



BESSY - Annual Report

2003



Berliner Elektronenspeicherring-Gesellschaft für Synchrotronstrahlung m.b.H.

Published by:
Berliner Elektronenspeicherring-Gesellschaft
für Synchrotronstrahlung m.b.H. (BESSY)

Albert-Einstein-Str.15
12489 Berlin
Tel. +49 30 6392 2999
Fax +49 30 6392 2990
info@bessy.de
www.bessy.de

Edited by :
Dr. Kai Godehusen



Dear user and friends,

it is mankind's inherent curiosity which urges humans to have a look beyond the horizon. This is still true today as it was several thousand years ago. We know from civilisations in China, Egypt, and the Middle East that they already observed the sky and conducted "astronomical research" and in Europe places like Stonehenge are well known examples for early bronze-age observatories. Meanwhile people in Central Europe were apparently still "sitting-in-the-trees" and drinking met. An unbelievable find near Nebra in Saxony-Anhalt yet tells us another story. The Nebra Skydisk is a more than 3,500 year old bronze disk with gold inlays showing the moon, stars and several other features. Contemporary and bronze-age high-tech met when scientists from Halle and Freiberg investigated the composition of the gold inlays using synchrotron radiation at BESSY. The presentation of the results made BESSY to a one-day "Centre of Archaeology". This is only one scientific highlight of 2003.

Due to the expanded research opportunities, like providing broadband THz radiation within the beamtime schedule, and a steady growth of the user community which includes industrial users and bio-medical researchers, we look forward to more exciting research in the coming years. We try continually to improve on user service which is by now becoming a real challenge, since for the first time in our history we exceeded the number of 1,000 users a year. More accommodation was urgently needed and we are pleased that the third house of the IBZ was completed by end of 2003. As a regular user you might have noted, that the campus Adlershof is now livelier. This is due natural sciences faculties of the Humboldt University moving on site and also due to several new shops and cafes which have opened their business.

We keep on developing BESSY and pushing hard on our future light source - the FEL - and on cutting edge instrumentation. Two FEL test facilities have been constructed: The Horizontal Bi-Cavity Test Facility (HoBiCaT) to a test stand for the FEL accelerator section and the femtosecond slicing approach which includes a new beamline design and modifications of the storage ring. The FEL project group has worked out the technical design of the new light source which will be published beginning of 2004. But there is even "more light" at the horizon, since our long term partner PTB received the approval to construct of a new Metrology Light Source (MLS) in close proximity to BESSY. Ground braking will take place in the summer of 2004.

BESSY also becomes more and more attractive for visitors of all kind and we had more than 9,000 visitors including "Lange Nacht der Wissenschaften". This is only the publicly seen part of a successful year, which would not have been possible without the commitment of our staff and the exciting research of our numerous users. We would like to thank all of them.

The BESSY Board of directors
Berlin, March 2004

High spatially resolved characterization of a superconducting tunnel junction detector in the soft X-ray range

S. Bechstein, B. Beckhoff, R. Fliegau, J. Weser, and G. Ulm

Physikalisch-Technische Bundesanstalt, Abbestraße 2-12, 10587 Berlin, Germany

Superconducting tunnel junction detectors are very sensitive energy-dispersive detectors. Offering an energy resolution about one order higher than that of conventional semiconductor detectors, STJ detectors are very attractive for several applications [1]. For instance, the STJs are used for synchrotron X-ray fluorescence analysis (XRF) applications involving light and transition elements, X-ray induced microanalysis [2,3] and potentially even in electron microprobe analysis, or for biological [4,5] or astrophysical [6,7] research.

Important characteristics of the detector performance are both the energy resolution and the spectral artifacts. To get more information about the dependence of the energy resolution on the detector area or about the influence of the leads and edges of an STJ, we performed spatially resolved measurements. Therefore, we scanned the detector area of an $141 \times 141 \mu\text{m}^2$ -sized Nb/Al/AlO_x/Al/Nb-STJ with the small step size of $10 \mu\text{m}$.

In these measurements we employed monochromatized undulator radiation of high spectral purity, which is available at the PTB Radiometry Laboratory at the electron storage ring BESSY II [8]. The beam was collimated with the aid of a nominal $5 \mu\text{m}$ -pinhole. We used a rather short distance of about 25 mm between this pinhole and the STJ detector, mounted in the snout of the cryostat, to minimize both diffraction at the pinhole and broadening of the beam profile due to the initial beam divergence. The cryogenic system [3] and the STJ detector [9] were provided by the Lawrence Livermore National Laboratory. For more details on the instrumentation and experiments conducted see [10].

The spatially resolved measurements were started with the scans in the two axes of the STJ (long, dashed lines in Fig. 1). Two scans in the y-direction at a distance of $40 \mu\text{m}$ from the axis followed (short lines in Fig. 1). Details of this measurement are listed in Table 1.

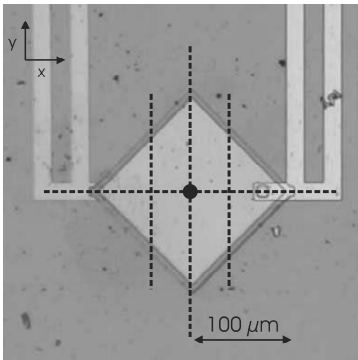


Fig. 1. Photograph of the $141 \mu\text{m} \times 141 \mu\text{m}$ -sized STJ with dashed lines indicating the performed line scans. The point in the center of the STJ demonstrates the origin of our coordinate plane.

Detector area	$141 \times 141 \mu\text{m}^2$
Photon energy	928 eV
Scan step size	$10 \mu\text{m}$
Length of the scan (x-axis, y-axis)	$300 \mu\text{m}$
Length of the scan ($ x = 40 \mu\text{m}$)	$200 \mu\text{m}$
Number of spectra	104
Net measurement period per spectrum	60 s
Maximum input count rate	about 1500 s^{-1}

Table 1. The scan data illustrated in Fig. 1.

During the two-dimensional scan we measured a total of 104 energy spectra similar to the two depicted in Fig. 2. Note that the energy scales employed in the current work always relate to the spectra recorded in the central position.

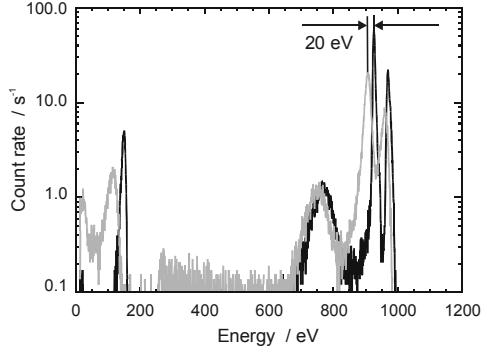


Fig. 2. Energy spectra at two different locations on the STJ. The black spectrum was measured in the center of the STJ, the gray one 70 μm away from the center ($y = -70 \mu\text{m}$, $x = 0$). The photon energy is 928 eV.

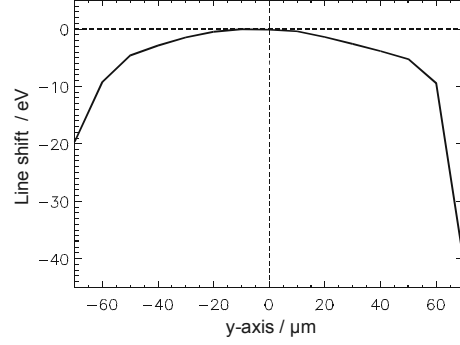


Fig. 3. Line shift of the 141 μm x 141 μm -sized STJ at $x = 0$. The line shift is as high as 10 eV within a distance of 60 μm from the center. The photon energy is 928 eV.

For each spectrum, the energy resolution E_{FWHM} and the maximum of the photon energy line of 928 eV were calculated using a Gaussian fit. Surprisingly, both the energy resolution and the pulse height scale change strongly over the area of the STJ. Noticeable changes are even observed in the central area of the detector. As a quantitative measure of these changes in the pulse height scale we defined a so-called line shift as the deviation of the maximum of the photon energy line from the maximum of the same line measured at the center of the STJ ($x = y = 0$). A positive deviation means a shift towards higher energies. Fig. 3 shows the shift along the y -axis ($x = 0$). Note that the line shift, estimated with an uncertainty less than 0.5 eV, is as high as 10 eV within a distance of 60 μm from the center. At a distance of more than 70 μm from the center of the STJ, the energy resolution degrades rapidly, so the Gaussian fitting becomes impossible. The line shift thus was calculated only at a length of 140 μm in the axes and at a length of 60 μm in the scans 40 μm beside the y -axis.

To illustrate the spatial dependence of the line shift, a contour map (Fig. 4) was created, based on the data obtained from the four line scans described above. The white area close to the center of the STJ shows the maximum, surrounded by the contour line of zero, which is not located at the center of the STJ. The difference in the x -direction might be caused by the different effects of the leads (top and bottom).

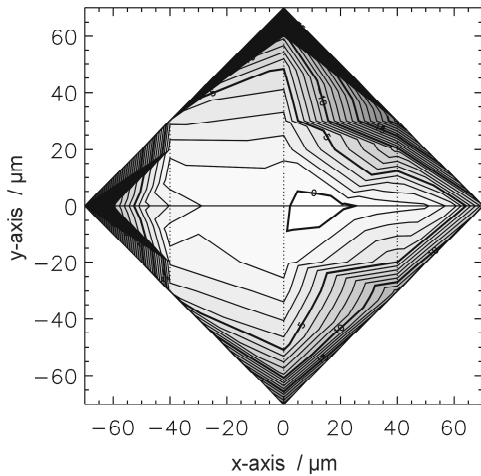


Fig. 4. Spatially resolved line shift in the center of the 141 μm x 141 μm -STJ. The white area shows the maximum, surrounded by the contour line of zero. The difference between two contour lines is 1 eV. The photon energy is 928 eV.

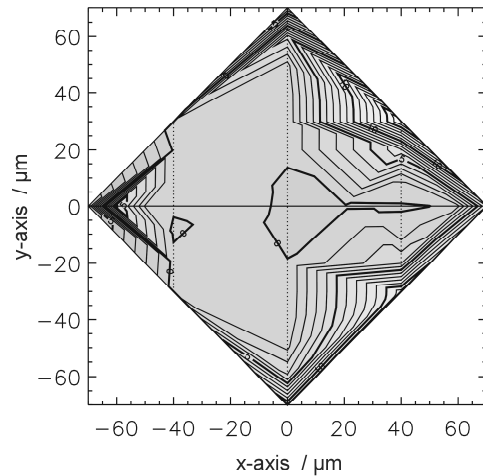


Fig. 5. Variation of E_{FWHM} in relation to the energy of the center of the 141 μm x 141 μm STJ. The maximum resolution is surrounded by the contour line of zero. The difference between two contour lines is 1 eV. The photon energy is 928 eV.

The contour diagram of the energy resolution (Fig. 5) depicts the difference between the local energy resolution and the energy resolution of the center of the STJ (ΔE_{FWHM}). The energy resolution in the center is $E_{\text{FWHM}} = 7.17$ eV. This diagram shows a similar dependence on the location, the main difference being a second, small maximum in the inner area.

Both the line shift and the energy resolution loss within the central area of the STJ, describe the difference in the energy resolution even without illuminating the leads and edges of the STJ.

Furthermore, with the aid of the employed 5 μm -pinhole we investigated the edges and leads. In a wide edge zone (the residual space between the edges of the STJ and the central area examined above), the quality of the investigated STJ degraded dramatically, more than expected. Apart from only a drastically reduced number of events with a photon energy of 928 eV we detected an additional line with an energy of about 270 eV (see Fig. 6). Only in the area of the upper electrode, this line was broadened due to additional lines, originating from different layers.

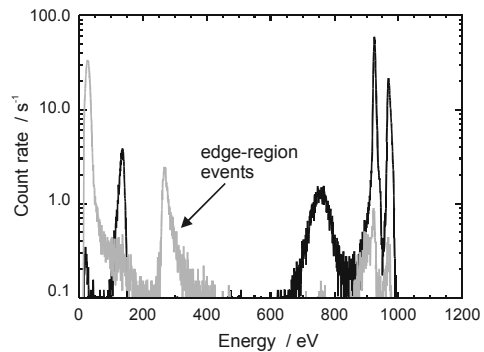


Fig. 6. Typical spectrum at the edge-region ($x = 40$ μm , $y = 50$ μm , gray line) compared to that at the center (black line) of the STJ. An additional line occurs at an energy of about 270 eV. The photon energy is 928 eV.

The local response changes within the central STJ region can lead to a better understanding of why larger illuminated areas have lower energy resolutions even if the diameter of the illuminated spot is chosen small enough to be far away from the edges. Furthermore, the assumption of local defects of the tunnel barrier that degrade the resolution could not be confirmed due to the absence of anomalies even in the inner area of the STJ. We expect that such spatially resolved measurements will prove to be a proper means of detector evaluation and contribute to improving future detector layouts.

- [1] For a recent overview of STJ detector research see "Proc. 9th Intl. Workshop on Low-Temperature Detectors (LTD-9)", AIP Conf. Proc. 605 (2002)
- [2] B. Beckhoff, R. Fliegauf and G. Ulm, *Spectrochim. Acta B* 58 (2003) 615-626
- [3] S. Friedrich, T. Niedermayr, O. Drury, M.F. Cunningham, M.L. van den Berg, J.N. Ullom, A. Loshak, T. Funk, S.P. Cramer, J.D. Batteux, E. See, M. Frank, S.E. Labov, *Nucl. Inst. Meth. A* 467-468 (2001) 1117-1120
- [4] G.W. Fraser, J.S. Heslop-Harrison, T. Schwarzacher, A.D. Holland, P. Verhoeve, A. Peacock, *Rev. Sci. Inst.* 74 (2003) 4140-4144
- [5] J.N. Ullom, M. Frank, J.M. Horn, S.E. Labov, K. Langry, W.H. Benner, *Nucl. Inst. Meth. A* 444 (2000) 385-388
- [6] P. Verhoeve, *AIP Conf. Proc.* 605 (2002) 559-564
- [7] A.P. Reynolds, J.H.J. de Bruijne, M.A.C. Perryman, A. Peacock, and C.M. Bridge, *A&A* 400 (2003) 1209-1217
- [8] F. Senf, U. Flechsig, F. Eggenstein, W. Gudat, R. Klein, H. Rabus, and G. Ulm, *J. Synchr. Rad.* 5 (1998) 780-782
- [9] M. Frank, L.J. Hiller, J.B. le Grand, C.A. Mears, S.E. Labov, M.A. Lindeman, H. Netel, D. Chow, A.T. Barfknecht, *Rev. Sci. Inst.* 69 (1998) 25-31
- [10] S. Bechstein, B. Beckhoff, R. Fliegauf, J. Weser, and G. Ulm, *Spectrochimica Acta B* 59, in print (2004)

Measurement of the thermal expansion coefficient for Mo/Si multilayer coatings

C. Buchholz, F. Scholze

Physikalisch-Technische Bundesanstalt, Abbestraße 2-12, 10587 Berlin, Germany

A major challenge for EUV lithography is the development and production of the projection optics with a total wave-front error below $\lambda/20$ at $\lambda=13.5$ nm [1]. This requires a figure accuracy of the Mo/Si multilayer coated mirrors of better than 0.2 nm. In the production process, the mirror substrate is polished to the required figure and afterwards the multilayer coating with a total thickness of about 200 nm is deposited. The thickness of this periodic coating can be determined from the number of layers, which is known from the coating process and the period which can be determined by reflectometry. To achieve the required uncertainty of 0.2 nm in the stack thickness, a relative uncertainty of 10^{-4} must be achieved in the determination of the stack period. This low uncertainty requires the investigation of even minor contributions like thermal expansion. So thermal behaviour must be known to design the coatings for the first mirrors in an EUVL-tool which are exposed to high thermal load from the high-power source. The operation temperatures of the optical components in an EUV stepper might thus differ from room temperature.

All mechanical drives of the PTB EUV reflectometer are driven by in-vacuum stepper motors with a total power of the order of 100 W [2]. Therefore the sample is measured at slightly elevated temperatures of 25°C to 30°C. The linear expansion coefficients for Mo and Si are $5.35 \cdot 10^{-6} \text{ K}^{-1}$ and $2.49 \cdot 10^{-6} \text{ K}^{-1}$, respectively [3]. For these values, temperature differences of up to 20 K would be needed to cause a relative variation of 10^{-4} in thickness.

In the Mo/Si multilayer, however, the material is amorphous and there is a significant internal stress in the layers. Therefore, the linear expansion coefficient for a layer system might be different. We measured the spectral reflectance of a Mo/Si multilayer for 6 temperatures in the range from 27 °C to 55 °C, see Figure 1. The lower temperature limit is due to the thermal environment in the reflectometer, see above and the higher limit is caused by the multilayer thermal stability. It is known that for temperatures above about 80 °C, the formation of Mo-silicides starts. This causes a shrinkage in layer thickness because the silicide density is higher.

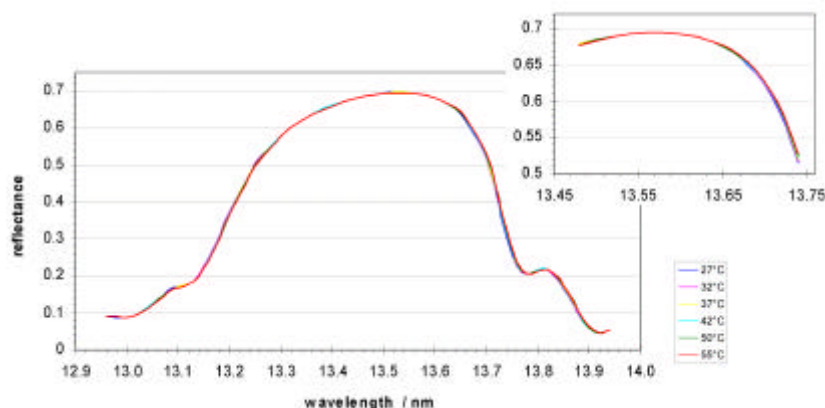


Figure 1 Spectral reflectance of a Mo/Si multilayer for 6 temperatures in the range from 27 °C to 55 °C.

Although there is no change in reflectance directly visible in Figure 1, the determination of the center wavelength at 50 % relative peak height yields a systematic shift of the wavelength with temperature, Figure 2 and Table 1. Because of the high stability of the storage ring and

the reproducibility of the beamline operation, the reflectance measurements can be reproduced within the statistical uncertainty of the detector signal measurement. Pure statistical considerations therefore are sufficient to derive the measurement uncertainty for subsequent measurements of the center wavelength. The spectral reflectance curve is very steep at the 50 % relative reflectance level, see Figure 3. The center wavelength therefore can be determined with only 0.06 pm uncertainty.

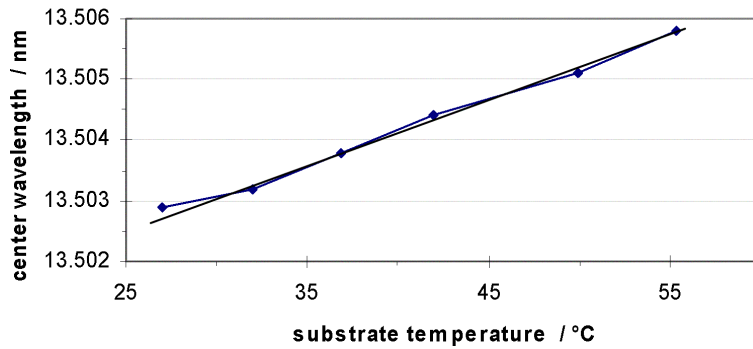


Figure 2 Center wavelength of the spectral reflectance from Figure 1 as function of substrate temperature. The black line shows a linear fit.

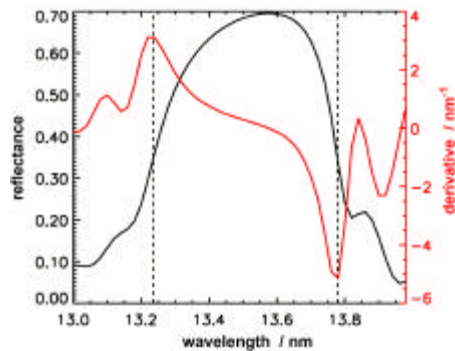


Figure 3 Spectral reflectance and derivative. The 50 % threshold positions are indicated by dashed lines. The derivative has its respective maxima at these positions, therefore statistical fluctuations of the measured signal have only minor influence on the determination of the peak position.

temperature / °C	center wavelength / nm	peak reflectance / %
27	13.5029(1)	69.51(8)
32	13.5032(1)	69.48(8)
37	13.5038(1)	69.50(8)
42	13.5044(1)	69.46(8)
50	13.5051(1)	69.46(8)
55	13.5058(1)	69.46(8)

Table 1 Center wavelength and peak reflectance for different substrate temperatures. The uncertainties given are only the reproducibility without the systematic contributions for the expansion factor $k=2$ (2σ).

A clear linear relationship is observed between center wavelength and substrate temperature. The thermal expansion coefficient derived from this correlation is $8.1(4) \cdot 10^{-6} \text{ K}^{-1}$. The first point was omitted in the regression. For this point no extra heating was applied and thus a temperature gradient between heater, sample, and thermometer would differ from the other points with the heater operated. The thermal expansion of the multilayer is about twice as big as for the pure materials. Therefore, if the temperature changes by more than 10 K, this effect has to be taken into account for the design of multilayer coatings for operation at elevated temperatures and for the determination of the center wavelength or layer period.

References

- 1 P. Gargini,
“Worldwide technologies and the ITRS in the current economic climate,”
Proc. SPIE **4688**, 25 – 28, (2002)
- 2 J. Tümmler, G. Brandt, J. Eden, H. Scherr, F. Scholze, G. Ulm
“Characterization of the PTB EUV reflectometry facility for large EUVL optical components,”
Proc. SPIE **5037**, 265-273 (2003)
- 3 MatWeb Material Data Sheet – online, <http://www.matweb.com/>

High-accuracy measurement of the angular sample positioning in the PTB EUV-reflectometer

C. Buchholz, A. Fischer, S. Plöger, F. Scholz, F. Scholze, H. Wagner

Physikalisch-Technische Bundesanstalt, Abbestraße 2-12, 10587 Berlin, Germany

A major challenge for EUV lithography is the development and production of the projection optics with a total wave-front error below $\lambda/20$ at $\lambda=13.5$ nm [1]. This requires a figure accuracy of the Mo/Si multilayer coated mirrors of better than 0.2 nm. In the production process, the mirror substrate is polished to the required figure and afterwards the multilayer coating with a total thickness of about 200 nm is deposited. The thickness of this periodic coating can be determined from the number of layers, which is known from the coating process and the period which can be determined by reflectometry. To achieve the required uncertainty of 0.2 nm in the stack thickness determination, a relative uncertainty of 10^{-4} must be achieved in the determination of the stack period. For off-normal incidence, this low uncertainty requires the accurate knowledge of the angle of incidence of the radiation. For 20° angle of incidence, a deviation of $60''$ shifts the reflected wavelength by 10^{-4} relative. Therefore, the angle of incidence must be known within this uncertainty.

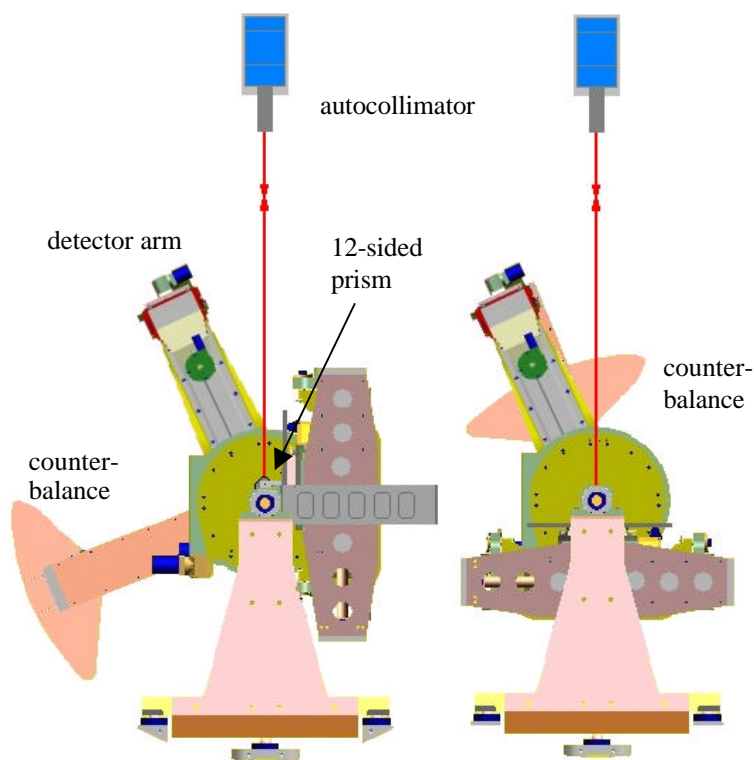


Figure 1 Scheme of the measurement set-up. An autocollimator with sub-arcsec resolution is mounted on top of the reflectometer, looking down to the main axis. A 12-sided regular prism is mounted in the axis of rotation. The reflectometer sample stage is moved from normal incidence (0° , shown left) to grazing incidence (90° , shown right) in steps of 30° . The autocollimator measures the difference between the actual rotation and the nominal 30° realized by the sides of the prism.

A practical alignment procedure for flat substrates is to align the sample surface parallel to the photon beam at 90° in grazing incidence. From this position the sample is rotated to the angle of choice using the rotation of the positioning stage. Therefore, the deviation of this rotation from the nominal values was measured. The scheme of the measurement is shown in Figure 1. A high-accuracy calibrated 12-sided prism with $0.5''$ uncertainty was mounted in the sample position to serve as an angle standard. The angular position of the planes of this prism was measured using an autocollimator looking downwards. So, we were able to achieve data for the angular positions in 30° steps. Because of the large sample weight and size, an active

counterbalance is needed to compensate the angular momentum at the rotation axis to below 100 Nm, to protect the goniometer [2].

A first test was made to investigate the influence of the residual moment on the angular position. We moved the sample horizontally at angles of 90° and 60° with the active counterbalance switched on and off. Figure 2 shows the influence of the angular momentum at the main axis on the angle. It was measured as the difference between the sample angle for counterbalance control on and off. Although the angular momentum is well below the limit of 100 Nm for the goniometer, significant deviations are observed. They follow a linear relation with a proportionality factor of 0.4 ″/Nm. Therefore, the algorithm for the counterbalance control was modified for a better compensation, specially with the goal to keep the angular momentum constant. The result is shown in Figure 3. Initially, the residual moment varied by about 150 Nm (changing its direction). The angular position at 0° deviated by 140″, from the one at the starting point at 90°. With improved compensation, this deviation is reduced to 75″. The values in Table 1 also show the excellent reproducibility of the angular position.

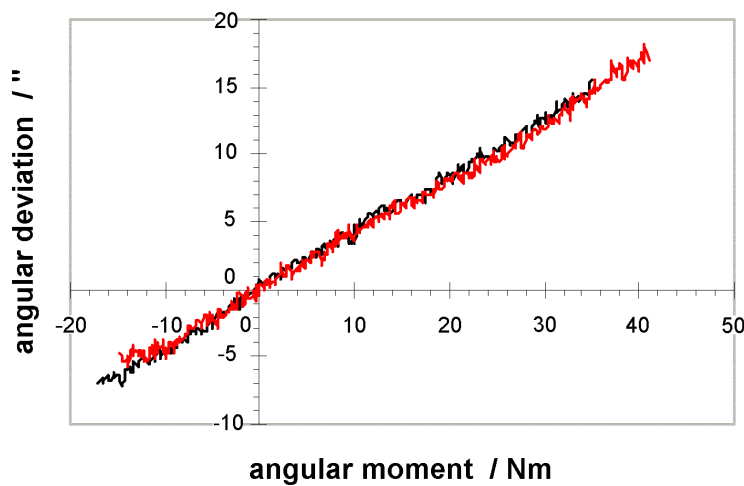


Figure 2 Correlation between angular moment at the sample axis and shift in angular position. Data are shown for angles of 90° (black) and 60° (red).

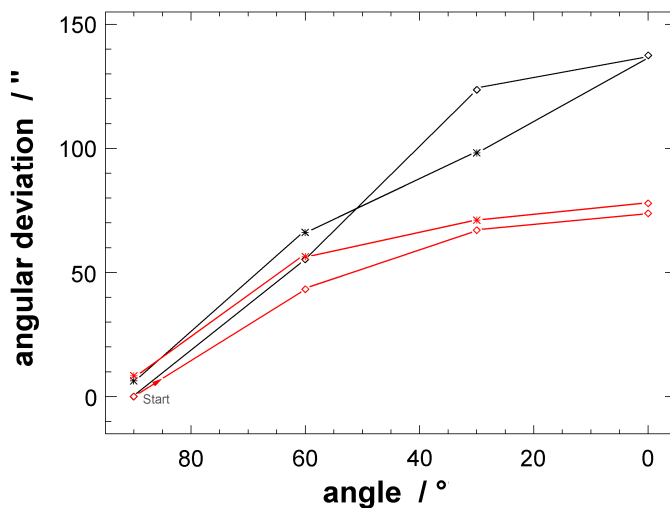


Figure 3 Measured difference of nominal angular position and actual position for operation with low sample weight. Shown are data for uncompleted compensation of the angular moment (black) and for ideal compensation (red). For optimum compensation, the remaining deviation is 78″ maximum and all values are reproduced within 15″ for forward/backward movement. The stage was first moved from 90° to 0° (diamonds) and afterwards back to 90° (crosses).

nominal angle / °	deviation move forward / “	deviation move back / “
90	0 (start)	8
60	43	56
30	67	71
0	74	78

Table 1 Difference of nominal angular position and measured position for operation with low sample weight. The maximum deviation is 78” and all values are reproduced within 15” for forward/backward movements.

It has been shown that large samples can be positioned in the EUV reflectometer with low uncertainty of the angle of incidence for the radiation. For the range from normal to grazing incidence, the deviations remain below 80” and are reproduced within 15”. In the range between 0° and 30° which is of most importance for the characterization of normal incidence EUV mirrors, the systematic shift is below 10”. No correction is needed in this angular range. It was also shown that movements of the linear sample axis do not change the angle of incidence by more than 15”. This result assures the mechanical quality of the EUV reflectometer for large samples and is a main prerequisite for the accurate determination of sample properties like multilayer stack periods from the reflected wavelength, using the Bragg-equation.

References

- 1 P. Gargini,
“Worldwide technologies and the ITRS in the current economic climate,”
Proc. SPIE **4688**, 25 – 28, (2002)
- 2 J. Tümmler, G. Brandt, J. Eden, H. Scherr, F. Scholze, G. Ulm
“Characterization of the PTB EUV reflectometry facility for large EUVL optical components,”
Proc. SPIE **5037**, 265-273 (2003)

High-accuracy calibration of energy-dispersive detectors using undispersed and monochromatized synchrotron radiation

F. Scholze,

Physikalisch-Technische Bundesanstalt, Abbestraße 2-12, 10587 Berlin, Germany

M. Procop

Bundesanstalt für Materialforschung und –prüfung, Unter den Eichen 87, 12205 Berlin, Germany

X-ray fluorescence analysis is a powerful nondestructive method for elemental composition analysis. Presently, this method is expanded into quantitative light-element analysis using soft X-ray excitation and detection. Here, a major challenge is the accurate calibration of the detection systems. PTB at BESSY has a long experience in using undispersed as well as monochromatized radiation for detector calibration in the soft X-ray region [1, 2, 3, 4]. The measurement schemes are shown in Figure 1.

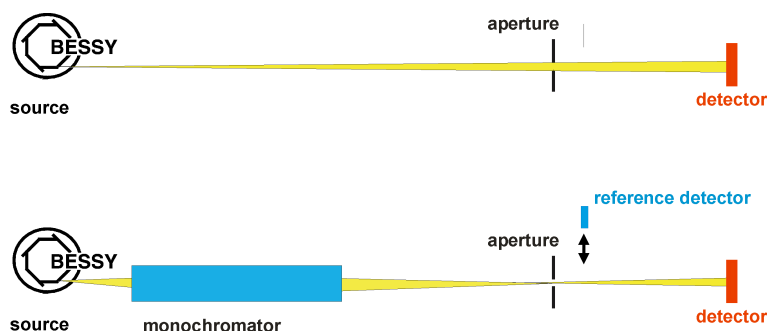


Figure 1 Scheme of the measurement set-up for detector calibration. The upper scheme shows the measurement using the storage ring as a source standard, the lower scheme is the comparison of the detector to be calibrated to a detector standard.

By the use of calculable undispersed synchrotron radiation from a bending magnet, the efficiency of energy-dispersive detectors can be determined up to a photon energy of about 20 keV at a dedicated beamline [3]. At low photon energy, however, the measurement uncertainty of this method is reduced by the limited energy resolution of the spectrometer, which makes it difficult to determine the efficiency by deconvolution of the continuous spectra measured below a photon energy of about 1 keV.

The best way to obtain reliable detector response functions and detection efficiency at low photon energy is to illuminate the detector with monochromatized radiation of small bandwidth and known flux. Monochromatized bending magnet radiation of high spectral purity, provided by the PTB soft X-ray radiometry beamline, is used for detector calibration at photon energies below 1.9 keV. This method requires to reduce the high photon flux at a synchrotron radiation beamline, which is measured with low uncertainty using calibrated photodiodes, reliably by several orders of magnitude [5].

The combination of both methods yields reliable and accurate data for the energy range from 0.1 keV to 20 keV [6]. The measurement with undispersed radiation is specially suited to obtain information on the pulse-rate linearity of the detector because measurements at different numbers of stored electrons can be compared, see Figure 2. Furthermore, because the spectral dependence of the efficiency is rather smooth in this energy range, rather broad energy intervals of about 1 keV can be binned to improve the statistics. This allows to determine the detection efficiency up to about 20 keV at a BESSY II bending magnet. It can also be seen from Figure 2 that it is hard to obtain reliable information for the detection

efficiency below 1 keV from this measurement because the spectral dependence is too steep and the spectrum is broadened by the detector.

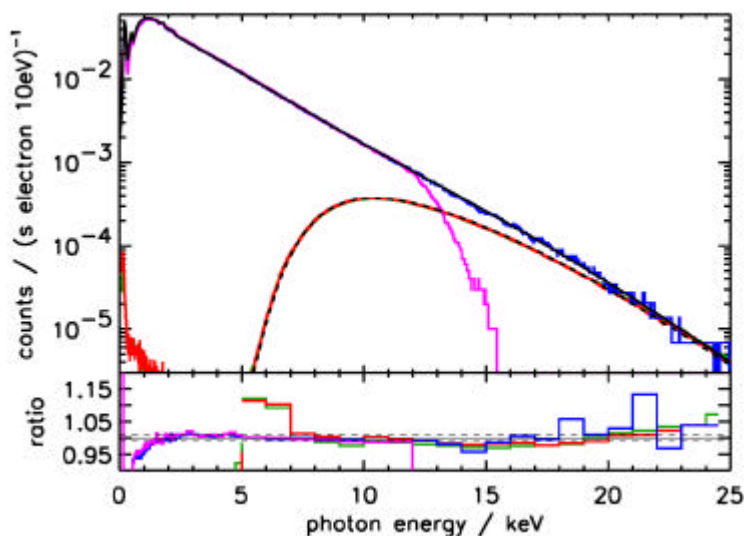


Figure 2 Pulse height spectra measured for different numbers of stored electrons. The red spectrum is measured with an additional Al-filter of 0.225 mm thickness to suppress low energy photons at a average number of 7670 electrons stored. The green blue and magenta curves represent measurements with 140, 100, and 50 electrons stored, respectively. The black curve is a calculation using the known photon flux from the standard source BESSY II and a model for the detector efficiency. The lower part shows the ratio between measured and calculated spectrum.

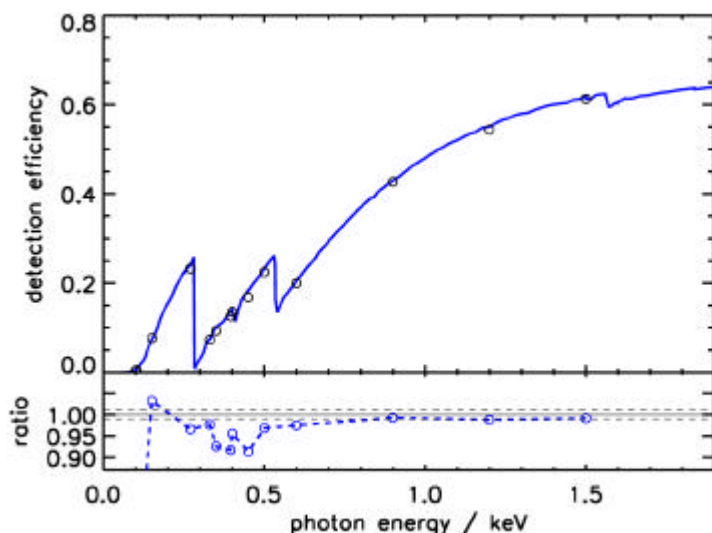


Figure 3 Measured detection efficiency for low-energy photons using monochromatized radiation at the soft X-ray radiometry beamline and a calibrated photodiode as reference detector. The model curve is the same as shown in Figure 2 and Figure 4. The deviation of the measured values from the model in the range below 0.5 keV is due to X-ray absorption fine structure effects, not included in the model.

The higher energy resolution to determine the efficiency in the low energy region between the various absorption edges of the window foil is obtained by using monochromatized radiation at the soft X-ray radiometry beamline. Here, the photon energy is known for each point, so the broadened pulse height spectra can be integrated to obtain the number of detected photons for each energy. This number is compared to the number of photons incident at the detector as determined using a calibrated photodiode [7]. By proper selection of the photon energies measured, it is therefore possible to determine the contribution of each elemental component of the detector radiation entrance window, see Figure 3.

In Figure 4, the detection efficiency is shown as determined by both methods in combination. It has a rather complex spectral dependence. This detector was equipped with a window from Moxtek, consisting of a thin polyimide based foil supported by a silicon grid with 50 μm wide bars, 380 μm thick and an open area of about 73 %. The low energy part of the efficiency curve is defined by the foil transmittance and can be derived from the detailed measurements with monochromatized radiation, see Figure 3. The high energy part specially the increase

between 10 keV and 15 keV can be determined with the undispersed radiation, see Figure 2. It is caused by partial transmission through the silicon support grid bars.

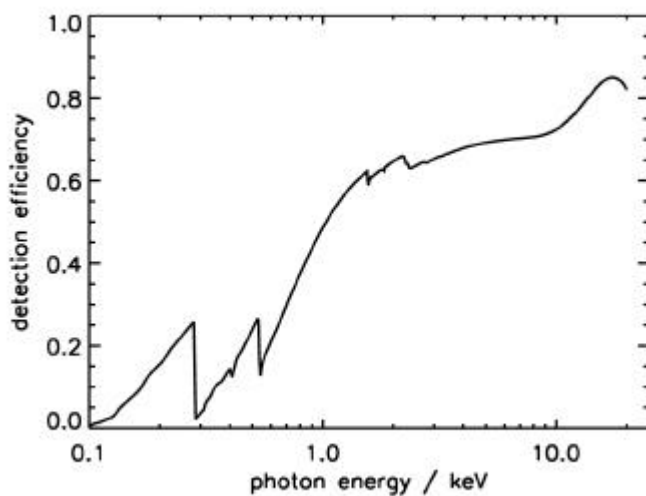


Figure 4 Detection efficiency of the Si(Li) with a low-energy window from Moxtek. This window consists of a thin polyimide based foil, supported by a silicon grid with 50 μm wide bars, 380 μm thick and an open area of about 73 %. The low energy part of the efficiency curve is defined by the window foil transmittance and can be derived from the detailed measurements with monochromatized radiation, see Figure 3. The higher energy part, specially the increase between 10 keV and 15 keV, can be determined with the undispersed radiation, see Figure 2. It is due to transmission through the silicon support grid bars.

From Figure 4 it is evident that a large number of parameters must be known to determine the detection efficiency of an energy dispersive detector specially for the low energy range. This is not possible using only a few fluorescence lines from radioactive sources. Using the calibration facilities of PTB it is possible to achieve an accurate calibration of such a system, which then can be used as a reference detector for the calibration of other detectors for certain selected fluorescence lines. The calibrations presented here are performed in the frame of EU-project EDS-CRM contract no. G6RD-2002-00851.

References

- 1 H. Rabus, F. Scholze R. Thornagel, and G. Ulm, "Detector calibration at the PTB radiometry laboratory at BESSY", Nucl. Instrum. Meth. **A377**, 209-216 (1996)
- 2 Beckhoff, Burkhard; Klein, Roman; Krumrey, Michael; Scholze, Frank; Thornagel, Reiner; Ulm, Gerhard; "X-ray detector calibration in the PTB radiometry laboratory at the electron storage ring BESSY II" Nucl. Instrum. Meth. **A444**, 480 – 483, (2000)
- 3 F. Scholze, R. Thornagel, G. Ulm, "Calibration of energy dispersive X-ray detectors at BESSY I and BESSY II" Metrologia **38**, 391-395 (2001)
- 4 R. Klein, M. Krumrey, M. Richter, F. Scholze, R. Thornagel, G. Ulm, "Radiometry with Synchrotron Radiation at the PTB Laboratory at BESSYII" Synchrotron Radiation News **15**, 23-29 (2002)
- 5 S. Kraft, F. Scholze, R. Thornagel, G. Ulm, W.C. McDermott, and Edwin M. Kellogg, "High accuracy calibration of the HXDS HPGc detector at the PTB radiometry laboratory at BESSY" Proc. SPIE **3114**, 101-112 (1997)
- 6 F. Scholze, M. Procop, "Measurement of detection efficiency and response functions for an Si(Li) X-ray spectrometer in the range 0.1 to 5 keV", X-ray spectrom. **30**, 69-76 (2001)
- 7 F. Scholze, J. Tümmeler, G. Ulm, "High-accuracy radiometry in the EUV range at the PTB soft X-ray radiometry beamline" Metrologia **40**, S224-S228 (2003)

Absolute Pulse-Resolved Measurement of EUV Radiation from the PTB Undulator at BESSY II

A. Gottwald, R. Müller, A.A. Sorokin, M. Richter

Physikalisch-Technische Bundesanstalt, Abbestr. 2-12, 10587 Berlin, Germany

In the spectral range of the vacuum ultraviolet (VUV) and extreme ultraviolet (EUV), the radiation of highly intense sources, like EUV-lithography plasma sources or VUV Free-Electron-Lasers (FEL), is strongly bunched by short radiation pulses of high intensity. Radiant power measurements with widely used solid state detectors (e.g. photodiodes) suffer from saturation, degradation, and even destruction under such intense irradiation. Furthermore, for radiometric use as a transfer standard, a detector system must show high linearity and reproducibility. Even with synchrotron radiation, there is a need for accurate EUV radiant power measurement and intensity monitoring e.g. for irradiation experiments [1]. In the PTB radiometry laboratory at BESSY II, a beamline for deflected, undispersed undulator radiation from the PTB U49 undulator is in use for EUV system metrology development and lithographic print testing [2]. At this beamline, the high intensity of the radiation (compared to a bending magnet beamline) as well as its non-monochromatic spectral distribution complicates accurate measurement of radiant power by photodiodes. The use of a gas-detector system [3] primarily developed for metrology of FEL radiation [4] overcomes these complications and, furthermore, offers the possibility of measuring the pulse energy of single radiation pulses emitted in the single-bunch operation mode. The detector (see figure 1) is based on atomic photoionization of rare gases at low particle densities. Electrons and ions created by photoionization are extracted and accelerated by an almost homogeneous electric field before being detected by simple Faraday cups, preventing the device from saturation even at high photon intensities. The signal electronics provides single-pulse read-out for electron and ion signal which can be measured at the same time. Moreover, ions may also be detected by a slow averaging ion-current signal with a time constant of a few seconds which

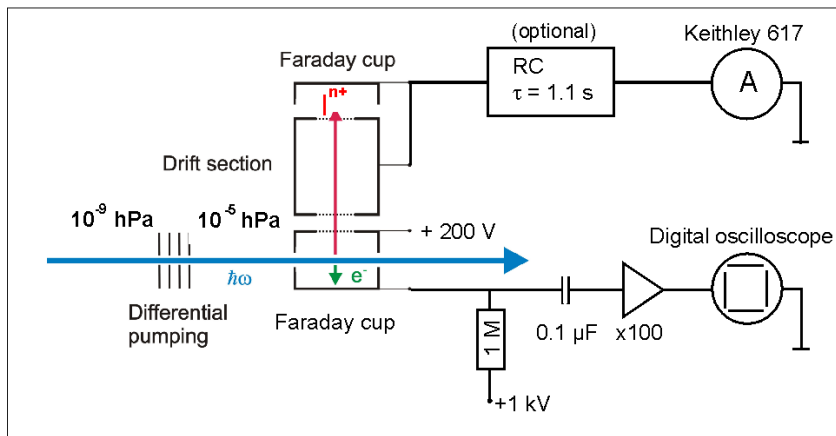


Fig. 1: Schematic view of the gas-monitor detector and the signal electronics used for single-pulse detection

is not affected by any time structure of the radiation. In contrast to conventional ionization chamber detectors, the low particle densities ensure high linearity over a wide dynamic range, since the contributions of secondary ionization are negligible.

In the normal operation mode of BESSY II, radiation can be regarded as quasi-cw. Here, calibration of the detector has been performed for the slow ion signal. Due to the time-integrating nature of the signal, this calibration does not depend on the radiation time

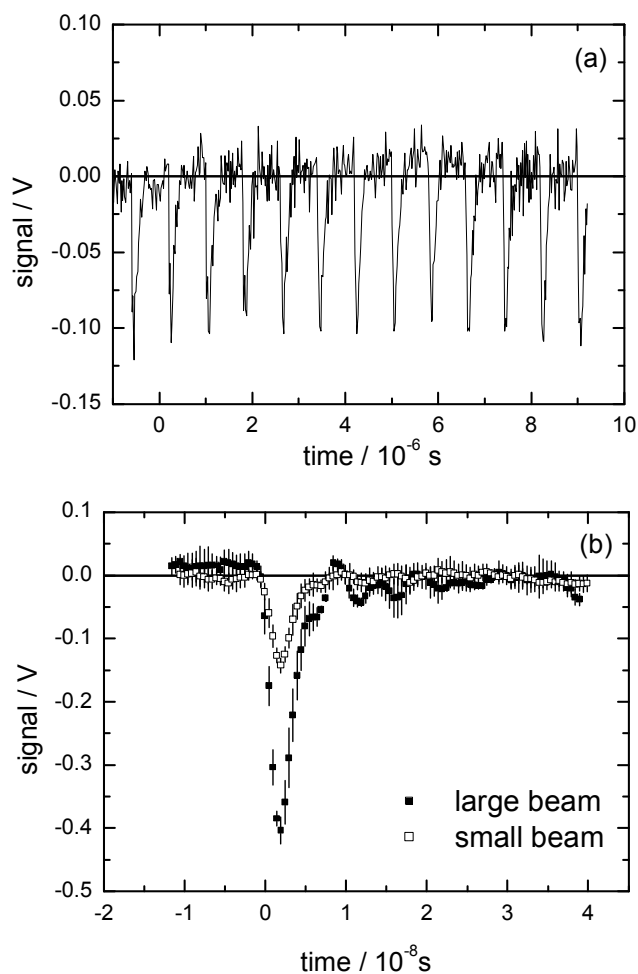


Fig. 2: Pulse-resolved measurement of EUV undulator radiation pulses in single-bunch operation. (a) overview, (b) detail for two different beam sizes.

structure. In the case of pulsed radiation, only the average pulse energy can be derived from the averaged ion current. In contrast, the pulse-resolved electron signal allows the determination of the pulse energy for each single pulse, if the electron signal is cross-calibrated to the simultaneously measured ion current.

In figure 2 (a), a typical pulse-resolved electron signal from the gas detector in the single-bunch mode is depicted. It shows a series of pulses arising from the EUV photon pulses emitted by the undulator. The different intensities arise from e.g. instabilities of the signal electronics, or statistical fluctuations, and limit the accuracy of single-pulse energy determination. Figure 2 (b) shows the mean of a pulse sequence for two different beam sizes (shaped by apertures). The measured pulse width of a few nanoseconds is mainly determined by the electronics and the electron time-of-flight distribution and does not depend from the beam size, while the pulse integral was shown to scale linearly with the average radiant power [5].

References

- [1] F. Scholze, R. Klein, T. Bock, *Appl. Opt.* **42**, 5621 (2003)
- [2] H. Meiling, J. Bishop, R. Hartman, P. Kürz, P. Hoghoj, R. Geyl, N. Harned, *Proc. SPIE* **4688**, 52 (2002)
- [3] M. Richter, A. Gottwald, U. Kroth, S. V. Bobashev, A. A. Sorokin, L. A. Shmaenok, J. Feldhaus, C. Gerth, K. Tiedtke, Patentanmeldung 10244303.3, DPMA, München (2002)
- [4] M. Richter, A. Gottwald, U. Kroth, A. A. Sorokin, S. V. Bobashev, L. A. Shmaenok, J. Feldhaus, C. Gerth, B. Steeg, K. Tiedtke, R. Treusch, *Appl. Phys. Lett.* **83**, 2970 (2003)
- [5] A. Gottwald, R. Müller, M. Richter, A. A. Sorokin, G. Ulm, *Meas. Sci. Technol.* **15**, 437 (2004)

VUV-Reflectometry on CaF₂ samples with different temperatures

A. Gottwald, H. Schoeppe, U. Kroth, M. Letz¹, M. Richter

Physikalisch-Technische Bundesanstalt, Abbestr. 2-12, 10587 Berlin, Germany

¹Schott Glas, Research and Development, 55014 Mainz, Germany

Fluoride crystals are strongly ionic and have the largest band gaps known for crystalline solids. As a consequence, they are transparent even in the wavelength region of deep ultraviolet (DUV) radiation. Driven by the need of miniaturization from the semiconductor industry, photolithography using DUV radiation is currently applied at a wavelength of 193 nm and under development for 157 nm. For F2 laser radiation at 157 nm, precision transmission optics built from CaF₂ are the key components of a lithographic imaging system. For this purpose, pure crystals of CaF₂ with extremely low impurity concentrations have been grown at Schott Lithotec.

Recently, the effect of an optical anisotropy for CaF₂ has been observed at 157 nm which is of great importance for the 157-nm technology [1]. Already the measured weak birefringence of the refractive index ($\Delta n/n \approx 10^{-6}$) considerably influences the design of the imaging optics. Optical anisotropies seem to be unexpected in perfectly cubic crystals, but are already known from semiconductor materials at optical wavelengths. For explanation, the breaking of symmetry by incident radiation in the vicinity of a strong absorption line was first described by Ginzburg [2], resulting in the possibility of observing the “spatial dispersion-induced

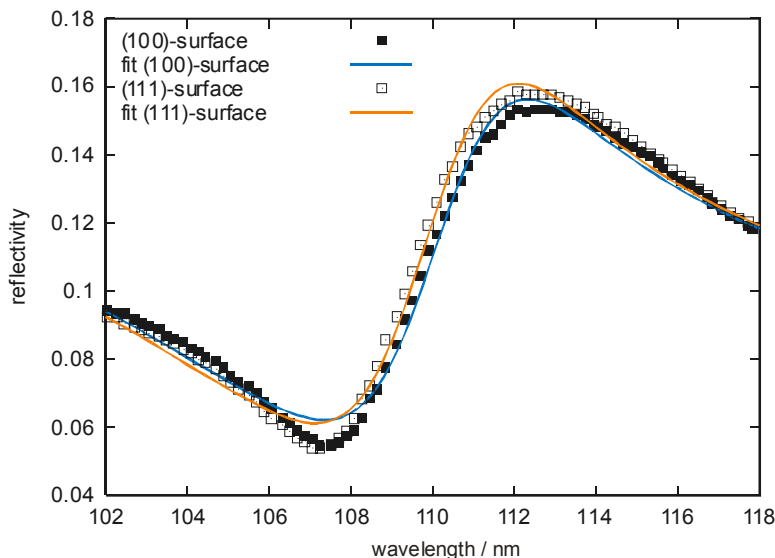


Fig. 1: Normal incidence reflectivity around the Γ point of CaF₂ for a (100) and (111) surface.

birefringence” close to such a resonance. Strongly ionic crystals show deep excitonic bound states: For CaF₂, the most pronounced one (the Γ exciton) arises at 11.1 eV, yielding a strong and narrow absorption structure at a wavelength of about 112 nm.

In this context, reflectometry measurements on high-purity CaF₂ samples from Schott Lithotec had been performed at the NIM-

beamline for detector calibration and reflectometry in the Radiometry Laboratory of the PTB at BESSY II. By determination of the sample reflectivity near the exciton resonance, the

spatial anisotropy of this absorption line is measured for samples with different surface orientations, namely (100) and (111) (figure 1). The measurements revealed a small but significant shift of about 0.2 nm towards smaller wavelengths of the resonance structure for the sample with the (111)-orientated surface. These experimental data were interpreted in a model related to the previously measured optical anisotropy at 157 nm and are in agreement with these data [3]. The fitting parameters of the model are the resonance position and

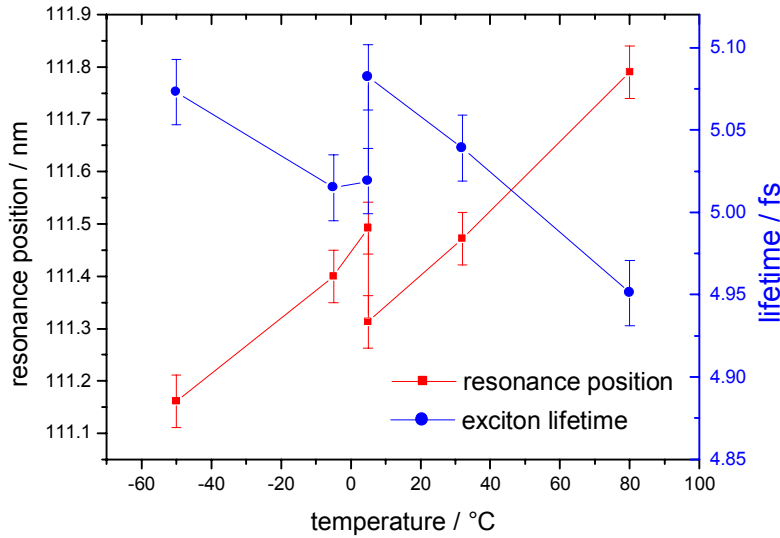


Fig. 2: Resonance position (left/red) and lifetime (right/blue) for the CaF_2 Γ -exciton for a sample with prepared (111) surface at different sample temperatures.

lifetime: Both can be expected to depend on the temperature of the sample. Furthermore, sample imperfections may influence the resonance structure and might be detectable only if the natural resonance width is reduced at lower temperatures. To realize such measurements, the reflectometer system has been improved by a sample holder equipped with a liquid nitrogen cryostat cooler and a Peltier heater unit. The sample temperature is selectable between -50 °C and $+80$ °C and stabilized with a feedback controller. Figure 2 shows results for the relative shifts of the resonance position and exciton lifetime for different temperatures for a specially prepared (111) sample. Generally, the resonance position shifts toward higher wavelength (lower photon energies) with increasing temperature, while the exciton lifetime decreases. Around 0 °C, both curves show an inconsistency: At the temperature of $+5$ °C where the measurement was taken, the values are not reproduced. This is assumed to be an effect of the surface contamination by water which was frozen on the sample surface at low temperature. Removing the surface contamination by heating the sample results in the second value which is consistent with the values at higher temperatures.

References

- [1] J. H. Burnett, Z. H. Levine, E. L. Shirley, Phys. Rev. B **64** 241102R (2001)
- [2] V. L. Ginzburg, JETP **34**, 1593 (1958)
- [3] M. Letz, L. Parthier, A. Gottwald, M. Richter, Phys. Rev. B **67**, 233101 (2003)

Absolute Responsivity and Homogeneity of Silicon Photodiodes in the X-ray Range

M. Krumrey, M. Hoffmann, P. Müller and G. Ulm

Physikalisch-Technische Bundesanstalt

Abbestraße 2-12, 10587 Berlin, Germany

Silicon photodiodes are used as easy-to-operate detectors from the visible range to the X-ray region. For absolute flux measurements, their responsivity has to be determined by calibration against a primary detector standard, typically a cryogenic electrical substitution radiometer (CESR). This technique is well established in the radiometry laboratory of the PTB at BESSY II. Radiation of high spectral purity is provided for this purpose at the four-crystal monochromator (FCM) beamline in the photon energy range from 1.75 keV to 10 keV [1].

Radiation from a 7 T wavelength shifter (WLS) is used at the *BAMline* to extend the procedure to photon energies up to 60 keV [2]. This beamline is equipped with a double multilayer monochromator (DMM) and a double crystal monochromator (DCM) which can be operated independently or in series. For photon energy above 25 keV, the higher order contribution is already well below 0.5 % with the DCM. For photon energies below 25 keV, the high spectral resolving power of the DCM can be combined with the efficient suppression of higher orders provided by the DMM, resulting in a higher harmonic content below 10^{-5} . The diode homogeneity has been investigated at this beamline especially around the Ag K absorption edge with a raster scan of the diodes through a 0.3 mm x 0.3 mm monochromatic beam.

As the existing CESR is no longer an absolute detector for photon energies above about 23 keV because the finite thickness of the copper absorber is no longer sufficient for complete absorption, a free-air ionization chamber (FAIC) of the PTB department for dosimetry has been used as additional primary detector standard at higher photon energies.

Several types of silicon photodiodes with active areas of about 1 cm² have been investigated. Earlier measurements in the soft X-ray range have shown the superior stability of diodes with n-on-p structure (like IRD AXUV 100) over p-on-n devices. However, the responsivity of these diodes decreases towards higher photon energies due to the thin active layer. Devices with similar structure but thicker depletion layer (IRD AXUV 20 HE) are only available with smaller active area. Due to a special mounting with a hole in the ceramic support, this diode can also be used in transmission. In the harder X-ray region, PIN diodes have higher responsivities because they are almost fully depleted. In the soft X-ray range, their responsivity is often reduced due to a thick oxide layer at the surface (Hamamatsu S3590) or the 0.3 µm Al front contact (SINTEF CHICSi 280). The SINTEF diodes, originally designed for an experiment in high energy physics, can be operated in transmission and are available with different Si thicknesses [3].

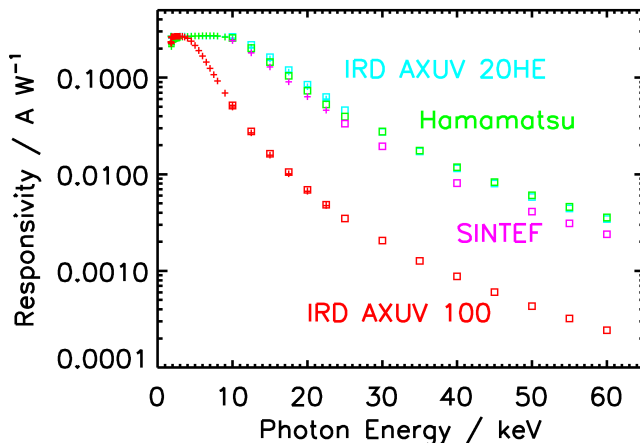


Fig. 1:

Responsivity of the investigated diodes. Crosses refer to calibrations against the CESR while open symbols (\diamond , \square , Δ) denote calibrations against the FAIC.

At photon energies between 2 keV and 10 keV, all investigated diodes showed perfect homogeneity over the entire surface. However, inhomogeneities were found for some diodes at higher photon energies where the radiation penetrates the silicon chip. While the diodes which can be operated in transmission (IRD AXUV 20 and SINTEF) exhibit good homogeneity to better than 2 % also at high energies as shown in Fig. 2a and 2b, the diodes with a backside contact which is attached to the support by conductive silver exhibit large spatial variations especially at photon energies above the Ag K absorption edge. This effect is most pronounced for the Hamamatsu diode. Below the Ag K edge, the relative responsivity varied between 94 % and 100 % (Fig. 2c), while the variation above this edge ranges between 84 % and 100 % (Fig. 2d). Obviously, the responsivity is enhanced by the absorption of the radiation in the silver layer which can give rise to fluorescence, backscattering or photoemission into the silicon [4].

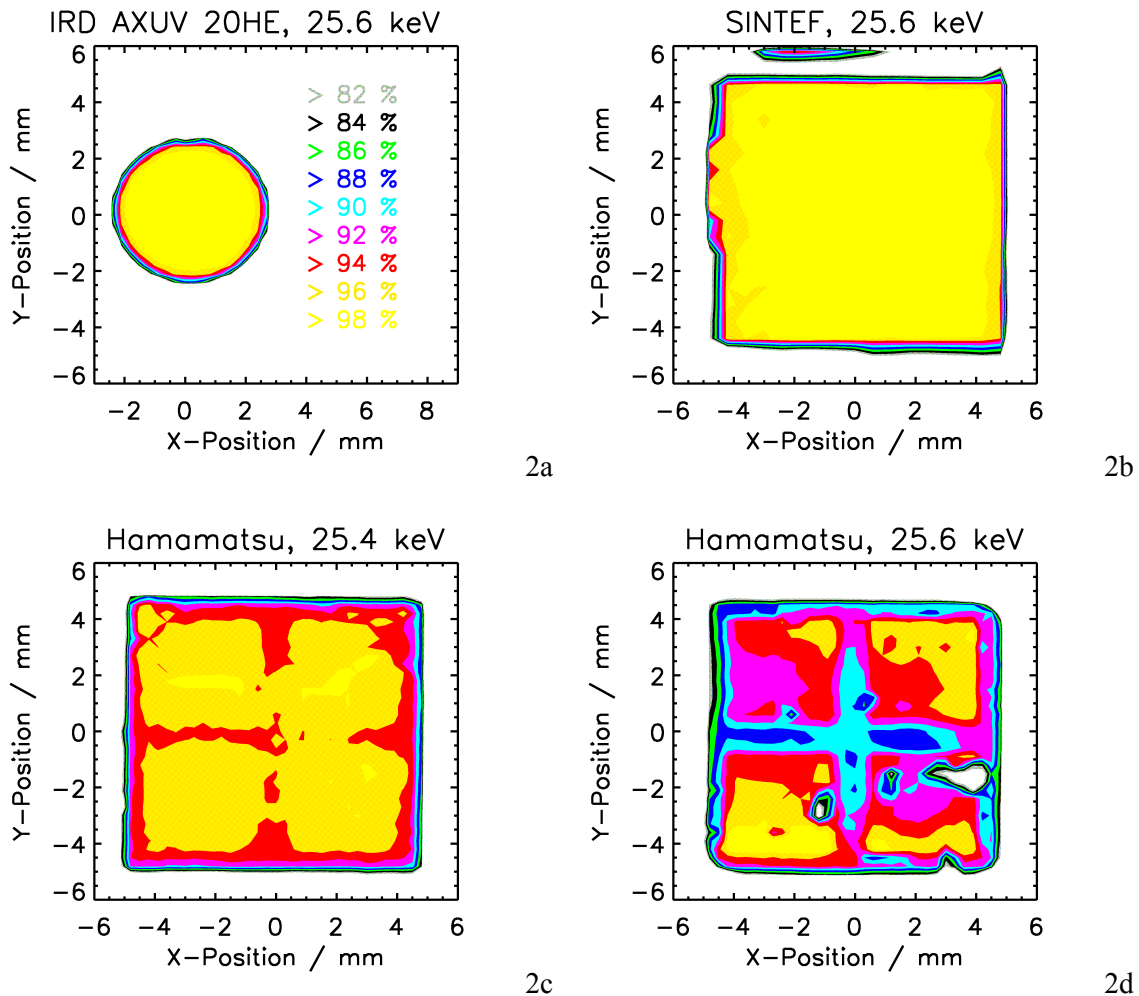


Fig. 2: Homogeneity of the responsivity at photon energies around the Ag K absorption edge at 25.5 keV

References

1. Krumrey, M. and Ulm, G., *Nucl. Instr. and Meth. A* **467-468**, 1175 - 1178 (2001).
2. Görner, W., Hentschel, M. P., Müller, B. R., Riesemeier, H., Krumrey, M., Ulm, G., Diete, W., Klein W., and Frahm, R., *Nucl. Instr. and Meth. A* **467-468**, 703 - 706 (2001).
3. Evensen, L., Westgaard, T., Avdeichikov, Carlen L., Jakobsson, B., Murin, Y., Martensson, J., Oskarsson, A., Siwek, A., Withlow, H. J., van Veldhuizen, E. J., Westerberg, L., Guttormsen, M., *IEEE Trans. on Nucl. Sci.* **44**, 629 – 634 (1997).
4. M. Krumrey, L. Büermann, M. Hoffmann, P. Müller, F. Scholze, and G. Ulm, Proceedings of the 8th International Conference on Synchrotron Radiation Instrumentation, San Francisco, August 2003

Thickness determination for SiO₂ films on Si by X-ray reflectometry at the Si K edge

M. Krumrey, M. Hoffmann, P. Müller and G. Ulm

Physikalisch-Technische Bundesanstalt

Abbestraße 2-12, 10587 Berlin, Germany

An absolute and highly accurate method for the thickness determination of thin films is X-ray reflectometry (XRR). In this technique, the reflectance of the sample is measured as a function of the grazing incidence angle of X-rays. Due to interference effects of radiation reflected on the layer surface and radiation reflected on the layer/substrate interface, oscillations occur in the reflectance curve which can be fitted by recursive application of the Fresnel equations. While the oscillation amplitude at a fixed photon energy depends on the densities and the surface and interface roughness, the oscillation period is mainly determined by the layer thickness. In commercial instruments, Cu K α radiation with an energy of 8048 eV is used and has been applied also to thin SiO₂ films. Unfortunately, the optical constants of Si and SiO₂ are very similar at this energy so that the reflection at the layer/substrate interface, and therefore also the oscillations, are very weak.

In the energy region just above the Si K absorption edge at 1838 eV, the attenuation coefficients of Si and SiO₂ differ significantly because the rise of the attenuation coefficient is shifted in SiO₂ towards higher energies due to the bonding state of Si. At 1841 eV the attenuation coefficient of Si has a local maximum while it is still low for SiO₂ [1].

The X-ray reflectance has been determined with monochromatized synchrotron radiation at the four-crystal monochromator (FCM) beamline of the PTB at BESSY II. At this bending magnet beamline, the photon energy can be tuned between 1.75 keV and 10 keV by using either four InSb(111) or four Si(111) crystals [2]. The measurements presented here were performed with InSb crystals at 1841 eV and with Si crystals at 8048 eV. The energy calibration is based on back reflection in silicon crystals and is therefore traceable to the Si lattice constant.

The reflectance curves obtained for samples with nominal oxide layer thicknesses between 6 nm and 1 μ m were fitted using the program IMD [3] assuming a single oxide layer and interface and surface profiles described by an error function. The weak oscillations in a $\theta/2\theta$ scan at 8048 eV on the thinnest oxide layer (nominal thickness 6 nm) and the much more pronounced oscillation at 1841 eV on the same sample are shown in Fig. 1.

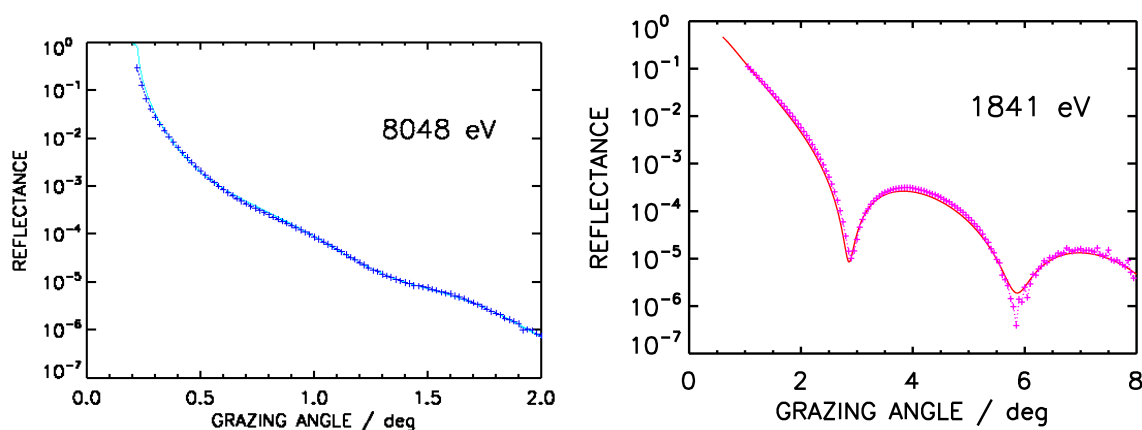


Fig 1: Reflectance of a SiO₂ film on Si with a nominal thickness of 6 nm at two different photon energies. The energy of 1841 eV is just above the Si K absorption edge.

Direct comparison of the results for the reflectance R measured at different energies is possible if the grazing angle θ is converted to the vertical component of the momentum transfer $q_z = 4 \cdot \pi / \lambda \cdot \sin(\theta)$, where λ is the wavelength. For perfectly flat surfaces, the quantity $R \cdot q_z^4$ should be almost constant above the critical angle and oscillations and a decrease due to roughness effects are clearly seen. The quantity $R \cdot q_z^4$ is shown in Fig. 2 for the 6 nm layer mentioned above and in Fig. 3 for a 160 nm SiO₂ layer. In both cases, the oscillations are much more pronounced at 1841 eV, allowing for a layer thickness determination with lower uncertainties [4]. The determined layer thicknesses are (6.2 ± 0.2) nm and (160.1 ± 1.0) nm, respectively.

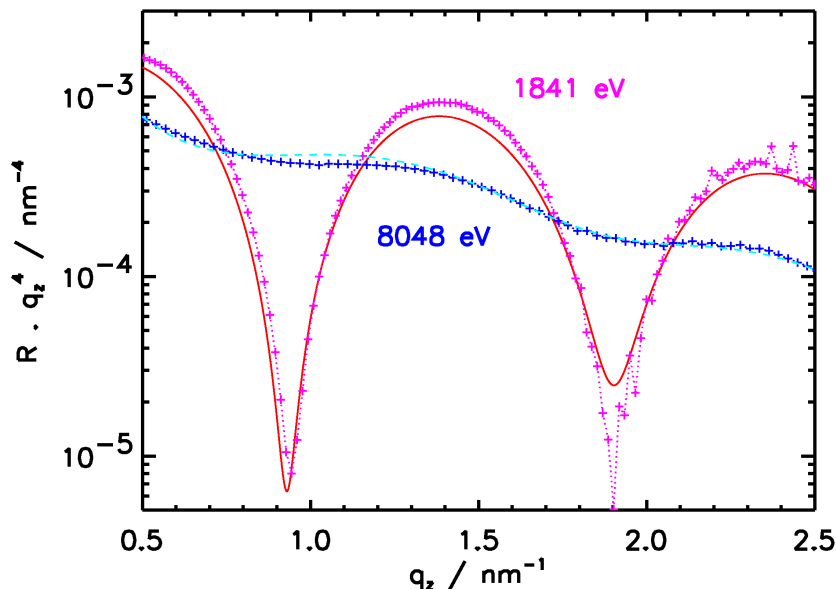


Fig. 2:

Comparison of the quantity $R \cdot q_z^4$ for measurements at 8048 eV (blue) and 1841 eV (red) on a 6 nm layer of SiO₂ on Si.

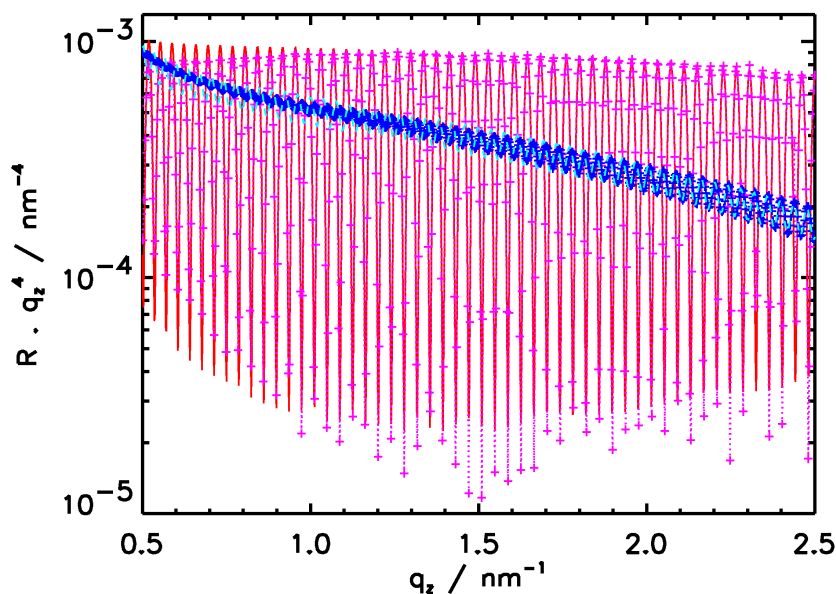


Fig. 3:

Same as above for a 160 nm layer of SiO₂ on Si.

References

1. A. Owens, G.W. Fraser, S.J. Gurman, *Rad. Phys. and Chem.* **65** (2002) 109
2. M. Krumrey, G. Ulm, *Nucl. Instr. and Meth. A* **467-468** (2001) 1175
3. D.L. Windt, *Computers in Physics* **12** (1998) 360
4. M. Krumrey, M. Hoffmann, G. Ulm, K. Hasche, P. Thomsen-Schmidt, *Thin Solid Films* (accepted for publication)

First Year of Measurements at the Reflectometer for Large EUVL Optics at PTB

C. Laubis, F. Scholze, G. Brandt, A. Fischer, S. Plöger, F. Scholz, H. Wagner, and G. Ulm.

Physikalisch-Technische Bundesanstalt, Abbestraße 2-12, 10587 Berlin, Germany

Concerning EUV optics for EUV lithography (EUVL) the pace of development has quickened. Especially after Intel declared its skipping of 157 nm process technology [1], the next step in diminishing wavelength for optical lithography is EUV at 13.5 nm [2].

Also the transition point from basic research to first applications has been reached. Therefore not only samples for basic investigations and process qualifications which tend to be small flat mirrors but also larger complex shapes designed for lithographic optics need to be measured.

The requirements towards EUV reflectometry generated by the development of EUVL are threefold:

First, any shape or configuration of EUV-optics should be measurable, requiring a range of mechanical degrees of freedom for sufficiently large samples. In 2003 the new reflectometer for large EUVL optics [3] at the PTB laboratory at BESSY II has proven to be a versatile tool for all measurements, the diversity of samples ranging from gratings, filters, flat and aspheric multilayer mirrors, EUVL mask blanks and masks to diodes, even scatterometry [4]. Figure 1 illustrates the freedoms of movement for the new reflectometer. The Ψ – drive (rotation of the detector) allows for easy reference measurements of the incident beam in front of the sample, without the need for long sample movements.

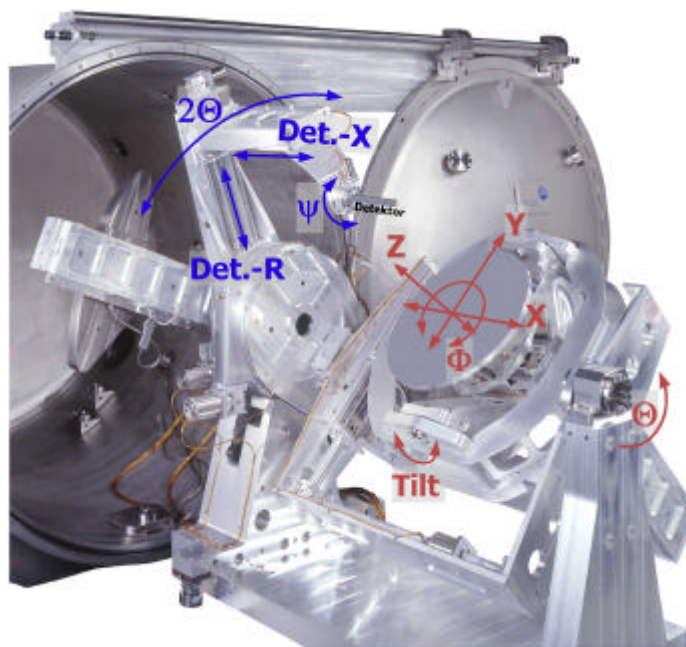


Figure 1 Picture of the large goniometer in front of the reflectometer vacuum chamber with degrees of freedom indicated.

Secondly, as lithography tools use a number of mirrors, this optical train is more sensitive to errors. This increases the need for accuracy in reflectance and wavelength measurements. The wavelength for the peak mirror reflectance should be matched better than 0.02% relative and the uniformity of reflectance should be better than 0.2%.

Here PTB continued to provide measurements with low uncertainties [5].

And thirdly, as more national and international companies concentrate their efforts on EUVL an increasing number of measurements is needed.

Due to the larger number of samples which can be placed in the instrument, we were able to increase the number of mirrors measured to about 930 in 2003. Considering the finite availability of laboratories able to measure in the EUV [6], this situation can slow the development process of EUVL in the future. Therefore PTB also works on the transfer of know-how for EUV metrology to help the industry to set-up their own measurement equipment close to the production line. In cooperation with the Fraunhofer IWS and institutes and companies from the Berlin-Adlershof area, an EUV reflectometer with a LPP source was developed and is now in operation at the CZ SMT AG [7].

To monitor the quality of EUVL masks, especially the accuracy of the structures on the mask, scatterometry can be used. In Figure 2, a typical result for scatterometry at a regular structure of lines and spaces on a EUV multilayer mask is shown. The quantity which is directly correlated to the geometrical structure of the surface is the scattering vector. The horizontal component (q_x) yields information on the lateral structure and the vertical (q_z) scattering vector on the periodicity of the multilayer coating. Shown are the results from a measurement with a fixed entrance beam and varying detector angle at a fixed wavelength. Here, not only q_x but also q_z changes with angle, see right axis in Figure 2. So, for every point along q_x , also q_z differs. This causes additional changes in the scattering amplitude, because the multilayer coating reflects only for values of q_z matching the multilayer period. At larger values of q_x this causes an additional decrease in scattered intensity as can be seen in comparison to the dashed line, indicating the envelope for Fraunhofer diffraction of a planar regular structure.

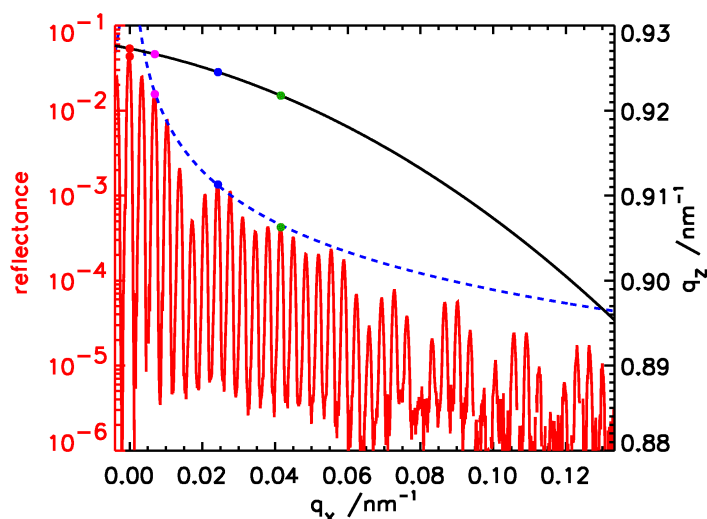


Figure 2 Reflectance at regular lines and spaces of an EUV mask measured as function of the angle of the reflected beam ($\lambda=13.5\text{nm}$). The data are shown here with the horizontal (q_x) and vertical (q_z) scattering vector. The periodicity in q_x yields information on the lateral structure. The blue dashed line indicates the envelope for Fraunhofer diffraction at a planar regular structure.

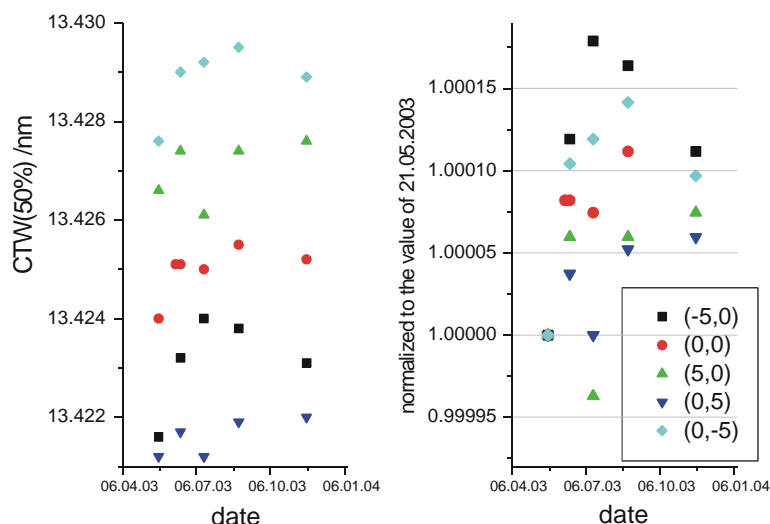


Figure 3 Measured center wavelength of a test mirror over the year. The sample has been kept in a dry-box between measurements. The left side shows repeated reflectance-measurements. On the right side the wavelength for the peak mirror reflectance is normalized to the value of may 21th 2003. Coordinates in millimeters of the spots measured are indicated in the box in the lower right corner.

We checked the stability of our reflectance measurements by repeated measurements of a group of samples. Between measurements the samples were kept in a dry-box. Each sample was always measured in several spots. Coordinates in millimeters of the spots measured are indicated in the box in the lower right corner of Figure 3. The left side of Figure 3 shows repeated reflectance-measurements of one sample. On the right side of Figure 3 the wavelength for the peak mirror reflectance normalized to the value of may 21th 2003 is shown.

As can be seen in the normalized data, the shift over time in the peak mirror reflectance is less than 0.02% for every single point over all the dates. This shows repeatability and comparability of our reflectance measurements as well as stability of the multilayer mirror over time.

Thus with the reflectometer for large EUVL optics, PTB is fully prepared to provide most accurate at-wavelength measurements for a multitude of reference- and basic research samples as well as for the large and aspheric mirrors for lithographic tools.

References

- 1 ElectronicNews – online, www.reedelectronicsgroup.com/esecc/Article_301016.htm
- 2 P. Gargini, Worldwide technologies and the ITRS in the current economic climate, *Proc. SPIE* **4688** (2002), 25 – 28
- 3 J. Tümmler, F. Scholze, G. Brandt, B. Meyer, F. Scholz, K. Vogel, G. Ulm, M. Poier, U. Klein and W. Diets, New PTB reflectometer for the characterization of large optics for the extreme ultraviolet spectral region, *Proc. SPIE* **4688** (2002), 338 – 347
- 4 A. Ehrmann, J. Rau, A. Wolter, F. Kamm, J. Mathuni, F. Scholze, J. Tümmler and G. Ulm, Mask CD characterization with EUV reflectometry at the electron storage ring BESSY II, *GMM-Fachbericht* **39** ISBN 3-8007-2748-x (2003), 59-64
- 5 F. Scholze, J. Tümmler, and G. Ulm, High-accuracy radiometry in the EUV range at the PTB soft x-ray beamline, *Metrologia* **40** (2003), 224 – 228
- 6 G. Ulm, Radiometry with synchrotron radiation, *Metrologia* **40** (2003), 100 – 106
- 7 Ludwig van Loyen, Thomas Böttger, Stefan Braun, Hermann Mai, Andreas Leson, Frank Scholze, Johannes Tümmler, Gerhard Ulm, Herbert Legall, Peter V. Nickles, Wolfgang Sandner, Holger Stiel, Christian Rempel, Mirko Schulze, Jörg Brutscher, Fritz Macco, and Stephan Müllender, A New Laboratory EUV Reflectometer for Large Optics using a Laser Plasma Source *Proc. SPIE* **5038** (2003), 12-21

Linearity of silicon photodiodes for EUV radiation

R. Müller, F. Scholze, R. Klein, S. Plöger, U. Schwarz, G. Ulm

Physikalisch-Technische Bundesanstalt, Abbestr. 2-12, 10587 Berlin, Germany

During the last decades electronic chips have become ever more powerful and more compact with the cost being lowered at the same time. The optical lithography techniques used for their production have however been pushed to the possible extent. Extreme ultraviolet (EUV) lithography is an attractive next generation lithographic technology since it will support imaging dense 1:1 line-space features smaller than 40 nm. EUVL uses radiation of about 13 nm wavelength. So there is a strong need for accurate EUV radiant power measurement and intensity monitoring e.g. for irradiation experiments and optics testing [1].

Photodiodes are used as easy-to-operate detectors in the extreme ultraviolet spectral range. The Physikalisch-Technische Bundesanstalt calibrates photodiodes with an uncertainty of the spectral responsivity of 0.3% or better. These calibrations are based on the comparison of the photodiodes to a cryogenic radiometer as primary detector standard using monochromatized synchrotron radiation, a quasi DC-radiation with a rather low radiant power of about 1 μ W [2]. At the customer, these diodes may be used for strongly pulsed radiation and very different radiant power. Therefore, the linearity of the diode signal with incident radiant power was studied with EUV radiation. We also investigate the influence of the photon beam spot size on the diode responsivity at high radiant power. Here we present first results of these investigations.

The measurements were performed at the EUV system metrology beamline at the undulator U49 of PTB at BESSY II [3, 4]. To achieve sufficiently high levels of photon flux to saturate the photodiode, direct undulator radiation was used. At a distance of 18 m from the undulator, the radiation is deflected by a water-cooled plane mirror with platinum coating at a deflection angle of 13° with respect to the direct beam. By this, high-energy harmonics of the undulator are suppressed. For the use in the EUV spectral range around 13 nm, further purification of the undulator spectrum is achieved by using different thin metal filters or foils. For details of the beamline and the EUV radiant power see references 3, 4 and 5. On the diode position, the undulator beam is 4 mm in size, FWHM. We therefore were not able to illuminate the full photodiode active area of 10 by 10 mm². The largest aperture size used in the investigations was 6 mm in diameter. For this aperture, the intensity already was significantly lower at the corner than in the center. The results however fit well in the trend of the other data.

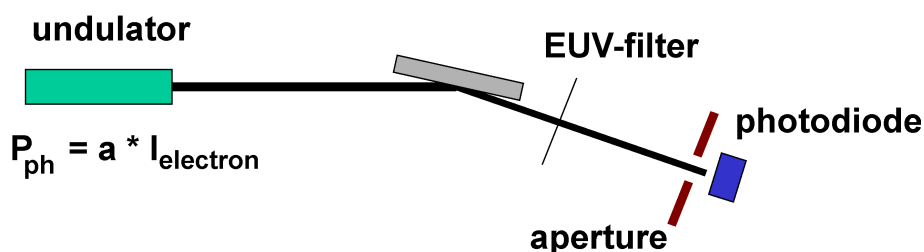


Figure 1. Scheme of the measurement set-up. EUV radiation from an undulator is spectrally filtered by plane mirror reflection for high-energy cut-off and an additional transmission filter for low energy suppression. The photodiode is placed behind an aperture of variable size and the radiant power P_{ph} is proportional to the stored electron current.

As a reference of the diode linearity, the photon flux from the storage ring was used. The storage ring can be used by PTB as standard source. The photon flux scales linear with the stored electron current. Therefore we measured the photocurrent of the photodiode as a function of the stored electron current. For each value of the stored electron current, we measured the photocurrent for a set of apertures which were successively placed in front of the diode. This measurement was repeated for stepwise decreased electron current until the photocurrent and electron current ratio was constant. As the total power incident on the photodiode scales with the aperture size, the photocurrent differs for the different aperture sizes. The measurements were done twice with two sets of apertures, the first set having diameters of 0.125 mm, 0.25 mm, 0.5 mm, 1 mm, 1.25 mm, 1.5 mm, 2 mm, and 4 mm, and the second set diameters of 0.5 mm, 1 mm, 2 mm, 3 mm, 4 mm, and 6 mm.

In figure 2 the ratio between photodiode current and stored electron current is shown. Derivations from linear behavior occur as changes in this ratio. The data for the different apertures were normalized to the region of low photocurrent, where the diodes are linear. The maximum radiant power incident at the diode for the 6 mm aperture and a stored current of 140 mA was of the order of 500 mW, corresponding to an irradiation level of about 2 W/cm². This level was not sufficient to saturate the diode with the smallest aperture (0.125 mm). For all other apertures, an appropriate signal was available. It was shown previously that the special SXUV type diodes used here, are stable for irradiation under UHV-atmosphere up to 150 kJ/cm² [6]. So because the measurements at the highest flux took only a few minutes, effects of the diode damage should not be observed in the measurements.

Figure 2 (left) shows the normalized diode photocurrent to stored electron current ratio for aperture sizes from 0.25 mm to 4 mm, see figure caption. Figure 2 (right) shows the same data for the second set of apertures from 1 mm to 6 mm. The ratio is shown as a function of the external diode current. In this presentation the asymptotic behaviour of the external current in the high saturation region is clearly visible. This asymptotic maximum current increases with the aperture size. The dashed curves in figure 2 have been calculated using a simple model equation for the measured current. The model is based on an equivalent electrical circuit with an electrometer. In this circuit the photodiode is characterized mainly by its equivalent serial resistance (for details see references 7 and 8). The best fit values for the serial resistance has are given in the caption of figure 2.

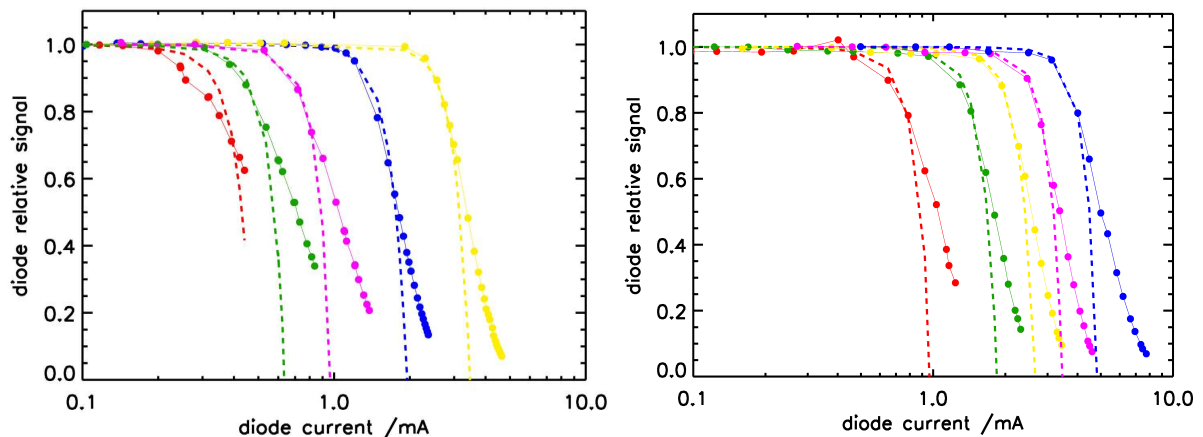


Figure 2. left: diode photocurrent normalized to input power for different aperture sizes of 0.25 mm, 0.5 mm, 1 mm, 2 mm, and 4 mm, data points in red, green, magenta, blue and yellow, respectively. The dashed lines are model curves for the saturation behaviour yielding serial resistance of 540 Ω , 410 Ω , 280 Ω , 155 Ω , and 90 Ω , respectively. Right: diode photocurrent normalized to input power for different aperture sizes of 1 mm, 2 mm, 3 mm, 4 mm, and 6 mm, data points in red, green, yellow, magenta, and blue, respectively. The dashed lines are model curves for the saturation behaviour yielding serial resistance of 280 Ω , 160 Ω , 115 Ω , 90 Ω and 65 Ω , respectively.

Especially for the large aperture sizes, at which the diode was operated in high saturation, this calculation does not agree well with the data at high irradiation. The measured current is systematically too high. Our explanation is that the effective serial resistance might change with the current. The charge carriers generated in the p-n junction are transported in the thin n-conducting front layer to the electrode at the border of the active area. So the carrier density in this almost completely depleted layer increases and the resistivity decreases.

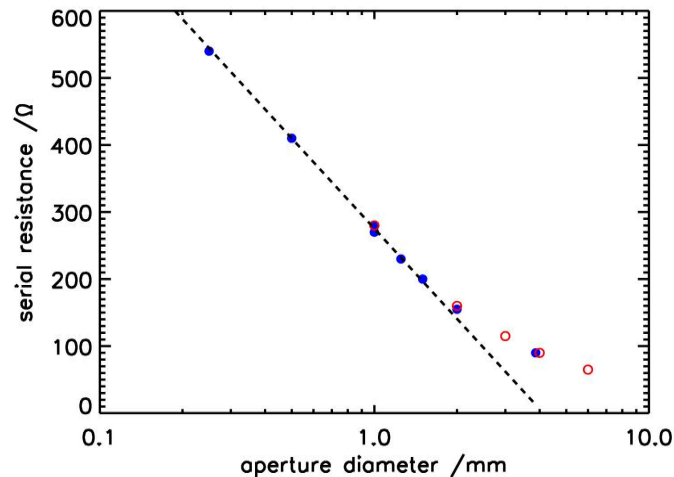


Figure 3. Presentation of the serial resistance obtained from the saturation curves (solid circles from figure 2 (left) and open circles from figure 2 (right)) as a function of aperture size. The ordinate is scaled logarithmically in aperture size. Please note the almost ideal logarithmic dependence up to an aperture size of about 2 mm. For larger aperture sizes, the slope decreases and the values appear to converge to a finite value for full diode illumination.

In summary the linearity of the photodiodes was tested in quasi-DC illumination for different photon beam spot sizes. A systematic and significant variation of the maximum external photocurrent with the photon beam spot size is shown. The maximum current in linear operation (1% relative saturation) decreased from about 3 mA for 6 mm photon beam diameter to 0.2 mA for a 0.25 mm diameter. The corresponding irradiance increased from 30 mW/cm² for the 6 mm aperture to about 2 W/cm² for a 0.25 mm aperture. The behaviour is explained by a change in the effective serial resistance with photon beam size. The values derived from the saturation measurement vary between 65 Ω for a 6 mm beam and 540 Ω for 0.25 mm. This effect can be attributed to the finite conductivity of the thin front contact layer carrying the current to the electrode [8]. For spot sizes much smaller than the diode's active area, the serial resistance scales logarithmically with the spot size.

- [1] H. Meiling et al., Proc. SPIE **4688**, 52 (2002)
- [2] H. Rabus, V. Persch, G. Ulm, Appl. Opt. **36**, 5421 (1997)
- [3] F. Scholze et al., Proc. SPIE **4344**, 402 (1998)
- [4] R. Klein et al. Synchrotron Radiation News **15**, 23 (2002)
- [5] A. Gottwald, R. Müller, A.A. Sorokin, M. Richter, G. Ulm, Meas. Sci. Technol. **15**, 437 (2004)
- [6] F. Scholze, R. Klein, T. Bock, Appl. Opt. **42**, 5621 (2003)
- [7] R. Korde, C. Prince, D. Dunningham, R. Vest, E. Gulliksen, Metrologia **40**, 145 (2003)
- [8] F. Scholze, R. Klein, R. Müller, submitted for publication

Evaluation of Complete Standardless Quantitation for Synchrotron Radiation Induced X-Ray Fluorescence Analysis

B. Beckhoff¹, M. Mantler², M. Bavdaz³, G. Fraser⁴, M. Kolbe¹, M. Krumrey¹
A. Owens³, A. Peacock³, D. Pullan⁴, F. Scholze¹, G. Ulm¹

¹Physikalisch-Technische Bundesanstalt, Abbestr. 2-12, 10587 Berlin, Germany

²Technische Universität Wien, Wiedner Hauptstr. 8-10, 1040 Wien, Austria

³Science Payloads Technology Division, ESA/ESTEC, 2200AG Noordwijk, The Netherlands

⁴Dept. Physics and Astronomy, Leicester University, Leicester LE1 7RH, England

Abstract. Employing synchrotron radiation of high spectral purity and well known radiant power for the specimen excitation and detecting element-specific fluorescence radiation by means of a calibrated detector behind a calibrated diaphragm allows for complete standardless quantitation in X-Ray Fluorescence (XRF) analysis. In view of future spectrometer developments and in order to assess this fundamental-parameter based quantitation approach several planetary analogue rock samples and thin layered materials were investigated at several photon energies of interest using monochromatized synchrotron radiation. Initial results demonstrate the potential of this quantitation approach to obtain reliable analytical results without having to use any reference materials.

Introduction. The experiment described below intends to contribute to the assessment of a genuine standard-free quantitation procedure by XRF in view of the evaluation of future XRF instrumentation such as the spectrometer specifically to be developed for the European Space Agency's BepiColombo mission. For the methodical investigation in the PTB radiometry laboratory at BESSY II, two photon energy ranges covering 78 eV to 1.9 keV and 1.75 keV to 10.5 keV were selected in correspondence to the radiation available at the plane grating monochromator (PGM) beamline for undulator radiation and at the four crystal monochromator (FCM) beamline. For the low energetic XRF analysis a versatile UHV irradiation chamber was designed and put into operation at the PGM beamline for undulator radiation. Here, all relevant parameters such as the incident radiant power, the solid angle of detection as well as the detection efficiency and response are well known or can be controlled absolutely during the XRF measurements.

Fundamental Parameter Methods. The number of fluorescence photons emitted from the sample can be described as a function of sample properties (elemental composition and concentrations, thickness, layer structure, size, etc.), geometrical setup, and the characteristics of the exciting radiation. The physical interactions between radiation and atoms are described by interaction coefficients (absorption and scattering), transition probabilities, and fluorescent yields, i.e., by the fundamental parameters. Primary (direct) and secondary (indirect) excitation effects are normally accounted for, but in the case of light elements the excitation by photo- and Auger-electrons as well as cascade-effects (e.g., L-emission after K-ionization) are essential (occasionally dominating) contributions. Electron interactions must be quantitatively known on an absolute scale for a complete computation.

Experimental arrangement. The primary beam was set to hit the specimen surface at 90° (perpendicular to the surface) for the minerals and at 45° for all other specimens including glass. The detector was positioned at 45° at a distance of 67 mm from the sample; the accepted solid angle (0.00037305 sterad) was defined by a carefully measured diaphragm of 1.46 mm diameter. As shown to the right in fig.1 other relevant XRF beam geometries are accessible, too. In order to validate the quantitation and spectrometer design approaches we have measured the fluorescent radiation from a variety of samples including one-elemental foils of Cu, Ni, Si, and Al, multilayer structures made of these materials, steels, glasses, as well as soil and rock samples provided by the Department of Physics and Astronomy of the Leicester University, England.

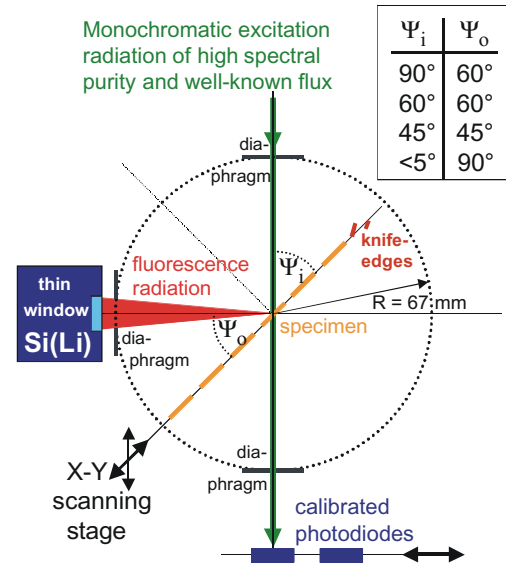


Fig.1 Accessible XRF beam geometries

The samples were mounted in holders corresponding to their size (cf. fig. 2).

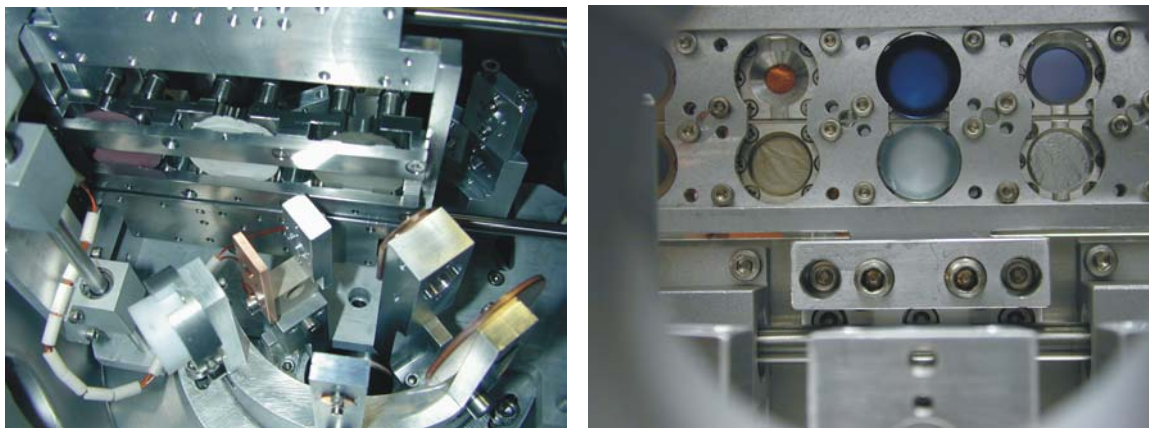


Figure 2. Experimental arrangement showing to the left the mineral or rock samples mounted on their holder. The incident beam passes through the entrance diaphragm towards the samples. The fluorescence radiation then passes through the diaphragm systems. The picture to the right shows the sample holder for the thin metal foils and layered materials with diameters of up to 10 mm.

Spectra evaluation and estimated errors. In order to validate the XRF quantitation employed, samples were excited at various photon energies allowing different spectral regions of interest to be enhanced. During these XRF measurements the incident photon flux was either monitored by a transmission photodiode or by the stored electron beam current. The detected count rates of relevant fluorescence lines were determined from the respective XRF spectra (cf. fig. 3) employing experimentally based detector response functions. The total uncertainty is composed of the relative uncertainty of both experimental and spectra deconvolution contributions ranging between 6 % to 9 %, the relative uncertainty in the fundamental parameters, which is element and energy dependent and smaller than 5 % for photon energies above 2 keV to 3 keV, and the accuracy of the mathematical model for the computations (less than 1 % uncertainty for medium or high Z-elements). The uncertainty is rather unpredictable for light elements, where secondary effects involving cascades and photo-electrons are dominating and the influence of the chemical state of the elements is not negligible.

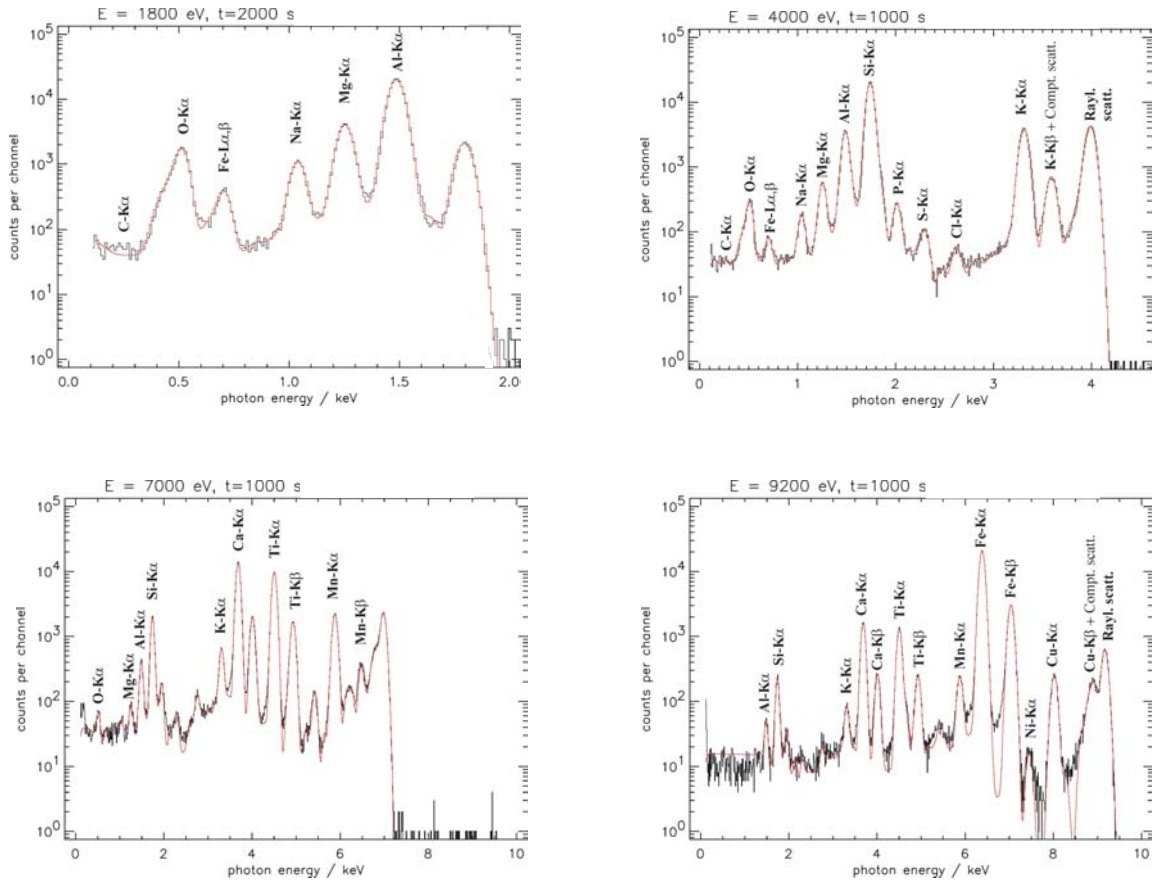


Figure 3. EDXRF spectra of an anorthosite sample excited with monochromatic radiation of four different photon energies. During these measurements the respective incident radiant power was well known.

Results. Employing standardless, fundamental parameter based quantitation procedures the experimental data were evaluated. Numerical data for a mineral specimen (anorthosite) as well as for layered and bulk materials are shown in the table below.

Obtained Concentrations							Ratio of Measured and computed counts									
Mineral	9.2 keV	7.9 keV	4.0 keV	1.8 keV	Average	StdDev	Sample	E / keV	SiKa	CuKa	CuKb	NiKa	NiKb	FeKa	CrKa	AlKa
O	0.11	0.11	0.12	0.10	0.11	0.01	2um Al	9.7								1.54
MnO	0.20	0.27	0.16	0.17	0.20	0.05	500nm Cu	9.7	0.90	0.84						
Fe2O3	13.81	11.71	13.29	13.78	13.15	0.99	50nm Cu/50nm Ni/Si	9.7	1.45							
Ni	0.01	0.00	0.01	0.01	0.01	0.00	50nm Cu/50nm Ni/Si	9.7				1.05	1.00			
Cu	0.07	0.05	0.06	0.03	0.05	0.02	50nm Cu/50nm Ni/Si	9.7	1.12	1.08						
Na2O	3.19	3.12	2.04	1.90	2.56	0.69	50nm Ni/50nm Cu/Si	9.7	1.43							
MgO	3.19	3.12	4.36	4.66	3.83	0.79	50nm Ni/50nm Cu/Si	9.7				1.06	1.00			
Al2O3	15.17	17.95	15.94	14.25	15.83	1.58	50nm Ni/50nm Cu/Si	9.7	1.11	1.04						
SiO2	49.65	46.84	49.60	49.78	48.97	1.42	Steel	9.7							1.09	
CaO	8.86	10.93	8.59	9.22	9.40	1.05	Steel	9.7	1.46					1.15		
K2O	0.63	0.52	0.45	0.60	0.55	0.08	Steel	9.7	1.33			1.70				
CO2	0.28	0.27	0.31	0.33	0.30	0.03	Steel	9.7				1.58				
P2O5	0.23	0.62	0.71	0.28	0.46	0.24	500nm Ni	9.7	1.34			1.00	0.92			
TiO2	3.98	4.06	3.90	4.18	4.03	0.12	12um Si	9.7	1.46							
Cl	0.01	0.01	0.01	0.02	0.01	0.00	12um Si		3	1.33						
Pd	0.00	0.00	0.00	0.00	0.00	0.00	12um Si		5	1.34						
Cd	0.02	0.02	0.02	0.02	0.02	0.00	Glass SRM610	9.7	1.28							
Ag	0.06	0.06	0.00	0.08	0.05	0.03										
S	0.18	0.06	0.05	0.21	0.12	0.08										
V	0.21	0.14	0.23	0.25	0.21	0.05										
Ba	0.14	0.13	0.15	0.16	0.15	0.01										

Conclusion. Best results with deviations of a few percent were obtained for medium Z elements, where fundamental parameters are most reliable and the computational models are accurate for bulk materials as well as for thin film structures. Silicon and aluminum exhibited significant systematic deviations which are apparently independent of sample properties and excitation conditions. In view of the widely varying literature values for transition probabilities it must be assumed that this is mainly a consequence of unreliable parameters, e.g. the transition probabilities for Si-K β given by Johnson et al. - which are close to our findings - and Elam et al. differ by a factor of 5.

References.

1. B. Beckhoff, R. Klein, M. Krumrey, F. Scholze, R. Thornagel, G. Ulm, Nucl. Instr. Meth. A **444**, 480-483 (2000)
2. N. Kawahara, T. Shoji, T. Yamada, Y. Kataoka, B. Beckhoff, G. Ulm, M. Mantler, Adv. X-Ray Anal. **45**, 511-516 (2002)
3. W.T. Elam, B.D. Ravel and J.R. Sieber Radiation Physics and Chemistry **63**, 121-128 (2002)
4. G.G. Johnson, Jr. and E.W. White, Amer. Soc. Test. Mater. Data Ser. DS-**46**, 38 pp. (1970)

Röntgenmaskentechnologie und alternative Maskentechniken

Martin Bednarzik, Alexander Firsov, Linke Jian, Harald Köhrich, Bernd Löchel, Heinz-Ulrich Scheunemann, Daniel Schondelmaier, Ingrid Wichert
 BESSY GmbH, Anwenderzentrum Mikrotechnik, Albert-Einstein-Str. 15, 12489 Berlin

Maskenmaterialien sollten eine hohe mechanische Stabilität, gute thermische Eigenschaften, eine hinreichende Prozessierbarkeit und eine hohe Röntgentransparenz aufweisen. Weiterhin sollten diese Materialien kommerziell erhältlich sein und die Substrate möglichst wenig nachbehandelt werden müssen. Schließlich sollten die Kosten möglichst niedrig sein.

In Tabelle 1 sind die bestrahlungstechnischen Eigenschaften dargestellt. Viele der Materialien sind nur bei sehr geringer Dicke ausreichend röntgentransparent. Membranen aus diesen Materialien sind besonders fragil und sollten deshalb Spezialanwendungen vorbehalten sein. Des Weiteren sind diese Membranen nur von speziellen Herstellern zu beziehen, so dass nur eine geringere Bezugssicherheit gegeben ist. Siliziumcarbid gibt es zwar als 200 µm Folie jedoch ist die Röntgentransparenz für diese Folienstärke sehr niedrig. Bornitrid ist zwar von seinen Eigenschaften geeignet, jedoch verändert sich dieses Material bei Bestrahlung. Polyamidmasken sind sehr preisgünstig herzustellen, jedoch nur für eine äußerst geringe Anzahl von Belichtungen benutzbar. Die starke Zersetzung des Materials durch Röntgenlicht bewirkt enorme Verzüge. Glaskohlenstoff (keine optische Transparenz) ist inzwischen auf dem Markt erhältlich. Jedoch ist die Oberfläche solcher Substrate noch nicht genügend eben. Sie ist gekennzeichnet durch eine gewisse Welligkeit und Kratzspuren auf der Oberfläche. Diamant ist zwar hervorragend als Maskenmembranmaterial geeignet (gute Röntgentransparenz, hohe optische Transparenz, jedoch ist der Preis sehr hoch und die Verfügbarkeit gering).

Tabelle 1: Materialeigenschaften von Maskenmembranmaterialien

Membranmaterial	Typische Dicke [µm]	Röntgen-transparenz [µm]***	Röntgen-absorptions-koeffizient [µm]	Dosis hinter Membran [W/cm]*	Dosis hinter Absorber [mW/cm]*	Masken-contrast	Oberflächen-dosis [kJ/cm²]	Belichtungs-zeit [min]**	Bemerkungen
Silizium	15	12	0.057095	0.56	2.24	250	10.5	80	
Siliziumnitrid	15	12	0.055183	0.57	2.24	254	10.3	79	
Siliziumcarbid	15	12	0.057365	0.55	2.16	255	10.1	82	
Bornitrid	15	150	0.00492	1.09	2.32	470	25.2	41	
Titan****	3	~15	~0.044	0.85	2.18	389	28.5	54	Standard Material FZK
Beryllium	500	860	0.000803	0.76	2.32	325	13.4	56	MODULIGA Material
Graphit	150	200	0.003526	0.70	2.34	297	12.1	62	Alternativ Material
Diamant	30	100	0.006705	0.92	2.40	384	18.3	46	
Glaskohlenstoff	200	230	0.002961	0.69	2.32	295	9.1	86	Alternativ Material
Glas (Displayglas)	30	20	0.04374	0.43	2.00	214	9.6	112	Alternativ Material
Polyimid (Kapton)	125	190	0.003631	0.73	2.34	312	12.9	59	Sonderanwendungen

* BESSY Dipol Ringstrom 200 mA

** PMMA 300 µm 30 mm hoch, Bottem-Dosis 4 kJ/cm²

*** Foliendicke bei der die Transparenz 50% beträgt (Photonenenergie 5 keV)

**** Circa-Werte da Absorptionskante

Beim Glas handelt es sich um sogenanntes Flat-Panel-Display-Glas, das von der Schott AG Mainz angeboten wird und hauptsächlich in der Elektronik Anwendung findet. Die breite Anwendungspalette erhöht die Verfügbarkeit des Materials enorm. Das Glas muss mechanisch nicht weiter bearbeitet werden, da die Dicke, die Planarität und die

Oberflächenrauigkeit den hohen Anforderungen an Membranmaterialien entsprechen. Das Material ist zudem mechanisch und chemisch stabil. Besonders hervorzuheben ist die außerordentlich hohe optische Transparenz, welche für justierte Röntgenbelichtungen wichtig ist. Negativ wirken sich die geringe Wärmeleitfähigkeit und die im Vergleich zu Beryllium geringere Röntgentransparenz aus. Allerdings ist für die ultratiefe Röntgenlithographie (> 1mm PMMA) der Unterschied nicht mehr so hoch (20% - berechnet für BESSY WLS 4 Tesla). Allerdings werden die Nachteile umso größer, je dicker das Glas gewählt wird.

Kohlenstoff als Graphit ist verhältnismäßig einfach zu beziehen und hat auch sehr gute Eigenschaften. Das Material ist mechanisch und chemisch stabil, die Röntgentransparenz ist ähnlich der von Beryllium, auf optische Transparenz wie beim Displayglas muss aber verzichtet werden. Nachteil ist jedoch, dass bisher das Graphit-Rohmaterial noch mechanisch nachbearbeitet werden muss, um die Oberflächenrauigkeit zu verbessern, um somit eine Qualitätssteigerung zu erreichen.

Inzwischen wurde ein Zulieferer gefunden, der feinkörnigeres Graphit (1µm Korngröße) mit einer Rautiefe von besser als 0.4 µm anbietet. Dieses Material ist derzeit bei BESSY in der Testphase.

Das Strukturieren der Membran aus Graphit mit Goldabsorbern ist verhältnismäßig einfach und damit preisgünstig. Da das Trägermaterial elektrisch leitend ist, wird keine Startschicht für die Galvanik benötigt, so dass die Membranen unmittelbar lithographisch strukturiert werden können. Speziell für die Herstellung so genannter "Low-Cost"-Masken ist dieses Material ideal. Der Herstellungsprozess ist in Abb. 1 dargestellt. Die Maskenmembran wird mit SU-8 in den erforderlichen Dicken beschichtet (ca. 30-50 µm). Nach dem Belichten über eine Chrom-Maske mit UV-Licht und dem anschließenden Entwickeln wird der Absorber mittels Goldgalvanik aufgebracht. Da der SU-8 Resist nach dem Prozessieren stabil ist und gleichzeitig eine hohe Röntgentransparenz aufweist, muss er nicht entfernt werden.

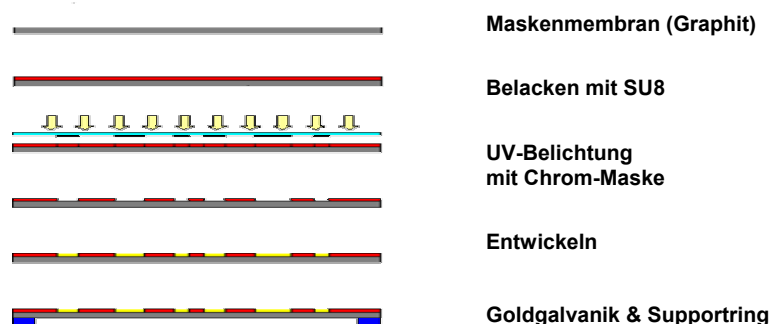


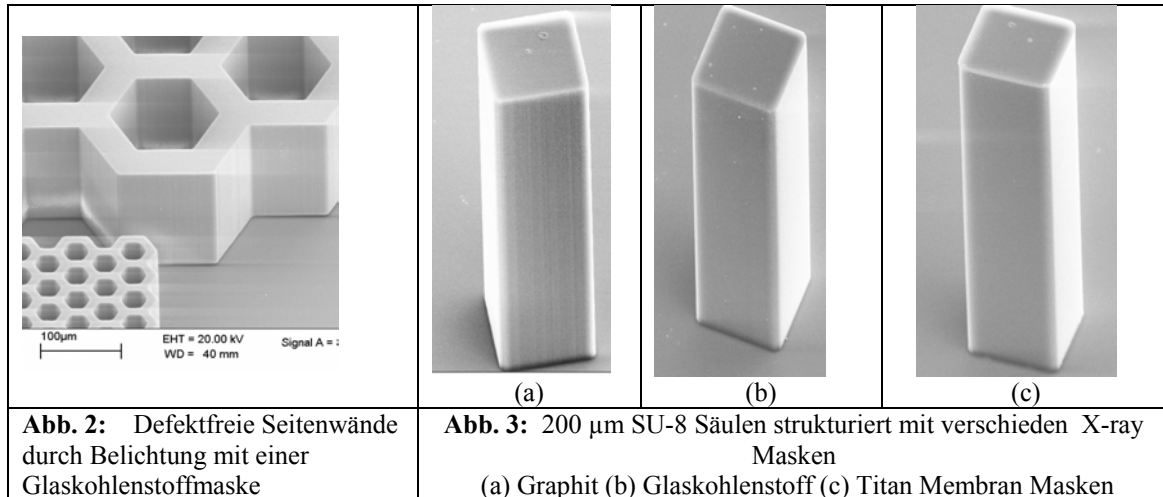
Abbildung 1: Strukturierung von "low-cost"-Graphitmasken

Nach bisherigen Erkenntnissen können mit diesem Maskenmaterial bei höchstauflösenden Belichtungen Probleme auftreten. Das Maskenmaterial ist nach unserer Meinung erste Wahl für Masken, die sehr schnell zur Verfügung stehen müssen und bei denen der Maskenpreis niedrig gehalten werden muss.

Masken aus Graphit wurden von BESSY in größerer Menge hergestellt und den Projektpartnern zur Erprobung zur Verfügung gestellt (Abb. 3.4). Die Produktion von solchen Masken ist sehr preisgünstig und das Strukturfeld ist sehr groß (Ø ~8 cm bzw. Fläche ~50 cm²). Die Anwendung solcher Masken aus Graphit ist jedoch eingeschränkt, da an den Strukturen Defekte, so genannte "Mouse Bites", auftreten und die Seitenwände eine hohe

Rauhigkeit aufweisen. Die Ursache dafür ist im Graphitmaterial selbst zu suchen. Zum einen hat das Graphitsubstrat eine sehr poröse Struktur welche Defekte im Goldabsorber induziert.

Um diese Defekte zu reduzieren wurde ein verfeinerter Maskenprozess erarbeitet. Dazu wird eine dünne SU8-Schicht auf das Graphit aufgeschleudert, um eine glatte und kavernenfreie Oberfläche zu erhalten. Danach wird eine Platingbase auf gesputtert. Dadurch verringern sich die Defekte auf der Maske. Glaskohlenstoff wurde als Trägermaterial verwendet. In diesem Fall ist auch die Oberfläche sehr glatt, so dass die Fehlstellen im Absorber nicht mehr auftreten. Erste Belichtungsergebnisse sind in Abbildungen 2 und 3. gezeigt. Die Oberflächenrauigkeit ist auf 40 nm Ra reduziert im Gegensatz zu 300 nm Ra bei normalem Graphit.



Weitere Untersuchungen betrafen das Displayglas als Trägermaterial. Da dieser Werkstoff insbesondere für justierte Belichtungen interessant ist, muss beim Prozessieren der Maske darauf geachtet werden, dass der Vorteil der optischen Transparenz erhalten bleibt. Da Glas nichtleitend ist muss für den Absorberaufbau eine Platingbase aufgebracht werden. Metalle sind in der Regel nicht transparent. Deshalb wurde bei BESSY ein Verfahren entwickelt die Startschicht für die Goldgalvanik aus transparentem und elektrisch-leitendem Indium-Zinn-Oxid (ITO) herzustellen.

ITO als Galvanikstartschicht für transparente Masken

Martin Bednarzik, Alexander Firsov, Linke Jian, Harald Köhrich, Bernd Löchel, Ivo Rudolph, Heinz-Ulrich Scheunemann, Daniel Schondelmaier, Ingrid Wichert
BESSY GmbH, Anwenderzentrum Mikrotechnik, Albert-Einstein-Str. 15, 12489 Berlin

Für bestimmte Anwendungen, z.B. der Herstellung dreidimensionaler Mikrokomponenten mit Hilfe der Röntgentiefenlithographie sind justierte Mehrfachbelichtungen notwendig. Voraussetzung dafür sind neben der Ausstattung der Belichtungsgeräte mit einem Justiersystem auch Röntgenmasken mit Justiermarken, deren Trägermaterial für das Justiersystem an den entsprechenden Stellen transparent ist. Das Justiersystem der von BESSY verwendeten Scanner der Fa. Jenoptik arbeitet mit Licht im sichtbaren Bereich. Eine Voraussetzung für die Herstellung justierbarer Röntgenmasken ist deshalb ein im sichtbaren Bereich transparentes Trägermaterial. Wenn man auf kommerziell erhältliches Material zurückgreifen möchte, kommt hierfür vor allem Displayglas (Borsilikatglas) der Fa. Schott in Frage. Dieses Material ist in sehr geringen Dicken bis zu 30 μm erhältlich und vor allem für den Einsatz im Bereich hochenergetischer Strahlung gut geeignet, da es auch die gewünschte Röntgentransparenz besitzt.

Einzig bekanntes Material für solche Anwendungen ist Indium-Zinn-Oxid (ITO). Es wird zur Fertigung von elektrischen Leiterbahnen bei der Herstellung von Flachbildschirmen eingesetzt. ITO kann durch Sputtern auf ein Trägermaterial aufgebracht werden.

Bei BESSY wird zum Aufbau von ITO-Schichten die Magnetron-Sputter-Anlage „HV-Sputtersystem-8A“ der Firma BesTec benutzt.

Die gewünschte Rauigkeit der ITO-Oberflächen konnte durch Prozessdruck- sowie Prozessgasveränderungen eingestellt werden, damit die mechanische Adhäsion von Gold auf ITO optimal ist. Durch die Zugabe von Sauerstoff zum Prozessgas konnte die kristalline Struktur sowie die Anzahl der Körner auf den ITO-Oberflächen beeinflusst werden. Dies wirkt sich nicht nur auf die mechanische, sondern auch auf die spezifische Adhäsion positiv aus. Zum anderen ist eine ausreichende elektrische Leitfähigkeit des ITO erreicht worden.

Die gewonnenen Erkenntnisse können zur Herstellung von optisch transparenten Röntgenmasken angewendet werden, um schlussendlich für die Herstellung von Mikrostrukturen mit hohen Aspektverhältnissen zu dienen.

Galvanische Abscheidung von Gold auf ITO-Schichten

Wie in der nachstehenden Abbildung im linken Bild zu sehen ist, sind die Goldabsorberstrukturen in allen Bereichen aufgewachsen. Zur Beurteilung der Haftung der Goldschichten konnte nur eine optische Kontrolle erfolgen, da ein Klebestreifen- oder Ritztest zur Zerstörung des dünnen Displayglases führen würde. Bei der optischen Kontrolle wurden auf der Vorder- sowie Rückseite der Maske keine Ablösungen der Goldstrukturen festgestellt. Weitere Aussagen über die Haftung werden sich im Laufe des Gebrauchs der entstandenen Röntgenmaske feststellen lassen.

Da die Transparenz im sichtbaren Bereich für das Justiersystem der Scanner eine wichtige Größe ist, wurden Transmissionsmessungen bei Wellenlängen von 510 nm bis 920 nm an den Glas/ITO-Maskenmembranen durchgeführt. Dabei wurde die Transmission für Displayglas ($d_{\text{Glas}} = 100 \mu\text{m}$), Displayglas mit ITO-Schicht ($d_{\text{ITO}} = 200 \text{ nm}$), und Displayglas mit

aufgebrachter ITO-Schicht und dem Photoresist SU-8 ($d_{\text{SU8}} = 35 \mu\text{m}$) als Formgeber für die Goldabsorberstrukturen bestimmt.

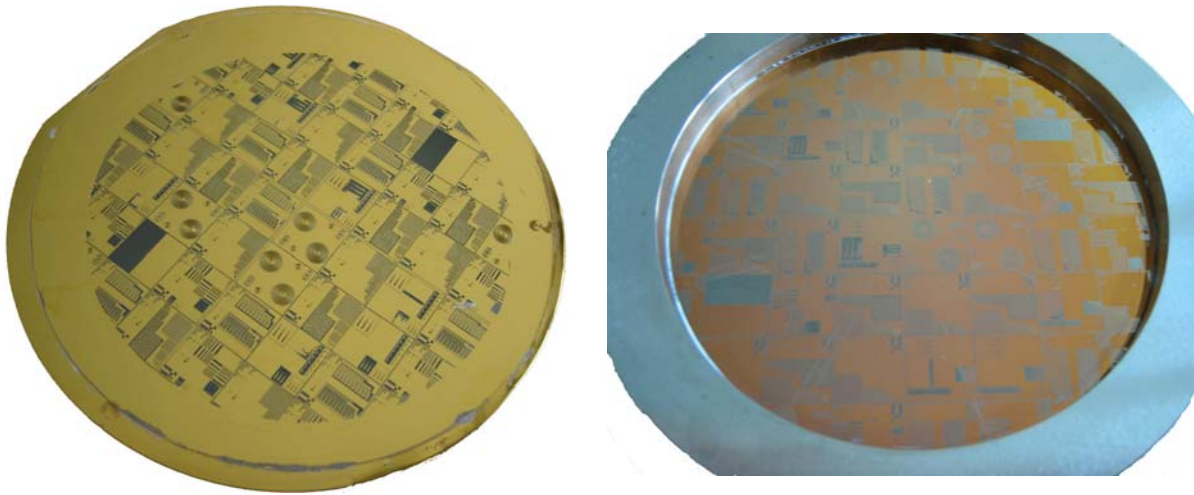


Abbildung 1: Röntgenmaske mit TESMA3D- Design aus Displayglas mit guten optischen und röntgentransparenten Eigenschaften als Trägermaterial (links: Vorderseite mit Goldabsorberstrukturen, rechts: Ansicht auf die Rückseite)

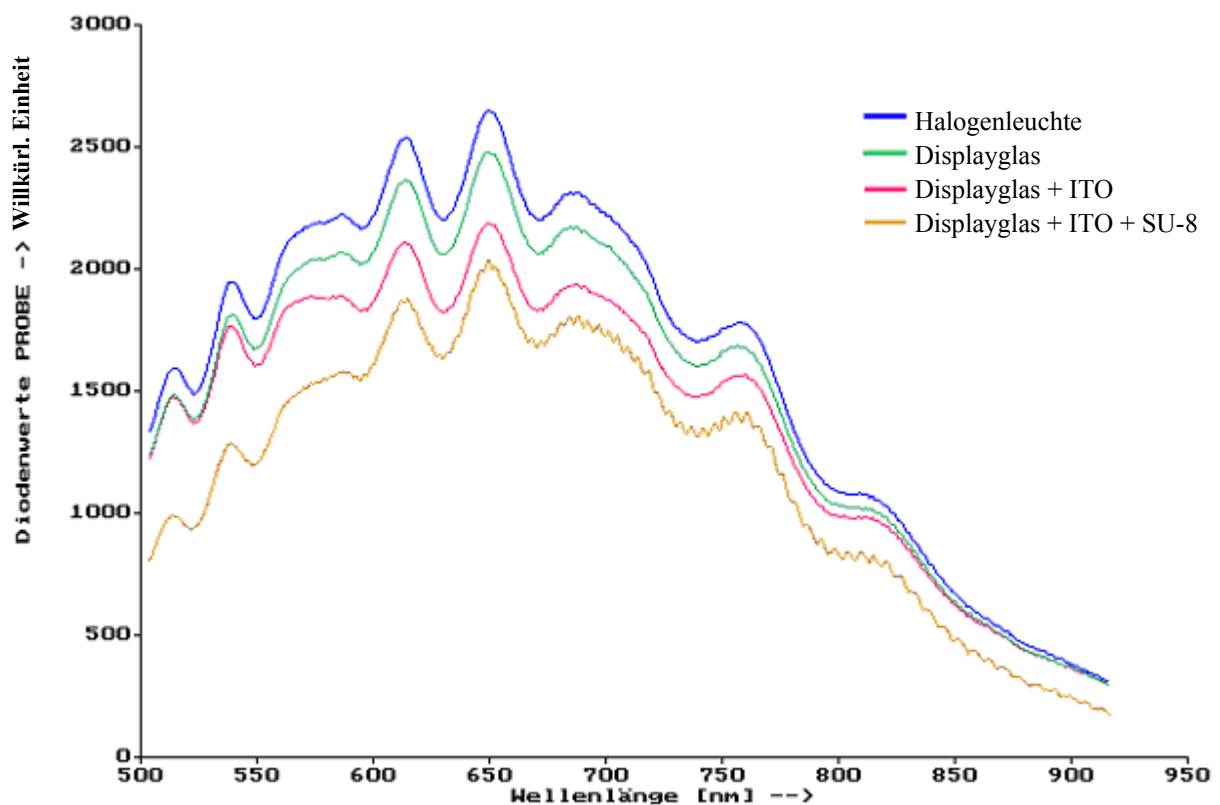


Abbildung 2: Transmission der Röntgenmaske im sichtbaren Bereich

Aus Abbildung 2 geht hervor, dass ITO, Glas und SU-8 erwartungsgemäß eine unterschiedlich starke Transmission zeigen. Das Displayglas hat in einem

Wellenlängenbereich von 550 nm bis 850 nm eine Transmission von 93 % und 95 %. Die Transmission der ITO-Schicht liegt im gleichen Wellenlängenbereich zwischen 89 % und 97 %. Der Resist SU-8 ist mit einer Transmission von 73 % bis 93 % am wenigsten

lichtdurchlässig. Die Transmission der untersuchten Materialien ist in Tabelle 1 für ausgewählte Wellenlängen dargestellt.

	550 nm	600 nm	650 nm	700 nm	750 nm	800 nm	850 nm
Displayglas	94 %	93 %	94 %	93 %	95 %	95 %	94 %
Glas + ITO	90 %	84 %	84 %	84 %	87 %	91 %	92 %
Glas + ITO + SU-8	65 %	64 %	77 %	78 %	77 %	77 %	71 %
ITO	96 %	90 %	89 %	90 %	92 %	96 %	97 %
SU-8	73 %	85 %	82 %	93 %	89 %	83 %	74 %

Tabelle 1: Prozentuale Bewertung der Transmission für ausgewählte Wellenlängen

Zusammenfassung

Das Scannerjustiersystem arbeitet mit Sensoren, die bei ca. 630 nm empfindlich sind. Zur Funktion ist eine Transmission von >30% notwendig. Im Rahmen dieser Untersuchungen konnte gezeigt werden, dass die Masken auf Displayglas mit ITO-Galvanikstartschicht diese Anforderungen erfüllen.

Die Untersuchungen zur Optimierung der Startschicht zeigen, dass Veränderungen am Prozessdruck und an der Prozessgaszusammensetzung die Haftung zwischen dem galvanisch abgeschiedenen Gold und ITO wesentlich beeinflussen.

Es wurde beobachtet, dass mit Druckerhöhung und Argon als Prozessgas die Haftung des Resists SU-8 und der Goldabsorberstrukturen verbessert wurden. Messungen am AFM¹ bestätigen, dass dies auf größere Oberflächenrauigkeiten der ITO-Schicht zurückzuführen ist und diese die mechanische Adhäsion begünstigen. Es wurden Rauigkeiten (RMS) bis zu 12 nm erreicht.

Die bei einem Argonpartialdruck von $1 \cdot 10^{-2}$ mbar gesputterten Proben mit dem größten gemessenen RMS-Wert weisen zwar die besten Haftungen auf dem Displayglas auf, zeigten aber eine schlechte Haftung von Gold auf ITO. Bei noch höheren Drücken steigt die Prozesszeit erheblich an und der Arbeitsdruck der Anlage bewegt sich nahezu am Limit.

Die Messungen der Korngrößen zeigen, dass mit Druckerhöhung beim Sputterprozess auch die Korngröße abnimmt. Dabei zeigen Proben mit Korngrößen des ITO zwischen 50 nm und 60 nm die beste Haftung.

Durch Variation der Prozessparameter konnte eine optimierte und eine elektrisch leitfähige ITO-Oberfläche erzeugt werden, so dass die mechanische und spezifische Adhäsion groß genug ist, um auf diesen Gold mit sehr guter Haftung galvanisch abscheiden zu können.

Eine Röntgenmaske mit 100 µm dicken Displayglas als Trägermembran, 200 nm ITO als Platingbase und 35 µm SU-8 als Resist weist eine optische Transmission von 64 % bis 78 % in einem Wellenlängenbereich von 510 nm bis 920 nm auf. Durch die Verwendung von PMMA-Resists, die auch wieder entfernt werden können, kann die optische Transmission der Röntgenmaske sogar auf 84 % bis 92 % gesteigert werden.

¹ Atomic Force Microscope

Lithographie mit Röntgenstrahlung

H.-U. Scheunemann, H. Köhrich, A. Barth, B. Löchel

BESSY GmbH, Anwenderzentrum Mikrotechnik, Albert-Einstein-Str. 15, 12489 Berlin

Bei BESSY stehen derzeit zwei Beamlines für die Röntgentiefenlithographie zur Verfügung. Die Belichtungsmöglichkeiten und die apparativen Voraussetzungen an den beiden Strahlrohren sind sehr unterschiedlich, die Auswahl erfolgt entsprechend den Anforderungen.

Das Synchrotronlicht eines Strahlrohres kommt aus einem Dipolmagneten mit einem Magnetfeld von 1.3 Tesla. Dies entspricht einer kritischen Photonenenergie von 2.5 keV ($\lambda_c=0.5$ nm). Damit ist diese Strahlungsquelle insbesondere für Standardbelichtungen geeignet. (Resisttiefe: PMMA bis 0.6 mm, SU8 bis 2 mm).

Bei der zweiten Strahlungsquelle sind zwei verschiedene Quellen benutzbar. Eine Möglichkeit ist der Wellenlängenschieber (WLS 4 Tesla). Die kritische Energie wird damit auf 7.7 keV ($\lambda_c=0.16$ nm) erhöht. Diese Quelle ist besonders für die Ultratiefenlithographie geeignet. (Resisttiefe: PMMA bis 5 mm).

Wird der Wellenlängenschieber ausgeschaltet, können noch die Steerer-Magnete (~ 0.4 Tesla) zur Lichterzeugung genutzt werden. Dadurch erniedrigt sich die kritische Energie auf 0.8 keV ($\lambda_c=1.5$ nm). Diese Strahlung eignet sich besonders für hochpräzise Abbildungen z.B. für die Maskenkopie. (Resisttiefe bis 100 μ m).

Die Belichtungsapparaturen sind ebenfalls unterschiedlich, das Dipolstrahlrohr ist mit einem Jenoptik Scanner DEX02 ausgerüstet. Dieses Gerät ist mit einer Kipp-Drehvorrichtung und einem Justiersystem ausgestattet. Am anderen Strahlrohr steht eine ältere Version DEX01. Dieser Scanner ist nun nachträglich mit einer Kipp- Drehvorrichtung ausgerüstet worden.

Für zahlreiche Anwendungen sind Schrägbelichtungen notwendig wie z.B. Auskoppelspiegel in Anwendungen im optischen Bereich, Präge- und Spritzgussformen mit leicht schrägen Kanten zur besseren Ablösung der Formkörper usw. Deshalb wurde auch der "ältere" Scanner nachträglich im Rahmen eines Projektes mit einer unabhängigen Kipp- und Drehvorrichtung ausgestattet.

Erste Schrägbelichtungen wurden schon früher vorgenommen. Sie sollten die Leistungsfähigkeit des Systems zeigen. Dazu wurden Belichtungen in 340 μ m dicke PMMA-Platten unter einem Einfallswinkel von 45° durchgeführt. Abb. 1 zeigt eine dieser 340 μ m hohe Strukturen. Die erhaltenen Ergebnisse hinsichtlich Kantensteilheit und Kantenrauigkeit entsprechen den Erfahrungswerten wie sie für diese Materialien erwartet werden.

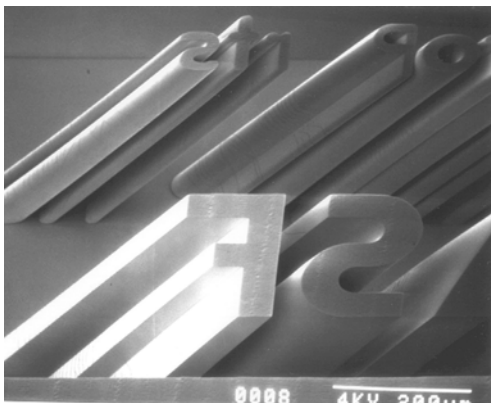


Abb. 1: Schrägbelichtung unter 45° belichtet in 340 μ m dicken PMMA

Kipp- und Drehmodul

Im Rahmen dieses Projekts wurde der Scanner DEX01 mit einer Vorrichtung ausgerüstet, mit der eine ähnliche Performance wie beim DEX02 erreicht wird. Die Kipp- und Drehvorrichtung kann in den vorhandenen Scanner ohne Umbaumaßnahmen bei Bedarf ein- und ausgebaut werden. Sämtliche anderen Funktionen des Scanners bleiben unverändert. Auch in die Steuerung des Scanners wird nicht eingegriffen. Die Kipp- und Drehvorrichtung hat ihre eigene unabhängige Steuerung. Die Sicherheit ist mechanisch gewährleistet.

Abbildung 2 zeigt das Gerät in seiner technischen Realisierung. Zu sehen ist die Montageplatte, mittels derer die Vorrichtung anstelle der bisherigen Masken- und Resistaufnahme in den Scanner eingeschraubt wird. Die Haltevorrichtung für Maske und Substrat ist in Drehkranzgehäuse eingelassen, die eine Drehung um die Strahlachse von 360° erlaubt. Dieses Gehäuse kann mittels des Kippmotors um $\pm 90^\circ$ gekippt werden. Die Vorrichtung ist so gebaut, dass beide Bewegungen unabhängig von einander sind. Zur Bestückung der Vorrichtung wird der Masken-Substrathalter aus dem Drehkranzgehäuse entnommen. Die Maske wird mit Hilfe eines Spannbügels im Maskenhalter fixiert; ebenso das Substrat in seinem Halter. Beide Teile werden nach der Bestückung zusammengeführt und mittels der Klemm- und Zentriervorrichtungen in festem Kontakt zu einander gebracht. Den Abschluss bildet eine Kühlplatte, an die ein steckbarer Kühlwasseranschluss angebracht ist. Diese Kühlung ist erforderlich um das Substrat und damit die Maske während der Belichtung auf nahezu konstanter Temperatur zu halten und damit thermisch bedingte Verzüge zu minimieren.

Abbildung 3 zeigt die Kipp- und Drehvorrichtung wie sie im Scanner eingebaut ist. Dabei ist ein Kippwinkel von 50° dargestellt.

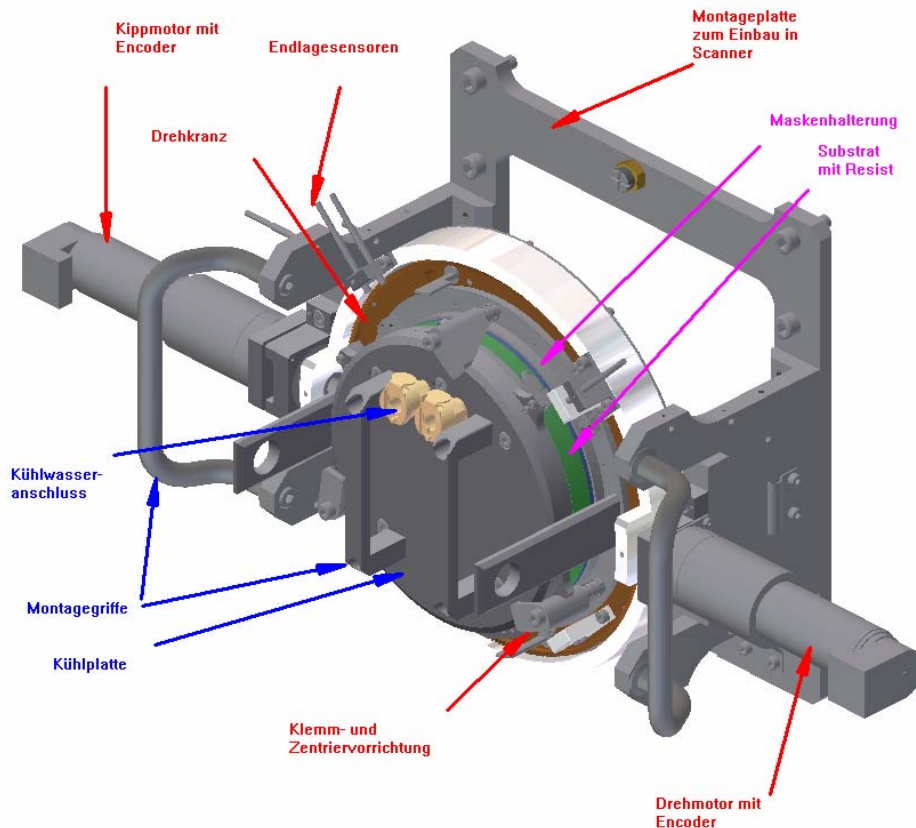


Abb.1: Technische Realisierung des Einbaumoduls für Kippung und Drehung im Scanner DEX 01

Datei: (Main assy)08.jpg
Beschreibung: Hauptbaugruppe
Betriebsposition
Drehung=0°
Kippung=50°
Lage=+65 mm

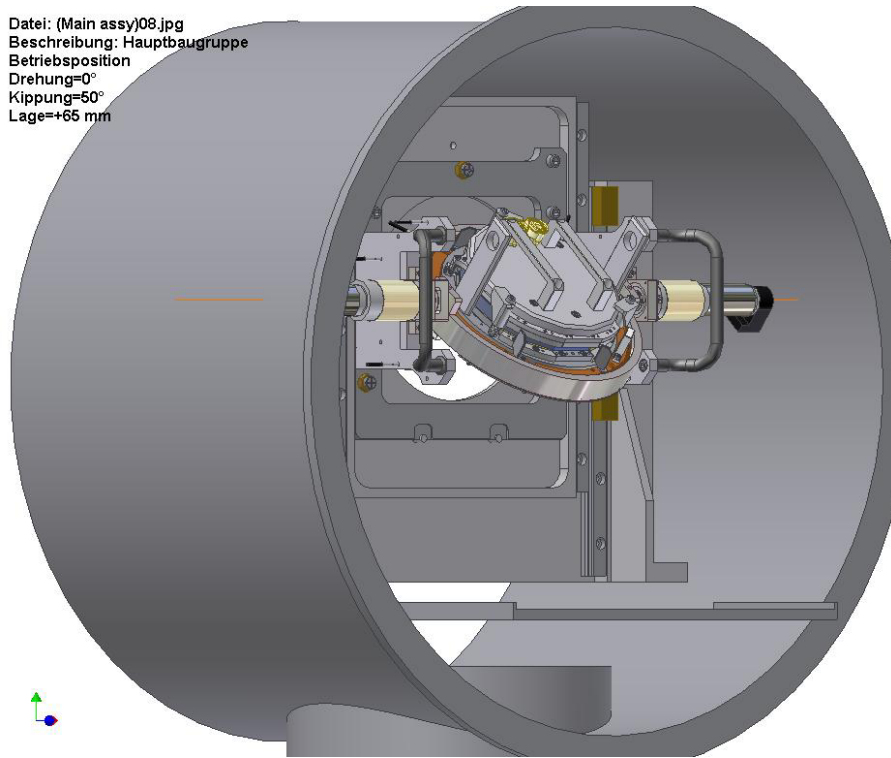


Abb. 3: Kipp- und Drehmodul unter 50° Kippung im Scanner Dex 01

Strahldiagnostik.

Weitere Neuerungen ergaben sich in der Strahldiagnostik. Im Rahmen einer Diplomarbeit wurde dazu ein Strahlprofilmessgerät entwickelt. Dies Gerät besteht aus einem x-y-Schlitten mit Hilfe dessen eine röntgenempfindliche Diode im Strahl bewegt werden kann. Mit Hilfe dieses Geräts ist eine automatische Vermessung des Strahlprofils möglich. Abbildung 4 zeigt die Messvorrichtung, die sehr einfach in beide Scanner eingebaut werden kann.

Dieses Gerät steht auch für andere Gruppen zur Verfügung, die Röntgenlithographie betreiben.

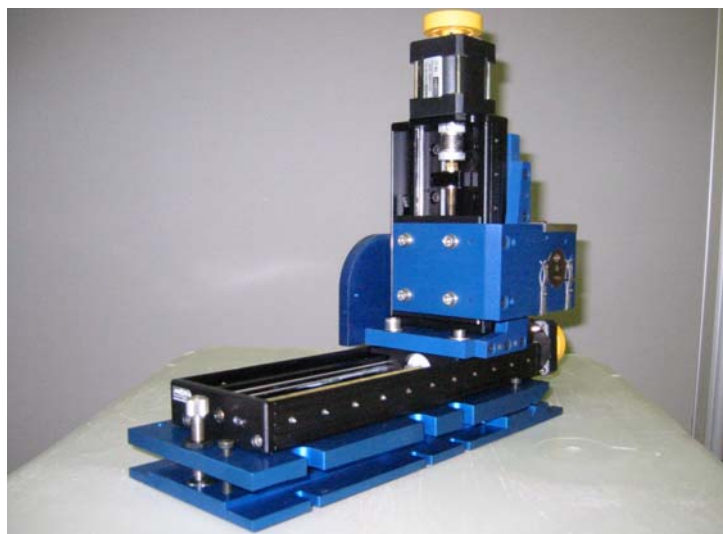


Abbildung 4: X-Y-Tisch der Vorrichtung zum Messen des Strahlprofils

Photophysics of Pyrrolobenzenes

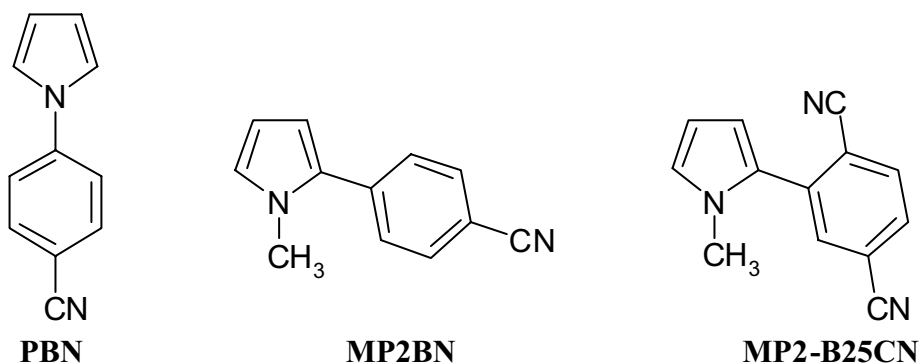
S. Murali^{a)}, Wolfgang Rettig^{a)} and René Lapouyade^{b)}

^{a)} *Institut für Chemie, Humboldt-Universität zu Berlin,
Brook-Taylor-str. 2, D-12489 Berlin, Germany*

^{b)} *Ecole Nationale Supérieure de Chimie et de Physique de Bordeaux
16 avenue Pey-Berland, F-33607, Pessac Cedex, France*

INTRODUCTION

The photophysics of donor-acceptor substituted benzenes are of great interest in the study of Intramolecular charge transfer (ICT) states. These states are commonly observed in N-phenylpyrrole (PBN) and several sterically hindered derivatives.¹ These compounds showed a large fluorescence red shift in medium and strongly polar solvents. Phenyl pyrroles contain an sp² hybridised nitrogen, thus the inter-moiety twist angle ϕ is better defined, and these derivatives can populate the twisted intramolecular charge transfer (TICT) state in a twisted geometry close to $\phi=90^\circ$. This TICT emission is usually connected with a reduced value of the transition moment due to the small π overlap in the twisted arrangement of the chromophores. In this aspect, MP2BN and MP2-B25CN have been synthesized and characterized photophysically, and have been compared with PBN.



Scheme 1. Molecular structures and their abbreviated formulas of the compounds investigated in the text.

RESULTS AND DISCUSSION

Fig. 1. shows the steady state absorption and fluorescence spectra of the investigated compounds in the solvents of low polarity, hexane and high polarity, acetonitrile. The maxima of both absorption and emission of MP2BN and MP2-B25CN significantly red-

shifted with respect to the model compound (PBN) in hexane and acetonitrile indicating the stabilization of the highly polar emitting state. The emission spectrum of MP2BN in acetonitrile is significantly blue shifted in comparison to PBN due to the different orientation of the conformer. The data below show that this is due to a different nature of the CT-state.

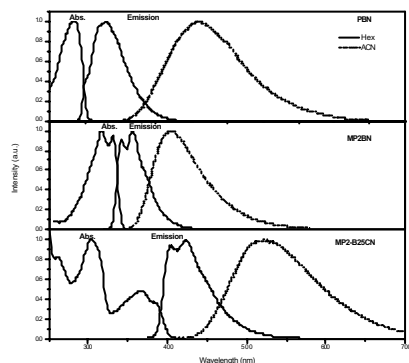


Fig. 1. Normalised absorption and fluorescence spectra of PBN,MP2BN and MP2-B25CN in hexane and acetonitrile.

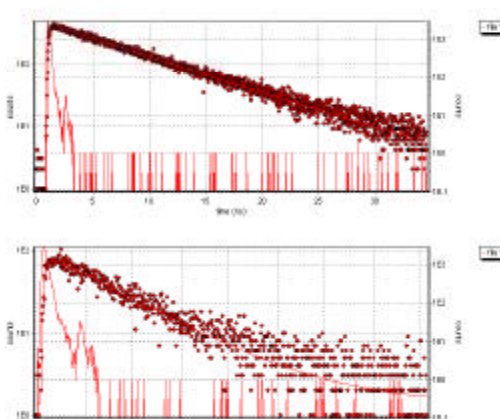


Fig. 2. Fluorescence decay curves of MP2-B25CN in n-hexane (above) and acetonitrile (below).

Fig. 2. exhibits the time resolved measurements carried out at BESSY.

With the aid of lifetime and quantum yield values, both radiative and non radiative rate constant have been calculated and are listed in Table 1. The radiative rate constants in acetonitrile are below 10^7 s^{-1} in PBN and MP2-B25CN indicating a forbidden emission from a TICT state whereas in the case of MP2BN the CT emission is tenfold more allowed. We assign it to a CT-state with partial twisting and mesomeric stabilization. The second cyano group in MP2-B25CN lowers the TICT state below the mesomeric CT-state and thus converts

Compounds	Sol	Φ_f	τ_f/ns	k_f/s^{-1}	k_{nr}/s^{-1}	the emission to forbidden TICT-emission.
PBN	Hex	0.028	2.42^1	1.16×10^7	4.0×10^8	
	ACN	0.036	8.20^1	0.43×10^7	1.2×10^8	
MP2BN	Hex	0.92	1.8	5.11×10^8	4.4×10^7	
	ACN	0.51	5.4	0.94×10^8	9.0×10^7	
MP-B25CN	Hex	0.378	7.47	5.06×10^7	8.3×10^7	
	ACN	0.024	2.78	0.86×10^7	34.9×10^7	

Table 1. Quantum yields, lifetimes and rate constants of PBN, MP2BN and MP2-B25CN in n-hexane and acetonitrile.

REFERENCES

- (1) Cornelissen-Gude, C.; Rettig, W. *Journal of Physical Chemistry A* **1998**, *102*, 7754.

Model Compounds for the Study of the Photochemical Mechanism and the Spectral Tuning in Photoactive Yellow Protein

Hani El-Gezawy^{a)}, Wolfgang Rettig^{a)}, Andrzej Danel^{b)}

^{a)} Institut für Chemie, Humboldt-Universität zu Berlin, Brook-Taylor-str. 2, D-12489 Berlin, Germany

^{b)} H. Kollataj University of Agriculture, Department of Chemistry, Mickiewicz Ave. 24/28, 30-059 Cracow, Poland

Introduction:

The Photoactive Yellow Protein (PYP) is a small water-soluble protein found in the purple sulfur bacterium *Ectothiorhodospira halophila*. PYP is thought to be the photoreceptor for the negative phototaxis of the host bacteria [1]. The chromophore in PYP is a simple donor-acceptor substituted benzene derivative, the thioester of PYPE-H, yet it shows a remarkable spectral tuning of its absorption in response to the surrounding protein environment [2, 3] (Fig. 1). The isomerization capability may strongly depend on the D-A strength: the latter is stronger in $-O^-$ than OH and OCH_3 . We plan to compare with a $N(CH_3)_2$ donor. Here first steps are shown for selective bridging of the flexible bonds to quantify the tendency for double and single bond isomerization.

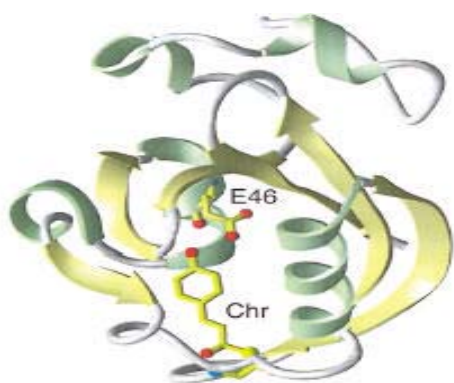


Fig. 1. Overall view of the PYP ground state structure [4].

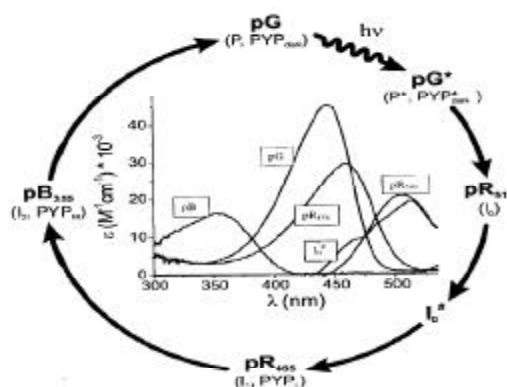
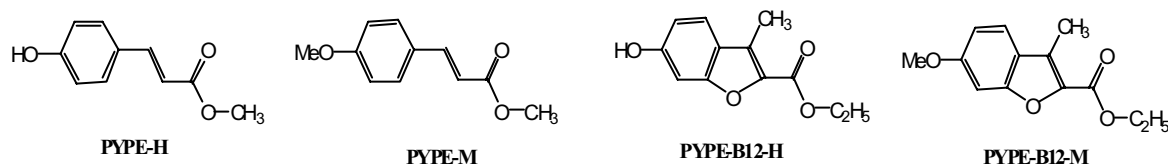


Fig. 2. Overview of the photocycle of PYP [5].

When the chromophore absorbs light this leads to excited state formation, followed by a series of intermediates leading back to the starting material as seen in Fig. 2. This photocycle of PYP proceeds by changing the structure of the twisted ethylene bond of the chromophore. Moreover, the changes of absorption spectra during the photocycle (Fig. 2) are connected to the change of the donor and the environment of the chromophore.

The Investigated Model Compounds:



We compared the nonradiative decays of flexible and rigidized PYP-models by measuring lifetimes and quantum yields at low temperatures.

Temperature Dependence of the Fluorescence Spectra:

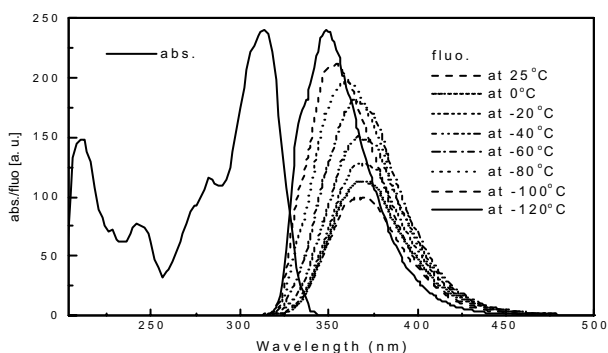


Fig. 3. Absorption spectrum at room temperature and Fluorescence emission spectra of PYPE-B12-H at different temperatures in ethanol

With decreasing temperature the fluorescence intensity increases, and the Stokes shift decreases (Fig. 3).

The fluorescence decay at 153 K (-120 °C) was performed at different emission wavelengths in the rather broad emission spectrum of PYPE-B12-H in ethanol resulting in a single exponential decay with the same time constant. This excludes several emissive products in slow equilibrium.

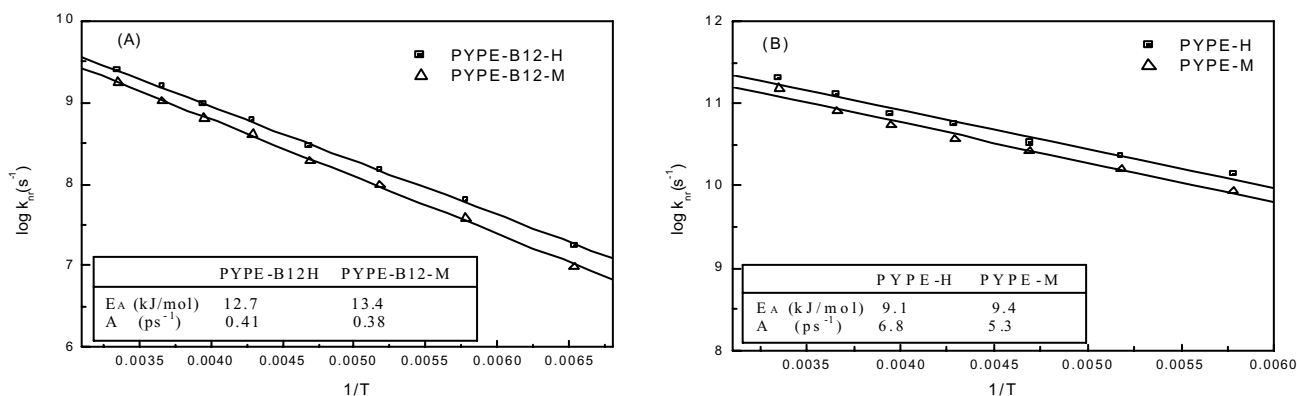


Fig. 4. Arrhenius plots of the nonradiative decay rate constants derived from the fluorescence quantum yields and constant k_f according to τ_f at 77K for (A) PYPE-B12-H and PYPE-B12-M, (B) PYPE-H and PYPE-M in ethanol.

The Arrhenius plots, Fig. 4, are linear for all compounds within the investigated temperature range. The significantly larger E_A values for the bridged compounds indicate the involvement of a different deactivation process. Note, however, that the rate constants are significantly smaller

Conclusion:

Quite unexpectedly, also the bridged compounds PYPE-B12H and PYPE-B12-M, which cannot isomerize, show some definite temperature dependent nonradiative losses. However, the activation energy is larger than in the case of the unbridged compound PYPE-H and PYPE-M.

References:

- [1] W.W. Sprenger, W.D. Hoff, K.J. Hellingwerf, *J. Bacteriol.* 175 (1993) 3096.
- [2] A.R. Kroon, W.D. Hoff, H.P.M. Fennema, J. Gijzen, G.J. Koomen, J.W. Verhoeven, W. Crielaard, K.J. Hellingwerf, *J. Biol. Chem.* 271 (1996) 31949.
- [3] M. Yoda, H. Houjou, Y. Inoue, M. Sakurai, *J. Phys. Chem. B* 105 (2001) 9887.
- [4] R. Brudler, R. Rammelsberg, T.T. Woo, E.D. Gotzoff, K. Gerwert, *Nature Structural Biology* 8 (2001) 265.
- [5] K.J. Hellingwerf, J. Hendriks, T.H. Gensch, *J. Biol. Phys.* 28 (2002) 395.
- [6] M. Sczepan, W. Rettig, *Phys. Chem. Chem. Phys.* 3 (2001) 3555.

PHOTOABSORPTION SPECTROSCOPY AT MEDIUM RESOLUTION. THE C₂HXYZ (X,Y,Z = H, F, Cl and/or Br) MOLECULES.

R. Locht¹, B. Leyh¹, H.W. Jochims² and H. Baumgärtel².

¹Département de Chimie, Université de Liège, Institut de Chimie, Bât. B6c,
Sart-Tilman par B-4000 Liège 1, Belgium.

²Institut für Physikalische Chemie, Freie Universität Berlin, Takustrasse 3,
D-14195 Berlin, Germany.

Since several years we proceed with the systematic investigation of halogenated derivatives of ethylene (C₂H₄). The photoabsorption and/or the photoionization of C₂H₃F and 1,1-C₂H₂F₂ [1], C₂H₃Cl [2,3] and C₂H₃Br [4,5] has been studied. The dissociation dynamics of the C₂H₃F⁺, 1,1-C₂H₂F₂⁺ [1] and C₂H₃Br⁺ [6] cations were investigated. The photoabsorption and photoionization spectroscopy of C₂H₂Cl₂ [7] and C₂H₂FCl [8] have also been examined by synchrotron radiation.

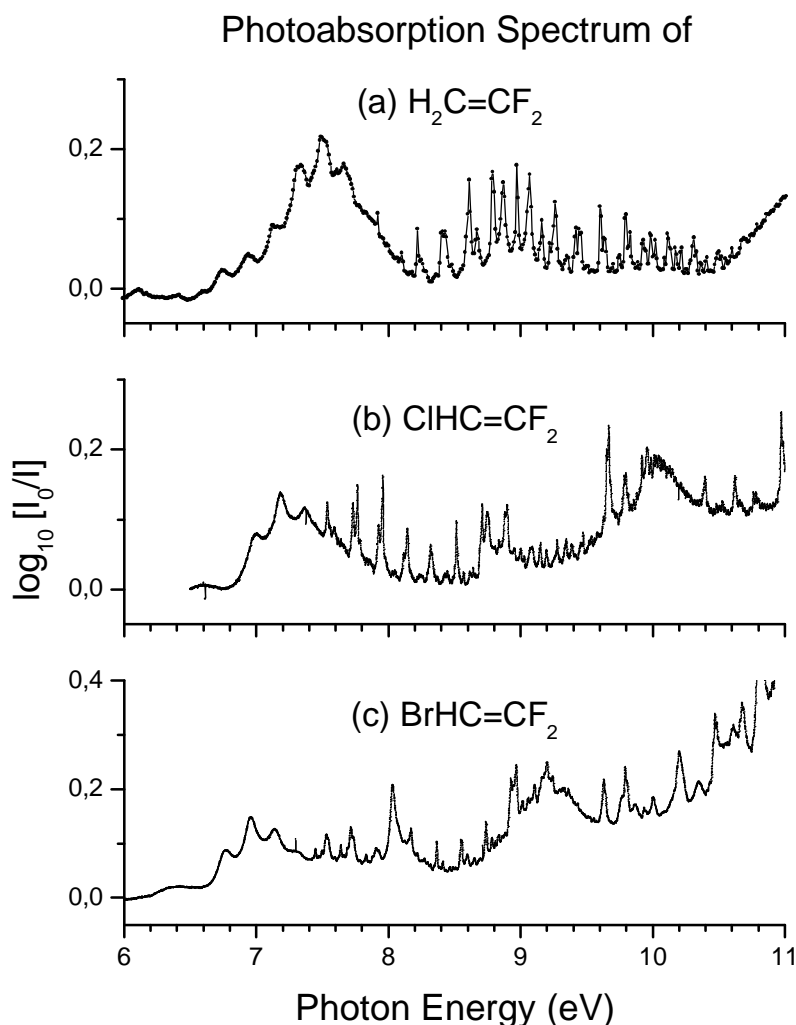


Fig.1 : Photoabsorption spectra in the 6-11 eV photon energy range : (a) 1,1-difluoro- (b) 1,1-difluoro-2-chloro- and (c) 1,1-difluoro-2-bromo-ethylenes.

Recently, for the last two mentioned compounds, the photodissociation of the cations and the kinetic energy distribution of the most abundant fragments have been measured by fixed wavelength photoionization (HeI, NeI and ArI/ArII resonance lines) in our laboratory.

We already measured their threshold-(TPES) and HeI-photoelectron spectra. The photoabsorption spectra recorded earlier with the 1.5m-NIM monochromator at BESSY I were of too low resolution. The aim of this work was to obtain the desired resolution, i.e. at least comparable to that obtained in the TPES spectra.

With the help of the 3m-NIM (on the 3m-NIM-2 beamline), equipped with the 2 400 l/mm Pt-grating, we didn't succeed to record any reliable photoabsorption spectrum, even over an energy range as small as 1 eV.

This experimental problem has been observed in the 5-25 eV region. Therefore, we switched over to the 600 l/mm Al-grating coated with a MgF₂ layer. An important disadvantage of this type of grating is the presence of a reflectivity gap between 15-18 eV photon energy. Entrance and exit slit widths were adjusted at 25 μm and 10 μm respectively. Under these experimental conditions a resolution of 5000 is obtained.

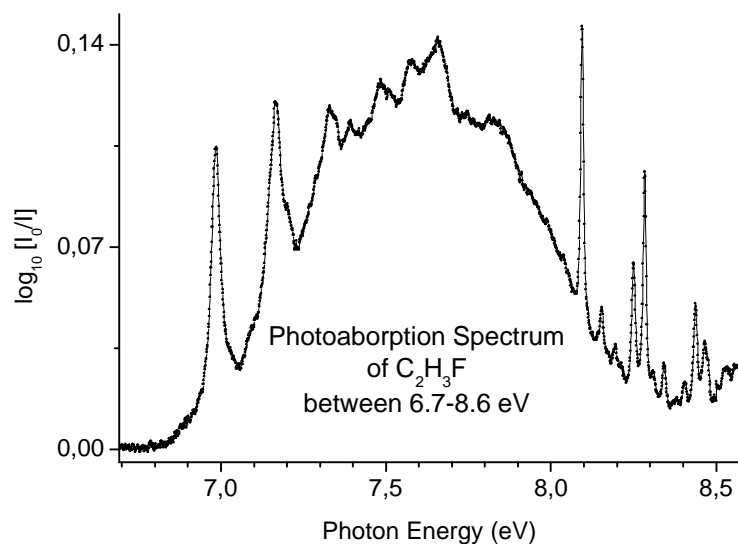


Fig.2 : Detail of the C₂H₃F photoabsorption spectrum between 6.7-8.6 eV photon energy.

Fig.1 shows typical photoabsorption spectra of 1,1-C₂H₂F₂, 1,1-difluoro-2 chloro- and 1,1-difluoro-2-bromoethylene between 6-11 eV photon energy. The spectra have all been recorded between 5-25 eV photon energy. The resolution achieved in the present experiment, as shown in fig.2, allows us to reconsider the Rydberg series assignments and to make a detailed vibrational analysis in most cases, for the first time. Many spectra show extended vibrational structures, with long progressions, at high energies, i.e. above 12 eV excitation energy. The analysis of the spectra

leading to the assignment of the Rydberg transitions is in progress.

Acknowledgment.

R.L. and B.L. gratefully acknowledge the Communauté Française de Belgique for the “Actions de Recherche Concertée” (A.R.C.) contract.

References.

- [1]. F. Güthe, R. Locht, B. Leyh, H. Baumgärtel and K.M. Weitzel, J. Phys.Chem. 103 (1999) 8404.
- [2]. R. Locht, B. Leyh, K. Hottmann, and H. Baumgärtel, Chem.Phys. 220 (1997) 207.
- [3]. R. Locht, B. Leyh, K. Hottmann and H. Baumgärtel, Chem.Phys. 220 (1997) 217.
- [4]. A. Hoxha, R. Locht, B. Leyh, D. Dehareng, K. Hottmann and H. Baumgärtel, Chem.Phys. 256 (2000) 239.
- [5]. A. Hoxha, R. Locht, B. Leyh, D. Dehareng, K. Hottmann, H.W. Jochims and H. Baumgärtel, Chem.Phys. 260 (2000) 237.
- [6]. A. Hoxha, R. Locht, A.J. Lorquet, J.C. Lorquet and B. Leyh, J. Chem.Phys. 111 (1999) 9259.
- [7]. G. Tornow, R. Locht, R. Kaufel, H. Baumgärtel and H.W. Jochims, Chem.Phys. 146 (1990) 115.
- [8]. R. Locht, B. Leyh, K. Hottmann and H. Baumgärtel, BESSY Jahresbericht (1999) 150.

HIGH RESOLUTION PHOTOABSORPTION SPECTROSCOPY OF CH_3Br , CH_3I AND THEIR ISOTOPOMERS.

R. Locht¹, B. Leyh¹, H.W. Jochims² and H. Baumgärtel².

¹ Département de Chimie, Université de Liège, Institut de Chimie, Bât. B6c, Sart-Tilman par B-4000 Liège 1, Belgium.

² Institut für Physikalische Chemie, Freie Universität Berlin, Takustasse 3, D-14195 Berlin, Germany.

In the latest issue of the BESSY Jahresbericht [1] we reported on the investigation and testing of the newly commissioned 3mNIM monochromator on the 3m-NIM-2 beamline at BESSY II. The aim of this preliminary work was to evaluate the performance of this instrument which has to provide us with high resolution photoabsorption spectra.

The present work has been achieved with the same experimental setup, i.e (i) a 30 cm long absorption cell mounted on the monochromator equipped (ii) with a 2 400 l/mm Pt grating. Most of the time, the entrance and exit slits were maintained at 25 μm and 40 μm respectively. The absorbance [$\log_{10} (I_0/I)$] is obtained by scanning successively the absorption spectrum of the considered compound and the transmission spectrum of the monochromator.

First, the spectra of CH_3Br and CD_3Br have been measured between 5-25 eV photon energy, at a "coarse" level. A detailed Rydberg series analysis has been performed. Several series, corresponding to $2e \rightarrow ns$ and np transitions, have been assigned. For the first time, two np -type transitions, i.e. transitions to np_a1 and npe orbitals have been assigned on the basis of characteristic quantum defects. Furthermore, fairly extended nd - and nf -type transitions account for many lines on the high energy side of the spectrum. All these Rydberg transitions are observed twice, converging to the two spin-orbit split 2E ionic states.

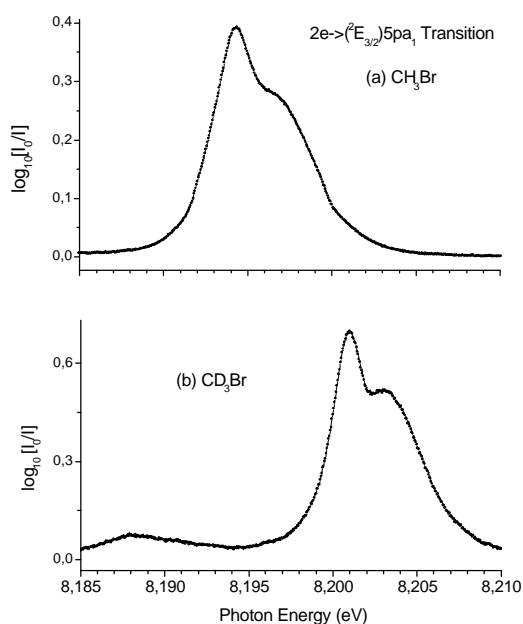


Fig. 1: $2e \rightarrow ({}^2E_{3/2}) 5p_a1$ line profiles in CH_3Br and CD_3Br

In the "coarse" photoabsorption spectrum, fine structures could be guessed for several lines on a meV scale. Therefore, short spectral regions of interest were scanned with 50 μeV intervals. Fig.1 shows a typical example of the observed line profile corresponding to the $2e \rightarrow ({}^2E_{3/2}) 5p_a1$ Rydberg transition in both CH_3Br and CD_3Br . Such a manifold of these lines is highlighted for the first time. Remarkably, the same type of manifold has been observed for the $2e \rightarrow ({}^2E_{1/2}) 5p_a1$ line in CD_3Br , whereas this feature is absent in CH_3Br . The structures are separated by 2.0-4.0 meV (16-32 cm^{-1}). The lines corresponding to $2e \rightarrow ({}^2E_{3/2}/{}^2E_{1/2}) npe$ Rydberg transitions don't show any of these structures at the same scale. On the other hand, in the same way, the

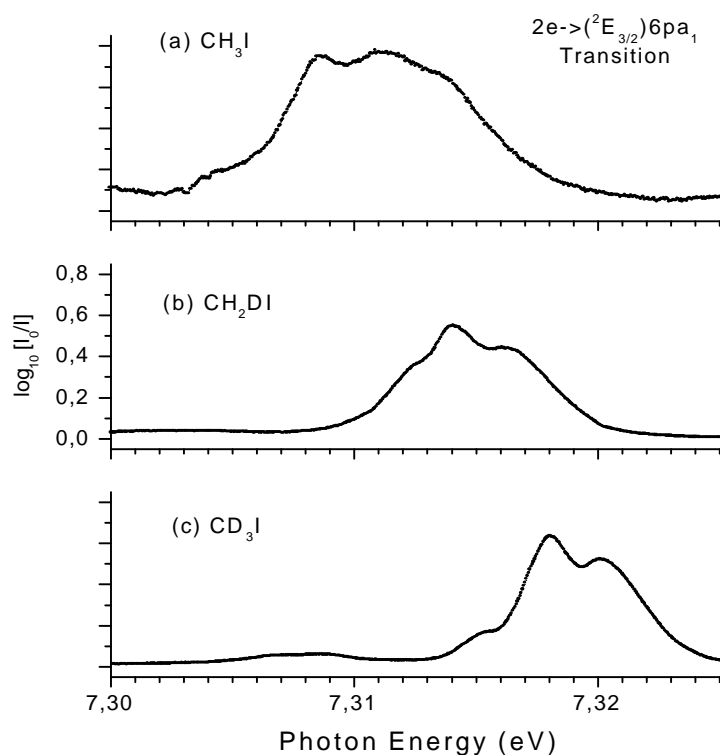


Fig. 2 : $2e \rightarrow ({}^2E_{3/2}) 6p_{a_1}$ line profiles in CH_3I , CH_2DI and CD_3I .

nd- and nf-type transitions show fine structures with energy differences ranging from 4.0-12.0 meV ($32\text{-}96\text{ cm}^{-1}$).

The photoabsorption spectrum of CH_3I , and of its two isotopomers CH_2DI and CD_3I , has been recorded under the same experimental conditions between 5.0-10.5 eV photon energy in a “coarse” scan and several fine scans. This enabled us to resolve Rydberg transitions characterized by high principal quantum numbers, i.e. $n \geq 30$. Typical results of the fine scans are displayed in fig.2 where also, for the first time, the manifold of the $2e \rightarrow ({}^2E_{3/2}) 6p_{a_1}$ line is highlighted for the three isotopomers. Well resolved

structures are observed with 1.6-3.2 meV ($13\text{-}25\text{ cm}^{-1}$) energy spacings. It has further to be noticed that the heaviest isotopomer exhibits the narrowest line profiles and the line shape drastically changes with the number of isotopic substituents.

The magnitude of the splittings observed in the $2e \rightarrow np_{a_1}$ lines is smaller by one order than those measured e.g. in the $2e \rightarrow nd$ lines observed in the spectrum of CH_3I in this work. In this latter case the fine structure was ascribed to the perturbation of the Rydberg electron by the quadrupole moment of the 2E ionic core [2]. The test of this hypothesis is in progress. On the other hand, the symmetry lowering from C_{3v} to C_s upon excitation of a $2e$ electron to a np_{a_1} orbital causes the splitting of degeneracies.

Acknowledgment.

R.L. gratefully acknowledges the Bundes Ministerium für Forschung und Technologie for a grant. R.L. and B.L. wish to thank the Communauté Française de Belgique for the “Actions de Recherche Concertée” (A.R.C.) contract.

References.

- [1]. R. Locht, H.W. Jochims and H. Baumgärtel, BESSY Jahresbericht, **2002**,
- [2]. B.P. Tsai and T. Baer, J.Chem.Phys. 61 (**1974**) 2047.

Rotating the linear polarization at UE52: A new approach to determine the angular distribution of photoelectrons

K. Godehusen¹, Ph. Wernet¹, T. Richter², P. Zimmermann², M. Martins³

¹BESSY GmbH ²Institut für Atomare Physik, TU Berlin ³Institut für Experimentalphysik, Universität Hamburg

The APPLE-II type undulator UE52 (magnetic period length 52 mm) has four identical rows of permanent magnets, two on top and two below the stored electron beam. Two of these rows can be moved along the direction of the electron beam (determined by the so-called 'shift parameter'). This makes it possible to operate the undulator in a way that it produces circularly ('parallel mode') or linearly ('antiparallel mode') polarized synchrotron radiation. The special feature of this type of undulator is that the angle of polarization can be continuously tuned to any value between 0° and 90° with respect to the horizontal plane. Whilst rotating the angle the focus of the SR stays fixed in space within 2 μm. This is negligible compared to the size of the light spot, therefore for any polarization angle the identical sample volume is probed.

A typical time needed for changing between two polarization angles is below 15 seconds. The experimental setup is shown in figure 1.

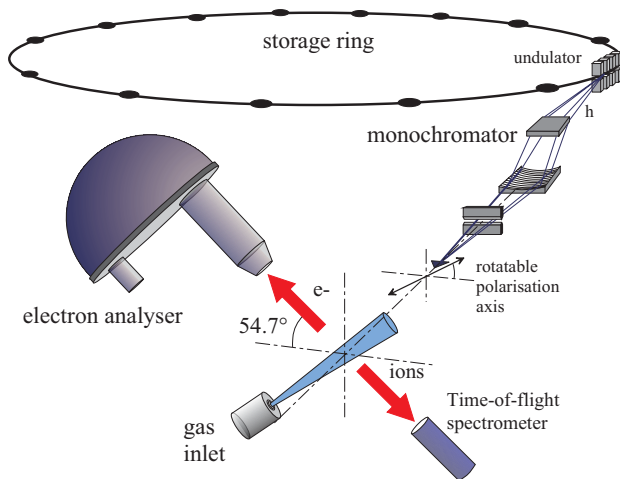
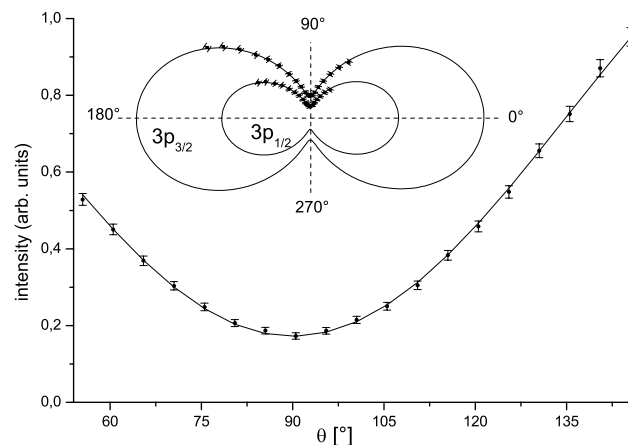


Figure 1: *The photoelectron spectra were recorded by a Scienta SES-2002 hemispherical electron analyzer mounted under the magic angle with respect to the horizontal plane. In addition, the charge and mass distribution of the photofragments could be analyzed by a time-of-flight ion spectrometer.*

The measurement of the electron angular distribution for the Krypton 3p photoemission is depicted in figure 2. It demonstrates the high precision of the method used. For details on the method and the results for Kr see [1].

Figure 2: *Main panel: Cartesian plot of the angular distribution of the Kr 3p_{1/2} photoelectrons as a function of the angle θ at a photon energy of 500 eV together with the fitted angular distribution curve. Insert: Polar plot of the angular distributions for 3p_{1/2} and 3p_{3/2} at 500 eV (data points and fitted curves).*



Our new experimental approach enabled us to measure the asymmetry parameter β for the 2p photoemission of free Mn atoms with high precision and multiplet resolved. As a result it could be shown that for Mn the values for β are uniform over the whole multiplet.

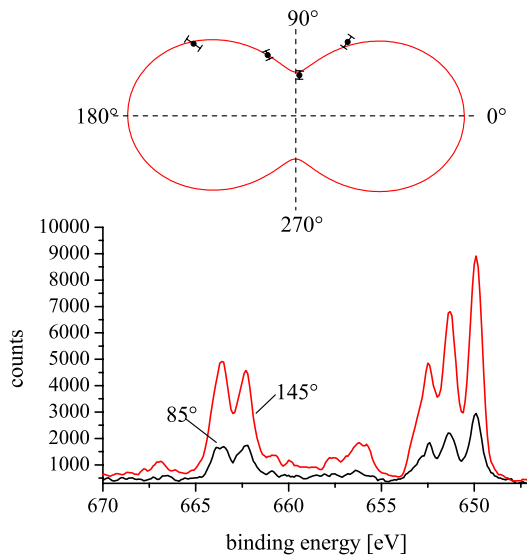
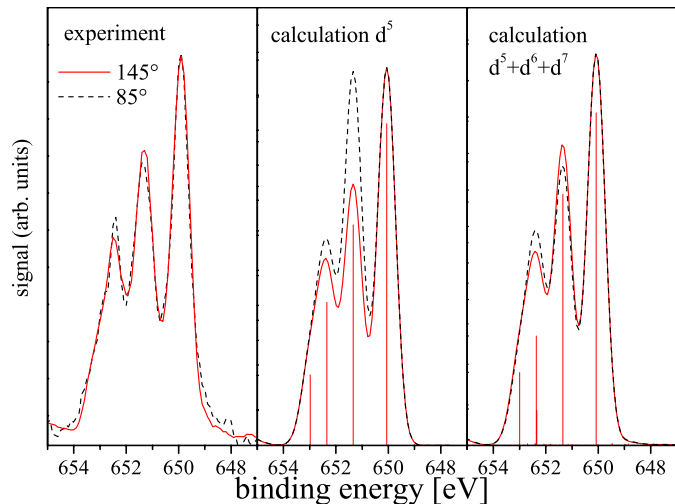


Figure 3: *Bottom: 2p photoelectron spectrum of Mn at 850 eV photon energy, measured for the angles 85° and 145°. Top: polar plot of the intensity of the strongest Mn photoemission line (at 650.06 eV binding energy), for four different angles.*

The single configuration approximation calculations, which up till now have been sufficient to describe the cross section and the dichroism of free Mn atoms, fail to reproduce the values for β . Additional configurations had to be included. This means that multiplet splitting and valence shell recoupling determine the shape of the photoelectron and dichroism spectra while the dynamics of the 2p photoionization process are more sensitive to configuration interaction.

Figure 4: *Comparison of the single and the multi configuration calculations with the experimental results for Mn. The spectra of the 2p_{3/2} multiplet measured under the angles of 85° and 145° are scaled to the most intense line, the same is done with the calculated results, the bar graphs shown correspond to an angle of 145°.*



For details on the calculations and the results for free Mn and Cr atoms see [2].

[1] K. Godehusen, H.-C. Mertins, T. Richter, P. Zimmermann, M. Martins
Electron-correlation effects in the angular distribution of photoelectrons from Kr investigated by rotating the polarization axis of undulator radiation, Phys. Rev. A **68**, 012711 (2003)

[2] K. Godehusen, Ph. Wernet, T. Richter, P. Zimmermann, M. Martins
Determination of the β parameter for atomic Mn and Cr 2p photoemission: A benchmark test for core-electron photoionization theories, Phys. Rev. A **68**, 052707 (2003)

Photodissociation processes of Rydberg states in N_2 in the exciting-photon energy ranges from 23 eV to 24.3 eV and from 25.6 eV to 26.7 eV

A Ehresmann†, L Werner†, S Klumpp†, S Lucht†,
H Schmoranzer†, S Mickat§, S Kammer§,
R Schill§, K-H Schartner§ and G Reichardt‡

† Fachbereich Physik, Technische Universität Kaiserslautern, D-67653 Kaiserslautern, Germany

§ I Physikalisches Institut, Justus-Liebig-Universität, D-35392 Giessen, Germany

‡ Berliner Elektronenspeicherring-Gesellschaft für Synchrotronstrahlung m.b.H., D-12489 Berlin, Germany

E-mail: arnauld@rhrk.uni-kl.de

It has been recently shown that some neutral photodissociation processes of the O_2 ($c^4 \Sigma_u^-$) $n l \lambda \ ^3 \Sigma_u^-, (v = 0, 1)$ and the CO ($^4 \Sigma_u^-$) $n s \sigma_g \ ^- \Sigma_u^-$ Rydberg states are fragment-state selective (Liebel et al. 2002, Liebel et al. 2001, Liebel et al. 2000, Ukai et al. 1995). The molecules dissociate into neutral fragments where one of the fragments is in a Rydberg state as well and where the effective principal quantum number of the Rydberg electron is conserved during the transition from the molecular Rydberg state to the fragment Rydberg state.

N_2 Rydberg states ($C^2 \ ^- \Sigma_u^+) n s \sigma (v)$ were investigated in the present work using monochromatized synchrotron radiation to clarify whether such a behavior can also be observed in N_2 . Dispersed fluorescence from excited NI fragments in the spectral ranges from 114 nm to 135 nm and simultaneously from 82 nm to 102 nm in the exciting-photon energy ranges from 23 eV to 24.3 eV and from 25.6 eV to 26.7 eV was investigated. The exciting-photon energy ranges were chosen such that they lie just beneath the thresholds for dissociative ionisation into the fragments $NII(^3P) + NI(^4S)$ and $NII(^3P) + NI(^2D)$. In these exciting-photon energy regions intensities from NI fragment fluorescence transitions in the visible region $2p^2(^3P)3s \ ^4P \rightarrow 2p^3 \ ^4S$ and $2p^2(^3P)3d \ ^2P \rightarrow 2p^3 \ ^4S$ and from $2p^2(^3P)nd \rightarrow 2p^3 \ ^4S$ and $2p^2(^3P)ns \rightarrow 2p^3 \ ^4$ in the VUV region were measured as functions of the exciting-photon energy with the very narrow bandwidth of 2meV.

Figure 1 shows a two-dimensional plot of the dispersed fluorescence intensities as a function of both the exciting-photon energy and the fluorescence wavelength in the exciting-photon energy region from 23 eV to 24.3 eV in the two spectral ranges between

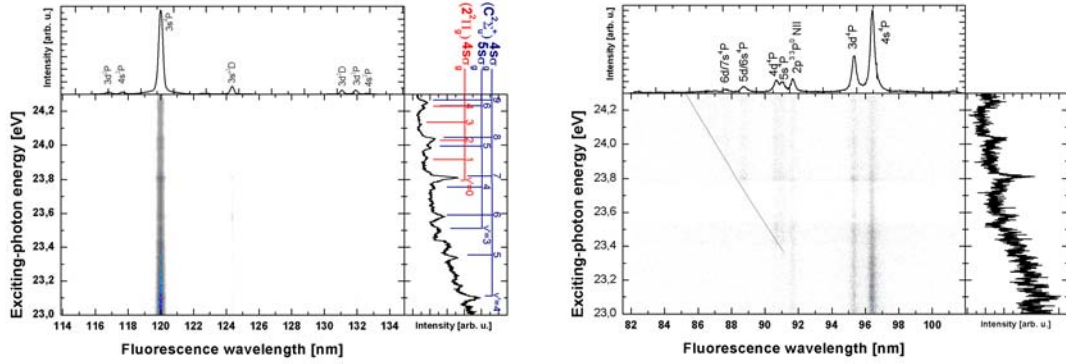


Figure 1. Two-dimensional dispersed fluorescence excitation spectrum of N_2 , normalized for the exciting photon flux. Fluorescence intensities are plotted in a linear 15-step colour scale as a function of the fluorescence wavelength and excitation energy. Upper panels show fluorescence intensities integrated over the exciting-photon energies. Right panels display integrated intensities over the fluorescence wavelength range between 114 and 135 nm as a function of the exciting-photon energy. a) Fluorescence wavelength range between 114 nm and 135 nm. b) Fluorescence wavelength range between 82 nm and 102 nm.

114 nm and 135 nm (Fig. 1a) and between 82 nm and 102 nm (Fig. 1b). The upper panels represent fluorescence intensities integrated over the exciting-photon energies and the right panels display integrated intensities over the fluorescence wavelength range. Vibronic bands of the N_2 ($C^2\Sigma_u^+$) $4s\sigma_g(v)$, $5s\sigma_g(v)$ and ($2^2\Pi_g$) $4s\sigma_g$ progressions according to (Codling 1966) and (Hiyama & Iwata 1993) are indicated as horizontal bars in the right panel of Fig. 1a. These energies clearly correspond to observed peaks in the fluorescence excitation function of Fig. 1a, right hand panel. In Fig. 1b a line has been drawn in corresponding to dissociation limits into fragment pairs $NI\ 2s^22p^3\ ^4S_{3/2}^o + NI\ 2s^22p^3\ ns/nd^4L_J$. The line was calculated according to

$$E_{exc} = E_{Diss} + \frac{hc}{\lambda_{fl}} \quad (1)$$

E_{Diss} corresponds to the dissociation limit into two NI fragments in the ground state $^4S_{3/2}^o$. As is evident from Fig. 1b, all dissociation fragments in Rydberg states are populated right from their dissociation limits. However, a state-selective dissociation of molecular Rydberg states into fragments (with one dissociation fragment in a Rydberg state) where there is a correlation between the Rydberg electron's quantum numbers when going from the molecular Rydberg state to the fragment Rydberg state cannot be identified here. Figure 2 shows a two dimensional plot of the dispersed fluorescence in the exciting energy range between 25.6 eV and 26.7 eV in the same two spectral regions as above. In Fig. 2b a line has been drawn in corresponding to the dissociation limits into the fragments $NI\ 2s^22p^3\ ^2D_{5/2} + NI\ 2s^22p^3\ ns/nd^4L_J$ being calculated according to Eq. 1, however with E_{Diss} corresponding to the dissociation energy into two fragments $NI\ 2s^22p^3\ ^4S_{3/2}^o + NI\ 2s^22p^3\ D_{5/2}$. Again here high intensities are observed just above

the dissociation limits of the Rydberg fragments, however a state-to-state dissociation was not observed.

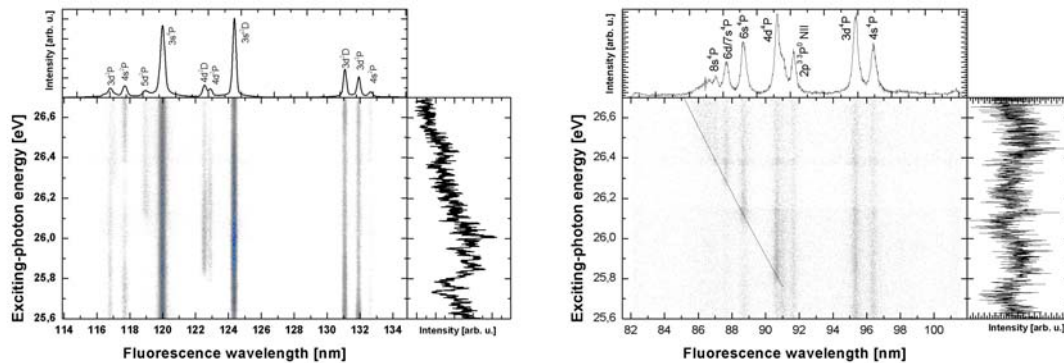


Figure 2. Same as Fig. 1, but for the exciting-photon energy range between 25.5 eV and 26.7 eV.

Acknowledgments

The BESSY staff is gratefully acknowledged for their continuous and very effective support. This work has been supported by the Deutsche Forschungsgemeinschaft (DFG) under the contract number DFG Schm 379/11.

Codling K 1966 *Astrophys. J.* **143**, 552.

Hiyama M & Iwata S 1993 *Chem. Rev. Lett.* **211**, 319.

Liebel H, Ehresmann A, Schmoranzer H, Demekhin P V, Lagutin B M & Sukhorukov V L 2002 *J. Phys. B: At. Mol. Opt. Phys.* **35**, 895–905.

Liebel H, Lauer S, Vollweiler F, Müller-Albrecht R, Ehresmann A, Schmoranzer H, Mentzel G, Schartner K H & Wilhelmi O 2000 *Phys. Lett. A* **267**, 357–369.

Liebel H, Müller-Albrecht R, Lauer S, Vollweiler F, Ehresmann A & Schmoranzer H 2001 *J. Phys. B: At. Mol. Opt. Phys.* **34**, 2581–2596.

Ukai M, Machida S, Kameta K, Kitajima M, Kouchi N, Hatano Y & Ito K 1995 *Phys. Rev. Lett.* **74**, 239.

Probing the Degree of Core Hole Localization in Isotope Substituted N_2 via Angle-Resolved Photoelectron Spectroscopy

D. Rolles, M. Braune, S. Cvejanović, R. Hentges, S. Korica, G. Prümper, A. Reinköster, J. Viehhaus, and U. Becker

Fritz-Haber-Institut der Max-Planck-Gesellschaft, Faradayweg 4-6, 14195 Berlin, Germany

The localization or delocalization of core holes in photoexcited homonuclear molecules has been subject of fierce debates over several decades. Recent studies have found convincing evidence for both localization as well as delocalization under certain conditions and in certain systems [1, 2]. Our work has focussed on the showcase molecule N_2 [3], for which we prove that the core hole (after $1s$ ionization) is delocalized and the photoelectron is emitted coherently from both centers. In order to study the coherence properties of the emission process, we performed angle-resolved photoelectron spectroscopy experiments on molecular nitrogen as well as on the isotope substituted species $^{14,15}N_2$ ("single label nitrogen") using six rotatable electron time-of-flight (TOF) analyzers in the single bunch mode of BESSY at beamline UE56/2-PGM1. Since the $N(1s)$ -doublet with a splitting of less than 100 meV (Fig. 1a) had to be resolved while data was acquired over several days, the experiment required extremely high energy resolution of both the beamline and our setup as well as a very high photon beam stability.

From our measurements, we were able to determine for the first time the photoelectron angular distribution parameter β of the two symmetry components *gerade* (g) and *ungerade* (u) of the $N_2:N(1s)$ photo line (Fig. 1b). The existence of those two components and their different photon energy dependent behavior is a clear signature of a coherent and delocalized emission process, in which the electron wave is emitted simultaneously from both indistinguishable molecular centers. In comparison to "normal" N_2 , the photoelectron spectrum of isotope substituted $^{14,15}N_2$ shows very small but distinct differences, which are best illustrated in the ratio of the two spectra (Fig. 1c) and the ratio of their spectral angular distribution parameter β (Fig. 1d). The most obvious difference is a smaller vibrational constant in the isotope-substituted species (both experiment and model calculations yield a difference of about 4.5 meV) due to an increased reduced mass, leading to pronounced oscillations in the intensity ratio (Fig. 1c), which coincide with the position of the vibrational progression. A simulation of the vibrational effect (dashed line) reproduces those oscillations very well, but fails to explain the additional "wiggle" (shaded areas) at the high-energy end of both the cross-section as well as the β -ratios. This additional structure can only be explained by a change in both relative intensity as well as angular distribution of the g and u components in $^{14,15}N_2$ compared to normal N_2 . A simulation including these changes (solid lines) reproduces the experimental data even at the high-energy end of the $1s$ photo line.

We attribute this effect on the cross section and the angular distribution to the broken inversion symmetry in the isotope substituted species leading to a partial localization of the core hole. While the inversion symmetry of N_2 creates two indistinguishable emitters comparable to the two slits in a Young's type experiment, the electron wave function in $^{14,15}N_2$ is slightly modified due to the broken symmetry mediated by a different nuclear spin in each center. As g and u lose their character as parity eigenfunctions in the no longer inversion symmetric molecule, they mix and consequently become more similar in their cross section and angular distribution. However, the mixing should be very small since the nuclear spin induced difference in the electron spectrum is very small compared to the g-u line splitting. The unexpected size of the effect in the percentage range is the result of multiple scattering in the shape resonance which enhances the average mixing approximately by a factor of ten.

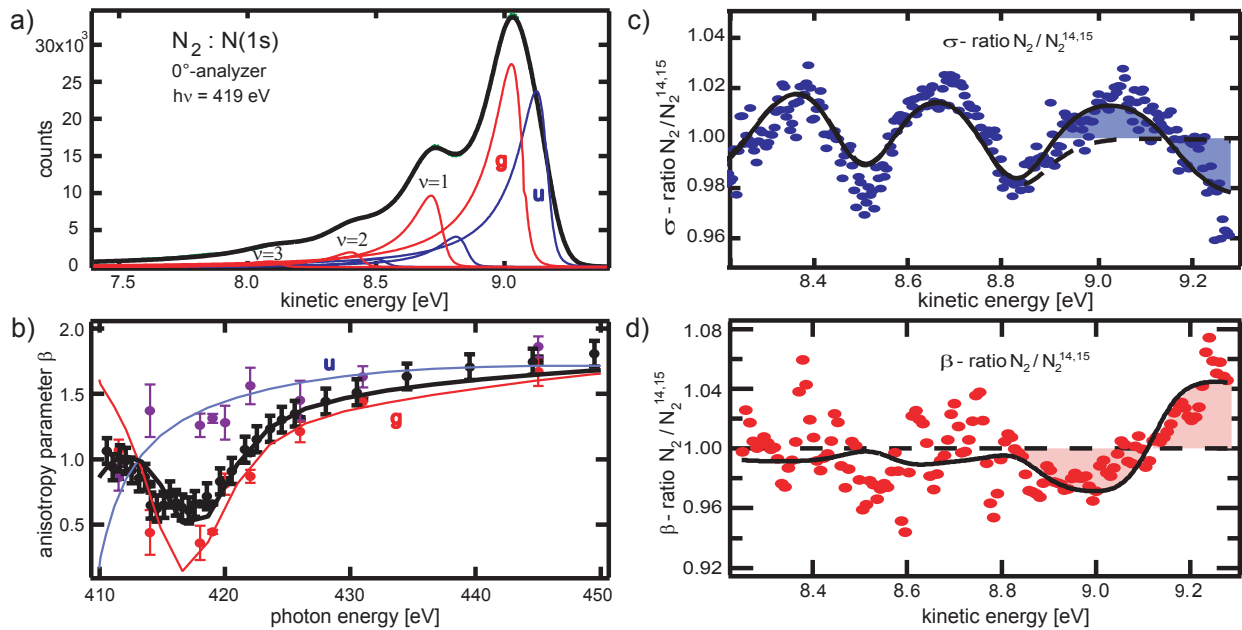


Figure 1: (a) $N_2:N(1s)$ photoelectron spectrum measured at UE56/2-PGM1 and fitted with a doublet of PCI-deformed peaks including vibrational progression. (b) Angular distribution parameter β of the g (red) and u (blue) components as well as their unresolved sum (black); the data points are a combination of the BESSY data and previous measurements at HASYLAB. The solid lines are theoretical predictions from the relaxed-core Hartree-Fock (RCHF) method [4]. Right panels: Ratio between normal N_2 and isotope-substituted $^{14,15}N_2$ for the photoelectron intensity (c) and the photoelectron angular distribution parameter (d) in the range of the $N_2:N(1s)$ photo line together with model calculations (solid) and those including the vibrational effect only (dashed).

In summary, the above results are the first angle-resolved high-resolution data available for the $N_2:N(1s)$ photoionization process and open up a regime of symmetry dependent behavior that has been believed to be inaccessible until very recently. The experiment on unsubstituted N_2 proves that the photoelectron emission in this case is delocalized and coherent from two spatially separated sites due to the indistinguishability of the two molecular centers. The comparison to isotope substituted $^{14,15}N_2$ shows that isotope substitution leads to a partial localization of the core hole due to the broken inversion symmetry of the molecule. The g and u components lose their purity as parity eigenstates, resulting in a change of their relative cross sections and photoelectron angular distribution by several percent. To our knowledge, this is the first time an isotope effect on the electronic structure has been observed in photoelectron spectroscopy.

This project has been supported by the Deutsche Forschungsgemeinschaft (Be 860/18-2) and the Bundesminister für Bildung und Forschung (BMBF-05KS1EB12).

References

- [1] O. Björneholm et al., Phys. Rev. Lett. 84, 2826 (2000).
- [2] G. Prümper et al., BESSY-Highlights 2002.
- [3] U. Hergenhahn et al., J. Phys. Chem. A 105, 5704 (2001).
- [4] B. Zimmermann and V. McKoy, *private communication*.

The photoionization and fragmentation of C_{60} in the energy range 26–130 eV

A. Reinköster,¹ S. Korica,¹ G. Prümper,¹ K. Godehusen,² O. Schwarzkopf,² M. Mast,²
J. Viefhaus,¹ and U. Becker¹

¹Fritz-Haber-Institut der MPG, Faradayweg 4–6, 14195 Berlin, Germany

²BESSY, Albert-Einstein-Str. 15, 12489 Berlin, Germany

1 Abstract

We report on the ionization and fragmentation of C_{60} with synchrotron radiation in the energy range from 26 to 130 eV under single photon conditions. The energy dependence of the cross sections of the produced C_{60}^{q+} ions ($q = 1, 2, 3$) and the charged fragments is analysed. The C_{60}^{q+} -ion yields ($q = 2, 3$) are explained within the framework of the model of T. D. Thomas [1].

2 The experiment

The measurements were performed at the dipole beam line TGM4 of the Berliner synchrotron radiation facility BESSY II. The photon beam crosses the effusive beam of neutral C_{60} molecules after energy selection (toroidal grating monochromator with a 950- ℓ /mm grating). We recorded spectra with photon energies from 26 to 130 eV in 1-eV steps. The positive charged C_{60} ions or fragments are separated by a pulsed 820-Volt field (pulse duration: 10 μ s, repetition rate: 12 kHz); the pulse also serves as a start signal for the coincidence electronics. In a short, second electrical field (2.8 kV) the ions are accelerated, drift through a field-free region (200 mm) before they hit the detector (3.3 kV) with three MCPs (Z -stack, diameter: 40 mm). The ion spectrometer works under Wiley-McLaren conditions, and it has, in principle, the possibility of multi-hit resolution.

C_{60} powder with a 99.95% purity was evaporated in a resistively heated oven with a rather moderate temperature of $\approx 425^\circ\text{C}$ (internal C_{60} energy ≈ 3.6 eV). Some measurements were taken with temperatures between 420 and 500°C to exclude temperatur driven effect as discussed in [2,3].

Typical spectra are shown in fig. 1; the changes with photon energy are illustrated in fig. 2.

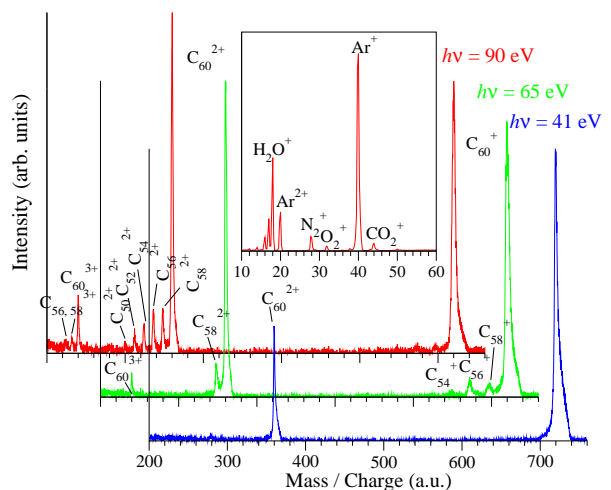


Figure 1: Parts of spectra (converted to a mass-per-charge scale) for photon energies of $h\nu = 41, 65,$ and 90 eV. The inset shows the low-mass region of the spectrum taken with 90 eV. Contributions of small fragment ions of C_{60} are negligible in this mass region.

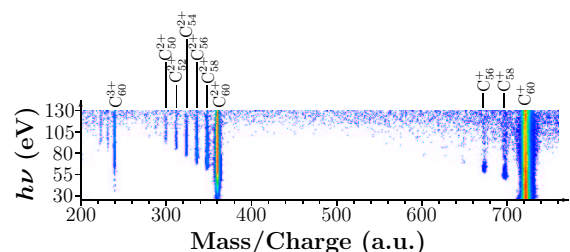


Figure 2: The intensity of converted spectra as a function of the ion mass per charge for different photon energies (26–130 eV). Each spectrum is normalized to its own maximum and the normalized yield increases from blue to red on a linear scale.

3 Results

3.1 Ionization of C₆₀

Experimental cross sections of C₆₀⁺, C₆₀²⁺, and the sum of C_{60-2m}^{q+} ions ($m \geq 0, q = 1, 2, 3$) are shown in fig. 3.

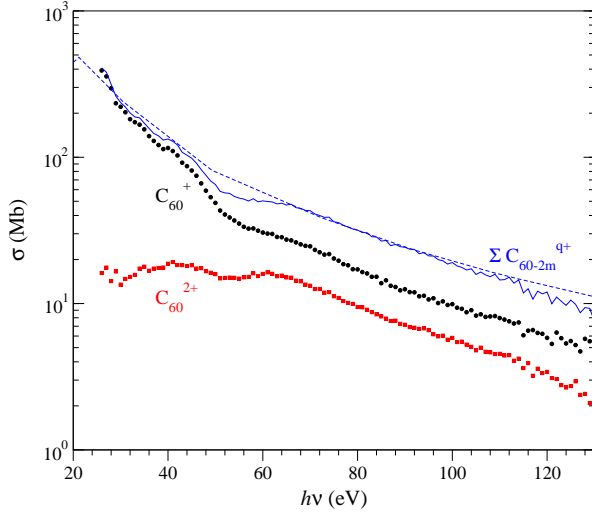


Figure 3: Photoionization cross section for the production of C₆₀⁺ (●) and C₆₀²⁺ (■) calculated with equation (1). The solid line (—) marks the cross section of all charged fullerene ions. The dashed line (---) gives 60 times the total photoabsorption cross section of a single C-atom [4] (scaled down by 2/3).

Photoionization cross section $\sigma(X)$ for the production of the fullerene type X can be deduced from the following formula:

$$\sigma(X) = N \frac{Y(X)}{Y(\text{Ar}^+)} \sigma(\text{Ar}^+). \quad (1)$$

Here, $Y(\dots)$ stands for the observed yield of the fullerene or argon ions. Cross sections of argon ions have been taken from [4]. A normalization factor N was chosen in a way that our total cross section at 26 eV corresponds to the total C₆₀ photoabsorption cross section reported by Jaensch and Kamke for this energy [5]. The changes of our cross sections with photon energy resemble the relative cross sections reported recently by another group [6].

The relative cross sections of C₆₀^{q+} ions are shown in fig. 4 (top panel). The ratios of C₆₀^{q+}/C₆₀⁺ ions ($q = 2, 3$) can approximately be described by the general model of T. D. Thomas for *shake-off* processes [1]:

$$\mu = \mu_\infty \exp\left\{-\left(r[\text{\AA}]\Delta E[\text{eV}]\right)^2 / (15.32E_{\text{ex}}[\text{eV}])\right\} \quad (2)$$

- μ : intensity ratio of the C₆₀^{q+} ions,
- μ_∞ : asymptotic value of μ ,
- r : the distance until the electrons are separated from the molecule:
 $r = 1.76 \text{ \AA}$ for C₆₀²⁺, 0.8 \AA for C₆₀³⁺,
- ΔE : the required excitation energy,
- E_{ex} : the kinetic energy of the electrons.

This finding indicates that the doubly and triply charged fullerene ions are probably formed via shake-off processes of super-excited C₆₀⁺ ions.

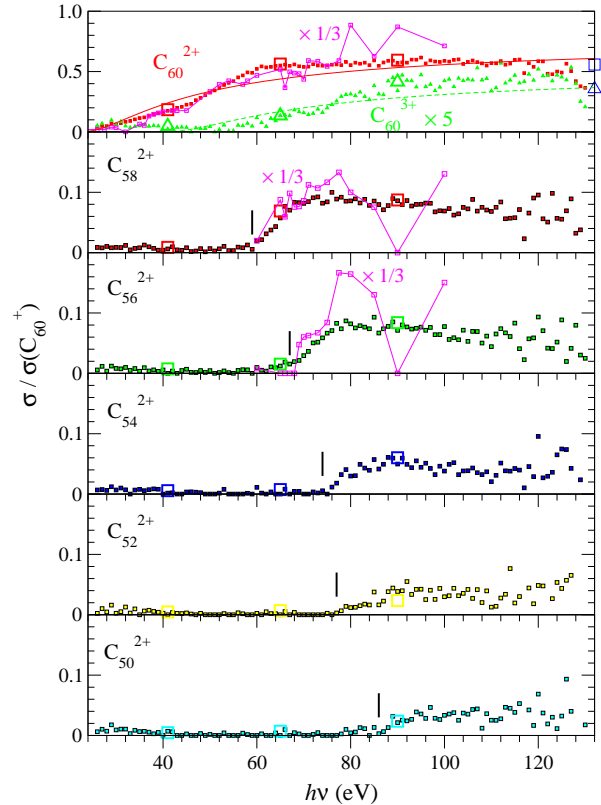


Figure 4: The relative cross section of C₆₀²⁺, C₆₀³⁺, and C_{60-2m}²⁺ (normalized to the C₆₀⁺ cross section). Some measurements recorded with a longer time are marked by big symbols. For comparison values of Fieber-Erdmann *et al.* [2] (magenta, hollow symbols with a line, scaled down by 1/3) and Aksela *et al.* [7] (the almost right, blue symbols in the top panel, taken with a photon energy of 280 eV) are also shown. All values for C₆₀³⁺ are multiplied with 5. The lines in the top panel are calculated with equation (2). Vertical lines indicate the appearance energies of the C_{60-2m}²⁺ ions.

3.2 C₆₀ fragmentation

Besides the pure ionization of C₆₀ the fragmentation of the buckminster fullerene is observed at high photon energies, leading to smaller

C_{60-2m}^{q+} ions ($m = 1, \dots, 5$) which are supposed to originate from a successive emission of C_2 units. The relative cross sections of the small fullerenes are given in fig. 4 and 5. Very small, charged fragments were not observed. Therefore, fullerene fission (like $C_{60}^{3+} \rightarrow C_{58}^{2+} + C_2^+$) or complete cage break-ups are unimportant in the energy range under study.

The yield of fullerene ions at high photon energies is similar to those reported by Aksela *et al.* [7] for energies below the $C(1s)$ threshold. Propably, nothing in the relative yields will change in the energy range between 130 and 280 eV.

So far it was unclear, if the singly charged C_{60-2m}^+ ions can be produced with photon energies ≤ 100 eV or not. A very small amount of C_{58}^+ was observed by Yoo *et al.* [8] at $h\nu = 41$ eV. No C_{60-2m}^+ fragments could be observed by Fieber-Erdmann *et al.* [2] even at higher energies. We found clear evidence for C_{60-2m}^+ ions ($m = 1, 2, 3$). The curves for C_{60-2m}^+ ($m = 1, 2$) pass through a maximum before they reach a lower final value (fig. 5). The appearance energy of the C_{60-2m}^{q+} ions are similar to values observed after electron impact [9].

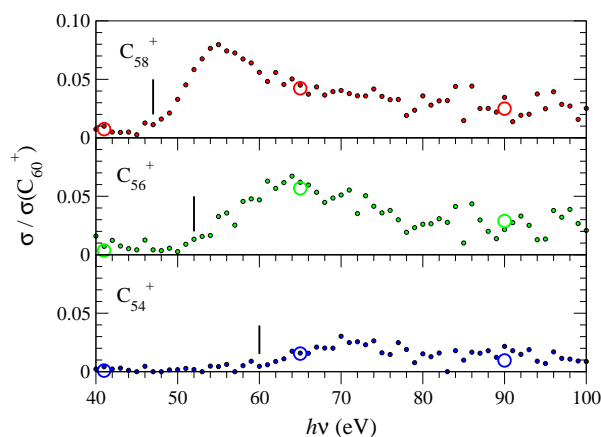


Figure 5: The relative cross sections of singly charged fullerene fragments as a function of the photon energy. Some measurements recorded with a longer time are marked by big symbols. Vertical lines mark the appearance energy of the fullerene fragments.

4 Summary

We studied the ionization and fragmentation of the buckminsterfullerene in the photon energy range from 26 to 130 eV. At high photon energies the photoionization cross section is similar

to the photoabsorption cross section of 60 carbon atoms. Relative C_{60}^{q+}/C_{60}^+ ($q = 2, 3$) cross sections can roughly be described by the theoretical model of Thomas. The energy dependence of singly charged fullerene fragment ions and values of small, doubly charged C_{60-2m}^{2+} ions ($m \geq 3$) were observed for the first time in the photon energy region under study. After excitation of the fullerenes with high photon energies ($h\nu \geq 90$ eV) the relative ionization/fragmentation is similar to values just below the $C(1s)$ threshold.

References

- [1] T.D. Thomas, *Phys. Rev. Lett.* **52**, 417 (1984).
- [2] M. Fieber-Erdmann M, W. Krättschmer, and A. Ding, Supplement to *Zeitschr. f. Phys. D* **26**, S308 (1993); T. Drewello, W. Krättschmer, M. Fieber-Erdmann, and A. Ding, *Int. J. Mass Spectrom.* **124**, R1 (1993).
- [3] M. Sai Baba, T.S. Lakshmi Narasimhan, R. Balasubramanian, C.K. Mathews, *Int. J. Mass Spectrom. Ion Processes* **130**, L1 (1994).
- [4] U. Becker and D.A. Shirley, in *VUV and Soft X-Ray Photoionization* (Plenum Press, New York, 1996), p. 148.
- [5] R. Jaensch and W. Kamke, *Mol. Materials* **13**, 143 (2000).
- [6] J. Kou, T. Mori, M. Ono, Y. Haruyama, Y. Kubozono, and K. Mitsuke, *Chem. Phys. Lett.* **374**, 1 (2003).
- [7] S. Aksela, E. Nömmiste, J. Jauhiainen, E. Kukk, J. Karvonen, H.G. Berry, S.L. Sorensen, and A. Aksela, *Phys. Rev. Lett.* **75**, 2112 (1995); J. Karvonen, E. Nömmiste, H. Aksela, and S. Aksela, *J. Chem. Phys.* **106**, 3466 (1997).
- [8] R. K. Yoo, B. Ruscic, and J. Berkowitz, *J. Chem. Phys.* **96**, 911 (1992).
- [9] P. Scheier, B. Dünser, R. Wörgötter, M. Lezius, R. Robl, and T.D. Märk, *Int. J. Mass Spectrom. Ion Processes* **138**, 77 (1994).

Angular distribution of Sc 3p photoelectrons measured by rotating the polarisation axis of undulator radiation

T. Richter, P. Zimmermann

Institut für Atomare Physik und Fachdidaktik, Technische Universität Berlin

K. Godehusen

Berliner Elektronenspeicherring-Gesellschaft für Synchrotronstrahlung mbH

M. Martins

Institut für Experimentalphysik, Universität Hamburg

Despite its rather limited technological relevance Scandium, ($Z = 21$) at the beginning of the 3d elements, has become a kind of key element with respect to the theory for inner shell processes. With Scandium having only one bound 3d electron in its ground state $3p^6 3d 4s^2 {}^2D$ one would expect a rather simple 3p photoelectron spectrum. The study of the multiplet structure of the 3p photoelectron spectrum, however, revealed a rather complex situation [1, 2].

A first theoretical analysis of the Sc 3p electron spectrum was published by Altun and Manson [3]. The calculations were based on many-body perturbation theory (MBPT), the close-coupling approximation and the multi-configuration Hartree-Fock approach (MCHF). However there is only marginal agreement between experiment and theory.

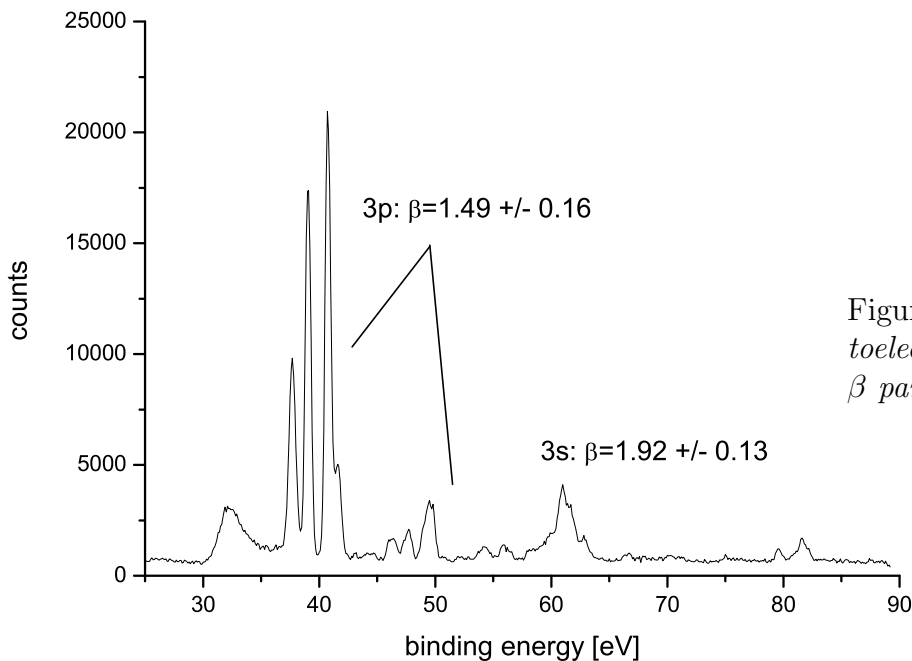


Figure 1: 3p and 3s photoelectron spectrum and β parameters of Sc

One reason for this is a peculiar anomaly in the term structure due to the $3p^5 3d$ configuration. For such a two-electron configuration with one hole $3p^{-1}$ and one electron 3d in an open subshell the electrostatic exchange interaction represented by the Slater

integrals G^k has a very pronounced effect on the singlet components. Especially the 1P_1 component is shifted by about 10 eV to higher binding energy due to the large value $g_1 = 1,27$ of the angular part in the exchange interaction $g_1 \cdot G^1$.

The second reason for the complex situation in the Sc $3p$ photoelectron spectrum are strong correlation effects of the valence electrons $3d$, $4s$ and $4p$ which result in a breakdown of the single configuration approximation.

On one hand the mismatch between experimental data and theory shows deficiencies in current models, but at the same time this data can be used to improve the situation. So a further study of this system should be fruitful.

For example A. Müller and coworkers focused on the recombination of Sc^{3+} ions[4]. The process can be seen as a reversed photoionization of Sc^{2+} which has a similar electronic configuration as the neutral atom.

For Mn and Cr $2p$ the analysis of the anisotropy parameter β for photoionization revealed a strong correlation between β and interconfiguration effects [5].

The β parameters for the Scandium $3p$ and $3s$ photoionization are shown in figure 1, together with a photoelectron spectrum of the $3p$ and $3s$ region. The measurements were carried out by rotating the polarisation axis of the undulator radiation, the technique was very successfully employed for Kr [6] before.

References

- [1] S. B. Whitfield, K. Kehoe, R. Wehlitz, M. O. Krause, C. D. Caldwell, Phys. Rev A 64, 022701 (2001)
- [2] K. Tiedtke, Ch. Gerth, M. Martins, B. Obst, P. Zimmermann, J. Phys. B. 33, L755 (2000)
- [3] Z. Altun, S. T. Manson, Europhys. Lett. 33, 17 (1966), J. Phys. B 32, L255 (1999), Phys. Rev. A 59, 3576 (1999)
- [4] S. Schippers, A. Müller, S. Ricz, M. E. Bannister, *et.al.*, Rev. Lett. 89 193002 (2002)
- [5] K. Godehusen, Ph. Wernet, T. Richter, P. Zimmermann, M. Martins, Phys. Rev. A 68, 052707 (2003)
- [6] K. Godehusen, H.-Ch. Mertins, T. Richter, P. Zimmermann, M. Martins, Phys. Rev. A 68, 012711 (2003)

Partial wave analysis of interfering resonant Auger (RA) transitions in the Raman regime using fluorescence polarization spectroscopy

R.H. Schill, S. Kammer, S. Mickat, D. Hasselkamp, B. Zimmermann, K.-H. Schartner

I. Physikalisches Institut der Justus-Liebig-Universität Giessen, D-35392 Giessen, Germany

L. Werner, S. Klump, A. Ehresmann, H. Schmoranzner

Fachbereich Physik der Technischen Universität Kaiserslautern, D-67653 Kaiserslautern, Germany

B.M. Lagutin, I.D. Petrov, V.L. Sukhorukov

Rostov State University of Transport Communications, 344038 Rostov-on-Don, Russia

The resonant Auger effect for Kr describes the decay of the $3d^9 5p/6p$ configuration of the Kr atom yielding Kr ions in the ground or the excited state. The dominating spectator decay [1] transitions have been investigated during the nineties by the Aksela group [2] using photoelectron spectroscopy with increasing resolution. Interference of the transition amplitudes on resonances which overlap within their natural line width were discussed in the earlier publications. A quantitative treatment of interfering amplitudes for each electron partial wave including the four $3d^9_{5/2} 5p_{3/2}$, $3d^9_{3/2} 5p_{1/2}$, $3d^9_{3/2} 5p_{3/2}$, $3d^9_{5/2} 6p_{3/2}$ resonances (R1...R4) was only recently carried out in our collaboration [3].

The interference results from the coherent summation of the direct population amplitude and of the above mentioned RA transitions

$$D(E_i J_i, \varepsilon l j_{el}) = \langle E_i J_i, \varepsilon l j_{el} | d | 0 \rangle + \sum_R \frac{\langle E_i J_i, \varepsilon l j_{el} | H^{ee} | R \rangle \langle R | d | 0 \rangle}{(\varepsilon + E_i - E) + i\Gamma(R)/2}. \quad (1)$$

The knowledge of the relative contribution of the three electron partial waves which are emitted in the photoionization of rare gas atoms is a first step towards a quantummechanically complete description of the process. Polarization fluorescence spectroscopy allows access to this contribution through the relations between alignment parameter A_{20} and orientation parameter O_{10} of the photoion and the relative partial cross sections $\sigma_{j_{el}}(J_i) / \sigma(J_i)$. J_i denotes the total angular momentum of the ion state and j_{el} of the photoelectron:

$$A_{20} = \sum_{j_{el}} A_{20}^{j_{el}}(J_i) \cdot \frac{\sigma_{j_{el}}(J_i)}{\sigma(J_i)} \quad \text{and} \quad O_{10} = \sum_{j_{el}} O_{10}^{j_{el}}(J_i) \cdot \frac{\sigma_{j_{el}}(J_i)}{\sigma(J_i)} \quad (2)$$

with $j_{el} = J_i + 1, J_i, J_i - 1$.

The coefficients $A_{20}^{j_{el}}(J_i)$ und $O_{10}^{j_{el}}(J_i)$ denote the kinematic partial alignment and orientation parameter [3]. An unambiguous determination of the relative partial wave distribution demands the measurements of both A_{20} and O_{10} . Due to the incoherent summation in (2), the relative contribution of the partial waves is the complete information accessible from a fluorescence analysis. Combined with spinpolarisation and angular asymmetry parameter of the photoelectron yield sufficient information for the quantummechanically complete description becomes available [4].

Our experimental setup consists of two 1m VUV normal incidence spectrometers and an interference filter and photomultiplier combination which is polarization sensitive due to a quarterwave plate and a rotating polarizer. The latter is oriented under an angle of 54° with respect to the exciting photon beam. O_{10} and A_{20} can be determined from the analysis of the fluorescence intensity as function of the polarizer angle.

Selected excited Kr^+ 5p fine structure resolved states were studied scanning the energy range of the $3d^9_{5/2} 5p_{3/2}$ resonance at 91.2eV and of the $3d^9_{3/2} 5p_{1/2}$, $3d^9_{3/2} 5p_{3/2}$, $3d^9_{5/2} 6p_{3/2}$

resonances at 92.5eV with circularly or linearly polarized radiation from the UE56 beamline. A bandwidth of the exciting photons of 11 meV was sufficient to measure within the so called Raman regime due to the 80 meV of the natural width of the $3d^95p$ resonances.

In the following we present the experimental results and the calculated values and discuss their comparison for the population of the $(^1D)5p^2F_{7/2}$ and of the $(^1D)5p^2D_{5/2}$ states. Fig.1 and Fig.2 display the values for A_{20} and O_{10} , and in the upper part for the relative electron partial wave contributions. The lower part of the figures shows the intensities of the Auger transitions. The experimental data points were obtained at different undulator beam lines. Cascade corrections were so far only applied for the $^2F_{7/2}$ state at selected energies. Accumulated spectra allow a more complete cascade analysis which is in progress. Moreover error bars have to be worked out. Statistical errors will contribute only in the wings of the resonances.

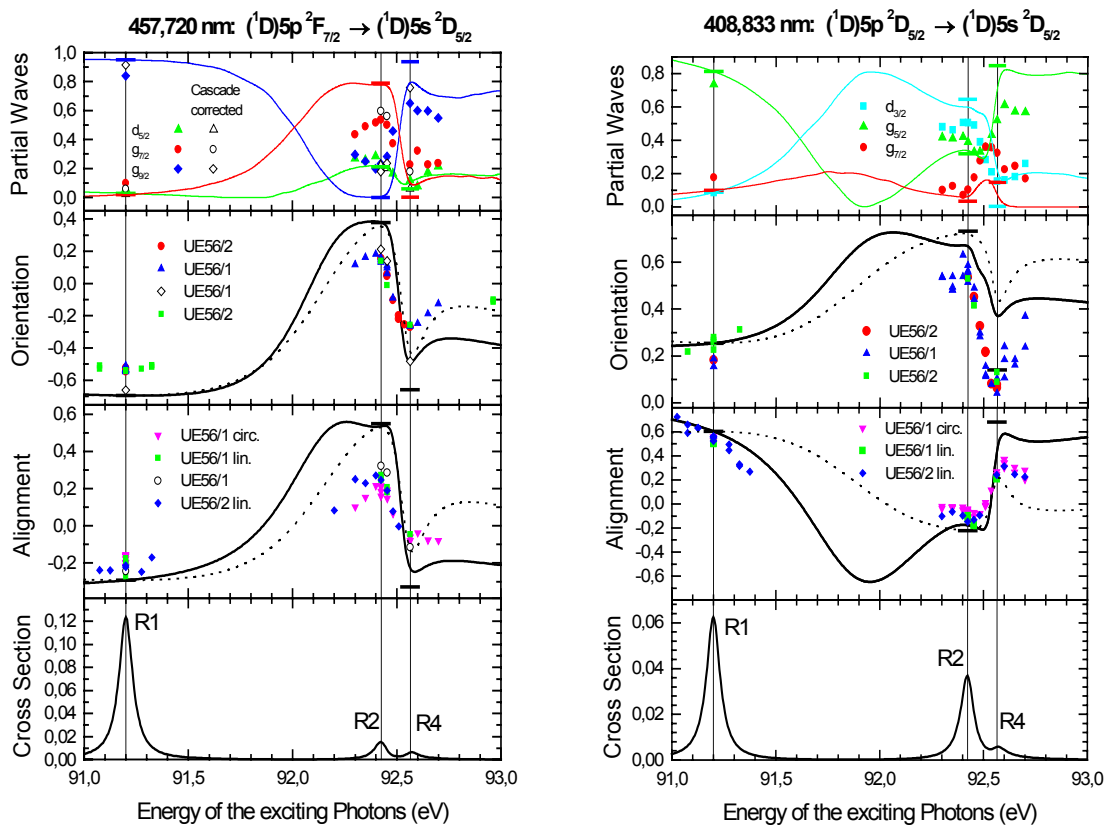


Fig.1 and 2: Calculated and experimental energy dependence of O_{10} , A_{20} and cross section for the $(^1D)5p^2F_{7/2}$ and the $(^1D)5p^2D_{5/2}$ states of Kr^+ . Calculation including coherent (—) or statistical (- - -) summation of overlapping resonances, horizontal bars showing values for two-step decay (length corresponding to natural line width). Symbols: experimental values using circularly and linearly polarized undulator radiation. Relative contribution of partial waves derived from (1). Open symbols: cascade corrected values.

The two selected states differ with respect to their relative intensities. For the $(^1D)5p^2F_{7/2}$ state R1 dominates. Effects in the population of R1 resulting from the tails of R2...R4 are expected to be weak. To the contrary, R1 and R2 should influence each other for the $(^1D)5p^2D_{5/2}$ state. Calculations and experiment confirm this expectation even quantitatively. Across R1 we observe energy dependent A_{20} and O_{10} values for the $^2D_{5/2}$ state while these are constant for the $^2F_{7/2}$ state. This is a clear interference effect. The statistical summation of the two-step values, weighted by the energy dependent cross section of R1...R4, does not result in an energy dependence of A_{20} and O_{10} across R1. In Fig.3 the intensity variation with

polarizer angle setting for the (1D) $5p^2D_{5/2}$ state, normalized to the mean intensity, is plotted for the seven energies across R1. On the resonance, the full harmonic intensity variation was verified, while for the energy positions on the low and high energy wing of R1 only the extrema could be measured with sufficient statistics.

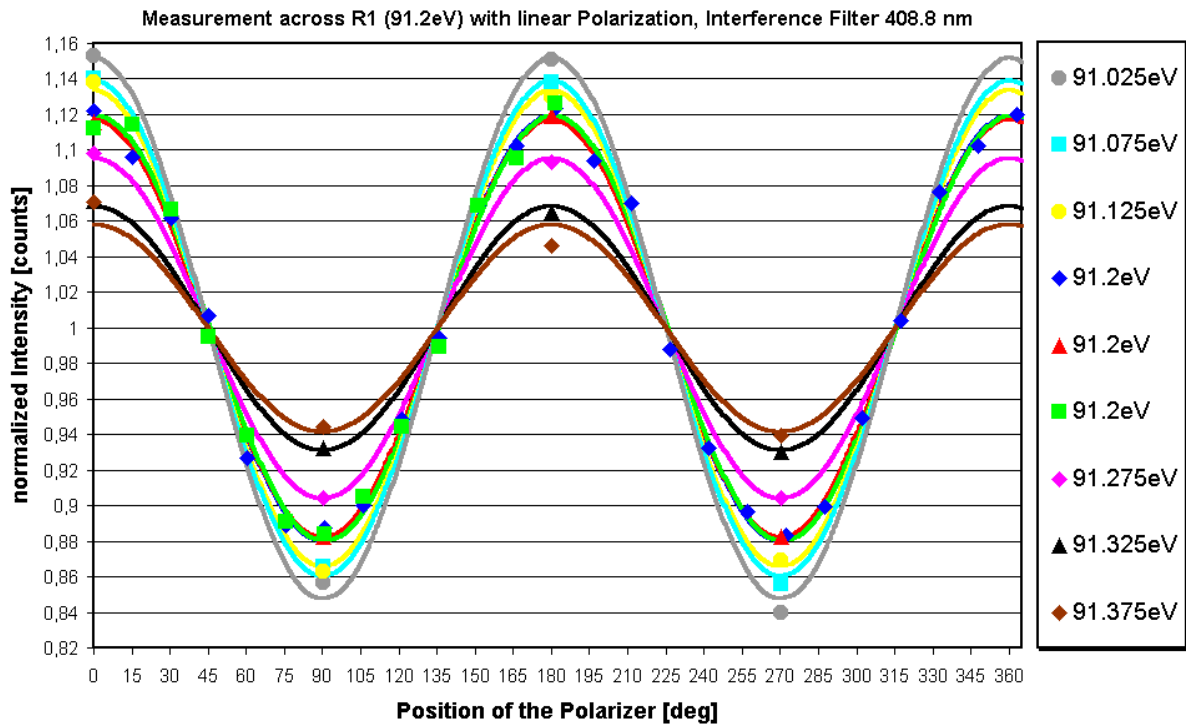


Fig.3: Normalized intensities as function of polarizer angle for the (1D) $5p^2D_{5/2}$ state for energies on R1 and on the low and high energy wing of R1 with linear polarization of the exciting photons. Observation angle 54° due to the beam direction.

For the energy range of R2...R4 there is so far a good qualitative agreement between experiment and calculation, also for the derived partial wave distributions. The differences between calculation and experiment on R2 for $^2F_{7/2}$ state and on R4 for the $^2D_{5/2}$ state can not result from cascade transitions but should be investigated within the calculations.

Interference resulting from the direct non resonant population according to the first term of (1) is only expected for 2P states. Calculations for the (1D) $5p^2P_{3/2}$ state show an interesting decrease of A_{20} and O_{10} on the low and high energy wing of R1 underlining the interest in further experiments. The presented results for the wings of R1 demonstrate the feasibility of these experiments.

- [1] W. Eberhardt, G. Kalkoffen and C. Kunz, Phys.Rev.Lett. **41**, 156 (1978)
- [2] G.B. Armen, H. Aksela,T. Aberg and S. Aksela, J. Phys. B: At. Mol. Opt. Phys. **33**, R 49 (2000)
- [3] B.M. Lagutin, I.D. Petrov, V.L. Sukhorukov, Ph. Demekhin, B. Zimmermann, S. Mickat, S. Kammer, ,K.-H. Schartner, A. Ehresmann, Yu.A. Shutov, and H. Schmoranzer, J.Phys.B: At-Mol.Opt.Phys. **36**, 3251 (2003)
- [4] B. Schmidtke, T. Khalil, M. Drescher, N. Müller, N.M. Kabachnik, and U. Heinzmann, J. Phys. B: At. Mol. Opt. Phys. **33**, 5225 (2000)
- [5] R.H. Schill, D. Hasselkamp, S. Kammer, S. Mickat, B. Zimmermann, K.-H. Schartner, A. Ehresmann, H. Schmoranzer, B.M. Lagutin, V. L. Sukhorukov, J. Phys. B:At.Mol.Phys.: **36**, L57 (2003)

Core Level Photoelectron Circular Dichroism Spectroscopy of Pure Enantiomers of the Chiral Natural Product Molecule, Carvone

C. J. Harding^a, S. Marburger^{b,c}, F. Zhang^a, U. Hergenahn^{b,c} and I. Powis^a

^a The School of Chemistry, The University of Nottingham, Nottingham NG7 2RD, UK

^b Fritz-Haber-Institut der Max-Planck-Gesellschaft, Faradayweg 4-6, 14195 Berlin, Germany

^c Max-Planck-Institut für Plasmaphysik, Boltzmannstraße 2, 85748 Garching, Germany
EU-HPP HPR1-1999-CT-00028

Many important bio-molecules are chiral and may adopt distinctively 'handed' forms (called enantiomers). Indeed, the fundamental molecular building blocks of terrestrial life display a unique invariant handedness, or homochirality, such that, for example, only left-handed amino acids occur naturally. In consequence, at the chemical level living organisms can show enantiomer-specific interactions with chiral species in the environment, with profound consequences for the pharmaceutical and food odour industries. This creates a demand for the detection and identification of molecular chirality at the laboratory level, and more broadly for the development of an understanding of the conditions which may have first led to homochirality on earth.

In both these spheres molecular interaction with circularly polarized radiation (which itself has an intrinsic handedness or helicity) is deemed important – with the proviso and consequent limitation, that it is typically a very weak effect, the difference between left and right handed interaction being typically $\leq 10^{-4}$. This comes about because the origin of such difference, or dichroism, lies in an interference between the electric dipole and (typically much weaker) magnetic dipole or electric quadrupole radiation—matter interaction terms.

In this report we detail measurements of much larger effects in a new form of circular dichroism spectroscopy in the soft X-Ray region, as observed with the natural product molecule carvone ($C_{10}H_{14}O$ – see Fig. 1). One enantiomer, R(-) carvone, has a minty odour, while the other S(+) enantiomer has a readily distinguished odour of caraway seed.

It has been recognized for some time that a novel form of circular dichroism is feasible in an angle resolved, differential photoionization cross-section measurement made on randomly oriented chiral molecules [1, 2] and we recently reported the first computational studies of this Circular Dichroism in the Angular Distribution (CDAD) [3, 4] indicating it to be a readily measurable effect of magnitude 10^{-2} or more. The general form of the predicted electron distribution for randomly oriented molecules is:

$$I(\theta) = 1 + b_1 P_1(\cos \theta) + b_2 P_2(\cos \theta)$$

where b_2 is essentially just the conventional photoelectron asymmetry parameter, β , and b_1 will be zero for all but chiral molecules and circularly polarized light. P_n are the Legendre polynomials, and θ the angle of electron emission with respect to the photon propagation direction. The sign of b_1 will reverse if either the handedness of the radiation or of the molecule is changed. This therefore predicts the CDAD (difference) signal to be $2b_1 \cos \theta$, i.e. a difference in emission forwards and backwards along the light beam.

Exactly this expected behaviour has now been observed in the valence ionization of camphor type molecules [5, 6], with magnitudes of a few % that vary with photon energy. We have also recently detected this phenomenon in the C 1s core ionization of camphor [7] with a maximum asymmetry of 12%. This is perhaps more surprising because of the well-defined spherical (even parity) nature of the initial orbital; since

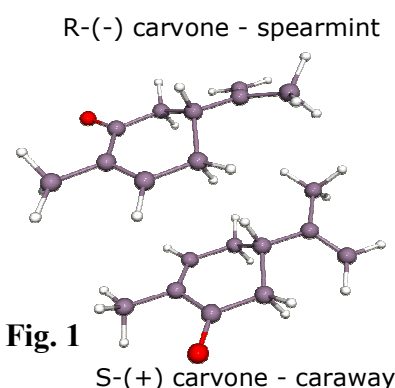


Fig. 1

CDAD arises from interference between partial waves of adjacent l values it clearly must arise here purely as a final state effect due to scattering of the photoelectron off the chiral molecular potential with a consequent parity mixing.

A major limitation to these earlier experiments were count variations attributable to the significant time interval (several minutes) taken to switch an undulator between the two states of circular polarization. For the present work we have carried out the first user experiments using the newly commissioned two-beam chopped mode of the dual undulators on the UE 56/2-PGM1 beamline. With the more rapid helicity switching achieved at 20 s intervals we saw an anticipated significant gain in sensitivity in our measurements. In consequence we can now present CDAD spectra taken across the photoelectron band profiles, rather than as before forming an average over each photoelectron band.

The C 1s core region of the carvone PES is shown in the top of Fig. 2. Three peaks can be observed. The most strongly bound peak (lowest kinetic energy) pertains to the carbon atom bound in the carbonyl (C=O) group. Other assignments are made with the aid of *ab initio* calculations with ionization energies shown (red bars) in the figure. It is apparent that many individual orbital contributions are unresolved, but contribute

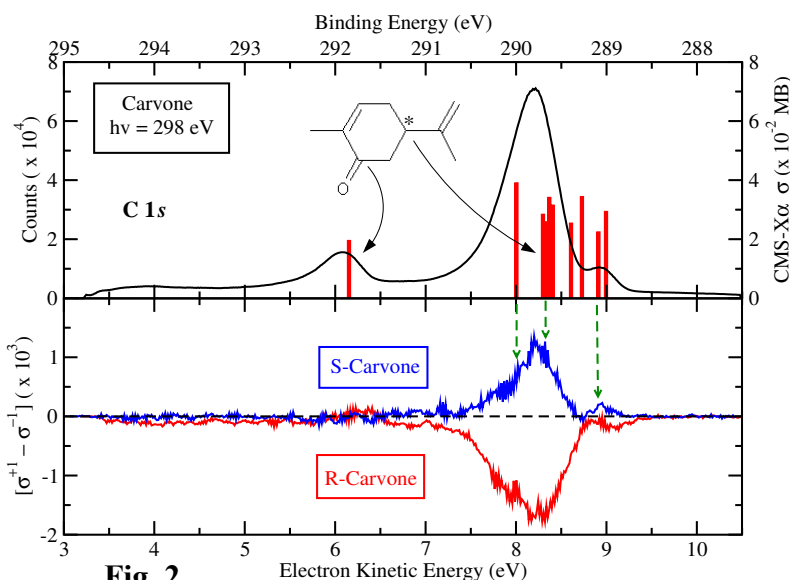
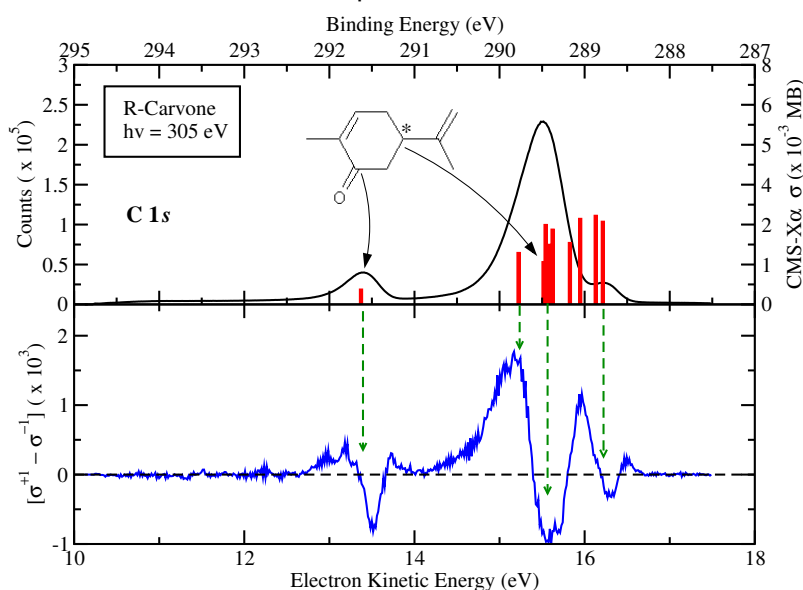


Fig. 2

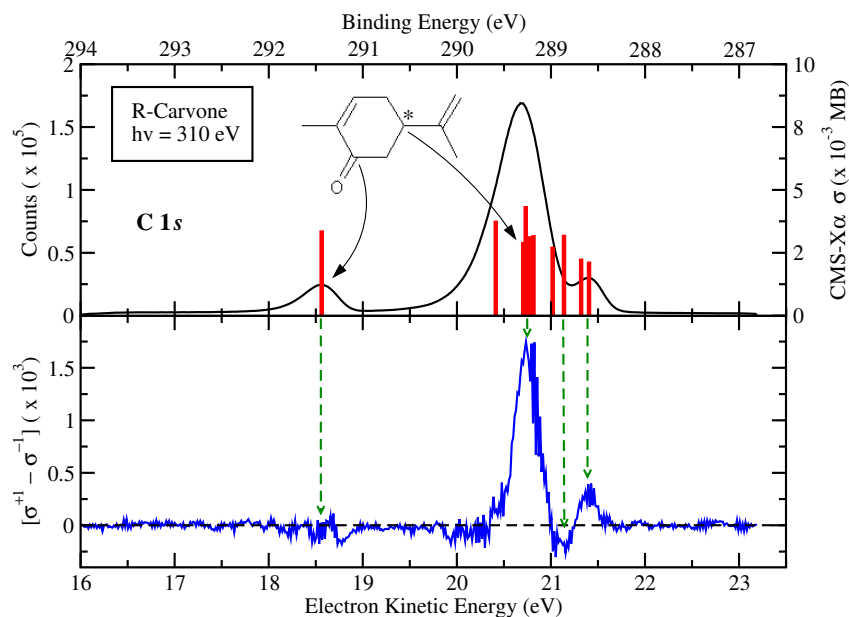
to the two other broad bands in the photoelectron spectrum. At $h\nu=298$ eV a relatively featureless CDAD signal is seen arising from the non-CO ionizations. The two enantiomers display opposite asymmetry, in accordance with expectations.

At higher photon energies more structured CDAD spectra are recorded showing for the first time dramatic variations across the width of a PES band. A preliminary analysis and comparison with the indicated ionization energies of individual C 1s levels suggests that the photoelectron circular dichroism spectrum provides a higher resolution than the normal photoelectron spectrum, allowing a partial identification of individual orbital contributions to the broad photoelectron bands.



However, it may also be observed that the CDAD signal varies, indeed may even undergo a sign reversal, across the width of the well isolated C=O C 1s band. This rather challenges current theoretical models which provide no explanation for such variations associated with the ionisation of a single orbital. A plausible hypothesis may be formulated in terms of vibronic effects influencing the photoelectron

scattering, but such influences have yet to be incorporated into any computational models for molecules of such size.



The asymmetries exhibited here are of the order of 1–2 %, smaller than the maximum asymmetry observed for the $\underline{C}=\text{O}$ C 1s orbital in camphor [7], yet still *much* larger than in natural absorption CD. Further improvements in sensitivity may be anticipated, making this new technique a potentially powerful adjunct to conventional XPS for the investigation of chiral molecules.

References

1. Ritchie, B., *Theory of the angular distribution of photoelectrons ejected from optically active molecules and molecular negative ions*. Physical Review A, 1976. **13**: p. 1411-1415.
2. Cherepkov, N.A., *Circular-dichroism of molecules in the continuous absorption region*. Chemical Physics Letters, 1982. **87**(4): p. 344-348.
3. Powis, I., *Photoelectron spectroscopy and circular dichroism in chiral biomolecules: L-alanine*. Journal of Physical Chemistry A, 2000. **104**(5): p. 878-882.
4. Powis, I., *Photoelectron circular dichroism of the randomly oriented chiral molecules glyceraldehyde and lactic acid*. Journal of Chemical Physics, 2000. **112**(1): p. 301-310.
5. Böwering, N., T. Lischke, B. Schmidtke, N. Müller, T. Khalil, and U. Heinzmann, *Asymmetry in photoelectron emission from chiral molecules induced by circularly polarized light*. Physical Review Letters, 2001. **86**(7): p. 1187-1190.
6. Garcia, G.A., L. Nahon, M. Lebech, J.-C. Houver, D. Doweck, and I. Powis, *Circular Dichroism in The Photoelectron Angular Distributions from Randomly Oriented Enantiomers of Camphor*. J. Chem. Phys., 2003. **119**(17): p. 8781-4.
7. Hergenbahn, U., E.E. Rennie, O. Kugeler, S. Marburger, T. Lischke, I. Powis, and G.A. Garcia, *Photoelectron Circular Dichroism in Core Level Ionization of Randomly Oriented Pure Enantiomers of the Chiral Molecule Camphor*. Journal of Chemical Physics, 2004.

Partial cross sections of doubly excited helium below the ionization threshold I_7

Y. H. Jiang,^{1,2} R. Püttner,¹ R. Hentges,³ J. Viefhaus,³
M. Poiguine,¹ U. Becker,³ J. M. Rost,² and G. Kaindl¹

¹*Freie Universität Berlin, Institut für Experimentalphysik, D-14195 Berlin*

²*Max-Planck Institut für Physik komplexer Systeme,
Nöthnitzer Strasse 38, 01187 Dresden*

³*Fritz-Haber-Institut Berlin, Faradayweg 4-6, D-14195 Berlin-Dahlem*

Double-excitation states in helium have been considered to be prototypical for two-electron systems with strong electron correlation. In the region close to the double ionization threshold, the interferences due to the overlap of several perturbers with different Rydberg series render the observed spectra highly complicated. In this case, the approximate quantum numbers begin to lose their meaning, and the regularities in the two-electron resonance spectrum start to dissolve. For this reason, the last eV below the double ionization threshold has drawn considerable attention in both experimental and theoretical studies, which mainly focused on the total photoionization cross section (TCS). Menzel *at al.* were the first who reported on measurements of partial cross sections (PCSs) up to the ionization threshold I_5 employing two spherical-sector-plate electrostatic analyzers [1, 2]. In the last year we measured the PCSs up to the ionization threshold I_7 with improved signal-to-noise-ratios using a time-of-flight (TOF) spectrometer.

State-of-the-art high-resolution monochromators in combination with TOF photoelectron spectrometers allow one to explore the autoionization of resonances in the region close to the double-ionization threshold of helium. The experiments were performed at the undulator beamline U125/2-SGM (BUS-beamline) of the Berliner Elektronenspeicherring für Synchrotronstrahlung (BESSY) using a photon energy resolution of $\Omega \cong 6$ meV (FWHM). The TOF spectrometer was mounted at the magic angle, i.e. in the dipole plane at an angle of $\theta = 55^\circ$ relative to the polarization direction of the incoming light. A needle (10 cm long, less than 500 μm inner diameter) directs an effusive jet of gas to the interaction region; the background pressure in the chamber was $\cong 10^{-4}$ mbar. From the count-rate and the calculated cross sections we estimated the pressure in the interaction region to be of the order of $\cong 10^{-2}$ mbar. TOF photoelectron spectra were taken for each photon energy and converted into photoemission spectra (PES) by a time-to-energy conversion procedure. In order to eliminate the influences caused by the decrease of the ring current and fluctuations of the gas pressure in the interaction region during data taking, the spectra were normalized to the intensity of the $n=1$ line.

The measured double-excitation $^1P^o$ resonances of helium can be identified in a simplified classification scheme $N, K_{n'}$ [4, 5], with N and n' standing for the ionization threshold of a given channel and the running index of the considered Rydberg series, respectively; K represents the angular-correlation quantum number. In an independent particle picture, $N(n')$ can be understood as the quantum number of the inner (outer) electron. The partial cross sections are described employing the notation σ_n^N . The lower index n refers to the principal quantum number of the single electron in the ionized final state, $\text{He}^+(n)$.

Fig. 1 displays an example of our results for the PCSs σ_n^7 (with $n = 2, 3, 4$, and

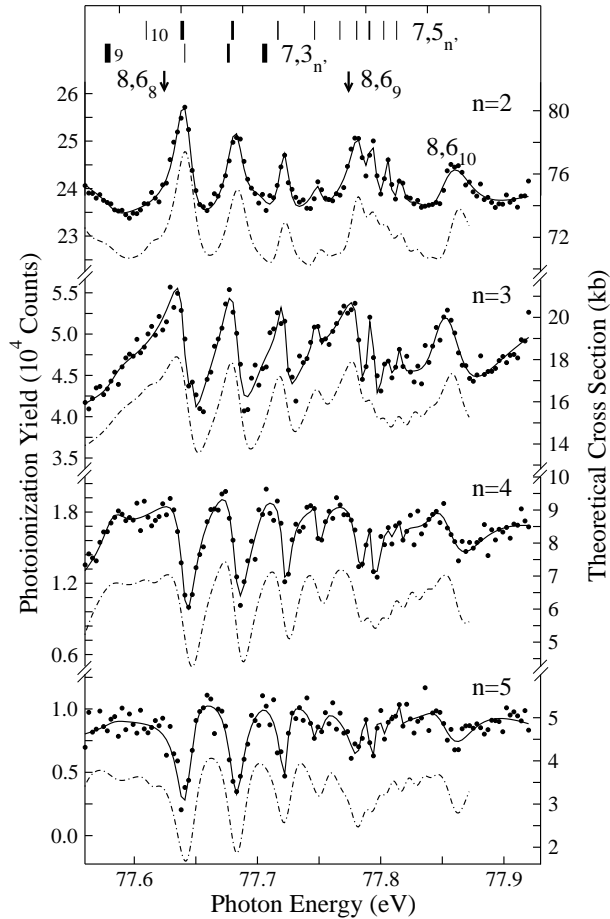


Figure 1: Experimental partial cross sections, σ_n^7 , leading to the final states $\text{He}^+(n)$, with $n = 2, 3, 4$, and 5 , along with the results of the eigenchannel R-matrix calculations. The data were taken in the photon-energy region between 77.56 eV and 77.92 eV. The two vertical-bar diagrams in the upper part of the figure give the assignments of the double-excitation resonances by specifying n' ; with the widths of bars being proportional to the linewidths of the corresponding resonances [6]. The vertical arrows mark the calculated energies of the perturber. The filled data points are the present experimental results, with the solid curves through the data points representing the fit results. The dash-dotted curves are the results of the R-Matrix calculations convoluted with a Gaussian of 6 meV width (FWHM) to simulate finite experimental resolution.

5) along with results of eigenchannel R-matrix calculations. In general, an excellent agreement between experiment and theory is observed. The present measurements confirm the general patterns [2] in the PCSs σ_n derived from the propensity rules [6] (not shown here; for details see Ref. [3]).

The present data were also used to test the predictions on mirroring behavior in the PCSs given by Liu and Starace [7]. For this, one has to divide the total cross section, σ_T , into two groups of partial cross sections, σ_P and σ_Q , with $\sigma_T = \sigma_P + \sigma_Q$. Liu and Starace predicted for the case that the fractional part of the TCS, ρ^2 , tends towards zero, i.e. the variations in the TCS caused by the resonances is small as compared to the background cross section, a mirroring of σ_P and σ_Q with respect to the energy axis [see Fig. 2(c)]. However, Fig. 2 demonstrates that this prediction is not generally fulfilled for the principal series in helium, although $\rho^2 \cong 0.01$. This is due to the fact that the variations in the PCSs caused by the resonances are in the same order as in the TCS [3]. The observed mirroring in Fig. 2(c) is only accidentally since σ_P mirrors σ_T .

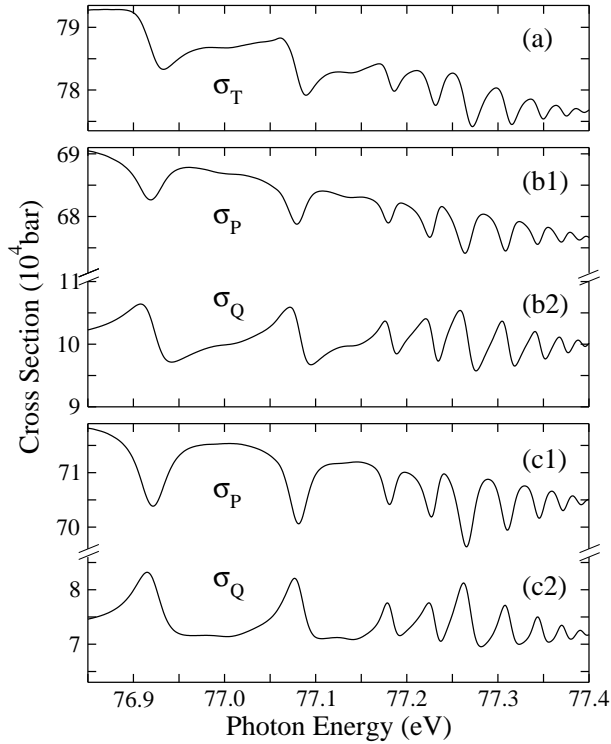


Figure 2: Cross sections below the ionization threshold I_6 obtained from eigenchannel R-matrix calculations and convoluted with a Gaussian resolution function of 6 meV width (FWHM). (a) Total cross section σ_T . In (b) and (c) the PCS σ_P and σ_Q were established in different ways: (b1) $\sigma_P = \sigma_1$ and (b2) $\sigma_Q = \sigma_2 + \sigma_3 + \sigma_4 + \sigma_5$; (c1) $\sigma_P = \sigma_1 + \sigma_3 + \sigma_4 + \sigma_5$ and (c2) $\sigma_Q = \sigma_2$.

References

- [1] A. Menzel, S. P. Frigo, S. B. Whitfield, C. D. Caldwell, M. O. Krause, J. Z. Tang, and I. Shimamura, *Phys. Rev. Lett.* **75**, 1479 (1995).
- [2] A. Menzel, S. P. Frigo, S. B. Whitfield, C. D. Caldwell, and M. O. Krause, *Phys. Rev. A* **54**, 2080 (1996).
- [3] Y. H. Jiang, R. Püttner, R. Hentges, J. Viefhaus, M. Poiguine, U. Becker, J. M. Rost, and G. Kaindl, *Phys. Rev. A* (submitted).
- [4] D. R. Herrick and O. Sinanoğlu, *Phys. Rev. A* **11**, 97 (1975).
- [5] C. D. Lin, *Phys. Rev. A* **29**, 1019 (1984).
- [6] J. M. Rost, K. Schulz, M. Domke, and G. Kaindl, *J. Phys. B* **30**, 4663 (1997).
- [7] Ch. N. Liu and A. F. Starace, *Phys. Rev. A* **59**, R1731 (1999).

Mass-filtered FeCo alloy nanoparticles on surfaces - a soft-magnetic material with high magnetic moments

J. Bansmann, A. Kleibert, R.P. Methling, F. Bulut¹, R.K. Gebhardt¹, M. Getzlaff¹,
E. Holub-Krappe², D. Schmitz², H. Maletta², K.H. Meiwes-Broer

Department of Physics, University of Rostock, D-18051 Rostock

¹ Institute of Applied Physics, University of Düsseldorf, D-40225 Düsseldorf

² Hahn-Meitner-Institut, D-14109 Berlin

supported by DFG via BA 1612/3-1 (in the DFG priority call 1153).

The reduced atomic coordination number of magnetic nanoparticles gives rise to properties being different from the respective bulk behaviour. Especially the large surface - to - volume ratio of clusters deposited on surfaces leads to an enhancement of the orbital moment in such nanoparticles. Here, we will focus on investigations related to very high total magnetic moments in soft-magnetic transition metal alloy clusters. For bulk material the Slater-Pauling curve gives an overview about the total magnetic moments of binary alloys consisting of 3d-metals. FeCo alloys with nearly equal contributions of iron and cobalt exhibit the highest magnetic moments with values of about $2.5 \mu_B$. Keeping in mind the fact that enhanced magnetic moments have been observed in small clusters deposited on surfaces [1,2], the question arises, whether the formation of alloy clusters might even more enhance this physical property. Using this

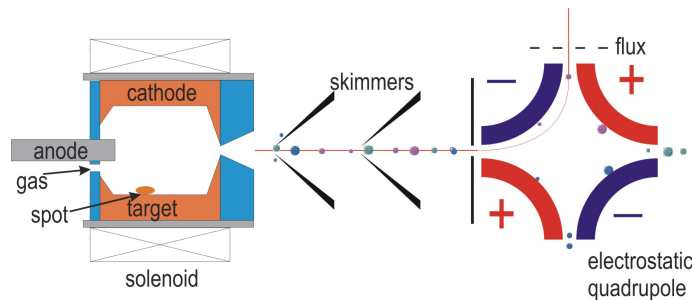


Figure 1: Schematic drawing of the arc cluster ion source ACIS and the electrostatic quadrupole deflector for the mass-filtering process of clusters in the size regime from 4 nm to 15 nm.

approach we have produced mass-filtered FeCo clusters with sizes of 6 nm and 7.5 nm from a commercial $\text{Fe}_{0.5}\text{Co}_{0.5}$ alloy target. The clusters have been created using the arc cluster ion source and mass filtered in an electrostatic quadrupole deflector, cf. fig. 1 [3]. Finally, the clusters were deposited under UHV and soft-landing conditions onto a substrate. In order to magnetize these clusters remanently without additional external

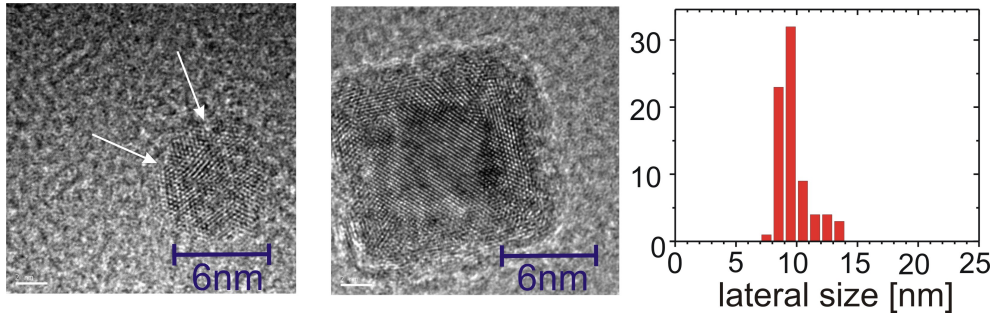


Figure 2: Left and middle: HR-TEM images from FeCo alloy clusters (size: 6 nm and 12 nm) on a TEM grid. Right: size distribution of mass-filtered FeCo alloy clusters with a mean size of 9 nm.

magnetic fields a ferromagnetic thin Ni(111) film on W(110) with a uniaxial in-plane anisotropy has been chosen as support for the clusters. Additionally, ex-situ HR-TEM and EDX- measurements were carried out in the group of Farle and co-workers (Univ. of Duisburg-Essen). Two high-resolution TEM images of mass-filtered FeCo clusters are shown in fig. 2 together with a size distribution of FeCo nanoparticles with a mean size of 9 nm from the ACIS source (cf. right part). The EDX measurements yield a ratio of 56:44 for iron to cobalt compared to 50:48 in the target material (composition of target given by the manufacturer, the remaining 2% consist of nickel and vanadium), the uncertainty of the EDX data is less than 5%. Thus, the results confirmed that the stoichiometry in deposited FeCo clusters is very similar to the chosen bulk material [4]. The spin and orbital moments of iron as well as cobalt contributions in the alloy have been investigated in-situ using the element-specific X-ray Magnetic Circular Dichroism (XMCD) technique at the UE46-beamline of the storage ring BESSY. The corresponding absorption spectra are shown in fig. 3, the radiation impinges on the surfaces at an angle of 60° with respect to the surface normal. The spectra clearly show strong intensity differences in all peaks induced by a reversal of the magnetization. The spin moments of iron and cobalt are parallel (ferromagnetic coupling) according to the sign in the respective 2p core levels.

A quantitative XMCD analysis based on the "sum-rules" yields large total magnetic moments of both elements (Fe and Co) when compared to their respective pure bulk properties, cf. fig. 4 However, the spin moments obtained in this first study do not exceed experimental or theoretical results [5] for FeCo alloys. Analogously to pure clusters in this size regime [6], the orbital moments in FeCo alloy clusters on Ni(111) are significantly enhanced with respect to theoretical values for bulk material. Thus, the orbital moments from FeCo clusters will play the dominant role for reaching total magnetic moments above the known bulk value although their contributions are about

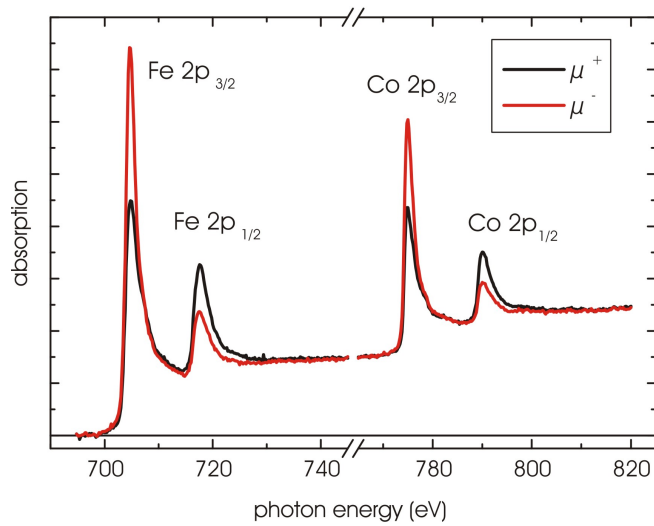


Figure 3: Photoabsorption spectra of FeCo alloy clusters taken with circularly polarized radiation for opposite in-plane magnetization direction.

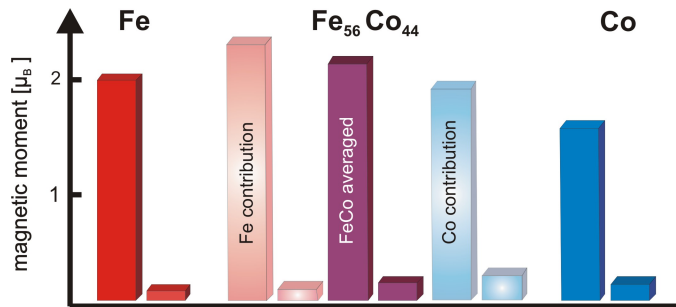


Figure 4: Element-specific quantitative XMCD analysis of the spin and orbital moments (large and small columns) of $\text{Fe}_{56}\text{Co}_{44}$ alloy clusters on a nickel film with respect to the bulk properties of both pure materials, cf. left (Fe) and right part (Co).

one order of magnitude smaller than the spin moments. Further investigations will be carried out on smaller FeCo alloy clusters and materials containing larger amounts of iron, which may increase the total magnetic moments.

References:

- [1] K.W. Edmonds et al., *J. Magn. Magn. Mat.* **220**, (2000).
- [2] J.T. Lau et al., *Phys. Rev. Lett.* **89**, 057201 (2002).
- [3] R.P. Methling et al., *Europ. Phys. J. D* **16**, 173 (2001).
- [4] M. Getzlaff et al., *Surf. Sci.*, **in press** (2004).
- [5] H. Ebert et al., *Solid State Commun.* **98**, 785 (1996).
- [6] A. Kleibert et al., *BESSY Annual report 2002*, p. 89.

Spectral Shifts in Core-to-Valence-Transitions of Molecular Van der Waals Clusters

R. Flesch, I. L. Bradeanu, A. A. Pavlychev*, and E. Rühl

Institut für Physikalische Chemie, Universität Würzburg,
Am Hubland, 97074 Würzburg

* St. Petersburg State University, St. Petersburg 198904, Russian Federation

Inner-shell absorption spectra of isolated molecules and the corresponding condensed phase are known to be quite similar to each other [1]. Substantial energy shifts have been reported for the evolution of molecular Rydberg states into the corresponding exciton states [2]. However, the situation is much less clear for the gas-to-solid shift in the regime of core-to-valence transitions. For example, high resolution spectra of gaseous and condensed nitrogen show a striking similarity at the N $1s \rightarrow \pi^*$ -transition near 400.9 eV. Recent high resolution work on free clusters indicates that Van der Waals clusters of diatomic molecules, give rise to very small spectral redshifts in clusters compared to the isolated molecule [3-5]. These shifts are of the order of 2-5 meV, which can be reliably measured with high resolution beam lines. There are also small changes in line profiles, which accompany these spectral shifts, corresponding essentially to Gaussian line broadening [5]. These results have been interpreted using a qualitative model that is based on the quasiautomatic approach [3-5]. More recently, we reported on gas-to-cluster shifts of C $1s$ -excited benzene clusters (C_6H_6)_n [6]. We observed a substantially larger redshift of the C $1s \rightarrow \pi^*$ -transition for clusters relative to

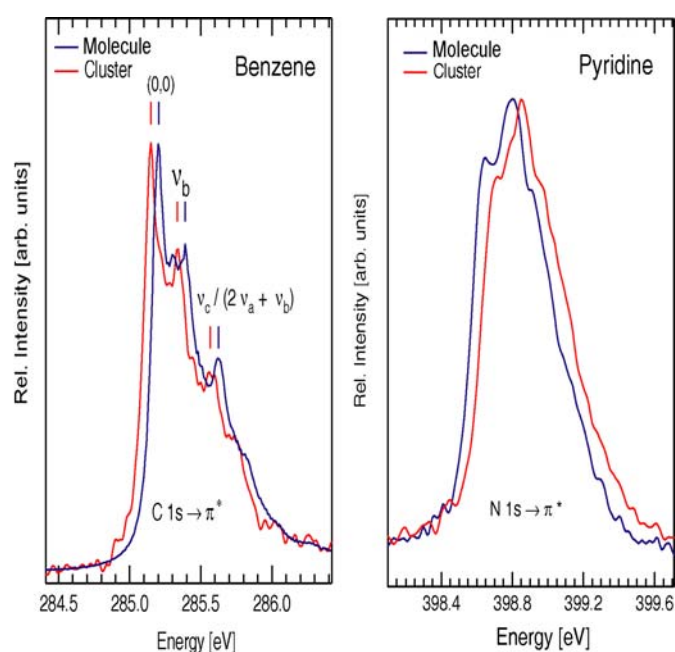


Fig. 1: left: Comparison of the C $1s \rightarrow \pi^*$ -transition of molecular benzene (C_6H_6 -yield) and benzene clusters ($(C_6H_6)_n$ -yield); right: Comparison of the N $1s \rightarrow \pi^*$ -transition of molecular pyridine (C_5H_5N -yield) and pyridine clusters ($(C_5H_5N)_n$ -yield).

isolated molecules (90 ± 5 meV) as well as broadening of the spectral profile by 30 ± 5 meV. This result is the motivation for the present work, where we have reproduced the earlier results and investigated N $1s$ -excited pyridine clusters ($(C_5H_5N)_n$) (cf. Fig. 1). The experiments were carried out at the UE 52-SGM beamline at BESSY with an energy resolution of $E/\Delta E \approx 5000$. The clusters are produced by seeding the liquid samples in argon or helium at room temperature. The mixture is expanded at $p_0 \geq 1$ bar through a nozzle ($d=50 \mu m$). This leads to the formation of homogeneous and heterogeneous clusters. The skimmed jet is transferred

into the ionization region of a time-of-flight (TOF) mass spectrometer, where it is excited by monochromatic undulator radiation. The TOF serves for cation separation and detection.

Fig. 1 shows a comparison of the spectral shifts of benzene and pyridine clusters. The photoabsorption of molecular benzene near the C 1s edge is dominated by an intense C 1s (a_{1g}) $\rightarrow\pi^*$ -transition (cf. blue curve on the left hand side of Fig. 1). The photoion yield of homogeneous benzene clusters (red curve) shows a band that is similar in shape to that of the isolated molecule, but it is redshifted by 50 ± 2.5 meV. This shift is somewhat smaller than in previous work [6], where likely larger clusters were formed. The band shows for the isolated molecule and in clusters the same vibrational fine structure, which is a result of the

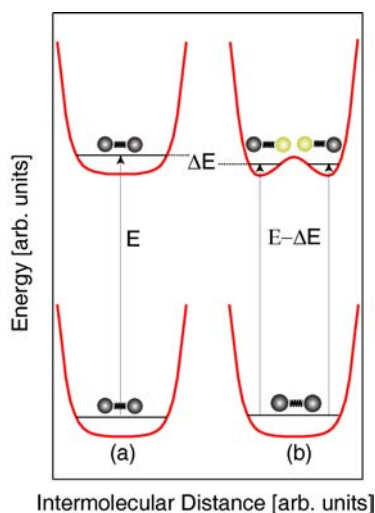


Fig. 2: Schematic diagram for two different situations of dynamic stabilization in core-excited clusters: (a) no stabilization; (b) dynamic stabilization.

change in the molecular potential upon core-level excitation. The photoabsorption of pyridine near the N 1s edge is dominated by the intense N 1s $\rightarrow\pi^*$ -transition, which is also vibrationally resolved (blue curve in Fig. 1, right hand side). The corresponding cluster spectrum (red curve) is blueshifted by 60 ± 5 meV. Changes in the energy positions of pre-edge core-to-valence transitions in clusters are rationalized by the influence of the local surroundings of the absorbing atom in clusters: (i) core-hole delocalization is observed in isolated highly symmetric molecules, such as benzene; (ii) the asymmetric environment of the absorbing site within the cluster leads to strong dynamic core-hole localization in the core-excited state. This is schematically visualized in Fig. 2 (b). As a result, a dynamic dipole moment is induced in benzene clusters. This dipole moment is extremely short-lived and exists only during the life time of the core-hole. However, it leads to a stabilization ΔE of the core-excited cluster that gives rise to a redshift. In contrast, N 1s excitation in pyridine leads to a localized excitation. Thus, no dynamic stabilization occurs in core-excited pyridine clusters (cf. Fig. 2(a)). The blueshift (cf. Fig. 1) is similar to the conversion of Rydberg states into the corresponding excitons, where commonly polarization screening is used to rationalize such blueshifts.

References

- 1 R.A. Rosenberg, P.J. Love, P.R. La Roe, V. Rehn, C.C. Parks, Phys. Rev. B **31**, 2634 (1985).
- 2 B. Kassühlke, P. Averkamp, S. Frigo, P. Feulner, W. Bertholt, Phys. Rev. B **55**, 10854 (1997).
- 3 R. Flesch, A.A. Pavlychev, J. J. Neville, J. Blumberg, M. Kuhlmann, W. Tappe, F. Senf, O. Schwarzkopf, A.P. Hitchcock, E. Rühl, Phys. Rev. Lett. **86**, 3767 (2001).
- 4 R. Flesch, W. Tappe, A. A. Pavlychev, E. Rühl, Surf. Rev. Lett. **9**, 99 (2002).
- 5 R. Flesch, A.A. Pavlychev, E. Rühl, Phys. Rev. A, submitted (2003).
- 6 R. Flesch, A.A. Pavlychev, E. Rühl, BESSY Annual Report 2001.

Financial support by the Deutsche Forschungsgemeinschaft is gratefully acknowledged.

Anisotropy of Cation Emission from Core-Excited Atoms, Molecules, and Clusters

R. Flesch, I. L. Bradeanu, A. A. Pavlychev^{*}, and E. Rühl

Institut für Physikalische Chemie, Universität Würzburg,
Am Hubland, 97074 Würzburg

^{*} St. Petersburg State University, St. Petersburg 198904, Russian Federation

Angle-resolved cation detection of isolated core-excited molecules has been investigated in the past [1-3]. This allows to derive symmetry-resolved spectra, providing for diatomic molecules a complete symmetry resolution between $\Delta\Lambda=0$ (parallel) and $\Delta\Lambda=\pm 1$ (perpendicular) transitions. Similarly, complete symmetry resolution is found for dipole allowed transitions in linear polyatomic molecules. However, incomplete symmetry resolution is found in transitions of triatomic molecules that undergo vibronic coupling, where e. g. $1s \rightarrow \pi^*$ -transitions are Renner-Teller split. To the best of our knowledge the experimental approach of angle-resolved ion-yield spectroscopy has not been applied to free, variable size clusters in the gas phase. This is the motivation for the present work, where we report on the commissioning of a new detector that allows us to measure simultaneously angle-resolved ion yields at various angles relative to the electric vector of linearly polarized synchrotron radiation, i. e. parallel and perpendicular to the polarization plane.

The experimental setup consists of a cluster jet and two identical channeltron multipliers (DeTech 206-03). One detector is mounted in the plane of the linearly polarized synchrotron radiation from the U49-2-PGM1 beam line at BESSY. The other one is mounted perpendicular to this plane (*out of plane* detector). The general setup of the detectors is similar to previous works on isolated molecules [1-3]. Cations are formed in the interaction region of the cluster jet by linearly polarized monochromatic soft X-rays. The interaction region is kept field free, so that the emission of cations with sufficient kinetic energy is detected simultaneously within an angle of $\pm 10^\circ$ by both channeltrons. A grid is mounted in front of each detector, so that a small retarding potential can be applied. The cluster jet and the beam of synchrotron radiation are crossed perpendicular to each other. The *in plane* detector was initially mounted at 45° scattering angle relative to the cluster jet. Other orientations of this detector at 0° and 135° were also tried out. Moreover, an effusive jet was used instead of the cluster jet in order to verify the proper operation of the setup in comparison with earlier work [2] and to avoid artifacts in cation detection. We used for the initial commissioning of the setup molecular nitrogen from an effusive and a supersonic jet, where the N $1s$ -excitation regime was investigated. The results shown in Fig. 1 indicate that similar findings compared to earlier work are obtained (cf. [1,2]). Cation detection of the *out of plane* channel shows Rydberg states of p^π -symmetry, whereas the other (*in plane*) detector probes for example the $3s^\sigma$ -Rydberg state as well as the N $1s \rightarrow \sigma^*$ -transition.

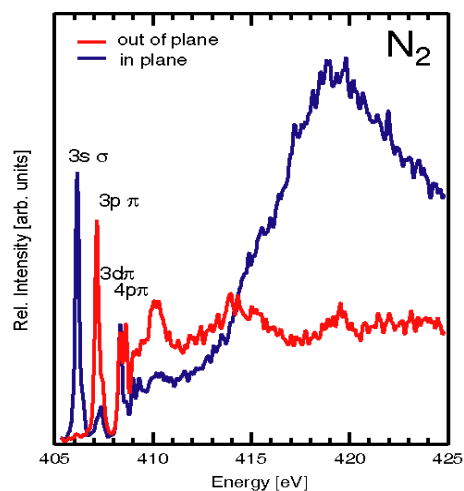


Fig. 1: Total ion yields of molecular nitrogen parallel (*in plane*) and perpendicular (*out of plane*) to the electric vector of linearly polarized synchrotron radiation in the N 1s excitation regime.

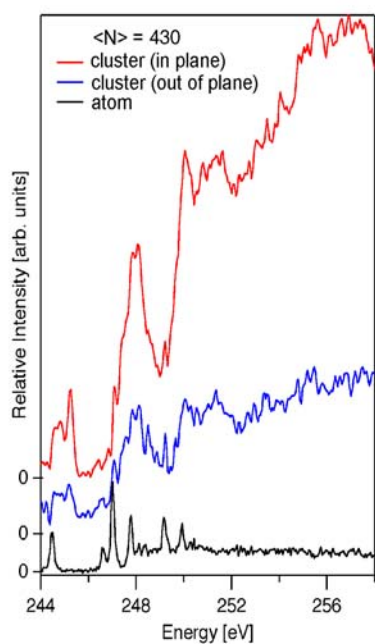


Fig. 2: Total ion yields of atomic argon and argon clusters ($\langle N \rangle = 430$) parallel (*in plane*) and perpendicular (*out of plane*) to the electric vector of linearly polarized synchrotron radiation in the Ar 2p excitation regime.

References

- 1 A. Yagishita, E. Shigemasa, Rev. Sci. Instrum. **63**, 1383 (1992); E. Shigemasa, K. Ueda, Y. Sato, T. Sasaki, A. Yagishita, Phys. Rev. A **45**, 2915 (1992); N. Kosugi, E. Shigemasa, A. Yagishita, Chem. Phys. Lett. **190**, 481 (1992).
- 2 J. Adachi, N. Kosugi, E. Shigemasa, A. Yagishita, Chem. Phys. Lett. **309**, 427 (1999).
- 3 T. Gejo, Y. Takata, T. Hatsui, M. Nagasono, H. Oji, N. Kosugi, E. Shigemeasa, Chem. Phys. **289**, 15 (2003).
- 4 E. Rühl, Int. J. Mass Spectrom. **229**, 117 (2003).

Financial support by the Deutsche Forschungsgemeinschaft is gratefully acknowledged.

We have also studied angle-resolved ion yields of 2p-excited Ar and Ar clusters (see. Fig. 2). In the case of isolated atoms one finds, as expected, identical signals for both ion detectors. This situation changes as soon as clusters are present in the jet. The cluster spectra shown in Fig. 2 correspond to the average cluster size $\langle N \rangle = 430$, where the atomic component has been subtracted. We observe for clusters distinct differences between the cation signals parallel (*in plane*) and perpendicular (*out of plane*) to the polarization plane. The *in plane* detector shows higher sensitivity for sites that are bound in the bulk interior of clusters. This becomes evident for the lowest exciton transition (Ar $2p \rightarrow 4s_{3/2}$ near 245 eV), where bulk excitons dominate. Moreover, the regime of continuum resonances shows only for this channel intense EXAFS oscillations ($E > 250$ eV). It is well-known that the EXAFS signal comes primarily from bulk sites in clusters [4]. On the other hand, the *out of plane* detector is mostly sensitive to surface-bound sites, so that this signal is distinctly different compared to the atomic ion yield and the *in plane* detector signal (see Fig. 2). Different orientations of the *in plane* detector indicate, that the bulk-site intensity is significantly increased for forward scattering, whereas backward scattering (135° relative to the jet axis) favors the detection of the atomic component and surface bound atoms. The detailed assignment of these results is currently in progress.

Self-assembled Tb(0001) nanoparticles on Nb(110) surface : a polarized soft X-ray resonant magnetic scattering study

J.M. Tonnerre¹, C. Meyer², S. Pokrant², E. Schierle³, E. Weschke³, E. Bontempi⁴, L. Ortega¹

¹ *Laboratoire de Cristallographie, CNRS, B.P. 166, 38042 Grenoble Cedex 09 (France)*

² *Laboratoire Louis Néel, CNRS, B.P. 166, 38042 Grenoble Cedex 09 (France)*

³ *Institut für Experimentalphysik Freie Universität Berlin, Arnimallee 14, 14195 Berlin (Germany)*

⁴ *Laboratorio di Strutturistica Chimica, Università di Brescia, Via Branze 38, 25123 Brescia (Italy)*

In contrast to 3d metal systems, studies of the magnetic properties of rare earth particles are rare and have been performed up to now almost exclusively on isolated particles in a molecular beam. Since it is not possible to obtain detailed structure information on isolated particles, the reduction of the magnetic moment is not well understood. The aim of this project is to contribute to the understanding of the size and matrix (interface) dependence of the magnetic properties of Tb nanoparticles embedded in a Nb matrix. This study has been initiated in Grenoble: Laboratoire Louis Néel (S. Pokrant, C. Meyer) and Laboratoire de Cristallographie (J.M. Tonnerre), with the collaboration of E. Bontempi in Brescia (Italy) and E. Weschke in Berlin.

The self-assembled particles have been epitaxially grown on a Nb(110) buffer layer deposited on a sapphire Al₂O₃(11-20) substrate. To protect the particles against oxidation, the films were covered with Nb (20 Å) and Al (25 Å) or Si (30Å) layers. In order to obtain first insight into the magnetic properties of Tb particles, we performed macroscopic SQUID measurements as a function of temperature (10 K-300 K). Below 150 K, the particles exhibit remanent magnetic order. Elastic strain effects in the particles have been observed by grazing incident X-ray diffraction (L. Ortega, LdC). They might induce some change in the transition temperatures for the antiferromagnetic and ferromagnetic phases with respect to the Tb bulk values (Curie temperature is 219.5K and Néel temperature is 231.5K).

In order to investigate the magnetic order of the Tb particles as a function of size and temperature, we have performed soft x-ray resonant magnetic scattering (XRMS) measurements using polarized photons corresponding to the region of the Tb $M_{4,5}$ edges (1241.1 eV, 1276.9 eV), on two samples with different size and structural correlation length, as well as on a continuous Tb film. A previous hard X-ray reflectivity experiment using Cu-K α radiation has been performed to determine thicknesses and roughnesses of the different stacking layers of samples (Fig. 1). For the continuous films, the thickness derived from

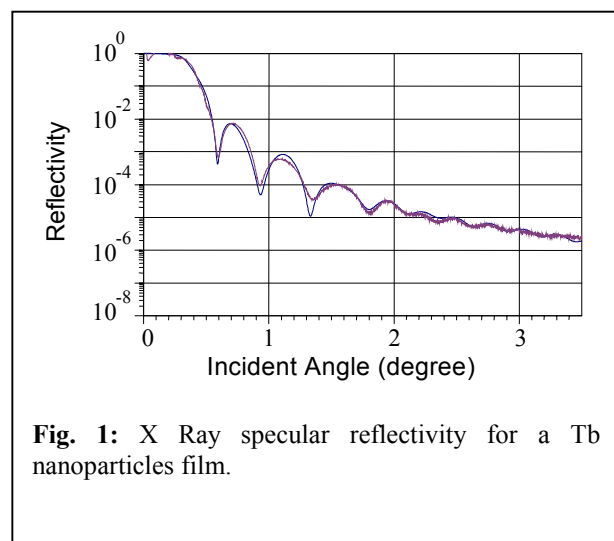


Fig. 1: X Ray specular reflectivity for a Tb nanoparticles film.

the fitting of the reflectivity angular dependence agrees very well with the nominal values. Also for a particle sample, the reflectivity could be well simulated by introducing a mixed Tb-Nb layer, 1.85 nm thick, with a 1.97 nm roughness and a Nb layer, 1.3 nm thick, with a roughness of 0.8 nm.

The strong resonant enhancement in the soft x-ray region at the $3d \rightarrow 4f$ transitions leads to an enormous increase in the sensitivity with respect to the small amount of Tb in the particle films (equivalent ≈ 3 continuous atomic layers), as demonstrated in a previous experiment on a continuous Ho films¹. The measurements performed at BESSY to probe the lateral arrangement of the particles, show satellite peaks in the diffuse scattering region, which correspond to in-plane statistical correlation lengths of 125 or 185 nm, respectively, for the two different samples labelled sp85 and tb98 (Fig. 2). These satellite peaks are resonantly enhanced, showing that they are related to the structural properties of Tb.

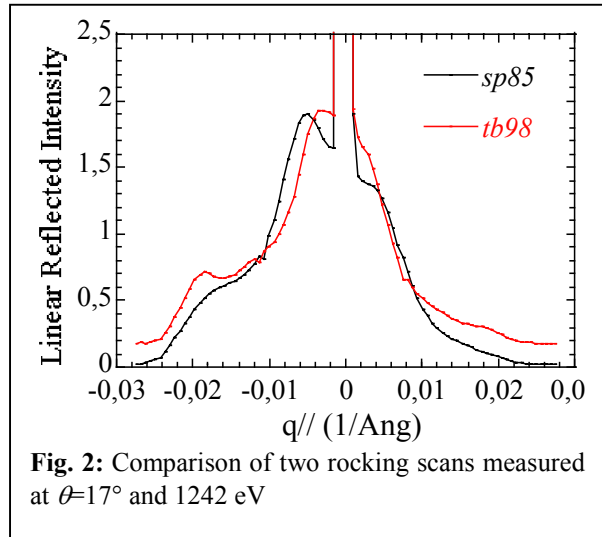
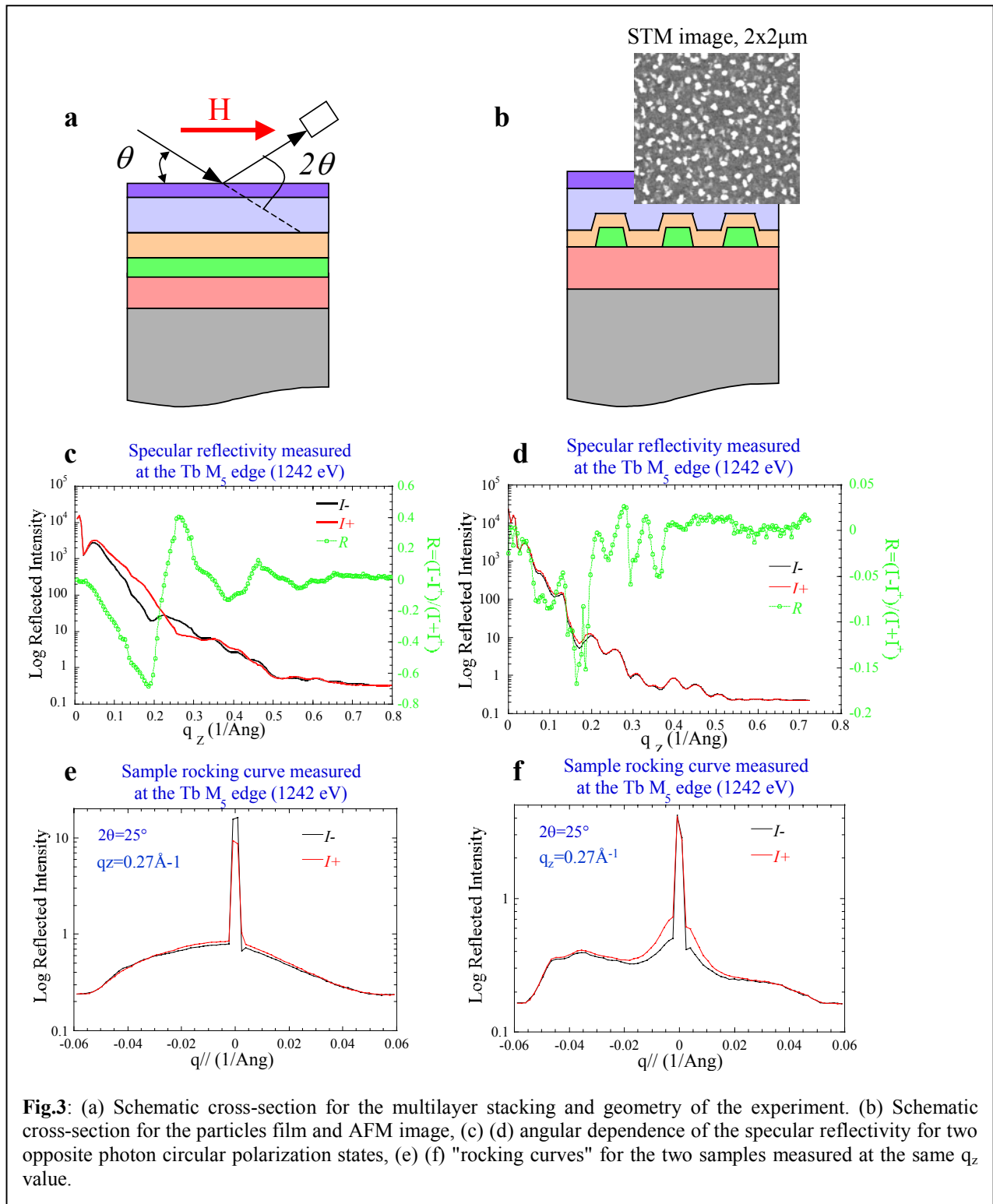


Fig. 2: Comparison of two rocking scans measured at $\theta=17^\circ$ and 1242 eV

Magnetic contrast was obtained by using left (I^-) and right (I^+) circularly polarized light from the UE52-SGM undulator beamline. Figure 3 shows raw data and corresponding asymmetries for the continuous Tb film and for a particle sample. In both cases, a pronounced dichroic contrast is observed in the specular scans. It turns out, however, that in the case of the particle sample, a relatively large contrast is observed in the diffuse direction, which is much weaker in the continuous film, as can be inferred from the rocking scans shown in the lowest panel in figure 3. Further analysis of the magnetic contrast for the specular and diffuse scattering data requires a detailed modeling of particle form factors, which is work in progress. They will provide information about the magnetization profile along the growth direction as well as the magnetic correlation in the plane.

The work in Berlin was supported by the BMBF, project 05 KS1 KEE/8.

¹ C.Schüßler-Langeheine et al., J. Electr. Spectrosc. Relat. Phenom. **114-116**, 953 (2001)



Photoionization of Single Stored Nanoparticles

M. Grimm^{a,b}, B. Langer^b, C. Graf^a, T. Lischke^c, S. Schlemmer^d,

W. Widdra^e, D. Gerlich^f, U. Becker^c, E. Rühl^a

^aInstitut für Physikalische Chemie, Universität Würzburg, Am Hubland, 97074 Würzburg

^bMax-Born-Institut Berlin, Max-Born-Straße 2a, 12489 Berlin

^cFritz-Haber-Institut der Max-Planck-Gesellschaft, Faradayweg 4-6, 14195 Berlin

^dRaymond and Beverly Sackler Laboratory for Astrophysics at Leiden Observatory, Leiden (NL)

^eFachbereich Physik, Universität Halle-Wittenberg, 06099 Halle

^fInstitut für Physik, Technische Universität Chemnitz, 09107 Chemnitz

Studies on solid and liquid particles with sizes in the range between small clusters and objects up to several micrometers have a tremendous potential for applications in various fields, such as basic research, nanoscopic and mesoscopic materials science, biology, environmental research, and astronomy. Experiments on such species are often dealing with averages over different particles with respect to size, shape, and related properties. In contrast, experiments on single, isolated nanoparticles provide specific information from the time average. Moreover, this approach allows us to control the environment of the particles, since any contact to a substrate is avoided. Single SiO₂ particles ($r = 250$ nm) are stored in the center of a three dimensional electrodynamic quadrupole trap, that is located in a UHV chamber, over long time periods reaching up to several days. After injection, the particle is illuminated by a frequency doubled Nd:YAG laser ($P < 50$ mW, $\lambda = 532$ nm). The scattered light is collected by a lens and detected by an avalanche photodiode. The scattered light is modulated by the eigenfrequencies of the trapped particle due to the particle motion through the Gaussian laser beam. These frequencies can be obtained from a fast Fourier transform of the photodiode signal. The charge-to-mass ratio Q/M of the particle is very precisely derived, once the parameters of the electrodynamic trap are known. At low charge states ($Q < 1000$ e) and low photon flux of monochromatic synchrotron radiation in the soft X-ray regime the charge state of the particle increases in steps of one or integer multiples of the elementary charge, leading to a stepwise change of the eigenfrequencies. The least common multiple of the frequency changes corresponds to the change of one elementary charge, which is the smallest step height in such particle charging experiment. This allows us to determine the absolute charge state and the absolute mass of the particle (see refs. [1-3] for more details).

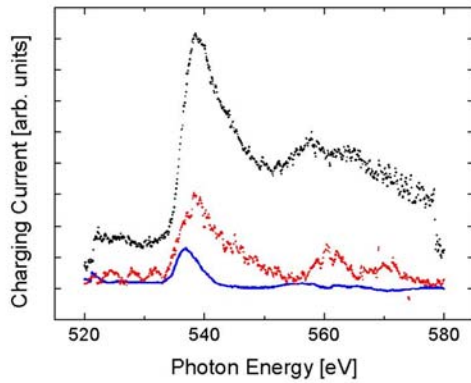


Fig. 1: O 1s spectra of a single stored nanoparticle ($r = 250$ nm) at different charge states (see text for further details).

After the charge and mass determination of the particle we recorded charging curves in the energy range of the O 1s-edge, i.e. from 520 eV to 580 eV. By scanning the photon energy the charging current of the particle is determined from the temporal evolution of the charge state in this spectral regime. Fig. 1 shows the first derivative of three charging curves for different average charge states. For low charge states ($Q \approx 15,000$ e - black curve) the first derivative of the charging curve is similar to the NEXAFS spectrum of quartz [4]. One can clearly observe intense near-edge features below the O 1s-ionization energy near 538 eV and a broad resonance in the O 1s-continuum near 554 eV. At higher charge states (red curve: $Q \approx 35,000$ e; blue curve: $Q \approx 50,000$ e) the intensity of the resonance as well as the intensity in the 1s-continuum drops. In addition, the resonance structure becomes narrower and it is also slightly redshifted with increasing charge state. These results are rationalized as follows: In the O 1s-continuum charging occurs primarily via the normal or double Auger decay. Assuming that the charges are located on the particle surface, the local electrical field increases with increasing charge state. As a result, only those electrons with sufficient kinetic energy can contribute to photoionization of the particle, corresponding to an increase in charge state. The other electrons will be retained by the field of the charged particle. The fraction of electrons that contribute to charging decreases with increasing charge state, so that the intensity of the differentiated charging curves decreases (cf. Fig. 1). The fastest electrons that can be emitted after resonant core level excitation with considerable flux come from resonant Auger processes. These processes occur mostly in the near-edge regime, i. e. between 535 eV and 540 eV.

This work is supported by the BMBF (contract no. 05KS1MPA/8, 05KS1OC1/2, and 05KS1BMA/0).

References

- 1 S. Schlemmer, J. Illema, S. Wellert, and D. Gerlich, *J. Appl. Phys.* **90**, 5410 (2001); S. Schlemmer, S. Wellert, F. Windisch, M. Grimm, S. Barth, and D. Gerlich, *Appl. Phys. A*, in press (2004).
- 2 M. Grimm, B. Langer, S. Schlemmer, T. Lischke, W. Widdra, D. Gerlich, U. Becker, and E. Rühl, *AIP Conf. Proceedings*, in press (2004).
- 3 M. Grimm, B. Langer, T. Lischke, E. Rühl, W. Widdra, D. Gerlich, U. Becker, and S. Schlemmer, *BESSY Annual Report 2002*.
- 4 Z. Wu, F. Seifert, B. Poe, and T. Sharp, *J. Phys.: Condens. Matter* **8**, 3323 (1996).

XPEEM investigation of 2D hierarchical array of Ni nanorods using block copolymer templates.

A. Sidorenko*¹, I. Tokarev¹, R. Krenek¹, Y. Burkov², D. Schmeisser², M. Stamm¹
¹*Institut für Polymerforschung, Dresden, and* ²*Brandenburgische Technische Universität, Cottbus.*

Methods of fabrication of ordered arrays of nanowires/nanorods are in the focus of many investigations. Such nanostructures are considered to be of significant interest for both fundamental and application aspects. Several approaches have been proposed based on the self-organization phenomenon [1-3].

Recently, we have published the results of the investigation of self-organization in thin films of BC supramolecular assembly (SMA). Based on the O. Ikkala approach [4,5], we have synthesized SMA from poly(styrene – b – 4-vinylpyridine) (PS-PVP) using hydrogen bonding of low molar mass additive (2-(4'-hydroxybenzeneazo)benzoic acid, HABA) with pyridine fragment of PVP [15]. The SMA demonstrates ability to form smooth thin films on solid substrate. PS-PVP+HABA is able to fast self-organization via vapor annealing in solvent selective for both PS and PVP+HABA solvent (1,4-dioxane) with perpendicular alignment of hexagonally packed cylinders of minor component (PVP+HABA) dispersed in the matrix of PS (Figure 1a). Moreover, rinse of thin films of the SMA in methanol results in ordered array of channels oriented either perpendicularly or parallel to the substrate plane [6]. The channels of 8-10 nm in diameter are distributed over the entire film surface with periodicity of 24-30 nm. Using the obtained membrane as a template for electrodeposition of metal, e. g. Ni, we obtained an array of ordered Ni nanorods (Figure 1b).

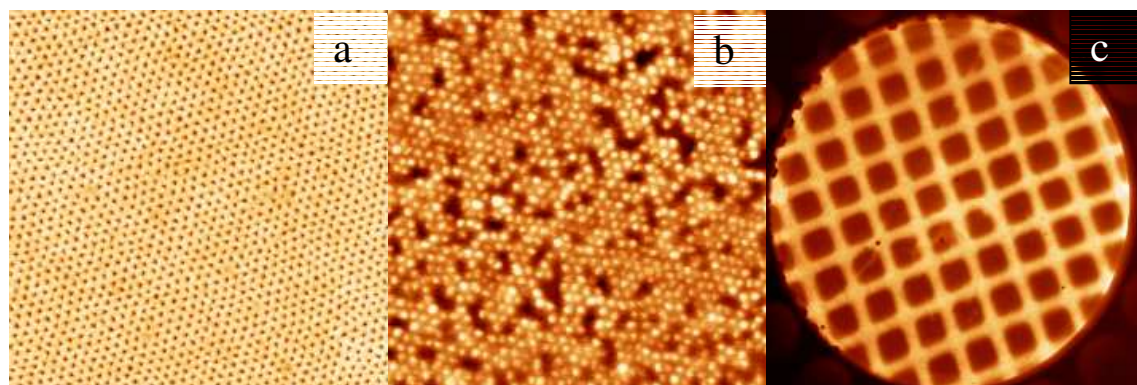


Figure 1. AFM images (topography, 1×1 μm lateral scale) of polymer template (a) and array of Ni nanorods obtained by electrodeposition of Ni through the nanotemplate (b). XPEEM image (120×120 μm) of Pbd micropatterned film at Cr2p contrast.

In order to obtain hierarchical structure of Ni covering, we modified the sample for electrodeposition. First, we deposited 30 nm thick chromium layer on top of Si{100} using

sputtering to provide electroconductivity. Second, we deposited thin micropatterned film of cross-linked poly(1,2-butadiene) (PBd) by photolithography. XPEEM image of the sample on this stage is acquired at Cr2p (574eV binding energy), Figure 1c. Third, we deposited 40 nm SMA layer and turned it into nanotemplate as described in details elsewhere [6]. Afterwards, we performed Ni electrodeposition through the combined template in order to obtain the hierarchical array of Ni nanorods.

The NEXAFS measurements of Ni deposition were performed prior the XPEEM measurements to find the exact Ni2p bonding energy as well as the peak width (Figure 2a). The result of subtraction of XPEEM images before (851.5 eV) and after (854.0 eV) Ni2p peak from the image required at the Ni2p peak (853.0 eV) is shown on the Figure 2b. It undoubtedly demonstrates distribution of Ni in the space between the PBd masked electrode surface. Thus, we obtained two scale hierarchy patterning combining electrode photolithography with insulating layer and nanotemplating.

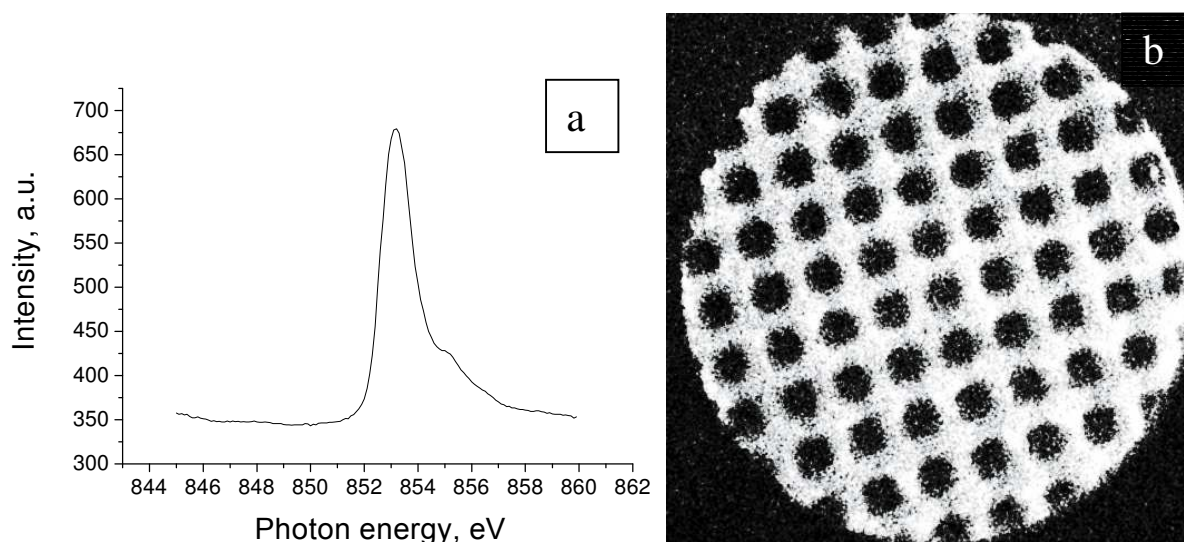


Figure 2. NEXAFS of hierarchical array of Ni nanorods and XPEEM image with Ni2p contrast (c), $120 \times 120 \mu\text{m}^2$ lateral scale.

Experimentals.

X-ray photoelectron emission microscopy (XPEEM.) and Near Edge X-ray Absorption Fine Structure (NEXAFS) spectroscopy measurements were performed on the U49/2-PGM2 beam line at the Bessy-II synchrotron radiation facility [7]. Details of the electron spectrometer used and the beam line parameters are published elsewhere [8]. The spectromicroscopic characterization by PEEM was performed with a FOCUS-IS PEEM (Omicron). The setup is equipped with a CCD camera. The camera total intensity is used to record the NEXAFS signal

which in principle can be used to obtain local spectroscopic information from the PEEM images as this information can be collected pixel resolved (μ -NEXAFS).

Acknowledgement

BMBF (grant 05KS1BPA/4) is gratefully acknowledged for financial support.

1. I. W. Hamley, *Nanotechnology* 2003, 14, R39.
2. H.X. He, N.J. Tao, Electrochemical fabrication of metal nanowires in *Encyclopedia of Nanoscience and Nanotechnology*, Eds., N.S. Nalwa, American Scientific Publishers, in press, 2003.
3. J. C. Hulteen, C. R. Martin, Template Synthesis of Nanoparticles in Nanoporous Membranes, in *Nanoparticles in Solids and Solutions*. Ed.: J. Fendler, Willey, 1998, Chapter 10, p. 235-260.
4. R. Mäki-Ontto, K. de Moel, W. de Odorico, J. Ruokolainen, M. Stamm, G. ten Brinke, O. Ikkala. *Adv. Mater.* 2001, 13, 117-121.
5. J. Ruokolainen, R. Mäkinen, M. Torkkeli, R. Serimaa, T. Mäkelä, G. ten Brinke, O.T. Ikkala. *Science* 1998, 280, 557.
6. A. Sidorenko, I. Tokarev, S. Minko, M. Stamm, *J. Am. Chem. Soc.* 2003, 125, 12211-12216.
7. P. Hoffman, D. Schmeißer, G. Roters, Z. Nenyai, *Thin Solid Films* 428 (2003) 216.
8. D.R. Batchelor, R. Follath, D. Schmeißer, *Nuclear instruments and Methods in Physics Research A* 467-468 (2001) 470.

Magnetic properties of deposited Gadolinium atoms and dimers and their monoxides

M. Reif, L. Glaser, M. Martins, and W. Wurth
*Universität Hamburg, Institut für Experimentalphysik
Luruper Chaussee 149, D-22761 Hamburg*

Small deposited metal clusters have unique physical properties which are connected to their cluster size [4]. The uniqueness of the clusters holds for many properties like chemical, optical or magnetic properties. In this study we have investigated the magnetic properties of Gd- atoms and dimers and their monoxides using x-ray circular dichroism (XMCD) to study the influence of the cluster size and the chemical environment on the Gd magnetism.

The magnetic properties of small, free Gadolinium clusters have already been studied with Stern Gerlach type experiments [1–3]. The magnetism of free Gd atoms is accounted for by seven unpaired 4f electrons and one 5d electron, which means, that the magnetism is mainly influenced from the character of the f shell. The 4f shell is well localized at the atomic site, hence the magnetic properties should be rather unaffected by the surrounding. However in order to obtain ferromagnetic properties in the bulk state, some interaction between the localized atomic magnets has to take place. This interaction is called RKKY interaction, which couples the local magnetic moments through an indirekt coupling mediated by the conduction electrons. Thus, the magnetic state might be strongly influenced by the structure and the filling of the conduction band.

Free Gadolinium atoms have an overall magnetic moment of $6.53\mu_B$ [2, 3], whereas Gd bulk has an increased magnetic moment of $7.55\mu_B$ per atom [2, 3]. The reason for this behavior is the coupling of the 5d electron. In contrast to this results, small ($N=10..33$ atoms per cluster) isolated Gd clusters have a reduced magnetic moment ($\approx 5\mu_B$ per atom for $Gd_{13,21}$ [3]) at low temperature.

The experimental setup of Gerion et al. [3] does not allow to measure pure Gd_N ; they always had some contributions of Gd_NO included. Nevertheless, they are able to tune the fraction of oxides in their cluster beam to some extent. Varying the parts of the oxide contribution, the magnetization of the cluster changes only slightly, indicating only a small influence of an oxygen adatom.

The clusters in our experiment are created by high energy ion bombardment of a gadolinium target with Xe. Mass separation is done using a dipole magnet. The spectroscopy chamber is equipped with the common surface science tools. Our experiments have been performed under UHV conditions at a base pressure below $3 \cdot 10^{-10}$ mbar. A detailed description of the experimental setup is given in [5].

The clusters are deposited onto an ultrathin iron film (3-4 monolayers (ML)) on a copper (100) single crystal. The ultrathin iron film provides a magnetic field perpendicular to the crystal surface (Peterka et al.[6]) to align the cluster moments. By the use of a coverage of 3% of a ML of clusters it is ensured that cluster-cluster interaction is small. In order to prevent the cluster from fragmentation, up to 5 ML of Argon are freezed on the iron surface (soft landing). Before taking spectra, the crystal is flash heated to 100K, to measure the clusters without the argon matrix.

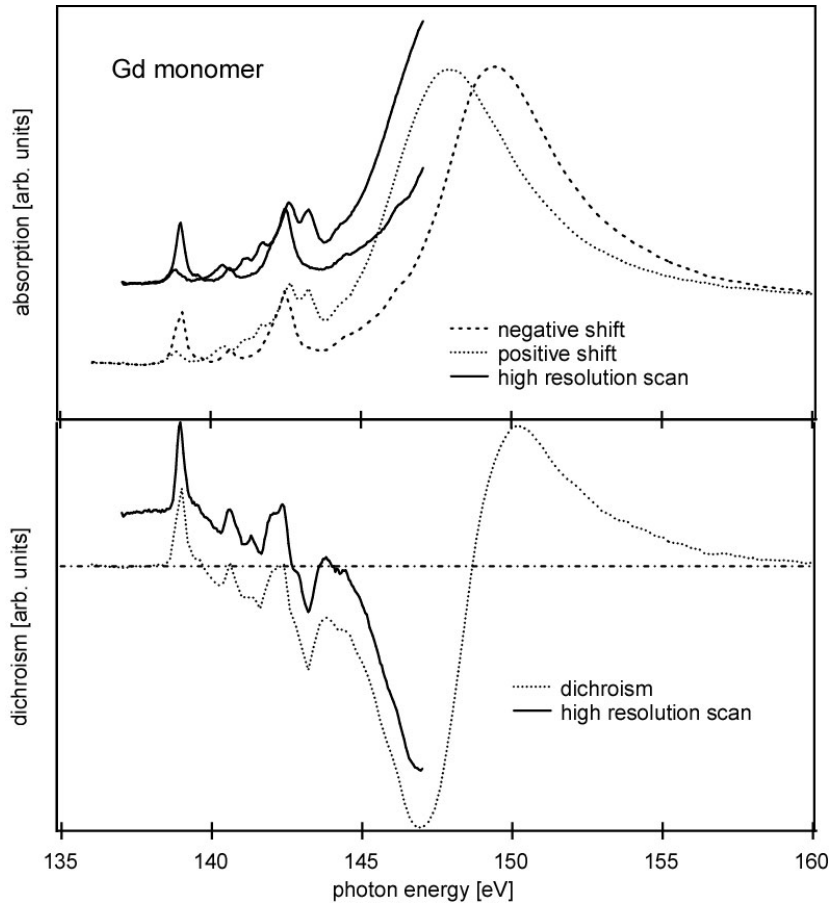


Figure 1: (a) XMCD measurements of Gd_1 with left and right circular polarized light. (b) Dichroism of Gd_1 .

The XMCD measurements have been performed at beamline UE56/1 PGM. Gd atoms and dimers and their monoxides have been investigated. The sample current is taken as a measure of the total absorption yield. The spectra are taken with a step width of 200meV, whereas high resolution scans were taken with 50meV resolution.

Figure (1a) shows absorption spectra of Gadolinium atoms deposited on the iron surface in the region of the 4d-4f excitation. The spectra are taken with left and right circular polarized light, whereas figure (1b) shows the difference spectrum. Figure 2 shows the spectra of the Gadolinium dimer. The spectra of the monoxide clusters (GdO, Gd_2O) look very similar. No difference in peak position and ratio have been observed. It is remarkable that also the spectra from GdO and Gd_2O are undistinguishable from the pure Gd monomer and dimer. Furthermore, also the XMCD spectra of Gd films on a W(0001) single crystal presented by Starke et al [7] are very similar to our cluster XMCD spectra.

The antiferromagnetic coupling to the substrate is mediated via the conduction electrons of the substrate. Since Gerion et al. [3] report that even oxygen does not affect the magnetic properties of isolated clusters drastically, the effect of oxydation should be even smaller in deposited clusters because the influence of an oxygen adatom does not affect the localized inner 4f shell very strong. The same should be true for the coupling of the pure Gd atoms and dimers to the substrate.

We thank the BESSY staff for the great support during beamtime.

Financial support for the work was given by the BMBF under grant KS1 GUB/5.

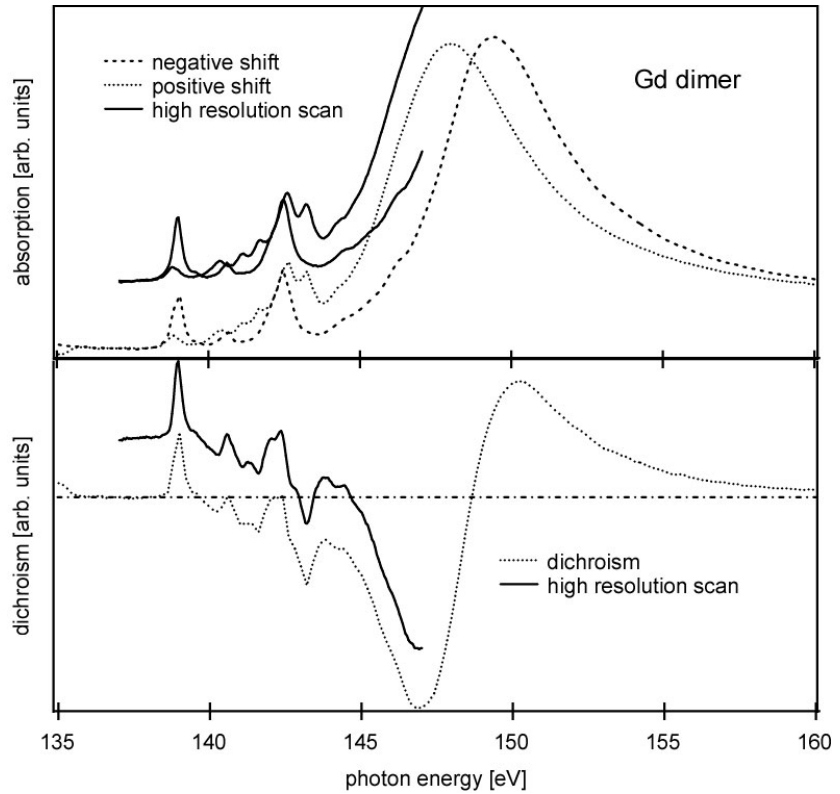


Figure 2: (a) XMCD measurements of Gd_2 with left and right circular polarized light. (b) Dichroism of Gd_2 .

References

- [1] D. C. Douglass, J. P. Bucher, and L. A. Bloomfield, *Phys. Rev. Lett.* **68**, 1774 (1992).
- [2] D. C. Douglass, A. J. Cox, J. P. Bucher, and L. A. Bloomfield, *Phys. Rev. B* **47**, 12874 (1993).
- [3] D. Gerion, A. Hirt, and A. Châtelain, *Phys. Rev. Lett.* **83**, 532 (1999).
- [4] J. Lau, A. Föhlisch, R. Nietubyc, M. Reif, and W. Wurth, *Phys. Rev. Lett.* **89**, 57201 (2002).
- [5] J. Lau, *Magnetische Eigenschaften kleiner massenselektierter Übergangsmetallcluster* (Desy-Thesis-2002-016, Notkestr. 85, 22607 Hamburg, 2002).
- [6] D. Peterka, A. Enders, G. Haas, and K. Kern, *Phys. Rev. B* **66**, 104411 (2002).
- [7] K. Starke, E. Navas, E. Arenholz, Z. Hu, L. Baumgarten, G. van der Laan, C. T. Chen, and G. Kaindl, *Phys. Rev. B* **55**, 2672 (1997).

Effect of Quenching Photoemission Resonance in Solid C₆₀ by Synchrotron Radiation

V.M. Mikoushkin, V.V. Shnitov, V.V. Bryzgalov, and Yu.S. Gordeev
*Ioffe Physical-Technical Institute, Russian Academy of Sciences, 194021, St.-Petersburg,
Russia*

S. L. Molodtsov, D.V.Vyalich, S.Danzenbacher
*Institut für Oberflächen- und Mikrostrukturphysik, Technische Universität Dresden,
D-01062 Dresden, Germany*

Abstract. Effect of quenching photoemission resonance (HOMO - ϵ_1 / Auger) in fullerite by Synchrotron Radiation (SR) has been revealed. The effect manifests itself in drastic decrease of molecular photoemission line intensities under SR. The effect can be used as a very sensitive tool for characterization of the extent of the radiation induced modification of fullerite at the first stages of this process.

Introduction

Study of fullerene fragmentation and modification has been one of the hot topics of the problem of interaction of large molecules with irradiation and atomic particles since the discovery of fullerenes [e.g. 1-2]. In particular, it was known that fragmentation of aggregated fullerenes (fullerites) can be modified by soft ultraviolet radiation of Hg- discharge sources due to polymerization of fullerenes [3]. The fullerite polymerization is caused by the creation of chemical bonds between carbon atoms of neighbor molecules instead of weak Van-der-Waals couplings. This process was supposed to be stimulated by direct photo-excitation of the HOMO-LUMO electron transitions in the vicinity of the maximum of the photo-excitation cross section (2.4–2.7 eV). This mechanism seemed to be ineffective in the case of high-energy radiation when the cross section is very small. Indeed, the process of fullerite modification by x-rays wasn't observed earlier. On the other hand, modification of fullerite C₆₀ by continuous ("zero order") Synchrotron Radiation (SR) has been revealed recently [4]. This process is reflected in a "red" shift of photoelectron spectra, in a "blue" shift of Auger electrons and in increasing continuous background of the valence band spectrum. The question has remained open whether the fullerite modification is induced by SR of ultra-violet or x-ray ranges. The answer to this question has been one of the main objectives of the research because it is very important both for the understanding fundamental mechanisms of fullerene fragmentation and of development of physical background for lithography [5] with nano-resolution provided by using x-rays and fullerite as a photo-resist. Another important objective was to reveal physical process sensitive to the fullerite modification. Such a process would give a tool for study of the modification, which is characterized by low rate even in the case of intensive fluxes of non-monochromatic continuous SR. It has been supposed that the process must be a resonant one, namely C1s - π^*2p_z photoemission resonance, which enhances the rate of HOMO - ϵ_1 photoemission of valence electrons.

Experimental procedure

Fullerite films were grown in the preparation chamber of the spectrometer of the Russian-German beam-line by evaporation of pure fullerene C₆₀ soot directly before the experiment. Photoelectron and NEXAFS spectra were measured before and after irradiation of the film by monochromatic SR in the energy range $h\nu = 120 \text{ eV} \div 600 \text{ eV}$. Of particular interest was the energy range in the vicinity of $h\nu = 284 \text{ eV}$ corresponding to the resonance C1s - π^*2p_z , which enhances the rate of HOMO-1 photoemission of valence electrons.

Modification of fullerite C₆₀ by monochromatic SR and mechanism of this modification

Modification of fullerite structure by monochromatic SR in the x-ray range has been revealed. The modification manifests itself in transformation of molecular peaks (HOMO) in photoelectron spectra of the valence electrons under irradiation. Fig.1 shows spectra of pristine fullerite (1, $Q = 0$) and of modified (2 and 3, $Q > 0$) one. As in the case of "zero order" SR [4], the molecular peaks undergo "red" shift under SR, their intensities diminish and continuous background increases towards the spectrum of amorphous carbon. The revealed transformation of the spectra of valence electrons evidences the transformation of electronic and atomic structure of fullerenes towards that of amorphous carbon. Analogous transformation of loss spectra, "red" shift of the C1s binding energy, "blue" shift of Auger electrons confirm this conclusion. The mechanism of such a radiation-induced modification of fullerenes includes an excitation of valence electrons, creation of intermolecular chemical bounds, losing small fragments and decreasing high symmetry of large fragment [4]. Excitation of valence electrons is induced by photoelectrons and a swarm of secondary electrons. As a result, the density of delocalized electrons near the Fermi-level increases resulting into increase of the relaxation energy. The increase of the relaxation energy is known to be the reason of decrease of the binding energy ("red" shift) and of the increase of the Auger electron energy ("blue" shift).

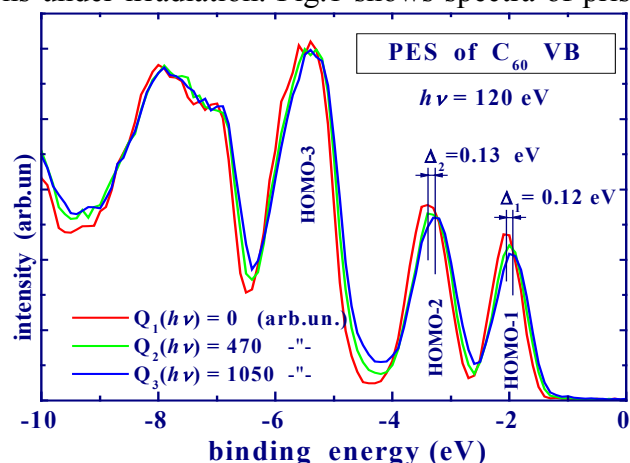


Fig.1. Photoelectron spectra of fullerite C_{60} valence band measured in the course of irradiation by monochromatic SR

Transformation of density of unoccupied states under SR

To find the resonance process sensitive to the fullerite modification, one needs information about the structure of unoccupied states through which the resonance photoemission of valence electrons occur. This information was obtained from the NEXAFS spectra in the vicinity of the transition "C1s - unoccupied (LUMO) states". Fig.2 demonstrates a set of NEXAFS spectra measured for pristine fullerite (1, $Q = 0$), fullerite irradiated by different doses of "zero order" SR (2-3, $Q > 0$) and a spectrum of amorphous carbon (4). Important experimental fact has been observed in the spectra in the course of irradiation: peaks of the unoccupied valence band radically decrease due to structure modification, especially the LUMO-1 (π^*2p_z) peak. The assumption has been made that the process of LUMO states decay must destroy the resonance photoemission.

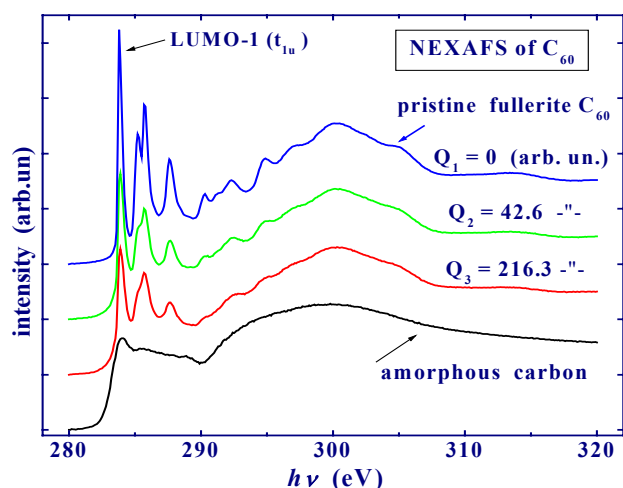


Fig.2. NEXAF spectra of fullerite C_{60} film measured in the course of the irradiation by "zero order" SR

Quenching photoemission resonance in fullerite by SR

Effect of resonance photoemission through LUMO-1 (π^*2p_z) state is illustrated by Fig.3. The figure shows photoelectron spectra of the valence band (HOMO) measured at the resonance C1s- π^*2p_z photon energy ($h\nu = 284.1$ eV) and near the resonance ($h\nu = 283.6$ and

284.9 eV). Radical increase of valence electron photoemission cross section at the resonance photon energy is caused by interference of amplitudes of direct (HOMO - ϵ) and Auger (C1s- π^*2p_z ; HOMO+ π^*2p_z) transitions. Unfortunately, the second order of SR was rather intensive in the experiment and C1s photoelectron line initiated by this order coincided with HOMO-1 peak at the resonance energy. Therefore, the most intensive line in Fig.3 is the sum of two contributions and HOMO-2 was chosen to study the influence of SR on resonance quenching. Fig.4 demonstrates this effect. The figure shows a set of resonance photoemission spectra ($h\nu = 284$ eV) measured for practically pristine fullerite (1, $Q \sim 0$), and irradiated one (2, 3, $Q > 0$).

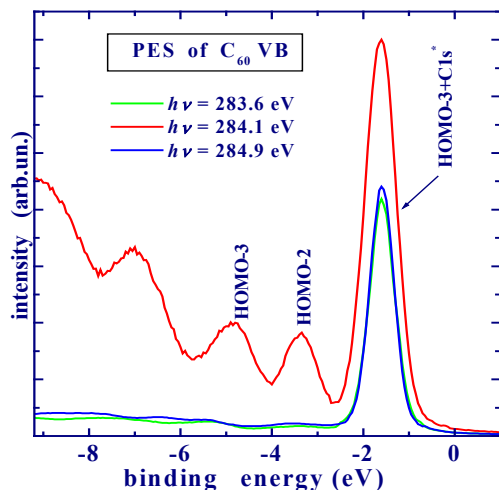


Fig. 3. PES spectra of fullerite C_{60} valence band measured in the course of irradiation by SR in the vicinity of resonance

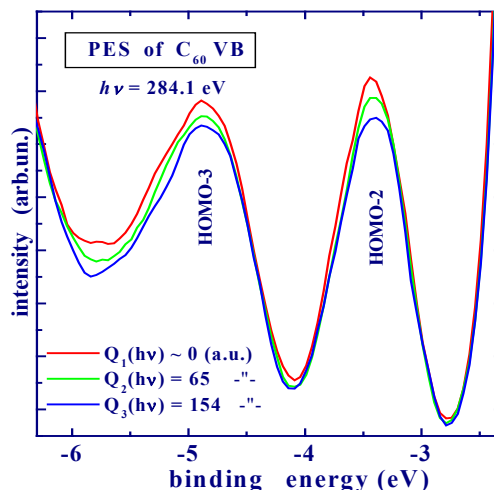


Fig.4. PES spectra of fullerite C_{60} valence band measured in the course of irradiation by SR in the vicinity of resonance

A reliable decrease of HOMO peak intensities (13%) is seen in the figure in spite of the fact that the irradiation doses were two orders of magnitude smaller than doses of SR with wavelength far from the resonance ($h\nu = 120$ eV), which induce comparable changes.

Conclusion

The process of radiation induced modification and effect of quenching photoemission resonance in fullerite C_{60} by SR have been revealed. It has been shown that the effect manifests itself in drastic decrease of molecular photoemission line intensities and can be used as a very sensitive tool for characterization of the extent of fullerite modification.

Acknowledgements

The project was supported by BESSY-II, INTAS grant № 2136, NWO grant № 047.009.012 and by the research program of the Russian Academy of Sci. "Low-Dimensional Quantum Structures". Authors thank Prof. A.S. Vinogradov for fruitful discussions.

References:

1. I.V.Hertel, H.Steger, J.de Vries, B.Weisser, C.Menzel, B.Kamke, and W.Kamke. Phys.Rev.Lett., **68**, 784 (1992).
2. O. Hadjar, P. Földi, R. Hoekstra, R. Morgenstern, T. Schlathölter, Phys. Rev. Lett. **84**, (2000) 4076-4079.
3. Y. Wang, J.M. Holden, A.M. Rao, P.C. Eklund, U.D. Venkateswaran, D. Eastwood, R. Lidberg, G. Dresselhaus, M.S. Dresselhaus. Phys. Rev. **B51**, 7, 4547 (1995).
4. Yu.S.Gordeev, V.M. Mikoushkin, V.V.Shnitov, S.L. Molodtsov, Abstr. XXIII Int. Conf. on the Phys. of Electronic and Atomic Collisions (XXIII ICPEAC), Stockholm, 2003, We 187.
5. V.V.Shnitov, V.M.Mikoushkin, and Yu. S.Gordeev, Microelectronic Engineering, v.69 (2003), p.p. 429-434.

Study of Element Composition and Shape of InAs/GaAs Quantum Dots

V.M. Mikoushkin, V.V. Bryzgalov, Yu.S. Gordeev, V.V. Shnitov, V.P. Evtikhiev,
A.S. Shcolnic, V.M. Ustinov, A.E. Zhukov
*Ioffe Physical-Technical Institute, Russian Academy of Sciences, 194021, St.-Petersburg,
Russia*

S. L. Molodtsov, D.V. Vyalich
*Institut für Oberflächen- und Mikrostrukturphysik, Technische Universität Dresden,
D-01062 Dresden, Germany*

Abstract. Indium-depth concentration profiles of the InAs/GaAs nanoheterostructures with quantum dots have been measured by the combination of layer-by-layer ion sputtering and element concentration control by means of photoelectron spectroscopy. It has been shown that these profiles gave direct information about geometrical shape of quantum dots.

1. Introduction

Investigation of a new generation of nanoheterostructures with self-organized semiconductor clusters inside a semiconductor matrix belongs to one of the basic lines of the modern physics and nano-electronics [1]. Of particular interest are systems of nanometer clusters with more narrow band gap than that in a semiconductor matrix, for instance, InAs and InGaAs clusters in a GaAs matrix, or Ge clusters in silicon. Cluster heterostructures are very promising in developing new generation of electronic devices. A number of optical devices are already designed on the basis of quantum dot systems. The basic studies of electron structure of real quantum dots have been performed mainly by the optical and volt-capacitance spectroscopy [2] that allow one determining energy position of electron and hole levels of quantum dots. Electron spectroscopy and other surface-sensitive methods, which are typically the most effective methods in studying electron structure of materials, fail in this case, since the depth of analyzed layer is much less than the thickness of matrix and cap layers. Of course, electron spectroscopy could be used for studying clusters in the course of quantum dot growth but there is no information about such studies. In any case one should take into account that semiconductor cluster without semiconductor matrix is not a quantum dot and studying clusters on the surface gives information about quite different physical object. A different way of quantum dot investigation has been developed in this research. It includes a photoelectron spectroscopy in combination with layer-by-layer ion etching of real quantum dot structure. Apart from information about element composition and electron structure, the developed way gives a possibility to estimate the shape of clusters. It is known that, depending on growth conditions, clusters of different shapes can be formed: pyramidal with different vertex angles or dome-shaped. The shapes are typically studied by the destructive (in sample preparation stage) method of transmission electron microscopy [2]. Therefore, it is difficult to simultaneously study the cluster shape and electron structure. The suggested way gives such an opportunity. Developing experimental techniques and studying element composition and shape of InAs clusters in the GaAs matrix (InAs/GaAs quantum dots) by photoelectron spectroscopy in combination with layer-by-layer ion etching were the main goals of the research.

2. The technique of opening quantum dot layer of InAs/GaAs nanoheterostructure.

The technique includes layer-by-layer ion sputtering and element concentration control by means of photoelectron spectroscopy in intervals between the sequential ion sputtering. Previously this technique was used for studying interfaces with high temperature superconductors. Diffusion profiles of about 10 nm thicknesses were measured [3]. The adapted tech-

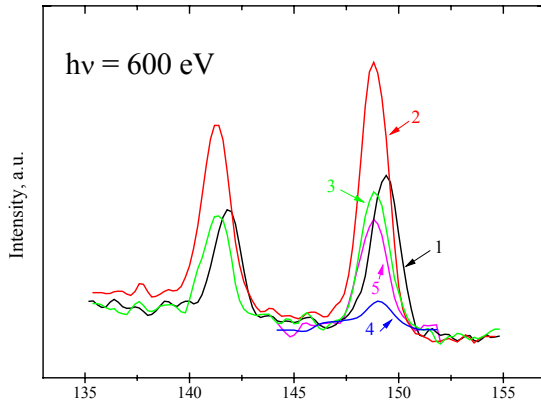


Fig. 1. In3d photoelectron spectra. Spectra numbers correspond to certain points in the In-depth profile in Fig.2a.

from the large one were used for the solution of this task. As a result, the technique providing simultaneous access to the quantum dot layer over the whole surface has been developed. One of the studied samples (A) was prepared by this technique before the BESSY experiment by removing the cap layer.

3. Depth profile and chemical state of In in InAs/GaAs nanoheterostructure.

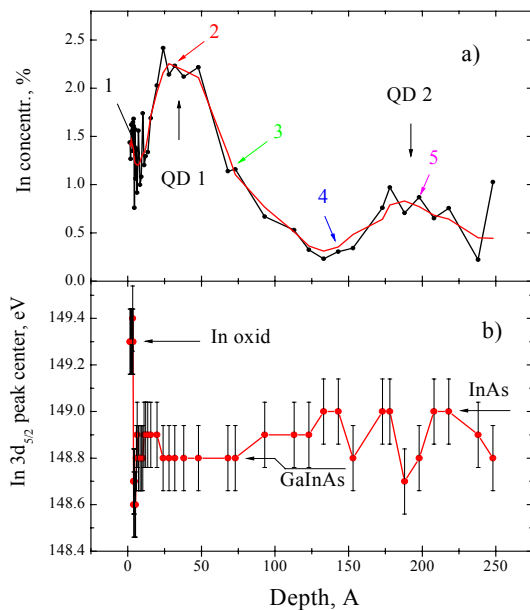


Fig. 2. a). In-depth concentration profile of the InAs/GaAs nanoheterostructure (sample A).

b). Kinetic energy of In3d_{5/2} photoelectrons throughout all the depth profile of the structure (sample A)

The point $d = 190$ Å corresponds to the position of the center of the second quantum dot layer (QD-2) being characterized by lower density of dots. The extensions of the QD-regions characterize the average height of quantum dots. They are close to each other in both QD-layers. Fig. 2b shows the kinetic energy of In3d_{5/2} photoelectrons throughout all the depth profile of the structure. Except of the region of native oxide near the initial surface ($d < 10$ Å), the In3d_{5/2} line practically doesn't show any chemical shift both in the dot layer (InAs) and bury-

nique provides a uniform remove of the GaAs cap layer with thickness of about several tens of nanometers and enables to stop sputtering in the immediate region before quantum dot layer. The etching rate calibrations in the course of removing the cap, intermediate (burying) and quantum dot layers were carried out mainly at Ioffe Institute by using electron spectrometer LHS-11. Final calibration was made at Russian-German beam-line of BESSY II by using SR as a diagnostic tool. Several identical samples obtained

Fig.1 shows In3d_{5/2, 3/2} photoelectron spectra measured at $h\nu=150$ eV irradiation after ion sputtering layers of the sample A of different thickness. Intensity of the line characterizes concentration of indium at different depth of the sample. Photoionization cross-sections of In 3d and As3d [4] were used to relate the line intensity with the concentration. As a result In-depth concentration profiles of the InAs/GaAs nanoheterostructures were obtained. Fig. 2a demonstrates the In-depth profile of the sample A. As was mentioned above, thick cap layer of this sample was removed before the experiment. Profile shows two layers of quantum dots (QD-1 and QD-2) separated by the burying layer. Regions of the dots and burying layer differ from each other by the In- concentration: the large concentration (0.5-2.5%) in the region $d = 50-70$ Å with the center at $d = 30$ Å corresponds to the first dot layer (QD-1).

ing one (GaAs). This fact evidences similar chemical positions of In in both layers and implies that In occupies site of GaInAs alloy rather than of interstitials or of In-metallic segregates.

4. Determination of quantum dot shape by photoelectron spectroscopy in combination with layer-by-layer ion etching.

Measuring element concentration profiles throughout the depth of quantum dot layer has been shown to enable determination of quantum dot geometrical shape. To better illustrate the idea, the depth profile of the sample **B** was measured (Fig. 3). Strong asymmetry of the profile presented in Fig.3 evidences a pyramidal type of clusters.

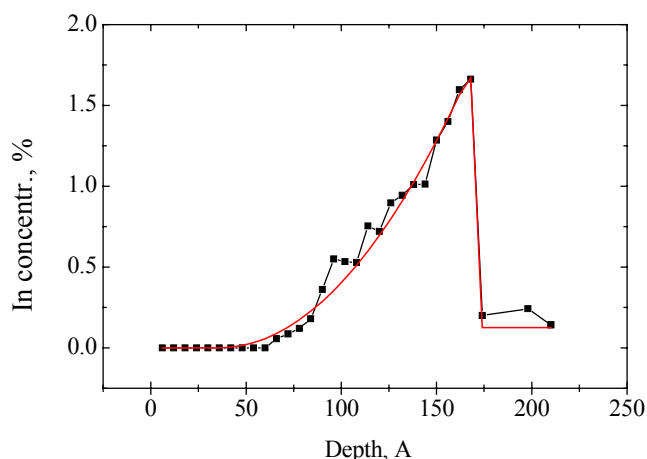


Fig. 3. In-depth concentration profile of the InAs/GaAs nanoheterostructure (sample **B**).

The width of the profile corresponds to the height of the quantum dot and the intensity rate increase gives information about the angle of pyramid. The following preliminary geometrical parameters of the quantum dots was obtained by comparing the experimental and calculated depth profiles: the height is ~ 110 Å, the side of the basis is ~ 90 Å. Fig. 2 demonstrates quantum dots of quite different shape of truncated pyramid or even towers. The solution of the problem of quantum dot shape determination is assumed to open the way to the complex research of geometrical characteristics and electron structure of quantum dots of real

heterostructures and to find out their interrelations.

Conclusion

1. The technique of opening quantum dot layer of InAs/GaAs nanoheterostructure has been developed. The technique provides simultaneous access to the quantum dot layer over the whole surface studied by electron spectroscopy methods.

2. The idea of determination of quantum dot shape by photoelectron spectroscopy in combination with layer-by-layer ion etching has been proposed.

Acknowledgements

The project was supported by BESSY-II and by the research programs “Physic of Solid-State Nanostructures” and “Low-Dimensional Quantum Structures”.

References

1. Grundmann et al., Phys. Rev. Lett., 74, 4043 (1995); Phys. Rev. B, 56 (10), 506 (1997).
2. C.M.A.Kapteyn, M.Lion, R.Heitz, D.Bimberg, P.N.Brunkov, B.V.Volovik, S.G.Konnikov, A.R.Kovsh, and V.M.Ustinov, Appl.Phys.Lett. **76** (12), p.1573-1575, 2000.
3. V.M.Mikoushkin, V.V.Mamutin, S.E.Sysoev, V.V.Shnitov, and Yu.S.Gordeev, Microelectronic Engineering, v.69 (2003), p.p. 480-484.
4. J.-J.Yeh, Atomic Calculations of Photoionization Cross Sections and Asymmetry Parameters, Gordon and Breach, Langhorne, PA, 1993.

Studying band gap opening in CdS nanoparticles by a combination of photoemission and x-ray absorption spectroscopy

Sanjeev Joshi, S. Rügamer, C. Kumpf, T. Schmidt, R. Fink, C. Heske, and E. Umbach
Experimentelle Physik II, Universität Würzburg, Am Hubland, 97074 Würzburg

S. K. Kulkarni

Department of Physics, University of Pune, Pune 411 007, India

The study of semiconductor nanoparticles has been an interesting field of research for more than a decade. This is because it gives an opportunity to understand physical properties in low dimensions and to explore their vast potential for applications, e.g., in optoelectronics. When one reduces the dimensions of a solid to a nanometer size (nanoparticles), the exciton radius becomes larger than the particle. This results in a splitting of energy bands into discrete quantized levels, and the band gap opens as the size of the particles is decreased [1-3]. With decreasing cluster size, the distinction between excitonic absorption and excitation into the (delocalized) conduction band becomes meaningless as exciton and unoccupied states both are localized within the nanoparticle. In this limit, the excitation is generally referred to as excitonic absorption [1]. We have reported earlier on the surface properties of CdS-nanoparticles, probed with high-resolution photoemission [3]. Various sulfur species are present in these particles, which can be identified as "surface" or "bulk" species by tuning the photon energy and hence the inelastic mean free path of the emitted photoelectrons. Furthermore, photoemission data can be discussed and understood in microscopic detail by analyzing the intensity variations of the various species as a function of excitation energy [4]. In this report we present data of combined valence band photoemission (VBPEs) and near edge x-ray absorption (NEXAFS) experiments in order to monitor the band gap opening in CdS nanoparticles. The nanoparticles were prepared with a wet chemical synthesis technique using Thioglycerol (TG) as a capping agent and deposited on a Au substrate, as reported in [4]. The experiments were performed at the UE52-PGM beam line with an energy resolution better than 40 meV. NEXAFS spectra were recorded in the partial electron yield mode. For VBPEs, photon energies of 200 eV and 120 eV were used. The spectra were collected for a large number of sample positions in order to account for sample inhomogeneities and radiation damage. From the position of UV-VIS absorption maxima, the sizes of the

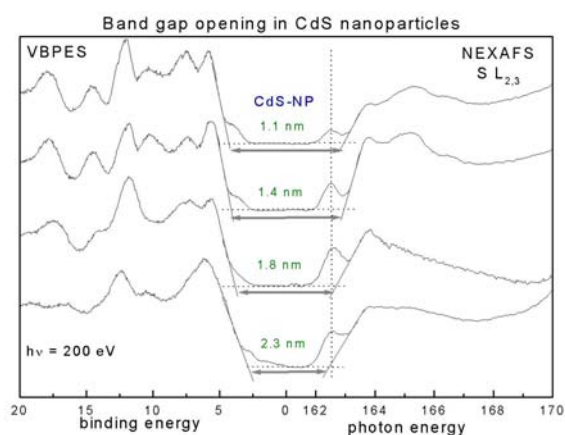


Figure 1: Left: Valence band photoemission (VBPEs) of four differently sized nanoparticles at a photon energy of 200 eV. Right: S L_{2,3} X-ray absorption spectra. Linearly extrapolated grey lines show the valence band edge and the absorption edge. Grey arrows give the distance between the two edges and hence indicate the band gap opening. The sizes of the particles are given above the grey arrows.

nanoparticles are determined using the tight binding approximation [5]. A band gap opening in CdS nanoparticles was reported previously by Lüning *et al.* [6], using a combination of NEXAFS and X-ray emission spectroscopy. They found that the band gap opening has about equal contribution from the valence and conduction band shift, in good agreement with an effective mass approximation with finite potential walls. The first shoulder in NEXAFS (at a photon energy of 162.7 eV) was assigned to a Wannier-type core exciton. With decreasing size, the energy separation between the exciton and the conduction-band related absorption features increased.

Thus, the apparent absorption onset is size independent, while there is a shift of the unoccupied states to higher binding energies. In contrast to the data in [6], Nowak *et al.* [7] observe a drop in intensity of this core exciton with decreasing particle size, which is interpreted as a Frenkel-type exciton (in contrast, for a Wannier-type exciton, the oscillator strength increases with decreasing particle size).

Figure 1 shows a plot of the band gap opening in our CdS nanoparticles. The spectra are calibrated using a Au reference sample. S 2p photoemission experiments (not shown) do not exhibit any shift in the (bulk) component with lowest binding energy as a function of size. In contrast, we find a shift of the valence band edge (as shown by grey lines linearly extrapolated to the dotted base line) to higher binding energies with decreasing particle size, in agreement with the work of Colvin *et al.* [8]. The right part of Fig. 1 shows the x-ray absorption of the nanoparticles at the S $L_{2,3}$ edge. The results are similar to those published in [6], i.e., they show a shift of the absorption edge (as shown by grey lines) with decreasing size and a size-independent core exciton peak at 162.5 eV (dotted vertical line). In contrast to [6], the intensity of this peak decreases as a function of particle size, in agreement with the results of Nowak *et al.* [7]. Figure 2 gives a schematic diagram of the electronic band structure of our CdS nanoparticles, plotted using the energy separation ($\Delta E \pm 0.1$ eV) of the valence band edge (VBM) with respect to the Fermi energy and the absorption edge with respect to the S 2p

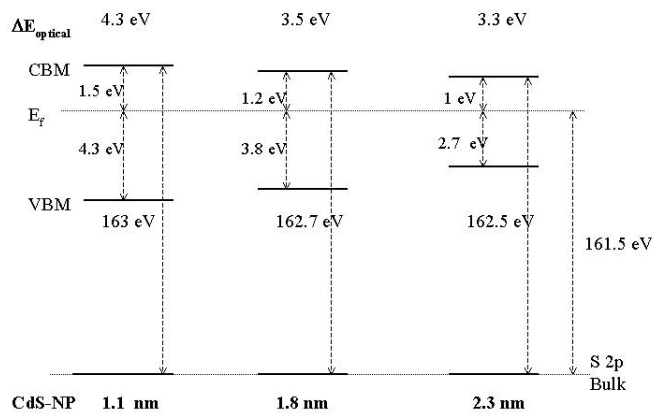


Figure 2. Schematic energy level diagram of 2.3 nm, 1.8 nm, and 1.1 nm CdS nanoparticles. The distance ($\Delta E \pm 0.1$ eV) of the valence band maximum (VBM) and the absorption onset ("conduction band minimum", CBM) with respect to the Fermi energy (E_f) are shown. The optical band gap ($\Delta E_{optical}$) is given at the top of the diagram.

core level binding energy (161.5 ± 0.1 eV). The optical band gap values for the particles, as derived from the UV-VIS spectroscopy, are given for comparison. For the larger particles the measured gap is comparable to the optical gap, while for the smallest particles (1.1 nm), the measured gap is by about 1.5 eV larger. This difference is attributed to the enhanced electron-hole correlation for optical absorption in small particles and to the difference between exciton and band edge in our NEXAFS data. Further detailed investigations of edge positions and final state effects are underway to interpret the results in a detailed quantitative picture.

References:

- [1] S. V. Gaponenko, "Optical Properties of Semiconductor Nanocrystals", Cambridge Univ. Press (1998).
- [2] Y. Kayanuma, Phys. Rev. B 38 (1988) 9797; Y. Wang and N. Herron, Phys. Rev. B 42 (1990) 7253 and J. Phys. Chem. 95 (1991) 525; L. E. Brus, J. Phys. Chem. 90 (1986) 2555.
- [3] U. Winkler, D. Eich, Z. H. Chen, R. Fink, S. K. Kulkarni, and E. Umbach, Chem. Phys. Lett. 306 (1999) 95; S. Joshi, R. Fink, C. Kumpf, T. Schmidt, C. Heske, S. K. Kulkarni, and E. Umbach, BESSY Annual Report (2002) 94.
- [4] Sanjeev Joshi, C. Heske, L. Weinhardt, C. Kumpf, R. Fink, S. K. Kulkarni, and E. Umbach, in preparation.
- [5] P. E. Lippens and M. Lannoo, Phys. Rev. B 39 (1989) 10935.
- [6] J. Lüning, J. Rockenberger, S. Eisebitt, J.-E. Rubensson, A. Karl, A. Kornowksi, H. Weller, and W. Eberhardt, Solid State Commun. 112 (1999) 5.
- [7] C. Nowak, H. Döllefeld, J. Friedrich, A. Kolmakov, M. Riedler, A. Eychmüller, J. O. Löfken, A. Wak, H. Weller, M. Wolff, and T. Möller, J. Chem. Phys. 114 (2001) 489.
- [8] V. L. Colvin and A. P. Alivisatos, Phys. Rev. Lett. 66 (1991) 2786.

Doping Dependence of the Mass Enhancement in $(\text{Pb,Bi})_2\text{Sr}_2\text{CaCu}_2\text{O}_8$ at the Antinodal Point in the Superconducting and Normal States

A. Koitzsch¹, T. K. Kim¹, A. A. Kordyuk^{1,3}, S. V. Borisenko¹, M. Knupfer¹, H. Berger², and J. Fink¹

¹*Leibniz-Institute for Solid State and Materials Research Dresden, P.O.Box 270116, D-01171 Dresden, Germany*

²*Institut de Physique de la Matière Complex, Ecole Polytechnique Fédérale de Lausanne, CH-1015 Lausanne, Switzerland*

³*Institute for Metal Physics of the National Academy of Sciences of Ukraine, 03142 Kyiv, Ukraine*

To understand the most unusual behavior of the high- T_c cuprates both in the superconducting state as well as in their normal state it is crucial to understand the low-energy electronic structure of these materials. Recently it became clear that an important milestone on this road is represented by the identification of a coupling of the electronic states to a bosonic collective mode [1, 2]. It is known that classical superconductivity is caused by the coupling of electrons to bosonic modes (phonons), which underlines the potential importance of this finding. This coupling causes a mass renormalization as well as an increased scattering rate of the electronic states on the energy scale of the mode. We investigate these effects as a function of doping and temperature in the k-space region where they are strongest [3]. A precondition is the ability to resolve the bilayer splitting, caused by the presence of two copper-oxyde layers in $(\text{Pb,Bi})_2\text{Sr}_2\text{CaCu}_2\text{O}_8$. Figure 1 shows a collection of so called Energy Distribution Maps (photoemission intensity as a function of energy along a certain k-direction – in this case the (π,π) - $(\pi,0)$ - $(\pi,-\pi)$ direction) for different dopings and different temperatures. Bonding and antibonding band contribute differently (left and middle row) to the spectral weight when different excitation energies are used. Applying a subtraction procedure yields the contribution of the bonding band (right column). It is already visually clear that there is an apparent doping dependence in the superconducting state: the bands are much flatter for the underdoped case than for the overdoped ones at the Fermi energy. Away from the Fermi energy there are no coherent band states for the underdoped case. Above T_c the situation is completely different: Coherent band states are visible for the underdoped case away from the Fermi level (which by itself is surprising and of great importance) and the slope of the bands is steeper. These results can be explained as follows: there is a bosonic mode which couples to the electronic states below T_c . Its impact on the electronic structure increases rapidly with underdoping.

For quantitative analysis a fitting procedure is applied to obtain the values of the slopes of the dispersions above and below T_c (i.e. the mass enhancements, see Figure 2). The results of this analysis are collected in Figure 3. The coupling parameter λ describes the mass enhancement compared to the unrenormalized dispersion. λ increases continuously with doping reaching huge values around $\lambda = 8$ for the most underdoped samples. In the normal state, however, the coupling appears to be doping independent and, as further studies along different k-directions suggest [4], rather isotropic.

The observed characteristics of the mass enhancement are inconsistent with a classical coupling to phonons. Instead an interpretation in terms of a coupling to spin fluctuations seems promising: in the normal state there is an isotropic coupling to a spin continuum whereas below T_c a magnetic resonance mode appears [5, 6]. This resonance mode causes the severe renormalizations of the electronic structure below T_c .

Financial support by the DFG (Fi-439/10-1) is gratefully acknowledged.

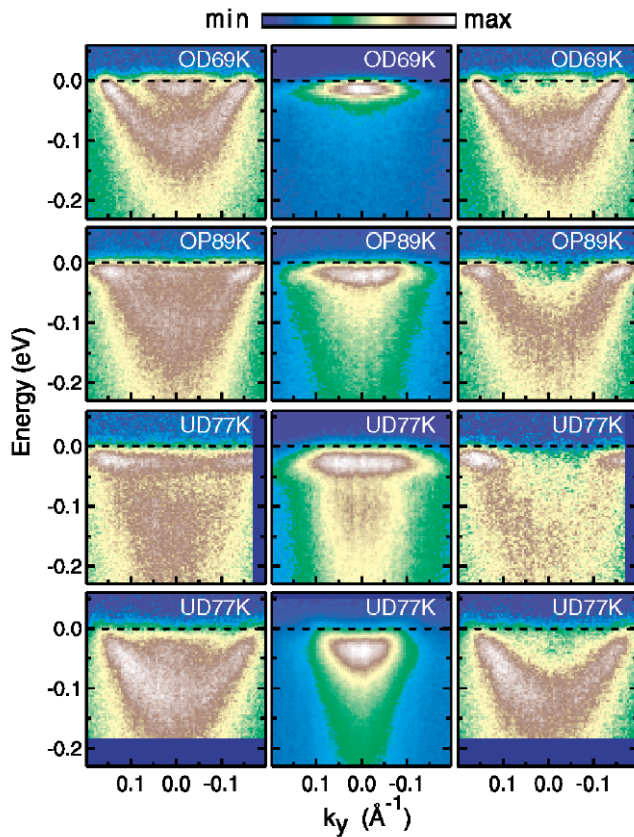


Figure1: ARPES intensity plots as a function of energy and wave vectors along the (π,π) - $(\pi,0)$ - $(\pi,-\pi)$ direction of overdoped (OD), optimally doped (OP), and underdoped (UD) Pb-Bi2212 superconductors taken at $T = 30$ K (upper three rows). Zero corresponds to the $(\pi,0)$ point. Bottom row: data for an UD sample taken at $T = 120$ K. Left column: data taken with a photon energy $h\nu = 38$ eV, at which the signal from the bonding band is maximal. Middle column: data taken at $h\nu = 50$ eV (or 55 eV), where the signal from the antibonding band is dominant. Right column: subtraction of the latter from the former yielding the spectral weight of the bonding

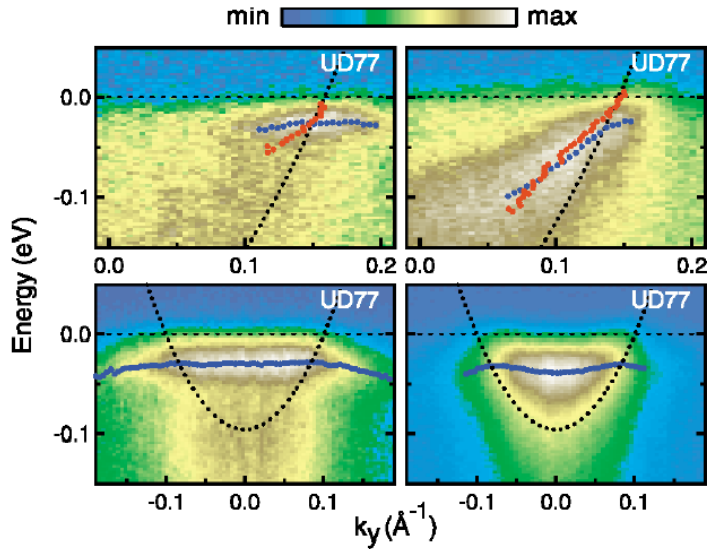


Figure 2: Dispersion of the bonding band near the antinodal point in an underdoped Pb-Bi2212 sample at $T = 30$ K (left) and at $T = 120$ K (right) as derived from Energy Distribution Curves (blue points) and Momentum Distribution Curves (red points) together with the bare electron dispersion (black points). Middle row: the same data for the antibonding band.

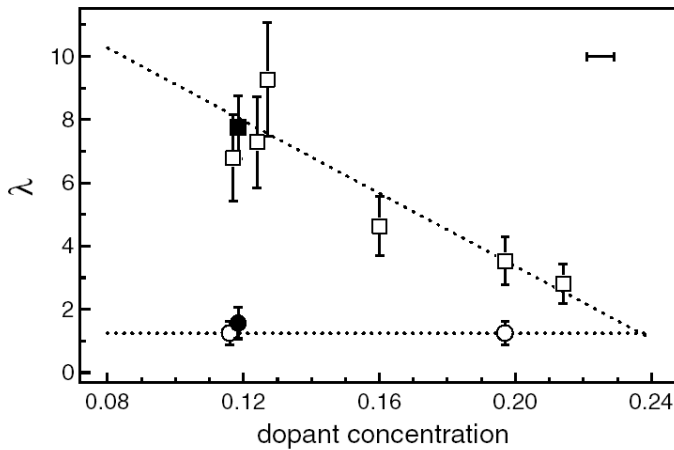


Figure 3: The coupling strength parameter λ as a function of dopant concentration. Squares: superconducting state; circles: normal state; open (solid) symbols: bonding (antibonding) band. The dashed lines are fits to the data using a straight line. Horizontal bar: experimental error in the dopant concentration.

[1] A. D. Gromko, A. V. Fedorov, Y.-D. Chuang, J. D. Koralek, Y. Aiura, Y. Yamaguchi, K. Oka, Yoichi Ando, and D. S. Dessau, *Phys. Rev. B* **68**, 174520 (2003)

[2] S. V. Borisenko, A. A. Kordyuk, T. K. Kim, A. Koitzsch, M. Knupfer, J. Fink, M. S. Golden, M. Eschrig, H. Berger, and R. Follath, *Phys. Rev. Lett.* **90**, 207001 (2003)

[3] T. K. Kim, A. A. Kordyuk, S. V. Borisenko, A. Koitzsch, M. Knupfer, H. Berger, and J. Fink, *Phys. Rev. Lett.* **91**, 167002 (2003)

[4] A. Koitzsch, S.V. Borisenko, A.A. Kordyuk, T.K. Kim, M. Knupfer, J. Fink, H. Berger, and R. Follath, cond-mat/0305380

[5] J. Rossat-Mignod, L. P. Regnault, C. Vettier, P. Bourges, P. Burlat, J. Bossy, J. Y. Henry and G. Lapertot, *Physica (Amsterdam)* **185–189C**, 86 (1991)

[6] M. Eschrig and M. R. Norman, *Phys. Rev. Lett.* **85**, 3261 (2000); *ibid.* **89**, 277005 (2002).

Origin of the shadow Fermi surface in Bi-based cuprates

A. Koitzsch¹, S. V. Borisenko¹, A. A. Kordyuk¹, T. K. Kim¹, M. Knupfer¹, J. Fink¹, M. S. Golden², W. Koops², H. Berger³, B. Keimer⁴, C. T. Lin⁴, S. Ono⁵, Y. Ando⁵, and R. Follath⁶

¹ *Leibniz-Institute for Solid State and Materials Research, IFW-Dresden, P.O. Box 270116, D-01171 Dresden, Germany*

² *Van der Waals-Zeeman Institute, University van Amsterdam, Valckenierstraat 65, NL-1018 XE Amsterdam, The Netherlands*

³ *Institute of Physics of Complex Matter, EPFL, CH-1015 Lausanne, Switzerland*

⁴ *Max-Planck Institute für Festkörperforschung, Heisenbergstrasse 1, D-70569 Stuttgart, Germany*

⁵ *Central Research Institute of Electric Power Industry, Komae, Tokyo 201-8511, Japan*

⁶ *BESSY GmbH, Albert-Einstein-Strasse 15, 12489 Berlin, Germany*

The term “shadow” Fermi surface refers to a long-standing problem of Fermi surface mapping in the Bi-based high- T_c cuprates. It appears, at a first glance, to be a shifted replica of the main Fermi surface (Figure 1). Its origin is controversial: initially a magnetic mechanism has been suggested [1] but also an explanation in terms of a structural effect has been put forward [2, 3]. In particular the magnetic scenario sparked a profound theoretical effort – and continues to do so. In the light of recent results, which emphasize the importance of magnetic fluctuations for the low energy excitations of the cuprates [4, 5], the problem seems especially pressing.

We investigated the characteristics of the shadow bands in one and two-layer Bi-based cuprates and collected evidence against the magnetic scenario (Figure 2) [6]. In particular we found i) no indication for an increased scattering rate due to the coupling of electronic states to antiferromagnetic fluctuations, ii) no signs of renormalization of the dispersion relation of the shadow band compared to the main band, iii) no energy dependence of the intensity ratio between shadow and main band, which has been forecast on theoretical grounds for the magnetic scenario, iv) and no temperature dependence of the same ratio (Figure 3). Moreover the obtained results for the shadow bands resemble closely that of the true diffraction replicas well known for the Bi-based cuprates. Therefore an explanation in terms of a structural scenario seems plausible. The shadow Fermi surface can be considered as the result of a back-folding of the bands due to a doubling of the unit cell, which would occur, for instance, if two neighboring copper atoms were structurally inequivalent, due to lattice distortions.

Financial support by the DFG (Fi-439/10-1) is gratefully acknowledged.

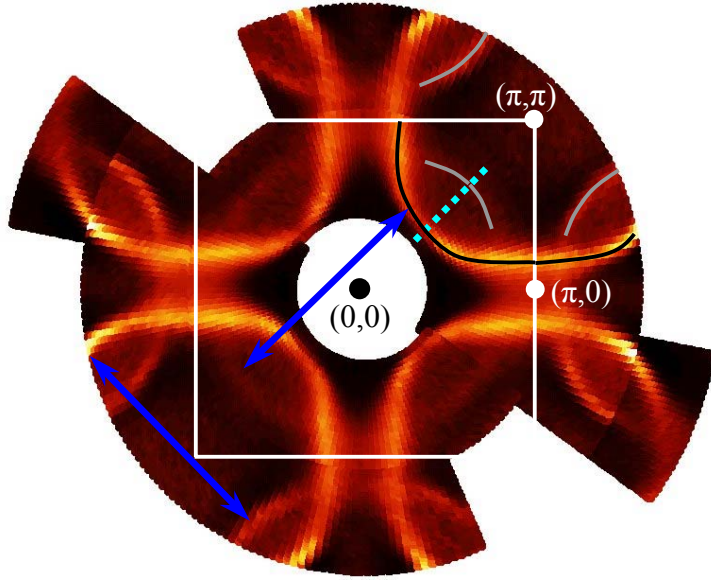


Figure 1: Fermi surface map of an overdoped (Bi,Pb)-2212 ($T_c=69$ K) crystal at room temperature taken with excitation energy 21.2 eV. Bright yellow denotes regions of high intensity. The white square represents the first Brillouin zone. The “barrels” around the (π,π) and equivalent points are the main Fermi surface (black underlined in the upper right quadrant). The additional

weaker barrel centered around $(0,0)$ is the shadow Fermi surface (gray underlined in the upper right quadrant). The blue arrows represent the (π,π) and equivalent vectors. The dashed light blue line marks the location of the binding energy dependent measurements performed in this study (see Fig.2).

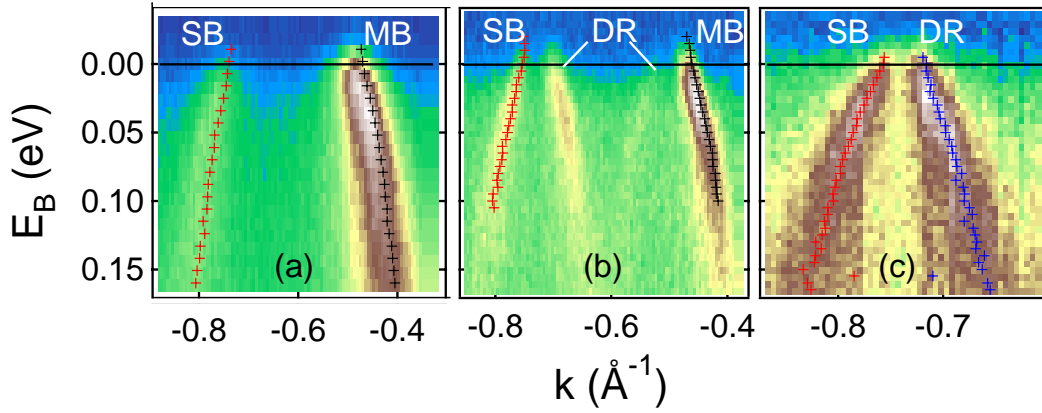


Figure 2: Energy distribution maps along the $(0,0)$ - (π,π) direction marked in Fig. 1 for (a) underdoped-(Bi,Pb)-2212, taken with excitation energy 55 eV at $T=30$ K; (b) slightly underdoped lead-free Bi-2212, excitation energy 50 eV at $T=30$ K (c) optimally doped Bi-2201, excitation energy 50 eV at $T=65$ K. The intense feature on the right hand side in (a) and (b) corresponds to the main band (MB), the weaker feature on the left hand side to the shadow band (SB). In between, diffraction replicas (DR) are found in pure Bi-2212 in panel (b). Panel (c) shows only the shadow band (left) and a diffraction replica of the main band (right). The black, red and blue markers denote the experimental dispersions of main band, shadow band and diffraction replica, respectively.

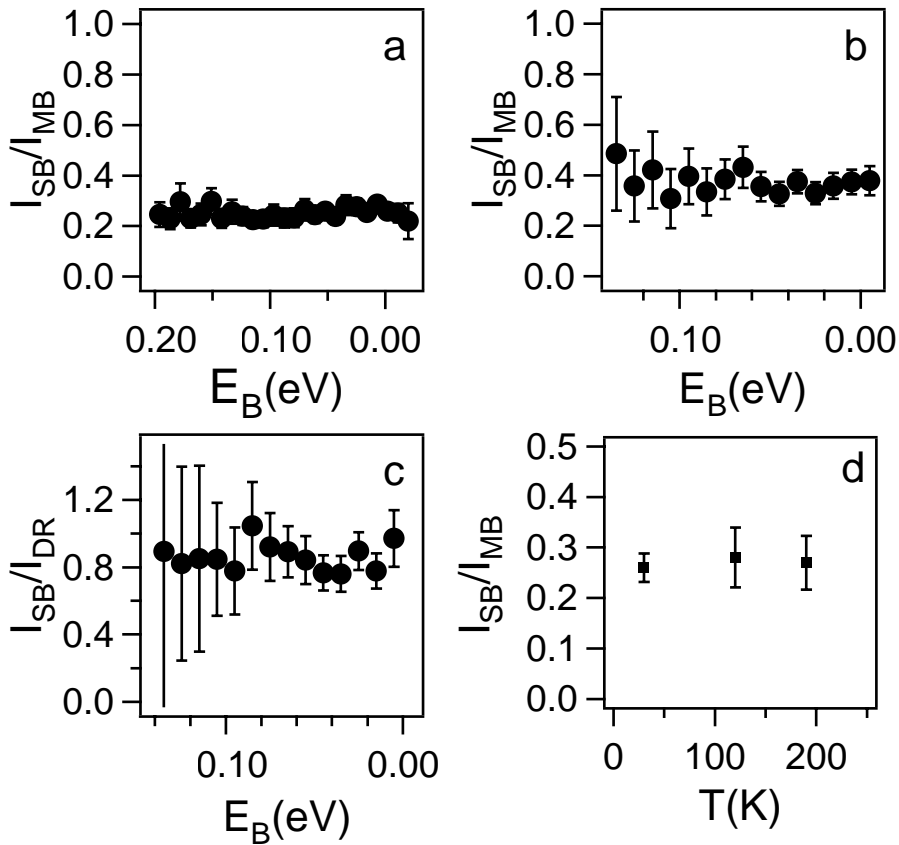


Figure 3: Ratio of the peak areas of the shadow and main band extracted from the data shown in Fig. 2. (a) (Bi,Pb)-2212 and (b) Bi-2212. (c) shows the ratio between shadow band and first diffraction replica of the main band for Bi-2201. (d) shows the temperature dependence of the ratio at the Fermi energy for (Bi,Pb)-2212.

- [1] P. Aebi, J. Osterwalder, P. Schwaller, L. Schlapbach, M. Shimoda, T. Mochiku, and K. Kadowaki, *Phys. Rev. Lett.* **72**, 2757 (1994)
- [2] S. Chakravarty, *Phys. Rev. Lett.* **74**, 1885 (1995)
- [3] D. J. Singh and W. E. Pickett, *Phys. Rev. B* **51**, 3128 (1995)
- [4] A. D. Gromko, A. V. Fedorov, Y.-D. Chuang, J. D. Koralek, Y. Aiura, Y. Yamaguchi, K. Oka, Yoichi Ando, and D. S. Dessau, *Phys. Rev. B* **68**, 174520 (2003)
- [5] S. V. Borisenko, A. A. Kordyuk, T. K. Kim, A. Koitzsch, M. Knupfer, J. Fink, M. S. Golden, M. Eschrig, H. Berger, and R. Follath, *Phys. Rev. Lett.* **90**, 207001 (2003)
- [6] A. Koitzsch, S. V. Borisenko, A. A. Kordyuk, T. K. Kim, M. Knupfer, J. Fink, M. S. Golden, W. Koops, H. Berger, B. Keimer, C. T. Lin, S. Ono, Y. Ando, and R. Follath, *cond-mat/0401114*

Electronic structure and electronic holes in defect Li_xCoO_2 oxides

V. R. Galakhov^{1*}, S. N. Shamin¹, N. A. Ovechkina¹,
D. G. Kellerman², K. Küpper³, M. Neumann³,
D. V. Vyalykh⁴, and S. L. Molodtsov⁵

¹*Institute of Metal Physics, Russian Academy of Sciences —
Ural Division, 18 S. Kovalevskaya str., 620219 Yekaterinburg GSP-170, Russia*

²*Institute of Solid State Chemistry, Russian Academy of Sciences —
Ural Division, 91 Pervomayskaya str., 620219 Yekaterinburg GSP-145, Russia*

³*Universität Osnabrück — Fachbereich Physik, D-49069 Osnabrück, Germany*

⁴*Freie Universität Berlin — Institut für Experimentalphysik, Fachbereich Physik
D-14195 Berlin-Dahlem, Germany*

⁵*Technische Universität Dresden — Institut für Oberflächen- und Mikrostrukturphysik,
Fachrichtung Physik, D-14195 Berlin-Dahlem, Germany*

Recent discovery of superconductivity in $\text{Na}_{0.35}\text{CoO}_2 \cdot 3\text{H}_2\text{O}$ layered compounds is a very exciting event because it shows a marked resemblance with superconducting cuprates [1]. These compounds consist of two-dimensional CoO_2 layers separated by insulating layer of Na^+ ions and H_2O molecules [1]. By the analogy with cuprates, it is supposed that superconductivity in layered cobaltites occurs in CoO_2 -layers and these materials are considered as electron-doped systems for a low-spin Co^{4+} lattice [1]. To elucidate the mechanism of superconductivity the studies of electronic structure of alkaline metal-doped cobaltites are of great interest.

Cobaltites Li_xCoO_2 have similar crystal structure as Na_xCoO_2 ($R\bar{3}m$ space group). The ground state of the Co^{3+} ions in LiCoO_2 can be written as $t_{2g\uparrow}^3 t_{2g\downarrow}^4 e_g^0$. To obtain charge neutrality due to Li-ion deintercalation these oxides should have, in addition to Co^{3+} , Co^{4+} ions. As shown in measurements of the Co $2p$ and O $1s$ X-ray absorption spectra of deintercalated samples of $\text{Li}_{1-x}\text{CoO}_2$ [3], charge compensation takes place due to holes in the O $2p$ band rather than as result of the formation of tetravalent cobalt.

Samples of the Li_xCoO_2 ($x = 1, 0.7, 0.6$) oxide were prepared by solid-phase reaction from $\text{Li}_2\text{C}_2\text{O}_3$ and Co_3O_4 compounds in air at 850°C for 25 hrs. Phase composition was checked by X-ray diffraction analysis. The X-ray photoelectron spectra (XPS) were obtained with a PHI 5600 ci Multitechnique System XPS spectrometer using monochromatized Al $K\alpha$ radiation.

The Co $L\alpha$ ($3d4s \rightarrow 2p_{3/2}$ transitions) and oxygen $K\alpha$ ($2p \rightarrow 1s$ transition) X-ray emission spectra (XES) were measured on a RSM-500 X-ray spectrometer under electron excitation. Co $2p$ and O $1s$ X-ray absorption spectra (XAS) were carried out at BESSY, at the Russian-Germany Beam Line.

*e-mail: galakhov@ifmlrs.uran.ru

Figure 1 presents the XPS valence-band spectrum and O $K\alpha$ and Co $L\alpha$ XES spectra of LiCoO_2 . X-ray emission spectra are brought to a common energy scale using the O $1s$ and Co $2p_{3/2}$ core-level electron binding energies.

Near the Fermi level, the Co $3d$ states are concentrated. The strongest peak A and the feature B derive from the t_{2g} orbitals. The XPS feature C , according to calculations made by Czyżyk *et al.* [5], is forming by t_{1u} orbitals, which derive primarily from the O $2p$ states with a slight admixture of the Co $4p$ states. The band D reveals the hybridized O $2p$ -Co $3d$ (e_g) states. The band E reflects hybridization of the Co $4s$ and $4p$ states (a_{1g} and t_{1u} orbitals) with O $2p$ states. The D and E features manifest themselves in the O $K\alpha$ spectrum. The XPS features A - E originates from the states in which the hole created in photoemission is screened as a result of electron transfer from the oxygen $2p$ band to form the $3d^6L^{-1}$ final-state configuration and the F satellite is formed by the $3d^5$ configuration. Here, L^{-1} denotes a hole in the O $2p$ states due to the charge-transfer process. One can see that the t_{2g} states form strong narrow peak near the Fermi level. One can suggest that the narrow t_{2g} peak reflects electron-phonon coupling in cobaltites Li_xCoO_2 and Na_xCoO_2 .

Figure 2 shows the O $1s$ and Co $2p$ XAS spectra of LiCoO_2 , $\text{Li}_{0.7}\text{CoO}_2$, and $\text{Li}_{0.6}\text{CoO}_2$. The deficiency of alkali metal ions in cobaltites leads to changes of both, Co $2p$ and O $1s$ absorption spectra. By this is meant that electronic holes are localized both in cobalt $3d$ and oxygen $2p$ states. These results are in contradiction with those obtained for $\text{Na}_{0.7}\text{CoO}_2$ [4] where, according to the analysis of Co $3s$ and Co $2p$ photoelectron spectra, de-

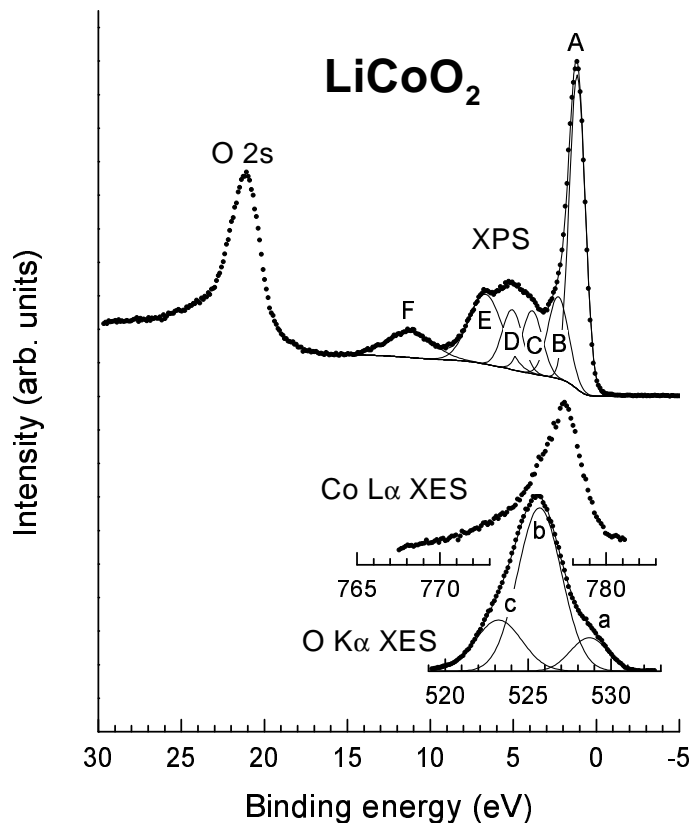


Figure 1: X-ray photoelectron spectrum of the valence band and Co $L\alpha$, O $K\alpha$ X-ray emission spectra of LiCoO_2 .

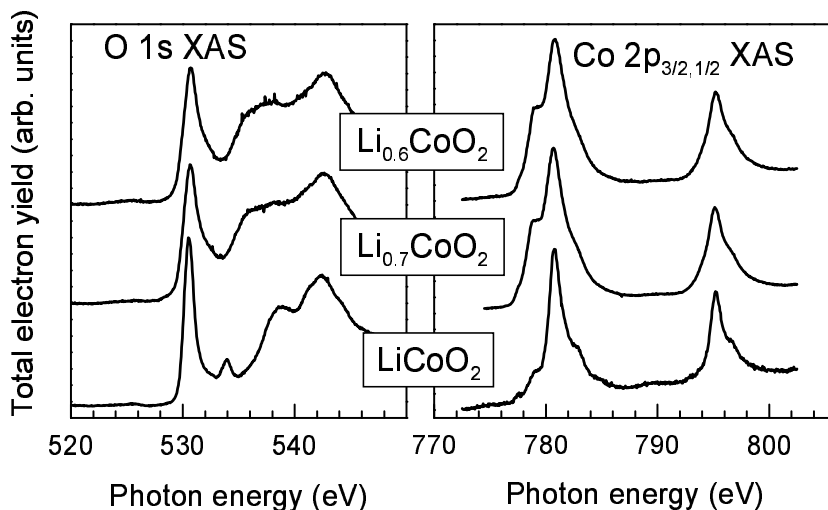


Figure 2: O $1s$ and Co $2p$ X-ray absorption spectra of LiCoO_2 , $\text{Li}_{0.7}\text{CoO}_2$, and $\text{Li}_{0.6}\text{CoO}_2$.

iciency of alkali metal ions should be resulted in the formation of holes, \underline{L} , in the oxygen $2p$ band (the $3d^6\underline{L}$ ground-state configuration).

The multiplet calculation made for the low-spin states of Co^{3+} ions accounts well for the Co $2p$ XAS spectra of LiCoO_2 [6]. These suggest that the Co $3d$ states are in the low-spin configuration ($S = 0$). On the other hand, the Co $2p$ XAS spectra of Li_xCoO_2 closely resemble the multiplet calculation carried out for the high-spin configuration ($S = 2$) of Co^{3+} ions [6].

Funding by the Research Council of President of Russian Federation (Project NSH-1026.2003.2) and Russian Ministry for Industry and Science (Project on Superconductivity of Mesoscopic and Strongly Correlated Systems), is gratefully acknowledged.

- [1] K. Takada, H. Sakurai, E. Takayama-Muromachi, F. Izumi, R.A. Dilanian, and T. Sasaki, *Nature* **422**, 53 (2003).
- [2] Y. Ono and T. Kajitani, in *Oxide Thermoelectrics*, (eds. K. Koumoto, I. Terasaki and N. Murayama), ISBN, p. 59 (2002).
- [3] L. A. Montoro, M. Abbate, J. M. Rosolen, *Electrochemical and Solid-State Letters* **3**, 410 (2000).
- [4] V. R. Galakhov, V. V. Karelina, D. G. Kellerman, V. S. Gorshkov, N. A. Ovechkina, and M. Neumann, *Phys. Solid State* **44** (2002) 266. An English translation of the journal *Fizika Tverdogo Tela* (St. Petersburg) **44**, 257 (2002).
- [5] M. T. Czyżyk, R. Potze R., G. A. Sawatzky, *Phys. Rev. B* **46**, 3729 (1992).
- [6] M. Abbate, J. C. Fuggle, A. Fujimori, L. H. Tjeng, C. T. Chen, R. Potze, G. A. Sawatzky, H. Eisaki, and S. Uchida, *Phys. Rev. B* **47**, 16124 (1993).

Spin-polarised photoemission spectroscopy of the MgO/Fe interface on GaAs(100)

F. Matthes^{*}, L.-N. Tong^{**}, C.M. Schneider^{***}

^{*} Leibniz-Institute for Solid State and Materials Research Dresden, Helmholtzstr. 20, 01069 Dresden, Germany

^{**} Institute of Material Science and Engineer, Anhui University of Technology, Ma-An-Shan, 243002, Anhui, China

^{***} Institute of Solid State Research, Research Centre Jülich, 52425 Jülich, Germany

We performed spin-polarised valence band photoemission spectroscopy to study the electronic band structure of the MgO/Fe interface for Fe films grown on GaAs(100). A precise knowledge of the electronic band structure of this interface is of essential importance to understand the microscopic mechanisms that control the properties of the tunnelling magneto-resistance (TMR) effect in the epitaxial Fe / MgO / Fe / GaAs(100) system : the system of choice for the theoretical calculation of the TMR. Mathon and Umerski predicted theoretical values for the TMR of 1200% that are much larger than those measured experimentally. Possible reasons for this discrepancy are the existence of an interfacial roughness or structural disorder at the interfaces that the existing models did not yet take into account. Another possibility that will alter the TMR effect is a possible interfacial layer of FeO between the first Fe electrode and the MgO barrier.

The experiments were performed in ultrahigh vacuum. The vacuum base pressure was $2 \cdot 10^{-10}$ mbar. The GaAs(100) substrates have been cleaned with Ar-ions until no carbon or oxygen contaminations were seen by Auger electron spectroscopy (AES). Subsequently, the substrates have been annealed up to temperatures of 560°C. The Low Energy Electron Diffraction (LEED) pattern exhibited a 4x6 reconstruction, indicating a Ga-terminated surface. On such prepared substrates 16 ML thick Fe films were grown by molecular beam epitaxy. Subsequently performed AES studies revealed no carbon or oxygen contaminations of the Fe surface. LEED investigations proved the bcc structure of the Fe film. In-situ magneto-optical Kerr-effect measurements confirmed a ferromagnetic ordering at room temperature with the easy axis oriented along the [110] direction.

The spin- and angle-resolved photoemission experiments were performed at the linear polarized undulator beam line U-125-1 PGM (BESSY) using a cylindrical mirror type analyser with integrated LEED spin-polarization detector (CSA200-SPLEED combination). Our geometry (45° incident light, normal emission) allows direct transitions from initial states with Δ_1 and Δ_5 spatial symmetry into final states with Δ_1 spatial

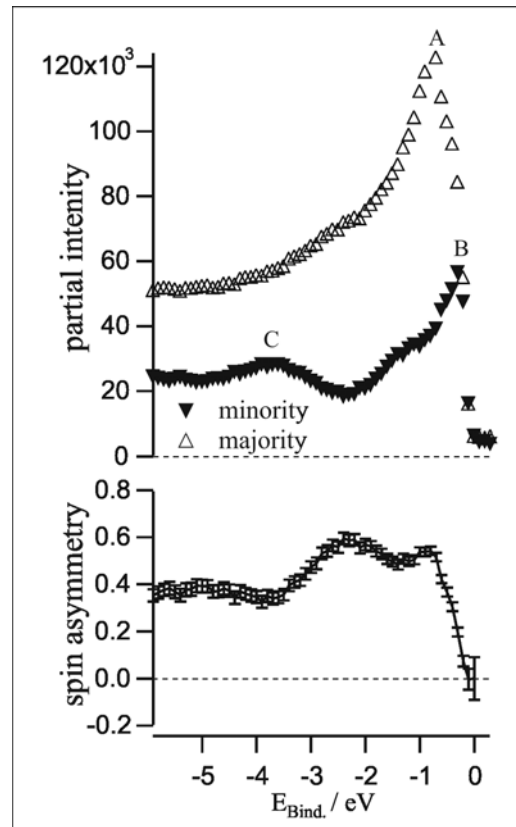


Figure 1: Spin-resolved photoemission of 16 ML Fe on GaAs(100) using a photon energy of 35 eV. Labelled are direct transitions to final states with Δ_6^1 symmetry from initial bulk Fe bands, A = Δ_6^{\uparrow} , B = $\Delta_{6,7}^{5\downarrow}$, C = Δ_6^{\downarrow} .

symmetry [1]. The overall energy resolution was nominally 200 meV. The spin polarization components of the photoelectrons perpendicular to the sample surface and in-plane along the [110] direction were determined simultaneously.

Figure 1 depicts a set of spin-resolved photoemission spectra from a 16 ML thick Fe film on GaAs(100) measured at a photon energy of 35 eV. On the basis of a spin-polarized relativistic Korringa-Kohn-Rostocker band structure calculation for bulk bcc Fe(100) [2], we can identify 3 direct transitions presumably originating from the initial state bands $\Delta_6^{\downarrow}, \Delta_{6,7}^{5\downarrow}, \Delta_6^{\uparrow}$. Our result is consistent with the interpretation of Turner and co-workers [3].

In a next step we have grown MgO films onto the 16 ML thick Fe film by electron-beam evaporation from a Mg rod and simultaneous oxidation. The success of the oxidation procedure was verified by comparing the Auger electron spectrum of the oxidized Mg film with that of a MgO crystal. Figure 2 depicts the spin-resolved data for a nominal coverage of 0.5 ML and 1 ML MgO. With increasing thickness of the MgO film we observe two features: the spectral intensity originating from the valence band of MgO [4] increases, while the intensity of direct transitions from the Fe bulk-related states Δ_6^{\uparrow} and $\Delta_{6,7}^{5\downarrow}$ is suppressed. As a surprising finding, our spin-resolved measurements reveal that the attenuation for the direct

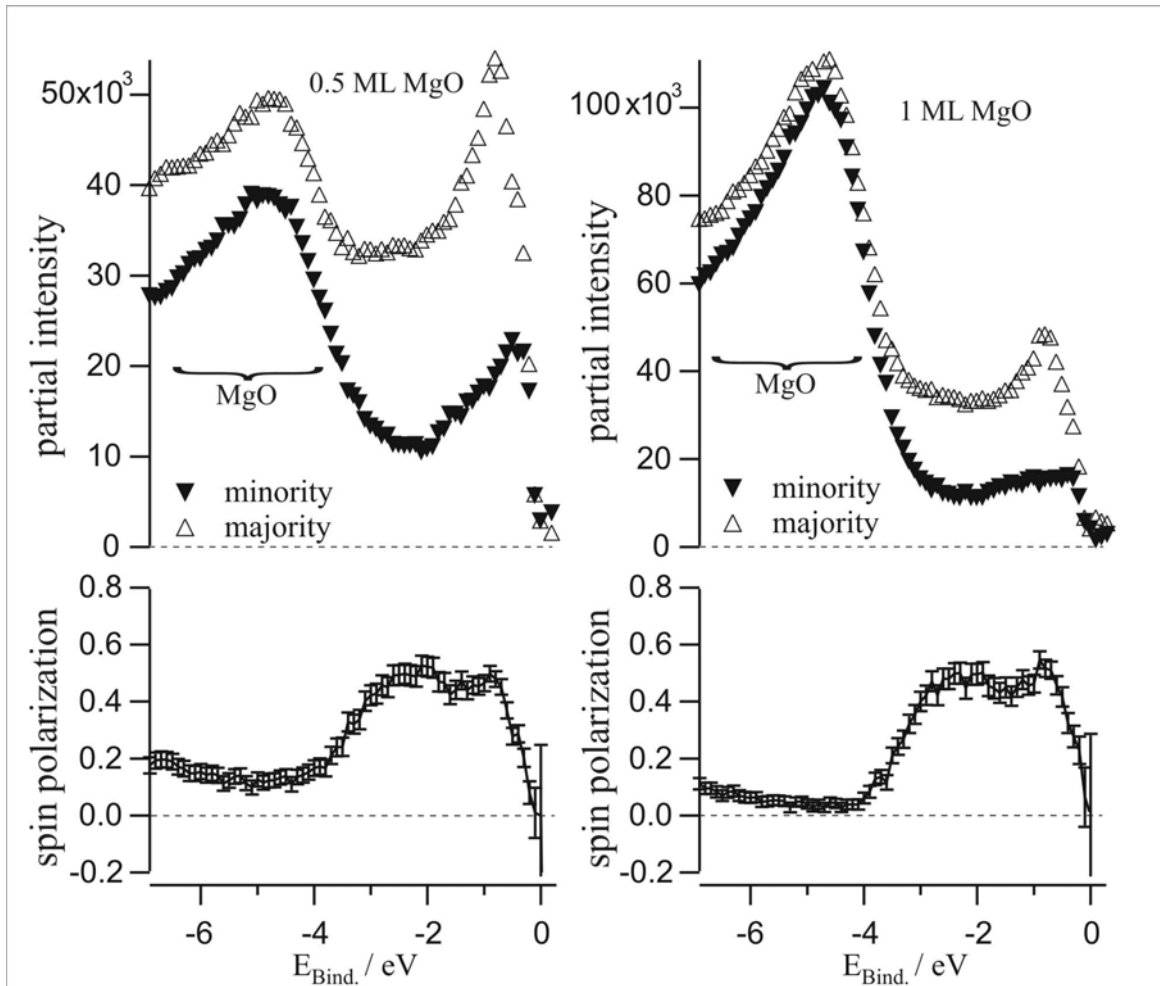


Figure 2 : Spin-resolved photoemission of nominal 0.5 ML thick MgO (left side) and 1 ML thick MgO (right side) on 16 ML Fe / GaAs(100).

transition from the $\Delta_{6,7}^{5\downarrow}$ band is stronger than the one from the Δ_6^{\uparrow} band. This behaviour

cannot be simply related to differences in the spatial symmetry of the photoelectron wave functions, as the final states for both transitions have Δ_6^1 symmetry. We also tend to exclude any spectral contributions from MgO in the region of 2 eV below the Fermi, as even for ultra thin films of MgO Klaua and co-workers [5] measured a thickness dependent tunnelling barrier with a minimum value of 2.6 eV for 2 ML. We also neglect the influence of photoemission emerging from surface states. In the case of Fe(100), these transitions have been found to be dominant for excitation energies between approximately 15 eV and 30 eV [3,6].

There are several possible mechanisms, which may be important to explain our observation. First, a possible formation of interface and half-space states and the scattering of the excited electrons at the interfaces and within the MgO film, which can be taken into account only by a proper 1-step photoemission calculation. The second mechanism bases on the fact that the final states of Fe are exchange-split. The Δ_6^{\downarrow} - and Δ_6^{\uparrow} are shifted in energy and may thus couple to different final states in the MgO film, or to the same final state at different k_{\perp} values. Thus, different coupling coefficients at the interface may be involved, causing a spin-dependence. The third mechanism relates to a possible FeO layer at the interface. In this case, Zhang and co-workers [7] predicted a charge transfer and an induced magnetic moment of $0.19 \mu_B$ at the O atoms of the interfacial FeO. Thus, one can assume that the spin-split density of states at the Fe/FeO/MgO interface will be altered, giving rise to an additional spin-dependent contribution. Which of these mechanisms is the dominant one cannot be decided on the basis of the present experimental data. Further investigations backed by theoretical 1-step photoemission calculations will be necessary to elucidate the behaviour of the Fe/MgO interface.

In conclusion, we have observed a spin-dependent attenuation for direct transitions related to Fe bulk initial states as a function of the MgO thickness. As this attenuation was measured also at photon energies of 40 eV and 60 eV (not shown here), we consider it a general property of the interface. To clarify its origin, theoretical calculations of the photoemission and may be further experimental work have to be performed.

References

- [1] W. Eberhardt and F.J. Himpsel, Physical Review B **21** 5572 (1980)
- [2] F. Matthes, Liu-Niu Tong, C.M. Schneider, Journal of Applied Physics (accepted)
- [3] A.M. Turner, A.W. Donoho, and J.L. Erskine, Physical Review B **29** 2986 (1984); A.M. Turner, and J.L. Erskine, Physical Review B **30** 6675 (1984)
- [4] M. Grass, J. Braun and G. Borstel, Surface Science **334** 215 (1995)
- [5] M. Klaua, D. Ullmann, J. Barthel, W. Wulfhekel, and J. Kirschner, Physical Review B **64** 134411 (2001)
- [6] E. Kisker, K. Schröder, W. Gudat and M. Campagna, Physical Review B **31** 329 (1985)
- [7] X.-G. Zhang, W. H. Butler, and Amrit Bandyopadhyay. Physical Review B **68**, 092402 (2003)

The structure of the Ni(100)c(2x2)-N₂ surface: a chemical-state-specific scanned-energy mode photoelectron diffraction determination

D.I.Sayago, M.Kittel, J.T.Hoeft, M.Polcik

Fritz-Haber-Institut der MPG, Faradayweg 4-6, D 14195 Berlin, Germany

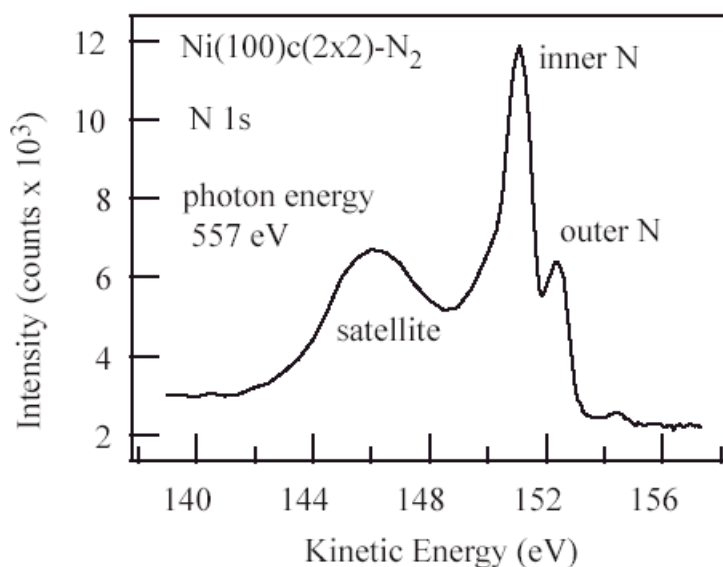
M.Pascal, C.L.A.Lamont

Centre for Applied Catalysis, Department of Chemical and Biological Sciences, University of Huddersfield, Queensgate, Huddersfield, HD1 3DH, UK

R.L.Toomes, J.Robinson and D.P.Woodruff

Physics Department, University of Warwick, Coventry CV4 7AL, UK

In many ways the adsorption phase formed by molecular N₂ on Ni(100) represents something of an enigma; the desorption energy is low, suggesting a weak chemisorption, yet the photoelectron spectra obtained from this surface are remarkably similar to those of the strongly chemisorbed CO on the same surface, and would suggest much stronger absorption. There is considerable evidence that the N₂ adsorbs with the N-N axis perpendicular to the surface, and it is generally believed that the molecule occupies atop sites, a view supported by the one published



quantitative structure determination of the c(2x2) phase from the Berkeley group [1] using so-called angle-resolved photoemission fine structure (ARPEFS), another name for scanned energy mode photoelectron diffraction (PhD). An important conclusion of this earlier structural study was that the Ni-N bondlength was a surprisingly long 2.25 Å, rationalised in terms of the weak bonding.

Fig. 1 Typical N 1s photoemission spectrum from Ni(100)/N₂

Because the two N atoms are inequivalent in the end-on bonding geometry, the N 1s photoemission spectrum is well-known to show two distinct chemically-shifted peaks in addition to strong satellite structure. This inequivalence means that with an appropriately-equipped modern undulator beamline such as UE49-1 at BESSY II, it is possible to extract separate PhD modulation spectra from each N atomic emitter, providing far more incisive structural information than could be achieved in a measurement (like that of the Berkeley group) which integrates over both components, leading to PhD spectra which represent an incoherent sum of the spectra of each emitter. We are also able to apply our more comprehensive methodology for

unique structure determination using many emission geometries rather than one single spectrum used in the earlier study.

Making full use of this chemical-state-specific PhD method we have conducted a new study of the Ni(100)c(2x2)-N₂ surface phase. Our study confirms that the N₂ adsorbs atop surface Ni atoms with the N-N axis perpendicular to the surface, but in contrast to the earlier study we find the Ni-N nearest-neighbour distance to be 1.81 ± 0.02 Å. This value is far more consistent with expectations for a chemisorption bond than the previous value of 2.25 Å. The reason for the earlier error appears to be the well-known problem of multiple near-coincidences in modulation periodicity at different bondlengths which is known to occur on both PhD and LEED but is readily

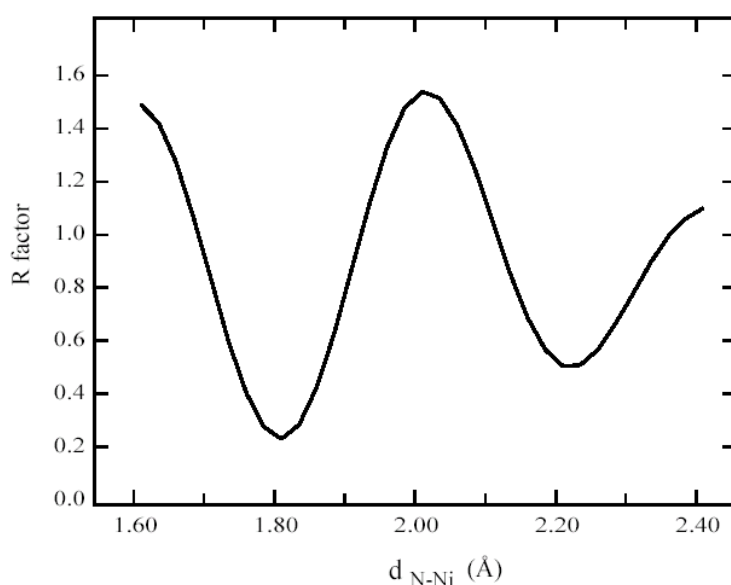


Fig. 2 Variation of the *R*-factor quantifying the agreement between theory & experiment as a function of the N-Ni distance. Note the ‘false’ minimum at 2.23 Å

surmounted by enlarging the data set with PhD spectra in different directions or additional diffracted beam spectra in LEED. In the present case, of course, the chemical-state-specificity makes the resolution even more effective, because the PhD from the ‘inner’ N (i.e. the N atom bonded to the Ni) is much more sensitive to the Ni-N distance than that from the outer.

N which provides a more reliable bonding measurement of the N-N distance

This bondlength is very significantly shorter than the value (2.25 Å) found in an earlier published study. An independent density functional theory (DFT) slab calculation yields a value of 1.79 Å, in excellent agreement with the results of the current experiment. Analysis of the PhD modulations of the N 1s photoemission satellite peak show that these are consistent with this comprising separable components localised at the two N atoms as has previously been assumed in an earlier investigation based on (angle-scan) X-ray photoelectron diffraction. Both experiment and theory indicate a small extension of the N-N distance due to the adsorption (0.03 ± 0.03 Å and 0.02 Å respectively)

1 E.J. Moler, S.A. Kellar, W.R.A. Huff, Z. Hussain, Y. Zheng, E.A. Hudson, Y. Chen and D.A. Shirley, Chem. Phys. Lett. 264 (1997) 502

XANES studies of chemically modified surface layers of metal sulphides

Yu. Mikhlin¹, Ye. Tomashevich¹, D. Vyalikh², L. Zhang³

¹ *Institute of Chemistry and Chemical Technology SB RAS, K.Marx st., 42, Krasnoyarsk, 660049, Russia*

² *Institut für Oberflächenphysik und Mikrostrukturphysik, TU Dresden, D-01062, Germany*

³ *Institut für Physikalische und Theoretische Chemie, Universität Tübingen, Auf der Morgenstelle 8, D-72076 Tübingen*

Metal sulphides are of interest as minerals and have important applications in materials science. Deposition of metals, oxidation in atmosphere, and conditioning in aqueous electrolytes often give rise to distortions of the metal sulphide surface layers, effectively modifying their structures and properties as compared with intrinsic materials. The real surfaces as intermediate products of metal sulphide decomposition are also expected to reflect relevant reaction mechanisms. XANES spectroscopy is a powerful tool to study the unoccupied density of states of solids but there are only a few works employing XANES to investigate reacted metal sulphides (e.g., [1-2]). The samples examined in this work were natural pyrrhotites, Fe₇S₈ and Fe₉S₁₀, arsenopyrite, FeAsS, chalcopyrite, CuFeS₂, sphalerite (Zn,Fe)S, ZnS/GaP(001) epitaxial films, and synthetic bornite, Cu₅FeS₄. Compact specimens were cut from massive minerals, abraded on silicon carbide sandpaper, cleaned with filter paper and washed with distilled water. The samples were treated in 1 M HCl (releasing H₂S), 1 M HCl + 0.4 M FeCl₃, 0.5 M H₂SO₄ + 0.2 M Fe₂(SO₄)₃ or 1 M HNO₃ + 0.4 M Fe(NO₃)₃ media at 50 °C for 1 h, rinsed with water and transferred into a vacuum chamber. ZnS films grown by molecular beam epitaxy were examined after prolonged air exposure. Spectra were collected in the TEY mode at room temperature at the Russian-German beam-line at BESSY II. The estimated energy resolution was better than 0.1 eV.

Pyrrhotite represents a series of iron sulphides with a system of ordered Fe vacancies, in which high-spin ferrous iron is octahedrally coordinated with sulfur, and S has six or five Fe neighbours, with an occurrence of Fe³⁺ being disputable [3,4]. The Fe L-edge spectra (Fig.1, 1,5) related with transitions from 2p states mainly to vacant 3d states (minor spin t_{2g}β and

e_gβ “crystal field” orbitals) show only minimal Fe³⁺ content for vacuum-cleaved pyrrhotites.

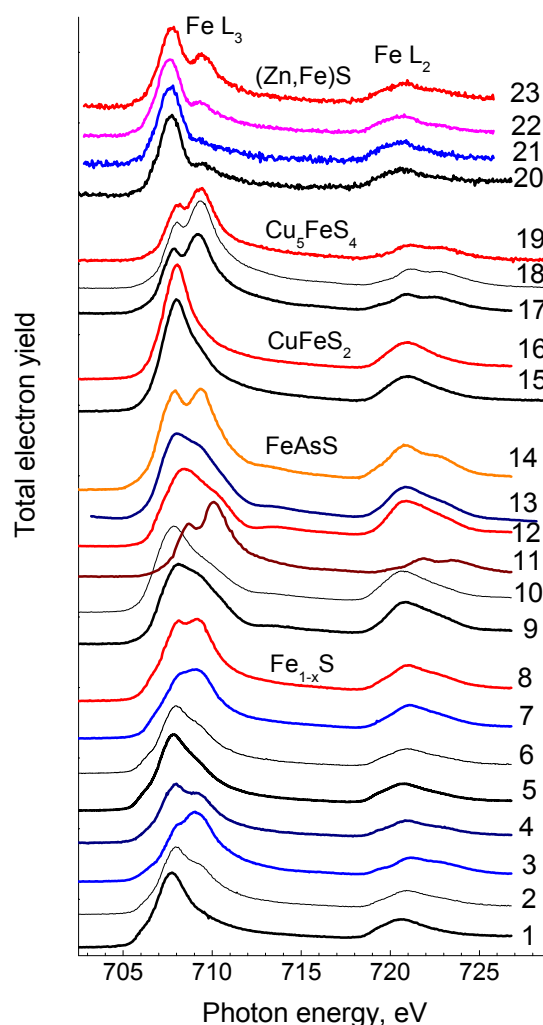


Fig.1. Fe L_{2,3} edge X-ray absorption spectra of (1) hexagonal pyrrhotite cleaved in vacuum, (2) abraded in air, (3) etched in 1 M HCl, (4) etched and aged in air for 1 week, (5) monoclinic pyrrhotite cleaved in vacuum, (6) abraded in air, (7) etched in 1 M HCl, (8) etched in 0.4 M FeCl₃, (9) arsenopyrite cleaved in vacuum, (10) abraded in air, (11) aged in air for 1 week, (12) etched in 0.4 M FeCl₃, (13) etched and aged in air for 1 week, (14) 1 M HNO₃ + 0.4 M Fe(NO₃)₃, (15) chalcopyrite cleaved in vacuum, (16) etched in FeCl₃ solution, (17) bornite cleaved in vacuo, (18) abraded in air, (19) etched in FeCl₃ solution, (20) sphalerite abraded in air, (21) etched in 1 M HCl for 45 min, (22) for 3 h, (23) 1 h etched in 0.4 M FeCl₃ solution.

After the acidic etching that produces essentially metal-depleted surfaces involving polysulphide anions [4,5], responses of Fe^{3+} species and an intermediate state of iron(II) with an energy of the vacant t_{2g} orbitals increased by 0.5-0.8 eV were observed (Fig.1, 3,4,7,8). Singlet Fe^{2+} found earlier [5] was not distinguished owing probably to its rapid oxidation. In the S L-edge spectra (Fig.2, 1-8), the changes of the pre-edge maxima, which corresponds to admixture of S s,p states to the Fe 3d crystal field orbitals, reflect the Fe^{3+} presence, and those above ~177 eV are due to the S-S bonding and a tentative fourfold coordination of S atoms instead of initial distorted octahedral one. Strong pre-edge maxima, which are characteristic of pyrite and S^0 , were not observed.

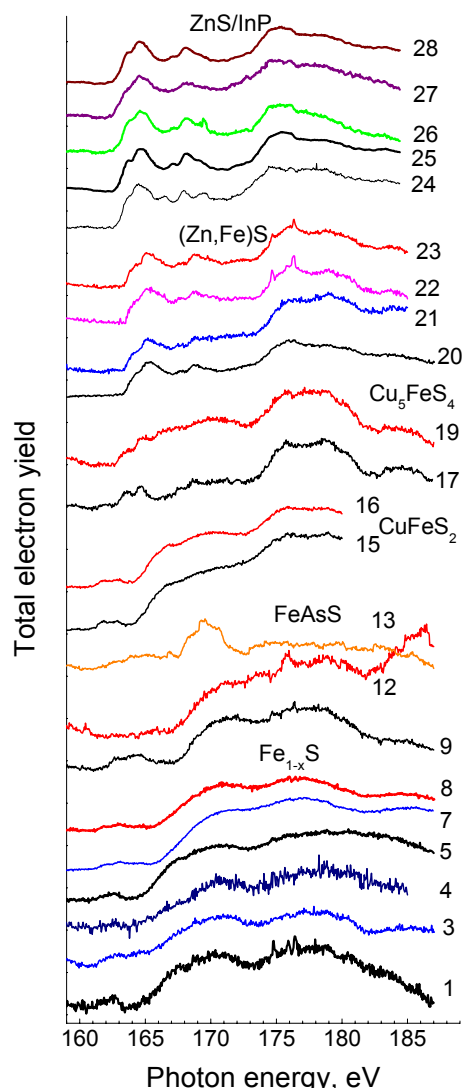


Fig. 2. S $L_{2,3}$ edge X-ray absorption spectra of (24) wurtzite, ZnS, powder, (25) ZnS(64ML)/GaP(001), (26) In(32ML)/ZnS(16ML)/GaP(001), (27) Cu(16ML)/ZnS(16ML)/GaP(001) annealed at 370 °C, (28) In(32ML)/ZnS(16ML)/GaP(001) annealed at 320 °C; other notation is the same as for Fig.1.

Arsenopyrite contains singlet ferrous iron octahedrally bonded to $(\text{AsS})^{2-}$ dimers, with As^{-1} and S^{-1} each coordinating three Fe atoms and another anion. Unlike pyrrhotite, iron retains its chemical state in the sulphur-excessive layer formed by the oxidative etching. At the same time, both aerial oxidation and the ferric nitrate treatment produce surface ferric iron compounds, which, but not the e_g^* band split by differences in Fe-S and Fe-As bonding assumed previously [6], are responsible for the additional maximum at the Fe L_3 -edge. The S $L_{2,3}$ -edge XANES of arsenopyrite etched in the ferric chloride solution (Fig.2, 12) shows considerably reduced pre-edge maxima, indicating a seemingly small Fe-S interaction in the iron-depleted surface layer. The main element in the spectrum of arsenopyrite etched in the ferric nitrate solution (Fig.2, 13) is a maximum at 169.5 eV attributed to sulphur species in oxidation state between +2 and +4.

XPS and Mössbauer spectroscopy clearly prove Cu^+ and Fe^{3+} species in a tetrahedral coordination (somewhat distorted in Cu_5FeS_4) for both chalcopyrite and bornite [3,7]. However, Fe L-, S L-, and Cu L-edge XANES of these compounds are essentially different. The Fe L-edge of chalcopyrite (Fig.1, 15) may be considered as a typical one for predominant Fe^{2+} , and the Cu L-edge spectrum (Fig.3, 1) would be interpreted, judging from the intensity of the peak A at ~932 eV, in terms of a formal Cu valence between +1 and +2 [2]. The Fe L-edge pattern of Cu_5FeS_4 indicates that the quantity of Fe^{3+} is notably larger than Fe^{2+} , and a contribution of Cu^{2+} is low. While the spectra of chalcopyrite suffer surprisingly moderate changes after the etching despite the formation of heavily metal-depleted layers, the Cu L- and S L-edge spectra of bornite are considerably modified. They become more similar to those of chalcopyrite, although the Fe L-edge shows only a small increase in the Fe^{2+} content. Van der Laan et al. have recently reported [8] that the peak A in Cu L_3 -edge spectra critically depends upon small changes in bornite composition and ascribed it to $2p^6d^{10}\underline{L}s \rightarrow 2p^5d^{10}\underline{L}s^2$ transitions, where \underline{L} stands for a hole localized on S ligand. We argue that this feature is attributable to transitions from initial configurations with d^9 electrons into final d^{10} configurations, which intensity is much more sensitive to the density of vacant Cu

3d states. The multiparticle effects certainly play an important role in the spectra, and the discrepancies between them and other methods may be explained in terms of notably increased contribution of the electronic configurations with a hole at S atoms in X-ray absorption. Further research is required to validate this phenomenon and to describe the spectra in detail.

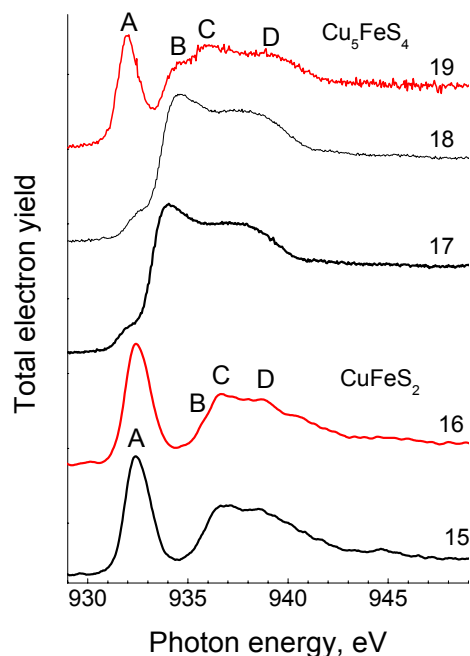


Fig. 3. Cu L_3 -edge X-ray absorption spectra of chalcopyrite and bornite. For notation see Fig.1.

The surface layers of sphalerite undergo rather small changes due to deposition of metals, oxidation in air or etching in acidic solutions. S L -, Fe $L_{2,3}$ -edge and, in lesser extent Zn L_3 -edge (not shown in Figs) X-ray spectra reveal two stages of the acidic etching of natural sphalerite, with the first one showing, in particular, lower concentration of Fe^{3+} and less

sharp features above the S L -threshold than for intrinsic material and samples etched for longer periods or under severer conditions. This appears to be due to diverse defect centers, which distort chemical bonds and flank the Fermi level in a different way in the metal-deficient layers formed at these stages. We believe that donor-like centers D^+ form initially, and then D^+/D^- pairs arise, akin to disordered chalcogenide semiconductors.

The S L absorption spectra measured on five heterostructures and ZnS powder that was a raw material for the ZnS epitaxial films are different (Fig. 2, 24-28), demonstrating that the powder has a wurtzite crystalline lattice, whereas the film has a zinc blende structure. The effect of the deposited Cu film was significant, with the spectrum features nearly vanished (not shown in Fig. 2). After annealing of the Cu/ZnS/GaP, the features in the S L -edge spectrum reappear. It should be noted that the Cu deposition influence on the S L emission spectra of ZnS was also considerable [9], suggesting that copper affects both the valence and the conduction bands of the ZnS epitaxial film. The In film induces minimal changes of the S L spectra, implying much less impact of sp metals than transition metals.

Summarizing, the XANES spectra allow determining both surface oxidation products and alterations of the reacted and/or buried sulphide phases. The L -edge spectra of sphalerite, pyrrhotite and arsenopyrite are reasonably described using static DOS pictures, whereas multiparticle interactions should be taken into account for chalcopyrite and bornite.

The authors gratefully acknowledge the support of the BESSY II and Russian-German Laboratory staff and RFBR (project 01-03-32687a).

1. K.H. Hallmeier, I. Uhlig, R. Szargan, *J. Electron Spectr. Rel. Phenom.* 2002, **122**, 91.
2. E.C. Todd, D.M. Sherman, J.A. Purton, *Geochim. Cosmochim. Acta*, 2003, **67**, 2137.
3. D.J. Vaughan, J.R. Craig *Mineral chemistry of metal sulfides*, 1978, Cambridge University Press.
4. A.R. Pratt, H.W. Nesbitt, *Am. J. Sci.* 1997, **297**, 807.
5. Yu.L. Mikhlin, Ye.V. Tomashevich, G.L. Pashkov, A.V. Okotrub, I.P. Asanov, L.N. Mazalov, *Appl. Surf. Sci.* 1998, **125**, 73; Mikhlin Yu. et al. *Phys. Chem. Chem. Phys.* 2000, **2**, 4393.
6. J.F.W. Mosselmans, R.A.D. Patrick, G. van der Laan, J.M. Charnock, D.J. Vaughan, C.M.B. Henderson, C.D. Garner, *Phys. Chem. Minerals*, 1995, **22**, 311.
7. E.Z. Kurmaev, J. van Ek, D.L. Ederer, L. Zhou et al., *J. Phys.: Condens. Matter.* 1998, **10**, 1687.
8. G. van der Laan, R.A.D. Patrick, J.M. Charnock, B.A. Grguric, *Phys. Rev. B.* 2002, **66**, 045104.
9. K.H. Hallmeier, L. Zhang, D. Wett, D. Schulze, B. Flemmig, J. Reinhold, T. Chasse, R. Szargan, *BESSY Annual Report* 2002, 134.

Quantum well states in Ag-stripes on stepped W(145)

A. Shikin, O. Rader, A. Varykhalov, W. Gudat
BESSY

Recently, the literature reflects enhanced interest in the electronic structure of stepped surfaces. Stepped surfaces are produced by cutting a monocrystal under a certain small angle relative to a high symmetry plane and are for this reason sometimes termed "vicinal surfaces". Of particular interest is the possibility to achieve lateral confinement of electrons on the steps leading to lateral quantum-size effects. Angle-resolved photoemission spectra from stepped Au(111) show a strongly anisotropic behavior (parallel and perpendicular to the steps) and have been interpreted along these lines. It should be mentioned that besides lateral quantization also superlattice effects due to the step array on the surface are possible reasons for anisotropic behavior of electrons on stepped surfaces, and both effects have been observed in the literature [1].

All photoemission work up to date studied an L-gap centered surface state of fcc(111) noble metals, and this limits the energy range of observable effects from the Fermi energy down to 0.4 eV binding energy [1]. Moreover, only clean stepped surfaces have been studied by angle-resolved photoemission where only two-dimensional surface states are expected to lead to one-dimensional confinement. Our intention is to create nanostripes using a stepped surface as template. The valence-band electron states of ultrathin metal stripes or wires formed in this way show also inherently two-dimensional behavior if the orbitals are chosen such that only relatively weak interaction with the substrate results. This two-dimensional electronic structure is then subject to the influence of the regular superlattice of steps. The energy range of low-dimensional behavior depends on the details of the stripe-substrate interaction but may extend to the whole valence-band range of the deposited material. Again, angle-resolved photoemission is the ideal method to study the resulting dimensionality via the k-vector-resolved electronic structure.

The current work is a first step towards studying the influence of lateral confinement and quantum-size effects on the valence band quantum-well states which are known to form in ultrathin Ag layers on W(110). We make particular use of the well-known thickness-dependence of energy positions of quantum-well states (QWS's). As stepped substrate we use W(145). The W(145) surface is characterized by regularly arranged terraces with (110)-orientation. Among the three possible low-Miller-index step-edge orientations, this surface features the most dense [111]-orientation. Returning to the reference system Ag/W(110), we note that besides good layer-by-layer growth enabling the separation of QWS's of individual layers [2], Ag is characterized by sp- and d-derived QWS's well separated from each other [2,3]. It is not *a priori* known whether electron confinement, which is along the film normal in the case of the two-dimensional quantum-well system, will be realized to the same perfection when the film is deposited on narrow steps. The intensity behavior of quantum-well states as a function of thickness has been found to be a good indicator of layer-by-layer growth and of a narrow distribution of thicknesses in the film. If Ag quantum-stripes grow perfectly wire-by-wire on the stepped W surface, the intensity behavior of quantum-well states if formed should oscillate with a similarly strong amplitude as for the flat system. The first step of the present work presented in this report is therefore the observation of QWS formation in the direction normal to the surface, their identification and analysis of their behavior in dependence on the deposited mass measured in monolayer equivalents or time of deposition.

In Fig. 1 a series of angle-resolved normal-emission spectra for Ag on W(145) is presented measured at the UE-56/1-PGM beamline at a photon energy of 62.5 eV. The spectra are characterized by attenuation of W-derived features under Ag-deposition and appearance of new features, which can be described as sp- and d-QWS's by analogy with the Ag/W(110) system [2]. The spectra corresponding to formation of 1, 2 and 3 ML are marked by full red lines. The spectra and the QWS-identification presented in Fig. 1 closely correspond to those characteristic of ultrathin Ag films on flat W(110) [2,3]. With formation of each new monolayer the energies of the observed QWS's change abruptly. Thickness-dependences of the QWS binding energies are shown in Fig. 2a together with their identification. Here, the theoretical estimates of QWS binding energies on the basis of the «extended phase accumulation» model [2] are for comparison shown by dotted lines and crosses. The maxima of intensities of different QWS's both of sp- and d-character (Fig. 2b) correspond to the formation of Ag stripes of 1, 2, and 3 ML thickness. Due to weak intensities of QWS's for 1 ML, we assume that the corresponding spectra rather reveal the formation of a Ag-W interlayer. The more pronounced behavior of QWS's of 2 and 3 ML indicate that on top of this interlayer the growth occurs in a relatively good wire-by-wire fashion. This is prerequisite for lateral confinement, and an analysis of the angle dispersion for k-vectors parallel and perpendicular to the photoemission spectra will be published later.

Ag/W(145) Normal emission

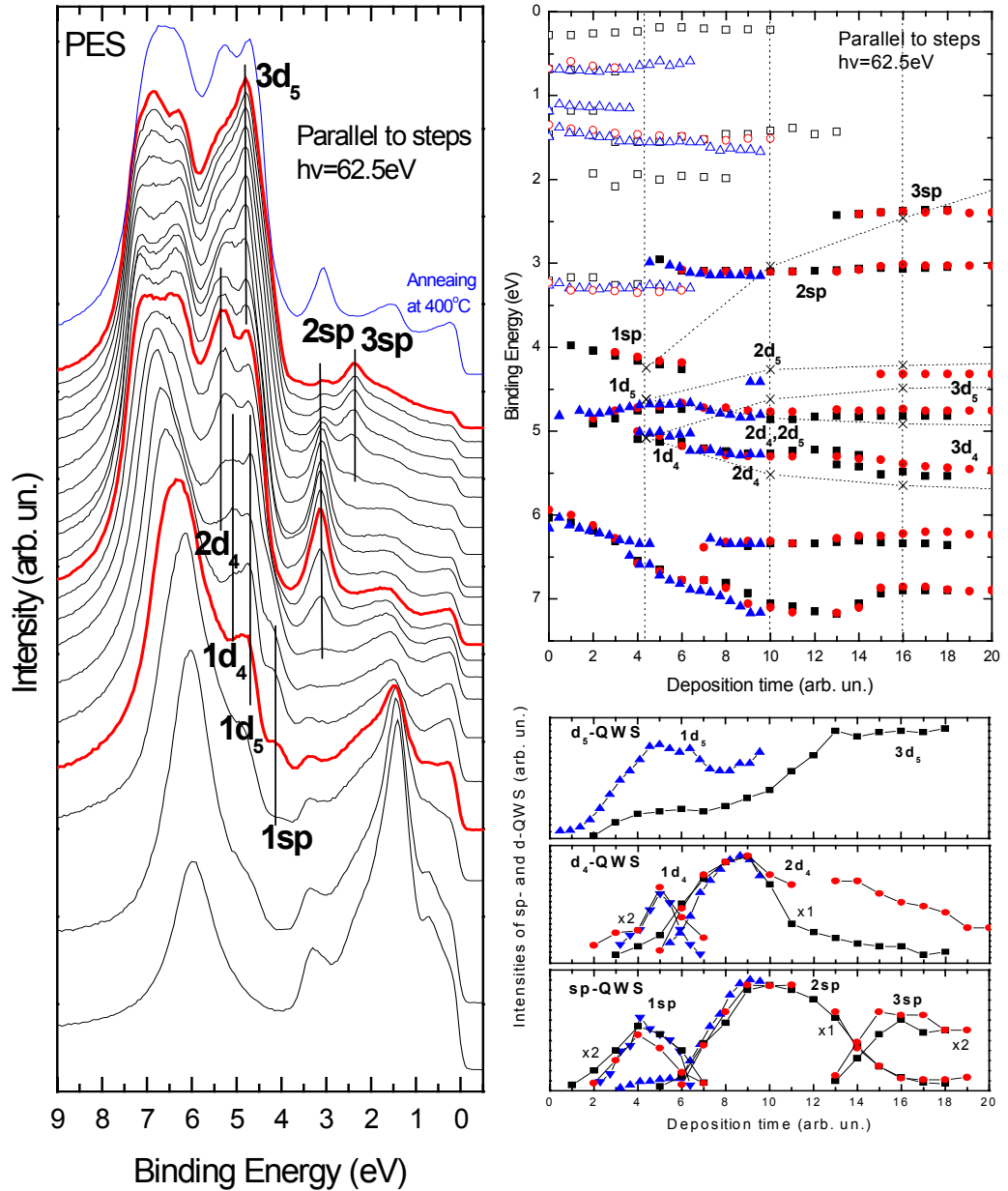


Fig.1 Series of normal emission valence band photoemission spectra for increasing thickness (0 - 3 monolayers) of Ag on W(145). Light polarization is parallel to the step edges.

Fig.2. Binding energies (a) and intensities (b) of sp- and d-derived quantum-well states.

1. J.E. Ortega et al., Phys. Rev. Lett. **84**, 6110 (2000); A. Mugarza et al., Phys. Rev. Lett. **87**, 107601 (2001). 2. A.M. Shikin, D. Vyalikh, G.V. Prudnikova, V.K. Adamchuk, Surface Science **487**, 135 (2001).
3. A.M. Shikin, O. Rader, W. Gudat, G.V. Prudnikova, V.K. Adamchuk, Surf. Rev. Lett. **9**, 1375 (2002).

Observation of step-derived lateral superlattice effects for graphite nanostripes on top of stepped Ni(755)

A.M. Shikin^{1,2}, D. Popov¹, I. Aliev¹, V.K. Adamchuk¹, W. Gudat², O. Rader²

1) St.Petersburg State University, St.Petersburg, 198904 Russia

2) BESSY

Recently, a number of detailed investigations has been published in the literature devoted to lateral quantization and lateral superlattice effects on the electronic structure. Such behaviour can occur on vicinal surfaces of monocrystals some of which form regularly arranged steps of monoatomic height (see, for instance, refs. [1-3]). In this context, we have to distinguish two types of low-dimensional systems with the potential of unique electronic properties: These are on the one hand pure stepped surfaces where lateral superlattice effects can be expected mainly for two-dimensional electronic states, namely surface states and surface resonances. Such systems have hitherto been studied almost exclusively [1,2]. On the other hand, the stepped surface can serve as template for the growth of nanowires and nanostripes, and in this case the electronic structure of the deposited film may as a whole be influenced by the step superlattice of the substrate. There are many parameters involved, and varying the step width has been identified as leading to a qualitative change from macrosurface-based electron wave functions at large widths to microsurface-based ones for small widths [1,2]. In order to decide between the two cases, the k -vector dependence of the two-dimensional surface states has to be measured with angle-resolved photoemission.

The system studied in the present work is stepped Ni(755) covered by graphite nanostripes of monolayer thickness. The influence of step-derived superlattice on the graphite valence band states is studied by angle-dependent photoemission for wave vectors parallel and perpendicular to the step direction. It is hoped that the large energy range of the graphite band structure allows to study the step-derived superlattice to more detail. The Ni(755) surface is characterized by regularly arranged terraces of about 1.3 nm width, monoatomic height, and a (111) surface crystallographic structure. We have previously investigated a related system: graphite monolayer stripes on top of vicinal Ni(771) with (110) terrace structure [3]. It was possible to distinguish superlattice effects as appearance of additional graphite π - and σ -bands shifted by an electron wave vector parallel to the surface ΔK_{\parallel} in close agreement with the lateral translation vector of the stripe superlattice. In addition, the extra branches appeared energetically shifted. The aim of our current investigation is to get an additional proof of the previously observed effects including the energy shift of the repeated bands for a different system. A major difference between the two systems is that while in the graphite/Ni(771)-system there is no obvious correlation between the structural parameters of the (110) terraces and the graphite (0001) structure, the Ni(775)-based system with its (111) terraces is characterized by good epitaxial correlation to graphite(0001).

The experiment was carried out at the Russian German beamline (RGLB) in the photon energy region 50 to 90 eV using a VG CLAM spherical electron analyser. Graphite stripes on top of Ni(755) were prepared by cracking of propylene ($p=1 \times 10^{-6}$ mbar) at a sample temperature of 450°C during 5 min.

In Fig.1 a,b, photoemission spectra are shown which were measured in the directions parallel and perpendicular to the steps (and to the graphite stripes formed), respectively. Where the polar angle corresponds to the terrace normal, the spectrum is colored red. Main characteristic of the spectra measured for wave vectors parallel to the steps is an arrangement in k -space symmetric to the terrace normal which, in this case, is identical to the macrosurface normal. This series of spectra is, moreover, similar to the ones observed for the corresponding flat system graphite/Ni(111). In the direction perpendicular to steps the main π - and σ -branches are centered around the terrace normal and are shifted away from the macrosurface

Fig.1 Angle-resolved PE spectra for graphite stripes measured for different polar angles in the direction parallel - (a) and perpendicular - (b) to the steps.

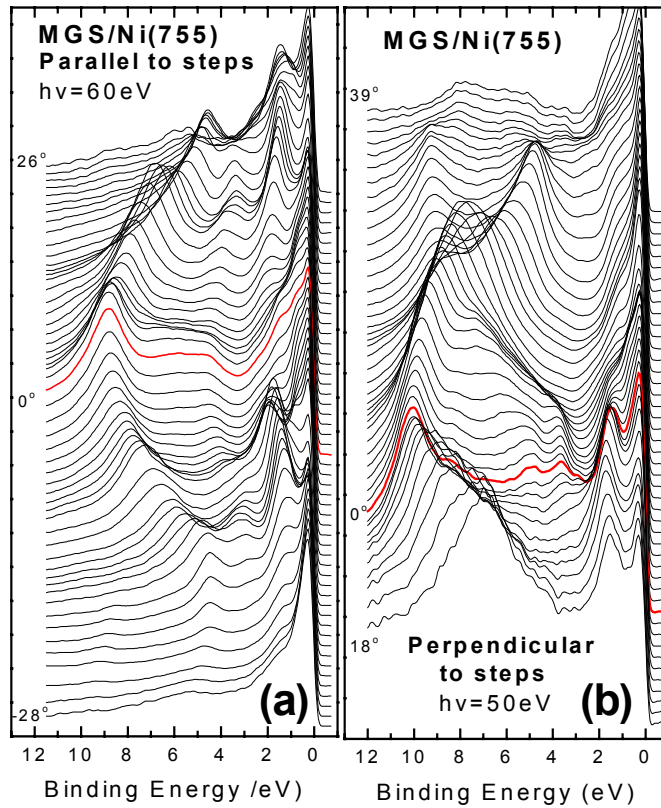
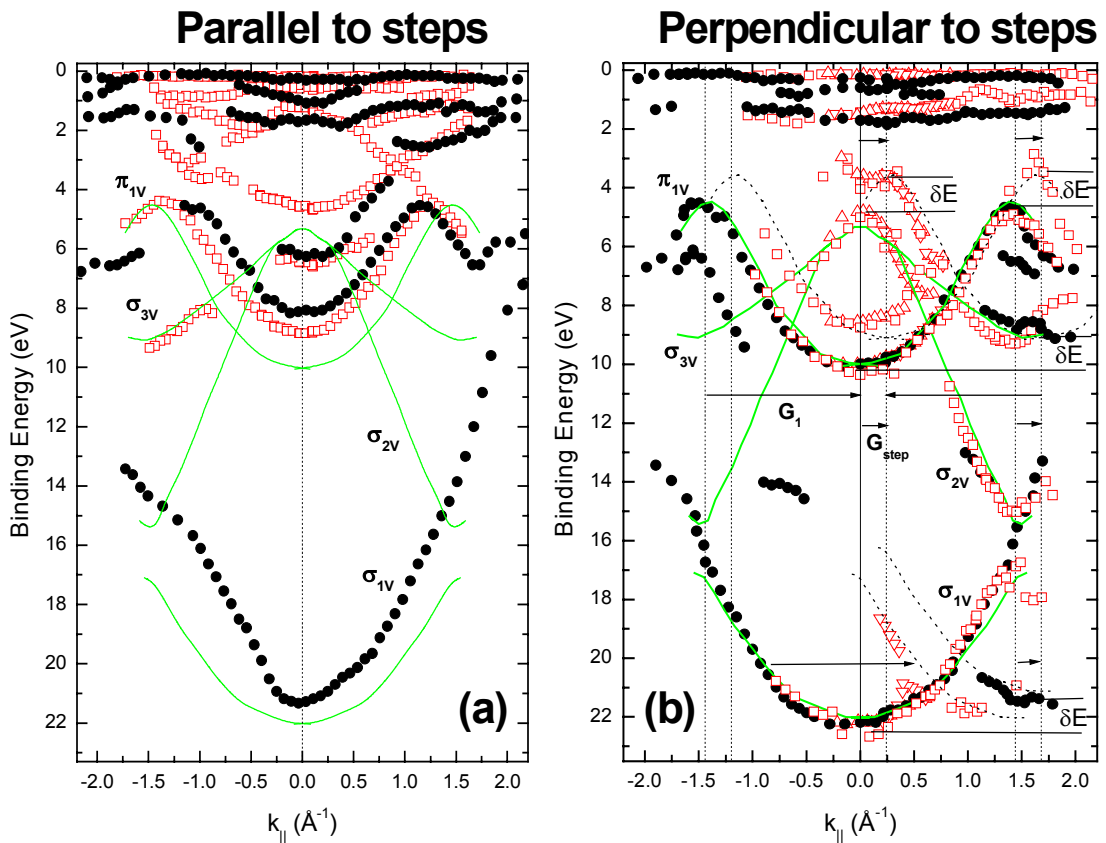


Fig.2 Valence band electron state dispersion dependences for graphite stripes measured in the directions parallel - (a) and perpendicular - (b) to the steps. Opened red symbols - $h\nu=50\text{eV}$ and black symbols - $h\nu=90\text{eV}$. Solid green lines correspond to the MG/Ni(111) system.



normal. This means, first of all, that the graphite follows indeed the geometry of the terrace planes which may be considered a proof of stripe formation. The second and more important observation is the appearance of an intense graphite π -like branch shifted relatively to the main branch in terms of angle as well as energy.

This can more clearly be seen in Fig. 2 a,b where the corresponding dispersions in parallel and perpendicular directions extracted from the photoemission spectra are shown. Data from measurements at different photon energies are superimposed. For comparison, dispersions of π - and σ -states for flat monolayer graphite (MG) on Ni(111) measured along the ΓM -direction are shown as solid green lines. In the parallel direction there appears good correlation between flat and stepped systems. There is only a small energy shift depending on the photon energy which can easily be explained by the terrace inclination in the present sample geometry: $k_{\parallel} = 0$ corresponds in Fig. 2 a to emission normal to the (755) macrosurface. As opposed to this, for the perpendicular direction we can distinguish two types of extra branches: one additional branch (for π and σ states) can be considered as main branch but shifted by the wave vector $\Delta k_{\parallel} = G_1 = 1.45 \text{ \AA}^{-1}$ which approximately corresponds to the size of Brillouin zone in the ΓM -direction. The second additional branch can be constructed by an energy shift relative to the main one by $\sim 0.9 \text{ eV}$ towards lower binding energies and in the k_{\parallel} -direction by the wave vector $G_2 = G_1 + G_{\text{step}}$, where G_{step} is the superlattice translation vector equal to $2\pi/L = 0.24 \text{ \AA}^{-1}$ with L corresponding to twice the terrace width on Ni(755). Such value of L is expected on the basis of unequal arrangement of the step edge atoms on the nearest terraces. The energy shift is marked in Fig. 2 as δE . Appearance of the additional branch of π -states with a Δk_{\parallel} -shift of G_1 (without any visible energy shift) can in principle be ascribed to a doubling of the π -branch due to umklapp corresponding to the Brillouin-zone size or, alternatively, to some surface reconstruction or facet formation. However, the disappearance of corresponding branches in photoemission spectra measured at $h\nu = 90 \text{ eV}$ and the absence of a corresponding spot in the LEED pattern for the same energy support the assumption of an umklapp-derived nature of the observed features.

In conclusion, we observed a step-derived superlattice effect in the direction perpendicular to the steps for graphite nanostripes probably due to umklapp scattering. The effect leads to the appearance of intense additional branches of π - and σ states shifted away from the terrace normal by a Δk_{\parallel} -value in accordance with the superlattice translation vector and shifted energetically. The observed effects call for detailed theoretical analysis in the future.

References:

1. A. Mugarza, A. Mascaraque, V. Perez-Dieste, V. Repain, S. Rousset, F.J. Garcia de Abajo, J.E. Ortega, Phys. Rev. Lett. 87, 107601 (2001); A. Mugarza, A. Mascaraque, V. Repain, S. Rousset, K.N. Altmann, F.J. Himpsel, Yu.M. Koroteev, E.V. Chulkov, F.J. Garcia de Abajo, J.E. Ortega, Phys. Rev. B 66, 245419 (2002).
2. J.E. Ortega, S. Speller, A.R. Bachmann, A. Mascaraque, E.G. Michel, A. Naermann, A. Mugarza, A. Rubio, F.J. Himpsel, Phys. Rev. Lett. 84, 6110 (2000).
3. A.M. Shikin, S.A. Gorovikov, V.K. Adamchuk, W. Gudat, O. Rader, BESSY Annual Report 2001, p. 190; Phys. Rev. Lett. 90, 256803 (2003);

Growth mechanism and electronic structure of Eu-Si(100) interface at various stages of its formation

D. V. Buturovich, M. V. Kuzmin and M. A. Mittsev

A. F. Ioffe Physico-Technical Institute, Russian Academy of Sciences, 194021 St. Petersburg, Russia

A. Varykhalov

BESSY, Albert-Einstein-Str. 15, D-12489 Berlin, Germany

A great deal of interest has been attracted to rare earth (RE) – silicon interfaces for two last decades, due to their fundamental and technological importance (see Refs. 1 and 2 for example and references therein). In particular, this attention was caused by fascinating physical and chemical properties of epitaxial RE silicides which can be grown on Si(111), and therefore, the interaction of RE metals with this face has been thoroughly studied up to date [2]. In contrast, little is known about the growth mechanisms and electronic and structural properties of RE/Si(100) interfaces. In 2002 we have started the characterization of RE-Si(100) systems and investigated the interface in which Yb was employed as an adsorbate. Utilizing core-level photoelectron spectroscopy with synchrotron radiation excitation (SR-PES) in combination with the other experimental techniques, it was shown that the growth mode and electronic structure of Yb-Si(100) system is strongly dependent on substrate annealing temperature and a charge transfer from Yb to Si can play an important role in formation of Yb films and Yb silicide overlayers on Si(100) [3].

The further progress in studying the RE-Si(100) interfaces can be achieved by changing the RE adsorbate. Europium is a good candidate for this purpose because, firstly, the electronic structure of isolated Eu atoms is different from that of Yb atoms, that is, 4f shell is half-filled for Eu, whereas it is occupied completely for Yb. Therefore, the comparison of Yb-Si(100) and Eu-Si(100) systems can provide the information about the role of electronic structure of RE atoms in mechanism of RE interaction with Si(100). Secondly, the crystallographic structure and lattice parameters are rather distinct for both RE metals. Yb exhibits a fcc structure with the lattice parameter $a_0 = 5.486 \text{ \AA}$, which is mismatched to Si ($a_0 = 5.43 \text{ \AA}$) within not more than 1%. While Eu has a bcc structure with $a_0 = 4.582 \text{ \AA}$, which is considerably different from that for Si (by 16%). Therefore, one may expect that both systems will exhibit different surface morphologies and growth modes depending on the atomic properties of RE adsorbates. Likewise, Eu and Yb silicide lattice types and lattice constants are sufficiently different. EuSi_2 silicide exhibits the tetragonal lattice, while YbSi_2 the hexagonal AlB_2 structure. For this reason, the comparison of Yb and Eu silicide films may give further information on the influence of the type and parameter of silicide structure on properties of silicide films formed by RE deposition onto Si(100)2×1.

From these perspectives, we have for the first time examined the initial stages of Eu-Si(100)2×1 interface formation by SR-PES. The measurements were performed in the Russian German laboratory at BESSY II. The end station of the beamline was equipped with an angle-resolved photoelectron spectrometer with a multichanneltron detector. The base pressure in the UHV chamber for measurements was better than 2×10^{-10} mbar. The angle of the incident photons was kept fixed at 67° relative to the sample surface normal. The *n*-type Si(100) substrates were cleaned *in situ* by resistive heating up to ~ 920 K and flashing at ~ 1500 K. Eu was deposited onto the Si(100) surface from a well-degassed Knudsen cell with typical evaporation rate of ~ 0.01 ML/s. The pressure was less than 1×10^{-9} Torr during Eu deposition.

The Si 2*p* and Eu 4*f* photoemission spectra were measured for Eu-Si(100) systems grown by the two different means. In the former one, Eu deposition onto Si(100)2×1 was done at room temperature

(RT), and the substrate was not heated then. In the other, Eu was also deposited at RT, however, the substrate was heated at 900 K for 4 min thereafter. According to the results of our measurements carried out at both BESSY II and Ioffe Institute, the processes of Eu-Si(100) interface formation are remarkably different for the cases described above and, for this reason, we will consider them separately.

(1) Interfaces grown at RT (Fig. 1). In this case, the silicide formation does not occur at any thickness of metal film. Only a limited intermixing of Eu and Si atoms is found. The Eu film is disordered, which is evident from the fact that the LEED spots for clean Si(100)2×1 disappear gradually with increasing the Eu coverage, whereas a new spots do not appear. Upon Eu deposition, the Si 2*p* feature S_U originated from Si dimers decreases. Simultaneously, the feature near the Fermi level decreases in the valence band spectra. As known, this feature is due to surface states on Si(100)2×1.

With increasing Eu content, the peaks with binding energies of 99.2 and 99.8 eV, which are characteristic of Si 2*p* spectrum for clean surface, reduce gradually. While the shapeless tail appears on the high-energy side of Si 2*p* spectra at >0.6 ML, with its width being > 1 eV. Both these facts are well evidence that the continuous metallic Eu film grows on the substrate at RT. The Si atoms are dissolved in this film. Since such a film is disordered (based on data obtained at Ioffe), the dissolved Si atoms can have a distinct coordination number, and therefore, different binding energy of 2*p* electrons. This is why there appears a long tail. Its location on the side of high kinetic energy can be due to a charge transfer to electronegative Si atoms from surrounding electropositive Eu atoms. As known, such a transfer should result in decreasing the binding energy of 2*p* electrons.

At 6.5 ML the above peaks with characteristic binding energies of 99.2 and 99.8 eV as well as the above tail practically disappear. Whereas the Eu 4*f* spectrum exhibits the lineshape resembling that for bulk three-dimensional Eu samples.

(2) Interfaces grown at RT and annealed afterwards at 900 K for 4 min (Fig. 2). In this case, the appearance of Si2*p* spectra depends on the Eu content on Si(100) in the whole coverage range studied (0 –30 ML). In the range of 0 – 1.5 ML, the transformation of Si2*p* spectra resembles the evolution of the spectra for non-heated Eu layers. However, at the Eu coverage higher than 1.5 ML, the spectra for heated system are very different from those for un-annealed one. Such a difference is due to formation of silicide phase upon heating. Obviously, the electronic state of Si atoms in this phase should be apparently distinguishing from that in the disordered Eu-Si(100) system.

The final shape of Si2*p* spectra at 30 ML is characterized by the presence of four clear features. One of them (kinetic energy is 24 eV) is very broad (~ 3 eV). One can suggest that it is caused by adsorbate atoms which have different environment upon Eu silicide film formation. The distinction of position of these atoms results in a large width of the peak.

The three other features form the spectrum, in which the energy difference between components is almost the same as that for clean Si(100) surface. However, this spectrum is shifted to high-energy side relatively to the spectrum for clean surface. The preliminary analysis shows that the transition from spectrum at 0 ML to spectrum at ≥20 ML shows a complex character. This transition is due to a change of chemical surrounding of Si atoms upon formation of Eu silicide. It can be also affected by the charge transfer from Eu atoms to Si atoms. We expect that the fitting of these spectra, which we are planning to perform further, will provide additional important information about the electronic structure and growth mode of Eu-Si(100) system.

[1] G. Rossi, Surf. Sci. Rep. 7 (1987) 1 and references therein.

[2] F. P. Netzer, J. Phys.: Condens. Matter, 7 (1995) 991.

[3] M.V. Kuzmin, M.A. Mittsev, D.V. Vyalikh, S.L. Molodtsov, BESSY Annual Report, 2002, p. 104

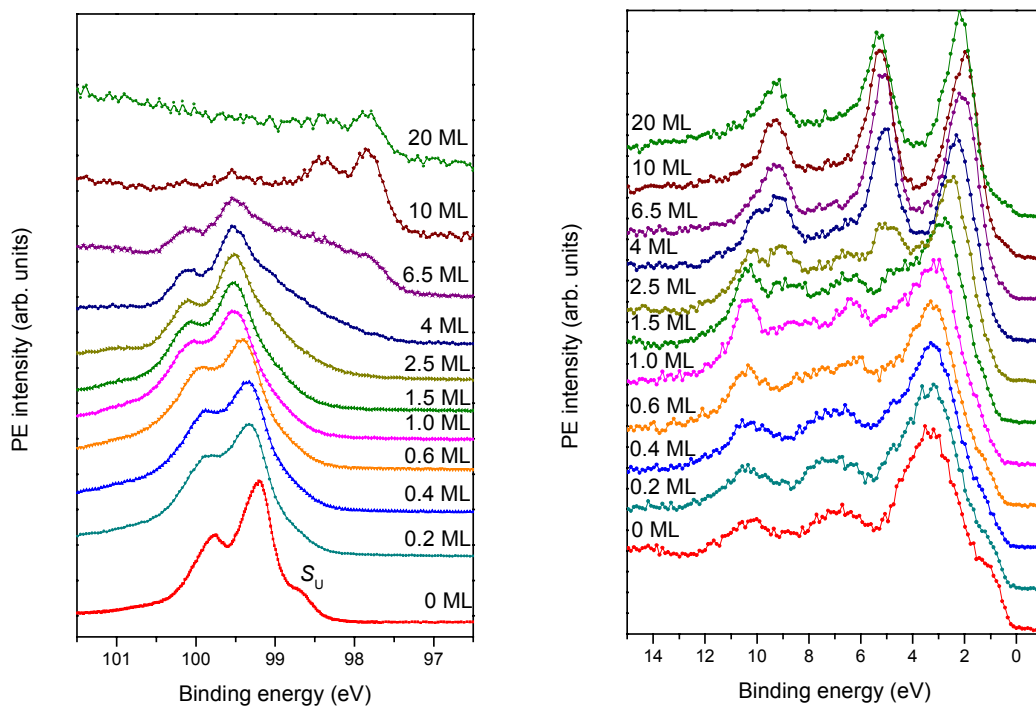


Fig. 1. Si $2p$ (left panel) and Eu $4f$ (right panel) photoelectron spectra taken at normal emission angle for Eu-Si(100) system formed at $T = 300$ K. The photon energy is 130 eV.

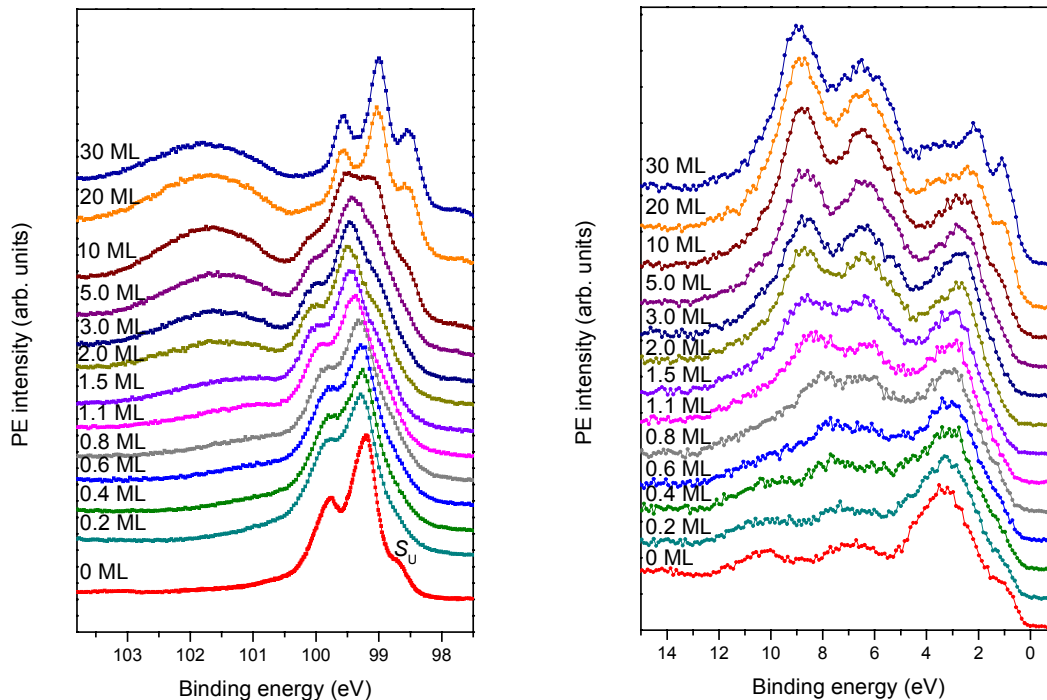


Fig. 2. Si $2p$ (left panel) and Eu $4f$ (right panel) photoelectron spectra taken at normal emission angle for Eu-Si(100) system formed upon annealing at $T = 900$ K. The photon energy is 130 eV.

X-ray absorption and circular magnetic dichroism of epitaxial Heusler compound films $\text{Co}_2\text{Cr}_{0.6}\text{Fe}_{0.4}\text{Al}$ on SiO_x and $\alpha\text{-Al}_2\text{O}_3$

S. Wurmehl², F. Casper¹, A. Gloskovskii¹, S. A. Nepijko¹, G. Jakob¹, G. H. Fecher¹, C. Felser², G. Schönhense¹, H. J. Elmers^{1,*}

¹ Institut für Physik, Johannes Gutenberg-Universität Mainz, D-55099 Mainz, Germany

² Institut für Anorganische Chemie und Analytische Chemie, Johannes Gutenberg-Universität Mainz, D-55099 Mainz, Germany

Heusler compounds are potential candidates for providing a complete spinpolarization at the Fermi edge since some of these compounds are predicted to be halfmetallic ferromagnets[1]. Halfmetallic ferromagnets are ideal materials for spintronic devices. For all applications it is necessary to grow epitaxial thin films with the correct composition and chemical order on appropriate substrates. Moreover, the magnetic properties at the interface between the Heusler compound and the unpolarized material are of crucial importance for the functionality of spintronic devices. Therefore we investigate chemical and magnetic properties using the element specific tool of magnetic circular dichroism in x-ray absorption. Surface sensitivity is achieved by measuring the total electron yield of photoemitted electrons. We focus on films consisting of the Al based Heusler compound $\text{Co}_2\text{Cr}_{0.6}\text{Fe}_{0.4}\text{Al}$ that should be a halfmetallic ferromagnet according to theory (Ref. [2]). Large magnetoresistance effects were observed in powder pellets at room temperature [3].

The Heusler compound films were prepared by magnetron sputtering under an argon atmosphere using a $\text{Co}_2\text{Cr}_{0.6}\text{Fe}_{0.4}\text{Al}$ target. After the deposition of the Heusler compound some of the films were capped by an ultrathin Au capping layer in order to protect the film surface from oxidation. We investigated epitaxial films that could be grown on $\alpha\text{-Al}_2\text{O}_3$ and polycrystalline films grown on a silicon wafer covered by native oxide (SiO_x). Structural properties were measured using X-ray diffraction as a standard method. The homogeneous cubic phase with a lattice constant of $a = 5.74 \text{ \AA}$ was confirmed for the epitaxial films grown on $\alpha\text{-Al}_2\text{O}_3$, while polycrystalline films deposited at room temperature on SiO_x showed no diffraction peaks. Magnetic circular dichroism (MCD) in the $2p \rightarrow 3d$ x-ray absorption spectroscopy (XAS) was measured at the Undulator beamline U56/1-SGM by the total electron yield method. Samples were measured in the remanent magnetization state switching the circular polarization.

The Cr XAS shows a clear deviation from the pattern that is characteristic for metallic Cr. Two distinct peaks are observed at the L_{III} edge separated by 1 eV and the peak at the L_{II} edge is accompanied by a shoulder. The peak positions and relative intensities are characteristic for the XAS spectrum obtained

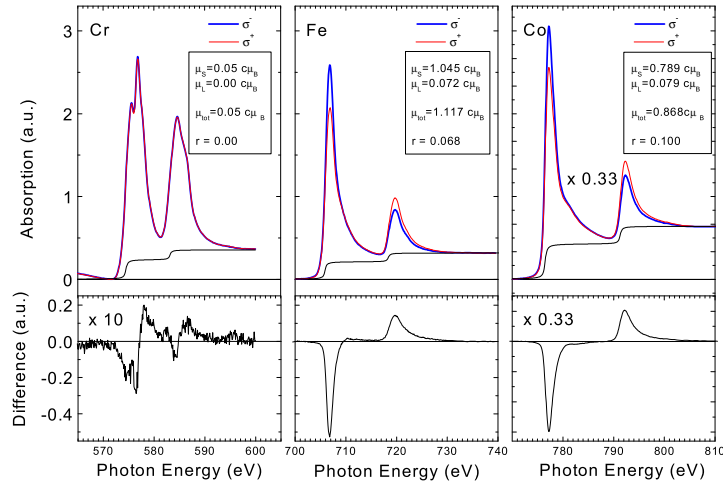


FIG. 1: Cr, Fe and Co $2p \rightarrow 3d$ XAS-MCD spectra for an uncoated polycrystalline $\text{Co}_2\text{Cr}_{0.6}\text{Fe}_{0.4}\text{Al}/\text{SiO}_x$ film. Thick (σ^-) and thin (σ^+) lines show the XAS spectra measured with left and right circular polarization. The bottom panels represent the MXCD spectra (note the different scales). The common factor c accompanying absolute values of μ_i accounts for the sample not being in saturation.

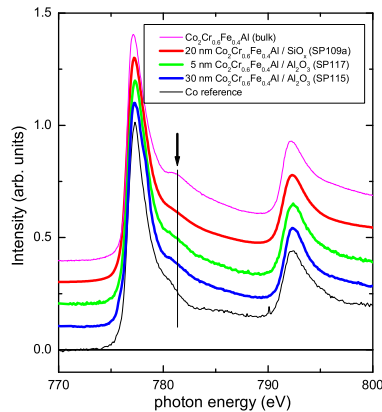


FIG. 2: Co $2p \rightarrow 3d4s$ XAS spectra for $\text{Co}_2\text{Cr}_{0.6}\text{Fe}_{0.4}\text{Al}$ films as indicated in the figure. Spectra measured for a pure Co film on $\text{Mo}(110)/\text{Al}_2\text{O}_3$ in the same run and for bulk $\text{Co}_2\text{Cr}_{0.6}\text{Fe}_{0.4}\text{Al}$ taken from Ref. [2] are shown for comparison. The extra peak at the Co L_{III} adsorption edge (indicated by an arrow) observed previously for the bulk sample is caused by the particular band structure of the Heusler compound.

from Cr_2O_3 [4]. The XAS spectra for Fe and Co, instead, show no extra oxide peaks. Obviously, the Cr is at least partly oxidized. This selective oxidation of Cr was already observed for uncoated bulk samples. Although the epitaxial samples grown on Al_2O_3 were capped by Au the XAS spectra look similar for all samples. Moreover, we did not observe any change of the magnetic properties during a time period of three months. Since x-ray diffraction confirms a pure phase for the deposited films, we conclude that the oxidation is restricted to the interface between the Heusler film and the Au capping or to the free surface, respectively. The most probable explanation for the observed oxidation of coated films is a contamination during the long cooling period before the Au capping could be deposited.

All three magnetic elements show a magnetic dichroism qualitatively similar to bulk samples. Using the sum rules for the integrated MCD signals A, B at the L_3, L_2 edges, orbital (m_L) and spin (m_S) magnetic moments can be separated [5]. We determine the orbital magnetic moment per spin according to $r = \mu_L / (\mu_S + \mu_T) = \frac{2}{3}(A + B) / (A - 2B)$ [6]. From the data shown in Fig. 1 we obtain for Fe (and Co) a value of $r = 0.07 \pm 0.02$ ($r = 0.10 \pm 0.02$ for Co), being larger than values measured for the pure elements ([7]) but similar to values measured for bulk samples of $\text{Co}_2\text{Cr}_{0.6}\text{Fe}_{0.4}\text{Al}$. The MCD signal for Cr is too small to obtain a reliable value for r .

For bulk samples of the $\text{Co}_2\text{Cr}_{1-x}\text{Fe}_x\text{Al}$ Heusler compounds the Co - XAS spectra (see Fig. 2) revealed a characteristic extra peak at 4 eV above the Co L_{III} peak position [2]. This peak was attributed to the particular band structure of the Heusler compound [8]. The pure Co element sample does not show this extra peak. For the thin films samples, however, a pronounced shoulder can be observed. The reduced intensity of the extra peak might be attributed to the fact that the Cr and probably the Al is selectively oxidized at the interface leaving partly a metallic FeCo compound.

In summary, we showed that the sputtered films possess chemical and magnetic properties similar to bulk samples. In particular, the orbital to spin moment ratio, the magnetic circular dichroism at the Cr absorption edge and a characteristic feature in the x-ray absorption spectra of Co are specific features for the properties of bulk $\text{Co}_2\text{Cr}_{1-x}\text{Fe}_x\text{Al}$ Heusler compounds. The absorption spectra at the Cr edge reveals a feature that could be attributed to Cr_2O_3 . The selective oxidation of Cr might be attributed to a contamination during the sample preparation process.

- [1] R.A. Groot, F.M. Müller, P.G. van Engen, and K.H.J. Buschow, Phys. Rev. Lett. 50, 20243 (1983).
- [2] H. J. Elmers, *et al.* Phys. Rev. B 67, 104412 (2003).
- [3] T. Block, *et al.* J. Solid State Chem. 176, 646 (2003).
- [4] C. Theil, J. van Elp, and F. Folkmann, Phys. Rev. B 59, 7931 (1999).
- [5] B.T. Thole, *et al.* Phys. Rev. Lett. 68, 1943 (1992).
- [6] H. A. Dürr, *et al.* Phys. Rev. B 58, R11853 (1998).
- [7] C.T. Chen, *et al.* Phys. Rev. Lett. 75, 152 (1995).
- [8] C. Felser, *et al.* J. Phys.: Condens. Matter 15, 7019 (2003).

NaI Aqueous Solution Surface Probed by Photoemission

R. Weber¹, B. Winter¹, P. M. Schmidt¹, W. Widdra²,
I. V. Hertel¹, and M. Faubel³

¹*Max-Born-Institut, Berlin, Germany*

²*Martin-Luther-Universität Halle-Wittenberg, Halle (Saale), Germany*

³*Max-Planck-Institut für Strömungsforschung, Göttingen, Germany*

For a NaI aqueous solution negative surface excess is inferred from the evolution of the ion photoemission signal as a function of the salt concentration. The experiments were performed using a $6\mu\text{m}$ diameter liquid microjet providing a free vacuum surface, which allows water molecules to evaporate without collisions, and hence enables the direct detection of photoelectrons originating from the liquid. Photons, 90 to 110 eV, were obtained from the MBI undulator beamline (U125-SGM).

Despite its importance, aqueous solvation constitutes one of the less understood interaction in chemical physics [1]. One reason for this is the difficulty to correctly account for the polarizability of water, and likewise for the polarizability of solvated ions [2]; this property is crucial for treating the respective interaction energies [3]. In fact, highly polarizable ions have been predicted to have a propensity for the surface, which may have consequences for the anion vs. cation concentration profile at the very near solution surface, and may hence affect the surface (atmospheric) chemistry [4, 5].

At 100 eV photon energy, corresponding to the maximum of the shape resonance in the $\text{I}^-(4d)$ photoionization cross section of aqueous iodide, the iodide signal may be detected for a concentration as low as 0.1 m in the present experiment. Hence, the evolution of the photoemission spectra can be followed over a large range of concentrations, up to saturation, which is about 13 m for aqueous NaI solutions. Notice that even for the lowest concentration studied the ions are no longer perfectly separated by the polar solvent molecules (Debye-Hückel model for electrolytes). Instead, some type of solvent-shared solvation structure must exist, having consequences for the relative distribution of anions vs. cations near the surface.

Fig. 1 displays photoemission spectra of aqueous NaI solutions for the low (0.1 to 1.0 m - inset) and high (0.5 to 12 m) salt concentration range, respectively. In order to infer the emission intensities of both ions as a function of the concentration, the corresponding peak integrals of the $\text{I}^-(4d)$ and the $\text{Na}^+(2p)$ features were evaluated. The result is presented in Fig. 2. The main figure shows the photoemission intensities for both anions and cations over the full range of concentrations, whereas the inset displays data for the lower concentrations only.

Our data indicate no differential behavior of the ion intensities since the anion to cation signal ratio remains constant. Hence the present result won't necessarily support any sur-

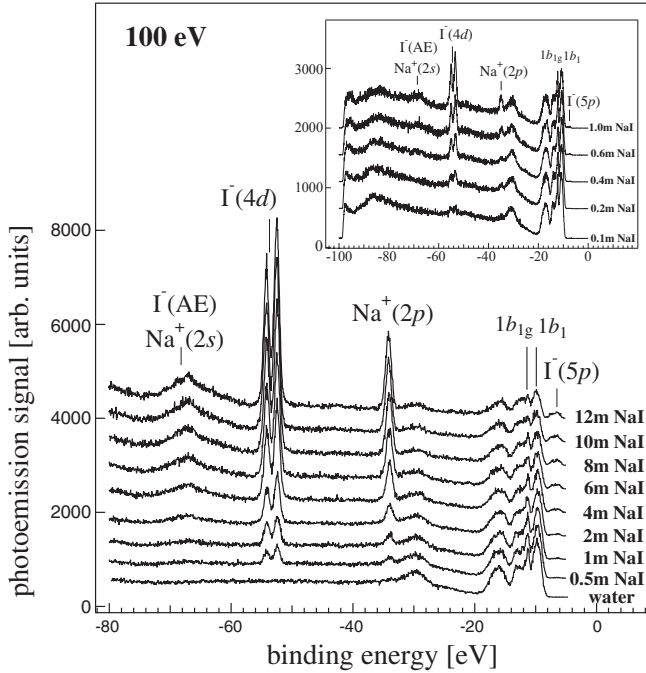


Fig. 1: Photoemission spectra of NaI aqueous solution obtained for different salt concentrations, 0.5 m to 12 m. The inset displays the spectra of low concentrated solutions up to 0.1 m. The excitation photon energy was 100 eV. Intensities have been normalized to the synchrotron photon flux. From this comparison constant electron binding energies of both $\text{I}^- (4d)$ and $\text{Na}^+ (2p)$ as a function of the salt concentration are inferred.

face excess of anions as theoretically predicted for aqueous NaI (and other sodium halides) at the air/solution interface [4]. Yet, such an enhancement of the anion concentration at the interface cannot be ruled out because the surface sensitivity of the present experiment, a few layers, would still be insufficient to resolve density profile changes within a region being small compared to the electron information depth. Indeed, molecular dynamics simulations predict that at the interface of a NaI aqueous solution highest anion and cation densities are separated by a distance which is smaller than the diameter of one water molecule [4].

The observed *saturation* behavior of the ion signal for concentrations above 2 m NaI would be consistent with a depletion of ions in the sub-surface region, in qualitative agreement with the aforementioned MD simulations [4]. The effect is related to solute-induced surface tension changes, which can be described by the Gibbs adsorption equation [6]. Then, the increase of surface tension of 'hard' water corresponds to negative adsorption of the ions, which in turn correlates with lower ion concentrations near the interface than in the bulk solution [5, 6]. This thermodynamic description (Gibbs equation) cannot be used, however, to infer the molecular structure of the interface. The depletion region may possess a characteristic ion density profile - as mentioned, I^- is likely to be enriched right at the interface (iodide surfactant activity), as compared to cations [4, 7]. Yet, the overall ion concentration would still be lower in the sub-surface region than in the bulk, but for neutrality equal amounts of anions and cations must exist. These microscopic structural details cannot be discerned in the present experiment.

Notice that ion binding energies (aq. I^- and Na^+) are found to be strictly constant to within ± 30 meV for all concentrations studied. This is rather surprising since 12 m concentration only allows for shared solvation shells; the situation is certainly well beyond

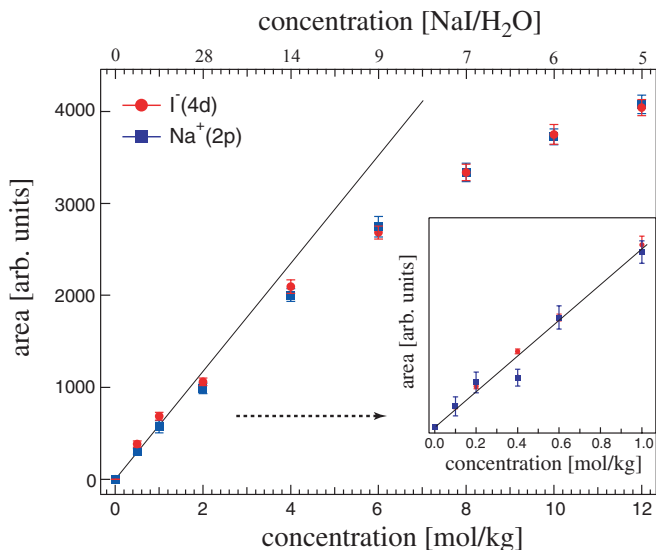


Fig. 2: Increase of the $I^{-}(4d)$ and $Na^{+}(2p)$ photoemission signal as a function of the NaI concentration (based on peak fitting and integration of spectra in Fig. 1). The inset presents data for low concentrations, up to 1.0 m. The sub-linear increase for concentrations larger than 2 m is attributed to a slower increase of ions near the surface as compared to the bulk solution.

the Debye-Hückel description. The fact that electron binding energies are not affected by the change of the solvation shell coordination is attributed to the balance of reduced binding of surface solvated iodide to one or two water molecules in the first solvation shell, and the gain in polarizability of asymmetrically solvated surface iodide [7]. Therefore the binding energy is not sensitive to the position.

References

- [1] M.F. Kropman and H.J. Bakker, *J. Chem. Phys.* **115**, 8942 (2001).
- [2] P. Jungwirth and D.J. Tobias, *J. Phys. Chem. B* **104**, 7702 (2000).
- [3] P. Silvestrelli and M. Parrinello, *Phys. Rev. Lett.* **82**, 3308 (1999).
- [4] P. Jungwirth and D.J. Tobias, *J. Phys. Chem. B* **105**, 10468 (2001).
- [5] P. Jungwirth and D.J. Tobias, *J. Phys. Chem. B* **106**, 6361 (2002).
- [6] A.W. Adamson, *Physical Chemistry of Surfaces*, J. Wiley, New York, 1990.
- [7] S. Bradforth and P. Jungwirth, *J. Phys. Chem. A* **106**, 1286 (2002).

Electronic structure and magnetism of GdN thin layers: X-ray absorption and XMCD at the N-K edge

F. Leuenberger¹, A. Parge¹, W. Felsch¹, K. Fauth^{2,3}, M. Heßler², and G. Schütz³

¹ *I. Physikalisches Institut, Universität Göttingen, Tammannstr. 1, D-37077 Göttingen*

² *Physikalisches Institut, Universität Würzburg, Am Hubland, D-9704 Würzburg*

³ *Max Planck Institut für Metallforschung, Heisenbergstr. 3, D-70569 Stuttgart*

After a controversial discussion over the years [1] it seems to be established by now that stoichiometric GdN is a ferromagnet [2]. It crystallizes in the sodium chloride structure, the Curie temperature T_C is around 60 K,. There has been speculation that in its ground state the compound may be half-metallic with complete spin polarization [3]. This becomes strong support from very recent ab-initio calculations using the self-interaction-corrected local-spin-density approximation (SIC-LSD) [4]. These calculations predict a band gap of ~ 1 eV for the minority spin channel only, and a principal Gd s-d and N p-like symmetry of the majority electrons at the Fermi energy. If the half-metallic character is verified the material will have potential applications in spin filtering devices.

Magnetism of GdN is dominated by the local magnetic moment of the half-filled Gd-4f shell (ground state $^8S_{7/2}$). There are small contributions, resulting from hybridization and exchange, from the Gd s-d and N p band electrons. This indicates that the N p states lie in the same energy range as the valence Gd states. The itinerant magnetic moments induced on the Gd 5d-derived and N 2p-derived states are expected to oppose each other. To our knowledge, little has been reported to determine the electronic structure of GdN using modern methods such as electron spectroscopy.

We have succeeded in preparing high-quality thin films of GdN by N⁺ plasma-assisted reactive sputtering. They show good stoichiometry, the Curie temperature T_C of the bulk material and the Hund's-rule value of the saturation moment ($\sim 7 \mu_B/\text{Gd ion}$) [5]. The electrical conduction is thermally activated down to T_C where is evidence of a transition to metallic behavior. The transition is considerably shifted in a sufficiently high magnetic field, as is reflected in a giant magnetoresistance. Measurements of x-ray magnetic circular dichroism (XMCD) at the Gd-M_{4,5}(3d \rightarrow 4f) edges performed at LURE in Orsay, France, reveal that the magnetic polarization of the Gd-4f moments mirrors the behavior of the macroscopic magnetization.

We have measured x-ray absorption (XA) and XMCD spectra on GdN at the nitrogen K edge (1s \rightarrow 2p transition) on beamline PM-3 of BESSY. Measurements at the Gd-M_{4,5} edges confirmed the previous results obtained at LURE. Prior to the experiment, the protective Cr cap layer was partially removed from the GdN layer (100 nm thick, Si substrate) by ion etching. The UHV environment warranted a clean sample surface during data acquisition. The spectra were recorded in the total electron yield mode, in photon energy steps of 100 meV and with light of 90% circular polarization; an external magnetic field of ± 1 T was flipped at each data point. The result obtained at low temperature is shown in the figure. The data provide information on low-lying unoccupied N 2p-derived conduction band states and their magnetic polarization. The XMCD signal is quite small ($\sim 0.5\%$ of the isotropic spectrum) but clearly resolved; it shows a characteristic structure that was well reproduced for different acquisitions. Its intensity varies with temperature as that of the Gd-M_{4,5}-edge dichroic signal; both disappear above T_C of the GdN layer. This observation reveals that the

Spin-resolved Photoemission Spectroscopy on Epitaxial Fe₃O₄(100) Films

M. Fonin,¹ Yu. S. Dedkov,¹ M. Sperlich,¹ L. N. Tong,² F. Matthes,²
C. M. Schneider,³ U. Rüdiger,⁴ and G. Güntherodt¹

¹ *II. Physikalisches Institut, Rheinisch-Westfälische Technische Hochschule Aachen,
52056 Aachen, Germany*

² *Leibniz Institute for Solid State and Materials Research Dresden,
PF 270116, D-01171 Dresden, Germany*

³ *Institut für Festkörperforschung, Forschungszentrum Jülich GmbH,
52425 Jülich, Germany*

⁴ *Fachbereich Physik, Universität Konstanz,
78457 Konstanz, Germany*

Since years ferromagnetic transition-metal oxide (TMO) films have been a subject of intensive research due to possible applications in various fields of technology. Highly spin-polarized TMO films, among them magnetite (Fe₃O₄) are claimed to have a large potential for future applications in spin-electronic devices. Theoretical calculations of the density of states (DOS) of magnetite (Fe₃O₄) predict only minority spin states at the E_F [1]. Spin-resolved photoelectron yield measurements performed on single crystalline Fe₃O₄ samples showed a large spin polarization of -60% near the photothreshold [2]. The possible half-metallic ferromagnetic nature of epitaxial Fe₃O₄(111) thin films grown on Fe(110) was experimentally confirmed by means of spin- and angle-resolved photoemission spectroscopy (SPARPES). In this experiment a negative spin polarization of $-(80\pm 5)\%$ at E_F was measured at RT [3].

In the present study the surface structure and electronic properties of epitaxial Fe₃O₄(100) films prepared *in situ* by MBE on single crystal MgO(100) substrates were investigated. The Fe₃O₄(100) surface shows in scanning tunneling microscopy (STM) a $(\sqrt{2}\times\sqrt{2})R45^\circ$ reconstruction. The spin-dependent electronic structure of the epitaxial Fe₃O₄(100) films was studied by means of spin-resolved photoemission spectroscopy using synchrotron radiation over a wide range of photon energies. At RT a maximum spin polarization of about $-(55\pm 10)\%$ was found at E_F .

Magnetite has a cubic inverse spinel structure. The structure can be considered as a stacking sequence of (100) layers containing either oxygen and iron ions in octahedral B sites or iron ions in tetrahedral A sites. The vertical distance (along [001]) between two crystal planes containing B sites or A sites is 2.10 Å, whereas the distance between A-B layers is 1.05 Å. Two terminations are possible for the bulk-truncated Fe₃O₄(100) surface. In one termination, the topmost layer consists of oxygen and iron in octahedral B sites located in the same plane (hereafter referred to as the B termination). Alternatively, the surface can consist of a monolayer (ML) of tetrahedral A iron (hereafter referred to as the A termination). Neither of these terminations is autocompensated, or non-polar. Thus, Fe₃O₄(100) tends to reconstruct. A $(\sqrt{2}\times\sqrt{2})R45^\circ$ reconstruction is commonly observed on the Fe₃O₄(100) surface during MBE growth.

The scanning tunneling microscopy characterization of the prepared thin films was carried out in an ultra-high vacuum (UHV) system with a base pressure of 8×10^{-11} mbar equipped with a commercial Omicron UHV AFM/STM. All STM measurements were carried out at room temperature using electrochemically etched polycrystalline tungsten tips cleaned in UHV by Ar⁺ sputtering. The presented STM images were taken in the constant-current-mode. The photoemission experiments were carried out at the U125/1-PGM beamline at the BESSY II storage ring. The U125/1-PGM undulator beamline provides a tunable source of photons over a 20-1500 eV energy range with a linear polarization of the light. The UHV system for the spin-resolved PES consists of a UHV chamber equipped with LEED optics, gas

inlet, e-beam evaporation cells, and an Omicron SPLEED analyzer for spin-resolved PES measurements. The spin-resolved photoemission spectra were recorded in normal emission. The total energy resolution was set to 150 meV and the acceptance angle was 6° . High quality 150-300 Å thick $\text{Fe}_3\text{O}_4(100)$ films were initially prepared *in situ* by e-beam evaporation of Fe on $\text{MgO}(100)$ substrates in O_2 atmosphere. During the growth, the O_2 pressure was maintained at 2×10^{-6} mbar and moderate substrate temperatures of 250-300°C were used to prevent magnesium interdiffusion.

Fig. 1 shows a LEED diffraction pattern (a) and a STM image (b) of an epitaxial $\text{Fe}_3\text{O}_4(100)$ film grown on the $\text{MgO}(100)$ substrate. The LEED image of the $\text{Fe}_3\text{O}_4(100)$ shows a $(\sqrt{2} \times \sqrt{2})R45^\circ$ reconstruction with respect to the (100)-terminated Fe_3O_4 surface unit cell. The same LEED pattern has been observed on *in situ* MBE-grown $\text{Fe}_3\text{O}_4/\text{MgO}(001)$ samples [4,5]. Fig. 1 b) shows a high-resolution STM image taken on a typical terrace representing a detailed picture of the rows consisting of bright protrusions. The distance between two bright protrusions within the same row was measured to be about 3 Å, and the distance between two rows is about 6 Å. Alternating pairs of bright protrusions within each row are shifted into the same direction perpendicular to the rows, resulting in a wave-like surface structure. Regularly ordered large dark depressions appear at the wide parts of the waves. These depressions are separated by 8.4 Å and have a $(\sqrt{2} \times \sqrt{2})R45^\circ$ symmetry.

Fig. 2 shows representative spin-resolved valence band photoemission spectra of the $\text{Fe}_3\text{O}_4/\text{MgO}(100)$ system as a function of photon energy (spin up: solid triangles up, spin down: solid triangles down). The position of the Fermi level corresponds to that of a pure epitaxial $\text{Fe}(100)$ film grown on $\text{MgO}(100)$. The photon energy was tuned in 2 eV steps over the range 40 - 60 eV, including the $\text{Fe } 3p \rightarrow 3d$ excitation threshold at 58 eV, where strong resonant photoemission was observed. The photoemission spectra show the $\text{Fe } 3d$ -derived emission extended over 1.5 eV below E_F and $\text{O } 2p$ -derived emission between 1.5 and 10 eV of binding energy. The general trend of the resonant enhancement of various features is very similar to those already reported in the $\text{Fe}_3\text{O}_4(100)/\text{MgO}(100)$ system [6]. Only weak

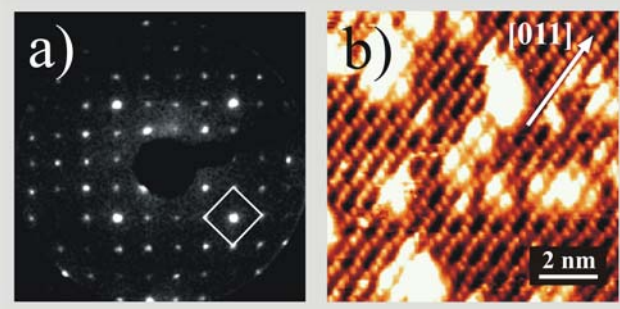


Fig.1. (a) LEED diffraction pattern of a $\text{Fe}_3\text{O}_4(100)$ film grown on $\text{MgO}(100)$. The energy of the electron beam is 107 eV. (b) STM image ($11 \times 11 \text{ nm}^2$) of a $(\sqrt{2} \times \sqrt{2})R45^\circ$ reconstructed $\text{Fe}_3\text{O}_4(100)$ surface showing a wave-like structure (1.1 V, 1.2 nA).

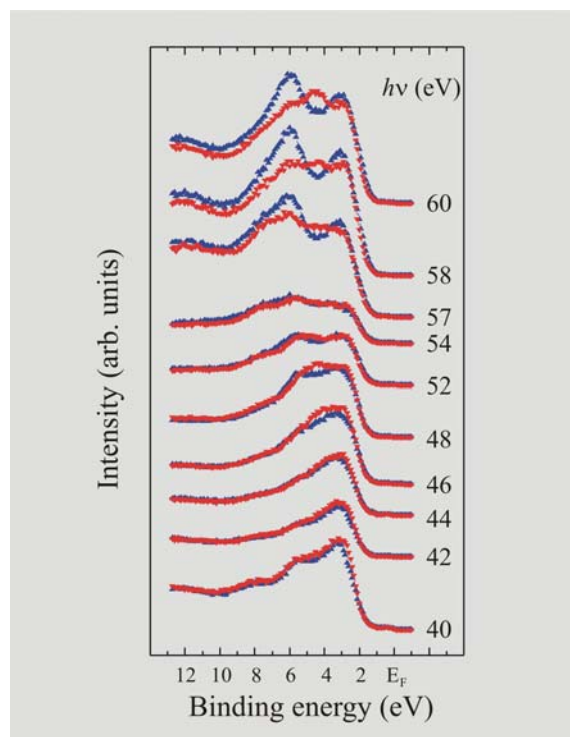


Fig.2. Spin-resolved valence band photo-emission spectra (spin up: solid up triangle; spin down: solid down triangle) of a $\text{Fe}_3\text{O}_4(100)$ thin film surface as a function of photon energy recorded at RT in normal emission.

dispersions of the O $2p$ and Fe $3d$ states in the valence-band structure of $\text{Fe}_3\text{O}_4(100)$ can be observed along the Γ -X direction of the Fe_3O_4 Brillouin zone.

Fig. 3 shows the spin-resolved photoemission spectra together with the total photoemission intensity recorded in normal emission with $h\nu = 58$ eV (a), the same spectra in the region near E_F (b), and the resulting spin polarization values (c) as a function of the binding energy relative to the Fermi level of the $\text{Fe}_3\text{O}_4(100)$ film. The $\text{Fe}_3\text{O}_4(100)$ film shows a negative spin polarization at E_F of about $-(55 \pm 10)\%$. The measured spin polarization is significantly different from that theoretically predicted by LSDA calculations. The magnetic moments at the $\text{Fe}_3\text{O}_4(100)$ surface might be reduced due to the $(\sqrt{2} \times \sqrt{2})R45^\circ$ surface reconstruction (see Fig. 1), leading to a reduction in the average spin polarization near E_F .

The negative polarization near E_F of about -55% on epitaxial $\text{Fe}_3\text{O}_4(100)/\text{MgO}(100)$ films is comparable to that previously observed in spin-resolved photoemission spectroscopy experiments [7,8]. However, a detailed theoretical analysis of the photoelectron spectra on the basis of LSDA and LSDA+ U band structure calculations with an inclusion of surface reconstruction is needed for the full understanding of the experimental spectroscopic results.

This work was supported by the German Federal Ministry of Education and Research (BMBF) under grant No. FKZ 05KS1PAA/7. The authors (M. F., Yu. S. D., and M. S.) would like to thank BESSY II for financial support.

1. Z. Zhang and S. Satpathy, Phys. Rev. B **44**, 13319 (1991).
2. S. F. Alvarado, W. Eib, F. Meier, D. T. Pierce, K. Sattler, H. C. Siegmann, and J. P. Remeika, Phys. Rev. Lett. **34**, 319 (1975); S. F. Alvarado, M. Erbudak, and P. Munz, Phys. Rev. B **14**, 2740 (1976).
3. Yu. S. Dedkov, U. Rüdiger, and G. Güntherodt, Phys. Rev. B **65**, 064417 (2002).
4. Y. J. Kim, Y. Gao, and S. A. Chambers, Surf. Sci. **371**, 358 (1997).
5. B. Stanka, W. Hebenstreit, U. Diebold, and S. A. Chambers, Surf. Sci. **448**, 49 (2000).
6. H.-J. Kim, Ph. D. Thesis, Seoul National University, 2001.
7. D. J. Huang, C. F. Chang, J. Chen, L. H. Tjeng, A. D. Rata, W. P. Wu, S. C. Chung, H. J. Lin, T. Hibma, and C. T. Chen, J. Magn. Magn. Mater., **239**, 261 (2002).
8. S. A. Morton, G. D. Waddill, S. Kim, I. K. Schuller, S. A. Chambers, and J. G. Tobin, Surf. Sci. **513**, L451 (2002).

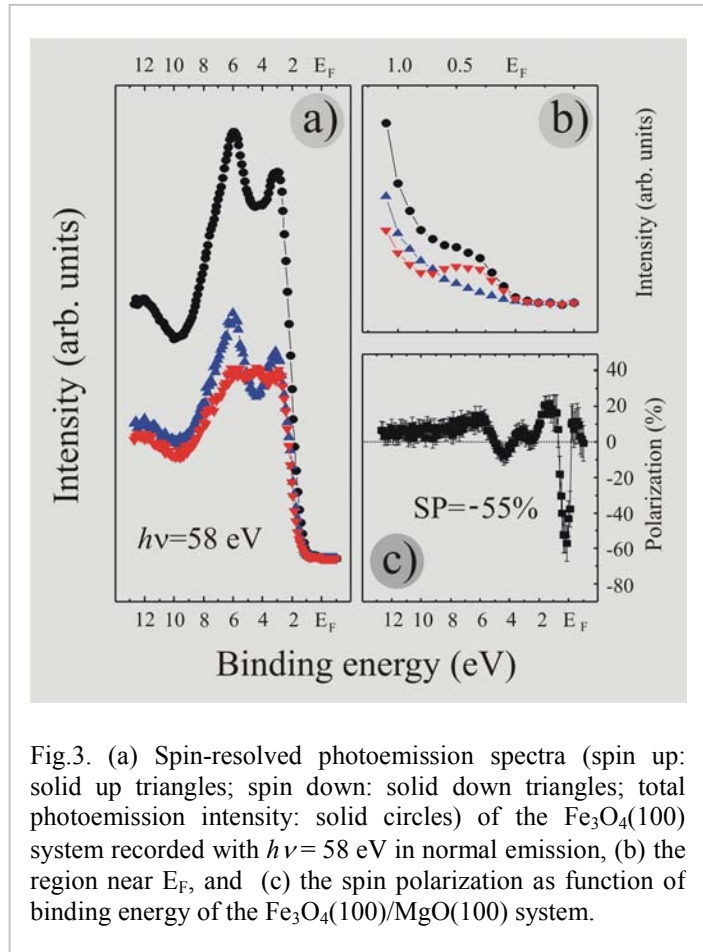


Fig.3. (a) Spin-resolved photoemission spectra (spin up: solid up triangles; spin down: solid down triangles; total photoemission intensity: solid circles) of the $\text{Fe}_3\text{O}_4(100)$ system recorded with $h\nu = 58$ eV in normal emission, (b) the region near E_F , and (c) the spin polarization as function of binding energy of the $\text{Fe}_3\text{O}_4(100)/\text{MgO}(100)$ system.

low-lying unoccupied p bands of nitrogen are spin-split by the exchange field created by the partially-filled Gd-4f states.

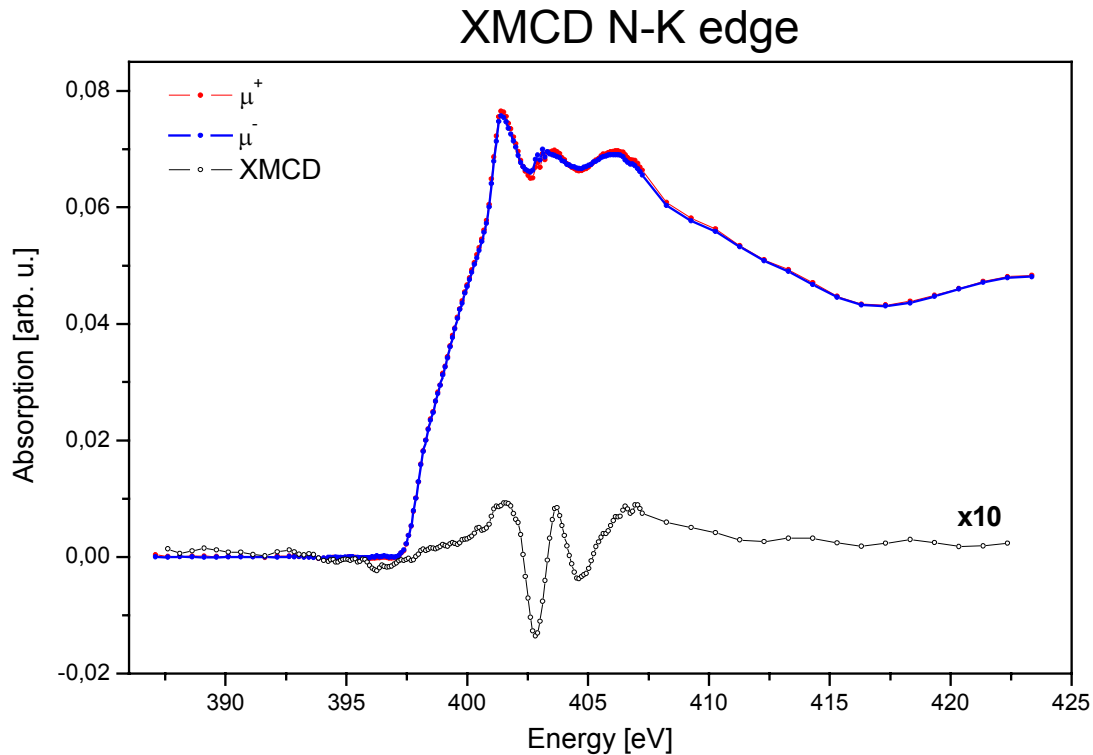


Figure: Total electron yield XA spectrum μ^+ (red) and μ^- (blue) and XMCD signal ($\mu^+ - \mu^-$) at the N K-edge in GdN at 15K.

The isotropic N-K spectrum exhibits a shoulder just above the onset of the absorption and three distinct maxima separated by a few eV. It varies only little with temperature between 300 K and 15 K and primarily probes the N-2p projected partial density of unoccupied states above the Fermi level. Efforts are under way to compare the result with the recent band-structure calculations [4]. Magnetic dichroism at the N-K edge sets in together with the onset of the absorption; the three local maxima in the dichroic spectrum appear at the same energies as the peaks in the isotropic spectrum. This indicates that their spectral shape is closely related to the spin-split N-2p-derived bands above the Fermi level. The integrated intensity reflects the orbital magnetization density of the unoccupied N-2p states [6]. We believe that the N K-edge XMCD spectra are of particular interest (even beyond the actual system) since no information on such spectra of a magnetic system is available in the literature yet.

We are indebted to Professor H. Ebert for theoretical support. Financial support was provided by the Deutsche Forschungsgemeinschaft within SFB 602.

References

- [1] P. Wachter and E. Kaldis, *Solid State Commun.* **34**, 241 (1980).
- [2] D. X. Li *et al.*, *J. Phys.: Condens. Matter* **9**, 10777 (1997).
- [3] see, e.g, A. Hasegawa and A. Yanase, *J. Phys. Soc. Japan* **42**, 492 (1977).
- [4] C. M. Aerts *et al.*, *Phys. Rev. B*, at press; cond-mat/0308354
- [5] F. Leuenberger *et al.*, to be published.
- [6] H. Ebert, *Rep. Prog. Phys.* **59**, 1665 (1996).

Temperature dependence of the hole distribution in Sr₁₄Cu₂₄O₄₁

**C. Hess¹, T. Kim², M. Knupfer², B. Büchner², N. Nücker³, P. Nagel³,
S. Schuppler³**

¹Department of Condensed Matter Physics, University of Geneva, CH-1211 Geneva, Switzerland

²Institute for Solid State Research, IFW-Dresden, P.O.Box 270116, D-01171 Dresden, Germany

³Forschungszentrum Karlsruhe, Institut für Festkörperphysik, D-76021 Karlsruhe, Germany

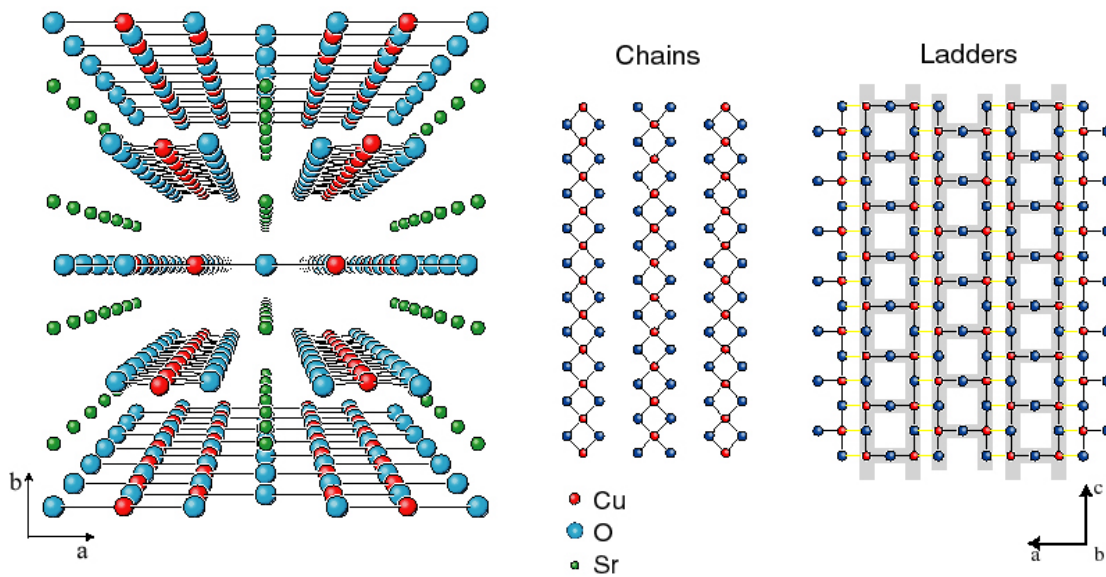


Fig 1.: The crystal structure of Sr₁₄Cu₂₄O₄₁.

The paradigmatic “ladder compound” Sr₁₄Cu₂₄O₄₁ consists of two types of low-dimensional structural units, CuO₂ chains and Cu₂O₃ two-leg ladders (see Fig. 1). Stoichiometry gives a total hole count per formula unit of 6, and the holes are located mainly in the chains although some fraction does dope the ladders as well [1]. As usual in cuprates the holes occur predominantly at the O sites and have mainly O2*p* character. In addition to magnetic and other peculiarities, a charge ordering transition is present at T_C ≈ 220 K, which affects the physical properties of both the doped spin chains and spin ladders [2].

Near-edge x-ray absorption fine structure measurements at the O1*s* edge (O1*s*-NEXAFS) directly detect these hole states due to their O2*p* character. The polarization dependence allows to assign spectral features to inequivalent O sites in the structural units. We investigated the *temperature dependence* to look for a possible redistribution of holes between sites and units, especially at the charge-order transition. Data were taken at beamline UE52-PGM in bulk-sensitive fluorescence detection mode; energy and self-absorption corrections were applied.

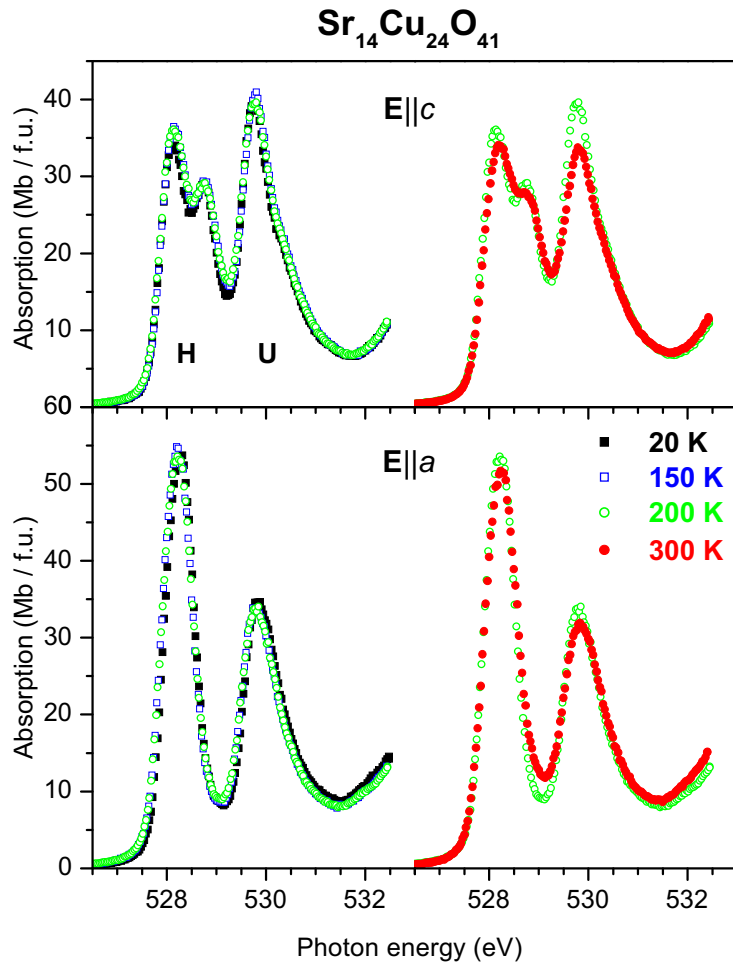


Fig. 2: Temperature-dependent O1s NEXAFS of $\text{Sr}_{14}\text{Cu}_{24}\text{O}_{41}$ for the light polarization set along the a and c axis.

Fig. 2 displays the resulting NEXAFS spectra with the incident light polarization oriented along the a and the c axis and for different temperatures. Two main structures can be seen: H corresponds to hole states in the various units and U to the upper Hubbard bands [1]. The data give clear evidence that the NEXAFS spectra are practically identical for $T \leq 200$ K and that significant changes take place only for $T > 200$ K, most obviously and profoundly for the U feature for $\mathbf{E}||c$. These observations seem to support a scenario which involves a redistribution of holes upon charge ordering. More detailed analysis is expected to yield further information on whether holes redistribute between chains and ladders, and/or within each structural unit. All this will lead to a better understanding of the charge-ordered state and its evolution with temperature.

[1] N. Nücker *et al.*, Phys. Rev. B **62**, 14384 (2000).

[2] L. P. Regnault *et al.*, Phys. Rev. B **59**, 1055 (1999); M. Takigawa *et al.*, Phys. Rev. B **57**, 1124 (1998); V. Kataev *et al.*, Phys. Rev. B **64**, 104422 (2000); G. Blumberg *et al.*, Science **297**, 584 (2002); T. Vuletić *et al.*, Phys. Rev. Lett. **90**, 257002 (2003); C. Hess *et al.*, Phys. Rev. B **64**, 184305 (2001).

Surface Electronic Structure of Epitaxial Fe₃O₄(100) Films

Yu.S. Dedkov¹, M. Fonin¹, D.V. Vyalikh², S.L. Molodtsov², U. Rüdiger³, and G. Güntherodt¹

¹ *II. Physikalisches Institut, Rheinisch-Westfälische Technische Hochschule Aachen, 52056 Aachen, Germany*

² *Institut für Festkörperphysik, Technische Universität Dresden, D-01062 Dresden, Germany*

³ *Fachbereich Physik, Universität Konstanz, 78457 Konstanz, Germany*

Since many years ferromagnetic transition-metal oxide (TMO) films have been a subject of intensive research due to possible applications in various fields of technology. Highly spin-polarized TMO films, among them magnetite (Fe₃O₄) are claimed to have a large potential for future applications in spin-electronic devices. The electronic band structure of Fe₃O₄ films was extensively investigated by means of different photoelectron spectroscopy techniques. However, the interpretation of the valence-band photoemission spectra of Fe₃O₄ has been a matter of debate since decades. Up to now the surface electronic structure of magnetite was investigated mostly in normal emission photoelectron spectroscopy. This particular method does not reflect the symmetry properties of the surface electronic states of magnetite.

Here we report on investigations of the surface electronic band structure of *in situ* prepared epitaxial, well characterized Fe₃O₄(100) thin films by means of angle resolved photoelectron spectroscopy (ARPES) using synchrotron radiation.

Magnetite has a cubic inverse spinel structure. The structure can be considered as a stacking sequence of (100) layers containing either oxygen and iron ions in octahedral B sites or iron ions in tetrahedral A sites. The vertical distance (along [001]) between two crystal planes containing B sites or A sites is 2.10 Å, whereas the distance between A-B layers is 1.05 Å. Two terminations are possible for the bulk-truncated Fe₃O₄(100) surface. In one termination, the topmost layer consists of oxygen and iron in octahedral B sites located in the same plane. Alternatively, the surface can consist of a monolayer (ML) of tetrahedral A iron. Neither of these terminations is autocompensated, or non-polar. Thus, Fe₃O₄(100) tends to reconstruct. A $(\sqrt{2} \times \sqrt{2})R45^\circ$ reconstruction is commonly observed on the Fe₃O₄(100) surface during MBE growth.

The scanning tunneling microscopy (STM) characterization of the prepared thin films was carried out in an ultra-high vacuum (UHV) system with a base pressure of 8×10^{-11} mbar equipped with a commercial Omicron UHV AFM/STM. All STM measurements were carried out at room temperature using electrochemically etched polycrystalline tungsten tips cleaned in UHV by Ar⁺ sputtering. The presented STM images were taken in the constant-current-mode. The photoemission experiments were carried out in the Russian-German Laboratory at the BESSY II storage ring.

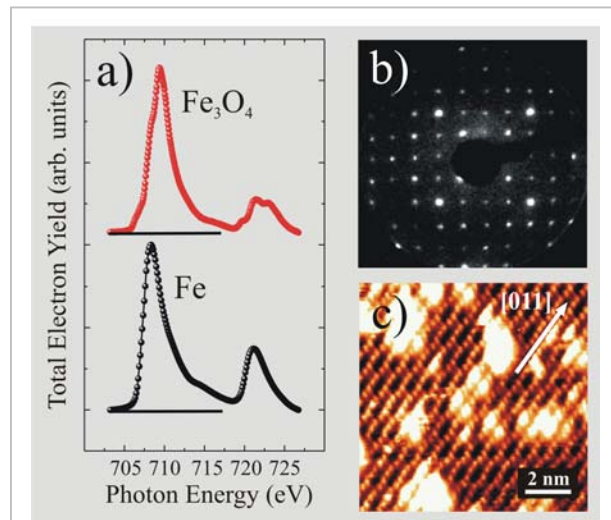


Fig.1. (a): XAS spectra of the epitaxial Fe₃O₄ and Fe films. (b) LEED image of the Fe₃O₄(100) film surface is presented. (c) STM image of a $(\sqrt{2} \times \sqrt{2})R45^\circ$ reconstructed defect free surface of the epitaxial Fe₃O₄(100) film.

The dipole beamline DIP-16-1A provides a tuneable source of photons over a 30-1500 eV energy range. The ultrahigh vacuum (UHV) system for ARPES at room temperature consists of a UHV chamber equipped with low energy electron diffraction (LEED) optics, a gas inlet, *e*-beam evaporation cells, and a 127° CLAM4 analyzer for ARPES measurements. The total energy resolution was set to 100 meV and the angle resolution was 1°. The base pressure in the vacuum chamber was 1×10^{-10} mbar. X-ray absorption spectra (XAS) spectra have been collected in the total electron yield (TEY) mode and normalized to the maximum intensity.

Fig.1 (a) shows a Fe $L_{2,3}$ edge XAS spectrum of a thin epitaxial $\text{Fe}_3\text{O}_4(100)$ film grown on the MgO(100) substrate (Fig.1(a)) in comparison with the XAS spectrum of the epitaxial iron thin film. The corresponding LEED picture of the $\text{Fe}_3\text{O}_4(100)$ film surface exhibits a $(\sqrt{2} \times \sqrt{2})R45^\circ$ reconstruction with respect to the (100)-terminated Fe_3O_4 surface unit cell. The same LEED pattern has been observed on *in situ* MBE-grown $\text{Fe}_3\text{O}_4/\text{MgO}(001)$ samples [1,2]. Fig. 1 (c) shows a high-resolution STM image taken on a typical terrace representing a detailed picture of the rows consisting of bright protrusions. The distance between two bright protrusions within the same row was measured to be about 3 Å, and the distance between two rows is about 6 Å. Alternating pairs of bright protrusions within each row are shifted into the same direction perpendicular to the rows, resulting in a wave-like surface structure. Regularly ordered large dark depressions appear at the wide parts of the waves. These depressions are separated by 8.4 Å and have a $(\sqrt{2} \times \sqrt{2})R45^\circ$ symmetry. All presented data show: (i) characteristic multiplet structure of XAS spectrum at the Fe $L_{2,3}$ and the O K -edges (not shown here) [3-5], (ii) $(\sqrt{2} \times \sqrt{2})R45^\circ$ reconstruction in LEED patterns, (iii) STM images exhibiting defect free $(\sqrt{2} \times \sqrt{2})R45^\circ$ reconstructed $\text{Fe}_3\text{O}_4(100)$ surface evidence the high bulk and surface quality of the investigated $\text{Fe}_3\text{O}_4(100)$ films.

Fig. 2 shows experimental results of the work function measurements of W(100), Fe(100), and $\text{Fe}_3\text{O}_4(100)$ surfaces. These results were extracted from the cutoff of the photoelectron spectra, which determine the work function of the surface. The values obtained on the epitaxial Fe(100) film surface are in a good agreement with those values measured on the surface of a Fe(100) whisker [6]. The experimentally obtained work function

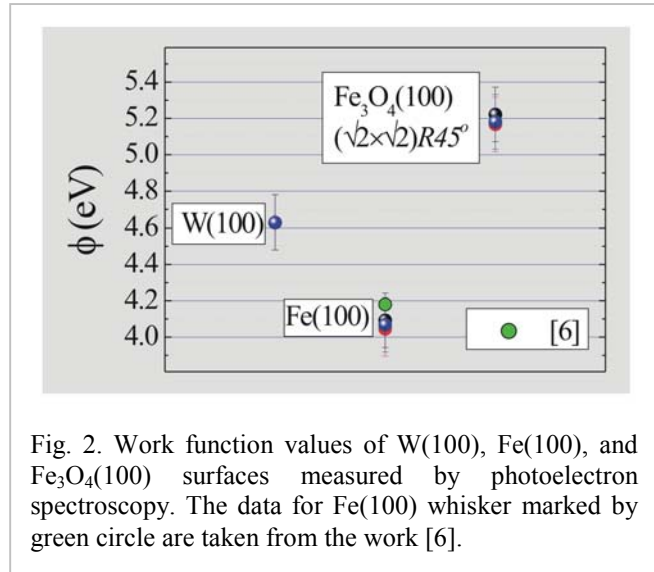


Fig. 2. Work function values of W(100), Fe(100), and $\text{Fe}_3\text{O}_4(100)$ surfaces measured by photoelectron spectroscopy. The data for Fe(100) whisker marked by green circle are taken from the work [6].

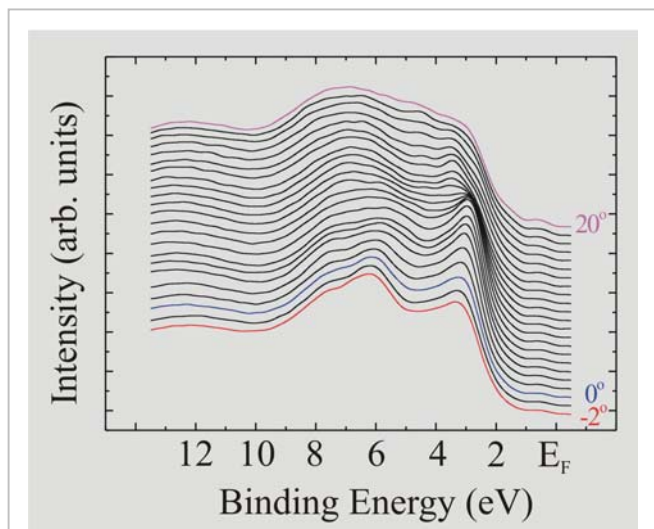


Fig. 3. ARPES spectra of a $\text{Fe}_3\text{O}_4(100)$ thin film surface at RT recorded at $h\nu=58$ eV for emission polar angles of 0-20° along the Γ -X direction of the $\text{Fe}_3\text{O}_4(100)$ surface Brillouin zone.

values of Fe₃O₄(100) film surface were compared to the values extracted from LSDA calculations [7]. In these LSDA calculations a model surface consisting of Fe B sites forming a wave like pattern (see STM image in Fig. 1c) with a $(\sqrt{2} \times \sqrt{2})R45^\circ$ symmetry was considered. The theoretically calculated work function value of $\Phi = 5.3$ eV is in a good agreement with the experimentally measured value of $\Phi = (5.23 \pm 0.15)$ eV.

Fig. 3 shows representative valence band spectra of an epitaxial Fe₃O₄(100) thin film as a function of the emission polar angle θ (0-20°) along the Γ -X direction of the surface Brillouin zone (SBZ). All spectra are normalized to the maximum intensity for each spectrum and an offset was introduced. A photon energy of $h\nu = 58$ eV, which corresponds to the $3p \rightarrow 3d$ resonance, was used in all photoemission experiments yielding an increased photoemission intensity from Fe $3d$ states near E_F . The ARPES spectra in Fig. 3 show the Fe $3d$ derived emission extended over 1.5 eV below E_F and the O $2p$ derived emission between 2 and 10 eV of binding energy. Pronounced dispersions of the O $2p$ derived states are clearly visible whereas the Fe $3d$ ones are almost non-dispersive. For a complete understanding of the observed structure of the photoelectron spectra detailed LSDA calculations are needed.

This work was supported by the German Federal Ministry of Education and Research (BMBF) under grant No. FKZ 05KS1PAA/7 and by the bilateral Project Russian-German Laboratory at BESSY II. The authors (M. F., Yu. S. D., and M. S.) would like to thank BESSY II for financial support.

1. Y. J. Kim, Y. Gao, and S. A. Chambers, *Surf. Sci.* **371**, 358 (1997).
2. B. Stanka, W. Hebenstreit, U. Diebold, and S. A. Chambers, *Surf. Sci.* **448**, 49 (2000).
3. F. M. F. de Groot, J. C. Fuggle, B. T. Thole, and G. A. Sawatzky, *Phys. Rev. B* **42**, 5459 (1990).
4. H.-J. Kim, J.-H. Park, and E. Vescovo, *Phys. Rev. B* **61**, 15284 (2000).
5. F. M. F. de Groot, M. Grioni, J. C. Fuggle, J. Ghijsen, G. A. Sawatzky, and H. Petersen, *Phys. Rev. B* **40**, 5715 (1989).
6. J. J. Paggel *et al.*, *Phys. Rev. B* **66**, 233403 (2002)
7. R. Pentcheva *et al.*, to be published.

Resonant photoemission study of half-metallic ferromagnetic CrO₂(100) films at the Cr 2p absorption edge

A.S. Vinogradov,¹ Yu. S. Dedkov,² M. Fonin,² D.V. Vyalikh,^{1,3} A.B. Preobrajenski,^{1,4} S.A. Krasnikov,^{1,5} E.Yu. Kleimenov,^{1,6} M.A. Nesterov,¹ C. König,² M. Sperlich,² S. L. Molodtsov,^{1,3} U. Rüdiger,⁷ and G. Güntherodt²

¹*V.A. Fock Institute of Physics, St.-Petersburg State University, 198504 St.-Petersburg, Russia*

²*II. Physikalisches Institut, Rheinisch Westfälische Technische Hochschule Aachen, 52056 Aachen, Germany*

³*Institut für Festkörperphysik, Technische Universität Dresden, D-01062 Dresden, Germany*

⁴*MAX-Laboratory, Lund University, P.O. Box 118, Lund S-22100, Sweden*

⁵*Wilhelm-Ostwald-Institut für Physikalische und Theoretische Chemie, Universität Leipzig, D-04103 Leipzig, Germany*

⁶*Fritz-Haber-Institut der Max-Planck-Gesellschaft, D14195 Berlin, Germany*

⁷*Fachbereich Physik, Universität Konstanz, D-78457, Konstanz, Germany*

The electronic structure of the strongly correlated transition metal oxides, among them chromium dioxide (CrO₂), has long been a matter of debate because of their unusual and practically important magnetic properties. CrO₂ is a ferromagnetic conductor for which first principles calculations on the basis of LSDA and LSDA+*U* approaches predict the finite density of electron states with only 3*d* spin-up electrons at the Fermi level (*E_F*) resulting in the so-called “half-metallic” behavior [1-3]. In the beginning these predictions were in contradiction to the experimentally observed low photoelectron emission intensity from valence band at *E_F* [4]. While strong correlation effects of the Cr 3*d* electrons might be responsible for such discrepancies between theoretical and experimental results, a complete description of the electronic structure of half-metallic CrO₂ is still missing. For a better understanding of its unusual properties additional information on the Cr 3*d* electrons in CrO₂ is required.

The 3*d* electron configuration of a metal atom is best probed in an x-ray absorption spectroscopy (XAS) experiment by exciting atomic 2*p* core electrons to unfilled electron states. In this case the dipole – allowed transitions are 2*p* → 3*d* and 2*p* → 4*s*, but transitions to 3*d* states dominate by a factor of more than 10 - 20 over transitions to 4*s* states. Therefore, in this work we use for the first time high-resolution x-ray absorption spectroscopy (XAS) in combination with resonant photoemission spectroscopy (ResPES) at the Cr 2*p* edge of well characterized, high quality CrO₂(100) films. The goal is to obtain new information on properties and energy distribution of filled and unfilled Cr 3*d* electron states in CrO₂ as well as on decay processes of the Cr 2*p* → 3*d* excitations which are strongly affected by features of electronic structure of CrO₂. It should be emphasized that similar investigations are lacking for CrO₂ and are few in number for other 3*d*-atom compounds. Up to now, ResPES measurements on transition metal compounds were mainly performed at the 3*p* edges despite the fact that the 2*p* levels give better possibilities studying the resonance than the shallow 3*p* ones. They are narrower and have the larger 2*p* spin-orbit splitting which results in well-separated 2*p*_{1/2} and 2*p*_{3/2} resonances instead of the overlapping 3*p*_{1/2, 3/2} ones.

The present high-resolution ResPES study is restricted to consider Cr 2*p* → 3*d* excitations only with Coster-Kronig decay channels involving the 3*d* electrons located below the Fermi level.

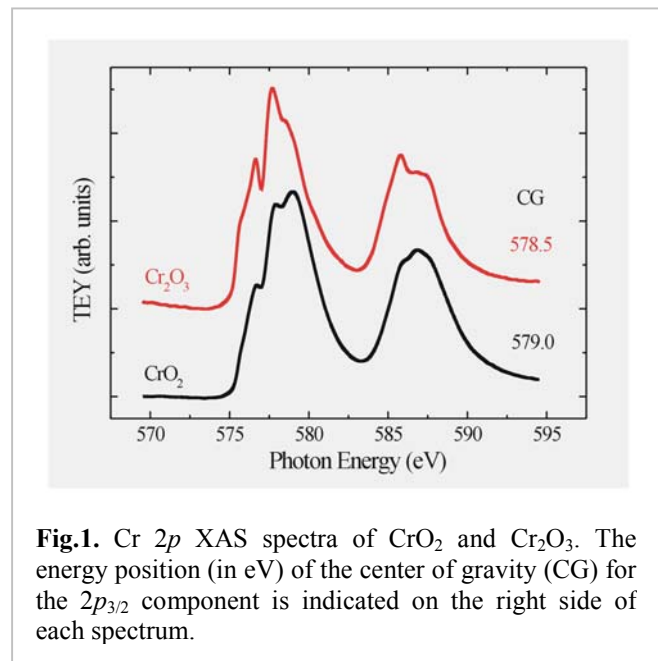


Fig.1. Cr 2*p* XAS spectra of CrO₂ and Cr₂O₃. The energy position (in eV) of the center of gravity (CG) for the 2*p*_{3/2} component is indicated on the right side of each spectrum.

In the present study the high quality CrO₂(100) films have been prepared on isostructural TiO₂(100) substrates. The bulk and surface high quality structural and magnetic properties of the CrO₂ films was verified using a x-ray diffraction, SQUID, MOKE, LEED and STM.

XAS and ResPES experiments were carried out at the Russian-German beam-line. The photon energy resolution was set to 100 meV at the Cr 2*p* edge. XAS spectra were recorded in the TEY mode. ResPES spectra were collected in the angle-integrated mode with the total energy resolution of 150 meV. The absorption and photoemission spectra were normalized to the incident photon flux, which was monitored by detecting the photocurrent from a gold mesh placed at the beamline exit. The [001] axis of CrO₂(100) films was oriented perpendicular to the plane of the storage ring, i.e. *c*-axis $\perp \vec{E}$. After introducing the sample into the UHV chamber at BESSY II its surface was cleaned by moderate Ar⁺ ion sputtering. XPS analysis carried out after such treatment does not show any presence of carbon contaminations.

Fig. 1 shows Cr 2*p* XAS spectra of CrO₂ and Cr₂O₃ for comparison. Changes in spectral shape and a high-energy shift of the center of gravity for the 2*p*_{3/2} component in going from Cr(III) in Cr₂O₃ to Cr(IV) in CrO₂ allow us to think that we deal with the Cr 2*p* spectrum of pure CrO₂. The detection of the latter with surface sensitive total electron yield is very difficult because CrO₂ is metastable at room temperature and atmospheric conditions and its surface is commonly covered by thin layers of Cr₂O₃. The XAS spectrum of CrO₂ was simulated on the basis of the LSDA and LSDA+*U* approaches. From a comparison of the experimental and calculated spectra a good agreement between Cr 2*p*_{3/2} XAS and the envelope of the Cr 3*d* unoccupied DOS obtained by LSDA+*U* method is found (not shown here).

Figure 2 (bottom panel) shows valence-band photoemission spectra of CrO₂ at the Cr 2*p*_{3/2,1/2} absorption edges. The numbered bars in the XAS spectra show the *hν* (from 500 eV to 605 eV) at which the photoemission spectra are measured. The bands located in the off-resonant photoemission spectrum (curve 1, before O 1*s* and Cr 2*p* absorption resonances) at 21.7 eV, 5.0 eV and 1.9 eV are associated with the valence O 2*s*, O 2*p* and Cr 3*d* electron states, respectively. The peak at the binding energy of approximately 30 eV in this spectrum is due to the emission from the O 1*s* state with photons of second order radiation. The Cr 3*d* band can be described as a low Hubbard band in the valence band of CrO₂ [6]. Earlier LSDA and LSDA+*U* band structure calculations predict the position of Cr 3*d* peak in PES spectra at approximately 0.5 and 1 eV, respectively, with weak photoemission intensity at *E_F* [5]. Recent LSDA+DMFT calculations [6] find a different position of the Cr 3*d* peak in the PES spectra around 1.9 eV. This value is in good agreement with the presented PES spectra where the position of Cr 3*d* PES peak is determined to be 1.9 eV.

In the valence band photoemission spectra of CrO₂ the Cr 3*d* states (*E*_{bind} = 1.9 eV) are strongly enhanced and additional structures A₁ – A₄ (Auger electron emission lines) appear as the *hν*

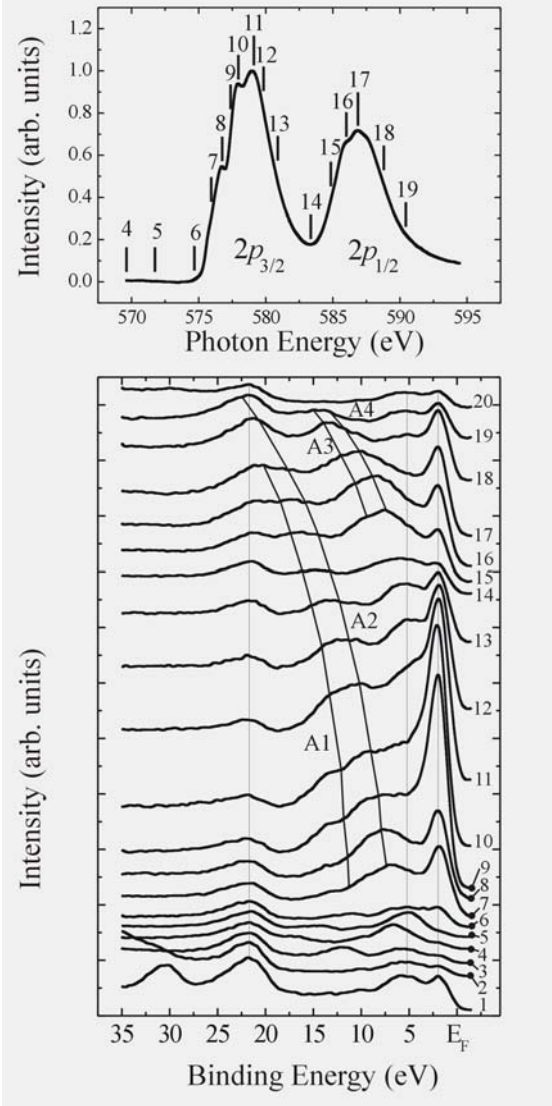


Fig.2. The valence-band photoemission spectra of CrO₂ film at the Cr 2*p*_{3/2} and 2*p*_{1/2} edges (lower panel). The photon energies used to excite these spectra are marked by the numbered bars in the XAS spectrum of the CrO₂ film (top panel); additional spectra with numbers 1, 2, 3, and 20 were taken at: 1 - 500 eV, 2 - 555 eV, 3 - 565 eV, 20 - 605 eV.

approaches the energies of absorption resonance in the Cr $2p_{3/2}$ and Cr $2p_{1/2}$ spectra from the low-energy $h\nu$ side. This enhancement of the $3d$ signal should be evidently ascribed to the electron emission due to the Coster-Kronig decay of the chromium core – excited $2p^5 3d^5$ electron states which result from $\text{Cr}^{4+} 2p^6 3d^2 \rightarrow 2p^5 3d^3$ absorption transitions. An interference of such a nonradiative process ($2p^5 3d^3 \rightarrow 2p^6 3d^1 + e$) with the direct photoemission one ($2p^6 3d^2 + h\nu \rightarrow 2p^6 3d^1 + e$) yields the Fano-resonance behavior for the resonant photoemission signal [7,8]. On this basis, the experimentally observed photon energy dependence of the photoelectron intensity from the valence Cr $3d$ states located close to the Fermi level was fitted to a sum of two Fano lineshapes, as shown in Fig.3. A good agreement is found between the experimentally observed dependence of photoemission intensity and the sum of two fitting lines with the asymmetry (q) and lifetime-width (Γ) parameters which are given in the inset of Fig.3. The matrix elements of the Coster-Kronig transitions from the core-excited $2p^5 3d^3$ electron states with the excited $2p_{3/2}$ and $2p_{1/2}$ electrons, V_{CK} , are equal to 0.69 eV and 0.59 eV, respectively. It is interesting to mention that the parameter Γ for the state with the excited $2p_{3/2}$ electron is larger than in the case of the excited $2p_{1/2}$ electron: an opposite relation between them should be expected owing to the probable Coster-Kronig $L_2L_3M_{4,5}$ process. Furthermore, the energy positions of the Fano resonances and absorption bands are different: the resonance takes place on the low-energy side of absorption band. It is possible that all these effects are related to features of the electronic structure of half-metallic ferromagnetic CrO_2 .

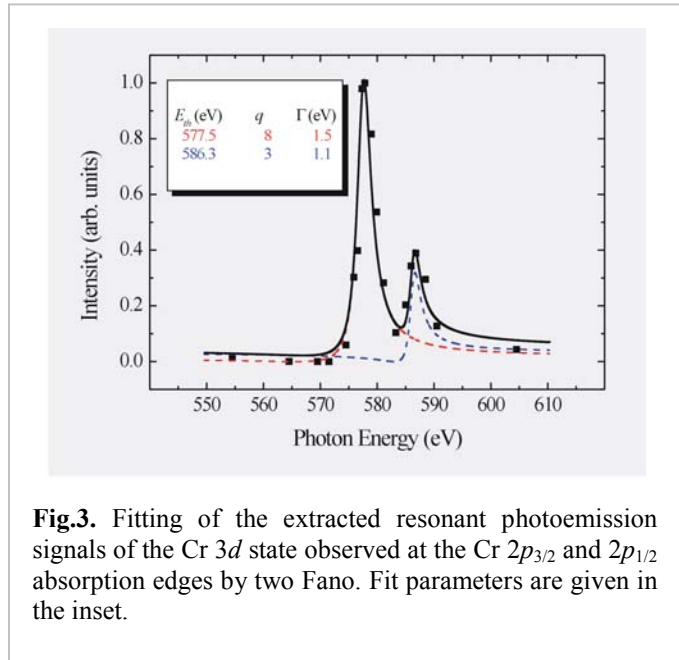


Fig.3. Fitting of the extracted resonant photoemission signals of the Cr $3d$ state observed at the Cr $2p_{3/2}$ and $2p_{1/2}$ absorption edges by two Fano. Fit parameters are given in the inset.

Acknowledgements

This work was supported by the Russian Foundation of Basic Research (grant No.01-03-32285), the German Federal Ministry of Education and Research (BMBF) under grant No. FKZ 05KS1PAA/7 and FKZ 13N7988, and by the bilateral Project "Russian-German Laboratory at BESSY". A.S. Vinogradov and M.A. Nesterov gratefully acknowledge the financial support by BESSY and by the Technische Universität Dresden. A.B. Preobrajenski warmly acknowledges the support by the Swedish Foundation for International Cooperation in Research and Higher Education (STINT).

References

1. K.-H. Schwarz, J. Phys. F: Met. Phys. **16**, L211 (1986).
2. S. P. Lewis, P. B. Allen, and T. Sasaki, Phys. Rev. B **55**, 10253 (1997).
3. M. A. Korotin, V. I. Anisimov, D. I. Khomskii, and G. A. Sawatzky, Phys. Rev. Lett. **80**, 4305 (1998).
4. K. P. Kämper, W. Schmitt, G. Güntherodt, R. J. Gambino, and R. Ruf, Phys. Rev. Lett. **59**, 2788 (1987).
5. T. Tsujioka, T. Mizokawa, J. Okamoto, A. Fujimori, M. Nohara, H. Takagi, K. Yamaura, and M. Takano, Phys. Rev. B **56**, R15509 (1998).
6. L. Craco, M. S. Laad, and E. Müller-Hartmann, Phys. Rev. Lett. **90**, 237203 (2003).
7. C.-O. Almbladh and L. Hedin in *Handbook of Synchrotron Radiation* (North-Holland, Amsterdam, vol.1, 1983).
8. U. Fano, Phys. Rev. **124**, 186 (1961).

Self-assembled Au nanowires on two-dimensional surface carbide: W(110)/C-R(15×3)

A. Varykhalov, O. Rader and W. Gudat
BESSY, Albert-Einstein-Str. 15, Berlin, 12489, Germany

Electronic properties of metallic nanosystems which dimensions comparable to the wavelength of the electron have been in the focus of research activities for several decades due to intrinsic quantum-size effects. Au as a classical *spd*-metal is of high importance for research in this field. Therefore, the fabrication of a uniform array of Au nanostructures, enabling studies with photoelectron spectroscopy, remains a challenge for quite a long time. In order to achieve electronic effects in systems of lower dimensionality than 2 - in nanowires (1D) or in quantum dots (0D) - one can employ self-organization effects for fabrication of such ordered arrays. Almost a standard way is the application of a vicinal surface (with high Miller-index) as substrate [1]. In more particular cases, one can also obtain a low-dimensional ordering on flat surfaces through strain effects or the phenomenon of surface alloying [2]. While the function of stepped surfaces is studied well with respect to self-organization, the role of surface reconstructions or superstructures of adsorbed materials (like W(110)/C-R(15×3)) as template for the fabrication of the nanoscaled systems has lacked attention until now.

Here we report on temperature induced self-organization of Au nanostructures on the two-dimensional surface carbide W(110)/C-R(15×3). The electronic structure was studied with photoemission techniques using a VG ESCALab electron analyser featuring 50meV and 1° resolution at beamlines UE56/1 and UE52 as tunable source of the photons. The surface geometry is revealed by scanning tunneling microscopy (STM). The sample was prepared *in situ* keeping the base pressure in the chamber below 2×10^{-10} mbar. Formation of the 15×3 carbide overlayer was achieved by heating the clean W(110) surface for several minutes at 500-550°C under a partial pressure of propylene of 5×10^{-8} mbar. A short flash to 2200° produced the R(15×3) superstructure (Fig. 1(a)) over the whole area of the sample surface. Subsequent deposition of 0.7ML of Au and annealing at 600°C leads to self-assembly of a regular nanowire array (Fig. 1(b)).

STM (Fig. 1) shows the carbon R(15×3) superstructure of the template in atomic resolution. Similar results, as well as the general crystallographic model, were reported earlier [3, 4]. Stoichiometrical analysis of the superstructure with Auger electron spectroscopy reported previously has revealed that it consists of a single atomic layer of carbon [5]. Fig. 1(a) demonstrates consistently with the literature [3] that R(15×3) is build up from rows of C atoms interconnected by zig-zag chains of carbon. Above that, the R(15×3) superstructure is rotated for 14° relative to the [1-11] direction of the W substrate. While the sites of the zig-zag-like carbon groups supply a high resolution in STM measurements, the atoms in linear chains can hardly be resolved. This phenomenon is determined by the properties of chemical bonding in the overlayer and likely by effects of W substrate relaxation [3].

From the comparative study of the W(110), W(110)/C-R(15×3) and self-assembled Au nanowire arrays with the technique of LEED (results are not reported here), we have to note that the nanowires orientation is strictly determined by the surface structure of the W(110) substrate but *not* by the geometry of the interface layer of C atoms. Orientation of the W substrate is marked with white vectors in Fig. 1. A notable feature of this self-assembly effect can be observed in Fig. 1(b). Actually, the nanowires are doubled and form arrays of *pairs* across the surface. Another notable point is the internal structure of the wires. Fig. 1(b) demonstrates that every first nanowire in the pair has a dense continuous structure while every second one consists of uniform and periodically arranged clusters. The most characteristic topographic sections are shown for illustration in Fig. 1(c)-i and 1(c)-ii.

The electronic structure of the nanowire array studied by angle-resolved photoelectron spectroscopy (AR-PES) is reported in Fig. 2. Angle-dependent spectra were measured for k-vectors of photoemitted electrons parallel (Fig. 2(a)) and perpendicular (Fig. 2(b)) to the wire orientation. The Au-induced states are marked with black lines, identified from comparison of the spectra to AR-PES data for W(110)/C-(15×3) without Au. Spectra in Fig. 2(a) exhibit an almost non-dispersing state d_1 , which has a binding energy of about 6.7 eV, as well as the state sp_1 dispersing in the range from 4 eV to 5.5 eV. In the perpendicular direction one can still observe the d_1 demonstrating the same behavior, but the band sp_1 is now split into a couple of weakly or nondispersing states having binding energies 4.5 eV and 5.3 eV respectively. The strongly anisotropic character of the dispersion proves the quasi-one-dimensional character of the structure [2, 6, 7], This electronic effect can be identified as quantization of the band labeled sp_1 in the self-assembled array of Au nanowires the one-dimensional geometric structure of which is already apparent from

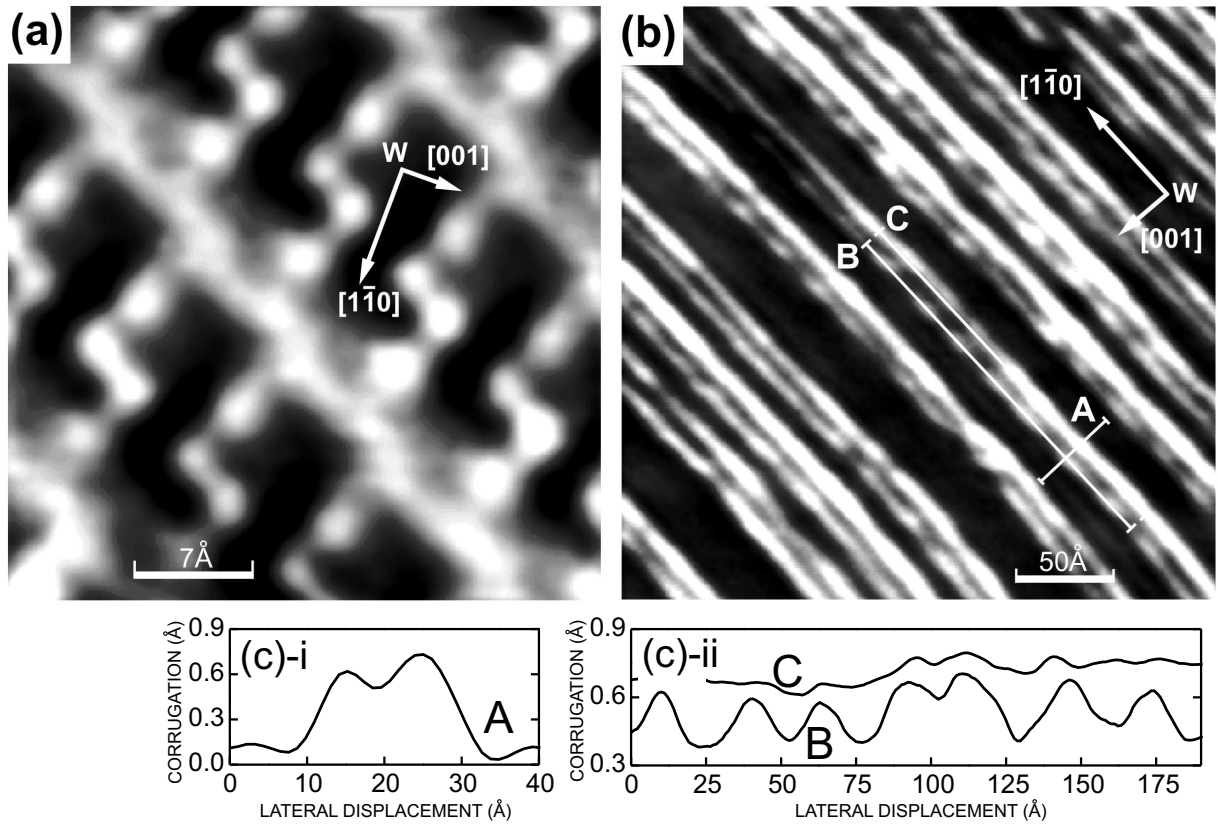


FIG. 1: STM study of the self-organization in Au/W(110)/C-R(15×3); verification of the C-R(15×3) superstructure with the atomic resolution provides an information about the internal structure of the surface carbide unit cell (a); STM measurement on the Au nanowires (b) shows that the nanowires appear in pairs (c)-i. While every first nanowire has a continuous and dense structure, every second one consists of periodically arranged Au clusters (c)-ii.

the STM.

Looking into the origin of the self-organization discovered, two different kinds of phenomena can be taken into account. A more geometrical explanation may be based on a one-dimensional substrate relaxation of W(110) under high symmetry tendencies of the chemical bonds in the carbide interlayer. Such relaxation was reported in Ref. [3] and could have a controlling role in the assembly of the Au overlayer as well. However, more likely is another explanation which refers the self-organization to the effect of the surface alloying between Au and W. While a bulk alloy between these two elements does not exist, it was shown in several studies that this can occur at the interfaces inducing, in some cases, a self-assembly effect [8, 9].

An independent confirmation for this assumption can be found in photoelectron spectra of $W4f_{7/2}$ core-level taken with high energy resolution. Four spectra shown in Fig. 2(c) correspond to the clean W(110) (with perfectly resolved surface component), carbonized W(110)/C-R(15×3), 0.7ML Au/W(110)/C-R(15×3) (after annealing and obtaining the self-assembled structure) and 0.7ML Au annealed on the clean W(110). The appearance of a spectral component at 31.7 eV likely manifest a chemical interaction between Au and the W leading to the self-assembly. Such interaction can obviously take place only in the open (free from carbon) areas of W substrate, i.e. in between the zig-zag carbon chains. Absence of any chemical shifts in $W4f$ for annealed Au/W(110) proves the stimulating role of R(15×3) interlayer for the Au-W surface alloying, possibly due to the C-induced modification of the surface structure of the W substrate.

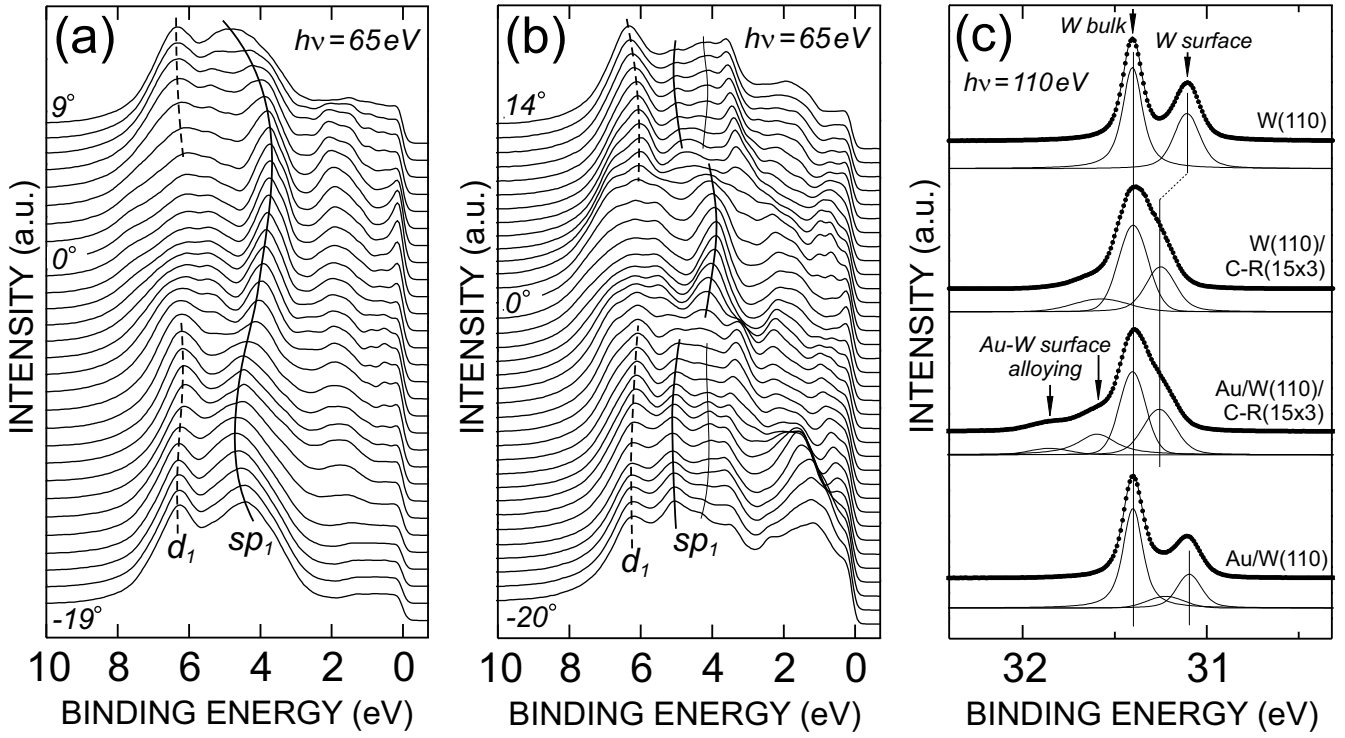


FIG. 2: Photoemission study of the Au nanowire array. While the band structure measured for k -vectors of the photoemitted electrons in the direction parallel to the nanowires demonstrates an obviously dispersing sp_1 state (a), the electronic structure mapped in the perpendicular direction reveals a quantization of that band (b). Comparison of the chemically-sensitive $W 4f$ spectra taken from $W(110)$, $W(110)/C-R(15 \times 3)$, $Au/W(110)/C-R(15 \times 3)$, and Au on the clean $W(110)$ shows that Au - W surface alloying is likely involved in the process of nanopatterning.

-
- [1] Adam Li, Feng Liu, D.Y. Petrovykh, J.-L. Lin, J. Viernow, F. J. Himpsel, and M. G. Lagally, *Phys. Rev. Lett.* 85, 5380 (2000)
 - [2] C. Pampuch, O. Rader, T. Kachel, and W. Gudat, C. Carbone, R. Klaesges, G. Bihlmayer, S. Blugel, and W. Eberhardt, *Phys. Rev. Lett.* 85, 2561 (2000)
 - [3] M. Bode, R. Pascal, R. Wiesendanger, *Surf. Sci.* 334, 185 (1995)
 - [4] M. Bode, R. Pascal, R. Wiesendanger, *Z. Phys. B.* 101, 103 (1996)
 - [5] J. G. Macmillan, A. J. Slavin and K. J. Sunderland, *Surf. Sci.* 173, 138, (1986)
 - [6] A. Mugarza, A. Mascaraque, Perez-Dieste, V. Repain, S. Rousset, F. J. Garcia de Abajo, and J. E. Ortega, *Phys. Rev. Lett.* 87, 107601 (2001)
 - [7] A. Mugarza, A. Mascaraque, V. Repain, S. Rousset, K. N. Altmann, F. J. Himpsel, Yu. M. Koroteev, E. V. Chulkov, F. J. Garcia de Abajo, and J. E. Ortega, *Phys. Rev. B* 66, 245419 (2002)
 - [8] U. Bardi, *Rep. Prog. Phys.* 57, 939 (1994)
 - [9] X.K. Shu, P. Jiang, J.G. Che, *Surf. Sci.* 545, 199 (2003)

Anisotropic Sexithiophene Thin Films Studied by EUV Angle-Resolved Photoemission Spectroscopy Combined with Laser Irradiation

C. Heiner¹, B. Winter¹, W. Widdra², I.V. Hertel¹

¹*Max-Born-Institut, Berlin, Germany*

²*Universität Halle-Wittenberg, Halle (Saale), Germany*

Electronic and optoelectronic devices using small π -conjugated polymers and oligomers, such as sexithiophene (6T), can already be found on the market and are still promising for new technological developments. Physical properties and hence device performance of such devices not only depend on the physical properties of the individual organic molecules but also on their relative orientation, which in turn affects their mutual interaction and thus *fundamental* film properties. Using an (1x2)-Au(110) single-crystal substrate an ordered structure within the film can be induced for the monolayer regime [1] wherein the molecules grow with their long axis along the $[1\bar{1}0]$ direction. Continual deposition of 6T leads to island formation, however, these islands still possess the same aforementioned preferred orientation within the macroscopic film. Presented here are valence band photoemission spectra of thin sexithiophene films grown on Au(110) obtained, for 50 eV photon energy, at the MBI-BESSY Undulator beamline (SGM-U125).

Fig. 1: Photoemission spectra of a ca. 2000Å 6T film with (bottom) and without (top) the addition of laser irradiation. The incoming polarization vector of the synchrotron light was at either perpendicular (blue) or parallel (red) to the long axis of the 6T molecules. Arrows indicate the rigid shift back that appears in the presence of laser irradiation.

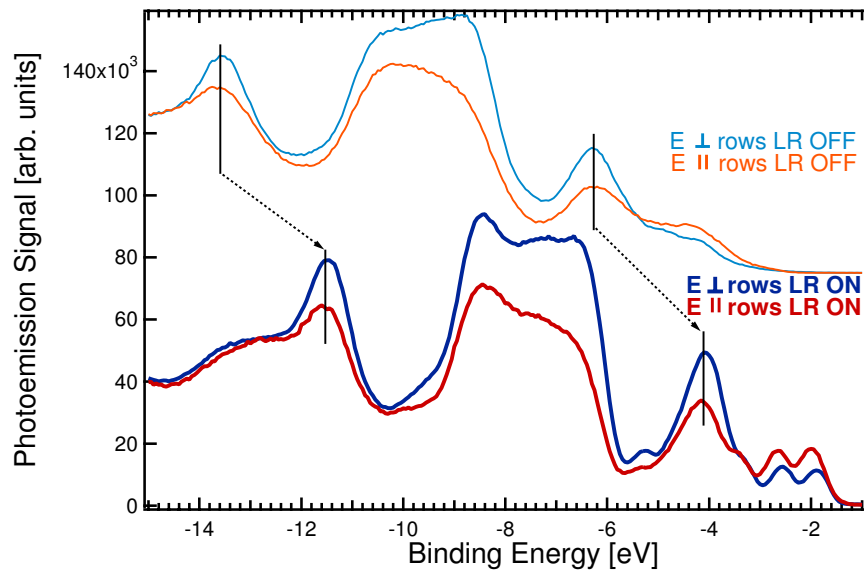


Figure 1 shows photoemission spectra of a ca. 2000Å 6T film with (below) and without (above) exposure to laser irradiation. Spectra were consecutively measured at grazing incidence in normal emission; the binding energies are with respect to the Fermi edge. The laser

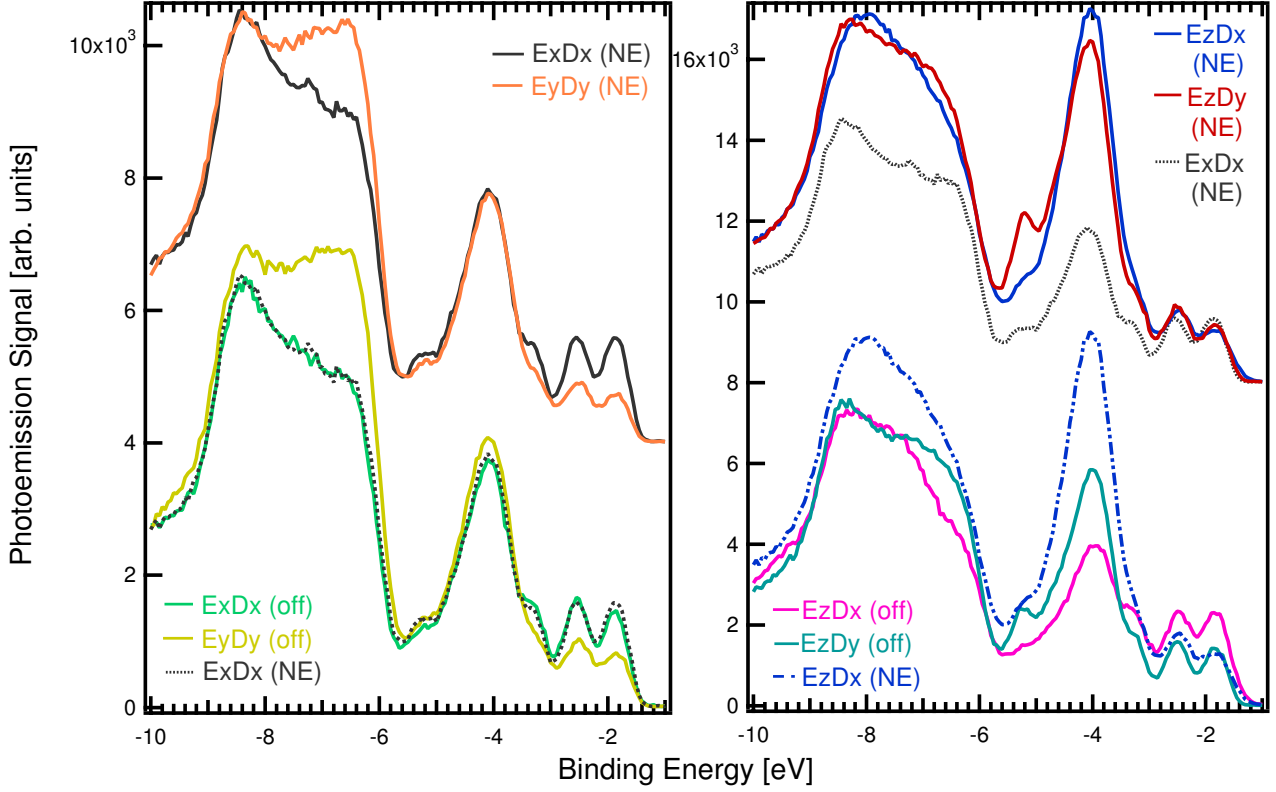


Fig. 2: Photoemission spectra from ca. 2000Å 6T film obtained in several experimental geometries for 50 eV photon energy with an additional 2.4 eV laser irradiation. See text for description of spectra.

irradiation, provided by either a Nd:YVO₄ laser ($\lambda = 532$ nm, 1.25 MHz) in single-bunch or a Ti:Sa ($\lambda = 400$ nm, 83 MHz) in multi-bunch, was necessary in order to compensate for the large amount of synchrotron induced film charging [2] typical for organic films. This is clearly visible in comparing the laser off/on spectra; the large backshift to the correct binding energies as well as an overall sharpening of the features in the latter spectra are all results of the film's de-charging. The pair of spectra on each tier contrasts the E vector of the synchrotron light either being perpendicular (blue) or parallel (red) to the 6T long axis, serving to further highlight the film's anisotropy.

In addition to changing the direction of the polarization vector we varied the electron detection angle; the resulting photoemission spectra are displayed in Figure 2. Here the top and bottom frames of spectra represent the geometry when the synchrotron polarization vector, E , in- (even) or out-of- (odd) the sample plane, respectively. Moreover, the spectra within each tier contrast in the azimuth of the sample (as in Fig. 1), positioning the light polarization vector either along (E_x) or across (E_y) the long axis of the molecules. The compared spectra within each frame show the change of electron detection from normal emission (above) to 20 degrees off normal emission (below), within both the x-z (D_x) and y-z (D_y) plane. The nomenclature for each labeled spectrum ($E_n D_n$) has the subscript $n = x, y, z$, to denote the direction of the polarization vector of the incident synchrotron light (E) and of photoelectron detection (θ_e) plane, respectively. The dotted spectrum is a reproduced $E_x D_x$ at normal emission and the dashed spectrum is a traced $E_z D_x$; their presence is intended to guide the reader in the spectra comparison, in which all peak intensity variations reflect the relationship to the reference

spectrum $E_x D_x$. The most dramatic effect can be seen in the delocalized π -region of HOMO, HOMO-1, and HOMO-2, at approximately 1.85 eV, 2.55 eV, and 3.3 eV respectively, where the binding energy scale is with respect to the Fermi edge. Regardless to the detection angle the aforementioned HOMOs' emission signals are enhanced (ca. doubled) in the x-detection plane. Furthermore in the even spectra, a reversal phenomena of a stronger signal when using y-direction excitation light is seen between the σ -regime of 5.7 eV and 8.0 eV binding energies. Noteworthy in the odd geometry is the 2.5 increase of the localized π -feature in normal emission in both detection planes and again a doubling of the HOMO and HOMO-1 (*delocalized* π -features) in just the x-detection plane.

The success of obtaining clear anisotropic HOMO's and other spectral features in our PE spectra of sexithiophene multilayers on Au(110), after the accompaniment of laser irradiation, gives us the opportunity and sensitivity necessary to observe distinct feature evolution (intensity variations) as a function of the experimental geometry. These experimental results directly correlate to symmetry-derived selection rules [3]. By applying group theory to the C_{2h} point symmetry group, as reported for 6T in films [4], no signal change should be observed when contrasting x and y light polarization directions or detection angles. Although this particular 6T conformer (trans) was calculated here and elsewhere [5] as the most stable conformation in the gas phase, the potential barrier for this conformer to align all of its sulfur atoms on the same side (cis) is quite small. Moreover, the symmetry rules applied here to a C_{2v} symmetry, due to the C_2 symmetry axis lying in-plane, yields a variation in signal expectations for x and y polarization and detection directions; this agrees fairly well with the intensity dependency observed here. The additional broken symmetries of C_2 or C_s , and the primary C_1 symmetry, allow for emission in every geometry, which accounts for the small signals still detected for what would otherwise be forbidden transitions within both strict C_{2h} and C_{2v} symmetries. In conclusion, using charge compensation to obtain the better-resolved presented spectra, the changing intensity effects, as said to reflect molecular orientation, shows that contributions from the surface and bulk must be considered separately. Various conformers, such as cis-oligomers, may be energetically stable for *surface monolayers* in thin films and must be included in such photoemission analysis.

References

- [1] S. Prato et. al. J. Phys. Chem. B **103**, 7788 (1999).
- [2] N. Koch et al. Thin Solid Films **391**, 81 (2001).
- [3] G. Koller, F.P. Netzer, M.G. Ramsey, Surface Science **421**, 353 (1999).
- [4] R. N. Marks et al. J. Phys. Chem. B **102**, 7563 (1998).
- [5] R. Telesca et al. Phys. Rev. B **63**, 155112 (2001).

X-ray magnetic circular dichroism sum rule correction for the light transition metals

Eberhard Goering

Max-Planck-Institut für Metallforschung, Heisenbergstrasse 3, 70569 Stuttgart, Germany

Quantum mechanical mixing of the L_2 and L_3 edge excitations strongly increases with reduced $2p$ spin-orbit-splitting. For a large number of $2p \rightarrow 3d$ absorption spectra the shape has been fitted nearly perfectly by a model, which takes into account lifetime and jj -mixing effects. X-ray magnetic circular dichroism (XMCD) sum rule correction factors have been determined for V and Cr, which are consistent to complementary investigations. This fitting procedure and the estimated correction factors are the basis for a future light element XMCD effective spin renormalization technique.

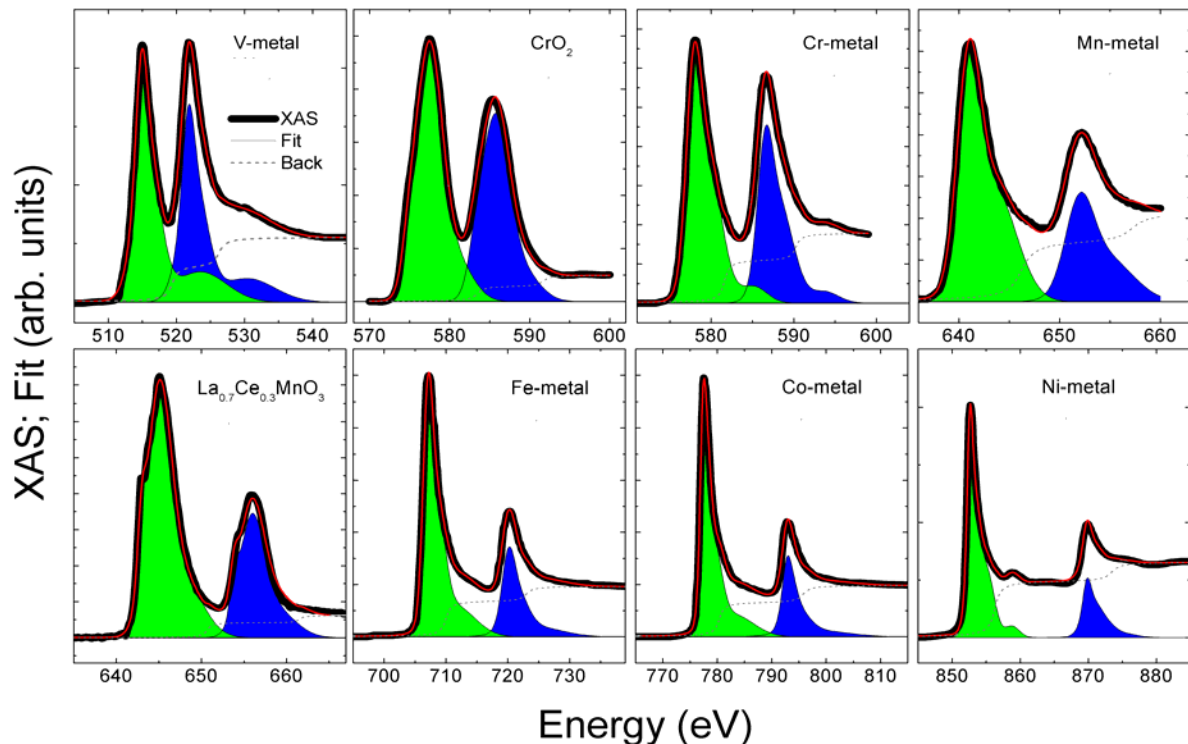


Figure 1 : Nonmagnetic $L_{2,3}$ TM XAS spectra (broad black line) and the corresponding fit results (red line) for V^1 , CrO_2^2 , Cr^3 , Mn^4 , $La_{0.7}Ce_{0.3}MnO_3^5$, Fe^6 , Co^6 and Ni^7 . The fitted L_3 and L_2 intensities are shown as green and blue areas respectively. The fitted background function is shown as the dotted grey line.

X-ray magnetic circular dichroism (XMCD) has become a widely used and powerful tool for magnetic investigations of complex systems. The major advantage is the quantitative determination of spin and orbital magnetic moments in an element specific way by the use of so called sum rules^{8,9}. The validity of the sum rules has been confirmed at first for Co and Fe metal thin layers⁶. Unfortunately, one important requirement for the applicability is the separation of $2p_{3/2}$ and $2p_{1/2}$ ($2p \rightarrow 3d$) excitations, which is valid for the heavy 3d transition metals (TM) like Fe, Co and Ni, but for Ti, V and Cr the L_2 and L_3 edges overlap and the $2p$ absorption process is now a quantum mechanical combination of $2p_{3/2}$ and $2p_{1/2}$ excitations¹⁰. One important finding was that this results in deviations of the so called branching ratio (BR) from the pure statistical value ($B_0 = 2/4$ for $p \rightarrow d$ excitations), observable in the non magnetic X-ray

absorption spectroscopy (XAS)^{10,11}. In addition, the BR is also influenced by the unbalance between $d_{3/2}$ and $d_{5/2}$ excitation channels, related to the expectation value of the angular part of the spin-orbit-operator in the initial state

$$\langle \Psi | \sum_i \mathbf{l}_i \cdot \mathbf{s}_i | \Psi \rangle^{11}.$$

The above mentioned very important problems in the applicability of sum rules have been handled here by a reliable fitting procedure of the XAS data, shown in Fig. 1 which gives well determined experimental BR values. Based on the BR ($r_{23}=L_2/L_3$), the $p_{1/2} - p_{3/2}$ -mixing for bulk material has been estimated quantitatively by a relative simple model. This gives experimentally determined effective spin-sum-rule-renormalization factors for the spin S_z and the magnetic dipole term T_z . This procedure allows the

application of sum rules for the light TM in combination with moment analysis^{2,12,13} and a quantitative experimental analysis of the BR and its above mentioned implications.

The fit results are shown in Fig. 1 for eight different XAS spectra. A large fraction of the XAS data has been scanned and digitized from the literature (see ref. # in the figure caption). For the fit of the spectra 3-4 pairs of Gaussian lines have been used to give a good shape approximation. All pairs are separated in energy by the same 2p-spin-orbit-splitting (SOC) and the L₂ parts are multiplied with the same factor r_{23} , which gives the BR. The continuum background, also influenced by the mixing, has been approximated by an *arctan* step function, which is again duplicated and shifted by the same 2p-SOC energy as for the Gaussian pairs and multiplied with the same factor r_{23} . In addition, a Coster-Kronig-Auger L₂L₃M₄₅ process, which decreases the 2p_{1/2} core-hole lifetime has been used by an additional broadening factor. It should be emphasized, that all pure metal spectra of the 3d TM series have quite similar shape, i.e. the main absorption lines are associated by an asymmetric shoulder at the high energy site. This result is quite unexpected, because theoretical atomic multiplet calculations show much larger differences in the spectral shapes for different 3d TM ions and between the L₂ and L₃ edges.

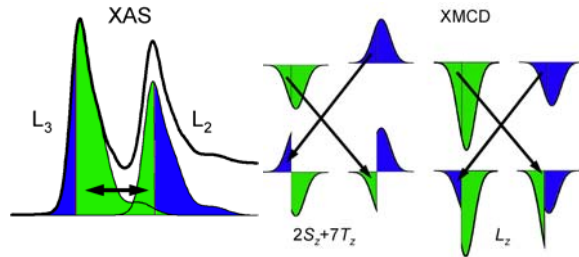


Figure 2: (Left) Schematic integral XAS intensity transfer between the L₂ and the L₃ edges, due to the *jj*-mixing. Schematic integral XMCD intensity transfer between the L₂ and the L₃ edges for the effective spin (middle) and the orbital (right) contributions. In the shown example the linear mixing related intensity transfer is $X = 1/3$ (small area fraction), where $1/3 I(j_{3/2}) \rightarrow L_2$ and $1/3 I(j_{1/2}) \rightarrow L_3$. Where $(1-X)$ (large area fraction) is the remaining $j_{3/2}$ ($j_{1/2}$) intensity at the L₃ (L₂) edges, respectively

In the following the *jj*-mixing will be estimated quantitatively, by neglecting the above mentioned angular part of the spin-orbit-operator. Figure 2 shows a schematic XAS spectrum with slightly overlapping L_{2,3} features and the corresponding L₃ and L₂ intensities. The green shaded area symbolizes the $j_{3/2}$ and the blue shaded area the $j_{1/2}$ related integral intensities. A factor

$$X = \frac{2r_{23}-1}{r_{23}+1}$$

could be calculated from the r_{23} , which is a direct linear measure for the *jj*-mixing. X is the transferred relative area from the pure *jj*-coupled states to the opposite L-edge $X I(j_{3/2}) \rightarrow L_2$ and $X I(j_{1/2}) \rightarrow L_3$

(fig. 2). For $X = 0$ no mixing is present, while for full mixing $X = 0.5$, 50% of $j_{3/2}$ and 50% of $j_{1/2}$ transitions are present, where the $j_{3/2}$ intensity is two times the $j_{1/2}$ intensity at each of both edges (L₂ and L₃).

The mixing influences the XMCD signal. As shown in the middle and right part of fig. 2. In the case of orbital moment related intensity, the L₂ and L₃ edge contributions have the same sign and the total integrated L_{2,3} intensity does not change by mixing. Therefore, the orbital sum rule is not affected, but for the spin (or T_z) moment a XMCD reduction factor $1-2 \cdot X$ is present, which is 1 for no mixing ($X=0$) and 0 for full mixing ($X=0.5$). Therefore, measured XMCD and sum rule related S_z and T_z moments must be multiplied by the inverse reduction factor of $1-2 \cdot X$. For Mn, nearly no reduction is present, while for Cr the correction factor is 2.0 and for V 3.6. In combination with XMCD moment analysis, these spin correction factors give consistent results for pure V and CrO₂. Further details of the fitting procedure and detailed discussions will be described elsewhere¹⁴.

In conclusion, the TM 3d L₂ XAS spectra could be interpreted by shifted, scaled and slightly broadened L₃ spectral shapes. The quantum mechanical *jj*-mixing of the 2p \rightarrow 3d excitation has been quantitatively determined from the fitted BR by a simple model, valid for systems with nearly quenched orbital moments, as present in bulk TM. A XMCD related spin moment correction factor for the light TM has been deduced from fitted XAS spectra, which results in consistent effective spin values compared to complementary experimental and theoretical investigations, while Mn, XMCD sum rule results are not significantly influenced by the mixing.

I would like to thank T. Kachel at BESSY II. In addition, I appreciate the helpful discussions with S. Gold, C. Ederer, and G. Schütz. Particularly I thank the other XMCD working groups, mentioned here, for the reproduced XMCD spectra and the Max-Planck-Society for financial support.

References

1. A. Scherz et al., PRB **66**, 184401-1 (2002).
2. E. Goering et al., PRL. **88**, 207203-1 (2002).
3. M. A. Tomaz et al., PRB **55**, 3716 (1997).
4. W. L. O'Brien et al., PRB **51**, 617 (1995).
5. S. Gold, E. Goering et al., in preparation (2003).
6. C. T. Chen et al., PRL. **75**, 152 (1995).
7. C. T. Chen et al., PRB **42**, 7262 (1990).
8. P. Carra et al., PRL **70**, 694 (1993).
9. B. T. Thole et al., PRL **68**, 1943 (1992).
10. B. T. Thole et al., PRB **38**, 3158 (1988).
11. G. van der Laan et al., PRL **60**, 1977 (1988).
12. E. Goering, et al., J.Sync.Rad. **8**, 422 (2001).
13. E. Goering et al., Appl. Phys. A, accepted (2003).
14. E. Goering, submitted to Phys. Rev. (2003)

Element-specific, in-situ investigation of the magnetization at the interface of Fe on V(110)

D. Schmitz, P. Imperia, H. Maletta
Hahn-Meitner-Institut Berlin, Glienicke Str. 100, 14109 Berlin, Germany

Fe on V(110) belongs to the class of systems where a ferromagnetic overlayer is deposited onto a non-ferromagnetic substrate. This system was measured for coverages of a few atomic layers with Polarized Neutron Reflectometry (PNR) and X-Ray Magnetic Circular Dichroism (XMCD) in order to study the surface and interface magnetization of Fe and the induced interface moment of V. According to the earlier PNR investigation [1,2] the total magnetization sets on at an Fe coverage of 2 monolayers (ML) which may be due to the coalescence of the Fe islands observed with Low Energy Electron Diffraction [3]. Moreover, for higher coverages it was found that the total magnetization is reduced as if 2 ML Fe were magnetically dead.

In order to check these findings, XMCD measurements at UE46-PGM were performed, making use of the advantages of XMCD to be element-specific and surface sensitive. According to these XMCD measurements, the onset of the Fe magnetization takes place at a thickness of 2 ML, in accordance with the earlier PNR results. In the critical Fe thickness regime between 2 ML and 5 ML the Fe magnetization increases rapidly with Fe coverage and asymptotically reaches the bulk magnetization at 5 ML. Since the magnetization reaches the bulk value already at 5 ML, the two magnetically dead Fe layers found earlier with PNR are not confirmed. The results summarized so far were obtained earlier at room temperature as reported in Ref. [4].

During the last year further investigations of Fe/V(110) have been performed with the end station at the UE46-PGM beamline. Thereby we focused on the temperature dependence of the Fe magnetization, on a state-of-the-art evaluation of the Fe XMCD spectra in order to determine the magnetic moments, and on the influence of a V buffer layer deposited onto the V substrate before Fe deposition.

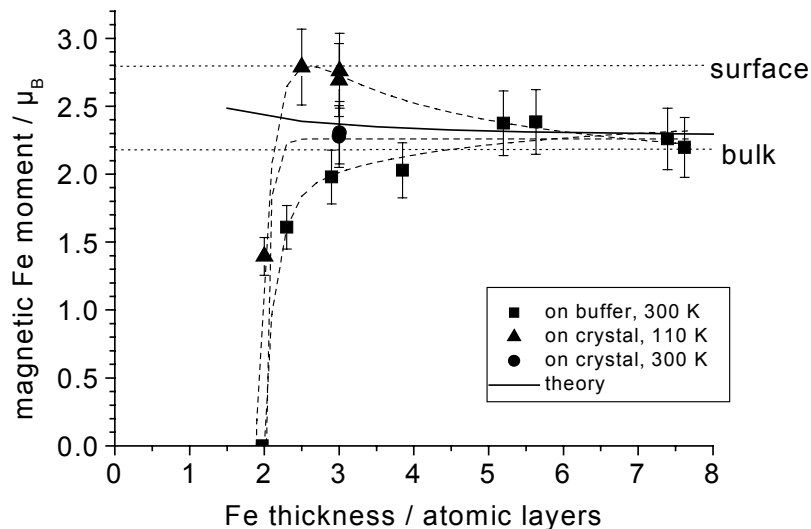


Fig.1: Average magnetic Fe moment per atom as a function of Fe thickness at room temperature (circles) and at 110 K (triangles) for Fe deposited onto the annealed V(110) single crystal. The Fe moments for deposition onto a V buffer layer (squares) and from ab initio calculations [5] assuming an $Fe_{0.5}V_{0.5}$ alloy of 1 ML thickness at the interface (solid line) are also shown.

In the critical Fe thickness regime between 2 ML and 5 ML (see Fig.1) the magnetization increases significantly by cooling from room temperature (circles) to 110 K (triangles) due to the reduced Curie temperature of the ultrathin Fe film. In contrast, the onset of the Fe magnetization at 2 ML is barely influenced by cooling because it is likely to be due to the coalescence of the Fe islands observed earlier with Low Energy Electron Diffraction [3].

The magnetic Fe moments presented in Fig. 1 were determined from the saturation corrected XMCD spectra using the well known sum rules [6,7]. The values were corrected for the incomplete degree of circular polarization and the angle between the incident light and the in-plane magnetization direction. At Fe thicknesses around 3 ML an enhanced average Fe moment of about $2.8 \mu_B$ is observed in the XMCD experiment at 110 K. This enhancement results from a combination of different effects. First of all, according to the area between the isotropic spectra and the step function the number of 3d holes is enhanced by 18% with respect to the bulk value due to a charge transfer from Fe to V and to a reduction of the coordination number at the surface [8]. At 7.5 ML Fe thickness the bulk value of 3.43 [9] was taken for the number of d holes. Secondly, the reduced Fe moment at the interface to V of $1.71 \mu_B$ [5] is overcompensated by the enhanced surface Fe moment of $2.82 \mu_B$ [8]. Finally, the contribution of the spin magnetic dipole term - which only vanishes for cubic symmetry - to the Fe spin moment in the surface layer of $-0.23 \mu_B$ [8] was taken into account, also enhancing the value of the Fe moment.

In order to suppress the small residual C contamination at the surface of the V single crystal, a V buffer layer of 1.5 nm thickness was deposited before the Fe. Obviously, the resulting average magnetic Fe moments (squares in Fig.1) are significantly reduced in comparison with the Fe films deposited directly onto the V crystal. During sample preparation Auger electron spectra [10] were taken after sputtering, annealing and V deposition in order to control the development of the surface contaminations. They reveal that the surface contamination by O is larger on the V buffer layer than on the annealed crystal surface. Therefore, the formation of Fe oxide is more likely on the V buffer layer than on the annealed crystal surface which may cause the observed reduction of the average Fe moment.

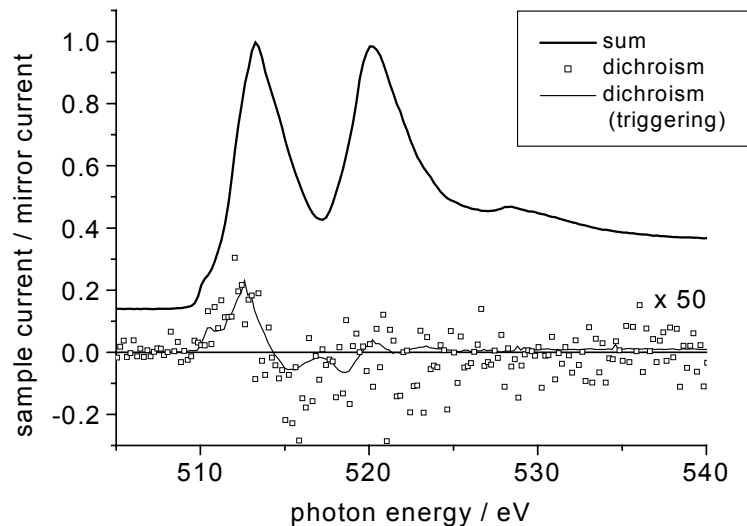


Fig.2: Normalized absorption (fat line) and circular dichroism spectra (squares) of V with 5 ML Fe coverage at room temperature. The latter have been multiplied by 50 for illustration. The noise is significantly reduced by triggering the electrometers (thin line).

In Fig.2 the absorption (fat line) and circular dichroism spectra (squares) of V with 5 ML Fe coverage at room temperature are shown. Please note that the V dichroism signal has been

multiplied by 50 for illustration because the corresponding asymmetry is very small, i.e., at most 0.4%. The reversed sign of the V dichroism signal at the rising edge of the L_3 line compared with Fe indicates the presence of a net V moment with antiparallel coupling to the Fe moment. In addition, the V moment can be crudely estimated comparing with the measurement of an $\text{Fe}_{90}\text{V}_{10}$ alloy in Ref. [11]. For this purpose the relative dichroism signals were determined by dividing the area under the dichroism signal by the area under the isotropic spectrum without background subtraction. The integration was performed only over the L_3 edge until the local minimum between the L_3 and the L_2 line because according to Ref. [11] the dichroism above this minimum is almost completely governed by the L_2 contribution. Assuming that the V magnetization is completely located in the interface layer to Fe and that the escape depth of the secondary photoelectrons is 2 nm provides a value of $-0.8 \mu_B$ per V atom. This value is consistent with the results obtained by other groups with *ab initio* calculations and experiments for single V overlayers on Fe, Fe/V superlattices and Fe/V/Fe(110) trilayers. In any case the V magnetization is too small to explain the reduced total magnetization found with PNR.

The XMCD results are published in Ref. [10].

- [1] T. Nawrath, H. Fritzsche, F. Klose, J. Nowikow, H. Maletta, Phys. Rev. B 60, 9525 (1999)
- [2] T. Nawrath, H. Fritzsche, H. Maletta, J. Magn. Magn. Mater. 212 (2000) 337-346
- [3] T. Nawrath, H. Fritzsche, H. Maletta, Surface Science 414 (1998) 209
- [4] D. Schmitz *et al.*, BESSY annual report 2001, p. 351
- [5] J. Izquierdo, R. Robles, A. Vega, M. Talanana, C. Demangeat, Phys. Rev. B 64, 060404 (2001)
- [6] B.T. Thole, P. Carra, F. Sette, G. van der Laan, Phys. Rev. Lett. 68, 1943 (1992)
- [7] P. Carra, B.T. Thole, M. Altarelli, Xindong Wang, Phys. Rev. Lett. 70, 694 (1993)
- [8] R. Wu, A.J. Freeman, Phys. Rev. Lett. 73, 1994 (1994)
- [9] G.Y. Guo, H. Ebert, Phys. Rev. B 50, 3861 (1994)
- [10] D. Schmitz, P. Imperia, J. Hauschild, Y.T. Liu, H. Maletta, J. Magn. Magn. Mater. 269/1 (2003) 89-94
- [11] A. Scherz, H. Wende, K. Baberschke, J. Minár, D. Benea, H. Ebert, Phys. Rev. B 66, 184401 (2002)

Surface induced ferromagnetism in the Ti doped p-wave Superconductor Sr_2RuO_4

E. Goering¹⁾, S. Gold¹⁾, J. Deisenhofer²⁾, K. Pucher²⁾, A. Loidl²⁾, S.G. Ebbinghaus³⁾, R.J. Cava⁴⁾, and G. Schütz¹⁾

¹⁾ Max-Planck-Institut für Metallforschung, Heisenbergstrasse 3, 70560 Stuttgart, Germany

²⁾ Experimentalphysik V, Center of Electronic Correlations and Magnetism, Institute for Physics, Augsburg University, D-86135 Augsburg, Germany

³⁾ Lehrstuhl für Festkörperchemie, Universität Augsburg, Universitätsstr. 2, 86135 Augsburg, Germany

⁴⁾ Department of Chemistry and Princeton Materials Institute, Princeton University, Princeton, NJ 08544, USA

For the p-wave superconductor Sr_2RuO_4 ferromagnetic fluctuations of the $4d_{xy}$ orbitals have been shown to be an important issue to the coupling mechanism. We clearly could identify a ferromagnetically ordered low temperature surface state of the Ru ions in the Ti doped system by the use of x-ray magnetic circular dichroism at the Ru $M_{2,3}$ edges. This has been previously predicted by first principle calculations, which suggest a rotational symmetry breaking at the surface correlated with ferromagnetic spin fluctuations as the origin of the spin-triplet pairing mechanism.

In the last decade Sr_2RuO_4 , which is isostructural to the High- T_c -superconductor $(\text{La,Sr})_2\text{CuO}_4$, has attracted a lot of attention because it is the only reported oxide spin-triplet superconductor¹ with a p-wave order parameter^{2,3}. Substituting Ru^{4+} by non-magnetic Ti^{3+} ($3d^0$) strongly suppresses superconductivity as a result of impurity scattering⁴. The critical Ti concentration is as low as 0.15%. Ti-doping obviously induces local magnetic moments with a pronounced anisotropy, and at low temperatures magnetic ordering is observed for $x \geq 2.5\%$ (e.g. $T_m \cong 15$ K for $x = 0.2$)^{5,6}. The nature of the magnetically ordered ground state is still under debate. It has been suggested that the tendency of the Σ_3 phonon mode towards a structural instability decreases⁷. Additionally, Matzdorf et al. detected a surface reconstruction in pure Sr_2RuO_4 suggesting a FM ground state of the surface⁸ in connection with a rotational symmetry breaking of the frozen Σ_3 phonon mode, that reportedly characterizes Sr_2RuO_4 as being close to a structural instability⁹. In contrast, a non-magnetic ground state of the surface has been proposed to explain recent photoemission data¹⁰. In order to reveal the origin of the magnetically ordered state in Ti-doped Sr_2RuO_4 , and the relation to the spin correlations in the pure compound, we investigated the Ru-4d and Ti-3d derived magnetism by x-ray circular dichroism (XMCD).

Single crystals of $\text{Sr}_2\text{Ti}_x\text{Ru}_{1-x}\text{O}_4$ with $x = 0.2$ and $x = 0$ have been grown by the floating-zone melting technique using sintered rods of polycrystalline powders, which were synthesized by conventional solid state reactions. The single-crystalline samples have been previously characterized and extensively investigated by X-ray diffraction, *dc*-resistivity, magnetic susceptibility, low temperature heat capacity and optical conductivity⁶. The crystals are platelets with 1-4mm along the *a* and *b* directions and less than 1mm thick along the *c* direction. X-ray diffraction results are comparable to earlier

published values. The $x = 0.2$ sample shows Curie-Weiss like magnetic ordering below 20K, with a strong easy axis behaviour along the *c* direction^{5,6}. Further details about the sample preparation are published elsewhere⁶.

X-ray Absorption Spectra (XAS) were recorded at the new bending magnet beamline SX 700 III at BESSY II. The monochromator energy resolution was set to about $E/\Delta E \approx 10000$ and the degree of circular polarization was 0.95 ± 0.03 . Two Keithley 6517A electrometers were used for simultaneous measurements of the total drain sample current and from an Au coated Cu grid, which monitors the intensity of the incoming photon beam. A split coil superconducting magnet system was used with a centre bore of 5cm and a maximum magnetic field of 30kOe. All spectra have been recorded at magnetic fields of ± 5 kOe in normal incidence geometry, with the *c* axis aligned parallel to the surface normal and the photon *k*-vector. The photon beam was aligned parallel to the magnetic field. Due to the normal incidence geometry, absolute nonmagnetic offsets signals ΔI in the raw XMCD total electron yield (TEY) signal *I* are smaller than $\Delta I/I = 3 \cdot 10^{-4}$. Nevertheless, this very small offset has been numerically corrected¹¹. The external magnetic field was flipped at each measurement point. Further details of the normalization and background subtraction method are described elsewhere¹¹. We would like to emphasize, that the achieved noise level is quite near to the statistical noise limit, which corresponds to the total number of electrons leaving the sample. In our case the effective sample current is in the range of 10-30pA and the corresponding noise level in the resulting XMCD signal is about 5-15fA for a single spectrum. The sample has been cleaved on air and instantaneously put into the load lock of the UHV system. All XMCD measurements have been performed under UHV conditions.

In Fig. 1a the normalized and background subtracted absorption at the Ti- $L_{2,3}$ and the Ru- $M_{2,3}$ edges are shown. Due to the low Ti doping concentration and the small radial matrix elements of the Ru- $M_{2,3}$ absorption the relevant total absorption signal is **less than 4%** of the background. In Fig. 1c the corresponding 10 point smoothed XMCD signal is shown, which is also an average over 10 single XMCD spectra. We want to emphasise that the resulting noise level from the unsmoothed sum is only 0.01% of the total absorption signal. A small negative intensity is observable at about 465eV and positive intensity at 485eV indicating the Ru 4d magnetization.

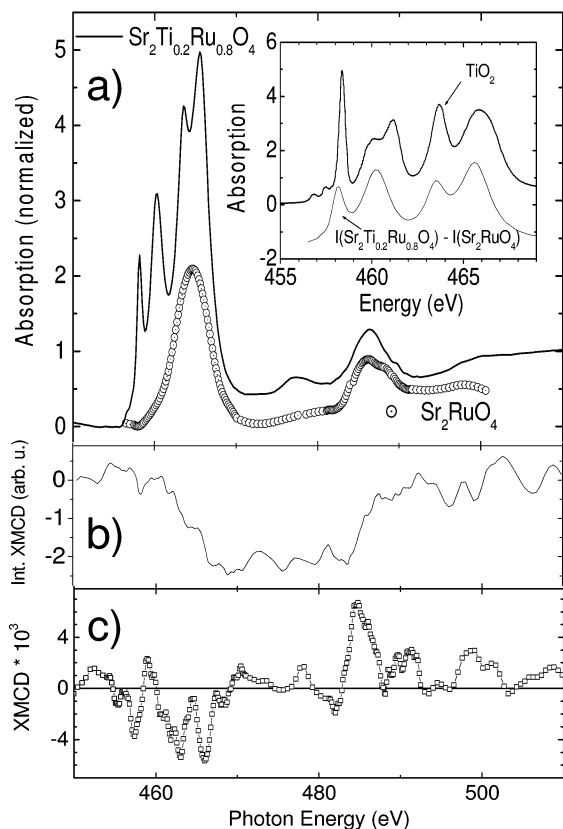


Figure 1: (a) Edge normalized XAS spectra of the Ti doped and the undoped sample. The undoped spectrum has been normalized to match the Ru M_2 peak areas at 486.5eV. The inset shows the estimated Ti $L_{2,3}$ intensity after subtraction of the normalized undoped Ru $M_{2,3}$ signal and a comparison to the $3d^0$ model compound TiO_2 . (b) Integrated XMCD signal from Fig. 1c. Double step like behaviour correspond to the projected spin moment of Ru 4d electrons. The edge height, indicated by the arrow, has been used for sum rule estimation of the projected Ru 4d spin moment. (c) Corresponding edge normalized XMCD signal smoothed by 10 point averaging.

Unfortunately, the Ru- M_3 edge is positioned at the same energy as the Ti L_2 edge. The inset of fig. 1a shows a TiO_2 Ti $L_{2,3}$ XAS spectrum, which has been measured previously at the PM5 bending magnet beamline at BESSY I utilizing an equivalent spectral resolution. For a quantitative estimation of the Ru-

M_3 intensity, we measured the undoped Sr_2RuO_3 system and scaled the Ru- M_2 to give matching areas to the doped signal (see Fig 1a). To extract the Ti- $L_{2,3}$ part in the spectrum we have subtracted the undoped and area scaled Ru- M_3 spectral weight from the doped absorption spectrum. The XMCD related projected spin moments are estimated by the use of sum rules and neglecting the magnetic dipole term T_z ¹²⁻¹⁴. The XMCD areas of the $L_{2,3}$ ($M_{2,3}$) edges were collected by simple integration. The integral of the XMCD signal from Fig. 1c is shown in Fig 1b. This integral clearly shows a downward and upward step. This undoubtedly indicates a Ru 4d magnetic moment. The resulting averaged sum rule related Ru 4d spin moment is $0.03 \mu_B/Ru$ ion using an effective number of 4d holes of $n_h=5.2$. We have measured the total sample magnetization (SQUID) at the same applied magnetic field of 5kOe giving a magnetic moment of $2.8 \cdot 10^{-3} \mu_B/f.u.$ or $3.4 \cdot 10^{-3} \mu_B/Ru$, which is at least one order of magnitude smaller compared to the above derived XMCD value. Due to the enhanced surface sensitivity of XMCD in TEY mode, we conclude that the surface has an enhanced magnetic moment compared to the bulk material, which could be estimated to $0.11 \mu_B/Ru$. Therefore, our results support the Σ_3 phonon model for FM correlations and suggest that electronic correlations at in the d_{xy} related Fermi surface and this phonon coupling are probably the dominating spin-triplet pairing mechanism in Sr_2RuO_4 .

We would like to thank T. Kachel for beamline support at BESSY II, and Y. Maeno for fruitful discussions. This work was supported by the BMBF via VDI/EKM 13N6917, partly by the DFG via SFB 484 (Augsburg), and the Max-Planck-Society.

References

1. Y. Maeno et al., Nature 372, 532 (1994).
2. G. M. Luke et al., Nature 394, 558 (1998).
3. K. Ishida et al., Nature 396, 658 (1998).
4. N. Kikugawa, et al. ; A. P. Mackenzie, and Y. Maeno, J.Phys.Soc.Jap. 72, 237 (2003).
5. M. Minakata and Y. Maeno, Phys.Rev.B 63, 180504-1 (2001).
6. K. Pucher et al., Phys.Rev.B 65, 104523-1 (2002).
7. M. Braden et al., Phys.Rev.Lett. 88, 197002 (2002).
8. R. Matzdorf et al., Science 289, 746 (2000).
9. M. Braden et al., Phys.Rev.B 57, 1236 (1998).
10. K. M. Shen et al., Phys.Rev.B 64, 180502(R)-1 (2001).
11. E. Goering et al., J.Sync.Rad. 8, 434 (2001).
12. P. Carra et al., Phys.Rev.Lett. 70, 694 (1993).
13. C. T. Chen et al., Phys.Rev.Lett. 75, 152 (1995).
14. B. T. Thole et al., Phys.Rev.Lett. 68, 1943 (1992).

Optical constants of UPtGe and UN between 10 meV and 10 eV

U. Barkow, M. Marutzky, A.-M. Cârsteanu, D. Menzel, A. Navratil, H. Schröter, S. Weber, J. Schoenes, C. Cobet¹, and R. Troć²

Institut für Halbleiterphysik und Optik, TU Braunschweig, Mendelssohnstr. 3, 38106 Braunschweig, www.iho.tu-bs.de

¹Institut für Festkörperphysik, TU Berlin, Hardenbergstr 36, 10623 Berlin

²W. Trzebiatowski Institute for Low Temperature and Structure Research, Polish Academy of Sciences, Wroclaw, Poland

Compounds of uranium are of special interest due to the intermediate localization of the 5f electrons. Elemental uranium, in which the 5f electrons are predominantly itinerant, has a metallic character and displays Pauli paramagnetism only. As the distance between the U-atoms in a compound increases, the 5f electrons become more localized and a magnetic coupling occurs via RKKY exchange. UN and UPtGe are both antiferromagnetic, but they differ remarkably in their optical and electrical properties.

Optical spectroscopy constitutes a powerful, nondestructive tool to study the electronic structure of solids since light as an electromagnetic wave interacts directly with the electrons. The response can be described by the complex dielectric function $\tilde{\epsilon}_{xyz}(\omega)$ which in most cases is a tensor of rank two. To determine one complex component of this tensor as a function of energy two separate measurements e.g. a transmission and a reflection measurement are necessary. Another method is used in ellipsometry where one obtains these values simultaneously from the conversion of linearly into elliptically polarized light. Due to recent progress in band-structure computation it becomes possible to compare experimental and theoretical optical spectra for complex materials with many atoms per unit cell. Therefore, ellipsometry over a wide spectral range allows one a good comparison of theory and experiment even for opaque single crystals which is done in the following.

UPtGe crystallizes in the orthorhombic EuAuGe-structure with the lattice constants $a=4.33$, $b=7.19$ and $c=7.52$ Å. The bindings have mostly metallic character. Below 50 K an antiferromagnetic, helical spinstructure occurs. The electric and magnetic properties of UPtGe are strongly anisotropic in that the properties along the b-axis differ significantly from those along the a- and c-axis [1].

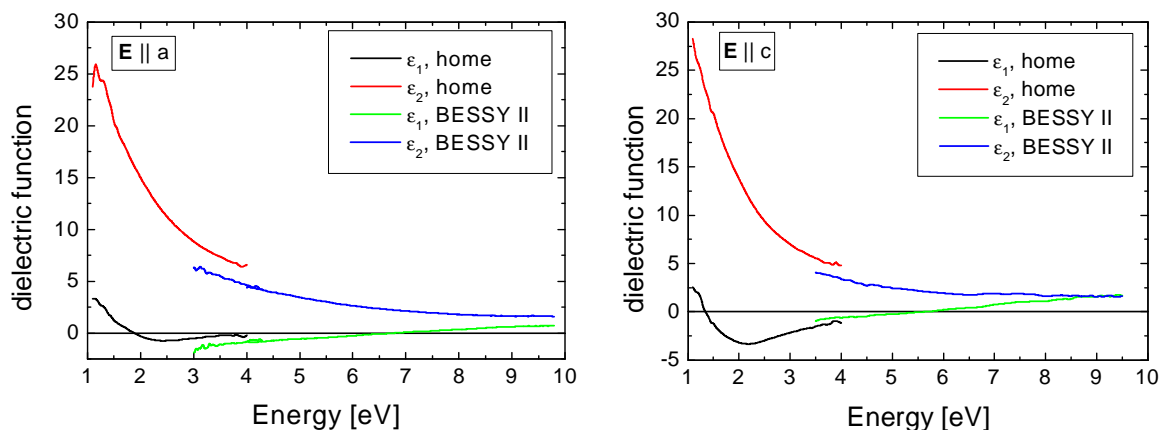


Fig 1a: Dielectric functions of UPtGe along the a- and c-axis

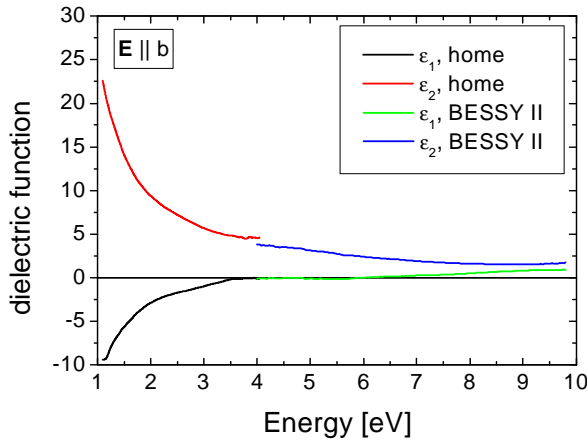
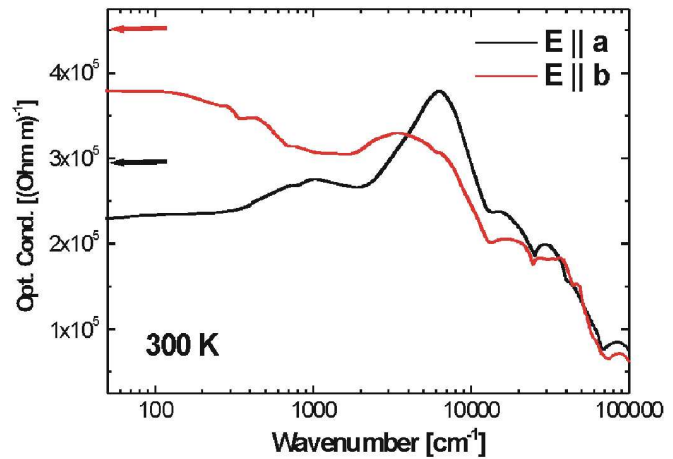


Fig. 1b: Dielectric function of UPtGe along the b-axis

Figs. 1a and 1b show measurements of the optical properties with the electric field vector parallel to the different crystal axes. While the dielectric constants for the a- and the c-axis are similar, the b-axis shows a different behaviour of ϵ . The dielectric functions in the range from 1 to 4.3 eV were measured with a home-made ellipsometer, and from 4 eV to 10 eV with the BESSY II VUV-ellipsometer.

Fig. 2: Optical conductivity parallel to the a- and b-axis



Joining the ellipsometric measurements of the reflectivity with home made FT-IR spectra one obtains wide range reflectivity spectra which can be transformed into the optical conductivity by Kramers-Kronig-transformation. Fig. 2 shows that the optical anisotropy between the a- and b-axis corresponds to the anisotropy of the dc-conductivity (indicated by the red and black arrow on the left) [1]. At higher energies some structures appear in the spectra. A fit with the Drude-theory is in progress in order to obtain more information about the conduction bands of UPtGe.

UN crystallizes in the cubic NaCl structure with a partial ionic bonding. Oppeneer *et al.* Have calculated the electronic structure from first principles and consecutively the spectrum of the isotropic optical conductivity [2].

An experimental spectrum as measured on one of our samples is shown in fig. 3. The optical conductivity of UN obtained from the ellipsometry data shows some structures in the high energy range above 4 eV marked by arrows. They can be related to structures which appear in the calculated spectrum of the optical conductivity with the LDA+U method taking only interband transitions into account [2].

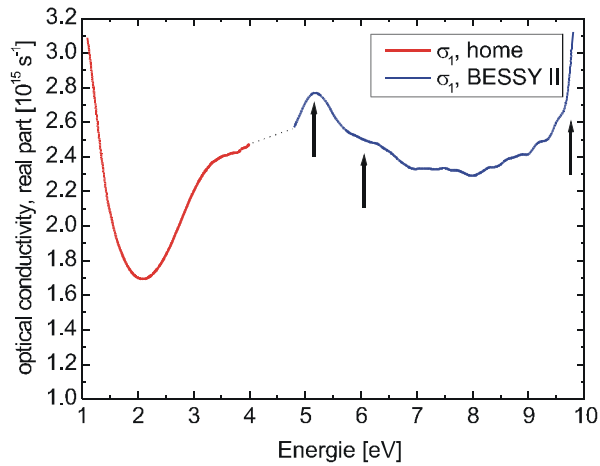


Fig. 3: Measured optical conductivity of UN

Thus, our measurements agree quite well with the theory. At lower energies, a difference between theory and experiment occurs which is due to the contribution of free electrons since in the calculation only interband transitions are taken into account.

Acknowledgments

We acknowledge the research group of Dr. N. Esser for the possibility to use the VUV ellipsometer and the BESSY company for beam time and financial support.

References:

- [1] R. Troć *et al.*, Phys. Rev. B, in press
- [2] P. M. Oppeneer *et al.*, private communication

Chemical bonding effects in nickel compounds studied by x-ray absorption.

A.S. Vinogradov¹, S.A. Krasnikov^{1,2}, A.B. Preobrajenski^{1,3}, E.V. Nikolaeva¹,
D.V. Vyalikh^{1,4}, S. L. Molodtsov^{1,4} and R. Szargan²

¹ V.A. Fock Institute of Physics, St. Petersburg State University, St. Petersburg, 198504 Russia;

² W. Ostwald-Institut für Physikalische und Theoretische Chemie, Universität Leipzig, D-04103, Leipzig, Germany;

³ MAX-lab, Lund University, S-22100 Lund, Sweden;

⁴ Institut für Festkörperphysik, Technische Universität Dresden, 01062 Dresden, Germany

X-ray Absorption Spectroscopy (XAS) has been widely used for several decades in order to gain information on the energy distribution and spatial localization of unoccupied electron states in transition metal (TM) compounds. Nevertheless, systematic XAS studies of the role of the covalent bonding (hybridization) in the formation of electronic structure and x-ray absorption spectra of these compounds are nearly not available. Recently we have studied the impact of chemical bonding on the absorption structures in the Fe 2*p* spectra for Fe(II) and Fe(III) compounds [1] and F 1*s* ones for TM fluorides [2]. Here we extend our study to the case of nickel compounds.

The Ni 2*p* absorption spectra were measured with high photon energy resolution for Ni metal and a series of its compounds: NiF₂, NiO, Ni(NO₃)₂, Ni(acac)₂, Ni(Pc), and K₂Ni(CN)₄. To support our analysis we have also measured certain absorption spectra of the ligand atoms: F 1*s* spectrum for NiF₂, O 1*s* spectrum for NiO, C 1*s* spectrum for Ni(Pc), and N 1*s* spectra for K₂Ni(CN)₄, Ni(Pc), Ni(NO₃)₂, LiNO₃, NaNO₃, KNO₃, CsNO₃, Cr(NO₃)₂, and Co(NO₃)₂. The main goal of this study was (i) to elucidate the character of the chemical bonding and the way it is displayed in x-ray absorption spectra and (ii) to obtain information on characteristics of low-energy unoccupied electronic states for investigated nickel compounds.

The XAS measurements on nickel compounds were performed at the Russian-German beamline at BESSY II [3] in the total electron yield detection mode. The metal sample was a nickel foil cleaned

by scraping with a diamond file in vacuum. A thin film of Ni(Pc) was prepared by thermal evaporation *in situ* onto Cu substrate. The samples of other compounds were prepared by rubbing the powder in a scratched copper plate. The XA spectra were recorded at the photon-energy resolution of 144 meV (Ni 2*p*), 115 meV (F 1*s*), 90 meV (O 1*s*), 70 meV (N 1*s*), and 50 meV (C 1*s*). Photon energies in the range of the fine structure of absorption spectra were calibrated using the known positions of the 1*s*-3*p* transition (867.13 eV) in the absorption spectrum of Ne [4], the 1*s*- π^* , $\nu=0$ transition (400.88 eV) in the spectrum of N₂ [4] and the first narrow peak (683.9 eV) in the F 1*s* absorption spectrum of K₂TiF₆ [5].

Fig.1 shows the Ni 2*p* absorption spectrum of Ni metal in comparison with the spectra of the most ionic compound, NiF₂, and the strongly covalent complex [Ni(CN)₄]²⁻ in solid K₂Ni(CN)₄. All spectra are normalized to the intensity of the main absorption peak *a*. The relative absorption intensity of the continuum (at the photon energy of 885 eV) is given by the number in parenthesis. The Ni(II) atom has formally the same 3*d*⁸ electron configuration in nickel metal, difluoride and cyanide complex. Ni2*p*_{3/2} absorption spectra of these compounds show considerable changes in going from Ni to NiF₂ and [Ni(CN)₄]²⁻: (i) the main absorption band *a*

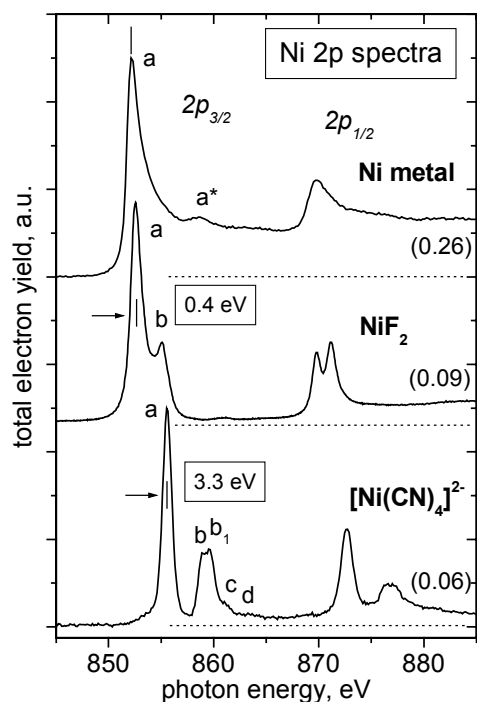


Fig. 1. High-resolution Ni 2*p* absorption spectra of Ni metal, NiF₂ and [Ni(CN)₄]²⁻.

(Ni $2p_{3/2} - 3d$) is split into two bands *a* and *b* with additional structures *b*₁, *c*, *d* for the latter in the case of the covalent complex; (ii) the main band *a* undergoes pronounced high-energy shifts: 0.4 eV (ionic NiF₂) and 3.3 eV (covalent complex). We assume that the covalent bonding between the Ni3*d* and ligand 2*p* electrons is responsible for the splitting of the main absorption band: *a* is associated with the transitions of Ni2*p*_{3/2} electrons to the unoccupied non-bonding 3*d* states, while *b* reflects those to the

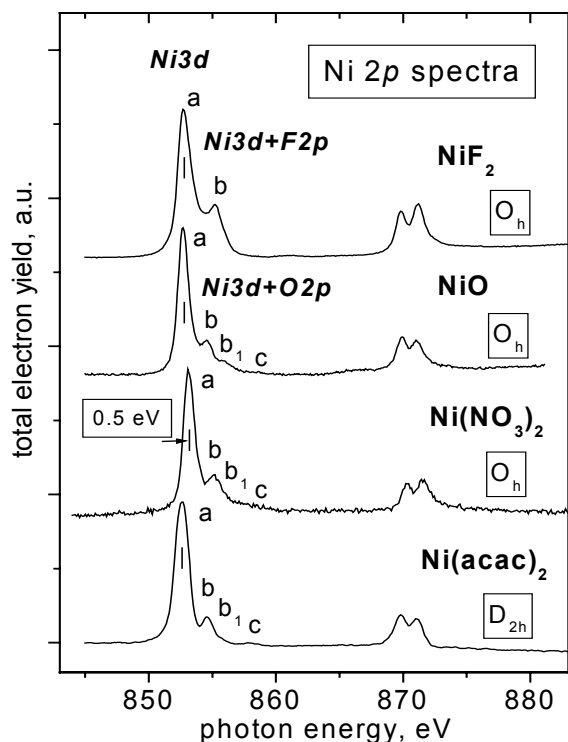


Fig. 2. High-resolution Ni 2*p* absorption spectra of the ionic nickel compounds.

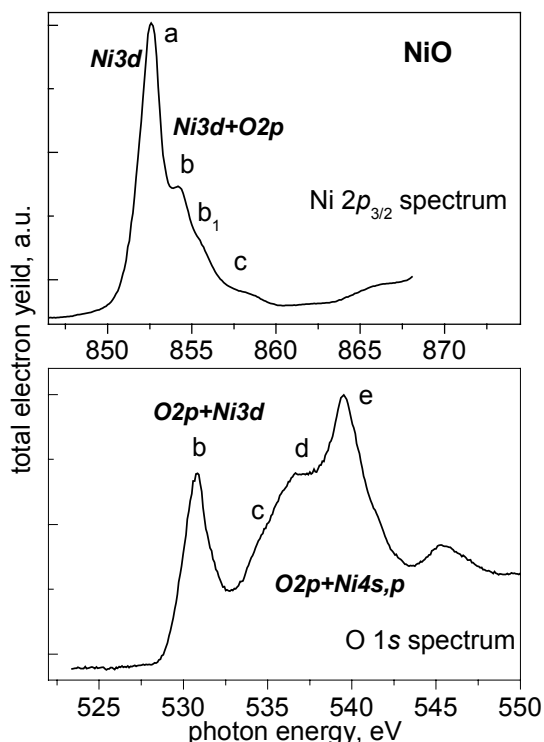


Fig. 3. Ni 2*p*_{3/2} and O 1*s* spectra of NiO aligned in energy using $\Delta E(\text{Ni}2p_{3/2}-\text{O}1s)=324.5$ eV.

empty states with the hybridized Ni 3*d*+ligand 2*p* character. The large high-energy shifts of Ni2*p* absorption are indicative of a considerable increase of the Ni3*d*-ligand 2*p* bonding and a decrease of the effective number of 3*d* electrons for the nickel atom in going from Ni metal to NiF₂ and [Ni(CN)₄]²⁻.

The Ni 2*p* spectra of ionic nickel compounds are compared in Fig.2. The nickel atom is coordinated octahedrally (or nearly octahedrally) to the fluorine atoms (NiF₂) or the oxygen ones (NiO, Ni(NO₃)₂). In Ni(acac)₂ the metal atom has a nearly square-planar environment by the four oxygen atoms of two acetylacetonates anions CH₃CO=CHCOCH₃⁻ [acac]. The ionicity of chemical bonding decreases along the NiF₂ – NiO – Ni(NO₃)₂ – Ni(acac)₂ series. The Ni2*p*_{3/2} absorption spectra of these ionic compounds are characterized by (i) the similar spectral profile for all compounds and additional weak structures *b*₁ and *c* for oxygen compounds; (ii) the close energy position of the main band *a* (~852.7 eV) for all compounds except Ni(NO₃)₂ for which the high-energy shift of 0.5 eV is observed; (iii) the appreciable broadening of the main band *a* in Ni(acac)₂. The origin of individual features in the Ni 2*p*_{3/2} absorption spectra for the ionic compounds can be understood within the framework of a quasi-molecular NiF₆ (NiO₆ or NiO₄) approach [2], which implies a partial participation of Ni3*d* electrons in the covalent bonding with the ligand (F, O) 2*p* electrons, as follows:

- As follows from the comparison between the Ni 2*p* and O(F) 1*s* spectra of NiO (Fig.3) and NiF₂ (not shown), Ni2*p*_{3/2} electrons pass into the empty molecular orbitals (MO's) of a quasi-molecule with the pure 3*d* character (nonbonding MO), resulting in band *a*, or the hybridized Ni3*d*+F(O)2*p* character (anti- and/or bonding MO's), resulting in structures *b*, *b*₁, *c*.
- The 3*d*^{*n*} electron configurations are very close for the Ni atoms in NiF₂, NiO and Ni(acac)₂, while in Ni(NO₃)₂ the number of 3*d* electrons is smaller due to the additional 3*d* – O2*p* π electron transfer (back-donation) between the Ni atom and ligands (NO₃⁻), which is responsible for the high-energy shift of the spectrum.

- The broadening of *a* may result from the lowering of the ligand-field symmetry ($O_h - D_{2h}$) causing the nonbonding $Ni3d$ states to split.

The covalent bonding was found to play the important role in the formation of absorption structures in $Ni2p_{3/2}$ spectra of the square-planar complexes $Ni(Pc)$ and $[Ni(CN)_4]^{2-}$ (Fig. 4). It causes a delocalization of the $3d$ states, decreasing the $3d$ electron density on the nickel atoms and thus lowering a screening of the $Ni 2p - 3d$ transitions and increasing their energy (high-energy shift). The absorption structures in the spectra of $[Ni(CN)_4]^{2-}$ (Fig. 5), $Ni(Pc)$ and $Ni(acac)_2$ can be also treated within the framework of the quasi-molecular approach.

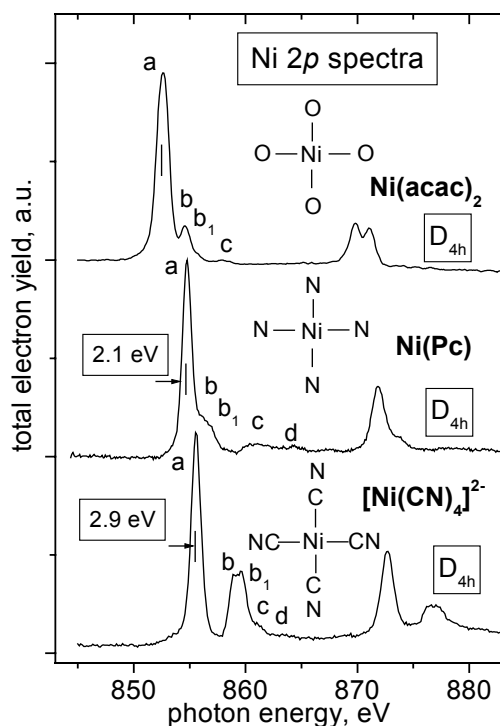


Fig. 4. $Ni2p$ absorption spectra of covalent $Ni(acac)_2$, $Ni(Pc)$ and $[Ni(CN)_4]^{2-}$.

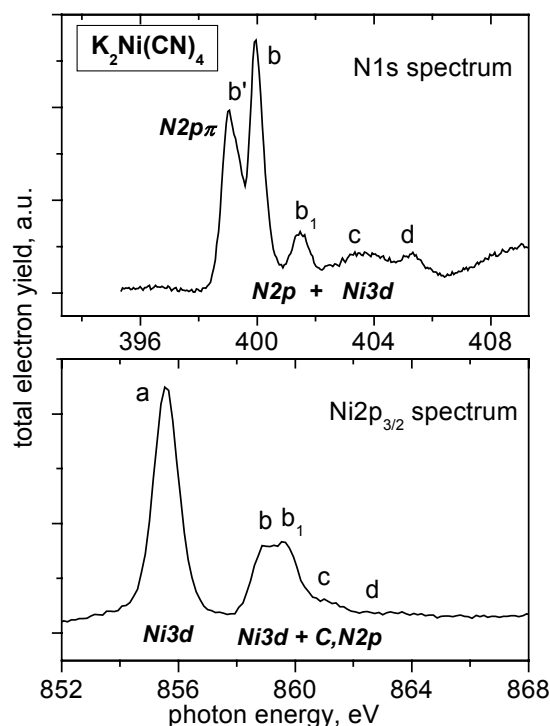


Fig. 5. $Ni2p_{3/2}$ and $N1s$ absorption spectra of $[Ni(CN)_4]^{2-}$ complex aligned in energy using $\Delta E(Ni2p_{3/2}-N1s)=458.7$ eV.

In conclusion, the basic results of our study provide a strong experimental evidence for importance of covalent bonding in the formation of unoccupied electron states in the nickel compounds. A strong influence of covalent bonding onto the spectral structure is clearly observed in the $Ni2p_{3/2}$ absorption, as well as in the $1s$ spectra of ligands (F, O, N, C). Thus, the quasi-molecular consideration of structures in x-ray absorption spectra from Ni compounds is proposed.

Acknowledgements

This work was supported by the Russian Foundation for Basic Research (project no. 01-03-32285), the Deutsche Forschungsgemeinschaft (SFB 463, TP B4 and B16), and the bilateral program Russian-German Laboratory at BESSY II. We thank the staff of BESSY II for valuable technical assistance. A.S. Vinogradov gratefully acknowledges the financial support by the Technische Universität Dresden. A.B. Preobrajenski acknowledges the support by the Swedish Foundation for International Cooperation in Research and Higher Education (STINT).

References

1. A.S. Vinogradov, A.B. Preobrajenski, A.S. Krasnikov et al., *Surf. Rev. and Lett.* **9** (2002), 359-364; A.S. Vinogradov, A.B. Preobrajenski et al., *BESSY Annual Report 2001*, p.137-139 (2002); in preparation.
2. A.S. Vinogradov, S.I. Fedoseenko et al., *Optika i Spektrosk.* **93**, 935-943 (2002) [*Optics & Spectrosc.* **93**, 862-867 (2002)]; A.S. Vinogradov, S.I. Fedoseenko, S.A. Krasnikov et al., *Physica Scripta*, in print (2004).
3. S.I. Fedoseenko, I.E. Iossifov, S.A. Gorovikov et al., *Nucl. Instrum. Methods Phys. Res. A* **470**, 84 (2001).
4. R.N.S. Sodhi, C.E. Brion, *J. Electron Spectr. Relat. Phenom.* **34**, 363 (1984).
5. A.S. Vinogradov et al., *Fiz. Tverd. Tela (Leningrad)* **24**, 1417 (1982) [*Sov. Phys. Solid State* **24**, 803 (1982)].

Electronic structure of $\text{La}_{1-x}\text{Sr}_x\text{MnO}_3$: Resonant Inelastic X-ray Scattering (RIXS)

K. Kuepper¹, V. R. Galakhov², A. Takacs¹, M. Neumann¹, and Ya. M. Mukowskii³

¹Universität Osnabrück, FB Physik, Barbarastr. 7, D-49069 Osnabrück, Germany

²Institute of Metal Physics, Russian Academy of Sciences - Ural Division, 620219
Yekaterinburg GSP-170, Russia

³Moscow State Steel and Alloys Institute, 117936 Moscow, Russia

1. Introduction

LaMnO_3 is an A-type antiferromagnetic insulator with a Néel temperature of 141 K, and is of special interest as the parent compound of doped lanthanum manganites showing colossal magneto resistance (CMR), which are the possible magnetic materials for applications in the next generation of hard disc reading heads [1,2]. Hole doping with Sr leads to a remarkable rich phase diagram as a function of temperature, magnetic field and doping that is due to the intricate interplay of charge, spin, orbital and lattice degrees of freedom which have been the subject of many studies during the last few years [3,4]. This variety of properties is often due to the different behavior of $3d$ electrons, which may be more or less localized, giving rise to intra-atomic correlation effects of different strength. Resonant Inelastic X-ray Scattering (RIXS) is well known to be a powerful spectroscopic tool in order to probe optically inaccessible bands, such as $d-d$ transitions in transition metal compounds. Recently, $d-d$ transitions between upper and lower Hubbard band in the Mott insulator NaV_2O_5 have been investigated by RIXS, furthermore Butorin *et al.* report RIXS spectra of MnO to be due to low-lying $d-d$ and charge transfer excitations [5,6]. We present here XAS and RIXS data of the Mn L edge of $\text{La}_{1-x}\text{Sr}_x\text{MnO}_3$ ($x=0.12, 0.34$) single crystals. The measurements were performed at beamline 12-2, U-41 PGM in combination with the rotateable spectrometer apparatus (ROSA).

2. Results and discussion

Fig. 1 displays the Mn L XAS and RIXS spectra performed for various excitation energies (labeled a.-d.) for $\text{La}_{1-x}\text{Sr}_x\text{MnO}_3$ ($x=0.12, 0.36$). The Mn $L_{2,3}$ XAS spectra, which are dominated by transitions to Mn $3d$ states but also contain contributions from Mn $4s$ states, consist of two broad multiplets which can be explained by the spin-orbit splitting of the Mn $2p$ core hole. A chemical shift of the Mn L_3 maximum of around 0.2 eV to higher photon energies can be observed for $\text{La}_{0.66}\text{Sr}_{0.34}\text{MnO}_3$. This indicates a change of the chemical environment of the Mn ions due to the higher amount of doped holes, this result is in agreement with the findings of Abbate *et al.* [7]. The Mn L RIXS spectra are strongly dependent on the excitation energy, the RIXS spectra recorded at excitation energies below and on the Mn L_3 XAS edge consist of three distinguishable main features, an elastic recombination peak and two resonant loss features which appear at constant loss energies of around 2.5 eV and 7 eV below the elastic peak. With help of complementary XPS valence band measurements (not shown here due to brevity) and recent band structure calculations [8] we can identify the loss features, the feature which is located 2.5 eV below the elastic peak is due to $d-d$ transitions between Mn t_{2g} bands in the valence band and unoccupied Mn e_g states in the conduction band, whereas the second loss feature can be associated with transitions between strongly hybridized Mn $3d - \text{O } 2p$ states in the valence band and unoccupied Mn $3d$ bands. The spectra taken at excitation energy d., on the maximum of the Mn L_2 XAS show an intensity ratio of L_α to L_β of about 0.5. This is consistent with the results of Yablonskikh *et al.* [9] on Mn based Heusler alloys, where it was found that magnetic ordering decreases the L_α to L_β branching ratio.

We have demonstrated that resonant inelastic x-ray scattering is a powerful spectroscopic tool to investigate correlation and hybridization mechanisms, such as low lying $d-d$ transitions or charge transfer excitations, in magnetic oxides. Especially in combination with complementary spectroscopic tools such as XPS or XAS and theoretical approaches it is possible to reveal a rather complete picture

of the interplay of the spatial distribution of the electronic density and the different inter- and intra-atomic correlation and hybridization effects, which determine both, the magnetic properties and the metal to insulator transition of these compounds.

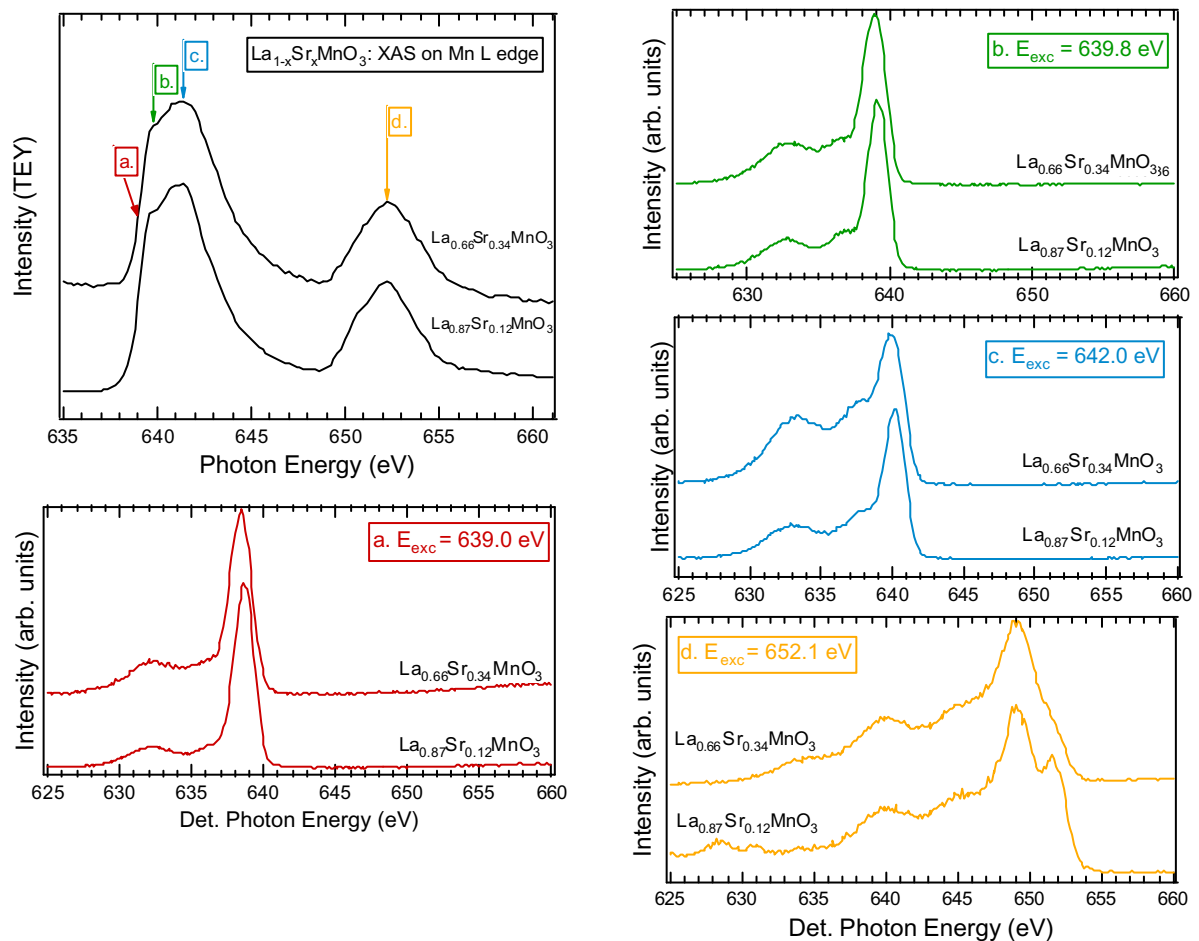


Fig. 1: XAS and RIXS spectra of the Mn L edge of $\text{La}_{1-x}\text{Sr}_x\text{MnO}_3$. The XAS spectra were recorded in total electron yield (TEY). The RIXS spectra were obtained at different excitation energies along the Mn L edge as indicated by the labels a-d in the XAS and the corresponding RIXS spectra.

Acknowledgements

Financial support of the PhD program of Lower Saxony is gratefully acknowledged. This project was supported by BMBF 05 SR8 OL1-2. VG acknowledges funding by the Research Council of the President of the Russian Federation (Project NSH-1026.2003.2), Russian Ministry for Industry and Science (Project on Superconductivity of Mesoscopic and Strongly Correlated Systems). We are grateful to O. Fuchs for support and advice during the experiments.

References

- [1] A. J. Millis, *Nature* **392**, 147-151 (1998)
- [2] M. Ziese, *Rep. Prog. Phys.* **65**, 143 (2002)
- [3] M. B. Salamon and M. Jaime, *Rev. Mod. Phys.* **73**, 583, (2001)
- [4] Y. D. Chuang, A. D. Gromko, D. S. Dessau, T. Kimura and Y. Tokura, *Science* **292**, 1509 (2001)
- [5] G. P. Zhang, T. A. Callcott, G. T. Woods, L. Lini, B. Sales, D. Mandrus, and J. He, *Phys. Rev. Lett.* **88**, 077401 (2002)
- [6] S. M. Butorin, J.-H. Guo, M. Magnuson, P. Kuiper, and J. Nordgren, *Phys. Rev. B* **54**, 4405 (1996)
- [7] M. Abbate, F. M. F. de Groot, J. C. Fuggle, A. Fujimori, O. Strebel, F. Lopez, M. Domke, G. Kaindl, G. A. Sawatzky, M. Takana, *et al.*, *Phys. Rev. B* **46**, 4511 (1992)
- [8] P. Ravindran, A. Kjekshus, H. Fjellvag, A. Delin, and O. Eriksson, *Phys. Rev. B* **65**, 064445 (2002)
- [9] M. V. Yablonskikh, Y. M. Yarmoshenko, I. V. Solovyev *et al.*, *cond-mat* p. 0203169 (2002)

Investigations on the transverse magneto-optical Kerr-effect in the vicinity of the 3p edges of Fe and Co

A. Kleibert, S. Valencia*, H.-C. Mertins*, and J. Bansmann
Fachbereich Physik, Universität Rostock, D-18051 Rostock
**BESSY GmbH, Albert-Einstein-Str. 15, D-12489 Berlin*

Magneto-optical effects in the visible regime are well known and commonly used for studying magnetic materials. Since the availability of high brilliance synchrotron radiation sources magneto-optical spectroscopy techniques were extended from the visible to the EUV- and soft X-ray regime, respectively. Especially, resonantly strong enhanced magneto-optical effects in reflection were found at the 2p edges of the magnetic 3d transition metals exceeding those known from visible light by orders of magnitude [1]. This in addition with element-specificity made synchrotron radiation based methods ideally suited for the investigation of magnetic nanostructures [2]. While most research activities in the past were focussed on the 2p edges we present here a study of the transverse magneto-optical Kerr-effect (T-MOKE) at the 3p threshold and compare our data with calculations using magneto-optical constants obtained independently by Faraday rotation measurements [3].

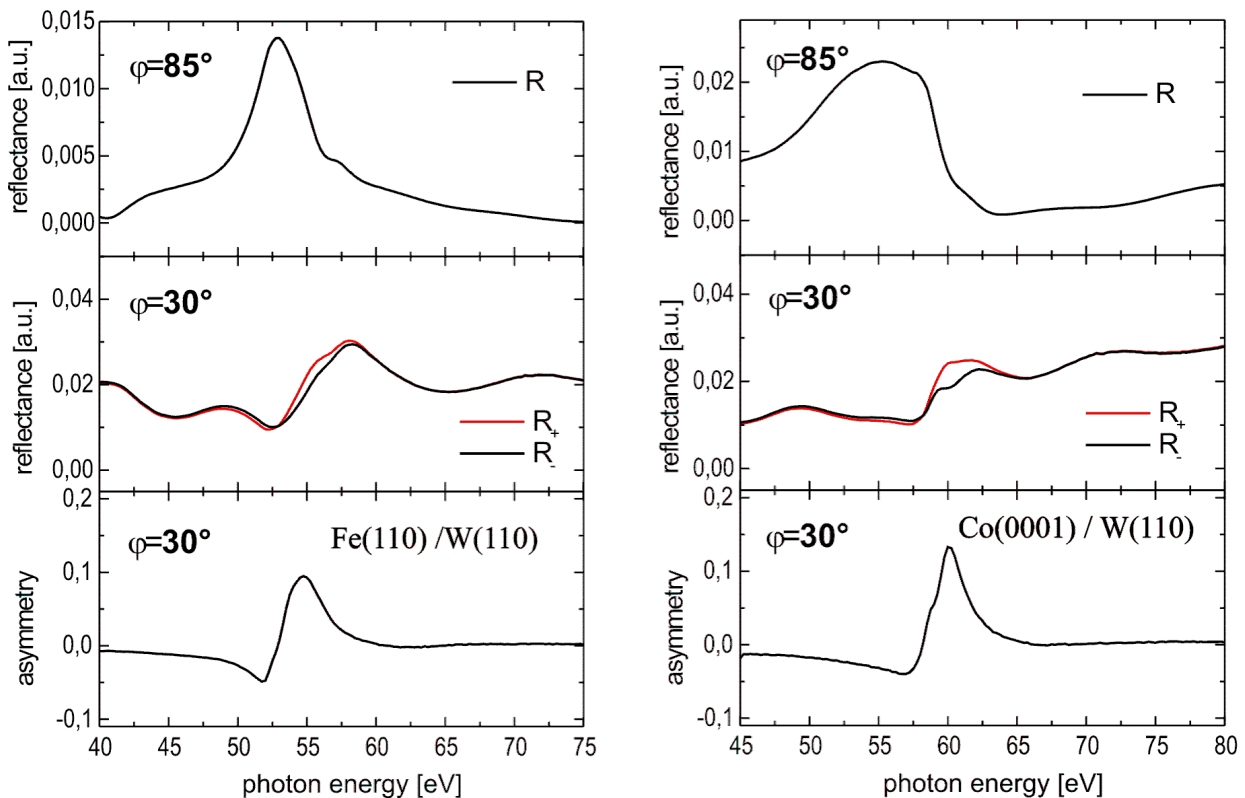


Figure 1: Upper panels: reflectivities of Fe (left) and Co (right) at nearly perpendicular incidence ($\varphi=85^\circ$). Middle panels: reflectivity at $\varphi=30^\circ$ and opposite magnetization (red and black, respectively). Lower panels: asymmetries $A = (R_+ - R_-)/(R_+ + R_-)$ at $\varphi = 30^\circ$.

Experiments were carried out using the BESSY Polarimeter [4] at the U125 PGM Beamline. In fig. 1 reflectivity data of thin Fe(110) and Co(0001) films on W(110) covered with Ag are displayed. Both topmost panels show the reflectance at an angle of incidence of $\varphi=85^\circ$, i.e. nearly perpendicular incidence. These spectra are dominated by the enhanced reflectivity in the vicinity of the 3p threshold around 53eV and 56 eV for Fe and Co, respectively. In agreement with theory no magnetic asymmetry was found at this angle of incidence. Reflectivities at more grazing incidence ($\varphi = 30^\circ$) are given in the middle parts of fig. 1. While the broad structures shown in the upper parts are not more observed noticeable changes in the reflectivity can be found when reversing the magnetization of the samples. The respective asymmetries $A = (R_+ - R_-)/(R_+ + R_-)$ are shown in the lower part and reach values up to 0.15 (=15%) close to the threshold energies.

The angular dependence of the reflectivity and asymmetry, respectively, is demonstrated in fig. 2. As a sample a 60nm Fe film sputtered on Si and capped with 3nm Ta to protect against oxidation was chosen. The measured reflectivities at a fixed photon energy of 55 eV with opposite magnetizations are depicted in the left part of fig. 2 (open red and black circles). The related asymmetry is displayed in the right part (open circles). One can see vanishing asymmetries for grazing and perpendicular incidence and a sharp transition from a strong positive to a negative maximum, respectively, in the vicinity of the pseudo-Brewster angle where the reflectivity of p-polarized light is strongly suppressed.

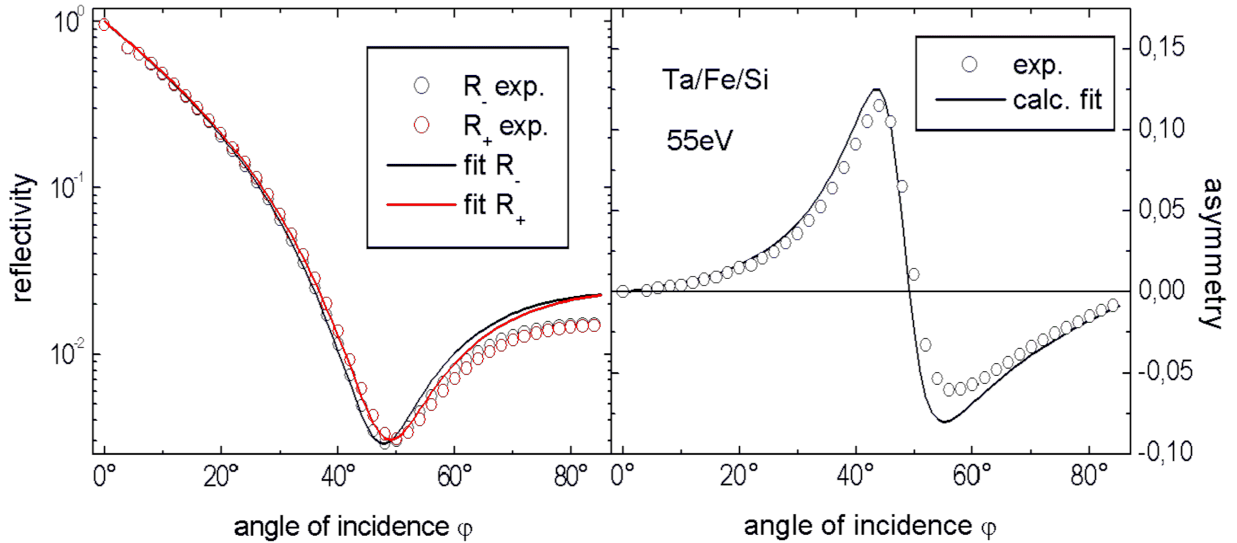


Figure 2: Left: measured reflectivities of Fe at 55eV (open black and red circles), solid lines denote calculated reflectivities. Right: Experimental (open circles) and calculated (solid line) asymmetry.

In order to get a more quantitative insight in the magneto-optical properties of the Fe film and the influence of the capping layer we used a formalism suggested by Zak et al. [5] to calculate the reflectivity and asymmetry of the sample. Nonmagnetic refractive constants N were taken from tabulated values [6], while the magneto-optical Voigt parameter Q for Fe was determined from independent experiments by Valencia et al. [3] (see tab. 1). The best

	n	k	q	p
Ta_2O_5	0.8799	0.1364	0	0
Fe	1.0341	0.1805	-0.00121	0.02255

Table 1: Refractive constants $N = n + i \cdot k$ from ref. [6] and Voigt parameter $Q = q + i \cdot p$ from ref. [3] used for the calculation of reflectivity and asymmetry shown in fig. 2.

fit for reflectivities and asymmetry shown as solid lines in fig. 2 was obtained by assuming a 4.9 nm Ta oxide layer at the top of the Fe layer. The oxidation of the capping layer results from air exposure of the sample. Further calculations (not shown here) yielded a strong influence of the capping layer on the reflectivity and the asymmetry of the sample. Especially, we found calculated asymmetries of up to 60% for an uncovered Fe sample. This value is comparable to effects found at photon energies near the 2p edges and therefore we expect a similar potential of experiments concerning the 3p thresholds for investigations on magnetic nanostructures.

References:

- [1] C. Kao et al., Phys. Rev. Lett. **65**, 373 (1990).
- [2] J. B. Kortright et al., J. Magn. Magn. Mat. **207**, 7 (1999).
- [3] S. Valencia et al., to be published
- [4] F. Schäfers et al., Appl. Optics **38**, 4079 (1999).
- [5] J. Zak et al., Phys. Rev. B **43**, 6423 (1990).
- [6] B. L. Henke et al., Atomic Data and Nuclear Data Tables **54**, 181 (1993).

Dynamics of the Surface Photovoltage on SiO₂/Si(100) Surfaces: Temperature and Excitation Density Dependence

D. Bröcker¹, T. Gießel¹, I. V. Hertel^{1,2}, W. Widdra³

¹*Max-Born-Institut, D-12489 Berlin, Germany*

³*FU-Berlin, Fachbereich Physik, D-10623 Berlin, Germany*

³*Martin-Luther-Universität Halle-Wittenberg, D-06099 Halle, Germany*

Over the last decade time resolved photoemission has evolved into a very successful technique. Several experiments use lasers for both, excitation of the sample and probing the excited surface states. Nevertheless laser sources are limited to the wavelength range from the infrared to the near ultraviolet, which leads to certain limitations of purely laser based photoemission experiments. On the other hand synchrotron radiation (SR) provides a huge photon energy range from some electronvolts up to several KeV with a characteristic pulse length of some picoseconds. The picosecond and nanosecond timescale is the relevant region for many excitations of – organic an classical – semiconductors. These considerations motivated the setup and further development of our experiment for time resolved pump probe experiments using laser and SR.

In many semiconductor surfaces and interfaces partially filled electronic states within the bandgap are pinning the fermi level. The reason is, that – in the case of p-doping – some of the electrons from the surface states are trapped by the bulk acceptors. This leads to a positive surface charge which is compensated by a – typically several 100 nm thick – depletion layer. The typical length scale is given by the Debye length $\mathcal{L}_d = \sqrt{kT\epsilon\epsilon_0/e_0^2p_0}$, where p_0 is the hole density in the bulk. This depletion layer, due to Poisson's equation $\Delta\Phi = -\rho/\epsilon\epsilon_0$, leads to a surface potential, well known as band bending. The band bending can be partially compensated by electrons excited to the conduction band by laser illumination. This process is well known as surface photovoltage (SPV) effect. The laser excited electrons are trapped by the surface potential until they decay via recombination with holes in the valence band. While the flattening of the band takes place on ps and sub-ps time scale, the recombination is somewhat slower and occurs typically on a ns time scale.

The MBI-Bessy beamline provides a specially designed Nd:YVO₄ laser system with 25 MHz repetition rate pulse picked to 1.25 MHz, which coincides with the single bunch repetition rate. The system is synchronized to the storage ring and provides typically 100 mW average power of the second harmonic at 532 nm. The laser system as well as the surface ap-

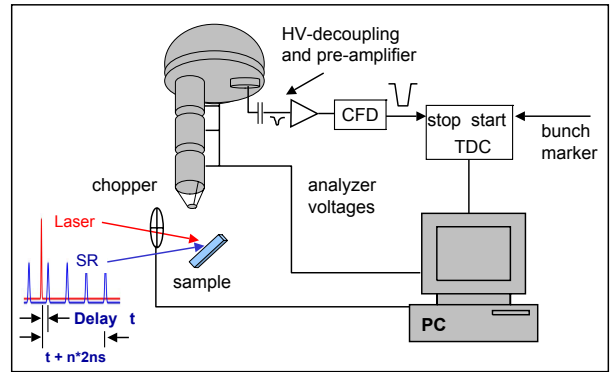


Fig. 1: Experimental setup for pump–multi-probe electron spectroscopy using laser and SR.

paratus has already been used for studies on the SPV under single bunch conditions [1]. For time resolved experiments under multi bunch conditions we developed a special real time resolved detection scheme [2]. Fig. 1 shows the principal setup of the experiment. We use a hemispherical electron analyzer (EA125, Omicron). The signal is coupled out and preamplified by a 250 MHz preamplifier and digitalized by a constant fraction discriminator (Canberra). Afterwards the digital signal is processed by a time to digital converter (TDC) (GPTA GmbH, Berlin), where a bunch marker serves as start signal. The TDC is read out by a PC, which also communicates to the electronics of the analyzer setting the lens voltages and triggers a chopper for the laser. Using appropriate settings for the pass energy and the entrance and exit slits of the analyzer, an experimental time resolution of about 1 ns is achieved. This allows for the separation of the photoemission signal of individual bunches. Note that the time resolution of the experiment is therefore only limited by the temporal overlap of the laser and the SR. Under normal operation conditions this is dominated by the bunch length of about 30 ps, while the synchronization jitter and the pulse length of the laser are 5 ps and 14 ps, respectively.

The time and energy resolved detection scheme was used in a study on surface photovoltage decay. Time

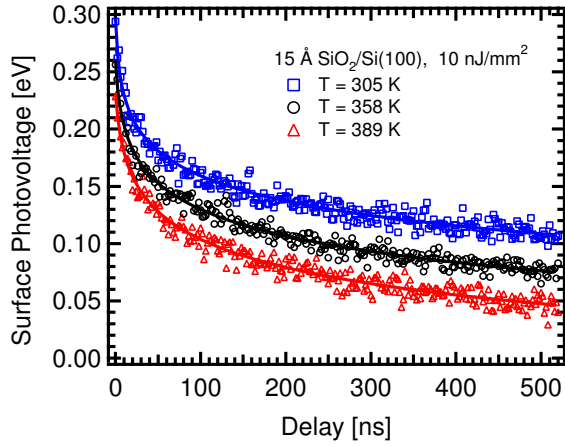


Fig. 2: Temperature dependence of SPV-decay for SiO₂/Si(100) at various temperatures.

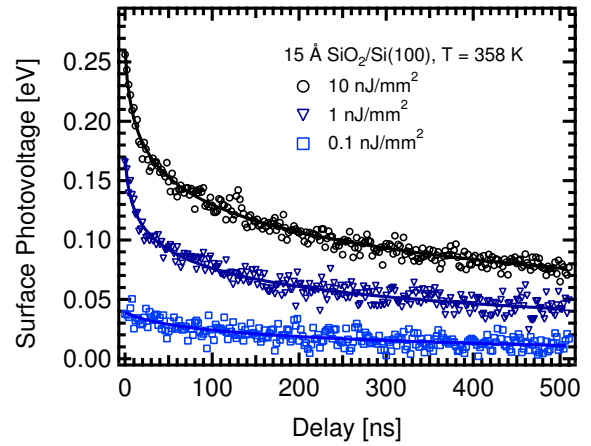


Fig. 3: Decay of surface photovoltage at T=358 K for various laser intensities.

resolved kinetic energy spectra of the Si 2p region were taken under various experimental conditions. The time of flight histograms were fitted in order to extract the photoemission intensity per bunch and kinetic energy. The result of this procedure is one spectrum per bunch of the storage ring filling in multi bunch. By comparing carefully peak positions with and without laser excitation, the peak shift due to the SPV could be extracted with an accuracy of about 5 meV. The measurement leads finally to a set of several hundred consistent data points within about one hour of measurement time. The fully parallel setup reduces many long time systematic errors due to changes of the laser/SR spatial overlap and the filling of the storage ring.

Fig. 2 shows the decay curves of the SPV on thin layers of SiO₂ on Si(100) for three different temperatures: 305 K, 358 K and 389 K. All three curves show the characteristic non-exponential decay as discussed in [3]. At time-zero, directly after the laser excitation, the SPV is 300 meV at room temperature and decreases to 240 meV at 389 K. Additionally a faster decay is observed at higher temperatures. The smaller starting value at higher temperature can be explained by the reduction of the Debye length as well as by the higher charge carrier density in the bulk, which aggravates the saturation. The faster decay at higher temperatures was expected from an quasi-equilibrium model based on thermionic emission. The decay of the excited charge carriers causes a recombination current, given by:

$$j_{rec} = j_{rec}(V_{bb}, T) = c \cdot T^2 e^{V_{bb}/\beta kT},$$

where c and β are constants, T is the temperature and V_{bb} is the band bending. The temperature dependence of the decay characteristic was predicted by this model and could be demonstrated and quantified by this set of measurements.

Fig. 3 shows SPV decay curves at fixed temperature T=358 K of the same surface for three different

excitation densities. As expected from previous measurements and the theory of the photovoltaic effect, the data show logarithmic dependency on the laser fluence. Additionally the decay becomes slower for smaller excitation densities, as expected from a model, in which the decay rate is depending on the band bending itself [3].

The large set of independent data for the SPV as a function of time intensity and temperature enables us to recheck the validity of the thermionic emission based model which describes very well the SPV decay at one given temperature and intensity. The quantitative analysis of the data shown in Fig. 2 and Fig. 3 reveals, that indeed the decay rate for a given sample preparation is not only a function of temperature and band bending: For any quasi equilibrium model the decay rate $\tau = -(dSPV/dt)^{-1}$ should be a function only of the SPV and the temperature. This is obviously not the case as becomes clear from the experimental data in Fig. 3. A possible explanation for this discrepancy is, that the assumption, that the surface potential represents the charge carrier distribution at all times, is not always true.

References

- [1] W. Widdra, D. Bröcker, T. Gießel, I.V. Hertel, W. Krüger, A. Liero, F. Noack, V. Petrov, D. Pop, P.M. Schmidt, R. Weber, I. Will, and B. Winter, *Surf. Sci.* **548**, (2003)87-94.
- [2] T. Gießel, D. Bröcker, P. Schmidt, and W. Widdra, *Rev. Sci. Instr.* **74**, (2003)11.
- [3] D. Bröcker, T. Gießel, and W. Widdra, *Chem. Phys.* in press (2003).

Investigation of the spin singlet and spin triplet character of the first removal state in Y-Bi2212 and La-Bi2201

R.-St. Unger, U.Seidel, M. Schneider, A. Krapf, H. Dwelk, C. Janowitz, R. Manzke
Humboldt Universität zu Berlin, Germany
V.A.Gavrichkov, S.G.Ovchinnikov

L.V.Kirensky Institute of Physics of the Siberian Branch of the Russian Academy of Science,
Krasnoyarsk, 660036, Russia

High temperature superconductivity is achieved by hole doping of parent compounds, which undergo a phase transition from the antiferromagnetic, insulating state to the metallic and superconducting state. This development can only be studied continuously on few members of the cuprate family. $\text{Bi}_2\text{Sr}_2\text{Ca}_{1-x}\text{Y}_x\text{Cu}_2\text{O}_{8+\delta}$ single crystals where the hole concentration in the two CuO_2 -planes per unit cell ($n=2$) is controlled by the substitution of Ca by Y and $\text{Bi}_2\text{Sr}_{2-x}\text{La}_x\text{CuO}_{6+\delta}$ single crystals where this concentration in the one CuO_2 -plane per unit cell ($n=1$) is controlled by the substitution of Sr by La enable this study of the doping dependence over a wide range of hole concentrations with ARPES. Investigations of antiferromagnetic parent compounds have so far mostly been reported for oxychlorides, like e.g. $\text{Sr}_2\text{CuO}_2\text{Cl}_2$ [1] and discussed within the t - t' - t'' - J model. Since the character of the CuO derived state near the Fermi level is decisive it will be discussed whether this or other models like the generalized tight binding method (GTBM) [2] give an appropriate description.

In the well equipped crystal growth laboratory of our group crystals were grown out of the melt, their quality was proved by Laue and LEED, the super-conducting properties by susceptibility measurements. The stoichiometry and, in particular, the Y- resp La- content was determined by energy dispersive x-ray analysis (EDX). Thus, a wide range of transition temperatures between 93K ($n=2$) resp. 29K ($n=1$) for optimal hole doping and 0K of strongly underdoped superconductors as well as the weakly hole doped insulators have been obtained. For an Y content of $x>0.9$ ($n=2$) resp. La content of $x>0.8$ ($n=1$) the crystals are obviously in the antiferromagnetic insulator phase. The ARPES-experiments were in the early stages of our investigations performed at HASYLAB and then at the U125/2 SGM beamline at BESSY. For the measurements discussed here 18 eV (at HASYLAB) and 40eV and 80 eV (at BESSY) photon energy was used.

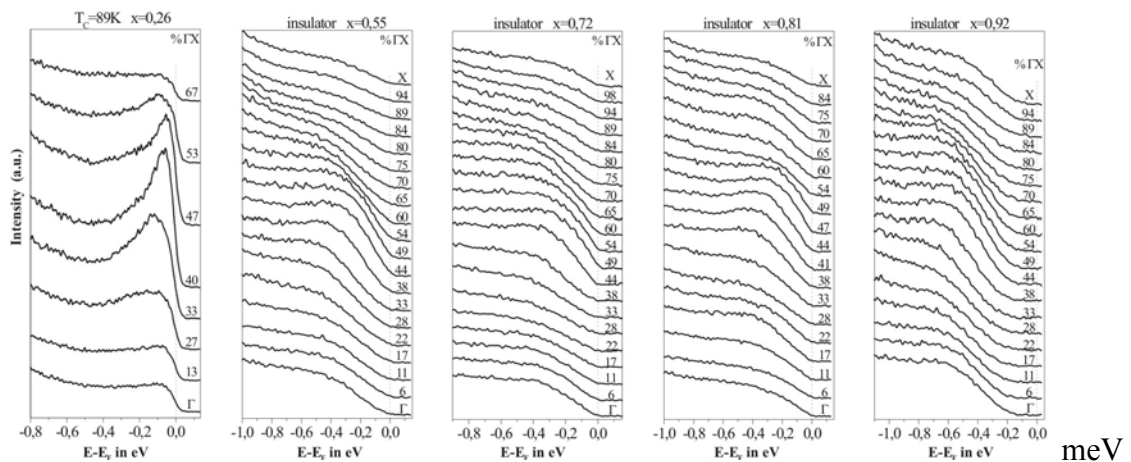


Fig.1. EDC's of $\text{Bi}_2\text{Sr}_2\text{Ca}_{1-x}\text{Y}_x\text{Cu}_2\text{O}_{8+\delta}$ single crystals along the TX direction of the Brillouin zone for different Y- content. The polarization plane of the synchrotron radiation lies in the TM direction. $T=90\text{K}$. Left spectrum: $h\nu=80\text{eV}$, other spectra: $h\nu=18\text{eV}$

The energy distribution curves (EDC) were recorded with hemispherical deflection analysers with a total acceptance angle of 1° and an energy resolution of 40 at BESSY [3] and 80 meV at HASYLAB [4], as determined from an Au Fermi edge.

In fig.1 spectra series of the metallic/superconducting and insulating state of the $\text{Bi}_2\text{Sr}_2\text{Ca}_{1-x}\text{Y}_x\text{Cu}_2\text{O}_{8+\delta}$ single crystals are shown for the ΓX -direction of the Brillouin zone and $T=90\text{K}$. The origin of the dispersing spectral weight near the Fermi level is due to strongly correlated CuO states located in the CuO_2 -planes. For the insulators with Y-content of $0.5 < x < 0.9$ the maximum of the dispersion curve which is very pronounced for $x=0.55$ smears more and more out for larger x . A dramatic change is observed for the $x=0.92$ insulator. The centroid of the band has now been shifted to about 600meV and instead of one dominating maximum in the dispersion curve three equally strong maxima are observable at positions 0%, 50%, and 100% of the ΓX distance of the Brillouin zone. While the 600meV shift is hard to ascribe to a definite reason and possibly due to pinning by defects [5], the appearance of this new state is exciting and new.

All our attempts to obtain the 3 peaks in the dispersion at $(0,0)$, $(\pi/2, \pi/2)$, and (π, π) in the framework of the $t-t'-t''-J$ model failed. That is why we started with a more general model, the 5 band $p-d$ model that takes into account $\text{Cu } d_{x^2-y^2}, d_{z^2}$, in-plane $\text{O } p_x, p_y$, and apical $\text{O } p_z$ single hole atomic states. The effect of strong electron correlations is certainly very important in the insulating phase and in a framework of the multiband pd - model the GTB –method takes into account different intra- atomic Coulomb and Hund exchange interactions at Cu and O sites as well as Cu-O nearest neighbour repulsion. While in the 3-band pd - model the top of the valence band is formed by a dispersion of holes excited into the ZRS state, the new physics in the multiband $p-d$ model results from the ${}^3B_{1g}$ triplet contribution. The triplet counterpart for the ZRS is also known in the 3 -band pd - model with the energy much higher than the ZRS , $\Delta E = E_T - E_S \approx 2eV$, so the triplet is not relevant in the low energy region. This irrelevance appears to be a model dependent result. In the multiband model presented here ΔE sharply decreases due to Hund exchange contributions from $d_{x^2-y^2}^\uparrow d_{z^2}^\uparrow$ configuration and additional bonding with apical oxygen induced t'_{pd} and t'_{pp} hopping (here “ ’ ” refers to the apical p_z orbital). For realistic parameters fitted well the ARPES – results for $\text{Sr}_2\text{CuO}_2\text{Cl}_2$ the value $\Delta E \approx 0.7 \text{ eV}$ and excitation of the extra hole added to the b_{1g} initial state to the triplet ${}^3B_{1g}$ state gives strong admixture near the $(0,0)$ and (π, π) points to the ZR - singlet.

To describe the ARPES in the insulating phase of $\text{Bi}_2\text{Sr}_2\text{Ca}_{1-x}\text{Y}_x\text{Cu}_2\text{O}_{8+\delta}$ we take into account the strong lattice parameter dependence on the Y – content: parameter c decreases and in-plane parameters a, b increase with the Y - concentration x , and neglect the small changes in the hole concentration. Correspondingly changes of the in-plane oxygen t_{pp} hopping and the in-plane apical oxygen hopping t'_{pp} appear. For simplicity the other model parameters are the same as in the undoped CuO_2 layer. The dispersion of the top of the valence band for different Y concentration has then been calculated by the GTB method, whose details will be published elsewhere [5], is shown in FIG.2.

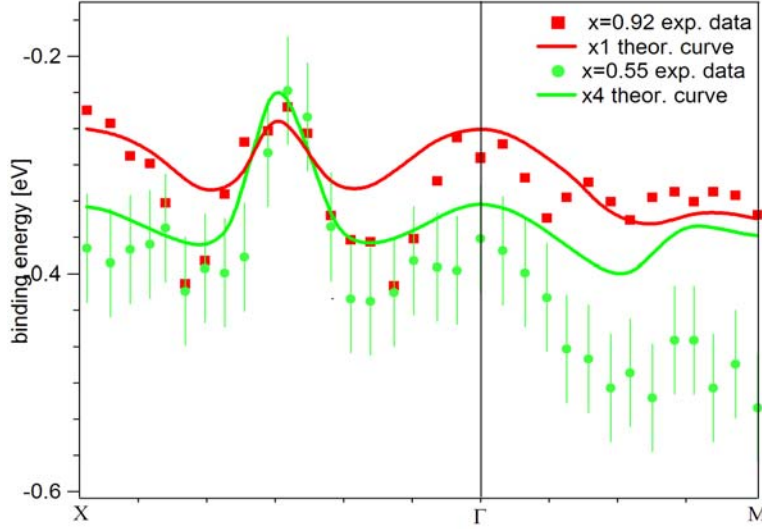


Fig. 2: Comparison of experimental ((red) dots : $x=0.55$, (green) squares: $x=0.92$) versus theoretical (drawn line: $x=0.55$, broken line $x=0.92$) dispersions for the samples with the highest ($x=0.92$) and lowest ($x=0.55$) Y-concentration along . The experimental $x=0.92$ - dispersion has been shifted to obtain a common valence band maximum with the $x=0.55$ -dispersion.

With increasing Y content the three peak structure along the $(0,0) \rightarrow (\pi, \pi)$ direction is clearly observed with the $(\pi/2, \pi/2)$ peak slightly decreasing its energy. Along the $(\pi, \pi) \rightarrow (\pi, 0)$ line there is no significant effect of the Y substitution. These results are in a good agreement to the *ARPES* data. Both states well mix to the one band of first removal states, in spite of the fact that there is essential difference between them. To exclude effects due to the orbital environment of the CuO_2 -planes or due to the photon energy, similar spectra series were done on antiferromagnetic ($n=1$) La-Bi2201. Generally similar dispersions were observed.

In conclusion we have measured that due to the “chemical” pressure effect induced by Y-substitution in $\text{Bi}_2\text{Sr}_2\text{Ca}_{1-x}\text{Y}_x\text{Cu}_2\text{O}_{8+\delta}$, the dispersion of the first removal state shows, at least near the AF phase at $x = 0.92$, a pronounced three peak structure at the $(0,0)$, $(\pi/2, \pi/2)$, (π, π) symmetric points of the BZ. Modeling the changes of the a,b,c lattice parameters in the GTB method with an essential 3-dimensional 5-band pd-model we reproduced the experimental three peaks structure and its concentration dependence. One may say our results indicate that the $(0,0)$ and (π, π) peaks result from the two-hole ${}^3B_{1g}$ counterpart for the Zhang-Rice state near E_F , which appears at far higher binding energies in 2-dimensional 3-band pd-models or t-J models. Our data also support the earlier scenario that the dispersion along the $(\pi/2, \pi/2) \leftrightarrow (\pi, 0)$ direction is strongly reduced by the inclusion of the apical oxygen orbital, and their inclusion is absolutely essential for obtaining the weak dispersion observed experimentally. Thus we offer new good testing ground for the theory of band structure in high-Tc cuprates.

References

- [1] C. Dürr et al., Phys. Rev. B **63**, 014505 (2000) and references therein
- [2] V. Gavrichkov, A. Borisov, S. G. Ovchinnikov, Phys. Rev. B **64**, 235124 (2001)
- [3] C. Janowitz et al., J. Electr. Spectr. & Rel. Phen. **105**, 43 (1999)
- [4] K. Roßnagel et al., Nucl. Instrum. Methods Phys. Res. A **467**, 1485 (2001)
- [5] F. Ronning et al., Phys. Rev. B **67**, 035113 (2003), and references therein

This work is supported by the BMBF (project no. 05 KS1KH11)

TEMPERATURE-DRIVEN CROSSOVER BETWEEN ANTIFERRO- AND FERROMAGNETIC INTERLAYER COUPLING

J.E. Prieto, K. Döbrich, O. Krupin, G. Kaindl, and K. Starke

Institut für Experimentalphysik, Freie Universität Berlin, Germany

We have studied the temperature dependence of the interlayer exchange coupling in rare-earth metal trilayers, using Gd/Y/Tb as a prototype example of a heterostructure with nearly identical lattice parameters of all components. Samples were grown epitaxially by metal vapor deposition on a single crystal W(110) substrate [1]. The thicknesses of the layers were in the range of a few nanometers. While Gd and Tb layer thicknesses were kept fixed, the Y spacer thickness was varied between 0.4 nm and 2.0 nm. Element-specific hysteresis loops of the Gd top layer (magnetically soft) and the Tb bottom layer (magnetically hard) were measured *in situ* by means of x-ray magneto-optical Kerr effect (XMOKE) [2,3]. To this end, the photon energy was tuned to the peaks of the M_5 absorption edges of either Gd or Tb (see Fig. 1).

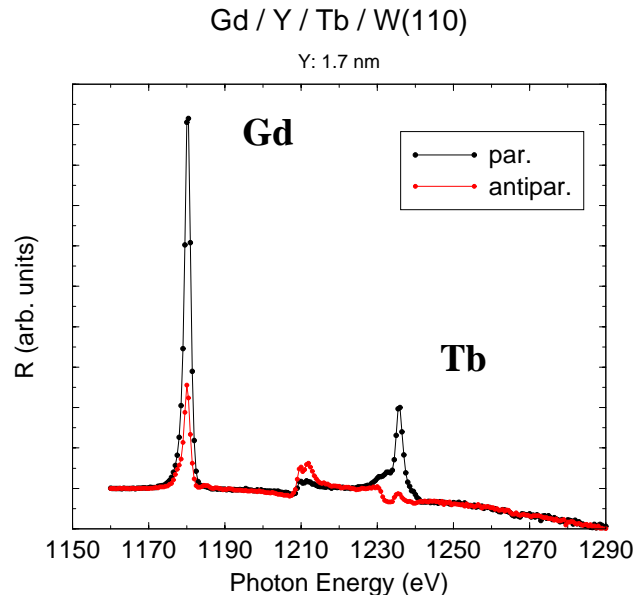


FIG. 1. Soft x-ray reflectivity spectra in the energy range of the Gd $M_{4,5}$ and Tb $M_{4,5}$ absorption edges, recorded at **Beamline UE56/1-PGM**. The angle of incidence was set at 8° with respect to the trilayer film plane. Individual layer thicknesses are $d_{Gd}=2$ nm, $d_Y=1.7$ nm, and $d_{Tb}=10$ nm.

Figure 2 shows hysteresis loops of Gd (a) at temperatures between 12 K and 217 K, each one recorded after a positive or negative *field cooling* (FC), i.e. after cooling the trilayer in an external field (~ 0.2 Tesla) of in plane orientation, along the easy axes of both Gd and Tb. Figure 2(b) shows Tb hysteresis loops over the same temperature range, taken before recording the Gd loops. They allowed us to determine the range of magnetic fields in which the Tb layer magnetization stays nearly constant; it is given by the (temperature dependent) Tb coercive field. The strength of the interlayer exchange coupling (IEC) is determined as a function of temperature from the shifts of the Gd hysteresis loops.

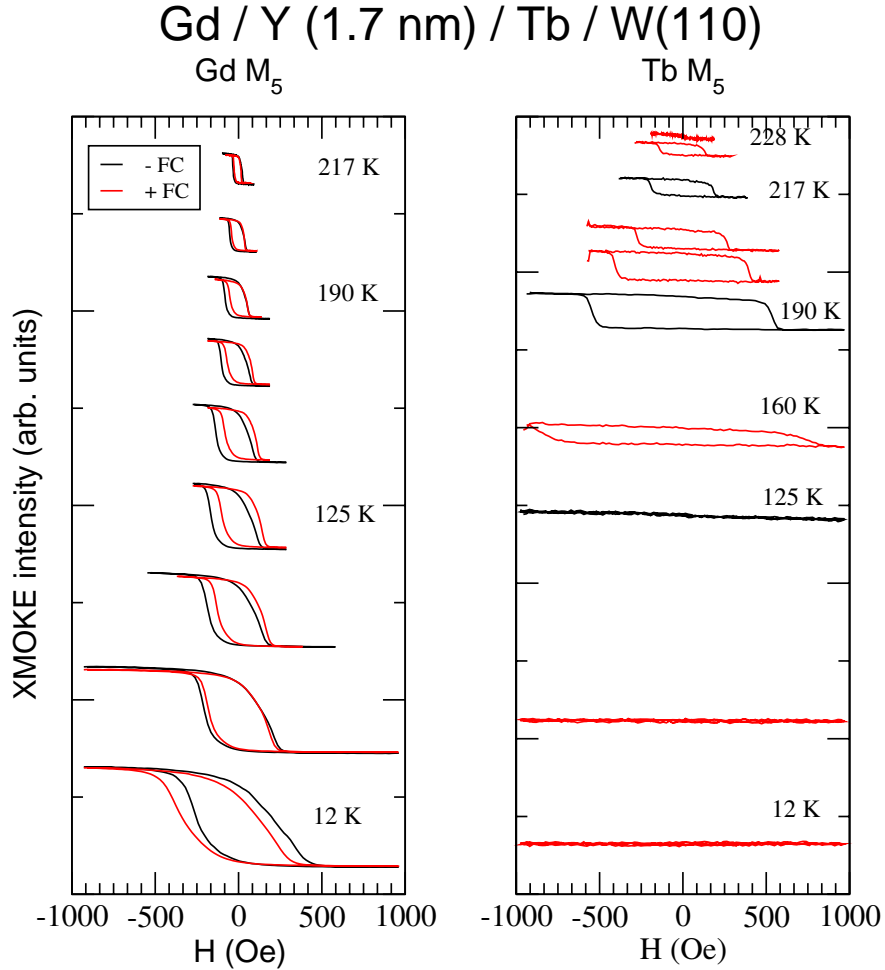


FIG. 2. Element-specific hysteresis loops recorded by XMOKE with the photon energy tuned to the M_5 edge of Gd (left panel) and Tb (right panel). +FC and -FC refer to opposite in plane orientations of the external magnetic field applied during the cooling of the trilayer down to the measurement temperature prior to the recording of each hysteresis loop. The magnetic field applied for the measurement of the Gd loops was kept always below the (temperature dependent) Tb coercive field, as determined by the Tb loops.

The Gd hysteresis loop shifts shows a crossover with temperature from antiferromagnetic (AF) to ferromagnetic (FM) coupling mediated by the Y spacer layer. This behavior has been found for different (but not all) Y spacer thicknesses in the range $d_Y = 0.4..2.0$ nm. While the well-known sign change of IEC with varying spacer thickness is inherent to the indirect (RKKY-type) coupling across metal spacer layers, such a temperature driven AF-F crossover has not been observed before. The phenomenon is tentatively attributed to a magnetization-dependent change in the matching conditions of the valence-band wave functions at the interfaces.

We thank H.-Ch. Mertins for experimental support. This work was financed by the German BMBF, Contract No. 05 KS1 KEC/2.

- [1] K. Starke: *Magnetic Dichroism in Core-Level Photoemission* (Springer, Berlin, Heidelberg, 2000), pp. 29-37.
- [2] K. Starke *et al.*, Phys. Rev. Lett. **86**, 3415 (2001).
- [3] J. E. Prieto *et al.*, Phys. Rev. B **68**, 134453 (2003).

X-ray absorption and resonant photoemission on $\text{Bi}_{2-y}\text{Pb}_y\text{Sr}_{2-x}\text{La}_x\text{CuO}_{6+\delta}$ single crystals

M. Schneider*, N.Z. Timergaleev[#], R.-St. Unger*, A. Krapf*, H. Dwelk*, C. Janowitz*,
R. Mitdank*, R. Manzke*

*Humboldt University Berlin, Germany

[#]Lomonosov University Moscow, Russia

The hole concentration in the copper oxide layers of $\text{Bi}_{2-y}\text{Pb}_y\text{Sr}_{2-x}\text{La}_x\text{CuO}_{6+\delta}$ has been determined directly from X-ray absorption spectroscopy. A series of crystals with varying La-concentration and with roughly the same Pb-concentration around $y = 0.13$ were grown out of the melt. While the concentration of the former element mainly determines the hole concentration, the partial substitution of Bi by Pb suppresses the 1×5 superstructure in the BiO-planes. Besides that the Pb is also known to influence the hole concentration. Also the oxygen concentration, which can be adjusted by annealing in vacuum or oxygen environment, has an effect on the hole concentration. Spectra were recorded at the German-Russian beamline with our XAS-detector attached to the experimental chamber of the beamline. Due to the limited time only three samples could be investigated, two with more than optimal hole concentration (sample X207 with $x(\text{La}) = 0.27$, $y(\text{Pb}) = 0.13$, $T_c = 8\text{K}$, not annealed and sample X203 with $x(\text{La}) = 0.31$, $y(\text{Pb}) = 0.15$, $T_c = 21\text{K}$, 4h annealed in vacuum at 300°C) and one with less than optimal hole concentration (sample X206 with $x(\text{La}) = 0.49$, $y(\text{Pb}) = 0.11$, $T_c = 16\text{K}$, 65h tempered in oxygen at 650°C), as determined by XAS resp. susceptibility measurements. By the temper process the critical temperature was enhanced to the optimum value for the respective doping level. Also the sharpness of the transition to the superconducting state and the purity of the phase increased. The optimum T_c is expected from previous investigations at $x(\text{La}) \sim 0.40$. The measurements at the Cu- L_3 threshold were performed with a resolution of 550meV at LN2-temperature and are depicted in Fig. 1.

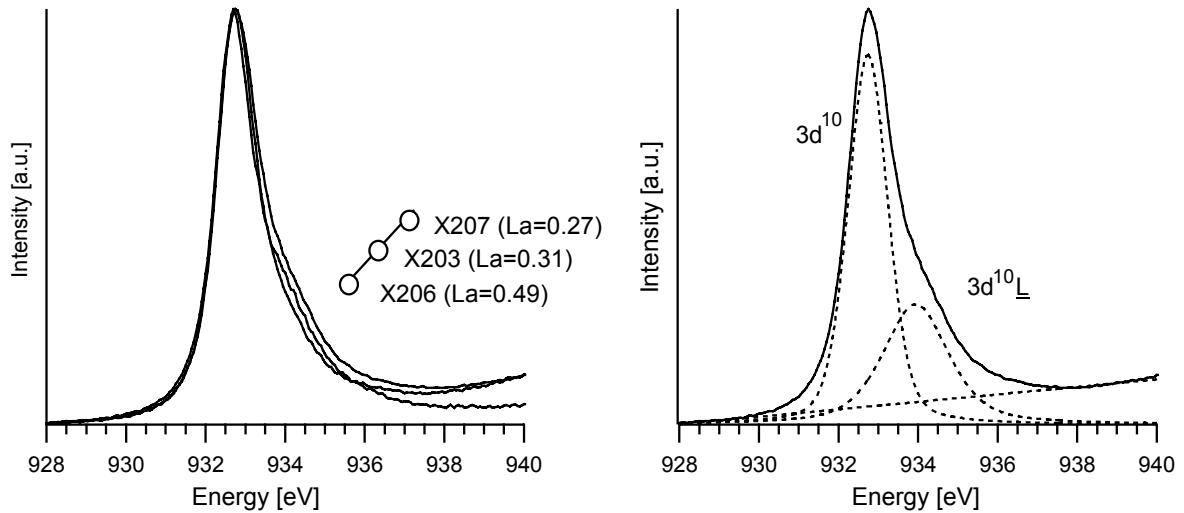


Fig. 1. Direct comparison of spectra with La content as depicted (left) and example of a fit with two Voigt-profiles and subtraction of a linear background on sample X207 ($x(\text{La})=0.27$) (right). The best fit was obtained for an energy difference of 1.4eV.

Besides the main line corresponding to the transition $2p^63d^9 \rightarrow 2p^53d^{10}$ an additional shoulder from the oxygen ligand $2p^63d^9 \underline{L} \rightarrow 2p^53d^{10} \underline{L}$, with \underline{L} representing a hole on the oxygen 2p orbital, occurs. From the relative intensities of the two peaks the hole concentration can be

determined. This method, whose details can be assessed in the literature, was applied for the first time on the BISCO-system by Pham [1], after having been used previously for LSCO [2, 3]. The results from the fit (Fig. 2.) gives absolute hole concentrations for our samples. The method is distinctly different from transport measurements like Hall effect. It is known that optimum T_c should occur at hole concentrations between 0.19 and 0.16.

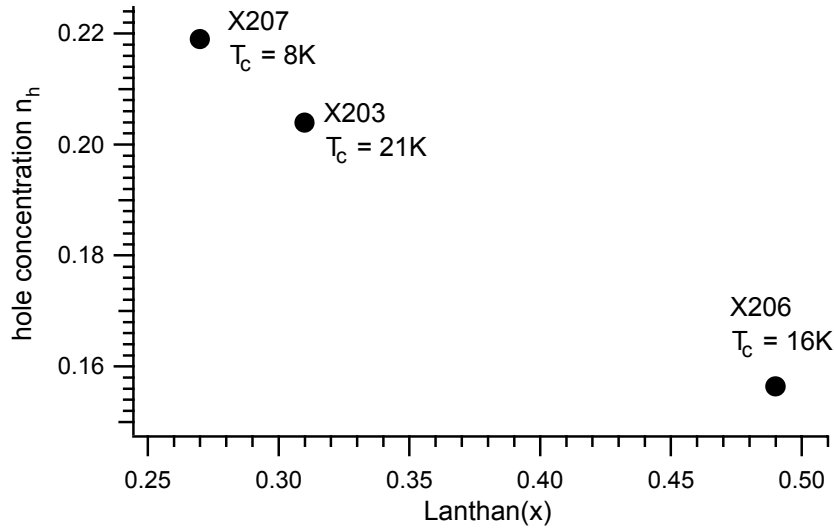


Fig. 2. Hole concentrations as obtained by fits to the data of Fig. 1. From left to right samples X207, X203, X206.

Additionally we also performed resonant photoemission at the Cu- L_3 threshold on the hole underdoped sample X206. In the valence band region mainly the peak corresponding to the Cu $3d^8$ final state at -17.6eV and at higher binding energies the Cu $3p^5 3d^9$ and Cu $3p^5 3d^9$ satellites at -90.0eV and -97.4eV were strongly enhanced, while the Cu $d^9 \underline{L}$ -like state at -9.6eV and the Cu $3p$ -main line at -82.2eV were less affected. The assignment of the structures was performed in reference to Qvarford et al. [4]. A theoretical description of the satellite structure has been given by Seino et.al. [5]. The measurements are to be continued on more samples to enhance the data basis for the cognition of common trends.

- [1] A.Q. Pham, F. Studer, N. Merrien, A. Maignan, C. Michel, and B. Raveau, Phys. Rev. B **48**, 1249 (1993)
- [2] M. Ronay, A. Santoni, A. G. Schrott, L. J. Terminello, S. P. Rowalczyk, and F. J. Himpsel, Solid State Commun. **77**, 699 (1991)
- [3] M. Merrien, A. Studer, C. Michel, P. Srivastava, B. R. Sekhar, N. L. Saini, K. B. Garg, and G. Tourillon, J. Phys. Chem. Solids **54**, 499 (1993)
- [4] M. Qvarford, J.F. van Acker, J.N. Andersen, R. Nyholm, I. Lindau, G. Chiaia, E. Lundgren, S. Söderholm, U.O. Karlsson, S.A. Flodström, and L. Leonyuk, Phys. Rev. B **51**, 410 (1995)
- [5] Y. Seino, H. Ogasawara, A. Kotani, B.T. Thole, and G. van der Laan, J. Phys. Soc. Jpn. **61**, 1859 (1992)

This work is supported by the BMBF (project no. 05 KS1KHA0).

Co/Cu/Ni trilayers close to their Curie temperature: An XMCD study

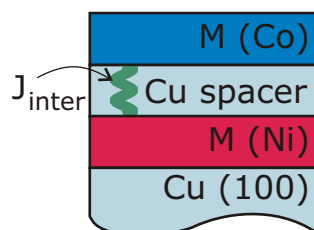
C. Sorg, A. Scherz, H. Wende, M. Bernien, T. Gleitsmann, Z. Li, S. Rüttinger,
Ch. Litwinski, and K. Baberschke

*Institut für Experimentalphysik, Freie Universität Berlin,
Arnimallee 14, D-14195 Berlin-Dahlem, Germany.*

Co/Cu/Ni trilayers are used as a prototype system to study the interlayer exchange coupling J_{inter} [1–5]. In these trilayers the ferromagnetic layers of Ni and Co are coupled through the Cu spacer (Fig. 1). Earlier experiments (carried out in remanence) revealed a separate onset of the magnetization for the different ferromagnetic Ni and Co layers [1]. A remarkable increase ΔT of the lower ordering temperature was observed in the presence of J_{inter} [1, 2]. Theoretical investigations addressed this effect to 2D spin-fluctuations [6]. Generally, the influence of spin-fluctuations is enhanced in 2D systems leading to a reduction of the Curie temperature T_C for ultrathin films compared to the bulk. An interlayer exchange coupling suppresses these spin-fluctuations and therefore the ordering temperature rises. The exchange coupling acts not only as a static exchange field but it influences also by higher order contributions the dynamics of the fluctuating spins. Therefore, a tail in the temperature-dependent magnetization of the Ni film is expected near the order-

ing temperature [6, 7]. However, this tail was not observed in the earlier experiments. As the earlier experiments were carried out in remanence they could not entirely exclude effects that might arise due to the formation of magnetic domains near the ordering temperature. Therefore, new investigations under a small applied magnetic field are done. The question of a tail of the Ni magnetization is clarified thanks to the new undulator beamlines at third generation synchrotrons like BESSY II. Taking advantage of the high-photon flux together with the high and constant degree of circular polarization small magnetic signals near T_C can be measured with sufficient signal to noise ratio. In the present work the individual magnetizations of Co and Ni in coupled Co/Cu/Ni trilayers are studied by the virtue of the element-specific X-ray magnetic circular dichroism (XMCD) in remanence as well as in a small applied magnetic field [8]. Hysteresis loops and temperature-dependent magnetization curves are investigated with particular interest in the Ni magnetization near the Ni ordering temperature T_C^{*Ni} .

Figure 1: In Co/Cu/Ni/Cu(100) trilayers the ferromagnetic layers of Co and Ni are coupled through the Cu spacer.



The Co/Cu/Ni trilayers were prepared *in situ* like in the earlier experiments [1, 3]. We measured the drain current while applying a positive voltage to a metallic grid near the sample to ensure the complete extraction of the emitted electrons also under a small magnetic field at the undulator beamline UE56/1-

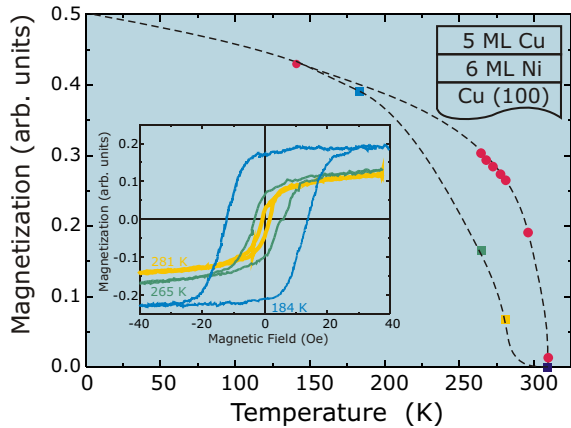


Figure 2: Temperature-dependent Ni magnetization of a 5ML Cu/6ML Ni/Cu(100) bilayer system in a constant applied magnetic field ($H = 40$ Oe, open circles), and at remanence determined from hysteresis loops (solid squares). The dashed lines serve as guides to the eyes. The inset shows the Ni hysteresis at three different temperatures.

PGM. The XMCD signal at the maximum of the L_3 edge (normalized to a constant edge jump) is proportional to the element-specific magnetization $M(T)$. To determine the hysteresis loops we measured the field-dependent XMCD signal at the L_3 maximum.

Figure 2 presents the magnetization of a 5ML Cu/6ML Ni/Cu(100) bilayer system in a constant applied magnetic field ($H = 40$ Oe, open circles), and at remanence determined from hysteresis loops (solid squares). The inset shows the Ni hysteresis. Above $T \approx 200$ K the remanent magnetization decreases considerably faster than the one in the applied magnetic field. Such a behavior has been observed in ultrathin Ni/Cu(100) films [9] using the polar magneto-optical Kerr effect. It can be explained by the formation of magnetic domains near the Curie temperature of these films. Applying a small magnetic field of $H \approx 30$ Oe is, in our case, sufficient to bring the sample into a single domain state even close to the Ni ordering temperature. Only by measuring on a single domain film one will obtain the proper magnetization in vicinity of T_C . However, the applied magnetic field should be small so that

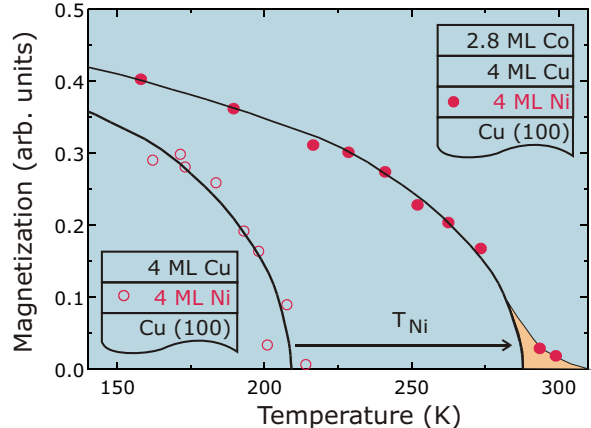


Figure 3: Ni magnetization of a trilayer before (open circles) and after (solid circles) evaporation of the Co layer measured at $H = 40$ Oe.

it does not produce additional field-induced magnetization in the sample.

In Fig. 3 the temperature-dependent magnetization of Ni in a coupled trilayer measured at $H = 40$ Oe both before (open circles) and after evaporation of the Co layer (solid circles) is shown. At first, a 4 ML Ni film capped with 4 ML Cu was studied (open circles). Then we ‘turned on’ the coupling by evaporating 2.8 ML Co onto the same sample. The Ni magnetization in the trilayer (solid circles) vanishes at a temperature $T_C^{*Ni} \approx 290$ K which is $\Delta T_{Ni} \approx 80$ K higher than for the bilayer system. The large ΔT_{Ni} confirms the results of Refs. [1, 2]. They cannot be addressed to effects of magnetic domains any more.

Theoretical investigations in a Heisenberg, i.e. localized, model have to take spin-fluctuations, i.e. higher order contributions in the spin dynamics, into account to explain the shift of the Curie temperature [6]. A second theoretical study within an itinerant single-band Hubbard model reveals the same effects [7]. Although an itinerant model is more appropriate for 3d transition metals, the results of both approaches are in good agreement with the experiment yielding a strong shift ΔT_{Ni} to larger values after the Co film has been evaporated on top, i.e. after the exchange coupling has been switched on.

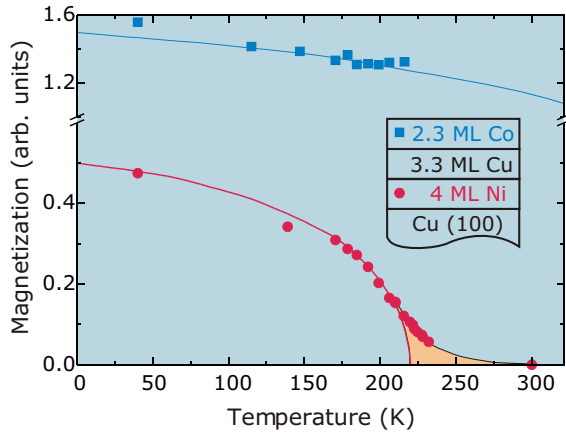


Figure 4: Individual Ni and Co magnetization of a Co/Cu/Ni trilayer. A tail in the Ni magnetization near the ordering temperature is clearly visible.

Figure 4 shows the individual Ni and Co magnetization curves for a 4 ML Ni/3.3 ML Cu/2.3 ML Co trilayer sample measured under a small applied field. In our new experiments in a temperature range close to T_C , we observe a tail of the Ni magnetization which is clearly out of the noise. This tail in $M(T)$ is predicted in both theoretical investigations the itinerant approach and the localized Heisenberg model [6, 7].

In summary, we have investigated the element-specific magnetization curves of Co/Cu/Ni trilayers under applied magnetic fields up to $H = 40$ Oe. We rule out the formation of magnetic domains and observe a considerable large shift of the Ni ordering temperature upon evaporation of a Co layer on top of a Cu/Ni bilayer. Close to the Ni ordering temperature a tail in $M(T)$ is evidenced. Both findings are in agreement with theoretical investigations in an itinerant approach as well as in a localized picture. They demonstrate that spin-fluctuations are of much more importance in 2D systems than in bulk.

This work was supported by the BMBF (05 KS1 KEB 4).

References

- [1] U. Bovensiepen, F. Wilhelm, P. Srivastava, P. Pouloupoulos, M. Farle, A. Ney, and K. Baberschke, Phys. Rev. Lett. **81**, 2368 (1998).
- [2] A. Scherz, F. Wilhelm, U. Bovensiepen, P. Pouloupoulos, H. Wende and K. Baberschke, J. Magn. Magn. Mat. **236**, 1 (2001).
- [3] P. Pouloupoulos and K. Baberschke, Lecture Notes in Physics, Springer **580**, 283 (2001).
- [4] W. Kuch, L. I. Chelaru, K. Fukumoto, F. Porrati, F. Offi, M. Kotsugi, and J. Kirschner, Phys. Rev. B **67**, 214403 (2003).
- [5] C. Won, Y. Z. Wu, A. Scholl, A. Doran, N. Kurahashi, H.W. Zhao, and Z.Q. Qiu, Phys. Rev. Lett. **91**, 147202 (2003).
- [6] P. J. Jensen, K.H. Bennemann, P. Pouloupoulos, M. Farle, F. Wilhelm, and K. Baberschke, Phys. Rev. B **60**, R14994 (1999).
- [7] J. H. Wu, T. Herrmann, M. Potthoff, and W. Nolting, J. Phys: Cond. Mat. **12**, 2847 (2000).
- [8] C. Sorg, A. Scherz, H. Wende, T. Gleitsmann, Z. Li, S. Rüttinger, Ch. Litwinski, and K. Baberschke, XAFS XII, June 2003, Sweden, accepted Physica Scripta (2003).
- [9] P. Pouloupoulos, M. Farle, U. Bovensiepen, and K. Baberschke, Phys. Rev. B **55**, R11961 (1997).

Interfaces of reactively evaporated In_2O_3 films

Y. Gassenbauer, A. Klein

Darmstadt University of Technology, Institute of Materials Science, D-64287 Darmstadt

L. Korte, A. Schöpke, T. Lußky, M. Schmidt

Hahn Meitner Institut, Abt. Silizium Photovoltaik, D-12489 Berlin

Transparent conducting oxides (TCOs) are widely used as electrodes in thin film solar cells and other optoelectronic devices. ITO ($\text{In}_2\text{O}_3:\text{Sn}$) and SnO_2 are used in CdTe and a-Si:H solar cells, while ITO is also used as contact to organic LEDs. In the latter case ITO is used for hole injection although being a degenerated n-type semiconductor. In order to optimise contact properties it is necessary to understand TCO surface and interface properties. This shall be achieved by systematic studies of in situ prepared and therefore contaminant free TCO films and different contact materials. We have studied the electronic properties of In_2O_3 films prepared by reactively evaporated metallic In and the interface properties with Si as well as ZnPc as a widely used organic semiconductor. The deposition chamber was attached to a photoelectron spectrometer system connected to the U49-2/PGM2. In_2O_3 was made by reactively evaporated metallic In from a homemade effusion cell in an atmosphere containing O^{2-} ions from an oxygen ion source. Hydrogen passivated crystalline Si substrates were prepared by wet chemical treatment. The ZnPc Films were thermally deposited using homemade effusion cells.

Si2p photoelectron spectra of a crystalline Silicon substrate with increasing In_2O_3 thickness are shown in Fig.1(a). The evolution of the In_2O_3 valence band maximum is determined from In3d and O1s binding energies with respect to the measured valence band. For silicon the evolution was calculated from the Si2p binding energies where the distance to the valence band is taken as 98.74eV^1 . Whereas the valence band position of the silicon remains constant, big changes can be observed for In_2O_3 . This can be due to variations in the oxygen vacancy concentration with increasing film thickness² leading to a doping gradient. The lower valence band position for low coverages can be explained by an increased oxygen vacancy concentration since oxygen reacts to SiO_x as can be observed in the Si2p spectra. The valence band position after a deposition time of approximately 1900 s indicates almost midgap Fermi level position at the In_2O_3 surface ($E_g(\text{In}_2\text{O}_3) = 3.6\text{eV}$).

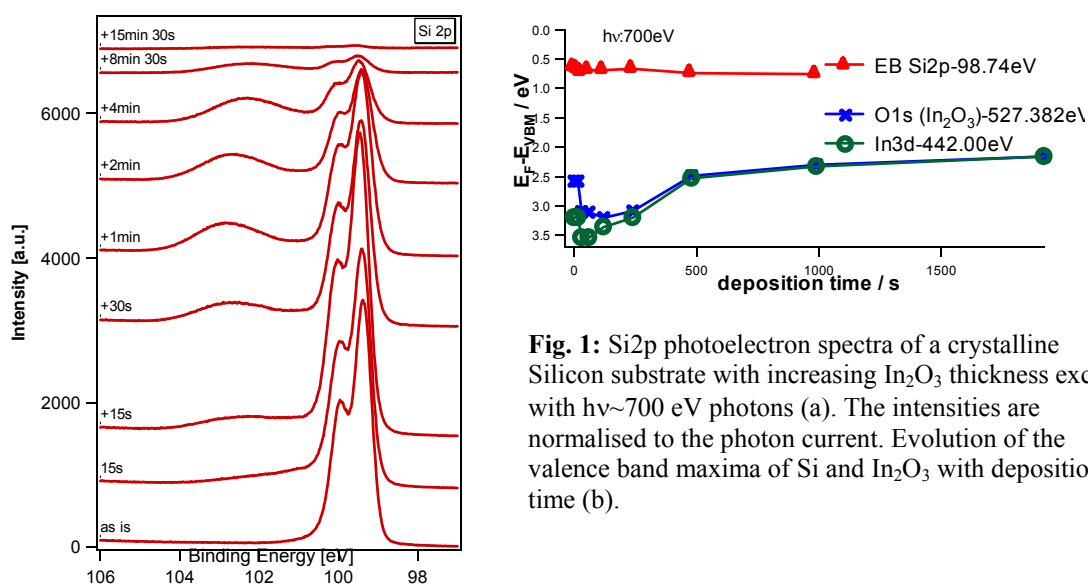


Fig. 1: Si2p photoelectron spectra of a crystalline Silicon substrate with increasing In_2O_3 thickness excited with $h\nu \sim 700\text{eV}$ photons (a). The intensities are normalised to the photon current. Evolution of the valence band maxima of Si and In_2O_3 with deposition time (b).

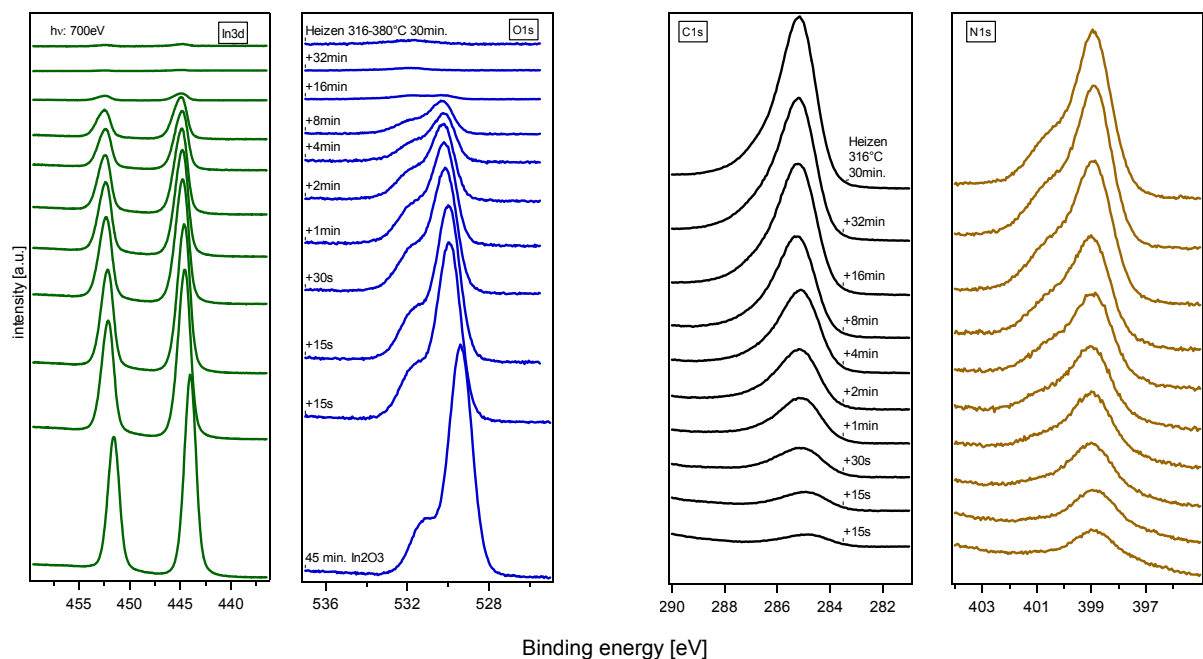


Fig. 2: In3d, O1s, C1s and N1s photoelectron spectra of an In₂O₃/ZnPc interface with increasing ZnPc thickness excited with $h\nu \sim 700$ eV photons. The intensities are normalised to the photon current.

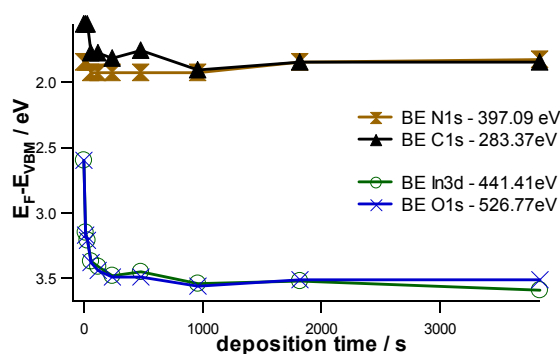


Fig. 3: Evolution of the valence band maximum of In₂O₃ and ZnPc with deposition time. The evolutions are determined for different core levels where the distance to the valence band maxima are well known.

To examine the influence of an organic semiconductor on the Fermi level position and therefore electronic properties of the interface, ZnPc was directly deposited on freshly prepared In₂O₃ films by thermal evaporation. The photoelectron spectra of the ZnPc deposition on In₂O₃ are shown in Fig.2, the evolution of the valence band maximum of In₂O₃ and the HOMO level of ZnPc with deposition time in Fig.3. Again the evolution of the valence band was calculated by the mentioned core levels and the known energy shift with respect to the valence band and HOMO level, respectively. Little changes with film thickness can be observed in the HOMO-level of the organic semiconductor. The large changes in the In₂O₃ valence band position point to a rearranging of the Fermi level leading to a higher hole injection barrier. This can be explained by taking into account the O1s spectra considering the intensity ratio between the high energetic shoulder and the main emission line. With increasing deposition time the intensity ratio change can be associated to an interface reaction with the ZnPc causing an oxygen depletion in the In₂O₃. Consequently a metallic shoulder appears in the In3d spectra of high coverages. The reaction products can not be indentified so far as no changes in the C1s and N1s spectra are observed. In addition the ZnPc valence band spectra are different to earlier experiments using nonreactive substrates. This could indicate that the entire deposited ZnPc is involved in the interface reaction. To clarify the origin of the modified Fermi level position further experiments are required. The interface reactions depend strongly on the film properties, which can be modified by the preparation process. To achieve the necessary energy resolution and surface sensitivity it is important to take the advantage of synchrotron radiation.

¹ G. Hollinger et al., J. Vac. Sci. & Tech. A 1, 640 (1983).

² A. Klein, Appl. Phys. Lett. 77, 2009 (2000).

A systematic study of embedded atom EXAFS: the (2×1)O/Cu(110) reconstruction as an ideal prototype system

H. Wende¹, Ch. Litwinski¹, A. Scherz¹, T. Gleitsmann¹, Z. Li¹, C. Sorg¹, K. Baberschke¹,
A. Ankudinov², J.J. Rehr², Ch. Jung³

¹Institut für Experimentalphysik, Freie Universität Berlin, Arnimallee 14, D-14195 Berlin-Dahlem, Germany

²Department of Physics, Box 351560, University of Washington, Seattle, Washington 98195, USA

³BESSY GmbH, Albert-Einstein-Str. 15, D-12489 Berlin-Adlershof, Germany

This work provides further insight into the so-called atomic EXAFS (AXAFS) effect by investigating the angular dependence of the x-ray absorption coefficient for a strongly anisotropic surface system [1]. While the regular EXAFS stems from the backscattering of the photoelectron at neighboring atoms the AXAFS contribution is assigned to the scattering at the charge densities placed between the atoms. Therefore, the AXAFS contribution to the entire fine structure of the x-ray absorption coefficient should be highly directional for systems with strong anisotropic bonding. This is the case for the reconstructed (2×1)O/Cu(110) surface system discussed here. There is general agreement that the O atoms are located in a long-bridge position along the [001] direction (see figure 1) forming O-Cu rows on the surface [2]. This C_2 symmetry results in a non-spherical scattering potential for the photoelectron. Therefore, a definite angular dependence of the AXAFS features is expected and reported for the first time in [1]. Obviously, the O-Cu bond in the surface plane is highly directional. There are two different types of bonds between the oxygen atoms and the first two Cu layers: The first bonding is between the O atoms (being located nearly in the surface plane) and the two Cu atoms of the first layer. The second bond is to the second layer. This local structure makes the (2×1)O/Cu(110) surface an ideal candidate to study the angular dependence of the atomic EXAFS contribution. Therefore, temperature-dependent surface EXAFS (SEXAFS) measurements at the

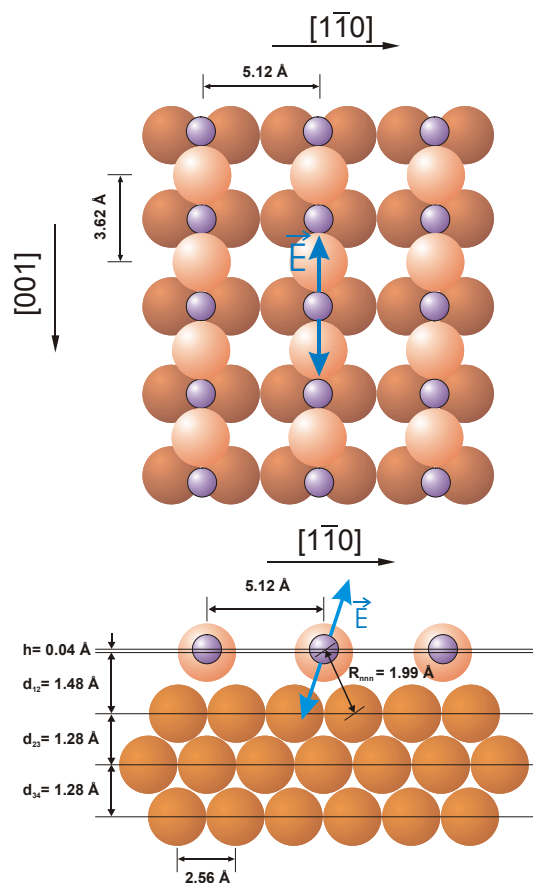


Fig. 1: Schematic representation of the adsorption geometry for the (2×1)O/Cu(110) system in top view (top) and side view (bottom) as determined from this work [1]. Small spheres: oxygen atoms, large lighter spheres: Cu atoms of the first layer, darker spheres: Cu atoms of the second and following layers.

oxygen K-edge were carried out for various polar and azimuthal orientations.

The presence of the controversial AXAFS effect (see e.g. [3-9]) was definitively observed for the low Z elements nitrogen and oxygen for the (2×3) N/Cu(110) and $(\sqrt{2} \times \sqrt{2})R45^\circ$ O/Cu(100) systems [10,11]. However, the lack of

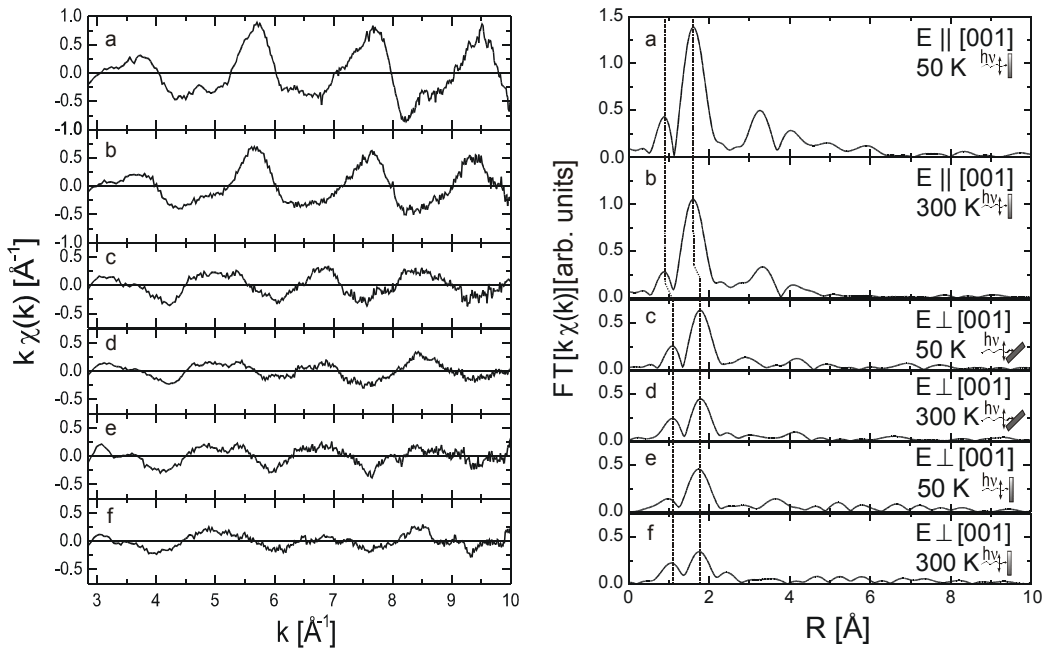


Fig. 2: SEXAFS oscillations $k \cdot \chi(k)$ (left) and the corresponding Fourier transforms $|FT[k \cdot \chi(k)]|$ (right) for the system (2×1)O/Cu(110). The AXAFS and nearest neighbor contributions are marked with the dotted vertical lines.

attention to the AXAFS effect over years was partly due to the non-availability of high quality EXAFS data. These data can be nowadays achieved at the new 3rd generation synchrotron sources where the gap of the undulator is scanned parallel to the monochromator. Light adsorbates on metal surfaces are established as a model systems for this kind of investigation since no multi-electron excitations can mimic the long-range oscillatory fine structure in the x-ray absorption coefficient [10,11] as it can be the case for heavier atoms [6-9].

The detailed analysis of the SEXAFS wiggles is carried out in k -space as it is presented in the left side of figure 2. The temperature-dependent data (50 K, 300 K) for the various polar and azimuthal orientations of the crystal are shown. The damping of the SEXAFS signals at 300 K is due to the larger dynamic disorder described by the mean square relative displacement $\sigma^2(T)$ which enters into the EXAFS Debye-Waller factor. At normal incidence with the E-vector parallel to the O-Cu rows ($E \parallel [001]$) the nearest neighbor bond R_{nn} is probed (figure 2a,b). Whereas

at grazing and at normal x-ray incidence with the E-vector perpendicular to the O-Cu rows ($E \perp [001]$) the next nearest neighbor bond R_{nnn} of the O-atoms to the second layer is analyzed (figure 2c,d,e,f). That indeed two different bonds are probed can be seen by looking at the different phases of the SEXAFS oscillations in the k -space (figure 2 left) for a,b compared to c,d,e,f. Correspondingly, the main peak position in the Fourier transform (figure 2 right) is shifted to larger distances for c,d,e,f as indicated by the right vertical lines. Now we turn to the investigation of the peak located at about half of the nearest neighbor distance (Fourier transforms a,b in figure 2) or at half of the next nearest neighbor distance (Fourier transforms c,d,e,f in figure 2), respectively. These contributions marked by the left vertical lines are assigned to the AXAFS contribution. Obviously these contributions shift systematically according to the bond which is probed. This demonstrates that these structures located at about 0.9 \AA (AXAFS nearest neighbor) and 1.1 \AA (AXAFS next nearest neighbor) cannot be artifacts due to

possible multi-electron excitations (MEEs) as discussed by Filipponi *et al.* [6,7]. This is because MEEs lead to structures at a fixed energy in the x-ray absorption coefficient $\mu(E)$. Therefore, features that originate from MEEs would show up at the same distance R in the Fourier transform, independent of the measuring geometry. The same argument is true for experimental artifacts which could be due to improper normalization of the data. Hence, the dependence of the AXAFS peak position on the bond being probed is a strong indication that this feature indeed stems from the scattering at interstitial charges between the absorbing and the backscattering atom.

In conclusion, we present surface EXAFS data nearly free of noise measured at a third generation synchrotron radiation facility. This enabled us to clearly identify the atomic EXAFS contribution in the spectra for the $(2\times 1)\text{O}/\text{Cu}(110)$ surface system where the oxygen coverage is 0.5 atomic layer only. It turns out that this system is an ideal prototype system for investigating the AXAFS since the O-Cu bonding is highly directional. Our angular-

dependent study showed that the position of the AXAFS contribution in the Fourier transform reflects the anisotropy of the bond being probed. This gives the unique opportunity to measure the anisotropy of the local embedded atom potential for the first time. Since the x-ray absorption of the low Z atom oxygen is investigated, no multi-electron excitations can mimic such a contribution. Therefore, the appearance of this feature can indeed be related to the scattering of the photoelectron at interstitial charge densities. The comparison to *ab initio* calculations [1] shows that the position and the lineshape of the AXAFS contribution in the Fourier transform can be modeled theoretically. A full-potential calculation is needed in the future to reproduce the experimentally determined angular dependence. Our combined experimental and theoretical work [1] may help to study the charge densities, that are responsible for the bonding for instance in oxides, in more detail in future works. This work is supported by the BMBF (05 KS1 KEB 4).

References:

- [1] H. Wende, Ch. Litwinski, A. Scherz, T. Gleitsmann, Z. Li, C. Sorg, K. Baberschke, A. Ankudinov, J.J. Rehr and Ch. Jung, *J. Phys.: Condens. Matter* **15** (2003) 5197
- [2] U. Döbler, K. Baberschke, J. Haase, A. Puschmann, *Phys. Rev. Lett.* **52** (1984) 1437
- [3] B.W. Holland, P. Pendry, R.F. Pettifer and J. Bordas, *J. Phys. C: Solid State Phys.* **11** (1978) 633
- [4] J.J. Rehr, C.H. Booth, F. Bridges, S.I. Zabinsky, *Phys. Rev. B* **49** (1994) 12347
- [5] A. Di Cicco, A. Filipponi, *Phys. Rev. B* **49** (1994) 12 564
- [6] A. Filipponi, A. Di Cicco, *Phys. Rev. A* **52** (1995) 1072
- [7] A. Filipponi, A. Di Cicco, *Phys. Rev. B* **53** (1996) 9466
- [8] J.J. Rehr, C.H. Booth, F. Bridges, S.I. Zabinsky, *Phys. Rev. B* **53** (1996) 9468
- [9] G.E. van Dorssen, D.C. Koningsberger, D.E. Ramaker, *J. Phys.: Condens. Matter* **14** (2002) 13529
- [10] H. Wende, P. Srivastava, R. Chauvistré, F. May and K. Baberschke, *J. Phys.: Condens. Matter* **9** (1997) L427
- [11] H. Wende and K. Baberschke, *J. Electr. Spectr. Relat. Phenom.* **101-103** (1999) 821

X-ray absorption and Mössbauer spectroscopy study of magnetic oxide nanostructures of a given topology.

E.G. Zemtsova^a, V.M. Smirnov^a, A.S. Vinogradov^b, S.I. Fedoseenko^b, V.G. Semenov^a,
V.V. Panchuk^a, D.V. Vyalikh^c, S.L. Molodtsov^c, I.V. Murin^a

^a *St. Petersburg State University, Department of Chemistry, 198504 St. Petersburg, Russia*

^b *V.A. Fock Institute of Physics, St. Petersburg State University, 198504 St. Petersburg, Russia*

^c *Institut für Festkörperphysik, Technische Universität Dresden, D-01062 Dresden, Germany*

According to studies of the recent decade, the substances of nanoscale size have properties distinguished them both from molecules and bulk solids. We should like to note that while physical-chemical parameters of three-dimensional oxide nanoparticles were studied in detail, the features of quasi-two-dimensional oxide nanostructures (nanolayers) were less studied. A such situation is possible because scientific base of synthesis of these nanostructure was not developed.

For realization of the reproducible synthesis of oxidation nanostructures it is important to reveal the chemical structures of the nanolayers (from 1 up to several tens) of element-oxygen groups on a surface of the substrate. In the present work we have carried out measurements of the high resolution on the Fe $2p_{3/2}$ и Si $2p$ adsorption spectra, and also measurements by a method of the Mössbauer spectroscopy. The quasi two-dimensional nanostructures (nanolayers) of the Fe-O of various thickness on the flinty monocrystalline substrates (Fe-O) n/Si (III) was used as objects.

Synthesis of the samples, containing on a surface of silicon various quantities element-oxygen monolayers, carried out at temperature 200 °C by the method molecular lay-up (ML-ALD) [1]. The industrial monocrystalline silicon of mark SD, 14-20 class of cleanliness was used in work. The firm FeCl₃ of mark of chemical cleanliness, temperature of sublimations - 312 °C was used as a reagent. Thickness of the put layers was defined by the ellipsometric method on the laser photometric ellipsometer LEPH-2. The light wave-length for exhausted laser is $\lambda = 0.63 \mu\text{m}$, the hade of ray is 45°. Mössbauer spectra by way of sliding geometry [2] were made to the laboratory of the Mössbauer spectroscopy of the Chemical Institution of the St.-Petersburg State University by using the Co band source in matrix of Ra. For realization of the elaboration of obtained results, except for the spectra of sliding drop, to received the spectrum of conversion electrons at $\theta = \mu/2$ for the preliminary determination of operation factors of compounds lying on surface.

The X-ray absorption investigation of similar structures has been conducted at the first time. In the first stage of the present study the main aim was to elucidate capabilities of X-ray absorption spectroscopy to characterize a quality of the nanostructures prepared ex situ at different times and a chemical state of iron atoms in systems under study. Therefore, the Fe $2p_{3/2}$ absorption spectra of FeO, FeCO₃, Fe(acac)₃, and Fe₂O₃ were also taken under the same experimental conditions for reference. All of the absorption spectra of nanostructures were taken detecting the total electron yield from the samples fixed onto a manipulator holder with a cohesive carbon tape. For the reference compounds the total electron yield spectra were measured from powder samples on the carbon tape. The estimated photon-energy resolution at the Fe $2p_{3/2}$ edge (~710 eV) and at the Si $2p$ edge (~100 eV) was about 120 and 20 meV, respectively. The spectra were normalized to the photocurrent acquired from a gold mesh placed at the beamline exit. The photon energy in the range of the fine structure of the Fe $2p$ absorption edge was calibrated using the known position (683.9 eV) of the first narrow peak in the F $1s$ absorption spectrum of K₂TiF₆ [3]. The Si $2p$ spectra were calibrated energetically with the Si $2p_{3/2}$ absorption edge of the crystalline silicon of which the energy position (99.8 eV) is well known [4].

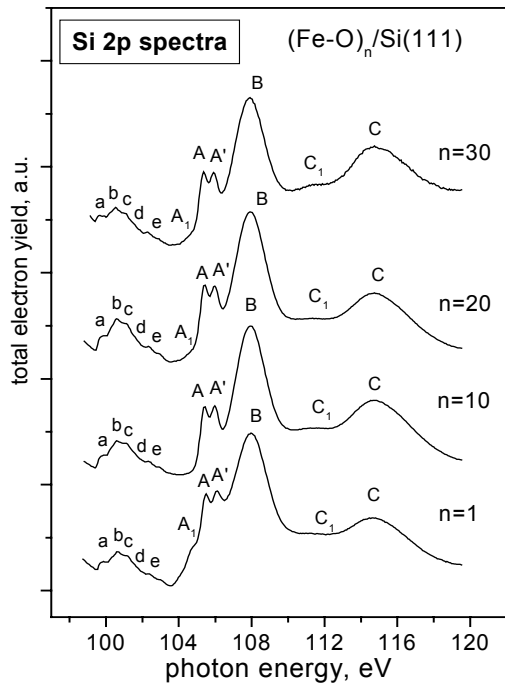


Fig. 1. Si 2*p* absorption spectra of $(\text{Fe-O})_n/\text{Si}(111)$ nanostructures.

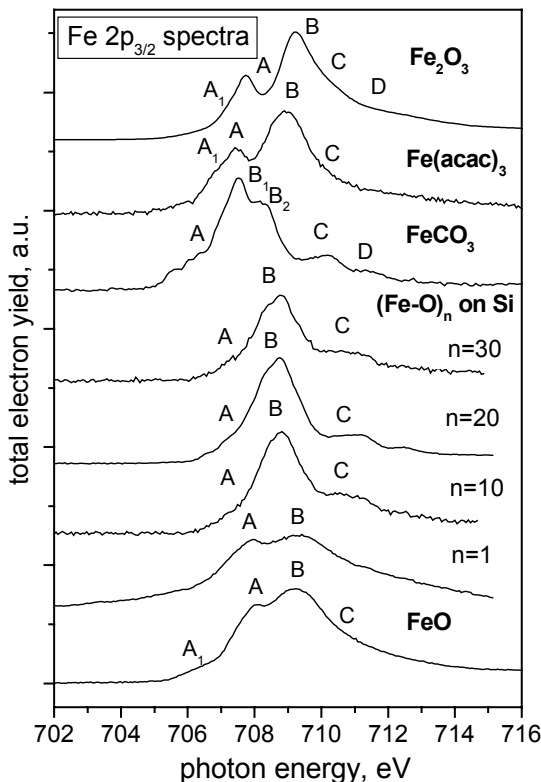


Fig.2. Fe 2*p*_{3/2} absorption spectra of $(\text{Fe-O})_n/\text{Si}(111)$ nanostructures.

in more accordance with those of the absorption structures in the spectrum of $\text{Fe}(\text{acac})_3$ with the three-valence iron atoms. On this basis, the mixed valence of the Fe atoms in the ordered $(\text{Fe-O})_n/\text{Si}(111)$ is suggested.

The distinct spectral shape of the one- monolayer spectrum and its much larger width in comparison to the spectra of the structures with $n \geq 10$ is evidence for a bad structural ordering in the one-monolayer Fe-O structure on the silicon surface.

Fig. 1 shows the Si 2*p* absorption spectra of the $(\text{Fe-O})_n/\text{Si}(111)$ nanostructures with a different number (*n*) of the Fe-O layers. These spectra involve the absorption structures from the crystalline silicon substrate, *a – e*, and those from the silicon oxide interface layer between the $(\text{Fe-O})_n$ layers and substrate, *A₁ – C*.

This identification results from the direct comparison between the spectra obtained and the well known ones of the crystalline silicon and silicon oxides, e.g. [3]. It is very interesting that the spectral shape of the absorption structures from the substrate and the interface as well as their energy positions and relative intensities depend only slightly on the number of the (Fe–O) layers. This is indicative of a very good reproducibility of the ML-CLD method used for the preparation of the above nanostructures. At the same time, the very high intensity of the interface structures in comparison to those of the Si substrate should be noted. Taking into account

results of the Ref. [5], the interface silicon oxide layer can be considered as a SiO_2 (*A*, *A'*, *B*, and *C*) and SiO_x (*A₁*) composition and its thickness can be estimated at several tens of Å. The measured Fe 2*p*_{3/2} spectra of the $(\text{Fe-O})_n/\text{Si}(111)$ nanostructures and reference iron compounds are presented in Fig. 2. The reference ones correlate well in absorption structures and their energy positions with the high-resolution Fe 2*p*_{3/2} spectra measured previously [6]. As is seen from the figure, the absorption spectra of the thick ($n=10, 20, 30$) nanostructures are very similar in appearance and differ considerably from the spectrum of the monolayer ($n=1$). This means that for the thick ($n \geq 10$) nanostructures most of the iron atoms have closely related chemical states and thus these structures are already organized

by an orderly fashion. By comparing with the spectra of the reference compounds, the most similarity in shape is observed for the spectra of the nanostructures and FeCO_3 in which the iron atoms are two-valence. At the same time, the absorption structures in the spectra of the nanostructures are shifted to higher photon energies and have the energy positions which are

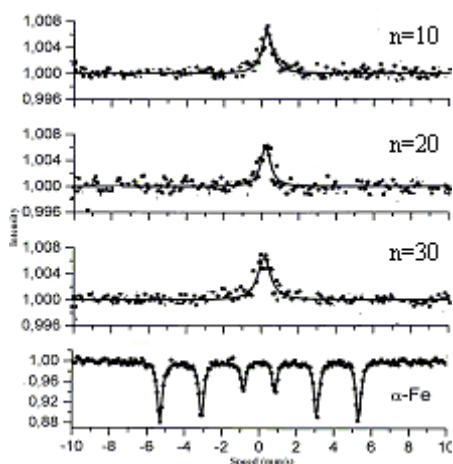


Fig.3. Mössbauer spectra of samples 10 Fe-O/Si, 20 Fe-O/Si, 30 Fe-O/Si

At the same time the Mössbauer spectra indicate to presence of Fe-O groups as Fe⁽⁺³⁾-O groups. Really the operation factors of chemical shift (value Δ from 0.17 to 0.31 mm/sec) shows that Fe in Fe-O groups find as the trivalent low pertaining to spin condition. The singlet line in an experimental spectrum indicates to absence of quadruple expansion. It shows that there is no the gradient of electric field, i.e. the spherical symmetry of electric environment takes place. On the other hand the presence of wide singlet in experimental spectra allows to draw a conclusion, that the educated structures be at the amorphous condition. The small consecutive increase of singlet height for samples with the 10, 20, 30 and 40 monolayers can point to the consecutive increase of plotted oxidation substances.

Acknowledgements:

The authors gratefully acknowledge V.K. Adamchuk (St. Petersburg State University) for support. This research was supported by Russian Foundation for Basic Research (grants № 02-03-32748 and № 03-02-17168), Program “Integration” (grant № Б 0028) and the bilateral program Russian-German Laboratory at BESSY II. We wish to thank the staff of BESSY for valuable technical assistance.

References:

1. V. M. Smirnov , Chemistry of Nanostructures: Synthesis, Structure, and Properties (in Russian) ; Izd. SPbGU: St.Petersburg, 1996
2. V.M. Smirnov, A.A. Shellich, V.G.Semenov, S.M. Irkaev, I.V.Murin, Int. Conf. ”Mossbauer spectr. and its application”, St.Petersburg, Russia, July 8-12, 2002, p.110
3. A.S. Vinogradov, A.Yu. Dukhnyakov, et al., Fiz. Tverd. Tela (Leningrad) **24**, 1417 (1982) [Sov. Phys. Solid State **24**, 803 (1982)].
4. F.C. Brown, R.Z. Bachrach, M. Skibovski, Phys. Rev. B **15**, 4781 (1977).
5. A.Bianconi, R.S. Bauer, Surface Science **99**, 76 (1980).
6. A.S. Vinogradov, A.B. Preobrajenski, et al., Surface Review and Letters, **9**, 359 (2002).

Initial stages of oxide mediated growth of CoSi₂ at the Si(100)2x1 surface

M.V.Gomoyunova¹, I.I.Pronin¹, N.R.Gall¹, D.V.Vyalikh², S.L.Molodtsov²

¹ A.F.Ioffe Physico-Technical Institute, 194021, St.Petersburg, Russia

² Institut für Oberflächenphysik und Mikrostrukturphysik Fachrichtung
Physik Technische Universität Dresden, D-01062 Dresden, Germany

Ultrathin cobalt disilicide films epitaxially grown on the silicon surface are important for nanoelectronics. Fabrication of perfect nano-sized CoSi₂ layers is limited by the rise of pinholes and another structural defects. Recently it has been shown by TEM and STM that morphology of CoSi₂ films can be noticeably improved by the use of preliminary oxidation of the substrates [1-3]. However, the mechanism responsible for the effect is still unclear. The aim of the present work was to study for the first time the initial stages of oxide mediated growth of CoSi₂ onto the Si(100)2x1 surface by means of high resolution photoelectron spectroscopy with synchrotron radiation.

The experiments were carried out in UHV at photon energy of 130 eV. The overall energy resolution of the electron energy analyser and the monochromator was 140 meV. Samples were produced from the Si(100) wafers with a misorientation of less than 0.1°. Before introduction into UHV they were subjected to wet chemical treatment according to the method of Shiraki and then flashed up to 1200°C in UHV to ensure the clean Si(100)2x1 surface without carbon and oxygen contaminations. The element composition of surfaces was monitored by PES. Cobalt was deposited at a rate of ~1 ML/min (1 ML = 6.8×10¹⁴ Co atoms/cm²).

At the first stage of the study silicon crystals were oxidized by exposure to high-purity oxygen at the pressure of ~1×10⁻⁷ Torr both at room and elevated temperatures. The sets of Si2p and valence-band spectra were taken for different doses of oxygen (3, 10, 100 and 10000 L). In the second stage cobalt were deposited onto the oxidized Si surfaces (the total doses ≤10 ML) and the same photoelectron spectra were taken for different Co coverages. Afterwards the samples were subjected to stepwise annealing until the temperature of 1000°C to investigate both the solid phase reaction between Co and Si and the behavior of silicon oxide layer.

The results obtained are illustrated in Fig. 1. Exposure of the Si(100)2x1 surface to oxygen at RT results in decrease of main components of the silicon surface, disappearance of the 2p_{3/2} mode of upper dimer atoms and in rise of a new suboxide (Si¹⁺ - Si³⁺) and oxide (Si⁴⁺) components with large positive energy shifts (~1 - 3.5 eV). The valence band spectra (Fig. 2) agree with the conclusion about formation of a complex oxide layer on the sample surface.

Deposition of Co onto prepared oxide layer considerably modifies the spectra. As it is seen from Fig. 1, the heights of Si 2p_{3/2} and Si 2p_{1/2} peaks not only diminish with the growth of the coverage, but also become almost equal in the case of the dose of 8 ML. At the same time the intensity of oxide components undergo much weaker changes. Such a behavior of spectra can be explained by assumption that adsorption of Co atoms is accompanied by not their accumulation on the surface but penetration under oxide layer. Nearly equal heights of 2p_{3/2} and 2p_{1/2} lines can be interpreted as rise of a new mode with the positive energy shift. It should be emphasized, that such mode does not exist in the case of Co/Si system, where deposition of cobalt onto the Si(100)2x1 surface leads to formation of Co-Si solid solution characterized, on the contrary, by a negative energy shift [4]. Thus, the effect is caused by the presence of oxygen. Analysis of changes of the Si⁺¹ and Si⁺² components confirms participation of suboxide phases in formation of ternary Co-Si-O complexes localized at the SiO_x-Si interface.

Diffusion of cobalt through the formed oxide layer is also supported by the data of Fig.2. It follows from both insignificant weakening of the valence band oxygen peak at the binding energy of ~ 7 eV due to deposition of Co and the relatively small intensity of Co 3d peak at ~ 0.7 eV as compared to the case of the binary system [4]. Thus, cobalt directly contacts with silicon even at room temperature, and consequently silicon oxide layer does not play a role of a diffuse barrier between them, as it was supposed in Ref. [1].

Annealing of the samples up to the temperature of 200°C does not affect the Si 2p and the valence band spectra. Strong changes associated with the start of solid phase reaction between cobalt and silicon is revealed at $\sim 250^{\circ}\text{C}$. It should be noted that the reaction in the ternary Co/O/Si system begins at practically the same temperature as in the binary Co/Si system. Further growth of the temperature also leads to transformation of the spectra, which is evidence for both gradual formation of CoSi_2 film buried under SiO_x layer and destruction of Co-Si-O complexes. The end of the process at the temperature of $\sim 800^{\circ}\text{C}$ is related to removal of the capping silicon oxide layer. Thus, the role of this layer in oxide mediated epitaxy of CoSi_2 consists in elimination of migration and mass transport during the solid-phase reaction between Co and Si.

The work was supported by Russian Foundation for Basic Research (grant № 01-02-17288) and the Russian-German laboratory at BESSY II.

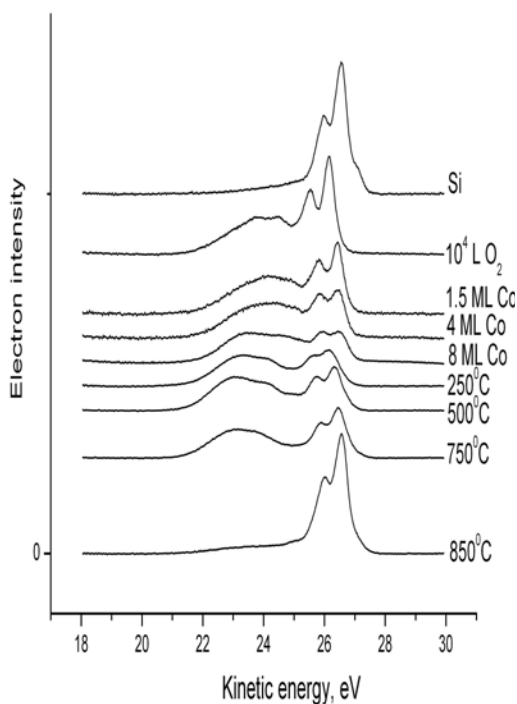


Fig.1. Si 2p core-level spectra taken with $h\nu = 130$ eV at different stages of oxide mediated growth of CoSi_2 .

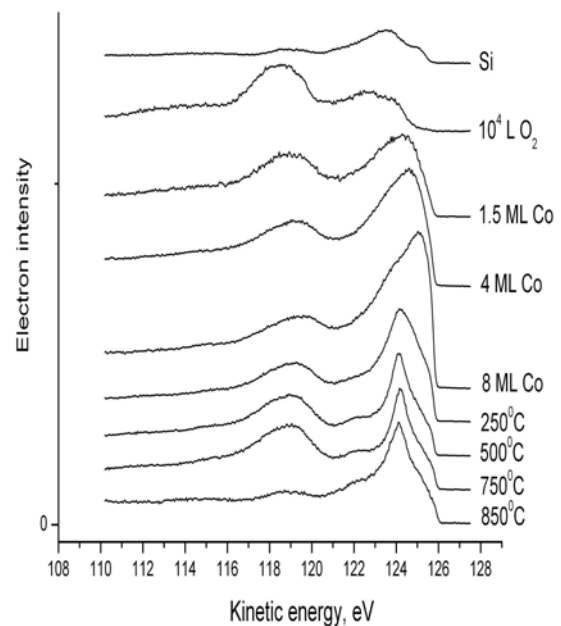


Fig. 2. Valence-band photoelectron spectra taken with $h\nu = 130$ eV.

References

1. R. T. Tung. Appl. Phys. Lett. **68**, 3461 (1996).
2. R. T. Tung. Jpn. J. Appl. Phys. **36**, 1650 (1997).
3. Y. Hayashi, M. Yoshinaga, H. Ikeda, S. Zaima, Y. Yasuda. Surf. Sci. **438**, 116 (1999).
4. M.V.Gomoyunova, I.I.Pronin, N.R.Gall, S.L.Molodtsov, D.V.Vyalikh. BESSY - Annual Report 2002, p. 117.

X-ray magnetic circular dichroism above and below the Verwey-transition of a Fe_3O_4 single crystal

S. Gold¹, E. Goering¹, G. Schütz¹

¹Max-Planck Institut für Metallforschung, Heisenbergstr. 3, Stuttgart, 70569, Germany

Recently Fe_3O_4 has become an intensively studied system, due to its proposed and experimentally observed high spin polarization at the Fermi-energy and its related applicability in future spin electronic devices. In addition, at the so called Verwey transition, which has been investigated over many decades, a dramatic change in the electrical resistivity appears. The origin of this phase transition is still under discussion. We show detailed X-ray magnetic circular dichroism (XMCD) experiments at 1T applied magnetic field performed above and below the Verwey transition and along different crystallographic directions ((100), (110) and (111)) in total electron yield (TEY) mode.

In the last few years magnetite (Fe_3O_4) has attracted revived interest due to its remarkable high spin polarization at the Fermi energy, theoretically predicted to be 100% [1] and recently investigated to be up to $-(80\pm 5)\%$ at room temperature by spin- and angle-resolved vacuum ultraviolet photoemission spectroscopy [2]. The reason for this revival is mainly related to promising future technological spintronics applications on the basis of Fe_3O_4 -electrodes, such as magnetic tunneling and spin injection devices. Fe_3O_4 is a promising candidate of the halfmetallic ferromagnets due to its high Curie temperature (895 K). Magnetite has an inverse spinel structure with two different iron sites (octahedral and tetrahedral coordinated) with average 2.5^+ and 3^+ configurations respectively. In addition magnetite undergoes at about $T_V = 125$ K a first-order metal-insulator transition, the so called Verwey-transition [3]. This transition is characterized by an abrupt decrease in resistivity by about two orders of magnitude (see for example [4]) and was explained by Verwey as an localization-delocalization transition at the octahedral sites from 2^+ and 3^+ configurations below T_V to a mixed valence 2.5^+ configuration above T_V . But up to now it is still unknown if there exists 2^+ and 3^+ charge ordering below T_V [5,6]. The still open question is: What is the driving mechanism for this transition?

We have investigated a Fe_3O_4 single crystal with X-ray magnetic circular dichroism (XMCD) for three crystallographic orientations ([100], [110] and [111]) and at three different temperatures (20 K, 80 K, and 150K) above and below T_V . All spectra were recorded in total electron yield mode at the new high resolution bending-magnet-beamline SX700 III at BESSY II in an applied magnetic field of ~ 10 kOe (flipped at each data point). The degree of circular polarization was about $95\pm 3\%$. Two Keithley 6517A electrometers were used for simultaneous measurements of the total drain sample current and from an Au coated Cu grid, which monitors the intensity of the incoming photon

beam. We have measured with two different angles of incidence of 45° and 0° to probe the different orientations. Further details of the experimental setup and the data analysis are reported elsewhere [7]. The Fe_3O_4 crystal has a $T_V \approx 123.8$ K and was characterized by F. Walz performing magnetic-after effect measurements. The sample reveals high quality.

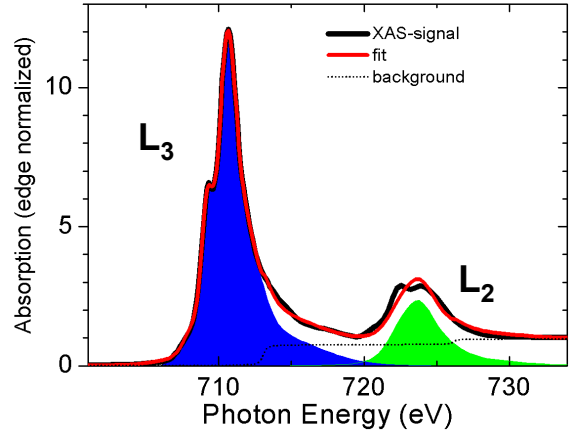


Figure 1: XAS spectrum of Fe_3O_4 , measured along the [110] direction at 150K, and corresponding L_3 (blue) and L_2 (green) edge fit results, including the background step-function.

As an example, Fig. 1 shows normalized XAS (X-ray absorption spectroscopy) spectrum at 150 K and 110 orientation. The very high branching ratio BR of 3.8 ± 0.2 of the XAS-spectra, extracted by a new fitting method [8], suggest a presence of large orbital moments in Fe_3O_4 by the expectation value of $\langle \Psi | \sum_i \mathbf{l}_i \mathbf{s}_i | \Psi \rangle$ [9].

The upper part of Fig. 2 shows the XMCD- spectra at [111] orientation at all three temperatures and the lower part at 150 K for all three orientations. The spectrum is clearly different compared to bulk Fe XMCD, especially the presence of three clear separated peaks in the spectrum, formerly assigned to the three different ion places in Fe_3O_4 antiparallel

oriented due the ferrimagnet behavior. Surprisingly at passing through T_V there are nearly no changes in the XMCD spectra for all temperatures and orientations. From comparison to SQUID magnetization curves, which clearly shows changes at T_V for the same sample, the absence of changes in XMCD behavior is not understood up to now. A sum rule analysis gives a total orbital moment below $< 0.03 \mu_B$ and seems to be in contradiction with the XAS branching ratio results. We have applied a relative new analysis method to our XMCD-data, so called moment analysis (Fig. 3), which takes into account the shape of the XMCD-spectra. Therefore one has to build a set of ground state moments, first introduced by G. van der Laan, with a convenient broadening and prefactors and fit the spectrum with several sets of ground state moments, separated in energy. The method is described elsewhere [10]. We can now extract for the different subparts of the spectra non-quenched and antiparallel oriented orbital moments at tetrahedral and octahedral coordinated sites in the range up to $0.3 \mu_B$. This explains the observed branching ratio. The sum rule related spin moments exhibit no significant changes, including the absence of a change in the easy axis behavior (extracted by SQUID measurements).

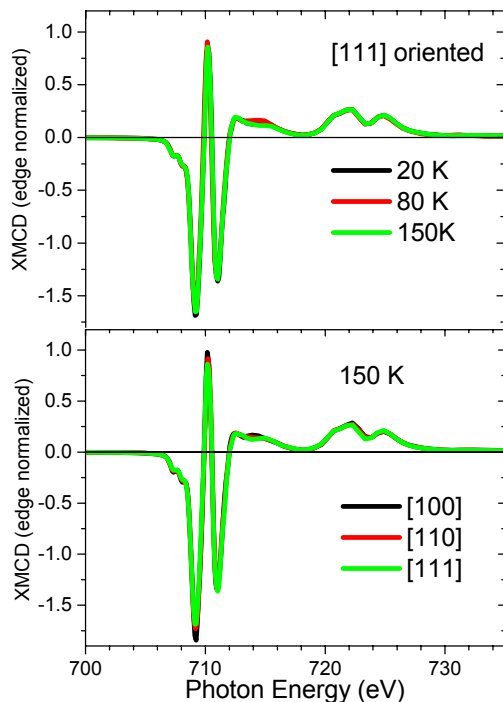


Figure 2: (top) Fe $L_{2,3}$ edge XMCD spectra of Fe_3O_4 at three different temperatures at an applied field of 10kOe. The photon beam was aligned along the [111] direction. (bottom) Fe $L_{2,3}$ edge XMCD spectra of Fe_3O_4 at three different directions. The temperature was held above the Verwey transition at 150K, and at an applied field of 10kOe

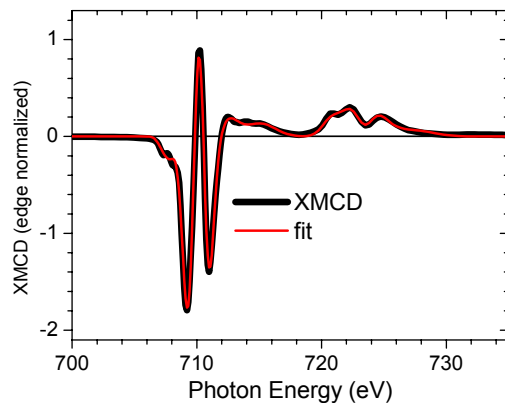


Figure 3: The black line shows a Fe $L_{2,3}$ edge XMCD spectrum of Fe_3O_4 at 80K. The photon beam was aligned along the [100] direction at an applied field of 10kOe. Red curve is a moment analysis fit, which has been used to separate the three different Fe contributions.

We have investigated a Fe_3O_4 single crystal for three temperatures and three different crystallographic orientations with XMCD and SQUID measurements. An evidence for a strong non-quenched orbital moment could be found in the branching ratio of the XAS-spectra and verified by the moment analysis. Sum rule related values show a nearly compensated orbital moment, so we conclude that the orbital moment in Fe_3O_4 is not completely quenched, but antiparallel aligned. The XMCD data and related hysteresis loops show no changes passing through T_V , what is still an open question.

We grateful thank T. Kachel at BESSYII for very kind support during the measurement time and F. Walz for helpful discussions.

References:

- [1] Antonov, V. N., Harmon, B.N., et al. Phys. Rev. B **64** (2001) 134410
- [2] Dedkov, Yu. S., Rüdiger, U., et al.; Phys. Rev. B **65** (2002) 64417
- [3] Verwey, E.J. and Haayman, P.; Physica (Amsterdam) **8** (1941) 979
- [4] Walz, F., J. Phys.: Cond. Mat. **14** (2002) 285
- [5] Garcia, J., Subias, G., et al. ; Phys. Rev. B **63** (2001) 54110
- [6] Wright, J. P., Attfield, P.J. et al. ; Phys. Rev. B **66** (2002) 214422
- [7] Goering, E., Justen, M., et al.; Appl. Phys. A. **74** (2002) 747
- [8] Goering, E., Phys. Rev. Lett. submitted
- [9] B. T. Thole et al., PRB **38**, 3158 (1988), and G. van der Laan et al., PRL **60**, 1977 (1988).
- [10] Goering E. et al ; J. Sync. Rad. **5** (1999) 537, and Goering E. et al., Appl.Phys.A., in press.

Orientation of pentacene molecules on SiO₂ and GeS(0001) studied with X-ray absorption spectroscopy

T. Schwieger, X. Liu, D. Olligs, M. Knupfer

Leibniz Institute for Solid State and Materials Research (IFW) Dresden, D-01069 Dresden, Germany

Th. Schmidt

Universität Würzburg, Am Hubland, D-97074 Würzburg, Germany

During the last years the interest in the field of thin organic films has grown dramatically due to their successful application in optical and electronic devices, such as light emitting diodes or field effect transistors. One of the most successfully applied organic materials is the organic semiconductor pentacene. Its planar molecular structure allows pentacene to grow in highly oriented organic films. The transport properties of organic films have been shown to be highly dependent on the morphology of the organic films. Furthermore it is known that the transport in organic crystals is highly anisotropic. In this context the detailed knowledge of the morphology of pentacene films is crucial for the functionality of organic semiconducting devices. Nevertheless previous investigations often refer to either submonolayer and monolayer films of pentacene on various substrates or to the structural properties of bulk-like pentacene films.

The orientation of organic molecules like phthalocyanine is known to depend strongly on the structure of the substrate. Phthalocyanine molecules are lying flat on single crystalline surfaces like GeS(0001) and Au(110), whereas they are standing on polycrystalline surfaces like SiO₂, polycrystalline gold or ITO. Polarisation dependent X-ray absorption spectroscopy is an ideal tool to investigate the geometric alignment of organic adsorbates. Here we have measured the relative intensity of the core level excitation from the C1s-level into the unoccupied π^* and σ^* molecular orbitals of pentacene as a function of the angle of incidence θ , of the linearly polarised synchrotron radiation, enabling an analysis of the molecular orientation of the pentacene molecules in the film.

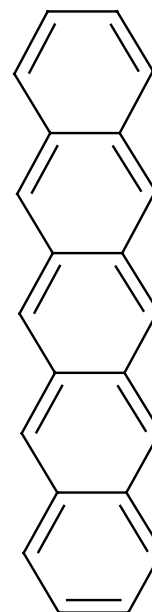


Fig. 1 Chemical structure of pentacene

Pentacene films have been prepared with a thickness of about 1 monolayer and 10 monolayers on SiO₂ and GeS(0001). This experimental approach allows us to analyze possible differences between the monolayer and bulk like regime of the pentacene films. The charge transport in organic field effect transistors mainly occurs in the first monolayer of the organic film, in contact to the gate insulator.

The experiments were performed at BESSY II using the UE 52-PGM beamline with an energy resolution set to 100 meV. The absorption was monitored by measuring the partial electron yield. The data have been corrected for the energy dependence of the incident X-ray beam and subsequently normalized to the absorption edge step height well above the

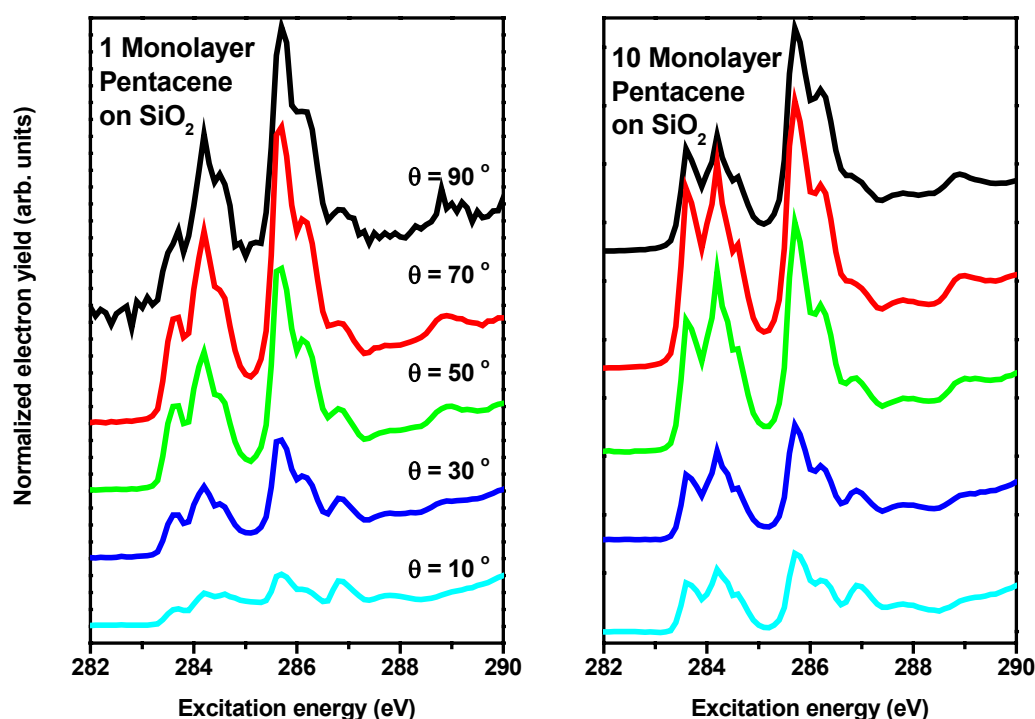


Fig. 2 X-ray absorption spectra from pentacene films (1 and 10 monolayers thick, respectively) on SiO₂ as a function of the angle of the incident photon beam. θ is the angle between the surface normal and the electric field vector of the synchrotron radiation.

threshold. The film thickness was determined by measuring the attenuation of the photoemission signal from the corresponding substrate. The SiO₂ substrate was heated prior to the pentacene deposition. After this treatment only very small contaminations of carbon could be detected. The GeS(0001)-surface was prepared by cleaving the GeS-crystal *in situ*. Pentacene was thermally evaporated and deposited onto the substrates held at ambient temperature.

All pentacene films reveal a strong dependence of the intensity of the C1s - π^* -transitions on the incident angle of the polarized photon beam. Thus both films are highly ordered. Series of C1s π^* - excitation spectra of a monolayer- and multilayer pentacene film on SiO₂ are depicted in Fig. 2. Both samples have their maximum intensity of the excitation around normal incidence, whereas at grazing incidence (10°) the intensity is minimal. This leads to the conclusion that the orientation of the molecular plane of the pentacene molecules at either film thickness is perpendicular to the substrate surface. The intensity of the C1s- π^* transitions is plotted versus the angle of incidence of the photon beam in Fig. 3. Furthermore this plot contains the according data from pentacene (1 and 10 monolayers) on single crystalline

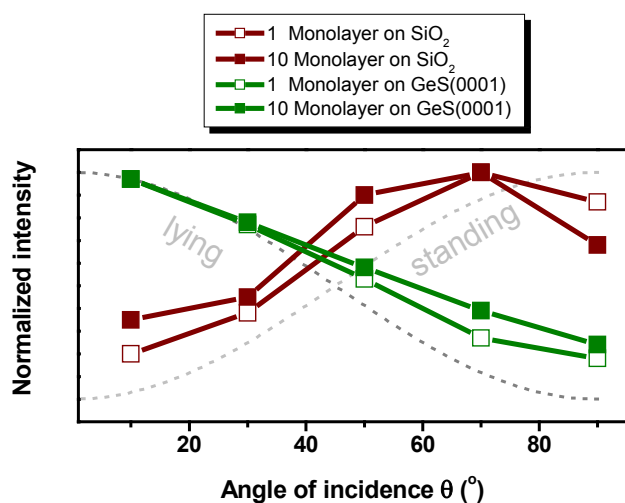


Fig. 3 Angular dependence of the intensity of the π^* -resonances of pentacene on SiO₂ and GeS(0001) with a film thickness of 1 and 10 Monolayer, respectively.

GeS(0001). The degree of ordering on both substrates is similar. However the orientation of the pentacene molecules is radically different. The molecules are standing on the SiO₂-surface and lying on the GeS(0001) substrate. Furthermore in both cases no dependence of the orientation or even the degree of order could be found for different film thicknesses of the pentacene film. On both substrates, the orientation of the molecules in the monolayer regime does not change with more organic material deposited on the substrate. This means that the orientation is predominantly determined by the substrate-molecule interaction. In Fig. 3 one can see that the maximal intensity for the π^* -transition for the pentacene on SiO₂ is at an angle of incidence of 70°. This might indicate, that the pentacene molecules on the SiO₂-surface are tilted by 20°.

In summary, we have measured the orientation of pentacene on SiO₂ and GeS(0001). We find standing molecules on SiO₂ and lying molecules on GeS(0001). The orientation of the pentacene molecules is independent of the film thickness.

This work was supported by the BMBF under grant no. 01 BI 163.

see also: T. Schwieger, X. Liu, D. Olligs, M. Knupfer, Th. Schmidt, J. Appl. Phys. (sub.)

Investigation of ZnO (0001) – single crystals and $Zn_xMn_{1-x}O$ and $Zn_xFe_{1-x}O$ PLD-films by means of X-ray absorption and resonant X-ray emission

D. Wett¹, D. Schulze¹, M. Lorenz², H. Schmidt², E. G. Ramirez² and R. Szargan¹

¹*Wilhelm-Ostwald-Institut für Physikalische und Theoretische Chemie, Universität Leipzig, D-04103 Leipzig, Germany*

²*Institut für Experimentelle Physik II, Universität Leipzig, D-04103 Leipzig, Germany*

Zinc oxide (ZnO) is a promising material because of its excellent optical, electronic and dielectric properties and, last but not least, because of its low price. The field of applications includes numerous products of semiconductor and sensor technology as well as photo catalysis. ZnO can be used as transparent, conductive material for solar cell caps. Recent success in p-doping of ZnO has paved the way for the production of light emitting diodes or transistors, for instance. Another important field is that of ferromagnetic semiconductors. By combining electric (ZnO) and magnetic (transition metal oxide) properties “spintronic” applications like spin-valve transistors and spin-LEDs were created. This study of XANES and X-ray emission spectra was carried out in order to obtain information on the valence band composition and orbital mixing of ZnO. Furthermore, the

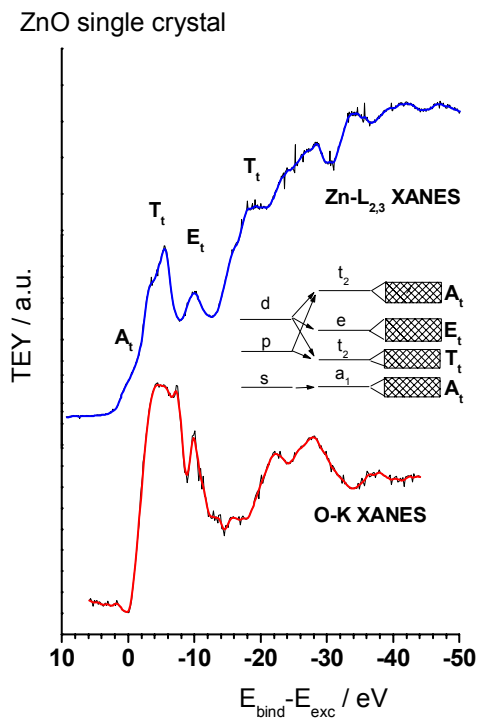


Fig. 1: Zn- $L_{2,3}$ and O-K XANES for the ZnO single crystal

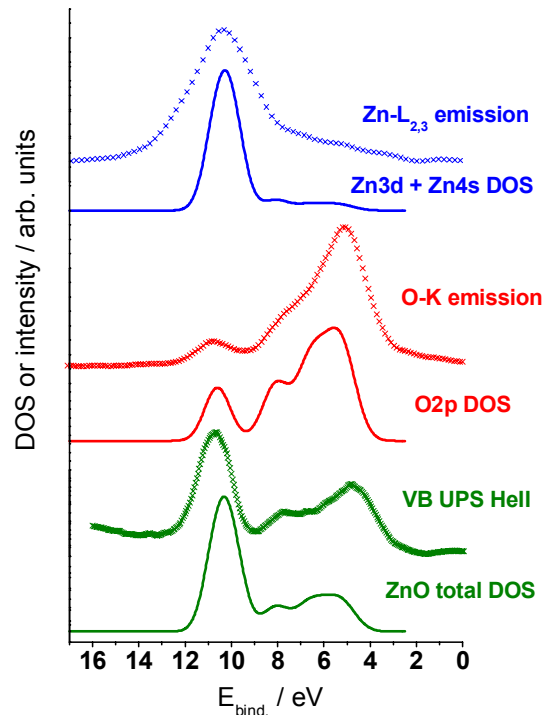


Fig. 2: Comparison between measured XES and UPS spectra and calculated DOS (smearing of 0.5 eV included, energy scale linearly shifted by 4.5 eV)

oxidation state of the transition metal (TM) in mixed ZnO/TM-oxide pulsed laser deposited (PLD) films should be found out.

All measurements were carried out at beamline U41-PGM by using the rotatable spectroscopy apparatus (ROSA).

The structure of the Zn-L XANES of the single crystal (fig. 1) agrees well with a simple molecular orbital approach [2] for a ZnO_4^{6-} tetrahedron. The splitting of the L_2 edge is caused by the mixing of Zn4s, 4d and O2p orbitals.

Further we measured the O-K and Zn- $L_{2,3}$ X-ray emission spectra of a ZnO single crystal at excitation energies of 1100 eV for Zn and 600 eV for O, respectively. Additionally, the He II (40.8 eV) UPS of the valence band was recorded. Aligning of the spectra (fig. 2) shows both Zn3d, 4s and O2p states distributed in an energy range of 12 eV indicating 3 sub-bands in the limits of the experimental resolution. The high energy O2p component at 10.5 eV overlaps well with the most intense feature of the Zn3d related structure. This gives evidence for the orbital mixing between ligand and metal. In order to verify this experimental effect we performed a DFT-GGA calculation of ZnO. The calculated partial densities of states for both Zn and O are in good agreement with the experimental data. The valence band of ZnO is dominated by Zn3d-O2p-mixed states. Also the less populated O2s- and Zn4s4p-states show mixing (not shown).

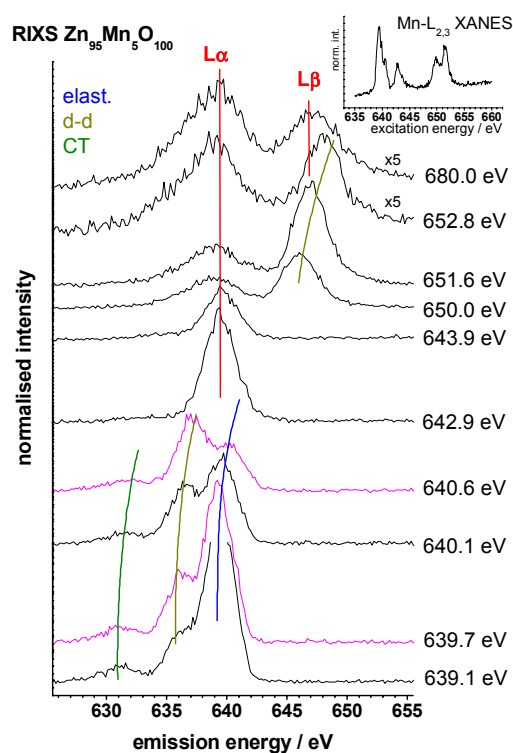


Fig. 3: Mn- $L_{2,3}$ XANES and RIXS of the $\text{Zn}_{95}\text{Mn}_5\text{O}_{100}$ sample

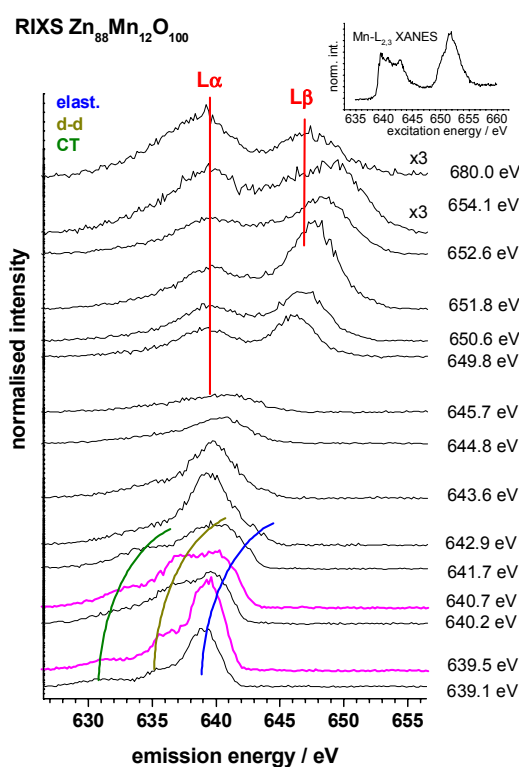


Fig. 4: Mn- $L_{2,3}$ XANES and RIXS of the $\text{Zn}_{88}\text{Mn}_{12}\text{O}_{100}$ sample

PLD (pulsed laser deposited) films taken from a test series for the preparation of ferromagnetic semiconductor material were characterised by X-ray absorption (XANES) and resonant inelastic X-ray scattering (RIXS). The composition of the films was $\text{Zn}_{95}\text{Fe}_5\text{O}_{100}$ (target material: mixture of ZnO and Fe_2O_3 powder), $\text{Zn}_{95}\text{Mn}_5\text{O}_{100}$ (ZnO and MnO) bzw. $\text{Zn}_{88}\text{Mn}_{12}\text{O}_{100}$ (ZnO and MnO_2).

Comparing our Mn-L XANES (insets fig. 3, 4) with reference spectra [3] one can see that in the $Zn_{95}Mn_5O_{100}$ film Mn has oxidation state +2 whereas in the $Zn_{88}Mn_{12}O_{100}$ sample in addition to Mn^{2+} there is a large amount of Mn^{3+} and Mn^{4+} to find, respectively. These differences are obviously related to the reduction of MnO_2 during the PLD process. The resonant Manganese-L emission spectra recorded at excitation energies between 639 and 654 eV (fig. 3, 4) show energy loss structures in the range of 2-8 eV, which may be attributed to d-d as well as charge transfer transitions (CT) [4].

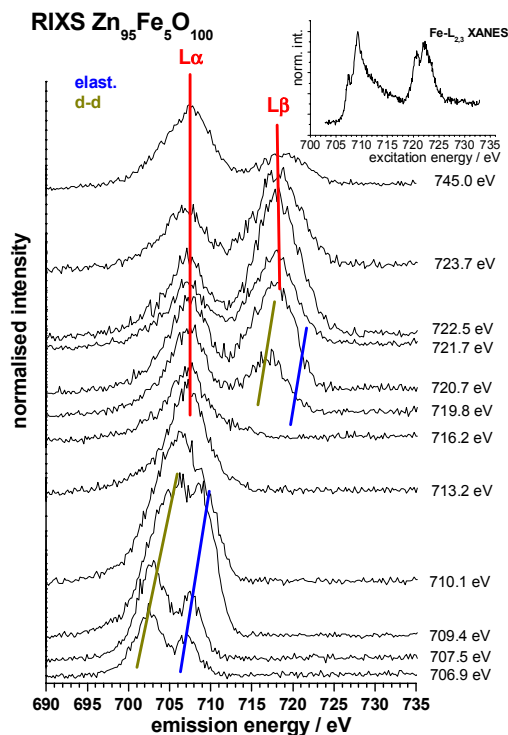


Fig. 5: Fe-L_{2,3} XANES and RIXS of the $Zn_{95}Fe_5O_{100}$ sample

For the $Zn_{95}Mn_5O_{100}$ sample the RIXS spectra are very similar to that of MnO [5]. In case of the Manganese rich sample the loss structures are broadened (Fig. 4). This broadening should be caused by the existence of several oxidation states and thus by the superposition of several groups of final states. The calculation of the energy loss spectra in order to interpret the features are worthwhile but still difficult to perform, however. Structural investigations (TEM) with respect to probable cluster formation are under way.

Comparing the Fe-L XANES (inset fig. 5) of the $Zn_{95}Fe_5O_{100}$ sample with XANES of different Fe oxides [6] we conclude that the oxidation state of iron is +3 in this case. The CT features in the RIXS spectra of the Fe containing sample are weak because of the low energy resolution.

Acknowledgement:

This work was financed by DFG FOR 404-SZ58/15 and BMBF, grant number 05KS10L1/3. We are grateful for technical support by C. Jung and M. Mast at the U41-PGM beamline, BESSY. The assistance from PD Dr. C. Engler in performing the DFT calculations is gratefully acknowledged.

References:

- [1] S. W. Jung, S.-J. An, Gyu-Chul Yi, C. U. Jung, Sung-Ik Lee and Sunglae Cho, *Appl. Phys. Lett.* 80(24) **4561** 2002
- [2] T. Mizoguchi, M. Yoshiya, J. Li, F. Oba, I. Tanaka and H. Adachi, *Ultramicroscopy* 86 **363** 2001
- [3] H. Kurata and C. Colliex, *Phys. Rev. B* 48(4) **2102** 1993
- [4] B. Fromme, U. Brunokowski and E. Kisker, *Phys. Rev. B* 58(15) **9783** 1998
- [5] S. M. Butorin, J.-H. Guo, M. Magnuson, P. Kuiper and J. Nordgren, *Phys. Rev. B* 54(7) **4405** 1996
- [6] A. S. Vinogradov, A. B. Preobrajenski, S. A. Krasnikov, T. Chassé, R. Szargan, A. Knop-Gericke, R. Schlögl and P. Bressler, *Surf. Rev. and Lett.* 9(1) **359** 2002

Electronic structure of polycrystalline LiCoO₂ thin films

D.Ensling^a, F.J.Fernandez-Madrigal^a, R.Hunger^a, C.Pettenkofer^b, A.Thißen^a, W.Jaegermann^a

*Fachbereich Materialwissenschaften - Oberflächenforschung der TU Darmstadt^a
Hahn-Meitner-Institut, Abteilung SE6, Berlin^b*

Transition metal oxides with layered crystal structures like V₂O₅, LiCoO₂, LiNiO₂, LiCo_xNi_{1-x}O₂ and LiMn₂O₄ can be used as cathode materials in thin film Na- or Li-intercalation batteries. In an all-solid-state device the thin film cathode is deposited onto a thin film solid electrolyte that had been deposited before onto the anode material. The battery can be charged by an external voltage, leading to deintercalation of the alkaline metals from the cathode, transport through the ionic conducting electrolyte and insertion into the anode material. The discharge process leads to an intercalation of alkaline metal ions into the transition metal oxides. The electrochemical data of the cell are mostly determined by the change of the electronic structure of the cathode material during intercalation or deintercalation. For materials with complicated electronic structures like transition metal oxides these changes can not be described by a simple filling of rigid bands by electrons. Therefore, the valence band structure must be determined as a function of the Li concentration. In this study the partial valence band density of states (PVBDOS) for the fully intercalated host material LiCoO₂ is studied by resonant photoelectron spectroscopy (ResPES) [1-2]. The resonant superposition of the different excitation processes (direct photoemission, autoionization and super-Coster.Kronig transition) leads to a Fano-like profile of the photoionization cross section superposed to the common values calculated for example by Yeh and Lindau [3]. For early transition metals like V and Ti the 3p-3d resonance leads to an significant enhancement of the 3d-cross section some eV above the 3p-3d-excitation threshold. This has already been used to determine, for example, the PVBDOS of TiO₂(110) [4] and polycrystalline V₂O₅ films [5]. In the left graph of Figure 1 a ResPES series for LiCoO₂ is shown. The most intense VB-emission around E_b=1.4eV is according to DFT calculations [6] mainly originating from Co3d-like states. Its intensity shows a clear drop for excitation energies of about 62eV that cannot be explained by the calculated cross sections for Co3d or O2p (right graphs in Figure 1). Taking the 3p-3d-threshold energy of about 59eV into account, the intensity drop can be explained as a 3p-3d-anti-resonance. As illustrated in the upper right graph of Figure 1, the off-anti-resonance spectrum can be calculated as the sum of spectra for $h\nu < 62\text{eV}$ and $h\nu > 62\text{eV}$. This has been done for 4 excitation energy combinations resulting in a normalized mean off-anti-resonance spectrum. By the calculation of difference spectra off- and in-anti-resonance [4-5] the O2p- and Co3d-contributions to the VB-DOS can be separated. This is shown in the left graph of Figure 2, compared with the in-anti-resonance spectrum (62eV) where the O2p-contribution is enhanced and with a standard XP spectrum with a significantly higher Co3d-cross section (Figure 1, lower right graph). A comparison with calculated PVBDOS shows good agreement with the ResPES data of this study.

This work was supported by the SFB595 of the Deutsche Forschungsgemeinschaft (DFG).

- [1] U. Fano, Phys. Rev. 124 (1961) 1866
- [2] L.C. Davis, L.A. Feldkamp, J. Appl. Phys. 59 (1986) R25
- [3] J.J. Yeh, I. Lindau, Atomic Data and Nuclear Data Tables 32 (1985) 1
- [4] R. Heise, R. Courths, S. Witzel, Solid State Comm. 84 (1992) 599
- [5] Q.-H. Wu, D. Ensling, R. Hunger, A. Thißen, W. Jaegermann, BESSY Annual Report 2002, 345
- [6] M.T. Czyzyk, R. Potze, G.A. Sawatzky, Phys. Rev. B 46, 3729-3735 (1992)

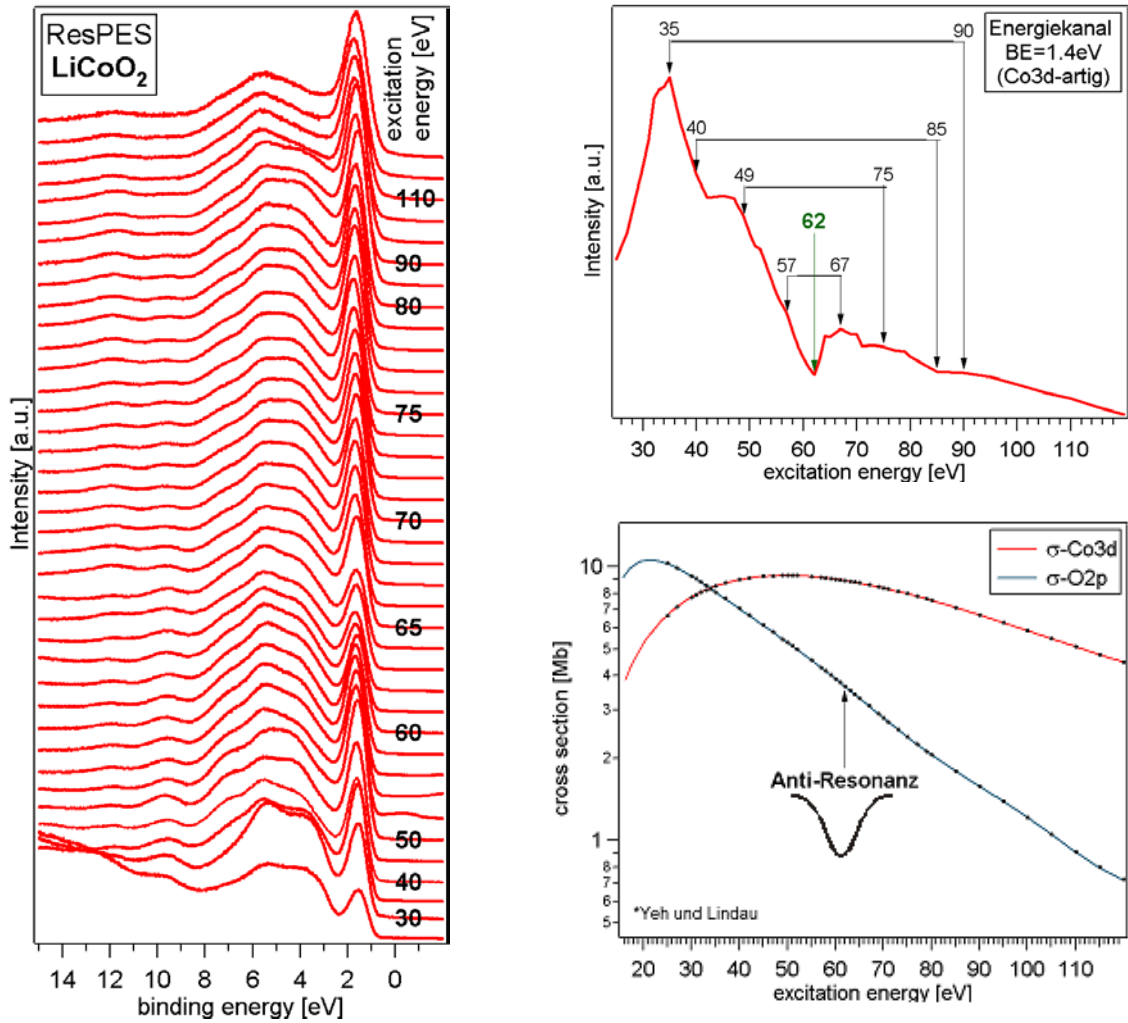


Figure 1: ResPES series of a LiCoO_2 (left), intensity of the $\text{Co}3d$ -like VB-state (upper right), and $\text{Co}3d, \text{O}2p$ photoionization cross sections [3] as a function of $h\nu$ (lower right).

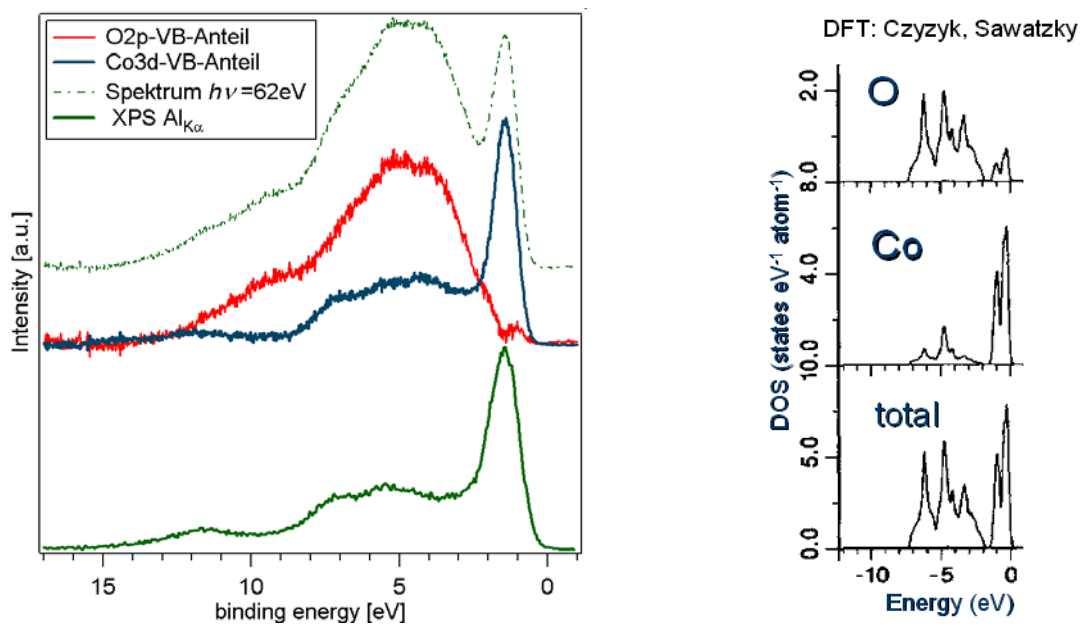


Figure 2: PVBDOS from ResPES series (left) and DFT-calculated PVBDOS [6] (right) of LiCoO_2 .

Chemical reaction at Cu/ZnS(001) and In/ZnS(001) interfaces detected by S L_{2,3} X-ray emission spectroscopy

L. Zhang^{1,2}, M. Nagel¹, H. Peisert¹, D. Schulze², R. Szargan², T. Chassé¹

¹*Institut für Physikalische und Theoretische Chemie, Universität Tübingen, Auf der Morgenstelle 8, D-72076 Tübingen*

²*Wilhelm-Ostwald-Institut für Physikalische und Theoretische Chemie, Universität Leipzig, Linnéstr. 2, D-04103 Leipzig*

Soft X-ray emission spectroscopy (XES) excited by synchrotron radiation is a “photon-in-photon-out” technique with information depth of about 100 nm. It is bulk sensitive compared to the surface-sensitive photoemission spectroscopy (PES), the latter has an information depth of about 1-5 nm. The power of the XES, especially combined with PES, has already been demonstrated in investigating buried interfaces.^[1-3] Following creation of core holes by incident photons, the X-ray emission process (fluorescence decay) is governed by the dipole selection rule. This makes X-ray emission spectroscopy both atom and angular momentum specific. By exciting appropriate core-level electrons, the partial density of states (PDOS) of different atom species in the valence band can be determined from the X-ray emission spectrum. The summation of these PDOS corresponds to the valence band spectrum obtained by photoemission spectroscopy. Therefore, XES can be used to characterize electronic and chemical properties of materials. The low fluorescence yield, due to the predominant Auger electron decay mode, can be overcome by employing high-brightness third-generation synchrotron radiation as excitation source.

In S L_{2,3} emission spectrum, S 2p_{3/2} (L3) and 2p_{1/2} (L2) core levels are excited, S 3s and S 3d-related states can be measured according to the dipole selection rule. In (transition) metal sulfides, it is usual to find metal d states-related features in the S L_{2,3} emission spectra, resulting from metal-S bonding. The appearance of the metal d states-related features is explained by: (1)

the involvement of the S 3d states in chemical bonding;^[4] (2) a wave function overlap between the S 2p and the metal d orbitals.^[2] The emitted photon energy of the metal d states-related feature is determined by the difference of the binding energies of the S 2p core levels and the metal d states (shallow core levels or dispersive valence states). The binding energy of the metal d states is atom specific. Hence, different emitted photon energy of the metal d states-related feature may reflect different metal-S chemical bonding. From the change of the position and intensity of the metal d states-related feature in the S L_{2,3} emission spectra, we can probe formation and/or decomposition of different metal sulfides.

Although photoemission spectroscopy is powerful to detect chemical reaction from the chemical shifts of the core levels of the involved atoms, in some cases the chemical shift may not be readily recognized. For example, reacted component may be smeared by bulk component when a chemical reaction is not remarkable and confined to the interface of a heterojunction. X-ray emission spectroscopy may work as a complementary method to photoemission spectroscopy, and in some cases it may even be a decisive method.

Cu(In,Ga)(S,Se)₂ (CIGSS) thin film with chalcopyrite structure is one of the most promising solar cell absorber materials and has been investigated extensively. “Alloy” between ZnS and CuInS₂ (the so-called ZCIS) may also be an attractive solar cell absorber material. In addition to its environmentally friendly character, the band gap of the ZCIS may change with

composition from 3.7 eV (ZnS) to 1.5 eV (CuInS₂), well matching the energy range of the visible light of the solar spectrum. As preliminary work, we have prepared Cu/ZnS(001), In/ZnS(001) heterojunctions by depositing Cu, In onto ZnS(001) films which were grown by molecular beam epitaxy on GaP(001). These heterojunctions have already been characterized *in situ* by X-ray photoemission spectroscopy and low energy electron diffraction (LEED).^[5] We have measured the S L_{2,3} emission spectra of these samples in the end station of ROSA at U41-PGM beamline in BESSY. As the samples were exposed to air before the XES measurement, the measurement is *ex situ*.

Core level X-ray photoemission spectra were measured in order to detect chemical reaction at the metal/ZnS(001) interfaces. However, in the stepwise deposition of Cu and In, the S 2p core level spectra display hardly any change. On the other hand, the Cu 2p_{3/2} core level spectra of Cu films below 1 monolayer (1 ML = 0.081 nm) are located at about 0.4 eV higher binding energy than those of thicker Cu films (16 ML). Note that distinguishing the reacted component (Cu-S) at higher binding energy from the dominant metallic component at lower binding energy is disturbed by the asymmetric character of the metallic component. In addition, one may argue that the higher Cu 2p_{3/2} binding energy of the initial Cu layers may result from a less screening due to non-structured Cu atoms rather than Cu-S bonding. In 3d_{5/2} core level spectra display similar results. To remove this unclearness, S L_{2,3} emission spectra of Cu (1.3 nm)/ZnS(001) (4.3 nm) and In(4.4 nm)/ZnS(001)(4.3 nm) have been measured.

As reference, S L_{2,3} emission spectra of ZnS (powder and film), CuS (powder), In₂S₃ (powder) and CuInS₂ (bulk crystal) have been measured, as shown in Fig. 1. All spectra were normalized to the same height of the peak around 148.2 eV. Besides the predominant S 3s → S 2p⁻¹_{3/2, 1/2} feature at about 148.2 eV, Zn 3d-, Cu 3d- and In 4d-related features are clearly revealed in the corresponding sulfides. The Zn 3d- and

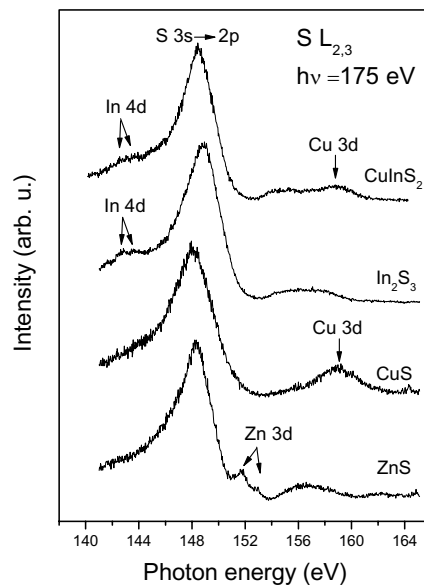


Fig. 1 S L_{2,3} emission spectra of ZnS, CuS, In₂S₃ and CuInS₂

In 4d-related features exhibit a doublet feature, the distance between the two peaks is about 1.2 eV, which is equal to the spin-orbit splitting of the S 2p core level. The Cu 3d-related feature is much broader due to the valence-band characteristic of Cu 3d. The occurrence of these features implies that in these sulfides, the d states of the sp metal (In) as well as the transition metals (Zn, Cu) are involved in the chemical bonding between S and metal atoms. It can also be seen that the photon energy of the S 3s → S 2p⁻¹_{3/2, 1/2} feature is not fixed in these sulfides. This may reflect the minor difference of the S 2p core level binding energy in different sulfides. The energy of this dominant feature in CuInS₂ is between those of CuS and In₂S₃. From the S 2p_{3/2} binding energy (161.8 eV in ZnS) and the emitted photon energy of these d features, the binding energy of these d-related states can be calculated to be 10.1, 2.9 and 18.9 eV for Zn 3d, Cu 3d and In 4d, respectively. The results for Zn 3d and Cu 3d are in agreement with their characteristic binding energies obtained in photoemission spectroscopy, but the In 4d binding energy is

about 2 eV higher than PES results. It is not uncommon that such a “deep” level as In 4d (compared to the shallow Cu, Zn 3d levels) is involved in bonding, in N K emission spectrum of GaN film, a fine feature originated from hybridization of Ga 3d (19.5 eV) with N 2p was also found.^[6] In CuInS₂ both Cu 3d- and In 4d-related states appear, implying the bonding of S atoms to both In and Cu atoms.

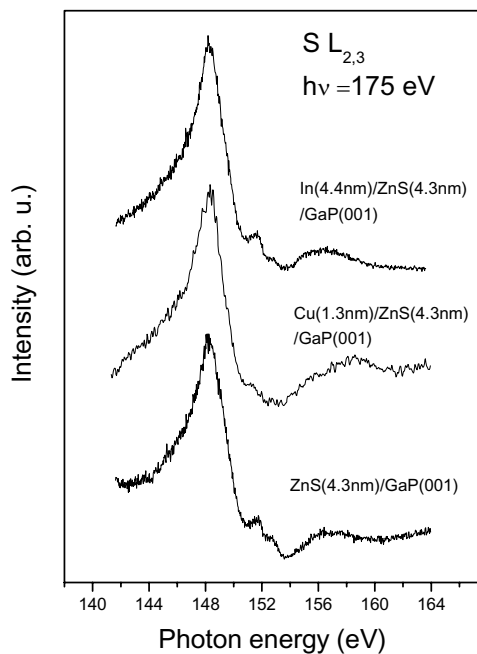


Fig. 2 S $L_{2,3}$ emission spectra of ZnS/GaP(001), Cu/ZnS/GaP(001) and In/ZnS/GaP(001) heterojunctions

Figure 2 displays S $L_{2,3}$ emission spectra of ZnS(4.3nm) / GaP(001), Cu (1.3nm) / ZnS(4.3nm) / GaP(001) and In(4.4nm) / ZnS(4.3nm) / GaP(001) heterojunctions. The spectrum of the ZnS film is essentially the same as that of ZnS powder sample, including features originated from S 3s, Zn 3d and upper valence band. After 1.3 nm Cu was deposited on the ZnS film, the S $L_{2,3}$ spectrum changes significantly. The Zn 3d-related doublet is suppressed considerably and a new feature arises at the higher energy side of the upper valence band of ZnS. From the reference spectra in Fig. 1,

we may conclude that this new feature results from Cu 3d, implying occurrence of Cu-S bonding. Therefore, at the Cu/ZnS interface, Cu_xS_y forms accompanied by decomposition of ZnS. This process is not so evidently revealed in the measurements employing photoemission spectroscopy. On the other hand, such a reaction does not clearly exist at the In/ZnS interface, since the S $L_{2,3}$ spectrum of the In/ZnS is nearly the same as that of the bare ZnS film, the In 4d-related feature does not appear and the Zn 3d-related feature hardly changes. Therefore, chemical reaction at the Cu/ZnS interface is much more extensive than at the In/ZnS interface. It is worth noting that these results are in agreement with the *in situ* LEED observation, in the latter experiment, the spots from ZnS film disappear after deposition of much smaller thickness of Cu film than In film.

Acknowledgements:

The financial support by the BMBF 03WKI 10 and BESSY as well as the support of the BESSY staff especially by C. Jung and M. Mast are gratefully acknowledged.

References:

- [1] J. A. Carlisle, L. J. Terminello, E. A. Hudson, R. C. C. Perera, J. H. Underwood, T. A. Callcott, J. J. Jia, D. L. Ederer, F. J. Himpsel and M. G. Samant, Appl. Phys. Lett. 67 (1995) 34.
- [2] C. Heske, D. Eich, R. Fink, E. Umbach, T. Van Buuren, C. Bostedt, L. J. Terminello, S. Kakar, M. M. Grush, T. A. Callcott, F. J. Himpsel, D. L. Ederer, R. C. C. Perera, W. Riedl and F. Karg, Appl. Phys. Lett. 74 (1999) 1451.
- [3] C. Heske, U. Groh, O. Fuchs, L. Weinhardt, E. Umbach, M. Grün, S. Petillon, A. Dinger, C. Klingshirn, W. Szuszkiewicz and A. Fleszar, Appl. Phys. Lett. 83 (2003) 2360.
- [4] E. Z. Kurmaev, J. van Ek, D. L. Ederer, L. Zhou, T. A. Callcott, R. C. C. Perera, V. M. Cherkashenko, S. N. Shamin, V. A. Trofimova, S. Bartkowski, M. Neumann, A. Fujimori, and V. P. Moloshag, J. Phys.: Condens. Matter 10, (1998) 1687.
- [5] L. Zhang, R. Szargan and T. Chassé, J. Appl. Phys. (in press).
- [6] C. B. Stagarescu, L. C. Duda, K. E. Smith, J. H. Guo, J. Nordgren, D. Doppalapudi, and T. D. Moustakas, Phys. Rev. B 54 (1996) R17335.

Orientation of soluble phthalocyanines on disordered substrates

H. Peisert¹, I. Biswas¹, L. Zhang¹, T. Schwieger², M. Knupfer², M. Hanack³,
D. Dini³, T. Chassé¹

¹University of Tübingen, IPC, Auf der Morgenstelle 8, 72076 Tübingen, Germany

²Leibniz Institute for Solid State Research Dresden, P.O. Box 270116, D-01171 Dresden

³University of Tübingen, Inst. Organ. Chem., Auf der Morgenstelle 18, D-72076 Tübingen

Thin films of organic semiconductors on various substrates have attracted much attention due to their successful application in optical and electronic devices, such as light emitting diodes or field effect transistors. Due to the anisotropic transport properties the ordering and orientation of such molecules is crucial for device efficiency. The family of the phthalocyanines (Pc's) represents one of the most promising candidates for ordered organic thin films in organic electronics, as these systems possess advantageous attributes such as chemical stability, excellent film growth on various substrates and electronic properties. It was shown, that CuPc forms highly ordered thin films, the molecular orientation however can be radically different: the CuPc molecules are standing on the technical substrates such as ITO, oxidised

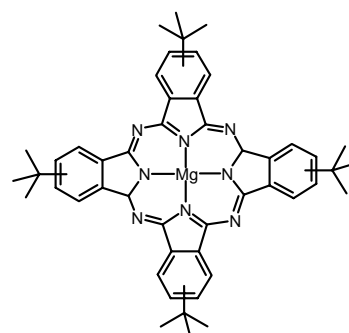


Fig.1 Structure of Tetra (tert-) butyl PcMg ($(t\text{Bu})_4\text{PcMg}$).

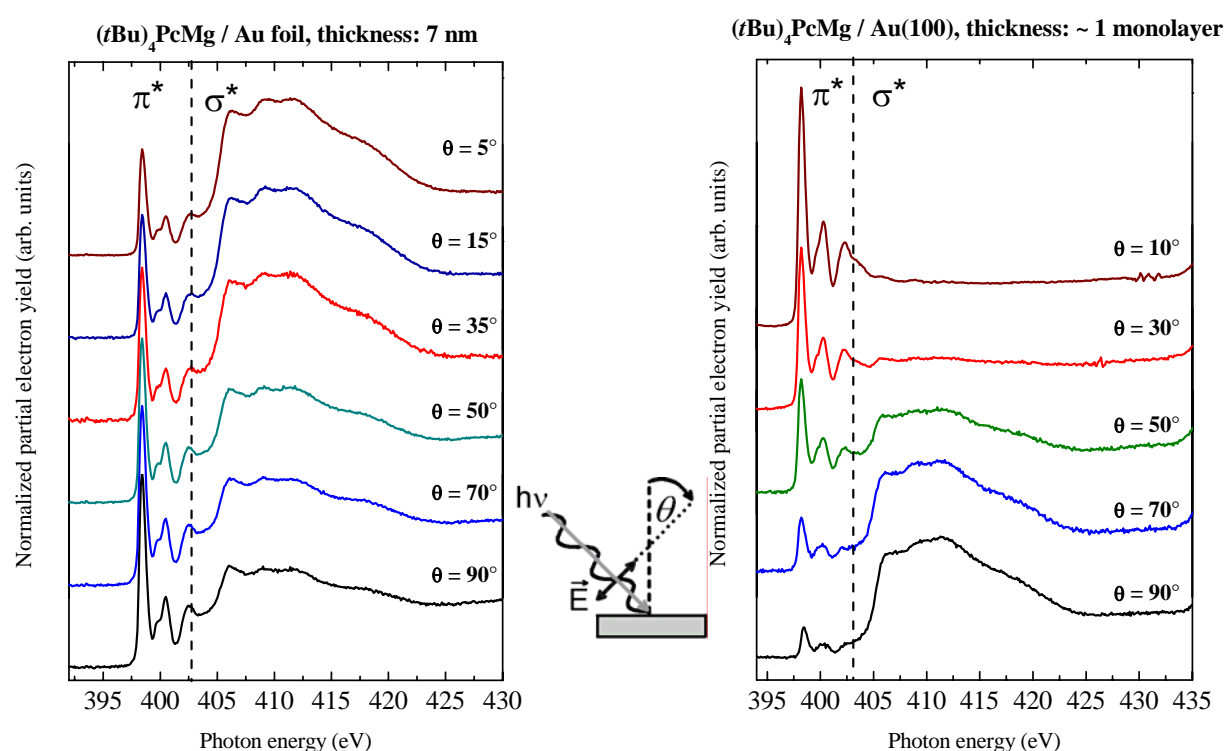


Fig. 2 N1s excitation spectra of $(t\text{Bu})_4\text{PcMg}$: a 7 nm thick film grown on polycrystalline Au (left) and about 1 monolayer on Au(100) (right). The sketch characterizes the photon incidence and polarization for p-polarized light (this corresponds here to a horizontal polarization).

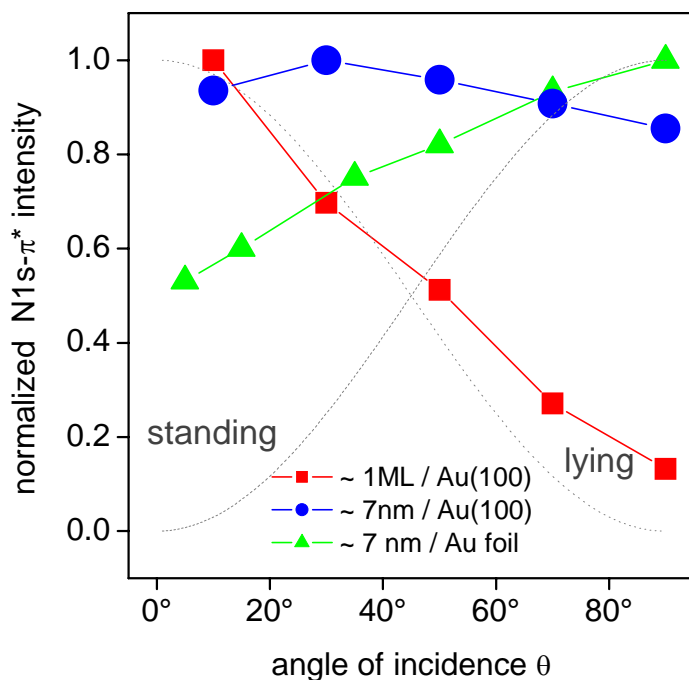


Fig. 3 Symbols: angle-dependence of the intensity of the π^* resonances on Au foil and Au(100). The expected intensity profiles for standing and lying Pc molecules are indicated by dotted and dashed lines, respectively.

Si and polycrystalline gold [1], whereas they are lying on many single crystalline substrates [2]. Due to the possible modification of Pc's a large variety of chemical properties is accessible. For instance, the studied tert-butyl metallophthalocyanines are highly soluble and thus they are especially suitable for processing organic semiconductor thin films from solution. However, the influence of substitution on the ordering and orientation of the molecules is not yet clear. For this purpose, x-ray absorption spectroscopy measurements were performed at the UE-52 undulator beamline.

In Fig. 1 N 1s excitation spectra of $(t\text{Bu})_4\text{PcMg}$ on a polycrystalline gold foil and on Au(100) are displayed as a function of the incidence angle of the synchrotron radiation. The lower energy features (398-405 eV) represent the π^* resonances, whereas those features above 405 eV are related to the σ^* resonances. A very clear angular dependence of the π^* resonances is observed in both cases. For a 7 nm thick film on polycrystalline gold (Fig. 2, left), the maximum intensity of the π^* resonances is observed at normal incidence. In contrast, the angle-dependence of the N 1s \rightarrow π^* intensities for a ultra-thin organic film on a single crystalline gold substrate [Au(100)] behave in an analogous, but opposite manner (Fig. 2, right). The integrated π^* intensities are summarized in Fig. 3. The data for the monolayer on Au(100) fit almost ideally to expected curve for lying molecules, whereas at higher coverages the angle dependence (spectra not shown) has nearly disappeared. This can be explained by i) completely disordered molecules or ii) a change of the preferred orientation at this film thickness. The different behaviour for the orientation on single crystalline and technically relevant polycrystalline substrates reminds now to the recently measured adsorbate geometry for the non-substituted CuPc: The organic molecules are well ordered on *both* substrates. But that the adsorbate geometry in each case is radically different: for Au(110) the CuPc molecular plane is parallel to the substrate surface and for polycrystalline (rough) substrates it is perpendicular. The different growth modes observed on various substrates can be understood in terms of different molecule-substrate interactions.

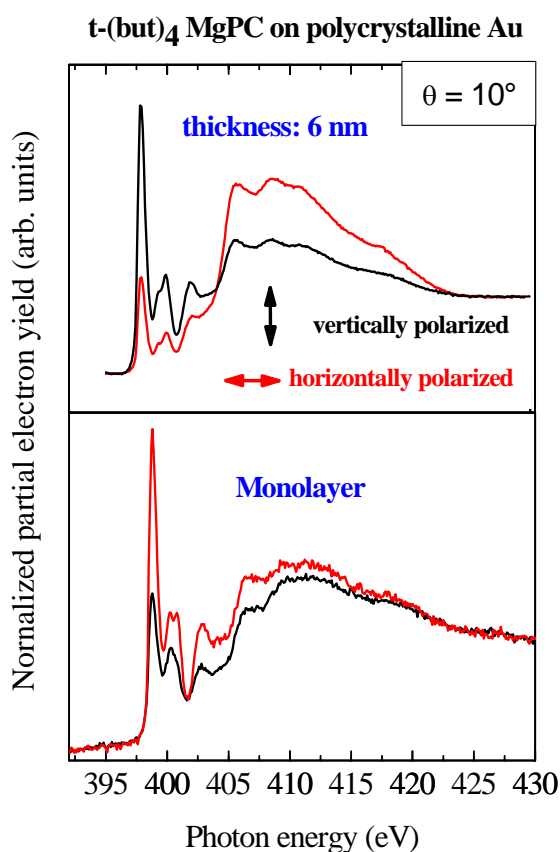


Fig. 4 Comparison of N1s excitation spectra of a 6-8 nm thick film and for a monolayer of *t*Bu₄PcMg grown on polycrystalline Au at grazing incidence. The variation of \underline{E} shows the *different* molecule orientation without sample rotation.

For valuable discussions and technical assistance we thank T. Schmidt (Uni Würzburg), H. Kuhlenbeck and S. Pohl (FHI Berlin), Ch. Jung (BESSY), as well as W. Neu (Uni Tübingen). Financial support by BESSY is gratefully acknowledged.

- [1] H. Peisert, T. Schwieger, M. Knupfer, M. S. Golden, J. Fink, J. Appl. Phys. **88**, 1535 (2000).
 [2] see e.g. S.R. Forrest, Chem. Rev. **97**, 1793 (1997).

For technological applications, the molecules directly at the interface are mainly responsible for the device properties. Therefore, we have measured more in detail the orientation of a (sub-)monolayer on the technically relevant polycrystalline gold substrate. Fig. 4 shows XAS spectra at grazing incidence for a monolayer compared to the thicker film. Alternatively in Fig. 4 not the polar angle of the sample, but the direction of the \underline{E} vector of the synchrotron radiation was changed. For lying molecules the excitation into π^* orbitals occurs for horizontally polarized light. Consequently, one can conclude from Fig. 4, that the *first layer* of the organic molecules *lies on the substrate surface*. This fact is also supported by angle dependent XAS spectra as shown in Fig. 2. These data suggest that the extrapolation of thin film data to the first monolayer could be highly misleading.

Electronic structure of [Fe(FeL₂)]*4CHCl₃ where L=NO₂: Normal X-ray emission (XES)

A. F. Takács¹, K. Kuepper¹, M. Neumann¹, T. Crainic¹, D. Wett², R. Szargan²,
R.W. Saalfrank³ and A. Scheurer³

¹Fachbereich Physik, Universität Osnabrück, Barbarastr. 7, D-49069 Osnabrück, Germany

²Wilhelm-Ostwald-Institut, University of Leipzig, Germany

³Institut für Organische Chemie, Universität Erlangen-Nürnberg, D-91054 Erlangen
Germany

Oxo-bridged polynuclear complexes of transition metal ions belong to a very interesting class of molecular materials. Among molecular magnets exhibiting intramolecular magnetic ordering, there are not many whose ground-state possesses an uncompensated spin. Antiferromagnetic molecules are much more common.

The “Ferric Star” molecule [Fe(FeL₂)]*4CHCl₃, is a new material, which has uncompensated magnetic moments and this is due to the antiferromagnetic coupling of the three Fe ligands to the central 3d ion, yielding a ferrimagnet configuration below 20 K.

In this work we investigate in a first step the occupied density of states in this molecule. Therefore we have performed XES (X-ray emission spectroscopy) measurements. The measurements were performed with the ROSA end-station at beamline U41-PGM at BESSY II.

In addition to XES measurements we have performed also XPS (X-ray photoelectron spectroscopy) measurements. The XPS spectrum of the valence band region is plotted in Figure 1 along with the element selective emission spectra of iron, oxygen and nitrogen. The excitation energies used for the XES spectra were chosen to correspond to the L_α edge for Fe and K_α threshold for O, C and N resulting from the absorption spectra. The emission spectra are correlated with the occupied density of states in the valence band region by taking into account the binding energies of core levels, as extracted from the XPS core-level spectra. The calibration of the XES spectra was performed by recording the reference lines of a pure iron sample (Fe L_α edge at 705.0 eV [1]) and MgO (O K_α edge at 525.0 eV [2]). The emission spectra were located in the valence band region by accounting for the proper XPS binding energy of the core-level (400.7 eV for N 1s, 532.3 eV for O 1s and 710.4 eV for Fe 2p_{3/2}).

Accordingly to the emission spectra the maximum at around 5.5 eV binding energy in the shape of the XPS valence band spectrum corresponds mainly to the Fe 3d_{4s} states. The shape of the emission spectra of the iron in the valence band region, near to the Fermi level is due to the small distance between the L₂ and L₃ edges. The oxygen 2p states, whose contribution is visible in the O K_α spectrum, are located approximately in the same region at about 6.6 eV binding energy. The contribution of the N 2p states is also visible, and is located around 8.4 eV binding energy. A comparison with the electronic structure results confirm this assignment. The states around 15 and 25 eV binding energy can be easily attributed to carbon, nitrogen and oxygen 2s states.

A strong hybridization between iron, oxygen and nitrogen atoms can be deduced from the XES spectra. A pronounced chemical bonding between Fe 3d and O 2p, gives rise to magnetic

polarization in the oxygen 2p shells. The 2p states of nitrogen and carbon are more separated in energy from the Fe3d states and therefore exhibit a smaller but not vanishing polarization[3].

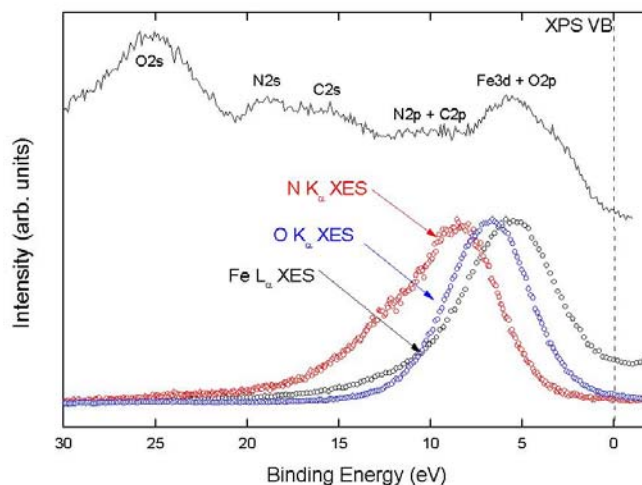


Figure 1: XPS valence band spectrum of $[\text{Fe}(\text{FeL}_2)] \cdot 4\text{CHCl}_3$ with $\text{L}=\text{NO}_2$ and along with element sensitive XES spectra of iron, oxygen and nitrogen.

References:

- [1] A. C. Thompson, D. T. Attwood, E. M. Gullikson, M. R. Howells, J. B. Kortright, A. L. Robinson and J. H. Underwood, *X-ray data Booklet*. Lawrence Berkeley national Laboratory, University of California, Berkeley, California, 2001
- [2] B. Schneider, *Untersuchungen zur elektronischen und geometrischen Struktur ausgewählter oxidischer und sulfidischer Materialien mittels Photoelektronen – und Röntgenspektroskopie*. PhD thesis, Universität Osnabrück, 2001
- [3] A.V. Postnikov, S.G. Chiuzbăian, M. Neumann, S. Blügel, Electron spectroscopy and density-functional study of “Feeric Wheel” molecules, *Cond. Mat.* 0306430 v1 17 Jun 2003

Acknowledgements:

Financial support of the PhD program of Lower Saxony is gratefully acknowledged. This project was supported by BMBF 05 SR8 OL1-2. We are grateful to O. Fuchs for support and advice during the experiments.

Reactivity and electronic structure of vanadium oxides

M. Abu Haija, S. Guimond, H. Kuhlenbeck and H.-J Freund
Fritz Haber Institute of the Max Planck Society, Chemical Physics Department
Faradayweg 4-6, 14195

Vanadium oxides exhibit a number of interesting physical and chemical properties that make them useful for many technological applications like optical switching devices, light sensors and heterogeneous catalysis. In the framework of an extended project dealing with the catalytic activity of vanadium oxides (Sonderforschungsbereich 546), the preparation and the properties of well-ordered $V_2O_3(0001)$ and $V_2O_5(001)$ surfaces have been studied over the past few years. New results are presented here concerning the chemical reactivity of $V_2O_3(0001)$ and the electronic structures of $V_2O_3(0001)$ and $V_2O_5(001)$ surfaces. For these studies, thin films (thicknesses ranging from 60 to 120 Å) of $V_2O_3(0001)$ were grown on Au(111) or W(110) by evaporation in an oxygen atmosphere. In the case of $V_2O_5(001)$, bulk single crystals were cleaved in-situ.

Using different methods (IRAS, HREELS, photoelectron spectroscopy), it has been shown that the surface of as-prepared $V_2O_3(0001)$ thin films is terminated by vanadyl groups, which are thermally stable in UHV up to about 1000 K [1]. These groups may be removed by electron bombardment, leaving behind a reduced surface that is possibly terminated by vanadium atoms. Structural details of this surface are still to be investigated. Motivated by the catalytic activity of vanadium oxides for oxidative propane de-hydrogenation we have investigated the interactions of these two differently terminated surfaces with propane and water using XPS and NEXAFS. Water is usually expected to be a by-product of this de-hydrogenation reaction. Following adsorption at 88 K, the samples were sequentially heated to different temperatures and analyzed. Figs. 1 displays a set of XPS spectra acquired for the adsorption of propane on the reduced surface of $V_2O_3(0001)$. Heating the surface causes a decrease in the intensity of the peak at about 283.5 eV (which represents the propane), while a new peak appears at about 289 eV. This peak may be attributed to a species containing oxygen atoms [2] as also found in the course of the oxidative dehydrogenation process. The O1s and V2p spectra in Fig. 1 show that a new species develops in the O1s region upon annealing (marked with a question mark). This species is neither water nor OH as revealed by a comparison with the spectrum at the top. Further experiments are currently carried-out to identify the chemical nature of the present species (TPD and IRAS). The vanadyl-terminated surface (results not presented here) showed little or no reaction.

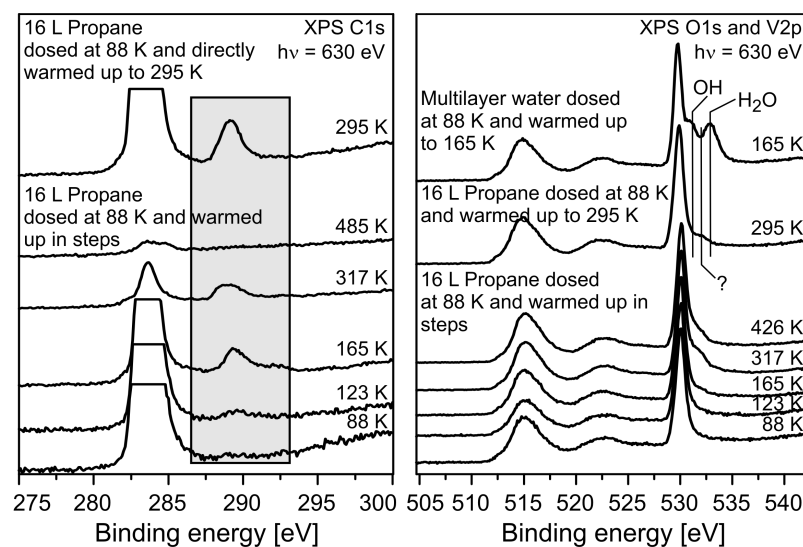


Figure 1: XPS spectra of the reduced $V_2O_3(0001)$ surface covered with propane at 88 K and heated to different temperatures. right: C1s region, left: O1s + V2p region.

Water interacts only weakly with the vanadyl-terminated surface. The interaction with the reduced surface is significantly stronger, as can be observed in Fig. 3. Heating the surface causes the formation of hydroxyl groups, which are detectable up to 540 K. Chemisorbed molecular water is gone at about 300 K.

The band structure of vanadyl-terminated $V_2O_3(0001)$ has been calculated from a series of UPS spectra ac-

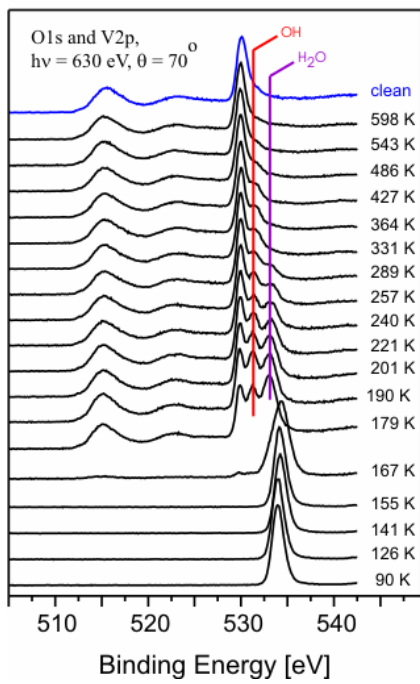


Figure 2: XPS spectra of the reduced $V_2O_3(0001)$ surface in the O1s + V2p region. The surface was exposed to water at 90 K and annealed at different temperatures.

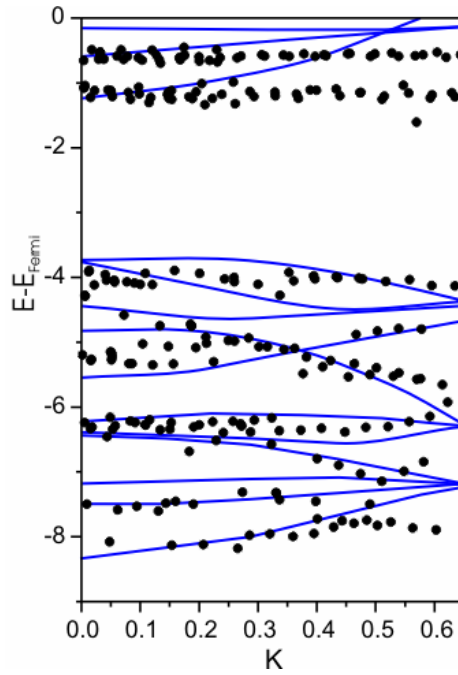


Figure 3: $V_2O_3(0001)$ band structure calculated from experimental UPS spectra, compared with theoretical data [2] (solid line).

quired at different photon energies at normal emission. Results are presented in Fig. 3, where the experimentally determined band structure is compared to one calculated by Mattheis [3]. For the determination of the experimental band structure it was assumed that the final state band can be represented by a parabola with an inner potential of 8 eV below E_F . The agreement with theory is reasonable. However, the two bands near the Fermi level (attributed to V3d states) do not

show any dispersion in the experimental data, as opposed to the theoretical predictions. The origin of this discrepancy is still unclear and may be a topic of future calculations.

To further investigate the electronic properties of vanadium oxides, angle-resolved NEXAFS spectra have been acquired for $V_2O_3(0001)$ thin films and $V_2O_5(001)$ single crystals. This work has been done as a cooperation with the group of K. Hermann (Fritz-Haber-Institut, theory department), in order to verify their theoretical calculations with experimental data. Spectra were recorded using partial yield detection. The incidence angle of the beam

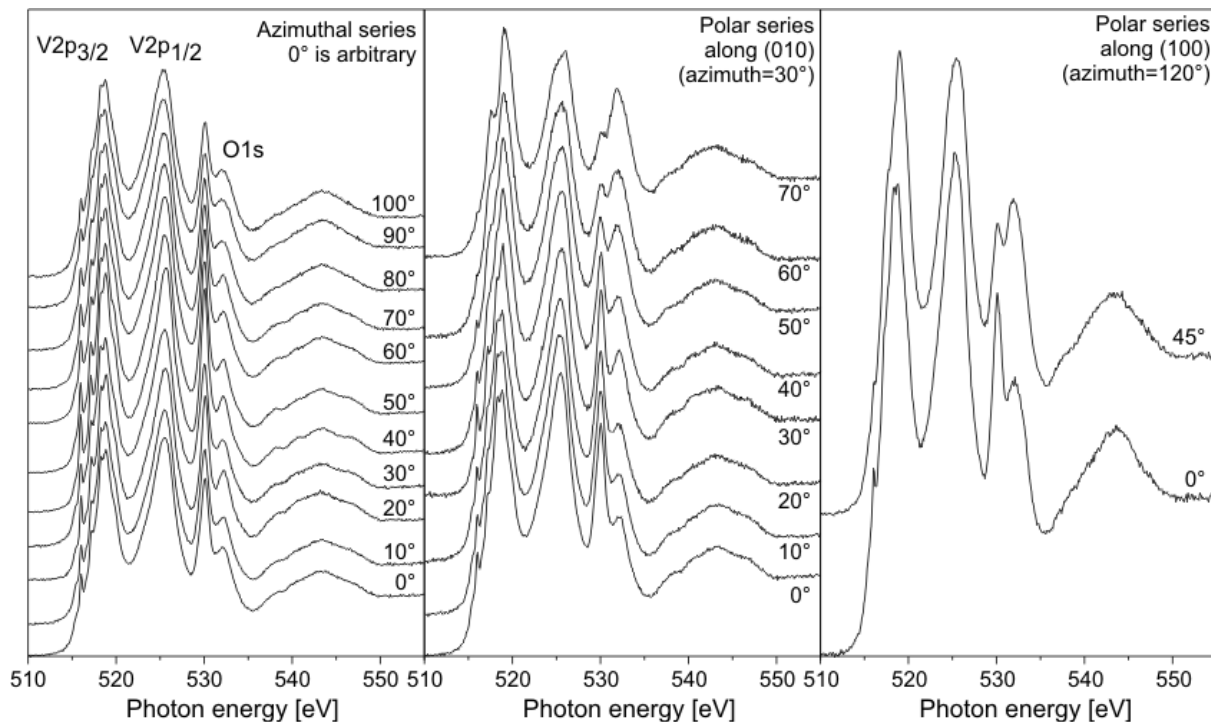


Figure 4: $V_2O_5(001)$ NEXAFS spectra acquired at different azimuthal and polar angles (partial yield detection mode).

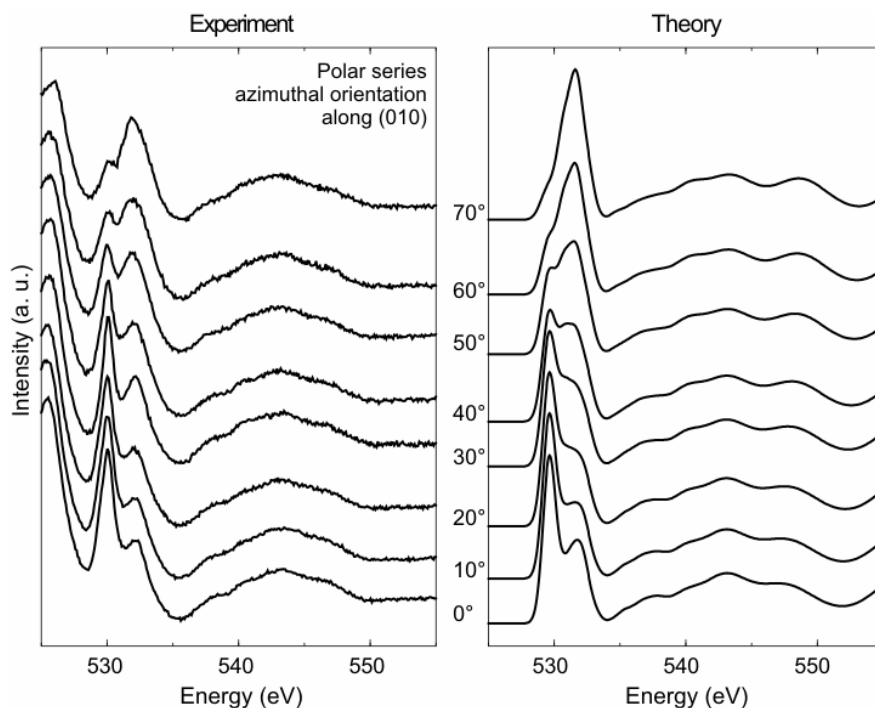


Figure 5: Comparison of experimental and theoretical [5] $V_2O_5(001)$ NEXAFS data (O1s region) for different polar angles (azimuthal orientation along (010)).

tions from the O1s core level to O2p states hybridized with unoccupied V3d (around 530 eV) or V4sp (535-550 eV) states [4]. The doublet observed around 530 eV arises from the splitting of the V3d bands by crystal field effects. The relative intensity of each band varies as a function of the polar and azimuthal angles because of the dipole selection rules. Obviously the theoretical and the experimental results are very similar which means that the applied theoretical model is suitable for a description of the real situation.

References

- [1] A.-C. Dupuis, M. Abu Al-Haija, B. Richter, H. Kuhlenbeck and H.-J. Freund, *Surf. Sci.* **539**, 99 (2003).
- [2] J. F. Moulder, W. F. Stickle, P.E. Sobol, K.D. Bomben, *Handbook of X-Ray Photoelectron Spectroscopy: A Reference Book of Standard Spectra for Identification & Interpretation of XPS Data*, Perkin-Elmer-Corporation, Eden Prairie, Minnesota, USA, 1992.
- [3] L. F. Mattheis, *J. Phys. Condens. Matter* **6**, 6477 (1994).
- [4] R. Zimmermann, R. Claessen, F. Reinert, P. Steiner, S. Hüfner, *J. Phys.: Condens. Matter* **10**, 5697 (1998).
- [5] C. Kolczewski and K. Hermann, *Surf. Sci.*, submitted.

(polar angle) and the azimuthal orientation of the samples with respect to the E-vector of the polarized beam have been varied. For $V_2O_3(0001)$, NEXAFS results only show small variations as a function of the polar orientation, and the results are not presented here due to the lack of space. In the case of $V_2O_5(001)$ (Fig. 4), more obvious differences are observed when varying either the polar or the azimuthal angle, especially in the O1s region (528 – 550 eV). This region corresponds to transi-

VUV – Spectroscopic Ellipsometry Investigations of DNA Base Layers Grown onto Flat H-passivated Silicon Surfaces

S. D. Silaghi, Yu J. Suzuki, O. D. Gordan, C. Himcinschi, G. Salvan,
M. Friedrich, T. U. Kampen, D. R. T. Zahn

Institut für Physik, TU Chemnitz, 09107 Chemnitz, Germany

C. Cobet, N. Esser, W. Richter

Institut für Festkörperphysik, TU Berlin, 10623 Berlin, Germany

W. Braun

BESSY GmbH, 12489 Berlin-Adlershof, Germany

The DNA base molecules (guanine-G, cytosine-C, adenine-A, thymine-T ; *shown in Figure 1*) may be considered as potential candidates in the field of nanotechnology. Their electronic properties are comparable to wide-gap semiconductors. Due to its low ionization potential, guanine is considered to be a key molecule for the enhancement of charge migration [1]. Guanine aggregates have been employed to build conducting nanoscale materials [2, 3]. Therefore the knowledge of the optical properties especially the dielectric function of DNA base layers is a prerequisite in the view of the above mentioned nanotechnological applications. Vacuum Ultraviolet (VUV) Spectroscopic Ellipsometry (SE) measurements were applied for the *in situ* optical characterization of DNA base layers grown onto flat H-passivated Si(111) surfaces. The DNA base layers were grown onto H-Si(111) surfaces by organic molecular beam deposition (OMBD) under ultra-high vacuum conditions. The silicon substrates were wet-chemically H-passivated by dipping in HF(40%) solution for 2 min. Such surfaces give rise to a (1x1) surface reconstruction. During the OMBD process H-Si(111) substrates were kept at room temperature. The VUV-SE measurements were performed at VUV ellipsometer either at 3m-NIM1 or 3m-NIM2 monochromators at BESSY II. The spectra were recorded in the energy range between 2.75 - 10 eV at an angle of incidence about 68°.

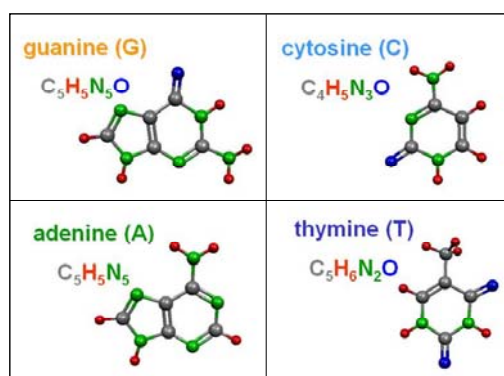


Figure 1. Chemical structure of DNA bases.

In the figure 2 the imaginary part of measured effective dielectric functions of DNA base layers on H-passivated Si(111) surfaces is shown. *Ex situ* FTIR measurements revealed that the organic layers are optically isotropic in the substrate plane as it was expected for the

3-fold symmetry of H-Si(111) surfaces. *In situ* VUV-SE measurements are limited to a single angle of incidence. For an accuracy determination of dielectric functions of DNA base layers a multi-sample analysis is required. Therefore different layer thicknesses were measured in order to compensate the variable incidence angle measurements. The layer thicknesses were determined from *ex situ* variable angle spectroscopy ellipsometry (VASE) spectra

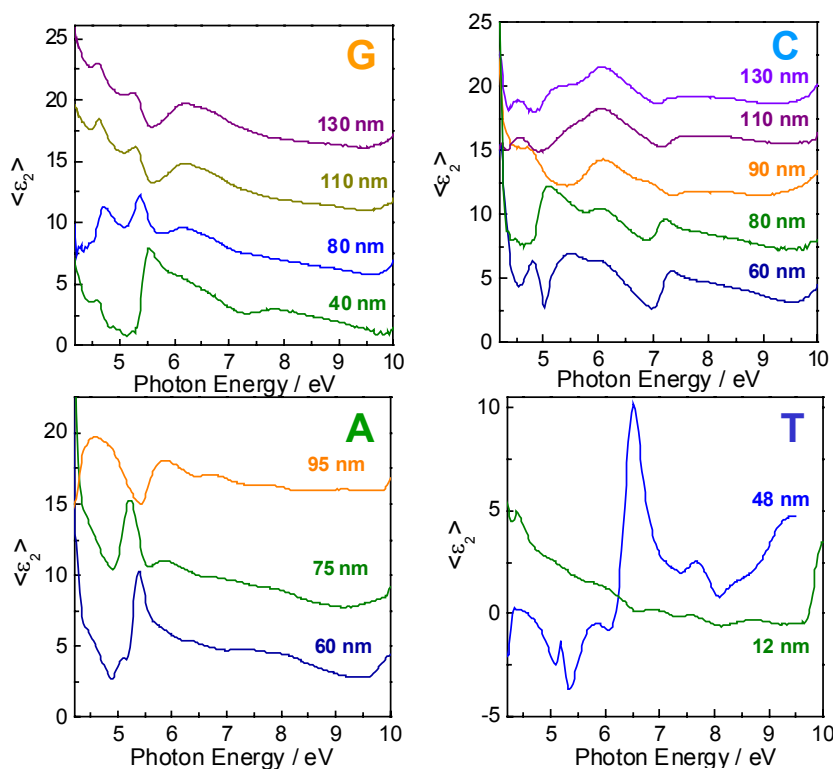


Figure 2. Measured effective dielectric function $\langle \epsilon_2 \rangle$ of DNA bases (G, C, A, T) for different layer thicknesses on H-Si(111) surfaces.

assuming a Cauchy layer in the non-absorbing energy range between 0.8-2 eV. The organic layers start to absorb above 4.6 eV. For thinner layers than 60 nm the interference effects due to substrate absorption around 5.2 eV (E'_1 – the interbandgap transition in bulk Si) are present in VUV-SE spectra. In thicker layers the absorption of the organic overlayers dominates in VUV-SE spectra. The thymine layers are found to strongly depolarize the light due to a very rough morphology. Therefore thicker layers than 48 nm could not be measured. Even very low evaporation rate of 1Å/min could not prevent the roughness of the thymine layers.

Knowing that the organic layers are azimuthally optical isotropic the aim is to determine the dielectric functions by applying a uniaxial model using VASE program. The dielectric functions of DNA base layers have not been reported in literature so far.

References

- [1] (a) M. Bixon, B. Giese, S. Wessely, T. Langenbacher, M. E. Michel-Beyerle, J. Jortner, Proc. Natl. Acad. Sci. U.S.A. **96** (1999) 11713; (b) G. B. Schuster, Acc. Chem. Res. **33** (2000) 253
- [2] D. Porath, A. Bezryadin, S. de Vries, C. Dekker, Nature (London) **403** (2000) 635
- [3] R. Rinaldi, E. Branca, R. Cingolani, S. Masiero, G. P. Spada, G. Gottarelli, Appl. Phys. Lett. **78** (2001) 3541

Electronic Properties and Chemistry of 3,4,9,10- Perylenetetracarboxylic dianhydride (PTCDA) upon Mg Deposition

G. Gavrilă¹, M.Gorgoi¹, T.U. Kampen¹, B.Tepper², W. Braun² and D.R.T Zahn¹

¹*Institut für Physik, Technische Universität Chemnitz, D-09107, Chemnitz, Germany*

²*BESSY GmbH, Albert-Einstein-Straße 15, D-12489 Berlin, Germany.*

Metal/organic/semiconductor hybrid structures may have a technological impact on the development of the high frequency Schottky diodes for telecommunications. The main parameters, which determine the operating range of a Schottky diode are the critical frequency and the operating voltage, both being determined by the properties of the organic/semiconductor and metal/organic interfaces. The operating voltage of such devices is closely related with the effective transport barrier heights at the interfaces. An understanding of the mechanisms responsible for the modification of the barrier height can be achieved by a detailed investigation of the electronic properties at the interface.

We present a detailed study of the interface formation between PTCDA (see Figure 1) and Mg using high resolution PES and NEXAFS

The organic layer is evaporated onto the sulphur passivated GaAs substrates followed by Mg evaporation with the thicknesses monitored by a quartz microbalance. The experiments were performed at the Russian-German beamline at Bessy II using the MUSTANG spectroscopy chamber. The photoelectron spectra as well as the NEXAFS spectra were detected with a PHOIBOS 150 (SPECS) analyser. The C1s NEXAFS raw data were divided by the current of the incident X-ray beam, background subtracted and normalized to the absorption step at 315eV photon energy.

The evolution of the C1s, O1s and Mg 2p core levels as a function of Mg coverage on PTCDA is shown in Figures 2(a)-(c). The C1s core level of the bare PTCDA consists of two main components. The high binding energy component (C₂) corresponds to the anhydride group while the low binding

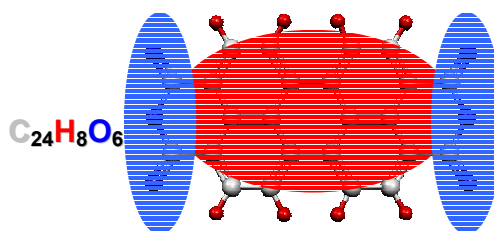


Figure 1. Molecular structure of 3,4,9,10-Perylene tetracarboxylic-dianhydride

energy component (C_1) corresponds to the perylene core. Moreover, this peak has a clear asymmetry due to the different carbon environments within the aromatic system. For the O_{1s} core level the two components stem from different oxygen environment within the carboxylic group, $O=C$ (O_2) and $C-O-C$ (O_1), respectively.

At low Mg coverage (0.1nm) the intensity of C_1 , C_2 , O_1 and O_2 components decreases significantly compared to the spectrum of bare PTCDA. The Mg_{2p} signal consists of a single high BE component. These observations are consistent with a strong chemical interaction between Mg and the carboxylic group of PTCDA resulting in either Mg-oxide complexes or Mg attached to the molecule. The perylene core of the PTCDA molecule retains its original structure as can be seen from the C_1 component which remains unchanged except for an energy shift of about 0.7eV towards lower BE. This shift can be attributed to a metal-induced polarization. At low coverage reacted molecules are surrounded mostly by unreacted ones experiencing strong polarization resulting in a decrease in binding energy.

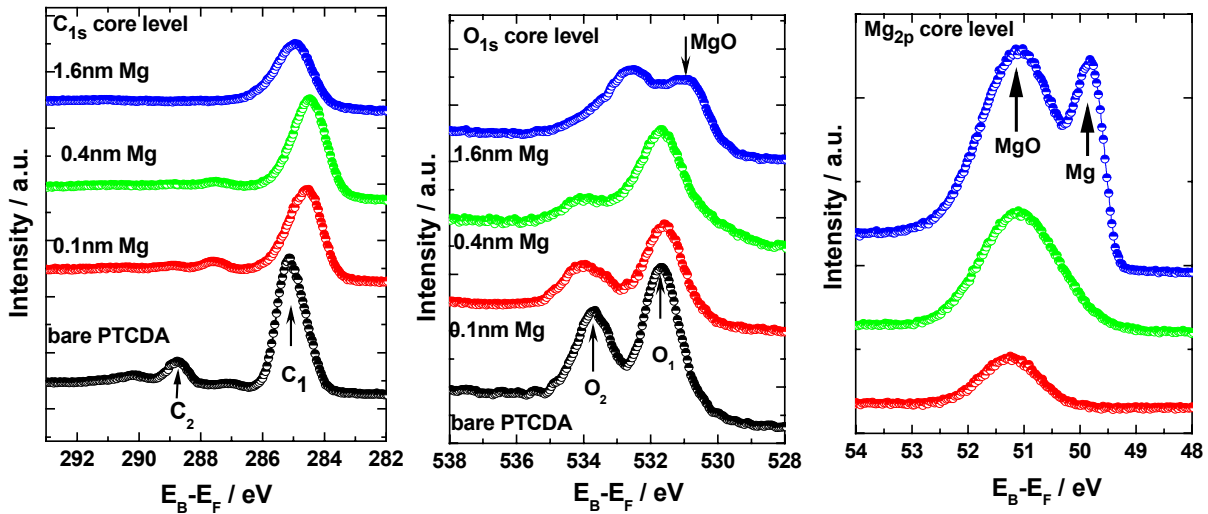


Figure 2. (a) C_{1s} , (b) O_{1s} and (c) Mg_{2p} core levels as a function of Mg coverage on PTCDA

With increasing the Mg coverage (0.4nm) the C_2 and O_2 components are decreasing significantly in intensity. Moreover, this observation is accompanied by the increase in intensity of the Mg_{2p} core level. C_1 , on the other hand, increases in intensity. We interpret this observed signal changes as a redistribution of charges in the molecule,

or in other words, as an increase in electron density on the perylene core due to the reduction of charge in the carboxylic group.

For coverage above 1.6nm of Mg, the C₂ component of the C1s core level vanishes and a new component in O1s core level being attributed to Mg-O complex arises. This observation may support the idea of formation of Mg-O complex detached from the molecule. The shift towards higher BE energy of the C₁ component may correspond to metal-induced polarization. When a large fraction of PTCDA is reacted the polarization decreases and the core level shifts back towards high BE. Moreover, a metallic Mg 2p component appears indicating that the chemical reaction is limited to the first few layers.

Figure 3 presents high-resolution C1s-NEXAFS measurements as a function of Mg coverage. With the first layer of Mg drastic changes are observed that can be interpreted as a partial occupation of the lowest unoccupied molecular orbital. These changes continue for high Mg thicknesses, the peaks corresponding to π^* transition start to be diminished, this indicates a change in the structure of the molecule.

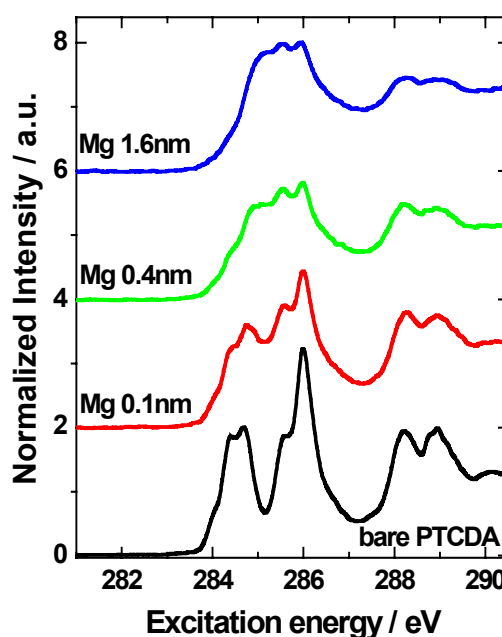


Figure 3. C1s NEXAFS - fine structure region measured as a function of Mg coverage on PTCDA

Acknowledgements

The authors gratefully acknowledge the BMBF (No. 05 KS1OCA/1) and the EU funded Human Potential Research Training Network DIODE (Contract No.: HPRN-CT-1999-00164)) for the financial support. Also to Dr. S. Molodsov, Dr. D. Vyallikh, Dr. D. Batchelor and Mike Sperling for the fruitful scientific discussions and technical support.

Imaging the exchange correlation hole in a $(\gamma, 2e)$ experiment from NaCl

J. Kirschner, G. Kerhervé and C. Winkler

Max-Planck Institut für Mikrostrukturphysik, Weinberg 2, D-06120 Halle

1 Introduction

Correlation between electrons is a fundamental characteristic of systems containing many electrons. The influence of correlation on the electronic structure of solids manifests itself in enhanced or suppressed magnetic susceptibilities of paramagnetic metals, large electronic coefficients of the heat capacity, or in differences between experimental and theoretical one-electron band widths, to name only a few examples. A quite promising way to investigate these correlation effects is to study the double photoemission (DPE), where the absorption of a single photon leads to the simultaneous excitation and emission of two (correlated) electrons. This simultaneous two-orbital excitation following the absorption of one VUV photon is exclusively caused by the interelectronic interaction because in the case of excitations by electron dipole transitions, a photon can only interact with one electron at a time [1],[2]. Recent theoretical calculations, carried out by Fominikh et al [3] on Cu(001) at a photon energy of $h\nu = 21.2$ eV, yield a striking structure in the angular distribution of photoemission from a surface, namely zones of strongly reduced intensity when distribution of the momenta parallel to the surface of one electron with a certain energy is mapped while the second electron is fixed in its momentum at the same energy. This observation can be understood from electron-electron repulsion, where the exchange interaction prevents two electrons from escaping with comparable wave vectors within a proximity determined by the screening length. Therefore, this so-called *exchange correlation hole* can be seen as a direct manifestation of exchange and correlation between two photoelectrons, where the size of the hole reflects the strength of the interaction between two electrons.

In the present work, the energy- and angle-distributions of correlated photoelectrons

ejected from a NaCl single crystal surface were studied in order to image the *exchange correlation hole* experimentally. This work was carried out at the dipole beamline CP-NIM of the BESSY II synchrotron radiation source in Berlin in the single-bunch-mode with photon energies of $h\nu \leq 50$ eV.

2 Experimental details

In the present experiment, the time-of-flight technique was utilised to determine the energy of the electrons released from the surface by an incoming photon. The momentum of one electron is determined by using a microchannel plate (MCP) in combination with a

position sensitive resistive anode. The corresponding coincident electron is detected with a central collector. With a distance of $l \simeq 55$ mm between sample and detector, the flight time of the electrons is typically about a couple of tens ns, and the solid angle covered with this set up is $\Omega \simeq 1.8$ steradian. The experiments were carried out under UHV conditions at a base pressure of $p_b \leq 10^{-10}$ mbar. In order to increase the energy resolution of the TOF-spectrometer, external magnetic distortions were compensated. Furthermore, the sample was held continuously at a temperature of $T_s = 110^\circ$ C to avoid charging effects and to anneal the probe. A schematic view of the experimental set up is given in fig. 1.

The flight times of the two electrons were measured with a set of time-to-amplitude converters (TAC) and the signals of the resistive anode were recorded with digitizers, while the bunchmarker of the beamline was taken to synchronise the system. Finally, an additional electronic coincidence unit extensively suppresses the background and selects events due to time-correlated electrons.

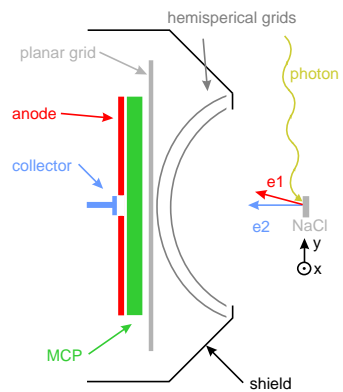


Figure 1: Schematic view of the experimental set up. e1, e2: photoelectrons, MCP: multichannelplate.

3 Results

In the following, results will be presented on photoelectron coincidence spectroscopy that was carried out on a NaCl(100) single crystal at a photon energy of $h\nu = 34$ eV with non-polarised synchrotron light. The surface normal of the probe was pointing to the center of the detector, marking the 0° polar angle of the emission direction.

Fig. 2 shows the momentum distribution of the first photoelectron with a kinetic energy of 8 eV, if its measured intensities of the momenta parallel to surface k_x and k_y are plotted, while the momentum of the second (correlated) electron with an energy of 7 eV is fixed along the surface normal. In fig. 2, the position of this second electron, which corresponds to the *blue* electron e2 in fig. 1, can be seen as a white spot in the center. The most striking feature in fig. 2 is an area of rather low intensity that appears almost as a disk with a diameter of about 1 \AA^{-1} around the center. This structure is principally very much alike to the calculated angular distribution of photoemission performed by Fominykh et al[3], and implies that the lack of intensity reflects the *exchange correlation hole*, as discussed above.

It should be noted that the full momentum distribution cannot be deduced from this data, since the accessible momentum range is strictly limited by the finite size of the MCP, so that the apparent structure in fig. 2 at the edge of the spectrum is meaningless. The actual dimension of the correlation hole becomes clearer from the symmetrised radial line scan done to the data in fig. 2, where the measured intensity is summed up along the parallel momentum k , see fig. 3. Here it is interesting to note that the dimensions of the calculated copper case and measured NaCl are comparable, which suggests that the size of the hole is not very much depending on the photon energy and

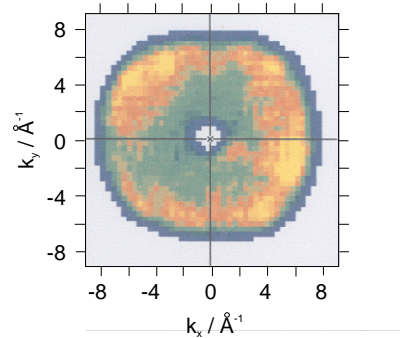


Figure 2: Momentum distribution of one electron while the momentum of the second electron is fixed around the surface normal. The energies of the two electrons are 8 eV and 7 eV, respectively.

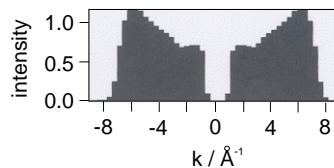


Figure 3: Symmetrised radial line scan of the momentum distribution shown in fig. 2.

the probe material. However, much further experimental and theoretical work, i.e. at various photon energies and on different samples, has to be done.

References

- [1] J. Berakdar, *Phys. Rev B* **58** (1998) 9808
- [2] J. Berakdar, *Appl. Phys. A* **69** (1999) 497
- [3] N. Fominykh, J. Berakdar, J. Henk and P. Bruno, *Phys. Rev. Lett.* **89**, 086402 (2002)

Resonant soft x-ray emission spectra of FeF₂ and CrO₂

A.S. Vinogradov¹, S.A. Krasnikov^{1,2}, A.B. Preobrajenski^{1,3}, R. Szargan², D.V. Vyalikh^{1,4},
S. L. Molodtsov^{1,4}, C. Laubschat⁴, Yu. S. Dedkov⁵, M. Fonin⁵, and G. Güntherodt⁵

¹ V.A. Fock Institute of Physics, St. Petersburg State University, St. Petersburg, 198504 Russia;

² W. Ostwald-Institut für Physikalische und Theoretische Chemie, Universität Leipzig, D-04103, Leipzig, Germany;

³ MAX-lab, Lund University, S-22100 Lund, Sweden;

⁴ Institut für Festkörperphysik, Technische Universität Dresden, D-01062 Dresden, Germany

⁵ II Physikalisches Institut, Rheinisch Westfälische Technische Hochschule Aachen, D-52056, Aachen, Germany.

The soft x-ray emission (SXE) spectroscopy is traditionally used to study electronic structure of solids via electron transitions from the valence band to an empty core level. Due to the binding energy

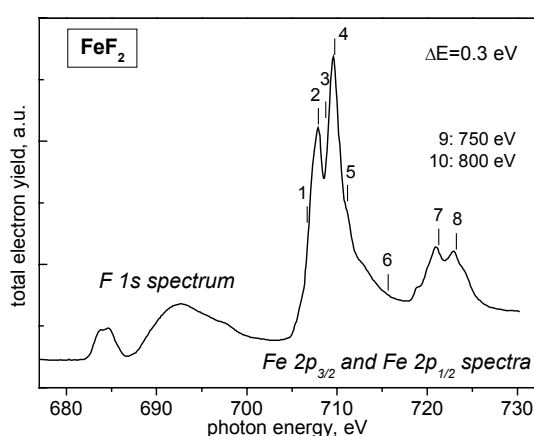


Fig. 1. F 1s and Fe 2p absorption spectra of FeF₂. The numbered bars mark photon energie used to excite Fe 2p emission spectra.

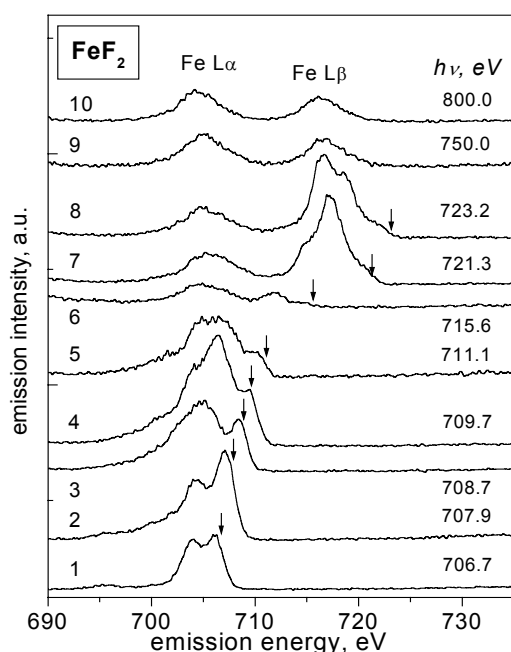


Fig. 2. Resonant Fe 2p emission spectra of FeF₂. The vertical arrows show recombination peaks.

separation of core levels in different atomic species and dominant atomic dipole selection rules that govern the x-ray emission process, SXE spectra give the elementally resolved partial density of states [1]. Recent developments of synchrotron radiation sources producing intense tunable monochromatized x-ray beams opened up new possibilities for SXE spectroscopy [2]. In particular, the possibility to select the energy of the excitation allows to perform resonant excitation, i.e. to produce a hole in the core electron shell exciting the core electron to localized empty states. These resonant SXE spectra lead to a better understanding of excitation-emission dynamics and give more specific information about electronic structure.

This report briefly discusses results of our use of resonant SXE spectroscopy to obtain new information on the valence electronic structure of FeF₂ and CrO₂. These 3d atom compounds are of great technological interest owing to their important physical-chemical properties. Metal fluorides, among them FeF₂ and FeF₃, have attracted considerable attention in high-resolution electron beam nanolithography because of their self-developing properties [3] while half-metallic ferromagnetic CrO₂ is considered as a promising material for magnetoelectronic devices [3]. For a better understanding of these important properties of FeF₂ and CrO₂ detailed information on their valence band electronic structure is necessary. It should be noted that both solids have the same rutile crystal structure.

All measurements were performed at the U41-PGM beam-line at BESSY II. The x-ray absorption spectra were measured in the total electron yield mode and are normalized to the incident photon flux. Resonant SXE spectra were recorded using a grazing-incidence x-ray spectrometer XES 300 of the end station ROSA. The energy resolution of x-ray spectrometer was set to 0.85 eV, 0.6 eV and 0.5 eV for Fe 2*p*, Cr 2*p* and O 1*s* spectra, respectively. The axis of x-ray spectrometer was set perpendicular to the beam-line axis in the plane of polarization of incident radiation in order to avoid the elastically scattered peak. The angle between the sample normal and the monochromator axis was 30°. The powder sample of FeF₂ was pressed into metallic indium plate attached to the sample holder. The high quality CrO₂(100) films were prepared on isostructural TiO₂(100) substrates.

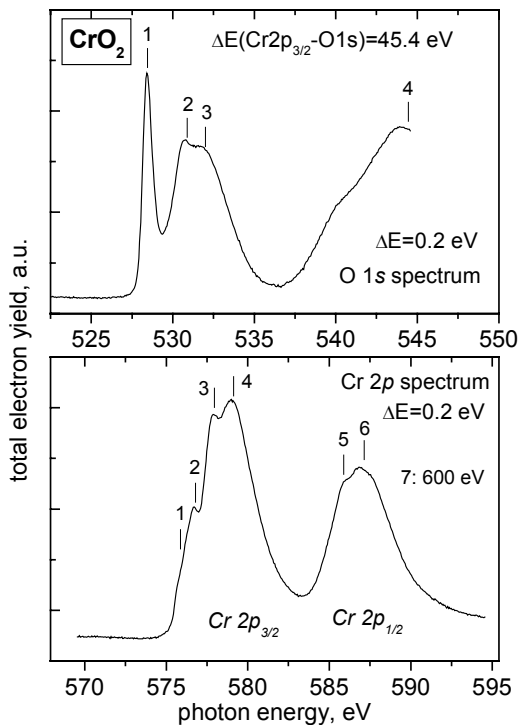


Fig. 3. Cr 2*p* and O 1*s* absorption spectra of CrO₂ aligned in energy using $\Delta E(\text{Cr}2p_{3/2}-\text{O}1s)$.

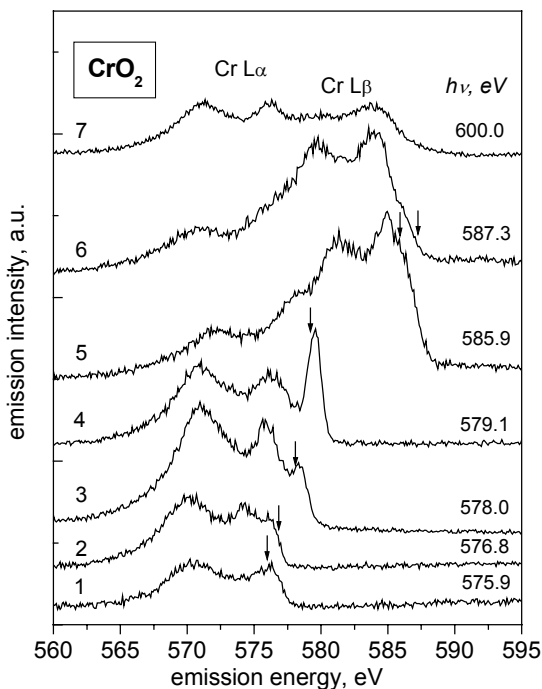


Fig. 4. Resonant Cr 2*p* emission spectra of CrO₂. The vertical arrows show recombination peaks.

The absorption and emission measurements for FeF₂ involving the Fe 2*p* electrons are shown in Figs. 1 and 2. The emission spectra are normalized to the acquisition time and the incoming photon flux. The Fe 2*p*_{3/2} and 2*p*_{1/2} emission spectra correspond to transitions of valence band electrons with the 3*d* character to the 2*p*_{3/2} and 2*p*_{1/2} core levels, respectively. In the case of nonresonant excitation (well above the absorption resonances, curves 9 and 10), both transitions denoted commonly by Fe *L*α and Fe *L*β are excited simultaneously. The curves 1-6 present the resonant Fe 2*p*_{3/2} spectra which are excited without the Fe 2*p*_{1/2} ones. It is seen from Fig.2 that the resonant Fe 2*p*_{3/2} spectra as well as the Fe 2*p*_{1/2} ones differ considerably in their spectral shapes from the nonresonant Fe *L*α and Fe *L*β spectra. These differences are indicative of an impact of the 2*p* electron excited to a localized empty 3*d* electron state on the x-ray emission process. Two types of processes determine the shape of resonant SXE spectra, which are commonly referred to as spectator and participator radiative decay. The term "spectator" implies that the electron promoted from a core level to an empty state remains in this state during the x-ray emission giving rise to spectator structures in spectra which are often considered as a result of the resonant inelastic x-ray scattering. In contrast, in the case of the "participator" decay the excited electron returns to the initial core level and annihilates the core hole causing reemission or recombination peaks

and attendant inelastic structures which are often associated with the resonant elastic x-ray scattering processes. In Fig. 2 the vertical arrows show the energy positions of the recombination peaks which are coincident with the photon energies used to excite the emission spectra. One can see from Fig. 2 that the similar intense peaks are available in the Fe 2*p*_{3/2} spectra and they are lacking in the Fe 2*p*_{1/2}

ones. Obviously the emission structures at the lower energies relative to the recombination peak reflect features due to the resonant inelastic x-ray scattering. It is interesting to note that the intensity relationship between the recombination peak and the inelastic structures in the Fe $2p_{3/2}$ and Fe $2p_{1/2}$ spectra changes considerably when the exciting photon energy is scanned across the Fe $2p_{3/2} \rightarrow 3d$ and Fe $2p_{1/2} \rightarrow 3d$ absorption resonances.

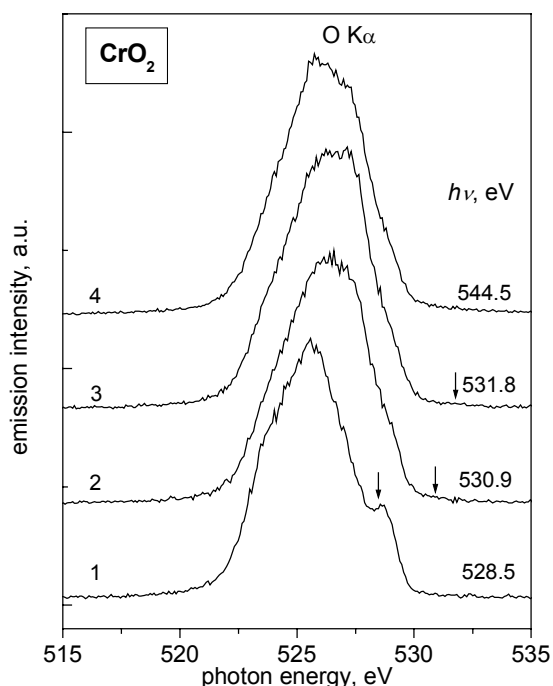


Fig. 5. Resonant O $1s$ emission spectra of CrO_2 .

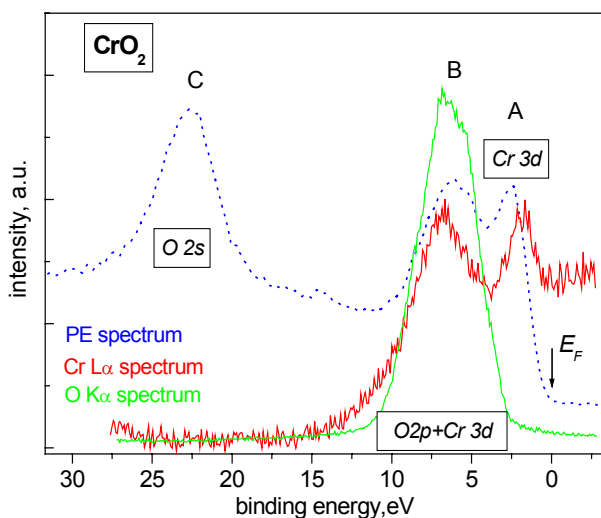


Fig. 6. Comparison between the nonresonant Cr $2p_{3/2}$ and O $1s$ emission spectra and valence band photoemission spectrum of CrO_2 .

The Cr $2p$ and O $1s$ absorption spectra of CrO_2 (Fig. 3) are aligned in energy using measured energy separation (45.4 eV) between the Cr $2p_{3/2}$ and O $1s$ core levels [5]. Resonant Cr $2p$ and O $1s$ emission spectra are presented in Figs. 4 and 5, respectively. The chromium emission spectra under changes of the excitation energy show the features which are similar to the ones observed in the resonant Fe $2p$ spectra of FeF_2 . The recombination peak in the resonant O $1s$ emission spectra is observed only at the lowest excitation in the absorption spectrum. It is worth noting that the O $1s$ emission spectrum undergoes distinct changes in the shape with increasing the excitation energy. In the Fig. 6 the nonresonant Cr $L\alpha$ and O $K\alpha$ emission spectra are compared with the valence band photoemission spectrum of CrO_2 taken at the

photon energy of 400 eV [5]. These spectra are displayed on the common binding energy scale: the photoemission and O $K\alpha$ are aligned at the position of the band B, while for alignment of the Cr $L\alpha$ and O $K\alpha$ spectra the measured $\Delta E(\text{Cr}2p_{3/2}\text{-O}1s)$ separation of 45.4 eV is used. This comparison indicates that the valence band of CrO_2 is composed from two subbands A and B with the pure Cr $3d$ and hybridized Cr $3d + \text{O } 2p$ character, respectively.

Acknowledgements

This work was supported by the RFBR (project no. 01-03-32285), the BMBF (grants no. FKZ 05KSIPAA/7 and FKZ 13N7988), the DFG (SFB 463, TP B4 and B16), and the bilateral program Russian-German Laboratory at BESSY II. We thank the staff of BESSY II for valuable technical assistance. A.S. Vinogradov gratefully

acknowledges the financial support by the Technische Universität Dresden and the W.-Ostwald-Institut für Physikalische und Theoretische Chemie der Universität Leipzig. A.B. Preobrajenski acknowledges the support by the Swedish Foundation for International Cooperation in Research and Higher Education (STINT).

References

1. L.G. Parratt, *Rev. Mod. Phys.* **31**, 616 (1959)
2. B.J. Nordgren, *J. Electron Spectr. Relat. Phenom.* **78**, 25 (1996)
3. J. Fujita et al., *Appl. Phys. Lett.* **66**, 3064, (1995); H. Watanabe et al., *Jpn. J. Appl. Phys., Part 1* **34**, 6950 (1995)
4. K.-H. Schwarz, *J. Phys. F: Met. Phys.* **16**, L211 (1986); S.P. Lewis et al., *Phys. Rev. B* **55**, 10253 (1997); M.A. Korotin, V.I. Anisimov, D.I. Khomskii, G.A. Sawatzky, *Phys. Rev. Lett.* **80**, 4305 (1998)
5. A.S. Vinogradov, Yu.S. Dedkov, M. Fonin, D.V. Vyalikh, et al., *BESSY Annual Report 2003*, in print.

X-ray longitudinal Kerr rotation and ellipticity spectra at the 2p edges of Fe, Co, and Ni

S. Valencia, H.-Ch. Mertins*, D. Abramsohn, A. Gaupp, and W. Gudat
BESSY, Albert-Einstein Strasse 15, D-12489 Berlin, Germany
P.M. Oppeneer

Leibniz-Institute of Solid State and Materials Research, P.O. Box 270016,
D-01171 Dresden, Germany

Key words: Magneto-optics, Kerr spectra, Polarimeter

Among the available magneto-x-ray spectroscopies resonant magnetic scattering and specular reflectometry of circularly and linearly polarized soft x-rays are becoming increasingly popular since the observed magnetic responses can exceed those of XMCD absorption experiments [1]. Moreover, the large size of the dichroic effects observable over a wide range of incident angles, as well as their sensitivity to layer thickness and interface roughness, designates x-ray reflection spectroscopies to be extremely useful techniques for the study of element-specific magnetic depth profiles of magnetic films or multilayers. Thus an improvement of our knowledge in such techniques as well as a tool able to obtain the maximum information from the scattered light is desired.

In the course of our systematic investigations of polarization effects in the soft X-ray region we report here on the first longitudinal magneto-optical Kerr (L-MOKE) rotation and ellipticity spectra measured across the 2p absorption edges of amorphous Fe, Co, and Ni (30nm thick sputtered layers capped with 3nm Al to prevent oxidation). We demonstrate theoretically and experimentally the close relation between such spectra taken at grazing incidence and those of two other reflection-type techniques, the X-ray magnetic circular dichroism (XMCD) and the transversal magneto-optical Kerr effect (T-MOKE). In addition the origin of the spectral features is analysed by means of numerical simulations.

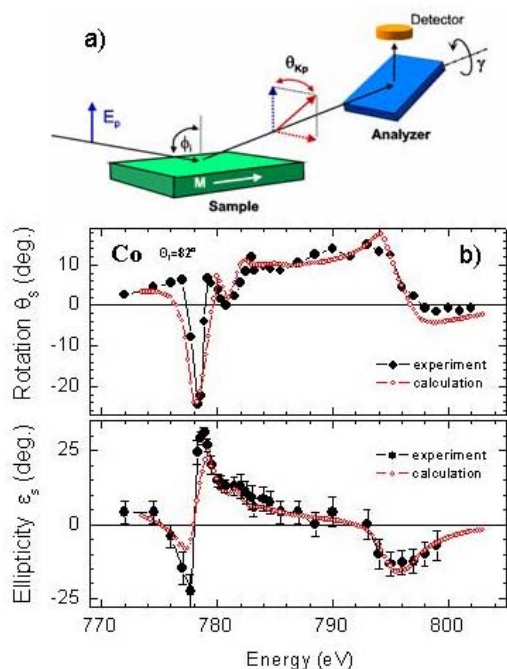


Fig 1. a) Experimental set up for the polarization analysis of the L-MOKE measurements and b) comparison between experimental (black circles) and calculated (red dots) rotation and ellipticity for the Co sample.

The L-MOKE effect consists in a rotation of the polarization plane and the appearance of elliptically polarized light, when linearly polarized light is reflected from a material which has a magnetic component parallel or anti-parallel to the propagation direction of the in-coming radiation. Thus a complete polarization analysis is needed to evaluate the phenomena.

The room temperature experiments were done at U49-1-PGM and UE56-1-PGM-1 beam lines at BESSY using the UHV polarimeter [2]. The experimental set-up is shown in Fig. 1a. The sample is set to an angle of incidence θ_i with respect to the normal and the polarization analysis is performed at selected energies across the 2p edges; the reflected intensity is recorded for two different magnetic field directions, while azimuthally rotating the analyser (γ) (W/Si multilayer of

150 periods of 1.12nm each). The data are fitted by the relation

$I(\gamma) = I_R [1 + P_{Lin} P_A \cos 2(\gamma + \theta_s)]$, which allows to obtain the Kerr rotation (θ_s) as well as the ellipticity (ϵ_s), once the polarizing power of the analyser (P_A) is known and considering fully polarized light, $\sin(2\epsilon_s) = P_{Circ} = \sqrt{1 - P_{Lin}^2}$.

In order to reduce the exposition of the data we will show only the results for Co ($\theta_i=82^\circ$). Those of Fe and Ni can be found in reference 3.

Fig 1b shows the Kerr rotation and ellipticity spectra for Co. Large Kerr rotations of up to 24° have been measured, thus being larger by two orders of magnitude than those detected at the visible energy range [4]. The rotation spectra have been analysed in order to identify the different contributions to their final shape. Using a macroscopic light propagation formalism with Fresnel reflection coefficients r_{ss} and r_{ps} for s polarized light an analytical expression for the Kerr effect can be derived [5]:

$$\theta_s + i\epsilon_s = -r_{ps}/r_{ss} \approx \frac{-in_0 n Q \cos \phi_i \tan \phi_t}{(n^2 - n_0^2) \cos(\phi_i - \phi_t)} \quad (1)$$

where $Q=2*(-\Delta\delta+i\Delta\beta)/n$ is the Voigt parameter, n the non magnetic reflection coefficient for the layer and n_0 that of the vacuum or cap layer.

Equation 1 allows to identify two main contributions to the spectra:

- i) The large Kerr rotations at the $2p_{3/2}$ and $2p_{1/2}$ edges are directly related to the magneto-optical constants $\Delta\delta$ and $\Delta\beta$.
- ii) In between the edges the dichroic contrast ($n^2-n_0^2$) approaches to zero thus dominating the shape in this region. This effect was recently predicted by *ab initio* calculations [6].

A third contribution is responsible for the pronounced minimum at 778.5 eV in Fig. 1, where no feature is expected, since the energy is already below the $2p$ resonance. In order to identify such a contribution we have performed numerical simulations by means of a computer code being currently developed at BESSY and by using previously determined optical constants for Co and Fe [7]. This code is based on a formalism of Zak *et al.* for determining magneto-optic coefficients in multilayer systems with arbitrary directions of their magnetizations [8]. The validity of the formalism is demonstrated in Fig. 1a where the calculated rotation and ellipticity spectra for Co are plotted together with the experimental ones. The computer simulations have shown that the origin of such strong negative rotation is due to the interferences of the waves being reflected at the magnetic surface and at the Si substrate. This is corroborated in Fig. 2b where the simulations for the Fe are plotted, the variation of the thickness of the layer causes a change in its position as well as in its magnitude, disappearing for the thickest layer (500 nm), where no reflection from the

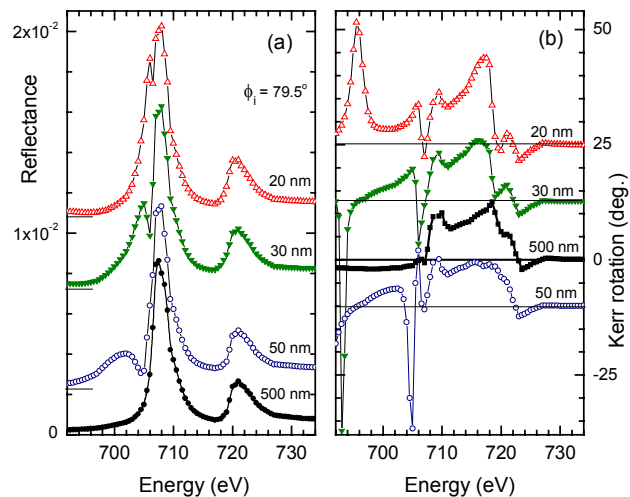


Fig 2. Simulated reflection (a) and Kerr rotation (b) spectra for a Fe layer of various thicknesses on top of a Si wafer.

substrate is expected. It can also be observed its correlation with the minima in the reflectance spectra (Fig 2a) which appears at the same energy position.

Using the above mentioned macroscopic light propagation formalism, we have shown that a theoretical relation holds analytically for grazing angles of incidence between the XMCD (measured in reflection) and the T-MOKE with the longitudinal Kerr rotation and ellipticity spectra [3]. This two reflection techniques are purely intensity measurements where polarization analysis is not necessary. In the XMCD measurements the reflectance $R_{C\pm}$ for left-right circular polarized light is measured and the so called Asymmetry parameter, $A_C = (R_{C+} - R_{C-}) / (R_{C+} + R_{C-})$, is defined. The same can be done for T-MOKE where the reflection of linear p-polarized light is recorded ($R_{T\pm}$) for two inverted magnetization directions transversal to the scattering plane. In this case $A_T = (R_{T+} - R_{T-}) / (R_{T+} + R_{T-})$. It can be shown that for small grazing angles of incidence the following relations hold:

$$\theta_s = A_T \operatorname{Re}\{\cos(\phi_i - \phi_t) / 4 \cos \phi_t\} \approx A_T \operatorname{Re}\left\{n_0 / 4 \sqrt{n^2 - n_0^2} + \cos \phi_i / 4\right\} \quad (2)$$

$$\varepsilon_s \approx \frac{1}{2} A_C + \cos \phi_t \operatorname{Im}\{r_{ps} \sqrt{n^2 - n_0^2} / n_0 r_{ss}^2\} \quad (3)$$

As can be seen in Fig. 3 the rotation spectra calculated this way does not present the minimum at 778.5 eV. This feature has been also verified by the computer simulations.

In conclusion by a complete polarization analysis we have measured the first experimental rotation and ellipticity L-MOKE spectra at the 2p edges of Fe, Co and Ni. The development of a new computer code at BESSY has allowed to identify the different contributions to the spectral shape of the Kerr rotation, separating contributions arising from atomic transitions from those arising from interference effects. Finally a close relation between L-MOKE and two other reflection-type magneto-optical techniques have been found to hold for grazing incident angles (θ_i between 90° and 75°). Such a relation allows the measurement of Kerr rotation and ellipticity spectra without the need of a polarization analysis, just by doing two simple XMCD and T-MOKE intensity-measurements.

References:

- [1] H.-Ch. Mertins et al. Phys. Rev. B **66**, 184404 (2002).
- [2] F. Schäfers et al. Appl. Opt. **38**, 4074 (1999).
- [3] H.-Ch. Mertins et al. Accepted for publication in Phys. Rev. B. (2004).
- [4] J.M. Ballantyne, Phys. Rev. B **54**, 1352 (1964)
- [5] P.M. Oppeneer, in *Handbook of Magnetic Materials*, edited by K. H. J. Buschow (Elsevier, Amsterdam, 2001), Vol. **13**, pp. 229-422.
- [6] J. Kunes et al. Phys. Rev. B **64**, 174417 (2001).
- [7] H.-Ch. Mertins et al. J. Magn. Magn. Mater. **240**, 451, (2002).
- [8] J. Zak et al Phys. Rev. B **43**, 6423 (1991).

* New permanent address: Univ. of Appl. Sciences Münster, Stegerwaldstrasse 39, D-48565 Steinfurt, Germany

This work has been done with support of the BMBF project 05KS1-IPB/8

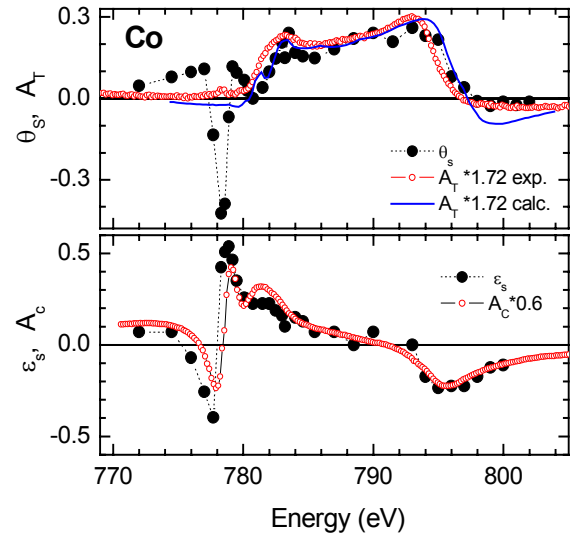


Fig 3. Experimental Kerr rotation and ellipticity spectra for Co at the 2p edges (black diamonds) together with the calculated ones (red open circles) using eq. 2 and 3 and the experimentally measured XMCD and T-MOKE. The blue line shows the calculated rotation by using eq. 2 and the simulated T-MOKE spectrum.

Cooper minimum observed for the Pr5s and Pr5p states in Pr₂O₃

Dieter Schmeißer

Angewandte Physik – Sensorik, BTU Cottbus, Postfach 10 13 44, 03013 Cottbus

We study the properties of Pr and its oxides at the interface regime on Si and SiC substrates. We find that at this highly reactive interface many intermediate reaction products occur /1,2/. Our goal is to understand the chemical stability of each individual species at the interface, the variation in the valence band population, and the influence of the localized Pr4f states. One of the coexisting phases is the bulk phase of Pr₂O₃, and we have succeeded to prepare it without other components in a thin layer on a SiO₂ covered Si(001) substrate. Here, we report on a very surprising particular feature of the bulk Pr₂O₃ phase and give evidence that the Pr5s and Pr5p states show a Cooper minimum in the photo ionization cross section (PIX). A Cooper minimum is the consequence of the nodes in the wave function which occurs and is characteristic for d-states with an angular momentum quantum number of $l=2$ /3-5/. It is observed in atoms, in theoretical calculations of the PIX /4/, and is observed in solids /5/.

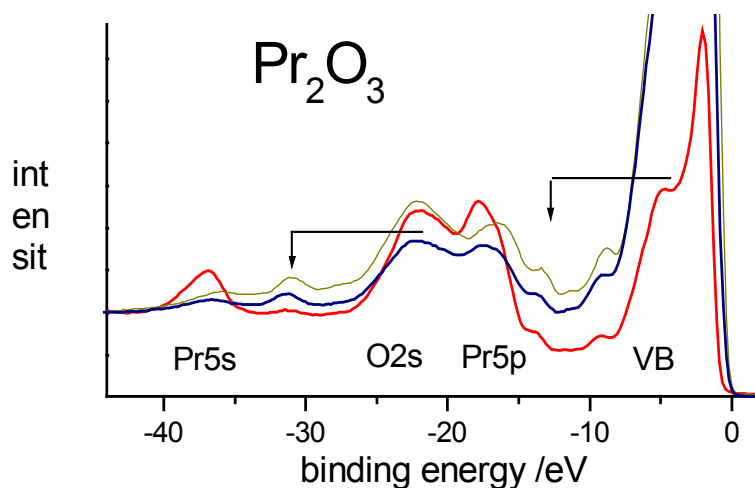


Fig.1
Pr₂O₃ valence band spectra
taken at photon energies of
360eV, 150eV, and 240eV.

In fig.1 we have depicted the valence band emission of bulk Pr₂O₃ with the well separated emission ranges of the Pr5s, O2s, Pr5p, as well as the valence band range consisting of Pr6s, O2p, and Pr4f states /1,2/. To show the Cooper minimum, in our experiment the photon energy is varied between 150eV and 450eV and its dependence on the individual valence band features is shown in fig.2. We observe in that range above the Pr4d-4f resonance a significant variation in the cross section of the Pr4d core levels which shows a broad Cooper minimum with the weakest intensity around 200eV. The original data are normalized to the intensity of the oxidic Si2p emission at 103eV and indicate that the Pr4d intensity is quenched to about 15% at a photon energy of 200eV. The shape of the Cooper minimum is rather broad, at low photon energies an assignment of the Pr4d intensity is not possible because of overlap with an Auger transition and the Pr4f resonance. Very remarkably, the valence band features also show characteristic variations in that photon energy range. We notice that the PES signals belong to two different classes. The first one (Fig.2a) includes the valence band (Pr4f and O2p) states as well as the shake off peaks (arrows). The intensity of these features falls off continuously within the investigated range. The second one (Fig.2b) follows the intensity variation of the Pr4d states and it includes the Pr5s and the Pr5p states. This surprising observation reflects the presence of the exchange interaction Xi in the intermediate state as will be discussed below.

The Cooper minimum in the X-section of the Pr5s shallow core level is addressed now. We consider that besides the direct photo ionization there coexists a two step process in which the

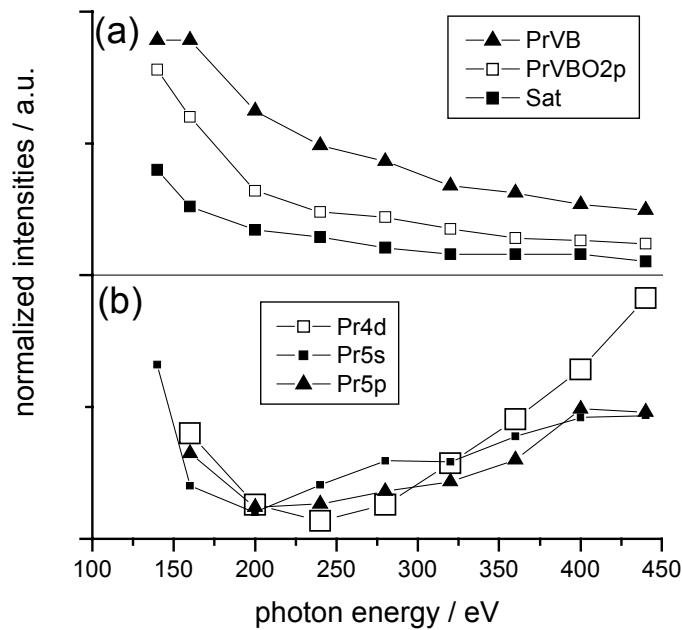


Fig.2
The intensities of the individual Pr atomic features upon varying the photon energies (normalized to that of the Si2p emission) are collected in (a) for the valence band signals (Pr4f and O2p), the satellite features (Sat), and in (b) for the Pr5s, Pr5p, and Pr4d states, respectively.

photo electron first is excited into an intermediate state and is released afterwards. It is another point of interest to find out by what mechanisms the intermediate state becomes filled and which of the empty states are involved. In Pr₂O₃ the most probable state is that the electron may intermediately occupy Pr5d states in the empty CB. The excited electron in that intermediate state it will interact via the exchange interaction Xi with all possible atomic like valence states and shallow core levels to give significant contributions such as

$$Xi(Pr5s, Pr5d) = \langle Pr5s \bullet CB(Pr5d) \mid 1/r \mid CB(Pr5d) \bullet Pr5s \rangle.$$

As a consequence, the escaping photoelectron may originate from an Pr5d state while initially an electron was excited out of the Pr5s core level. In our experiments that interaction is witnessed as the escaping electron now shows variations in its PIX which are characteristic for d-states (Cooper minimum) although its binding energy identifies an Pr5s initial state. In addition, the escaping photo electron experiences the interaction with all available CT complexes. This reflects in a significant broadening of the photoemission signal which corresponds to the total strength of the exchange interaction as well as the formation of shake up satellites as evident in fig.1.

In conclusions, we give experimental evidence for the exchange interaction to contribute in the photo ionization cross section of the valence states of Pr₂O₃. The exchange interaction shows up in our data in the width of the PES signals, in strong satellite intensities, and in the appearance of a Cooper minimum for Pr5s and Pr5p parent states.

Acknowledgement

The experimental assistance of Guido Beuckert and Ioanna Paloumpa is appreciated as well as the support at the U49/2 beam line of Patrick Hoffmann and the BESSY staff. This work is supported by DFG Schm745/9-1.

Literature

- 1 D.Schmeißer and H.J.Muessig, J.Phys.Cond.Matter 16 (2004)S153.
- 2 D.Schmeißer, Materials Science in Semiconductor Processing 6 (2003) 59.
- 3 J.W.Cooper, Phys. Rev. 128 (1962) 681.
- 4 J.Yeh and I.Lindau, At. Data Nucl. Data Tables 32(1985)1.
- 5 S.L.Molodtsov, S.V.Halilov, V.D.P.Servedio, W.Schneider, S.Danzenbacher, J.J.Hinarejos, M.Richter, C.Laubshat, Phys.Rev. Letters 85 (2000) 4184.
- 6 G.Wendin, Phys.Rev.Lett. 53 (1984) 724.

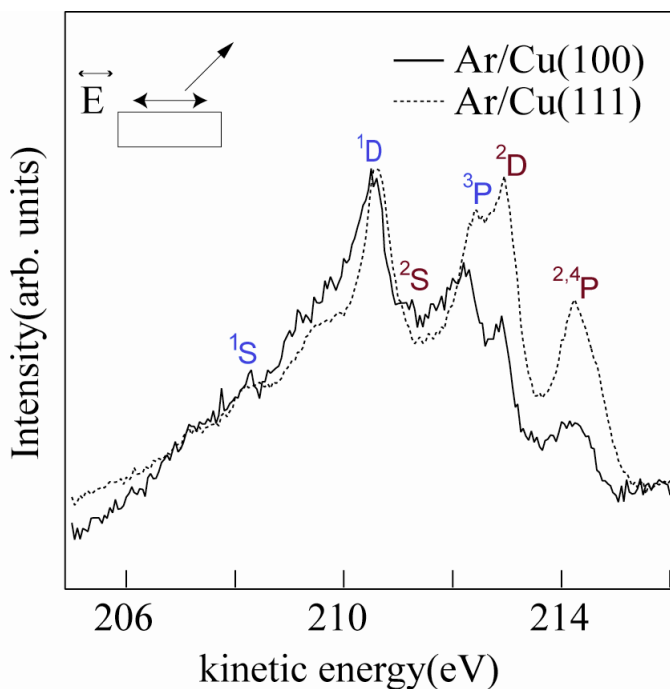
Influence of the surface projected band gap on the charge transfer dynamics between the adsorbate and the substrate

*S. Vijayalakshmi, A. Föhlisch, A. Pietzsch, F. Hennies, M. Nagasono, W. Wurth
Institut für Experimentalphysik, Universität Hamburg, 22761 Hamburg, Germany*

The surface projected band structure of single crystals is known to differ significantly for different crystallographic orientations. Consequently, the charge transfer dynamics between adsorbed atoms and molecules and the substrate are also highly sensitive to the surface projected band structure of the substrate. In particular, for Cu a surface projected band gap with a surface state is found on the Cu(111) face. In contrast, on the Cu(100) face, there is no surface projected band gap. Thus, on the Cu(111) surface charge transfer should be reduced in comparison to the Cu(100) surface. Both from the theoretical and experimental side the charge transfer dynamics between adsorbed Cs on the Cu-surfaces has been investigated. Time resolved 2 photon photoemission studies find for the Cs electronic resonance on the Cu(111) surface a charge transfer time approx. twice as large (~ 10 fs) as on the Cu(100) surface^(3,4). Also theoretical models of Cs on Cu(111) and Cu(100) surfaces show this influence from the band gap leading to large differences in charge transfer dynamics⁽²⁾.

We have now studied the charge transfer dynamics between Ar on Cu(111) and Cu(100) using the so called core-hole clock method. Here the charge transfer time for the Ar 4s electron of core-excited Ar($2p_{3/2}^{-1}4s$) to the surface is determined on the femtosecond timescale of the Ar($2p_{3/2}^{-1}4s$) core-hole lifetime. In previous work, we have determined for different metal substrates the charge transfer times in Ar adsorbed on Ag(111), Ni(111), Ru(001) and Cu(111)⁽¹⁾. This is done by the quantitative determination of the branching ratio of decay channels related to charge transfer channels vs. atomically localized decay channels at the adsorbate atom⁽⁵⁾.

Fig.1: Autoionization spectra of the resonantly excited Ar ($2p_{3/2}^{-1}4s$) adsorbed on Cu(111) and Cu(100) surfaces. The relative intensities of decay channels vary for the two surfaces. Using the core-hole clock method, we extract a shorter charge transfer time on Cu(100) in comparison to Cu(111).



The experiments were performed at the BESSY UE56/1-SGM Beamline using our new UHV spectroscopy chamber equipped with a SCIENTA SES2002 analyzer. A monolayer of Ar is prepared on the clean Cu(111) and Cu(100) surfaces. All the measurements were made with the electric field of the photons lying parallel to the surface. Excitation bandwidth is 120 meV.

In Fig. 1 the autoionization spectra of Ar adsorbed on Cu(100) and Cu(111) for resonant Ar($2p_{3/2}^{-1}4s$) excitation are shown. We observe autoionization features, where the Ar4s electron stays at the adsorbate (Auger Raman lines (2S , 2D , $^{2,4}P$)) and autoionization features representing charge transfer into the substrate (normal Auger lines (1S , 1D , 3P)). In particular, the relative intensity of Auger Raman channels to normal Auger channels is larger on the Cu(111) surface than on the Cu(100) surface. This finding directly indicates, that charge transfer of the Ar4s electron in the Ar($2p_{3/2}^{-1}4s$) excited state is faster for Cu(100) than for Cu(111) in agreement with the behavior expected from the projected band structure of Cu substrate. A detailed quantitative analysis is required to understand these effects and is underway.

Acknowledgements

We are grateful for the support given by S. Cramm, S. Eisebitt and the BESSY II crew. Financial support was given by the Deutsche Forschungsgemeinschaft under Schwerpunktprogramm SPP 1093 "Dynamik von Elektronentransferprozessen an Grenzflächen".

References

1. A. Föhlisch et al., Chem. Phys. 289 (2003) 107.
2. A.G. Borisov and J.P. Gauyacq, Phys. Rev. Lett. 86 (2001) 488.
3. M. Bauer et al., Phys. Rev. B 60 (1999) 501.
4. M. Bauer et al., Phys. Rev. B 55 (1997)10040.
5. W. Wurth and D. Menzel, Chem. Phys. 251 (2000) 141, and references therein.

Time Resolved Laser-Synchrotron 2 Photon Photoemission at the BaF_2/Si interface

A. Pietzsch, F. Hennies, S. Vijayalakshmi, A. Föhlisch, and W. Wurth
*Institut für Experimentalphysik, Universität Hamburg,
Luruper Chaussee 149, D-22761 Hamburg, Germany*

Two-Photon Photoemission (2PPE) is a variant of photoelectron spectroscopy which allows the investigation of unoccupied electronic states. A *pump* laser pulse excites electrons in the studied system and a *probe* laser pulse then photo-emits the electron. The measurement of its kinetic energy provides a means to determine the binding energy of the unoccupied state with respect to the vacuum level and also dynamical information of the system in time-resolved 2PPE by variation of the delay between the two pulses. However, the limited energy range of optical lasers does not allow to investigate every desired system. The excitation with a laser pulse followed by subsequent probing of a synchrotron pulse can be applied here. The use of a synchrotron probe pulse offers the great advantage of being tunable in energy which allows a wide range of systems to be studied and to enhance the photoemission cross section. Thus, these pump-probe techniques are very promising for studying excited state properties of adsorbate-surface systems.

In the present experiment, we investigated electron dynamics at a ns time scale where we observe band bending effects at the BaF_2/Si interface. An exponential intensity decrease of the time-resolved signal after laser excitation is found.

The experiment was performed at the Berliner Speicherring für Synchrotronstrahlung BESSY at the MBI-beamline U125/1-SGM (CRG). A laser beam was guided into the chamber to the focus of the electron analyzer (Omicron EA 125) to excite the sample during measurement. The laser pulses ($E = 2.33$ eV, pulse width 12 ns, $E/\text{pulse} = 200$ nJ) were synchronized with the synchrotron (time of circulation: 800 ns): using a pulse picker, a single laser pulse each synchrotron period of 800 ns is selected. The electron analyzer can be operated in two modes, the first one corresponding to the measurement of energy distribution curves (EDC) in photoemission spectroscopy. In the second mode, a time distribution curve (TDC) is measured [1]. The energy dispersed photoelectrons are detected by four energy channels. Depending on the pass energy, each channel detects electrons in a given energy interval. Then, all electrons within this interval are measured as a function of time.

BaF_2 is transparent for the exciting laser due to its large band gap of 9.07 eV at 300 K. Thus, the laser excites the lower-lying Si substrate and creates charges at the BaF_2 -Si interface. At semiconductor surfaces, band bending occurs: uncompensated ions establish an electric field within an adjacent bulk layer. The changes of the electron energy levels near the surface in response to this electrostatic potential cause the band structure to bend to higher binding energies [2].

Charge carrier surface recombination has been investigated before at the Si(001)/SiO₂ interface by Widdra *et al.* [3] by means of laser-synchrotron 2PPE. However, the problem in investigating the Si(001)/SiO₂ sample lies in the fact that the laser can excite the silicon atoms situated in the substrate as well as those in the adsorbate. Thus, the effects observed cannot clearly be assigned with the SiO₂ adsorbate. The situation at the Si/ BaF_2 interface

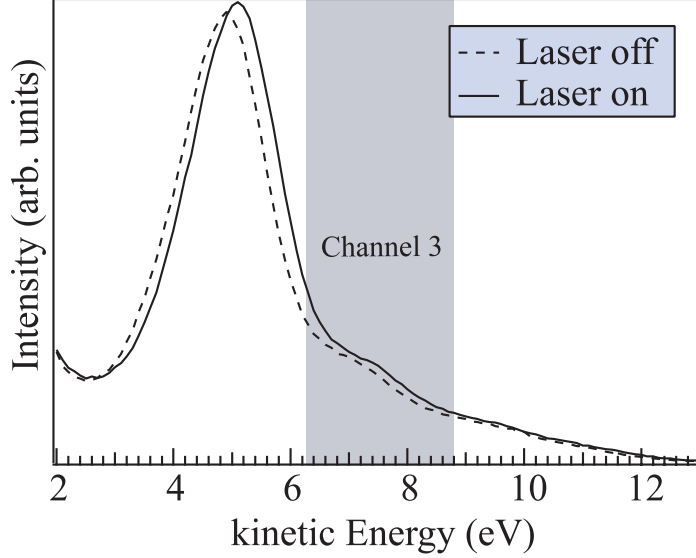


Figure 1: UPS spectra of BaF_2 on Si(100) with and without laser excitation. The dominating peak corresponds to the HOMO of BaF_2 . Comparison of the two spectra shows an energy shift of about 0.15 eV of the spectrum after laser excitation towards higher energies.

is similar to that at the Si(001)/SiO₂ interface with the difference that here, we excite the Si atoms and selectively probe the BaF_2 .

To give an overview of the measured energy channels, a UPS spectrum of the BaF_2 highest occupied molecular orbital (HOMO) is shown in Figure 1. It was measured with a probing energy of $h\nu = 18$ eV and a pass energy of 10 eV. As a reference, also the spectrum without laser excitation is shown. A clear shift of about 240 meV of the BaF_2 HOMO is observed to occur after laser excitation.

To investigate the charging effects at the BaF_2 /Si interface, time resolved measurements were performed using the TDC mode of the electron analyzer. The positioning of the energy windows used for the different channels of the TDC measurements have a width of 2.5 eV each. The position of channel 3 is marked in gray in Fig: 1.

Every channel shows a TDC spectrum which has a length of 800 ns. The data for channel 3 (i.e. the channel at the high-energy side of the HOMO) is presented in the inset of Fig. 2, showing an exponential feature. Coinciding with the delay time of synchrotron and laser, this effect is caused by the laser excitation. In Figure 2, all frequencies with $\nu \geq 0.45$ GHz (i.e. the 2 ns periodic structure of the synchrotron and the high frequency noise) are removed from the spectrum using Fourier transformation. There, it is assumed that there are no other periodic structures arising from the excitation and decay process. The observed exponential decrease can be fitted.

The silicon Fermi level is pinned by the experimental set-up and the Si/ BaF_2 interface electronic levels are coupled via the vacuum level. Due to the laser excitation, electron-hole pairs are created at the interface that are separated in the near-interface field until their electric field compensates the field in the absence of light. Thus, the band bending at the Si/ BaF_2 interface is lifted for a short time. This leads to a shift of the energy positions of the higher-lying states towards higher energies with respect to the Fermi level; the BaF_2 HOMO is now detected also in channel 3. After the laser pulse however, the charge

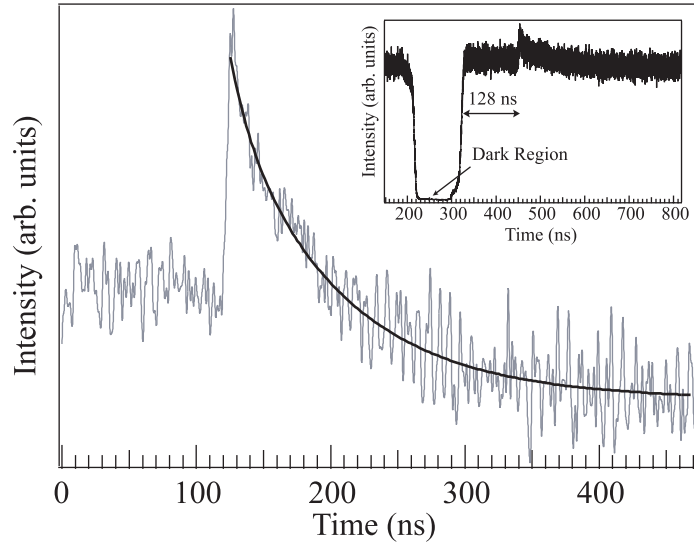


Figure 2: TDC signal of BaF_2 on Si from channel 3 in the time interval 150-820 ns (Inset). The exponential decay is shown enlarged with a relative time scale starting at the end of the dark region. Here, the 2 ns periodic structure of the synchrotron and higher frequency contributions have been removed using Fourier transformation. The exponential decay is fitted.

carriers will recombine (primarily at the interface) which leads to the reappearance of the band bending and thus a shift of the BaF_2 core level back to its initial value. Here, we observe the BaF_2 HOMO shifting back to higher binding energies. The reappearance of the band bending is not found to be a linear process, the best fit of the decay is delivered by a double exponential decay. The time constants obtained from it then are a measure for the relaxation time at the interface. They are determined to be $\tau_1 = (86.8 \pm 0.6)$ ns and $\tau_2 = (10.0 \pm 0.5)$ ns.

We acknowledge the support and assistance from the MBI beamline crew, in particular T. Gießel, D. Pop, D. Bröcker, R. Weber, R. Schumann and W. Widdra. This work was supported by the Deutsche Forschungsgemeinschaft under Schwerpunktprogramm SPP1093 "Dynamik von Elektronentransferprozessen an Grenzflächen" through grant Wu207/1-1.

References

- [1] T. Gießel, D. Bröcker, P. Schmidt, and W. Widdra, *Rev. Sci. Instr.*, **74**(11), 4620 (2003).
- [2] A. Zangwill, *Physics at Surfaces*, Cambridge University Press, 1988.
- [3] W. Widdra, D. Bröcker, T. Gießel, I. Hertel, W. Krüger, A. Liero, F. Noack, V. Petrov, D. Pop, P. Schmidt, R. Weber, I. Will, and B. Winter, *Surface Science*, **543**, 87 (2003).

Rotated spin polarization vector as experimental proof of coherence between direct and indirect photoemission from magnetized Gd/W(110)

N. Müller, T. Khalil, M. Pohl, T. Uphues, N. Kabachnik, U. Heinzmann

Fakultät für Physik, Universität Bielefeld, D-33501 Bielefeld

M. Polcik

Fritz-Haber-Institut der MPG, D-14195 Berlin

O. Rader

BESSY GmbH, D-12489 Berlin

F. Heigl

Freie Universität Berlin, Fachbereich Physik, 14195 Berlin

We describe an experiment in which two different preferential spin directions acting in combination are used to characterize the coherence of the direct and indirect photoemission channel in the first pre-edge peak of the $4d \rightarrow 4f$ – resonance in Gd appearing at a photon energy of about 138 eV. The two preferential spin directions are defined by using ferromagnetic order and circularly polarized radiation.

The basis of the experiment is the following property of the electron spin: if two different pure spin states χ_a, χ_b with the adjunct polarization vectors $\mathbf{P}_a, \mathbf{P}_b$ ($\mathbf{P}_a \neq \mathbf{P}_b, |\mathbf{P}_{a,b}| = 1$) are coherently superposed, the resulting new spin state $\chi = \chi_a + \chi_b$ is also a pure spin state and the adjunct polarization vector \mathbf{P} has a component P_{coh} perpendicular to \mathbf{P}_a and \mathbf{P}_b .

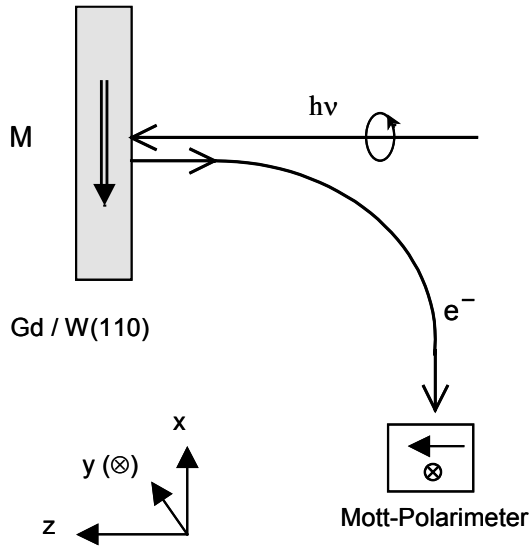


Figure 1: Scheme of the experiment

Figure 1 shows a scheme of the experiment. The Gd-layer grown on W(110) and cooled below 80 K is magnetized in plane by using a pulsed magnetizing coil. The preferential spin direction of the Gd 4f-electrons, which is antiparallel to the in plane magnetization \mathbf{M} , is aligned with the x-axis. Circularly polarized radiation from the beamline UE 56/2-PGM1 at BESSY hits the Gd-layer at normal incidence. Thus the preferential spin direction defined by the radiation lies normal to the Gd-layer, i.e. along the z-axis. In the electron energy analyzer the emitted electrons are deflected by 90° . Correspondingly the 4-counter Mott polarimeter following the energy analyzer measures the z component P_z (\leftarrow) and the y-component P_y (\otimes) of the polarization vector \mathbf{P} of the

emitted electrons. P_y is just the component, which can exist only if the direct emission channel

$$(4d^{10}4f^7) {}^8S_{7/2} \rightarrow (4d^{10}4f^6) {}^7F_J + \epsilon e^-$$

and the indirect autoionizing channel with the sequence of transitions

$$(4d^{10}4f^7) {}^8S_{7/2} \rightarrow (4d^94f^8) X \rightarrow (4d^{10}4f^6) {}^7F_J + \epsilon e^-$$

are coherently superposed.

The spin polarization \mathbf{P}_{dir} of the direct emission channel is mainly determined by the magnetization \mathbf{M} [1], the spin polarization $\mathbf{P}_{\text{trans}}$ of the indirect channel results from the primary excitation by the circularly polarized radiation [2].

For the indirect channel we expect the highest spin polarization $\mathbf{P}_{\text{trans}}$ for the first pre-edge peak of the Gd $4d \rightarrow 4f$ – resonance [2]. Hence we searched for the coherence effect in this peak. The result is shown in figure 2.

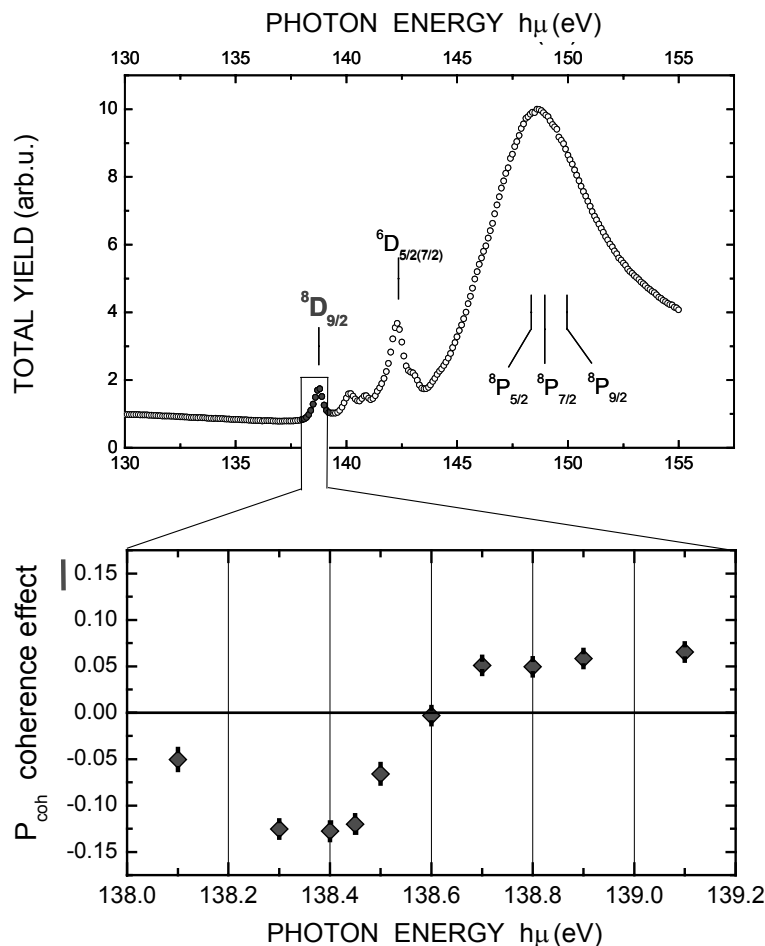


Figure 2: Total-yield spectrum measured at the Gd $4d \rightarrow 4f$ – resonance and the spin polarization component P_{coh} measured across the first pre-edge peak.

Our measurements reveal a significant coherence effect with a spin polarization $P_y = P_{\text{coh}}$ varying from

$$P_{\text{coh}} \approx -12\% \text{ to } P_{\text{coh}} \approx 6\%$$

within a photon-energy interval < 0.4 eV on the low energy side of the resonance. The existence of P_{coh} and its changing sign corresponds to a total spin polarization rotated out of the plane defined by the magnetization \mathbf{M} and the helicity of the radiation and to the phase shift π appearing between the two emission channels, respectively.

This work was supported by the Deutsche Forschungsgemeinschaft (He 1049/7-2).

1. T. Kachel, R. Rochow, W. Gudat, R. Jungblut, O. Rader, and C. Carbone, Phys. Rev. B **45**, (1992) 7267
2. N. Müller, T. Lischke, M. R. Weiss, and U. Heinzmann, J. Electr. Spectr. Rel. Phen. **114-116**, (2001) 777

Electronic Structure of Regular Bacterial Surface Layers

D.V. Vyalikh,¹ S. Danzenbächer,¹ M. Mertig,² A. Kirchner,² W. Pompe,²
Yu.S. Dedkov,³ and S.L. Molodtsov¹

¹ Institut für Festkörperphysik, Technische Universität Dresden, D-01062 Dresden, Germany

² Max Bergmann Zentrum für Biomaterialien and Institut für Werkstoffwissenschaft, Technische Universität Dresden, D-01062 Dresden, Germany

³ II. Physikalisches Institut, Rheinisch-Westfälische Technische Hochschule Aachen, D-52056 Aachen, Germany

Self-assembled regular biological structures find consistently increasing significance for the human being. They contribute to different fields of basic research and applications including biomolecular templating successfully used in the recent time for nanoscale engineering [1]. By analogy with organic and molecular systems [2], biocomposites might reveal superconducting or unique low-dimensional magnetic behavior. Further developments particularly in the field of nanobiotechnology of hybrid systems are slowed down, however, by a lack of information about electronic structure of the biological objects. Here we present the electronic structure of regular bacterial surface layer (S-layers) of *Bacillus sphaericus* NCTC 9602, which was for the first time measured with spectroscopic methods such as photoemission (PE) and x-ray absorption near-edge structure (NEXAFS) spectroscopy.

The S-layer of *Bacillus sphaericus* NCTC 9602 consists of a network of proteins, which contain in average 40-60% of hydrophobic amino acids linked together via the peptide bonds. Each of the amino acids (except proline) is built by an acidic carboxyl group and an amino group. A central carbon atom is bonded to these groups, with a hydrogen atom on one side and a side chain on the other side. The side chains consist of carbon, oxygen and nitrogen atoms and vary from one amino acid to another. Many of the side chains differ from each other in the number and type of double bonds between carbon atoms as well as between carbon atom and nitrogen or oxygen atom. The individual bonds are similar to those found in organic compounds.

In the present study the S-layers were grown *ex-situ* on SiO_x/Si substrate strictly following the procedure described in Ref. [3]. A characteristic transition-electron microscopy (TEM) image of the ordered S-layer is shown in Fig. 1. Immediately after preparation the samples were transferred into a photoemission spectrometer. The PE and the partial-electron-yield NEXAFS experiments were performed using radiation from the Russian-German beamline. This ultra-high energy resolution dipole beamline [5] was proven to be particularly eligible to investigate delicate objects with spectroscopic techniques:

In difference to mostly deployed in the present time undulator beamlines delivering extremely high photon flux in a form of a discrete spectrum, it provides low-intensity radiation distributed continuously in a wide range of photon energies (30 to 1500 eV). The latter is very important for NEXAFS studies. The overall-system energy resolution accounting for the thermal broadening in cases of the valence-band (VB) and the C

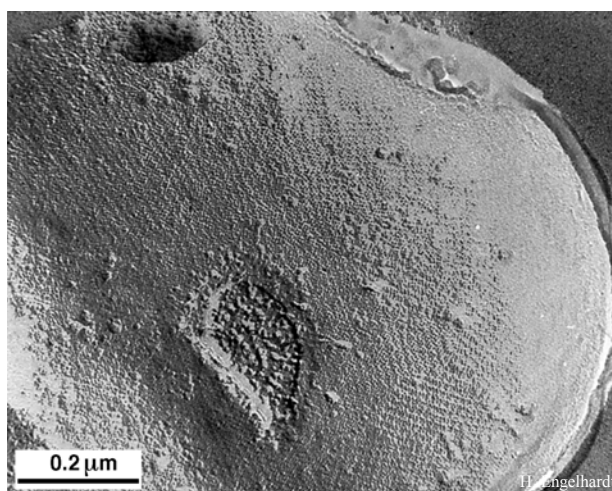


Fig. 1 TEM pattern of the S-layer [4]

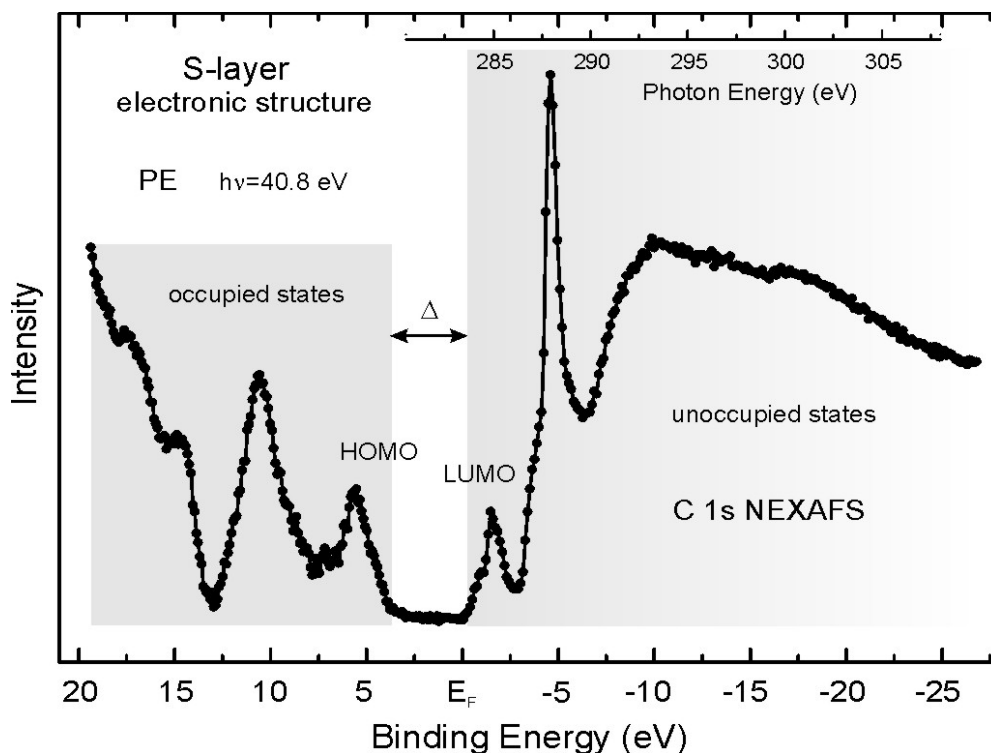


Fig. 2 Electronic structure of the S-layer as derived from the PE and NEXAFS experiments

1s core-level PE experiments was set to 150 meV and 200 meV full width at half maximum (FWHM), respectively. The resolution for the NEXAFS measurements is determined solely by the performance of the beamline and was varied from 80 meV to 100 meV when going from the C 1s (~283 eV) to the O 1s (~530 eV) threshold, respectively.

A typical C 1s core-level NEXAFS spectrum taken from the “as grown” S-layer with highly monochromatized light is shown in Fig. 2 (right). The spectrum consists of two main parts: rather sharp features in the region between 283 eV and 288 eV and broad structures above 290 eV photon energies. Previous studies of the C 1s NEXAFS in a series of individual amino acids [6,7], which reveal spectra with lineshapes similar to the one in Fig. 2, attributed the sharp low-energy features to the $1s \rightarrow \pi^*$ transition into the unoccupied orbitals originating from C atoms in different environments. The high-energy structures were related to the $1s \rightarrow \sigma^*$ transitions. These latter structures are very broad because of the short lifetime of the corresponding exciting states.

Based on the experimental NEXAFS spectra of a series of amino acids [6] and their interpretation on the basis of the *ab initio* static-exchange method calculations [7], we can assign the first manifold feature in the spectra of the “as grown” S-layer (~285 eV) predominantly to the transitions into the unoccupied orbitals of the C=C double bonds in the aromatic rings. Another peak of much larger intensity found in the C 1s NEXAFS spectra at 287.8 eV can be attributed to the $1s \rightarrow \pi^*$ excitation of the C=O double bond of the carboxyl group. Since the chemical environment of this bond does not change from one amino acid to another, there is no initial-state splitting of this resonance. Therefore this component represents less structure than the 285-eV one. Its shoulder at about 287 eV coincides in energy with the expected C=N $1s \rightarrow \pi^*$ resonance, which by the same reason as the discussed above one for the C=O transition, is not expected to reveal a pronounced manifold splitting.

The occupied valence electronic states were studied by means of angle-integrated VB photoemission. The photon energy of 40.8 eV (He II α) for this experiment was selected to

make a compromise between high cross-section of photoexcitation of primarily 2p states of the second row elements expected in the valence bands of proteins and relatively high surface sensitivity required to increase the contribution from the VB of the S-layer at the cost of the overlapping signal from the SiO_x/Si substrate. A difference valence-band PE spectrum, which was obtained by a proper subtraction of the separately measured pure substrate signal from the spectrum taken for the supported S-layer, is shown in Fig. 2 (left). Similar to results measured for other organic materials the difference spectrum consists of a series of separate lines originating from different molecular orbitals that are separated from each other by rather deep minima. Thereby the maximum of the highest occupied molecular orbital (HOMO) is located at 6 eV binding energy (BE). The other mostly intense feature is placed at 11 eV BE. There is a number of less pronounced structures at 7 eV, 15 eV, and 17 eV BEs. Note that in difference to NEXAFS experiments, valence-band PE is not element specific. Therefore, we cannot determine experimentally the origin of the occupied molecular orbitals. By analogy with the unoccupied states we believe, however, that the electronic states of different atoms in the VB are strongly hybridized with each other. Thereby one can assume that the HOMO and the intense peak at 11 eV BE are the bonding and the antibonding contributions originating in the interaction of the O-derived 2p states [relate to the peak at ~ 8 BE in the spectrum of the substrate (not shown)] with the electronic states of other ingredients of the proteins. Since the O atoms are mainly bound within the carboxyl groups they hybridize with the C 2p states forming predominantly the C=O double bonds with certain admixtures of the C-OH bonds.

As seen in Fig. 2 the top of the HOMO is located at about 3.5 eV below the Fermi energy disclosing semiconducting origin of the S-layer. Both the occupied and unoccupied electronic states are referred to the common E_F. (The E_F position for the NEXAFS was determined from the C 1s photoemission spectrum.) The obtained protein layers are moderate wide gap semiconductors with a gap value of Δ ~ 3.5 eV. The Fermi level is pinned close to the bottom of the lowest unoccupied molecular orbital (LUMO). The gained information is of high importance to make reliable predictions for possible chemical reactions and other chemical or physical phenomena in hybrid biological systems. It is expected that the position of the Fermi level can be shifted across the gap (as necessary for purpose of bioelectronics) by doping with appropriate materials. Similar to other molecular solids like alkali fullerenes [2] it may cause high-temperature superconducting properties of the S-layer intercalation compounds and be used in field effect transistor doped biocomposites.

Acknowledgment: This study was supported by the bilateral program "Russian-German Laboratory at BESSY II".

References:

- [1]. J.T. Moore *et al.*, Appl. Phys. Lett. **72**, 1840 (1998); S. Dieluweit *et al.*, Supramolecular Sci. **5**, 15 (1998); M. Panhorst *et al.*, J. Vac. Sci. Technol. B **19**, 722 (2001); W. Shenton *et al.*, Nature **389**, 585 (1997).
- [2]. *Organic Superconductivity*, eds. V.Z. Kresin and W.A. Little (Kluwer Academic Publishers, Hardbound, 1991); S. Uji *et al.*, Nature **410**, 908 (2001); A.F. Hebard *et al.*, Nature **350**, 600 (1991); S.P. Kelty *et al.*, Nature **352**, 223 (1991); M.J. Rosseinsky *et al.*, Phys. Rev. Lett. **66**, 2830 (1991).
- [3]. H. Engelhardt *et al.*, J. Bacteriol. **168**, 309 (1996); M. Mertig *et al.*, Eur. Phys. J. D **9**, 45 (1999).
- [4]. H. Engelhardt, *Electron microscopy of microbial cell wall proteins. Surface topography, three-dimensional reconstruction, and strategies for two-dimensional crystallization, Fungal Cell Wall and Immune Response*, eds J.P. Latge and D. Boucias, Vol. H53 NATO ASI Series (Springer-Verlag, Berlin, 1991).
- [5]. S.I. Fedoseenko *et al.*, Nucl. Instr. and Meth. in Phys. Res. A **505**, 718 (2003).
- [6]. J. Boese *et al.*, J. Electron Spectr. Rel. Phenom. **85**, 9 (1997).
- [7]. V. Carravetta *et al.*, J. Chem. Phys. **109**, 1456 (1998).

Atomic structure and initial oxidation of hydrogen saturated 4H-SiC($\bar{1}1\bar{2}0$)

Th. Seyller¹, N. Sieber¹, K.V. Emtsev¹, R. Graupner¹, L. Ley¹,
 A. Tadic², D. James², J.D. Riley², R.C.G. Leckey², M. Polcik³
¹ *Institut für Technische Physik II, Universität Erlangen-Nürnberg, Germany*
² *Department of Physics, La Trobe University, Bundoora, Vic 3083 Australia*
³ *Fritz-Haber-Institut, Berlin, Germany*

Introduction

Polar {0001} surfaces of 4H- and 6H-SiC have been intensively studied in the past and a wealth of information is now available on their structural and electronic properties. Recently, however, it was proposed that the non-polar ($\bar{1}1\bar{0}0$) and ($\bar{1}1\bar{2}0$) surfaces (a-planes) have a large potential as substrates for crystal growth [1,2], chemical vapor deposition [3], and fabrication of MOSFET devices [4]. In this contribution we present a study on the properties of H-saturated 4H-SiC($\bar{1}1\bar{2}0$) and the initial oxidation of this surface in O₂ at 800°C. The measurements were performed at UE56/2-PGM1. The hydrogenation was carried out by annealing the sample in ultra-pure hydrogen as described elsewhere [5-7].

Results and Discussion

Atomic structure of H-terminated 4H-SiC($\bar{1}1\bar{2}0$)

Figure 1(a) shows a LEED pattern of hydrogenated 4H-SiC($\bar{1}1\bar{2}0$) together with a sketch of the ideal (1×1) surface. The sharp spots seen in the diffraction pattern are indicative of an unreconstructed (1×1) surface. The surface exhibits a glide-plane symmetry which leads to systematic spot extinctions. In particular spots with indices (kl) with $k = \pm n$, n integer and $l \in \{\pm m, \pm 2m, \pm 3m\}$, $m \neq 0$ and integer are absent.

C1s and Si2p core level spectra of 4H-SiC($\bar{1}1\bar{2}0$) and their deconvolution into Voigt lines are displayed in Figure 1(b) and (c), respectively. Spectra were acquired at two different photon energies, thus varying the effective sampling depth from 3.0 Å to 4.6 Å for both core lines. This allows the identification of surface components in the spectra. The C1s core level spectra shown in Figure 1(b) are made up of three components. Two of them can be identified as surface components. Surface component ‘Si₃C-H’ with a chemical shift of 0.42 eV with respect to the bulk component is identified as due to carbon atoms bound to three silicon atoms and one hydrogen atom [7]. Its intensity agrees well with estimates based on a layer attenuation model for the surface in Figure 1(d). Di- and trihydrides expected at ~0.84 and ~1.26 eV are absent. The second chemically shifted component ‘C_xH_y’ at 2.2 eV with respect to the bulk component is caused by a minute hydrocarbon contamination (few percent of a monolayer) which results from the storage of the sample in a vacuum transport vessel [7].

The Si2p spectra in Figure 1(c) are made up of two spin-orbit split doublets. Component ‘SiC’ is due to photoelectrons emitted from the SiC bulk and surface component ‘C₃SiH’ at 0.23 eV is assigned to Si atoms bound to three carbon atoms and one hydrogen atom [7]. The SXPS data of H-terminated 4H-SiC($\bar{1}1\bar{2}0$)-(1×1) surface thus indicate the presence of monohydrides only which is consistent with a simple bulk-terminated and unreconstructed surface with one H-saturated dangling bond per surface atom as shown in Figure 1(d).

Oxidation of H-terminated 4H-SiC($\bar{1}1\bar{2}0$)

Oxidation of H-terminated 4H-SiC($\bar{1}1\bar{2}0$) was carried out by exposing the surface to O₂ at a sample temperature of 800°C. The largest exposure was 2×10⁵ L. The Si2p spectra revealed the formation of an SiO₂ layer with an interface layer containing silicon in various oxidation states in contrast to SiC(0001)/SiO₂, where only the oxidation state Si⁺ (C₃-Si⁺-O) was observed at the interface [8]. In order to identify the number of oxidation states present at the interface between SiC($\bar{1}1\bar{2}0$) and SiO₂ the spectra were deconvoluted into Voigt doublets. This is demonstrated in Figure 2 for the Si2p spectrum taken after exposure to 2×10⁵ L O₂. Plot (a) shows results of a fit with four chemically shifted components due to Si⁺, Si²⁺, Si³⁺, and Si⁴⁺ with equal separation

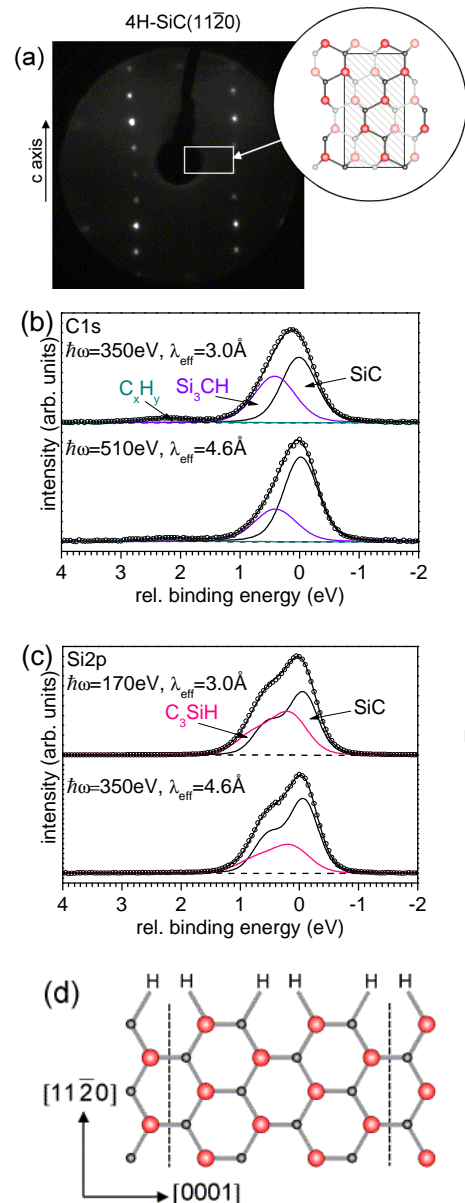


Figure 1: LEED pattern (a), C1s (b) and Si2p (c) core level spectra of H-terminated 4H-SiC($\bar{1}1\bar{2}0$). The binding energy is given with respect to the bulk line. (d) Proposed structure of the H-terminated 4H-SiC($\bar{1}1\bar{2}0$) surface in a side view projection.

between the doublets, i.e. assuming that the replacement of a Si-C bond by a Si-O bond adds a constant chemical shift of 0.61 eV per Si-O bond to the Si2p core level. Hoshino et al. [9] applied a similar procedure to the Si2p spectra of oxidized 6H-SiC(1120) yielding similar values (0.55 eV). In addition, the Gaussian widths were in good agreement with literature values [9].

On the other hand, Virojanadara and Johansson report the presence of only three chemically shifted components (Si^+ , Si^{2+} , Si^{4+}) on oxidized 4H-SiC(1120) [10]. Fitting our spectra with three chemically shifted components results in a fit as shown in Figure 2(b). A fit of similar quality is obtained with chemical shifts of 0.58, 1.55, and 2.47 eV, which agree well with the fit results Virojanadara and Johansson [10].

Although the residuum (see Figure 2) is somewhat larger for the three component model than for the model with four chemically shifted components, both models yield satisfactory fits. Furthermore, the complete set of spectra taken after each oxidation step can be fitted with both models. Figure 3 shows intensities of the different components of the four component model as a function of oxygen exposure. The Si^+ , Si^{2+} and Si^{3+} components are formed at very low exposures. The sum of these three components reaches its maximum value after 25 L oxygen, then remains constant, and finally decreases parallel to the bulk signal as SiO_2 (Si^{4+}) is formed. This shows that the suboxides are located at the interface, as was also confirmed by changing the surface sensitivity of the experiment. A qualitatively similar picture is gained for the three component model. Hence, the question whether there are two or three suboxide components located at the interface remains open. However, it is clear that the SiO_2 /4H-SiC(1120) interface is different from SiO_2 /SiC(0001), where only one suboxide species (Si^+) was observed [8,11-13]. The most likely reason for this is the different structure of the (1120) surface as compared to the (0001) surface.

Figure 4 shows C1s spectra taken after an oxygen exposure of 2×10^5 L. The spectra were taken with take-off angles of 0° and 60° thus providing a contrast in surface sensitivity. Both spectra have been fitted using three components: one bulk component (labeled SiC) and two interface components (labeled I_{c1} and I_{c2}). Both interface components are considerably broader than the bulk component. The chemical shift of these components are 0.7 eV for I_{c1} and 2.3 eV for I_{c2} , respectively. This points to the formation of C-O-C and Si-O-C bonds [12,14].

Summary

We have observed chemically shifted components in C1s and Si2p spectra of H-terminated, unreconstructed 4H-SiC(1120)-(1 \times 1) which were assigned to monohydrides. The spectroscopic results are compatible with a simple bulk-terminated and unreconstructed surface with one H-saturated dangling bond per surface. Oxidation of this surface in O_2 at 800°C leads to the formation of a SiO_2 layer with an interface layer containing more than one, possibly all three (Si^+ , Si^{2+} and Si^{3+}) suboxide species. Chemically shifted components were also observed in the C1s core level spectra as well, which is consistent with an interface containing both, Si-O and C-O bonds. Therefore, we suggest that the possibility to form more than one suboxide species and C-O bonds makes the interface softer and thus reduces the tendency to form of electrically active defects.

References

- [1] J. Takahashi, et al., J. Crystal Growth Vol. 181 (1997), p. 229.
- [2] T. Nishiguchi, et al., Mater. Sci. Forum Vol. 353-356 (2000), p. 69.
- [3] T. Kimoto, et al., Mater. Sci. Forum Vol. 353-356 (2001), p. 543.
- [4] H. Yano, et al., Appl. Phys. Lett. Vol. 78 (2001), p. 374.
- [5] N. Sieber, et al., Appl. Phys. Lett. Vol. 78 (2001), p. 1216.
- [6] N. Sieber, et al., Appl. Phys. Lett. Vol. 80 (2002), p. 4726.
- [7] N. Sieber, et al., Phys. Rev. B Vol. 67 (2003), p. 205304.
- [8] C. Virojanadara and L. I. Johansson, Surface Science Vol. 472 (2001), p. L145.
- [9] Y. Hoshino, et al., Surf. Sci. Vol. 531 (2003), p. 295.
- [10] C. Virojanadara and L. I. Johansson, Phys. Rev. B Vol. 68 (2003), p. 125314.
- [11] C. Virojanadara and L. I. Johansson, Mater. Sci. Forum Vol. 389-393 (2002), p. 701.
- [12] C. Virojanadara and L. I. Johansson, Surface Science Vol. 505 (2002), p. 358.
- [13] L. I. Johansson, et al., Surf. Sci. Vol. 529 (2003), p. 515-526.
- [14] B. Hornetz, et al., J. Mater. Res. Vol. 9 (1994), p. 3088.

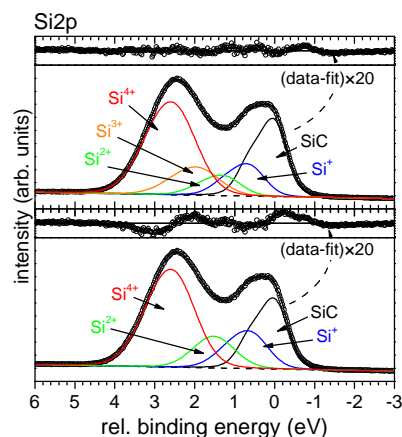


Figure 2: Fits of the Si2p core level spectrum of 4H-SiC(1120) taken after a total O_2 dose of 2×10^5 L at 800°C using (a) four and (b) three chemically shifted components.

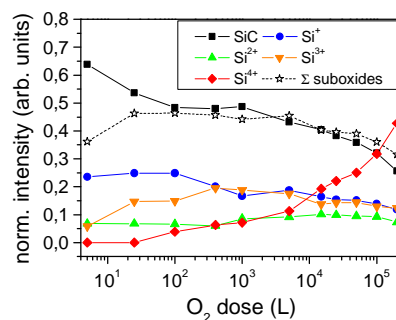


Figure 3: Intensities of the SiC bulk component and the four chemically shifted components Si^+ , Si^{2+} , Si^{3+} , and Si^{4+} as a function of oxygen exposure. In addition, the sum of the three suboxide species is given.

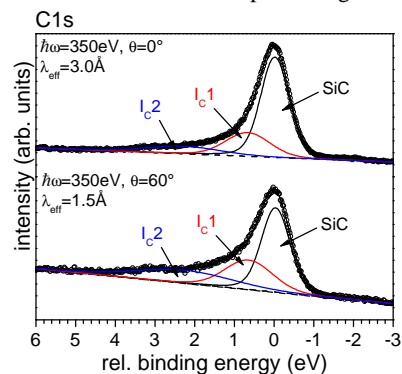


Figure 4: Fits of the C1s core level spectrum of 4H-SiC(1120) taken after a total O_2 dose of 2×10^5 L at 800°C . Spectra taken with a take-off angle of 0° and 60° degree are shown.

Doping of Single-Walled Carbon Nanotubes by H_2SO_4 and HNO_3

R. Graupner, J. Abraham*, Th. Seyller, A. Vencelová, A. Hirsch*, L. Ley

Universität Erlangen, Institut für Technische Physik, Erwin-Rommelstr. 1, 91058 Erlangen

** Universität Erlangen, Institut für Organische Chemie, Henkestr. 42, 91042 Erlangen*

Single Walled Carbon Nanotubes (SWCNTs) consist of graphite sheets which are rolled up into a cylindrical form. Typical diameters are in the range of nanometers and lengths may be several hundreds of micrometer or even millimeters, making them a true one-dimensional material. Moreover, the way the graphite sheet is rolled up to form a tube, described by the so called roll-up or chiral vector, determines whether this tube is semiconducting or metallic [1].

In our work we have investigated the influence of Brønsted acids, namely H_2SO_4 and HNO_3 on the electronic properties of thin films of SWCNTs which were prepared by the laser ablation technique [2]. The raw material was purified using HNO_3 and filtered to obtain free-standing films of SWCNTs ("bucky-paper"). To remove possible residual nitric acid from the purification process, the samples were first annealed in UHV at temperatures of 320-500 °C, immersed into the respective acid, dried, and then reinserted into the spectrometer. Photoemission measurement were taken at the undulator beamline U49/2-PGM 2. To monitor doping effects the binding energy of the C 1s core level binding was measured before and after immersion into the acids. Binding energies were calibrated with respect to the Au 4f 7/2 core level which was regularly measured and adjusted to an energy of 84.00 eV.

In figure 1 the influence of the immersion into 4 M H_2SO_4 (left) and 4 M HNO_3 (right) on the C 1s core levels are shown. It is evident that both treatments lead to a shift towards lower binding energies, i.e. a p-doping behaviour is observed. For the sulphuric acid treatment the change in Fermi-level position amounts to 0.5 eV (Fig. 1 left, middle curve). The binding energy shift of the core level is accompanied by a considerable broadening of the peak. Subsequent annealing of the sample restores both position and shape of the C 1s spectrum (top curve). For nitric acid, the shift is smaller (0.2 eV, Fig. 1 right, full line in the middle) and appears to be unstable. After one day's storage in UHV the shift of the core level is considerably reduced (dashed line in the middle of Fig. 1, right). Again both position and shape of the C 1s core level are restored to its initial values by annealing (top curve).

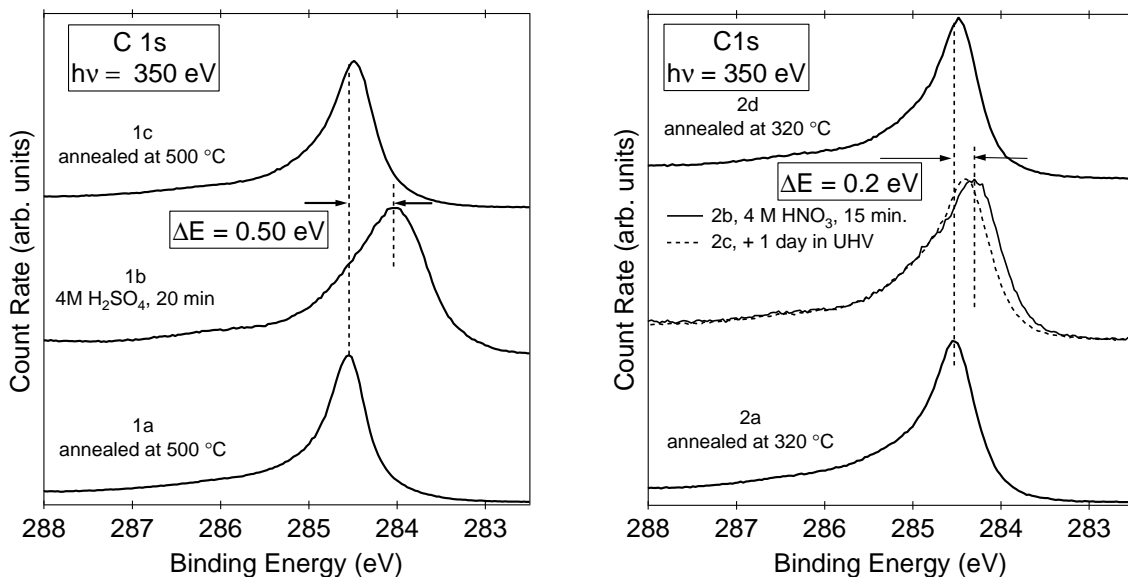


Figure 1: Influence of the immersion of a SWCNT sample into H_2SO_4 (left) and HNO_3 (right) on the C 1s core level spectra of SWCNTs in the form of a bucky-paper. For details see text.

A p-type charge transfer by acids is a well known phenomenon in graphite, where intercalation of H_2SO_4 and HNO_3 has been performed by electrochemistry [3]. In our case, a spontaneous charge transfer is observed which can be explained by the fact that the intertube volume in the bucky-paper is more easily accessible [4]. The fact that doping is caused by a mere intercalation of the respective acid also explains the fact that storage in UHV reduces the shift the Fermi-level upon desorption of HNO_3 .

The respective S 2p and the N 1s core levels are shown in Fig. 2. For H_2SO_4 (Fig. 2, left), the main S 2p emission intensity (S_A) is characteristic of sulphur in the oxidation state VI [5, 6] which supports the assumption of intercalation of the acids. For the N 1s spectra in the nitric acid case the situation is more complicated, as nitrogen is already present in the purified and annealed starting material (Fig. 2

right, bottom curve). Nevertheless, a new component in the N 1s core level which develops upon the nitric acid treatment can be attributed to N bound to three oxygen atoms (N_E in the upper curve of Fig. 2, right). Other components contributing to the N 1s core level can be identified as substitutional nitrogen in the graphene lattice (N_A), pyridine structures (N_B), and NO_2 groups (N_D) [2]. The origin of the broad structure N_C is still unclear.

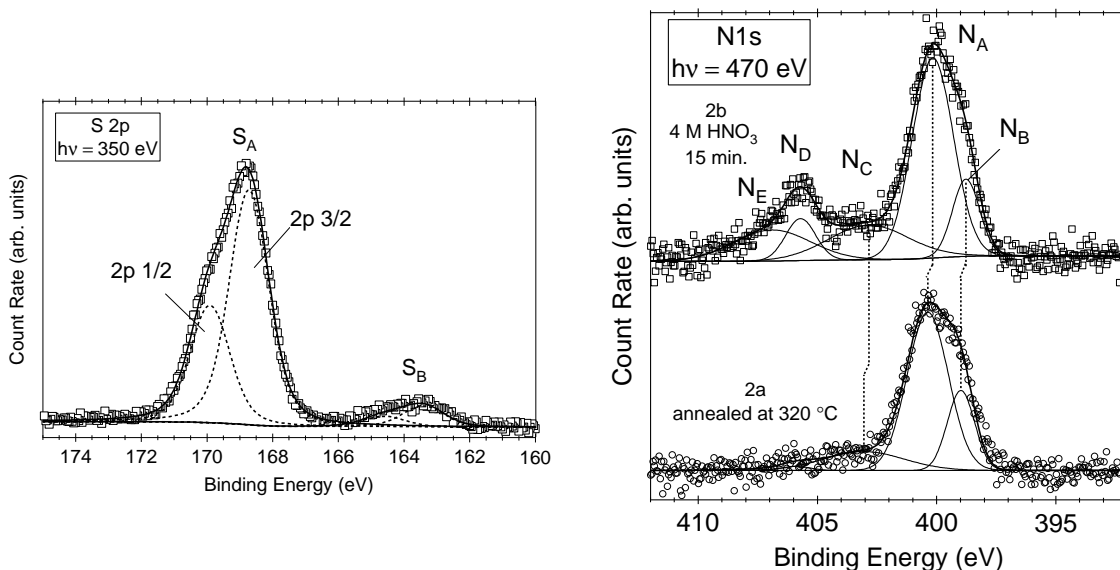


Figure 2: S 2p spectrum of bucky paper after immersion in H_2SO_4 (left) and N 1s core levels of the annealed starting material (right, bottom) and after immersion in HNO_3 (top).

To summarize, Single-Walled Carbon Nanotubes show a spontaneous hole doping by intercalation of Brønsted acids as H_2SO_4 and HNO_3 . Photoelectron Spectroscopy is able to resolve both the sign of the charge transfer as well as the amount of the Fermi-level shift. Moreover, due to its chemical sensitivity the doping species can be identified. These observations may have important implications for the study of intercalation processes in SWCNTs. This is of great technological relevance for the potential application of SWCNTs as electrode materials in batteries [7].

This work was supported by the Bayerische Forschungsstiftung under the auspices of the "Bayerischer Forschungsverbund für Werkstoffe auf der Basis von Kohlenstoff, FORCARBON".

References

- [1] R. Saito, G. Dresselhaus, and M. S. Dresselhaus, *Physical Properties of Carbon Nanotubes*, Imperial College Press, London, 1998.
- [2] R. Graupner, J. Abraham, A. Vencelová, T. Seyller, F. Henrich, M. M. Kappes, A. Hirsch, and L. Ley, *Phys. Chem. Chem. Phys.*, 2003, **5**, 5472–5476.
- [3] M. S. Dresselhaus and G. Dresselhaus, *Adv. Phys.*, 1981, **30**, 139–326.
- [4] G. U. Sumanasekera, J. L. Allen, S. L. Fang, A. L. Loper, A. M. Rao, and P. C. Eklund, *J. Phys. Chem. B*, 1999, **103**, 4292–4297.
- [5] B. J. Lindberg, K. Hamrin, G. Johansson, U. Gelius, A. Fahlman, and K. Siegbahn, *Phys. Scripta*, 1970, **1**, 286–298.
- [6] M. Descostes, F. Mercier, N. Thromat, C. Beaucaire, and M. Gautier-Soyer, *Appl. Surf. Sci.*, 2000, **165**, 288–302.
- [7] P. M. Ajayan and O. Z. Zhou in *Carbon Nanotubes, Synthesis, Structure, Properties, and Applications*, ed. M. S. Dresselhaus, G. Dresselhaus, and P. Avouris; Springer Verlag, Berlin, 2001; pp. 391–425.

Electronic Structure of Si Nanoparticles in SiO₂ Matrices studied by Soft X-ray Fluorescence Spectroscopy.

A.Zimina, S. Eisebitt, W. Eberhardt

BESSY m.b.H., Albert-Einstein-Str., 15, 12489, Berlin, Germany

J. Heitmann, M. Zacharias

Max-Planck-Institut für Mikrostrukturphysik, Halle, Germany

Nanoscaled structures play an important role in optoelectronic technologies. After the discovery of the strong, size dependent photoluminescence (PL) in the visible spectral range of porous silicon [1], further research focused on Si nanoparticles which are more stable under ambient conditions. In the past, Si nanoparticles were produced in a silicon dioxide matrix by ion implantation [2], sputtering of Si rich oxides [3] or reactive evaporation of Si rich oxides [4].

To obtain better control over the nanoparticle size distribution and spacing a synthesis technique has been developed in Max Planck Institute for Microstructure Physics (Halle) [5]. The process is based on the growth of a SiO/SiO₂ superlattice with subsequent high temperature annealing in N₂ atmosphere, which leads to the formation of Si particles in a SiO₂ matrix. Si nanoparticles as small as 1.5 nm in diameter can be produced with a narrow size distribution in this way. As an example, a high resolution transmission electron microscopy image from [5] is reproduced in Fig.1. Resonant and low temperature PL measurements indicate the existence of electronic quantum confinement with a strongly enhanced ratio of direct to phonon assisted transitions at low temperature due to momentum broadened band edge states [6]. An increase of the PL peak energy up to 0.5 eV compared to bulk crystalline Si has been observed [5].

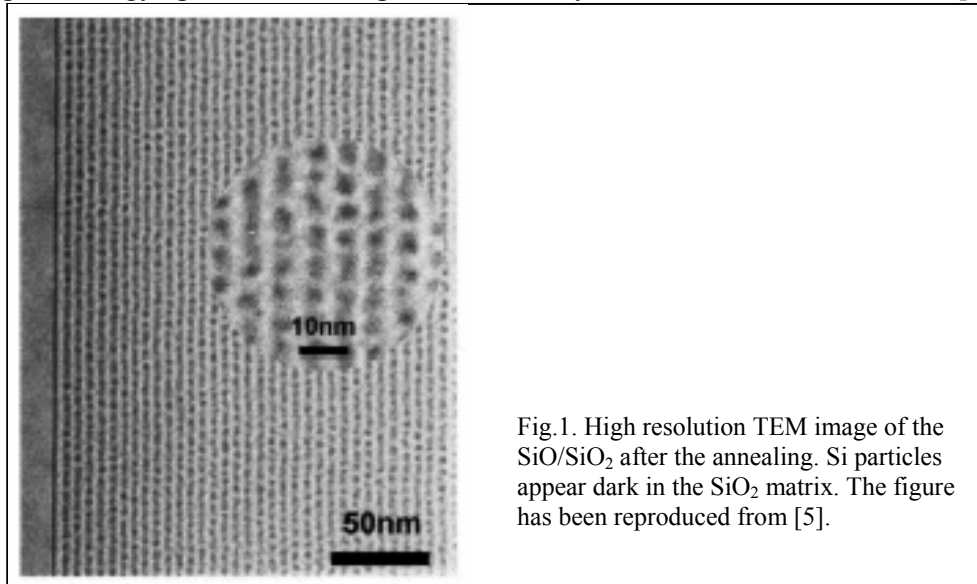


Fig.1. High resolution TEM image of the SiO/SiO₂ after the annealing. Si particles appear dark in the SiO₂ matrix. The figure has been reproduced from [5].

Details of the potential well acting as a confinement potential are difficult to access, as they depend on the detailed structure of the interface region between a Si nanoparticle and the surrounding SiO₂ matrix. In particular, the potential shape depends on which kinds of suboxides are present. Knowledge of this potential shape would enable quantitative models of the confinement energy as a function of particle size and interface

structure. Information on the presence of the various possible silicon oxides adjacent to a Si particle may also help to refine the synthesis procedure.

Using soft X-ray spectroscopy [7], we investigate changes in the electronic structure of Si nanoparticles in a SiO₂ matrix synthesized in the MPI for Microstructure Physics as described above. The local partial density of the electronic states (DOS) in the valence band (VB) and conduction band (CB) is probed independently by soft X-ray fluorescence (SXF) and soft X-ray absorption (SXA). Using photon excitation with monochromatized synchrotron radiation allows us to excite selectively different oxide species due to the presence of a Si 2p core level energy shift of about 1 eV per oxygen neighbor towards an increased binding energy [8].

Annealed samples initially consisting of 45 periods of SiO(n)/SiO₂(5nm), n=5, 4, 3, 2nm, on a quartz substrate have been investigated at the BESSY UE125-PGM beamline. The beamline energy resolution was set to 50 meV. Si 2p SXF was recorded in a Rowland-type soft x-ray fluorescence spectrometer with a resolution of 300 meV.[9]

As the bulk of the sample is not conductive and diffuse reflection of the incident x-rays is strong, Si 2p SXA was recorded by partial fluorescence yield (pFY), accepting only characteristic x-ray fluorescence in the Rowland spectrometer as a yield signal. Due to the inherently low x-ray fluorescence yield and the limited solid angle acceptance of the Rowland spectrometer, the counting statistics of this signal is only modest.

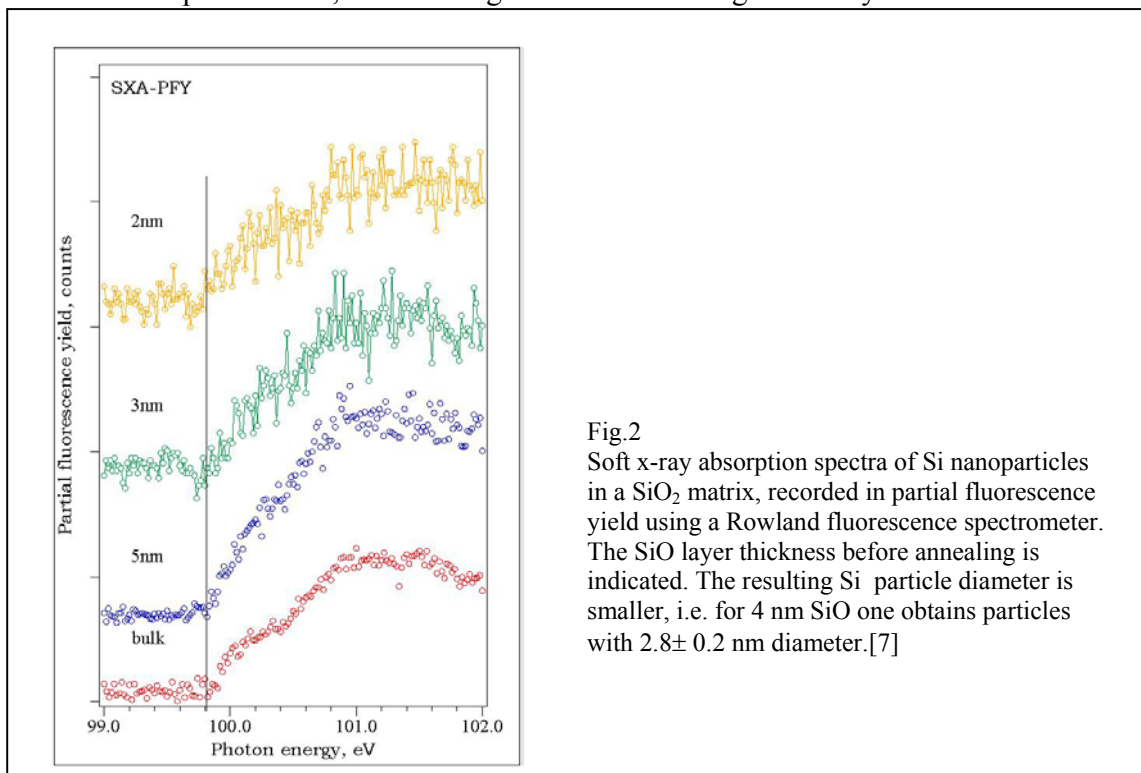


Fig.2
Soft x-ray absorption spectra of Si nanoparticles in a SiO₂ matrix, recorded in partial fluorescence yield using a Rowland fluorescence spectrometer. The SiO layer thickness before annealing is indicated. The resulting Si particle diameter is smaller, i.e. for 4 nm SiO one obtains particles with 2.8 ± 0.2 nm diameter.[7]

A comparison of the pFY-SXA spectra is presented in Fig.2. In spite of the limited signal to noise ratio, some conclusions can be drawn. The 2p_{3/2}-2p_{1/2} spin orbit splitting of 0.6 eV which is clearly visible in bulk crystalline silicon (edge inflection points at 99.8 eV and 100.4 eV) can still be observed in the Si nanoparticle samples. This indicates that inhomogeneous broadening *e.g.* due to particle size variation is small. At

the same time, the unoccupied (s+d)-DOS is not dramatically different from bulk crystalline Si. In particular, the peak at 101.0 eV with its spin-orbit partner at 101.6 eV produced by a LPDOS typical for *crystalline* Si [10] can be located in the nanoparticle spectra just above the noise level. In comparison, bulk amorphous silicon (a-Si:H) SXA spectra do not exhibit such a structure[11]. These observations are consistent with the formation of Si nanoparticles containing a core of crystalline silicon. No evidence for the formation of an exciton between the $2p_{3/2}$ core hole and the electron excited into the CB in the final state of the absorption process is detectable. We estimate that such an exciton should be visible in the pFY-SXA spectra if the exciton binding energy would exceed 100 meV. We cannot detect any quantum confinement shift of the CB minimum with decreasing particle size. Based on effective mass theory and experimental findings for porous silicon [12], one would expect about 40% of the increase in band gap to be due to a shift of the CB. For the 2 nm Si particle PL measurements indicate a band gap increase compared to bulk crystalline Si of 0.35 eV, which would amount to a CB fraction of 0.14 eV. It is questionable whether such a shift can be detected with the present signal to noise ratio.

SXF spectra excited at 100.0 eV incident photon energy were measured for all samples and are compared with spectrum of bulk crystalline Si in Fig.3. At this excitation energy only the $2p_{3/2}$ core level of the c-Si is excited and thus the observed spectra reflect the (s+d)-DOS in the VB of the Si nanoparticle *core*. The (s+d)-DOS observed for the 3 nm, 4 nm and 5 nm sample indicated the presence of crystalline Si, with its characteristic 3 peak structure. In amorphous Si, the peaks at 89.5 eV and 91.5 eV would merge to one structure due to the lack of long range order [13]. These findings are in agreement with our conclusions from the pFY-SXA spectra. The fluorescence signal from the 2 nm sample was too weak to interpret the observed spectral shape. The peak at 96 eV emission energy is more “step-like” in the Si nanoparticles as compared to the “peak-like” shape in bulk crystalline Si. Similar changes in the SXF spectral shape have been observed for nanoporous silicon in the past, where they could be attributed to changes in the (s+d)-DOS due to quantum confinement [14,15]. The exact position of the VB minimum is difficult to locate due to strong diffuse scattering of the incident radiation, giving rise to an elastic peak which obscures the top of the VB in the spectra under selective excitation conditions.

The suboxides potentially present in the interface region between the Si nanoparticles and the SiO₂ matrix were studied via the SXF spectra for increasing excitation energies. Series of SXF spectra were recorded for all samples, here we present the data for the sample with an initial SiO layer of 4 nm thickness in Fig. 4. With the lowest excitation energy the $2p_{3/2}$ core level of crystalline Si can be excited. Above 100.4 eV the $2p_{1/2}$ level is reached and the spectrum is the sum of L_{α} and L_{β} emission, but still related only to the Si atoms without a chemical bond to an oxygen neighbor. With further increase in the primary energy Si atoms with more oxygen neighbors will be excited. The SXF spectra then are a superposition of the valence band emission from all Si atoms with a 2p binding energy below the excitation energy. The spectra with excitation energies from 100.6 eV to 102 eV are virtually identical, indicating that suboxides with stoichiometry Si₂O₁ are not detectable. A slight change of the emission spectrum can be observed when raising the excitation energy to 103 eV. This spectrum, which is very similar to the 104 eV excitation spectrum, can not be described by a superposition of the

spectrum excited at 102 eV and the well known SiO₂ spectrum, which is obtained for excitation energies ≥ 108 eV. This spectral shape suggests the presence of small amounts of suboxides with a stoichiometry Si₂O₂ and/or Si₂O₃. We observe this general behavior for the all samples with different Si nanoparticle sizes. The observations are consistent with a relatively sharp interface region with only few suboxides present. If the transition region between the crystalline Si core and the surrounding matrix would contain suboxides over a shell with a volume e.g. comparable to the nanocrystal core volume, one would observe more dramatic spectral changes with every increase of the excitation energy by 1 eV.

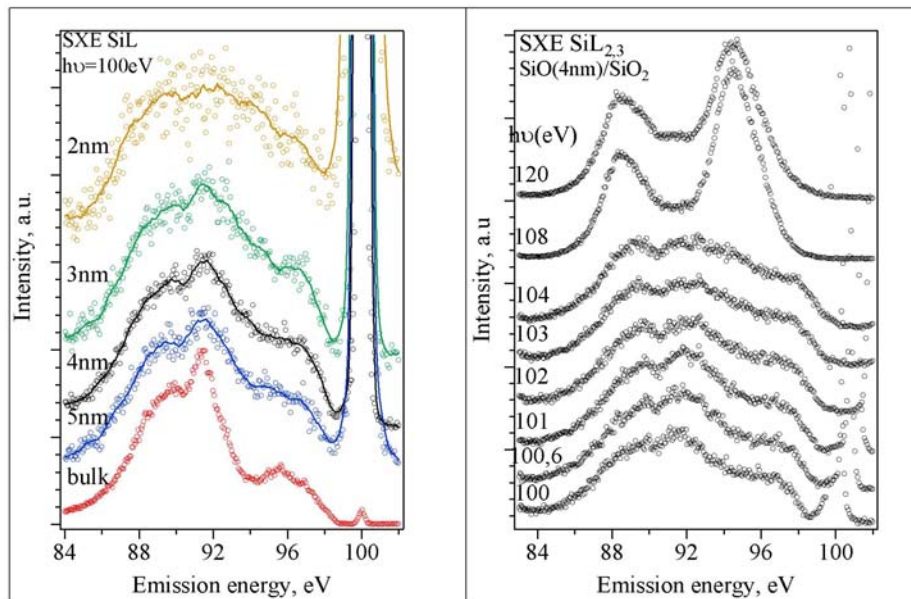


Fig. 3 (left): SXF spectra for Si nanoparticles in a SiO₂ matrix and bulk crystalline Si excited at 100 eV photon energy.

Fig. 4 (right): SXF spectral change as a function of excitation energy for a Si nanoparticle sample.

References:

- [1] T.Canham, Appl. Phys. Lett. **57**, 1046 (1990), V.Lehmann, U. Goesele, Appl. Phys. Lett. **58**, 856 (1919)
- [2] See, for example: M. L. Brongersma et al., J. Appl. Phys., **86**, 2, 759 (1999)
- [3] S. Hayashi, K. Yamamoto, J. Lumin. **70**,352 (1996)
- [4] U. Kahler, H. Hofmeister, Opt. Mapper. **17**,83 (2001)
- [5] M. Zacharias, J. Heitmann, R. Scholz, *et al.*, Applied Physics Letters **80**, 661 (2002)
- [6] J. Heitmann, D. Kovalev, F. Eichhorn, L.X. Yi, F. Müller, M. Zacharias, submitted for publication
- [7] S. Eisebitt and W. Eberhardt, *Soft x-ray spectroscopy as a probe of nanostructured solids* in Frontiers of Nano-Optoelectronic Systems, Ed. L. Pavesi and E. Buzaneva, NATO Science Series II **6**, 347 (Kluwer, Dordrecht,2000)
- [8] F.G. Bell and L. Ley, Phys. Rev. B **37**, 8383 (1988)
- [9] Experimental parameters: 600 l/mm spherical grating with 3710 mm radius; 20 μ m entrance slit; 2D 15° off-Rowland detection to obtain the entire spectrum in a parallel mode.
- [10] A. Bianconi, R. Delsole, A. Selloni, *et al.*, Solid State Communications **64**, 1313 (1987).
- [11] L. Yang, B. Abeles, W. Eberhardt *et al.*, Physical Review B **39**, 3801 (1989)
- [12] T. van Buuren, T. Tiedje, J. R. Dahn, *et al.*, Appl. Phys. Letters **63**, 2911 (1993).
- [13] K. E. Miyano, D. L. Ederer, T. A. Callcott *et al.*, Physical Review B **48**, 1918 (1993).
- [14] S. Eisebitt, J. Luning, J. E. Rubensson *et al.*, Solid State Communications **97**, 549 (1996).
- [15] S. Eisebitt, S. N. Patitsas, J. Lüning et al., Europhysics Letters **37**, 133 (1997).

k-space microscopy of high temperature superconductors: *around the ring in $(\text{Pb,Bi})_2\text{Sr}_2\text{CaCu}_2\text{O}_8$*

M. S. Golden¹, Y. Huang¹, J. van Vollenhoven¹, I. Santoso¹, S. Tavaddod¹, A. Mans¹
H. Berger², R. Follath³, P. Bressler³

¹ Van der Waals-Zeeman Institute for Experimental Physics, Universiteit van Amsterdam
NL-1018 XE Amsterdam, The Netherlands

² Institut de Physique Appliquée, Ecole Polytechnique Fédérale de Lausanne, CH-1015 Lausanne, Switzerland

³ BESSY GmbH, Albert-Einstein-Strasse 15, 12489 Berlin, Germany

Due to its provision of direct access to the frequency and momentum dependence of the elementary single-particle excitations in complex, correlated electron systems, high resolution angle-resolved photoemission has taken up a central role in the experimental investigation of unconventional quantum electron matter such as the high temperature superconductors and related systems. In particular, the coupling of high resolution in k-space (i.e. angular resolution) with high resolution and flexibility in energy offered by ID-based SR sources presents a powerful probe in which matrix-element effects can be exploited to help separate the contributions from - for example - different bands, thus allowing the isolation of the intrinsic spectral response of a particular state, which can then be compared with the predictions of theory. In this contribution, we present a status report on the use of SR-based k-space microscopy, carried out at the U125-1/PGM beamline, to study the near- E_F states of the bilayer high T_c superconductor $(\text{Pb,Bi})_2\text{Sr}_2\text{CaCu}_2\text{O}_8$.

The most widely studied high T_c superconductor (HTSC) using surface sensitive methods such as ARPES or STS is $\text{Bi}_2\text{Sr}_2\text{CaCu}_2\text{O}_8$, due to its excellent cleavage qualities and high T_c (optimal doping, depending on exact cation stoichiometry lies in the high 80's or low 90's Kelvin). This system is a bilayer HTSC, with two CuO_2 planes in close proximity, whose electronic states can hybridise to form a bonding and antibonding combination of the $\text{Cu-O } d_{p\sigma^*}$ bands of each CuO_2 plane.

A number of seminal HTSC ARPES results [1] are based upon the strong k-dependence of such quantities such as the lineshape (broad near $[\pi,0]$ in the normal state, sharper along the nodal $[0,0]$ - $[\pi,\pi]$ line), the superconducting and pseudogaps (maximal near $[\pi,0]$ going to zero along the nodal $[0,0]$ - $[\pi,\pi]$ line). In this context, the fact that the c-axis bi-layer splitting (referred to as BLS in the following) also has a strong k-dependence is highly relevant. It is minimal along the nodal line and maximal near $[\pi,0]$. Consequently, in the light of this, it is natural to ask to what extent either the quantitative or even qualitative conclusions drawn from angle-resolved photoemission data in the past have been hampered by our erstwhile inability to resolve the BLS [2].

Given recent improvements in both experimental resolution (analyser and beamline) and single-crystal quality, the BLS is now clearly visible in state-of-the-art k-space microscopy datasets, both in the superconducting and normal conducting states.

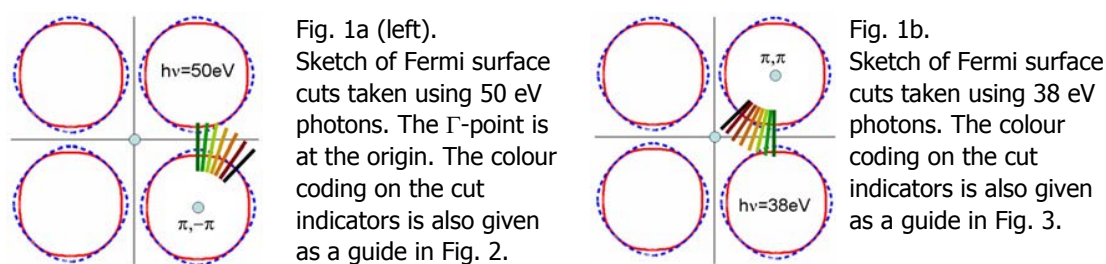
The aim of a set of experiments started in beamtimes at the U125/1-PGM beamline in 2003 is to trace out a series perpendicular Fermi surface cuts in differently doped $\text{Bi}_2\text{Sr}_2\text{CaCu}_2\text{O}_8$ -based HTSC systems, in which high resolution data was recorded using different photon energies and at different temperatures. The idea here is to attempt to explicitly resolve the BLS in a self-consistent database in which the position along the irreducible Fermi surface (FS) octant ($[0,0]$ - $[\pi,\pi]$ - $[\pi,0]$) is a running variable. In this way, when the series of experiments is completed, the following points, among others, can be addressed as a function of k-space location, doping level and temperature:

- many-body (renormalised) dispersion relation of the bonding and antibonding bands, presence of strong-coupling (feedback) effects [3] as a function of Fermi surface angle
- lineshapes and linewidths (in both energy and momentum space) for each band: where are there well defined quasiparticles ? what are the lifetimes of the states involved ?
- gaps (superconducting [4], pseudo), for each band.

In this way, we are confident to be able to better distinguish true many-body effects from those essentially resulting from an unresolved detail of band structure - not only at a particular k-point such

as $[\pi,0]$, but across the whole FS octant. It is the details of the k- and temperature dependence, coupled to the doping dependent behaviour that will finally allow a definitive assignment of the identity of bosonic modes which couple to the electronic system, an issue that is currently the subject of much debate.

Experimentally, such a programme is challenging as well as time intensive. We were fortunate to be able to have access to the IFW Dresden group's SES100-based ARPES end station, coupled to the IFW's new three angular axis cryo-manipulator. The latter offers unparalleled k-space manoeuvrability, and makes the perpendicular Fermi surface cuts shown here possible. The experiments carried out in 2003 concentrated on using 50 and 38 eV excitation energies. At least close to $[\pi,0]$, the former strongly favours emission from the antibonding BLS CuO_2 -related band (i.e. the bonding band is essentially invisible), whereas the latter also gives a relatively strong signal from the bonding band. For both photon energies, the superior resolving power of the U125/1-PGM enabled the total experimental resolution to be kept to 13 meV and below 0.2° in angle, without unacceptable inflation of the measuring time necessary for reasonable statistics.



In both cases (a and b), the FS's arising from the antibonding and bonding c-axis bilayer split CuO_2 -bands are shown schematically as blue dotted and solid red lines, respectively.

Fig. 1 illustrates the k-space location of the data presented in this report. The sample in question is Pb-doped $\text{Bi}_2\text{Sr}_2\text{CaCu}_2\text{O}_8$, the Pb-doping being vital as a suppressor of the incommensurate (5x1)-like modulation of the Bi-O planes that otherwise leads to a plethora of diffraction replicas over the whole FS quadrant, making a serious analysis of the data practically impossible. The crystal in question had a T_c of 85K, making it very close to optimal doping.

Fig. 2 shows data recorded at a photon energy of 50 eV: the upper row for a temperature of 30 K - well inside the superconducting state - the lower row for 100K, i.e. in the normal state. In Fig. 2 the antibonding band is clearly visible, and dominates the energy distribution maps (EDMs) for k close to $[\pi,0]$. Closer to the nodal direction (e.g. in the three right-most panels), the two bilayer-split components are apparent, also for $h\nu=50\text{eV}$. Fig. 3 shows the analogous dataset for a photon energy of 38eV, again with the upper row in the superconducting state (30K) and the lower row in the normal state (120K). Here the bonding band is much more prominent than in the 50eV data, as expected.

At this stage, the data shown in Figs. 2 and 3 are being analysed in terms of the loci of the maxima in the MDCs (horizontal cuts of the EDMs) and EDCs (vertical cuts of the EDMs). The intention is to generate self-consistent fitting results for the two BLS bands for both photon energies: only the relative intensities of the two components are free parameters between the datasets recorded with different photon energies. In this way, a higher precision and greater robustness of the conclusions extracted can be achieved.

[1] e.g. A. Damascelli, Z. Hussain and Z.-X. Shen, Rev. Mod. Phys. **75**, 473 (2003); M. R. Norman and C. Pepin, Rep. Prog. Phys. **66** (2003) 1547–1610

[2] A. A. Kordyuk et al., Phys. Rev. Lett. **89**, 077003 (2002)

[3] S. V. Borisenko et al., Phys. Rev. Lett. **90**, 207001 (2003); T. K. Kim et al, PRL **91**, 167002 (2003)

[4] S. V. Borisenko et al., Phys. Rev. B **66**, 140509 (2002)

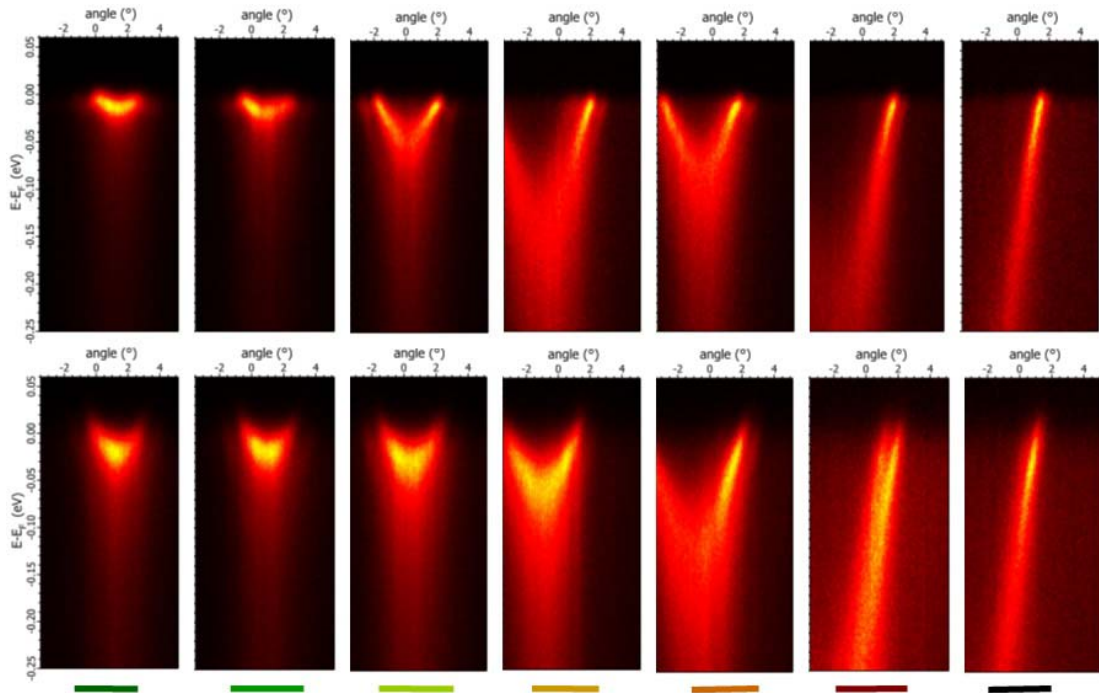


Fig. 2. Energy distribution maps from the colour-coded cuts shown in Fig. 1a recorded from Pb-Bi2212 with a photon energy of 50eV. Upper row: $T=30\text{K}$, lower row: $T=100\text{K}$.

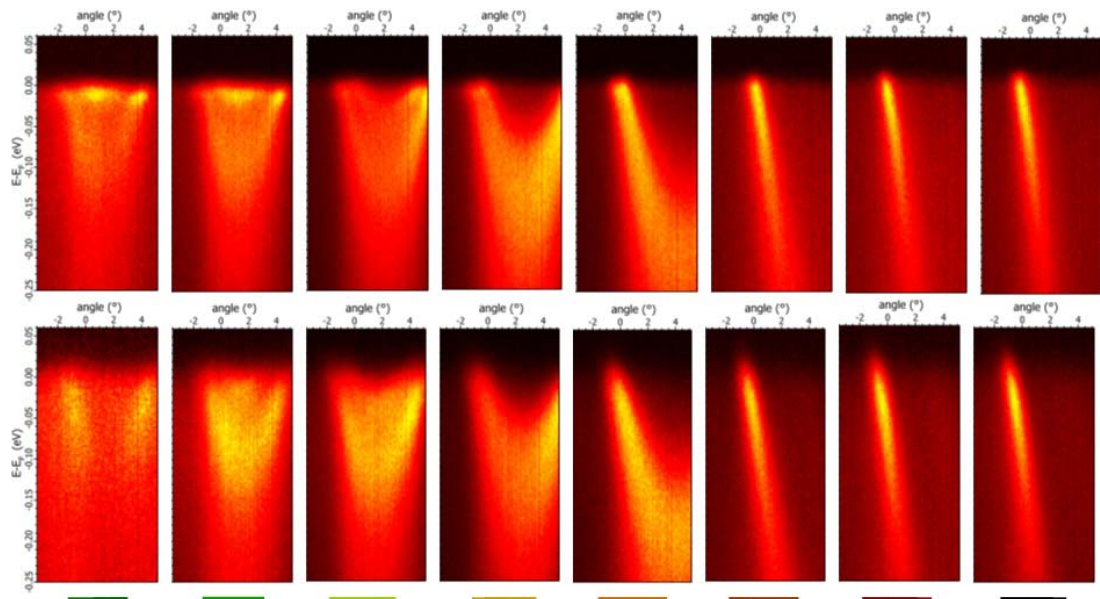


Fig. 3. Energy distribution maps from the colour-coded cuts shown in Fig. 1b recorded from Pb-Bi2212 with a photon energy of 38eV. Upper row: $T=30\text{K}$, lower row: $T=120\text{K}$.

We would like to thank the IFW Dresden's ARPES group for their generous technical support and the FOM, EU (via BESSY's large scale facility grant) and the Fonds National Suisse de la Recherche Scientifique for their financial backing of this research.

Self-organization of Pb thin films on Cu(111) induced by Quantum Size Effects

J. H. Dil, J. W. Kim, S. Gokhale,* M. Tallarida, and K. Horn

Department of Molecular Physics, Fritz-Haber-Institut der MPG, D-14195 Berlin

**Indira Gandhi National Open University, New Delhi, India*

Quantum well states, resulting from electron confinement in small artificial structures, offer access to an interpretation of many interesting physical properties of matter under conditions of reduced dimensions. In general, there is a connection between the occupancy of quantum well states and surface/thin film properties, which leads to an oscillatory behaviour of these properties as a function of film thickness¹. Among the predictions, specific “critical” and “magic” thicknesses, preferred over others because of their lower total energy similar to magic cluster sizes, have found considerable interest. Here we examine quantum well states in the Pb/Cu(111) system, and analyse their electronic structure and its interplay with film morphology, using angle-resolved photo-emission. We find that at low temperature, epitaxial layers are grown. Upon annealing, these rearrange into islands of different height influenced by quantum size effects, in that the stable layers have the topmost occupied well state further removed from the Fermi level than the less stable ones. Electron confinement in Pb films leads to the occurrence of quantum well states, as evident from the set of valence band photoelectron data (Figure 1), where several well-defined lines, absent in spectra from bulk Pb(111), are found. The lines shift in binding energy upon increasing the layer thickness, which confirms that they arise from individual quantum well states, and the binding energies of the peaks are analyzed within the phase

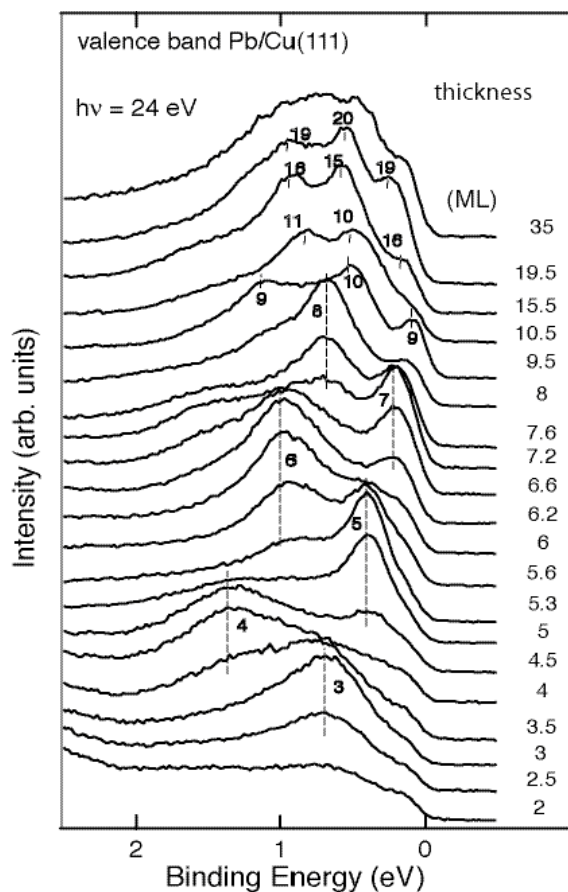


Figure 1: Valence level spectra from Pb layers on Cu(111) deposited at 100 K, for different depositions as indicated, recorded in normal emission at a photon energy of 24 eV.

accumulation model.² The peaks in Figure 1 are marked accordingly. This shows that at some coverages a mixture of layer thicknesses occurs, i.e islands of different height.

Annealing of Pb layers induces strong changes in the spectra, as shown in Figure 2, suggesting that a rearrangement is taking place when diffusion processes are enhanced.

The spectra for the as-deposited films (dashed lines) exhibit clear lines in an energy range right up to the Fermi level. Upon annealing, two processes can happen: either an existing peak increases, and the others vanish, or an entirely new peak occurs (e.g. for 17 ML). In either case, features with spectral weight at higher binding energy now dominate the spectrum. That structural changes are induced by annealing is also apparent from the intensity of the Cu 3d peak at 3 eV binding energy. This increases markedly for specific coverages, suggesting that more change occurs and the deposited thicknesses are therefore less stable. This can only be explained by a breaking-up of the Pb layer into islands with a well-defined height by diffusion of Pb atoms.

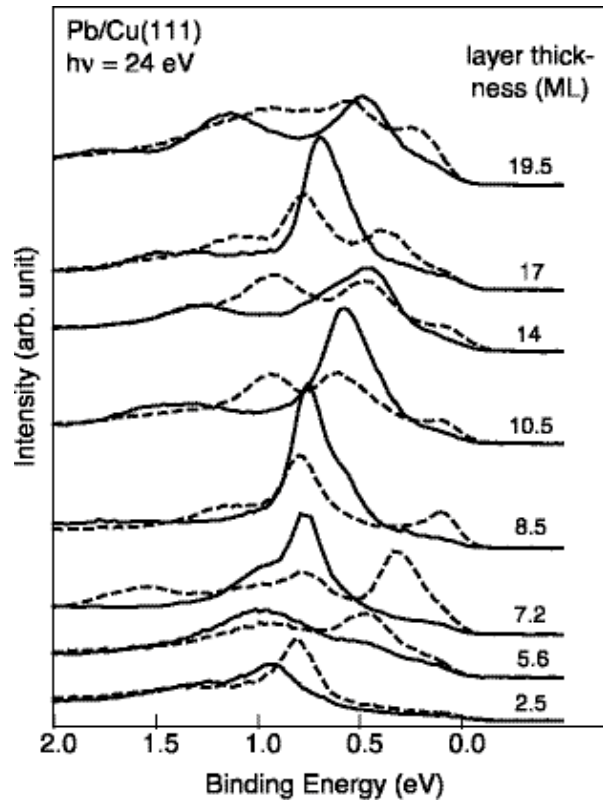


Figure 2: Close-up of spectra near E_F of as-deposited Pb films (dashed lines) of different thickness, and changes induced by annealing (solid lines), recorded in normal emission at a photon energy of 24 eV.

The reason for this process can be identified when considering the total energy of the film, by adding up all the energies of electrons in quantum well states from the bottom of the well up. The energy of the topmost occupied state can be lowered by changing the thickness to a width where the next higher state is just above the Fermi level; or, in other words, the islands rearrange their height to avoid the presence of quantum well states at the Fermi level. From the data it is obvious that this electronic driving mechanism is active here, offering a straightforward demonstration of preferential growth of specific island heights.

References

1. F.K.Schulte, Surface Sci. **55**, 427(1975).
2. P.Echenique and J.Pendry, J.Phys. C **11**, 2065(1978)

In-situ x-ray absorption of Co/TiO₂ Catalysts for Fischer-Tropsch Synthesis

Fernando Morales¹, Pieter Glatzel¹, Frank de Groot, Bert Weckhuysen¹,
Evgueni Kleimenov², Hendrik Bluhm², Michael Hävecker² and Axel Knop-Gericke²

¹ Department of Inorganic Chemistry and Catalysis, Utrecht University, Sorbonnelaan 16,
3584 CA Utrecht, The Netherlands.

² Fritz-Haber-Institut der MPG, Faradayweg 4-6, D-14195 Berlin, Germany.

Abstract

The reduction behaviour of Co/TiO₂ catalysts for Fischer-Tropsch synthesis has been investigated by soft X-ray absorption spectroscopy (XAS) at beam line U56/2-PGM-2 at the BESSY synchrotron in Berlin. In-situ XAS measurements of the L_{2,3} edges of Co has been carried out during reduction treatments of the samples in H₂ at temperatures up to 425 °C and at 2 mbar of pressure.

Introduction

The transformation process from syngas to hydrocarbons; i.e., Fischer-Tropsch synthesis (FTS) is gaining more and more importance due to the need for high purity fuels which can be obtained from other feedstocks than crude oil, i.e. natural gas, charcoal or biomass. Supported Co catalysts are claimed to be the most effective in achieving higher chain growth probability values (α) and turnover rates than other metal-based catalysts what makes them the catalysts of choice for FTS [1]. Reducibility of supported-cobalt particles strongly depends on the support used and on the preparation method [2]. For supports without a strong interaction with cobalt, such as silica, highly reducible cobalt oxide clusters are normally formed. TiO₂-supported catalysts have shown to have a strong metal-support interaction [3] what makes the cobalt species difficult to be reduced, most likely due to a strong CoO_x interaction with the support or the formation of other stable compounds such as CoTiO₃ that are reduced only at very high temperatures. The formation of cobalt titanate species has been reported before and it is thought to occur during the reduction from Co₃O₄ crystallites to CoO. During the reduction process Co²⁺ can diffuse into the support lattice leading to the formation of these compounds.

In the recent years it has become possible to perform XAS measurements at pressure ranges of 1-10 mbar [4] what allows carrying out *in-situ* treatments of the samples, e.g. calcinations and reductions, providing useful information about the surface composition of the catalysts under conditions that are closer to the actual operating conditions. We have performed *in-situ* XAS measurements during reduction treatments were carried out with two different Co/TiO₂ catalysts: one prepared by incipient wetness impregnation technique (IWI) with low cobalt dispersion and the other prepared by homogeneous deposition precipitation (HDP) with high cobalt dispersion. In addition, the same treatment was carried out for bulk Co₃O₄ in order to evaluate the reducibility of Co oxide compounds in the absence of TiO₂ support.

Results

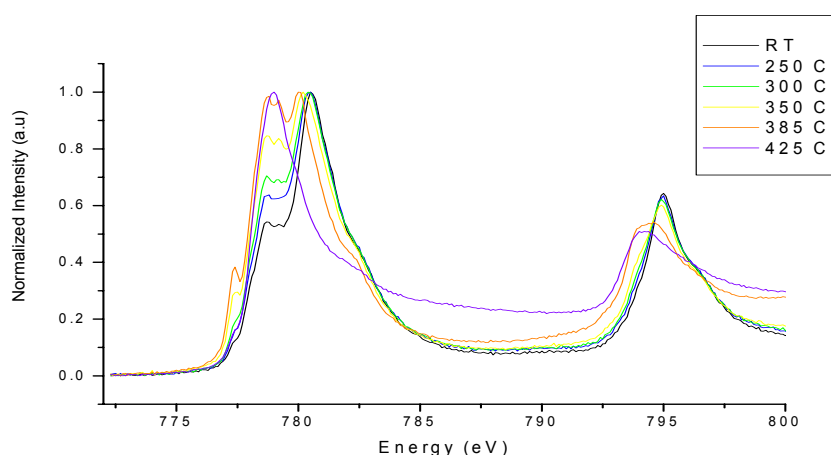


Figure 1: *Co L_{2,3} edges for bulk Co₃O₄ during reduction.*

Figure 1 shows the Co L_{2,3} edges spectra of the bulk Co₃O₄ measured during the reduction treatment in H₂ from room temperature up to 425 °C. It can clearly be observed that the spectrum shape changed by increasing the reduction temperature. At the same time the maximum energy peak shifted to lower energies. These spectral changes were due to a shift from higher to lower cobalt valence and variations in the symmetry of the cobalt states upon reduction. Comparison of the experimental spectra with the theoretical simulations leads us to a better understanding of these spectrum shapes. The spectra measured at room temperature correspond to a mixture of tetrahedral Co²⁺ and octahedral Co³⁺ states characteristic for Co₃O₄. As soon as the reduction temperature was increased, the shape of the spectra changed becoming partly due to octahedral Co²⁺ due to the reduction of Co₃O₄ to CoO. At a temperature of 385 °C the measured spectrum corresponds to pure CoO, as found by comparison to charge transfer multiplet calculations. This confirms the complete shift to Co²⁺. The consecutive reduction of CoO to Co⁰ easily occurred at the temperature of 425 °C at which the pure Co⁰ spectrum was measured. This spectrum consisted of a sharp single peak (L₃ edge) without any features, characteristic of Co metal.

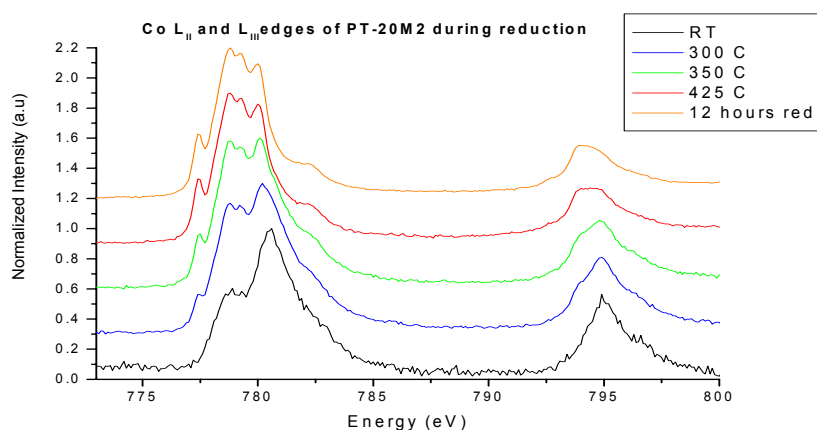


Figure 2: *Co L_{2,3} edges measured for the IWI-prepared Co/TiO₂ (PT-20M2) catalysts during reduction.*

Figure 2 shows the results for the IWI-prepared Co/TiO₂ catalyst. The reduction behaviour of the cobalt species was similar in both catalysts, though significantly different to the bulk cobalt oxide discussed above. At room temperature the spectra corresponded to mainly Co₃O₄ though some CoO was also present in both samples. In both catalysts the reduction of

Co₃O₄ to CoO occurred at lower temperatures than with the bulk Co₃O₄. In the HDP catalyst the pure CoO spectrum was measured at 350 °C whereas in the IWI catalyst a little amount of Co³⁺ was also present in addition to CoO. In both catalysts, the CoO compound did not further reduce to Co⁰ a high extent as shown in the spectra at 425 °C, which consists mainly of CoO and only a small amount of Co⁰. This result indicates that CoO supported on TiO₂ was hardly reducible to Co metal at the conditions used in this work.

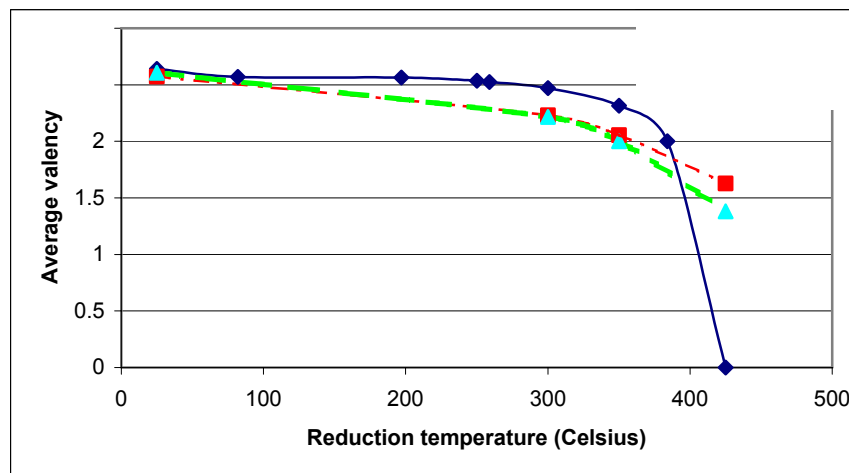


Figure 3: average cobalt valence for the three samples measured during the reduction treatments

Figure 3 shows the average cobalt valence for the three samples measured during the reduction treatments. These numbers are derived from linear combinations of the spectra measured at each temperature were used to calculate the average valence. At room temperature the cobalt average valence in the catalysts was lower than 2.66 what means that some CoO was present in the calcined catalysts in addition to Co₃O₄. It is clear from the figure that bulk CoO reduces quickly to Co⁰, whereas the supported CoO reduces only a little.

Conclusions

It can be conclude that the support strongly influences the reduction behaviour of the cobalt oxides by depleting the extent of reduced cobalt achieved in the catalysts at these working conditions. The final cobalt composition of the catalysts was mostly CoO and a small amount of Co⁰, whereas in the bulk cobalt oxide pure Co⁰ was obtained after the same treatment. This points towards the existence of a strong metal support interaction in both catalysts, which affects the surface composition of reduced catalysts.

References

- [1] E Iglesia: Design, synthesis, and use of cobalt-based Fischer-Tropsch synthesis catalysts. Applied catalysis A 161 (1997) 59-78.
- [2] M Kraum, M Baerns: F-T Synthesis: the influence of various cobalt compounds applied in the preparation of supported cobalt catalysts on their performance. Applied Catalysis A 186 (1999) 189-200.
- [3] M Vob, D Borgmann, Wedler.: Characterization of Alumina, Silica, and Titania Supported Cobalt Catalysts. Journal of Catalysis 212 (2002) 10-21.
- [4] A Knop-Gericke, M Havecker, T Schedel-Niedrig, R Schlogl: High-Pressure low-energy XAS: a new tool for probing reacting surfaces of heterogeneous catalysts. Topics in catalysis 10 (2000) 187-98.

Local adsorption sites and bondlength changes in Ni(100)/H/CO and Ni(100)/CO

J.T.Hoeft, M.Polcik, D.I.Sayago, M. Kittel, R.Terborg
Fritz-Haber-Institut der MPG, Faradayweg 4-6, D 14195 Berlin, Germany

R.L. Toomes, J. Robinson, D.P.Woodruff
Physics Department, University of Warwick, Coventry CV4 7AL, UK

M.Pascal, G.Nisbet, C.L.A.Lamont
*Centre for Applied Catalysis, Department of Chemical and Biological Sciences,
University of Huddersfield, Queensgate, Huddersfield, HD1 3DH, UK*

Studies of CO adsorption on Ni surfaces go back to the earliest stages of development of surface science, and indeed the $c(2 \times 2)$ phase of CO adsorbed on Ni(100) was the first model system used in the first quantitative structure determination of a molecular adsorbate using quantitative LEED. Partly because of this, and partly despite it, the CO/Ni system provides a valuable model for understanding some aspects of molecular interactions with surfaces. In the present study, using C 1s (and O 1s) scanned-energy mode photoelectron diffraction, the objective was to understand how molecule-surface bondlengths (in the present case the C-Ni distance) vary as the bond order and bond strength of the chemisorption vary. The experiments involved the study of 4 distinct structural phases: CO on Ni(100) in the $c(2 \times 2)$ 0.5 ML phase and in the high coverage $(3\sqrt{2} \times \sqrt{2})R45^\circ$ phase, and CO coadsorbed with atomic H in the low temperature $c(2 \times 2)$ phase and in the higher-temperature disordered phase [1, 2]. Conventional wisdom is that these four phases involve adsorption of the CO in atop, bridge, atop and bridge sites respectively, and indeed these local sites were confirmed in our study. Apart from these differences in Ni-C bond order (of 1.0 or 0.5), the $c(2 \times 2)$ -CO/H phase is known to have an adsorption energy about a factor of 2-3 less than the pure CO phases, in particular.

The complete structure determinations of these systems using PhD at BESSY II, and exploiting the photoelectron binding energy chemical shifts to distinguish CO in different coadsorbed states in some of the surface preparations, show that in the pure CO adsorption phases at approximately constant adsorption energy, the measured Ni-C bondlengths show an increase of 0.16 ± 0.04 Å in going from atop to bridge sites, while comparison with similar results for Ni(111)/CO for 3-fold coordinated adsorption sites using the same methodology [3] show a further lengthening of the bond by 0.05 ± 0.04 Å. These changes in the Ni-CO chemisorption bondlength with bond order (for approximately constant adsorption energy) are consistent with the standard Pauling rules.

However, comparison of CO adsorbed in the atop geometry with and without coadsorbed hydrogen shows that the coadsorption increases the Ni-C bondlength by only 0.06 ± 0.04 Å, despite the decrease in adsorption energy of a factor of 2 or more. There is therefore a pronounced difference between the change in the Ni-C bondlength when the bond order is halved at constant adsorption energy, and when the adsorption energy is halved at constant bond order. In order to gain a better

understanding of this we have also conducted density functional theory slab calculations, and find that these reproduce the effect observed experimentally.

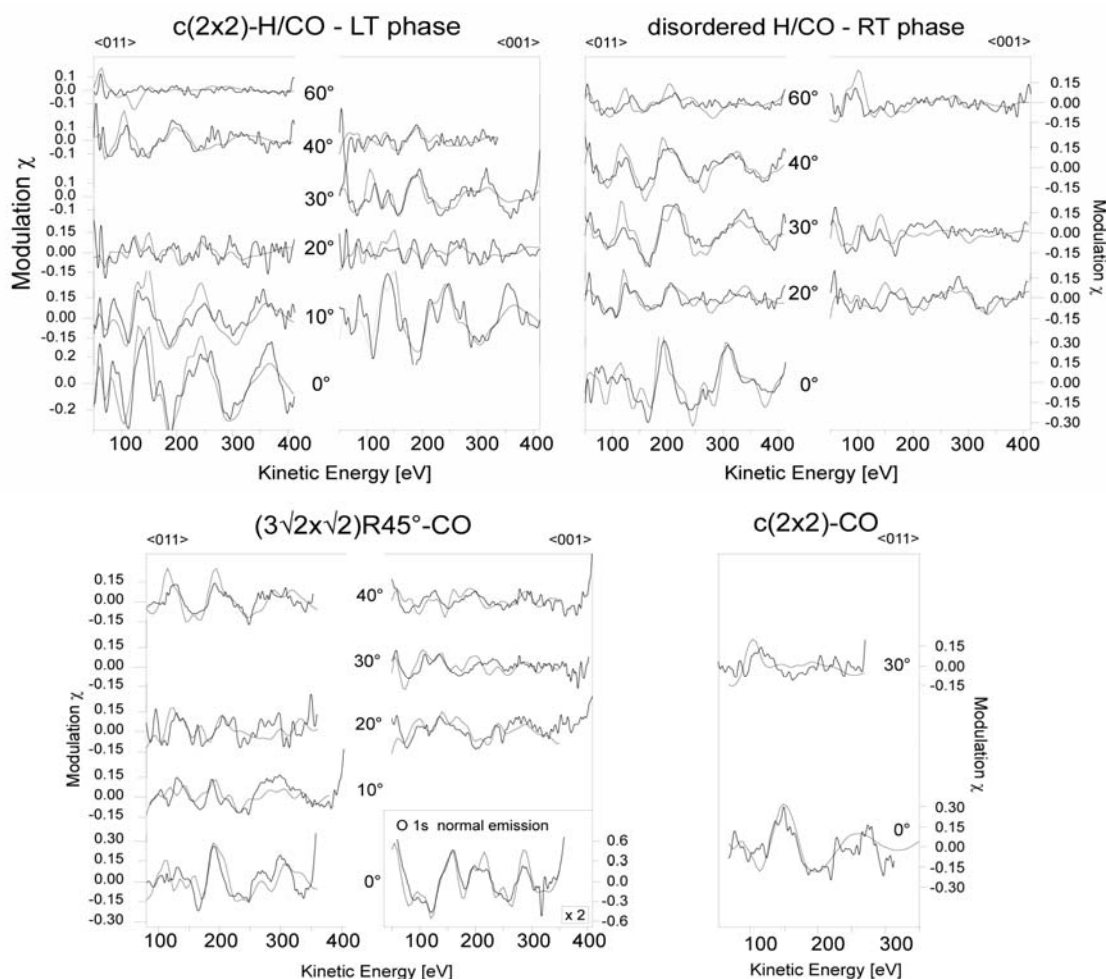


Fig. 1 Comparison of experimental and theoretical PhD modulations spectra for the best-fit structures of the four Ni(100)/CO surface phases

However, the results of both the experiments and the DFT calculations show that CO adsorption onto the Ni(100)/H surface is accompanied by significant structural modification. There is a large rumpling of the outermost layer distinguishing between Ni surface atoms bonded, or not bonded to CO, and the DFT calculations also show that the CO adsorption causes a very significant shift of the atom layer spacing of the adsorbed H atoms. It is argued that is the energy cost of these distortions which gives rise to the low total adsorption energy, the local Ni-C bond remaining quite strong and thus retaining a short Ni-C bondlength.

- 1 D.I.Sayago, J.T.Hoeft, M.Polcik, M.Kittel, R.L.Toomes, J.Robinson, D.P.Woodruff, M.Pascal, C.L.A.Lamont, G. Nisbet, *Phys.Rev.Lett.* **90** (2003) 116104
- 2 J.T.Hoeft, M.Polcik, D.Sayago, M. Kittel, R. Terborg, R.L. Toomes, J. Robinson, D.P.Woodruff, M.Pascal, G. Nisbet, C.L.A.Lamont, *Surf. Sci.* **540** (2003) 441
- 3 M.E.Davila, M.C.Asensio, D.P.Woodruff, K-M.Schindler, Ph.Hofmann, K-U.Weiss, R.Dippel, P.Gardner, V.Fritzsche, A.M.Bradshaw, J.C.Conesa and A.R.González-Elipe *Surf.Sci.* **311** (1994) 337

In situ XPS at a bending magnet beamline:

Study of the electronic structure of binary Cu/Zn catalysts

M. Hävecker, B.L. Kniep, H. Bluhm, E. Kleimenov, D. Teschner, A. Pestryakov, T. Ressler,

A. Knop-Gericke, R. Schlögl

Fritz-Haber-Institut der MPG, Faradayweg 4-6, D-14195 Berlin (Dahlem), Germany

Introduction

In situ X-ray photoelectron spectroscopy is a powerful tool for the investigation of dynamic processes studied in the field of material science and catalysis. Several examples of the application of this technique can be found in this and previous annual reports. The study of a catalyst under working conditions often requires a complex gas feed and an elaborated gas analytic to follow the conversion of the gas phase during the reaction. It might be frequently unavoidable to use hazardous substances (e.g. poisonous or flammable) as reactants. It is obvious that a permanent endstation at a beamline dedicated for spectroscopic *in situ* investigations can fulfill these requirements much more efficiently than a non-permanent installation. A broad range of spectroscopic investigations should be performed at this beamline. An optical setup based on a plane grating monochromator (PGM) working in the collimated light is most suitable because the operation of the beamline can be optimized for the specific needs of the users without any hardware modifications (e.g. setting of slit positions, mirrors). A schematic view of the proposed optical layout can be found in Fig. 1.

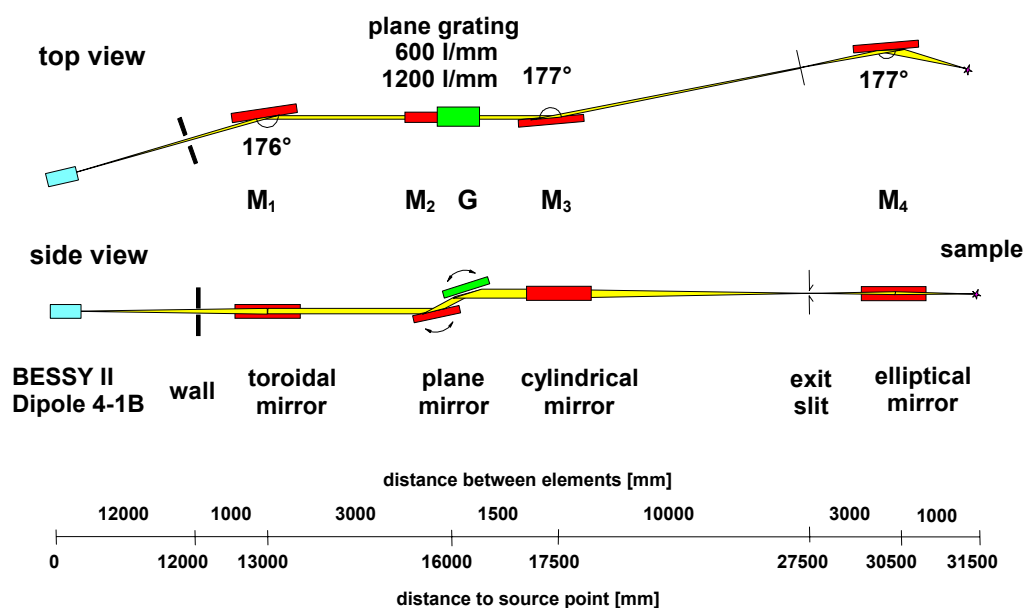
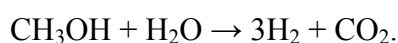


Figure 1: *Optical layout of a plane grating monochromator beamline in collimated light*

The Russian-German beamline (RGLB) operated at a BESSY bending magnet is based on a PGM working in collimated light [1]. Therefore, we used RGLB to test the opportunity for *in situ* XPS investigation at a bending magnet beamline in general, although this beamline is not optimized for operation with the already existing *in situ* XPS endstation.

Cu/ZnO (alumina) catalysts are common catalysts for the hydrogenation of carbon monoxide and carbon dioxide. These systems have found industrial use for the low-temperature methanol synthesis, for the low-temperature water-gas shift reaction, and for the steam reforming of methanol following the reaction [2]:



An important application could be the onboard production of hydrogen for fuel cell application. It is the proposed synergistic effect in the binary copper/zinc oxide that makes this system interesting for investigation [3-5]. The maximum activity is obtained in an intermediate compositional range, whereas Cu and ZnO alone exhibit only negligible activity [6].

Results and discussion

Fig. 2 shows *in situ* XP spectra of a Cu/ZnO catalyst in 1 mbar H₂. The lower set of spectra (a) shows the catalyst before the activation at room temperature and the upper set (b) was taken during the activation process in hydrogen at 250°C. Spectra with two photon energies resulting in different information depths were taken at each condition. The shift of the Cu3p core level indicates a reduction of Cu but not of Zn. It can be seen that during the activation the catalyst surface

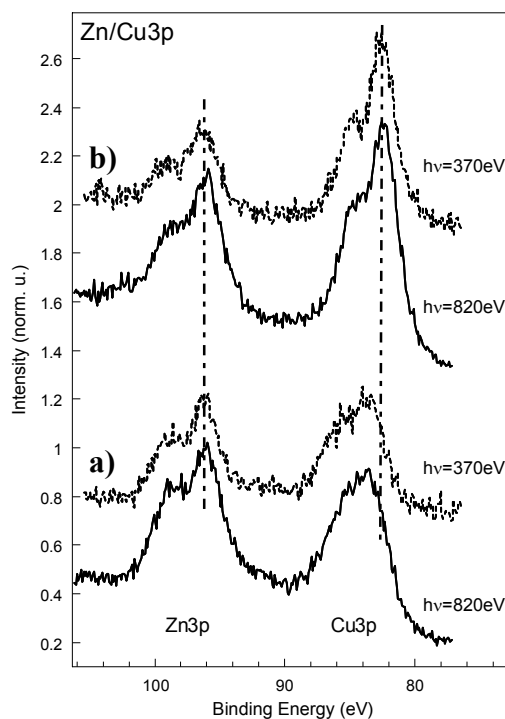


Figure 2: Zn3p and Cu3p core level spectra. The spectra were taken at 1 mbar H₂ before the activation at room temperature (a) and during the activation at 250 °C (b). The incidence photon energy was varied as indicated.

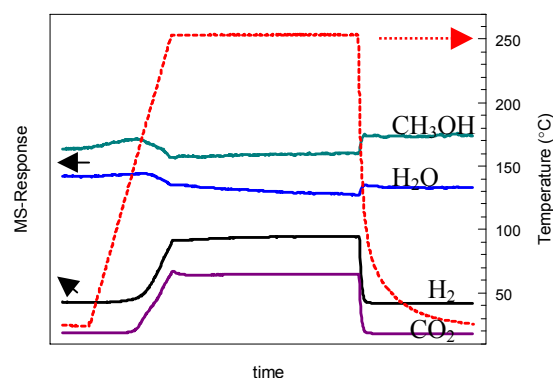


Figure 3: Mass spectrometer response while the catalyst was heated in a mixture of CH₃OH and H₂O. H₂O and CH₃OH were consumed and H₂ and CO₂ evolved at the same time.

got enriched with copper. Furthermore, this example shows a nice application of the depth-profiling technique by variation of the incident photon energy. A gradient of the Cu/Zn ratio was found by this technique with the higher Cu concentration at the outermost surface under this activation conditions. After the activation in hydrogen the sample was heated in a 1:1 mixture of methanol and water ($p_{\text{tot}}=0.25$ mbar). The mass spectrometer response during the reaction is shown in Fig. 3. It can be seen by the consumption of CH_3OH and H_2O and the evolution of H_2 and CO_2 at the same time that the activated catalyst presented in Fig. 2 is active in the methanol steam reforming reaction.

These results demonstrate that it is feasible to carry out successfully *in situ* XPS measurements at a PGM bending magnet beamline. It should be noted that a beamline specially designed for operation with the *in situ* XPS setup is expected to result in an even better performance.

Acknowledgement

The authors want to acknowledge Denis Vyalikh and Rolf Follath for their assistance during the beamtime at the Russian German Beamline. MH gratefully acknowledges Fred Senf for support and valuable discussions concerning beamline layouts.

References:

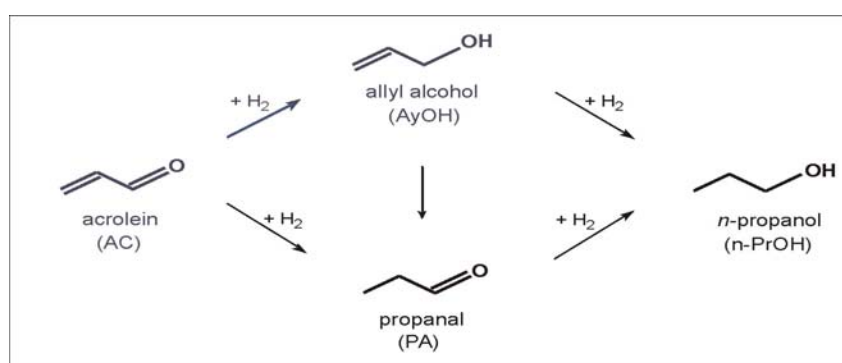
- [1] S.I. Fedosenko, I.E. Iossifov, S.A. Gorovikov, J.-S. Schmidt, R. Follath, S.L. Molodtsov, V.K. Adamchuk, G. Kaindl, Nucl. Instr. and Meth. A 70 (2001) 84.
- [2] P.J. Wild, M.J.F.M. Verhaak, Catal. Today 60 (2000) 3.
- [3] K. Klier, Adv. Catal. 31 (1982) 243.
- [4] M.M. Günter, T. Ressler, B. Bems, C. Büscher, T. Genger, O. Hinrichsen, M. Muhler, R. Schlögl, Catal. Lett. 71 (2001) 37.
- [5] B.L. Kniep, T. Ressler, A. Rabis, F. Girgsdies, M. Baenitz, F. Steglich, R. Schlögl, Angew. Chem. 116 (2004) 114.
- [6] B.S. Rasmussen, P.E.H. Nielsen, J. Villadsen, J.B. Hansen, in: *Preparation of Catalysts IV*, eds. B. Delmon, P. Grange, P.A. Jacobs, G. Poncelet (Elsevier, Amsterdam, 1987) p.785.

Selective hydrogenation of acrolein using silver catalysts:
studied by high-pressure XPS and XAS

D. Teschner¹, A. Knop-Gericke¹, A. Pestryakov¹, E. Kleimenov¹, B. Steinhauer¹, M. Hävecker¹, H. Bluhm¹, M. Bron², P. Claus², R. Schlögl¹
¹*Fritz-Haber-Institut der Max-Planck-Gesellschaft, Faradayweg 4-6, D-14195 Berlin*
²*TU Darmstadt, Petersenstr. 20, D-64287 Darmstadt*

Introduction

Selective hydrogenation of organic molecules containing numbers of unsaturated functional groups is an important step in the industrial preparation of fine chemicals. The hydrogenation of acrolein, an α,β -unsaturated aldehyde, can proceed either to the saturated aldehyde, propanal, or to the α,β -unsaturated alcohol, allyl alcohol (*Scheme 1*). From both products, the consecutive hydrogenation to n-propanol is possible as well as side reactions like decarbonylation. When using silver as catalyst, the selectivity to propanol or by-products is low (in most cases below 5 %), therefore mainly allyl alcohol and propanal are formed [1]. This joint multicenter project attempts to establish relationship between intramolecular selectivity (hydrogenation of C=C vs. C=O bond) and catalyst properties (surface structure, shape, support, precursor salt) and clarify the effect of reaction pressure.



Scheme 1: Selective and total hydrogenation of acrolein

Experimental

High-pressure XAS measurements were carried out on silver single-crystal (Ag(111)), polycrystalline Ag foil and supported catalyst (9Ag/SiO₂). The angle of incident beam to sample surface was varied on the single crystal (90°: normal incidence, 30°: grazing incidence). Carbon K-edge data were collected in the total electron yield mode (TEY). Gas phase and collector plate (surface related plus gas phase) signal were recorded. The reactor cell was operated in batch mode with a gas mixture of 0.01 mbar acrolein, 0.01 mbar argon and 7.48 mbar H₂. The reaction was monitored by online mass spectrometer (MS).

The high-pressure XP spectra were taken with another set-up. Its differentially pumped electrostatic lens system is the key feature, allowing us to investigate the sample in the mbar

pressure region. We used here polycrystalline Ag foil and supported catalysts (Ag/ZnO) with different Ag loading and precursor salt. The samples were measured in UHV (RT), in hydrogen and oxygen (RT, 250 °C) and in the reaction mixture of 0.1 mbar acrolein and 0.9 mbar hydrogen (flow mode) at 250 °C.

Results

In the flow experiment no conversion could be detected, most probably because of the very low contact time and pore diffusion problems in the mbar pressure range. However, in the batch experiments we observed the formation of propionaldehyde (hydrogenation of C=C double bond) and almost no allyl alcohol (if any). The conversion was $\sim 1\text{-}2\%$ /hour, and was not too sensitive to the silver samples. Considering the broad range of samples (from single crystal to supported sample) and the inactivity of non-supported samples at industrial conditions, the hydrogenation was found to be a beam enhanced process on the illuminated surface. However, the low allyl alcohol (and high propionaldehyde) selectivity fits very well to the pressure dependence of the intermolecular selectivity measured separately in the industrial relevant (1-20 bar) pressure range.

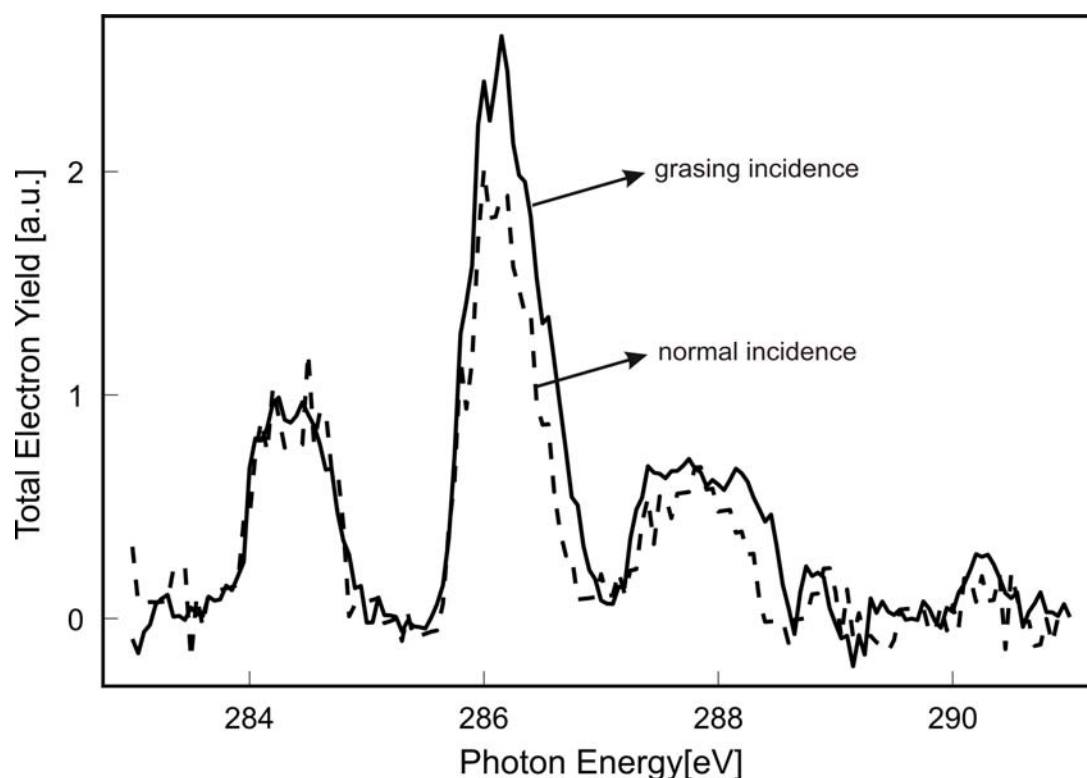


Figure 1: Angular dependent XAS of Ag(111) in the C K-edge (after background subtraction; gas + surface signal). The single crystal is in the gaseous ambient of 0.01 mbar acrolein, 0.01 mbar argon and 7.48 mbar H₂.

Angular dependent XAS measurements on the C K-edge shows that the π -like “C=O” orbital of acrolein lie parallel to the surface and σ^* (C-H) orbitals orientate rather perpendicular.

Consequently, the molecule is in the *lying-down* orientation under hydrogenation conditions. A closer analysis of the surface related spectra (not just for Ag(111)) reveals that the $1\pi^*$ transition corresponding to the “C=O part” of the molecule is clearly increased compared to the “C=C part”, relative to gas phase spectrum of acrolein. As a result, “C=O” is accumulated on the surface, or which is more in line with the catalytic data, C=C double bonds are almost not present on the surface. Therefore, it is very likely that the C=C double bond of acrolein is already hydrogenated and this hydrogenated species is what we detect on the surface.

In the high-pressure XPS set-up, we investigated a series of ZnO supported silver catalysts prepared from two different precursors (lactate or nitrate based Ag salt) with 5 or 10 % nominal Ag loading. Most of the samples were already tested catalytically at 20 bar before our measurements. In the information depth of XPS the apparent silver loading of 5 and 10% Ag/lactate/ZnO samples was nearly the same and was slightly dependent (8-10% Ag) on the gaseous ambient. The apparent silver content (metal dispersion) decreased in the reaction mixture (250 °C). The silver dispersion was low for the “calcined but not reduced” samples, which increases after reduction treatment. The “lactate” samples initially (stored in air) showed Ag₂O (6-8 % of the total Ag content) besides metallic silver. The oxide component was entirely reduced under reaction condition; therefore the reaction proceeds on metallic silver. The “nitrite” samples, exhibiting lower intrinsic activity, showed small residual oxidic part (~2%; ~ the detection limit). Additionally, we measured temperature dependently silver foil (Ag 3d core level) in oxygen (0.5 mbar) ambient, and surprisingly found Ag₂O (9.3%) at 350 °C, at which condition according to the silver/oxygen phase-diagram Ag₂O should be not stable. The oxygen content (mainly ZnO) of the supported samples decreases in the reaction mixture, due to desorption of adsorbed species (water, O-H, oxygenated C). The O/Zn ratio of the samples catalytically tested previously ex-situ were unexpectedly high (4-5), while the “calcined but not reduced” sample and the support itself showed ratios (1.5-2) much closer to the stoichiometric 1. The reason for this extraordinary O/Zn ratio might be in the high carbon content (up to 70%) of the used samples, carbon sitting mainly on Zn ions.

Acknowledgement

The authors thank the BESSY staff for their continual support during the measurements and the trust allowing us to carry out this study using acrolein. The work was supported by the German Research Foundation (DFG).

References

¹ Claus, P., *Topics in Catalysis* **5**, 51(1998).

Fig.2 - are attributed to the co-occupation of at least two distinct local sites. Quantitative modelling based on a two-site model indicates that the

	% bridge LT/RT	d_{C-C} (Å)	$d_{(C-Si,D)}$ (Å)	$d_{(Si,D-Si,D)}$ (Å)	$\langle u^2(c,z) \rangle$ ($\times 10^{-3} \text{ Å}^2$)	R
bridge parameters: all combined models		1.36	1.83	2.44	4	
bridge + rotated pedestal						0.45
rotated pedestal	69/37	1.28 ± 0.42	1.74 ± 0.12	2.05 ± 1.00	1 (+74/-1)	
bridge + rotated pedestal						0.46
rotated pedestal (constrained)	69/37	1.40	1.81 ± 0.08	2.40	1 (+28/-1)	
rotated pedestal theory		1.54-1.60	1.97-2.01	2.28-2.36		
bridge + pedestal						0.40
pedestal	65/37	1.19 ± 0.40	2.17 ± 0.07	2.82 ± 0.93	2 (+20/-2)	
bridge + pedestal						0.44
pedestal (constrained)	65/37	1.40	2.07 ± 0.07	2.40	2 (+30/-2)	
pedestal theory		1.58-1.62	2.00-2.07	2.34-2.37		
bridge + rotated bridge						0.39
rotated bridge	55/19	1.31 ± 0.37	2.46 ± 0.17	3.09 ± 0.98	5 (+19/-5)	
bridge + rotated bridge						0.48
rotated bridge (constrained)	68/49	1.40	1.84 ± 0.21	2.40	10 (+64/-10)	
rotated bridge theory		1.36-1.37	1.90-1.92	2.37-2.44		

Table 1 Structural parameters of acetylene

majority state at low temperature is bridge site adsorption with the C-C axis of the acetylene directly above, and parallel to, Si-Si surface dimers. At room temperature a second state accounts for more than 50% of the adsorbed acetylene molecules, and the favored model places these acetylene molecules midway between pairs of Si dimers, although the azimuthal orientation of the C-C axes is ambiguous. One possible geometry for this second species is the “pedestal site” tetra- σ species previously proposed by Xu *et al.*[2], although the specific geometry proposed by this group can be excluded. An alternative “rotated pedestal” site is comparably probable. There is no direct evidence for any occupation of a rotated bridge site across the ends of two adjacent Si dimers, but partial occupation of this site cannot be excluded. The quantitative structural parameters are summarised in Table 1.

References:

- [1] R. Terborg, P. Baumgärtel, R. Lindsay, O. Schaff, T. Gießel, J. T.Hoefl, M. Polcik, R. L. Toomes, S. Kulkarni, A. M. Bradshaw, and D. P. Woodruff, Phys. Rev. B **61**, 16 697 (2000).
[2] S. H. Xu, M. Keeffe, Y. Yang, C. Chen, M. Yu, G. J. Lapeyre, E. Rotenberg, J. Denlinger, and J. T. Yates, Jr. Phys. Rev. Lett. **84**, 939 (2000).

Combined application of XPS, XANES and mass-spectrometry to the *in-situ* study of ethylene epoxidation over silver

V.I.Bukhtiyarov, A.I.Nizovskii

Boriskov Institute of Catalysis, Lavrentieva prosp., 5, 630090, Novosibirsk, Russia

H. Bluhm, M.Hävecker, A.Knop-Gericke, R.Schlögl

Fritz-Haber-Institut der MPG, Faradayweg 4-6, D-14195 Berlin (Dahlem), Germany

Revealing the structure/activity relationship was a motivation for numerous studies using UHV-based surface science techniques to evaluate the nature of active centers on a catalyst surface. However, the results of such investigations can not be transferred directly to technical catalysis due to the pressure gap problem. A similar limitation is also found for the case of ethylene epoxidation over silver. In spite of several hundreds of the papers about this system, the nature of the oxygen species that are responsible for the ethylene oxide formation is still under debate. The pressure gap problem is one reason for this situation, since ethylene oxide has been observed among the reaction products only if the reaction pressure is higher than 1 mbar [1,2]. Practically all studies of this reaction, however, were post-reaction analysis under UHV conditions after evacuation of the reaction mixture, and not even a very fast transfer from the reaction zone to the UHV analyzer chamber (less than 20 seconds) did allow the observation of an active oxygen species [1,2].

To tackle this problem we have performed *in-situ* studies of the ethylene epoxidation reaction over a silver foil using a X-ray photoelectron spectrometer that is equipped with a high-pressure gas cell. This spectrometer is able to measure XPS spectra at pressures of up to 5 mbar. The high brightness of the synchrotron radiation source helps to compensate for the attenuation of the XPS signal at high pressures. The catalytic activity of the silver foil was characterized by proton-transfer reaction mass spectrometry. In addition, XANES spectra were measured to elucidate the atomic or molecular origin of the oxygen species.

All experiments were performed at beam line U49/2-PGM1 at BESSY in Berlin. The overall spectral resolution was 0.1 eV at the oxygen *K*-edge. All spectra were normalized by the incident photon flux, which was measured using a photodiode with known quantum efficiency. The ethylene and oxygen flows into the experimental cell were regulated using calibrated mass flow controllers. The sample was a polycrystalline Ag foil (99.99% purity) mounted on a temperature-controlled heating stage. The sample temperature was measured by means of an alumel-chromel thermocouple attached directly to the back of the sample. The

sample was cleaned by cycles of Ar^+ sputtering, annealing in 10 mbar of O_2 at 570 K, and flashing to 800 K in UHV.

In the first set of experiments we have tested the rate of ethylene epoxidation depending on the catalyst temperatures (300 –600 K). In agreement with the previous catalytic data, the reaction rate was low at room temperature and increases sharply after when the temperature is increased above 420 K. The XPS spectra show that at $T < 420$ K the silver surface is covered by carbonate groups, but that at $T \geq 470$ K silver is modified by subsurface (embedded) oxygen. We have then performed a detailed measurements using XPS and XANES at various partial pressures of ethylene and oxygen at $T = 420$ K.

Figure 1 shows a set of C1s and O1s spectra of the polycrystalline silver foil measured at $T = 420$ K during the exposure to different $\text{C}_2\text{H}_4 + \text{O}_2$ reaction mixtures, and at different total pressures. The exposure to pure oxygen removes the initial carbon contamination ($E_b(\text{C1s})=284.4$ eV) and produces nucleophilic oxygen with $E_b(\text{O1s})=528.2$ eV. The introduction of ethylene to the gas phase (oxygen/ethylene ratio = 10:1) decreases the equilibrium coverage of O_{nucl} , indicating the high reactivity of ethylene. In addition, a new O1s peak at 530.0 eV appears which is assigned to electrophilic oxygen. The nature of the

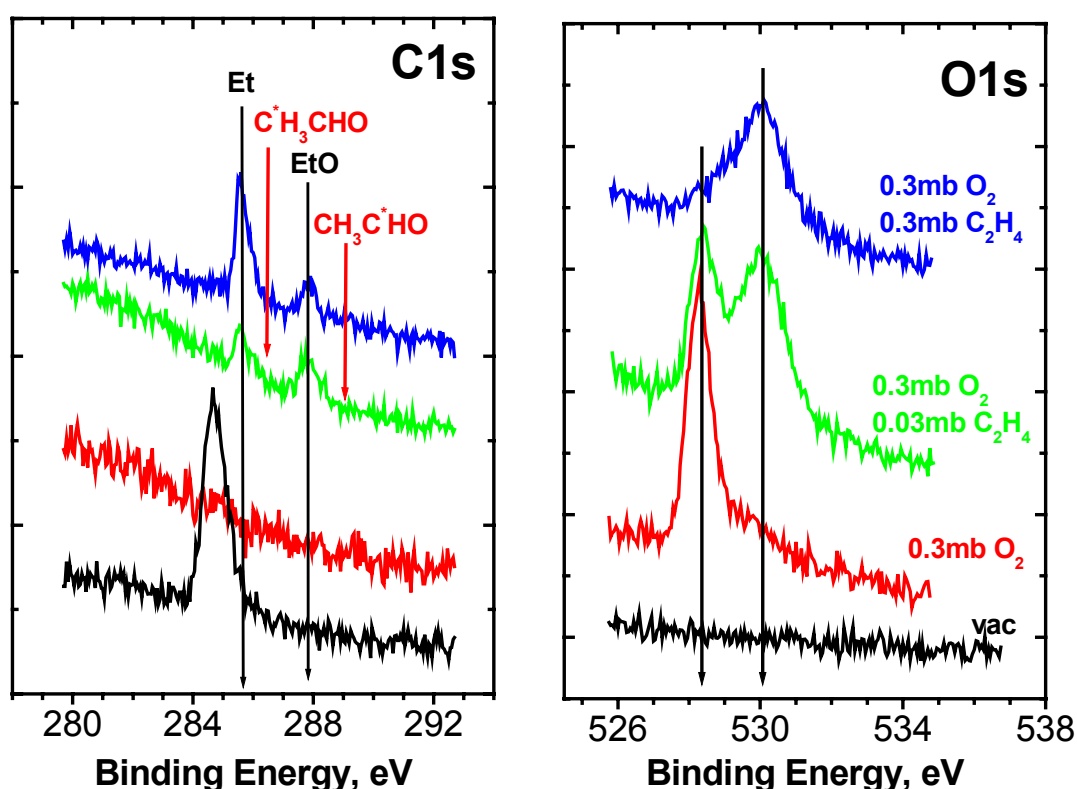


Fig.1. C1s and O1s spectra from the silver foil exposed to $\text{C}_2\text{H}_4 + \text{O}_2$ at 420 K and various partial pressures. The spectra measured in vacuum are also shown for comparison.

electrophilic oxygen was studied earlier by us using a combination of XPS, XANES, UPS, and Auger spectroscopy [3-4]. An increase of the partial pressure of ethylene (oxygen/ethylene ratio = 1:1) decreases sharply the surface concentration of the nucleophilic oxygen, whereas the concentration of the electrophilic oxygen remains practically constant.

Two features at ~ 285.8 and 287.9 eV are observed in the C1s spectra. They are assigned to gas phase ethylene and ethylene oxide, respectively. The former assignment is confirmed by the enhancement of the corresponding C1s signal which occurs when the ethylene pressure is increased. The assignment of the second line is based on the known shift in binding energy between C_2H_4 and C_2H_4O of 2.1 eV [5], and on the disappearance of this C1s signal after the removal of oxygen from the reaction mixture. This is the first observation of ethylene oxide in gas phase C1s spectra and is of great importance since it proves unambiguously the formation of ethylene oxide under our conditions. The detection of ethylene oxide using mass spectrometry is difficult since ethylene oxide is hard to distinguish from its isomer (acetaldehyde), which is a side product of the ethylene epoxidation reaction and gives a very similar mass spectrum. In the case of XPS the asymmetric carbon atoms in acetaldehyde would give rise to two different C1s signals (marked by red arrows in Fig 1) that are not observed in our spectra.

The XPS data in Fig. 1 also show that an increase in the ethylene partial pressure does not change the yield of ethylene oxide. This is also supported by the simultaneously obtained mass spectrometry data (not shown here). From this observation we conclude that electrophilic oxygen is the active species for the formation of ethylene oxide, whereas the nucleophilic oxygen is inactive in the reaction.

Acknowledgement. V.I.B. and A.I.N. gratefully acknowledge the financial support by the Max-Planck-Gesellschaft.

References:

1. C.T. Campbell and M.T. Paffett, Surf. Sci. 139 (1984) 396.
2. C. T. Campbell and M. T. Paffett, Surf. Sci. 143 (1984) 517.
3. V.I. Bukhtiyarov, M. Hävecker, V.V. Kaichev, A. Knop-Gericke, R.W. Mayer and R. Schlögl, Catal. Lett. 74 (2001) 121.
4. V.I. Bukhtiyarov, M. Hävecker, V.V. Kaichev, A. Knop-Gericke, R.W. Mayer and R. Schlögl, Phys. Rev. B 67 (2003) no.235422.
5. K. Siegbahn, C. Nordling, G. Johansson, J. Hedman, P.F. Hedén, K. Hamrin, U. Gelius, T. Bergmark, L.O. Werme, R. Manne, and Y. Baer, "ESCA applied to free molecules", North-Holland, Amsterdam, 1969.

The adsorption of NO on an oxygen pre-covered Pt(111) surface: in-situ high-resolution XPS combined with molecular beam studies

J.F. Zhu, M. Kinne, T. Fuhrmann, B. Tränkenschuh, R. Denecke and H.-P. Steinrück
 Physikalische Chemie II, Universität Erlangen-Nürnberg, Egerlandstr. 3, D-91058 Erlangen

Adsorption of NO on a Pt(111) surface pre-covered with a p(2x2) atomic oxygen layer has been studied *in-situ* by high-resolution X-ray photoelectron spectroscopy and temperature-programmed XPS using third-generation synchrotron radiation at BESSY II, Berlin, combined with molecular beam techniques [1], and *ex-situ* by low energy electron diffraction and temperature-programmed desorption. This coadsorption system is of interest because electro-

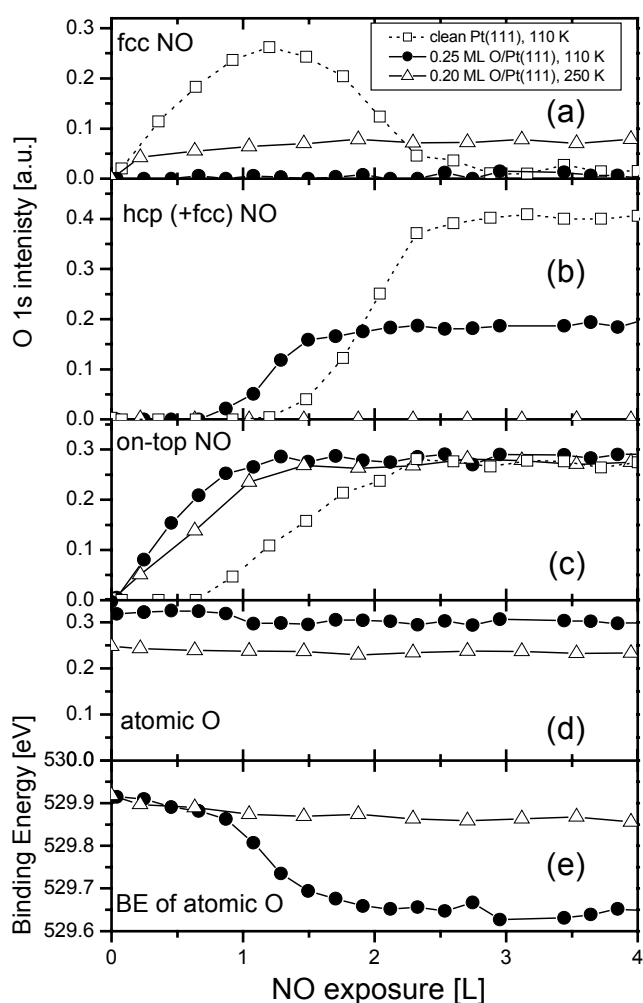


Fig. 1: Results of a quantitative analysis of O 1s spectra taken during NO adsorption on clean Pt(111) and Pt(111) precovered with 0.25 and 0.20 ML oxygen. The photon energy was 650 eV. Intensities for different species are given in (a) – (d). The O 1s binding energy of atomic oxygen as a function of NO exposure is given in (e).

negative modifiers such as O are known to greatly influence the catalytic behavior under realistic conditions [2]. O 1s XP spectra reveal that an ordered p(2x2)-O layer with an oxygen coverage of 0.25 ML dramatically changes the adsorption behavior of NO as compared to the clean surface. From a detailed quantitative analysis of the spectra by deconvolution into separate contributions, several conclusions can be drawn [3]; these are summarized in Fig. 1 for NO adsorption at 110 K together with results for clean Pt(111) [4] and for a lower O coverage at higher surface temperature. In all cases, NO is provided by the molecular beam with the nozzle at room temperature ($E_{kin}=0.09$ eV). The sample pressure corresponds to $5.3 \cdot 10^{-8}$ mbar.

The atomic oxygen in the (2x2) layer with an O 1s binding energy of $E_B = 529.9$ eV occupies fcc hollow sites, and therefore blocks NO adsorption on these sites (see solid circles in Fig. 1a), which are energetically preferred on clean Pt(111), with $E_B = 530.3$ eV. As a consequence, NO populates on-top sites ($E_B=532.0$ eV) at low coverages (Fig. 1c). At 110 K, NO can additionally adsorb on hcp hollow sites ($E_B = 530.6$ eV), thereby inducing a shift of the O

1s binding energy of atomic oxygen towards lower energies by about 0.25 eV (Fig. 1e). The bond strength of the hcp hollow NO species to the substrate is weakened by the presence of atomic oxygen, as is deduced from a shift in desorption temperature of this state from about 190 K for pure NO adsorption to about 140 K on p(2x2)-O/Pt(111) [3]. A sharp p(2x2) LEED pattern is observed for NO adsorption on the oxygen pre-covered surface, up to saturation coverage. Upon heating the surface, the uptake curve shown in of Fig. 1 is reversed, including the binding energy shift of the atomic oxygen upon desorption of NO from hcp sites.

Using a slightly smaller amount of 0.20 ML oxygen at a higher surface temperature of 250 K has some influence on two aspects of the NO adsorption. Firstly, not all fcc sites are blocked for NO adsorption, giving rise to the small intensity in Fig. 1a (open triangles). Secondly, at 250 K no hcp sites are occupied, as this temperature is above the desorption temperature of NO from these sites. As a consequence, the O 1s binding energy of atomic oxygen does not change in this case (see Fig. 1e).

The total NO coverage is calibrated using the O 1s intensities of the c(4 x 2)-CO/Pt(111) structure with a coverage of 0.5 ML. As a result, the total saturation coverage of NO on Pt(111) pre-covered with varying amounts of oxygen (below 0.25 ML) is found to decrease linearly with increasing oxygen precoverage. Inspecting the initial slope of the uptake curves of the total NO coverage, no influence of the presence of oxygen on the initial sticking coefficient is observed within the error bars. The adsorption behavior is found to be precursor-mediated for all oxygen precoverages, as seen by a linear coverage increase up to near saturation. Using the more accurate method of King and Wells [5] in a separate chamber, the initial sticking coefficient of NO is found to be reduced slightly from 0.96 on clean Pt(111) to 0.88 on a p(2x2) oxygen pre-covered surface.

This work is supported by DFG through Ste 620/4-2.

[1] R. Denecke, M. Kinne, C.M. Whelan, H.-P. Steinrück, *Surf. Rev. Lett.* 9 (2002) 797.

[2] W. F. Egelhoff Jr. *Fundamental Studies of Heterogeneous Catalysis* (Elsevier, Amsterdam, 1982).

[3] J.F. Zhu, M. Kinne, T. Fuhrmann, B. Tränkenschuh, R. Denecke, H.-P. Steinrück, *Surf. Sci.* 547 (2003) 410.

[4] J.F. Zhu, M. Kinne, T. Fuhrmann, R. Denecke, H.-P. Steinrück, *Surf. Sci.* 529 (2003) 384.

[5] D.A. King, M.G. Wells, *Surf. Sci.* 29 (1972) 454.

In-situ high resolution XPS studies on the adsorption behavior of CH₄ on Pt(111) at different surface temperatures

T. Fuhrmann, M. Kinne, B. Tränkenschuh, C. Papp, J.F. Zhu, R. Denecke and H.-P. Steinrück
Physikalische Chemie II, Universität Erlangen-Nürnberg, Egerlandstr. 3, 91058 Erlangen

The adsorption behavior of impinging molecules for changing coverages is a basic step in the understanding of heterogeneous catalysis. This information can be obtained from coverage-dependent sticking coefficient measurements. In general, these measurements are integral in nature, not revealing the chemical identity of the adsorbed species on the surface. On the other hand, from investigations of the thermal reactions of adsorbates, different species are known to exist for different surface temperatures. Combining a supersonic molecular beam system, which is necessary to measure sticking coefficients, with high-resolution x-ray photoelectron spectroscopy (HR-XPS), we performed in situ experiments studying both the adsorption behavior and the chemical nature of the adsorbed species simultaneously. In the case of hydrocarbons, especially the analysis of the vibrational splitting of the XPS signals is used as a fingerprint to classify the chemical nature of the species.

The apparatus has been described elsewhere [1]. A seeded beam of 5% methane in He, originating from a nozzle heated to 1073 K was used for adsorption, impinging at normal incidence and with a kinetic energy of 0.71 eV on the Pt(111) surface. The experiments were performed at beamline U49/2-PGM1 using an excitation energy of 380 eV for C 1s spectra; at a combined resolution of 160 meV an acquisition time of 8 s/spectrum is needed. The surface temperature during adsorption was varied between 110 and 500 K.

From previous temperature-programmed XPS experiments, CH₃ is known to be the stable chemical species on the surface up to about 260 K, followed by CH in the temperature range up to 500 K [2]. Above 500 K pure carbon in various modification (i.e., different C 1s binding energies) is the stable species on the surface. Figure 1 shows a typical spectrum taken at a surface temperature of 251 K during a TPXPS experiment. Three peaks at 282.48, 282.88 and 283.28 eV are assigned to CH₃, caused by vibrational splitting of the XPS signal. At 283.64 and 284.06 eV the two peaks of CH are observed, also caused by vibrational splitting. The signal of pure carbon occurs at 283.81 eV [2].

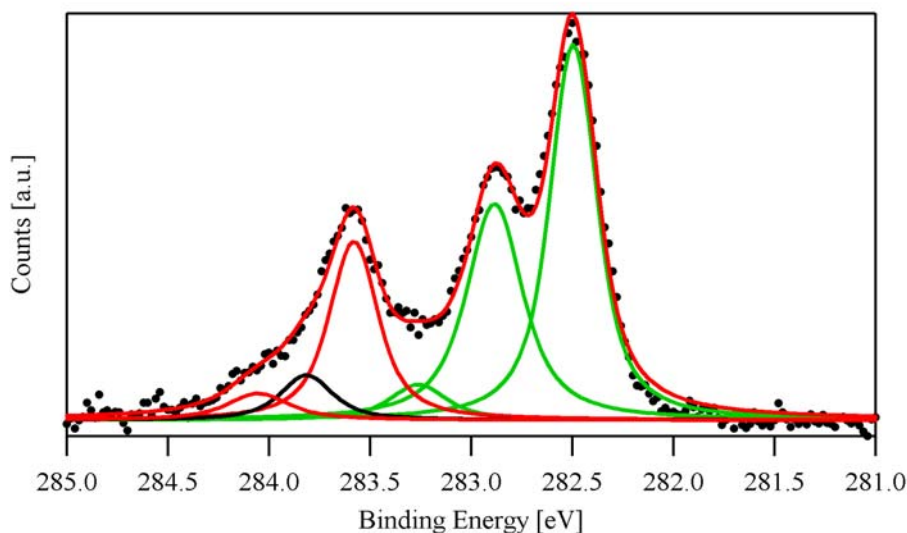


Fig. 1: C 1s spectrum annealed to 251 K, following methane adsorption with a kinetic energy of 0.71 eV at 110 K. The solid lines show results of a deconvolution procedure.

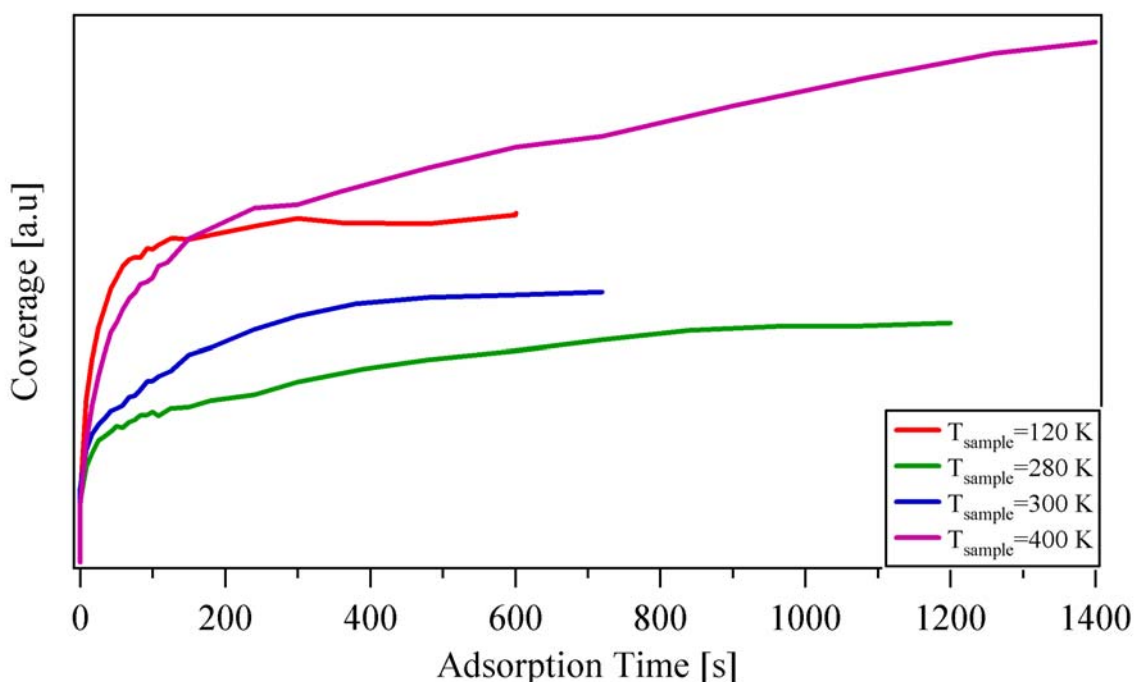


Fig. 2: Resulting total C 1s intensities for methane adsorption on Pt(111) at different surface temperatures. The kinetic energy of the impinging molecules was 0.71 eV.

Figure 2 shows the total C 1s intensity as a function of the adsorption time for different surface temperatures. As described in literature [3], the initial sticking coefficients obtained from the initial slopes of the adsorption curves, are in the same range. Comparing the coverage dependent sticking behavior, however, big differences are noticed in the measured surface temperature window. At 120 K, where CH_3 is populated, adsorption with a relatively high sticking coefficient up to nearly saturation coverage is observed. Interestingly, going to higher temperatures, the coverage dependent adsorption behavior shows a much smaller tendency to reach a saturation value, which itself seems to be smaller as for low temperature adsorption. The time to achieve saturation is largest at around 280 K, which is close to the formation temperature of CH. At 300 K where only CH is adsorbed on the surface, already a trend to slightly higher sticking coefficient and saturation coverage is observed.

Facing the situation at 400 K and above, no saturation is reached. More detailed analysis of the taken spectra shows a population of CH up to about 150 s, followed by the increase of a new species in the range of pure carbon. Interestingly, this is different to the observation by TPXPS. The carbon species shows no sign of saturation. A detailed analysis of the data is still in progress.

This work was supported by DFG (Ste620/4-2).

- [1] R. Denecke, M. Kinne, C.M. Whelan, H.-P. Steinrück, Surf. Rev. Lett. 9 (2002) 797.
- [2] T. Fuhrmann, M. Kinne, C.M. Whelan, J.F. Zhu, R. Denecke, H.-P. Steinrück, Chem. Phys. Lett. (submitted).
- [3] A.C. Luntz, Winters, H.F., J. Chem. Phys. 101 (1994) 10980.

CO adsorption and desorption processes on Pt(355) investigated by in-situ high resolution XPS

B. Tränkenschuh, T. Fuhrmann, C. Papp, J.F. Zhu, R. Denecke and H.-P. Steinrück
Physikalische Chemie II, Universität Erlangen-Nürnberg, Egerlandstr. 3, 91058 Erlangen

For many heterogeneously catalysed chemical reactions surface defects, like adatoms, steps or kinked steps play a key role. The starting point of any surface reaction is the adsorption of the reactants. In order to study the influence of steps on CO adsorption and desorption processes, we compare a stepped Pt(355) with a flat Pt(111) surface, previously studied in our group^[1]. The (355) surface contains five atom wide (111) terraces separated by monatomic (111) steps. Using high resolution x-ray photoelectron spectroscopy (HRXPS), the occupation of different adsorption sites can be quantitatively monitored in-situ during these processes^[1].

The experiments were performed at beamline U49/2 PGM1, using a transportable apparatus described elsewhere^[2]. It combines HRXPS with a supersonic molecular beam for gas dosing at varying pressures. C 1s spectra were acquired in-situ within 4 s, using synchrotron radiation of 380 eV with a resolution of 150 meV, while adsorbing CO. Subsequently heating the sample with a heating rate of 0.4 K/s during data acquisition allows to investigate the desorption process of CO up to 500 K.

Fig. 1 shows a CO uptake experiment on Pt(355) at 130 K ($p=1.3 \cdot 10^{-9}$ torr), until saturation is reached at 1.26 L. We can clearly distinguish different CO adsorption sites, both on the terraces and steps by their binding energy. The peaks at 286.1 and 286.7 eV are assigned to bridge and on-top bound species on terraces, respectively, having the same binding energy as on flat Pt(111)^[1]. The smaller peaks at 285.8 and 286.4 eV are allocated to 'bridge' and 'on-top' sites on steps, respectively^[3].

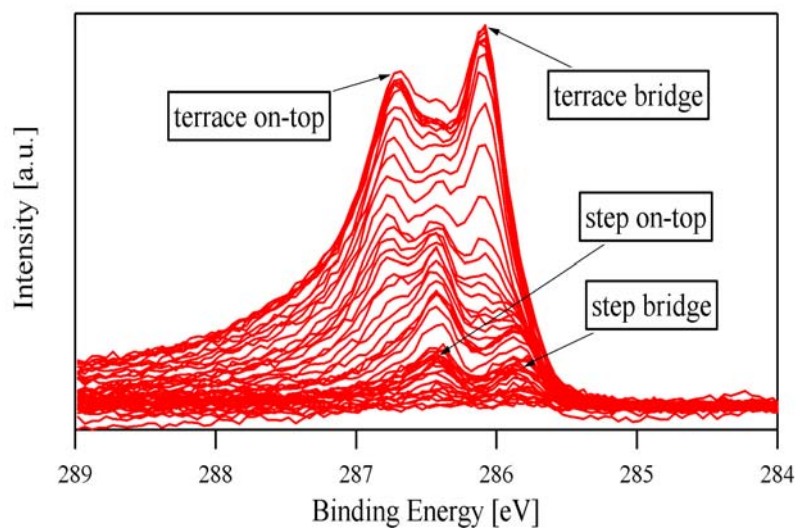


Fig. 1: C 1s spectra recorded during CO uptake on Pt(355) at $T_{\text{sample}} = 130$ K, $p = 1.3 \cdot 10^{-9}$ torr.

We also observe a slow temporal change in the CO occupation of the adsorption sites during a few months. There is a change from step 'bridge' species towards step 'on-top' species, which perhaps can be explained by a roughening of the step edges. As known in literature^[4], also for stepped Pt surfaces care has to be taken in cooling the sample at a slow rate (we used 1.7 K/s) to allow equilibrium of the step morphology.

As shown in Fig. 2 from a quantitative analysis using fixed peak shape parameters, step adsorption occurs first nearly to saturation, before terrace adsorption starts. The ratio of terrace to step coverage is about 3 : 1. In the case of the terrace adsorption the tendency that first on-top and then bridge adsorption sites are occupied is the same as for flat Pt(111). However, the details of the coverage-dependent site occupation are different, clearly showing the influence of the terrace width. In particular, no ordered adsorbate structure could be observed by LEED.

Therefore, the coverage calibration for Fig. 2 was done by comparing the peak areas of the C 1s spectra of CO on the stepped crystal with those on the flat Pt(111) surface. The resulting saturation coverage, being now lower for the stepped surface than for Pt(111) with 0.5 ML, has to be considered being preliminary.

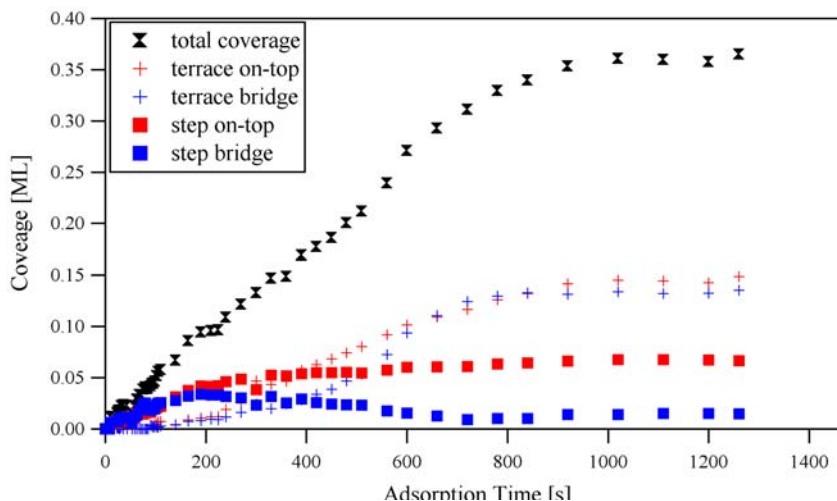


Fig. 2: Quantitative fitting results of the data shown in Fig. 1 for CO uptake on Pt(355) at 125 K.

The thermal evolution of the adsorbed CO was studied by temperature-programmed C 1s XPS experiments. Here one can see that CO desorption on the terraces starts at 350 K whereas the CO on the steps desorbs between 400 and 490 K.

Conclusions

In high resolution XPS experiments on the stepped Pt(355) surface, different adsorption sites are observed for CO on both terraces and steps. As one would expect, due to the lower coordination of step atoms, CO first adsorbs on these sites. However, also the site occupation on the (111) terraces is changed relative to the Pt(111) surface. From the quantitative analysis of the XPS data the adsorption and desorption kinetics for the various sites are studied in detail.

This work was supported by DFG (STE 620/4-2).

- [1] M. Kinne, T. Fuhrmann, C. M. Whelan, J. F. Zhu, J. Pantföerder, M. Probst, G. Held, R. Denecke, H.-P. Steinrück, *Journal of Chemical Physics* **2002**, 117, 23.
- [2] R. Denecke, M. Kinne, C. M. Whellan, H.-P. Steinrück, *Surface Review and Letters* **2002**, 9, 797.
- [3] J. S. Luo, R. G. Tobin, D. K. Lambert, G. B. Fisher, C. L. DiMaggio, *Surface Science* **1992**, 274, 53.
- [4] P. Gambardella, M. Blanc, H. Brune, K. Kuhnke, K. Kern, *Physical Review B* **2000**, 61, 2254.

In situ XPS investigation of VPO catalyst oxidation state at different catalytic conditions

E. Kleimenov, H. Bluhm, M. Hävecker, A. Knop-Gericke,
A. Pestryakov, D. Teschner, R. Schlögl

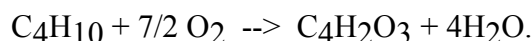
*Fritz-Haber-Institut der Max-Planck-Gesellschaft, Abteilung Anorganische Chemie,
Faradayweg 4-6, D-14195 Berlin, Germany.*

J. A. Lopez-Sanchez, J. K. Bartley, G. J. Hutchings

Cardiff University, Department of Chemistry, P.O. Box 912, Cardiff, UK CF10 3TB

Introduction

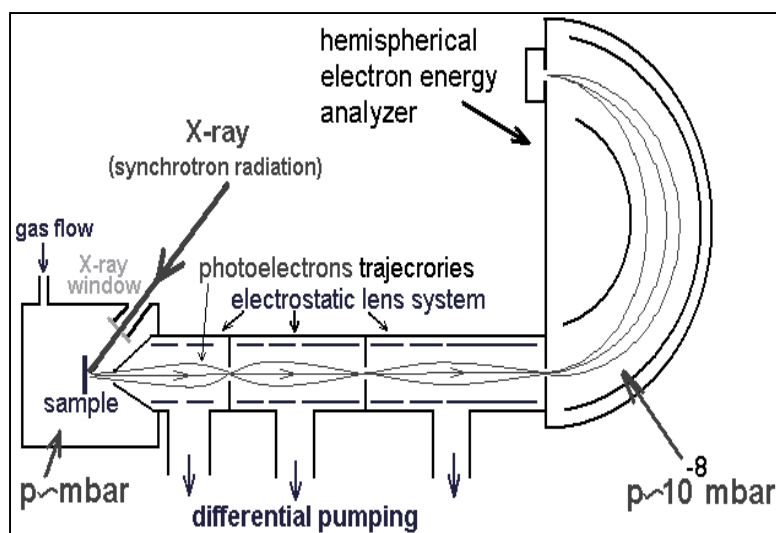
Vanadium phosphorous oxides (VPO) are well known as industrial catalysts for the selective oxidation of n-butane to maleic anhydride in the reaction



The usual industrial conditions for this reaction are $p=1$ atm and $T=375\text{--}480$ °C. Numerous studies of the catalyst were performed in order to reveal the structural properties (i.e., the active sites) that are responsible for the formation of maleic anhydride. The nature of the active sites is, however, still under discussion [1].

X-ray photoelectron spectroscopy (XPS) is a well-established technique for the determination of the surface oxidation state. Due to the short mean free path of electrons in a

Figure 1.
In situ XPS setup.



gas phase this technique generally must operate in high vacuum and cannot be applied for catalyst characterization during reaction. Our novel system (Fig. 1) overcomes this limitation.

Our earlier in situ XPS experiments on VPO catalysts [2] showed changes of the V oxidation state with temperature. In the present investigation both the temperature and the gas composition were changed to investigate the oxidation state of the surface during a DuPont-

type industrial process [3]. In this process there is a spacial and temporal separation between the oxidation of the *n*-butane and the reoxidation of the catalyst surface. The data represent the first XPS study of VPO under different reaction gas mixtures.

Experiment

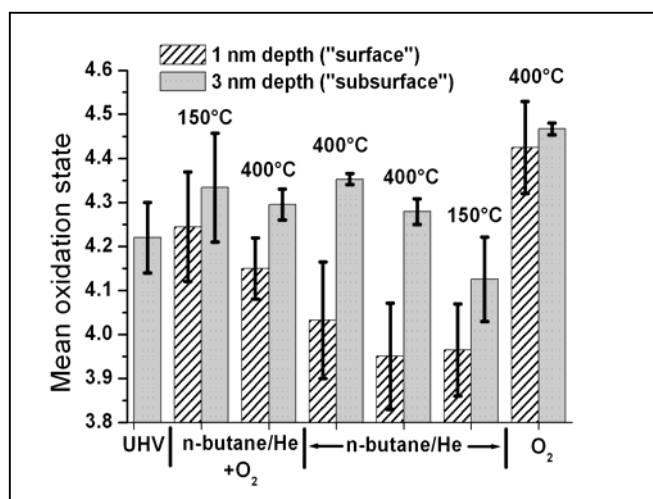
Our in situ XPS apparatus is a modified standard XPS spectrometer. The input lens of the analyzer is combined with a 3-stage differential pumping system. The pressure in the analyzer was in the 10^{-8} mbar range when the reaction cell pressure was several mbar. The reaction cell was separated from the synchrotron beamline by a 100 nm thick SiN_x window. The overall spectral resolution of the system as measured by the Ar2p_{3/2} gas phase peak was set to better than 0.2 eV. Photon energies of 720 eV and 1254 eV were used in our experiments. These energies correspond to approximately 1 nm and 3 nm information depth for the O1s/V2p spectral region (~510-535 eV binding energy). [4].

The VPO sample was prepared as described in [5] by heating the precursor (V₂O₄+H₃PO₄) at 145°C for 72 hours. Subsequently the sample was activated for 56 hours in a 1.7% *n*-butane-in-air mixture at 400°C. The catalytic characterization at standard conditions (1 bar) and structural characterization were done prior to the XPS measurements. The sample was investigated in a constant gas flow regulated by mass-flow controllers. The catalytic activity of the sample was registered by proton-transfer reaction mass spectrometry (PTRMS) that was performed simultaneously to the spectroscopic measurements. XP spectra were taken in the reaction mixture (*n*-butane/He+O₂) at 150°C and 400°C, under anaerobic conditions (*n*-butane/He) at 400°C and 150°C, and in pure O₂ at 400°C.

Results and discussion

The vanadium oxidation state was determined by a combination of two methods: by fitting the V³⁺, V⁴⁺ and V⁵⁺ components of the V2p_{3/2} peak, and by the determination of the

Figure 2.
Vanadium
oxidation state
depending on
conditions.



O1s-V2p_{3/2} first momentum difference. Both methods give systematic errors [6]. The first method has a positive systematic error because of the peak asymmetry, and the second one has a negative systematic error because of the contribution of adsorbates at the O1s region. The mathematical average between the two results was used in Fig. 2 to determine the true oxidation state, whereas the difference between them was used to determine the error bar. This error bar should not be misinterpreted as an experimental error, which is much smaller.

The oxidation state of the surface showed a dynamic response to the catalytic conditions in agreement with the data presented in Refs. 7 and 8. The maleic anhydride yield decreased with a decreasing amount of V⁵⁺ centers in the absence of gas phase oxygen. This supports the hypothesis that V⁵⁺ species participate in the *n*-butane oxidation process. The involvement of V⁵⁺ centers was also previously shown by in situ X-ray absorption studies [9]. In addition, our measurement indicate that the V⁵⁺ centers are located in the subsurface region.

References

1. J.-C. Volta, *Chemistry*, 3 (2000), pp. 717-723
2. E. Kleimenov, I. Ayub, H. Bluhm, M. Hävecker, K. Ihmann, A. Knop-Gericke, D. Teschner, R. Schlögl, BESSY annual report 2002, 232-234
3. R.M. Contractor, D.I. Garnett, H.S. Horowitz, H.E. Bergna, G.S. Patience, J.T. Schwartz, G.M. Sisler, *New developments in selective oxidation II* (1994), 233-242
4. M. P. Seah, *Surf. Interface Anal.*, 9 (1986), pp. 85-98
5. J.A.Lopez-Sanchez, L. Griesel, J. K. Bartley, R. P.K. Wells, A. Liskowski, D. Su, R. Schlögl, J.-C. Volta, G. Hutchings, *PCCP* 5 (2003), 3525-3533
6. G. W. Coulston, E. A. Thompson, N. Herron, *J.Catal.* 163 (1996), 122
7. H. Bluhm, M. Hävecker, E. Kleimenov, A. Knop-Gericke, A. Liskowski, R. Schlögl, D. S. Su, *Topics in Catalysis*, 23 (2003), pp. 99-107
8. M. Hävecker, R. W. Mayer, A. Knop-Gericke, H. Bluhm, E. Kleimenov, A. Liskowski, D. Su, R. Follath, F. G. Requejo, D. F. Ogletree, M. Salemon, J. A. Lopez-Sanchez, J. K. Bartley, G. J. Hutchings, R. Schlögl, *J. Phys. Chem. B*, 107 (2003), pp. 4587-4596
9. G. W. Coulston, S. R. Bare, H. Kung, K. Birkeland, G. K. Bethke, R. Harlow, N. Herron, P. L. Lee, *Science*, 275 (1997), pp 191-193

***In situ* X-ray photoelectron spectroscopy of ammonia oxidation on Pt(533)**

S. Günther, A. Scheibe, D. Albrecht, R. Imbihl

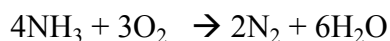
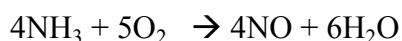
Institut für Physikalische Chemie, Universität Hannover, Callinstr. 3-3a, D-30167 Hannover

H. Bluhm, M. Hävecker, A. Knop-Gericke, E. Kleimenov

Fritz-Haber-Institut der Max-Planck-Gesellschaft, Faradayweg 4-6, D-14195 Berlin, Germany

Introduction

We have used *in situ* X-ray photoelectron spectroscopy (XPS) to investigate the catalytic oxidation of ammonia with oxygen on a Pt(533) surface. The high temperature oxidation of ammonia with oxygen to NO on platinum in the so-called Ostwaldt process is one of the most important industrial chemical reactions. At low temperature ($T < 800$ K) mainly N_2 and to a smaller degree also N_2O are obtained:



In a LEED/STM study it was shown that the Pt(533) surface (4(111)x(100) in Somorjai notation) undergoes restructuring under reaction conditions leading to a doubling of the step height of the (100) steps and to a doubling of the width of the (111) terrace units [1]. The restructuring was associated with a change in selectivity from preferential N_2 on the original surface to dominant NO production on the restructured surface. Our goal was to identify the reacting surface species over a broad pressure range and to determine whether the prevailing species change as a consequence of the pressure change and as a consequence of reaction-induced surface restructuring.

Experimental

The maximum pressure used during the experiments was ~ 1 mbar. X-rays are admitted to the experimental cell through a 100 nm thick SiN_x window. The photoelectrons emitted from the sample or the gas phase enter a differentially pumped electrostatic lens system through a 1 mm diameter aperture. They pass two additional apertures before being focused into the focal plane of a standard electron energy analyzer. The N 1s and the O 1s spectra shown in this report were obtained by using photons of 690 and 830 eV, respectively. The experiments were performed at the undulator beam line U49/2-PGM1.

Results:

During adsorption of NH_3 at least three different components in the N 1s spectra were detectable. These species are present on the Pt(533) in the low temperature regime ($T < 250 \text{ C}$) of ammonia oxidation in the 10^{-4} and 10^{-1} mbar range.

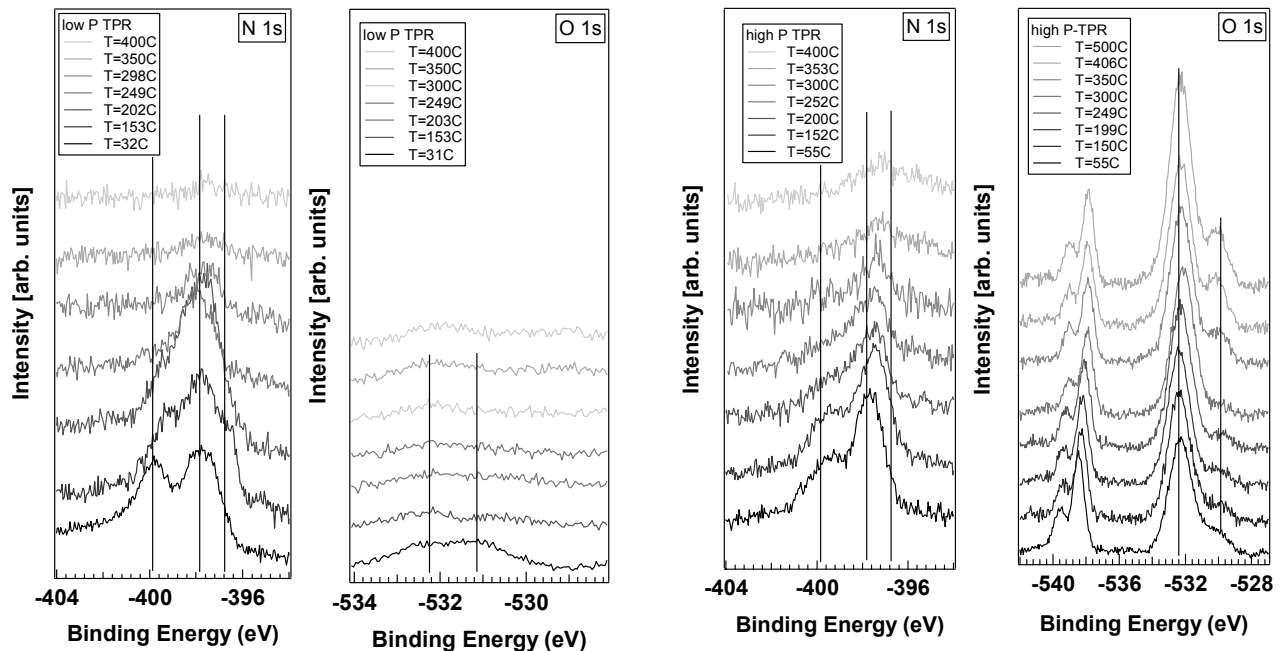


Fig. 1: In situ O 1s and N 1s spectra obtained during the catalytic ammonia oxidation at various temperatures. Low pressure experiment $P(\text{O}_2) = 3 \times 10^{-4}$ and $P(\text{NH}_3) = 1 \times 10^{-4}$ mbar, high pressure experiment $P(\text{O}_2) = 5.75 \times 10^{-1}$ and $P(\text{NH}_3) = 0.65 \times 10^{-1}$ mbar

Figure 1 shows the N 1s and O 1s spectra obtained from the Pt(533) sample (and the gas phase) *in situ* during the reaction. Clearly the N 1s species present on the sample during the reaction are very similar in the two pressure ranges.. The oxygen species present on Pt(533) in the low and in the high pressure experiment vary substantially. The main reason for this difference is that the surface is partially contaminated by carbon during the reaction in the low pressure regime. As a consequence oxygen is immediately reacted off from the surface.

Besides the O 1s peak obtained from molecular oxygen of the gas phase (between 538 and 540 eV) several adsorbed oxygen species are well visible in Fig. 1. At high pressure a new oxygen species at 532.2 eV is visible beside the known species at 529.7 eV of atomic adsorbed oxygen. Note that atomic oxygen is present on the surface at low temperature, then nearly no intensity is found in an intermediate temperature interval from 200 °C to 300 °C and a substantial amount of oxygen is again present at high temperatures above 350 C. This T-dependent behavior of the oxygen coverage as well as the of nitrogen containing adsorbates

could be reproduced in a realistic mathematical model simulating ammonia oxidation with mean field differential equations. One key input for the model is the fact that adsorbed NO already decomposes on Pt(533) above 70 °C.

The new oxygen component at 532.2 eV accumulated during the $\text{NH}_3 + \text{O}_2$ reaction in the high pressure experiment turned out to be highly stable because it could not be removed by NH_3 reduction at 500 °C and 1 mbar. This species is also built up during low pressure reaction conditions but only to a modest amount when repeating several temperature programmed reaction cycles.

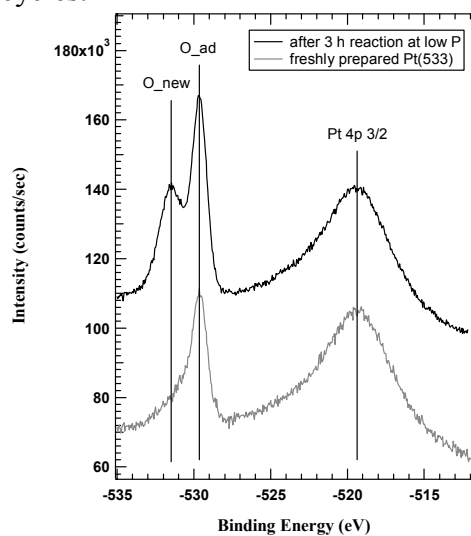


Fig. 2
O 1s and Pt 4p_{3/2} spectra of a freshly prepared Pt(533)-surface and the surface after 3 hours reaction in ammonia and oxygen.

Fig. 2 shows the O 1s spectrum from a freshly prepared Pt(533) surface and a surface which has been temperature cycled (3 ramps from 30 °C to 550 °C and back) in $p(\text{O}_2) = 1 \times 10^{-3}$ and $p(\text{NH}_3) = 1 \times 10^{-4}$ mbar for 3 hours. The accumulation of oxygen is clearly visible. The total oxygen coverage of this particular experiment is still below one monolayer assuming a saturation coverage of 0.25 ML for adsorbed oxygen on Pt(111). Although it is known that high oxygen coverages on Pt(111) are possible if other O-sources than O_2 adsorption are applied [2], to our knowledge the observed component is not reported in the literature. It should be noted that this species developed exclusively during the ammonia oxidation experiments. The identification of the new oxygen species at 532.2 eV and the clarification whether this species is a signature of the pressure gap will be the aim of future experiments.

Acknowledgements

The BESSY staff is acknowledged for its continuing support of our experiments.

References

- [1] A. Scheibe, S. Günther and R. Imbihl, Catal. Lett. **86**, 33 (2003).
- [2] N. A. Saliba, Y. L. Tsai, C. Panja, B. E. Koel, Surf. Sci. **419** (1999) 79-88.

Maleic Anhydride on ZnO

St. Gil Girol, Th. Strunskus and Ch. Wöll

Lehrstuhl für Physikalische Chemie I, Ruhr-Universität Bochum, D-44801 Bochum

(gil@pc.rub.de, <http://www.pc.rub.de>)

Maleic anhydride ($C_4H_2O_3$, “MA”, displayed in fig. 1) is an important starting material for the industrial production of 1,4-butanediol (BDO), which gives rise to engineering materials like polyurethanes and polybutylene terephthalates. The production of BDO is performed by catalytic hydrogenation of MA over Cu/ZnO catalysts [1]. Despite the fact that Cu/ZnO catalysts have been used in this process for more than a decade a detailed picture of the role of zinc oxide in the catalyst mixture has not emerged yet.

To shed light on the interaction between MA and pure ZnO, the behaviour of MA was investigated on ZnO single crystal surfaces, namely on the polar Zn-terminated ZnO(0001), the polar O-terminated ZnO(000 $\bar{1}$), and the non-polar ZnO(10 $\bar{1}$ 0) surface [2]. Using X-ray photoelectron spectroscopy (XPS), on all surfaces a temperature induced fragmentation of MA was observed at temperatures around 200 K, leading to coexistence of MA-fragments and intact MA-molecules at this temperature. The according XP spectra of the C1s and O1s regions, measured on the O-terminated sample, are shown in fig.1 and fig. 2, respectively. The stoichiometry changes caused by heating the sample from 165 to 220 K indicate a decarboxylation or decarbonylation of MA with subsequent desorption of CO and CO₂. This process was also confirmed by the TDS (thermal desorption spectroscopy) measurements. Between 200 K and 600 K the decomposition degree was found to further increase on all surfaces, proceeding towards total decomposition.

Above 600 K a carbonaceous, oxygen containing species was found in all cases.

To gain information about the bonding mode of the intact molecule and its fragments to the ZnO surfaces, C1s- and O1s-NEXAFS measurements were

performed, focussing on the low temperature regime, where spontaneous fragmentation was observed.

The NEXAFS spectra were recorded at the beamline HE-SGM in the partial electron yield mode using a channel plate detector. The base pressure of the system was below $5 \cdot 10^{-10}$ mbar. The evaluation of the adsorbate spectra included normalisation in the low energy regime prior to subtraction of the spectra obtained for the clean substrate. After subtraction the high energy regime of the resulting adsorbate spectra were normalised to one.

The π^* -NEXAFS resonances are assigned π_n^* (atomic species), which labels transitions from the involved atomic species into the molecular orbital n, with n=1 being the lowest unoccupied molecular orbital (LUMO) and n=2, 3,... being the subsequent unoccupied MOs.

In the following, the results obtained on the

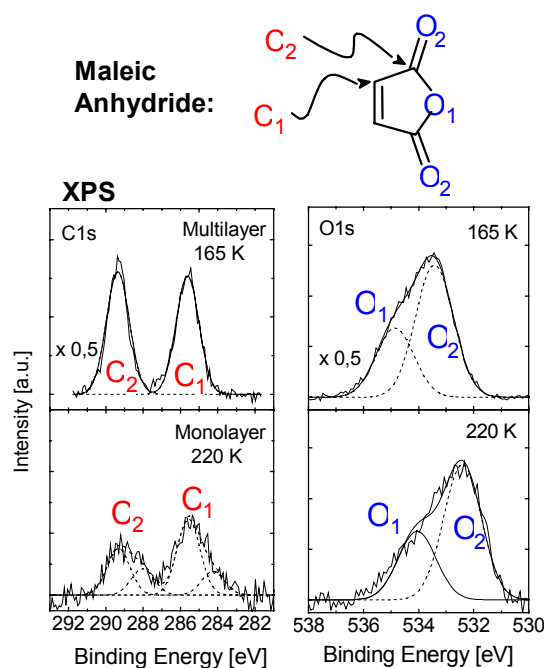


Fig. 1: XP spectra of MA recorded on the O-terminated ZnO surface. Spectra of the multilayer (intact MA) and the partially decomposed monolayer are shown.

O-terminated ZnO crystal will be discussed. The assignment of the resonances was carried out in accordance with the work of Lopez et al. [3] and is summarized in table 1.

In fig. 1 the C1s-NEXAFS spectra of a multilayer and a monolayer, both prepared at 165 K in separate experiments, as well as the spectrum of the monolayer tempered to 230 K are displayed. In agreement with the XPS data, NEXAFS shows that in both cases intact molecules are present on the surface. The π^* -resonance at 284.0 eV (" $\pi^*_1(C_1)$ "), which can be attributed to transitions from the olefinic C1s level to the LUMO, is present in the monolayer, indicating conservation of the olefin bond. Thus, significant interactions between the double bond and the surface, for example formation of a di- σ -bond, can be ruled out. The evaluation of the O1s-NEXAFS spectra was complicated by the O1s-contributions of the substrate spectra, leading to the intense resonance at 537.5 eV. However, in accordance with the spectra of Lopez et al. [3] three π^* -resonances can be identified for the multilayer as well as for the monolayer spectra at 165 K at 531.0, 534.7 and

535.6 eV, respectively, originating from transitions from the carbonyl O1s level. Comparing the MA-related π^* -resonances in the multilayer and monolayer spectra no additional features can be seen.

While in the case of the multilayer spectra no dichroism can be observed, resonances of the monolayer spectra at 165 K show an angular dependence indicating that the molecular plane of the molecules is slightly tilt towards the surface.

In the NEXAFS spectra taken at 230 K characteristic changes are observed. As is evident from the XPS results, at 230 K only a fraction of the monolayer is decomposed so that the NEXAFS spectra also show a superposition of both intact MA and the decomposed (decarboxylated) species.

The C1s spectra reveal decreased intensities of the carbonyl-related resonances, which is in accordance with the decarboxylation reaction. Also the $\pi^*_1(C_1)$ resonance decreases in intensity (while XPS still proves the presence of the related C atoms), pointing towards rehybridisation of the olefin bond. A weak new feature appears at 286.5 eV (see arrow in fig. 2).

Previous measurements of MA had been

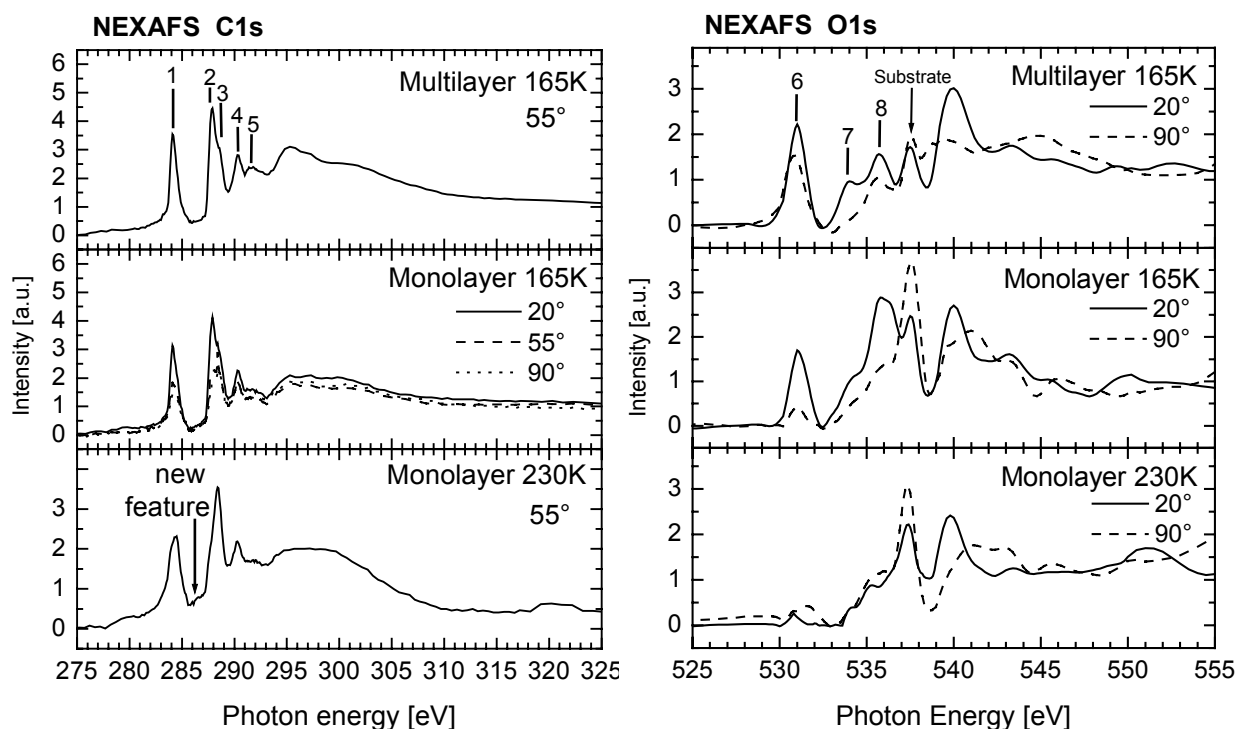


Fig. 2: C1s- and O1s-NEXAFS spectra of MA recorded on the O-terminated ZnO(000 $\bar{1}$) surface. Spectra of the multilayer and the monolayer, prepared at 165 K and spectra of the decomposed monolayer, prepared by heating the sample to 230 K, are shown, respectively.

Edge	Resonance	Transition	Photon energy [eV]
C1s	1	$\pi_1^*(C_1)$	284.0
	2	$\pi_1^*(C_2)$ $\pi_2^*(C_1)$	287.9
	3	$\pi_3^*(C_1)$	288.6
	4	$\pi_2^*(C_2)$	290.2
	5	$\pi_3^*(C_2)$	291.8
O1s	6	$\pi_1^*(O_2)$	531.0
	7	$\pi_2^*(O_2)$	534.0
	8	$\pi_3^*(O_2)$	535.8

Table 1: Assignment of the NEXAFS-resonances [3].

carried out on a more defective O-terminated ZnO crystal. Here, XPS revealed a clearly higher decomposition degree than observed for the sample discussed above. The related C1s-NEXAFS spectrum of the monolayer at 230 K is shown in fig. 3. Compared to the monolayer on the crystal described above, the decrease of the $\pi_1^*(C_1)$ -resonance as well as the intensity of the new resonance at 286.5 eV are clearly more pronounced. This can be explained with the higher decomposition degree. Thus, the rehybridisation of the olefin bond and the formation of the new feature can be regarded as being characteristic for the MA fragments formed on the surface. No angular dependence was found for the monolayer at 230 K.

The most noticeable change in the O1s-NEXAFS spectrum measured at 230 K is the nearly complete absence of the $\pi_1^*(O_2)$ resonance, which demonstrates the absence of carbonyl groups. From XPS it is evident that the adsorbed layer still contains CO groups, so that a rehybridisation to σ -bonded C-O groups has to be assumed. This

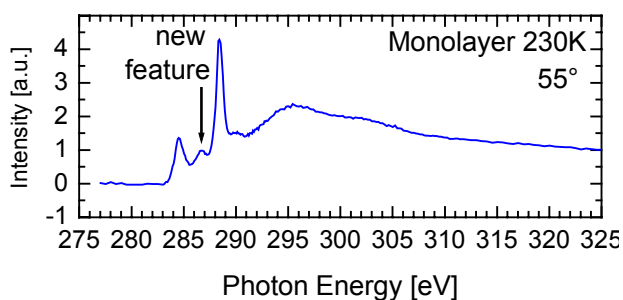


Fig. 0: C1s-NEXAFS spectrum of MA recorded on a defect-rich O-terminated ZnO surface.

does not only apply for MA fragments (which represent only a small fraction of the adsorption layer in this temperature regime) but also for the non-dissociated molecules. The change of the bonding state of the CO group indicates that the oxygen-containing part of the MA molecule preferentially interacts with the surface. Hence, a ring-opening can be assumed to be the first reaction step of the fragmentation. Saturation of cleaved bonds can either occur by bonding to the surface or by uptake of protons. It is likely that protons are available on the surfaces due to the characteristic property of ZnO to form hydroxyl groups even under UHV conditions [4-6]. Also the adsorbed MA species can act as a source of hydrogen if a surface promoted deprotonation [7] takes place.

Regarding the role of ZnO in Cu/ZnO catalysts, changes of the chemical state of the ZnO surfaces can also affect the chemical properties of the copper particles which are in contact with the ZnO phase. Also the wetting properties and hence the morphology of a catalyst might be changed due to the modification of the ZnO surface [8].

This work was supported by the DFG through SFB 558, A5.

- [1] U. Herrmann and G. Emig, *Ind. Eng. Chem. Res.* **36** (1997) 2885.
- [2] S. Gil Girol, Th. Strunskus, Ch. Wöll and M. Muhler, *in preparation*.
- [3] Lopez, T. Bitzer, T. Heller and N.V. Richardson, *Surf. Sci.* **477** (2001) 219.
- [4] M. Kunat, S. Gil Girol, T. Becker, U. Burghaus and C. Wöll, *Phys. Rev. B* **66** (2002).
- [5] V. Stämmler, K. Fink, B. Meyer, D. Marx, M. Kunat, U. Burghaus, S. Gil Girol and Ch. Wöll, *Phys. Rev. Lett.* **90** (2003) 106102.
- [6] M. Kunat, S. Gil Girol, U. Burghaus and Ch. Wöll, *J. Phys. Chem. B* **107** (2003) 14350.
- [7] J.M. Vohs and M.A. Barteau, *J. Phys. Chem.* **91** (1987) 4766.
- [8] N.-Y. Topsøe and H. Topsøe, *Journal of Molecular Catalysis A* **141** (1999) 95.

The Effect of Oxygen Adsorption on the chiral Pt{531} Surface

S. J. Pratt¹, L.B. Jones², G. Held¹

¹University of Cambridge, Department of Chemistry, Lensfield Rd, Cambridge, UK

²CCLRC Daresbury Laboratory, Warrington, UK

Single enantiomers of bio-relevant chiral molecules are essential in the production of most drugs; new technologies for enantioselective catalysis could therefore have a major impact on the design and production process of modern drugs. The further development of heterogeneous methods by introducing enantioselective catalyst surface geometries would, to this end, harness the distinct advantages of heterogeneous processes over the homogeneous methods predominantly in use [1]. One of the principal strategies for enantioselective heterogeneous catalysis is to use a chiral substrate to 'stereodirect' a surface reaction. Certain high Miller-index stepped-kinked surfaces of symmetric bulk crystal structures are intrinsically chiral because they have no mirror planes. There are some examples in the literature of enantioselective reactions on such surfaces of Pt and Cu [2,3,4,5]. However, it is rather difficult to discriminate between enantiomers with most conventional Surface Science techniques because they probe only scalar quantities (e.g. mass, vibrational frequency, electronic binding energy). Only crystallographic methods and polarisation-dependent optical methods are able to discriminate directly between enantiomers.

This preliminary study of the influence of oxygen adsorption on Pt{531} is part of a series, eventually aiming for the study of enantioselective reactions of chiral molecules on this surface. Pt{531} has the smallest surface unit cell of all chiral Pt surfaces for which enantioselective reactions have been reported, allowing parallel studies with LEED-IV and DFT alongside these experiments. Before enantioselective processes can be studied, however, the basic adsorption properties of this rather unusual surface must be studied. CO [6] and oxygen are the obvious adsorbates for such tests, for which a large database is available on their adsorption behaviour on low Miller index and some stepped surfaces of Pt.

The experiments were performed at the beamline UE52-PGM (CRG) at BESSY II using a Scienta 200 mm electron energy analyser with pass energies of 20 and 40 eV. For the O 1s and Pt 4f spectra shown here linearly polarised light was used with photon energies of 162eV (1st harmonic) and 700eV (3rd harmonic), respectively, and a spot size at the sample of about 100 μ x 200 μ . The photoelectrons were detected normal to the surface. All data were recorded at room temperature. The binding energies of all spectra were calibrated with corresponding measurements at the Fermi energy for the same photon energy and pass energy. The intensities were normalized with respect to the background at the low binding energy (BE) side of each spectrum. The base pressure of the uhv system was 2x10⁻¹⁰ mbar. Oxygen and CO were dosed by backfilling the chamber.

A typical cleaning procedure for low Miller index Pt surfaces involves annealing the sample at temperatures of around 900K in an oxygen atmosphere of 10⁻⁷ mbar. This removes carbon from the surface by forming gaseous CO or CO₂. The remaining layer of chemisorbed oxygen can be removed completely from the low index surfaces by flashing to 1100K. If the same procedure is applied to Pt{531} only part of the oxygen desorbs from the surface. Figure 1 shows the O 1s spectrum after a typical oxygen treatment (15 min at 900K in 2x 10⁻⁷ mbar oxygen) before and after annealing to 1100K (spectra 1 and 2). Before the annealing step the spectrum consists of two peaks around BE 529.6 eV (OC1) and 530.8 eV (OC2), respectively. After annealing, these two peaks have disappeared and a new intense peak is observed at a higher BE of 532.3 eV (OS). This peak persists even after annealing to 1200K, which is the highest temperature reached in the experiment. It was also found that the intensity of this peak can vary significantly when the sample is moved with respect to the X-ray beam. Molecular adsorbates (e.g. H₂O, CO from residual gas) can be excluded as the origin of this second XPS peak because the annealing temperature is well above their desorption temperatures. The high BE of 532.3 eV also excludes chemisorbed oxygen on the surface or surface oxides, for which the reported BE's are always around 530 (\pm 1) eV [7]. An extra O1s peak at similar BE's is found, however, for oxygen adsorbed on stepped surfaces of Rh [8.]. On rhodium the corresponding oxygen species is also stable up to much higher temperatures than those needed to remove chemisorbed

oxygen from the surface. On Rh the OS species can eventually be removed by annealing to temperatures above 1400K.

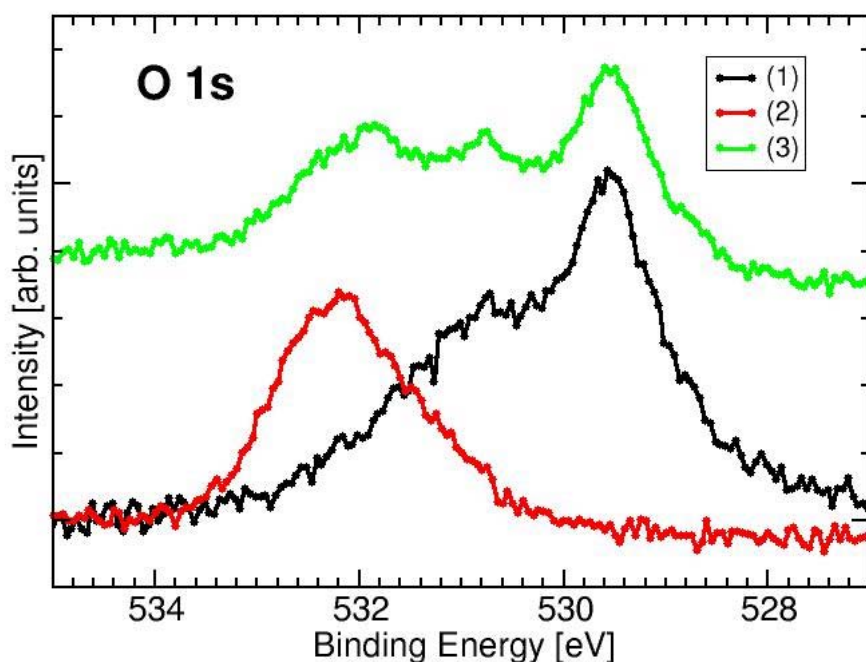


Figure 1: *O 1s* spectra after oxygen treatment of the Pt{531} surface (1), annealing to 1100K (2) and oxygen adsorption at room temperature onto the same surface ($h\nu = 700$ eV, normal emission).

When oxygen was adsorbed at room temperature onto the Pt{531} surface, for which the OS peak in spectrum 2 (Fig.1) was observed, the peaks OC1 and OC2 reappear (spectrum 3 in Fig. 1). In addition, the energy of the OS peak is shifted by 0.4 eV and its intensity is reduced by about a factor of 2. Our experiments also show that it is possible to adsorb similar amounts of CO on both the clean surface and the surface for which the OS peak is observed. From this we conclude that the corresponding oxygen species must reside underneath the topmost Pt layer ('subsurface oxygen').

This interpretation is corroborated by the shape of the Pt $4f_{7/2}$ line. On the low BE side of the bulk signal centred around 71.0 eV there is additional intensity which we assign to a surface core level shift (SCLS) of the low coordinated Pt atoms. This SCLS is seen for the clean surface (black spectrum in Fig. 2) and for the surface with subsurface oxygen (red spectrum). A layer of chemisorbed oxygen adsorbed at room temperature, however, causes the SCLS to disappear (green spectrum). In the green spectrum of Figure 2 there is an extra peak at 71.6 eV due to subsurface oxygen, which causes significant broadening of the Pt $4f_{7/2}$ line with respect to the clean surface.

As mentioned above, the intensity of the OS peak varies across the surface and can be significantly higher than the intensities of the OC peaks or the O1s signal of a saturated CO layer on this surface. Therefore it seems likely that the subsurface oxygen atoms contributing to this peak are distributed over several layers. One way of removing subsurface oxygen from Pt{531} is by dosing CO at room temperature followed by annealing to 600K. CO readily reacts with subsurface oxygen to form CO_2 , which then desorbs from the surface. After 2 such cycles most of the OS peak has disappeared. This indicates that diffusion from the subsurface oxygen sites to the surface sites, where CO resides, has a rather low barrier.

The chemical nature of the subsurface oxygen species is rather unclear at the moment. It was mentioned already that the O 1s binding energy does not match the energies usually found for chemisorbed oxygen or oxides. If a surface oxide were formed, one would also expect significant

shifts in the 4f levels of the Pt atoms involved. Shifts of 3eV and 4eV are reported for PtO and PtO₂, respectively [7]. Compared to these values, the effect of subsurface oxygen on the Pt4f spectrum is very small. The extra peak shifted by 0.6 eV with respect to the bulk peak is comparable to peak shifts due to CO adsorption [9]. The large shift in the O1s signal between chemisorbed ('ad-surface') oxygen and subsurface oxygen, on the other hand, points towards a rather large change of the electronic environment of the oxygen atoms. It remains an open question why this has so little effect on the XPS signal from the surface Pt atoms. A DFT study is currently carried out in our group trying to explain these findings.

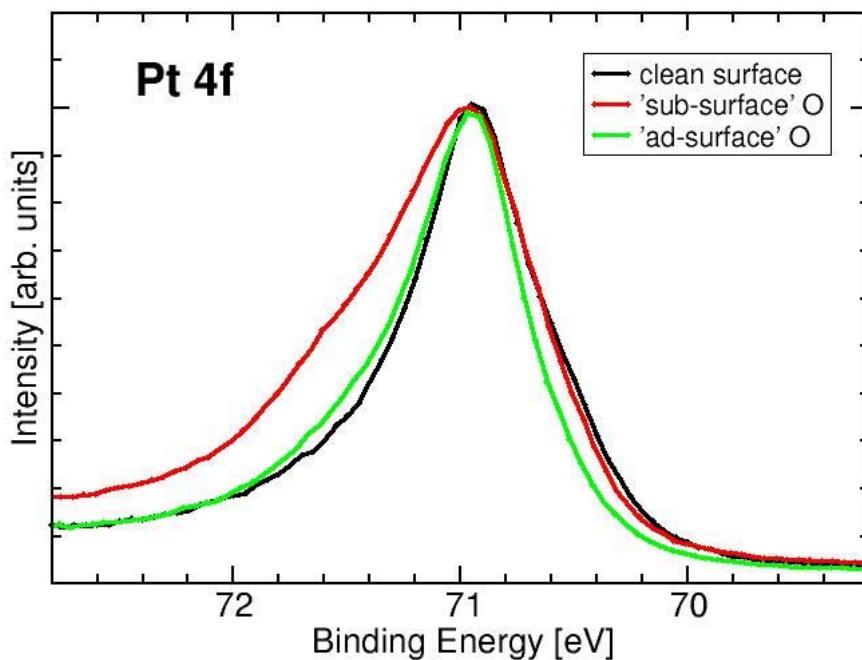


Figure 2: Pt 4f_{7/2} peak for the clean Pt{531} surface, subsurface oxygen and a chemisorbed layer of oxygen adsorbed on the clean surface ($h\nu = 162$ eV, normal emission).

This study was supported by the European Commission under the “Human Potential Programme, Transnational Access to Major Research Infrastructures”, Contract No HPRI-1999-00028 and by EPSRC. We also gratefully acknowledge many helpful discussions with Prof. Sir D. King and Dr S.J. Jenkins.

References:

- [1] R. Raval, CATTECH (2001) 5 12.
- [2] G. A. Attard, et al., J. Phys. Chem. B (1999) 103 1381
- [3] A. Ahmadi, G. A. Attard, J. Feliu and A. Rodes, Langmuir (1999) 15 2420
- [4] G. A. Attard, J. Phys. Chem. B (2001) 105 3158.
- [5] J. D. Horvath and A. J. Gellman, J. Am. Chem. Soc. (2001) 123 7953.
- [6] S.J. Pratt, E.A. Hawkins, G. Held, BESSY Annual Report 2002, 226
- [7] D. Briggs, M.P. Seah, „Practical Surface Analysis“, Wiley, 1990.
- [8] J.N. Andersen, priv. communication.
- [9] M. Kinne, et al., J. Chem. Phys. 117 (2002) 10852

In situ TEY cell for XAS measurements at the BAMline

L. Wilde^a, J. Radnik^a, M. Schneider^a, D. Herein^a, H. Riesemeier^b and M. Radtke^b

^a Institut für Angewandte Chemie Berlin-Adlershof, Richard-Willstätter-Str. 12, 12489 Berlin

^b Bundesanstalt für Materialforschung und –prüfung, Unter den Eichen 87, 12205 Berlin

Introduction

The BAM and the ACA jointly operate an EXAFS experiment at the BAMline for characterisation of catalysts, especially under working conditions. For the investigations of catalysts which have a relatively high concentration of the absorber atoms or have an inhomogeneous phase distribution, the TEY detection mode is probably most suited for XAS measurements, because of its relative insensitivity to XAFS amplitude reductions, compared to fluorescence detection [1]. Therefore, a TEY cell was developed, that can operate under a chosen atmosphere up to a temperature of 600 °C. The suitability of the cell for EXAFS analysis was checked at a copper foil. With the reduction of an oxidised copper sheet in the temperature range between 220°C and 330°C, it could also be demonstrated, that the cell works well under in-situ conditions.

Experimental

The cell, which is based on a KF element (see Fig. 1) has a modular design, that allows an easy handling. The synchrotron radiation hits the sample under an incidence angle of about 2°. The emitted electrons are then collected by a collector which is biased with >40V. The step height of the absorption edge was found to be independent on potential from voltages higher than 40V. The sample holder is connected to ground potential. Into the sample holder a high performance heating cartridge and a Pt100 thermoelement are integrated. The sample holder is integrated into a ground plate (but electrically isolated from it) which also contains the feedthroughs for the heating cartridge and the thermoelement. Gaseous educts/products can enter/leave the cell through a gas inlet/outlet.



Fig 1 TEY cell for in-situ XAS investigations (left), sample holder (right)

The absorption spectra were taken at the Cu-K edge ($E_K=8.9805\text{keV}$). For the in-situ measurements a gas stream of 10ml/min H_2 in 90 ml/min He was applied and strictly controlled by mass flow controllers. XANES spectra were taken every 10°C within the temperature range mentioned above. For the analysis of the EXAFS the Feff 7.0 code and WINXAS 2.0 were used [2, 3]. The analysis of the phase compositions during the reduction of the oxidised copper sheet the PCA and LC-XANES fit functions of WINXAS 2.0 were used.

Results

In Fig. 2 the normalised absorption spectra of a copper foil is shown. It shows of good signal/noise ratio up to an energy of 9.6keV (corresponding to $k=12.7\text{\AA}^{-1}$). This was good enough to reproduce the first five shells of the well known fcc copper structure. The Fourier transformed k^3 weighted $\chi(k)$ function and the best fit are shown in the insert of Fig. 2. The parameters of the best fit are summarised in Tab. 1.

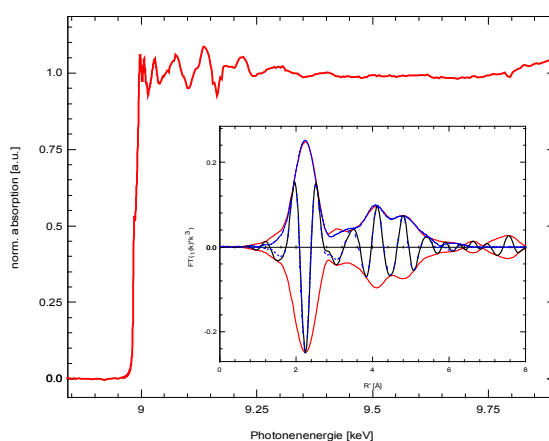


Fig. 2 TEY-EXAFS spectra of a copper foil and the corresponding analysis, for the fit the co-ordination numbers were kept fix, S_0^2 value was fixed at 0.9, all E_0 values were correlated and the length of the multiple scattering paths were correlated to those of the single scattering paths

Pair	CN	R (Å)	σ^2 (Å ²)	E_0 (eV)
Cu-Cu	12	2.540	0.0102	2.17
Cu-Cu	6	3.557	0.0181	2.17
Cu-Cu	24	4.409	0.0126	2.17
Cu-Cu	12	5.071	0.0192	2.17
Cu-Cu	24	5.713	0.0138	2.17

Tab. 1 Parameters of the best fit of the measurement to the Cu fcc structure

In order to demonstrate that the cell can be operated under in-situ conditions, a simple reaction (the reduction of an oxidised copper sheet) was performed. Depending on the reaction temperature the phase composition was determined. Therefore measurements of reference spectra (Cu, Cu_2O , CuO) have to be done. The initial state was found to be solely CuO . The evolution of the XANES spectra is shown in Fig. 3a. The PCA analysis of these spectra pointed to the presence of only two phases during the

reduction. These two phases were identified as CuO and Cu. The relative concentration of the both phases was then calculated for each temperature by fitting a linear combination of the reference XANES spectra to the measured spectra (see Fig. 3b).

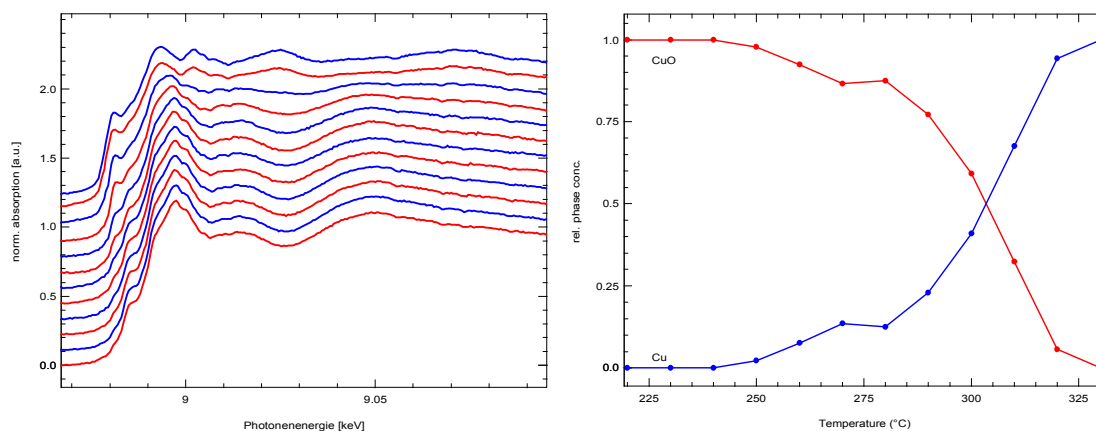


Fig. 3 XANES spectra during the reduction of CuO (a) and the subsequent phase composition (b) depending on the temperature

The reduction starts at about 260°C but a significant conversion to Cu takes place at about 300°C. At 330°C the former CuO is completely reduced to copper.

References

- [1] S.L.M. Schröder, Ph.D. Thesis, University of Cambridge 1996.
- [2] J.J. Rehr, J. Mustre de Leon, S.I. Zabinski and R.C. Albers, *J. Am. Soc.* **113** (1991) 5135.
- [3] T. Ressler, *J. Synchrotron Radiat.* **5** (1997) 118.

Acknowledgements

The authors gratefully acknowledge the financial assistance of the Senatsverwaltung für Wissenschaft, Forschung und Kultur and from the BMBF (03C3013). We thank Mr. G. Ackermann and Mr. Wilhelm for their technical support.

Light induced dry etching of cobalt with chlorine

V. Ney, N. Schwentner

Institut für Experimentalphysik, Freie Universität Berlin, Arnimallee 14, D-14195 Berlin

Light induced dry etching is a method to structure many materials, e.g. Si [1], GaAs [2] and Cu [3]. To monitor the reaction rates in situ, a new setup [4] was used at the beamline 3m-NIM-1 at BESSY II. The crystal of a quartz microbalance serves as substrate on which the material is evaporated. In the reaction cell, mass changes of the quartz, which are due to deposition of gas molecules or removal of material can therefore be observed directly. The sample is placed in the focal spot of the beamline monochromator with a 600 lines/mm grating of dispersion $d = 0.6 \text{ nm/mm}$, which is operated in a spectrograph mode without exit slit. With this setup, the light induced reaction of cobalt with chlorine was observed for the first time. Atomic force microscopy images taken after an etching experiment with a fine Ni-net as mask showed that indeed material was removed at the irradiated areas. Those measurements confirm the quartz microbalance observations which showed a mass reduction at certain wavelengths. Fig.1 displays the change of the frequency of the quartz versus time. A constant slope within a time interval corresponds to a constant reaction rate for the employed conditions. An increasing frequency represents a decreasing mass and thus a removal of material. In Fig.1 the sample was irradiated three times at a wavelength of 175 nm starting at the arrows. The beamshutter (BS) was closed for two intervals in order to separate a light induced reaction rate from a dark reaction rate. For the wavelength of 175 nm a clear rise of the slope can be observed, which implies that the reaction rate increases. The dark reaction, which can be observed as long as the beamshutter is closed, is significantly smaller than the light induced one.

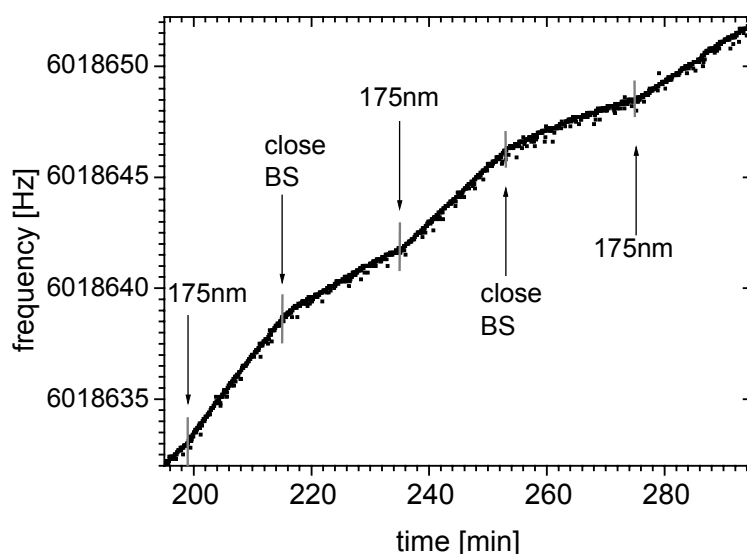


Fig. 1: Reaction rate measurements at a wavelength of 175 nm.

gas concentration:
chlorine:argon, 1:100

pressure etching cell:
0.2 mbar

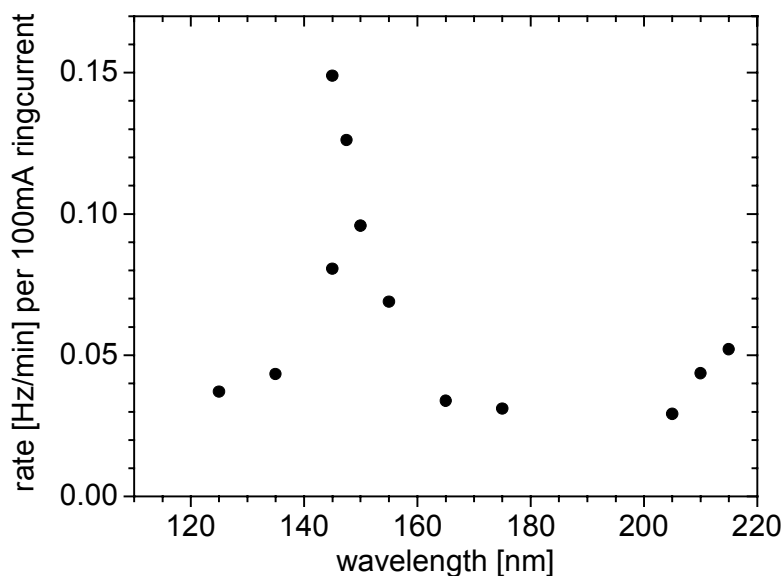


Fig. 2: wavelength dependence of the etching reaction of cobalt with chlorine

To measure a wavelength dependency of a reaction, steady conditions for several hours need to be ensured. Especially a stable irradiation of the evaporated Co spot is necessary to exclude thermal drifts and alternating surface conditions. Since grating movement of the monochromator leads to a laterally changing position of the focus, continuous measurements were difficult. Therefore point to point analysis, where the focal position could be adjusted to the sample, was performed. The experiment was carried out at a chlorine concentration of 1:100, diluted in argon, and a gas pressure of 2 mbar in the etching cell. Subtracting the dark reaction as reference yields the wavelength dependency shown in Figure 2. The normalized reaction rate per 100 mA ringcurrent is displayed for several wavelengths. A frequency change of 9 Hz corresponds to 1 nm Co. A clear maximum can be observed around 150 nm and another rise at 210 nm. At 150 nm the frequency change of 1 nm requires an irradiation time of 60 min. Taking the photon flux in the exposed area and the density of Co leads to an etching efficiency of about 0.35 Co atoms per photon.

- [1] M.V. Dobrotvorskaya, V. Stepanenko, U. Streller, H. Raaf, N. Schwentner: *Appl. Surf. Science* **136**, 331-337 (1998)
- [2] U. Streller, A. Krabbe and N. Schwentner: *Appl. Surf. Science* **106**, 341-346 (1996)
- [3] H. Raaf, N. Schwentner, *Appl. Surf. Sci.* **174**, 13 (2001)
- [4] V. Dietz and N. Schwentner, *Surf. Sci.* **528**, 215 (2003)

NEXAFS study of the interaction of glycine with ice layers

G. Tzvetkov^a, G. Koller^a, M. B. Casu^b, R. Bauchspiess^b, C. Heske^b, E. Umbach^b, M. G. Ramsey^a, F. P. Netzer^a

^a*Institut für Experimentalphysik, Karl-Franzens-Universität Graz, Universitätsplatz 5, A-8010 Graz, Austria*

^b*Experimentelle Physik II, Universität Würzburg, Am Hubland 97074, Würzburg, Germany*

Heterogeneous reactions on thin ice films are important for understanding a wide variety of phenomena. For instance, molecular adsorption on ice surfaces is of great interest in the fields of environmental chemistry and astrophysics [1]. The interaction of ice surfaces with biologically active molecules is also of importance for the development of bioengineered materials and for certain processes involved in cryo-electron microscopy [2].

This report considers the adsorption of glycine (the simplest amino acid, $\text{NH}_2\text{CH}_2\text{COOH}$) on ultrathin films of amorphous ice at 100 K, as probed by the O K-edge NEXAFS. Furthermore, to elucidate the nature of the glycine/ice interaction, the co-condensation of both molecules into mixed layers has also been examined. The ultra-thin ice films investigated in this work were prepared by condensing water onto Al_2O_3 films, epitaxially grown on NiAl(110). As shown in Ref. [3] water adsorbs non-dissociatively on the oxygen-terminated Al_2O_3 layer at 100 K.

The measurements were performed at the PM-3 bending magnet beamline. The O K-edge NEXAFS spectra were recorded in Auger yield detection mode by a spherical sector analyser (Vacuum Generators, CLAM 2). Vapour deposition of glycine was achieved from a specially designed Knudsen cell-type molecule evaporator; exposures are given in arbitrary doser units (DU). The water exposures were carried out by background dosing in the preparation chamber. A H_2O exposure of 1 Langmuir (1×10^{-6} Torr s) corresponds roughly to one nominal monolayer (ML) of water/ice.

Fig. 1 shows the evolution of the O K-edge NEXAFS spectra, recorded after exposure of a nominally ~ 50 ML thick ice film to various amounts of glycine. The spectra show the gradual suppression of the water-ice resonances and the evolution of the glycine peaks. After adsorption of 20 DU of glycine (~ 20 monolayers) the spectrum shows only the resonances characteristic for the zwitterionic form of glycine ($\text{NH}_3^+\text{CH}_2\text{COO}^-$) as judged from the comparison with the spectrum from the pure glycine multilayers (top curve). Specifically, a π^* -resonance at 532.6 eV ($\text{O } 1s \rightarrow \pi^*_{\text{COO}^-}$ transition) and shape resonances at 540 eV (σ_1) and at ~ 544 eV (σ_2) are observed. Warming up the ice/glycine layers to 200 K, where the H_2O is already desorbed, shows that water desorption does not influence the chemical state of the remaining glycine in the multilayers, i.e. there is no memory effect of the former presence of water in the spectra.

In Fig.2, bottom curve, the spectrum obtained after co-condensation of 50 L of water with 20 DU of glycine is shown. The spectrum is a superposition of the typical features of both glycine and amorphous ice. The O K-edge spectrum of the co-condensed film after heating to 200 K indicates again the presence of only zwitterionic glycine molecules in the multilayers.

The present results show that there is no detectable influence of the water-ice on the chemical state of the glycine molecules in the condensed layers. That is, there is no protonisation of the molecules and the zwitterionic state of glycine remains unaltered. Moreover, the O K-edge NEXAFS results indicate that the condensed water molecules exert no memory effect on the glycine layers after H₂O desorption.

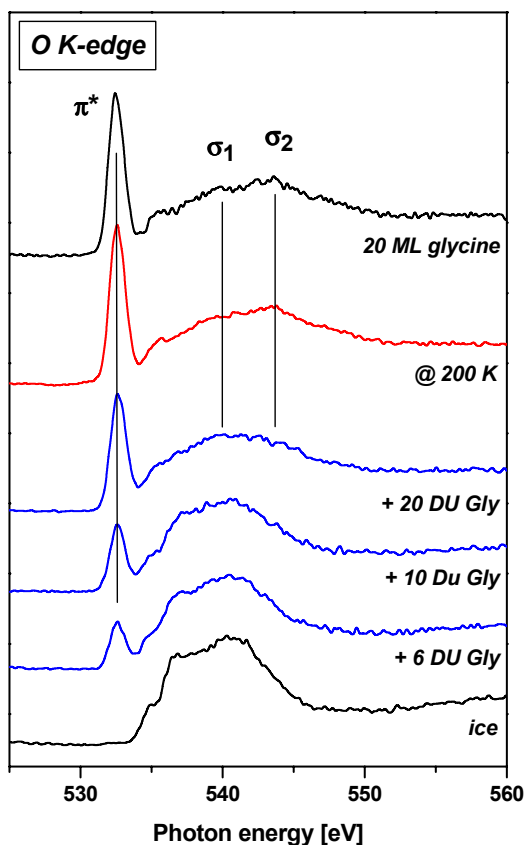


Fig. 1. Development of the NEXAFS spectrum of the water-ice film upon glycine adsorption. The spectrum of the heated to 200 K film is compared with the spectrum of the pure glycine multilayers (top curve).

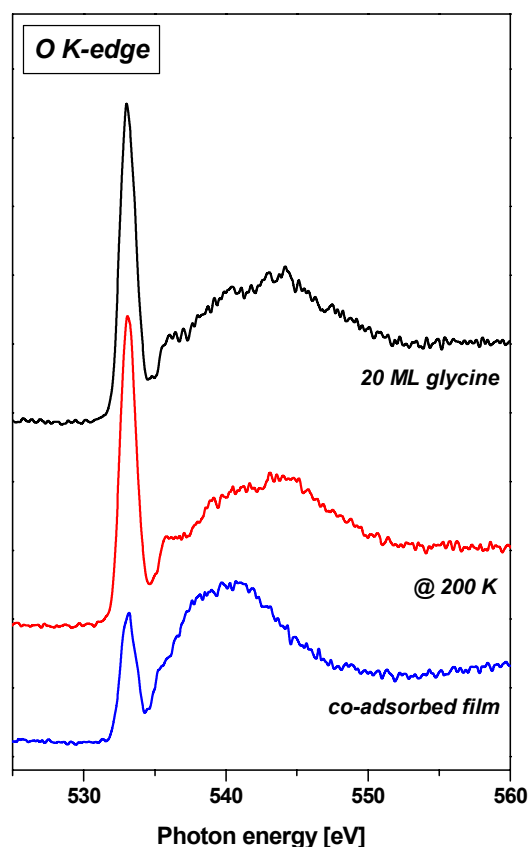


Fig. 2. NEXAFS spectrum of the co-condensed ice/glycine film (bottom curve). The spectrum of the heated to 200 K film is compared with the spectrum of the pure glycine multilayers (middle and top curves).

1. S. B. Barone, M. A. Zlondo, M. A. Tolbert, J. Phys. Chem. A 103 (1999) 9717.
2. H. G. Heide, Ultramicroscopy 14 (1984) 271.
3. G. Tzvetkov, Y. Zubavichus, G. Koller, Th. Schmidt, C. Heske, E. Umbach, M. Grunze, M. G. Ramsey, F. P. Netzer, Surf. Sci. 543 (2003) 131.

We are indebted to the BESSY staff for the support, in particular to Dr. W. Braun for his help and many discussions. This work was supported by the Austrian Science Foundation and German BMBF.

Adsorption of 2,3-butanediol on Si(100)

J.W.Kim^{a,*}, M.Carbone^{b,c}, M.Tallarida^a, J.H.Dil^a, K. Horn^a,
M.P.Casaletto,^d R.Flammini^e, M.N. Piancastelli^b

^a Fritz-Haber-Institut der Max-Planck-Gesellschaft, Faradayweg 4-6, 14195 Berlin, Germany

^b Dip. di Scienze e Tecnologie Chimiche, Università Tor Vergata, 00133 Roma, Italy

^c Sincrotrone Trieste, SS14 Km163, 5 in Area Science Park Basovizza, Italy

^d CNR-ISMN, Sezione di Palermo, Via Ugo La Malfa, 153 -90146 Palermo Italy

^e CNR-IMIP Sezione di Roma, Via Salaria Km 29.300-00016 Monterotondo Scalo, Italy

The interaction between organic molecules and silicon surfaces has drawn increasing attention, since current technology demands smaller and smaller functioning units, and their manufacturing in microelectronics involves many steps in which such interaction is important. Control of molecular reactions on the Si substrate may produce large arrays of self-assembled monolayers, which hold promise for future applications. The adsorption of alcohols on Si surfaces has revealed common phenomena irrespective of the surface phase. Methanol or ethanol adsorption on Si(100) or (111) surfaces react in a very similar fashion, *i.e.* the alcohol is dissociated into an alkoxy group and a hydrogen atom by O-H bond breaking. These fragments bond to a Si dimer atom spontaneously at room temperature. This observation can be linked to the fact that C-O bond breaking as another dissociation path needs a higher activation energy than breaking the O-H bond. Here we extend this common reaction scheme of adsorbed alcohols to a more complex system, 2,3-butanediol with two neighbouring alcohol groups. The essential functional group of diol molecules is the same as that of simple alcohols, but their electronic configuration is more like that of a diene group which has two double bonds in a molecule. The molecular nature of adsorbed 2,3-butanediol is revealed in the valence band spectrum (Fig. 1). Peaks due to molecular orbital-related show a close similarity to previous results on ethanol adsorption [1,2], probably because 2,3-butanediol has a molecular structure of two added units of ethanol. In order to relate the features in the valence band spectrum to molecular orbitals (MO's), we have calculated the energies of these for ethanol and 2,3-butanediol based on density functional theory with a B3LYP exchange-correlation potential and a 6-31G* basis set [3]. The calculated energy values are plotted on top of Fig. 1, shifted such that the highest binding MO is aligned at the same position as its experimental counterpart. The experimental spectrum and the calculated MO's exhibit great similarities. This indicates that the overall molecular bonds are not perturbed upon adsorption. Comparing the experimental and

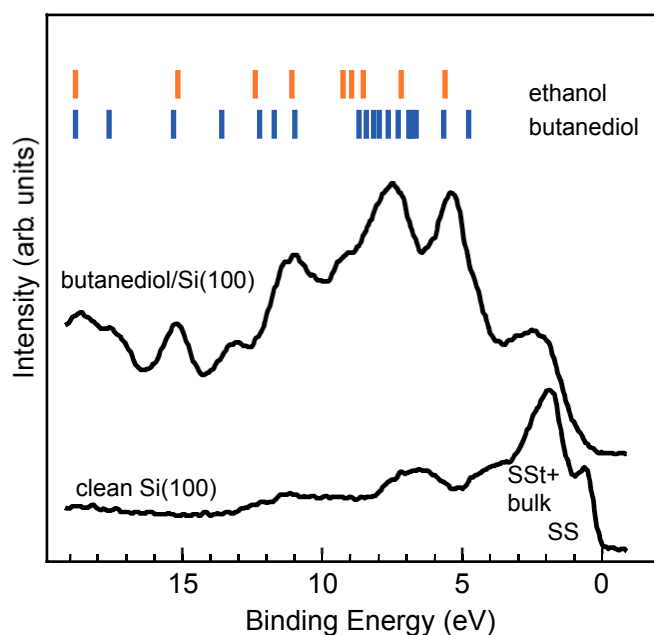


Fig. 1 Valence band spectra for clean Si(100) and with 2,3-butanediol adsorbed. Ionization potentials of calculated MO's for ethanol and 2,3-butanediol are plotted at the top.

adsorbed alcohols to a more complex system, 2,3-butanediol with two neighbouring alcohol groups. The essential functional group of diol molecules is the same as that of simple alcohols, but their electronic configuration is more like that of a diene group which has two double bonds in a molecule. The molecular nature of adsorbed 2,3-butanediol is revealed in the valence band spectrum (Fig. 1). Peaks due to molecular orbital-related show a close similarity to previous results on ethanol adsorption [1,2], probably because 2,3-butanediol has a molecular structure of two added units of ethanol. In order to relate the features in the valence band spectrum to molecular orbitals (MO's), we have calculated the energies of these for ethanol and 2,3-butanediol based on density functional theory with a B3LYP exchange-correlation potential and a 6-31G* basis set [3]. The calculated energy values are plotted on top of Fig. 1, shifted such that the highest binding MO is aligned at the same position as its experimental counterpart. The experimental spectrum and the calculated MO's exhibit great similarities. This indicates that the overall molecular bonds are not perturbed upon adsorption. Comparing the experimental and

theoretical results in more detail, two questions need further consideration. First, the highest occupied MO at 4.7 eV has no corresponding feature in the valence band spectrum for 2,3-butanediol. Since this MO has a mixed character of O non-bonding and C-C bond, we can assume that most changes upon adsorption are concentrated on this MO. Secondly, the feature at 12-13 eV has been regarded as belonging to an O-H bond for simple alcohols, and should disappear due to Si-O bond formation and consequent liberation of the H atom [4]. However, there remains a clear peak in our spectrum. We assign this feature not to a localized O-H bond but to C-O (and C-H₃) bonds, which also follows from the calculation.

Fig. 2 shows the C 1s core level spectrum for 2,3-butanediol on Si(100). There are two peaks at 284.8 and 286.1 eV. In the case of C-O bond cleavage, another lower binding feature due to a Si-C bond would occur, which produces a feature at 284.6-284.0 eV [18,20]. However, there is no evidence for this in Fig. 2. Thus, it is clear that there is no further decomposition or reaction of 2,3-butanediol on Si(100) except for O-H cleavage. From charge transfer considerations, these two peaks are assigned to the inner C atoms bonded to O (286.1 eV) and the C atoms in the methyl group (284.8 eV). Based on the above results, we conclude that 2,3-butanediol forms a bond made of Si-O bridges, and the remaining H atoms form Si-H bonds. An analysis of the Si 2p core level line supports our conclusion. From the valence band and C 1s spectra, it is obvious that the other molecular bonds remain intact. Since the LEED pattern does retain the (2x1) superstructure upon adsorption of 2,3-butanediol, we suggest that the Si dimer bonds remain intact as well. Concerning the final product after 2,3-butanediol adsorption, one system which closely resembles the present one is the [4+2] cycloaddition reaction between butadiene [H₂C=CH-CH=CH₂] and Si(100), where four C atoms and two Si atoms make a six-membered ring [1]. The formation of such a six-membered ring may also be achieved in our case, when 2,3-butanediol interacts with a dimer bond.

References

- [1] M. Carbone, M.N. Piancastelli, J.J. Paggel, Chr. Weidel, K. Horn, Surf. Sci. 412/413 (1998) 441.
- [2] M.P. Casaletto, R. Zanoni, M. Carbone, M.N. Piancastelli, L. Aballe, K. Weiss, K. Horn, Surf. Sci. 447 (2000) 237.
- [3] C.T. Lee, W.T. Yang, R.G. Parr, Phys. Rev. B 37 (1988) 785.
- [4] M.N. Piancastelli, R. Zanoni, M. Marsi, G. Margaritondo, Sol. State Comm. 79 (1991) 13.

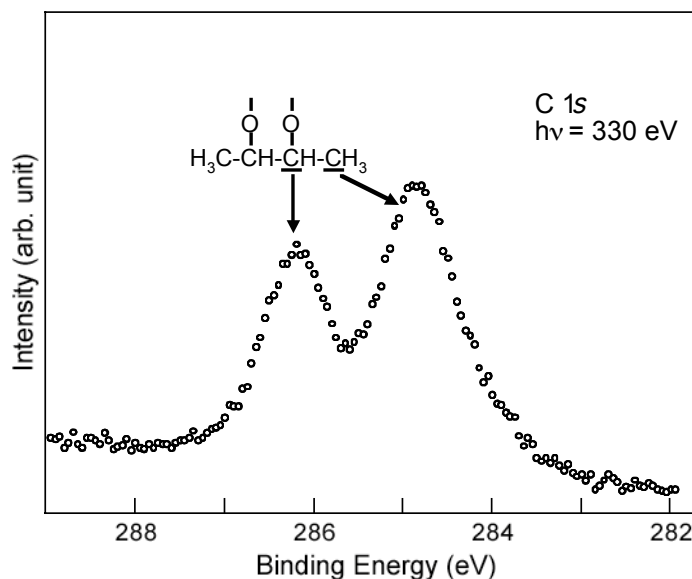


Fig. 3 C 1s core level spectrum for 2,3-butanediol on the Si(100) surface measured at $h\nu = 330$ eV

Structural and magnetic phase transition in MnAs(0001)/GaAs(111) epitaxial films

B. Jenichen, V. M. Kaganer, C. Herrmann, L. Däweritz, K. H. Ploog

Paul-Drude-Institut für Festkörperelektronik, Berlin

N. Darowski, I. Zizak

Hahn-Meitner-Institut, Berlin

Epitaxial films of ferromagnetic MnAs on semiconducting GaAs are of interest for spin injection. For MnAs films grown on GaAs(001) a strain-mediated coexistence of ferromagnetic α MnAs and paramagnetic β MnAs below the phase transition temperature of about 40°C is now well established. This coexistence is related to the epitaxial constraint and it is of interest to study the influence of other epitaxial orientations on the structural phase transition and to search for a possible shift of the ferromagnetic transition temperature to higher values. Here we present results for epitaxial MnAs films grown on exactly oriented GaAs(111)B substrates. Fig. 1 shows a schematic view of the epitaxial relationship of MnAs on GaAs(111).

The MnAs layers were grown by standard solid-source molecular beam epitaxy (MBE). A 100 nm thick GaAs buffer layer was grown first at 600°C and a growth rate of 250 nm h⁻¹. Then, a 2 nm thick MnAs nucleation layer was grown at 225°C with a growth rate of 20 nm h⁻¹ and an As₄/Mn beam-equivalent pressure (BEP) ratio of 230. A 400 nm thick main body of the MnAs layer was grown at 300°C with a growth rate of 200 nm h⁻¹ and an As₄/Mn BEP ratio of 22. Scanning electron microscopy revealed, that the surface exhibits smooth areas and some triangularly shaped depressions with a depth of about 100 nm.

Grazing incidence x-ray diffraction (GID) measurements were performed at the bending magnet beamline KMC2 at the storage ring BESSY using a double crystal graded SiGe(111) monochromator. A six-circle x-ray diffractometer with a temperature controlled sample stage was used. Temperature variations of the x-ray diffraction curves near the phase transition temperature were evaluated for the α MnAs($\bar{1}100$) reflection and the β MnAs(020) reflection. These reflections are most sensitive for the large deformations in the hexagonal base plane MnAs(0001), which occur during the phase transition. For the given sample orientation only GID allows the measurement of these reflections. Near the transition temperature, a continuous changeover from one peak to the other is observed. The temperature dependence of the

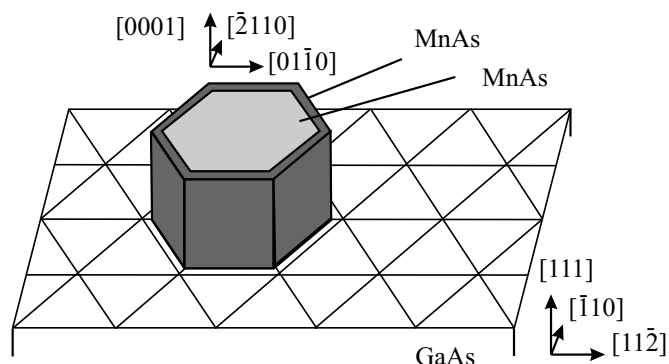


Fig. 1. Schematic view of the epitaxial relationship of MnAs on GaAs(111). The orthorhombic β MnAs unit cell is also indicated. The unit cell of GaAs can be considered as pseudo-hexagonal.

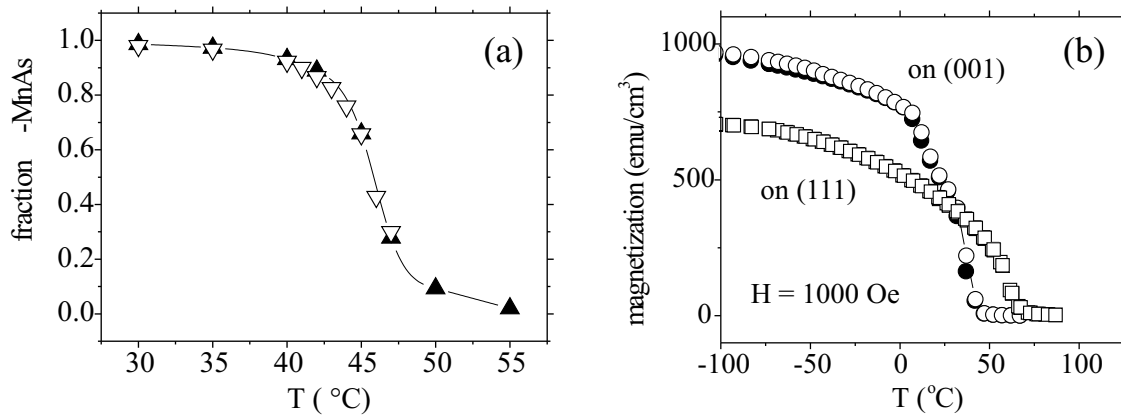


Figure 2: Temperature dependence of the α MnAs phase fraction (a) near the first order ferromagnetic-paramagnetic phase transition. Heating and cooling are marked by upward and downward pointing triangles, respectively. The lines are guides for the eye. The temperature dependence of the magnetization for MnAs layers on GaAs (001) (circles) and (111)B (squares) in the external field of 1000 Oe is shown in (b).

fraction of the α MnAs phase is presented in Fig.2(a). Heating and cooling are marked by upward and downward triangles, respectively. The phase coexistence is observed from 40 °C to 50 °C. No temperature hysteresis is seen. The phase coexistence found in the present study for MnAs(0001)/GaAs(111) films occurs at higher temperatures and in a narrower temperature range as compared to the phase coexistence in MnAs(1 $\bar{1}$ 00)/GaAs(001) films. There it occurs in a temperature range of 20 °C to 40 °C and shows a temperature hysteresis.

Temperature dependent magnetization measurements using a superconducting quantum interference device (SQUID) magnetometer with calibrated temperature stage have shown marked differences in the magnetization curves of MnAs(0001) epitaxial films on GaAs(111)B and MnAs(1 $\bar{1}$ 00) films on GaAs(001). Fig. 2(b) illustrates, that the temperature dependencies of the magnetization of the MnAs films grown on GaAs(001) and GaAs(111)B in the external field of 1000 Oe consist of two regions: a rapid increase of magnetization in the phase coexistence range and smooth further increase on cooling to low temperatures. The rapid increase of magnetization is the result of the increase of the fraction of the ferromagnetic α MnAs phase in the film. On GaAs(001) the magnetization obtained when the whole film transforms into the α MnAs phase is almost 80% of the maximal magnetization reached at $T = 0$ K. In contrast, the MnAs film on GaAs(111)B reaches just after the phase transition only 25% of the maximal magnetization.

Thus, the ferromagnetic phase transition in MnAs(0001) epitaxial films on GaAs(111)B proceeds through a phase coexistence of α -MnAs and β -MnAs, as in the case of MnAs(1 $\bar{1}$ 00) films on GaAs(001). The structural and also the ferromagnetic transition temperatures are notably higher than for MnAs/GaAs(001) films. However, the magnetization (after the whole film transforms into α MnAs phase) is 3 times smaller.

Creep-Induced Tetragonal Lattice Distortion of γ' Precipitates in Single Crystal Superalloys

I. Zizak, N. Darowski, G. Schumacher, N. Wanderka
Structure Research, Hahn-Meitner-Institut Berlin GmbH

H. Klingelhöffer
Federal Institute of Materials Research and Testing

W. Chen and W. Neumann
Institute of Physics, Humboldt University to Berlin

Single crystal nickel base superalloys are high temperature materials used for turbine blades in aero engines and industrial gas turbines. The superalloys are composed of γ' precipitates having the ordered $L1_2$ superlattice structure. The precipitates are embedded coherently in a solid solution matrix of fcc γ phase. For an effective precipitation hardening the single crystal superalloys are designed to contain a high volume fraction of γ' precipitates in a range of 40 – 70 %. In the as-heat treated state the γ' precipitates in superalloys have cuboidal morphology with the precipitate surfaces parallel to $\{100\}$ and are uniformly distributed in the γ matrix. Due to the coherency and the difference in lattice parameters between the γ' precipitates and γ matrix the internal stresses (so-called misfit stress) and the elastic lattice distortion govern in both the γ' and γ phases which are considered to be one of the major contributions of microstructure features in superalloys to the high temperature strength.

After full heat treatments the coherency between the γ' precipitates and γ matrix leads to a tetragonal lattice distortion in the γ matrix [1]. In case of negative lattice mismatch (γ' lattice parameter smaller than that of the γ phase) the cells of γ phase between two neighbouring γ' precipitates are compressed in direction parallel to the γ'/γ interface and elongated in the perpendicular direction due to the asymmetric distribution of the misfit stresses. The elastic lattice distortion of the γ' precipitates in non-deformed superalloys has approximately a hydrostatic nature and is independent of orientation. Their lattice structure remains essentially cubic. During creep deformation a dislocation substructure develops in the superalloys. It is expected that the built-up of dislocation substructure in the superalloys can result in an asymmetric lattice distortion in the γ' phase and causes the morphologic change of the γ' precipitates in the superalloys and therefore the change of deformation behaviour of the superalloys at high temperature.

A model single crystal superalloy SC16 [2] with a γ' volume fraction of about 40 % was used in the present investigation to study the tetragonal lattice distortion of the γ' precipitates induced by creep deformation. The superalloy has a negative lattice mismatch at high temperature and was deformed mechanically to a creep strain of 0.5 % at 1223 K under tensile as well as under compressive loading, respectively. High resolution synchrotron X-ray diffraction was used to determine the lattice parameters of the γ' precipitates in creep-deformed SC16 in two orientations, parallel (using the 001 reflection) and perpendicular (using the 100 reflection) to the

load axis of [001] at various temperatures up to 1173 K. Monochromatic synchrotron radiation at the KMC2 beamline at BESSY with the energy of 8,000 eV was used in the present study. Three functions, the Gaussian, the Lorentzian and the simplified Voigt (a combination of Gaussian and Lorentzian), were employed in data evaluation, see the example in Fig. 1. In most cases the same lattice parameter was obtained irrespective of the applied fitting function in the evaluation.

After tensile creep deformation a tetragonal lattice distortion in γ' phase could be measured on SC16. The γ' precipitates show a larger lattice parameter $a_{001}^{g'}$ in the orientation direction parallel to the load axis than $a_{100}^{g'}$ in the perpendicular directions, see Fig. 2. An inverse effect was observed in the specimen creep-deformed under compressive loading: $a_{100}^{g'}$ is larger than $a_{001}^{g'}$ after compressive creep deformation. The ratio $a_{001}^{g'}/a_{100}^{g'}$ selected for representation of tetragonal lattice distortion in the γ' precipitates are presented in Fig. 3 for both of the SC16 specimens creep-deformed under tensile and compressive loading, respectively. In both of the cases the tetragonal lattice distortion has a maximum value of the order of 10^{-3} at room temperature. With increasing temperature the tetragonal lattice distortion of the γ' precipitates becomes weaker.

Based on a dislocation model [2] the build-up of the tetragonal lattice distortion of the γ' precipitates in creep-deformed single crystal superalloys can be understood qualitatively as following: Under creep conditions the γ' precipitates are generally not sheared by dislocations. The inelastic deformation takes place essentially in the γ matrix. The glide of mobile dislocations generated in the γ matrix is stopped by the γ' precipitates. The dislocation substructure during tensile creep deformation is schematically shown in Fig. 4. The dislocation

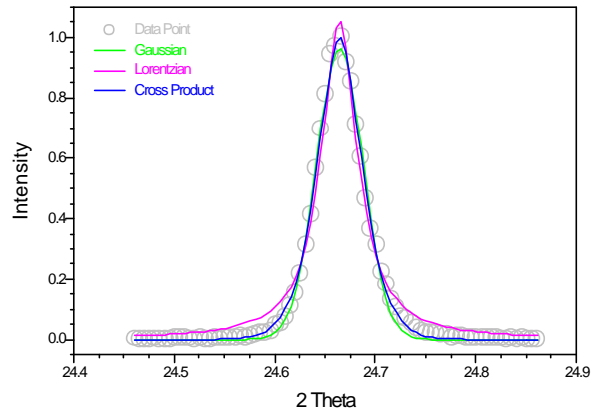


Fig. 1 Comparison of various fitting methods using Gaussian, Lorentzian and simplified Voigt functions, respectively

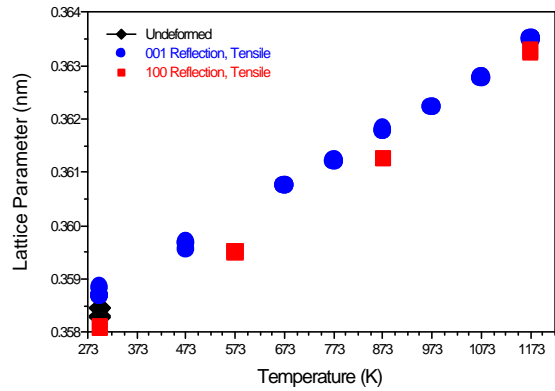


Fig. 2 Lattice parameters of γ' phase in direction parallel and perpendicular to load axis after tensile creep deformation

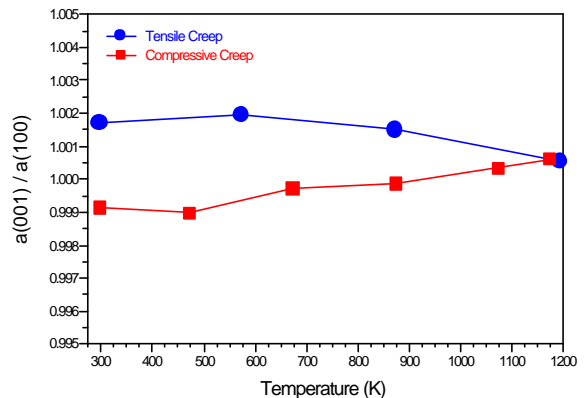


Fig. 3 Tetragonal lattice distortion at various temperatures

segments at the γ'/γ interfaces has the nature of a 60° mixed dislocation [3]. The edge component of the burgers vector of the segments is directed in the γ' phase at the γ'/γ interfaces normal to the load axis. This results in a compressive lattice distortion in [100] and [010] orientations. A smaller lattice parameter was therefore measured for the γ' phase in these crystal orientations (red squares in Fig. 2). At the γ'/γ interfaces parallel to the load axis the edge component of the burgers vector of the 60° dislocations lies in the γ matrix leading to a tensile lattice distortion in the neighbouring γ' phase. The lattice parameter of the γ' phase in [001] orientation becomes larger than that before creep deformation (blue circle data points in Fig. 2). The ratio $a_{001}^{g'}/a_{100}^{g'}$ is in this case larger than 1, see Fig. 4. An analogue analysis for SC16 after compressive creep deformation leads to an $a_{001}^{g'}/a_{100}^{g'}$ value smaller than 1.

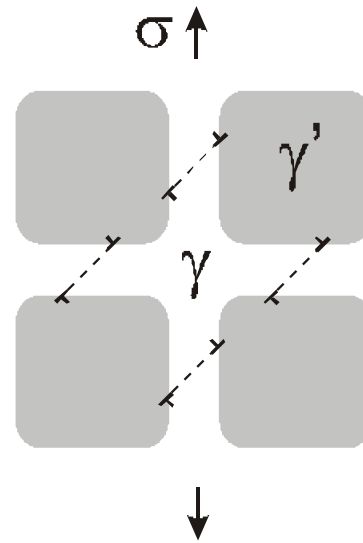


Fig. 4 Schematic presentation of dislocation substructure during tensile creep deformation in superalloys

The temperature dependence of the tetragonal lattice distortion in the γ' precipitates is thought to be caused either by the relative change of stiffness of the γ' precipitates and γ matrix with temperature or by relaxation due to re-arrangement of dislocations at g/g' interfaces. At high temperature the elastic constants of γ' phase are generally larger than those of the γ matrix. The lattice distortion is concentrated mainly in the relatively weaker γ matrix. With decreasing temperature the difference in the stiffness between the γ' phase and γ matrix becomes smaller. A measurement on two separate alloys corresponding to the γ' and γ component phases in CMSX4 [4] revealed that the γ phase alloy has a larger elastic modulus than that of the γ' phase ones at temperatures below 1023 K. This causes a shift of lattice distortion from the γ matrix at high temperature into the γ' phase at ambient temperature. As a result a stronger tetragonal lattice distortion was observed at ambient temperature. The temperature effect could also result from the relaxation caused by the changes in the dislocation substructure at high temperature. Further experiments are necessary to find out the reason for the observed temperature dependence in tetragonality.

Financial support of the Deutsche Forschungs-gemeinschaft under the grant number NE646/5-4 and SCHU 1254/3-4 is gratefully acknowledged. The authors are thankful to Ms. Ch. Förster and Mr. W. Becker for their technical assistance.

- [1] W. Chen, W. Neumann, N. Darowski, I. Zizak, N. Wanderka and G. Schumacher, Z. Kristallographie, Suppl. 20 (2003) 163
- [2] W. Chen, N. Darowski, I. Zizak, G. Schumacher, H. Klingelhöffer, N. Wanderka and W. Neumann, Mater. Sci. Forum, 426-432 (2003) 4555.
- [3] H. Gabrisch, D. Mukherji and R.P. Wahi, Phil. Mag., 74 (1996) 229
- [4] D. Siebörger, H. Knake and U. Glatzel, Mat. Sci. Eng., A298 (2001) 26

NEXAFS - Spectroscopy on Plasma-polymerized Films Prepared from Organic Molecules (Ethylene, Allyl alcohol, Styrene)

Sufal Swaraj, Umut Oran, Andreas Lippitz, Rolf-Dieter Schulze and Wolfgang Unger

Bundesanstalt für Materialforschung und –prüfung (BAM), D-12203 Berlin, Germany

The formation of plasma-polymerized materials made from organic molecules is a technologically attractive way to obtain films with unique properties, e.g. adhesion, wettability, conductivity or selected chemical functionalisation. A detailed chemical characterization of these films is a great challenge for the analyst because of the co-existence of a greater number of chemical species in plasma-polymerized films. We started to investigate this kind of organic films using photoelectron spectroscopy for chemical analysis (ESCA), near edge X-ray absorption fine structure (NEXAFS) spectroscopy and time-of-flight secondary ion mass spectroscopy. In order to do this a dedicated plasma preparation chamber was designed and added to the main analysis chamber of a NEXAFS/electron spectroscopy apparatus at the HE-SGM beamline at BESSY II. The same chamber can be moved to a laboratory ESCA facility as well as a TOF-SIMS instrument at BAM. This approach offers the possibility to study plasma-polymerized films without air exposure before analysis (often also called *in situ* analysis) and the influence of post-plasma reactions. This is the preferred way to study the result of a plasma based deposition process because it is well known that plasma-polymerized films undergo certain secondary chemical reactions when they are exposed to atmosphere. The important effect of air exposure, in terms of plasma technology denominated as the “ageing” of the film in air, can be studied additionally.

The investigations are dedicated to find correlations between basic chemical properties of the deposited films and a variation of plasma deposition parameters, e.g. pulsed or cw plasma condition, duty cycle in pulsed plasma, power of discharge, pressure of organic monomers and ratio of monomer partial pressures in co-polymerization. Co-polymerized products are of special interest because it is assumed that technologically requested film properties may be “tailored”. Monomers to be used are simple organic molecules with a polymerizable C=C bond, e.g. ethylene, allyl alcohol and styrene. Chemical properties of interest are:

- estimates of the numbers of C=C bonds remaining in the film,
- oxygen uptake and formation of oxygen species due to ageing,
- the retention of principal structure units of the used monomers in the film (e.g. the phenylene rings from styrene),
- estimates of the number of well defined functional groups (e.g. OH), and
- branching or/and cross-linking in the film.

The spectroscopy of NEXAFS is well suited to give answers to the questions raised above because the method is very sensitive to unsaturated carbon and carbonyl species. Usually we find intense C 1s or O 1s $\rightarrow \pi^*$ resonance features in the C-K-edge or O-K-edge spectra, respectively, when these species exist in the plasma deposited film.

In the following we describe our first results obtained with the ethylene-allyl alcohol co-polymer system. Films of around 100 nm thickness were deposited in a pulsed plasma at a duty cycle of 0.1 and a r.f. discharge power of 10 W on clean silicon wafers. Figs. 1 a-c present selected C-K-edge and O-K-edge spectra obtained with

grating 1 and 150 μm slit width at the HESGM beamline. All samples were analyzed without exposure to air before analysis.

Fig. 1a gives the C-K-edge of a plasma polymerized ethylene film. A relatively high concentration of C=C bonds is revealed which must be reduced by further optimization of the deposition process. (C-H)* and σ^* resonances but no carbonyl related features are found. Fig. 1b presents the C-K-edge of a plasma deposited co-polymer made from an ethylene/allyl alcohol monomer mixture. The C=C bond concentration is reduced, the (C-H)* featured disappeared and probably carbonyl related resonances appear in this spectrum. The plasma-technologically undesirable carbonyl bond formation is cross checked by the respective O-K-edge spectrum in Fig. 1c.

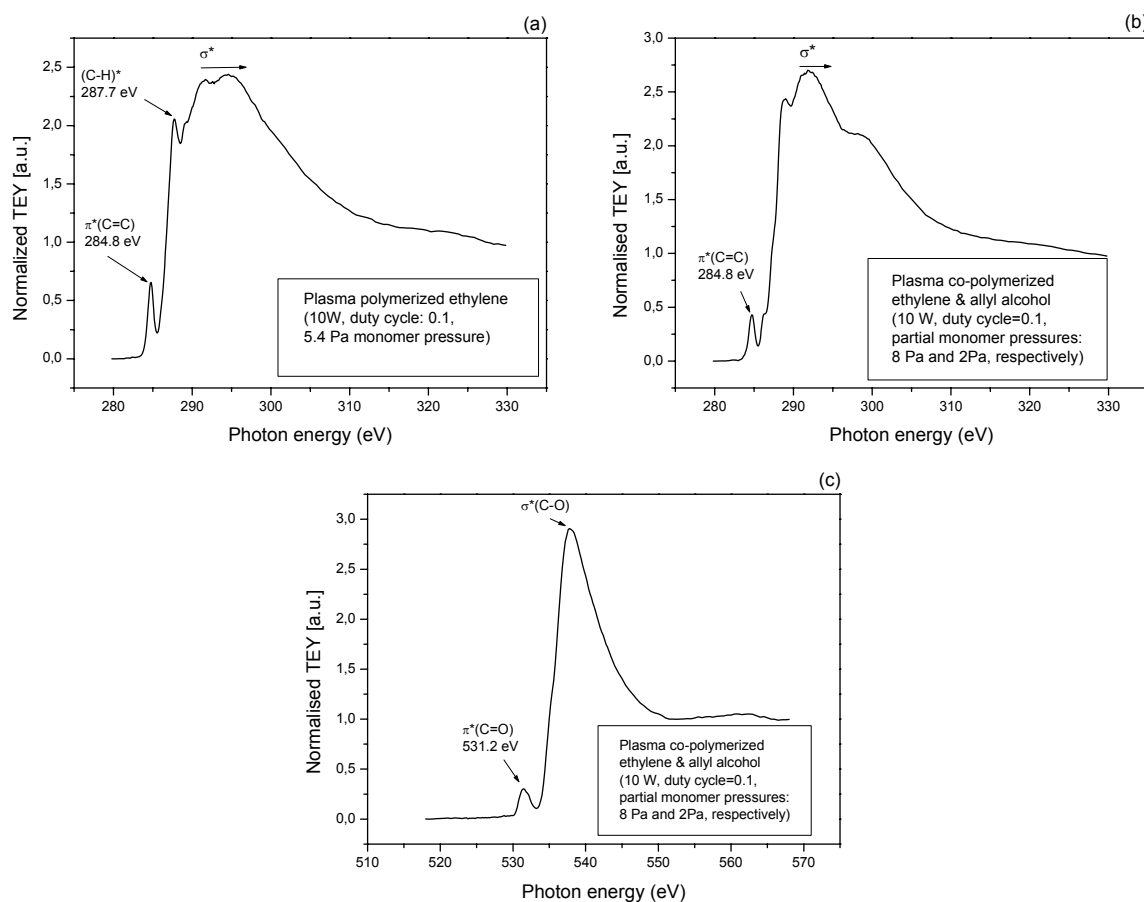


Figure 1

Another example is presented in Figs. 2a and b. Here we compare the C-K-edge spectra of a spin coated thin polystyrene reference sample with this of an air exposed plasma polymerized styrene sample. The plasma polymer film (thickness around 10 nm) was deposited in a pulsed plasma at a duty cycle of 0.1, a pressure of 5 Pa in the reactor chamber and a r.f. discharge power of 10 W on a clean silicon wafer.

A result is that we find intense C 1s $\rightarrow \pi^*_{\text{ring}}$ resonances in both cases clearly pointing to a good retention of the phenyl ring structure unit of the monomer in the plasma deposited film under the given deposition conditions. This result was successfully cross checked by TOF-SIMS and valence as well as core level spectra in XPS.

Additionally, semi-quantitative results can be derived from the NEXAFS spectra: The

π^*_{ring} resonance area for the plasma deposited film reaches ca. 90 % of this measured with the reference polystyrene. A striking difference between both spectra is the occurrence of a new $\text{C } 1\text{s} \rightarrow \pi^*$ resonance at ca. 286.1 eV in the plasma polymer spectrum. The new feature is interpreted to be due additional substitution(s) of aromatic rings, probably by methyl groups or short sequences of aliphatic carbon chains in the simplest cases, i.e. branching or even cross-linking in the plasma polymerized styrene film.

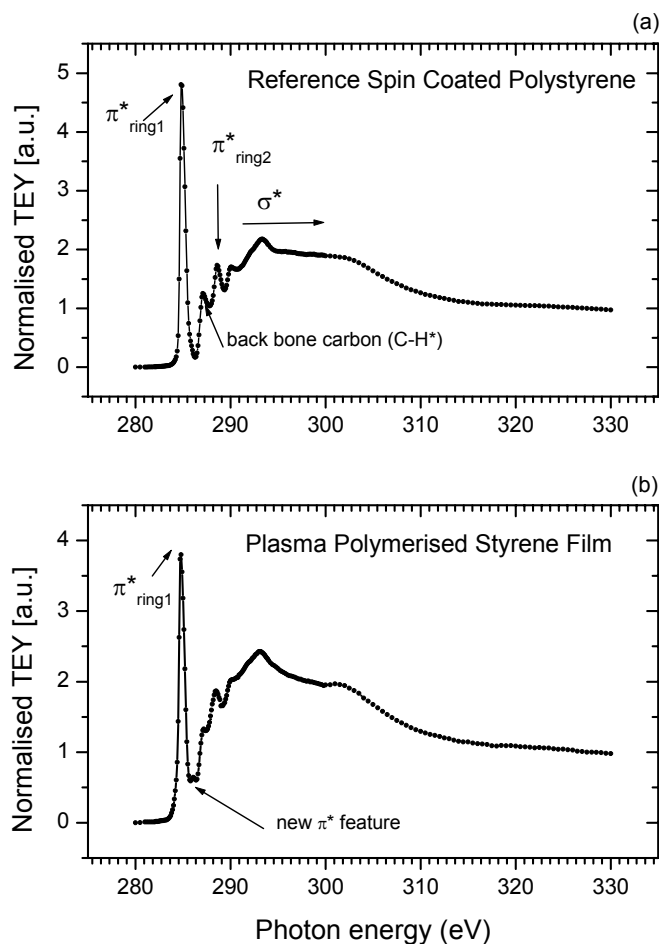


Figure 2

Acknowledgements:

Thanks are due to the BESSY staff and the other CRG members for the excellent collaboration during commissioning of the HESGM beamline. Special thanks are due to Matthias Mast (BESSY), Thomas Strunskus (RUB) and Olaf Schwarzkopf (BESSY) for support during the experiments.

Electronic state of carbons occurred in the carbonaceous chondrite meteorites

A.V. Okotrub¹, L.G. Bulusheva¹, Yu.P. Dikov², A.V. Gusel'nikov¹,
M. Poygin³, S.L. Molodtsov³

¹*Institute of Inorganic Chemistry, Siberian Branch of Russian Academy of Science – IIC SB RAS, Novosibirsk, Russia*

²*Institute of Geology of Ore Deposits, Petrography, Mineralogy and Geochemistry of the Russian Academy of Sciences, IGEM RAS, Moscow, Russia*

³*Russian-German Laboratory, BESSY-II, Berlin, Germany*

Carbon plays an important role in the universe evolution because of its abundance and its ability to form complex species. Investigation of processes of carbon generation and transformation in the interstellar space is an important problem in the revealing of origin of the Solar System and life on the Earth. One of the components of the Solar System, which are rich in carbon, is the carbonaceous chondritic meteorites. The occurrence of a specific form of carbon in a meteorite should depend on the condensation conditions and age of meteorite. So-called primitive meteorites include grains, which were formed before the Solar System birth and characterized by various anomalous [1]. We examined the samples of eight chondrites – *Kainsaz*, *Isna*, *Murray*, *Boriskino*, *Mighei*, *Murchison*, *Allende*, and *Orgueil* – listed in rising age. The last three meteorites are

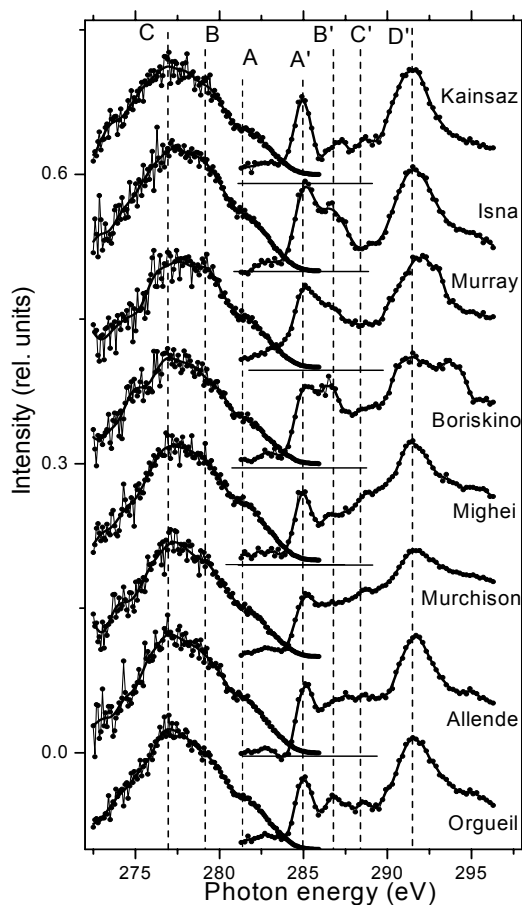


Fig. 1. CK α -spectra (left part) and CK-edge absorption spectra (right part) of chondritic meteorites.

qualified as primitive ones. The meteorites contain about 0.8-2.6% of carbon, which can constitute graphite, diamond, SiC particles, carbides of metals and hydrocarbons.

Electronic state of carbon occurred in the chondritic meteorites was probed by high-energy spectroscopy methods. Carbon K-edge X-ray absorption spectra (XAS), carbon and oxygen X-ray photoelectron spectra (XPS) of the samples were measured using the Berlin synchrotron radiation facility at the Russian-German laboratory BESSY-II. The XAS data were acquired in the total yield of electrons mode and normalized to the primary photon current from a gold-covered grid recorded simultaneously. The resolution of incident radiation was about 0.06 eV. XPS C1s- and O1s spectra were excited using photons with 600 eV. Carbon K α -spectra of the samples were measured using a laboratory X-ray spectrometer. A sample was located on a copper support and cooled down to the liquid nitrogen temperature in the vacuum chamber of

the X-ray tube operating with copper anode ($U = 6 \text{ kV}$, $I = 0.5 \text{ A}$). The single crystal of ammonium biphthalate NH_4AP was used as an analyzing crystal. Determination of X-ray band energy was accurate to $\pm 0.15 \text{ eV}$ with spectral resolution of $\sim 0.4 \text{ eV}$.

$\text{CK}\alpha$ - and CK -edge spectra of the meteorites are compared in Fig. 1. The spectra characterize the partial density of occupied and unoccupied states of carbon respectively. The main spectral features are labeled and variation in their intensity indicates the meteorites are distinguished by kinds of incorporated carbon. The maxima A and C of $\text{CK}\alpha$ -spectra correspond to π - and σ -systems, while the intensity of feature B is formed by both types of $\text{C}2\text{p}$ -electrons. The $\text{CK}\alpha$ -spectra of *Orgueil*, *Allende*, and *Mighei* meteorites have the most similarity with the graphite spectrum [2] and somewhat enhanced intensity of the feature B can be related to the presence of grains of carbides [3]. Lowering of the maximum A and broadening of main intense maximum in the $\text{CK}\alpha$ -spectra of other samples are attributed to large portion of diamond-like and hydrogenated carbon in the chondrites. The CK -edge XAS spectra of meteorites show two main peaks A' and D' located around 285 eV and 291.5 eV and corresponded to the transition $1s \rightarrow \pi^*$ states and $1s \rightarrow \sigma^*$ respectively. Furthermore, two features B' and C' positioned around 286.5 eV and 288 eV can be recognized in the certain spectra. The features B' is related to the transitions $1s \rightarrow \pi^*_{\text{C=O}}$ induced by the presence of oxygen [4]. The XAS spectrum of *Boriskino* meteorite exhibits maximal intensity of this feature, which is compared with the intensity of $\pi^*_{\text{C=C}}$ resonance. The feature C' at 288 eV corresponds to σ^* -resonances, which can be attributed to both C-H and Si-C bonds [5]. It is known that primitive chondrites are rich in SiC component and high intensity of the feature C' is characteristic of these meteorites. The C-H bonds are involved in hydrogenated amorphous carbon

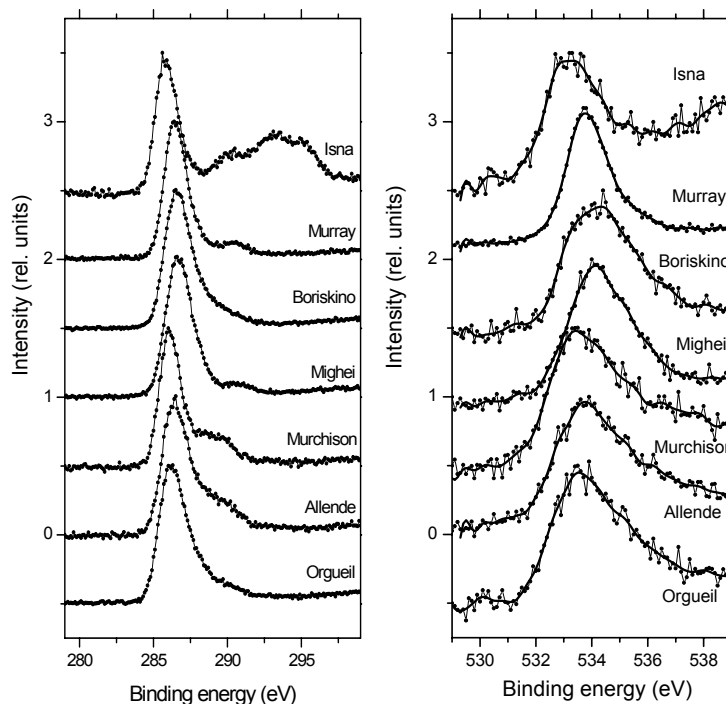


Fig. 2. $\text{C}1\text{s}$ - (left picture) and $\text{O}1\text{s}$ -spectra (right picture) measured for chondritic meteorites.

or hydrocarbon molecules. The reduced intensity of the feature C' was detected in the C K-edge spectra of *Isna* and *Murray* meteorites.

$\text{C}1\text{s}$ - and $\text{O}1\text{s}$ -spectra of the samples are presented in Fig. 2. One of the interesting findings is an energetic shift of the line in both types of spectra. The $\text{C}1\text{s}$ - and $\text{O}1\text{s}$ -spectra of *Orgueil*, *Murchison*, and *Allende* primitive meteorites are positioned around 286.1 eV and 533.5 eV, the spectra of *Mighei*, *Boriskino*, and *Murray* are shifted by

0.3–0.6 eV toward the higher binding energy, while the energy of the spectral lines of *Isna* meteorite is lowered by 0.3 eV. The detected shift of the spectra is more likely to be caused by sample charging during the XPS measurements and indicates the different composition of meteorites. The C1s- and O1s-lines of *Murray* and *Isna* meteorites have the smallest width that correlate with minimal intensity of the feature at 288 eV in the CK-edge XAS spectra. The XPS spectra of other meteorites reveal a significant portion of carbonyl and carboxyl groups in the samples.

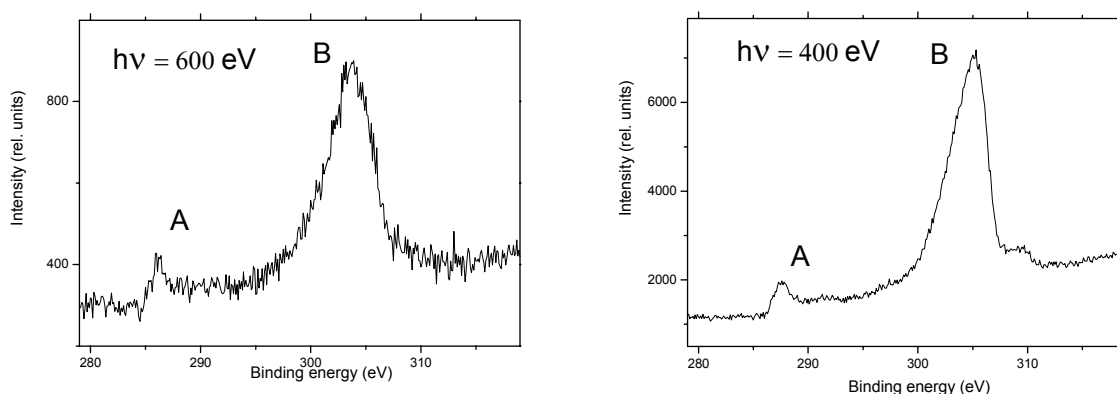


Fig. 3. C1s-spectra measured for *Kainsaz* meteorite measured with different excitation energy.

The XPS spectra of *Isna* and *Kainsaz* meteorites showed an anomalous, namely, the arising of intense feature far removed from the main line. In the case of *Kainsaz* meteorite the intensity of new line became dominant (Fig. 3). The separation of lines A and B was found to be independent from the energy of spectrum excitation. The separation of lines A and B was found to be independent from the energy of spectrum excitation. Nevertheless, we attribute the observed splitting of C1s-line to the induced charging of samples due to high inhomogeneity of the meteorite substance. Thus the spectral maximum A in the C1s-spectrum of *Kainsaz* meteorite corresponds to the graphite inclusions characterized by good conductivity and intense maximum B is likely related to diamond-like forms of nanocarbon. The O1s-spectra of *Kainsaz* and *Isna* meteorites also showed the splitting that suggests the diamond nanoparticles have developed oxidized surface. It is intriguing that anomalous of XPS spectra being indicative of specific composite of substance was observed for the youngest meteorites.

- [1] U.Ott “Interstellar grains in meteorites” *Nature*, 364 (1993) 25-33.
- [2] A.V.Okotrub, L.G.Bulusheva, V.L.Kuznetsov, Yu.V.Butenko, A.L.Chuvilin, M.I.Heggie “X-ray emission studies of the valence band of nanodiamonds annealed at different temperatures” *J. Phys. Chem. A* 105 (2001) 9781-9787
- [3] *Soft X-ray Band Spectra*, Ed. D.J.Fabian, Academic Press, London and New York, 1968, 382p.
- [4] C.Lenardi, P.Piseri, V.Briosis, C.E.Bottani, A. Li Bassi, P.Milani “Near-edge x-ray absorption fine structure and Raman characterization of amorphous and nanostructured carbon films” *J. Appl. Phys.* 85 (1999) 7159-7167.
- [5] C.Haluschka, H.-J.Kleebe, R.Franke, R.Riedel “Silicon carbonitride ceramics derived from polysilazanes/ Part I. Investigation of compositional and structural properties” *J. Europ. Ceram. Soc.* 20 (2000) 1355-1364.

A balance of structural forces in alkanethiolate self-assembled monolayers on noble metal substrates

A. Shaporenko¹, M. Brunnbauer², A. Terfort², M. Grunze¹, and M. Zharnikov¹

¹ *Angewandte Physikalische Chemie, Universität Heidelberg, Im Neuenheimer Feld 253, D-69120 Heidelberg, Germany*

² *Anorganische und Angewandte Chemie, Universität Hamburg, 20146 Hamburg, Germany*

Self-assembled monolayers (SAMs) are 2D polycrystalline films of chainlike or rodlike molecules that are chemically anchored to a suitable substrate. During the last two decades these systems attracted considerable attention because they allow preparation of organic surfaces with a specific chemical identity and provide a means to tailor the surfaces properties such as wetting, adhesion, lubrication, corrosion, and biocompatibility. At a given chemical composition of the SAM constituents, the properties of a SAM depend on its structure and packing density. These, in turn, result from the complex interplay of intermolecular and headgroup-substrate interactions, provided that the tail groups are weakly-interacting. In particular, for the ω -substituted alkanethiolate (AT) SAMs on gold and silver, which are probably the best studied SAM systems at present, intermolecular interaction and the corrugation of the sulfur-metal binding energy surface were believed to be the major factors affecting the film structure.¹

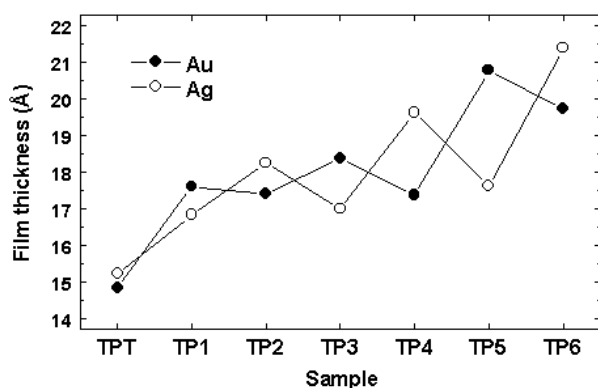


Fig. 1. The effective thickness of TPn/Au (full circles) and TPn/Ag (hollow circles) derived from the XPS data (C1s/Au4f and C1s/Ag3d intensity ratios).

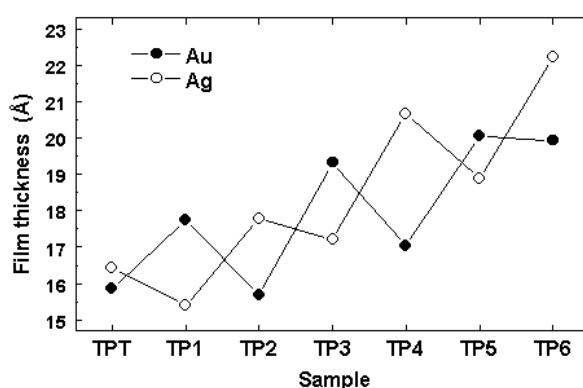


Fig. 2. The effective thickness of TPn/Au (full circles) and TPn/Ag (hollow circles) derived from the ellipsometry data.

There is, however, an additional factor, which is the character and geometry of the headgroup-substrate interaction. To clarify the importance of this factor, the chemical identity, packing density, and orientational and conformational order of 4,4'-terphenyl-substituted alkanethiolate SAMs (TPn: $C_6H_5(C_6H_4)_2(CH_2)_nSH$, $n = 1-6$) on polycrystalline (111) gold and silver substrates were studied by XPS, HRXPS, ellipsometry, IRRAS, NEXAFS spectroscopy, and water contact angle measurements. In the TPn SAMs, strongly interacting terphenyl moieties were combined with the short aliphatic linker. Provided that the intermolecular interaction plays a deciding role for the SAM packing, no influence of the aliphatic linker length on the film structure could be expected.

The TPn SAMs were found to be well-defined, densely-packed, and contamination-free. As indicated by the XPS (Fig. 1), ellipsometry (Fig. 2), and NEXAFS (Figs. 3 and 4) data, the packing density and the orientation of the terphenyl moieties in the TPn SAMs exhibited a pronounced zig-zag variation with n from TP1 to TP6, which was opposite on silver than on gold. A higher packing density and a smaller inclination of the terphenyl moieties was

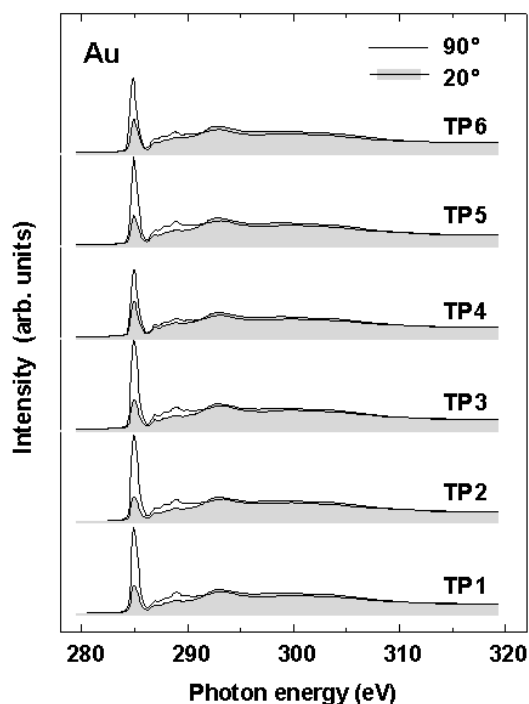


Fig. 3. Carbon K-edge NEXAFS spectra of TPn/Au acquired at X-ray incident angles of 90° and 20°.

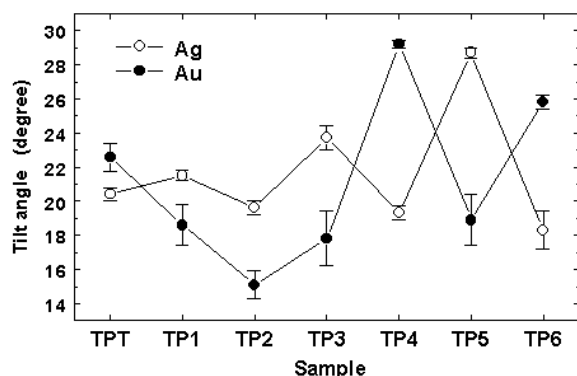


Fig. 4. The average tilt angle of the terphenyl moieties in TPn/Au (full circles) and TPn/Ag (hollow circles) derived from the NEXAFS data.

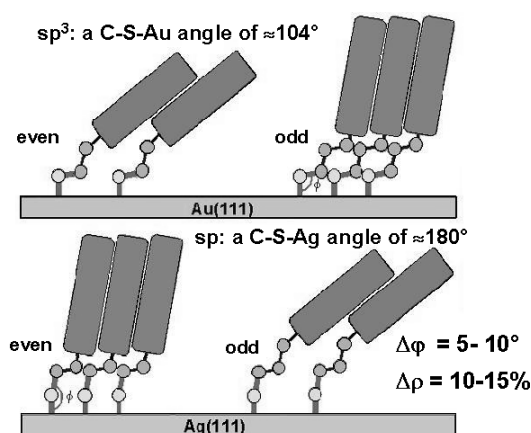


Fig. 5. Schematic drawing of the orientation and packing of the TPn molecules in the respective SAMs.

observed for an odd number of the methylene units in the aliphatic linker in TPn/Au, and an even number of these units in TPn/Ag. *Vice versa*, a lower packing density and a larger inclination of the terphenyl moieties was found for an even number of the methylene units in the aliphatic linker in TPn/Au, and an odd number of these units in TPn/Ag.

As shown in Fig. 5, the observed odd-even effects can be explained by assuming that the bending potentials of the substrate-S-C entity depends strongly on the deviation of the substrate-S-C bonding angle from an optimal value of $\approx 104^\circ$ (Au) and $\approx 180^\circ$ (Ag), respectively. The optimal substrate-S-C angles are associated with the bonding configurations of the sulfur headgroups, which are assumed to have an sp^3 hybridization on Au and an sp hybridization on Ag, respectively.²⁻⁴

The odd-even effects in the TPn films are very similar to those observed previously in SAMs of biphenyl-substituted alkanethiolates (BPn) on Au and Ag,²⁻⁵ both in their dependence on n and their extent. This suggests a common origin of the observed phenomena in all alkanethiolate SAMs, which we identify as a deciding role of the headgroup-substrate bond in the balance of forces determining the packing density and molecular orientation in these systems. Both for the BPn and TPn SAMs, the contribution of the substrate-S-C bending potentials obviously dominates over the intermolecular forces.

This work has been supported by BMBF (GRE1HD) and DFG (JA 883/4-2).

References:

- (1) A. Ulman, Chem. Rev. **96** (1996) 1533.
- (2) M. Zharnikov, S. Frey, H. Rong, Y. J. Yang, K. Heister, M. Buck, and M. Grunze, Phys. Chem. Chem. Phys. **2** (2000) 3359.
- (3) H.-T. Rong, S. Frey, Y. J. Yang, M. Zharnikov, M. Buck, M. Wühn, Ch. Wöll, and G. Helmchen, Langmuir **17** (2001) 1582.
- (4) M. Zharnikov and M. Grunze, J. Phys. Condens. Matter. **13** (2001) 11333.
- (5) W. Azzam, P. Cyganik, G. Witte, M. Buck, and Ch. Wöll, Langmuir **19** (2003) 8262.

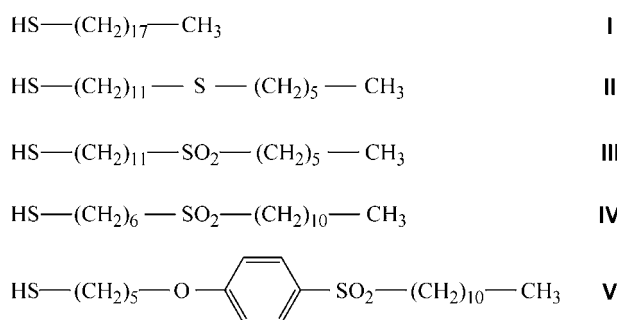
A tailored manipulation of a monomolecular resist: Introduction of a "weak link"

K. Heister¹, S. Frey¹, A. Ulman², M. Grunze¹, and M. Zharnikov¹

¹*Angewandte Physikalische Chemie, Universität Heidelberg, Im Neuenheimer Feld 253, D-69120 Heidelberg, Germany*

²*Department of Chemistry and the NSF MRSEC for Polymers at Engineered interfaces, Polytechnic University, Brooklyn, NY 11201, USA*

Self-assembled monolayers (SAMs) can be modified by electrons and X-rays, which ensures their application as a lithographic resist or a template.¹⁻³ Recently, we have shown that the effectiveness of alkanethiolate (AT) SAMs as a monomolecular lithographic resist can be noticeably enhanced by the insertion of functional entities, serving as a predetermined breaking point, into the molecular backbone.⁴ The aim of the present study was an extension of this approach by the investigation of the effect of the chemical identity and the position of the inserted functionality on the response of AT films toward electron irradiation. As test systems, we used several AT SAMs with introduced sulfide, sulfone, and sulfonyl-phenoxy groups (see Fig. 1). The pristine and irradiated (by electrons) SAMs were characterized by



XPS (Figs. 2 and 3), IR spectroscopy, and NEXAFS spectroscopy (Fig. 4).

The results imply that the insertion of a functional entity into the alkyl chain of AT SAMs affects the sensitivity of these systems toward ionizing radiation. In particular, the irradiation-induced thickness reduction could be significantly enhanced (by about 30%, see Fig. 5) by the incorporation of the sulfur-derived functionalities as predetermined breaking point, even though the chains were not exclusively cut at the position of the incorporated group, but the scission events related to the "weak links" were just added to those in the alkyl matrix. Among the investigated sulfide, sulfone, and sulfonyl-phenoxy groups, the identity of the chosen functionality was found not to be decisive for this effect. At the same time, the position of the incorporated group along the alkyl chain was very essential for its performance as a predetermined breaking point. The enhancement of irradiation-induced desorption was observed only when the groups were placed close to the SAM-ambient interface. Otherwise, the effect of the

Fig. 1. Chemical structures of materials used to fabricate the SAMs investigated in the present study. The numbers I -V are used below as the names of the corresponding films. I is taken as a reference system.

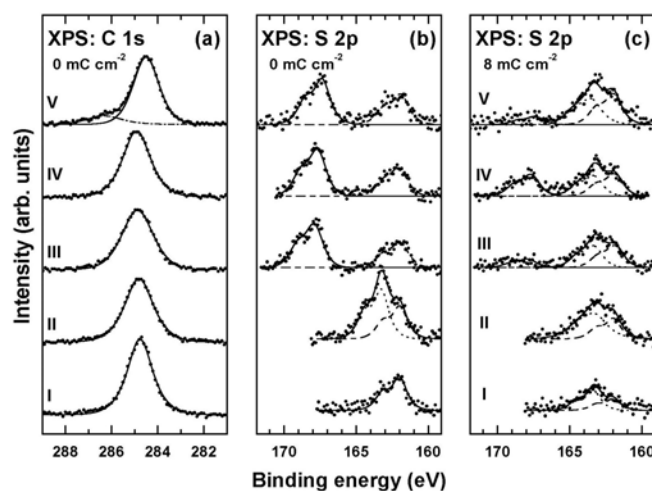


Fig. 2. C 1s (a) and S 2p (b,c) XPS spectra of pristine (a,b) and irradiated (c) I-V. The irradiation dose was 8 mC cm⁻². Individual spectral components are indicated.

"weak link" was neutralized by an enhanced quenching of the excited states via the dipole-dipole interaction with the substrate and a trapping of molecular fragments in the highly reactive (under electron irradiation) hydrocarbon layer.

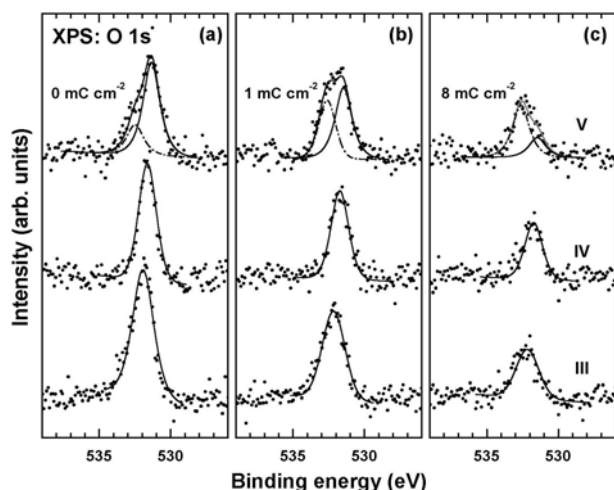


Fig. 3. O 1s XPS spectra of pristine (a), and irradiated (b,c) **III**, **IV**, and **V**. The irradiation dose was 1 mC cm⁻² (b) and 8 mC cm⁻² (c). Individual spectral components are indicated.

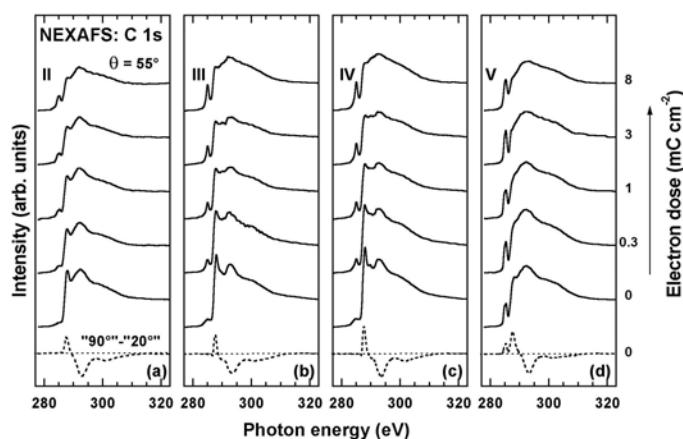


Fig. 4. Carbon K-edge NEXAFS spectra of pristine (bottom but one spectra) and irradiated **II-V** acquired at an X-ray incidence angle of 55°. Bottom curves: the difference between the spectra of the pristine films acquired at normal and grazing (20°) X-ray incidence.

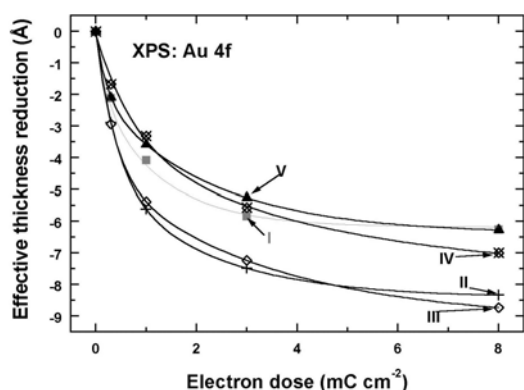


Fig. 5. Effective thickness reduction of the investigated films in the course of irradiation. The values were estimated based on the attenuation of the Au 4f XPS signal.

Apart from the enhanced irradiation-induced desorption, which affected the "outer" part of the films, the extent of damage at the thiolate-substrate interface was significantly reduced by the introduction of the sulfur-derived functionality into the alkyl spacer. This stabilizing effect on the "deeper" part of the film varied with the chemical identity of the incorporated functionality and was most pronounced for the sulfone and sulfonyl-phenoxy functionalities. It was tentatively explained by an enhanced coupling of the SAM constituents and an additional cross-linking mediated by the irradiation-modified "weak links".

The results clearly show that the response of monomolecular films towards electron irradiation is a complex process, which, however, can be tailored to a definite extent by a versatile architecture of the film constituents.

This work has been supported by BMBF (05 SL8V HA 2 and GRE1HD) and DFG (JA 883/4-2).

References:

- (1) M. Zharnikov and M. Grunze, *J. Vac. Sci. Technol. B* **20** (2002) 1793.
- (2) R. Klauser, I.-H. Hong, S.-C. Wang, M. Zharnikov, A. Paul, A. Götzhäuser, A. Terfort, and T. J. Chuang, *J. Phys. Chem. B* **107** (2003) 13133.
- (3) A. Götzhäuser, W. Geyer, V. Stadler, W. Eck, M. Grunze, K. Edinger, Th. Weimann, and P. Hinze, *J. Vac. Sci. Technol. B* **18**, **2000**, 3414.
- (4) K. Heister, S. Frey, A. Götzhäuser, A. Ulman, and M. Zharnikov, *J. Phys. Chem. B* **103** (1999) 11098.

Layer-resolved imaging of magnetic interlayer coupling by domain wall stray fields using photoelectron emission microscopy

*W. Kuch, L. I. Chelaru, K. Fukumoto, F. Offi, M. Kotsugi, and J. Kirschner
Max-Planck-Institut für Mikrostrukturphysik, Weinberg 2, D-06120 Halle, Germany*

BMBF 05KS1EFA6

Many interesting phenomena in thin film magnetism occur in trilayers in which two ferromagnetic layers are separated by an ultrathin nonmagnetic spacer layer. To explore these phenomena, it is necessary to understand and control the magnetic coupling between the two ferromagnetic layers. We used photoelectron emission microscopy (PEEM) in connection with x-ray magnetic circular dichroism (XMCD) for the element-resolved investigation of local coupling phenomena in epitaxial Co/Cu/Ni trilayers. With this technique, the local intensity of emitted low-energy secondary electrons is imaged by a set of electrostatic lenses. Magnetic contrast is obtained from the dependence of the absorption of circularly polarized x-rays on the local magnetization direction for excitation at the maxima of elemental absorption edges [1]. Since elemental absorption edges are excited, information about the local magnetization direction is obtained element-selectively. We found that besides the well-investigated laterally extended magnetic interlayer coupling, also a local coupling is present which is caused by magnetostatic stray fields emanating at magnetic domain walls.

The measurements were performed at the beamline UE56/2-PGM2. Co/Cu/Ni trilayers were deposited in-situ at room temperature on a Cu(001) single crystal. The commercially available PEEM (Focus IS-PEEM) was operated at 90 μm field of view and 300 nm lateral resolution. Fig. 1 shows layer-resolved magnetic domain images of a Co/Cu/Ni trilayer of 4 atomic monolayers (ML) Co, 6 ML Cu, and 15.5 ML Ni after application of an external magnetic field of 240 Oe in the direction indicated by the arrow labelled "H". For this Cu spacer layer thickness the magnetic interlayer coupling by indirect exchange through the Cu layer is relatively weak [2], so that the magnetization directions of the magnetic Ni and Co layers are along its individual easy axes, perpendicular to the film plane ("out-of-plane") for the Ni layer and along the film plane ("in-plane") for the Co layer. The left panel shows the domain pattern of the Ni layer, as seen through the Co and Cu layers, obtained at the photon energy of the Ni L_3 absorption edge (851 eV). A regular stripe domain pattern is observed, in which the magnetization in neighboring stripes is oriented out of the film plane and into the film plane, as indicated in the figure. The right panel shows the domain image of the Co layer at exactly the same sample position, obtained at the photon energy of the Co L_3 absorption edge (778 eV). The Co mag-

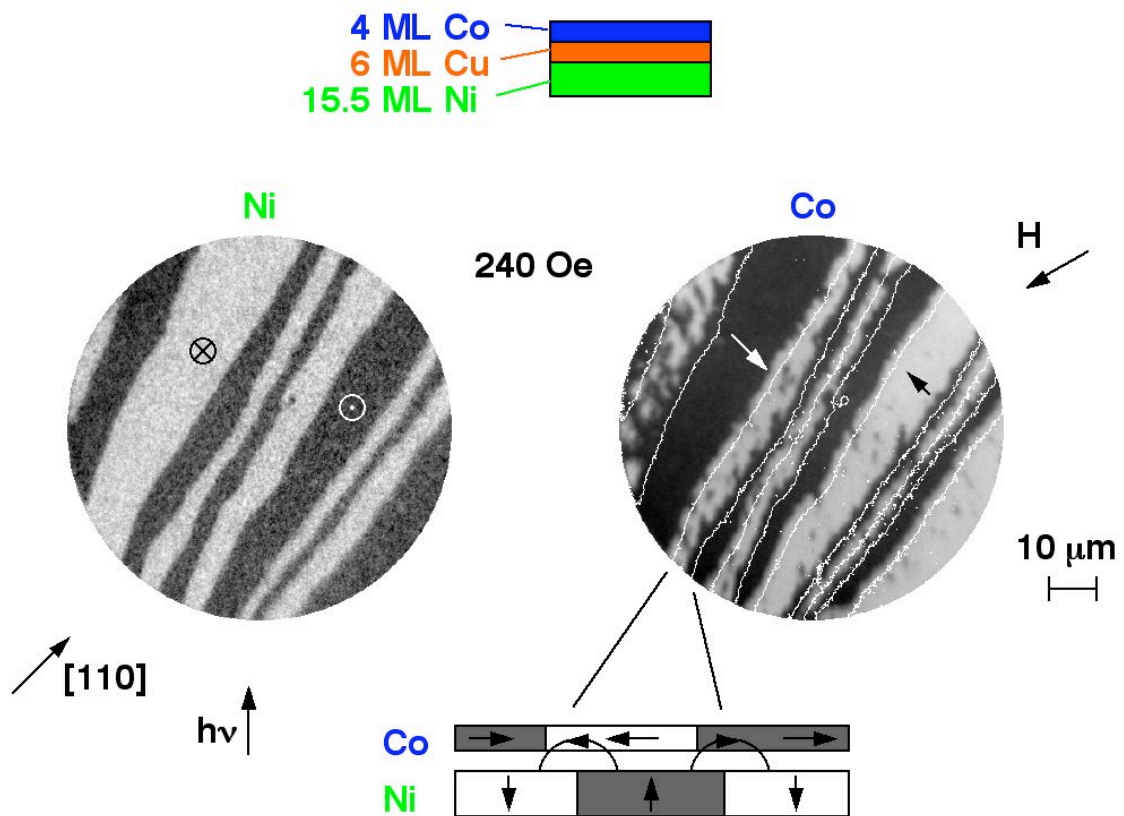


Fig. 1: Left: Magnetic domain image of the Ni layer of a 4 ML Co/6 ML Cu/15.5 ML Ni trilayer (see sketch at the top of the figure). The local Ni magnetization in the bright and dark stripes points into and out of the film plane, respectively. Right: Magnetic domain pattern of the Co layer at exactly the same sample position. A similar stripe domain pattern as in the Ni layer is recognized, in which bright and dark stripes correspond to local magnetization directions along $[-110]$ and $[1-10]$ in-plane directions, respectively, as indicated by arrows. Small white lines in the Co domain image mark the positions of the Ni domains. The observed lateral displacement of the Co domains with respect to the Ni domains is due to local magnetostatic coupling by magnetic stray fields from the Ni domain walls, as indicated in the sketch at the bottom.

netic domains qualitatively replicate the stripe pattern of the Ni layer, although the magnetization direction in the Co stripes is along two opposite in-plane directions and thus perpendicular to the Ni magnetization direction.

To facilitate the detailed comparison of the two domain images, white lines in the Co image (right) reproduce the contour lines at 50% contrast change of the Ni domain image, and indicate the position of domain walls in the Ni layer. A systematic lateral displacement of the Co in-plane domains with respect to the Ni domains to the upper left is observed. This shift is the consequence of a local magnetostatic interlayer coupling mediated by magnetic stray fields emanating from Ni domain boundaries. This is explained by the sketch at the bottom of Fig. 1. Magnetic flux closure between neighboring Ni domains leads to a magnetic stray field at the position of the Co layer with a component in the film plane, as indicated by the curved arrows. The interaction of the Co magnetization with

this stray field leads to a preferential Co magnetization direction perpendicular to the Ni domain walls, pointing either to the upper left or to the lower right of the image, depending on whether the Ni domain wall separates an “up” from a “down” domain or vice versa.

The effect can be quantified by applying external magnetic fields of different magnitude. We observed that a field of 265 Oe along the direction indicated by “*H*” is required to annihilate the white domains in the Co domain image [3]. Micromagnetic simulations revealed that while the maximum of the stray field of Ni domain walls at the position of the Co layer is calculated to be about a factor of two higher than that value, its lateral extension is quite narrow (about 50 nm), so that the effect on the Co layer magnetization becomes laterally averaged out and lowered by the exchange stiffness of the Co layer [3]. Despite the obvious importance of such local coupling mechanisms for the controlled separate manipulation of the magnetization of individual magnetic layers in a multilayered magnetic system, relatively little experimental work up to now has focused on the micromagnetic interactions in magnetic interlayer coupling [4,5]. This may be due to the lack of adequate techniques, which must not only provide microscopic lateral resolution, but also allow layer-selective probing of the magnetic domain structure. XMCD-PEEM has proven an ideal tool for such investigations, and is expected to provide valuable insights into micromagnetic interactions in coupled magnetic systems.

- [1] W. Kuch, Appl. Phys. A **76**, 665 (2003).
- [2] W. Kuch, X. Gao, and J. Kirschner, Phys. Rev. B **65**, 064406 (2002).
- [3] W. Kuch, L. I. Chelaru, K. Fukumoto, F. Porrati, F. Offi, M. Kotsugi, and J. Kirschner, Phys. Rev. B **67**, 214403 (2003).
- [4] L. Thomas, J. Lüning, A. Scholl, F. Nolting, S. Anders, J. Stöhr, and S. S. P. Parkin, Phys. Rev. Lett. **84**, 3462 (2000).
- [5] R. Schäfer, R. Urban, D. Ullmann, H. L. Meyerheim, B. Heinrich, L. Schultz, and J. Kirschner, Phys. Rev. B **65**, 144405 (2002).

X-ray investigations of a heat sink mounted disk laser device

J. Grenzer^{1,2}, U. Zeimer³, and U. Pietsch²

²University of Potsdam, Institute of Physics, Am Neuen Palais 10, 14469 Potsdam, Germany

³Ferdinand-Braun-Institut fuer Hoechstfrequenztechnik, Albert-Einstein-Str. 11, 12489 Berlin, Germany

Using the white beam setup at the EDR-beamline at BESSY we have investigated a semiconductor disk laser device. The optically pumped laser was mounted on a heat sink to ensure stable operation conditions. For a perfect optical device, i.e. for an homogeneous shaped Gaussian beam, it is necessary that the laser is mounted without any local stress.

The aim of the experiment was to characterize the local bending and uniformity of the laser after mounting. The laser device is mounted on a sapphire heat sink and consists of an AlAs/GaAs-Bragg grating and an InGaAs/GaAsP multilayer as active region. The overall thickness of the multilayer system is $6\mu m$. The lateral size of the laser is $2 \times 2mm^2$.

We have investigated the scattering of the laser device using an horizontal reflection geometry. Figure 1 shows the experimental setup. A cross section of the primary beam was defined by slits in front of the sample. The incident angle of the direct beam onto the sample was about $33degree$. Using either a narrow or a very broad white x-ray beam in order to illuminate the whole sample the diffracted intensity was detected using a CCD-X-ray camera at a diffraction angle of about $66degree$. Therefore, the measurement was carried out at the (004) reflection at an energy of about $8keV$. The adjustment of the sample was done by a point detector.

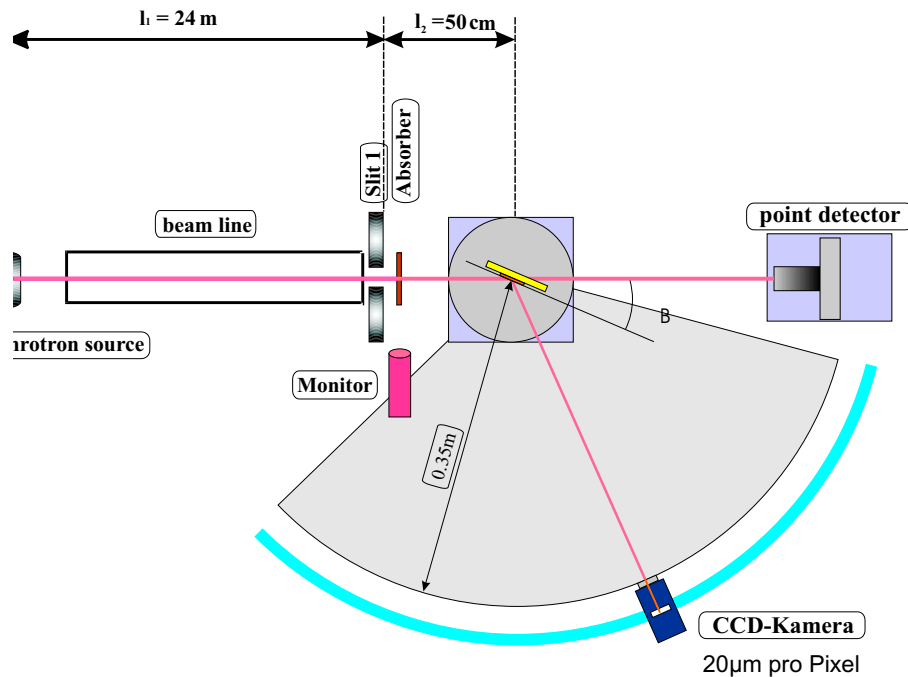


Figure 1: Experimental Setup to investigate the uniformity of a disk laser device.

¹e-mail: grenzer@rz.uni-potsdam.de

Using a broad rectangular beam ($7 \times 7\text{mm}^2$) it was very easy to find the imperfections of the device, and to decide whether the wafer is bent or not. However, a quantification is very complex. By illuminating the sample with a narrow beam ($< 0.25 \times 0.25\text{mm}^2$) and scanning the sample through the fixed beam the imperfections can locally be identified. Figure 2a shows a diffraction pattern of the laser measured with a broad beam. Instead of a rectangular sized diffraction pattern we found a complicated shaped pattern caused by the local bending of the laser crystal, i.e. the diffraction condition changes from point to point.

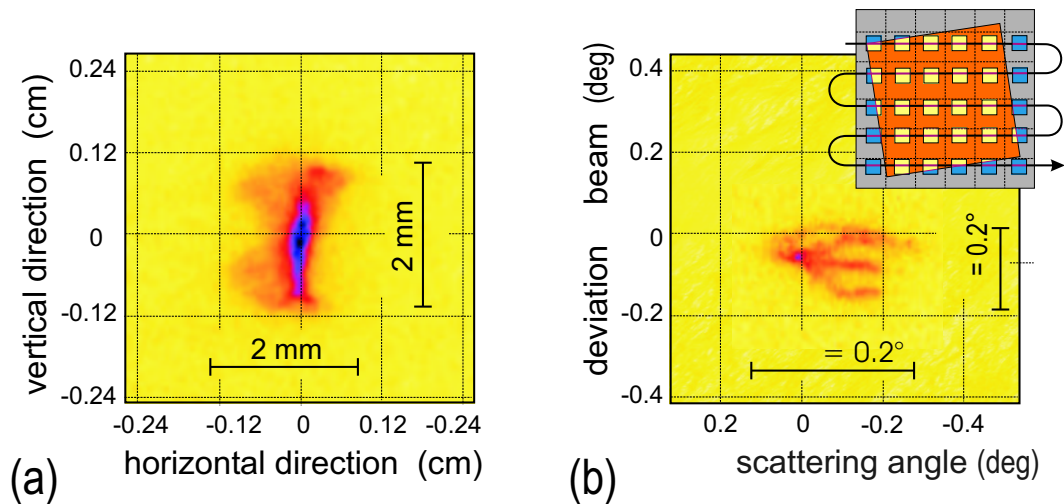


Figure 2: Diffraction patterns of an optically pumped disk laser measured at the (004) Bragg reflection either by illuminating the whole sample (a) or by a narrow beam at different positions (x,y) (b); the inset in (b) shows the measured points.

Figure 2b shows the same sample measured with a narrow beam at different positions of the sample with a step width of 0.5mm . The inset shows the pathway of the measurement. The diffraction pattern changes with each illuminated position. Figure 2b represents the integrated intensity of all positions. The whole device is bent by a radius of about 1m, however, the scanning shows that the laser is much more affected locally by the mounting.

We would like to acknowledge the help of A. Pucher to control the x-ray camera.

The sample was provided by Dr. Martin Zorn; FBH Berlin.

References

- [1] "Design and Characteristics of High-Power ($\approx 0.5\text{-W}$ CW) Diode-Pumped Vertical-Cavity Surface-Emitting Semiconductor Lasers with TEM₀₀ Beams", M. Kuznetsov, F. Hakimi, R. Sprague, A. Mooradian, IEEE Journal of Selected Topics in Quantum Electronics 5 (1999) 561

Growth and interface of MnAs/GaAs(001): An *in-situ* grazing incidence X-ray diffraction study

D. K. Satapathy, W. Braun, B. Jenichen, V. M. Kaganer
A. Trampert, L. Däweritz, K. H. Ploog

*Paul-Drude-Institut für Festkörperelektronik
Hausvogteiplatz 5–7, D–10117 Berlin, Germany*

At the PHARAO beamline, we have quantitatively studied the growth of MnAs/GaAs(001) layers under optimized growth conditions. Our aim is a detailed understanding of the structure of the MnAs/GaAs interface. MnAs epitaxy is performed at a substrate temperature of 250 °C on an As-rich $c(4\times 4)$ reconstructed GaAs surface. Under these growth conditions, the c -axis of the hexagonal unit cell is parallel to the GaAs $[1\bar{1}0]$ direction. Grazing incidence diffraction (GID) with synchrotron x-rays was used to measure the in-plane lattice parameters, and to follow the growth starting from the first monolayer. Under the conditions described above, MnAs grows epitaxially on GaAs(001) with the MnAs(11 $\bar{2}$ 0) plane parallel to the GaAs(220) plane which both are perpendicular to the surface and can be analyzed in a single radial scan along the $[110]$ substrate direction. The growth of MnAs proceeds in the Stranski-Krastanov growth mode. The evolution of the in-plane lattice parameter a measured from the peak position of MnAs(11 $\bar{2}$ 0) with respect to the substrate (220) peak is shown in Fig. 1(a). At the beginning of growth, the MnAs

layer is compressively strained. It relaxes with increasing thickness. This relaxation of the film is seen by a continuous increase of the in-plane lattice parameter a up to a layer thickness of 20 ML. When the in-plane lattice parameter has reached the final value, the strain energy is homogeneously distributed throughout the film and the growth proceeds smoothly. We estimate the average in-plane grain sizes in two perpendicular directions along the surface from the full-width at half maximum (FWHM) of the MnAs(11 $\bar{2}$ 0) and the MnAs(0002) peaks. The domain size increases with film thickness. It reaches a final value of ~ 27 nm along the MnAs

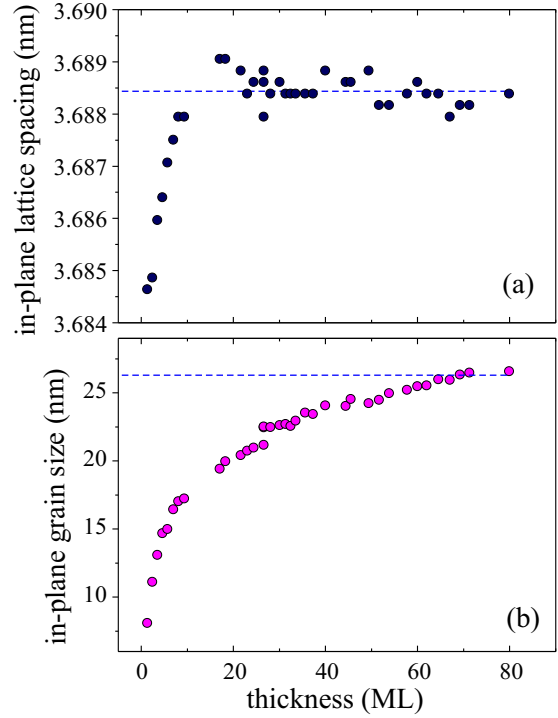


Figure 1: (a) Evolution of in-plane lattice parameter a with the thickness. The dotted line represents the lattice spacing after the final thickness is achieved. (b) Evolution of the in-plane grain size during growth. The dotted line represents the grain size after the final thickness is reached.

$[11\bar{2}0]$ direction at a layer thickness of about 75 monolayers as shown in Fig. 1(b). Along the perpendicular MnAs $[0001]$ direction, the final grain size is ~ 32 nm.

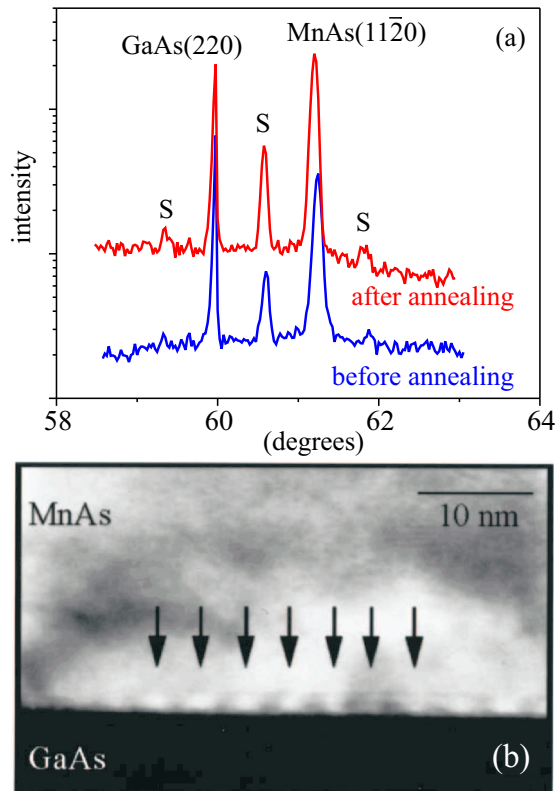


Figure 2: (a) Grazing incidence diffraction curves before and after the annealing of the sample. The angle of incidence is well above the critical angle of total external reflection. S denotes satellites due to dislocations. (b) Cross-section TEM micrograph of the interface between the MnAs epitaxial layer and the GaAs buffer layer. Arrows indicates the strain contrast due to the dislocation array.

From the X-ray reflection intensities along the crystal truncation rod (CTR) of the zeroth-order dislocation satellite, the thickness of the interface layer can be determined to 1.6 nm. Within this thickness the strain due to the dislocation array is inhomogeneously distributed. The MnAs layer was annealed at 400°C for 10 minutes to improve the crystallinity of the film. As shown in Fig. 2(a) after annealing the satellite reflections become more pronounced, showing an enhancement of the ordering of the dislocation array. The in-plane grain size increased by 20% along the MnAs $[11\bar{2}0]$ direction, indicating an improvement of the layer crystallinity.

GID allows to separate the signal of the interface structure from the signal of the epitaxial film. Depth resolution is achieved by changing the grazing incidence angle in the range from 0.2° to 0.8°. Additional satellites are seen when the angle of incidence exceeds the critical angle for total external reflection and penetrates into the film, which shows that the satellites are not a feature of the near surface region of the MnAs epitaxial layer but originate from the buried interface between MnAs and the GaAs buffer layer, Fig. 2(a). The satellites are found in scans along the MnAs $[11\bar{2}0]$ direction. They arise due to the formation of an ordered array of misfit dislocations, which accommodates the 7.5% lattice mismatch. From the positions of the satellites, the period of the dislocation array is calculated to be 4.9 nm in agreement with previous transmission electron microscopy (TEM) studies, Fig. 2(b). The number of satellites between the substrate and the layer reflection reveals that the component of the Burgers vector of this misfit dislocations is $1/3[11\bar{2}0]$. This result is in agreement with the Burgers vector determination by TEM. Such edge dislocations are most effective in stress relaxation. No dislocation satellites are found along the MnAs $[0001]$ direction.

From the X-ray reflection intensities along the

X-ray resonant magnetic scattering of Fe/Cr superlattices

A. Nefedov, J. Grabis, A. Bergmann, F. Radu and H. Zabel

*Experimentalphysik IV, Ruhr-Universität Bochum, Universitätstrasse 150, 44780 Bochum
Germany*

Magnetic heterostructures consisting of two or more ferromagnetic (F) layers separated by nonmagnetic or antiferromagnetic (AF) spacer layers have received much attention due to their importance in fundamental science and technology. The antiferromagnetic alignment of magnetic layers leads to a giant magnetoresistance effect (GMR) [1, 2], which is used in magneto-electronic devices, such as GMR reading heads, spin valves and tunnel junctions. The performance of these devices crucially depends on the chemical and magnetic structure, and especially on the quality of the AF/F interface.

During the last decade a growing number of experiments have been carried out, using atom and shell tunability of synchrotron radiation for the investigation of magnetic properties. Hannon *et al* [3] have shown that the corrective terms to the atomic scattering factor are sensitive to the magnetization of the sample. X-ray resonant magnetic scattering (XRMS) using either circularly or linearly polarized x-rays, has proven to be a highly useful technique for the study of magnetic properties of buried layers or interfaces and depth-dependent magnetic properties. In the case of magnetic multilayers, the periodicity of the magnetization amplitude leads to a magnetic contribution at the position of low-angle Bragg peaks for ferromagnetically ordered multilayers and at the half-order positions for antiferromagnetically ordered multilayers. Moreover, a varying external magnetic field can be applied during XRMS measurements, such that the magnetization reversal at corresponding L absorption edges can be followed, i.e. element-selective hysteresis loops can be measured.

We have grown an $[\text{Fe}(15\text{\AA})/\text{Cr}(8\text{\AA})] \times 20$ superlattice on a $\text{MgO}(001)$ substrate by molecular beam epitaxy. The Cr layer thickness of 8 Å corresponds to the first maximum in the AF interlayer exchange coupling [1, 2]. SQUID magnetometry indicated a strong AF coupling with a saturation field of $H_S \approx 30$ kOe. The XRMS experiments were carried out at different beamlines of BESSY II using a new UHV-diffractometer ALICE [4].

We start our discussion with experiments taken with circularly polarized light. By tuning the incident energy to just below the Fe L_3 edge, we observe strong magnetic Bragg peaks at the 1/2 and 3/2 positions in units of the reciprocal lattice vector of the first order structural peak associated with the superlattice periodicity (Fig. 1 a). Furthermore, from the presence of an 1/2-order peak in the off-specular reflectivity curve (open symbols) we can infer two additional properties: first, the individual ferromagnetic layers are decomposed into magnetic domains, and second, the ferromagnetic domains are strictly antiferromagnetically correlated from top to bottom.

Then we have investigated the field dependence of the intensity at the position of the half-order magnetic peak, which is reproduced in Fig. 1 b. As expected, the hysteresis loop has a maximum in the remanent state ($H = 0$ Oe) and decreases with increasing magnetic field. This decrease should continue until saturation is reached, but the background from charge scattering obscures this effect. Furthermore, in addition to the charge contribution in a scattering factor, the magnetic contribution is also present for all scattering angles, which results in a difference of the intensity for positive and negative field values. It should be noted that this difference takes only place when

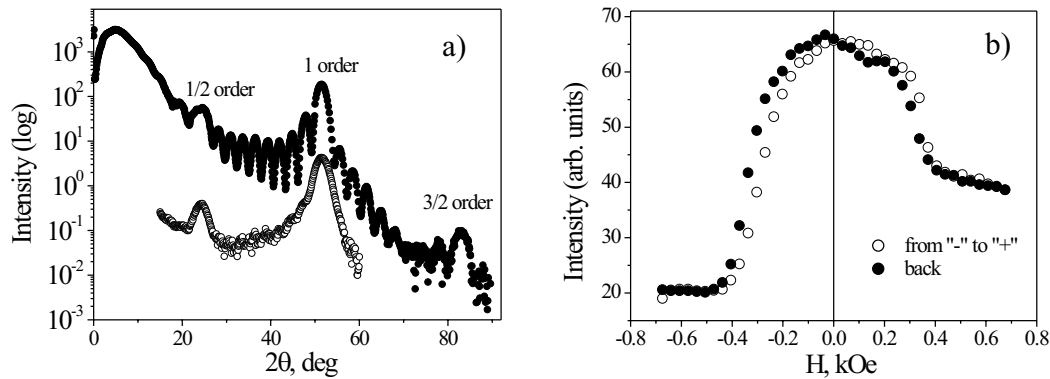


Figure 1: a) Specular (closed symbols) and longitudinal diffuse scans (0.4° offset) (open symbols) taken at the Fe L_3 edge for AF coupled superlattice with 20 repeats of [Cr(8 Å)/Fe(15 Å)] deposited on Cr(240 Å)/MgO(001) buffer-substrate system. b) Hysteresis loop measured at the position of the half-order magnetic peak ($2\theta = 24^\circ$) (circularly polarized radiation).

circularly polarized x-rays are used, which are sensitive to the in-plane sample magnetization in the scattering plane. The same hysteresis loop measured with linearly polarized x-rays exhibits the same background level for positive and negative fields, since in this case no in-plane magnetization component is detected.

Finally, it has been found that transverse scans across the half-order peak exhibit a sharp peak with a Lorentzian line profile superimposed on a flat shoulder of diffuse intensity. With increasing field the width of the central Lorentzian peak and the intensity of the diffuse intensity both drop by roughly a factor of two. From the Lorentzian line shape of the central half-order peak we infer a multidomain state in remanence, which diminishes with increasing field. At the same time the broad diffuse shoulder may reflect spin disorder at the Fe/Cr interface which decreases with increasing field.

We would like to thank J. Podschwadek for technical assistance during sample preparation, and T.Kachel and H.-Ch.Mertins (BESSY) for their help with the beamline operation. This work was supported by the German Federal Ministry of Education and Research (BMBF) under Contract No.03ZAE7BO.

References

- [1] P. Grünberg, R.Schreiber, Y. Pang, M.B. Brodsky, and C.H. Sowers, *Phys. Rev. Lett.* **57**, 2442 (1986)
- [2] S.S.P. Parkin, N. More, and K.P. Roche, *Phys. Rev. Lett.* **64**, 2304 (1990)
- [3] J.P. Hannon, G. T. Trammell, M. Blume, and D. Gibbs, *Phys. Rev. Lett.* **61**, 1245 (1988)
- [4] J. Grabis, A. Nefedov, H. Zabel, *Rev. Sci. Instr.* **75**, 4048 (2003)

Polarisation dependence of the x-ray reflectivity fine structure in hexagonal crystals

E.O.Filatova¹, E.Yu.Taracheva¹, J.-M. André², H.-Ch.Mertins³, D.Abramsohn³

¹ *Institute of Physics, St-Petersburg University, St-Petersburg, 198904, Russia*

² *Lab. de Chimie Physique, Université Pierre et Marie Curie, 75231 Paris, France*

³ *BESSY, Albert Einstein Str. 15, D-12489 Berlin, Germany*

*This work was supported by the bilateral program "Russian-German Laboratory at BESSY II".

The early experimental studies of the interaction of x-rays (s-polarised synchrotron radiation and unpolarised radiation of the x-ray tube) with one-axis crystals hex.BN [1] and hex.CdS [2] show that a very strong orientation dependence of K-shell near edge structure of both reflection and absorption spectra due to crystal orientation with respect to the electric field vector in both crystals exists. In the case of hex.BN a strong anisotropy of chemical bonding along and perpendicular to atomic layers results in the energy difference of π and σ resonances (the π are the lowest excitations and the σ are the highest ones) characterising the B and N K-shell absorption spectral dependence. This results in the orientation dependence of the polarisation vector \mathbf{E} of linearly polarised light with respect to the optical axis \mathbf{c} of the crystal ($\mathbf{E} \parallel \mathbf{c}$ or $\mathbf{E} \perp \mathbf{c}$). Strong effects are observed in transitions from the K shell to π ($2p_z a_2^-$ - component) and to σ ($e'(2p_{xy})$ -component) states of the conduction band. The hex.CdS is a cubic crystal in terms of nearest neighbours. The orientation dependence in this case is caused by virtual photoelectron scattering from the atoms located in distant coordination shells.

In this work the influence of the spatial crystal anisotropy on x-ray reflection spectra of polarised synchrotron radiation is investigated in detail.

The angular spectral dependencies of the reflection coefficients were carried out at the UE56/1-PGM line at the BESSY-UHV polarimeter [3]. The surfaces cut perpendicular to the optical \mathbf{c} axis of the crystal were analysed. B K-reflection spectra of hex.BN and S $L_{2,3}$ - reflection spectra of hex.CdS were measured for different grazing incidence angles.

As follows from traditional Fresnel's formulae in the case of isotropic crystal the x-ray reflectivity in the near – critical – angle region (region of the total external reflection) almost does not depend on the polarisation direction of the incident radiation. According to calculations, for example presented in [4], the reflection coefficients R_s and R_p are distinguished on the quantity $10^{-2} - 10^{-6}$ for $\lambda \sim 10 \text{ nm} - 0.1 \text{ nm}$ in the region of small grazing incidence angles.

For one-axis crystal the permittivity tensor is a diagonal tensor in a rectangular coordinate system x, y, z when one axis of this system coincides with the optical axis of the crystal. The Fresnel-like formulae for the reflectivity of the s- and p-polarised incident radiation can be written [5]:

$$R_s = \left| \frac{\sin \theta - (\varepsilon_{xx} - \cos^2 \theta)^{1/2}}{\sin \theta + (\varepsilon_{xx} - \cos^2 \theta)^{1/2}} \right|^2, \quad (1)$$

$$R_p = \left| \frac{(\varepsilon_{yy} \varepsilon_{zz})^{1/2} \sin \theta - (\varepsilon_{zz} - \cos^2 \theta)^{1/2}}{(\varepsilon_{yy} \varepsilon_{zz})^{1/2} \sin \theta + (\varepsilon_{zz} - \cos^2 \theta)^{1/2}} \right|^2$$

where θ is the glancing angle and the ε_{ij} are the components of the dielectric tensor.

In our case the optical axis coincides with the z axis so $\varepsilon_{zz} = \varepsilon_{\parallel}$ and $\varepsilon_{xx} = \varepsilon_{yy} = \varepsilon_{\perp}$.

One can see from equations (1) that the coefficient R_s is determined by only one component ε_{\perp} . In contrast the coefficient R_p depends on both components ε_{\parallel} and ε_{\perp} resulting in the dependence of the electric field vector \mathbf{E} either perpendicular or parallel to the \mathbf{c} -axis of the crystal. However, at small grazing incidence angles the dependence of R_p on ε_{\perp} becomes negligible. So in the case of one-axis crystal the reflectivity near the absorption edge depends on the polarisation and orientation of the incoming radiation if the grazing incidence angle is close to the critical angle. Using the experimental measured R_s and R_p coefficients one could determine all components of the permittivity tensor of the one axis crystal from equations (1).

Figures 1 and 2 show the S $L_{2,3}$ - reflection spectra of hex.CdS measured for 6° and 15° and the B K-reflection spectra of hex.BN measured for 4° and 20° . A strong dependence on the polarisation of the light is observed.

The analysis of S $L_{2,3}$ -reflection spectra fine structure of hex.CdS crystal (Fig. 1) indicates that the reflection spectra present for the different polarisation quite the same number of main features and

that the energy positions of these structures are independent on the type of the polarisation. The shape of the reflection spectra depends only slightly on the type of the polarisation at

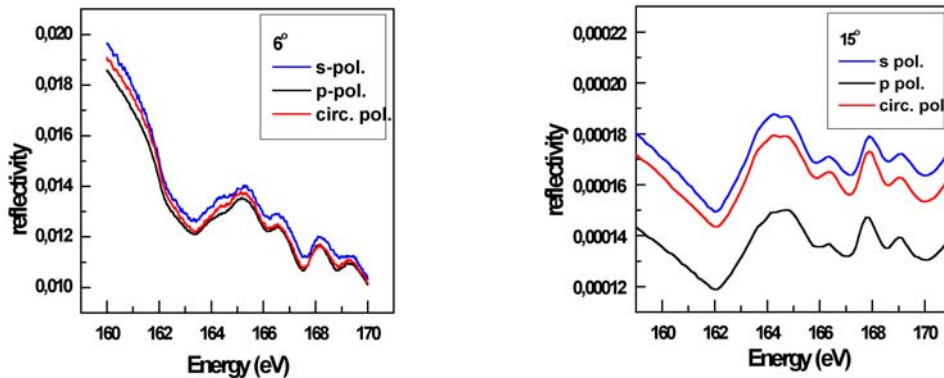


Fig. 1 $S L_{2,3}$ - reflection spectra of hex.CdS crystal obtained for different incidence angles (6° and 15°) with the help of s- and p-linearly polarised and circular (positive) polarised radiation.

all angles. (We emphasise that the polarisation dependence of the reflection spectra fine structure in the energy region 163-170 eV has been determined.) At the same time the polarisation dependence of the absolute values of the reflection coefficient is established. One can see that the tendencies in this polarisation dependence are in a good agreement with the traditional Fresnel's formulae.

The analysis of the fine structure in the B K-reflection spectra of hex.BN crystal (Fig. 2) indicates that the reflection spectra present for the different polarisation quite the same number of main features and that the energy positions of these structures are independent on the type of the polarisation and the same for all investigated angles. But in the case of hex.BN only for small grazing incidence angle $\theta = 4^\circ$ the shape of the reflection spectra depends only slightly on the type of the polarisation. The growth of the grazing incidence angle to 20° leads to a significant changing in the shape of all spectra. Strong intensity dependence due to type of the polarisation for peaks A and B takes place. One can see that the growth of the grazing incidence angle leads to considerable increasing of the intensity of peak A in the case of p- polarised radiation and of the intensity of peak B in the case of s- polarised radiation.

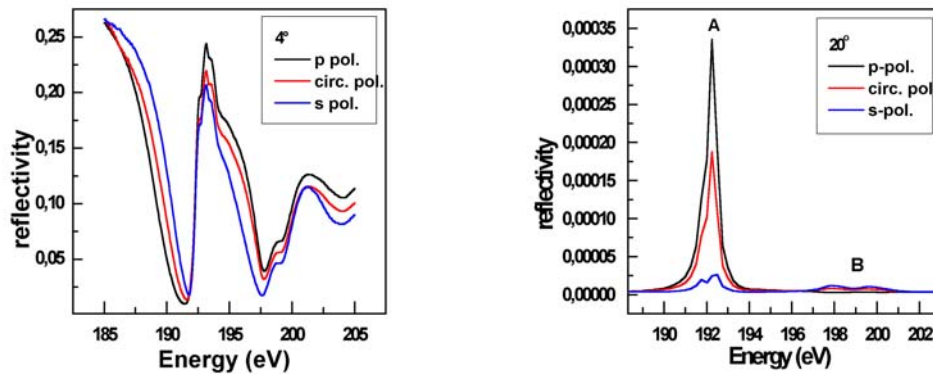


Fig. 2 B K-reflection spectra of hex.BN crystal obtained for different incidence angles (4° and 20°) with the help of s- and p-linearly polarised and circular (positive) polarised radiation.

Besides, in contrast with hex.CdS crystal there is the polarisation dependence of the absolute values of the reflection coefficient at small grazing incidence angle $\theta = 4^\circ$ in hex BN. One can see that only before energy 192 eV the coefficients R_s are larger in contrast to R_p . To understand this effect the angular dependencies of reflection coefficient $R(\theta)$ and angular distributions of scattered radiation for different incidence angles were measured. An additional maximum (the anomalous scattering peak) in the angular distribution of the scattering intensity at a glancing incidence angle exceeding the critical angle of total external reflection was discovered. Moreover the polarisation dependence of the angular position of this peak was established. The difference in anomalous scattering peak positions for p- and s-polarised radiation contributes approximately 0.8° . Taking into account the connection of the angular position of the anomalous scattering peak with the critical angle of total external reflection (anomalous scattering peak angular position coincides with critical angle [6]) and the equations (1) it is

reasonably safe to suggest that there are two critical angles for two different polarisation of the incident radiation. According to our investigations the critical angles for s-polarised radiation is smaller in comparison with p-polarisation. This result is in a good agreement with the theoretical predictions from [7] and with experimental investigations of orientation dependencies of B K-reflection spectra [1]. According to [1] the critical angles for two orientations of the crystal surface cut parallel to the optical axis in the region of π - resonance are distinguished on 1° .

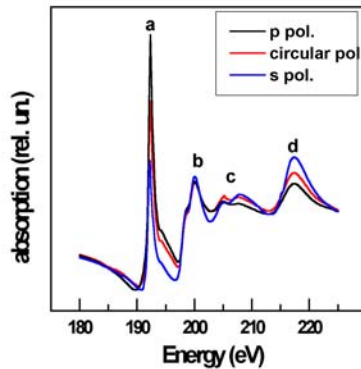


Fig. 3 B K-absorption spectra of hex.BN calculated from reflection spectra measured for $\theta = 4^\circ$ with the help of s- and p-linearly polarised and circular (positive) polarised radiation.

To interpret the reflection spectra polarisation dependence the absorption spectra were calculated from the reflection spectra measured for the grazing incidence angle 4° by means of Kramers-Kronig relations using the method described in [8]. The calculated spectra are plotted in the Figure 3. One can see the spectra for different type of the polarisation have similar numbers of features (a, b, c and d). The energy position of all features is independent on the type of polarisation whereas the intensity of all features depends on the polarisation. According to dipole selection rules with the regard to the crystal symmetry, in the simplest case of s-polarised radiation in hex.BN must originate from transitions from B 1s to σ states in the case when $\mathbf{E} \perp \mathbf{c}$ and from B 1s to π states when $\mathbf{E} \parallel \mathbf{c}$. According to experimental alignment the geometry $\mathbf{E} \perp \mathbf{c}$ is realised for s-polarised radiation and only transitions from B 1s states to σ states are expected in this case, so that the structure a is in agreement with our observations. On contrary when p-polarised radiation is used, the contribution of each component ($\mathbf{E} \parallel \mathbf{c}$ and $\mathbf{E} \perp \mathbf{c}$) to the overall reflection process is analysed. In the case of small grazing incidence angle the dependence of R_p on ε_\perp becomes negligible and one could consider that the coefficient R_p depends on ε_\parallel mainly that means that the alignment $\mathbf{E} \parallel \mathbf{c}$ is realised. So the transitions from B 1s to π states dominate in good agreement with our observations.

The dynamics of the polarisation dependence of the measured reflection and calculated absorption B K-spectra correlates well with the orientation dependencies obtained in the work [1]. However it should be emphasised that some differences in polarisation and orientation dependencies of reflection spectra exist. For example, an additional structure appears with the growth of the angle in the polarisation dependencies near peak A (from the side of small energies) in contrast with the orientation dependencies of the reflection spectra. The intensity of this structure depends on the type of the polarization and becomes largest in the case of s- polarisation. To understand this effect some additional measurements are necessary.

Acknowledgments

E.O.Filatova and E.Yu.Taracheva gratefully acknowledge the Russian-German Laboratory at BESSY II for financial support.

References

- [1] E.O.Filatova and V.A.Lukyavov. J. Phys.: Condens. Matter **14** (2002) 11643.
- [2] E.O.Filatova, J. -M André et. al.. J. Phys.: Condens. Matter (2004) in prints.
- [3] F. Schäfers et al., Appl. Opt. **38** (1999) 4074
- [4] L.K.Izraileva, I.B.Borovskiy. Izv.AN SSSR, ser.fiz. **36** (1978) 438
- [5] R.V.Vedrinskii et al., J. Phys.: Condens. Matter. **5** (1993) 8643
- [6] E.O.Filatova and T.A.Blagoveshenskaya. J. X-Ray Science & Technology **3** (1992) 204
- [7] V. Sh. Machavariani. J. Phys.: Condens. Matter. **8** (1996) 10687
- [8] E.O.Filatova et al., J. Phys.: Condens. Matter **11** (1999) 335

Investigation of Static Speckle Pattern by Energy-dispersive Coherent Scattering at the EDR-Beamline of Bessy II

T. Panzner^{a,b}, W. Leitenberger^a, J. Grenzer^a, K. Morawetz^a, U. Pietsch^a and H. Möhwald^b

^a Institut für Physik, Universität Potsdam, 14415 Potsdam, Germany

^b MPI für Kolloid- und Grenzflächenforschung, 14476 Golm

The investigation of energy-dispersive static speckle pattern from different samples under different scattering conditions was performed using the set-up shown in figure 1.

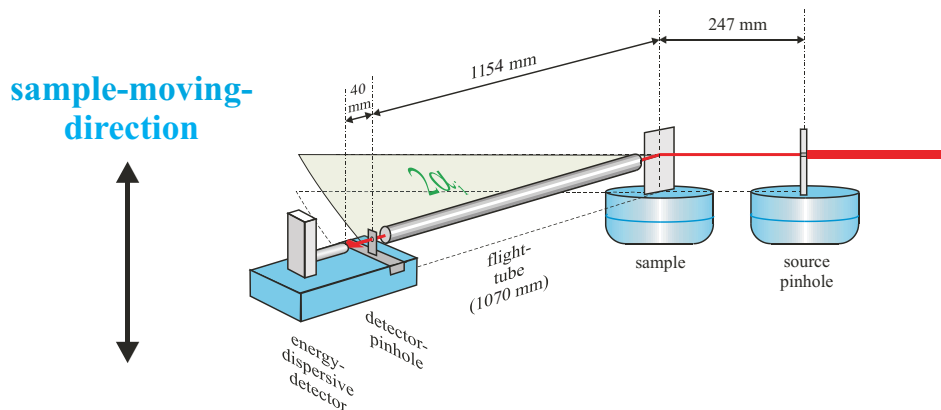


Figure 1: Experimental set up for the investigation of static speckle pattern in reflection geometry

In case of a thin polymer film on a Si-substrat we measured the reflectivity as a function of the sample position. As shown in fig.2 the shape and the intensity of certain features in the reflectivity curve changes with position. On the other hand the average of all scans corresponds to a conventional reflection curve measured with incoherent radiation (see left side of figure 2). The strong intensity fluctuations of local curves can be interpreted by : a) fluctuations of the surface height, b) fluctuation of the local film thickness, c) density fluctuations (important for polymers and other organic material) and d) heterodyne mixing of two scattering waves. We repeated the same measurement for different incident angles α_i being either smaller or larger compared to the critical angle of total external reflection α_c . This makes the measurement either more sensitive for the surface roughness or the fluctuations of film density, respectively. Figure 3 shows 3 line scans selected at one q_z value but measured at 3 different incident angles. The horizontal axis corresponds to vertical sample positions changed in steps of 10 μm . It is clearly shown that the speckle features measured at $\alpha_i < \alpha_c$ differ from that measured in opposite case. This gives a hope for the future to measure intensity fluctuations in organic films as a function of depth.

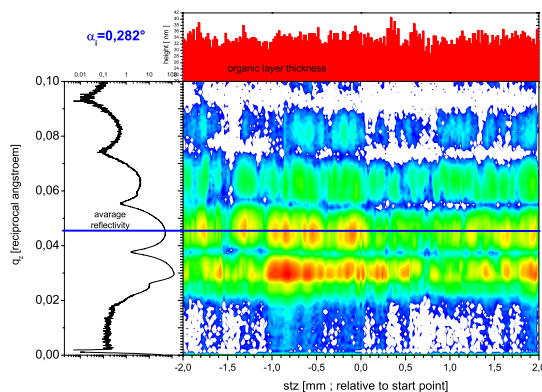


Figure 2: Coloured map of coherent scattering in reflectivity mode measured as a function of sample position

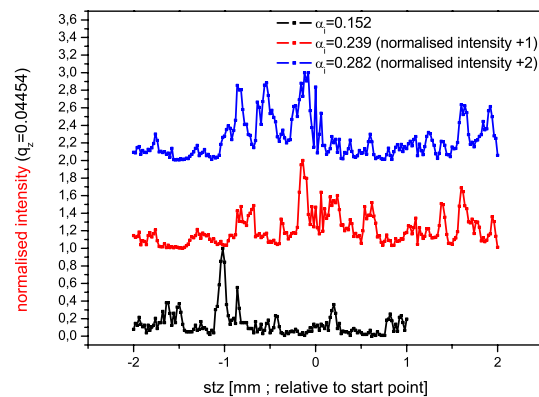


Figure 3: line scans for the same q_z but taken from different incidence angles

At last we recorded static speckle pattern at constant incidence angles but various angles of exit α_f , again as a function of the sample position. Figure 4 (top left) displays the appearance of several Fresnel fringes induced by diffraction at the incident pinhole if one changes the exit angle. After measuring the Fresnel fringes we performed scans for varying sample positions in the Fresnel pattern (black lines in Figure 4 bottom). Here we observed that the contrast of the speckles became improved measuring at an exit angle which corresponds to higher orders of Fresnel diffraction. This result will be considered for future measurements.

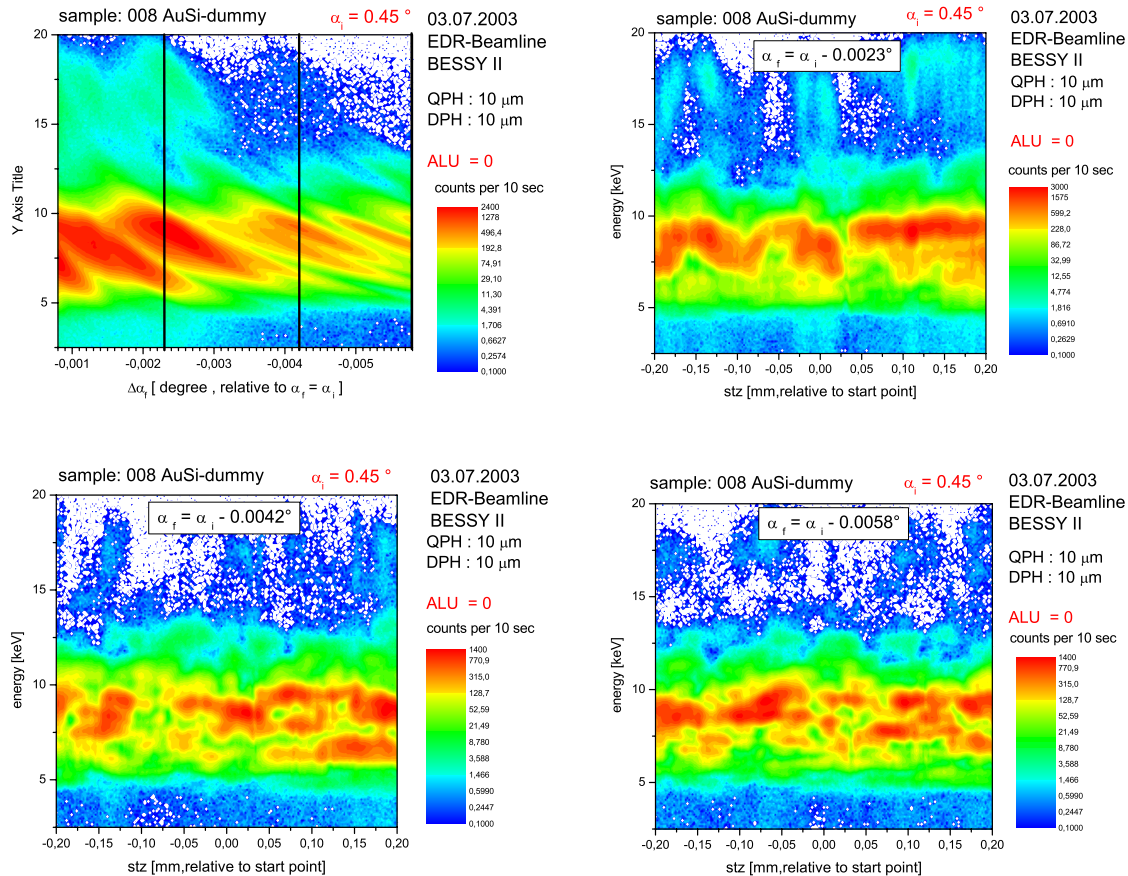


Figure 4 : Fresnel pattern after scattering at a gold sample (left upper corner) measured by changing the exiting angle. Sample-scan maps taken at different position of the Fresnel pattern (marked in the Fresnel pattern with black lines). The speckles becomes clearer for decreasing exiting angles, when the incidence angles kept fix.

The measurements have shown, that the EDR beamline at BESSY II can be used to perform coherent scattering experiments. We were able to detect static speckle pattern in reflectivity geometry which vary as a function of the incidence angle. This offers the opportunity to perform depth dependent speckle analysis. The estimated coherent flux through a 10 μm pinhole was measured to be $6 \cdot 10^6$ photons/100mA. This seems sufficient for an X-ray correlation spectroscopy experiment on the timescale of several seconds.

References

- [1] T. Panzner, W. Leitenberger, J. Grenzer, U. Pietsch, *J. Phys. D Appl. Phys.* 2003, 36, A93
- [2] W. Leitenberger, H. Wendrock, L. Bischoff, T. Panzner, U. Pietsch, J. Grenzer, A. Pucher, *Physica B, Condensed Matter* 2003, 336, 63
- [3] Poster GORDON research Conference , Bristol RI, 2003

Sub-Micrometer computed tomography at BAMline

Bernd R. Müller, Axel Lange, Michael Harwardt, Manfred P. Hentschel

Bundesanstalt für Materialforschung und -prüfung (BAM), D-12200 Berlin, Germany

Introduction

X-ray computed tomography is a powerful non-destructive investigation method, that has been applied in many fields of modern research. So far the major limitations were imposed by low detection efficiency and low spatial resolution. With the advent of third generation synchrotron facilities excellent high intensity X-ray sources became available that by far counterbalanced low efficiency. On the other hand the resolution of presently used detector systems is restricted by scintillator properties, optical light transfer, and CCD Granularity. They impose a practical limit of about one micrometer, while the Processing research demands urgently an advance in the submicron region. A break-through in this respect is being achieved by a novel detector type. It uses the properties of asymmetric Bragg reflection to increase the cross section of the reflected X-ray beam. A suitable combination of correspondingly cut Bragg crystals yields an image magnification that even at higher energies may surpass a factor of 1000. In this way the influence of the detector resolution can be scaled down accordingly.

Instrumentation and Measurement

During the last year such a device has been installed at the experimental stage of the BAMline [1]. At the first attempt the system consists of an asymmetric cut Si(111) crystal with an inclination between the net planes and the crystal surface of 5.7 degree. The Double Multilayer Monochromator delivers a parallel X-ray beam with photon energies up to 100 keV. The beam transmits the specimen which can be moved and rotated. The attenuated beam behind the specimen to be analyzed is then reflected by the asymmetric cut crystal which delivers a magnification up to 100 at a photon energy of 20 keV. The X-rays are converted to visible light by a 20 μm thick fluorescence layer made up of $\text{Gd}_2\text{O}_2\text{S:Tb}$. The light is projected by a set of camera objectives (see fig. 1) onto a charge coupled device (CCD). The CCD Camera consists of 2048 x 2048 Pixel with a Pixel size of 20 μm x 20 μm . It records the intensity of the light and this value is stored in a computer. The sample is then rotated by a small angle and another two-dimensional absorption image is obtained (see fig. 2 a). The process continues until 180 or 360 degree of the sample rotation has been recorded.

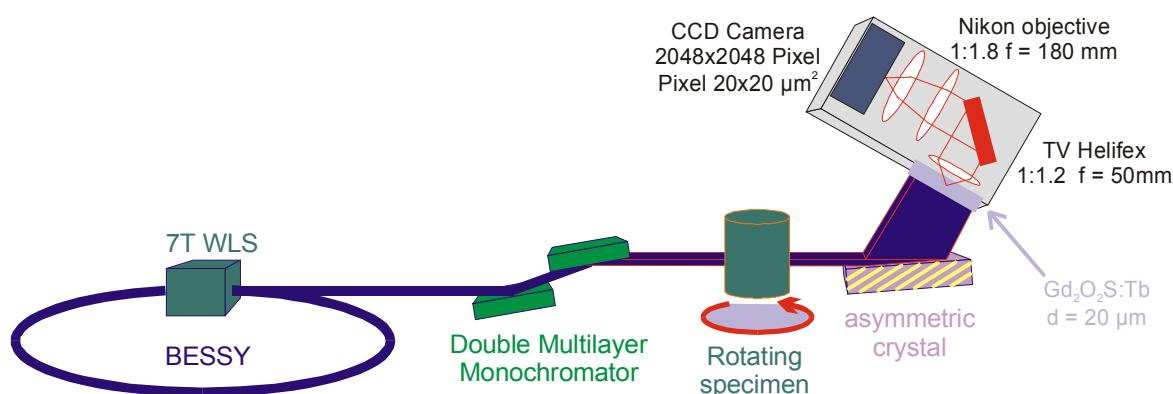


Figure 1: Experimental setup of the Computed Tomography test station with asymmetric Bragg-crystals as magnifier at the BAMline.

Results

In fig. 2 the result of the investigation of a glass capillary (left) and a stainless drill (right) is shown. The capillary has an outer diameter of about 200 μm and is filled with glass fibres of a diameter of about 12 μm . The drill has a diameter of about 100 μm . A moderate

magnification of about 20 for the glass capillary (at 17.9 keV) and about 45 for the drill (at 19 keV), respectively, was chosen.

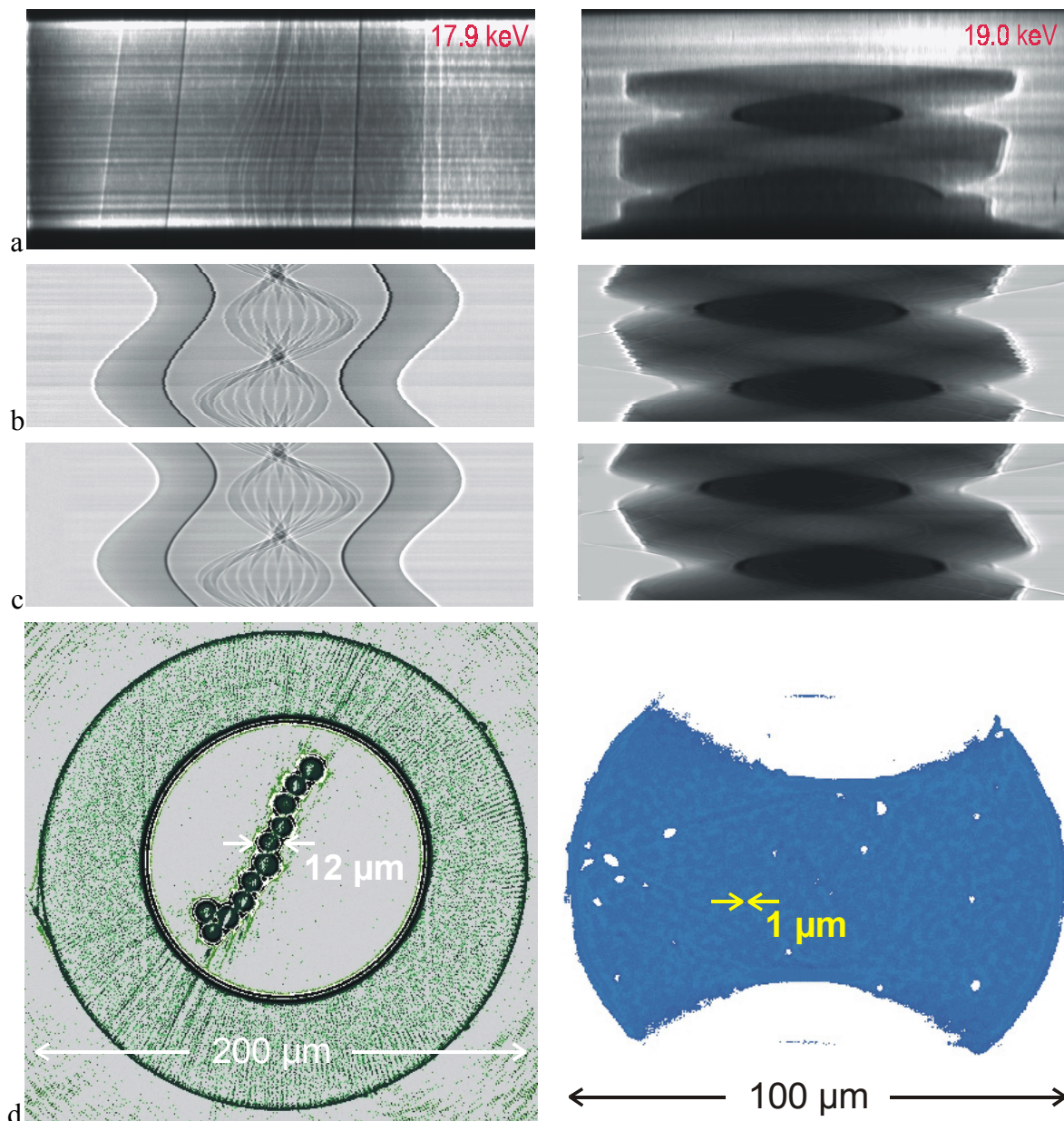


Figure 2: a) One of 360 projections of left: a 200 μm diameter glass capillary with 11 glass fibres with a diameter of about 12 μm , right: of a 100 μm diameter steel drill, respectively. b) Sinogram of one plain out of the CT data set. Due to the mechanical limits of the specimen manipulator lots of horizontal shiftings in the sine tracks are visible. c) After modifying the data set by the software “MODIFIEDB” the horizontal shiftings in the sine tracks are eliminated. d) Reconstruction from the modified Sinogram. At 17.9 keV the magnification by the crystal was 20, at 19.0 keV 45, respectively.

Even at the lower magnification the measurements highlights the mechanical limitations of the used specimen manipulator system (see the Sinogram, fig. 2 b). Lots of horizontal shiftings in the sine tracks are visible. To overcome the shortcoming of the manipulator system a software code was developed (and named “MODIFIEDB”). It compensates the horizontally shifting of the specimen caused by the ball bearing guideway of the manipulator (see fig. 2 c). After the modification of the data set by MODIFIEDB two-dimensional reconstructions of the linear attenuation coefficients in the sample interior where performed (See fig. 2 d). The reconstruction of the glass capillary shows artefacts which are caused by X-ray refraction at the interface between glass and air. This effect is up to now disregarded in the computer code for the reconstruction. The Reconstruction from the data set of the drill

measurement clearly shows pores with a diameter of less than 1 μm . The pixel resolution was about 150 nm x 150 nm.

References

- [1] W. Görner, M.P. Hentschel, B.R. Müller, H. Rieseemeier, M. Krumrey, G. Ulm, W. Diete, U. Klein, R. Frahm; "The first hard X-ray beamline at BESSY II", Nucl. Instr. and Methods in Phys. Res. A 467-468 (2001) 703-706.

Investigation of Pore Formation in Metallic Foams by Synchrotron Computed Tomography

A. Haibel¹, A. Rack¹, G. Weidemann², H. Riesemeier², J. Goebbels², J. Banhart¹

¹Hahn-Meitner-Institute Berlin, 14109 Berlin, Germany

²Federal Institute for Materials Research and Testing, 12200 Berlin, Germany

Metallic foams are highly porous materials. In most cases they consist of aluminium or zinc alloys mixed with titanium or zirconium hydride particles as blowing agent. Our research topics aim at the understanding of the physical processes during foaming and on the optimization of production by varying the manufacturing parameters.

One aim of our investigation is to understand the mechanism of pore stabilization by silicon carbide particles in aluminium foams. To achieve a sufficient stability of the aluminium foam during the foaming process, insoluble, partially wetted, micrometer-sized silicon carbide particles (SiC) were added to the alloy. Due to their partial wetting property, SiC-particles are assumed to accumulate on the pore surfaces.

As a first result of our measurements we see that the SiC-particles in the foamed material seem to accumulate preferentially on the pore surfaces (see Fig. 1).

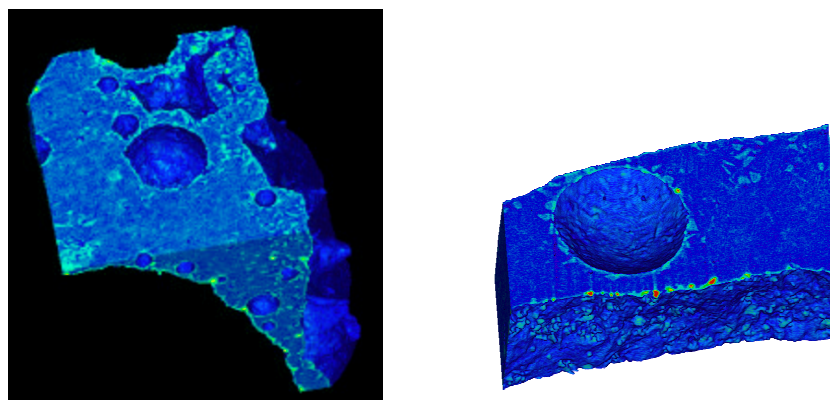


Figure 1: Left: Spatial arrangement of the silicon carbide particles (cyan) in the tomogram of the foamed material (blue, side length: 2 mm). The picture on the right side is a magnification of a single pore.

In order to quantify the spatial correlation between the pores and the SiC-particle positions we use a special 3d dilatation algorithm. Thereby the pores were sequentially dilated step by step. After each of these dilatation steps the SiC-particle voxels which became included in the increased pore volume were counted. If this fraction of added particles decreases while dilating a correlation between pore and particle position exists. Figure 2 represents the calculated results using this algorithm for the fully foamed material. The correlation between the pores and the particle accumulation is obviously for the investigated aluminium foams.

A second aim is to investigate the pore size distribution of zinc foams. In contrast to aluminium foam where a pore size distribution with a certain maximum is well-known, zinc foam shows a different behaviour. Figure 3 displays clearly that besides a pore population with big diameters also a population with tiny pores exists, a so called bimodular distribution. The calculated pore size distributions is displayed in Fig. 3, right.

The solubility of hydrogen in liquid zinc at a temperature close to the melting point is two orders of magnitude smaller than for liquid aluminium (< 0.002 at 516°C for liquid zinc and 0.69 at 660°C for liquid aluminium – measured in cm^3 of gas at atmospheric pressure and 0°C per 100 g metal). Our explanations for the different pore distributions in zinc and aluminium foam are based on that fact. In liquid aluminium smaller pores can not survive (pressure $\sim 1/\text{diameter}$) as the hydrogen always

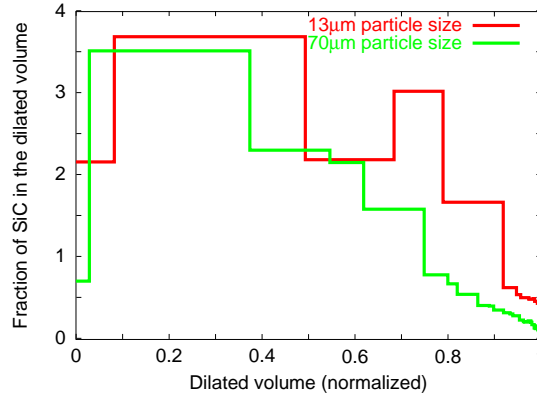


Figure 2: Correlation diagram of two fully foamed (right) alloys which differ by the SiC-particle size ($13\ \mu\text{m}$ and $70\ \mu\text{m}$).

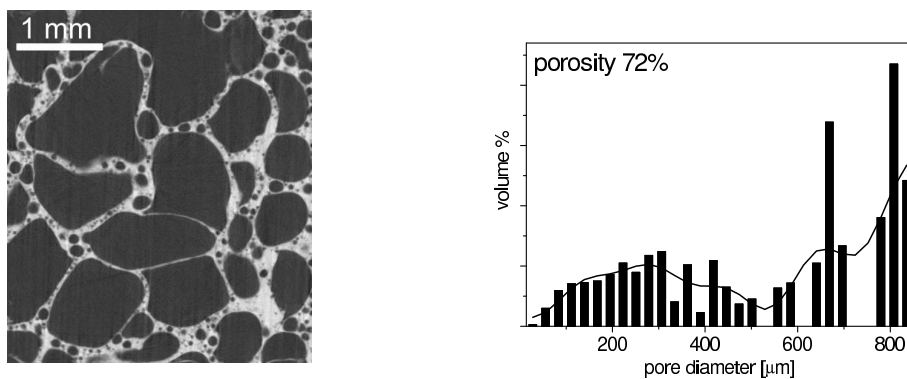


Figure 3: Left: Tomographic slice of a zinc foam with a porosity of $P=72\%$. Right: Pore size distribution for this zinc foam.

escapes. So we have a maximum for the pore size where an equilibrium of pressure-diffusion exists. For the zinc foam the hydrogen is trapped in each pore due to the small solubility and therefore even tiny pores can survive.

The investigations are done within the scope of the DFG-Project Ba 1170/4-2.

References

- [1] A. Haibel, J. Banhart, *Synchrotron-Tomography on Metallic Foams*, proceedings of the International Symposium on Computed Tomography and Image Processing for Industrial Radiology, 2003, ISBN 3-935538-12-X
- [2] A. Rack, A. Haibel, B. Matijasevic, J. Banhart, *Synchrotron Tomography on zinc and aluminium foams*, proceedings of the Metfoam conference "Cellular Metals and Metal Foaming Technology", 2003, ISBN 3-9311381-48-X
- [3] H. Kropf, A. Haibel, *Verifizierung von 3D-Tomographiedaten durch metallographische Untersuchungen*, proceedings of the Metallographie-Tagung, 2003, in press

Synchrotron- μ -Tomography on Complex Materials

A. Haibel¹, A. Rack¹, A. Bütow¹, H. Kropf¹, H.-M. Helwig¹, J. Banhart¹
G. Weidemann², H. Riesemeier², J. Goebbels²

¹Hahn-Meitner-Institute Berlin, 14109 Berlin, Germany

²Federal Institute for Materials Research and Testing, 12200 Berlin, Germany

Due to their special properties metallic foams are of high interest for the industry. They are used for light weight constructions, as energy and sound absorber, and for isolation. Further possible applications for metal foams arise by surface refinement in terms of spattering with other materials. Applications as corrosion, wearout, or heat protection, or as catalytic converter are conceivable. Surface coatings could be used also for electrical isolation or against adherence, for increasing mechanical stability, increasing thermal emission, or just as a decorative finish (for instance gold or silver coatings).

The focus of our research was the investigation of the bonding properties of this coatings. Therefore our metal foam samples were coated by the company “Berolina Metallspritztechnik Wesnigk GmbH” with five different metals (see Fig. 1).



Figure 1: Aluminium foams coated with a) titanium, b) brass, c) silver, d) copper, and e) zinc.

Based on non-destructive 3D studies (synchrotron-tomography) the metal skins on our aluminium foams were compared with results from 2D light microscopic and metallographic methods. Figure 1 shows the five aluminium foam samples, coated with titanium, brass, silver, copper, and zinc (from left to right). From these foams we prepared samples with $2 \times 2 \times 10$ mm size for the tomographic

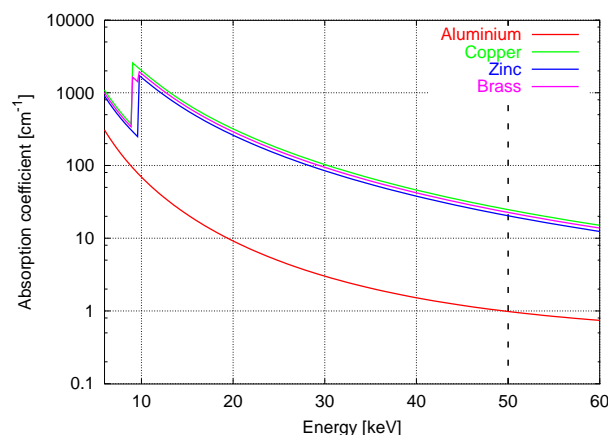


Figure 2: Absorption coefficients for the foam matrix (aluminium) and three different coating materials (copper, zinc, and brass) in the X-ray energy range between 6 and 60 keV. (The X-ray energy range at the BAMline is tunable between 6 and 60 keV.)

measurements. The measurements were carried out at the beamline “BAMline” at BESSY. By monochromizing the beam we are able to distinguish between regions of different absorption in the samples. Due to the high absorption coefficient of the metal coatings the X-ray energy was set to 50 keV (see Fig. 2). The spatial resolution was $3.6 \mu\text{m}$.

For discussing the results we chose three of the samples, the copper coated, the zinc coated, and the brass coated aluminium foams. As a first example Figure 3 (left) displays the tomographic picture of the copper coated foam. The center and the right part of Figure 3 shows 2D slices of

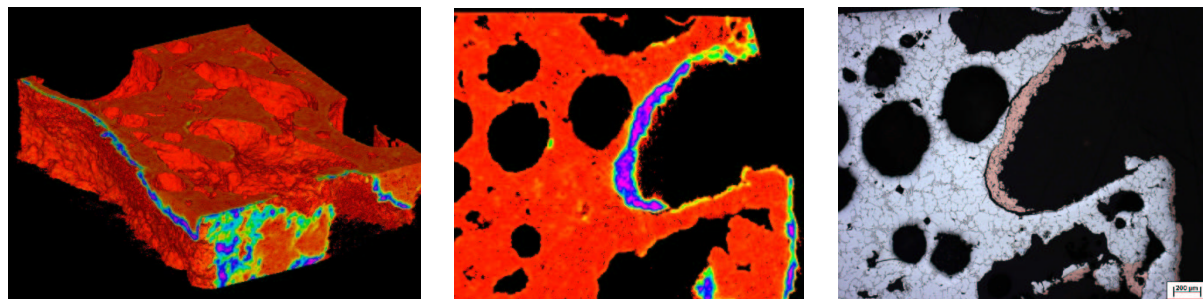


Figure 3: Left: Tomographic picture of a copper coated foam. Center: 2D tomographic slice. Right: metallographic cut of the sample. The tomographic slice and the metallographic cut (light microscopic image) shows the same layer of the sample.

the sample, a tomographic slice and a metallographic cut of the same layer as the tomographic one. The absorption coefficient of aluminium is for $E=50 \text{ keV}$ 1.1 cm^{-1} whereas the absorption coefficient of copper is 23.4 cm^{-1} . Therefore the copper coating is easily to distinguish from the matrix. In the tomographic images a good adherence of the copper coating can be recognized whereas in the microscopic picture a detachment is discernible. That implies, the detachment happens first during metallographic preparation, probably during the cutting, polishing or embedding the sample. Here the metallographic investigation method would provide an incorrect result.

In Figure 4 a 3D and a 2D tomographic image and a light microscopic picture of the zinc coated aluminium foam are plotted. Due to the high absorption contrast between the aluminium matrix

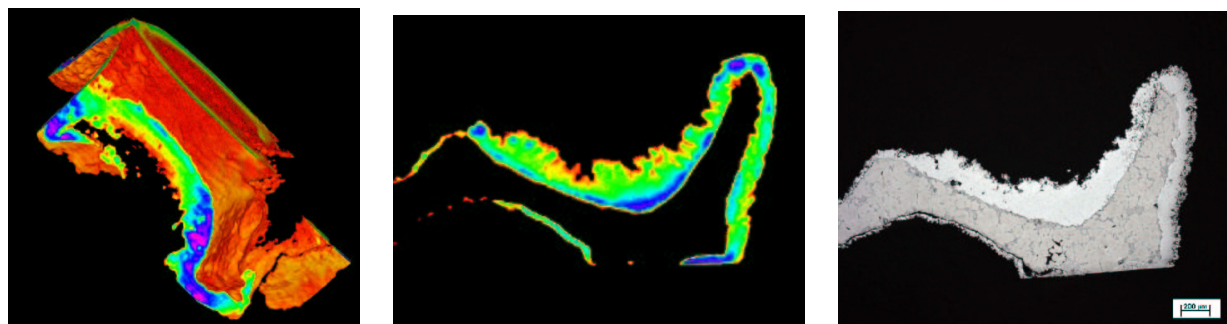


Figure 4: Left: Tomographic image of a zinc coated foam. Center: 2D tomographic slice. Due to the high thickness and the high absorption coefficient of the coating the aluminium matrix seems almost transparent and the coating is visible only. Right: metallographic cut of the same layer.

($\mu=1.1 \text{ cm}^{-1}$) and the thick zinc skin ($\mu=20.7 \text{ cm}^{-1}$) the aluminium occurs almost transparent in the tomographic images. Here the light microscopic measurement method presents the better result. One discerns a prevailing good bonding of the coating.

Two tomographic images (3D and 2D) and one metallographic cut of a brass coated foam are depicted in Figure 5. The absorption coefficient of brass is $\mu=23.0 \text{ cm}^{-1}$ and the coating is easily identifiable. Here a poor bonding can be verified in the tomographic image as well as in the light microscopic cut. Because the poor bonding of the coating is shown already in the nondestructive tomographic measurements it is obvious that the detachment occurred during or directly after covering.

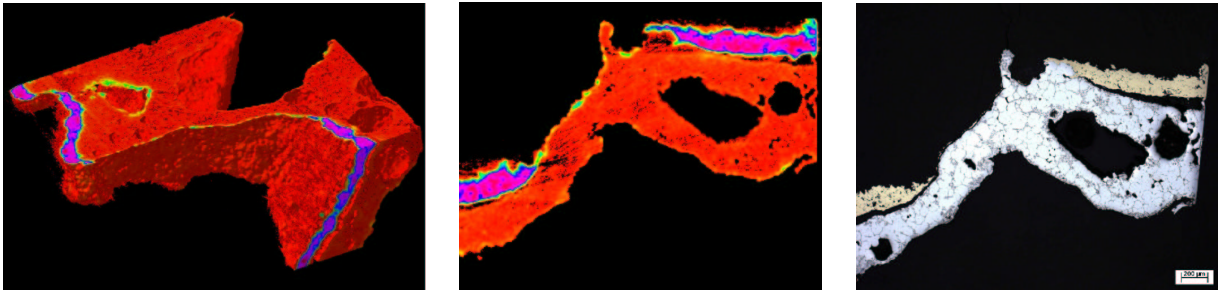


Figure 5: Left: Tomographic picture of a brass coated foam. Center and right: A tomographic and a light microscopic 2D slice of the same sample layer.

By means of 3D- μ -tomography we were able to visualize the bonding behaviour of metal coated aluminium foams and to analyze the complex structures of such materials non-destructively. In contrast to the metallographic investigation methods no additional preparation steps are necessary which leads to unsophisticated results.

References

- [1] H. Kropf, A. Haibel, *Verifizierung von 3D-Tomographiedaten durch metallographische Untersuchungen*, proceedings of the Metallographie-Tagung, 2003, Berlin, in press
- [2] A. Haibel, A. Rack, H. Kropf, H.-M. Helwig, H. Riesemeier, G. Weidemann, J. Goebbels, J. Banhart, *Synchrotron-Tomography on Complex Materials*, poster contribution of the BESSY user meeting, Dec. 2003

Ultra-Fast Probe of Magnetization Dynamics Using The New Low-alpha Mode of BESSY

A. Oelsner, A. Krasnyuk, S. A. Nepijko, A. Kuksov*, C. M. Schneider*, G. Schönhense

Institut für Physik, Johannes Gutenberg Universität Mainz

* Institut für Festkörperforschung IFF-6, Forschungszentrum Jülich GmbH

The imaging of magnetization reversal processes on the sub-nanosecond time scale by means of photoemission electron microscopy (PEEM) currently becomes an important research field, driven by applications of fast-switching spintronic devices such as magnetic RAM elements. The experimental approach to this problem consists of a combination of microstrip-lines [1] (or microcoils [2]) carrying ferromagnetic microstructures with a time-resolved imaging of their magnetic domains using PEEM, exploiting the inherent time structure of the light from a synchrotron facility [3, 4]. In the past, the best time resolution of PEEM-based stroboscopic experiments on magnetic domains that we could achieve was about 125 ps, which was mainly limited by the temporal width of the X-ray pulse (or equivalently, the bunch length of the storage ring) [5].

A new operation mode (low-alpha bunch mode) at BESSY together with improvements at the pulse generator / delay device of the instrument enabled us for the first time to observe magnetization dynamics with a time-resolution of about 10 ps. The experimental setup is shown in Fig.1. The magnetization changes are driven by a magnetic field pulse created by a current pulse passing the microstrip-line device. The field pulse was held in phase with the time structure of the synchrotron radiation and could be shifted in time via a precision delay generator.

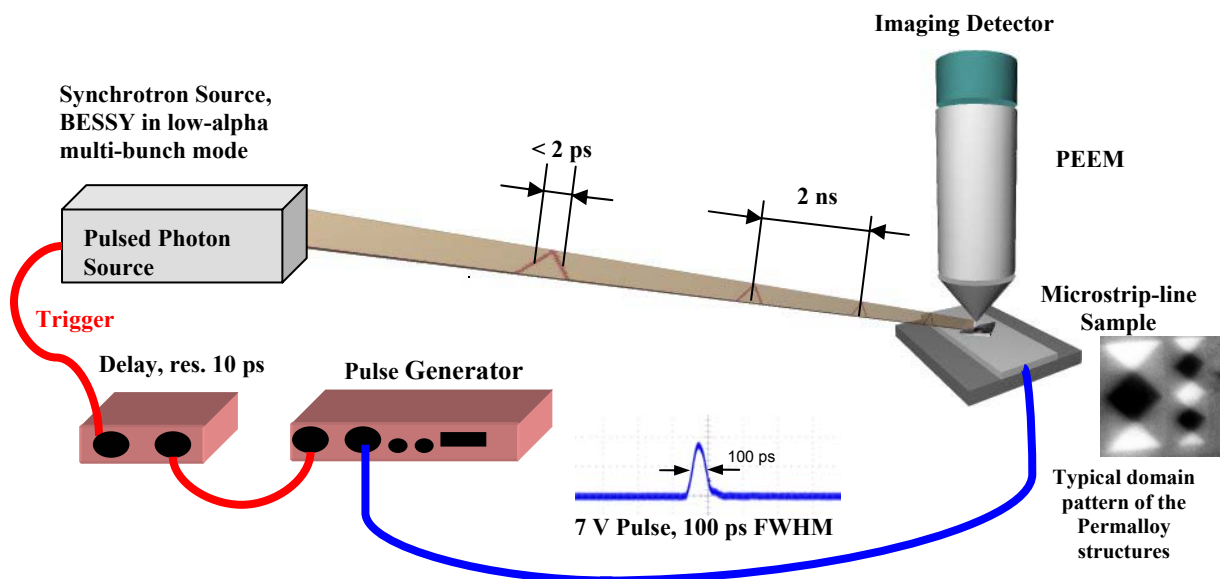


Fig. 1: Experimental setup for time-resolved observation of magnetization dynamics

In our experiments we used the low-alpha multi-bunch option providing a typical X-ray pulse length below 2 ps as probe to acquire MXCD images. The pulse generator produces pulse amplitudes of about 7 V (approx. 2 mT) with a FWHM of 100 ps at a frequency of 500 MHz synchronous with the X-ray time structure. An internal electronics unit controls the delay of the pulse generator with an accuracy of 10 ps, the delay being shifted stepwise for different probing times. Typically, a jitter between 8 ps and 14 ps was measured comparing synchrotron trigger and pulse generator output. After passing the strip-line and leaving the vacuum chamber, the pulse width was broadened to about 1.5 ns, while the rising edge (200 ps) was still remarkably steeper than the falling edge. From earlier experiments on these devices we know that the effective pulse shape at the sample is less broadened than the signal

observed far behind the strip-line due to additional cables and contacts. Thus, the true rising edge of the field pulse is expected to be shorter than 200 ps, when it arrives at the magnetic structure. Due to the fast rising edge, Fourier components up to several GHz are excited in the magnetic film. The ferromagnetic rectangular microstructures consisted of Permalloy (30 nm thick) with a maximum feature size of 40 μm . The MXCD probe of their domain structure has been done at the Ni - L_3 absorption edge. A static domain pattern of the structure investigated is shown in the lower right corner of Fig.1. As a response to the field pulse the domain walls are displaced and move in a damped oscillation around their initial position [7], shown in the preliminary analysis of this movement in the right-hand plot of Fig. 2. Note that the stroboscopic images consist of $6 * 10^{10}$ cycles.

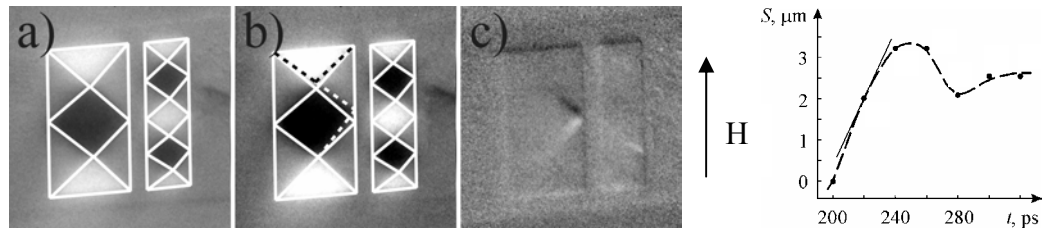


Fig. 2 left: Domain pattern movement at different probing times: a) 0 ps, b) 10 ps, c) difference between patterns in a) and b), the time zero (0 ps) is chosen at 1.25 ns after the rising edge of the field pulse, when the external field is supposed to be zero. H denotes the direction of the pulsed field.

Right: Preliminary analysis of the time-dependent domain wall displacement, the shift S of the domain wall in the centre of the image is plotted versus the probing time t with respect to the field pulse cut-off edge.

The time zero (0 ps) was taken at about 1.25 ns after the rising edge arrived at the structure (field pulse cut-off). With increasing probing times, the investigated area should be nearly field-free, thus reflecting the system response after the field pulse. The reference time is marked by a small change in magnification, while the 7 V amplitude reaches the area under investigation. This is caused by the PEEM electron optics' response to the electrical field of the pulse. A selected sequence of difference images is shown in Fig. 3 for probe time differences of 20 ps and 10 ps. The domain boundary motion can be observed in a reproducible way over the whole period of time until 420 ps after the 0 ps reference point. Occasionally, a non-reproducible total switching of a part of the domains was observed, indicated by the strong black and white contrast in the upper left difference image of Fig. 3 (0 ps - 20 ps). A total magnetization reversal could not be induced by the pulse itself, because the field pulse amplitude was too small (about 2 mT). It is very likely that this random switching arises from instabilities due to an increased sample temperature, caused by the high pulse frequency of 500 MHz.

The displacement of the domain boundaries, however, was reproducible; this behavior leads to comparably small changes as seen in all other difference images. In general, different domain wall regions seem to respond at different probing times, for instance, when comparing probing times (20 ps - 40 ps) with (80 ps - 100 ps) or (100 ps - 120 ps). The domain motion of the larger rectangular structure (left) seems to be more strongly damped than that of the smaller structure (right). At certain probing times (at about 60 ps, 220 ps and 380 ps) a concerted oscillation of all domain walls was observed, followed by smaller oscillations. In this time interval of damped oscillations we find an average domain wall speed of $6 * 10^4$ m/s (Fig. 2 right plot) being larger than the value observed in earlier experiments on 80 μm sized structures [6]. Besides the smaller feature size here, one reason for this difference could be the much smaller field pulse leading only to minor oscillation amplitudes in the motion of domain walls. Therefore the restoring forces of the domain pattern are remarkably smaller here. Another reason might be given by the higher temperature of the device which consumes much more power from the high frequency of the current pulses at 500 MHz.

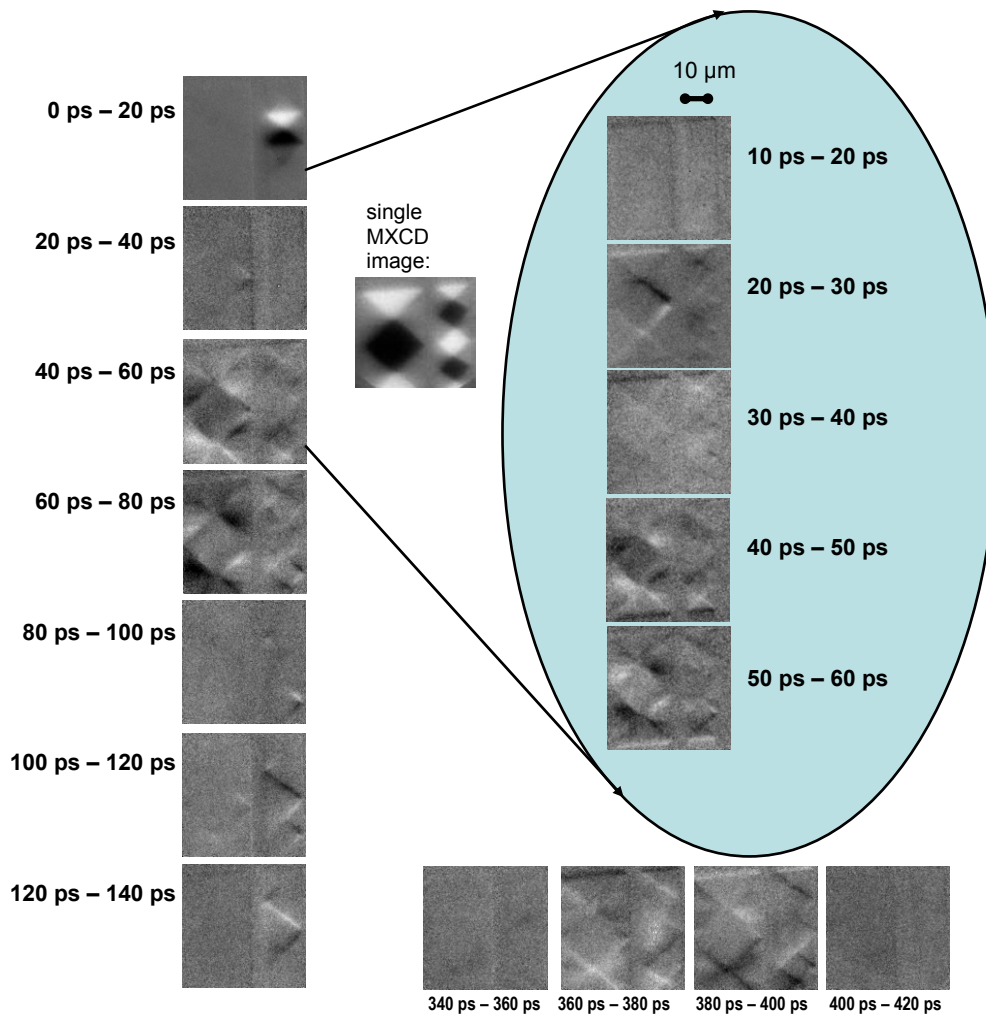


Fig. 3: Time dependent differences of the magnetic domain patterns, maximum changes in domain boundary positions appear at different times for two rectangular structures

Our first results using the BESSY low-alpha operation mode are very promising. Technically, we were able to reach a time resolution below 20 ps. Nevertheless, it needs more data and further systematical effort to understand the observed domain wall motion behavior in detail.

The experiments are funded by BMBF grants 05 KS 1 UM 1/5, 05 KS 1 BDA/9, 13 N 7675 /2 and 13 N 7863. The authors thank the staff at the Synchrotron facility BESSY in Berlin for the great support providing the low-alpha operation mode.

Literature:

- [1] A. Krasnyuk, A. Oelsner, S.A. Nepijko, A. Kuksov, C.M. Schneider, G. Schönhense
Appl. Phys. A **76** (2003) 863-868
- [2] J. Vogel, W. Kuch, M. Bonfim, J. Camarero, Y. Pennec, F. Offi, K. Fukumoto, J. Kirschner,
A. Fontaine, S. Pizzini, Appl. Phys. Lett. **82** (2003) 2299
- [3] A. Krasnyuk et al.; BESSY Annual Report 2002 (2003) p. 365
- [4] A.Oelsner, A. Krasnyuk, D. Neeb, S.A. Nepijko, A. Kuksov, C.M. Schneider, G. Schönhense
J. Electron. Spectr. Rel. Phenom, in print
- [5] A. Kuksov, C.M. Schneider, A. Oelsner, A. Krasnyuk, D. Neeb, G. Schönhense, C. de Nadai,
N. B. Brookes; J. Appl. Phys., in print
- [6] C.M. Schneider A. Krasnyuk, A. Oelsner, D. Neeb, and G. Schönhense, A. Kuksov and I. Mönch, J.
Morais, C. de Nadai and N.B. Brookes (submitted to Appl. Phys. Lett.)
- [7] M. Bauer, J. Fassbender, B. Hillebrands, R.L. Stamps;
Phys. Rev. B **61**, 3410 (2000)

Total reflection X-ray fluorescence studies of multilayer molecular films of liquid crystals

N.N.Novikova, S.I.Zheludeva, V.V.Lider, N.D.Stepina, W.Haase, A.I.Erko, A.A.Knyazev, Yu.G.Galyametdinov

A.V.Shubnikov Institute of Crystallography RAS

The technique used below is based on recording along with angular dependence of reflected x-ray beam the yield of characteristic fluorescence excited by incident x-ray beam at total external reflection (TER). Analysis of fluorescence angular dependence provides direct information of ion position in the layered systems in the direction of surface normal.

We studied rare-earth metallomesogens. These new highly magnetically anisotropic liquid-crystalline lanthanide complexes have received special interest as appropriate building blocks for easily aligned soft magnetic molecular materials. The mesogenic compound was synthesised at the Kazan Physical-Technical Institute, Russian Academy of Sciences.

The samples under investigation were multilayer films of Eu(III) compound deposited on silicon substrates by Langmuir-Blodgett technique. All samples were prepared on a Langmuir Trough Joyce Loebel. A 0,5 mg ml⁻¹ solution of Eu(III) compound in toluol was spread onto a triply distilled water and incubated during different exposure time before starting the compression. The transfer onto the substrate was carried out by the horizontal mode at $\pi=25$ mN/m. 3 films have been examined: 20 transfers, 7 transfers and 6 transfers. Experimental results only for 7 transfers film are presented in this report.

X-ray fluorescence measurements were carried out at the beamline KMC-2. The samples were mounted on a diffractometer to reflect in the horizontal plane. The bending magnet radiation was monochromated by a double crystal monochromator (SiGe graded crystals) to x-rays energy $E=13,2$ keV. The slit width of 100 μm (horizontal) and 1mm (vertical) was found to provide the optimal conditions for experimental measurements. The reflected x-ray beam was detected by scintillation detector. The fluorescent signal was measured by the Peltie cooled ROENTEC detector, the fluorescent spectrum was recorded at each point in the reflectivity curve in TER region.

X-ray fluorescence spectrum at $\theta < \theta_c$ (θ_c is the critical angles of TER for silicon) is shown in Fig. 1. The fluorescence peak of Eu L_α radiation is clearly distinguished. Besides the strong peaks of Ar K_α radiation (from argon of the surrounding atmosphere) and Si K_α radiation (from silicon substrate) can be seen. The most interesting in this spectrum is the set of additional peaks: Ca K_α , Fe K_α and Fe K_β , Cu K_α , Zn K_α and Zn K_β . From our point of view the presence of impurity ions in liquid crystal film may be explained by the incorporation of these ions from water subphase during deposition process. For all of these peaks the integrated intensity was plotted as a function of incident angle.

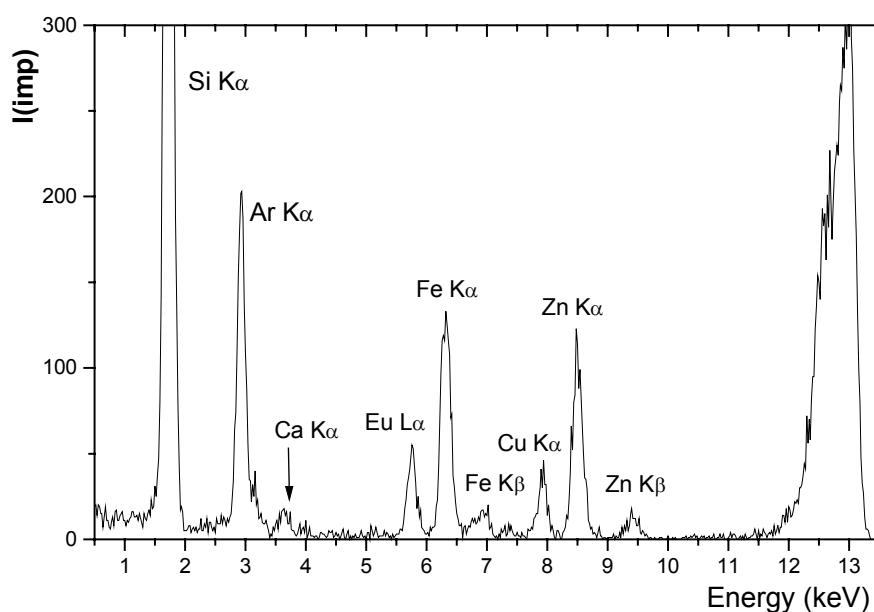


Fig. 1. X-ray fluorescence spectrum from molecular film of liquid-crystalline Eu(III) compound.

The angular dependence of Eu L_α -, Cu K_α - and Zn K_α -fluorescence yield are presented in Fig. 2. As can be seen the behavior of Eu L_α - and Cu K_α -fluorescence curves is nearly identical: these curves are sharply peaked at θ_c . The shape of Zn K_α -fluorescence is essentially different: it repeats reflectivity curve. Even qualitative observation of these experimental results indicates that Eu and Cu ions occupy similar position inside the film whereas Zn ions arrangement has an opposite nature. The complete analysis of experimental data will be published elsewhere.

This work was supported by the Russian-German Laboratory and by BMBF/DLR (grant RUS OO/203), DFG (grant 436 RUS/113/401/0-3).

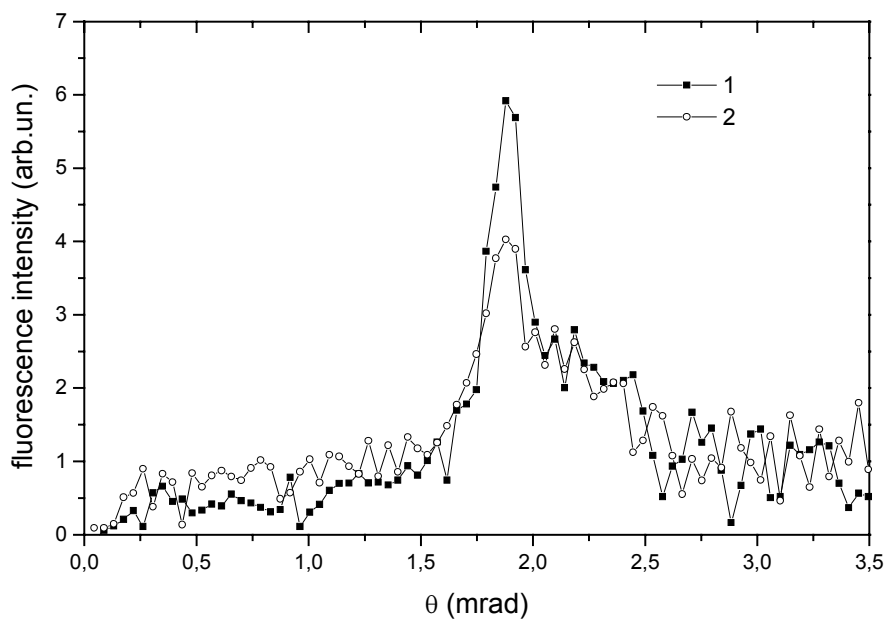


Fig. 2 a.

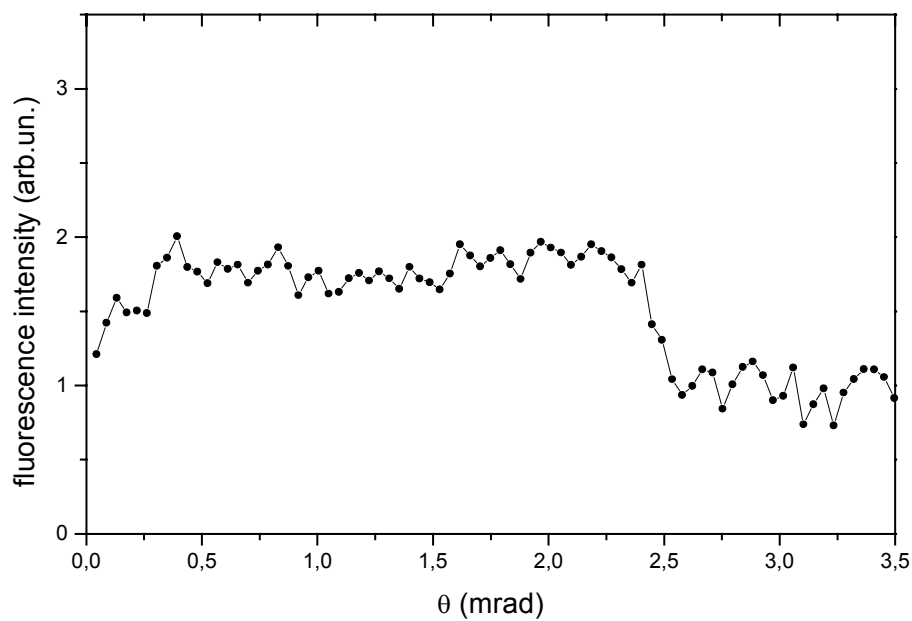


Fig. 2 b.

Fig. 2. Experimental fluorescence angular dependencies from molecular film of liquid-crystalline Eu(III) compound: a) Cu K_{α} (curve 1) and Eu L_{α} (curve 2) fluorescence yield; b) Zn K_{α} fluorescence yield.

L-edges EXAFS in Fe measured at UE46-PGM

H. Rossner, D. Schmitz, and H. Maletta

Hahn-Meitner-Institut Berlin, Glienicker Str. 100, 14109 Berlin

The gap scanning technique for long range energy scans ($\Delta E \sim 900$ eV) has been used to test performance and stability of the plane grating monochromator beamline installed at the elliptical undulator UE46 [1]. For this test the extended x-ray absorption fine structure (EXAFS) has been measured in Fe within the energy range of 680 eV - 1600 eV and a step size of 1.25 eV. The monochromator energy and the undulator gap size were moved together using set values based on magnetic field tables. This technique ensures the maximum light intensity for each monochromator energy. Energy scans have been performed for the third and fifth undulator harmonics using the symmetric mode with horizontal linear polarization, the 1200 l/mm blazed grating, an exit slit width of 100 μm , and the focussing mirror option for the last optical element (M4) of the beamline.

The energy dependence of x-ray absorption in Fe was measured in transmission mode using the same Si photodiode for collection of the incoming (I_0) and transmitted (I) light intensities. Moving the sample in and out of the beam, I and I_0 were accumulated alternately in successive energy scans and normalized separately to the corresponding mirror current of M4. The sample material was prepared under UHV conditions growing ~ 49 nm thick Fe films *in situ* by e-beam evaporation onto 2 μm thick semitransparent Parylene (C_8H_8)_n substrates. The crystal structure of the film is of polycrystalline bcc type [2]. The absorption functions of the Parylene substrate and of the Fe film on Parylene, measured at the peak intensity of the fifth undulator harmonics, are shown in Fig. 1. Similar results were achieved using the third undulator harmonics.

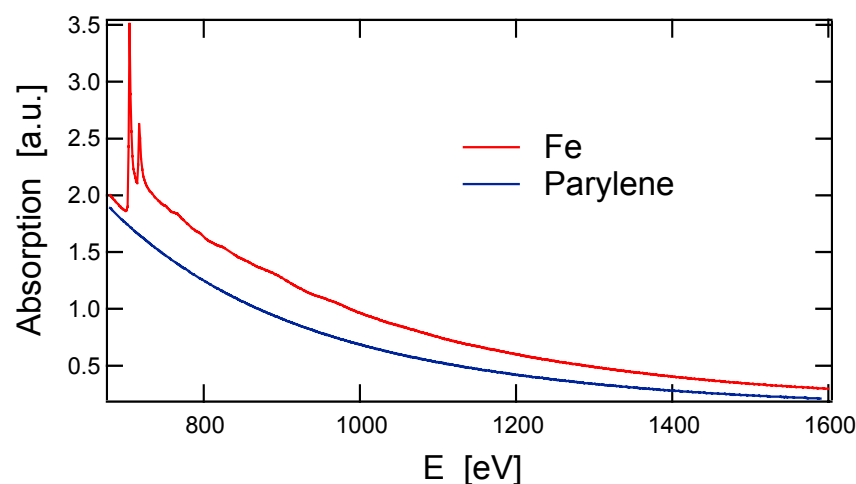


Fig. 1
Photon energy dependence of the X-ray absorption measured in 2 μm thick Parylene foil and in ~ 49 nm thick Fe film grown on this foil.

EXAFS measurements at the L-edges of 3-d transition metals offer the possibility to determine the geometric and magnetic local structures. However, due to the overlapping oscillations above the L_1 -, L_2 -, and L_3 -edges the analysis is getting cumbersome. We use the stochastic regularization of the Bayes-Turchin approach [3] for solution of the ill-posed problem to extract structure parameters from the measured data. This analysis requires the determination of the detection efficiency $A(k)$ as a function of the wave number k , and the embedded atom absorption $\mu_0(k)$ to obtain the EXAFS function $\chi(k)$. From the latter radial distances R_j , Debye-Waller (DW) parameters σ_j^2 , and anharmonicity parameters $C_{3,j}$ have to be inferred. The analysis of the EXAFS data is based on the results of the FEFF code [4] for $\mu_{0,L}(k)$ and $\chi_L(k)$ of the three L-edges and is performed in three steps:

- 1) Determination of $A(k)$, which involves the subtraction of the pre-edge background contribution, the decomposition of the measured absorption function into L_1 -, L_2 - and L_3 -contributions using the corresponding ratios of $\mu_{0,L}(k)^{\text{FEFF}}$, and the normalization of the smoothed function $\langle \mu_{L_3}(k) \rangle^{\text{exp}}$ to the smoothed function $\langle \mu_{0,L_3}(k) \rangle^{\text{FEFF}}$.
- 2) Assignment of uncertainties for the input parameters, and introduction of a cubic-spline correction-function $\Delta\mu_0(k)$ for the embedded atom absorption functions $\mu_{0,L}(k)^{\text{FEFF}}$.
- 3) Extraction of local structure parameters from the measured absorption $\mu(k)^{\text{exp}}$ using the iteration procedure of the Bayes-Turchin approach. The input of the procedure consists of an *a priori* guess of all model parameters. The results of the fit are *a posteriori* model parameters, including errors and error correlations, and *a posteriori* functions $\mu(k)^{\text{post}}$ and $\chi(k)^{\text{post}}$.

The decomposition of the normalized absorption $\mu(k)^{\text{exp}}$ into the contributions of the three L-edges is shown in Fig. 2. Note that the absorption is given in Mega barn using conversion factors of the FEFF code.

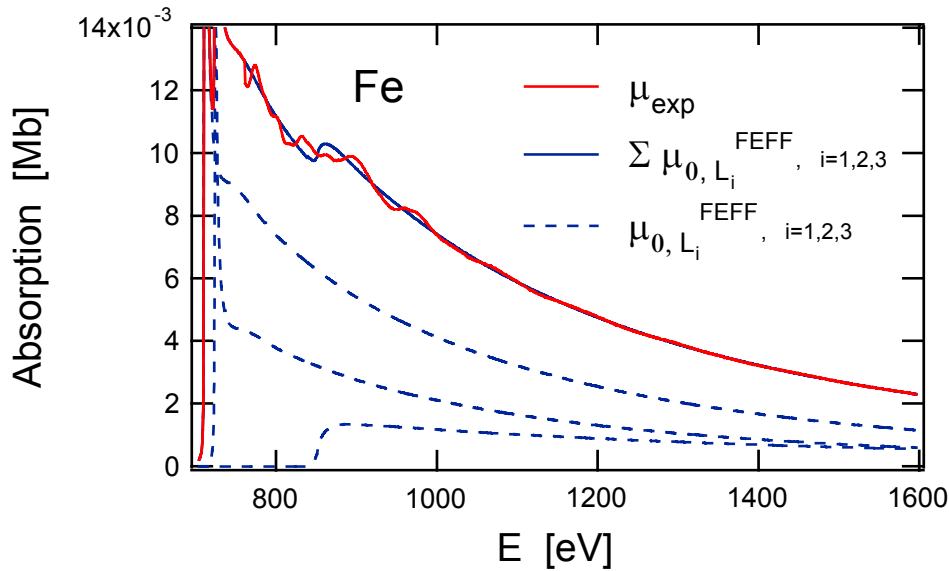


Fig.2 Normalized absorption $\mu(k)^{\text{exp}}$, the contributions of the three L-edges $\mu_{0,L}^{\text{FEFF}}$ computed by the FEFF code, and the total atomic like background $\Sigma\mu_{0,L}$.

A set of 84 parameters is used in the analysis: 11 cubic spline points for atomic background correction $\Delta\mu_{0,1}, \dots, \Delta\mu_{0,11}$, using the same correction function $\Delta\mu_0(k)$ for $\mu_{0,L}^{\text{FEFF}}$ of the three edges, the amplitude reduction factor S_0^2 , the L_3 -edge energy E_0 , the single scattering half path lengths R_1, \dots, R_9 of a nine shell atom cluster, the Debye-Waller parameters $\sigma_{1, \dots, 61}^2$ of the 61 scattering paths used, and the third cumulant $C_{3,1}$ of path one. The relative edge distances $E_{0,L2}-E_0$ and $E_{0,L1}-E_0$ were taken from the FEFF code results and were kept constant during the iteration procedure. Also the relations between the 9 single scattering path lengths of a cluster with radius $R=7.3 \text{ \AA}$ and the multiple scattering path lengths were taken from the FEFF code and applied during the iteration procedure using the actual parameters of R_1, \dots, R_9 . As *a priori* data an ideal bcc crystal structure was assumed with $a=2.8665 \text{ \AA}$, Debye-Waller parameters given by the correlated Debye model with Debye temperature $\theta_D=420 \text{ K}$ and an assumed sample temperature of $T=500 \text{ K}$. The FEFF code was used with the self-consistent potential option for a cluster radius of $R_{\text{SC}}=6 \text{ \AA}$ and a 4% threshold for the cutoff of the curved wave amplitudes. At the beginning of the iteration the edge energy E_0 was set to $E_0=713 \text{ eV}$, S_0^2 was taken from FEFF as $S_0^2=0.986$, and the third cumulant $C_{3,1}$ as well as the cubic spline values for the atomic background correction were set to zero.

During iteration the regularization parameter α is optimized, which divides the eigenvalue space of the parameters into a subspace where eigenvalues are determined by the experimental data and a subspace where eigenvalues are determined by the *a priori* data. The iteration procedure showed that 24 out of 84 eigenvalues were determined by the experimental data, and the following values of the *a posteriori* model parameters were obtained: all $\Delta\mu_{0,i}=0$, i.e. no corrections to the atomic background functions $\mu_{0,L}^{\text{FEFF}}$ of the three L-edges were needed, and the parameters S_0^2 , E_0 and $C_{3,1}$ retained their *a priori* values. The crystal structure, however, appears to be strongly distorted. For example the shifts and *a posteriori* errors of the first three shell radii got the values $\Delta R_1=(-0.024\pm 0.002)$ Å, $\Delta R_2=(-0.049\pm 0.001)$ Å, and $\Delta R_3=(-0.032\pm 0.003)$ Å. It is noted, that $S_0^2=0.67$ is obtained when the sample temperature is assumed to $T=300\text{K}$.

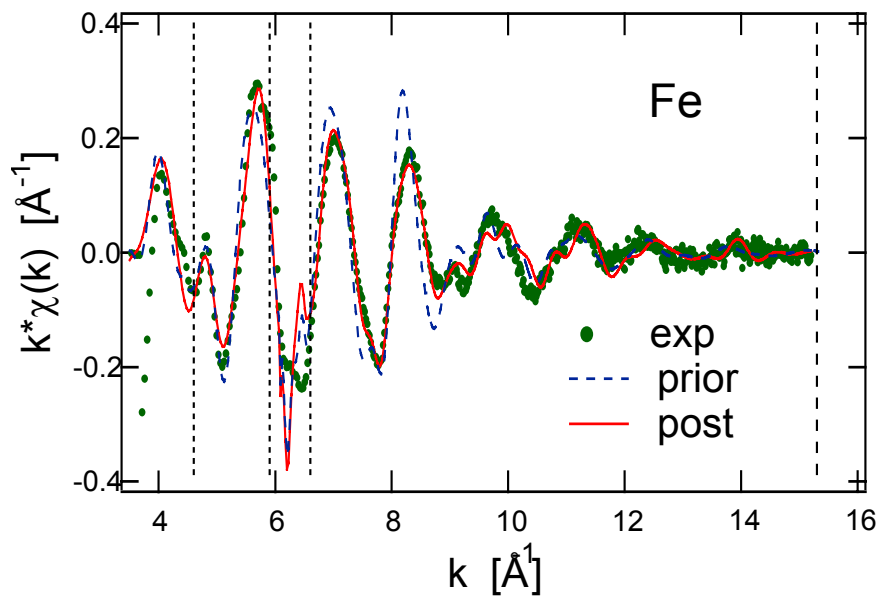


Fig. 3
Comparison of k -weighted EXAFS functions $k\chi(k)$ of the measured data, the *a priori* data and the *a posteriori* data. Two fit regions were used: $4.6 \text{ \AA}^{-2} \leq k \leq 5.9 \text{ \AA}^{-2}$ and $6.6 \text{ \AA}^{-2} \leq k \leq 15.3 \text{ \AA}^{-2}$, with limits indicated by the dotted vertical lines.

Our first experiment indicates that the combination of gap scanning technique for data collection and application of the Bayes-Turchin approach for data analysis enables the study of local geometric structures by L-edges EXAFS measurements at UE46-PGM. We are optimistic that these techniques can be extended to magnetic EXAFS measurements for the determination of local magnetic structures.

References

- [1] U. Englisch, H. Rossner, H. Maletta, J. Bahrtdt, S. Sasaki, F. Senf, K.J.S. Sawhney, W. Gudat, Nucl. Instr. and Meth. A467-468 (2001) 541
- [2] Y.U. Idzerda, V. Chakarian and J.W. Freeland, Synchrotron Radiation News, Vol. 10, No. 3 (1997)
- [3] H.J. Krappe and H.H. Rossner, Phys. Rev. B **61**, 6596 (2000); Phys. Rev. B **66**, 184303 (2002)
- [4] A.L. Ankudinov and J.J. Rehr, Phys. Rev. B **56**, R1712 (1997)

The excellent support of the BESSY group during beamtime, especially of W. Frentrup, is gratefully acknowledged. We also thank H.J. Krappe for valuable discussions and his numerous suggestions for data analysis.

Investigation of conducting band of titanium dichalcogenides by absorption spectroscopy

A.N. Titov^{1*}, Yu. M. Yarmoshenko¹, A. Zimina², A.V.Postnikov^{1,3}, S.Eisebitt², W.Eberhardt²

¹*Institute of Metal Physics, Ural Division of Russian Academy of Sciences, 620219*

Ekaterinburg, Russia

²*BESSY GmbH, 12489, Berlin, Germany*

³*University of Osnabrueck – Department of Physics, D-49069 Osnabrueck, Germany*

Corresponding author

A.N. Titov

Institute of Metal Physics UrD RAS, S. Kovalevskaya St. 18

Tel. +7 3432 184098

e-mail: alexander.titov@usu.ru

Introduction

Titanium dichalcogenides at present are widely used as electrode materials of electrochemical devices. They found the widest application as cathodes for lithium batteries. EMF arises in the battery due to a difference of positions of Fermi level of lithium metal and a cathode material, and the current is provided with electron transfer from metal in a conducting band of titanium dichalcogenide, formed, basically, by Ti3d-orbitals. Thus, position and form of Ti3d-band defines EMF value and capacity of the battery, and, hence, its efficiency.

At present it is established [1] that the shape of the Ti3d-band is influenced by the nearest chalcogenium environment of Ti-atom in the form of distorted octahedron extended along the hexagonal c-axis. It is known that the replacement of one chalcogenium type by another, as well as intercalation by transition metals, changes the distortion of the chalcogenium octahedron [2]. It seems reasonable to assume that such change should affect the form and, probably, energy position of a Ti3d-band.

On the other hand, an intercalation by transition metals can result in a redistribution of the electron density, hybridization of Ti3d- with valence states of intercalated metal and, probably, the change a degree of filling of the Ti3d-band. This effect can coexist with the deformation of local chalcogenium environments. It is possible to separate these two effects by investigating materials in which deformation is well pronounced without charge transfer from intercalant, on one hand, to Ti of a host matrix and, on the other hand, materials showing very small deformation alongside with appreciable charge transfer.

The dependence of lattice deformation value upon intercalation by transition metals in TiSe₂ has been reported in Ref. [3]. According to these results, an insertion of Fe and Cr leads to approximately similar deformation. At the same time, the bivalent state of iron is reliably established [4], whereas the most stable state of chromium is Cr³⁺. Thus, for these materials one can expect different charge transfer from intercalated metal to host lattice at approximately similar magnitude of lattice deformation, caused by intercalation. The choice of materials was motivated by the need to have examples of different degree of charge transfer, as well as of different value of deformation. The last was achieved in the study of Fe_{0.25}TiTe₂ in comparison with Fe_{0.5}TiSe₂, where the charge state of Fe is the same, but the lattice deformation differs.

Results and discussion

X-ray absorption spectra were measured on line UE-56/1-SGM with energy resolution 0.1 eV.

We begin with qualitative comparison of spectra and calculations of the investigated compounds, obtained using structural parameters from Table 1.

First principles calculations of the electronic structure were performed within Linear functional theory, using the full-potential augmented plane waves method, as implemented in the WIEN2k code. The details of calculations are given in [6].

In TiL- spectrum of TiSe_2 two brightly pronounced peaks with energies 456.3 eV and 459.3 eV (Fig. 1.) are observed. In the bottom part of Fig. 1 the spectrum of rough surface is shown. One can see that spectra taken from cleaned and rough surfaces differ by energy position and relative spectral intensity of peaks. Apparently, the material of a rough surface represented non-stoichiometric TiO_2 . It is close to the spectrum of TiO_2 in energy positions and the shape of peaks [5].

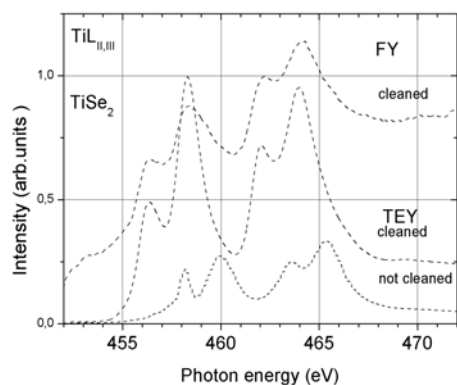


Fig.1 TiL absorption spectra in TiSe_2 .

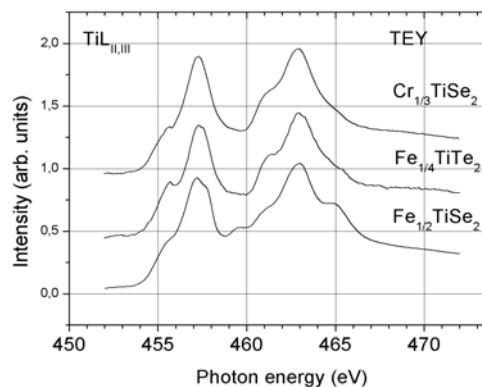


Fig.2 TiL absorption spectra in TiSe_2 and TiTe_2 Intercalated by Cr and Fe.

Fig. 2 depict the XAS TiL-spectra of TiSe_2 and $\text{Cr}_{1/3}\text{TiSe}_2$ are presented. Two peaks, which were observed for TiL_3 (and also in TiL_2) spectra, are possible to identify with e_g and t_{2g} orbitals, when d-states of metal are confined to octahedral symmetry. The value of energy splitting between e_g and t_{2g} -peaks for two examined compounds differs by 0.3 eV and makes 1,9 and 1,6 eV for TiSe_2 and $\text{Cr}_{1/3}\text{TiSe}_2$, respectively. The intensity of the t_{2g} -peak for TiSe_2 is less than in the intercalation compound. Model calculations [5], which demonstrate a reduction of lattice distortion accompanied by a degeneration of e_g and t_{2g} states and formation of a single d-state peak, are in a qualitative agreement with these experimental results.

Though octahedral distortion for $\text{Cr}_{1/3}\text{TiSe}_2$ only insignificantly decreases in comparison with TiSe_2 (Table 1), a strong change of a spectrum both in relative spectral peak intensity and in energy shift is observed. However lattice distortion mentioned at the comparative analysis of spectra and, finally, electronic structure of both materials is not the unique reason of change in the spectrum. In $\text{Cr}_{1/3}\text{TiSe}_2$ there is an additional occupancy of valence Cr3d-band resulting in spatial polarization of Se, formation of Cr-Se bonds and, according to our measurements, in an increase in energy of internal $\text{Ti}2p_{3/2}$ -level by 0.5 eV from 455.0 eV.

Chromium has formal valence state +3 in $\text{Cr}_{1/3}\text{TiSe}_2$, therefore the lowest empty $\text{Ti}3d_z^2$ -like band is occupied in intercalation compounds by one electron per formula unit. In other compounds - $\text{Fe}_{1/4}\text{TiTe}_2$ and $\text{Fe}_{1/2}\text{TiSe}_2$ - this band is occupied by 0.5 and 1 electron, respectively. Such difference in filling is reflected in the form of Ti-spectrum in these compounds.

Fig. 3 summarized densities of states DOS for TiSe_2 , $\text{Cr}_{1/3}\text{TiSe}_2$ and $\text{Fe}_{1/4}\text{TiTe}_2$. It is visible that metal 3d-states of each orbital symmetry are present throughout the width of valence bands for these compounds. It is impossible to extract their contribution except in special cases when in the limited energy interval the density of states of one certain symmetry prevails over others.

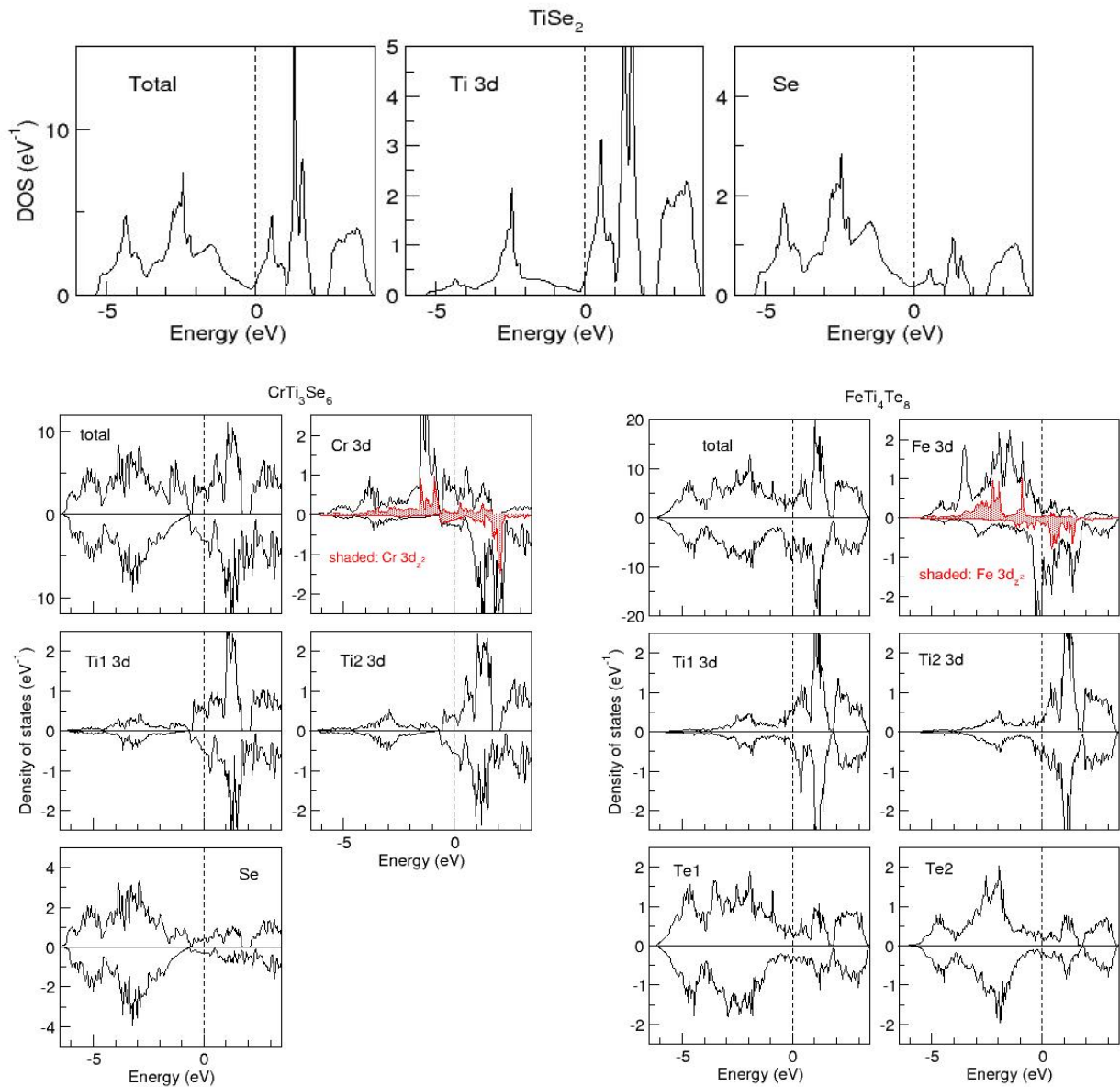


Fig.3 Calculated DOS of TiSe_2 , $\text{Cr}_{1/3}\text{TiSe}_2$, and $\text{Fe}_{1/4}\text{TiTe}_2$.

For example, in an empty part of a valence band, $3d_{xz, yz}$ -states prevail for energy higher than +2 eV. Nevertheless, the general picture of energy distribution of Cr3d-states in $\text{Cr}_{1/3}\text{TiSe}_2$ on one hand and Fe3d-states in $\text{Fe}_{1/2}\text{TiSe}_2$ and $\text{Fe}_{1/4}\text{TiTe}_2$ on the other hand considerably differ. For Cr3d-states the tendency to energy localization is characteristic. Centers of gravity of Cr3d-states with different spin projections are rather far on both sides from Fermi level, and the gap is observed near to energy -0,7 eV for the occupied states of majority spin. In Fig. 3 the area of $\text{Cr}3d_z^2$ -states is specially highlighted. These states are "smeared" in a broad energy interval, in empty part of a valence band their maximum of distribution corresponds to $E=+2$ eV. In a vicinity of this energy the Ti3d-states of majority spin have a gap, and density of states of minority spin is small. The vacant and lower-lying in energy Cr3d-states with other orbital symmetry occupy the same energy interval as Ti3d. It results in their mixing due to atoms of a Se-environment. The situation in the occupied part of a valence band is similar. In energy range -2– -1 eV, where density of Cr3d-states (including d_z^2) reaches maximum size, the density of Ti3d-states is minimal. From the analysis of distribution of Se4s4p-states in a valence band it follows that all Cr3d-states, except $3d_z^2$, mix up with Se. Hence, intercalation of Cr at filling of a valence band results in a hybridization, of basically empty 3d states of Ti and Cr. Such chemical bond is accompanied by the polarization of the layers of Se-atoms at boundaries of TiSe_6 and CrSe_6 octahedra. This

polarization arises due to mixing of Se4sp and Cr3d orbitals. Cr3d_{z²}- orbital practically does not participate in this process.

Table 1.

Structural data for intercalation materials based on titanium dichalcogenides, obtained by full profile analysis with powder samples at room temperature. The value $\gamma = 2zc_0/a_0$ is a characteristics of the form of local Ti environment. For ideal octahedron $\gamma = 0,8165$.

Compound	a(A)	b(A)	c(A)	2zc/a
TiSe ₂	3,540	3,540	6,008	0.8655
Cr _{1/3} TiSe ₂	3,589	3,589	5,982	0.8651
Fe _{1/2} TiSe ₂	6.2673	3.5915	11.9557	0.8552
Fe _{1/4} TiTe ₂	3.8109	3.8109	6.3451	0.8842

In comparison with Cr_{1/3}TiSe₂, in Fe_{1/4}TiTe₂ 0.5 electrons per formula unit occupy the valence band at intercalation of Fe. As we see from Fig. 3b, it essentially influences the distribution of density of Fe3d-states. Near the Fermi level the narrow band with high intensity is observed. This band is weakly hybridized with Ti3d-states in this energy area. At energy about 1.7 eV above of the Fermi level the band mixed with intense Ti3d-band is observed. As well as in Cr_{1/3}TiSe₂, the interaction between Fe3d- and Ti3d-states occurs due to their hybridization with valence states of boundary Te-atoms.

In Fig. 4 the absorption TiL_{2,3}-spectrum for Cr_{1/3}TiSe₂ is compared to the density of Ti3d-state in a conducting band. The density of states is smeared by the Lorentz function with 0.5 eV halfwidth.

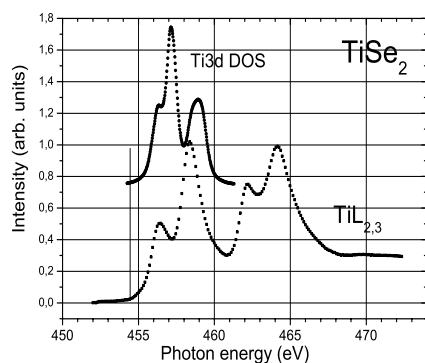


Fig.4 TiL absorption spectra in Cr_{1/3}TiSe₂ compared with calculated band. The DOS is smeared with Lorentz function of 0.5 eV halfwidth.

From the consideration of experimental spectra and the analysis of DOS-calculations it follows that the formation of electronic structure of chalcogenides, investigated in the given work, is influenced by two competing mechanisms. One of them is the filling of bottom empty Ti3d-like band and is determined by the valence state and concentration of intercalated atoms. The other mechanism consists of the formation of octahedral distortions of different size and hybridization of valence states of an impurity and host lattice atoms.

References

1. R.H.Friend, A.D.Yoffe Electronic properties of intercalation complexes of the transition metal dichalcogenides// *Adv. Phys.* **36**, № 1 (1987) P.1-94
2. T.Hibma Structural Aspects of Monovalence Cation Intercalates of Layered Dichalcogenides// *Intercalation Chemistry* eds. M.S.Wittingham and A.J.Jacobsen, London: Acad. Press, 1982, P.285-313.
3. A.N.Titov, A.V.Dolgoshein, I.K.Bdikin, S.G.Titova *Phys. Solid State* **42**, 1610 (2000)
4. D.R.Huntley, M.I.Sienko, K.Hiebel *J. Solid State Chem.* **52** (1974) 233
5. F.M.F. de Groot, X-ray absorption of transition metal oxides: an overview of the theoretical approaches. *J. of Electron Spectr. Rel. Phen.* **62**, (1993), 111-130.
6. A. V. Postnikov, M. Neumann, St. Plogmann, Yu. M. Yarmoshenko, A. N. Titov and A. V Kuranov,. *Comput. Mater. Sci.* **17** № 2-4 (2000) pp. 450

Bonding and Surface Chemistry of Polytopic Benzoic Acids on Cu(100): Combined STM and Synchrotron Observations

S. Stepanow¹, M. Lingenfelder¹, A. Dmitriev¹, N. Lin¹, J.V. Barth², K. Kern^{1,2}

¹Max-Planck-Institut für Festkörperforschung, Stuttgart, ²Institut de Physique des Nanostructures, Ecole Polytechnique Fédérale de Lausanne

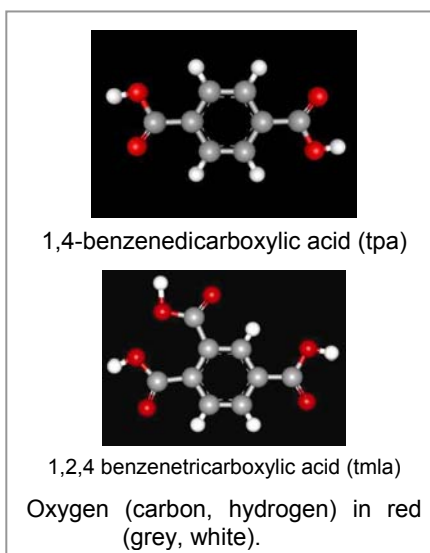
Th. Strunskus, Ch. Wöll

Lehrstuhl für Physikalische Chemie I, Ruhr-Universität Bochum

The deliberate construction of complex nanoscale assemblies using molecular building blocks is paramount for the development of novel functional materials. Particularly appealing is the engineering of supramolecular architectures, which are stabilized by non-covalent links such as hydrogen bonds or metal-ligand interactions. In order to develop a rationale for molecular engineering at surfaces, we need a solid understanding of the interaction of complex molecules and their functional groups with solid substrates and the resulting organization principles [1]. This will pave the way towards novel bottom-up strategies for the fabrication of supramolecular nanostructured materials potentially useful in molecular electronics, nano-templating, chemical sensing schemes, host-guest interactions or catalysis.

We have performed combined scanning tunneling microscopy (STM) and synchrotron investigations addressing the bonding, ordering and surface chemistry of the related molecules 1,4-benzenedicarboxylic acid (terephthalic acid - tpa) and 1,2,4-benzenetricarboxylic acid (trimellitic acid - tmla) on the Cu(100) surface. Polytopic benzoic acid molecules of this type are frequently employed in 3-D crystal engineering [2] and have proven to be useful for the fabrication of nanoporous supramolecular layers [3-5]. The molecule tpa and tmla with their respective twofold and threefold exodentate functionality are shown in fig. 1. While the formation of organic layers and nanostructures can be nicely monitored by STM, important questions when using such species in molecular engineering at surfaces (both for H-bonded or metallosupramolecular architectures) comprise carboxylic acid group deprotonation and molecular orientation. They can be addressed by X-ray photoelectron spectroscopy (XPS) and near-edge X-ray absorption fine structure (NEXAFS).

Distinct hydrogen-bonded assemblies could be obtained at low temperature (up to 275 K) with tpa. The STM image in fig. 1 reveals that molecular ribbons evolve on the square substrate. The corresponding C1s XPS data shown confirm that the tpa carboxyl groups remain largely complete, i.e., the well-known splitting of the C1s peak is observed reflecting the contribution from the atoms in carboxyl and phenyl moieties at an energy of 285.2 and 289.8 eV, respectively (cf. [6]). Accordingly the O1s peak appears broadened due to overlapping hydroxyl and carbonyl intensities (531.9 and 533.4 eV, respectively). The NEXAFS analysis of this phase indicates that adsorption with the aromatic ring parallel to the substrate prevails. Interestingly, the real-space modeling reveals that the H-bonds formed between the adsorbed molecules do not obey the typical R-COOH pairing motif, which accounts in pure tpa or other dicarboxylic acids for 1-D molecular chain elements [7], rather the interplay between substrate corrugation and functional group interactions makes a lateral



2-D interweaving scheme preferable. For the related case of low-temperature tmla adsorption ($T < 200$ K) the combined study reveals that flat adsorption of integral molecules similarly prevails. However, no supramolecular ordering could be obtained, which behavior is associated with the reduced symmetry and mobility of this molecule (no data shown).

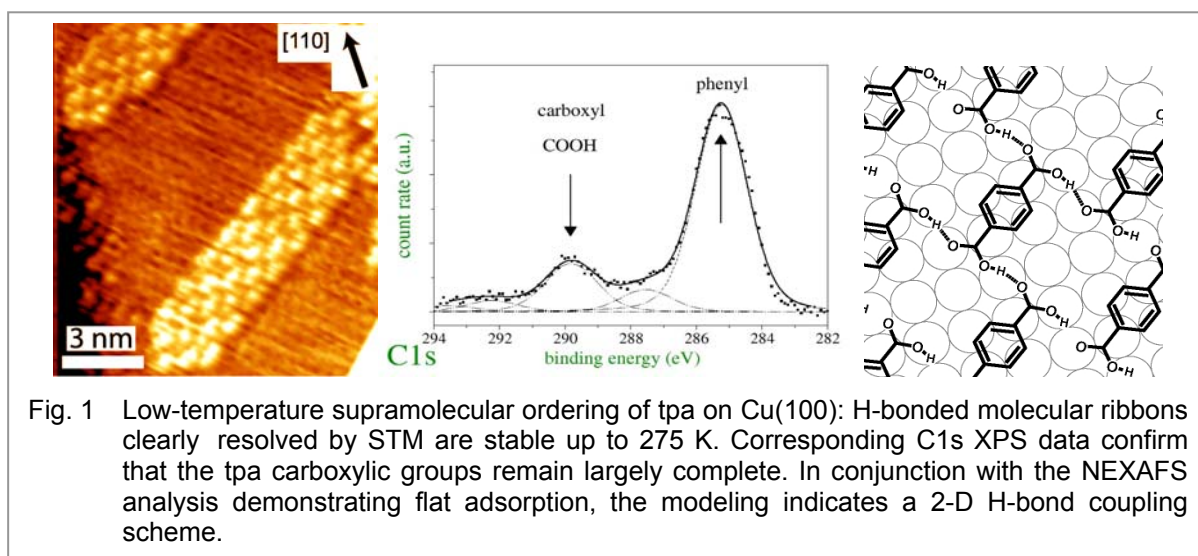


Fig. 1 Low-temperature supramolecular ordering of tpa on Cu(100): H-bonded molecular ribbons clearly resolved by STM are stable up to 275 K. Corresponding C1s XPS data confirm that the tpa carboxylic groups remain largely complete. In conjunction with the NEXAFS analysis demonstrating flat adsorption, the modeling indicates a 2-D H-bond coupling scheme.

At increased temperatures ($T = 300 - \sim 500$ K) for both molecules a (partial) deprotonation of the carboxylic acid groups occurs because of the chemical reactivity of the Cu substrate. With tpa the formation of a biterephthalate is encountered, as deduced from the reduced separation of the splitted C1s contributions (now at 285.1 and 288.2 eV, respectively) and the existence of a narrowed O1s peak centered at 531.4 eV. Again the NEXAFS analysis reveals that the phenyl ring is oriented parallel to the substrate lattice – the two pronounced C 1s $\rightarrow \pi^*$ resonances exhibit a marked intensity variation with the angle of incidence. Surprisingly the STM data show that the packing density with the negatively charged biterephthalate species is increased as compared to the integral molecule, which is associated with a lateral coupling scheme where the anionic tpa carboxylate groups are engaged in H-bonds with phenyl rings of adjacent molecules. For comparison, on Cu(110) under similar conditions an upright standing monoterephthalate layer is formed [8]. This demonstrates that the geometry and symmetry of the substrate can be used to tune the orientation and functionality of adsorbed tpa layers.

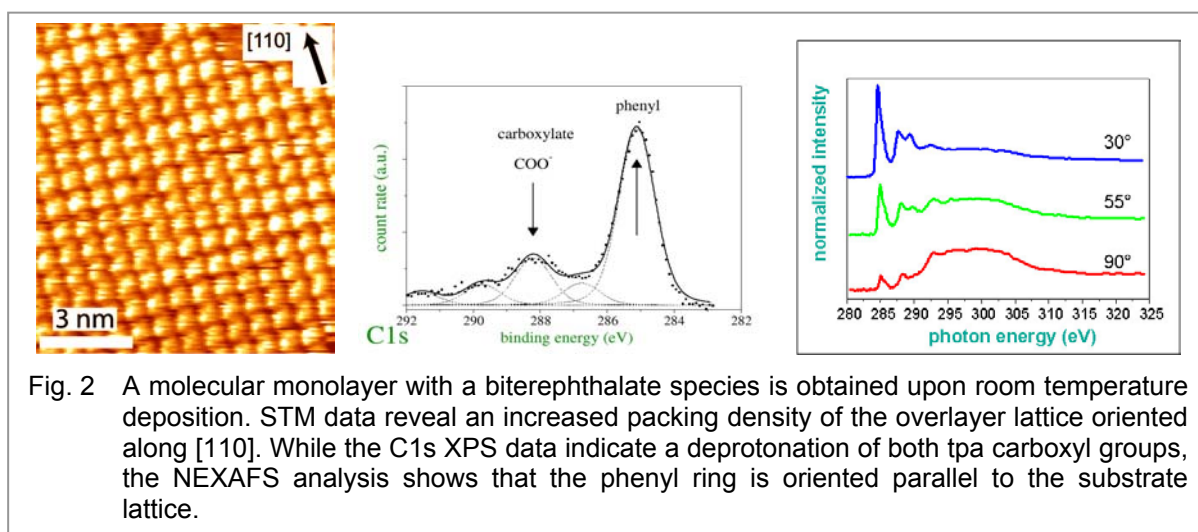


Fig. 2 A molecular monolayer with a biterephthalate species is obtained upon room temperature deposition. STM data reveal an increased packing density of the overlayer lattice oriented along [110]. While the C1s XPS data indicate a deprotonation of both tpa carboxyl groups, the NEXAFS analysis shows that the phenyl ring is oriented parallel to the substrate lattice.

A somewhat different scenario is encountered with the regular tmla layers evolving with the substrate held at elevated temperature (450 K). Now the XPS data indicate merely a partial deprotonation of the carboxyl groups, which signals the formation of a monocarboxylate species. Moreover, the NEXAFS analysis of this phase reveals that the pronounced C 1s $\rightarrow \pi^*$ resonances show only a small intensity variation with the angle of incidence and the 90° spectrum has the largest intensity. This corresponds either to an almost random orientation of the molecules or to a situation where the plane of the tmla molecules is oriented on average at a tilt angle slightly larger than 54 degrees relative to the Cu(100) surface. The latter is consistent with the only partial deprotonation of the tmla molecule, where just one of the three functional groups is engaged in the substrate carboxylate anchoring. Currently the data is further analyzed and complementary theoretical investigations are underway to clarify the question of the intriguing possibility of an intramolecular hydrogen bond at the carboxylic groups in the *ortho* position of the adsorbed species.

In conclusion, our results reveal that combined STM and synchrotron investigation of functional organic molecules at solid surfaces provide complementary insight in the ordering and chemical nature of such systems, which is useful to advance the field of molecular engineering at surfaces.

References

- [1] J. V. Barth *et al.*, Appl. Phys. A **76**, 645 (2003).
- [2] M. Eddaoudi *et al.*, Science **295**, 469 (2002).
- [3] A. Dmitriev *et al.*, J. Phys. Chem. B **106**, 6907 (2002).
- [4] A. Dmitriev *et al.*, Angew. Chem. Int. Ed. **42**, 2670 (2003).
- [5] M. A. Lingenfelder *et al.*, Chem. Eur. J., in print (2004).
- [6] M. Wühn, J. Weckesser, and C. Wöll, Langmuir **17**, 7605 (2001).
- [7] M. Sledz, J. Janczak, and R. Kubiak, J. Mol. Struct. **595** (2001).
- [8] D. S. Martin, R. J. Cole, and S. Haq, Phys. Rev. B **66**, 155427 (2002).

INVESTIGATION OF A LATERAL MODULATED SUBSTRATE DEFINED BY ION BEAM IMPLANTATION

J. Grenzer¹, N. Darowski[§], S. Klaumünzer[§], and U. Pietsch

University of Potsdam, Institute of Physics, Am Neuen Palais 10, 14469 Potsdam, Germany

[§]Hahn-Meitner-Institut Berlin, Glienicker Straße 100, D-14109 Berlin, Germany

The aim of the proposal was the X-ray characterization of a periodic strain field of as-implanted specimen and the in-situ measurement of the varying strain distribution in ion-implanted periodic nanostructures during annealing. The period of the produced lateral grating structures was about 500nm and created into a GaAs substrate. Due to the lateral periodicity on the mesoscopic length scale each fundamental Bragg peak is accompanied by satellites (so called grating peaks). The scientific problem consists in the non-destructive investigation of the shape and strain distribution of these peaks within the nanostructure. For the measurement, a high-resolution setup is needed.

A typical lateral periodicity of 500 nm the distance of these peaks in reciprocal space equals $\Delta q_x = 2\pi/D = 0.013 \text{ nm}^{-1}$, which requires an angular resolution and angle reproducibility of any goniometer of less than 0.001° , especially of the diffraction circles. In addition, the demand on the smallest as possible angular step width is a consequence of the extreme large lateral correlation length of these artificial nanostructures, which results in extremely narrow peaks defined only by the resolution function of the beam line.

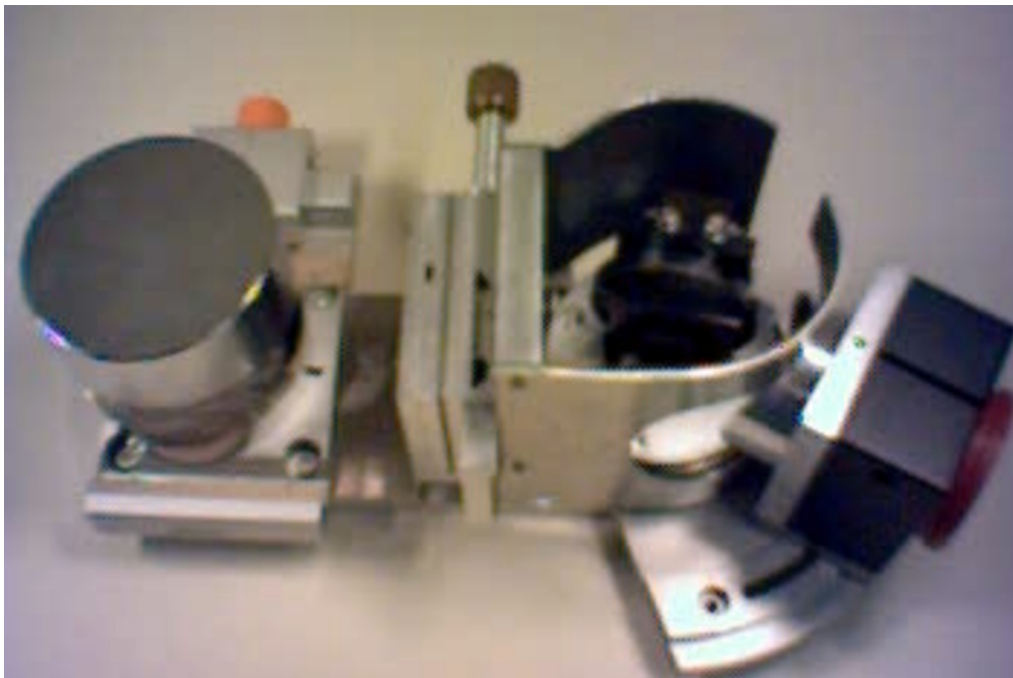


Figure 1: Analysator setup; using a moveable mechanical slit the beam can pass the analysator box trough an entrance slit directly into the scintillation counter without diffraction on the analyser crystal.

¹ e-mail: grenzer@rz.uni-potsdam.de

The experiment was carried out at the HMI 6-axis HUBER diffractometer at the KMC2 beam line at BESSYII. The incident beam was monochromatized ($\lambda=0.154$ nm) and collimated using a SiGe (111) double-crystal monochromator. To achieve highest-resolution in reciprocal space, a special analyser setup was build and mounted on the diffractometer using a Ge (111) crystal in front of the scintillation detector resulting in an in-plane resolution better than $2...3 \cdot 10^{-3}$ nm⁻¹.

The resolution function of the experimental setup was measured using a Si (001) crystal measured in grazing incidence diffraction (GID) at the (400) reflection and in high-resolution diffraction at the (004) reflection. Figure 2 shows both resolution functions.

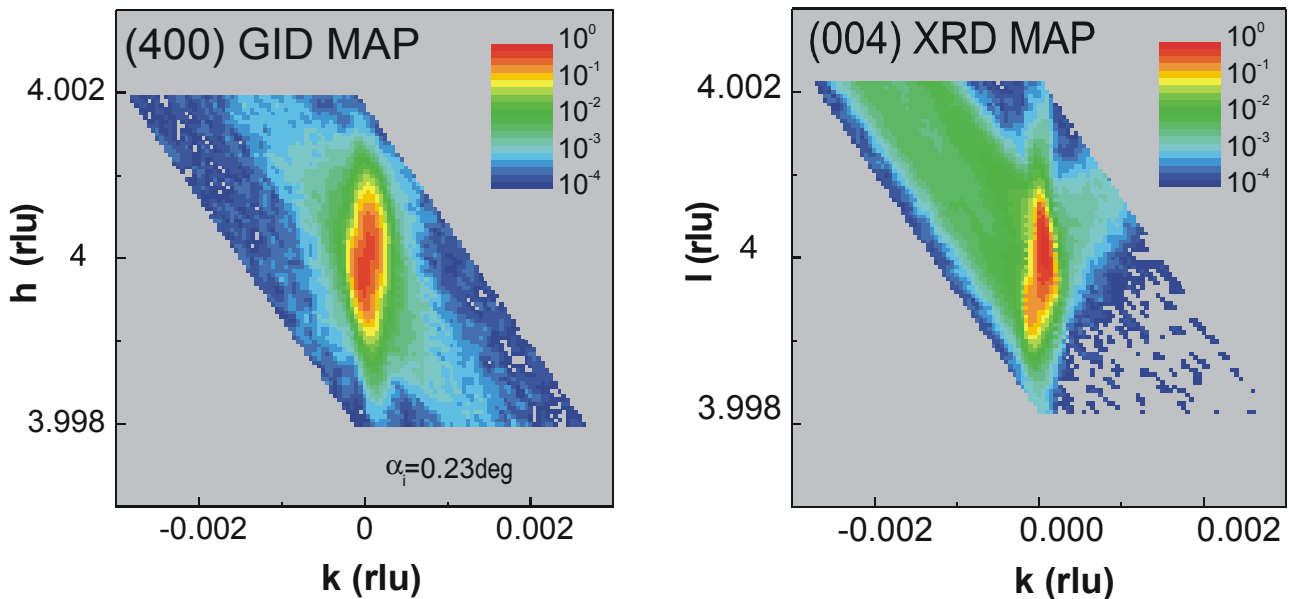


Figure 2: Resolution functions of the KMC2-Beamline at BESSYII

Both resolution functions show a typical behaviour, two crossing streaks the stronger one is the analyser streak and weaker one caused by the monochromator. However it can be seen that the both bragg peaks are slightly distorted and show a relatively large background, especially for the XRD measurement. The used beam line setup was dispersive and therefore the peaks are vertically enlarged due to the finite wavelength separation. Figure 2 shows that the achieved resolution function is not sufficient to investigate lateral surface gratings produced by ion beam implantation which require a very high resolution in reciprocal space. To make it possible the resolution function should be sharper and especially the background should be reduced and therefore the dynamical range of detection should be increased at least by two orders of magnitude. A better defined resolution function can be achieved by reducing the focusing during such measurements but this reduces as well the number of photons available for the experiment. However, the experiment showed that structure investigations requiring both, X-ray diffraction and grazing incidence diffraction, can be performed taking into account the lower resolution in reciprocal space.

References

- [1] V.Holy, U. Pietsch, T.Baumbach "*High Resolution X-ray Scattering from Thin Films and Multilayers*", Springer Tracts in Modern Physics Vol. 149, Berlin 1999.
- [2] J. Grenzer, N. Darowski, U. Pietsch, A. Daniel, S. Renon, J. P. Reithmaier and, A. Forchel, *Appl. Phys. Lett.* **77**, 4277 (2000).

Study of glasses containing industrial waste by means of μ -XRF mapping and μ -NEXAFS.

F. Pinakidou, M. Katsikini, E. C. Paloura*, P. Kavouras, Ph. Komninou, Th. Karakostas
Aristotle Univ. of Thessaloniki, Dept. of Physics, GR54124 Thessaloniki, Greece

A. Erko

BESSY GmbH, Albert Einstein Str. 15, 12489 Berlin, Germany.

EU, HPRI – 1999 – CT 00028

The solidification and stabilization of lead oxide-contaminated ash, which is a toxic industrial waste, is a process that allows for its safe disposal. The aim of this work is to determine the local environment around the Fe atoms (whose structural role depends on its oxidation state and the PbO concentration) in the glass matrix of lead-rich industrial wastes, by means of μ -XAFS spectroscopy. By making use of the advantages of X-ray fluorescence (XRF) mapping, it is possible to study the elemental distribution of iron in a vitrified industrial waste and furthermore to detect the existence of different phases that are formed in an inhomogeneous sample.

The under study sample is the vitrified product of lead-rich ashes, produced by incineration of sludges that contain large quantities of toxic organic compounds. The incineration process involves co-melting of lead contaminated ash with the appropriate quantities of vitrifying and flux agents (SiO_2 and Na_2O , respectively) at high temperatures (1400°C), followed by quenching in order to form vitrified materials¹. The under study sample consists of 70% ash, 20% SiO_2 and 10% Na_2O . A powder hematite ($\alpha\text{-Fe}_2\text{O}_3$) sample is studied as reference material.

The μ -XRF and μ -XAFS measurements were conducted at the KMC2 beamline at the electron storage ring BESSY-II in Berlin. The beamline is equipped with a double-crystal monochromator and capillary optics that allow the reduction of the beam diameter to $5\mu\text{m}$. The XRF maps were recorded using excitation photons of 7200eV, i.e. higher than the Fe-K absorption edge. The angle of incidence of the SR beam was 45° and the energy dispersive (Röntec) fluorescence detector was positioned normal to the beam. The Fe-K fluorescence photons emitted from the sample were discriminated by setting electronically the energy range of interest from 5919 to 7403 eV. The μ -XAFS spectra were recorded at the Fe-K edge at different positions of the sample in the fluorescence yield mode, while the spectrum of the Fe_2O_3 reference sample was recorded in the transmission mode using ionization chambers.

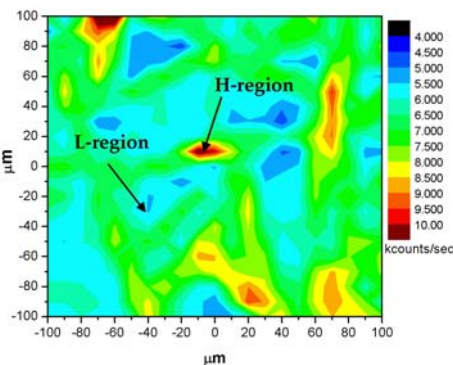


Figure 1: $100 \times 100 \mu\text{m}$ XRF map of the under study sample. The regions depicted as L and H, contain low and high iron concentration, respectively.

The XRF map shown in fig. 1, demonstrate that Fe is not homogeneously distributed in the under study sample. In particular, Fe appears to form islands where its concentration is about 2 times higher than the background Fe concentration.

In order to investigate the bonding environment around the Fe atoms at different positions of the sample, μ -XAFS spectra at the Fe-K edge were recorded at the regions with high and low Fe concentration (denoted as H and L, respectively). The Fe-K-edge NEXAFS spectra of the under study sample and the reference compound are shown in Fig. 2. The spectra were normalized for the transmission function of the monochromator, using the signal from an ionization chamber positioned in front of the sample, and were subjected to linear background subtraction (by fitting the spectrum far before the

* e-mail: paloura@auth.gr

absorption edge) and normalization to the edge jump. The NEXAFS spectra of Fe-containing compounds are characterized by a pre-edge feature that is attributed to $1s \rightarrow 3d$ transitions.² In a centrosymmetric environment (e.g. octahedral) the intensity of the pre-edge feature is weak due to the quadrupole character of the transition. Contrary to that, in a non-centrosymmetric environment (e.g. tetrahedral) the pre-edge peak gains intensity due to the d-p mixing of the final state, which gives dipole character to the transition. Thus, the intensity of the pre-edge peak is inversely proportional to the coordination number of the absorbing atom due to the loss of inversion symmetry of the iron site.^{3,4} As shown in Fig. 2, the Fe-K NEXAFS spectra exhibit differences in the intensity of the pre-edge peak, in the two distinct regions (H and L) of the under study sample. The increased intensity in the L-regions is therefore indicative of the alteration of the local environment around the Fe ion, i.e. the Fe atom tends to occupy tetrahedral sites into the glass matrix.

Not only the intensity but also the shape of the pre-edge feature depends on the local coordination around Fe. According to Westre et al.,² fitting of the pre-edge feature with one Lorentzian is a fingerprint of the tetrahedral coordination of the Fe atoms. Contrary to that, two Lorentzians are necessary to fit the pre-edge peak when Fe occupies octahedral sites. In the hematite sample, where Fe is octahedrally coordinated, two Lorentzians (centered at 7111.8 and 7115eV, respectively) were necessary to fit the pre-edge region. The same is valid for the spectra recorded at the H-region of the vitrified sample. The pre-edge peak of the spectrum recorded at the L-region, was fitted using one Lorentzian (positioned at 7112.3eV), which suggests a tetrahedral coordination around the Fe atom. This is consistent with previous work conducted in the under study sample which disclosed that the main crystal phase identified is hematite¹. SEM micrograph of the under study sample shown in fig. 3,

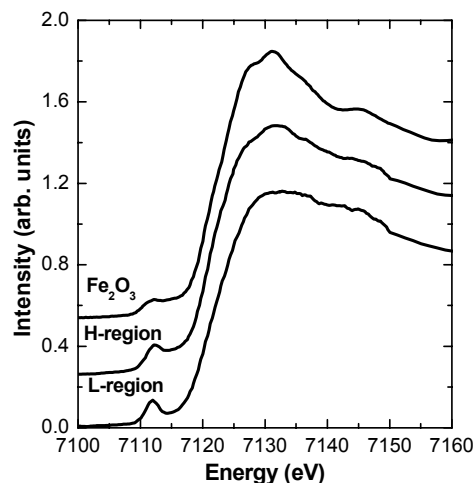


Figure 2: Fe-K NEXAFS spectra of the under study sample.

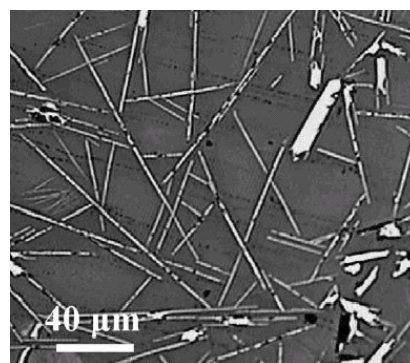


Figure 3: SEM micrograph of the under study sample.

reveals its compositional inhomogeneity. Furthermore, the position of the pre-edge peak, which is a measure of the portion of various oxidation states of Fe in a mixed valence sample,⁵ is found to be invariant and independent on the Fe concentration i.e., no alteration occurs in the $Fe^{+3}/\Sigma Fe$ ratio in both the H and L-regions.

Acknowledgements: F. Pinakidou acknowledges financial support from the Greek State's Scholarship Foundation.

References

- ¹ P. Kavouras et al., *Waste Manag.* **23**, 361 (2003).
- ² T. Westre et al., *J. Am. Chem. Soc.* **119**, 6297 (1997).
- ³ Ziyu Wu et al., *Apl. Phys. Lett.* **79**, 1918 (2001).
- ⁴ C. R. Randall et al., *Inorg. Chem.* **34**, 1036 (1995).
- ⁵ S. Bajt, S. R. Ruton and J. S. Delabey, *Geochim. Cosmochim. Acta*, **58** (23), 5209 (1994).

Effect of Si doping on the Debye-Waller factors of GaN.

M. Katsikini, E. C. Paloura, F. Pinakidou.

Dept. of Physics, Aristotle Univ. of Thessaloniki, 54124 Thessaloniki, Greece

EU, HPRI-1999-CT-00028

GaN is a wide-band gap semiconductor which finds applications in UV- and visible- light emitters and detectors as well as in data storage devices¹. GaN is also used in microelectronics because of its good thermal and chemical stability and physical hardness², while alloys of GaN with AlN and InN permit band-gap engineering and the fabrication of high brightness blue LEDs, based on GaN/InGaN/AlGaN heterostructures³. Si is the main n-type dopant of GaN with activation energy $\sim 17\text{meV}$ ⁴. In this report we apply EXAFS in order to study the effect of Si doping on the local microstructure around the Ga atom in epitaxially grown GaN.

The Si doped GaN samples used in the present study, were grown by plasma assisted molecular beam epitaxy on (0001)Al₂O₃ substrates as described previously.⁵ The carrier concentration (n) in the films was determined by room temperature Hall effect measurements using the van der Pauw method⁶ and varies from $2.2 \times 10^{15}\text{cm}^{-3}$ for the undoped sample to $1.0 \times 10^{20}\text{cm}^{-3}$. The Ga K edge EXAFS measurements were conducted in the KMC-2 beamline. The EXAFS spectra were recorded using a Si photodiode as a fluorescence yield detector at room temperature. The angle of incidence was 45° to the sample surface and the detection angle was 45° .

Prior to analysis, the EXAFS spectra were normalized to the flux of the monochromator using the signal from an ionization chamber positioned before the sample. Then the spectra were subjected to subtraction of the atomic absorption using the AUTOBK program. A model for hexagonal GaN ($a=3.18\text{\AA}$, $c=5.168\text{\AA}$) was constructed using the FEFF8 code.⁷ The $\chi(k)$ spectra were fitted using paths which correspond to the 4 nearest neighboring (nn) shells of N. The fitting was done using the FEFFIT program simultaneously for all the samples by iteration of the nn distance and the Debye-Waller factor (DWF) for each shell. The coordination numbers were kept fixed while the amplitude reduction factor and the energy shift (ΔE_0) were iterated in such a way that they take the same values for all the samples. Polarization effects were taken into account during the construction of the paths.

The Fourier Transforms (FT), in the k-range $3.5\text{-}12\text{\AA}^{-1}$, of the $k^3\chi(k)$ spectra are shown in Fig. 1. The first peak in the FT corresponds to the four nitrogen atoms of the tetrahedron around Ga. Deviations of the c/a

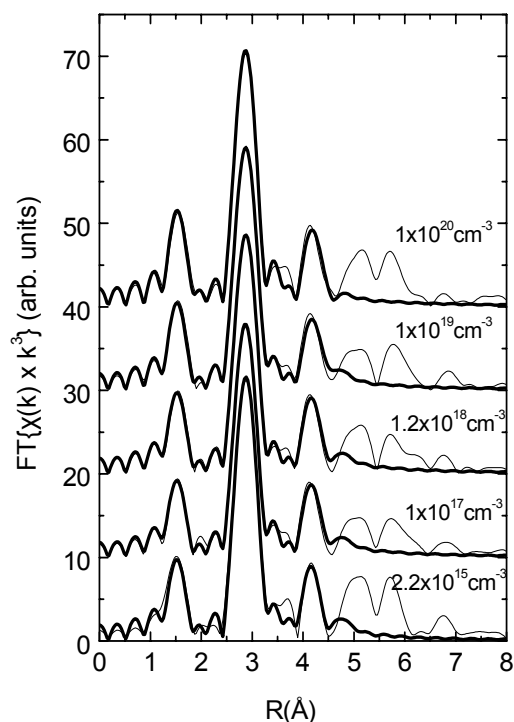


Fig. 1: Amplitude of the Fourier transform of the k^3 weighted $\chi(k)$ spectra of the under study samples. The experimental curve and the fitting are shown in thin and thick solid line respectively.

ratio and the u-parameter of the hexagonal unit cell from the ideal values of 1.63 and 3/8 respectively, lead to alteration of the length of the Ga-N bond along the c-axis. The second peak corresponds to the 12 Ga atoms that are second neighbors of Ga. Among them 6 Ga-Ga bonds lie on the c-plane. Biaxial stress-induced deviations of c/a and u-parameter from the ideal values lead to different lengths for the bonds on and off the c-plane. The fitting results show that the mean Ga-N and the Ga-Ga distances do not depend on the carrier concentration, contrary to the DWF's which decrease systematically with increasing carrier concentration. The dependence of the DWF's (σ) on the carrier concentration is shown graphically in Fig. 2. The error bars are determined from the analysis program.

The DWF which is defined as the mean square relative displacement of the neighboring atom relative to that of the absorbing atom, has two components: a static (σ_{stat}) which is due to the static disorder and a thermal (σ_{ther}) and can be written as $\sigma^2 = \sigma_{\text{stat}}^2 + \sigma_{\text{ther}}^2$. More specifically, σ_{stat} is related to the symmetric Gaussian pair distribution function of distance r:

$$g(r) = \frac{1}{\sqrt{2\pi}\sigma_{\text{stat}}} e^{-\frac{(r-r_0)^2}{2\sigma_{\text{stat}}^2}}$$

where $(r-r_0)$ is the deviation from the mean distance r_0 .⁸ It has been reported that Si doping causes relaxation of the thermal stress in GaN samples that are heteroepitaxially grown on sapphire, most probably due to the increase of misfit dislocations.⁹ This stress relaxation leads to a decrease of the deviation of the c/a ratio from the ideal value and thus reduces the standard deviation (σ_{stat}^2) of the N-Ga and Ga-Ga bond lengths from the mean value, r_0 . Therefore the observed reduction of the DWF could be attributed to Si-doping induced thermal stress relaxation.

References

- ¹ S. D. Lester, F. A. Ponce, M. G. Craford and D. A. Steigerwald, *Appl. Phys. Lett*, **66**, 1250 (1995).
- ² *Properties of Group III Nitrides*, edited by J. H. Edgar, (INSPEC, Exeter, 1994).
- ³ S. Nakamura, T. Mukai, M. Senoh, *Appl. Phys. Lett*, **64**, 1687(1994).
- ⁴ W. Götz, N. M. Johnson, C. Chen, H. Liu, C. Kuo, W. Imler, *Appl. Phys. Lett*, **68**, 3144 (1996).
- ⁵ T. D. Moustakas, R. J. Molnar, *Mat. Res. Soc. Proc.*, **281**, 753 (1993).
- ⁶ E. Iliopoulos, D. Doppalapudi, H. M. Ng, T. D. Moustakas, *Appl. Phys. Lett.*, **73**, 375 (1998).
- ⁷ J. Mustre de Leon, J. J. Rehr, R. C. Albers, S. I. Zabinsky, *Phys. Rev.* **B44**, 3937 (1992).
- ⁸ "EXAFS spectroscopy: techniques and applications", B. K. Teo, D. C. Joy, 1981 Plenum Press, New York.
- ⁹ In-Hwan Lee, In-Hoon Choi, Cheul-Ro Lee, Eun-joo Shin, Dongho Kim, Sam Kyu Noh, Sung-Jin Son, Ki Yong Lim, Hyung Jae Lee, *J. Appl. Phys.*, **83**, 5787 (1998).

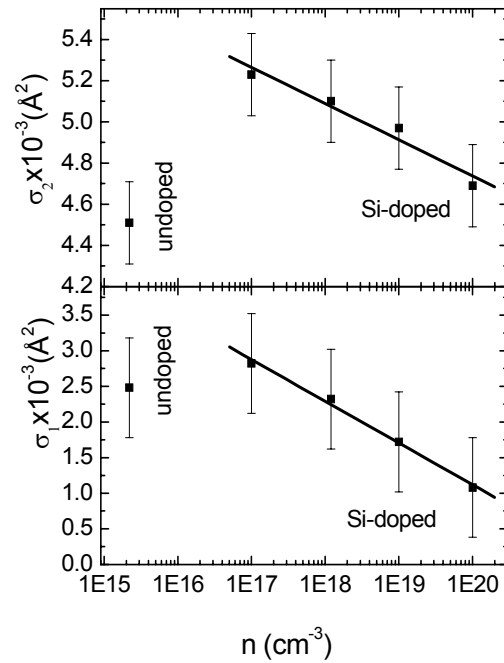


Fig. 2: Debye-Waller factors of the 1st (σ_1) and 2nd (σ_2) neighboring shells.

Nanostructures on Si: Initial Phases During por-Si Formation

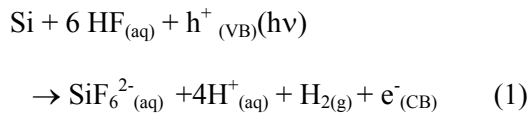
H. Jungblut, M. Aggour, J. Jakubowicz, C. Murrell, E. Goncalves, M. Kanis, E. R uthers, P. Cox¹
and H. J. Lewerenz

Hahn-Meitner-Institut Berlin, Interface Engineering Group, 14109 Berlin

Division of Solar Energy, Interface Engineering Group, Hahn-Meitner-Institut Berlin GmbH, 14109
Berlin, Germany

¹School of Pharmacy and Medical Sciences, Portsmouth University, Portsmouth, U. K.

The electrochemical micro- and nanostructuring of n-type silicon in HF containing aqueous solutions is based on the so-called divalent dissolution occurring via the net reaction



The term „divalent“ refers here to the consumption of two charge carriers for the dissolution of one Si atom: one light induced hole coming from the valence band (VB) and one electron being injected into the conduction (CB) band.

Despite numerous applications (e.g. luminescent porous silicon, photonic crystals), the very initial pit and nanostructure formation attracted minor attention. To get more insight into the respective processes, we use the parameter space of dilute ammonium fluoride with slightly acidic pH instead of the commonly used more aggressive and higher concentrated HF solutions. This enabled us to trace both, the chemical reaction path as postulated by the currently most elaborate model [1] by SRPES as well as the surface morphological changes by atomic force microscopy (AFM) during the initial nonroughening on n-Si(111). The experimental procedure for PES investigations after photoelectrochemical treatment is described elsewhere [2]. Fig. 1 shows Si 2p spectra obtained for electrochemically H-terminated n-Si(111) (a), after anodisation in dilute NH₄F and sample emersion slightly positive of open circuit potential (ocp) (b) and after emersion at the first photocurrent maximum (c). The deconvolution of the spectra leads to contributions due to surface species (2) – (6) whose shift in binding energy can be compared with partial charges of surface species sugges-

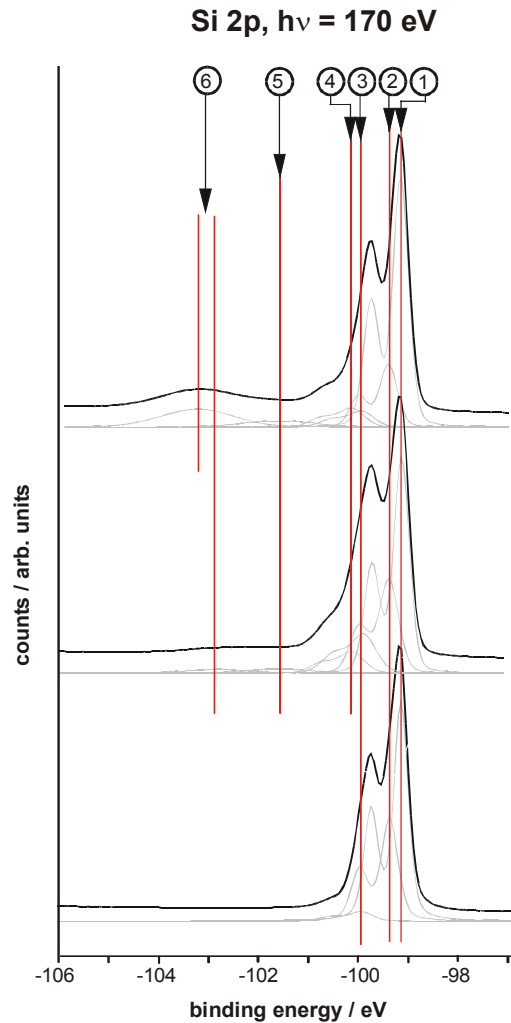


Fig. 1. Si 2p spectra obtained after electrochemical H-termination (a), after sample emersion slightly anodic of ocp (b) and after sample emersion at the 1st photocurrent maximum (c). 1: bulk signal; 2: surface core level shift (scl) due to H-termination; 3: scl due to Si-OH-H species; 4: scl due to Si-F-H species; 5: signal due to Si(OH)₃ species (precipitate); 6: twofold oxidised Si surface species being not attributable to SiO₂ (see text).

ted in the model which are obtained by density functional theory (DFT) calculations. The result is shown in Fig. 2. The evidence of the

respective surface species seems to confirm the chemical aspects of the model, but so far the

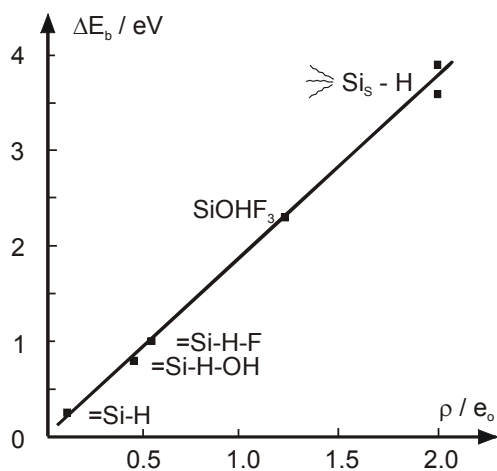


Fig. 2. Observed binding energy shifts ΔE_b vs. partial charges ρ for different surface species suggested in the model of ref. [1]. Species with $\rho = 2$: see text.

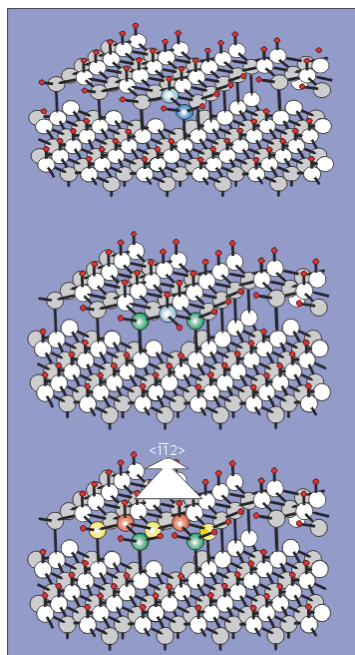


Fig. 3. Visualisation of the dissolution model suggested in ref. [1]. Top: a kink site atom (dark blue) is firstly attacked. Middle: After removal of the subsequent atom (light blue) the green atoms will be etched. Bottom: Subsequently the green, red and yellow atoms are taken away.

model describes no pit formation. In the model, a kink site atom at a terrace edge is assumed to start the dissolution process which then continues in lateral direction. This is

illustrated in Fig. 3. Only terrace removal and a smoothing of the saw-tooth like terrace edges being typical for Si(111) with a small miscut ($< 0.5^\circ$) will be the consequence of the suggested mechanism.

In contrast, a cautious anodisation with minute flown charge reveals first pits being 1 mono-layer (ML) deep at reentrant sites (Fig. 4a) and after slightly increased flown charge also at more linearly shaped terrace edges (Fig. 4b). Besides, one observes a smoothing of the zig-zag shaped terrace edges as being expected from the model.

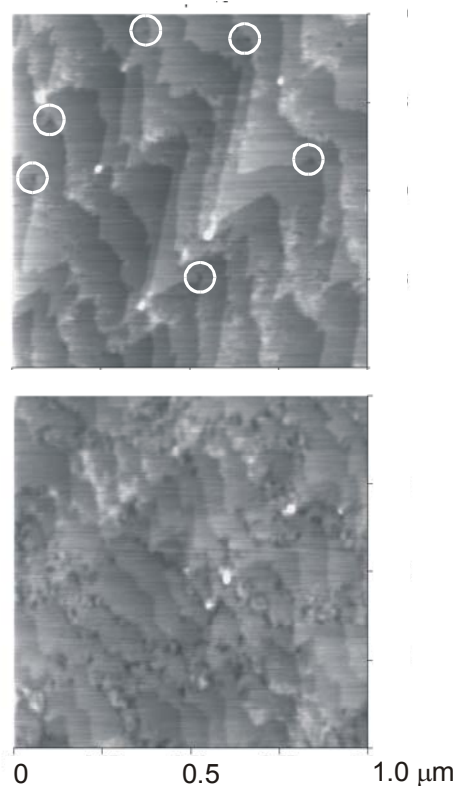


Fig. 4. AFM micrograph of FZ n-Si(111) (a): after anodisation from ocp to + 0.1 V positive of ocp in 0.1M NH_4F , pH 4.5. (b): after additional 15 s at 0.1 V for 15 s. Charge flown: 0.06 mCcm^{-2} (a) and 0.53 mCcm^{-2} (b). Grey scale indicates height.

Because the pit formation requests the removal of a fully coordinated surface atom a mechanism differing from the suggested model must act. A detailed analysis of the charge balance at the Si/electrolyte contact [3] under our experimental conditions leads to a potential drop of 0.096 V in the semiconductor while only 4 mV drop off in the Helmholtz layer.

The respective number of counterions is therefore extremely low: only about 1 F⁻ ion per 3x10⁴ Si surface atoms is necessary to build up the potential drop in the Helmholtz layer. Under these conditions, the usual double layer model assuming a smeared out electrolytic charge becomes invalid. Therefore the question arises at which places the counterions will be localised.

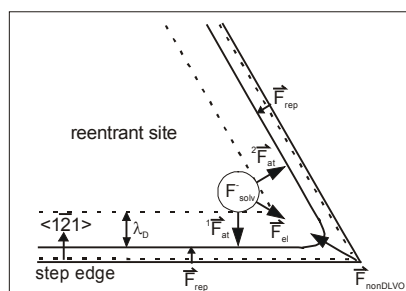
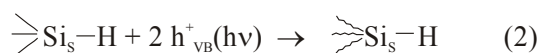


Fig. 6. Schematic of the origin of nanopit formation due to localisation of a F⁻ ion in a reentrant site. The acting forces are denoted as: F_{rep} : repulsive force due to hydrophobic-hydrophilic interaction; F_{at} : attractive force due to semiconductor charging; F_{el} resulting electrostatic force; λ_D : Debye length; F_{solv} : solvated fluoride anion.

Fig. 6 shows a reentrant site in detail. The combined electrostatic attraction forces due to semiconductor charging and field enhancement at terrace step edges will pull the F⁻ ion into the corner of the step edges. The solvated F⁻ ion, however, is hydrophilic while the H-terminated Si surface is hydrophobic. This results in a repulsive non-DLVO force [4]. The F⁻ ion will be immobilised if both forces counterbalance each other. The effect of counterion immobilisation will lead to a very local electric field at this site which will deflect photo-generated holes to Si atoms in the vicinity of the counterion where they can be oxidised. We suggest a reaction corresponding to



which will weaken considerably the respective Si atom backbonds. This renders possible a solvolytic splitting of backbonds. Assuming this model leads to a rate determining step in the dissolution process which involves a Si²⁺ surface species. A line which is shifted by $\Delta E_b = 3.6$ and 3.9 eV, respectively, is indeed observed (Fig. 1) and fits well with the hitherto

found ΔE_b vs. ρ correlation (Fig. 2). This shift cannot be attributed to Si in SiO₂ because the correspondingly obtained O 1s line does not show contributions due to O in SiO₂ [5]. It should be noted that a process according eq. (2) is still divalent but a charge carrier doubling effect as observed in the mechanism corresponding to eq. (1) will not occur. The effect, however, will be comparably small because we showed in a former study [6] that presumably only 10-20% of the total flown charge will be consumed for pit formation during initial nanoroughening while the predominant part of the charge is used for terrace removal.

J. Jakubowicz and E. Goncalves gratefully acknowledge financial support by the DFG in the Priority Program „Fundamentals of Electrochemical Nanotechnology“.

References

- [1] P. Allongue, V. Kieling and H. Gerischer, *Electrochim. Acta* **40**, 1353 (1995)
- [2] H.J. Lewerenz, H. Jungblut and S. Rauscher, *Electrochim. Acta* **45**, 4627 (2000)
- [3] A. Natarjan, G. Oskam and P. Searson, *J. Phys. Chem. B* **102**, 7793 (1998)
- [4] D. N. Petsev and P. G. Vekilov, *Phys. Rev. Lett.* **84**, 1339 (2000)
- [5] H. J. Lewerenz, M. Aggour, C. Murrell, M. Kanis, H. Jungblut, J. Jakubowicz, P. A. Cox, S. A. Campbell, P. Hoffmann and D. Schmeisser, *J. Electrochem. Soc.* **150**, E185 (2003)
- [6] J. Jakubowicz, H. Jungblut and H. J. Lewerenz, *Electrochim. Acta* **49**, 137 (2003)

Temperature dependent EXAFS measurements of thin metallo-supramolecular films

Y. Bodenthin^{1*}, U. Pietsch¹, D. G. Kurth², J. Grenzer¹, Th. Geue¹ and H. Möhwald²
²Max Planck Institute of Colloids and Interfaces, D-14424 Potsdam (Germany), Tel:
¹University Potsdam, Department of Physics, Potsdam (Germany)
^{*}bodenth@rz.uni-potsdam.de, Tel: +49331977-1580, Fax: -1133

The aim of the experiment is to study temperature dependent changes in the coordination sphere of metallo units in a supramolecular layer structure. In a ligand field of octahedral symmetry, the d-orbitals of the metal ions split into low-lying t_{2g} and high-lying e_g subsets. A lengthening of the metal ion–ligand bond due to the occupation of the anti-bonding e_g subset may give rise to a spin crossover. Above 318 K the system undergoes a transition from a low-spin (LS) t_{2g}^6 electronic configuration to a high-spin (HS) $t_{2g}^4 e_g^2$ electronic configuration. A reversible amphiphilic phase transition causes sufficient mechanical strain within the layer. This strain distorts the coordination sphere of the metal units resulting in a transition between low- to high-spin state.

The system consists of metallo-polyelectrolytes (MEPE **1**), prepared in an aqueous solution by self-assembly of ditopic 1,4-bis(2,2':6',2''-terpyridin-4'-yl)benzene and Fe^{2+} ions. The subsequent self-assembly of MEPE and dihexadecyl phosphate amphiphiles (DHP) lead to a completely non-covalent, hydrophobic polyelectrolyte-amphiphile-complex (PAC **2**)ⁱ. Thin films of PAC were prepared by means of Langmuir Blodgett technique (Fig. 1).

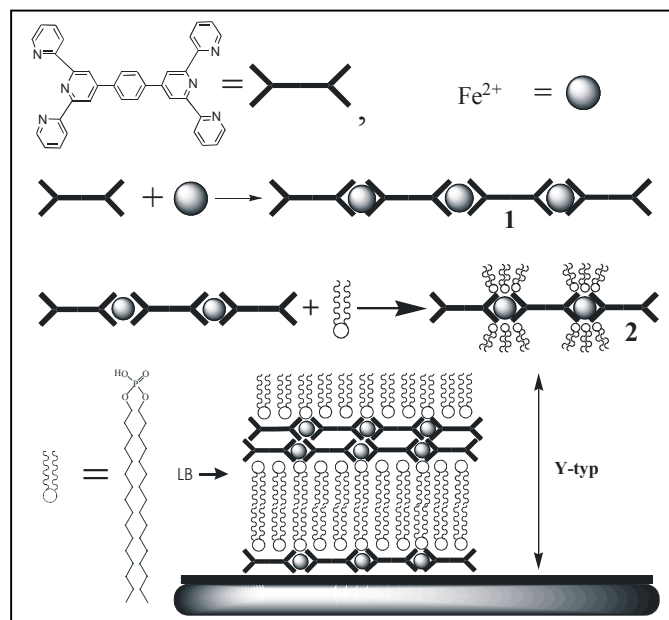


Fig. 1 Scheme of the metallo-supramolecular system used in the experiments

The experiments were performed at the KMC 2 beamline at BESSY II, exploiting the fluorescence yield $I_{\text{fluor}}(E) \sim \mu(E)$ of the Fe^{2+} ionsⁱⁱ. The incoming light strikes the sample under grazing incidence conditions ($\alpha_i = 0.15^\circ - 0.2^\circ$). We use an energy-dispersive Röntec detector attached perpendicular to the sample surface. The background-noise can be suppressed by setting a region of interest giving rise to higher accuracy of the measurements.

Fig 2. shows a typical EXAFS-function $\chi(k) = (\mu(k) - \mu_0(k)) / \mu_0(k)$ of Fe-PAC films and its theoretical fit at room temperature (RT). It is obvious that the EXAFS data cannot be fitted by a single shell model. The fit was done in terms of a two core approximation with two different iron-nitrogen distances $r_1 = 1.76 \pm 0.01 \text{ \AA}$ and $r_2 = 2.18 \pm 0.02 \text{ \AA}$ and occupation numbers 4 and 2, respectively. These numbers define a deformed octahedron with the long axis perpendicular to the film normal.

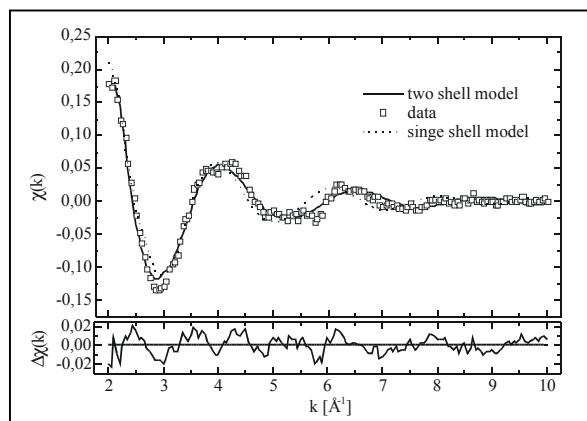


Fig.2: EXAFS function of a 11 Monolayer film and theoretical calculation

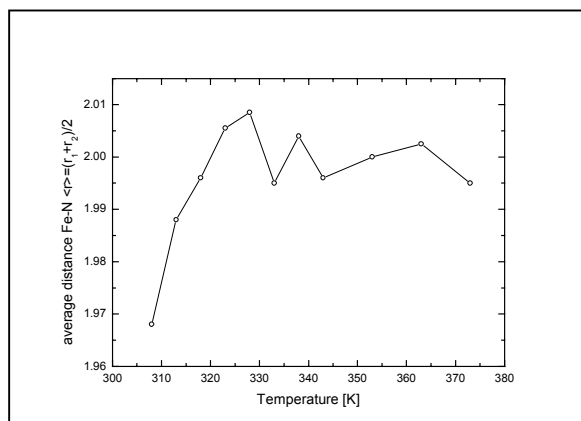


Fig.3: Increasing deformation of coordination sphere of metallo-centres

Temperature dependent EXAFS measurements indicate a structural change in the coordination geometry. Increasing the temperature the average distance $\langle r \rangle = (r_1 + r_2) / 2$ of the Fe-N bonds increase from 1.97 \AA at RT to 2.01 \AA at 328 K. The ratio r_2 / r_1 remains unchanged at 1.24 on the entire temperature scale. The increasing deformation of the Fe-N octahedron is in accordance with the strong rearrangement of the film structure found in temperature dependent simultaneous measurements of grazing incidence diffraction (GID) and specular reflection (XRR)ⁱⁱⁱ. This amphiphilic phase transition induce a mechanical strain to the MEPE and deforms the Fe-N octahedron opening the way for spin transitions in the material.

ⁱ D. G. Kurth, P. Lehmann, M. Schütte, *Proc. Natl. Acad. Sci.* 97, 5704- 5707 2000

ⁱⁱ A. Erko, I. Packe, C. Hellwig, M. Fiber-Erdmann, O. Pawlitzki, M. Veltkamp, W. Gudat, *AIP Conference Proc.* 521, p.p. 415-418, 2000, A. Erko, I. Packe, W. Gudat, N. Abrosimov, A. Firsov, *SPIE* 4145, p.p. 122-128, 2000

ⁱⁱⁱ Y. Bodenthin, J. Grenzer, R. Lauter, U. Pietsch, P. Lehmann, D.G. Kurth and H. Möhwald, *J. Synchr. Rad.* 9, 206-209, (2002)

Chemical State Depth Profiling of Ultra-Thin Oxynitride Layers by Photoelectron Spectroscopy

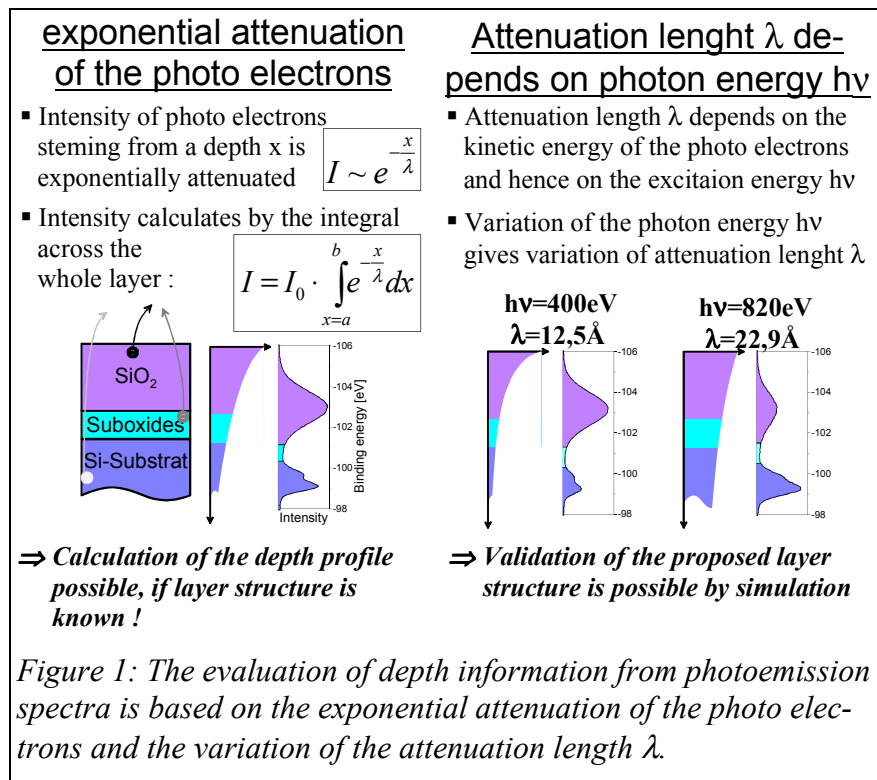
P.Hoffmann, D.Schmeißer

BTU Cottbus / Lehrstuhl Angewandte Physik-Sensorik / Universitätsplatz 3-4 / 03044 Cottbus

Introduction

Oxynitrides are supposed to replace the conventional SiO_2 for ultra-thin (<10nm) gate dielectrics. The main reasons therefore are the larger dielectric constant ϵ of oxynitrides (linear increase with nitrogen content from 3.9 of SiO_2 to 7.8 of Si_3N_4 [1]) and its easy integration into common semiconductor processes by replacing O by N. Therefore it is clear that the understanding of the formation process of oxynitrides grown by various methods (thermal oxidation and oxynitridation of Si by NO, N_2O and NH_3 / chemical deposition like CVD or ALD) is well investigated and is summarised in many review articles [2]. A main aspect of all these investigations always was the depth structure of the oxynitride films. But common depth profiling techniques suffer from limited depth resolution (SIMS) or limited information about bonding states (SIMS, Ion Scattering). This information can be derived from photoelectron spectroscopy (PES). Due to its extreme surface sensitivity PES is especially suitable for ultra-thin layers. Furthermore λ can be varied by the

kinetic energy of the photoelectrons and hence by the excitation energy. As PES always gives a sum signal from all layers within the analysed area the variation of the analysed depth can open up the possibility to derive a depth structure of the sample from the PES data.



Experimental

For application of this method described above the core levels of interest (on oxynitrides these are Si2p, N1s, and O1s) have to be measured at various photon energies from around 50eV above the ionisation threshold (highest surface sensitivity) to the highest available photon energy (highest bulk sensitivity). Furthermore the attenuation length λ has to be known in dependence of the kinetic energy of the photoelectrons. For Si, SiO_2 and Si_3N_4 these values were calculated [3] and validated on test samples [4].

We used samples prepared in-situ by heating Si(111) in a N_2O ambient at various pressures and temperatures [5] as well as oxynitride layers made by RTP- [6] and plasma-enhanced CVD-processes [7].

Results and Discussion

Performing a line decomposition of the measured PES data the main components like Si substrate, silicon dioxide SiO_2 , oxynitride SiO_xN_y , and nitride Si_3N_4 were detectable. An example

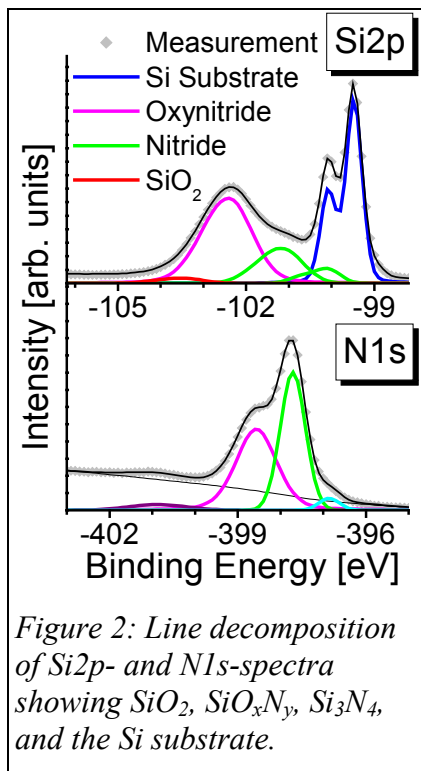


Figure 2: Line decomposition of Si2p- and N1s-spectra showing SiO₂, SiO_xN_y, Si₃N₄, and the Si substrate.

of a line composition for PES data of an oxynitride layer containing all, SiO₂, SiO_xN_y, and Si₃N₄, is given in Figure 2. This line decomposition was done for all spectra of a certain core level emission measured at different photon energies and hence at different information depths λ . On the in-situ prepared samples (heated in 10⁻⁴..10⁻²mBar N₂O) a strong variation of the intensity ratio [Si₃N₄]/[SiO_xN_y] was found. This is exemplary shown in Figure 3. The increase of the nitride signal intensity with increasing λ shows that the nitride must be located underneath the oxynitride and proves a layered structure of the film A model was created then ([6], [7]), that allows to calculate the thickness of the nitride layer from the N1s and the Si2p spectra redundantly. For the sample shown in Figure 3 it was calculated 3.0Å ±0.7Å (standard deviation) for the nitride layer at an overall layer thickness of 6.5Å ±0.8Å. This layered structure with Si₃N₄ at the Si substrate was found for all oxynitrides prepared in N₂O.

On the oxynitride prepared with RTP or PE-CVD methods only on samples with high nitrogen content Si₃N₄ could be found. The other samples exhibit exclusively oxynitride

SiO_xN_y. And even on those sample where nitride was found no layered structure like described above was detectable.

In conclusion it can be noted that photoelectron spectroscopy with variable excitation energy allows the investigation of the depth structure without destroying the sample especially on ultra-thin layers. On oxynitride layers it was possible to distinguish oxynitride and nitride and to figure out the preparation regime which gives the desired depth structure (layered or mixed distribution of nitride and oxynitride).

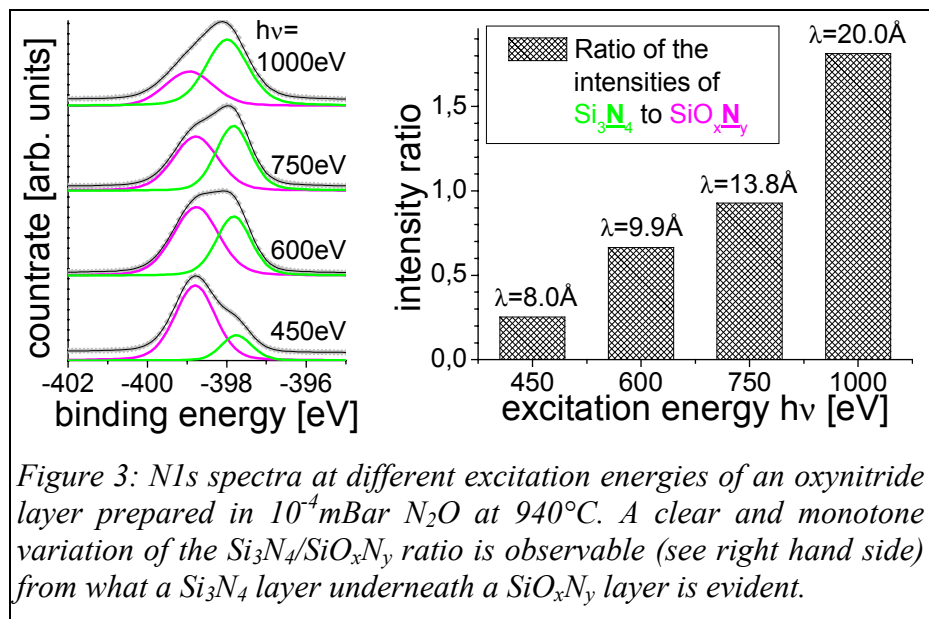


Figure 3: N1s spectra at different excitation energies of an oxynitride layer prepared in 10⁻⁴mBar N₂O at 940°C. A clear and monotone variation of the Si₃N₄/SiO_xN_y ratio is observable (see right hand side) from what a Si₃N₄ layer underneath a SiO_xN_y layer is evident.

Acknowledgement

We like to acknowledge Dr.G.Roter and Dr.Z.Nenyeyi from Mattson Thermal Products, Dornstadt for providing the RTP oxynitride layers and Prof.R.Beck from Warsaw Technical University for preparing the PE-CVD samples.

- [1] D.M.Brown, P.V.Gray, F.K.Heumann, H.R.Philipp, E.A.Taft: J. of the Electrochem. Soc. **115** (1968) 311.
- [2] E.P.Gusev, H.C.Lu, E.L.Garfunkel, T.Gustafsson, M.L.Green: IBM J.Res.Developm. **43** (1999) 265-286.
- [3] S.Tanuma, C.J.Powell, D.R. Penn: Surf. Interf. Anal. **17** (1991) 911.
- [4] H. Yamamoto, Y.J. Baba, T.A Sasaki: Surface Science **349** (1996) L133-L137.
- [5] P. Hoffmann, R.P. Mikalo, D.R. Batchelor, D. Schmeißer, R. Follath: BESSY Jahresbericht 2000, 165.
- [6] P.Hoffmann, D.Schmeißer, G.Roters, Z.Nenyeyi: Thin Solid Films **428** (2003) 216.
- [7] P.Hoffmann, D.Schmeißer, R.B.Beck, M.Cuch et al.: Journal of Alloys and Compounds, submitted.

Temperature-dependent surface photovoltage of polycrystalline Cu(In,Ga)Se₂

T. Schulmeyer, R. Hunger and A. Klein

Darmstadt University of Technology, Institute of
Materials Science, Petersenstrasse 23, D-64287 Darmstadt, Germany

Thin film solar cells using polycrystalline Cu(In,Ga)Se₂ chalcopyrite semiconductors have reached conversion efficiencies of about 19 %. High conversion efficiency solar cells are prepared on soda lime glass substrates using a film sequence Mo (back contact), Cu(In,Ga)(S,Se)₂ (absorber), CdS (buffer layer), ZnO (window). The p-Cu(In,Ga)(S,Se)₂ / n-CdS heterointerface is thereby of crucial importance for obtaining best conversion efficiencies. The surface of these polycrystalline films is Cu-poor, because of the slightly Cu-poor growth conditions. The existence of this Cu-poor surface layer with a lower valence band maximum and a wider band gap is also used to describe the recombination mechanisms of Cu(In,Ga)Se₂ chalcopyrite solar cells. The valence band offset between the Cu-poor Cu(In,Ga)₃Se₅ surface composition and the Cu-rich Cu(In,Ga)Se₂ bulk composition is predicted from theory to 0.34 eV [1].

In this contribution, temperature-dependent photovoltage measurements with synchrotron radiation induced photoelectron emission of polycrystalline Cu(In,Ga)Se₂ surfaces are presented. The photoemission characterization was performed at the TGM 7 beamline with a UHV preparation and a PHOIBOS 150 electron analyser. Contamination free Cu(In,Ga)Se₂ surfaces are prepared by the selenium decapping process, which is described elsewhere [2,3]. These Cu-poor grown Cu(In,Ga)Se₂ absorbers, which were used in this contribution show reproducible the Cu-poor Cu(In,Ga)₃Se₅ surface composition. Photoelectron spectra of the Ga 3d/In 4d emission line and the valence band maximum were taken with an excitation energy of 80 eV at room temperature. After the measurement, the sample was cooled down with a cryostatic temperature regulator filled with liquid nitrogen. After 30 minutes, a thermocouple, which is placed beneath the sample holder, displays a temperature of about -170°C. After a period of additional 30 minutes, a spectrum of the Ga 3d/In 4d emission line of the cooled sample was taken. The liquid nitrogen supply has been stopped and the sample started to warm up. A very slow heating rate was desired to fulfil temperature equilibrium, because of the used glass substrate. The heating rate was determined to 1 K/min. After every temperature increase of 2 K, a spectrum of the Ga 3d/In 4d emission line was taken. A heater was used to increase the sample temperature up to 100°C after reaching room temperature. The heating rate was kept in the range of 1 K/min. In Fig. 1, the spectra series of the Ga 3d/In 4d emission lines of the decapped Cu(In,Ga)Se₂ surface are displayed. The first spectrum was measured after cooling down the sample to -170°C. The following Ga 3d/In 4d emission lines were recorded during warming up the sample up to 100°C. The distance between the valence band maximum and the Ga 3d/In 4d core level was determined at room temperature to 17.23 eV.

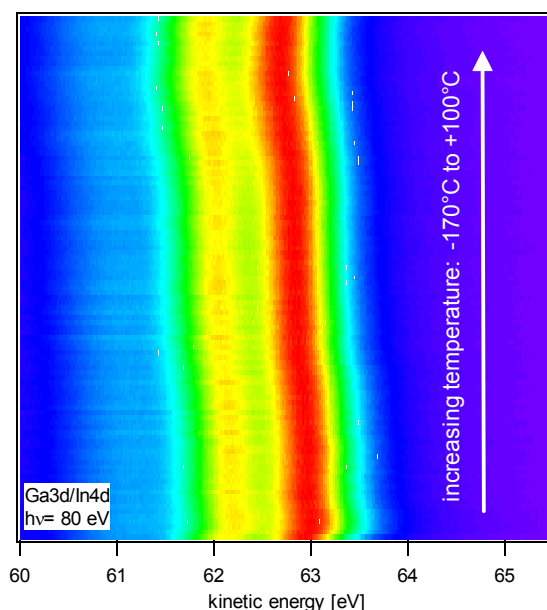


FIG. 1. Image plot of the Ga 3d/In 4d emission lines taken with increasing temperature starting from -170 °C (bottom of the picture) up to +100°C (top of the picture). An energetic shift induced by the temperature is clearly visible.

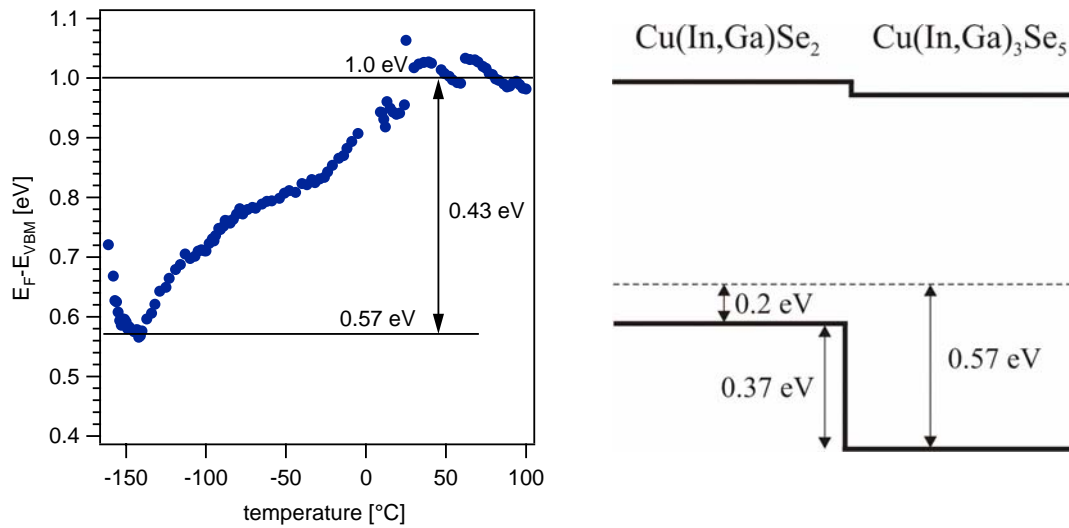


FIG. 2. Left: Evolution of the valence band maximum in dependence of temperature. The energetic shift of the core level was determined to 430 meV. Right: Valence band alignment between the Cu-poor surface layer and the Cu-rich bulk composition. A valence band offset of 370 meV was determined, by assuming flat band conditions at low temperatures and a bulk Fermi-level of 0.2 eV.

By adding this energy value to all kinetic energies at certain temperatures, the evolution of the valence band maximum in dependence of sample temperature can be calculated. The result of this procedure is displayed in Fig. 2 (left). The distance between the Fermi-level and the valence band maximum at room temperature can be determined to 1.0 eV. This value is in good agreement with the value determined by ultra violet measurements of decapped $\text{Cu}(\text{In,Ga})_3\text{Se}_5$ surfaces [2]. At low temperatures, we assume, that flat band conditions are achieved. The distance between the Fermi-level and the valence band maximum was determined to 0.57 eV. At temperatures between -170°C and -150°C , a slight decrease of the distance between the Fermi level and the valence band maximum is visible. We assume, that the sample didn't reach the lowest temperature at the time, when the measurement began to start, which might be due to the used glass substrate. For flat band conditions, the energy value at -150°C was therefore used. In Fig. 2 (right), the complete energy diagram of the decapped $\text{Cu}(\text{In,Ga})_3\text{Se}_5$ surface is given. Our results lead to a valence band offset of 0.37 eV by assuming a bulk distance of the Fermi-level of 0.2 eV. The latter seems reasonable, since solar cells with 14% efficiency can be prepared using identically prepared absorbers [2]. A good p-doping of the absorber is necessary to obtain such efficiencies. There is quite good agreement between the theoretical predicted valence band offset of 0.34 eV and the value of 0.37 eV determined from the SPV measurements, which indicates that the used experimental method might be appropriate to investigate the modification of the electronic surface structures.

This work was supported by the German Bundesministerium für Bildung und Forschung under contract no 01SF0114.

- [1] S.B. Zhang, S.-H. Wei, A. Zunger, and H. Katayama-Yoshida, *Phys. Rev. B* **57** (1998), 9642.
- [2] T. Schulmeyer, R. Hunger, W. Jaegermann, A. Klein, R. Kniese, and M. Powalla, *Proceedings of the 3rd World Conference on Photovoltaic Energy Conversion*, (Osaka, 2003).
- [3] T. Schulmeyer, R. Kniese, R. Hunger, W. Jaegermann, M. Powalla, and A. Klein, *Thin Solid Films* (in press).

Study of Co₂MnGe Heusler thin films and multilayers by soft x-ray resonant scattering

J. Grabis, A. Bergmann, A. Nefedov, K. Westerholt, H. Zabel

*Experimentalphysik IV, Ruhr-Universität Bochum, Universitätsstrasse 150, 44780 Bochum
Germany*

We report on the results of XRMS reflectivity and diffuse scattering studies on a [Co₂MnGe/Au]₅₀ superlattice. To obtain the magneto-optical constants in the region of $L_{2,3}$ Mn and Co absorption edges, XMCD spectra were measured in a separate experiment.

By electronic band structure calculations the Heusler alloy Co₂MnGe has been predicted to be a half metallic ferromagnet. This property is rare for intermetallics and attractive for application in spin dependent electron transport devices such as e.g. giant magneto-resistance (GMR) or tunnelling magneto-resistance (TMR) devices or for the injection of spin polarized electrons into semiconductors. RF-sputtered single films and superlattices with Au as non-magnetic spacer layer have been investigated by XMCD and XRMS in the range of Mn and Co L absorption edges.

All measurements have been performed at BESSY II using the ALICE diffractometer for soft x-ray resonant magnetic scattering which has been built at the Ruhr-University Bochum [1]. The diffractometer comprises a two-circle goniometer and works in a horizontal scattering geometry. The sample environment consists of a He closed-cycle cryostat ($T = 30\text{ K} - 400\text{ K}$) and a rotatable electro-magnet ($H_{max} = 2.7\text{ kOe}$), which makes it possible to apply the magnetic field in any direction of the scattering plane.

X-ray absorption spectra (XAS) of a single Co₂MnGe film have been measured at beamline PM3. The XAS spectra were recorded at the $L_{2,3}$ absorption edges of Mn and Co using circularly polarized light at an incidence angle of 40° measured from the surface of the in-plane magnetized sample. The total electron yield (TEY) detection mode was used, measuring the sample drain current. The XMCD was measured with constant polarization, switching the magnetic field. It is assumed, that the TEY signal is proportional to the absorption. While the Co XAS is similar to that of the pure metal, the Mn spectrum shows a multiplet structure. This effect is not expected theoretically and indicates disorder in our samples. To obtain absolute values of the imaginary part β of the refractive index, the background of the gold cap layer must be subtracted. Therefore the absorption spectra have been normalized to published tabulated values in the pre- L_3 and post- L_2 energy regions. The associated real part δ_{\pm} can be calculated by applying the Kramers-Kronig relations (Fig. 1 a). With knowledge of the optical constants the reflected intensities and asymmetries can be simulated using an optical approach [2]. For this purpose a program has been written and successfully tested for an antiferromagnetically coupled Fe/Cr superlattice. The simulation of Heusler reflectivities is still in progress at the moment.

By means of diffuse scattering, in- and out-of-plane structural and magnetic correlations as well as charge and charge-magnetic roughnesses can be studied. We used mainly two different scans to study the diffuse scattering: A longitudinal off-specular ($\omega - 2\theta$) scan, where the sample angle ω is slightly offset from the specular direction (corresponding to a scan in q_z at fixed $q_x \neq 0$), yields information about out-of-plane correlated roughness. A q_x scan at fixed q_z allows to determine in-plane correlation lengths. From the simulation of a reflectivity in the hard x-ray range the layer thicknesses ($d_{\text{Heusler}} = 29.8\text{ \AA}$, $d_{\text{Au}} = 22.6\text{ \AA}$) and roughness parameters ($\sigma_{\text{Heusler}} = 5.5\text{ \AA}$,

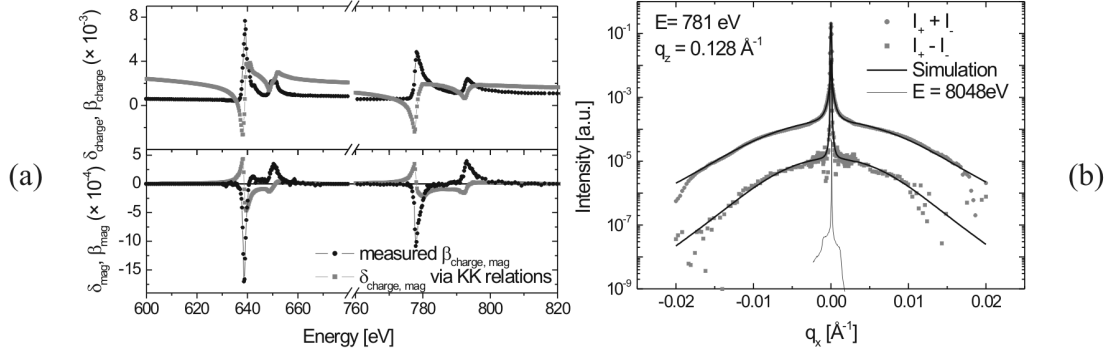


Figure 1: (a) Refractive index of Co_2MnGe (PM3). (b) q_x -scans at the position of the first order Bragg peak (UE56/2-PGM2).

$\sigma_{\text{Au}} = 3.4 \text{ \AA}$) can be determined. The large peaks in the diffuse scattering indicate that the roughness is correlated vertically almost through the whole layer system. We have measured the intensity along reciprocal-space vector q_x at the q_z position of the first order Bragg peak for the same superlattice. The incoming beam ($E=781 \text{ eV}$, Co L_3 edge) was circularly polarized and the magnetic field was applied parallel (I_+) and antiparallel (I_-) to scattering plane and sample surface, respectively. Sum (charge diffuse scattering) and difference (charge-magnetic diffuse scattering) of the intensities are depicted in Fig. 1 (b). For comparison the same scan at hard x-ray energies ($E=8048 \text{ eV}$) is shown in the same graph. A big advantage of soft x-rays is the large range of accessible q_x values. Due to the long wavelength and therewith large scattering angles the limiting sample horizon is at much higher values as compared to hard x-ray scattering. Therefore the short correlation length corresponding to the size of the crystallites can only be seen at low photon energies. There is no indication for multiple-scattering effects like Yoneda wings in the soft x-ray diffuse scattering. Therefore the experimental curves have been simulated using the Born approximation assuming self-affine roughness [3]. To reduce the number of free fit parameters it was assumed in a first step that the roughness is perfectly correlated through the whole superlattice, which is justifiable by longitudinal off-specular scans. There are two in-plane correlation lengths present in the diffuse scattering: One - as mentioned above - corresponding to the size of the crystallites ($\xi_1^c = 250 \text{ \AA}$) and one corresponding to a long-range roughness which might stem from steps in the sapphire substrate ($\xi_2^c \approx 6000 \text{ \AA}$). In the difference curve the short-range correlation is reproduced with a slightly higher value ($\xi_1^{cm} = 300 \text{ \AA}$), while the long-range correlation has increased much more and is now almost hidden in the specular peak ($\xi_1^{cm} \approx 12000 \text{ \AA}$).

We would like to thank T. Kachel, H.-C. Mertins, W. Mahler and B. Zada for their help with beam-line operation. This project is funded by BMBF O3ZAE7BO.

References

- [1] J. Grabis, A. Nefedov, H. Zabel, *Rev. Sci. Instr.* **74**, 4048 (2003)
- [2] J. Zak *et al.*, *Phys. Rev. B* **43**, 6423 (1991)
- [3] C. S. Nelson *et al.*, *Phys. Rev. B* **60**, 12234 (1999)

XMCD investigation of molecular magnetism in metallo-supramolecular films

Y. Bodenthin^{1*}, U. Pietsch¹, D. G. Kurth², J. Grenzer¹, Th. Geue¹ and H. Möhwald²
²Max Planck Institute of Colloids and Interfaces, D-14424 Potsdam (Germany), Tel:
¹University Potsdam, Department of Physics, Potsdam (Germany)
^{*}bodenth@rz.uni-potsdam.de, Tel: +49331977-1580, Fax: -1133

The aim of the experiment was to detect the spin crossover in a lamellar superstructure containing a quasi one-dimensional rigid metallo-supramolecular polyelectrolyte (MEPE) complex.

Reflectivity spectra of several metallo-supramolecular films were recorded using circular polarized light of the undulator U56. Both polarisation states of the incident light (left and right hand circular polarization) were measured close to the iron absorption edges (700 eV to 730 eV). The difference of the two reflection spectra (asymmetry ratio $A(E) = (I_r - I_l) / (2 \langle I \rangle)$) gives information about the spin and orbit momentum of the iron ions within the MEPE. The experiments were performed using a fixed reflectivity geometry ($\alpha_i = 2^\circ$) below the critical angle of the film and above the critical one of the substrate.

The investigated system is shown in Fig. 1. It consists of several thin layers of Fe-polyelectrolyte-amphiphile-complexes deposited in Y-conformation on a silicon substrate by means of Langmuir-Blodgett technique. In the polymer backbone **1** (Fig. 1) the Fe^{2+} ions are surrounded by ligands of 1,4-bis(2,2':6',2''-terpyridin-4'yl)-benzene creating a nearly octahedral crystal field. To build the complex **2** (Fig. 1) 6 dihexadecylphosphate-amphiphile chains (DHP) per molecule unit are electrostatically added. Previous investigations have shown that this system shows paramagnetic properties at temperatures near and above room temperature. This can be explained by the small concentration of Fe^{2+} within the sample and their relative long interionic distances.

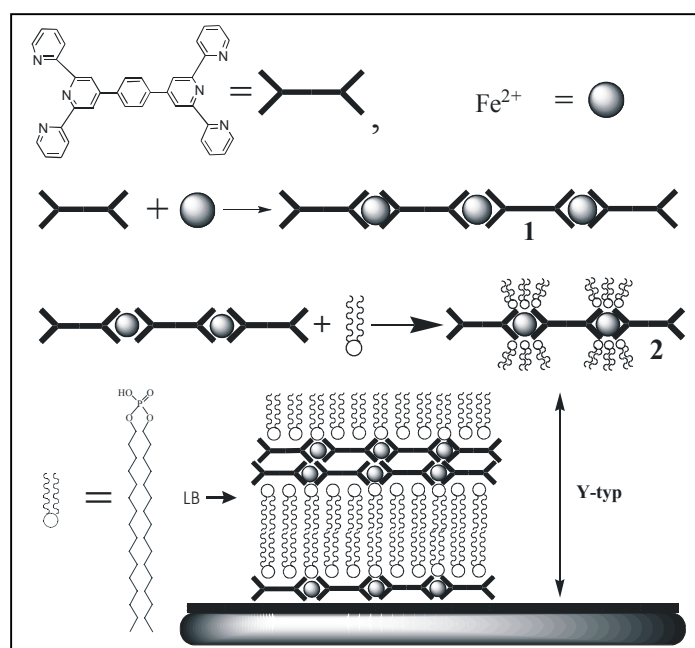


Fig. 1 Scheme of the metallo-supramolecular system used in the experiments

Figure 2 shows the reflectivity of the left and right circular polarized light vs. the energy of a 11 ML film. A magnetic field of about 300 Oe supplied by permanent magnets placed below the sample was applied in a longitudinal geometry. Due to the energy dependence of the reflectivity coefficient the overall reflectivity decreases as a function of energy of the probing light. Additionally, there are two minima at about 706 eV and 718 eV corresponding to the L_3 and L_2 absorption edges of iron. Figure 3 shows the calculated asymmetry ratio between the measured intensities vs. the energy of two different samples at room temperature. The measured background noise was about 0.1~0.2 %. Resonant dichroic signals of up to three percent were found at the Fe $2p_{3/2}$ resonance. This is a clear evidence for the magnetization of the iron-ions because no dichroic signals were found without an applied field. Unfortunately the refractive index $n = 1 - (\delta \pm \Delta\delta) + i(\beta \pm \Delta\beta)$ is a complex quantity and both, the real (dispersion δ) and imaginary parts (proportional to absorption) are subject to change due to the interaction with the magnetic moment of the sampleⁱⁱⁱ. For a rough estimate we used functional dependencies of the magnetic contributions $\Delta\delta$ and $\Delta\beta$ calculated by an ab-initio method for BCC iron for the evaluation of our asymmetry data^{iv}. Due to the lower iron density within the investigated system this dependencies have to be scaled by factors of 0.7 and 0.07, respectively. Applying sum rules^v to the absorption parts β_{\pm} of the refractive index n a magnetic moment of about $0.5 \pm 0.3 \mu_B$ per iron ion for the spin-momentum was calculated. This value is in qualitative agreement with the results of spin-resolved neutron reflectivity measurements^{vi}. In contrast to neutron scattering XMCD is much faster and more convenient in temperature dependent measurements.

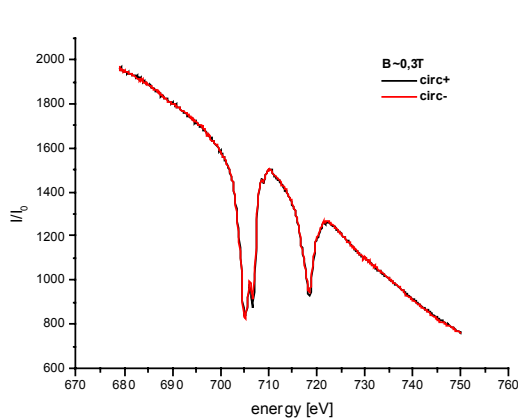


Fig.2: reflected intensities (circ.+ , circ.-) vs. incident photon energy

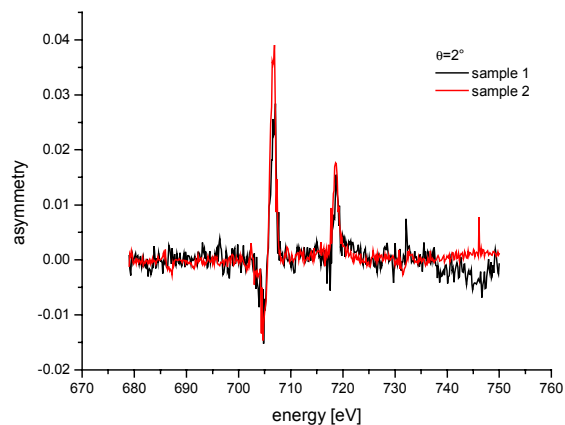


Fig.3: calculated asymmetry ratio(red, black) with an applied field $B \sim 0.3$ T and w/o field (blue)

ⁱ M. Schütte, D.G. Kurth, M.R. Linford, H. Cölfen, H. Möhwald, *Angew. Chem. Int. Ed.*, **37**, 2891 (1998)

ⁱⁱ Y. Bodenthin, U. Pietsch, *Bessy Annual Rep.* 239 (2001)

ⁱⁱⁱ H.-Ch. Mertins, D. Abrahamssohn, A. Gaupp, F. Schäfers, W. Gudat, O. Zaharko, H. Grimmer, P.M. Oppeneer, *Phys.Rev.*B66 184404 (2002)

^{iv} J. Kuneš, P.M. Oppeneer, H.-Ch. Mertins, F. Schäfers, A. Gaupp, W. Gudat, P. Novak, *Jour. Margn. Materials* 240 454-456 (2002)

^v C.T. Chen, Y.U. Idzerda, H.-J. Lin, N.V. Smith, G. Meigs, E. Chaban, G.H. Ho, E. Pellegrin, F. Sette, *Phys.Rev.Lett.* 75, 152 (1995)

^{vi} Y. Bodenthin, U. Pietsch, *ILL Experimental report*, 7-09-72, 2002

Soft x-ray resonant magnetic reflectivity of NiO/NiFe, NiO/Ni, and NiO/Fe bilayers modified by He-ion bombardment

D. Engel, A. Ehlers, H. Schmoranzer, A. Ehresmann
*Dept. of Physics, Kaiserslautern University of Technology,
 D-67663 Kaiserslautern, Germany*
 H.-Ch. Mertins, D. Abramsohn, W. Gudat
BESSY GmbH, D-14195 Berlin, Germany

The exchange bias field H_{eb} of magnetic layer systems consisting of a ferromagnetic layer adjacent to an antiferromagnetic layer can be modified by He-ion bombardment at defined ion doses both in magnitude and direction [1-3]. To gain more insight into the magnetic and structural modifications by the ion bombardment, $\theta / 2\theta$ -x-ray reflection measurements have been carried out with the BESSY polarimeter [4] at the beamline UE56/1-PGM at BESSYII. Samples were NiO/NiFe, NiO/Ni, and NiO/Fe exchange biased bilayer systems with polycrystalline structure. After preparation the samples have been bombarded with different ion doses in an applied magnetic field to obtain enhancement, reduction, and reversal of the original "as prepared" $H_{\text{eb},0}$. These samples together with an "as prepared" sample have been used for the experiments.

Structural information

A sketch of the investigated layer systems is shown in Fig. 1a). On Si as substrate NiO was grown as an antiferromagnetic (AF) layer of 50 nm thickness, followed by a ferromagnetic (F) layer (NiFe, Ni or Fe) of 5 nm thickness. To prevent oxidation, the system was capped by Ta.

The probe depth (see Fig. 1c)) of the used x-rays at energies of 851.7 eV (Ni

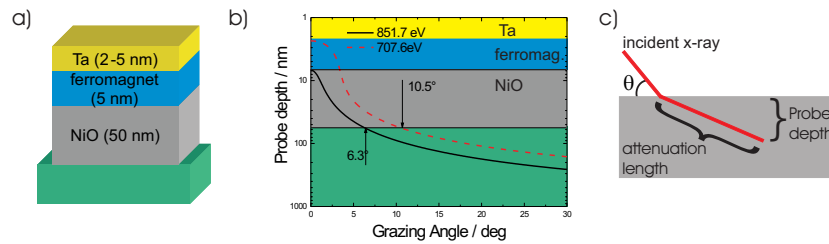


Fig. 1: a) Investigated layer system. As ferromagnet, NiFe, Ni and Fe was used. b) Probe depth of used synchrotron radiation: solid line 851.7 eV (Ni L_3 -edge), dashed line 707.6 eV (Fe L_3 -edge). c) Correlation between attenuation length and probe depth.

L_3 -edge) and 707.6 eV (Fe L_3 -edge) was simulated [5] and is shown in Fig. 1b). Until an energy-dependent angle θ_s the radiation is sensitive only to the Ta- and F-layer.

For the three investigated unbombarded layer systems the results of the $\theta / 2\theta$ -x-ray reflection measurements are shown in Fig. 2, where Fig. 2a), b) and d) were measured near the Ni L_3 -edge and c) was measured at the Fe L_3 -edge. From the width of the wiggles the thicknesses of the different layers can be computed. The broad structures (light grey) in Fig. 2a), b) and d) correspond to the added thicknesses of the Ta plus the F layers. The small wiggles (dark grey) correspond to the thickness of the total layer system. From 6.3° on, the wiggles of the layer systems with NiFe and Ni as ferro-

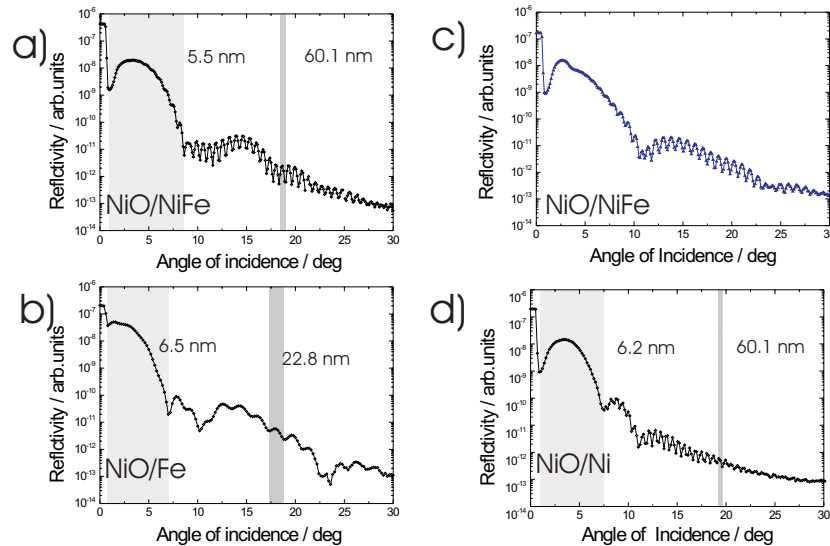


Fig. 2: $\theta / 2\theta$ -x-ray reflection measurements of unbombarded layer systems. a) NiO/NiFe, b) NiO/Fe, d) NiO/Ni, each measured near the Ni L_3 -edge. c) shows a NiO/NiFe layer system measured near the Fe L_3 -edge.

magnets are distinctive and the thickness of the total layer system fits well with fabrication data, whereas for Fe as ferromagnet, the wiggles do not represent the total layer system thickness. The reason for this is a different growth behaviour and/or a change in the refraction index due to chemical interactions at the AF/F-interface (e.g. formation of Fe_xO_y). In Fig. 2c) a $\theta / 2\theta$ -x-ray reflection measurement at an energy near the Fe L_3 -edge is shown for a sample with NiFe as AF. In comparison to a) it can be seen, that here beyond an angle of $\theta_s \approx 10^\circ$ the wiggles correspond to the full layer system. These different angles fit well with the ones indicated in Fig. 1b).

Interface modification by He-ion bombardment

One proposed mechanism of He-ion bombardment induced modifications of exchange-biased bilayers is structural modification due to defect creation in the AF volume as well as at the AF/F interface. In the first case, an enhancement of H_{eb} is due to creation of pinning centers of domains and change of the effective magnetic volume of the AF grains.

The comparisons of $\theta / 2\theta$ -x-ray reflection measurements for NiO/NiFe and

NiO/Fe, near the Ni L_3 -edge and Fe L_3 -edge, are displayed in Fig. 3a) and b), respectively, showing a pronunciation of the interference features after ion

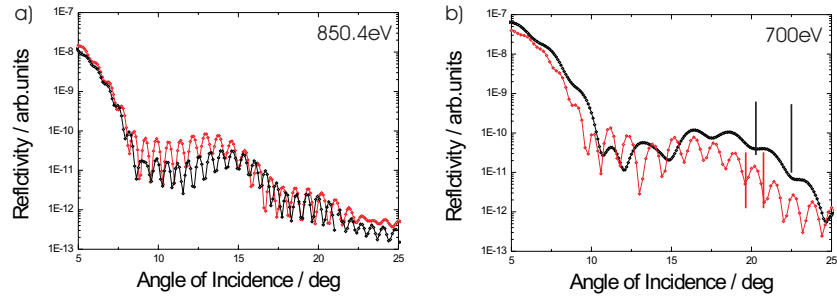


Fig. 3: $\theta/2\theta$ -x-ray reflection measurements of a) a NiO/NiFe-bilayer system near the Ni L_3 -edge, and b) a NiO/Fe-bilayer system near the Fe L_3 -edge. Black curves show the sample before and red curves after He-ion bombardment with 1×10^{14} ions/cm².

bombardment. In the case of the NiO/Fe-system the width of the wiggles decreases to a value close to the expected layer thickness, i.e. before bombardment a small wiggle corresponds to nearly 27 nm and after bombardment to 43 nm. The reason for a stronger pronunciation of the wiggles after ion bombardment is a sharpening of the gradient of the refraction index of all interlayer surfaces. This is due to a smoothing of the respective surfaces by the ion bombardment, which leads to a better exchange coupling at the AF/F interface and thus to a higher H_{eb} . The microscopic process of how the ions do smooth the interfaces, however, remain unclear.

References

- [1] T. Mewes, R. Lopusnik, J. Fassbender, B. Hillebrands, M. Jung, D. Engel, A. Ehresmann, H. Schmoranzler, Appl. Phys. Lett. 76, 1057 (2000).
- [2] A. Mougin, T. Mewes, M. Jung, D. Engel, A. Ehresmann, H. Schmoranzler, J. Fassbender, B. Hillebrands, Phys. Rev. B 63, 060409 (2001).
- [3] D. Engel, A. Kronenberger, M. Jung, H. Schmoranzler, A. Ehresmann, A. Paetzold, K. Röhl, J. Magn. Magn. Mater. 263, 275 (2003).
- [4] F. Schäfers, H.-Ch. Mertins, A. Gaupp, W. Gudat, M. Mertin, I. Packe, F. Schmolla, S. Di Fonzo, G. Soulli, W. Jark, R. Walker, X. Le Cann, M. Eriksson, R. Nyholm, Appl. Opt. 38, 4074 (1999).
- [5] Center for X-Ray Optics (CXRO), <http://cindy.lbl.gov/>

Acknowledgements

Prof. K. Röhl is acknowledged to let us use his Leybold Z700 sputter source. This work was funded by the Deutsche Forschungsgemeinschaft under contract number EH187/2.

Soft x-ray resonant magnetic scattering on CoO/Fe exchange bias bilayers

F. Radu, G. Nowak, J. Grabis, A. Nefedov and H. Zabel

Experimentalphysik IV, Ruhr-Universität Bochum, Universitätsstrasse 150, 44780 Bochum
Germany

When a ferromagnetic (F) thin film in contact with an antiferromagnetic (AF) thin film is cooled down through the Néel temperature (T_N) of the AF layer in an applied magnetic field, the hysteresis loop of the F layer develops a loop shift and an enhanced coercivity. Defects in the antiferromagnetic layer could lead to uncompensated spins inside it or/and at the AF interface that mediates the interaction between the F and AF layers. The search for such effective magnetic moment into the AF layer is subjected to element sensitive magnetic measurements provided by methods like x-ray magnetic circular dichroism (XMCD) or x-ray magnetic scattering (XRMS).

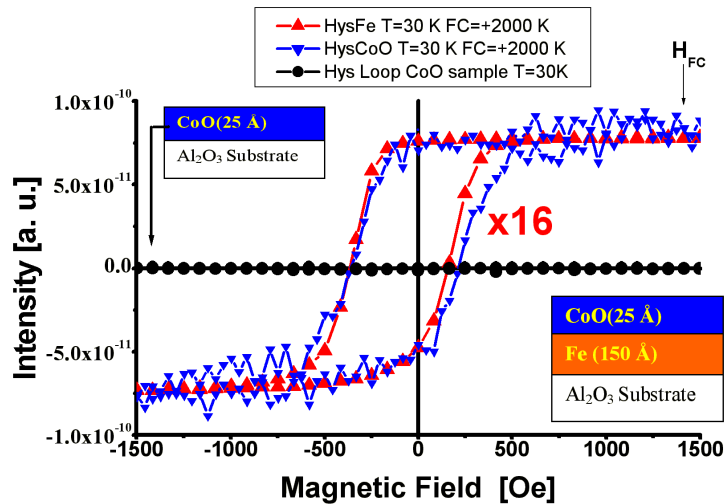


Figure 1: Elements specific hysteresis loops of the CoO/Fe exchange bias bilayer. The red curve is the hysteresis loop is taken on the CoO edge ($E=778.5$ eV). The blue curve is the hysteresis loop of Fe taken at $E=707.5$ eV. The black curve is the hysteresis loop of the virgin CoO layer deposited on the substrate.

We used for the present study the ALICE diffractometer [1], working in XRMS mode to search for the presence of effective magnetic moment into the AF layer. Using rf-sputtering technique we have prepared two samples: one is a Fe/CoO exchange bias system and another one is just a simple CoO layer deposited on a sapphire substrate. Both samples were grown in the same run. The CoO sample is used to confirm the good quality of the AF CoO layer which is not in contact with the ferromagnetic layer.

The systems were cooled in a field of +2000 Oe from above the $T_N=291$ K of the CoO AF layer to $T=30$ K. At this temperature we have measured element specific hysteresis loops of CoO layer and Fe layer. First observation is that the CoO layer of the Fe/CoO sample has a ferromagnetic hysteresis loop shown in Fig. 1. The coercive fields of the AF CoO layer are different than the ones

of the ferromagnetic Fe layer. Such differences in the coercive fields were constantly observed for other samples we have measured. In order to exclude that such ferromagnetic moment is not present in the virgin CoO layer we have measured the hysteresis loop and asymmetry of a single CoO layer deposited on the substrate. The curves shown in Fig. 1 and Fig. 2 (a) contain no ferromagnetic signal which confirms that the ferromagnetic moment of the CoO is directly related to the proximity of the Fe layer.

Such an effect is exemplified on Fig. 2, where the asymmetry $(I_+ - I_-)/(I_+ + I_-)$ is plotted function of energy. I_+ refers to the intensity for field applied parallel to the chirality of the circular light while I_- is the intensity for the field applied antiparallel to the same chirality. For the exchange biased sample we observed that the asymmetry is enhanced close to the absorption edge of CoO. Its maximum value is about 2 %. In the 2 (a) is plotted as well, the asymmetry of the CoO layer which is not in contact with any F layer and one can see that the asymmetry is zero. For the Fe layer the asymmetry (Fig. 2 (b)) is much higher reaching a maximum value of 50 % at an energy close to the absorption edge. From this measurements we conclude that the proximity of the F layer induces in the AF layer a magnetic moment. Such magnetic moment is related to the uncompensated spins of the AF layer and behaves in two ways. Part of the spins are frozen being strongly coupled to the AF itself. They do not rotate with the rotation of the F layer. Another part of this spins are, however coupled to the F layer and they show the same qualitative hysteresis loop.

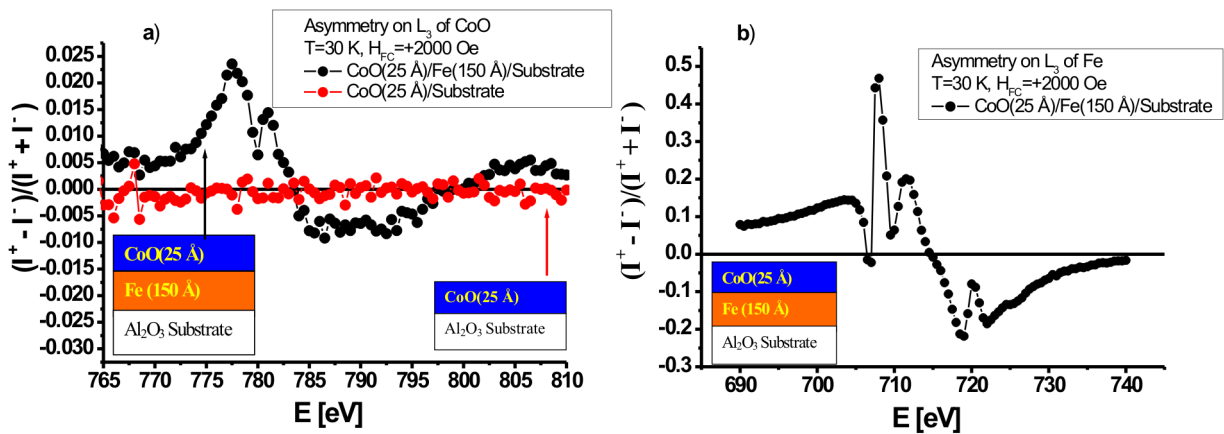


Figure 2: The asymmetry $(I_+ - I_-)/(I_+ + I_-)$ measured at the L_3 edge of the CoO for 2 samples: one substrate/Fe/CoO (black curve) and the other substrate/CoO (red curve) (a) and at the L_3 edge of the iron (b). The systems were cooled down in a field of +2000 Oe.

We would like to thank S. Erdt-Böhm for technical assistance during sample preparation, and T.Kachel and H.-Ch.Mertins (BESSY) for their help with the beamline operation. This work was supported by the German Federal Ministry of Education and Research (BMBF) under Contract No.03ZAE7BO.

References

- [1] J. Grabis, A. Nefedov, H. Zabel, *Rev. Sci. Instr.* **75**, 4048 (2003).

A PEEM study of lateral inhomogeneities on etched CdTe(110) surfaces

S. Taeger^a, D. Kraft^a, B. Jaeckel^a, P. Hoffmann^b, D. Schmeißer^b, A. Thißen^a, W. Jaegermann^a

*Fachbereich Materialwissenschaften - Oberflächenforschung der TU Darmstadt^a
Fachbereich Angewandte Physik – Sensorik der BTU Cottbus^b*

Thin film solar cells with polycrystalline CdTe as absorber material are on the threshold to commercial success. Stable conversion efficiencies of about 10% can be reached for single cells and of about 7% for large scale modules of the production line of ANTEC Solar GmbH. Higher efficiencies of about 15% can temporarily be realized for cells prepared with chemically and electronically unstable Cu-containing back contacts. From the viewpoint of electron affinity Ohmic contacts can only be prepared with chemically inert high work function materials of $\phi > 5.8\text{eV}$, or, alternatively, as tunneling contacts. To date no Ohmic back contact for CdTe has been found. The technologically relevant back contact has been developed by empirical optimisation. The preparation starts with a wet-chemical etching using NP etch as a solvent consisting of a mixture of nitric and phosphoric acid. The effect of this treatment is described in detail in literature [1]. Mainly oxides are removed from the CdTe surface and Cd is dissolved, leaving an elemental Te film on top. Onto this surface Sb_2Te_3 and finally the metallic back contact material NiV is deposited by magnetron sputtering.

The wet-chemical etching process is, besides the effect of preferential etching along grain boundaries, inhomogeneous for polycrystalline films as well as for single crystals. Optical microscopy studies (Figure 1, left) showed in both cases circular inhomogeneities, which have also been studied by ESMA (polycrystalline samples), AFM and EFM (single crystals). The lateral diameter of these etch circles differs from about 2-30 μm , so that also PEEM imaging combined with microspectroscopy can be applied. For this study a FOCUS PEEM equipped with a $\mu\text{-ESCA}$ analyser has been used at the beamline U49/II PGM2. The right image of Figure 1 shows a PEEM image of small etch circles on a NP-etched CdTe(110) sample illuminated by a Hg lamp with an excitation energy of $h\nu=4.9\text{eV}$. Images and spectroscopy data have been taken for a large etch circle on the same sample excited by synchrotron light with a photon energy of $h\nu=85\text{eV}$. The analysed surface areas are shown in Figure 2. Spectra have been taken for a homogeneous surface region without etch circle (“surrounding”, left image), the etch circle plus surrounding (middle), the isolated circle and in the centre of the etch circle (right image). The spectra are shown in Figure 3 together with the calculated Cd4d/Te4d intensity ratios and work functions calculated from the spectra. Obviously the Cd/Te concentration in the centre of the etch circle is significantly higher than in the homogeneous surrounding. Furthermore different oxygen species can be found in the O2s-emission in the homogeneous surrounding and in the centre of the circle. This result has also been shown from ESMA studies of NP-etched polycrystalline CdTe films. Obviously the etching process is stronger outside the circles, leading to the interpretation, that the circles are due to bubble formation of the gaseous etching products located at defined condensation seeds in the centre of the circles breaking the contact of the surface with the NP-etch. This interpretation is supported by AFM topography measurements showing the circles to be about 400nm higher than the surrounding. As a result of the inhomogeneous etching the work function is about 150meV higher in the circle than in the homogeneously etched surface regions. This result verifies the differences in the surface potentials determined by EFM measurements on similar samples.

- [1] D. Kraft, A. Thißen, J. Broetz, S. Flege, M. Campo, A. Klein, W. Jaegermann, J. Appl. Phys. 94 (2003) 3589

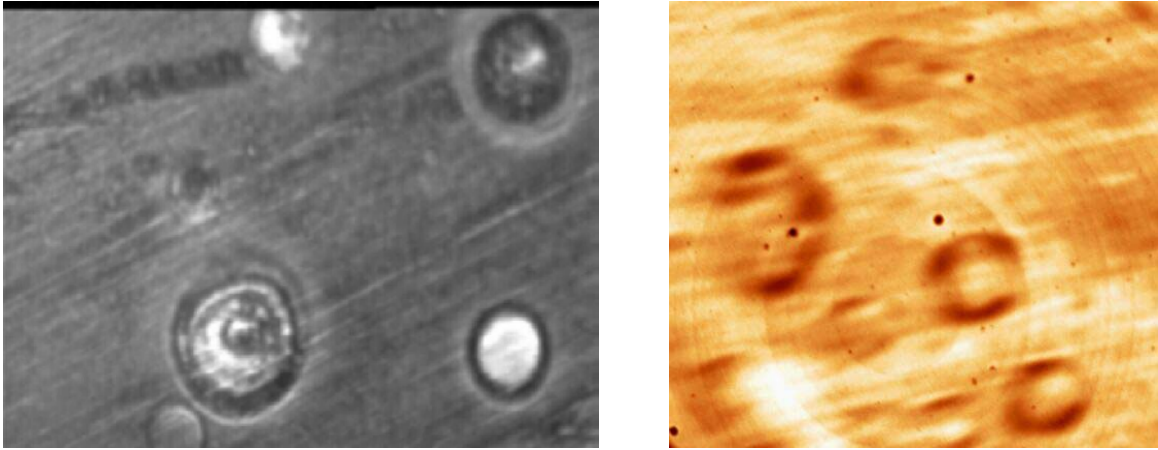


Figure 1: Optical microscopy image ($170 \times 130 \mu\text{m}$) (left) and Hg lamp-excited PEEM image ($40 \times 40 \mu\text{m}$) (right) of a wet-chemically NP-etched CdTe(110) surface.

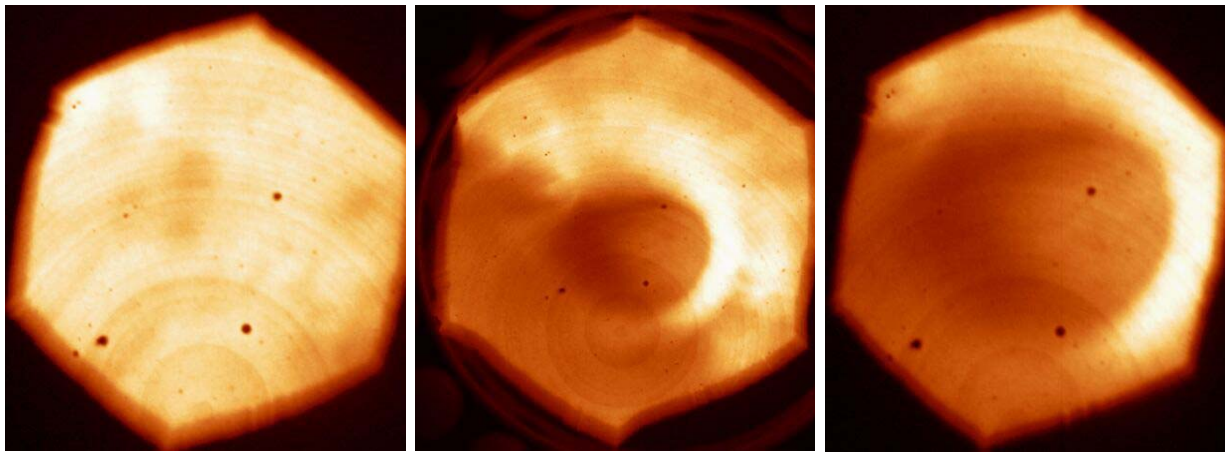


Figure 2: Synchrotron-excited ($h\nu=85\text{eV}$) PEEM images of the homogeneous surrounding ($40 \times 40 \mu\text{m}$) (left, a), etch circle with surrounding ($80 \times 80 \mu\text{m}$) (middle, b), and etch circle ($40 \times 40 \mu\text{m}$) (right, c) of a wet-chemically NP-etched CdTe(110) surface.

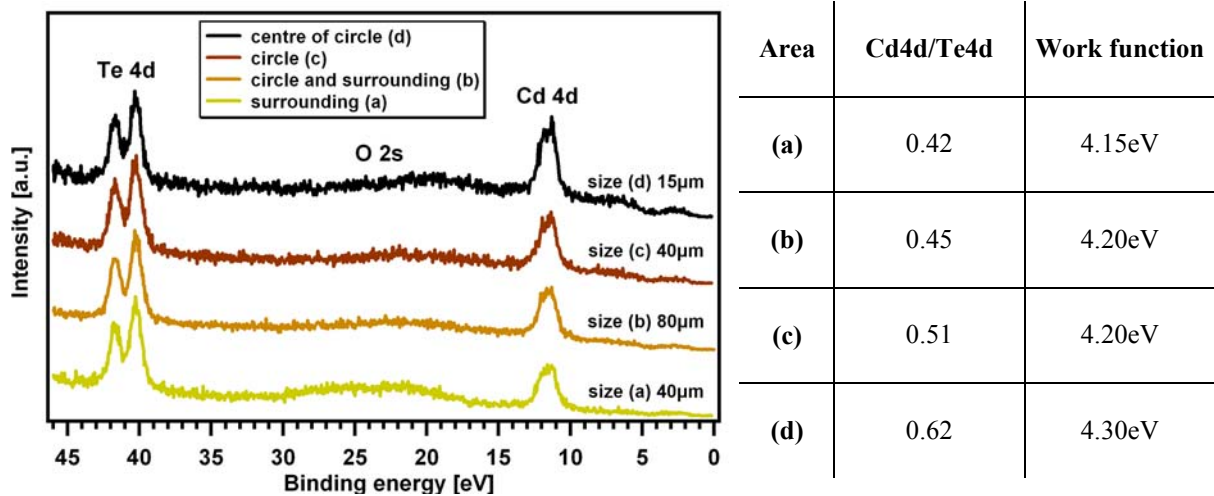


Figure 3: PEEM spectra taken at $h\nu=85\text{eV}$ in the regions shown in Figure 2 (left), Cd4d/Te4d intensity ratios and work functions determined from the spectra (right).

This work was supported by the Bundesministerium für Wirtschaft BMWi Grant No. 0329857.

Investigation of Oxidation and Migration Processes of Inorganic Compounds in Ink Corroded Manuscripts

Oliver Hahn¹, Birgit Kanngießer², Wolfgang Malzer², Max Wilke³, Bettina Nekat³, Alexei Erko⁴

¹ *Bundesanstalt für Materialforschung und –prüfung (BAM), Unter den Eichen 44-46, 12203 Berlin*

² *Institut für Atomare Physik und Fachdidaktik, Technische Universität Berlin, Hardenbergstr. 36, 10623 Berlin*

³ *Institut für Geowissenschaften, Universität Potsdam, Postfach 601553, 14415 Potsdam*

⁴ *BESSY GmbH, Albert-Einstein-Straße 15, 12489 Berlin*

Abstract

To continue former investigations¹ we studied the oxidation and migration processes of inorganic compounds in ink corroded material by means of a combination of micro X-ray fluorescence analysis (micro-XRF) and micro X-ray absorption near edge structure spectroscopy (micro-XANES). With elemental mapping by micro-XRF the correlation of the minor elements zinc and copper in the ink to the major element iron was investigated. Along concentration profiles of iron micro-XANES measurements were carried out in order to determine the oxidation state and the local environment. With the help of model inks we could show that copper is a further important element in the paper degradation process due to iron gall ink corrosion.

Experimental

The experiments were carried out at the bending magnet beamline KMC-2 at BESSY. A double Si-Ge gradient crystal (111) monochromator was used to monochromatize the primary beam providing an energy resolution of about $E/\Delta E = 4200$. After the monochromator the beam was focussed horizontally by a toroidal mirror. Final focussing to a spot size of about 17 μm at the experiment was done by use of a polycapillary half-lens. In order to achieve higher fluorescence intensities and to decrease effects by sample inhomogeneities, the data were collected with a bigger spot size of 30 μm . The elemental mapping was performed with a step width of 50 μm . Micro-XANES spectra at the Fe and Cu K-edge were collected in fluorescence mode using an energy step width around the absorption edge of 0.5 eV. Total acquisition time for one absorption spectrum is about 14 minutes. The XANES spectra were corrected for background absorption by subtracting a polynomial function that was fitted to the spectral region before the pre-edge. The spectra were then normalized for atomic absorption by fitting an arc tangent function and a gaussian function to the spectra and setting the arc tangent function to equal step height for all spectra. For the determination of the valence state we used the inflection point of the absorption edge as a figure of merit. The inflection point indicates the energetic shift of the edge position if the bulk chemical composition is not changing.

Results

Micro X-ray Fluorescence: We investigated historical manuscripts in different corrosion states, and in addition several model inks. These model inks were prepared according to historical recipes.

The micro-XRF elemental mapping mainly yielded two minor elements, Cu and Zn, beside the main element Fe in both inks. For further quantitative evaluation of the minor elements we used a fingerprint value W , which corrects for the interference effects of the elements in the paper². W is proportional to the ratio of the weight fraction of Cu and Zn, respectively, to the weight fraction of Fe. In a first step all fingerprint values obtained were sorted according to their magnitude. They are plotted in figure 1 as $W/\Delta W$, where ΔW means the distance between neighbouring values.

This curve is similar to a frequency distribution. The outer regions, marked with 1 and 5, contain results obtained from measurements on the pure paper. For these measurement points the calculation becomes numerically unstable, because the intensity measured in a certain point is subtracted from the mean value of all intensities measured on paper. The W -values obtained from the measurements on the ink spot constitute the peak between the marker a and d.

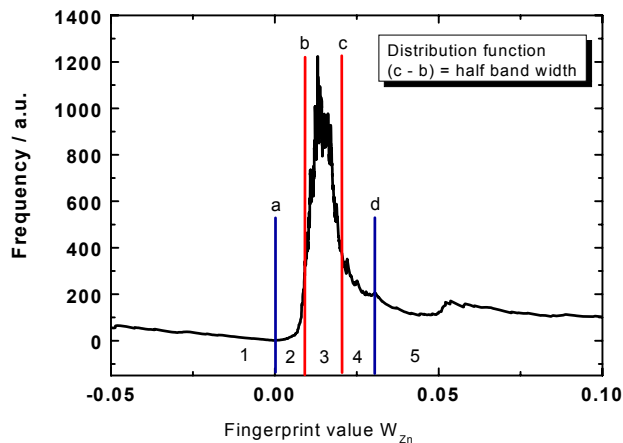


Fig. 1 Distribution function $W/\Delta W$ of W_{Zn} .

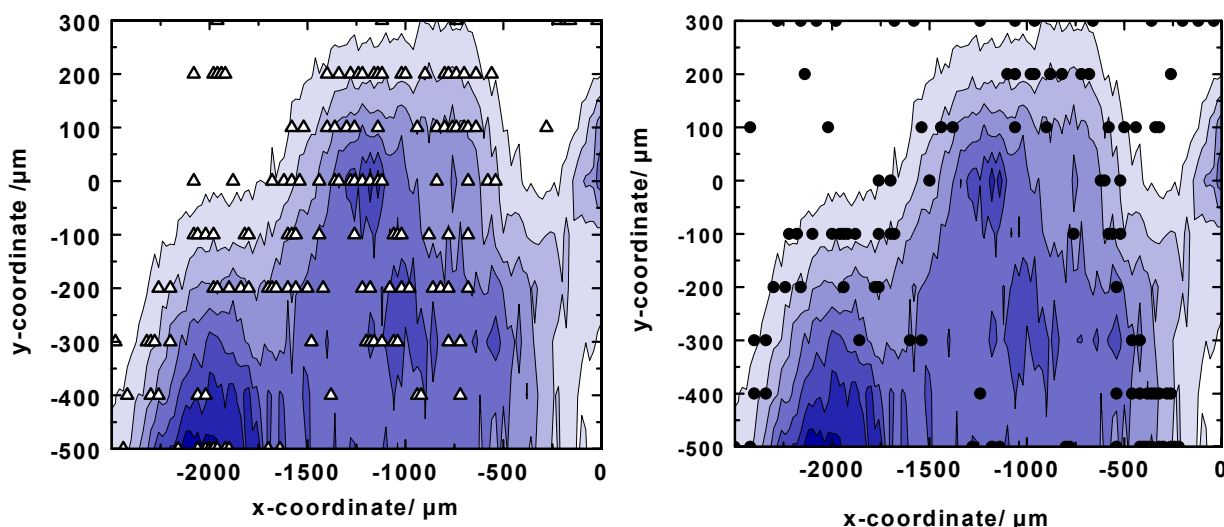


Fig. 2: Fingerprint value W_{Zn} in comparison to the distribution of Fe in the ink material. White triangles symbolise fingerprint values $0 < W_{Zn} < b$ (Interval 2); black circles indicate fingerprint values $c < W_{Zn} < d$ (Interval 4).

In figure 2 we mapped the fingerprint values of Zn lying in the lobes of this peak, i.e. outside the FWHM, onto the contour plot of Fe distribution. Values of the upper lobe (c-d) are depicted as black dots in the right image. Values of the lower lobe (a-b) are depicted as white triangles in the left image. It can be seen that higher fingerprint values occur more frequently in the edge region of the ink spot. The weight fraction of Zn increases relative the one of Fe. In contrast, the lower values of Zn are scattered over the entire ink spot. Therefore, one can exclude, that the right image only may reflect the increasing uncertainty of the fingerprint value. The same plots for copper, which are not depicted here, show the same behaviour for the values lying inside the upper wing. However, also the values of the lower wing occur more frequently in the edge region. Hence, these findings support the hypothesis, that the mobility of non iron metal ions through the paper is stronger than that of iron ions.

Micro X-ray Absorption Near Edge Structure: Along concentration profiles micro-XANES measurements have been carried out to determine a possible change in the Fe^{2+} to Fe^{3+} ratio. In order to get a qualitative impression of the ratio the spectra were compared to iron sulphates as references. The measurements confirmed former investigations that the Fe^{2+} to Fe^{3+} ratio depends on the preservation state of the manuscripts. Furthermore the objects with a strong corrosion revealed an

increase of the $\text{Fe}^{2+}/\text{Fe}^{3+}$ ratio with increasing iron amount, that in turn correlates with the degree of the ink corrosion. For a better understanding of the influence and the mechanics of a photon induced reduction of the Fe^{3+} -ions during the measurements systematic investigations based on self-made inks were started where composition and other parameters were changed in a well-defined way. According to historical recipes iron gall inks with and without copper as a minor element were prepared. Additionally, we used iron phytate as a reference substance, because the octahedrally coordinated iron is similar to the iron gallate complex.

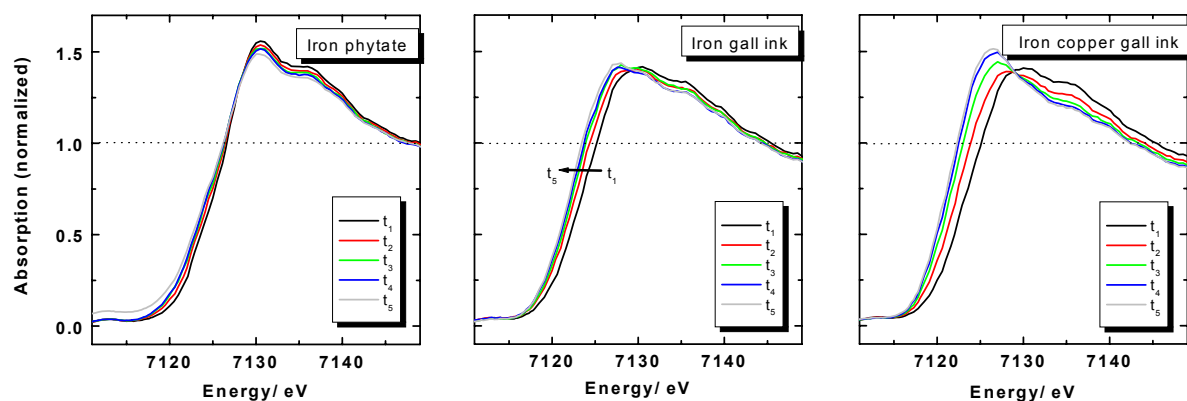


Fig. 3: Energetic shifts of the measured iron K-edges of different model inks depending from the radiation dose. The XANES spectra were collected at the same site (from 1 to 5)

The model ink doped with Cu showed the highest energetic shift of the measured iron K-edge with increasing radiation dose (see Fig. 3). The pure model ink exhibited a smaller energetic shift under the same experimental conditions. Further on, the iron phytate showed almost no energetic shift. In contrast, we could not observe any shift of the Cu K-edge during the time series measurements of the model ink doped with Cu. Apparently Cu reacts as a catalyst or, at least, enhances the photo-reduction process, although it does not itself show any apparent energetic shift in the K-edge during the same time regime. If Cu redox reactions occur at all, they are much faster than the experimental time resolution. In any case the reactions are reversible. We may conclude that Cu contributes to the iron induced degradation of paper based on synergetic effects³.

Conclusions

With the combination of micro-XRF and micro-XANES we investigated migration and oxidation processes in ink corroded manuscripts. The minor elements Zn and Cu were found to occur more frequently in the outer regions of the ink spots. Hence, one may conclude that the mobility of the non-iron metal ions through the paper is stronger than that of iron ions. This result is also important for the broadening of the ink corrosion process. The investigations reveal definitely that the presence of Cu-ions enforces the photo-reduction process of iron. The Cu-ions act as catalyst for the photo-reduction. Thus, the reduction/oxidation process of Cu is in any case reversible. Based on the experience that not only humidity but also light enhances the ink corrosion process we might confer these current results on the ink corrosion mechanism.

¹Hahn O, Malzer W, Kanngießner B, Investigation of oxidation and migration processes of inorganic in ink corroded manuscripts, BESSY, Annual Report 2002, 262-264.

²Malzer, W, Hahn, O, Kanngießner B, A fingerprint model for inhomogeneous ink paper layer systems, X-Ray Spectrometry, in press.

³Kanngießner B, Hahn O, Wilke M, Nekat B, Malzer W, Erko A, Investigation of Oxidation and Migration Processes of Inorganic Compounds in Ink Corroded Manuscripts, submitted to: Spectrochimica Acta B.

THz Spectroscopy of excited acceptor states in p-type germanium

H.-W. Hübers and S. G. Pavlov
*Deutsches Zentrum für Luft- und Raumfahrt (DLR),
Rutherfordstraße 2, 12489 Berlin, Germany*

K. Holldack, P. Kuske, U. Schade, and G. Wüstefeld
*Berliner Elektronenspeicherring-Gesellschaft für Synchrotronstrahlung mbH (BESSY),
Albert-Einstein-Straße 15, 12489 Berlin, Germany*

Introduction

Germanium doped with gallium (Ge:Ga) is widely used for sensitive detectors of far-infrared (FIR) or terahertz (THz) radiation [1]. The detection mechanism is based on a transition from the Ga ground state to the valence band. The long-wavelength cutoff of such detectors is determined by the energy of the ground state, for Ge:Ga $\sim 120 \mu\text{m}$ [2]. This cutoff can be extended to longer wavelengths ($\sim 240 \mu\text{m}$) by applying stress to the crystal [3]. A compressive force along the $\langle 100 \rangle$ crystal axis removes the degeneracy at the top of the valence band and decreases the acceptor binding energy [4]. Detectors of this type are utilized in many space or airborne observatories for infrared astronomy. Examples are ISO, ESA's Infrared Space Observatory [5], the Satellite Infrared Telescope Facility, SIRTf [6], which is currently in operation, and SOFIA, the Stratospheric Observatory for Infrared Astronomy, a DLR-NASA observatory [7]. Despite the wide use of this type of detector there remain some fundamental questions: A long wavelength response at $1\text{-}10 \text{ cm}^{-1}$ which increases with applied stress was observed by several groups in unstressed Ge:Ga [8,9]. However the origin of the response remains unclear. Another peculiarity of Ge:Ga, which is controversially discussed is, whether the cascade capture model is the appropriate explanation for hole capture by attractive hydrogen centers such as Ga in p-type germanium [10]. It has been proposed that direct capture into the ground state exceeds cascade capture for $T > 3\text{K}$ for singly ionized acceptors [11,12].

Experimental Setup

The experiments have been performed at the IRIS beamline [13] at the BESSY storage ring by using a polarizing step scan Fourier transform spectrometer (FTS) [14] at the THz port of IRIS. Single sided interferograms have been measured. The unapodized resolution was 0.15 cm^{-1} . BESSY was operated in a dedicated low α mode ($\alpha = 4 \times 10^{-5}$) with a current of about 40 mA. By this way powerful and coherent THz synchrotron (CSR) radiation below 50 cm^{-1} was generated [15,16]. The unstressed Ge:Ga is a cube of 4 mm side length with a doping concentration of $6 \times 10^{15} \text{ cm}^{-3}$ and a compensation of about 1%. The stressed Ge:Ga is a cube of $1 \times 1 \times 1 \text{ mm}^3$ with a Ga doping concentration of $2 \times 10^{14} \text{ cm}^{-3}$ and a compensation of less than 1%. Stress was applied by a screw and a piston. A ball bearing decoupled the torque from the screw from the detector. By this means a compressive force of $\sim 6 \times 10^8 \text{ Pa}$ was applied along the $\langle 100 \rangle$ crystal axis. The samples were mounted in a liquid Helium cryostat. The temperature of the samples was 4.5 K. A cold black polyethylene was mounted in front of the samples to reduce background radiation. The THz CSR radiation from BESSY passed through the FTS and was concentrated onto the samples by a parabolic mirror and a cone. The photocurrent induced by the CSR in the samples was detected by a lock-in amplifier with reference to the 1.25 MHz revolution frequency of BESSY.

Results and Discussion

A typical interferogram is shown in Fig. 1 while Fig. 2 displays the photoconductivity spectra for stressed and unstressed Ge:Ga.

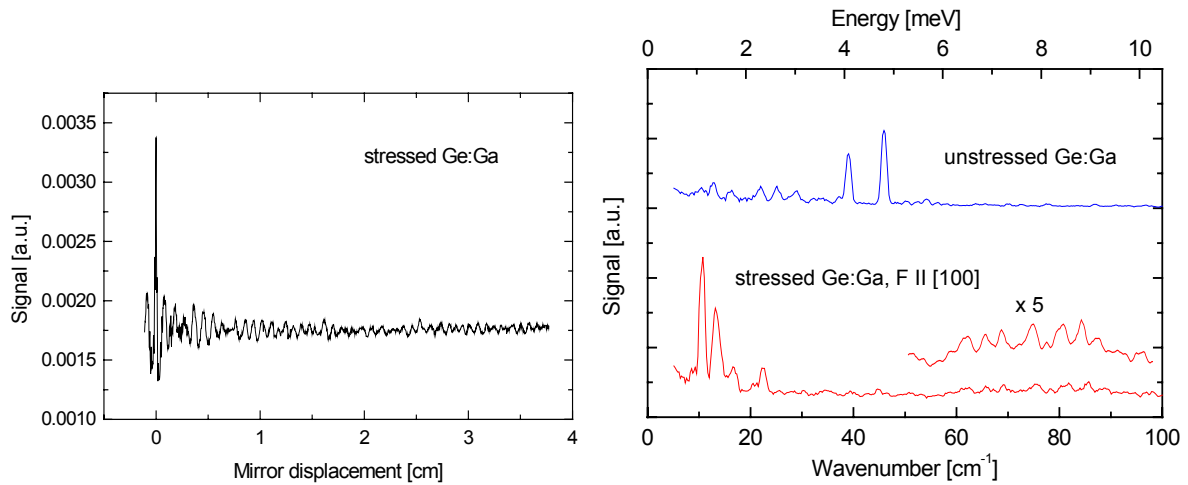


Fig. 1: Interferogram obtained from the stressed Ge:Ga crystal.

Fig. 2: Photoconductivity spectra of unstressed and stressed Ge:Ga.

The upper trace in Fig. 2 is the spectrum of unstressed Ge:Ga. The two highest peaks around 4-5 meV are due to the Sb donors, which are the compensating dopants in Ge:Ga. The larger peak at 5.72 meV corresponds to the transition from the $1s(A_1)$ ground state to the $2p_0$ state (5.71 meV [17]) and the smaller peak at 4.86 meV to the transition from the $2p_0$ state to the conduction band (4.74 meV [17]). The small peaks below 3 meV are due to transitions from bound excited states of Ga to the valence band and between bound excited states. The stressed Ge:Ga shows a broad response between 6 and 10 meV due to a transition from the ground state to the valence band (Fig. 3). This is the spectral range where the detector is made for.

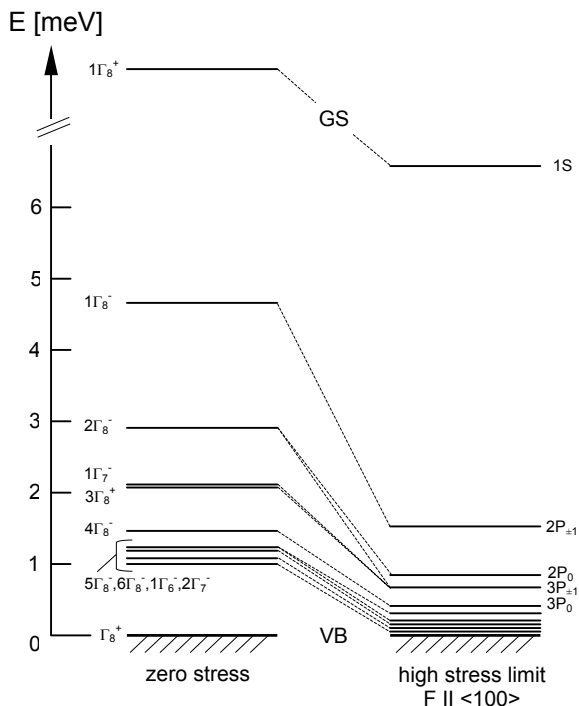


Fig. 3: Energy-level diagram of Ge:Ga with zero stress and in the high stress limit. The position of the energy levels are taken from [17,18].

However, there is a strong response below about 2 meV. Again, this is due to transitions from bound excited states of Ga to the valence band and between bound excited states (Fig. 3). It is important to note that the data are not calibrated for the CSR spectrum. Therefore the relative intensities are arbitrary. However, the results indicate that there is a significant responsivity of Ge:Ga detectors at long wavelengths. For any detector application care should be taken to block the long wavelength response by appropriate filters. In addition, our results indicate, that a cascade type of relaxation exists in Ge:Ga at 4.5 K. In case of direct capture to the ground state none of the excited states would be observable.

References

1. E. E. Haller, *Infrared Phys. Technol.* **35**, 127 (1994).
2. J. Beeman and E. E. Haller, *Infrared Phys. Technol.* **35**, 827 (1994).
3. A. G. Kazanskii et al., *Appl. Phys. Lett.* **31**, 496 (1977).
4. H. Hasegawa, *Phys. Rev.* **129**, 1029 (1963).
5. J. Wolf, *Optical Engineering* **33**, 1492 (1994).
6. R. Schnurr et al., *Proc. of the Conf. on Infrared Astronomical Instrumentation SPIE 3354*, 322 (1998).
7. D. Rabanus et al., *Proc. of the Conf on Airborne Telescope Systems, SPIE 4014*, 137 (2000).
8. M.F. Kimmitt et al., *Proc. of the 4th Conf. on Infrared Physics*, 289 (1988).
9. C. Meny et al., *Proc. of the 15th Int. Conf. on Infrared and Millimeter Waves*, 230 (1990).
10. M. Lax, *Phys. Rev.* **119**, 1502 (1960).
11. L. S. Darken, *Phys. Rev. Lett.* **69**, 2839 (1992).
12. I. Wilke et al., *Sol. State Comm.* **93**, 409 (1995).
13. U. Schade et al., *Rev. Sci. Instrum.* **73**, 1568 (2002).
14. D. H. Martin and E. Pulett, *Infrared Phys.* **10**, 105 (1969).
15. M. Abo-Bakr et al., *Phys. Rev. Lett.* **88**, 254801, (2002).
16. M. Abo-Bakr et al., *Phys. Rev. Lett.* **90**, 094801 (2003).
17. Landolt-Börnstein, *New Series II/22b*, 480 (1991).
18. J. Broeckx et al., *Phys.Rev. B* **35**, 6165, (1987).

Anisotropy of the dielectric function for hexagonal InN

R. Goldhahn¹, V. Cimalla², O. Ambacher², C. Cobet³, W. Richter³, N. Esser⁴, H. Lu⁵
and W.J. Schaff⁵

¹Inst. f. Physik, ²Zentrum f. Mikro- und Nanotechnologien, TU Ilmenau, PF 100565, 98684 Ilmenau, Germany

³Institut für Festkörperphysik der TU Berlin, Hardenbergstraße 36, 10623 Berlin, Germany

⁴Institute of Spectrochemistry and Applied Spectroscopy, Department Berlin-Adlershof, Albert-Einstein-Str. 9, 12489 Berlin, Germany

⁵Dept. of Electrical and Computer Engineering, Cornell University, Ithaca, New York 14853, USA

Among the group-III nitride semiconductor compounds, the physical properties of InN are known rather poorly. This is mainly attributed to the difficulties in growing high-quality crystals. Currently, the debate focuses on the question concerning the band gap of InN. Interband optical absorption measurements of sputtered polycrystalline InN films yielded a band gap of $E_g \sim 1.9$ eV. This value has been accepted for a long time and was frequently used as the end-point value for the extrapolation of the band gap in $\text{In}_x\text{Ga}_{1-x}\text{N}$ alloys. Studies of epitaxial layers grown by MBE or MOVPE, however, revealed a much narrower gap of $E_g \sim 0.7$ eV (for a recent review see e.g. Ref.1). Recently, we compared the DF's for both types of films, as obtained from spectroscopic ellipsometry (SE) measurements in the energy range from 0.7 eV up to 5.5 eV, with the results of *first-principles* calculations. It was demonstrated [2] that only the DF of MBE-grown films exhibits the characteristic features being expected for wurtzite InN. Therefore, it was concluded that the band gap is only $E_g \sim 0.7$ eV.

Calculations predict for hexagonal InN a pronounced optical anisotropy in the range of the higher-energetic critical points [3], i.e. the ordinary ϵ_o and extraordinary ϵ_e dielectric tensor components corresponding to the electric fields perpendicular and parallel to the *c*-axis, respectively, differ appreciably. Here we demonstrate for the first time that MBE-grown InN shows this characteristic behaviour.

The optical response of absorbing materials, measured by SE, depends mainly on the in-plane tensor components but only weakly on the component normal to the surface. Therefore, in order to get access to both tensor components, samples are required for which the *c*-axis lies in the surface plane. We succeeded recently in depositing high-quality InN on *r*-plane sapphire substrates with an AlN nucleation layer and GaN buffer using plasma-assisted MBE. The InN film with a thickness of 460 nm was identified to be non-polar *a*-plane which follows the *a*-plane GaN buffer (thickness of 160 nm). Further growth details as well as results of the structural, electrical and optical characterisation has been published elsewhere [4]. The ellipsometric parameters Ψ and Δ were determined for *c*-axis orientation either parallel or perpendicular to the plane of incidence. For the VUV measurements (3 to 9.5 eV), the **3m-Normal-Incidence-Monochromator 2** was used as light source. The data refer to an angle of incidence of 68.7° .

In order to obtain ϵ_o and ϵ_e and not only pseudo-dielectric functions, Ψ and Δ were fitted by taking in to account the sample orientation as well the rms surface roughness of ~ 6 nm. The corresponding results for the real (ϵ_1) and imaginary parts (ϵ_2) of ϵ_o and ϵ_e are shown by the full lines in Fig. 1(a) and (b), respectively. First of all, the excellent matching to the data recorded with a commercial ellipsometer (J.A. Wollam Co., Inc.) in the energy range from 0.7 up to 4.5 eV should be noted. At second, the low-energy results prove that the band gap of the *a*-plane InN film does not differ to the previous results for *c*-plane MBE-grown films and is

~ 0.7 eV (coinciding with the strong increase of ϵ_2 at this energy followed by nearly constant value up to 3.5 eV).

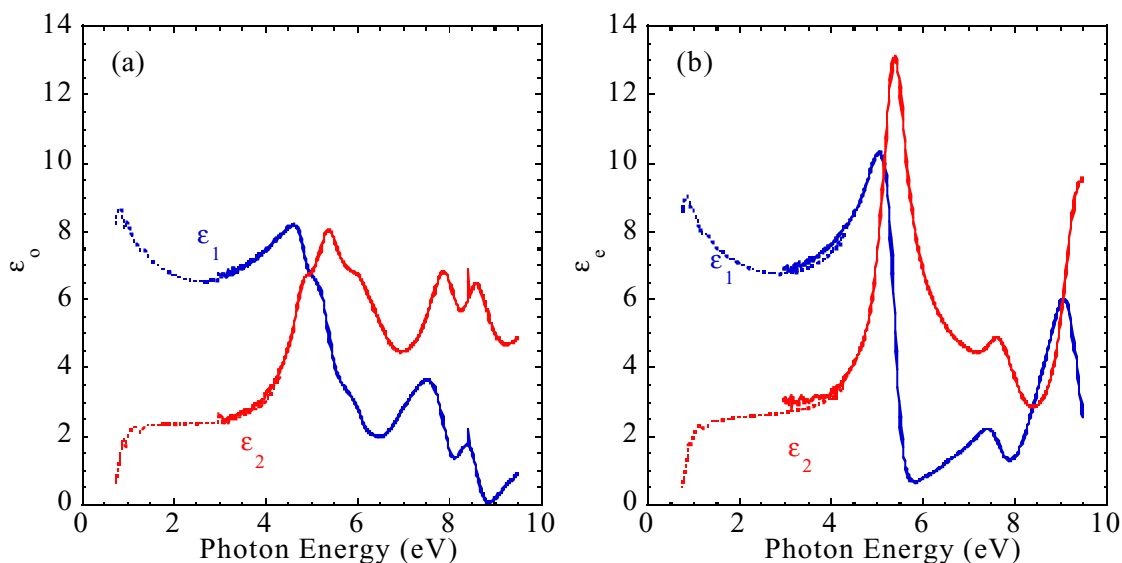


Fig. 1: Real (blue) and imaginary (red) part of the ordinary (a) and extraordinary (b) dielectric tensor components for wurtzite InN. The full lines refer to measurements at BESSy II while the dashed lines were obtained from studies using a commercial ellipsometer.

A comparison of Fig.1 (a) and (b) evidences that the ordinary and extraordinary dielectric tensor components differ appreciably in the range of the higher-energetic interband transitions. The imaginary part ϵ_2 of ϵ_o shows peaks at 4.88, 5.38, 6.02, 7.86, and 8.6 eV which are related to the critical points of the band structure. For the extraordinary component, however, only three peaks are resolved at 5.38, 7.63, and 9.44 eV. Furthermore, the magnitude of the peak found for both polarisation directions at 5.38 eV is much larger if the electric field is parallel to the c -axis. The qualitative shape of ϵ_o and ϵ_e as well as the intensity ratio agrees excellent with theoretical calculations [3]. It emphasises our conclusion that the low band gap (~ 0.7 eV) materials represent bulk-like InN with wurtzite structure.

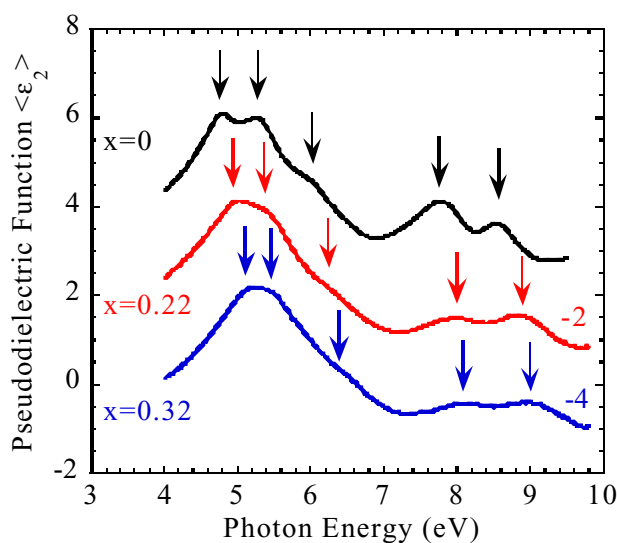


Fig. 2: Imaginary part of the pseudodielectric functions for $In_{1-x}Ga_xN$ alloys corresponding to electric field polarisation perpendicular to the c -axis. The lower curves are shifted for sake of clarity as indicated. The arrows mark the critical points of the band structure.

Studies of In-rich $In_{1-x}Ga_xN$ alloys provide further insight into the general behaviour, although only films with c -axis orientation normal to the surface are available until now, i.e. only the ordinary tensor component can be evaluated. Results for the low-energy range has

been reported in Ref. 2. Here we present preliminary data for the VUV range. Fig. 2 compares the imaginary part of pseudodielectric functions for two alloy layers with Ga contents of 22% and 32% with InN. As for InN, five critical points are clearly resolved demonstrating the high structural quality of the films, and as expected they shift continuously to higher energies with increasing Ga concentration. In the next step, the data have to be corrected for surface roughness allowing a comparison with the results of Fig. 1.

In summary, we have reported for the first time the ordinary and extraordinary dielectric tensor components for InN. The observed anisotropy agrees excellent with theoretical calculations, and transition energies for the critical points of the band structure have been determined.

The group from Berlin acknowledges financial support provided by the BMBF grant 05SE8KTA3. The Ilmenau group is supported by the Ministry of Science, Research and Art of Thuringia (B609-02004). The Cornell group acknowledges support from ONR contract No. N000149910936.

References

- [1] A.G. Bhuiyan *et al.*, J. Appl. Phys. **94**, 2779 (2003).
- [2] R. Goldhahn *et al.*, Mat. Res. Soc. Symp. Proc. **743**, L.5.9 (2003).
- [3] F. Bechstedt *et al.*, phys. stat. sol. (a) **195**, 628 (2003); C. Persson *et al.*, J. Phys.: Condens. Matter **13**, 8945 (2001).
- [4] H. Lu *et al.*, Appl. Phys. Lett. **83**, 1136 (2003).

Surface modification by irradiation with swift heavy ions

*W. Bolse, B. Schattat, H. Paulus [Institut für Strahlenphysik der Univ. Stuttgart];
I. Zizak, N. Darowski, S. Klaumünzer [Hahn-Meitner-Institut Berlin, Germany]*

Swift heavy ions at energies of the order of MeV/amu are slowed down in a solid predominantly by electronic excitation and ionization of the target atoms, while nuclear energy deposition by elastic collisions is negligible. Defect creation and amorphous track formation due to electronic energy deposition, which has been observed especially in insulators, demonstrate that part of the electronic excitation energy is transferred to the lattice. In thin film packages swift heavy ion irradiation results in atomic mixing at the interfaces. In former experiments it was shown that interface mixing in oxide bilayer occurs as soon as a certain threshold Sec is exceeded, which is given by track formation threshold of the less sensitive material of the bilayer [1]. The threshold for interface mixing of NiO/SiO₂ is given by NiO, where we have investigated the track formation, too. NiO single crystals prepared for transmission electron microscopy (TEM), as well as NiO bulk material and the thin layer system NiO/SiO₂ have been irradiated with 90 MeV to 350 MeV Ar, Kr, Xe and Au ions at $T = 80$ K and low fluences, ($\sim 10^{10} \text{ cm}^{-2}$), where the single ion impacts are clearly separated from each other.

The irradiations were performed at the ISL at Hahn-Meitner Institute, Berlin. No tracks were observed after irradiation with 90 MeV Ar ions, while discontinuous track fragments became visible after irradiation with 140 MeV Kr ions. This is in good agreement with the intermixing and self organization behaviour in NiO/SiO₂-bilayers, where the effects could only be observed after irradiation with ions heavier than Ar [3]. Continuous tracks, with their number density being in agreement with the ion fluence, were formed during irradiation with 230 MeV Xe and 350 MeV Au, respectively. On the left part of the figure 1, the top view of a NiO-sample irradiated with 350 MeV Au is shown, while on the right part of the figure the sample was tilted by 40°, displaying continuous tracks. Furthermore, spherical nanoparticles have been formed at the end of these tracks. Fresnel contrasts, which evidence voids, were observed along the tracks and prove that the center of the tracks is empty. The void formation conforms with the nanoparticle formation at the surface. Similar nanoparticles have been observed at the top of NiO/SiO₂ due to swift heavy ion irradiation with low fluences.

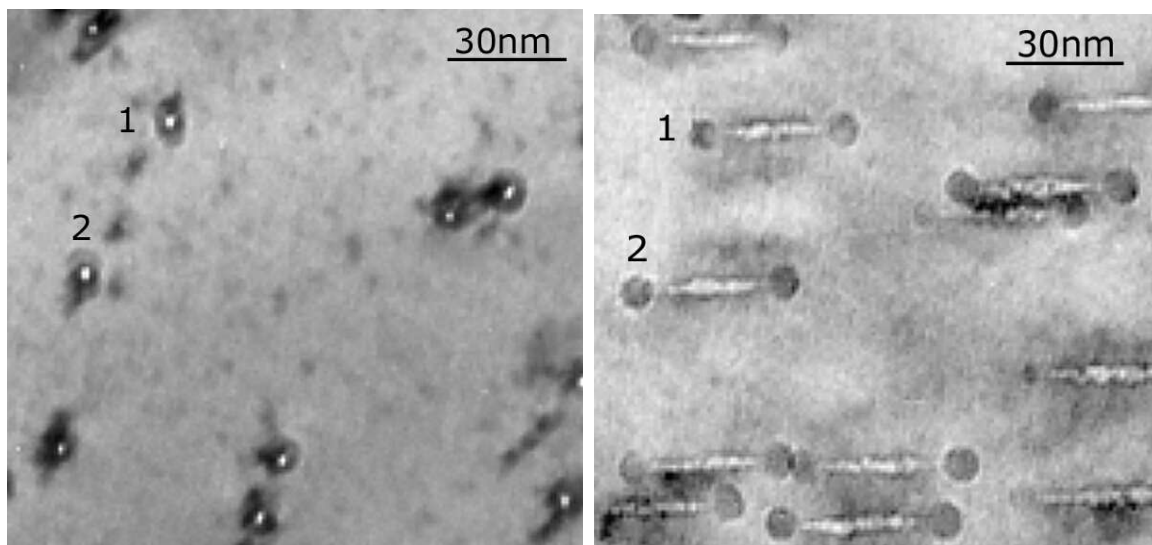


Fig.1: 200 kV TEM-images of a NiO single crystal irradiated with $4 \times 10^{10} \text{ cm}^{-2}$ 350 MeV Au. Left: top view of the sample, right: sample tilted by 40°. Note that two corresponding tracks are numbered.

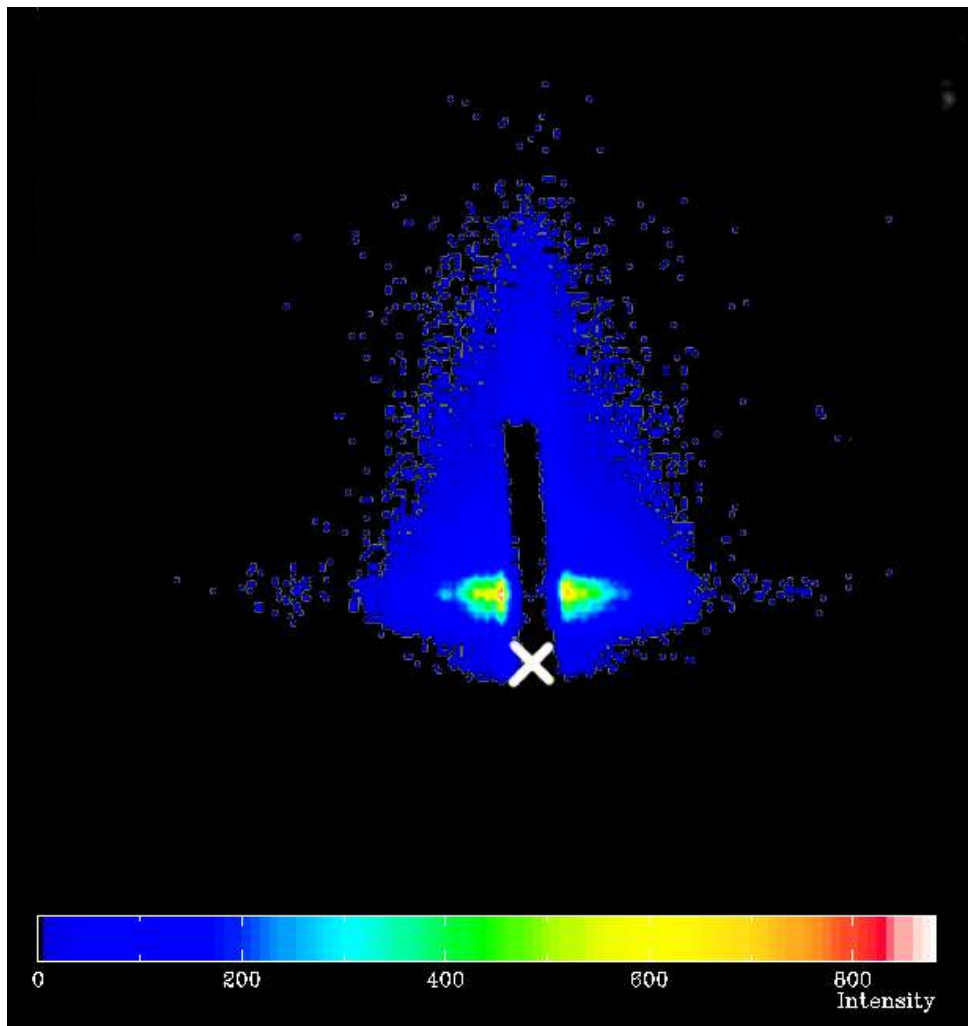


Fig. 3 Enlarged image from 2d area detector. The white cross marks the position of the primary X-ray beam. The sample surface is parallel to the x-axis of the detector, and the photons are reflected upwards. The dark box in the middle is the shadow of the beam stopper, which protects the detector from the directly reflected beam. The scattering in the surface direction can be seen left and right from the reflected beam.

X-ray scattering methods have been proven to be a powerful tool for non-destructive analysis of the shape, size distribution and density fluctuations of solid state matter. Using the 6-circle goniometer at the KMC2 beamline at BESSY and the available area sensitive detector, it was possible to study the diffuse small angle scattering (SAXS), recording the beam reflected from the sample surface (GISAXS). This geometry allows to gain information about structures at the surface with a size of a few nanometers, and is therefore well-suited for the investigation of the pellets on the irradiated NiO-samples. The shape of the pellets, their size distribution and parts of the ion track near the surface can be studied and characterized.

The goniometer at the KMC2 beamline is optimized for surface investigations using the grazing incidence angle geometries, and, in combination with the well collimated beam and the area sensitive detector, it is suitable for GISAXS measurements.

After the sample surface was aligned with the incident beam, fast qualitative reflectometry measurements were performed to estimate the angle of total reflection for the specific sample. Changing the incident angle in the GISAXS experiment allows the study of different depths under the surface. If the GISAXS measurement is performed with incident angle smaller than the total reflection angle, only objects which are above the surface are detected. If the incident angle is larger, part of the photons is penetrating the surface and being scattered on the objects below the surface. This way it the scattering of the pellets and from the hollow tracks can be measured separately.

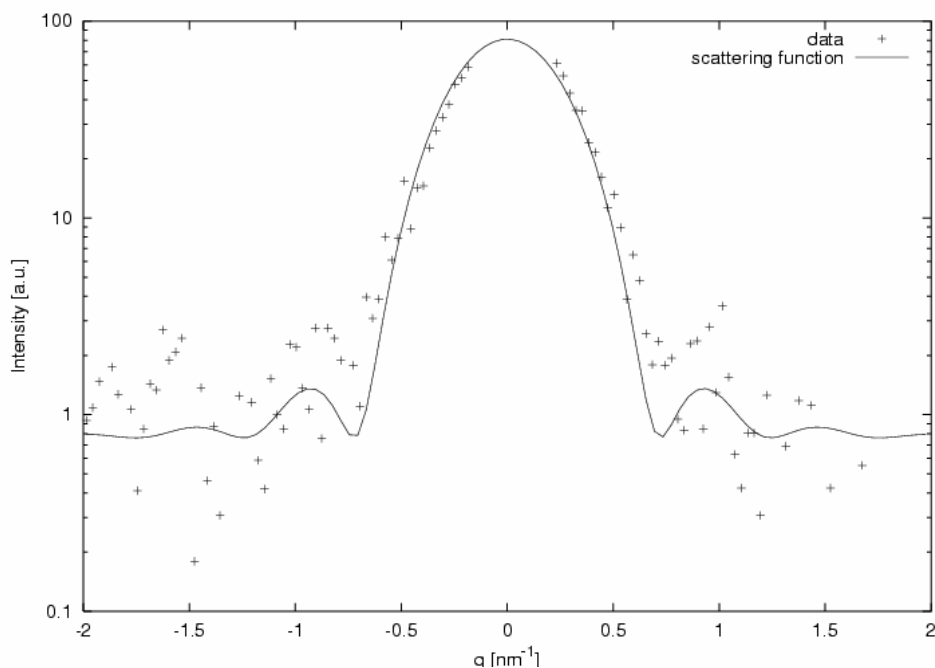


Fig. 4 Scattering function in the direction parallel to the surface. The solid line is the fit with the scattering function for the monodisperse solid spheres. The data behind the beam stopper are removed.

Since only one half of each sample was irradiated, we were able to measure the scattering from the unirradiated part, and use this measurements for the background correction. Figure 3 shows the detected scattered intensity from the thin NiO/SiO₂ irradiated with 5×10^{10} 350 MeV Au ions/cm². The resolution and the signal to noise ratio were not very satisfactory, so only part of the planned evaluation was performed. The scattering pattern measured on the unirradiated part of the sample was subtracted from the pattern measured on the irradiated part. The resulting scattering pattern was fitted with the model function of monodisperse spheres laying on the sample surface to obtain the radius of the pellets. The resulting radius of the pellets was **6.2 nm**.

Thick NiO single crystals showed no difference in scattering function between the irradiated and the unirradiated part.

Although GISAXS offers more information on the surface objects, it was not possible to evaluate the measured data with the expected success. Low intensity of the primary beam and large noise made the detection of the hollow tracks impossible. However, we were able to detect and estimate the size of the spheres on the surface of some irradiated samples. This experiment showed that GISAXS provides information on irradiated samples which are very hard to measure with other methods.

In 2005, a new SAXS experimental station is going to be operational at the 7T wiggler at BESSY. The new station is optimized for the surface scattering, and we plan to continue this experiment at the new device.

[1] W. Bolse, B. Schattat, Nucl. Instr. Meth. B 190 (2002) 173

[2] B. Schattat, W. Bolse, S. Klaumünzer, F. Habsmeier, A. Jasenek, Appl. Phys. A 76 (2002) 165.

[3] W. Bolse, B. Schattat, A. Feyh, Appl. Phys. A 77 (2003) 11.

Ti Texture Modification Using Swift Heavy Ions

*I. Zizak, N. Darowski, G. Schumacher, S. Klaumünzer [HMI, Berlin];
W. Assmann [LMU München]; J. Gerlach [IOM, Leipzig]; I. Großhans [Univ. Augsburg]*

Accelerated ions interact with the solid through nuclear and electronic interaction. At very high energies the nuclear energy loss (S_n) is much smaller than the electronic energy loss (S_e), and the interaction between the ions and the solid leads to excited electrons in the solid. A part of the electronic excitation energy is converted into atomic motion, e.g. via the electron-phonon coupling.

Recently a change in crystallite orientation of the polycrystalline Ti films was detected after the irradiation with 200 MeV Au ions [1]. To study the mechanisms of the texture modification, a new series of experiments was started. In this contribution variations of the angle of the incoming beam, the irradiation dose, and the grain size of the samples are reported.

A bulk Ti sample with an average grain size of approximately 5 μm was compared to the fine-grained Ti films deposited on the Si (001) wafer (grain size of the order of magnitude of 100 nm). The thickness of the film was 3 μm . All samples were cut into 8x8 mm square pieces and uniformly irradiated at room temperature up to 4×10^{14} Au ions/cm². Because the deposited Ti films already possessed a texture, we irradiated the thin samples under two different angles, 20° and 45°, to avoid the correlation effects between the ion beam direction and the existing orientation distribution. The textures of irradiated samples were studied using the synchrotron radiation beam at the KMC2 beamline at BESSY [2]. The samples were mounted on a six-circle goniometer (Huber). The built-in sample translator was used for the positioning of the sample into the X-ray beam. Used photon energy was 8 keV. To avoid absorption by the substrate, the diffraction was measured in reflection geometry. The size of the focused beam at the sample position was 200x200 μm .

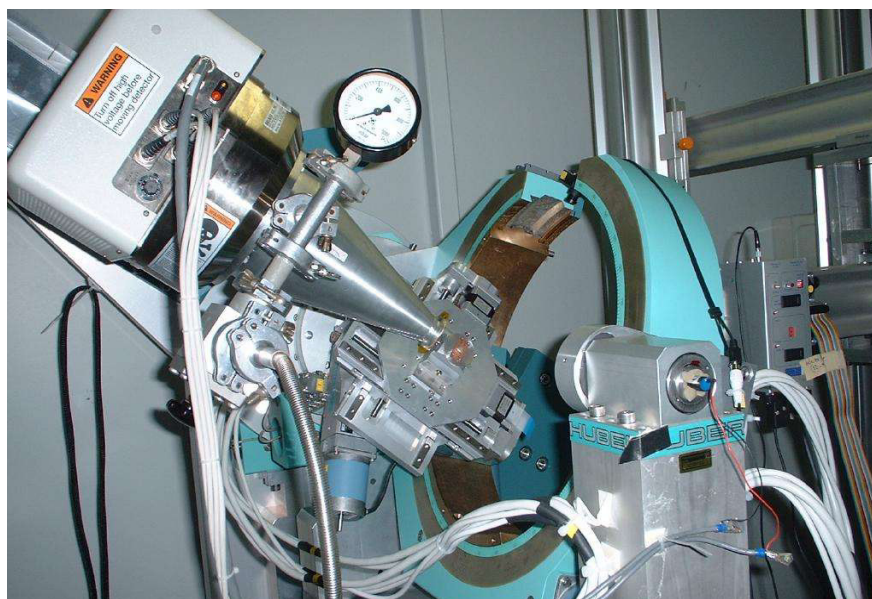


Fig. 1 Improved experimental device at the KMC2 beamline includes the evacuated photon path between the sample and the detector. Figure shows the sample mounted on the goniometer head and the area detector during the measurement. The incoming X-ray beam enters the figure from right.

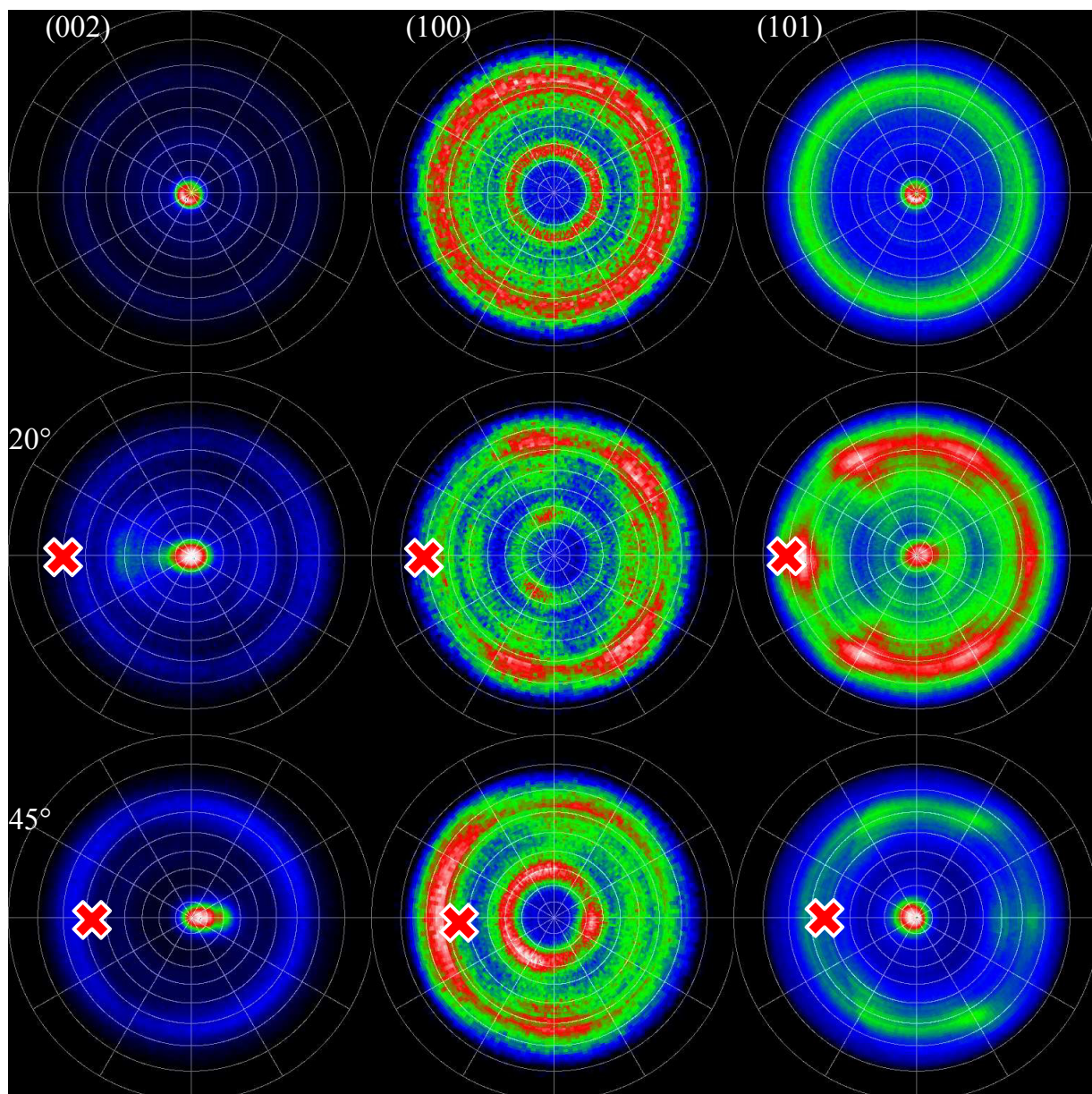


Fig. 2 Pole figures of the unirradiated sample (top row), sample irradiated with 5×10^4 ions/cm² under 20° incident angle, and the sample irradiated with the same dosis under 45° incident angle. From the left to the right: 002, 100, and 101 pole figure. The red cross marks the irradiation direction. The outer ring of the pole figures is dark because of the absorption of X-rays in the sample.

The stereographic projection of the intensity distribution is called the pole figure. In the pole figure the polar angle α is projected to the distance from the center and the azimuthal angle β the angular distance from the x-axis (pointing from the center to the right). The crystallographic planes which are parallel to the surface give rise to the maximum in the middle of the figure, and the planes whose normal lies in the surface plane will have a maximum on the perimeter of the figure.

Since the unambiguous determination of the crystal orientation in three dimensions requires at least two angles, the orientation distribution function (ODF) requires even in simple cases at least two pole figures of non-parallel plane sets in crystal, so the experiment has to be repeated for another Bragg angle.

For the acquisition of the scattered photons, a multi-wire area sensitive detector with 12 cm large sensitive area was used (HiStar, Bruker AXS). The distance between the sample and the

detector was 33 cm. The advantage of the area sensitive detector is that it can acquire a range of different azimuthal angles at once, so there is no need to scan the azimuthal angle in small steps. In the present experiment, the detector covered 20° in azimuthal angle, so only four steps in this direction were sufficient to cover the whole hemisphere.

The second advantage of an area detector is that the whole range of Bragg angles is acquired in the same frame. In the present experiment the detector acquired simultaneously (100), (002), and (101) Bragg reflex of Ti at 35.325°, 38.68°, and 40.43° respectively. This method also allows the background correction. The diffuse scattering is estimated by averaging the acquired intensities for 2- θ values slightly higher and lower than the Bragg reflection so the measured intensities could be corrected. It was also possible to exclude other possible phases of Ti, which would produce a Bragg reflection in the measured region, especially the high pressure ω -phase which is sometimes seen after the irradiation of Ti with swift heavy ions [3,4].

Below 10¹⁴ ions/cm² the textures of films showed no changes. First changes became visible after 10¹⁴ ions/cm² and the resulting textures depended on the beam direction. Since a complete coverage with tracks occurs already at the dose of about 10¹³ ions/cm², we conclude that texture modification does not occur in single ion tracks but reorientation of the crystallites requires multiple track overlap.

The thick sample showed in unirradiated state a texture specific for rolled metal sheets. This texture did not change even after 5x10¹⁴ ions/cm². The grain size seems to have an important influence on introduced grain orientation.

The rate of the texture change was similar for the samples irradiated under different incident angles, both textures showed the first changes only after 10¹⁴ ions/cm². The resulting textures are different, and depend on the ion beam direction.

Figure 2 shows three sets of pole figures, for unirradiated thin film, and for thin films irradiated with the maximal dosis, 5x10¹⁴ ions/cm². There is a maximum in the middle of the (002) and (101) pole figures for all three samples. We already showed in our previous experiment [5] that the Ti layer starts to grow with the (101) plane parallel to the surface, but after some certain thickness it grows with the (002) plane parallel to the surface. We assume that the maximum in the middle (101) pole figure comes from the deeper regions of the film. Which are nearer to the substrate, and the (002) maximum from the grains nearer to the surface. We also see that the maximum in the middle of the (101) pole figure is not much affected by ions. The angles 20° and 45° are chosen so that one of them lies below, and one above the direction of the (101) plane normal in the unirradiated sample (approximately 27° from surface). If we look at the (002) pole figures of the irradiated sample we can see that the (002) peak in the 20° sample moves to the left, and in the 45° sample to the right. This behaviour suggests the affinity between the (101) plane normal and the direction of the ion beam.

Also, as in the previous experiment, a break of the (101) fibre texture into six distinct maxima was observed. A more quantitative combination with the previous experiment is difficult due to the different qualities of the Ti layers used in experiments. Different growing rates and/or temperature resulted in different beginning state, and slight difference in the ion energy may cause a variation in the dynamics of the texture alteration.

- [1] H. D. Mieskes, W. Assmann, F. Grý uner, H. Kucal, Z. G. Wang, and M. Toulemonde, *Physical Review B* **67** (2003), 155414.
- [2] A. Erko, I. Packe, C. Hellwig, M. Fieber-Erdmann, O. Pawlitzki, M. Veldkamp, W. Gudat, *AIP Conf. Proc.* **521** (2000) 421
- [3] H. Dammak, A. Barbu, A. Dunlop, D. Lesueur, *Phil. Mag. Lett.* **67** (1993), 253
- [4] H. Dammak, A. Barbu, A. Dunlop, D. Lesueur, *Phil. Mag. A*, **79** (1999), 147
- [5] I. Zizak, N. Darowski, J. Gerlach, A. Wenzel, *BESSY Annual report 2002*, page 319

Exchange coupling in thin Fe films on NiO(001) – temperature and thickness effects

U. Mick, W.G. Park, E.Kisker

Institut für Angewandte Physik, Heinrich-Heine-Universität Düsseldorf

This work is supported by BMBF under grant 05KSIPFB/1

Thin film structures consisting of adjacent antiferromagnetic (AF) and ferromagnetic (FM) layers are widely used in novel electronic devices that utilize spin dependent transport like GMR-sensors or MRAM storage cells. The exchange coupling between the AF and the FM layer is responsible for pinning the magnetization of the FM layer, resulting in ‘exchange biasing’. Although exchange biased systems are already used in technical applications, the underlying mechanism in coupling is still in scientific debate.

Fe films deposited on a NiO surface can be used as a model system. However contradicting results and assumptions have been published in the last years. Matsuyama et al.¹ used SEMPA to investigate thin Fe-films on NiO(001) and found that the Fe-Moments are canted away from their crystallographic easy axis in accordance with the magnetic ordering as predetermined by the NiO substrate. They assumed a 90°-coupling between the NiO-moments and Fe-moments under theoretical considerations. Ohldag et al.² used PEEM to investigate Fe and Co on NiO and found a collinear coupling between the FM and the AF layer. They supposed a reorientation of the Ni-moments in the NiO substrate in accordance to the ferromagnetic ordering that showed no ‘canting’. Earlier results obtained by our group showed evidence for both spin reorientation in the NiO substrate as well as ‘canted’ Fe-moments.

During the beamtime at BESSY in July/August 2003 we investigated the system Fe/NiO(001) at the Beamline UE52-SGM by Photoemission Electron Microscopy (PEEM) utilizing magnetic linear (or circular) dichroism (MLD and MCD). In situ cleaved NiO single crystals provided atomically clean and defined NiO(001) surfaces as seen in complementary STM investigations. Annealing of NiO above the Néel-temperature leads to thermal relaxation of a cleaved surface. Fig. 1 shows the changing of the MLD contrast in the Ni-L₂ edge during the anneal process. These PEEM-images as well as x-ray absorption spectroscopy (XAS) (fig. 2) confirm the magnetic transition above the Néel temperature. The PEEM-images furthermore show a drastic reordering of the NiO domain pattern due to thermal relaxation.

After depositing thin Fe-films on the thermally relaxed surfaces of NiO(001) the formation of Fe FM domains had been investigated by PEEM using MCD with respect to film thickness and the azimuthal rotation of the sample.

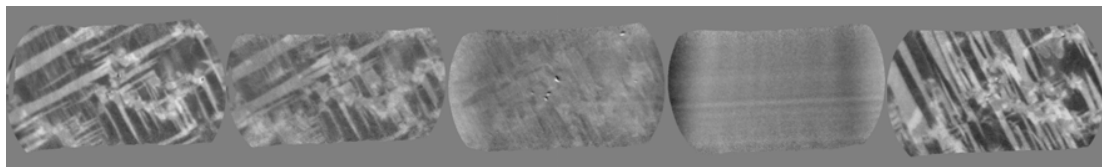


Fig. 1: Changing of MLD contrast on NiO(001) during annealing. Starting from room temperature (left) the domain contrast vanishes when exceeding the Néel temperature (4th PEEM-image). The 5th image on the right side shows the resulting domain pattern after cooling to room temperature. The size of full image is about 100µm.

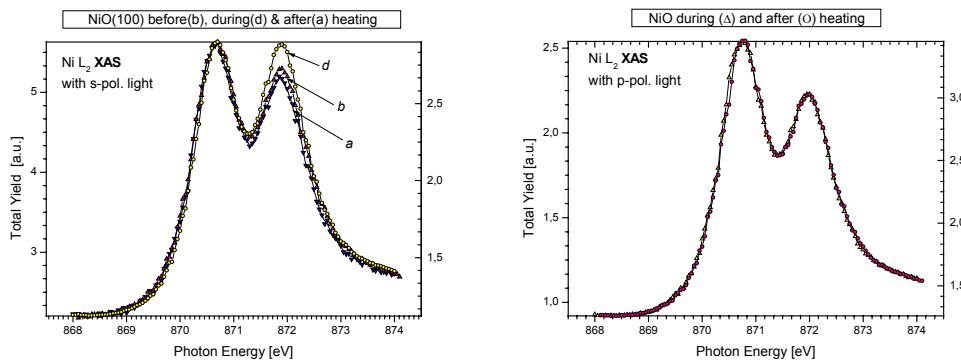


Fig. 2: X-ray absorption spectra at the Ni-L₂ edge. Above the Néel temperature the magnetic exchange part of spectrum vanishes³ in s-polarised light (left) but not in p-polarized light (right).

The Fe domains in Fe/NiO(001) disaggregate into small domains whose orientations are mostly collinear to the underlying Ni-moments in the NiO substrate (see in Fig 3). Some domains run along [110] directions while others are canted away (about 18° from [110]) what agrees to the bulk-like spin orientations in the NiO substrate.

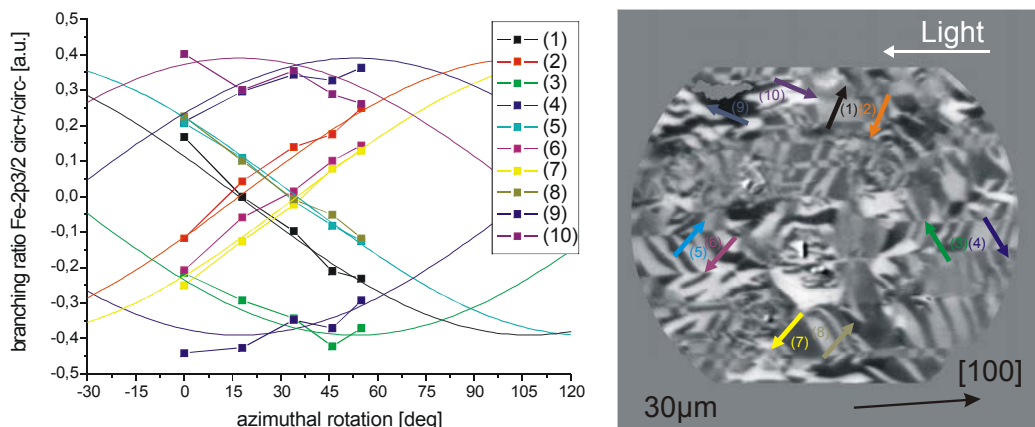


Fig. 3: Change of the Fe MCD-contrast with the azimuthal sample rotation (left) for selected domains on Fe/NiO (right). The Fitted curves correspond to the contrast progression that is expected from distinct directions of the magnetic moments.

These results support the findings of Matsuyama et al.¹ regarding the canted Fe-Moments. However they comply with the collinear coupling between FM and AF layers as observed by Ohldag et al.² and Nolting et al.⁴

When the thickness of Fe on NiO is increased step by step and the ferromagnetic domain formation on Fe is traced, PEEM images show a strong evidence for spin reorientation in the Fe layer. Ferromagnetic coupling inside the Fe layer occurs when the cluster like growing iron layer coalesces at about 6-8 ML. In some areas the Fe-moments seem to rotate with increasing film thickness while others remain unaltered (see Fig. 4). Angular dependent measurements show that the change in the domain contrast is clearly due to a rotation of the spin alignment.

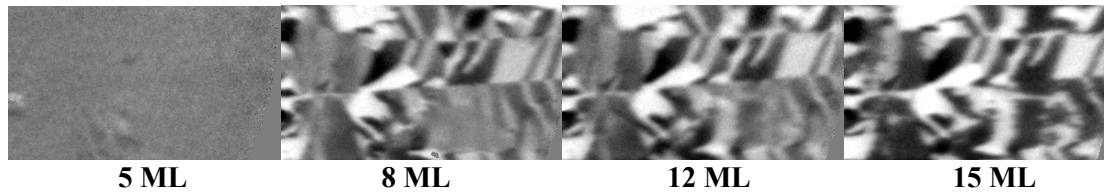


Fig. 4: Thickness dependence on the domain formation in the Fe layer. After the onset of ferromagnetic coupling at 8 ML some domain orientations seem to rotate with increasing film thickness (as seen in lower right or upper left region of each picture) while others remain unaltered.

To observe the interface reaction in Fe/NiO we took X-ray absorption spectra and PEEM-images with different polarized light for very thin (<1ML) and for thicker Fe coverages. However they gave no indication for any significant oxidation in the Fe film (as shown in Fig 5) or reduction in the NiO.

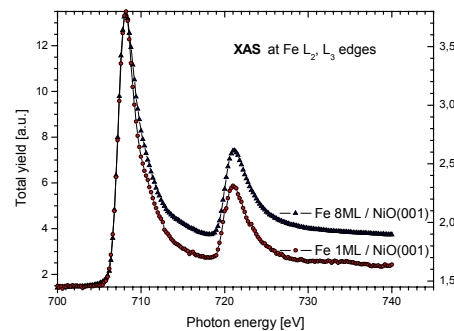


Fig. 5: XAS at the Fe-L-edges for different film thicknesses. No indication for significant interface reactions (namely oxidation) have been found

In summary, our results obtained by PEEM and XAS show clearly canted Fe moments on Fe/NiO(001). However they support also collinear arrangements between the AF and FM layers in some sense. With increasing Fe thickness some of ferromagnetic domains seem to rotate to the direction different from the ones in NiO. There was no evidence for any interface reaction during Fe coating. Annealing process of NiO above Néel temperature showed a different behavior with s- and p-polarized light. A full recovery of XAS-peak at the Ni L₂ edge was observed with s-polarization but no change with p-polarization. Spin reorientations have been observed on the ‘as cleaved’ NiO-surface during annealing for both the in-plane components and the out-of-plane moments in NiO (here not shown).

Acknowledgements: This work is supported by BMBF under grant 05KSIPFB/1. We would like to thank the user support and the beamline support team in BESSY, particularly Mr. Pfau, Dr Godehusen and Dr. Senf.

- [1] H. Matsuyama, C. Haginoya and K. Koike, Phys. Rev. Lett. 85, 646 (2000)
- [2] H. Ohldag, A. Scholl, F. Nolting, S. Anders et al., Phys. Rev. Lett. 86, 2878 (2001)
- [3] D. Alders, L.H. Tjeng, F. C. Voogt et al. Phys. Rev. B 57, 11623 (1998)
- [4] F. Nolting, A Scholl, J. Stöhr et al., Nature 405, 767 (2000)

Low-energy electron excitations in complex oxides studied by x-ray Raman spectroscopy

C. F. Hague^{1,2}, J.-M. Mariot¹, L. Journal¹, J.-P. Rueff¹, R. Delaunay¹, M. Sacchi²,
S. Eisebitt³

¹LCP-MR, Université Pierre et Marie Curie, Paris. ²LURE Orsay. ³BESSY, Berlin.

(Supported by BESSY-EC- HPRI-1999-CT-00028)

Introduction

The undisputed advantages of resonant x-ray Raman spectroscopy (RXRRS) are that probed sample-depths are one or two orders of magnitude larger than in photoemission experiments; there is element selectivity (via the involvement of a core-hole-excitation) and insensitivity to charging effects and magnetic fields. The major drawback is weak signal strength, here many orders of magnitude lower than that encountered in photoemission and Auger spectroscopy. The outcome is that the quality of the spectra is often poor (poor energy resolution and/or poor statistics) which is a handicap to breaking new ground in the study of the electronic properties of materials. We have designed a new soft x-ray spectrometer whose figure of merit, with a specialized beamline at SOLEIL in mind, is much improved compared to existing instruments. The relevant figure of merit must ensure both a high resolving power and an excellent signal-to-noise ratio. It is also important to closely match the spectrometer and beamline characteristics. In the case of SOLEIL, the beamline will provide a flux $> 10^{13}$ photons/s at a resolving power of ≈ 2000 , focused to $\approx 2 \mu\text{m}$ in the vertical plane. The U41-PGM beamline at BESSY II is a high flux microfocus beamline with similar characteristics. It is designed to provide $\approx 10^{13}$ photons/s over the 170 – 800 eV energy range with a resolving power ≈ 2000 for 12 μm focal spot. This, except for the size of the focal spot, is an excellent match for our spectrometer.

Our first session aimed at assessing the performance of the prototype spectrometer and initiating a study of phase transitions in 3d transition metal oxides. We will give a brief summary of the experimental performance and illustrate the present status by means of a preliminary experiment on the paramagnetic-metal–antiferromagnetic-insulator (PM–AI) first order phase transition in V_2O_3 .

Experimental

Our experimental station consists of the spectrometer and sample chamber. Positioning relative to the beam focus can be finely adjusted (x, y, z, and θ adjustments). The spectrometer uses two focusing mirrors and a plane-grating with variable line spacing. A flat-field image is obtained with energy dispersion in the vertical plane [1]. The sample surface lies perpendicularly to the scattering plane and is positioned by means of a high precision manipulator. The sample position relative to the incoming beam and the optical axes of the spectrometer is highly critical for maximum signal intensity. The intersection between the “point” source and the optical axis has to coincide to within $\pm 0.1 \text{ mm}$ in the x-direction (incoming beam) and $\pm 0.01 \text{ mm}$ in the y- and z-directions. The best focus was determined by means of a knife-edge fitted to the sample manipulator. The FWHM was 16 μm for a monochromator exit slit of 45 μm (see Fig. 1). Most measurements were performed using a 100 μm monochromator slit and a spot size $\approx 30\text{-}50 \mu\text{m}$ FWHM. The spot position was generally very stable between refills. At this stage however we found that repeated examination of the spot size and position was too time-consuming, so the results reported here did not use optimum focusing. We envisage installing a beam position monitor for future experiments.

Fig. 2 shows data for the V L_{III} -edge excitation for GdVO_4 taken with a back illuminated CCD detector. The absorption spectrum was obtained by measuring the total fluorescence yield (TFY) with the spectrometer by monitoring the zero-order intensity. From

an analysis of the Gaussian-like high energy edge of the elastic peak, we estimated the total resolving power to be 700. We are confident that this can be improved on.

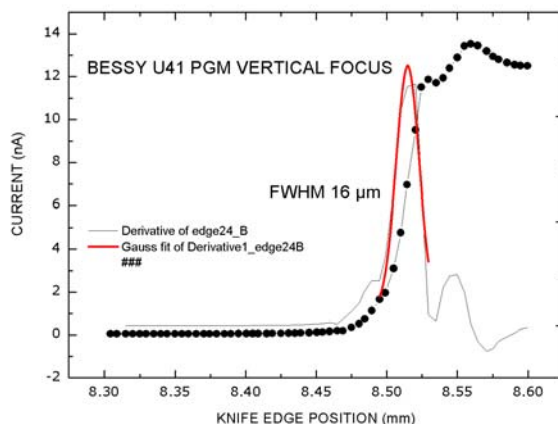


Fig.1. Best focus determined by the vertical displacement of a knife-edge. A value of $16 \mu\text{m}$ FWHM was measured with a monochromator exit slit of $45 \mu\text{m}$.

It should be noted that the signal strength is particularly satisfactory. The background-subtracted raw data shown in Fig. 2 is for a CCD exposure time of 100 s only.

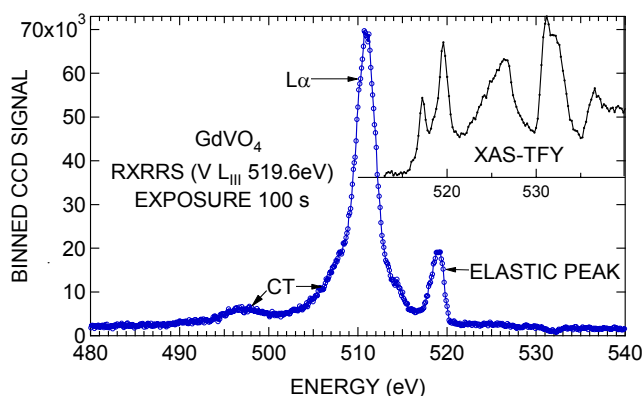


Fig. 2. Resonant x-ray Raman spectrum of V in GdVO_4 measured at the L_{III} edge. The inset shows XAS measured by total fluorescence yield. The XAS energy scale is that of the PGM monochromator. The XES energy scale is determined independently from the spectrometer grating-angle and assuming the $\text{V } M_{\text{I}}-L_{\text{III}}$ emission line energy is at 446.5 eV (not shown). The peak count rate according to the CCD manufacturer's current-to-counts conversion is $\approx 700 \text{ counts/s}$.

Vanadium sesquioxide

The electronic structure of V_2O_3 is complex and still not fully understood [1,2]. Dealing with the $\text{V } L$ x-ray emission spectrum (XES) data justifies in itself the use of resonant excitation because $\text{V } 3d$ and $\text{O } 2s2p$ hybridization is large in the covalent V_2O_3 compound. It is at the origin of marked structure $\approx 7\text{-}16 \text{ eV}$ below the main V emission band which shifts up by $+3 \text{ eV}$ compared to the metal. The $\text{V } 2p$ spin-orbit splitting is $\approx 7.7 \text{ eV}$ so the L_{III} and L_{II} related XES overlap and, furthermore, there is partial overlap with the $\text{O } K\alpha$ emission band. This is illustrated in Fig. 3 by data taken with an MCP detector covering a broad energy range. At the L_{II} resonance the $\text{O } K\alpha$ signal is eliminated. At the L_{III} resonance the L_{II} part of the signal is eliminated.

RXRRS data taken under higher resolution conditions using a CCD detector is presented Fig. 4. The spectra were recorded for excitations just below the L_{III} or L_{II} edges and measured above and below the metal-insulator transition temperature. A distinct change in

shape indicates a drop in the intensity of low energy excitations in the insulator phase and a possible change in the intensity of the elastic scattering. These measurements are to be resumed shortly at BESSY under improved resolution conditions, in order to study the low energy loss structure in more detail.

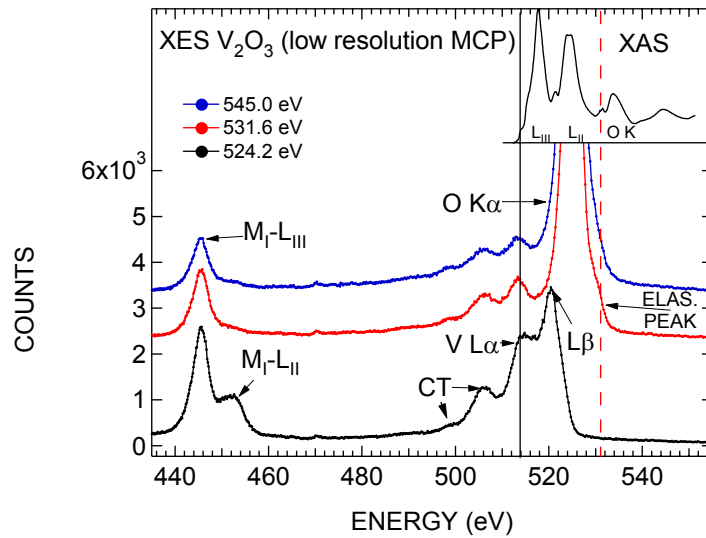


Fig. 3. Extended V_2O_3 XES spectrum (top curve) illustrating how resonant excitation (lower curves) can eliminate overlap between V and O components.

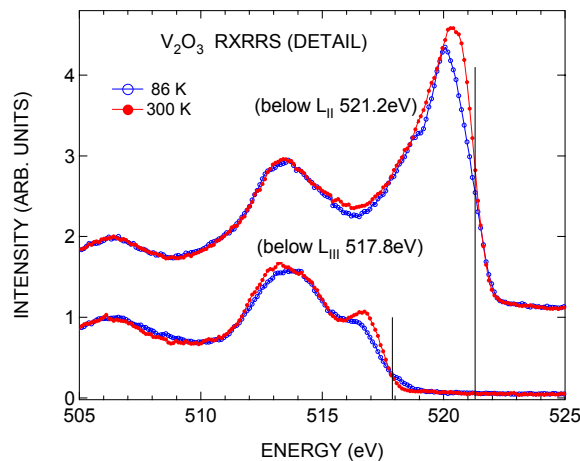


Fig. 4 Resonant x-ray Raman spectra taken just below the L_{III} and L_{II} edges. The elastic peak position is indicated. The interesting low-energy-loss features are expected within 1-2 eV of the elastic peak justifying further efforts to improve the resolving power of the experiment. It should be noted that raw data are presented except for CCD dark-current subtraction

Acknowledgements

We are indebted to Professor W. Felsch and collaborators for providing oriented thin film V_2O_3 samples and to Professor A. Revcolevschi and collaborators for providing single crystals of $GdVO_4$.

- [1] K. Held et al., Phys. Rev. Lett. **86**, 5345 (2001).
- [2] B. Sass et al., J. Phys. Condens. Matter. **16**, 77 (2004).

Resonant magnetic soft x-ray scattering from polycrystalline Ho metal films

E. Schierle, H. Ott, G. Kaindl, E. Weschke

Institut für Experimentalphysik, Freie Universität Berlin, Arnimallee 14, D-14195 Berlin, Germany

Resonant magnetic scattering is an emerging technique for the study of magnetic correlations in thin films. In particular in the soft x-ray region, i.e. at the $L_{2,3}$ edges of the 3d transition metals and at the $M_{4,5}$ edges of the lanthanides, a large increase of the magnetic scattering amplitude is obtained, which leads to a very high sensitivity that allows to study ultrathin films and dilute systems. So far, studies of magnetic superstructure studies in thin films have been largely carried out on high-quality monocrystalline thin films with narrow mosaic spread. Previous results on very thin Ho films [1], however, have indicated that the sensitivity should be sufficient to study polycrystalline material.

The experiments were carried out with a UHV-compatible Θ - 2Θ diffractometer that has come into operation in 2003 and which is based on a newly developed two-stage rotary feedthrough [2]. Fig. 1 (left) shows the instrument at the UE/52-SGM beamline. It is readily operated at a pressure of 6×10^{-11} mbar, Ho films were grown in situ in UHV on a W(110) single crystal substrate and on a polycrystalline Ta substrate, respectively. The right panel of Fig. 1 shows the internal setup with the W crystal, a set of seven evaporators and the diode detector behind a changeable slit. The W crystal is mounted on a closed-cycle He cryostat that allows cooling down to ≈ 35 K.

Fig. 2 displays the specular reflectivities of two different Ho films, recorded with a photon energy corresponding to the maximum of the M_5 resonance of Ho. The data were taken at a temperature well below the magnetic ordering temperature. Ho metal is characterized by long-period magnetic structure with a period of ≈ 10 ML at low temperatures. This magnetic superstructure gives rise to a magnetic diffraction peak at a wave vector transfer of ≈ 0.2 (in units of the reciprocal lattice parameter c^* of Ho), which is readily observed in both cases. The reflectivity of the 46-ML-thick monocrystalline film (solid data points) reveals a broad magnetic peak with a width corresponding to the finite number of layers contributing to the

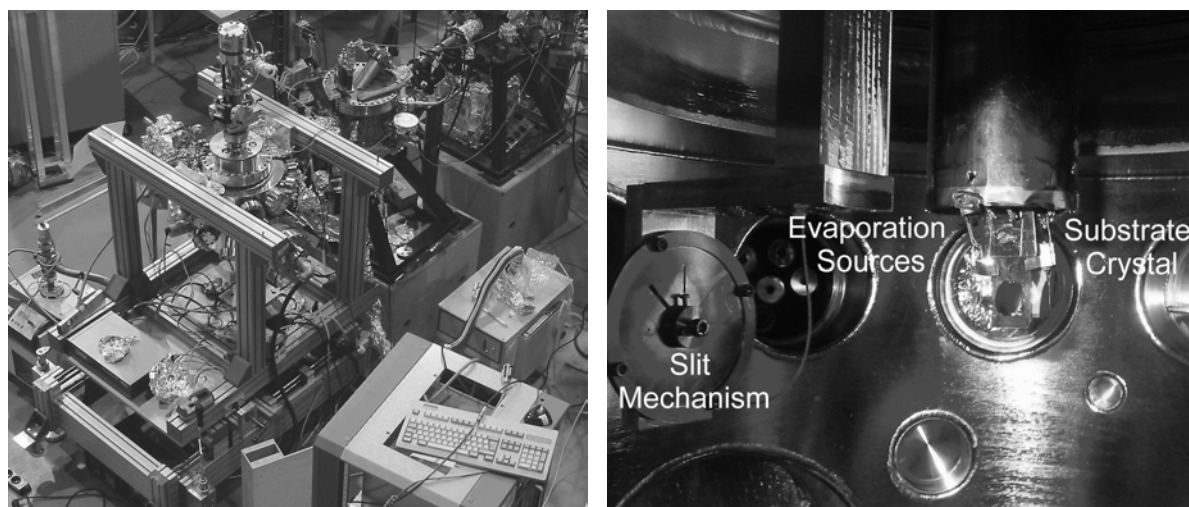


Fig. 1. UHV diffractometer at the UE/52-SGM beamline (left). The photograph on the right panel shows an internal view.

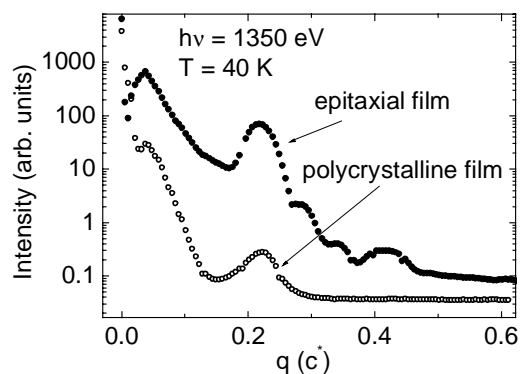


Fig. 2: Specular reflectivities, recorded at the Ho-M_5 resonance from a 46 ML thick monocrystalline film (solid data points) and from a 110 ML thick polycrystalline film (open circles). In both cases, a pronounced magnetic superstructure peak is visible.

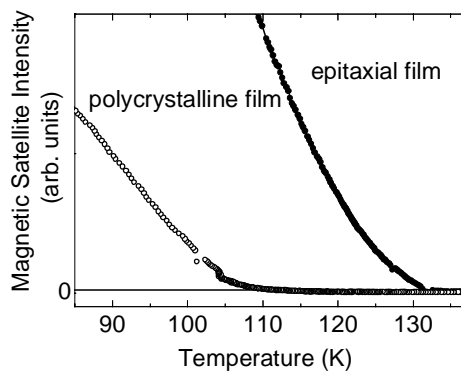


Fig. 3: Temperature dependence of the magnetic satellite intensity for two different Ho films of the same thickness. For the polycrystalline film, a distinct reduction of the ordering temperature from ≈ 132 K to ≈ 105 K is observed.

scattering signal. The reflectivity of the 110-ML thick polycrystalline film is characterized by a much faster decrease of the specular reflectivity. In addition, the magnetic superstructure peak is much broader than expected from the film thickness of 110 ML. Such a broadening is also observed in transverse scans (not shown here), indicating a finite grain size of the polycrystalline material. Assuming the same magnetic and structural coherence, a mean grain size of the order of 14 nm can be determined.

According to this grain size, a finite size effect on the ordering temperature may be anticipated, as observed in epitaxial thin Ho films [3]. And indeed, we observe a reduction of T_N in the polycrystalline films, as can be seen from the temperature dependences of the magnetic superstructure peaks displayed in Fig. 3. It is interesting to note that a film of 110 ML is in fact too thick to exhibit a finite size effect [3]. This means that there is no magnetic coupling across the structural grains, resulting in separated nanomagnets in a chemical homogeneous system. This is related to the local character the 4f magnetic moment and the coupling of the magnetic modulation wave vector to the c direction of the lattice.

The present results show that magnetic studies of polycrystalline material by resonant magnetic soft x-ray scattering are readily feasible, opening the way to magnetic powder diffraction.

This work was financially supported by the BMBF, project 05KS1KEE/8.

References:

- [1] C. Schüßler-Langeheine *et al.*, J. Electr. Spectrosc. Relat. Phenom. **114-116**, 953 (2001).
- [2] E. Weschke, Patentschrift Aktenzeichen 103 16 730.7, submitted to Deutsches Patentamt (7.4.2003).
- [3] V. Leiner *et al.*, Phys. Rev. Lett., submitted (2003).

Metal-organic Chemical Vapor Deposition (MOCVD) of Palladium: Spectroscopic Study of Cyclopentadienyl-allyl-palladium Deposition on a Palladium Substrate

A. Niklewski, T. Strunskus, G. Witte and Ch. Wöll,

Lehrstuhl für Physikalische Chemie 1, Ruhr-Universität Bochum, Bochum, Germany

Introduction

Metal-organic chemical vapor deposition (MOCVD) of metals is attractive in many applications because it offers a number of potential advantages over physical vapor deposition methods such as metal evaporation or sputtering. Among the advantages of MOCVD are low deposition temperatures, fast growth rates, the ability to cover complex topologies conformally, and the potential for selective area deposition. Despite the big potential very little is known about the exact precursor decomposition mechanism involved in the deposition of the metal thin films. Knowledge of the exact decomposition mechanism may aid to improve the MOCVD-Precursors, the decomposition process and the purity of the metal deposits obtained.

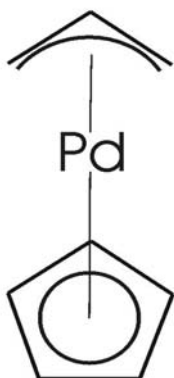


Fig.1 Chemical structure formula of Pd precursor

Here the initial steps of the adsorption and decomposition of cyclopentadienyl-allyl palladium, short $\text{Pd}(\eta^5 - \text{Cp})(\eta^3\text{-allyl})$ (see Fig.1), on a well defined Pd(111) single crystal surface are investigated. Previous work has shown that this palladium complex is a suitable precursor for low temperature palladium deposition[1-4].

Experimental

XPS and NEXAFS measurements at BESSY were done in a UHV system consisting of a loadlock, a preparation chamber and an analysis chamber attached to the HESGM beamline at BESSY. The Pd precursor was prepared and cleaned at the "Lehrstuhl für Anorganische Chemie II" of the "Ruhr-Universität Bochum" [5-7]. It was stored in an inert gas at temperatures below -18 °C and used without further purification. To avoid contact of the precursor with metallic surfaces a self-built dosing system with chemically inert walls was used. A thermostat with a coolant liquid was used to store the precursor at temperatures below -18°C prior to the experiments. Raising the temperature of the thermostate allowed outgassing of the precursor and adjustment of a desired vapor pressure of the precursor during the experiments. The Pd(111) crystal used for the experiments was cleaned by repeated cycles of ion sputtering (1kV sputter voltage, $p(\text{Ar}) = 1 \times 10^{-4}$ mbar) and flashing the crystal for less than one minute to about 900 K.

Results and Discussion

XP spectra

The Pd 3d and C 1s core level spectra of a multilayer deposit taken with Al K_{α} radiation are shown in Fig. 2. After deposition at 160 K the palladium $3d_{5/2}$ and $3d_{3/2}$ lines appear at binding energies of 337.7 and 343.0 eV, respectively. In the C 1s region one observes a single line at 284.5 eV binding energy and a "shake-up" satellite at around 289 eV (see Fig.2). Based on a quantitative analysis of the XPS data a C/Pd ratio of 8.0 is obtained in excellent agreement with the stoichiometric value expected for an intact precursor.

The palladium 3d lines of the precursor are shifted by 2.6 eV to higher binding energies compared to the Pd 3d lines of the palladium metal substrate appearing at 335.1 eV and 340.4 eV for the clean palladium substrate. This is an indication that the palladium is formally in a +2 oxidation state in the precursor complex. In the C 1s region only a single C 1s line is resolved indicating that the negative charge is evenly distributed over all carbon atoms. The shake-up peak at around 289 eV is typical for π - π^* -transition in conjugated π -electron systems. It is likely that it originates from the benzene like π -electron system of the cyclopentadienyl ligand in its anionic state.

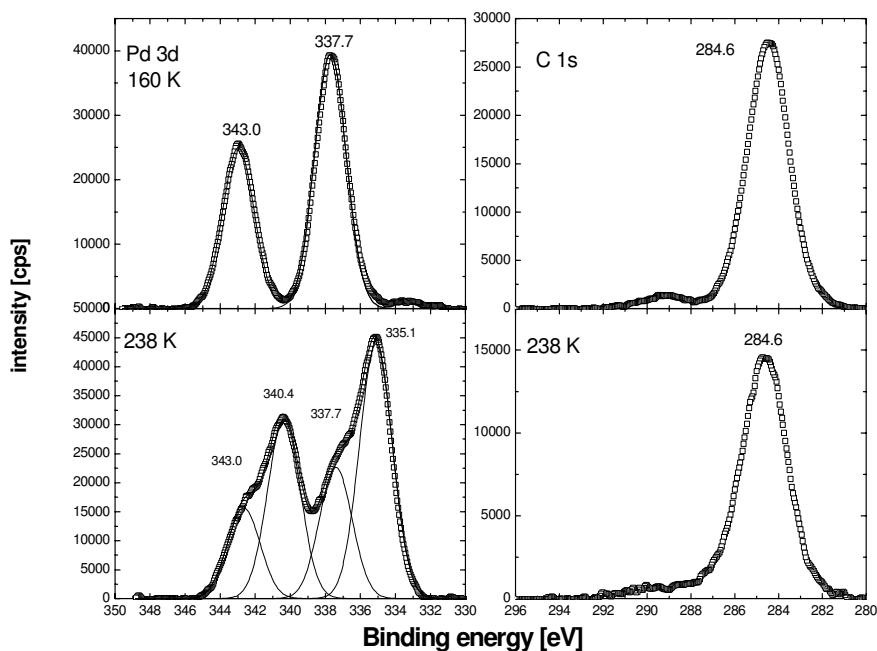


Fig. 2 Pd 3d und C 1s core level spectra of a multilayer deposit of the Cp(allyl)Pd precursor. Top: After deposition at 160 K. Bottom: After warming to 238 K.

Annealing the sample for 5 min to 238 K leads to significant changes in the Pd 3d and C 1s signal (see Fig. 2). The calculated thickness of the deposit decreases and the Pd 3d core level spectrum shows reduction of the Pd(II) signal and a corresponding growth of the substrate Pd(0) metal signal. The main C 1s line becomes asymmetric with increased intensity at higher binding energy. The decrease and finally vanishing of the Pd(II) signal (not shown) together with the lineshape changes in the C 1s region clearly indicate the decomposition of the (Cp)Pd(allyl) precursor on the Pd(111) surface. The data indicate that the transition of Pd(II) to (Pd0) occurs first prior to the complete removal of the ligands. Under UHV conditions on a clean palladium substrate the ligands do not desorb completely but a layer remains covering the palladium surface.

NEXAFS spectra

The corresponding NEXAFS spectra for the multilayer deposit are shown in Figure 3. The top spectra represent the thick multilayer of the intact precursor molecule. The spectra exhibit strong resonances at 284.5 eV, 285.1 eV, and 286.4 eV. These resonances are excitations of C 1s electrons into empty π^* orbitals. Based on quantum chemical calculations the first two resonances are assigned to the “cyclopentadienyl” ligand, whereas the resonance at 286.4 eV is assigned to the “allyl” ligand. The resonance at 287.8 eV is assigned to excitations into Rydberg states and the remaining broad resonances at 291 eV and at 297 eV are assigned to excitations into σ^* -orbitals. The π^* resonances allow to distinguish the two ligands. Corresponding to the changes detected in the C 1s core level

spectrum also the NEXAFS spectrum shows significant changes upon annealing to 238 K (see fig. 3). The splitting of the first two resonances is no longer resolved and a single resonance at 284.8 eV is

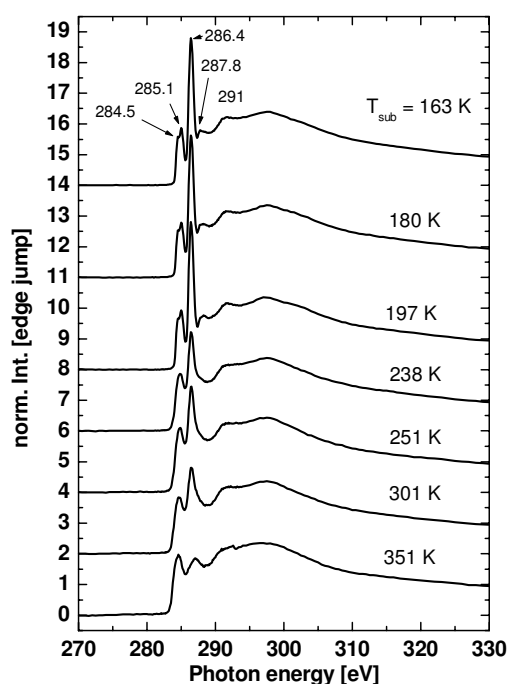


Fig. 3 NEXAFS spectra of *Cp(allyl)Pd* multilayer on a Pd(111) substrate after deposition at 163 K and after different annealing steps.

remaining precursor molecules undergo chemical changes. It can be speculated that the first step in the decomposition is the interaction of the central palladium atom with the palladium surface. The central Pd(II) atom is thereby changed to Pd(0). The precursor then loses first the allyl ligand and, while the Cp ligand remains bonded to the Pd atom as indicated by the NEXAFS results.

Acknowledgements

This work has been supported by the DFG SPP 1119 under the project number WO 464/19-2.

References

1. J.E. Gozum, D.M. Pollina, J.A. Jensen, and G.S. Girolami, *J. Am. Chem. Soc.* **110**, 2688 (1988).
2. J.-C. Hierso, P. Serp, R. Feurer, and P. Kalck, *Appl. Organomet. Chem* **12**, 161 (1998).
3. C.S. J.-C. Hierso, R. Feurer, P. Kalck, *Chem. Mater.* **8**, 2481 (1996).
4. Z. Yuan and R.J. Puddephat, *Adv. Mater.* **1**, 51 (1994).
5. R. Redon, R. Cramer, S. Bernes, D. Morales, and H. Torrens, *Polyhedron* **20**, 3119 (2001).
6. Z.Y. Y. Zhang, R.J. Puddephat, *Chem. Mater.* **10**, 2293 (1998).
7. U. Weckenmann, in *Lehrstuhl für Anorganische Chemie*. Ruhr-Universität Bochum: Bochum. (2002).

obtained. The intensity of the resonance at 286.4 eV is decreased and the resonance at 287.8 eV vanishes. The XPS results show that the layer thickness is reduced to about three monolayers of the precursor. Besides the presence of some intact precursor molecules there are significant contributions from excess ligands interacting with the Pd(0) substrate. This can lead to the observed broadening and small shifts of the π^* and σ^* resonances. Excitations into Rydberg states are often quenched by the interaction of molecules with metal surfaces. After heating to 301 K and 351 K a decrease in intensity of the allyl resonance at 286.4 eV is observed (Fig.3). The resonances attributed to the cyclopentadienyl units remain unchanged. The layer thickness is reduced to 0.5 nm and no Pd(II) is detected anymore in the Pd 3d core level spectrum.

Taken together the following picture evolves from the XPS and NEXAFS data. At 238 K most of the precursor molecules are desorbed. Precursor molecules not in contact with palladium desorb before decomposition. The

Interface sharpening instead of broadening by diffusion in ideal binary alloys

Z. Erdélyi, D.L. Beke, G.A. Langer, M. Kis-Varga, [Department of Solid State Physics, University of Debrecen, P.O. Box 2 H-4010 Debrecen, Hungary]; M. Sladeczek, L.-M. Stadler, B. Sepiol [Institut für Materialphysik der Universität Wien, Universität Wien, Austria], I. Zizak [Hahn-Meitner-Institut Berlin, Germany]

The presented project aimed at an astonishing new effect, which is in complete contrast to hands-on experience – namely the sharpening of interfaces in completely miscible binary systems due to diffusion on nanoscale, i.e. on short diffusion distances and short time. Using computer simulations based on deterministic kinetic equations [1] and Monte Carlo technique [2], we showed that on nanoscale and for strongly composition dependent D (large diffusion asymmetry), an initially diffused A/B interface can become abrupt even in an ideal system [3,4]. In the framework of this project, our goal was to prove it experimentally.

We prepared Mo/V multilayer samples with a modulation length of approximately 5-6 nm by magnetron sputtering [5]. The pure Mo and V epitaxial layers were separated by an about 1 nm thick diffused interface with a constant composition gradient. Such a initial profile (time $t = 0$) is illustrated in figure 1 for the Ni/Cu system. Note, that the preparation of the Mo/V samples described above is not a standard procedure but needed significant improvement.

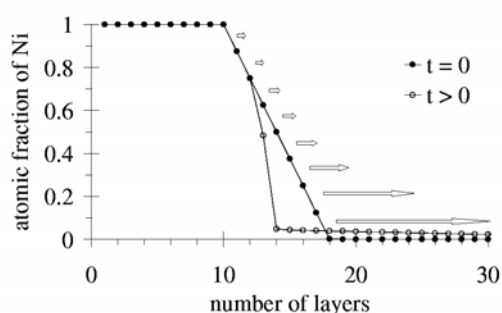


Fig.1 : Composition distribution of A (Ni) during the dissolution of 10 atomic layers of A into B(111) (Cu) calculated using deterministic kinetic equations. The initially 8 atomic layers width interface become abrupt due to the asymmetric diffusion (concentration dependent diffusivity). The arrows represent the schematic drawing of the 'flux distribution' (lengths is proportional to the absolute value of the atomic flux) in the initial state ($t=0$...filled circles).

Synchrotron reflectometry and diffraction measurements on the (002) Bragg reflection of the multilayer structure were performed at the KMC2 beamline at BESSY radiation facility using a 8 keV X-ray beam. The samples were mounted in a vacuum chamber with a Be hemisphere on a 6-circle diffractometer. The versatile design allowed for both geometries without remounting the sample. Starting from the room temperature the measurements were repeated for several temperatures up to 650°C. For each temperature θ - 2θ intensity profiles were recorded in both geometries using a scintillation point detector. The range of the reflectometry and diffraction measurements was set from 0.4° to 10° and 53° to 65°, respectively.

Figure 2(a) shows some diffraction patterns measured during the heat treatment, i.e. in different stages of the sample, whereas in Fig.2 (b) some simulated diffraction patterns can be seen. The calculation has been carried out with an improved model based on Fullerton's and his coworkers work [6]. In the improved model we can consider not only linearly diffused (initial profile in Fig. 1) and abrupt interfaces (final state after sharpening), but also intermediate ones. For the calculation of the initial state ($t_0 = 0$) we supposed a multilayer of 20 bilayers, each consisting of a 7 atomic layers thick Mo layer and a 20 atomic layers thick V layer. All interfaces are assumed as 7 atomic layers thick and linearly diffused. Thus each bilayer contains 41 atomic layers. The diffraction pattern for t_1 is calculated assuming that 2 atomic layers from the interface have already been dissolved into the V layer. At t_2 a dissolution of 5 atomic layers is supposed, whereas the last pattern corresponds to the final state, i.e. an abrupt interface. Comparing the measured and calculated patterns an agreement of the main features can be found, which confirms our theoretical predictions.

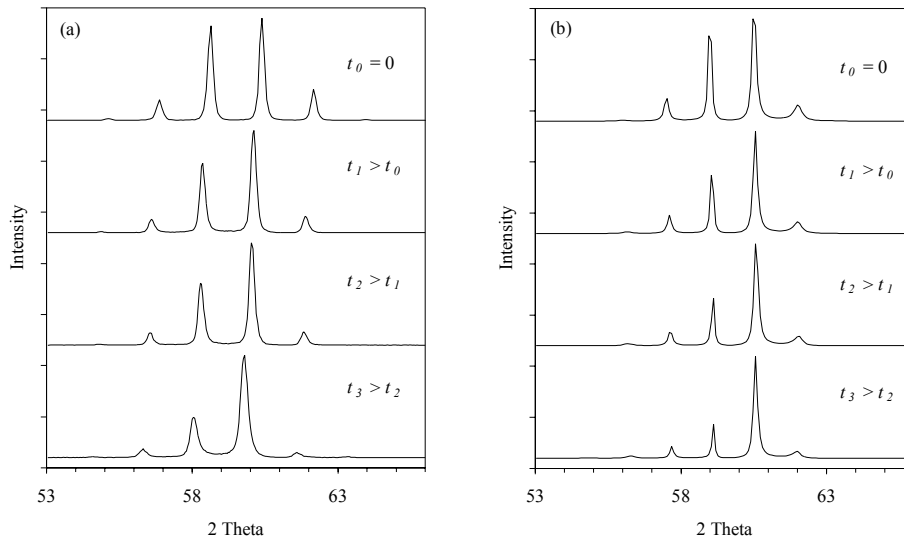


Fig. 1: (a) Diffraction patterns measured during the heat treatment, i.e. in different stages of the experiment (b) simulated patterns (see also the text).

Besides a qualitative comparison we would like to fit the measured data by our model. However, the quantitative structural refinement of superlattice structures is not a simple task. Figure 3 shows preliminary result of our new developed computer program. Even if our refinement software is not yet completed, the results obtained by it are promising.

Although we should still finalize the treatment of the data, we can conclude that practically we managed to prove the sharpening effect experimentally. Finally, we note that the measured reflection patterns are also in agreement with the reported results.

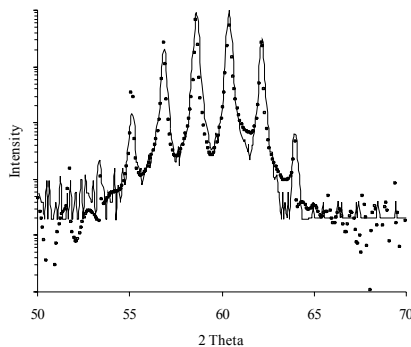


Fig. 2: Preliminary result of our structural refinement program. The circles represent the measured diffraction pattern, whereas the solid line is the model function. Note that the intensity is plotted on logarithmic scale in order to show all the details of the pattern.

- [1] G. Martin, *Phys. Rev. B*, **41** (1990), 2279.
- [2] D.L. Beke, C. Cserhádi, Z. Erdélyi, I.A. Szabó, *Nanoclusters and Nanocrystals* (Ed. H.S. Nalwa, American Scientific Publisher, 2003) chap.: Segregation in Nanostructures.
- [3] Z. Erdélyi, I.A. Szabó, D.L. Beke, *Phys. Rev. Letters*, **89** (2002), 165901.
- [4] Z. Erdélyi, D.L. Beke, *Phys. Rev. B*, **68** (2003), 092102.
- [5] D.L. Beke, G.A. Langer, M. Kiss-Varga, A. Dudas, P. Nemes, L. Daroczi, Gy. Kerkes, Z. Erdelyi, *Vacuum* **50** (1998) 373.
- [6] E.E. Fullerton, I.K. Schuller, H. Vanderstraeten, Y. Bruynsereade, *Phys. Rev. B*, **45** (1992), 9292.

nanoESCA on decorated grain-boundaries of poly-Cu

S. Schmidt¹, M. Escher³, F. Forster¹, D. Funnemann³, B. Krömker³, M. Merkel², F. Reinert¹, N. Weber²

¹Universität des Saarlandes,

FR 7.2 Experimentalphysik, Saarbrücken

²Focus GmbH, Görsroth

³Omicron Nanotechnology GmbH, Taunusstein

We present Imaging XPS measurements of polycrystalline Cu with a fraction of 2% Bi using the nanoESCA spectrometer. This spectrometer allows to resolve the grains and grain boundaries in polycrystalline samples. The spatially resolved XPS data show that small amounts of clean metallic Bi are deposited between the Cu grains and therefore serve as an element decoration of the grain-boundaries of the poly-Cu.

It is known that nature and size of grains and grain-boundaries mainly define the mechanical properties of nano- and polycrystalline materials. The decoration of grain-boundaries by addition of small amounts of non-alloying elements allows their imaging by, i.e., tomographic methods¹. For the investigation of chemical and spatial structures of grains and grain-boundaries in the poly-crystalline $\text{Cu}_{0.98}\text{Bi}_{0.02}$ we have used the nanoESCA, a newly designed instrument allowing Imaging XPS with good resolution in energy and an adequate spatial resolution better than 200 nm^2 . The energy resolution has been determined by measurements of the Fermi edge of the sample at room temperature using an excitation energy of $h\nu = 605\text{ eV}$ at beam-line UE-52/SGM (see inset in Fig. 2). In consideration of the broadening caused by the exciting radiation ($\Delta E(h\nu) \approx 80\text{ meV}$) and intrinsic thermal contribution of $4k_{\text{B}}T$ we obtain an energy resolution of the instrument of $\Delta E \lesssim 190\text{ meV}$. This good performance allows us to identify subtle differences in the chemical formation on different sample areas of sub- μ scale. Thus, one can perform a chemical analysis of single grain surfaces and grain-boundaries³. The $\text{Cu}_{0.98}\text{Bi}_{0.02}$ -polycrystal used in our measurements has been grown by a controlled cooling down of the melt of 98% Cu and 2% Bi and subsequent mechanical and chemical polishing cycles. Prior to the measurements the sample has been cleaned *in situ* by careful Ar^+ -ion sputtering in order to ensure a contamination-free surface. All measurements presented here were taken at room temperature and a base pressure of 5×10^{-10} mbar using only ion getter pumps to prevent vibration and assure good spatial resolution. The spectra in the center of Fig. 3 show four energy scans across

the $\text{Bi}4f_{7/2}$ core level taken on different sample areas (red, blue, cyan and green rectangles in the picture at binding energy $E_B = 156.83\text{ eV}$) at an excitation radiation of $h\nu = 600\text{ eV}$. The arrows in the spectra mark the energy positions where the corresponding pictures — with a field of view of $50\text{ }\mu\text{m}$ — were taken. White areas mean a high intensity of emitted electrons. It is obvious that the high intensity at the unshifted Bi-peak can only be found in the grain-boundaries while the areas on a grain surface (green rectangle) remains dark. This means that the Bi segregates between the Cu grains and therefore serves as a decoration of the grain-boundaries while the grains itself consist of clean Cu (see green curve in Fig. 3). The spatial extension of the Bi/Cu interface is below the spatial resolution.

In Fig. 2 we show a more detailed study of the $\text{Bi}4f_{7/2}$ peak. After background correction a Voigt line fit to the raw data shows a FWHM (full width at half maximum) of the peak of 313 meV . The peak position at $E_B = 156.8\text{ eV}$, the line-shape and the absence of any satellite structure indicates the purity of the metallic Bi in the grain-boundaries. From the calibration of the energy resolution (see inset in Fig. 2) and the Gaussian contribution of the exciting radiation we can estimate an intrinsic line-width of the Bi $4f_{7/2}$ core-level of about 240 meV .

We would like to thank C. Krill and M. Ziehmer from the Universität des Saarlandes for providing the $\text{Cu}_{0.98}\text{Bi}_{0.02}$ samples. This work was supported by the BMBF (FKZN 13N7865, 13N7863, 13N7864, 13N7847) and the DFG(SFB 277). We like to thank the BESSY II staff, esp. F. Senf for his help with the beam-line.

¹ C. Krill, K. Döbrich, D. Michels, A. Michels, C. Rau, T. Weitkamp, A. Snigirev, and R. Birringer, in *Developments in X-Ray Tomography III*, edited by U. Bonse (2002), vol. 4503 of *Proc. SPIE*, pp. 205–212.

² D. Funnemann, P. Bernhard, M. Escher, F. Forster, B. Krömker, M. Merkel, F. Reinert, S. Schmidt,

G. Schönhense, J. Westermann, et al., *Bessy Annual Report 2002* pp. 350–351 (2003).

³ S. Schmidt, P. Bernhard, M. Escher, F. Forster, D. Funnemann, Krömker, M. Merkel, F. Reinert, G. Schönhense, and C. Ziethen, *Bessy Annual report 2002* pp. 179–180 (2003).

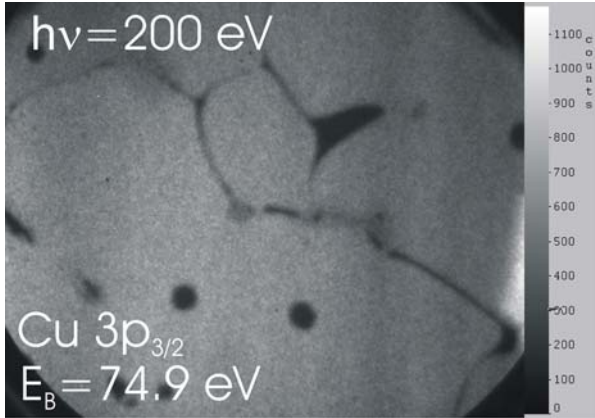


FIG. 1: The spatial photoemission intensity map taken at the binding energy of the $\text{Cu } 3p_{3/2}$ core level of $\text{Cu}_{0.98}\text{Bi}_{0.02}$ shows the exposed Cu grain surfaces (white=highest intensity) and the grain boundaries (dark).

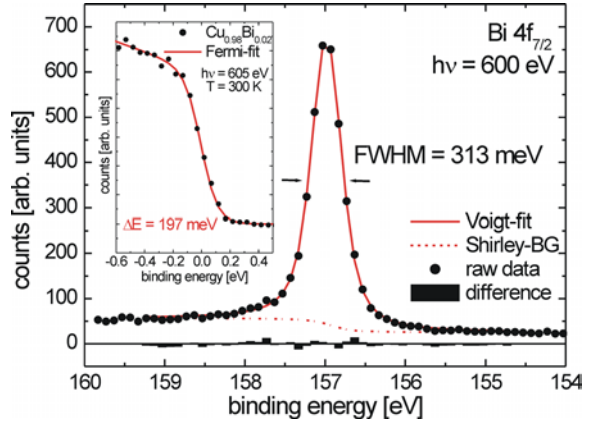


FIG. 2: Energy scan across the $\text{Bi } 4f_{7/2}$ XPS core-level. The FWHM of the core-level, as determined from the line, is 313 meV. The energy resolution of $\Delta E = 197$ meV is determined from a measurement of the Fermi-edge (displayed in the inset) by taking into account the intrinsic line-width of the light and the temperature broadening (see text).

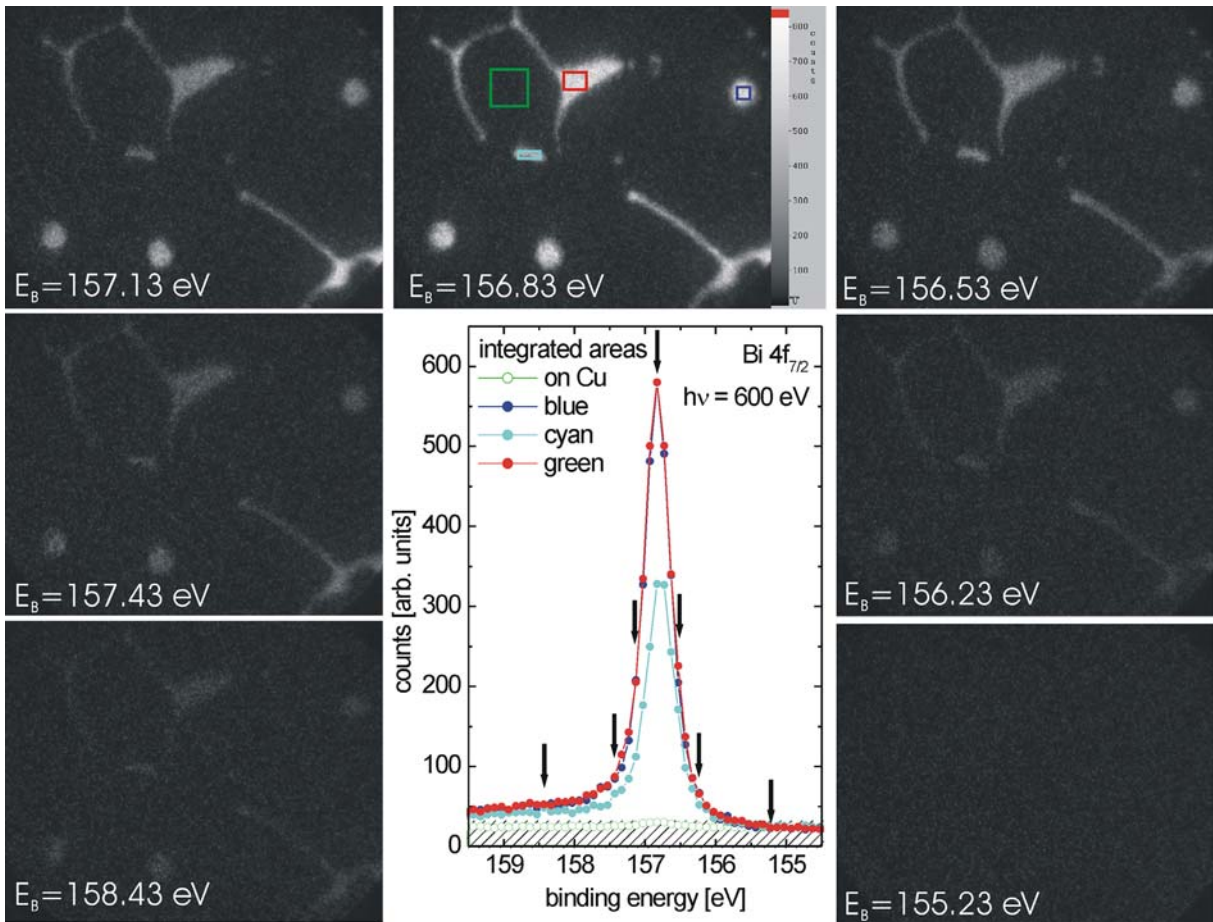


FIG. 3: In comparison to Fig. 1, this series of pictures taken from the energy scan over the $\text{Bi } 4f_{7/2}$ XPS core-level shows the element contrast inversion. The selected pictures are taken at the binding energies labelled in the pictures and indicated by arrows in the spectra. The color codes of the spectra indicate the corresponding sample areas (squares in the picture at $E_B = 156.83$ eV) over which they have been integrated.

Mapping of magnetic domains at the Fe 2p XPS core-level using the *nano*ESCA

S.Schmidt¹, M. Escher³, F. Forster¹, D. Funnemann², B. Krömker²,
M. Merkel³, F. Reinert¹, N. Weber³

¹Universität des Saarlandes, ²Omicron NanoTechnology GmbH, ³Focus GmbH

We report the first imaging ESCA results using the “*nano*ESCA” for the MLD/MCD mapping of magnetic domains in iron single crystals. Using a band-pass energy filter, this spectrometer allows imaging at typical XPS core-level binding energies. Compared to conventionally used X-ray absorption technique for the imaging of magnetic domains (XMCD with XPEEM) our results show that direct core-level XPS is well suited to create a map of the magnetic domains at crystal surfaces with high surface sensitivity. Thus, the technique simultaneously allows the imaging of the surface magnetic structure and the measurement of XPS spectra showing elemental and chemical contrast on the same sample region with high spatial resolution.

The “*nano*ESCA” imaging spectrometer is a newly developed system for imaging ESCA that consists of a PEEM in combination with a double hemispheric band-pass energy filter [1]. It is capable of taking images of the spatial distribution of photoelectron intensities emitted from the sample surface. With the integration of the band-pass energy filter into the electron-optics it is possible to confine the energy of the emitted electrons contributing to a single picture to a small range of kinetic energy. Due to the large range of detectable kinetic energies, XPS scans can be done from high binding energies above $E_B=1200$ eV to kinetic energies at the Fermi-edge, depending on the excitation radiation. The energy resolution of the system has been demonstrated to be better than 190 meV, measured at a photon energy of $h\nu=605$ eV on the Fermi-edge of $\text{Cu}_{0.98}\text{Bi}_{0.02}$ [2], the spatial resolution is better than 200 nm [1] and has been improved during the last beam-time to reveal spatial structures of 80 nm at low electron kinetic energies.

The grazing angle θ of the photon beam was 25° . As indicated in Figure 2 the photon beam is horizontal. The PEEM immersion lens has an acceptance angle of less than $\pm 4^\circ$ for electrons with 90 eV kinetic energy. Hence in all measurements at this kinetic energy (or higher) only electrons close to the surface normal are detected.

The single crystal iron sample was prepared in-situ by a sputtering-annealing cycle. The data presented in this report have been taken at the UE-52 SGM beam-line allowing a high degree of circular polarization and high photon flux in a small spot of ~ 40 μm at high photon energies up to 1.5 keV.

The Fe (100) sample was imaged in photoemission with a photon energy of $h\nu=850$ eV at the Fe2p_{3/2} core level with circularly polarized light (Figure 3). The field of view was about 100 μm . The domain pattern as presented in Figure 3 can be seen without any further data processing.

To understand the observed domain pattern one has to take into account the different dichroism effects:

clearly the MCD is present since circular light is used. The MLDAD occurs due to the p-polarized component in the \vec{E} -vector. The MLD can be neglected at the Fe2p core level (in contrast to the Fe3p core level). In case the relevant effects are small enough they will combine linearly.

In the upper part of the image taken with σ^+ polarization (Figure 3) a pattern with large domain sizes can be seen, which disappears in the image with σ^- polarization. This indicates that the MCD and the MLDAD are of the same order of magnitude: The MLDAD is present in both images with the same sign but the MCD changes sign from σ^+ to σ^- polarization. The disappearing domain pattern in the image with σ^- polarization is due to a compensation of MCD and MLDAD. The two effects can be separated easily by taking the sum (MLDAD) and the difference (MCD) as shown in Figure 4.

Assuming the magnetic vector to be in plane due to stray field minimization the sum image gives the vertical magnetization and the difference image the horizontal magnetization. To check the difference image an X-MCD image (with σ^+ polarization only, see Figure 5) at the Fe2p_{3/2} absorption edge was taken for comparison. The domain pattern in both images is in good agreement. The different probing depth (enhanced surface sensitivity in XPS) becomes obvious at the defect in the middle of the image, which seems not to contribute to the domain walls at the present scale of the image.

The PES spectra of the Fe2p_{3/2} core level in Figure 1 are taken from the large domains in the upper part of the image (see inset) with σ^+ polarization. The MLDAD and the MCD have the same line shape. The size of the dichroism ($\sim 30\%$ asymmetry) is in good agreement other spectroscopic data [5]. The missing negative structure in the dichroism at the shoulder of the peak is most likely due to a systematic error.

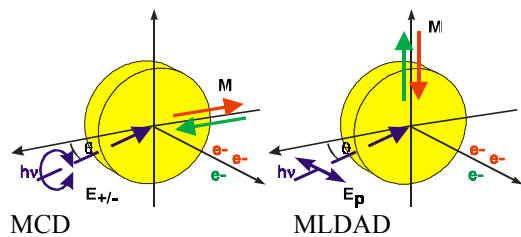


Figure 2: Geometry of the experiment. The indicated magnetization corresponds to the MCD and MLDAD respectively.

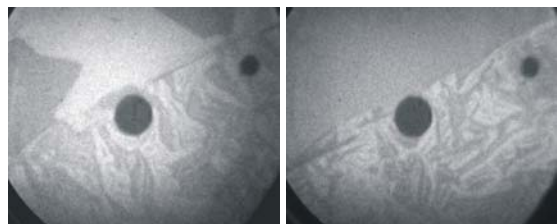


Figure 3: Domain contrast in photoemission at the $Fe2p_{3/2}$ threshold by σ^+ polarization (left) and σ^- polarization (right).

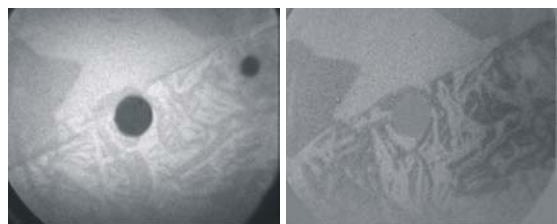


Figure 4: The sum image from σ^+ and σ^- polarization (left) corresponds to the MLDAD. The difference image from σ^+ and σ^- polarization (right) corresponds to the MCD.



Figure 5: X-MCD at the $Fe2p_{3/2}$ absorption threshold with σ^+ polarization.

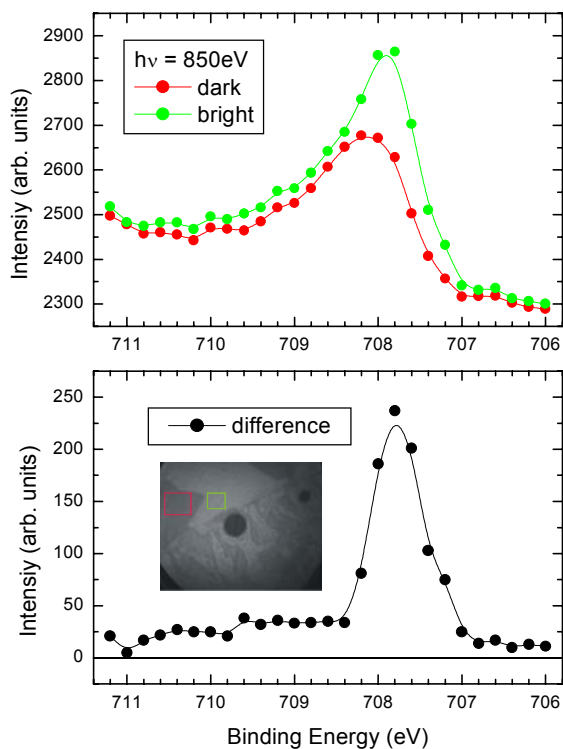


Figure 1: PES spectrum and dichroism of the $Fe2p_{3/2}$ XPS core level. The inset shows the picture of Figure 3 (left). The red and green rectangles mark the sample areas over which the corresponding spectra (above) have been integrated.

References

- [1] D. Funnemann *et al.*, Bessy Annual Report 2002 (2003)
- [2] S. Schmidt *et al.*, Bessy Annual Report 2003 (2004)
- [3] C.M. Schneider, G. Schönhense, Rep. Prog. Phys. **65** (2002), R1785-R1839 and references therein
- [4] S. Imada *et al.*, Surf. Rev. Lett. **9**, 2, (2002)
- [5] F.U. Hillebrecht *et al.*, Phys. Rev. B **53**, 18, 12182-12194 (1996)
- [6] W. Kuch *et al.*, J. Vac. Sci. Technol. B. **20**(6), 2543, (2002)

This work was supported by the BMBF (FKZN 13N7865, 13N7863, 13N7864, 13N7847) and the DFG (SFB 277). The authors like to thank the BESSY staff, esp. F. Senf for his help with the beamline.

Computed tomography experiments at BAMline

G. Weidemann, J. Goebbels, B. Illerhaus, Th. Wolk, H. Rieseemeier

Federal Institute for Materials Research and Testing (BAM)

Unter den Eichen 87, 12205 Berlin, Germany

In cooperation with HMI (cf. contribution of Banhart, Haibel et al.) a CCD camera with 2048 x 2048 pixel was integrated into the computed tomography experimental set-up at BAMline. Samples up to a diameter of 7 mm can be measured with a voxel size of $(3.65 \mu\text{m})^3$. The major field of investigations were further studies on bone remodelling

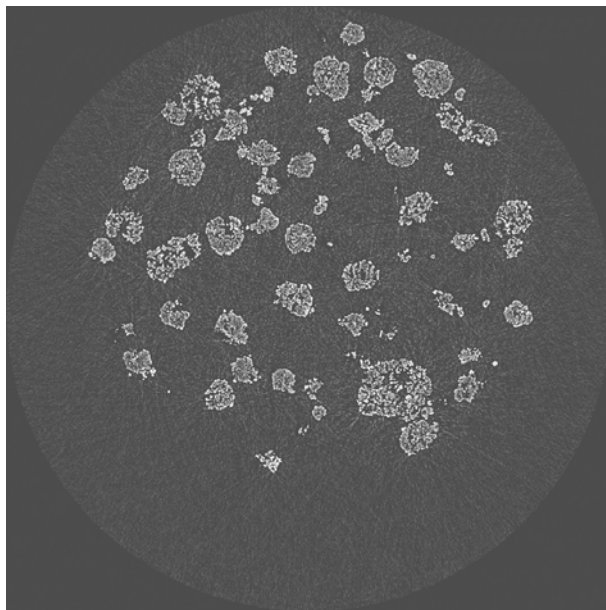


Fig. 1: Horizontal slice of a sample. The scan conditions are 10 keV; the voxel size was $(3.65 \mu\text{m})^3$.

and implants as well as the characterization of light metals and core samples in cooperation with partners from industry and research institutes. First studies were done on the hardening process of concrete and catalytic polymerisation of polyethylene as function of polymerisation time. Fig 1. shows a horizontal slice from the 3D image data set of a polymer powder obtained after 60 min of polymerisation. The fracture mechanism of the silica-supported catalyst due to the formation of polyethylene was deduced from the position of the silica particles.

As an example characterizing light metals fig. 2 shows results from a fatigue test sample of a cast magnesium alloy, measured with a voxel size of $5.5 \mu\text{m}$ at 30 keV. The part failed after about 10.000 cycles at a maximum load of 60 N/mm^2 (20 Hz, $R=0.1$). The left part of fig. 2 shows a vertical slice (bottom) together with the isosurface representation of the fractured surface of the sample (top). The excess material of the alloy segregated at the grain boundaries during casting is visible as thin filaments with higher attenuation. The section of a horizontal slice is shown in the right part of the figure together with a colour bar representing the different X-ray attenua-

tion of matrix material and alloy, 100 steps - increasing attenuation with increasing brightness.

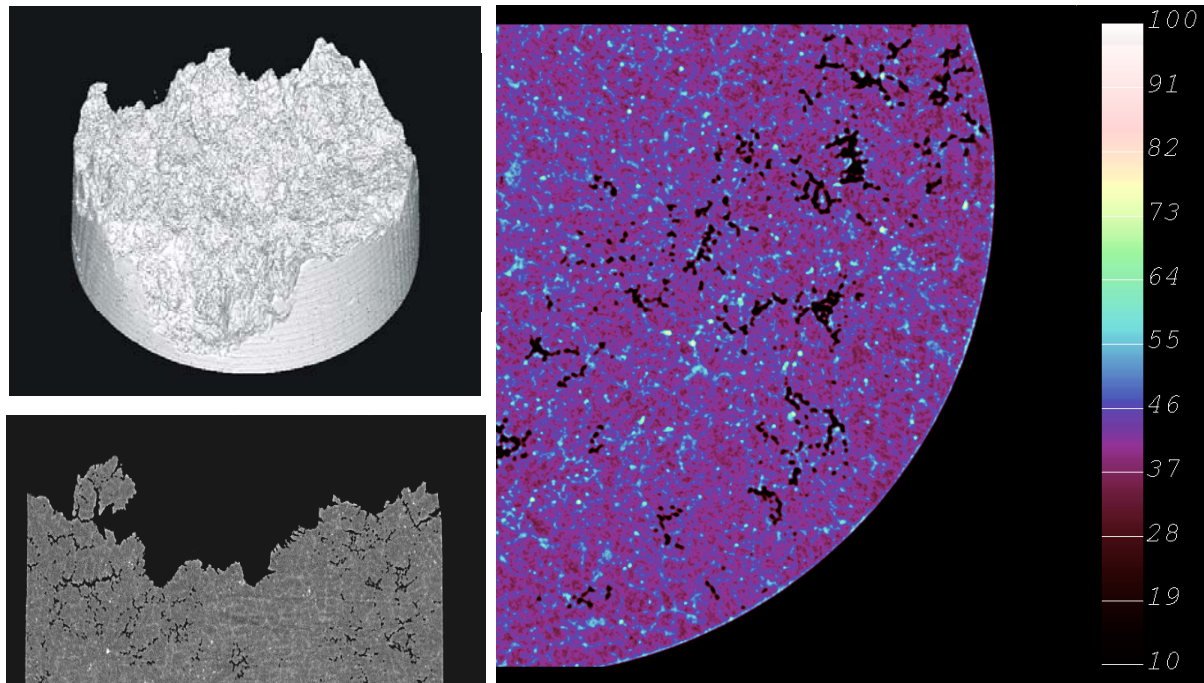


Fig. 2: Fatigue test sample of cast magnesium alloy. The left side of the image shows a vertical slice (top) from the 3D image data set together with the fractured surface of the sample (bottom). The right part represents a pseudo coloured display detail of a horizontal slice with a colour bar for quantified attenuation in the sample. The scan conditions are 30 keV; the voxel size was $(5.5 \mu\text{m})^3$.

References

J. Goebbels, B.R. Müller, H. Riesemeier, G. Weidemann
Special Solutions for CT-Investigations with Synchrotron Radiation
Proc. NDT in Progress, Prague, 2003, pp. 91-97
ISBN 80-214-2475-3

B. Illerhaus, N. Hort, C. Potzies, H. Frank, J. Goebbels
Non-destructive Testing of Cast Magnesium Alloys by Computerized Tomography
Proc. of the 6th Int. Conference Magnesium Alloys and their Applications, 18-20 Nov 2003,
Wolfsburg, Ed. K.U. Kainer, Wiley-VCH, 2003, pp. 746-751
ISBN 3-526-30975-6

Spectroscopic analysis of Cu(In,Ga)(S,Se)₂ thin film solar devices by combining x-ray emission and photoelectron spectroscopy in the CISSY endstation

Ch.-H. Fischer, M. Bär, A. Grimm, I. Kötschau, I. Lauermann, K. Rahne, J. Reichardt, S. Sokoll, and M.C. Lux-Steiner, *Hahn-Meitner-Institut Berlin, GmbH*
L. Weinhardt, O. Fuchs, G. Storch, and C. Heske, *Experimentelle Physik II, Universität Würzburg*
C. Jung and W. Gudat, *BESSY GmbH, Berlin*
T. P. Niesen, S. Visbeck, and F. Karg, *Shell Solar GmbH, München*

In the second year of operation, the investigation of chalcopyrite thin film solar devices and their relevant components with the CISSY apparatus was continued in order to enable a knowledge-based development of more efficient and more stable solar cells and modules. By X-ray emission (XES) and photoelectron (PES) spectroscopy [1], combined with in-system preparation, (buried) interface, surface, and layer compositions were studied in the multilayer systems of chalcopyrite solar cells and modules. Here, three examples are presented in more detail.

Electrochemically „etched“ CIS (CuInS₂) absorbers

In order to obtain the required material properties for high photovoltaic efficiencies, the CuInS₂ absorber layers are prepared copper-rich with the consequence of a copper sulfide segregation at the surface. This phase is typically removed by etching with a KCN solution, a highly toxic chemical. Lewerenz et al. [2] replaced this process by electrochemical etching, but so far resulting cell efficiencies reached only up to 3%. Fig. 1a shows the sulfur L_{2,3} XES spectra of CuInS₂ absorbers, as

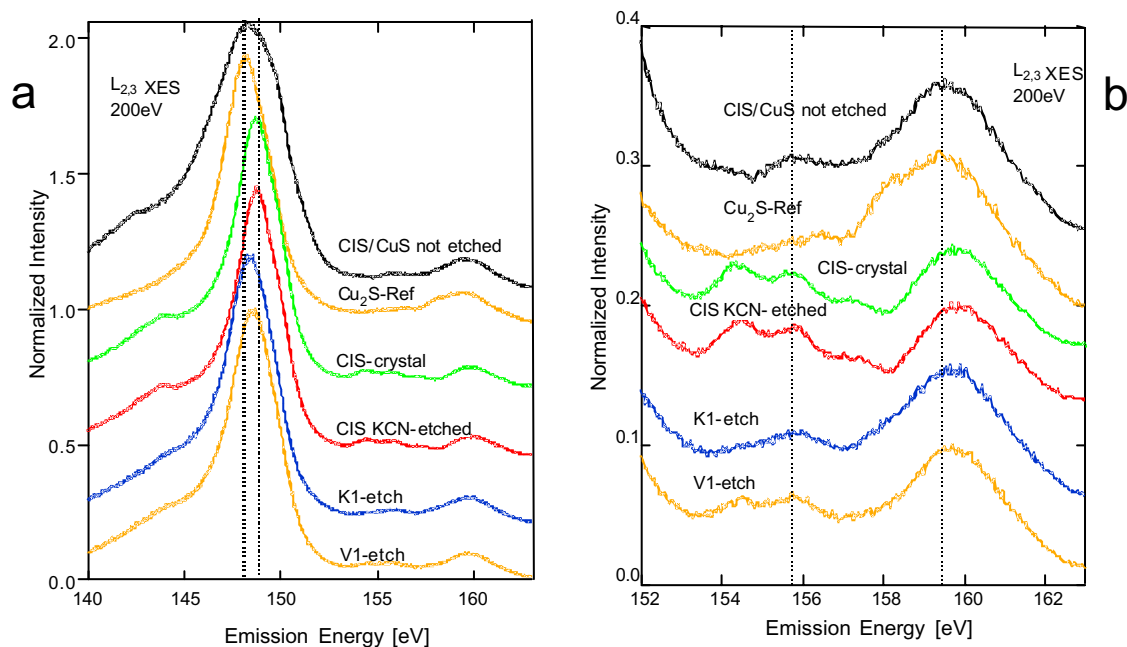


Fig. 1 a) S L_{2,3} XES spectra of CuInS₂ absorbers, as grown and after electrochemical etching under different conditions (K1 and V1), as well as reference spectra of Cu₂S, CuS, and CIS. b) The energy range of the transitions from the valence band is shown on an expanded intensity scale.

grown, after KCN and electrochemical etching under various conditions (K1, V1), as well as reference spectra of Cu₂S, CuS, and CIS. The comparison of the 3s → 2p main peak positions (close to 148 eV) as well as an analysis of the spectral features at higher energies (transitions from the upper valence band, Fig. 1b) reveals a reduction of the copper sulfide contribution in the electrochemically etched samples. However, the spectra still differ from that of the KCN-etched CIS reference. These spectroscopic results led directly to a modification of the etch conditions. So far, the resulting solar cell efficiency could be raised up to 8%.

Laterally resolved XES measurements

The CISSY chamber is equipped with a step motor-driven central manipulator allowing the precise scanning of the sample under the synchrotron spot during XES and PES measurements. For line or

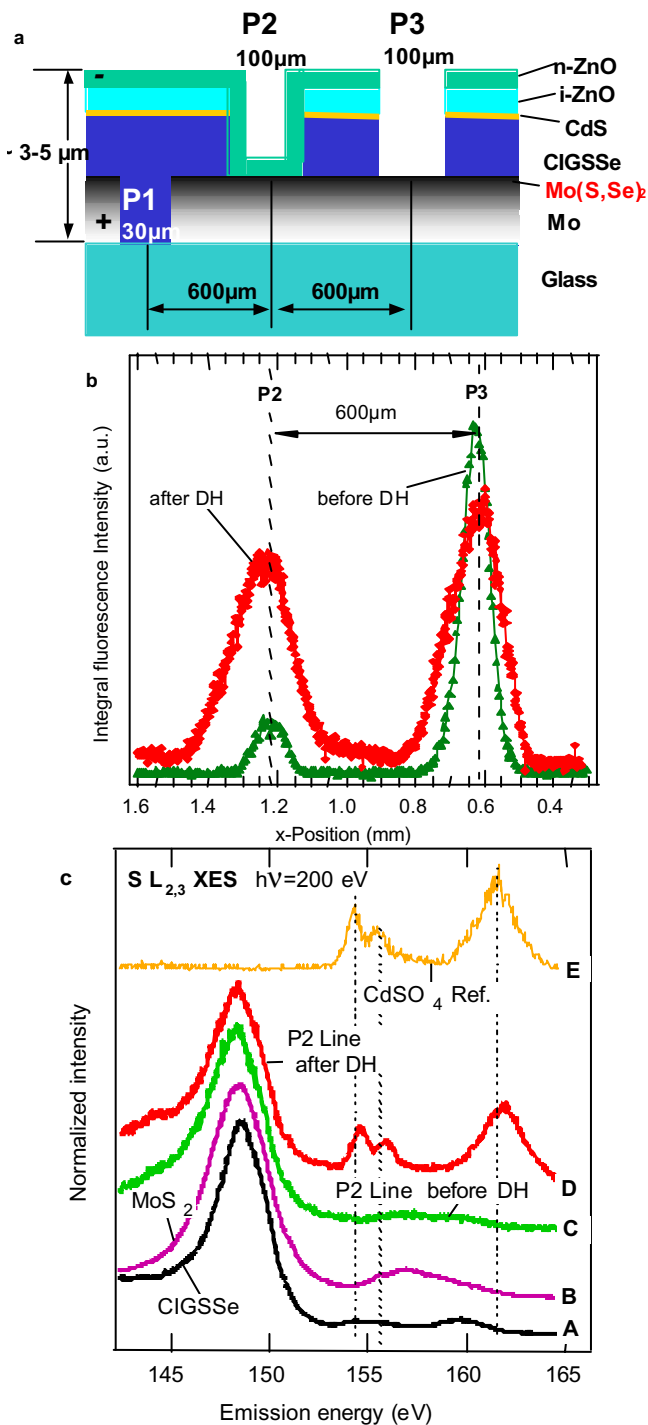


Fig. 2: a) Schematic cross-section of a special CIGSSe solar module (see text). b) Integral S-XES signal (140-165 eV) as a function of the position (scan perpendicular to the grooves) before (green) and after (red) DH. c) local, energy resolved S $L_{2,3}$ -spectra of the P2-line before (C) and after (D) DH. Reference-spectra of CIGSSe (A), MoS_2 (B), and a metal sulfate (E) are given for comparison. The spectrum in P2 before DH is interpreted as a superposition of CIGSSe and MoS_2 contributions. Thus, the strong increase of the integral SXES signal in b) after DH correlates with a high sulfate content in the corresponding spectrum in c).

area scans at a certain fluorescence x-ray energy range or electron kinetic energy, respectively, the spectroscopic signal is recorded as a function of the local position. On the other hand, XES- and PES spectra can be measured at well-defined positions on the sample. The probing synchrotron spot at the U41-PGM beamline typically has an effective size of about 100 μm by 800 μm for XES measurements and 50 μm by 30 μm for PES. By moving a MoS_2 /glass test structure with parallel grooves of various widths perpendicular to the grooves, it was possible to resolve grooves as narrow as 25 μm by a S-XES scan with a 60x30 μm^2 beam spot.

The chalcopyrite solar technology offers the possibility of manufacturing cost efficient monolithically integrated modules. The individual layers that form a solar device are deposited in large areas, and at certain process steps these layers are laterally separated by laser or mechanical "scribing". This leads to an array of solar cells, electrically connected just by an overlapping highly conducting n-ZnO layer without any soldering.

In order to obtain the required long-term stability, these solar modules have to be encapsulated in a costly process. A cost reduction, crucial for the economic success, seems possible if the intrinsic stability of the devices and, in particular, of the interconnects, can be improved, thus allowing a simpler lamination. The identification of local degradations demands spatially resolved characterization methods and accelerated aging tests, so-called damp-heat tests ('DH' 100 h, 85°C/85% rel. humidity).

For this purpose, a special CIGSSe module test structure was used, as shown in Fig. 2a (the thickness of the n⁺-ZnO window layer was reduced to 30 nm, thus allowing the XES detection of the underlying layer, and the distance between the P1, P2, and P3 scribe lines was increased to 600 μm). For XES line scans, such modules (before and after DH) were moved under the synchrotron spot (100x800 μm^2) perpendicular to the scribe lines while the integral sulfur fluorescence (140-165 eV) was recorded (Fig. 2b). One can clearly identify the scribe lines P2 and P3 as positive peaks indicating a higher sulfur concentration, since the surface of the Mo layer consists of $Mo(S,Se)_2$. In the P2 line, the S-XES signal is attenuated due to the attenuation in the thin n-ZnO film. In-between the grooves the attenuation is further increased due to the larger thickness of the cover layers (n-ZnO/i-ZnO).

After the DH-test of the un-encapsulated module, a strongly enhanced fluorescence is found in the P2 scribe. Once composition changes are localized, further information about the chemical environment is available from the individual spectra taken at

corresponding positions (Fig.2c). While the S-XES spectrum from the P2 scribe line before DH points to a mixture of MoS₂ and CIGSSe (probably due to particles remaining from the scribing process), after DH a pronounced contribution of sulfate is observed as visualized by the sulfate reference spectrum. Complementary PES measurements show the extension of this alteration up to the surface.

If the formation of insulating sulfate in the electrical contacts between the single cells of a module will also be observed in modules with thicker n-ZnO layers (standard thickness 400 nm), one potential source of efficiency loss under environmental conditions is localized and characterized and attempts can be undertaken to avoid this degradation in the manufacturing process.

Homogeneity

Homogeneous layer compositions are a prerequisite for good solar cell performance. In Fig. 3a, an ILGAR-ZnO/Mo(S,Se)₂ model system after DH is investigated. In contrast to the as-deposited sample, the S L_{2,3}-XES area scan (integral intensity 140-165 eV) shows bright and dark spots, corresponding to high and low intensities (Fig. 3a). The spectra taken from the bright and the dark spot, respectively, and more clearly the difference spectrum (see Fig. 3b) indicate a sulfate contribution. Thus, not only the inhomogeneous element concentration, but also the different chemical environment after DH could be analyzed.

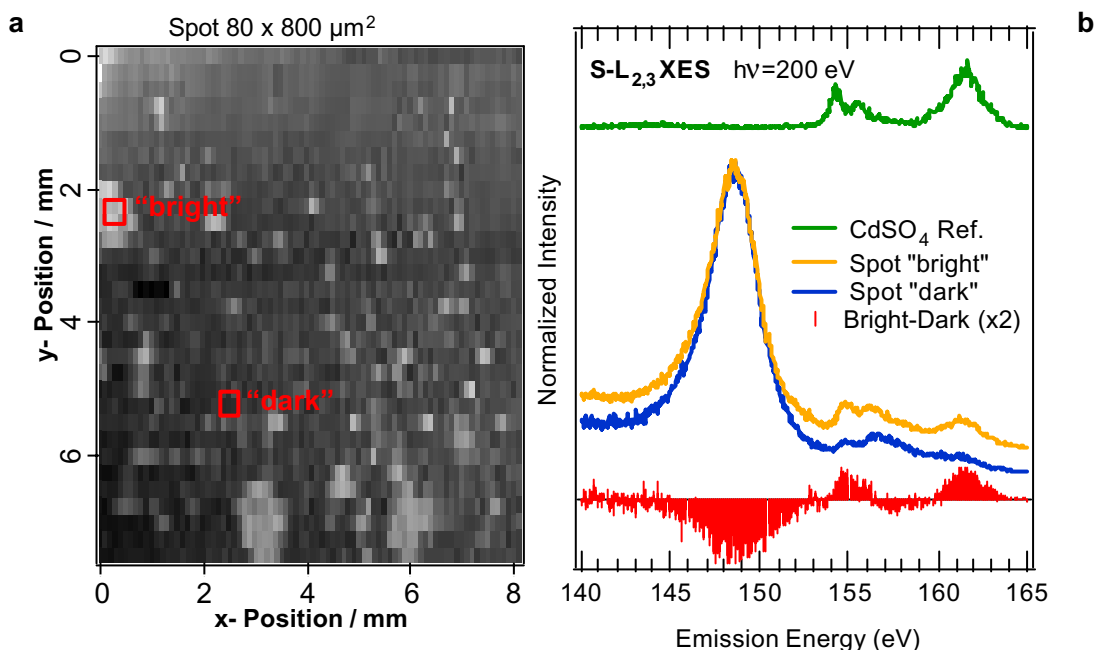


Fig. 3 S L_{2,3}-XES of an ILGAR-ZnO/Mo(S,Se)₂ model system after DH (beam spot 80x800 μm²). a) area scan (integral intensity 140-165 eV), bright = high intensity. b) S L_{2,3}-XES spectra taken from the bright (yellow) and the dark (blue) spot in Fig.3a. The difference spectrum (red) in comparison to the sulfate reference (green) indicates a sulfate contribution to the "bright" spectrum.

Acknowledgement

This work was supported by BMBF (contract no. 01SF0007) and BMWi (contract no.0329889)

Selected Publications

- [1] "Spectroscopic investigation of buried interfaces and liquids with soft x-rays", C. Heske, Appl. Phys. A, in press.
- [2] A. Lewerenz, private communication.
- [3] "Analysis of zinc compound buffer layers in Cu(In,Ga)(S,Se)₂ thin film solar cells by synchrotron-based soft X-ray spectroscopy", I. Lauer mann, M. Bär, A. Ennaoui, U. Fiedeler, C.-H. Fischer, A. Grimm, I. M. Kötschau, M. C. Lux-Steiner, J. Reichardt, B. R. Sankapal, S. Siebentritt, S. Sokoll, L. Weinhardt, O. Fuchs, C. Heske, C. Jung, W. Gudat, F. Karg, and T. P. Niesen, Mat. Res. Soc. Symp. Proc. Vol. 763 B4.5.1 (2003).
- [4] "Monitoring chemical reactions on surfaces in liquids: water on CuIn(S,Se)₂ thin film solar cell absorbers", C. Heske, U. Groh, O. Fuchs, E. Umbach, Th. Schedel-Niedrig, Ch.-H. Fischer, M.Ch. Lux-Steiner, S. Zweigart, F. Karg, J.D. Denlinger, B. Rude, C. Andrus, and F. Powell, J. Chem. Phys. (Comm.) 119, 10467 (2003).
- [5] "X-Ray Emission Study of the ZnO/Cu(In,Ga)(S,Se)₂ Interface before and after Damp Heat Treatment", I. Kötschau, M. Bär, Ch.-H. Fischer, A.Grimm, I. Lauer mann, J. Reichardt, I. Sieber, S. Sokoll, M. C. Lux-Steiner, L. Weinhardt, O. Fuchs, C. Heske, C. Jung, W. Gudat, T. P. Niesen, and F. Karg, Proceedings WCPEC-3, Osaka, 2003, in press.
- [6] "Studying buried interfaces with soft x-ray spectroscopy", C. Heske, Synchrotron Radiation in Natural Sciences 2, 35 (2003).
- [7] "CdS- and Cd(OH)₂-formation during Cd-treatments of Cu(In,Ga)(S,Se)₂ thin film solar cell absorbers", L. Weinhardt, Th. Gleim, O. Fuchs, C. Heske, E. Umbach, M. Bär, H.-J. Muffler, Ch.-H. Fischer, M.C. Lux-Steiner, Y. Zubavichus, T.P. Niesen, and F. Karg, Appl. Phys. Lett. 82, 571 (2003).

High reactivity of Pr on oxide covered 4H-SiC

D.Schmeißer¹, G.Lupina², H.J.Muessig²

Angewandte Physik – Sensorik, BTU Cottbus, Postfach 10 13 44, 03013 Cottbus¹
Ihp, Im Technologiepark 25, 15236 Frankfurt (Oder), Germany²

We use photoelectron spectroscopy to characterize the reactivity of Pr evaporated on SiO₂ covered 4H-SiC substrates. We analyze the Si2p, C1s, and O1s core levels and find that Pr reacts at RT with the SiO₂ layer. Pr-silicide is formed as well as Pr-carbides. These are reaction intermediates as upon annealing to 300°C a Pr-silicate layer is formed which is stable up to 800°C. However, the reaction at the SiC surface remain irreversible.

The application of SiC substrates for electronic devices is of current interest in materials science. ISFET are reported for high temperature sensors application /1/ as well as power FET /2/. For the latter interface engineering is of crucial importance to reach a low interface density, a prerequisite for electrical performance. In this context, we have previously studied the oxidation behavior of 6H-SiC /3/ as well as the interaction of Pr₂O₃ to 4H-SiC substrates /4/.

In Fig.1 we show the Si2p core levels recorded after exposure of Pr (two steps) onto the native oxide layer of a SiC substrate. The lower curves show the data after annealing to 300°C and 500°C. All data are taken at a photon energy of 440eV. Remarkably are the strong shift upon Pr evaporations which amount almost 4eV. Upon annealing these contributions shift again. The Si2p core levels show components which are shifted to lower binding energies and which show up after Pr evaporation and disappear after the annealing.

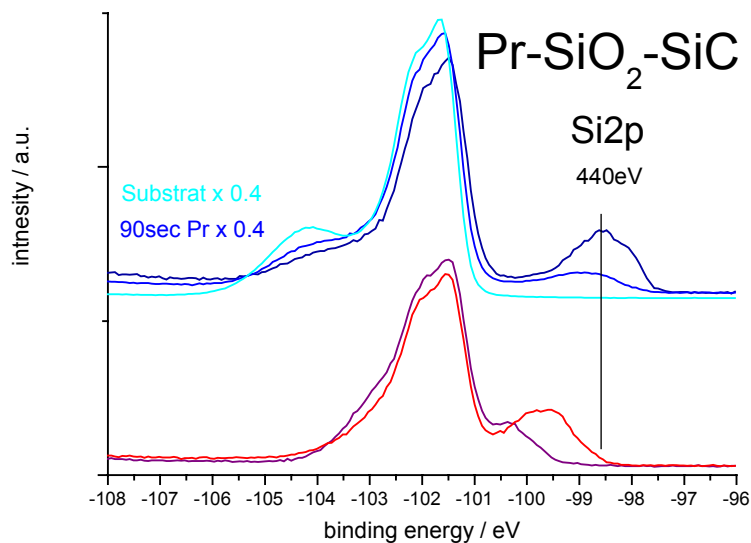


Fig.1:
Si2p core level spectra for the bare SiO₂ / SiC surface, after the evaporation of Pr (0.5nm, 1nm, top curves), and after the annealing steps (300°C, 500°C, lower curves).

In fig.2 we show the C1s core levels recorded after exposure of 1nm Pr onto the native oxide layer of a SiC substrate. The spectra are taken at photon energy of 440eV. The spectrum of the native oxide layer consists of the main SiC peak at 283.6eV as well of a strong feature at 285.6eV. The latter is assigned to a Si-carbonate layer in which Si-C tetra-eders are connected via oxygen bridges /5/. The spectra in Fig.2 are taken after two evaporation steps with the same amount of Pr. After the first step the intensity decreases by 45% and a Pr thickness of 0.5nm can be calculated. The weakening after the second step indicates that the resulting thickness is not doubled (1nm) but is 0.8nm only. This indicates that some of the Pr is already penetrated into the SiO₂ layer.

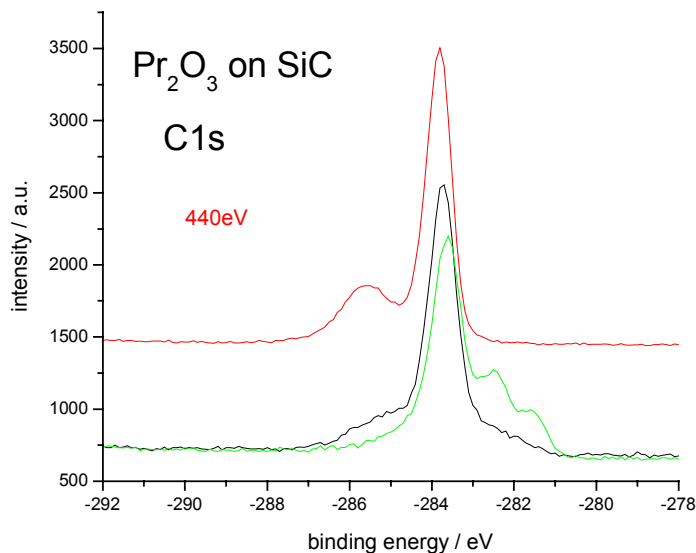


Fig.2:
C1s core level spectra recorded for the bare SiO₂ / SiC surface (top) and after evaporation of 0.5nm and 1nm Pr (bottom). The data are taken at 440eV.

As evident from these data there are considerably changes in the C1s peak positions upon evaporation of Pr. The first evaporation step causes the disappearance of the 285.6eV peak. It also creates unstructured features on the low binding energy side of the main C1s emission which develop into two well separated emissions at 282.6eV and at 281.6eV, respectively. Annealing causes a backward shift of these components and there are significant broadening and contributions after annealing. It should be mentioned that the O1s core levels which are characteristic for SiO₂, Pr₂O₃, and for Silicate /6,7/ also indicate that the SiO₂ in the native oxide is completely removed by the reaction with the Pr. In our experiments we learn that SiO₂ is completely decomposed after annealing the Pr exposed films to form Pr-silicides.

For a first interpretation we rather speak of Si-O, C-O, Pr-O bonds than of phases as the total thickness of our system is in the order of 1nm only. Initially we start with oxygen in bridging position between SiC and C-Si tetraheders /5/. This is a kind of carbonate and we do have Si-O-C-Si bonds which appear at a b.e. of 285eV in our data. Obviously, Pr is able to break the O-C bond as it forms Pr-C and Si-C species as well as Pr-Si species already at RT.

Our data suggest that there exist both, mono- and di-carbides with Pr-Si and Si-Pr-Si bonds because of the different shifts in the core level b.e. of 2eV and 4eV respectively. Similarly, for the carbon we deduce bonds like Si-C-Pr and Pr-C-Pr. Such species can account for the two well separated peaks in the C1s and Si2p emission pattern, respectively.

The Pr- and Si- carbides convert to the Pr-silicates which are more stable and form upon slight annealing. Thereby the silicides are not completely transformed after the annealing to 500°C. We deduce from the broad C1s emission and the remaining shoulder at the Si2p that Pr has attacked the SiC surface irreversible. Future experiments will find out whether this can be avoided by starting with an increased SiO₂ thickness.

We acknowledge the support at the U49/2 beam line of Patrick Hoffmann and the BESSY staff. This work is supported by DFG Schm745/9-1.

Literature

- 1 A.LloydSpetz, et al., Thin Solid Films, 299 1/2 (1997) 183.
- 2 V.V.Afanas'ev, A.Stesmans, F.Chen, S.A.Campbell, R.Smith, Appl.Phys.Lett. 82 (2003) 922.
- 3 D.Schmeißer, R.P.Mikalo, P.Hoffmann, Th.Seyller, L.Ley, A.Lloyd Spetz, Applied Surface Science 184 (2001) 342.
- 4 A.Goryachko J.Paloumpa, G.Beuckert, Y.Burkov, D.Schmeißer, Physica Stat.Solidi, submitted.
- 5 N.Sieber, B.F.Mantel, Th.Seyller, J.Ristein, L.Ley, T.Heller, D.R.Batchelor, D.Schmeißer, Appl.Phys. Letters 78 (2001) 1216.
- 6 D.Schmeißer and H.J.Muessig, J.Phys.Cond.Matter 16 (2004)S153.
- 7 D.Schmeißer, Materials Science in Semiconductor Processing 6 (2003) 59.

In-situ XRR and GIXRD measurements on growing oxide scales on PVD iron

D. Vogel (*), W. Leitenberger, M. Spiegel (*)

Institute of Physics, University of Potsdam, 14469 Potsdam, Germany

(*) MPI für Eisenforschung GmbH, 40237 Düsseldorf, Germany

1. Introduction

The research group 'High Temperature Reactions' at the MPI für Eisenforschung GmbH focuses on the growth kinetics and structure of ultrathin oxide scales that were formed by thermal oxidation of metals. Particularly the morphology and structure of oxides formed at relatively low temperatures (100-300 °C) is unknown. Previous experiments have shown that *in situ* energy-dispersive reflectometry is a useful tool to study temperature dependent oxide scale growth kinetics on a pure iron substrate with a time resolution of 10 min.

To obtain more well-defined experimental conditions with respect to metal thickness and surface roughness, iron- as well as iron/chromium layers were prepared on Si-wafers by PVD. Furthermore, a gas supply unit was installed which enables to exactly set the desired moisture content in the reactive gas atmosphere and to monitor the oxygen content during the experiments by an oxygen sensor. With this equipment it is feasible to oxidise and reduce the sample in a N₂-5%H₂ atmosphere at oxygen partial pressures down to 2E-5 bar and a dew point of -40°C. Hence, the aim of this work was to study the oxidation and reduction kinetics of PVD prepared metal substrates of iron.

2. Results

Figure 1 shows the change of reflectivity of the oxide layer on a 1000nm Fe thin film deposited onto a Si substrate as a function of energy. The sample was heated in air and isothermal spectra were obtained at different temperatures up to 237.5°C. At this temperature, the N₂-5%H₂ forming gas was introduced to reduce the preformed oxide scale. In addition, Figure 2 shows the corresponding GIXRD spectra obtained at the same time.

The spectra can be divided into several distinct areas: Between approx. 3 keV and 11 keV definite peaks are seen in the spectra. During heating up to 237.5°C the position and intensity of the main peaks remains unchanged, while an intensity loss of the minor peak at 11 keV is observed. Upon heating the peak is smearing out more and more. At 237.5°C it has disappeared almost completely. The room temperature spectra shows two broad oscillations, showing the presence of a thin oxide scale. This was also shown by ex-situ XPS-measurements, where some Fe³⁺ was indentified. This layer obviously remains stable during heating as the oscillations do not change with temperature. In addition, periodic oscillations appear in the higher energy range, superimposed with the broad fluctuation. Obviously, a second scale is formed at about 200 °C. Additional GI-XRD spectra were recorded at the same conditions (fig. 2). The intensities obtained have shown, that in a temperature range between 200°C and 212°C especially Fe₃O₄ is formed.

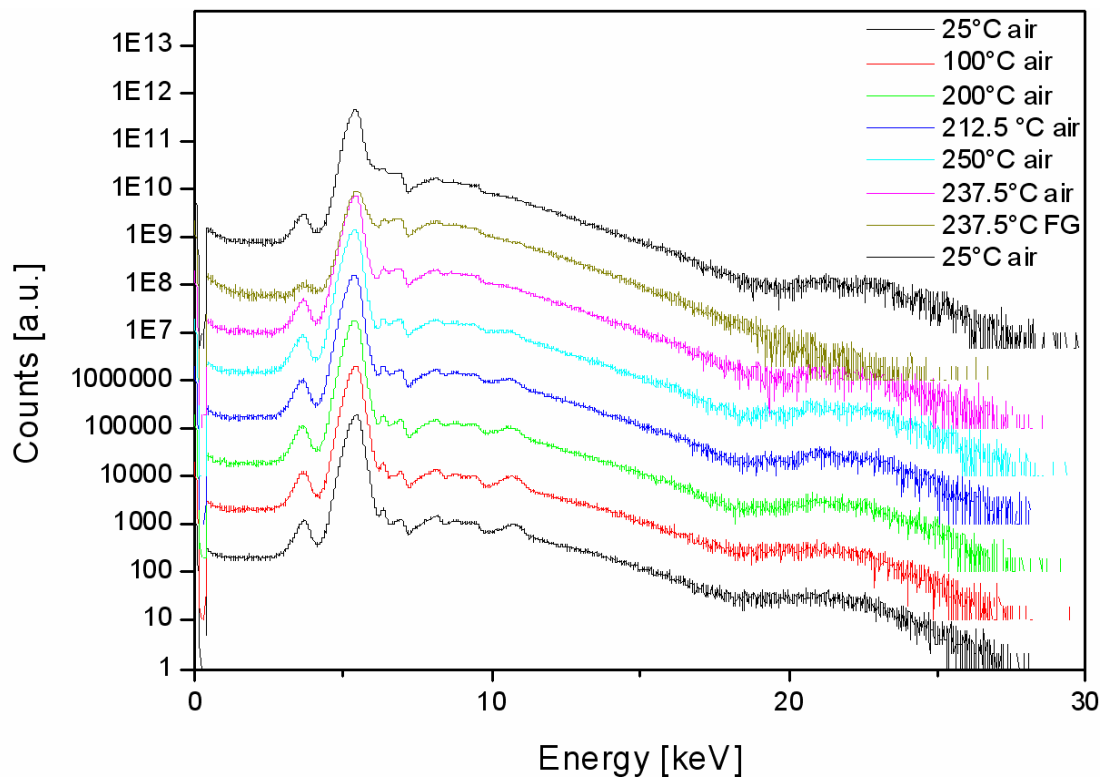


Figure 1: Change of reflectivity of the iron oxide layer evaporated onto PVD in two different atmospheres (air and forming gas, exposure time 15min, DP=-38°C, 27ppm O₂)

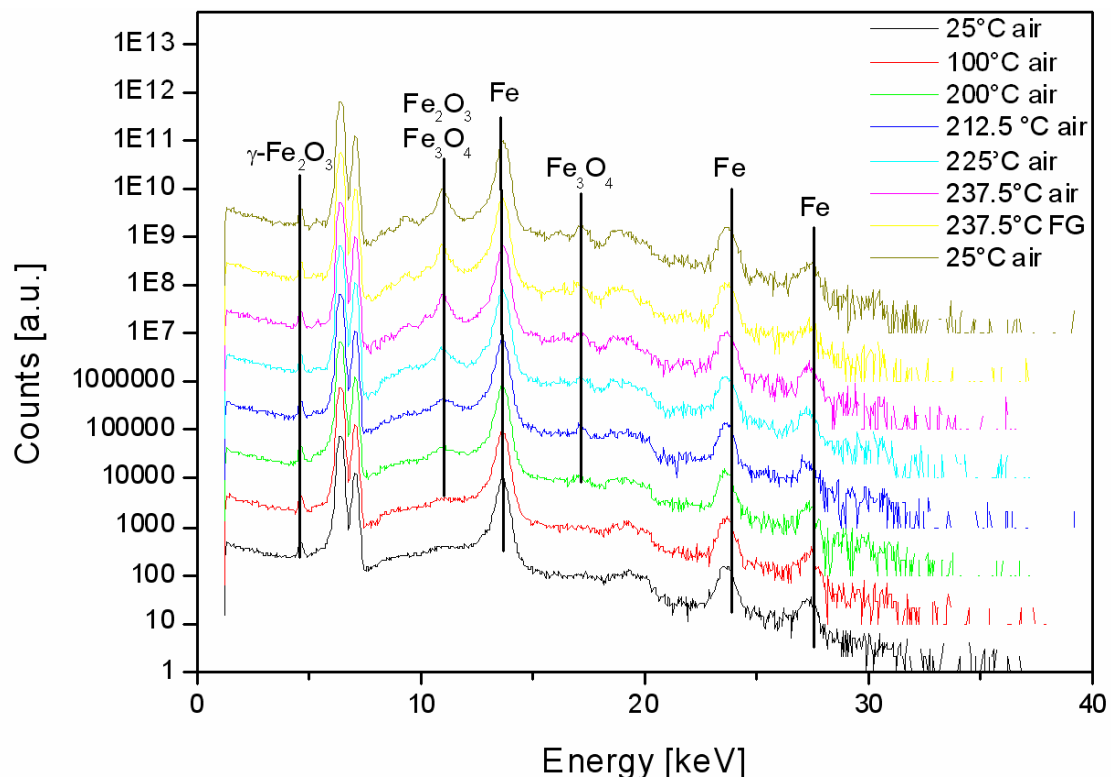


Figure 2: XRD spectra of the oxide layer at increasing temperature

If forming gas (N_2 -5% H_2 , $p_{O_2}=20E-6$, DP=-39°C) is introduced and the sample is flushed at 237.5°C for 5 min the broad peak at 18 keV disappears and significant changes in the intensities of the other peaks are observed. The GIXRD spectra show now significant difference, however, a slight decrease in the Fe_3O_4 intensity is observed. When the sample is subsequently cooled down to room temperature, the peak at 18 keV reappears again and the intensities of the other peaks have again a similar appearance as in the samples heated in air.

3. Conclusions

The experiments have shown that reproducible time resolved in-situ XRR and GIXRD spectra can be obtained from a growing oxide scale during heating of a PVD iron sample. The combination of GIXRD and XRR measurements revealed that, besides the room temperature oxide, a second oxide scale is formed at about 200 °C. Introduction of reducing gas into the reaction chamber results in a significant change in the reflectometry spectra, showing a reaction of the oxide with the reducing gas. The interpretation of the reflectometry spectra is difficult and can not be solved by normal simulation programs available (Berkeley Lab: www-cxro.lbl.gov) and, therefore, information concerning oxide scale thickness and interface roughness could not be obtained. More work is needed to understand the complex nature of the XRR spectra with more defined samples, especially with respect to surface roughness. This can be done by different sputter rates in the PVD process and AFM characterisation before exposure.

PEEM studies of KCN-etched CuInS₂ surfaces

K.Müller, Y.Burkov, D.Schmeißer, Brandenburgische Technische Universität Cottbus, Angewandte Physik-Sensorik, 03013 Cottbus, P.O.Box 101344, Germany

1. Introduction

Photo-emission-electron microscopy (PEEM) is used for studies of CuInS₂ surfaces. CuInS₂ (CIS) is used as polycrystalline absorber layer for thin film solar cells and a characterisation need to be performed in terms of morphological informations, but first of all, of the elemental distribution and of doping inhomogenities at the surface. We demonstrate that the method is capable for such surface studies with high resolution [1]. Excitation with Hg-illumination allows characterisation of doping inhomogenities. The use of synchrotron radiation allows visualisation of inhomogenities at the surface and in between of single grains. In addition, by taking images around the absorption edges of Cu, In or S, we are able to map elemental distributions in high resolution.

Generally, contrast of a PEEM-image is a contrast of electron recovery, bright areas represents regions with high emitting rate of electrons. The rate of electron recovery, the contrast, is influenced by topography (shadowing), work function (different materials or reduced work function at edges, doping level), chemical inhomogenities, resulting in a different recovery rate [1]. The amount of emitted secondary electrons often dominates the spectrum of photoelectrons and in consequence, the contrast of PEEM is strongly influenced by the recovery rate of secondary electrons. For smooth mc-Si wafers, topologic contrast can be excluded and a coincidence of doping level with the rate of emitted secondary electrons was demonstrated [2]. In order to minimise the problem of interpretation, excitation at different photon energies is useful: By taking two images with energies around the absorption edges of the elements searched for and by subtracting the intensities at the related pixels, contrast of this so called difference-image should be a contrast of elemental distribution.

2. Results

For our measurements, we used radiation of a standard high pressure lamp (4.9eV) and synchrotron radiation at the BESSYII-U49/2 beam line. The PEEM optics adapted is an OMICRON FOCUS-IS-PEEM with a CCD-camera and a simulated hemispherical analyser [1]. In Figure 1A we show a PEEM image of a CuInS₂ sample illuminated by Hg-radiation. The sample represents the state of the surface just after etching with KCN. Former XPS and UPS studies show that a stoichiometric surface is reached after a combined annealing- and sputter procedure [3, 4]. In Fig.1A we show a surface consisting of grains in homogeneous distribution of size with an average diameter of about 2µm. In addition, the Hg-image shows a distribution of bright areas, whereas synchrotron images (at 170eV) shows a surface morphology without any significant differences in brightness. This allows us to conclude that this difference in Hg-PEEM intensities should be due to a heterogeneity of work function, or in other words, due to differences of the doping level.

For a better resolution and for difference images we used synchrotron radiation. The PEEM-resolution enables us to analyse areas in the grain size range. The diameter of the recorded images was in the range of 20µm. We recorded difference images at the same position with energies around the absorption edges of Cu, In, S for KCN- etched CIS- samples again (see Figures 1B,1C,1D). The images shows structures of a size of about 2 µm, this is in the range of the poly crystalline grain size. A discussion of for elemental contrast in between single grains can be extracted if we compare the difference images for Cu (Figure 1B), In (Figure 1C), and S (Figure 1D). For Cu, bright and relatively homogeneous areas with dark spots are

recorded. For In and S the situation is reverse, here exactly these spots (in the Cu-image) appear brighter.

In conclusion, at the surface of KCN etched CIS, In-rich sulphides seems to be incorporated in a relatively Cu-rich matrix. Using synchrotron radiation, we are able to study spectromicroscopic information in the sub- μm range, at the surface and in between of single grains. In addition, due to the variable energy of the incident beam, characterisation of elemental distribution is possible.

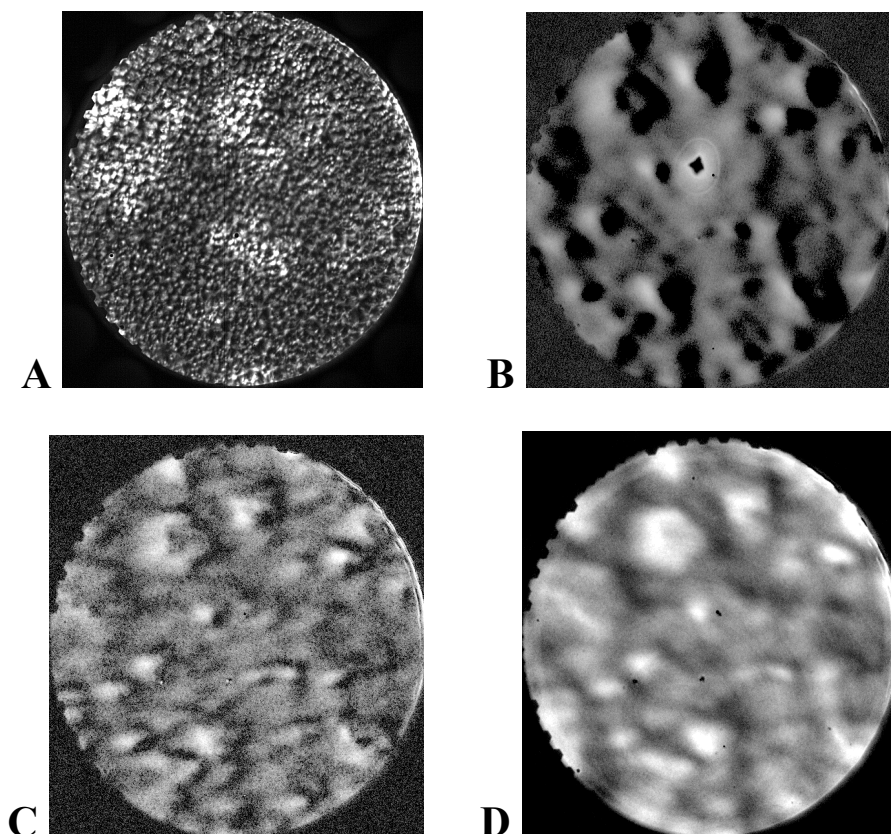


Figure 1: *A: PEEM image, as recorded by Hg-illumination (Diameter 140 μm). B, C, D: Difference-Images taken with synchrotron radiation. A: at the Cu 2p edge (935.3eV, 930eV) B: at the In3d edge (455eV, 430eV), C: at the S2p edge (175eV, 157eV), Diameter: 20 μm . The brightness in the difference images reflects the inhomogeneous elemental distribution.*

3. Acknowledgements

We thank H.J. Lewerenz and R.Scheer (HMI) for helpful discussions and providing CuInS_2 samples. The experimental assistance of P.Hoffmann, G.Beuckert, and of the BESSY staff is acknowledged. This work was supported by DFG under grant no. GEP-SCHM 745/3.

4. References

- [1] K Müller, Y.Burkov, and D.Schmeißer Thin Solid Films 431-432 (2003) 307-311
- [2] P.Hoffmann, R.Mikalo, D.Schmeißer, M.Kittler Phys. Stat. Sol.(b) 215 (1999) 743.
- [3] K.Müller, R.Scheer, Y.Burkov, D.Schmeißer, Thin solid Films 2004, in press.
- [4] K.Müller, P.Hoffmann, S.Milko, Y.Burkov, D.Schmeißer, Thin Solid Films 431-432 (2003) 312.

Solid-state reaction between Pr and SiO₂ studied by photoelectron spectroscopy

G. Lupina*, H.-J. Müssig*, and D. Schmeißer

*IHP, Im Technologiepark 25, D-15236 Frankfurt (Oder), Germany

Angewandte Physik-Sensorik, BTU Cottbus, Postfach 10 13 44, D-03013 Cottbus, Germany

Recently, investigations of high dielectric constant materials to replace silicon dioxide have been focused also on silicates. Praseodymium silicate is thermally stable in direct contact with Si and act more like the preferable SiO₂-Si interface[1-3].

In this work, we have studied by a non-destructive depth profiling using photoelectron spectroscopy at the undulator beam line U49/2-PGM2 the interfacial reactivity of Pr overlayers deposited at room temperature onto thin SiO₂ films on Si(001) substrates. Pr was evaporated from tungsten coil containing a piece of Pr. After Pr deposition, the sample temperature was increased step by step up to 800 °C and kept at each step for 1 min.

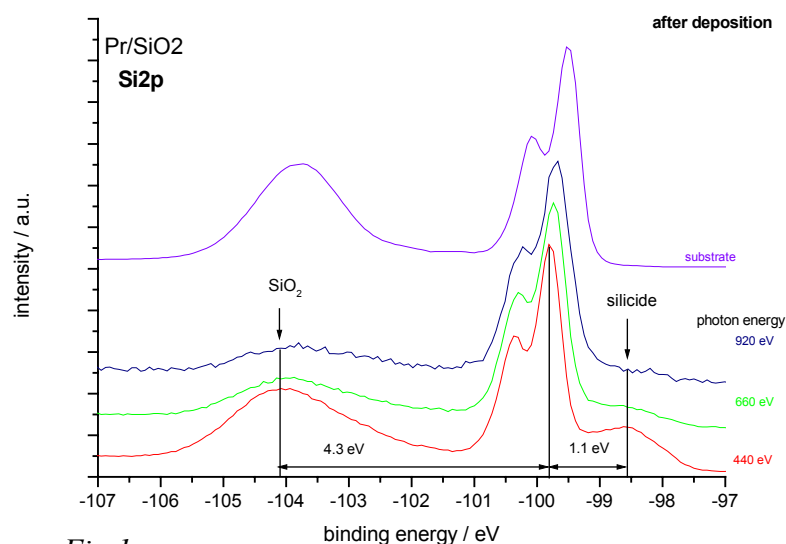


Fig.1.

Si2p core level spectra obtained before (upper curve) and after (lower curves) Pr deposition. Intensities demonstrating SiO₂ and Pr silicide are indicated.

The solid-state reaction between Pr and SiO₂ was monitored by Si2p and O1s core level spectra. In Fig.1 we compare the Si2p emission data obtained before and after Pr deposition and taken at different photon energies ($h\nu = 440\text{eV}$, 660eV , and 920eV). These spectra were measured after deposition of about 1nm Pr onto a 2nm thick SiO₂ film. The formation of Pr silicide is detectable by the peak intensity at -98.6eV . The decrease of the intensity at -104eV indicates that a partial reduction of the SiO₂ film occurs. A weak structure at about

102.3eV can be assigned to Pr silicate. Already at room temperature the chemical reaction between SiO₂ and Pr atoms takes place. Modification of the surface sensitivity by varying the incident photon energy, indicates that the chemical reaction is initiated at the SiO₂-Pr interface. From the most surface sensitive emission ($h\nu = 440\text{eV}$) at 98.6eV we can conclude that Pr silicide must be located on the top of the surface [4]. The composition of the layer stack is significantly altered upon annealing (Fig.2).

After annealing at 300°C a broad emission with a maximum at 102.2eV appears. This peak is clearly separated from the emission of the Si substrate at 99.3eV and is characteristic for Pr silicate. Pr silicide, one of the solid-state reaction products at room temperature, is completely removed after annealing. We should notice that the emission from SiO₂ is very weak. There are no significant changes after a second annealing step at 500°C . Only the silicate peak intensity is clearly increased.

The Pr silicate formation after heat treatment is also suggested by the corresponding O1s core level spectra represented in Fig. 3. The spectrum recorded after Pr deposition shows at least three components with binding energies of 533.4eV, 531.8eV, and 530.3eV which can be assigned to SiO₂, Pr silicate and Pr₂O₃, respectively. These data support our earlier suggestion that SiO₂ is partly reduced at RT by the Pr overlayer forming both Pr silicate and Pr₂O₃.

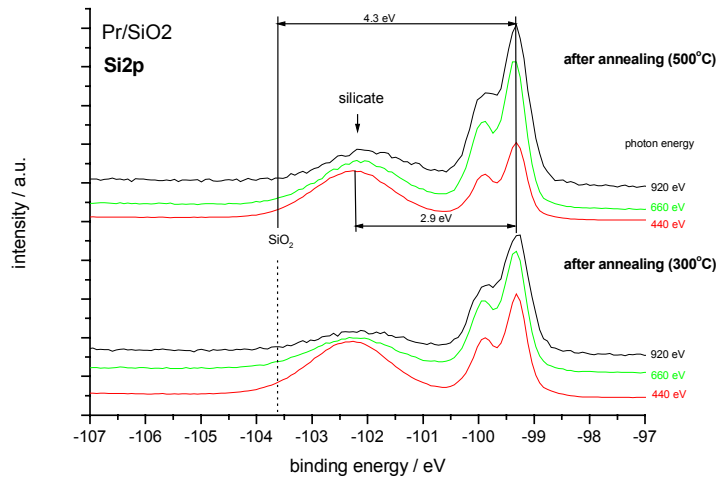


Fig. 2: The emission pattern from Si2p states taken after annealing steps: 300°C (lower curves) and 500°C (upper curves)

completely reduced and is located at the interface to the Si substrate.

In summary, the reaction between SiO₂ and Pr is studied by a non-destructive depth profiling using synchrotron radiation and XPS. About 1nm of Pr was deposited on top of about 2nm thick SiO₂/Si(001) films. The reaction is initiated at the outer SiO₂ surface. At RT a Pr silicide and a Pr oxide are formed and SiO₂ is partially reduced. Annealing at moderate temperatures leads to the formation of a silicate which is stable up to 800°C. The silicide, which should be avoided in interface design, is completely transformed to silicate at elevated temperatures. Such a mechanism can be used to produce a well-defined, insulating silicate layer which can serve as a buffer-layer between a high-k Pr₂O₃ film and the silicon substrate.

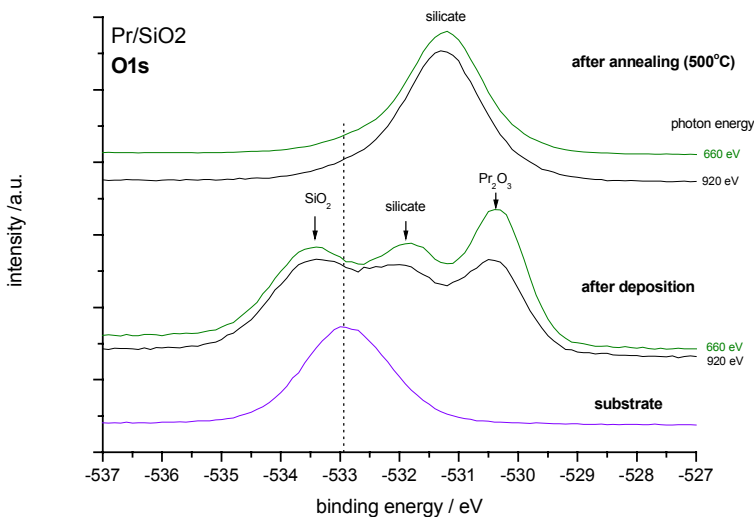


Fig. 3 Comparison of O1s spectra before and after annealing.

- [1] D. Schmeißer, H.-J. Müssig, J. Phys.: Condens. Matter **16** (2004) 153.
- [2] D. Schmeißer, J. Dąbrowski, H.-J. Müssig, Proceedings of the 2003 MRS Spring Meeting (Symposium D), in press.
- [3] D. Schmeißer, H.-J. Müssig, J. Dąbrowski, Appl. Phys. Lett., submitted.
- [4] W. A. Henle, F. P. Netzer, R. Cimino, W. Braun, Surf. Sci. **221** (1989) 131.

Surface magnetization deficit in (GaMn)As ferromagnetic semiconductors

F. Kronast, R. Osyannikov, A. Vollmer, H.A. Dürr, W. Eberhardt, BESSY, Berlin

P. Imperia, D. Schmitz, Hahn-Meitner-Institut, Berlin

G. Schott, K. Brunner, M. Sawicki, L. Molenkamp, University of Würzburg

The existence of a carrier induced ferromagnetic phase in the class of III-V based dilute semiconductors such as (GaMn)As is a phenomenon of large fundamental and technological interest. Despite the existence of various theoretical models the physics underlying these magnetic properties is still under discussion.^{1, 2} This is partially due to the diluted nature of the material. Mn is thought to replace Ga atoms. These Mn impurities are essential for establishing ferromagnetic order. In addition the limited solubility can lead to Mn residing in interstitial sites. The contribution of interstitial Mn to ferromagnetism is still unclear. A very sensitive quantity in this respect is the magnetic moment residing on Mn impurities and the number of Mn atoms contributing to long range ferromagnetic order. Both parameters are accessible to x-ray magnetic circular dichroism (XMCD). Comparing the lineshape of the Mn $L_{2,3}$ x-ray absorption spectrum detected in a total yield measurement to calculations Oldag et al.³ found a Mn d^5 high spin ($5\mu_B$) configuration. However, the measured XMCD asymmetry of 7.9% in samples with 2% Mn concentration was much smaller than expected (59%). The authors deduced that only a small fraction of 13% of the Mn atoms participate in the long range ferromagnetic order. Quite recently a very different result was published by Soo et al.⁴. Using a soft-x-ray fluorescence yield detector they found a exceptional large XMCD asymmetry of 39% in a sample with 3% Mn content. This corresponds to a large fraction of 66% Mn atoms participating in the ferromagnetic ordering. The temperature was in both cases 5K.

We conducted a systematic XMCD study to find out whether this discrepancy can be explained by variation of the Mn concentration throughout the (GaMn)As film and the different probing depth of fluorescence and total yield signal. The experiments were done at the UE 46-PGM beamline using the HMI spectroscopy chamber that allowed simultaneous recording of electron yield, fluorescence and reflectivity while the sample was kept at a constant temperature of 16K. A permanent field of ~ 300 Oe was applied to align the magnetization along the axis of the x-ray beam. We studied a series of ferromagnetic (GaMn)As samples grown by low temperature MBE with a Mn concentration ranging from 1 –6%.

In Fig 1 the electron yield and the fluorescence signal for a sample with 6% Mn content are displayed. Most obvious is the different lineshape of total and fluorescence yield x-ray absorption spectra. The total yield spectrum has a far more pronounced multiplet structure. It's maximum is also shifted by 0.6eV to higher photon energy compared to the total yield spectrum. The lineshape of the electron yield x-ray absorption spectrum is very similar to that reported by Ohldag et al.³ whereas the fluorescence lineshape matches the spectra of Soo et al.⁴. Interestingly the XMCD lineshape is identical for both detection methods although the XMCD asymmetry of $27 \pm 1\%$ in the fluorescence channel is approximately four times larger than the value of $6.7 \pm 1\%$ obtained for electron yield. The same behaviour was observed at all Mn concentrations ranging from 1 - 6% only the size of the asymmetry is reduced in the low concentration samples. This is presumably due to the fact that the temperature in our experiment (16K) was very close to the Curie temperature of the low concentration samples .

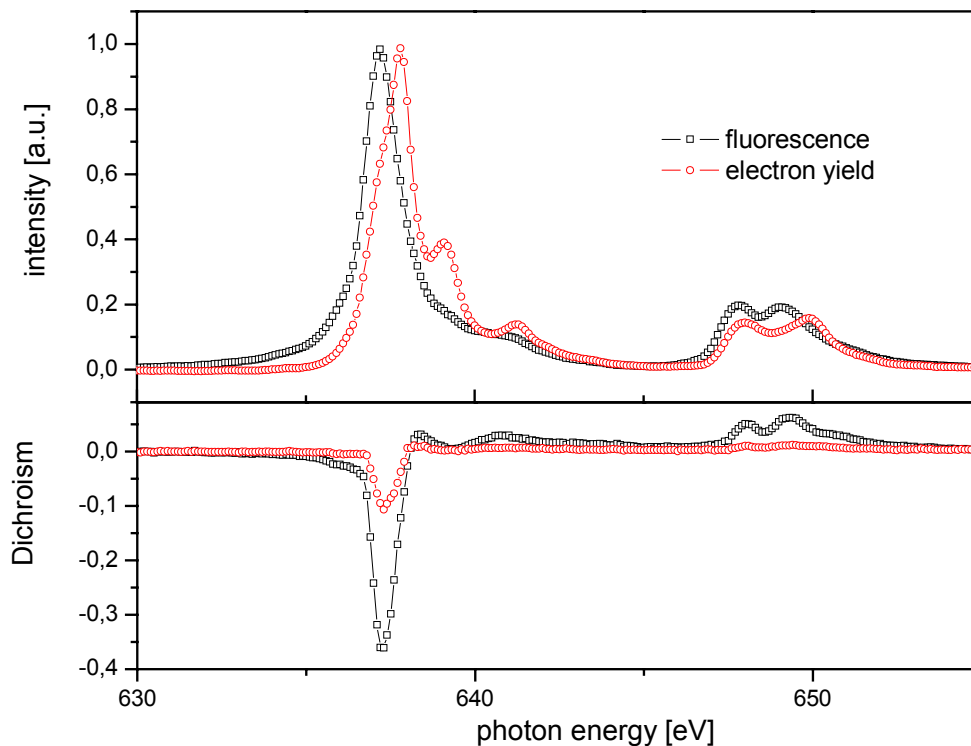


Fig.1 Mn x-ray absorption spectra (upper panel) $(\text{Ga}_{0.94}\text{Mn}_{0.06})\text{As}$ excited by circular polarized x-rays measured simultaneously by total electron yield and fluorescence yield detection at 16K. The angle of incidence was set to 22° . Lower panel shows circular dichroism i.e. the difference between left and right circular light.

The different spectra in fluorescence and electron yield indicates the presence of two Mn species in our samples. Taking into account the larger probing depth of the fluorescence signal we can conclude that the local configuration of the Mn atoms varies strongly from the bulk to the surface. The identical position and similar lineshape of the XMCD suggests that only the Mn species dominant in the volume is ferromagnetic. At the surface the dichroic signal is diminished by the contributions of a second Mn component in a non ferromagnetic Mn configuration possibly due to interstitial Mn impurities. This presence of a ferromagnetic Mn species in the bulk and a non ferromagnetic species at the surface could explain why the two XMCD studies mentioned at the beginning came to a different result. The spectra measured by Ohldag et al. [3] have an identical multiplet structure as our electron yield data and the values of the XMCD asymmetry are in good agreement too. Whereas the spectra of Soo et al. [4] match our fluorescence data and show a similarly enhanced XMCD signal.

References

- ¹ T. Dietl, H. Ohno, F. Matsukura, J. Cibert, and D. Ferrand, *Science* **287**, 1019 (2000)
- ² A. Kaminski, and S. Das Sarma, *PRL*, **88**, 247202 (2002)
- ³ H. Ohldag, V. Solinus, and F.U. Hillebrecht, *APL* **76**, 2928 (2000)
- ⁴ Y.L. Soo, G. Kioseoglou, S. Kim, X. Chen, H. Luo, and Y.H. Kao, *PRB*, **67**, 214401 (2003)

Strong temperature dependence of irradiation effects in thin organic layers

P. Feulner, T. Niedermayer, K. Eberle, R. Schneider, D. Menzel

Physikdepartment E20, Technische Universität München, D-85747 Garching

Y. Tai, M. Zharnikov,

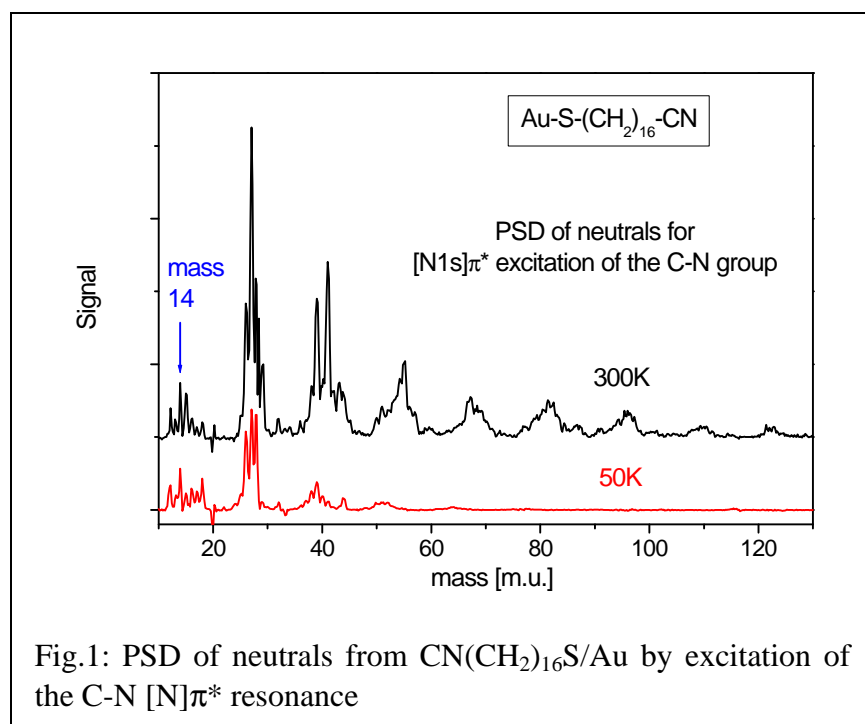
Angewandte Physikalische Chemie, Universität Heidelberg, Im Neuenheimer Feld 253,

D-69120 Heidelberg

E. Schmich, A. Lehner

Walter-Schottky-Institut, Am Coulombwall 3, D-85748 Garching

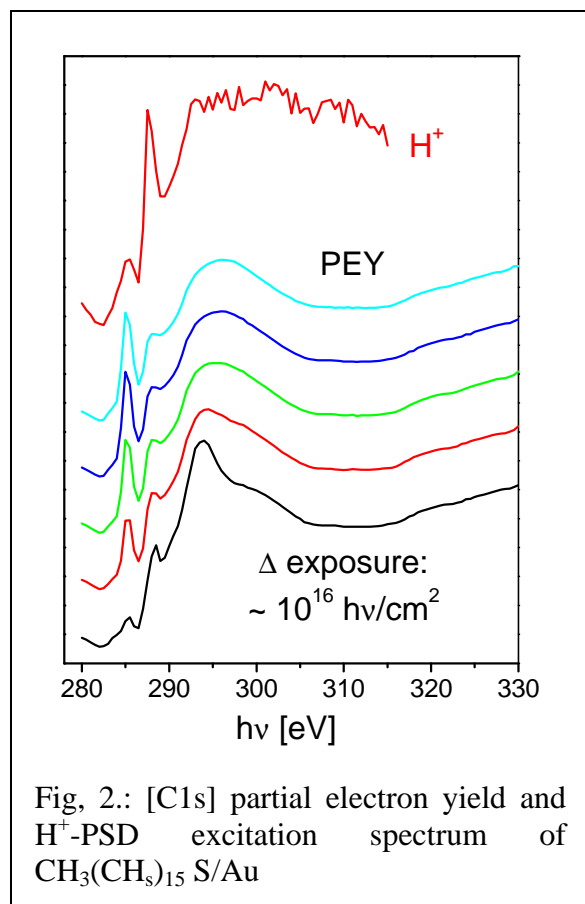
In recent years, thin organic layers on surfaces, and in particular self-assembling monolayers (SAMs) [1] have attracted broad interest due to their rich potential in applications such as, e.g., building blocks for chemical and biological sensors [2], or ultra thin resists for lithography with maximum resolution [3]. With suitably chosen molecules, SAMs can serve as both positive and negative resists, or tailored chemical templates [3]. An important basis required for this selection is the detailed knowledge of the behavior of these layers under ionizing radiation. As yet, related studies have been restricted to ambient temperature (see [4] for a review of previous work) although it is well known from electron and x-ray microscopy that cryogenic conditions can efficiently inhibit structural changes by irradiation. To investigate the influence of cooling on radiation damage of thin organic layers, we have performed a series of XPS, XAS, and photon stimulated desorption (PSD) experiments at the U41-PGM and U49-II-PGM-I beamlines at temperatures between 50K and 300K. Apart from some measurements on organic layers on Si and diamond, most experiments were done on different alkanethiolates on Au [1]. For this type of SAMs, detailed knowledge on radiation effects at ambient temperature exists from previous experiments [4]. In particular, strong selectivity in bond breaking by inner shell excitations has been concluded from PSD of ions [5].



We prepared the SAMs ex-situ by a standard immersion procedure. The measurements were performed in UHV. Fig.1 shows mass spectra of neutrals [6] desorbed from a monolayer of CN(CH₂)₁₆S/Au by π-resonant excitation of the CN group. Comparing the traces at 50K and 300K, two aspects become evident. Firstly, cooling reduces desorption particularly of heavy fragments very efficiently. We obtained similar results for organic layers on Si and

on diamond substrates (not shown). Secondly, selective breaking of the C-N bond yielding PSD of N atoms shows up as a peak at mass 14 in Fig.1. This maximum, however, is much smaller than the competing peaks at larger masses particular for 300K, although the π-reso-

nant excitation cross section is large in XAS. Obviously, selective bond breaking by inner shell excitations is of limited use for molecular tailoring on a microscopic scale if strong competing non-resonant or non-specific reaction channels exist in parallel. We note that heavy fragments desorb almost exclusively as neutrals. Monitoring only the desorption of charged particles, which are a minority species, yields an unrealistic picture of the radiation induced particle losses.



XPS and XAS data as a function of photon dose and sample temperature elucidate the radiation induced changes in our layers in more detail. C1s XAS from alkanethiolates and radiation induced changes have previously been studied in detail [4]. From the pristine SAMs, peaks at 288.3 eV, 294 eV, and ~300 eV are obtained which have been assigned to overlapping Rydberg and $\sigma^*_{\text{C-H}}$ resonances, and two kinds of $[\text{C1s}]\sigma^*_{\text{C-C}}$ states, respectively (Fig.2). XAS monitored by H⁺ PSD projects out the $[\text{C1s}]\sigma^*_{\text{C-H}}$ state (Fig.2). High resolution data (not shown) reveal distinct energy shifts between the Rydberg and the σ^* contributions enabling their untangling. Extended irradiation reduces the $[\text{C1s}]\sigma^*_{\text{C-C}}$ intensity [4], and gives rise to a new maximum at 285.1 eV which previously has been assigned to a π -resonance due to double bonds created by radiation induced de-hydration [4] (Fig. 2). Varying the temperature between 50K and 300K, we found no significant change of the rate of formation for this π -resonant feature.

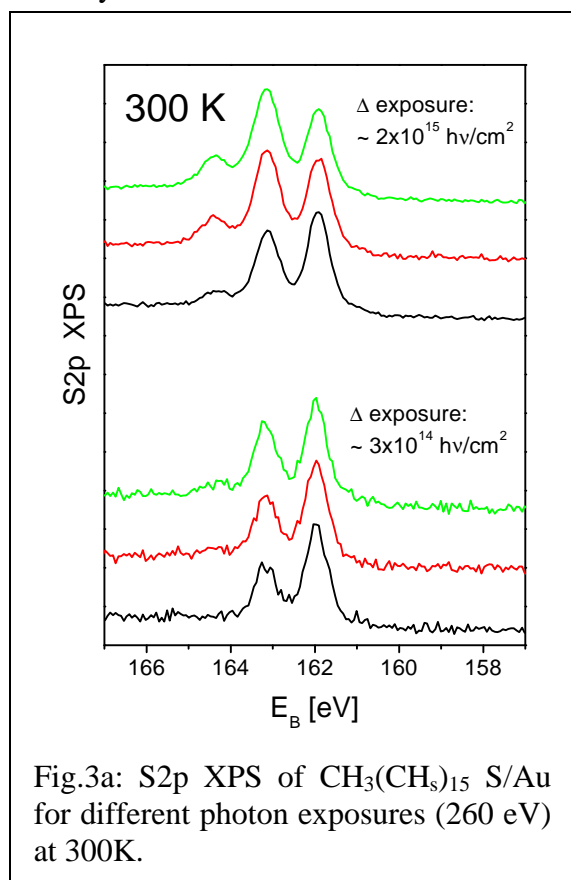
This was totally different for another prominent irradiation effect observed previously in alkanethiolates, namely the breaking of the Au-thiolate bond, and the formation of dialkylsulfide species [4], a process which requires movement of the whole S-(CH₂)_x-R chain. As a fingerprint of this reaction, an additional S2p_{1/2, 3/2} doublet appears in XPS which is blueshifted on the binding energy scale by 1.3 eV relative to the Au-thiolate related doublet of the pristine layer [4]. At 300K, this reaction monitored by its XPS signature proceeds very fast (Fig.3a). At 60K, it is essentially absent (Fig.3b). Only after extended irradiation, formation of atomic sulfur identified by a redshifted S2p doublet shows up as a competing reaction channel.

In summary, we found for the first time strong temperature effects in reactions of thin organic layers induced by ionizing radiation. Reactions connected with the intermolecular movement of large fragments, as PSD at higher masses or the thiolate to dialkylsulfide transformation, are efficiently quenched by cooling. We note that this rate depletion is not due to simply freezing the structure. Heating to 300K after irradiation at 60K had no effect on the XPS results. Obviously, sufficient mobility of the molecules inside the layer is required for the permanent breaking of the Au-S bond. We hope that the evaluation of data for inter-

mediate temperatures which is under way will reveal details of this reaction kinetics. The abstraction of small fragments, and in particular of H atoms leading to the π -resonant feature in Fig.2, is nearly independent of the sample temperature, certainly because of their larger mobility. We think that our results are of considerable importance for all applications where

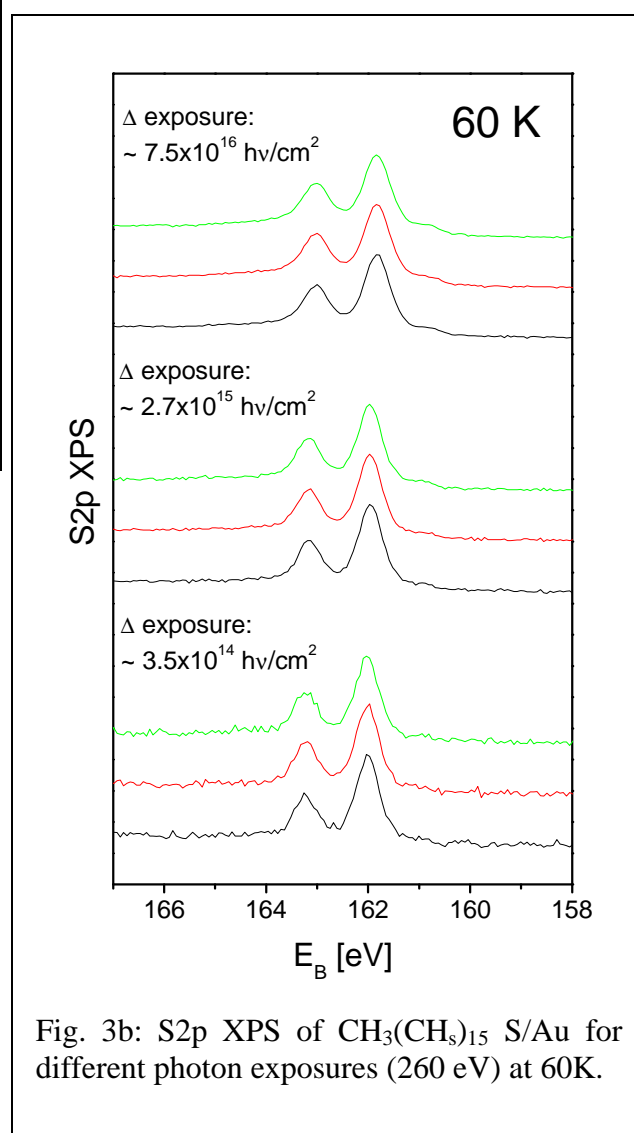
thin organic layers on metal or semiconductor substrates are exposed to radiation by electrons or photons.

We thank the staff of BESSY, in particular W. Braun, C. Jung, H. Pfau and O. Schwarzkopf for help during the experiments. MZ and YT thank M. Grunze for the support of this work.



References:

1. see, e.g., A. Ulman, *Thin Organic Layers* (Academic Press, New York 1991).
2. see, e.g., D.G. Castner and B.D. Ratner, *Surf. Sci.* 500 (2002) 28.
3. see, e.g., A. Götzhäuser et al., *J. Vac. Sci. Technol.* B18 (2000) 3414.
4. M. Zharnikov and M. Grunze, *J. Vac. Sci. Technol.* B20 (2002) 1793, and references therein.
5. S. Wada et al., *Surf. Sci.* 528 (2003) 242.
6. R. Romberg et al., *Surf. Sci.* 451 (2000) 116.



Optical Properties of thin InN layers

C. Cobet¹, M. Rake¹, T. Schmidtling¹, M. Drago¹, W. Richter¹ and N. Esser²

¹ Technische Universität Berlin, Institut für Festkörperphysik, PN 6-1, Hardenbergstrasse 36, 10623 Berlin

² Institut für Spektrochemie und angewandte Spektroskopie, Albert-Einstein-Str. 9, 12489 Berlin

Projekt: **Esser / Richter**

gefördert vom BMBF, Förderkennzeichen: 05SE8KTA3

The group III – Nitrides, including the prominent compound GaN, is one of the most successful and a widely investigated material class for optoelectronic devices in the last decade. The scientific and industrial interest has become even higher in the last two years, since new results on InN have been published. Up to the late 90's, InN properties were measured mostly on sputtered low quality thin films. The fundamental band gap of these samples was assumed to be around 2 eV [1,2]. But new theoretical investigation [3], as well as an experimental progress in the epitaxial growth of smooth layers by MBE [4-6] and MOVPE [7], has shown that the fundamental band gap is more likely located around 0.7 eV [8,9]. Therewith, group III – Nitrides could cover a very wide spectral range from the far ultra violet (AlN) to the near infrared including the whole visible spectral range. However, the reasons for the contradicting results concerning the fundamental band gap are still under discussion.

The determination of the dielectric function is essential for a fundamental understanding of optical and electronic properties, and can also be used as a criterion for crystal quality and surface perfection. We use the VUV-XUV-Ellipsometer setup at BESSY II to measure the dielectric function of InN in the spectral range of the higher interband transitions under UHV conditions. The BESSY ellipsometer is a worldwide unique setup using the particular advantages of a synchrotron light source. Depending on the used beamline, the available spectral range is between 2.5-10.0 eV (3m-NIM-1 beamline) and 6.5-35 eV (TGM 4 beamline).

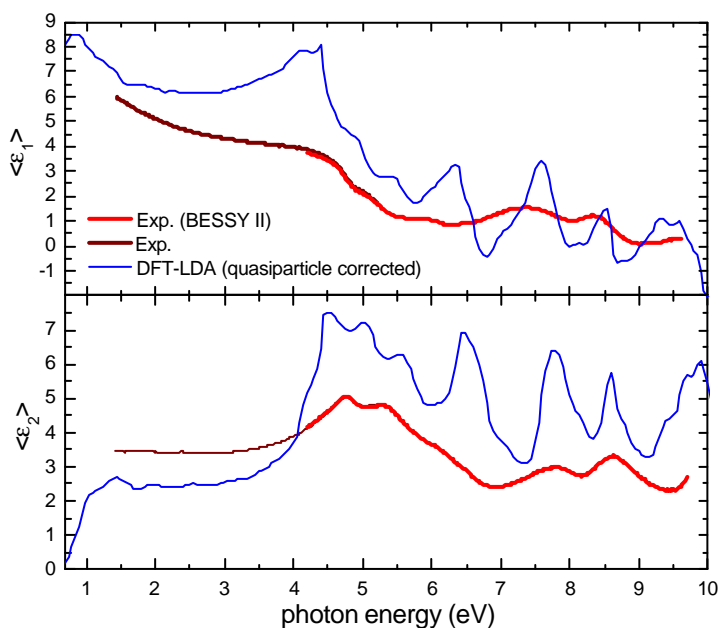


Fig. 1: Real- and Imaginary part of the effective dielectric function of MBE grown wurtzite InN sample (red curves) in comparison with the results of a DFT-LDA calculation.

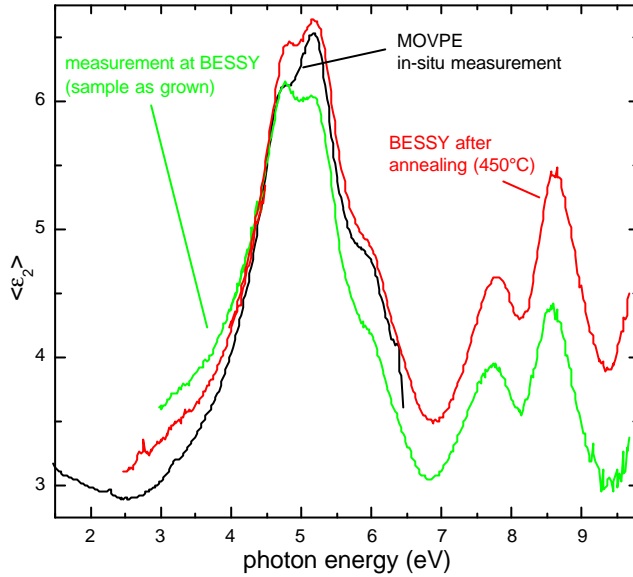


Fig. 2: Imaginary part of the effective dielectric function of MOVPE grown wurtzite InN measured in-situ after growth (black line), as grown with the BESSY ellipsometer (green line) and after annealing in UHV (red line).

In Fig. 1 the $\langle \epsilon_1 \rangle$ and $\langle \epsilon_2 \rangle$ spectra, i.e. the real- and imaginary part of the effective dielectric function, of a MBE grown InN sample are shown in comparison with results of a DFT-LDA calculation [3]. Above 4eV 5 or 6 distinct transition structures dominate both the experimental spectrum as well as the theoretical results, but the energy positions and the relative amplitudes differ considerably. The fundamental band gap of this sample was determined to 0.8 eV at room temperature. Fig. 2 shows the associated $\langle \epsilon_2 \rangle$ results for a MOVPE grown InN sample (green line). The black spectrum in Fig. 2 was measured in-situ in the MOVPE reactor directly after growth under inert nitrogen atmosphere. The comparison of both spectra shows remarkable differences in the over all amplitude and the amplitudes of the two interband transitions at 4.8 and 5.2 eV. We attribute this to a surface degeneration (oxidation) of the InN film while transporting the sample in air. As a first approach to recover the clean InN film, we annealed the sample in the ellipsometer chamber under UHV-conditions at 450°C for 15min. After cooling down to room temperature, the red spectrum shown in Fig.2 was measured. In comparison to the previous spectra the alteration of the sample is noticeably reduced and the relative peak amplitudes at 4.8 and 5.2eV are reversed again. An Auger investigation of the surface before and after this annealing process shows an oxide peak reduction of 75% in comparison to the nitrogen peak. This result supports the suggested surface oxidation. In order to further investigate this “oxidation” effect, we annealed the MOVPE grown InN layer at 400°C in an oxygen enriched atmosphere for one hour in an oven. After this treatment the InN $\langle \epsilon_2 \rangle$ spectrum was strongly damped and the transition related features were almost disappeared (Fig.3 red line). The most prominent difference is the appearance of a strong Fabry-Perot interference up to 3.3 eV indicating a new fundamental band gap of approx. 3.5 eV. These results were first observed with the BESSY ellipsometer providing a very small spot diameter of less than one millimeter on the sample surface. Former investigations of these oxidized layers with a standard ellipsometer gave no insight into these changes in the DF. Probably inhomogeneities occur during annealing in the epitaxial films leading to differently oxidized regimes inhibiting a clear evaluation of the absorption edge.

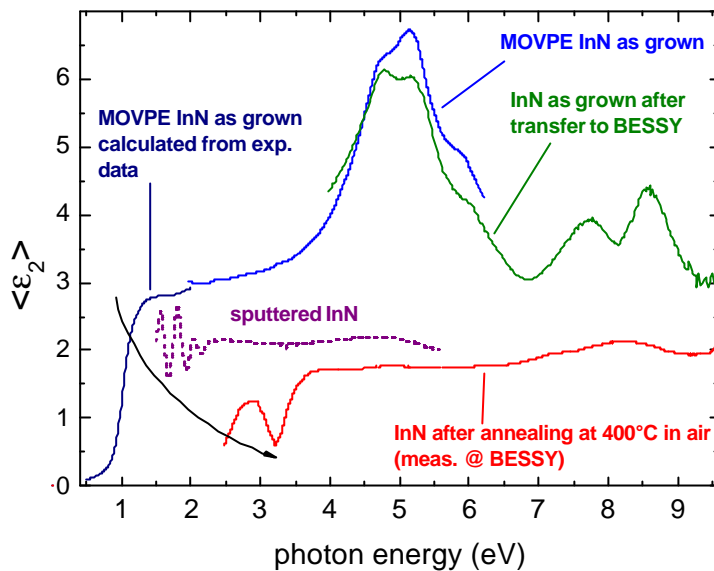


Fig. 3 Imaginary part of the effective dielectric function of MOVPE grown InN as shown in Fig. 2 in comparison with high temperature (400°C) oxygen annealed sample (red line) and an InN layer deposited in a sputtering process (dotted blue line).

In Fig. 3 this spectrum is plotted together with the previously shown as grown InN $\langle \epsilon_2 \rangle$ spectra and the result for a sputtered InN sample. Similar oxidation experiments under more defined conditions in UHV, do not show any oxidation effect in the measured spectra. We used an annealed sample as shown in Fig.2 (red line) and expose the sample for 30-60 min with pure oxygen (partial pressure: 10^{-2} mbar; sample temperatures: 400-200°C). According to this result, a pure oxidation seems to be unlikely and further influences like the effect of water or hydrogen have to be included. However, the comparison of all these results demonstrates the strong influence of the sample degeneration/oxidation or the influence of other contaminations on the optical properties in the range of the interband transitions and especially on the energetic position of the observed optical band gap. Finally these results may explain the wrong assumptions about the fundamental band gap of InN, but further work is needed for a detailed explanation.

Acknowledgements

We gratefully thank the BESSY GmbH and the BESSY coworkers for their help and support. Further on we thank the BMBF for financial funding under 05~KS1KTB/2.

References

- [1] K. Ikuta, Y. Inoue, and O. Takai, *Thin Solid Films* **334**, 49 (1998)
- [2] T.L. Tansley, C.P. Foley, *J. Appl. Phys.* **59**, 3241 (1986)
- [3] F. Bechstedt, J. Furthmüller, M. Ferhat, L. K. Teles, L. M. R. Scolfaro, J. R. Leite, V. Yu. Davydov, O. Ambacher, and R. Goldhahn., *phys. stat. sol. (a)* **195**, 628 (2003)
- [4] T. Inushima, V. V. Mamutin, V.A. Vekshin, S. V. Ivanov, T. Sakon, M. Motokawa, and S. Ohoya, *J. Crystal Growth* **227-228**, 481 (2001)
- [5] V. Yu. Davydov et al., *phys. stat. sol. (b)* **229**, R1 (2002)
- [6] J. Wu et al., *Appl. Phys. Lett.* **80**, 3967 (2002)
- [7] T. Matsuoka, H. Okamoto, M. Nakao, H. Harima, and E. Kurimoto, *Appl. Phys. Lett.* **81**, 1246 (2002)
- [8] Q. Guo, O. Kato, M. Fujisawa and A. Yoshida, *Solid State Commun.* **83**, 721 (1992)
- [9] R. Goldhahn, S. Shokhovets, V. Cimalla, L. Spiess, G. Ecke, O. Ambacher, J. Furthmüller, F. Bechstedt, H. Lu, and W.J. Schaff, *Mat. Res. Soc. Symp. Proc. Vol.* **743**, (2003)

Mapping Disorder-Order Induced Changes To The Fermi Surface Of Cu₃Au

Using A New Toroidal Electron Energy Analyser

A. Tadich^a, L. Broekman^a, J.Riley^a, R.Leckey^a, T. Seyller^b, K.Emtsev^b

^a*School Of Physics, Latrobe University, Bundoora Campus, Victoria 3083, Australia.*

^b*Institut fur Technische Physik II, Universitat Erlangen Nurnberg, 91058 Erlangen, Germany.*

Introduction

Many important physical properties of a crystalline material (transport, optical properties, magnetic properties) depend upon the topology of the Fermi Surface (FS). The binary alloy Cu-Au system displays a variety of unusual phases which, together with other properties such as the incommensurate long-period superlattice in CuAu, are believed by some to be related to FS topology[1, 2]. Knowledge of the FS of these materials is of fundamental importance in explaining these phenomena. With this in mind, an ARUPS investigation of the FS of Cu₃Au was performed.

The polytype Cu₃Au, is probably the best known example of a binary alloy that undergoes an order-disorder transformation. Below the critical temperature $T_c = 663\text{K}$, Cu and Au atoms reside on 2 interpenetrating simple cubic (SC) sublattices, resulting in an L1₂ structure. This is defined as the "ordered" state. Above T_c , the atoms are randomly distributed over the same sites, resulting in a fcc lattice where each lattice point is randomly occupied by atoms of either gold or copper character[3] (Fig 1).

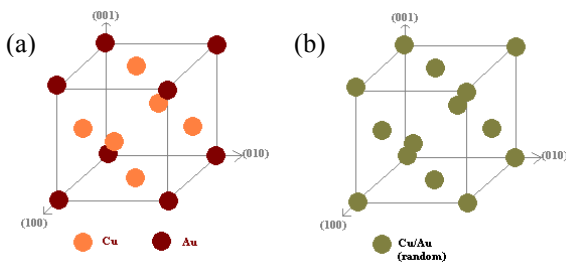


Fig. 1: Ordered (a) and disordered (b) structure conventional unit cells for Cu₃Au.

The changes expected to the electronic structure near the Fermi energy (E_F) are small [4], but due to the introduction of new Brillouin zone boundaries, back folding of the electron energy bands occurs. This results in the expected FS of the ordered structure possessing a more intricate structure, with closely spaced contours.

The Fermi surface of Cu₃Au has been previously studied by photoemission with a previous generation Toroidal analyser[5] in the Constant Initial State mode[6] (CIS) and by dHVA (de Haas Van Alphen)[1] Our earlier investigation used the Azimuthal Scan technique as previously described[7]

Sample Preparation

A Cu₃Au(111) crystal was cleaned by repeated cycles of argon ion bombardment at 500°C until sharp LEED patterns were obtained. The disordered state was obtained by rapidly quenching the crystal to room temperature within a matter of minutes. To obtain the ordered state, a three stage cleaning process was used to grow large ordered domains: (i) annealing at 340C to facilitate large domain growth, (ii) annealing at progressively lower temperatures over 5 days (iii) a light bombardment at 100eV followed by annealing overnight at 200C.

Experimental

Measurements of the bulk Fermi surface of Cu₃Au were performed on beamline TGM-4 using a newly developed Toroidal electron energy analyser as described elsewhere in this yearbook. The

energy resolution of this experiment was limited by the monochromator to approx. 200 meV. The angle resolution of the instrument was $<1^\circ$. Full hemispherical measurements were performed using the azimuthal scan technique at various photon energies, on both the disordered and ordered phases of the crystal. CIS measurements were also performed (not shown) along two high symmetry directions. In short, the azimuthal scan method of mapping the emission hemisphere involves measuring k over all polar angles at fixed E_k (in this case, at the Fermi Level) and stepping the azimuthal angle of the crystal (about the sample normal). Since our analyser accepts all polar angles, the crystal was rotated 180° to map the hemisphere. Azimuthal scan data reflects the distribution in the sample plane of the intersection of the photoemission final state with the bulk Fermi Surface. The Fermi energy was obtained by measuring an Energy Distribution Curve (EDC) over a window containing the Fermi energy, and setting the analyser at that kinetic energy which corresponded to the point of inflexion of the Fermi edge.

Shown below in Fig 2 is the stereographically projected data for photon energies of 41 and 46 eV. The data represents the parallel component of the electron wave-vector, $k_{||}$, measured over all emission angles from the sample surface. High intensity reflects high photocurrent. The photons were incident at 45° to the sample normal.

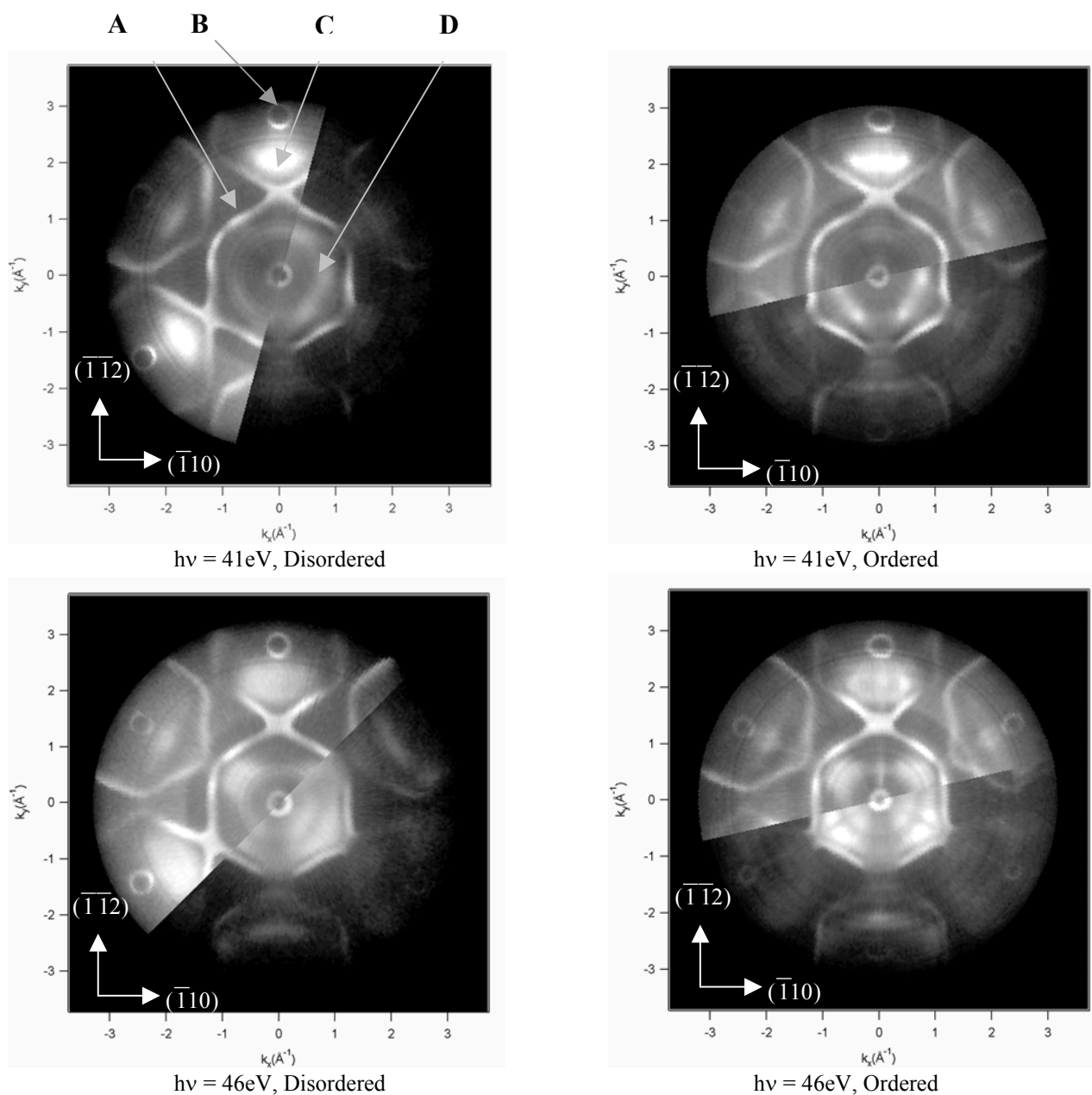


Fig 2: Disordered and Ordered Fermi Surface maps for $\text{Cu}_3\text{Au}(111)$, measured with $h\nu = 41\text{eV}$ and 46eV . Surface crystal directions are shown. Features A,B,C and D are described in the text. Note that the two scans were performed with different sample mounting orientations, hence the difference in the sampling positions of the FS as shown.

The data shows several interesting features. Of note is that the data is highly anti-symmetric about two halves. These halves are generated by the $0 \Rightarrow (+90)$ polar emission angles from the sample (measured relative to the sample normal) and the $0 \Rightarrow (-90)$ sector. This asymmetry has yet to be explained, but most likely has its roots in polarisation dependent matrix element effects. The contour labelled A is the bulk FS cut made at that photon energy. Both 41 and 46eV share this contour, which is sharp and shows intensity over all azimuthal angles. Clearly visible are the well-known "dogs bone" contours, which for disordered Cu_3Au , is in agreement with the expected FS. This contour remains unchanged upon crystal ordering for all photon energies used.

The feature labelled B is the well known surface state of the $\text{Cu}_3\text{Au}(111)$ surface, which disperses up to the Fermi level. This is visible in the central Brillouin zone and in adjacent zones. The origin of Features C and D is presently unknown. For both photon energies shown (and many others not shown) there exists a 3 fold structure in the centre BZ (D), and bright areas within adjacent zones (C). A similar 3-fold structure to feature D has previously been observed in $\text{Ag}(111)$ with less resolution[8], and was attributed to scattering of the final state. As far as we know, there exist no available states at the Fermi level in Cu_3Au at these locations in k_{\parallel} that would lead to these features.

For $h\nu = 41\text{eV}$, feature D is symmetric about the two emission halves. Two bright nodules develop on each wing as the crystal becomes ordered., and feature C elongates in k -space. On the other hand, for $h\nu = 46\text{eV}$, feature D is highly asymmetric. Upon ordering, a narrow "spike" develops along the $(-1-12)$ direction. It is suspected that this feature is part of the new FS of the ordered structure, since along the (111) direction a simple band back folding model has predicted a FS that includes a cube joined along its edges [9]. This would produce a tri-spoke structure if intersected along the (111) direction. For the other emission half, splitting of the intensity of feature D is observed as one goes to the ordered structure. In the outer BZ, the diffuse nature of feature C that was present in the disordered state has given way to a 3 spoke structure, clearly different from the disordered state. Overall, there seems to be a dependence upon the degree of order for these features.

Acknowledgements

The authors wish to thank the staff of BESSY and members of the HMI (Berlin) for invaluable support during beamtime.

1. Deimel, P.P., *Fermi Surface And Electronic Structure Of Ordered Cu_3Au* . Physical Review B., 1981. **24**(10): p. 6197.
2. Kevan, S.D., *Fermi Surface Studies Using Angle Resolved Photoemission*. Journal Of Electron Spectroscopy And Related Phenomena, 1995. **75**: p. 175-186.
3. Robinson, I.K. and P.J. Eng, *Near Surface And Bulk Short Range Order In Cu_3Au* . Physical Review B., 1995. **52**(14): p. 9955-9963.
4. Jordan, R.G. and B. Ginatempo, *Photoemission Form Ordered And Disordered Cu_3Au* . Mat. Res. Soc. Proc., 1991. **186**: p. 193.
5. Leckey, R.C.G. and J.D. Riley, Appl. Surf. Sci., 1985. **22/23**: p. 196.
6. Con Foo, J.A., et al., *The Fermi Surface Dimensions Of Disordered Cu_3Au As Determined By Angle Resolved Photoemission Spectroscopy*. Solid State Communications, 1998. **107**(8): p. 385-390.
7. Con Foo, J.A., et al., *Direct k -space imaging of the Fermi surface of Cu*. Physical Review B., 1995. **53**(15): p. 9649.
8. Greber, T., *Probing the electronic states of band ferromagnets with photoemission*. unknown, 2001.
9. Deimel, P.P., *de Haas-van Alpen measurements Of The Fermi Surface in Ordered Cu_3Au* . Physical Review B., 1982. **25**.

Sexiphenyl orientation on Al(111) and TiO₂(110)

G. Koller, S. Berkebile, G. Tzvetkov and M.G. Ramsey

Institut für Experimentalphysik, Karl-Franzens-Universität Graz, A-8010 Graz, Austria

The interface of active organic films with inorganic substrates is decisive to the function of organic devices. The nature of the interface, on the one hand, is crucial to the charge injection into the film. It can, on the other hand, also influence the growth, morphology and structure of the film, critical to its opto-electronic properties. Here we report investigations into the orientation of sexiphenyl molecules from monolayer coverages to thin films grown on Al(111) and TiO₂(110) substrates. Para-sexiphenyl (6P) is a promising material for light emitting diodes, solar cells and field effect transistors. Aluminium is one of the most commonly used metallic contacts in organic devices, while TiO₂ may be a promising transparent substrate as it can be prepared to be either conducting or electrically insulating. The surfaces were prepared in-situ under UHV and investigated in the MUSTANG end station attached to the Russian-German beamline with the NEXAFS obtained using a partial yield detector.

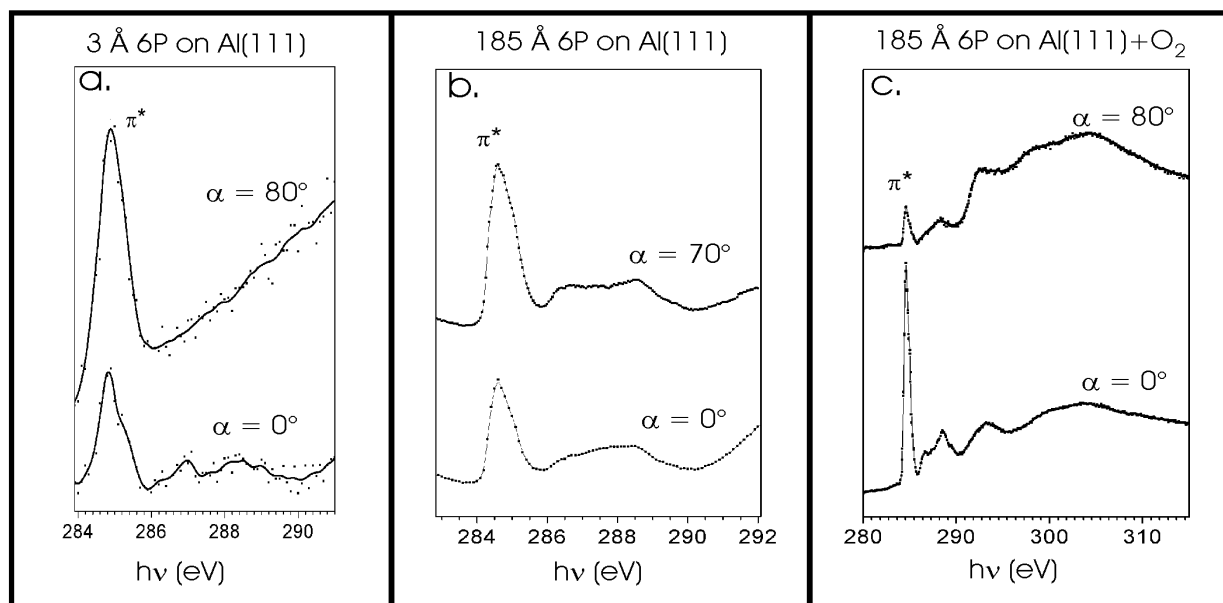


Fig1: *C K-edge NEXAFS of Sexiphenyl adsorption at room temperature on clean and oxygen modified Al(111).*

Figure 1a. displays the C_K edge as a function of incident angle for 3 Å of sexiphenyl on atomically clean Al(111). The π^* features are weak at normal incidence and have maximum intensity at glancing incidence. This suggests that the molecules are lying down with their aromatic rings near, though not perfectly, parallel to the substrate. This supports the orientation proposed from LEED and ARUPS investigations for the ordered, dense 6P monolayer of twisted 6P which saturates at $\sim 4\text{Å}$ [1,2]. For higher exposures (Fig 1b.) the

angular effects weaken consistent with expectations for the 6P(21-3) crystallite orientation we have observed in ex-situ x-ray diffraction studies of thick 6P films grown at RT on Al(111)[3]: such an orientation implies all the molecules are parallel to the surface with the film made up of alternating planes of molecule with aromatic planes on average parallel and tilted with respect to the substrate. If, however the Al surface is exposed to oxygen prior to adsorption of 6P the molecular orientation is changed dramatically. As seen in figure 1c. the maximum in π^* intensity is now observed at normal incidence and is weakest at glancing incidence. This could be due to the molecules in the film being oriented either edge-on or perpendicular to the substrate. The former is however extremely unlikely in such a thick film as 6P packs in an herring bone structure with the molecular planes of neighbouring molecules having a significant angle to each other. We therefore conclude that the molecules are oriented near perpendicular to the substrate. Presumably, the chemisorbed oxygen on the Al substrate has turned off the electrostatic bond of the molecules to the clean Al and they have arranged to present the lowest energy surface of the molecular film. The 6P(001) orientation, which has the molecules oriented at 17° to the surface normal, is the most commonly reported orientation for thick 6P films. Such an orientation is consistent with the results of figure 1c. This suggests that the disordered oxygen passivated Al(111) surface models the relatively ill characterised/dirty substrates that most structural studies of 6P films have been performed upon. Investigations of 6P grown at elevated temperature on clean Al were also undertaken. Contrary to the general conception that the higher mobility thus obtained leads to better order of upright oriented molecules the NEXAFS did not indicate a preferred orientation. The π^* region was also investigated in higher resolution to ascertain whether NEXAFS is sensitive to differences in electronic structure arising from differences in molecular conformation. On clean and oxygen passivated Al(111) the films formed are made up of twisted and planar 6P, respectively. These are clearly distinguishable in valence band photoemission by differences in the energy spread of the occupied π band and the ionisation potential of the HOMO [4]. This difference was not discernable in the π^* features as observed by NEXAFS. The NEXAFS is very similar to that of the monomer and dimer [5](benzene and biphenyl) although on close inspection the major π^* peak is somewhat broader and has an asymmetry suggesting it is made up of two unresolved features. The latter may be due to differences in the initial state carbons, and the inability to observe difference in the π^* band spread is presumably due to the localisation effects of the core hole created in the X-ray absorption process.

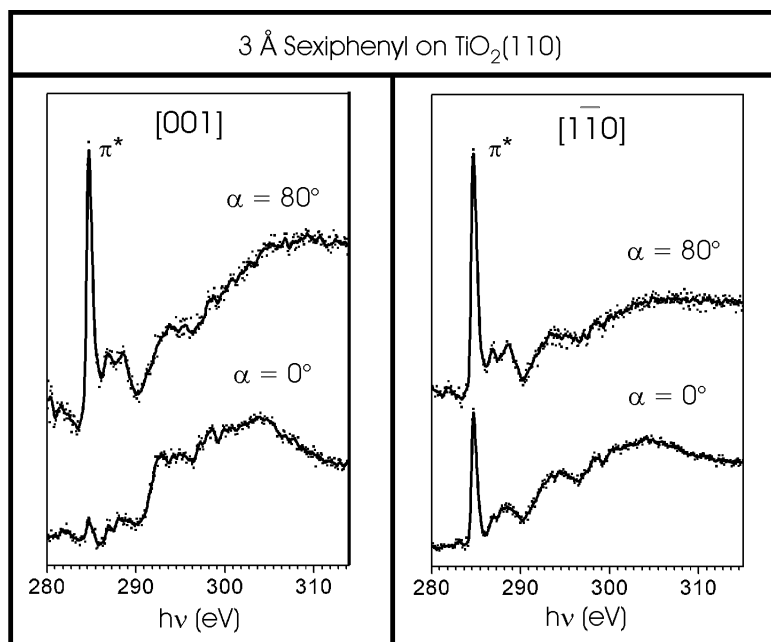


Fig2: C K-edge NEXAFS of 3Å of 6P grown at RT on TiO₂(110) in the [001] and [110] azimuths

On the TiO₂(110) surface sexiphenyl assembles into long rectangular nano-needles oriented parallel to the [110] azimuth, even at submonolayer exposures. For instance at 3Å exposure structures with lengths, widths and heights of the order of 60 x 6 x 0.6 nm are observed in STM with bare substrate between them. Ex-situ AFM of higher coverages has indicated that the dimensions of these structures approximately scale with exposure. NEXAFS with X-ray polarisation parallel to the [001] and [110] azimuthal directions of the substrate clearly reveal the molecular orientation in the self-assembled nano-structures. For 3 Å figure 2. shows that for normal incidence in [001] the π^* feature is all but invisible while in [110] it is quite distinct. In both azimuths the π^* intensity increases with the angle of incidence. The molecules can thus be concluded to be oriented with their molecular axes parallel to the surface and to [001] (i.e. perpendicular to the nano-needles) and their molecular planes at $35 \pm 10^\circ$ with respect to the surface plane. At higher exposures the azimuthal orientation of the molecules is no longer visible in the NEXAFS which shows a behaviour indicative of molecules with their molecular axes perpendicular to the substrate. In AFM of high coverages, along with the 6P-needle structures islands of circular morphology were also observed. The upright molecules observed in the NEXAFS at higher exposures are presumably correlated with these defect areas.

Acknowledgments: This work has been supported by the Austrian Science Foundation and the EU via HPRI-CT-1999-00028. The able assistance of Denis Vyalikh at the RG-BL is also gratefully acknowledged.

References:

1. B. Winter, J. Ivanco, F.P. Netzer, M. G. Ramsey, Thin Solid Films, **433**,269 (2003).
2. B. Winter, J. Ivanco, I. Salzmann, R. Resel, F.P. Netzer, M. G. Ramsey, Langmuir submitted.
3. R. Resel, I. Salzmann, G. Hlawacek, C. Teichert, B. Koppelhuber, B. Winter, J. Krenn, J. Ivanco, M.G. Ramsey, Organic Electronics, 2003 in press.
4. J. Ivanco, B. Winter, F.P. Netzer, and M.G. Ramsey, Adv. Mater.**15**,1812(2003).
5. M.G. Ramsey, F.P. Netzer, D. Steinmüller, D. Steinmüller-Nethl, D.R. Lloyd, J.Chem.Phys. **97**,4489(1992).

Surface core-level shift and impurity charge states of (100) PbTe(X) surface (X=Ge, Ga)

L.V. Yashina^{1*}, V.S. Neudachina¹, E.V. Tikhonov¹, V.I. Shtanov¹, S.L. Molodtsov²,
M. Poyguine³

¹*Department of Chemistry, Moscow State University, Leninskie gory, 119992 Moscow, Russia*

²*Institut für Festkörperphysik, Technische Universität Dresden, D-01062 Dresden, Germany*

³*Institut für Experimentalphysik, Freie Universität Berlin, Arnimallee 14, D-14195 Berlin-Dahlem, Germany*

Lead telluride belongs to narrow-gap semiconductors that are widely applied for infrared detectors production and thermoelectric materials preparation. However, some surface properties of the materials on the base of PbTe remain unexplored. Nowadays X-ray photoelectron spectroscopy with synchrotron radiation (SR XPS) becomes a powerful tool for the investigation of charge states of low-concentration dopants, as well as for detection of the surface spectral features.

Surface core-level shift is defined as the difference in binding energies (BEs) of core-level photoemission signals coming from surface and bulk atoms. It was shown previously for PbS, which may be regarded as PbTe analogue, that the SCLS effect cannot be detected at room temperatures due to high phonon broadening above the Debye temperature [1]. In order to detect the SCLS for the (100) surface of undoped PbTe, a single crystal was *in situ* cleaved in vacuum at room temperature and then cooled down by liquid nitrogen below its Debye temperature. The spectra were recorded with a photoemission spectrometer operating with CLAM 4 (Thermo VG Scientific) analyzer. The base pressure during the experiments was in the low range of 10^{-10} mbars. The Pb 5*d* and Te 4*d* spectra were recorded at 125 and 90 eV photon energies; several spectra were recorded for 125 eV energy in order to check the reproducibility. All the spectra underwent the integral background subtraction and were fitted by the Gaussian-Lorentzian convolutions. The Gaussian part accounts for the experimental resolution and phonon broadening effect, meanwhile the Lorentzian contribution originates from the finite life-time of the photoemission core-hole. The Lorentzian full width at half maximum (FWHM) was fixed for all the spectra during the fitting procedure.

The Pb 5*d* spectra taken at both 125 and 90 eV photon energies were best fitted with one doublet. The obtained value of phonon broadening for these spectra (0.20 ± 0.02 eV) is in accordance with the data for PbS(100) [1]. The observed phonon broadening value shows that

* - corresponding author, e-mail: yashina@inorg.chem.msu.ru

it is quite improper to fit the Pb $5d$ spectra with two doublets, which means that the Pb $5d$ SCLS cannot be detected for PbTe(100) surface at given experimental conditions. These results are similar to those obtained for PbS(100) in [1].

For Te $4d$ spectra the good quality of fitting was reached only when two doublets were used. The two-doublet fitting also gave reasonable phonon broadening values. Comparing the fitted spectra that were obtained at 90 and 125 eV phonon energies, it was found that the relative intensity of the component at lower BEs increases with the decrease of $h\nu$. This means that the component lying at higher BEs corresponds to the bulk, meanwhile that lying at lower BEs is the surface one. The Te $4d$ SCLS value derived from the two-doublet fitting is (-0.26 ± 0.01) eV.

The obtained negative SCLS is in good correlation with the value defined for PbS(100) surface ((-0.30 ± 0.01) eV for natural galena and (-0.27 ± 0.01) eV for synthetic sample [1]). To our opinion, these results confirm the dynamic LEED data for the PbTe(100) surface [2], which show the presence of the differential relaxation. Pb sublattice relaxes inward by 0.22 \AA relative to Te sublattice, which may lead to the compensation of Pb excessive charge density and, hence, the absence of the SCLS effect. At the same time, the excessive charge density of Te atoms is not compensated, as Te atoms cannot move into the bulk due to electrostatic interactions.

The impurity charge states of PbTe(X) (X=Ga, Ge) were investigated by means of SR XPS. The measurements of core-level spectra were carried out using PbTe(Ga) (1.0 mol.% GaTe) and PbTe(Ge) (2.5 mol.% GeTe) polished slices. Both samples underwent Ar^+ sputtering.

In order to determine the gallium charge state in the PbTe matrix, Ga $2p$ and Ga $3d$ spectra were recorded. Unfortunately, the intensity of the first peak was very low, so that we were not able to detect it for the sample under consideration. Ga $3d$ line in the case of PbTe superposes on the Pb $5d$ line, which makes the quantitative peak shape analysis quite complicated. Fig. 1(a) presents the results of (Ga $3d$ +Pb $5d$) peak fitting performed after the integral background subtraction.

The obtained Ga $3d$ FWHM value is in good agreement with other SR XPS measurements of this line, e.g. for GaAs [3]. This fact allows us to suppose that the observed line includes one component only. The position of the energy maximum (19.8 eV) corresponds to $3+$ charge state of gallium. It should be mentioned that a significant scattering of Ga $3d$ BE for different Ga^{3+} -compounds is observed. It varies between 19.1 eV for GaAs reconstructed surface and 21.4 eV for Ga_2O_3 [3]. Our result for Ga $3d$ BE lies between these

values, which corresponds to the difference in the electronegativity of the anions: $O > Te > As$. This result is also in line with different electrophysical properties measurements [4].

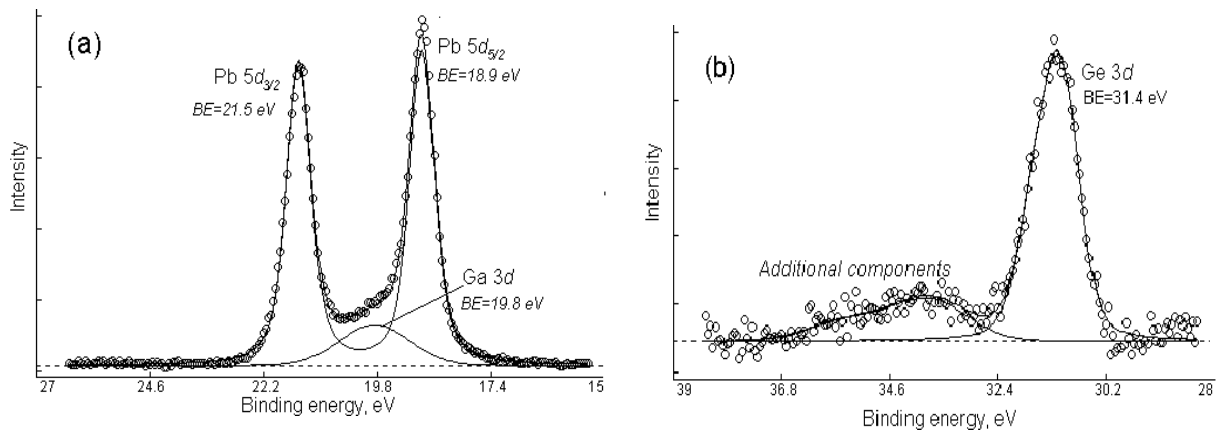


Fig. 1. The results of peak fitting for Ga 3d and Pb 5d superposition measured for PbTe(Ga) surface (a), and Ge 3p line measured for PbTe(Ge) surface (b).

Fig. 1(b) shows the results of peak fitting for Ge 3d spectra. In this case one intensive component is accompanied by at least two additional peaks positioned at higher BEs. This result confirms our previous observation of Ge 2p line in PbTe(Ge) using Al K $_{\alpha}$ source [5]. Germanium reveals donor properties when introduced into PbTe matrix [4], so that part of Ge atoms may exist in +4 oxidation state. However, we cannot directly attribute the observed additional peaks to Ge⁴⁺ state, as they may arise due to Ar sputtering or relaxation losses at the surface.

This work was performed as a part of the bilateral Program „Russian-German Laboratory at BESSY II“.

- [1] J.A. Leiro, K. Laajlehto, M.S. Peltoniemi, M. Torhola, A. Szczerbakow, *Surf. Interface Anal.* **33** (2002) 964.
- [2] A.A. Lazarides, C.B. Duke, A. Paton, A. Kahn, *Phys. Rev. B* **52** (1995) 14895.
- [3] T.S. Lay, K.H. Huang, W.H. Hung, M. Hong, J. Kwo, J.P. Mannaerts, *Solid-State Electron.* **45** (2001) 423-426.
- [4] B.A. Volkov, L.I. Ryabova, D.R. Khokhlov, *Uspekhi Fizicheskikh Nauk* **172** (2002) 875 (in Russian).
- [5] L.V. Yashina, S.P. Kobeleva, V.S. Neudachina, T.B. Shatalova, V.P. Zlomanov, *Surf. Interface Anal.* **34** (2002) 498.

Synchrotron Radiation Photoelectron Spectroscopy of Invar Alloys γ -(Ni_{0.9-x}Fe_x)Mn_{0.1} (x=0.2; x=0.5)

N.V. Lomova¹, E.A. Naymushina¹, I.N. Shabanova¹,
M.V. Poiguine², S.L. Molodtsov³, K. Starke⁴

¹Physical-Technical Institute, UBRAS, 426001, Izhevsk, Russia

²St. Petersburg State University, Institute of Physics, St. Petersburg, 198904, Russia

³Institut f. Oberflaechen-und Mikrostrukturphysik, TU Dresden, 01062 Dresden, Germany

⁴Freie Universitaet Berlin, Fachbereich Physik, Berlin, Germany

Most of the physical properties of the invar alloys are anomalous. These anomalies of physical properties allow to create important materials for the development of current technology. Invar alloys attract attention of many investigators; however the question concerning the reasons of the appearance of invar features has not been solved yet.

The invar alloys Fe₅₀Ni₄₀Mn₁₀ and Fe₂₀Ni₇₀Mn₁₀ with fcc structure were studied using the method of photoelectron spectroscopy with high resolution on the Russian-German Beamline in the synchrotron center BESSY II. The samples were made from high purity components with the use of the method of induction melting in argon atmosphere. Unlike Fe₅₀Ni₄₀Mn₁₀, the Fe₂₀Ni₇₀Mn₁₀ alloy has weakly expressed invar anomalies [1]. In order to study the features of the above alloys, the spectra of 3s core levels and valence bands of the samples were obtained using an electrostatic spectrometer RGLB together with synchrotron irradiation. The surface of the samples was purified mechanically (with a file) in vacuum of the sample preparation chamber. The alloys were investigated both in paramagnetic state (at room temperature, T_{room}) and ferromagnetic state (at T > T_C). The samples were heated in a furnace designed specifically for this purpose.

In Figs 1 and 2, the photoelectron 3s- spectra of d-metals in the Fe₅₀Ni₄₀Mn₁₀ and Fe₂₀Ni₇₀Mn₁₀ are presented. In work [2] we showed that the structure of the multiplet splitting of Me3s spectra indicated the nearest environment of a metal atom. Unlike pure metals, the changes of the parameters of the multiplet splitting of 3s- spectra of d-metals in the alloys gives the information on the tendencies of the changes of atomic magnetic moments and 3d – shell localization [2].

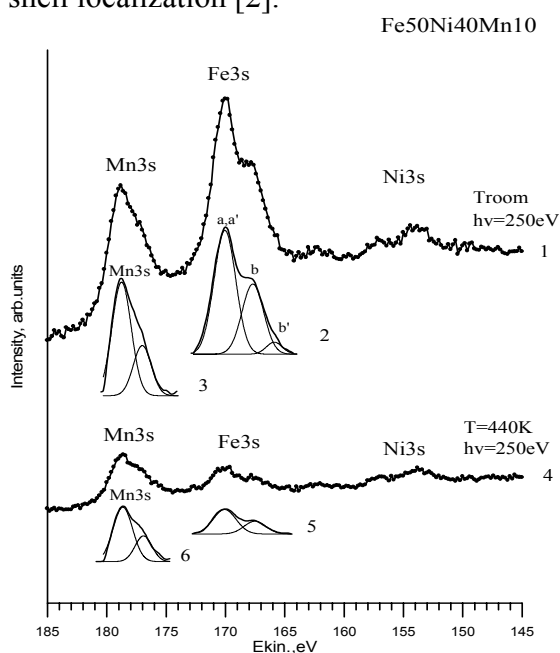


Fig.1 Photoelectron 3s-spectra of Fe₅₀Ni₄₀Mn₁₀ alloy: 1-at T_{room}; 4-at T>T_C; 2,3,5,6- Background subtracted Fe3s and Mn3s spectra and the results of their fitting.

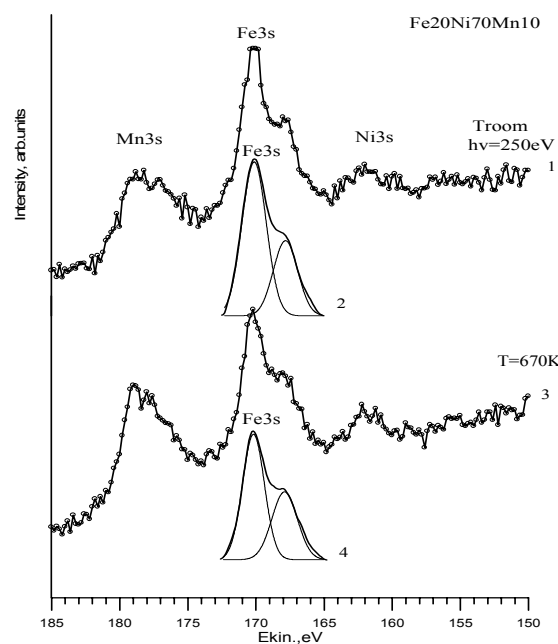


Fig.2 Photoelectron 3s-spectra of Fe₂₀Ni₇₀Mn₁₀ alloy: 1-at T_{room}; 3-at T>T_C; 2, 4 - Background subtracted Fe3s -spectra and the results of their fitting.

The study of the features of the Fe 3s- spectrum structure in the $\text{Fe}_{50}\text{Ni}_{40}\text{Mn}_{10}$ system in the ferromagnetic state (at T_{room}) shows the presence of three maxima in the Fe 3s- spectrum or two multiplet splittings (the maxima a and b – the first multiplet splitting, and a' and b' – the second multiplet splitting) in contrast to the $\text{Fe}_{20}\text{Ni}_{70}\text{Mn}_{10}$ alloy. The main maximum consists of the overlapping of the components from two multiplet splittings. Two multiplet splittings are due to the fact that the iron atoms in invar $\text{Fe}_{50}\text{Ni}_{40}\text{Mn}_{10}$ are in two non-equivalent sites and have different nearest environment and different d- electron density localization, consequently, their magnetic moments are different as well.

In the paramagnetic state the shape of the Fe 3s- spectrum of the $\text{Fe}_{50}\text{Ni}_{40}\text{Mn}_{10}$ alloy changes. Only one multiplet splitting indicating one state of iron atoms is present. According to the hypothesis of Tower and Weiss on the existence of two magnetic states for Fe atoms in invar alloys, one state has a big magnetic moment and effective volume and the other has a small magnetic moment and volume [3]. When the temperature grows, the iron atoms pass from the first state into the second state. As a result, anomalously small heat expansion occurs.

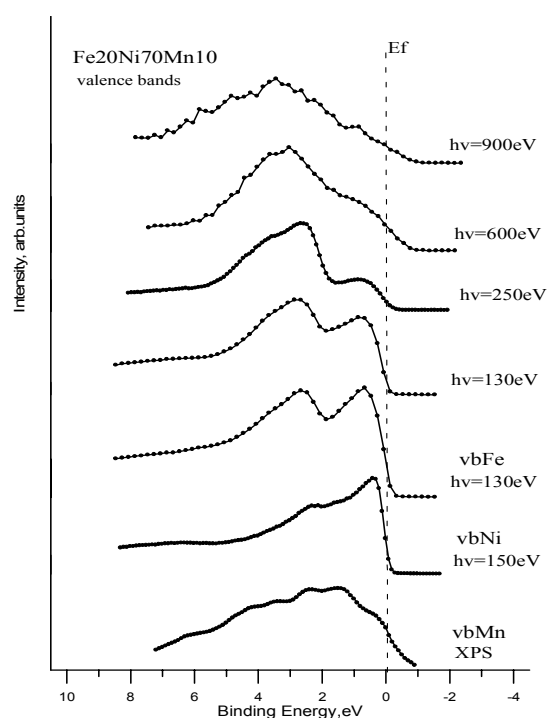


Fig.3. Valence band spectra of metallic Mn, Ni, Fe and $\text{Fe}_{20}\text{Ni}_{70}\text{Mn}_{10}$ alloys at different excitation energies ($h\nu$)

Fig.3 shows the spectra of the valence bands of the $\text{Fe}_{20}\text{Ni}_{70}\text{Mn}_{10}$ alloy at different excitation energies ($h\nu$) and the spectra of the valence bands of the Fe, Ni and Mn pure metals. The spectrum of the valence band of the alloy mainly consists of two maxima (low-energy and high-energy), and the structure of the valence bands of pure Fe, Ni and Mn is found in it. The analysis of the shape and the energy position of the features of the spectra of the alloy valence band shows that with an increase of the excitation energy, the section of photo-ionization of the high-energy part increases and it becomes more intensive than the low-energy part. Besides, its maximum shifts from E_f on the side of large energies. In accordance with [4], an increase of the energy of excitation leads to an increase of the probability of the photo-ionization, e_g components of d-electrons participating in the formation of the covalent bond.

Additional measurements and calculations are planned to verify this supposition. We gratefully acknowledge technical and financial support provided by Russian-German Laboratory and BESSY II staff.

References

- [1] Wassermann E.F., Ferromagnetic Materials, N5, North Holland, 1990, p.239-322.
- [2] Shabanova I.N., Keller N.V., Surf. Interface Anal. 2001, 32, p.114-116
- [3] Chikazumi S., J. Magn. Mater. 1980, 15, p.1130
- [4] Lomaeva S.F., Shabanova I.N., J. of Electron Spectr. 1995, 76, p.619-621

Orientation-controlled organic thin films for field effect transistors: Perylene/ $\text{Al}_2\text{O}_3/\text{NiAl}(111)$

M. B. Casu, A. Schöll, K. R. Bauchspieß, Th. Schmidt, C. Heske, and E. Umbach

Experimentelle Physik II, Universität Würzburg, Am Hubland, D-97074 Würzburg, Germany

Organic electronic devices offer an interesting alternative to inorganic semiconductor electronics due to low-cost deposition methods, flexible substrates, and simple packaging [1, 2]. Thin-film organic field effect transistors (OFETs) are part of this rapidly developing field and a technological challenge of modern solid-state physics [3]. One of the main goals is to prepare organic films with physical and electronic properties comparable to those of organic single crystals [4]. In this work we present the results of a near-edge x-ray absorption fine structure (NEXAFS) investigation of thin perylene films deposited on $\text{Al}_2\text{O}_3/\text{Ni}_3\text{Al}(111)$.

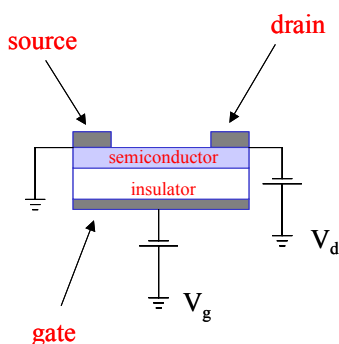


Fig. 1. Conventional geometry of a FET. In an OFET the semiconductor is organic.

Perylene [5, 6] single crystals are characterised by high hole and electron mobilities [7], which makes perylene one of the premier model candidates as OFET layer. However, due to the crystal structure and the overlap of the directional π orbitals, the transport is highly anisotropic and hence depends on the orientation of the molecules. As reported earlier [8], it is possible to tailor the molecular orientation of perylene thin films by using appropriate sets of preparation parameters during growth. Thus, it is possible to grow films in which the chosen molecular orientation is optimal for a charge transport between source and drain. For the geometry as shown in Fig. 1, the charge transport parallel to the surface requires

upright standing molecules, because then the charge propagation through the overlapping π orbitals is optimised [9].

We prepared thin films of perylene by organic molecular beam deposition (OMBD) in-situ using strictly controlled evaporation conditions for well-ordered films. The measurements were performed at the UE52-PGM beamline at BESSY. The $\text{Ni}_3\text{Al}(111)$ single-crystal substrate was oriented with an accuracy better than 0.4° and mechanically polished on one side. It was cleaned in ultra high vacuum (UHV) by means of repeated cycles of Ar-sputtering and subsequent annealing. The oxide preparation was carried out by exposing the single crystal to oxygen at 1050 K (partial pressure 3×10^{-8} mbar). This method gives a thin oxide layer of 5 Å [10], suitable for investigation by standard electron spectroscopies without any charging phenomena. In addition, the thin oxide layer is intended to simulate the electronic and structural properties of thick oxide layers employed in industrially relevant OFETs. Each step of the substrate preparation was checked by using X-ray photoelectron spectroscopy (XPS) and NEXAFS. Perylene was deposited on $\text{Al}_2\text{O}_3/\text{Ni}_3\text{Al}(111)$ with different deposition parameters. The deposition was monitored with a quadrupole mass spectrometer; the nominal thickness was determined by using the attenuation of the XPS substrate signals (Al_{2p} and Ni_{3p}). We carried out NEXAFS measurements in the partial electron yield mode in grazing incidence (70°). In order to investigate the molecular orientation on the surface we took advantage of the dependence of the NEXAFS spectra on the polarisation of the incident radiation [11]. Hence, we measured the spectra by using both in plane (s-pol) and out of plane (p-pol) polarised synchrotron radiation, tuning the polarisation by means of the undulator. Finally the spectra were normalised using the I_0 current and the clean substrate signal [12].

In this work we took three different deposition parameters into account: coverage, substrate temperature, and deposition rate. Figure 2 shows the molecular orientation, as calculated from a large number of C-K NEXAFS spectra, in the growth parameter space. We observe that the perylene molecular plane is parallel to the substrate surface when the film deposition rate and the substrate

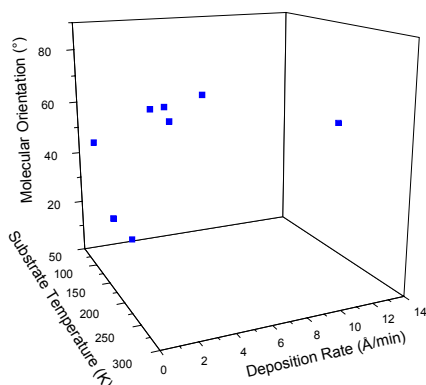


Fig. 2. Summary of the molecular orientation obtained for different sets of growth parameters.

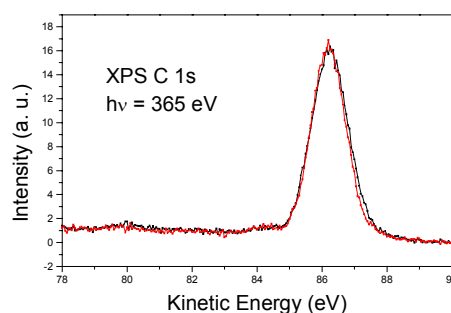


Fig. 3. XPS C 1s spectra of the film with a molecular orientation of 85°: freshly prepared (black curve) and after 16 hours in UHV (red curve).

temperature are low, while the molecules stand upright when a higher substrate temperature and a higher deposition rate are chosen. In the latter case, the highest average molecular orientation was 85°, using a deposition rate of 2nm/min and keeping the substrate at room temperature. Since perylene has a high vapour pressure, we checked the XPS C 1s spectra of the upright molecular orientation film as grown and after 16 hours in UHV (3×10^{-10} mbar). As shown in Figure 3, no major changes occurred in the XPS spectra. Furthermore, as derived from the NEXAFS spectra (not shown), the molecular orientation did not change either.

In conclusion, our NEXAFS investigations show that the growth parameters play a fundamental role in the molecular orientation of thin films of perylene deposited on $\text{Al}_2\text{O}_3/\text{Ni}_3\text{Al}(111)$. A high deposition rate, keeping the substrate at room temperature, causes the molecules to stand upright. Investigating the vacuum stability of these films as a function of time we find that they are relatively stable. The obtained results suggest that perylene thin films grown under these conditions facilitate the charge transport parallel to the substrate, which has to be shown in a separate experiment. We thus find that perylene/ $\text{Al}_2\text{O}_3/\text{Ni}_3\text{Al}(111)$ is an interesting organic/insulator/substrate model system for developing OFETs.

Acknowledgements

The authors would like to thank the BESSY staff for technical support, Stephan Pohl and Helder Marchetto, Fritz-Haber-Institut for the beamline support, and Prof. M. Sokolowski and Michael Voigt, Universität Bonn, Germany, for supplying the highly purified perylene. Financial support by the DFG through the OFET-Schwerpunktprogramm (Um 6/8-1 and Um 6/8-2) and by the BMBF (05KS1WWA/5) is gratefully acknowledged.

References

- [1] C. J. Drury, C. M. J. Mutsaers, C. M. Hart, M. Matters, and D. M. de Leeuw, *Appl. Phys. Lett.* 73 (1998) 108.
- [2] A. Bonfiglio, F. Mameli, and O. Sanna, *Appl. Phys. Lett.* 82 (2003) 3550.
- [3] H. E. Katz, A. J. Lovinger, J. Johnson, C. Kloc, T. Siegrist, W. Li, Y.-Y. Lin, and A. Dodabalapur, *Nature* 404 (2000) 478.
- [4] H. E. Katz and Z. Bao, *J. Phys. Chem. B* 104 (2000) 671.
- [5] A. Camerman and J. Trotter, *Proc. Royal Soc. A* 279 (1963) 129.
- [6] J. Tanaka, *Bull. Chem. Soc. Jpn.* 36 (1963) 1237.
- [7] N. Karl in *Landolt-Börnstein, Group III, Semiconductors, Vol. 17*, Springer, Heidelberg, 2000.
- [8] M. B. Casu, A. Schöll, D. Hübner, Y. Zou, K. R. Bauchspieß, Th. Schmidt, C. Heske, and E. Umbach, *Bessy Annual Report 2002* (2203) 173.
- [9] C. D. Dimitrakopoulos and P. R. L. Malefant, *Adv Mater* 14 (2002) 99.
- [10] A. Rosenhahn, J. Schneider, J. Kandler, C. Becker, and K. Wandelt, *Surf. Sci.* 433-435 (1999) 705.
- [11] J. Stöhr and D. A. Outka, *Phys. Rev. B* 36 (1987) 7891.
- [12] A. Schöll, Y. Zou, Th. Schmidt, R. Fink, and E. Umbach, *J. Electron. Spectrosc.* 129 (2003) 1.

Resonant inelastic X-ray scattering on amorphous silicon monoxide (SiO)

A. Hohl¹, T. Wieder¹, H. Fuess¹, A. Njeh², A. Zimina³, and S. Eisebitt³

¹*Institute for Materials Science, Darmstadt University of Technology, D-64287 Darmstadt, Germany*

²*Science Faculty, Materials Physics Laboratory, Sfax University, TN-3018 Sfax, Tunisia*

³*BESSY GmbH, D-12489 Berlin, Germany*

The atomic structure of the black, coal-like modification of amorphous silicon monoxide (SiO) is a still controversial issue. Recently, we developed a new structural model for this material, the interface clusters mixture model [1]. SiO is a frozen non-equilibrium system of a disproportionation in the initial state. Depending on the production conditions it consists of amorphous silicon dioxide (SiO₂) clusters, nano-sized clusters of amorphous silicon (Si), and a significant amount of sub-oxide (approximately 10 at.%) between the clusters. This sub-oxidic interface is a region with a very high degree of structural and chemical disorder. The morphology of the SiO can be seen as determined by the interface. An increased degree of disproportionation into Si und SiO₂ (i.e. increased cluster sizes) and a decreased volume amount of the interface can be observed for increased annealing temperature.

Here, investigations of the electronic structure of SiO are of particular interest as from the results one can get additional information about atomic structural parameters. The quantitative determination of structural parameters of this material requires methods, which allow to clarify best possible the distribution of sub-oxide states in the interface and the relationship between sample treatment (annealing temperature) and the cluster sizes. Thus, we perform RIXS (resonant inelastic X-ray scattering) measurements as a part of our structural characterization by combination of several experimental methods. RIXS spectroscopy gives information about the occupied states thus complementing results from NEXAFS (near-edge X-ray absorption fine structure) spectroscopy mapping the unoccupied states. And the possibility of partial yield spectroscopy can provide an improved resolution of the different oxidation states of Si atoms in the absorption spectrum.

The present experiments were performed at room temperature at the UE56-1/SGM beamline. We recorded spectra at the Si L-edge (about 100 eV). The estimated energy resolution on the primary side was 20 meV - 100 meV depending on slit and step width. The samples were measured in reflection mode. For RIXS the soft X-ray emission (SXE) spectrometer (Rowland geometry) was used, which had a fixed 90° angle between incident beam and detector. The SXE energy resolution was about 250 meV. For NEXAFS we detected the total fluorescence yield (TFY) by using a photodiode. Additionally, the total electron yield (TEY) was measured by directly detecting the sample current through a wire, which was in conductive contact to the sample. NEXAFS and RIXS data have to be corrected for the energy dependence of the incident beam intensity I_0 by division through a spectrum (for each absorption spectrum) or a constant value (for each SXE spectrum) of monitored I_0 , which was obtained using a gold mesh, that was fixed on the primary side of the sample chamber.

We investigated SiO samples in different modifications. Bulk samples were commercially available Patinal[®] from Merck KGaA (Darmstadt, Germany) which had been produced at approximately 600 °C with a deposition rate of about 200 nm/s in an induction vacuum sintering system. As an example we present here the results for two powder samples, which had been ground from bulk SiO immediately before they were mounted in the sample chamber. This had been done in order to minimize possible aging (oxidation) effects. One sample had been produced from a native (unannealed, amorphous), bulk SiO sample, the other had been produced from a bulk SiO sample, which had been annealed earlier under nitrogen flow for one hour at 1025 °C (thus containing a partly crystallized Si fraction).

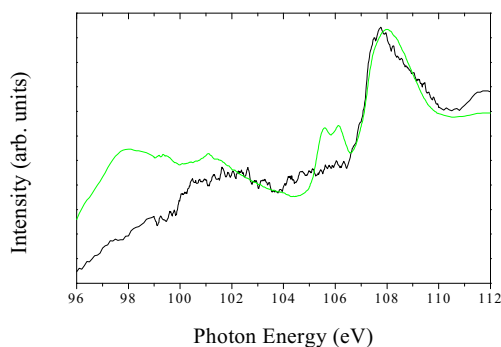


Fig. 1. Si L NEXAFS spectra for a native SiO powder sample, obtained from TFY (black) and TEY (green) detection, normalized to I_0 and scaled to equal intensity for clarity.

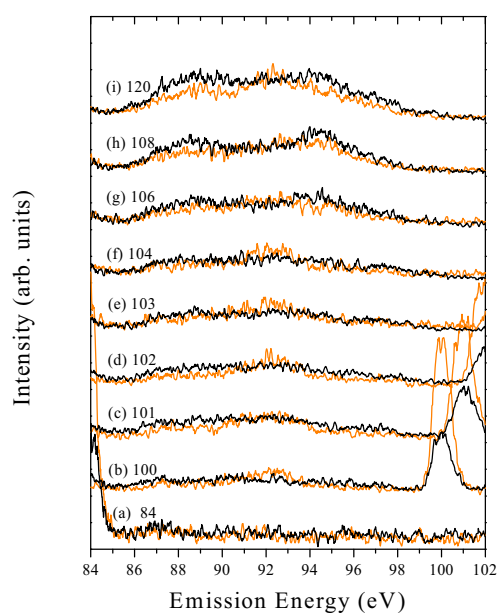


Fig. 2. SXE spectra for a native (black) and for an annealed (orange) SiO powder sample, normalized to equal data acquisition time and to I_0 . The excitation energies (eV) are assigned for the spectra (a) - (i).

The absorption spectra (Fig. 1) exhibit with moderate quality some features which can be attributed to pure silicon (the onset of the Si L-edge just below 100 eV) and to pure silicon dioxide (small features around 106 eV and a large peak at 108 eV), which can be found in the literature [2,3]. The origin of the features is the amount of $\text{Si}(\text{Si}_4)$ and $\text{Si}(\text{O}_4)$ tetrahedral building units in the measured sample volume. The shape of our TFY spectra could sometimes be affected by reflected light from the probed sample volume, which might indicate a large amount of internal interfaces. The TEY spectra could be affected by low conductivity of some samples. Features related to sub-oxide could not be resolved. The study of the influence of reflectivity requires further measurements on specially prepared samples.

Fig. 2 shows a comparison of the SXE spectra for the two powder samples mentioned above. The annealed sample shows a higher intensity of the elastic scattering peak and features more similar to crystalline Si (mainly around 92 eV) [4], whereas the native sample shows more and more SiO_2 -like features (around 89 eV and 95 eV) [5] with increasing excitation energy. As there is no stoichiometric difference between the two samples, the observed behaviour can be related to the different cluster sizes (including partial crystallization in the Si fraction of the annealed sample) and different interface morphology (affecting reflectivity and elastic scattering). The Si clusters in the native sample are probably too small (with sizes below 2 nm) to show electronic properties comparable to bulk Si. To resolve features related to the sub-oxide (interface) in the probed volume further measurements on an array of samples with varying parameters are necessary giving more supporting points for concluded relations.

First measurements of absorption spectra by partial fluorescence yield (PFY) detection with an energy window excluding elastic scattering in the spectrometer showed the possibility to obtain improved spectra from more measuring time. A continuation of the project is planned.

References

- [1] A. Hohl, T. Wieder, P.A. van Aken, T.E. Weirich, G. Denninger, M. Vidal, S. Oswald, C. Deneke, J. Mayer, and H. Fuess, *J. Non-Cryst. Solids* **320** (2003) 255.
- [2] F.C. Brown, R.Z. Bachrach, and M. Skibowski, *Phys. Rev. B* **15** (1977) 4781.
- [3] R. Williams, diploma thesis, Universität, Cologne, 1997.
- [4] K.E. Miyano, D.L. Ederer, T.A. Calcott, W.L. O'Brien, J.J. Jia, L. Zhou, Q.-Y. Dong, Y. Ma, J.C. Woicik, and D.R. Mueller, *Phys. Rev. B* **48** (1993) 1918.
- [5] G. Wiech, H.-O. Feldhütter, and A. Šimůnek, *Phys. Rev. B* **47** (1993) 6981.

Lensless imaging with soft X-rays of 3.1 nm wavelength

M. Lörger, S. Eisebitt, W. Eberhardt
BESSY m.b.H., Albert-Einstein-Str. 15, 12489 Berlin, Germany

J. Lüning, S. Andrews, J. Stöhr
SSRL, Stanford Linear Accelerator Center, 2575 Sand Hill Road, Menlo Park, CA 94025, USA

Introduction

The imaging of objects on a scale of micrometer to nanometer dimensions is an important scientific technique. The resolution is generally limited by the wavelength of the radiation or particles used. Soft X-rays push this limit into the nanometer regime. *Coherent small angle scattering* (SAS) of soft x-rays allows for object reconstruction, holography and dynamic investigations [1]. In this report we demonstrate the feasibility of object reconstruction from the coherent scattering intensity *alone* [2].

Coherent scattering recorded in 2D with spatial oversampling allows for reconstruction of the illuminated object by solving the phase problem [3,4]. This technique is often called "lensless imaging" or "oversampling phasing". The increase in brilliance of synchrotron radiation over the last years has enabled experimental progress in performing lensless imaging at x-ray wavelengths with spatial resolution down to 10 nm as well as tomographic imaging [5,6]. The development of free electron x-ray lasers will provide a coherent photon flux of many orders of magnitude higher than available today [7]. This will increase the spatial resolution and permit time resolved lensless imaging using a single x-ray pulse on a femtosecond time scale.

Generally, it is an experimental problem to collect reliable data in the direction of forward scattering ($\mathbf{q} = 0$), because (a) transmitted intensity is superimposed on the forward scattering and (b) most existing 2D spatially resolving detectors are limited in dynamic range. As a result, experiments are often performed with a central beam stop. Consequently, the low spatial frequency information is lost. As this information is important in order to perform lensless imaging, the long range shape of the object has been obtained in a separate experiment *e.g.* by low resolution optical microscopy in the past [5].

To obtain the object shape and its fine structure from its x-ray scattering intensity *alone* another approach is adopted: It has been proposed by Fienup and it is based on the convolution theorem exploiting the inverse Fourier transform of the diffraction pattern which is also known as PATTERSON map [8]. The PATTERSON map is equal to the autocorrelation of the diffracting object. If a spatially separated reference scatterer exists the autocorrelation becomes easily interpretable. This technique is equivalent to low resolution Fourier transform holography. A recent publication demonstrates how a reference object can be prepared by moving gold balls of 50 nm diameter with a scanning tunneling microscope (STM) [9]. Here we propose the use of a microstructured sample holder that allows to take advantage of the PATTERSON map to obtain low spatial frequency information and enables lensless imaging of a wide variety of samples based on x-ray diffraction data alone.

Experiment

Our test sample is produced in a Au-film of 2 μm thickness. The test object that shall be reconstructed consists of apertures drilled into the opaque Au-film by a focused ion beam (FIB). The apertures are arranged by forming two HI■-patterns (cp. Fig. 1(a)). The letter structure is inside an area of 3.3 $\mu\text{m} \times 3.7 \mu\text{m}$. As reference object a pinhole of 0.8 μm in diameter is drilled into the film at a lateral distance of 5 μm to the letter pattern.

The coherent x-ray diffraction pattern of the sample is measured in transmission geometry at beamline UE56/1-SGM of BESSY II. The wavelength of the x-rays is 3.1 nm with an energy resolution of $E/\Delta E \approx 5000$. The longitudinal coherence length is $\xi_l = \lambda^2/2\Delta\lambda \approx 8 \mu\text{m}$, which is larger than any optical path length difference in our setup. The transverse coherence length is defined by a collimating pinhole of $d = 50 \mu\text{m}$ in diameter located at a distance of $L = 723 \text{ mm}$ upstream of the sample. At the sample site the transverse coherence length is: $\xi_{tr} = \lambda L/\pi d \approx 13 \mu\text{m}$, hence, the sample and the reference hole are illuminated coherently because both lie within an area of 7 $\mu\text{m} \times 9 \mu\text{m}$. The diffraction pattern is recorded by a 2D position sensitive detector with 100 $\mu\text{m} \times 100 \mu\text{m}$ pixel size located 990 mm downstream of the sample.

The resulting coherent diffraction pattern is shown in Fig. 1(b). The vertical and horizontal cross-like diffraction pattern originates from the ■ apertures in the letter pattern. The high-frequency line pattern is due to interference between the reference hole and the letter pattern. This diffraction pattern is important to determine the relative position of both the reference hole and the sample apertures. The white circle indicates the area of specular diffraction that is omitted due to reasons mentioned above. For the 3.1 nm radiation the detector area covers a maximum momentum transfer of $q_{max} \approx 35 \mu\text{m}^{-1}$ corresponding to a spatial resolution of 180 nm.

Reconstruction and Discussion

As a first step for the reconstruction of the letter sample the inverse Fourier transform of its diffraction pattern is calculated and plotted in Fig. 1(c). This PATTERSON map corresponds to the autocorrelation of the object, hence, revealing the rough shape of the letter pattern and its position in real space. In Fig. 1(c) the convolution of the reference hole with the lattern pattern is clearly visible. The autocorrelation shows both the image and the mirrored twin-image of the object. The rough shape of the letters can be observed. The white circle and the black rectangles indicate the shape that is used as input to the reconstruction procedure. Only one of the twin-images is chosen, *i.e.* the obtained solution could also be the mirror image of the actual object.

The reconstruction algorithm performs consecutive Fourier transforms of complex waves between the object plane and the diffraction plane in order to retrieve the fine structure of the test object [3, 4]. The complex waves consists of a magnitude and phase. To force convergence of the algorithm towards the actual object, constraints are applied in real space (object plane) as well as in q -space (diffraction plane). In real space we use the shape obtained from the PATTERSON map (cp. Fig. 1(c)) such that the object is set to zero values *outside* the circle and rectangles, *i.e.* no scattering occurs from the opaque area of the *Au*-film. *Inside* the shape the calculated magnitudes and phases are maintained. In q -space the constraint is simple: the pattern of the magnitude of the complex wave calculated by Fourier transform of the preliminary object must correspond to the measured pattern and is, hence, set to the square root of the measured intensity.

The algorithm starts in q -space with an initial random phase of values between $-\pi$ and π . The error of the object determined by the normalized deviation of the calculated diffraction pattern from the measured diffraction pattern decays during each iteration step. After 180 iterative steps the algorithm converges towards the solution. The reconstructed object is shown in Fig. 1(d). The letters and the reference hole are recovered. The object fine structure is retrieved with a resolution of 180 *nm*, which is given by the maximum momentum transfer in our setup. The small features indicated by white arrows in (a) are not reconstructed because they have characteristic widths of 100 *nm* and are thus below the spatial resolution. The resolution limit is also confirmed by the scan-line in the inset of Fig. 1(d), where each square symbol indicates an image pixel of approximately 90 *nm* size. The same object is recovered for different initial phase sets.

We have demonstrated an image reconstruction based on coherent x-ray scattering. The only input used in addition to the measured diffraction pattern is that the sample is opaque outside the letter pattern and the reference hole. The location and the rough shape of the apertures is determined from experimental data alone due to the presence of the reference hole. The algorithm itself is able to reconstruct the fine structure within the rough shape. The resolution is limited by the recordable maximum momentum transfer. Using a suitable nanostructured sample holder, this approach is applicable to a wide variety of samples.

Acknowledgments

S. A. would like to thank the Fannie and John Hertz Foundation for financial support. The research of J. L. and J. S. is supported by the Office of Basic Energy Sciences of the U.S. Department of Energy.

References

- [1] E. Spiller, "Coherence effects from visible-light to x-rays," *Nuclear Instruments & Methods in Physics Research Section A - Accelerators Spectrometers Detectors and Associated Equipment*, vol. 347, pp. 161–169, 1994.
- [2] S. Eisebitt, M. Lörger, W. Eberhardt, J. Lüning, S. Andrews, and J. Stöhr, "A scalable approach for lensless imaging at x-ray wavelengths," *submitted to APL*, 2004.
- [3] R. Gerchberg and W. Saxton, "A practical algorithm for the determination of phase from image and diffraction plane pictures," *Optik*, vol. 35, no. 2, pp. 237–246, 1972.
- [4] J. R. Fienup, "Reconstruction of an object from modulus of its Fourier-transform," *Optics Letters*, vol. 3, no. 1, pp. 27–29, 1978.
- [5] J. W. Miao, P. Charalambous, J. Kirz, and D. Sayre, "Extending the methodology of x-ray crystallography to allow imaging of micrometer-sized non-crystalline specimens," *Nature*, vol. 400, no. 6742, p. 342, 1999.
- [6] J. Miao, T. Ishikawa, B. Johnson, E. H. Anderson, B. Lai, K. O. Hodgson, "High Resolution 3D X-Ray Diffraction Microscopy," *Physical Review Letters*, vol. 89, no. 8, p. 088303-1, 2002.

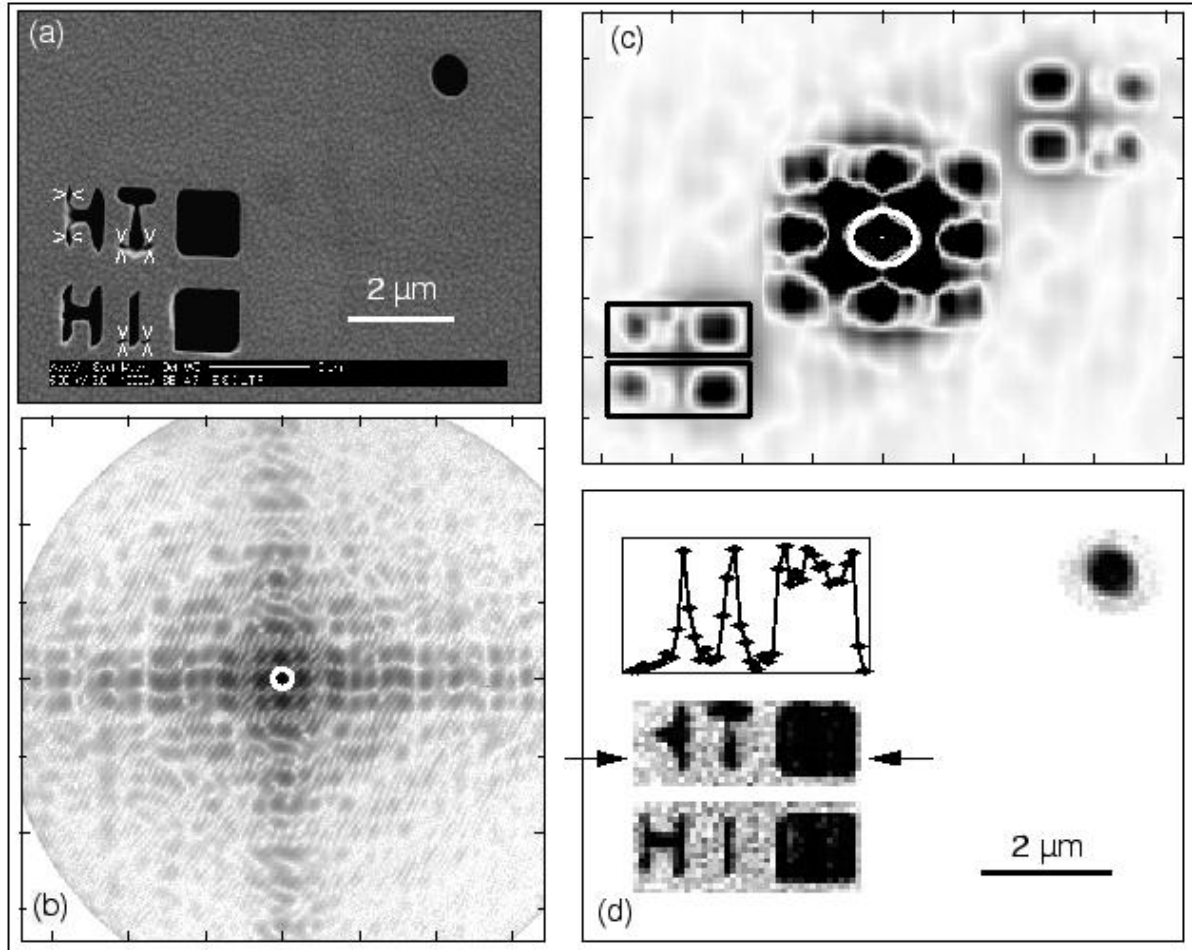


Figure 1: (a) Scanning electron micrograph of the test sample, containing the sample region (letters and squares) and the reference hole. (b) Coherent diffraction pattern on a logarithmic intensity grayscale over a range $-35 \mu\text{m}^{-1} \leq q \leq 35 \mu\text{m}^{-1}$. The central maximum indicated by the white circle was recorded but not used in the data analysis. (c) Patterson map obtained by Fourier transformation of (b) shown over a $\pm 8.5 \mu\text{m}$ horizontal and $\pm 7.5 \mu\text{m}$ vertical range. The regions indicated by two black rectangles and a white circle were chosen for image reconstruction. (d) Image reconstruction based solely on the x-ray diffraction pattern in (b), using the shape regions shown in (c). Inset: scan line between the arrows.

- [7] M. Abo-Bakr, W. Anders, J. Bahrtdt, R. Bakker, W. Eberhardt, B. Faatz, R. Follath, A. Gaupp, M. von Hartrott, E. Jaeschke, D. Krmer, P. Kuske, M. Martin, R. Mller, H. Prange, S. Reiche, W. Sandner, F. Senf, I. Will, G. Wstefeld, "The BESSY FEL project", *Proceedings of the 23. International Free Electron Laser Conference, Darmstadt*, published in NIM A, vol. 483 , p. 470-477, 2002.
- [8] J. Fienup, "Reconstruction of a complex-valued object from the modulus of its fourier transform using a support constraint.," *J. Opt. Soc. Am. A*, vol. 4, no. 1, pp. 118-123, 1987.
- [9] H. He, S. Marchesini, M. Howells, U. Weierstall, H. Chapman, S. Hau-Riege, A. Noy, and J. C. H. Spence, "Inversion of x-ray diffuse scattering to images using prepared objects," *Phys. Rev. B*, vol. 67, p. 174114, 2003.

Decomposition behaviour of as-received and oxidized TiH₂ powder

B. Matijasevic, J. Banhart [Technische Universität Berlin, HMI];
I. Zizak, N. Darowski, G. Schumacher [Hahn-Meitner-Institut Berlin]

Metallic foams are excellent engineering materials offering high energy absorbing capacity, reduced thermal and electrical conductivity, as well as enhanced mechanical and acoustic damping. This material combines properties of cellular materials together with those of metals.

One very promising and proved way to produce metal foams is the powder metallurgy route [1]. A precursor material tablet is produced by compacting a powder mixture including small amounts of blowing agent powder. Heating of this material causes gas release by decomposition of the embedded blowing agent and thus expansion of the material.

The overall aim is to produce a stabilized blowing agent compatible with the foaming process [2]. The alloy composition and the type of the blowing agent have to be chosen such that the blowing agent gives a rise to an ideal foaming behavior with formation of a homogeneous pore size.

Up to now titanium hydride showed up as the best foaming agent to reach homogeneous pore formation and pore size distribution. As there is a mismatch between the melting point of aluminum alloys (500-600°C) and the decomposition temperature of TiH₂ (400°C), the latter should be subjected to thermal and/or oxidizing treatments.

By this an oxide layer is formed on the surface of the titanium hydride powder particles. This layer delays gas release, from the particles, so that during heating up of the powder mixture the blowing first takes place when the melting temperature of the alloy is reached. The thickness and composition of the layer depends of the used temperature and time period of oxidation (Fig.1).

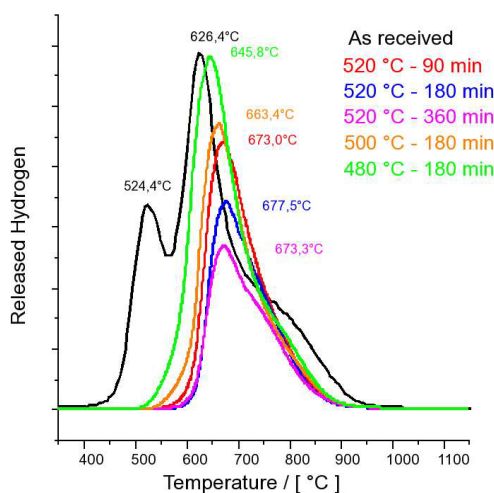


Fig. 2: Release of hydrogen as a function of heat treatment. The decomposition of the TiH₂ is impeded due to the slow diffusion of the hydrogen through the oxide layer.



Fig. 1: TiH₂ oxidized at different conditions. The color of the powder depends on the thickness of the oxygen layer.

By the present investigation the influence of various pre-treatments is investigated on the release of hydrogen from TiH₂. For this purpose the decomposition of TiH₂ powders is examined by differential scanning calorimetry (DSC) [3], thermogravimetric analysis (TGA) [1,4,5] and mass spectrometry (MS, Fig. 2).

Cold pressed TiH₂ powder pre-treated in air at 520°C for 180 minutes was studied in situ during the heating in air. Synchrotron radiation experiments were performed at the KMC2 beamline at BESSY synchrotron radiation source in Berlin. Powder diffractometry was performed using an area sensitive detector, which allowed the acquisition of the whole range of the diffraction pattern simultaneously. The sample was mounted on in the focus of a radiation heater (Fig. 3). The

temperature of the sample was controlled using two thermocouples mounted on the sample stage. In the preliminary experiment the temperature was changed from room temperature up to 700°C with the constant rate of 5K per minute.

The area sensitive detector was covering the angles between 34° and 45°, so it was possible to acquire the most important Bragg reflexes of the different compounds assumed in sample (Fig. 4).

Data evaluation showed that we were able to determine the content of hydrogen in the sample and to follow the evolution of the Ti/H ratio by the help of the phase diagram.

We identified the same titanium oxides, which were measured after the pre-treatment on a laboratory X-ray source (see Fig. 4). After the initial change of the TiO₂ intensity, the amount of oxides stayed constant, while the concentration of hydrogen increased considerably. The structure of titanium-hydride changed on higher temperatures to β-phase because of the loss of hydrogen. After the cooling the sample consisted of mixture of α-Ti and δ-TiH_{1.5}.

These preliminary in situ X-ray diffraction experiments at BESSY are combined with scanning electron microscopy (SEM) and energy dispersive X-ray analysis (EDX) to get some additional information.

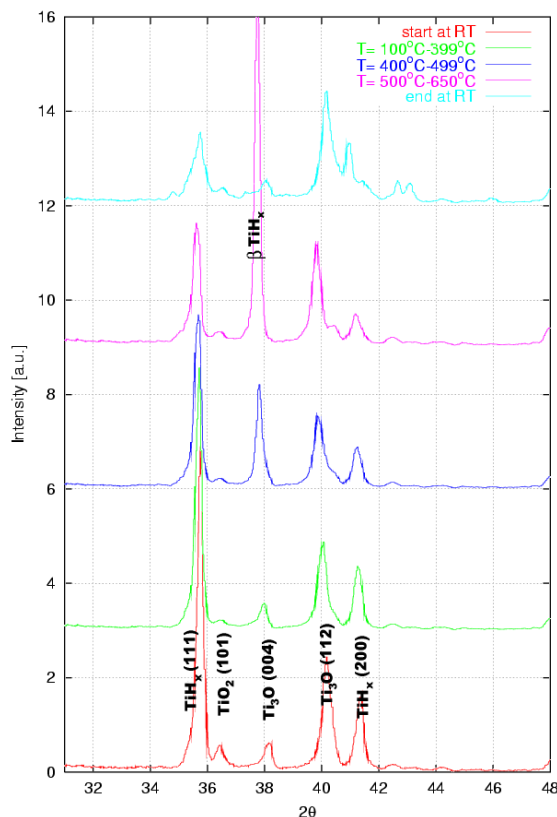


Fig. 4: Alterations of the peak intensities during heating and cooling of a pre-treated powder.

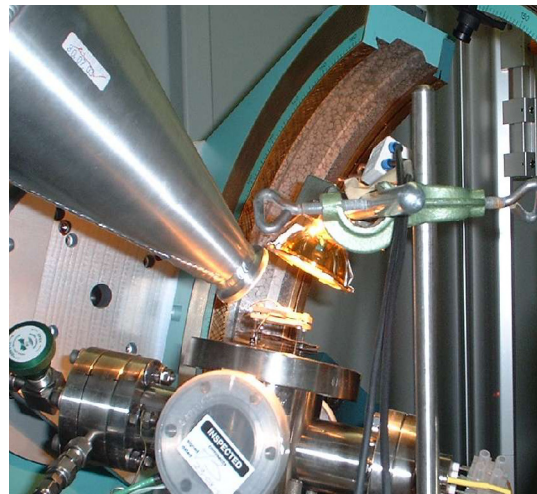


Fig. 3: The sample was mounted on a ceramic holder and irradiated with an halogen lamp. The incoming X-rays entered the figure from right. Scattered photons were reflected through the metal cone on the left side to the detector.

In future we plan to perform the in-situ diffraction experiment during the pre-treatment of the blowing agent at different temperatures and annealing time, as well as the decomposition of the hydride and in the inert atmosphere.

- [1] Baumgärtner F, Duarte I, Banhart, J. *Adv Engn Mat* 2 (2000) 168-74.
- [2] Banhart J. German Patent 100 (15) 2000.
- [3] Centeno-Sánchez RL, Kennedy AR, Wood JV. In: Banhart J, Ashby MF, Fleck NA, editors. *Cellular metals and metal foaming technology*. Bremen: MIT Verlag (2001) 69-76.
- [4] Gergely V, Clyne TW, In: Banhart J, Ashby MF, Fleck NA, editors. *Metal foams and porous metal structures*. Bremen: MIT – Verlag; (1999) 83-89.
- [5] Kresse R. In: Banhart J, Ashby MF, Fleck NA, editors. *Metal foams and porous metal structures*. Bremen: MIT – Verlag; (1999) 109-12.
- [6] Kennedy AR, Lopez VH, *Mater. Sci. Eng. A* 357 (2003) 258-263

Non-destructive depth profile analysis of ultra-thin surface layers

S. Oswald, R. Reiche, M. Zier
Leibniz-Institut für Festkörper- und Werkstoffforschung Dresden,
Postfach 270116, D-01171 Dresden, Germany

At present thin film applications are more and more focused to the thickness range of some nm. Prominent example for this trend is microelectronics where for instance diffusion barrier layers for next circuit generations have to reach a thickness below 10 nm. At such dimensions the properties of the interfaces become more and more of interest and have to be considered in particular. Beside investigations of the segregation process at semiconducting oxides [1] we have focused our interest especially on the investigation of the interface behaviour of diffusion barriers of the type Ta, TaN and TaSiN with Si and SiO₂ substrates by X-ray photoelectron spectroscopy (XPS) [2,3]. XPS is a preferred method for that purpose because beside the element composition also chemical states can be studied.

Depth profiling investigations of the interface chemistry using XPS with sputter depth-profiling are not promising because the chemical information can be destroyed by the energy impact from the sputter ions [4]. An alternative for the study of very thin films is the use of the depth information of the electrons analysed by its limited inelastic mean free path. Thus using angle-resolved XPS (ARXPS) and model calculations it is possible to get information on chemical composition and structure up to some nm in depth. We started investigations in this field at oxide layer structures developing a new modelling procedure [5]. Problems occur due to influences of multiple elastic scattering especially when using surface-near take-off angles for electron analysis. Additionally surface roughness leads to uncertainties when modelling with flat surfaces - the analysis of powders is not meaningful with traditional ARXPS. One alternative to overcome these disadvantages seems to be non-destructive analysis using a variable energy of the X-ray excitation from a synchrotron source. Then the experiment geometry is fixed and the influences due to changes in multiple scattering and roughness are minimised.

For our studies we used the beam-line Ue 52-PGM equipped with a SCIENTA photoelectron analyser. Used analyser conditions were: 75 eV pass energy, 0.8 mm entrance slit. The energy of X-ray radiation was varied from 200 to 1300 eV (3rd and 5th order of undulator). For higher energies, which would be of interest for reaching higher escape depth of the analysed electrons, there was not enough radiation flux available.

For calculations to quantify the measured photoelectron intensities an analyser transmission function determined at the used experimental condition is needed. We obtain this function using the sample current at a sputter cleaned Au foil as X-ray flux reference. The result is shown in Fig. 1 and agrees well with the expectations for such a hemispheric analyser.

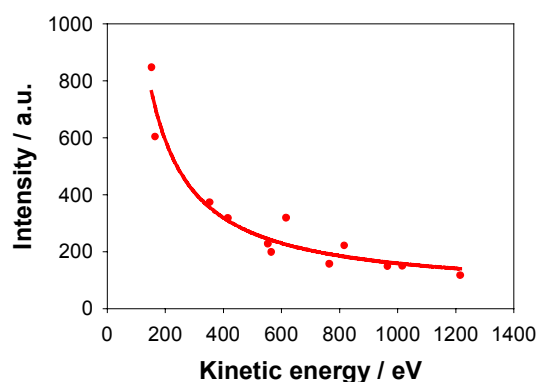


Fig. 1 Transmission curve determined for the SCIENTA analyser.

Based on this result, quantification of the energy dependent measurement was accomplished using the same algorithms as used for ARXPS [5]. The only difference is that instead of the variation of the angles for each measured point a different attenuation length must be used. Also the changes in the photoionisation cross section have to be considered.

Encouraged by previous investigations at doped Sn-oxide material where surface segregation of the dopant was observed [1], the investigation of Sn-doped In-oxides was started. In₂O₃ single crystals and powders doped with approximately 0.9 mol% Sn were annealed under oxygen atmosphere to study their surface behaviour. Fig. 2 shows the results of energy-dependent XPS and model calculations for the single crystal annealed for 20 h at 1000 °C.

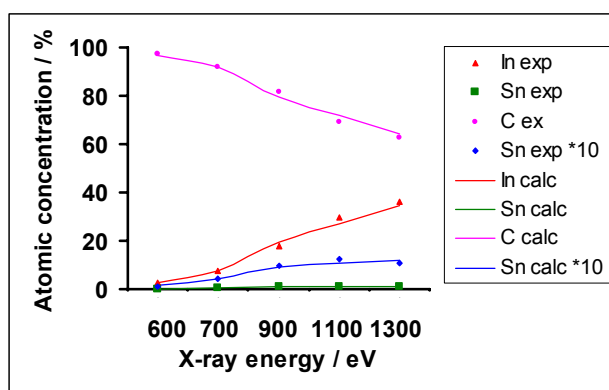


Fig. 2 Comparison of measured (dots) and calculated (lines) data for a Sn-doped in-oxide single crystal shows good satisfying agreement. The very low Sn values (green) are plotted once more scaled with factor 10 (blue) for better view.

As model structure a Sn segregation layer below a C surface contamination was assumed to be on the In₂O₃ material. With this assumption a satisfying approximation can be reached, as can be seen from the comparison of the values from the measurements and the calculated values in Fig. 2. The calculated thickness values were 2.2 nm for the contamination (untypically high for such oxide systems, maybe some residuals from preparation glue) and 0.04 nm for the Sn-oxide segregation layer. This is in accordance with the expectation that such segregation layers are typically in the range below one monolayer. In principle the results of the measurements at the powders (annealed at 700, 900 and 1100 °C) point also to segregation, nevertheless the quantification was not so successful because of obvious discontinuities in the measuring values. This may be caused by some problems in sample preparation (adhesion of the powders on the Au base foils) and with the spherical shape of the particle which should be included into the model for further calculation procedures.

As a second system we investigated different Ta compounds, namely Ta, Ta₅Si₃, TaSi₂ and TaN. Except for the TaSi₂ sample, which was a sputter target, all samples were 100 nm thick films, deposited by magnetron sputtering on a Si substrate. Core-level spectra taken of these samples at a X-ray energy of 900 eV (Fig. 3) show a substantial amount of Ta₂O₅, indicated by the large peak doublet at 26.5 eV (black dashed line), which stems from the native oxide layer grown on all samples in air. Besides this, different peak positions for the bulk material can be clearly seen and therefore distinguished from each other, even the two silicides (pair of blue and black dashed line) which show a very small difference in the Ta4f binding energy but a distinct one to Ta-nitride (green dashed line) and metallic Ta (red dashed line). It is obvious that for all these compounds the spectra are dominated by a thick natural oxide (and an additional contamination layer - not discussed here). Thus studies of the interface of a Ta-X to a substrate below seems to be only meaningful if in situ preparation of the films can be done.

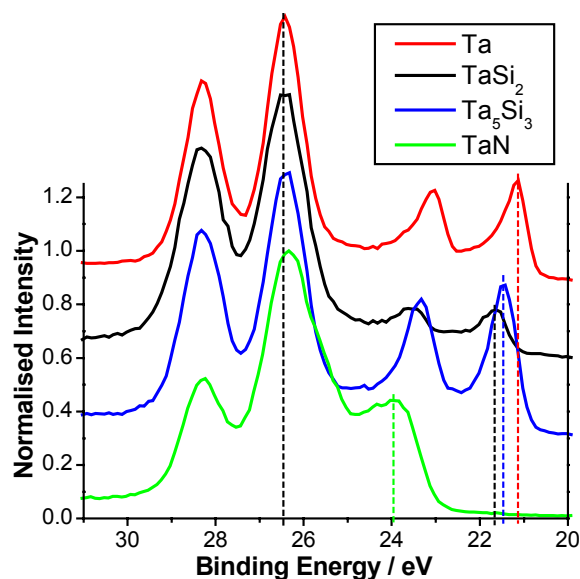


Fig. 3 Ta4f spectra of different Ta compounds, measured at 900eV excitation energy. Different chemical states are observed: Metal, two silicide components, nitride and oxide (dashed lines from right).

Ta was also used as a 2 nm thick cap layer in a Ta/Al(oxide)/Co trilayer structure to protect the oxidation state of the AlO_x barrier oxidised by oxygen plasma exposure. However, this oxide barrier could not be characterised, because within the whole energy range of X-ray radiation we were not able to measure any Al signal. The Ta cap layer was partly oxidised, as expected already from the results shown above, on top of it we found a submonolayer H₂O film beside the general CH_x contamination.

It was demonstrated that the method of non-destructive depth profile analysis using energy-dependent XPS measurements can be used for thin overlayer structures like segregation layers at oxides with low contamination. For metallic systems, as shown here for the very reactive Ta, effects of contamination and oxidation are dominating. Here a way out can be in situ preparation or the use of X-ray radiation of higher energy (higher electron mean free path).

Acknowledgement

The work was partly funded by the SMWA Saxony (Proj. 6918/1083).

References:

- [1] S. Oswald, G. Behr, D. Dobler, J. Werner, K. Wetzig, W. Arabczyk, *Anal. and Bioanalyt. Chem.* 378 (2004) 411 - 415.
- [2] M. Zier, S. Oswald, R. Reiche, K. Wetzig, *Anal. and Bioanalyt. Chem.* 375(2003) 902-905.
- [3] M. Zier, S. Oswald, R. Reiche, M. Kozłowska, K. Wetzig, *J. Elect. Spect. Rel. Phen.* 2004, submitted.
- [4] S. Oswald, R. Reiche, *Appl. Surf. Sci.* 179(2001)1-4, 307-315.
- [5] M. Kozłowska, R. Reiche, S. Oswald, H. Vinzelberg, R. Hübner, K. Wetzig, *Surf. Interface Anal.* 2004, submitted.

Investigations of Ge concentration micro-variations in a $\text{Si}_{1-x}\text{Ge}_x$ crystal.

A. Erko*, N.V. Abrosimov**

**Berliner Elektronenspeicherring-Gesellschaft für Synchrotronstrahlung (BESSY) m.b.H.*
Albert Einstein Str. 12489 Berlin, Germany

***Institut für Kristallzüchtung, Max-Born-Str. 2, 12489 Berlin, Germany*

Abstract

Ge concentration variations along the crystal growth axis in $\text{Si}_{1-x}\text{Ge}_x$ single crystals are investigated on a micrometer scale. The KMC-2 beamline with capillary microfocusing optics have been used to perform experiments with a spatial resolution on the order of $5\ \mu\text{m}$ at the photon energy of 11.4 keV. As a result the dependence of the oscillation amplitude and average Ge concentration is shown.

Introduction

Laterally-graded crystals are going to be used as neutron-, γ -ray and X-ray monochromators when spectral intensity of a divergent beam to be enhanced as compared to spectral intensities available from perfect periodic crystals. They are also of importance with the development of new high brilliance X-ray synchrotron radiation sources, optimized for very small source size of some μm and beam divergence less than $5 \cdot 10^{-4}$ radian. Accordingly the crystallographic quality and homogeneity of the crystals are very important for the practical applications.

The growth of the $\text{Si}_{1-x}\text{Ge}_x$ gradient crystals is based on one of the peculiarities of Czochralski technique: the segregation of the second component results the non-uniform distribution of Ge along the crystal length takes place during the growth. Since the distribution coefficient k of Ge in Si is less than 1, the Ge content increases with rise of crystal length and solidified fraction $g = M_{\text{cr}}/M_0$, where M_{cr} - is the mass of the crystal and M_0 - the mass of the charge, $0 < g < 1$. Such crystals were also grown using automatic diameter control.

The main structural defects of the $\text{Si}_{1-x}\text{Ge}_x$ single crystals grown from the melt are dislocations and rotational striation. The density of dislocations are generally increases with the Ge content and is less than $100\ \text{cm}^{-2}$ in crystals with Ge concentrations of up to 3 at. %. The striations are caused by the fluctuation of the microscopic growth rate on the solid-liquid interface because of the thermal asymmetry of the heating zone, melt convection and fluctuations of mechanical movements. In $\text{Si}_{1-x}\text{Ge}_x$ single crystals the Ge-rich striations lead to a local fluctuation of the lattice parameters and cause the generation of the misfit dislocations within striations limiting the application fields of monochromators. Up to now the real influence on a topograph contrast of this two sources – lattice strength defects and Ge concentration variations – are not completely clear.

The goal of the experiment is to investigate Ge concentration variations with a $\sim 5\ \mu\text{m}$ spatial resolution using the capillary microfocus system, installed at BESSY KMC-2 beamline. The average period of possible variations of Ge concentration depending on the crystal pulling rate is more than $50\ \mu\text{m}$ for the average Ge concentrations up to 8 at% investigated and can be successfully resolved by existing instrumentation.

Experimental setup.

The graded-crystal monochromator beamline KMC-2 was used to set-up of the microprobe system¹. The beam with the energy range of 11400 eV (above Ge K-edge) is monochromatized by the double-graded-crystal monochromator and focused onto an aperture slit with the size of $\varnothing\ 350\ \mu\text{m}$. The total flux in the spot is in the range of $10^9 - 10^{10}$

phot/sec/100 mA. The parameters of inner elliptical surface of the glass mono-capillary are shown in table 1.

Table 1. The Glass capillary ellipse parameters.

Large half-axis (mm)	Small half-axis (μm)	\varnothing of input aperture (μm)	\varnothing of output aperture (μm)	Focal Length (mm)	Focal Size (μm)
100	175	350	15	0.8	~ 5

The capillary is placed close to the focal position of the refocusing mirror of the beamline. In figure 1 is shown an optical scheme of the experimental set-up.

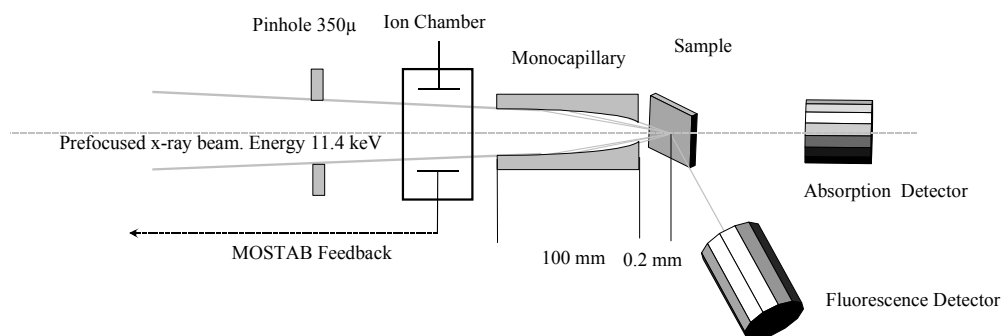


Figure 1. Optical scheme of the microprobe experimental set-up.
Energy range 3.5 keV - 15 keV.

The capillary holder is mounted on a special 5-axis goniometer with a remote control. High-resolution x-ray camera allows one to reduce an alignment time to several minutes and provides continuous control of the focused beam. Ionization chamber for the flux monitoring is located behind the slit system in front of capillary entrance aperture providing feedback signal for an intensity stabilization system (MOSTAB) and constant flux through the capillary aperture.

The microprobe-beamline provides an experimental set-up for EXAFS and XANES measurements in-air or He in the energy range of 3.6 keV – 15 keV. Beam intensity is stabilized by the MOSTAB electronics with an accuracy of 0.1 %. The detector system consists of a Si-PIN photodiode for fluorescence measurements, three ion chambers, a scintillation counter and an energy-dispersive detector Röntec.

A sample stage and detectors are mounted on a $\ominus -2\ominus$ goniometer. Precise X-Y-Z translation provides a 3-D scan with 1 μ reproducibility of the sample position.

Experimental results

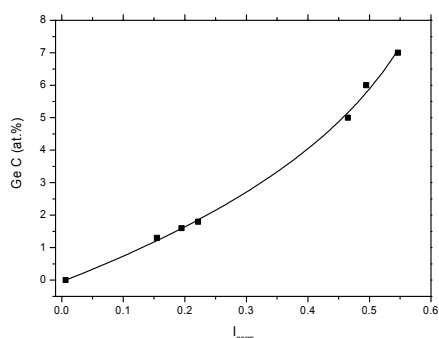


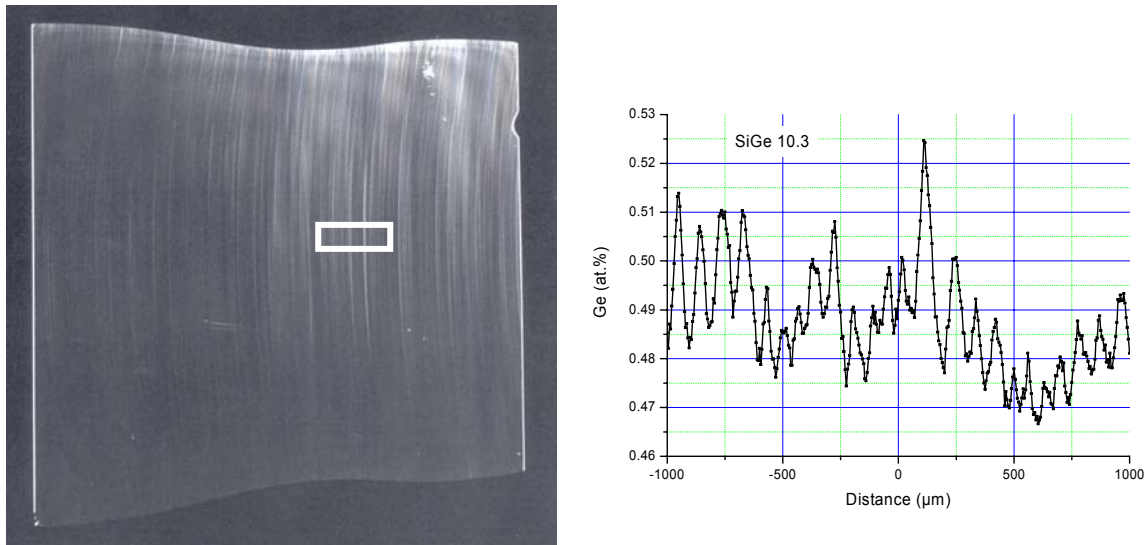
Figure 2. Calibration curve for the absolute measurements of Ge concentration in a $\text{Si}_{1-x}\text{Ge}_x$ single crystal. Experimental points are approximated by 3-rd order curve (solid line).

The fluorescence microprobe was first carefully calibrated using reference SiGe crystals with known Ge concentration. Pure Si and Ge samples were used at the ends of experimental range to obtain 0% and 100% Ge concentration accordingly. The calibration curve for absolute Ge concentration measurements in the range of 0% - 8% Ge atomic percents (at.%) is shown in Figure 2.

Each sample was measured simultaneously with Ge reference sample to calibrate average fluorescence intensity. Finally, an absolute Ge concentration $C(\text{at.}\%)$ is calculated as a function of normalized fluorescence intensity (I_{norm}). Experimental points are approximated with the third-order curve with parameters:

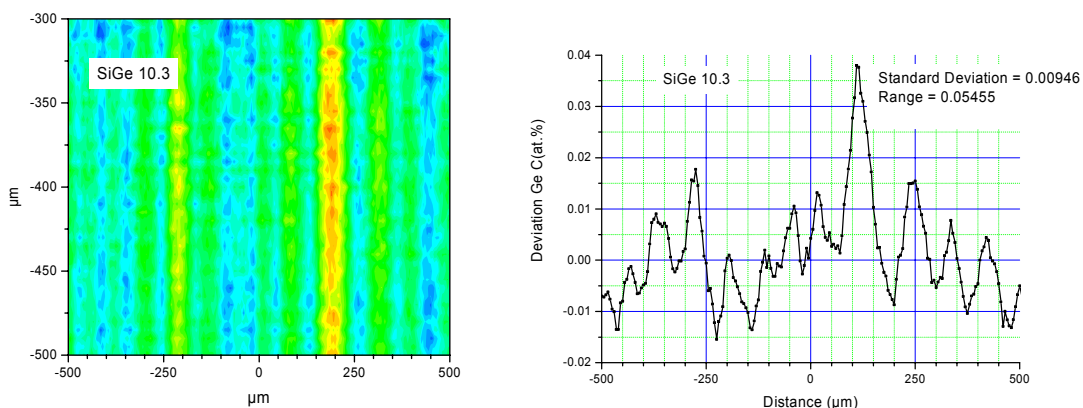
$$C(\text{at.}\%) = -0.125 + 9.64 I_{\text{norm}} - 9.62 I_{\text{norm}}^2 + 29 I_{\text{norm}}^3 \quad (1)$$

The samples were measured to perform two-dimensional plane scan in a focal plane of the capillary. Five samples with average concentration of 0.5 at.% Ge, 1.65 at.% Ge, 2.0 at.% Ge, 3.0 at.% Ge, 6.1 at.% Ge were investigated. Due to the physical properties of the fluorescence signal, the intensity oscillations have higher contrast for a low average Ge concentration in a sample. In figure 3 is shown one of the measured sample with the average Ge concentration of 0.5 at.%.



a) X-ray Lang transmission topograph of the (220) cut wafer from $\langle 111 \rangle$ grown $\text{Si}_{1-x}\text{Ge}_x$ single crystal (Mo $K\alpha_1$ radiation).

b) One-dimensional x-ray microprobe scan of the sample area indicated in figure a) in the white frame.



c) Two-dimensional x-ray microprobe image of a middle part of the sample area indicated in figure a) in white frame.

d) One-dimensional Ge concentration variations in the sample area shown in figure c) as a deviation from the average concentration.

Figure 3. The measurement results of the sample SiGe 10.3 with average concentration of 0.5 at.% Ge.

The main characteristics of the concentration oscillations for the five samples: standard deviation and maximum amplitude are shown in figure 4. These results will be used to

analyze influence of the growth parameters (temperature variations, rotation rate, pulling rate) on a mixed crystal characteristics.

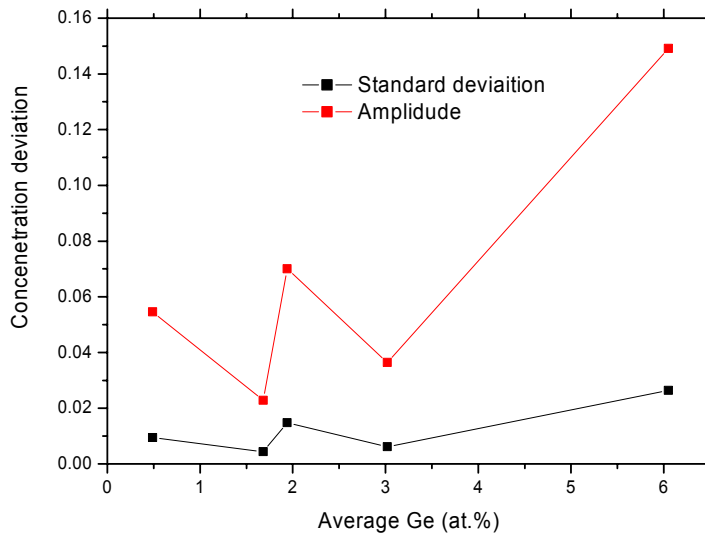


Figure 4. Standard deviation and maximal amplitude of the concentration oscillations depending of average concentration of Ge in SiGe sample.

The results of measurements are in good agreement with 3D computations of melt turbulent convection in the crystallization zone during the growth process and they will be very important to improve the growth technology of $\text{Si}_{1-x}\text{Ge}_x$ single crystals at the Institute of Crystal Growth, Berlin.

ⁱ A. Erko, I. Packe, W. Gudat, N. Abrosimov, A. Firsov "The Crystal Monochromator Based on graded SiGe Crystals" Nuclear Instruments and Methods in Physics Research A **467–468** (2001) 358–361

Metallic CoGaAs Nano-Wires on GaAs(001)(4x2)

P. Vogt¹, K. Lüdge¹, W. Braun², W. Richter¹, N. Esser³

¹Technische Universität Berlin, Institut für Festkörperphysik, Berlin, Germany

²BESSY GmbH, Berlin, Germany

³Institute of Spectrochemistry and Applied Spectroscopy, Department Berlin-Adlershof, Germany

Only recently it has been discovered that the Ga-rich (4x2) reconstruction of GaAs(001) refers to a very unusual surface structure: The so-called ζ (4x2) structure [1] which comprises a regular array of sub-surface voids of atomic size. Here we show for Co on GaAs(001) that this peculiar structure may be of great importance for the formation of particular well ordered sub-monolayer phases.

We demonstrate, that by growth of sub-monolayers of cobalt on the ζ (4x2) reconstructed GaAs(001) surface (Co deposition at substrate temperatures $>100^\circ\text{C}$) well-ordered, one-dimensional metallic nanowires are formed. The surface structure, chemical composition and its electronic nature were studied using Scanning Tunneling Microscopy (STM) and Soft X-ray Photoemission Spectroscopy (SXPS).

The evolution of the surface structure for Co deposition up to 0.75ML is shown in the figure. The regular row structure of the clean ζ (4x2) structure is preserved upon Co deposition. In filled state STM images (Fig. 1) the faint rows of the clean surface develop segments of bright contrast with increasing Co coverage without changing the row distance or regularity. Around 1ML of Co a regular array of bright stripes along the [110] direction with a spacing of four surface lattice constants has built.

To examine the chemical reactions that occur upon Co deposition SXPS core level spectra of As3d and Ga3d were analyzed. Fig.2 shows them together with the spectra obtained on the clean GaAs(001)(4x2) surface.

The dash-dotted black line belongs to the emission line of the bulk coordinated atoms, and the shaded peaks correspond to the surface/interface components as obtained after fitting. In agreement with earlier studies on equally prepared clean GaAs surfaces [2] there are two main surface components found in the Ga3d spectra shifted to lower and higher kinetic energy by -0.38eV and 0.34eV, respectively (see Fig.2a). The As3d emission line depicted in Fig.2b contains three surface components. Most predominant, and related to the dimer rows, is the one component shifted by 0.5eV to higher kinetic energies (labeled As-S₁). We attribute the two small components to the remains of the (1x6) reconstruction because they are more prominent in spectra taken on a surface with mainly (1x6) symmetry. In order to give further evidence for the interpretation of a surface contribution, the relative intensity of the components in the emission lines ($I_{\text{comp}}/I_{\text{bulk}}$) were analyzed as a function of the photon energy. The escape depth of the

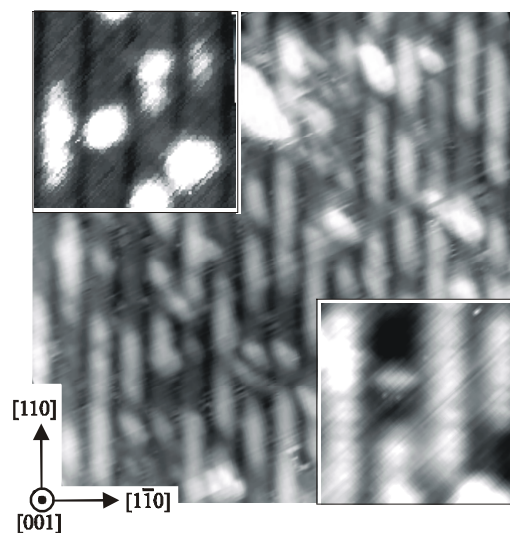


Fig. 1: STM image of 0.75ML Co on GaAs(001). The insets show high resolution images after deposition of 0.05ML and 0.25ML.

electrons is a function of their kinetic energy, therefore the surface sensitivity and thus the ratio between surface and bulk contribution is expected to show a maximum at a kinetic energy of about 50eV. Indeed, this is observed for the surface components (not shown here). Upon the deposition of 0.75ML Co at 150°C the line shapes of the Ga3d and the As3d emission lines change due to the new components that evolve in each spectrum as can be seen in Fig.2c,d. Since both Co induced contributions are shifted to higher kinetic (lower binding) energy with respect to the bulk component, they originate from Ga and As atoms at bonding sites with relative charge accumulation with respect to the bulk. The Ga component labeled Ga-I₁ (I: interface) is shifted by 0.42 eV and has a metallic character i.e. an asymmetric line shape described by a Doniach-Sunjic parameter of 0.15. Fitting the spectra without the asymmetry in the Ga-I₁ line shape lead to structures in the residuum that could not be explained with an additional component. Also the reacted component evolving in the As3d core level shifted by 0.75 eV (labeled As-I₁) has a metallic character that is induced by the presence of metallic Co atoms. The intensity variation with photon energy of the new I₁ components is the same as observed for the reconstruction related surface contributions with a maximum intensity around 50 eV kinetic energy. Thus, the metallic components stem from As and Ga atoms at the surface which react with adsorbed Co atoms. Consequently we conclude that the rows observed in the STM image in Fig.4b contain Co that is partially bonded to Ga and As. However, comparing the absolute

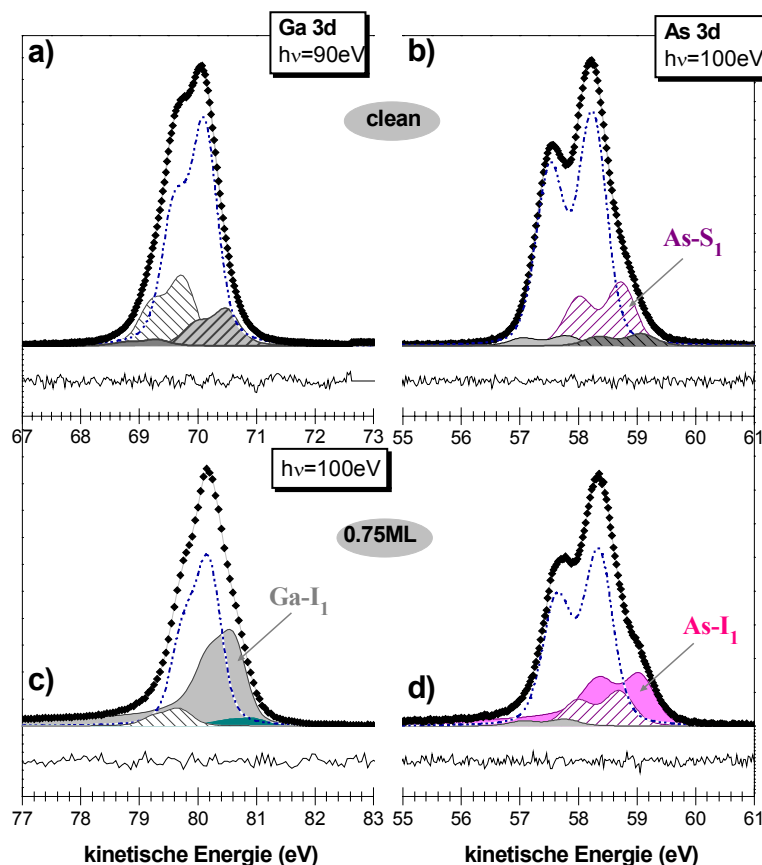


Fig.2: Ga3d and As3d core level spectra taken on the clean GaAs(001)(4x2) surface (a, b) and after deposition of 0.75ML of Co (c, d) (excitation energy 100eV).

intensities of the I_1 components in Fig.2c and d, a higher amount of Ga is involved. This can be explained if the Co adsorbs in the channel, i.e. subsurface between the first and the second atomic layer of the (4×2) structure, where according to the $\zeta(4\times 2)$ model Ga atoms face each other. The Co would be incorporated in the subsurface, and the row structure of the clean (4×2) reconstruction would essentially persist. The incorporated Co would have Ga nearest neighbors. The surface As atoms would be responsible for the corrugation along the rows seen in the Fig.1.

Summarizing, STM and SXPS results are consistent with a Co adsorption in the “nano-holes” of the $\zeta(4\times 2)$ structure leading to 1D-metallic nanowires along the $[110]$ -rows of the clean surface.

- [1] S.-H. Lee, W. Moritz, and M. Scheffler, Phys. Rev. Lett. **85**, 3890 (2000).
- [2] C. J. Spindt, M. Yamada, P. L. Meissner, K. E. Miyano, T. Kendelewicz, A. Herrera-Gomez, and W. E. Spicer, Phys. Rev. B. **45**, 11108 (1992).

**Structural studies of the outer membrane receptor (FptA) of the pyochelin from
*Pseudomonas aeruginosa***

**David Cobessi, Hervé Célia and Franc Pattus, Receptors and Membrane Proteins,
CNRS UPR 9050, ESBS, F-67412 Illkirch, France**

When grown under iron-deficient conditions, many bacteria synthesize and release into the environment iron chelators termed siderophores. By solubilizing the ferric iron of insoluble complexes that form under aerobic conditions at physiological pH, siderophores make iron available for use by the cell. In the host it is expected that siderophores sequester iron from iron-containing molecules such as transferrin and lactoferrin, and subsequently deliver iron to the microbial cell. *Pseudomonas aeruginosa* is an opportunistic human pathogen which infects injured, immunodeficient, or otherwise compromised patients. Under iron-limited conditions, the bacterium secretes different siderophores such as the pyochelin (MM < 2000 Da). The pyochelin is transported through the outer membrane by the pyochelin receptor FptA (MM: 75000 Da).

We crystallized the receptor in presence of different detergents in several crystallization conditions containing already a cryoprotectant solution. The crystals obtained in one crystallization condition diffracted beyond 3 Å resolution on the beamline BL2 at BESSY. There are very thin but long plates or rods. Several frames for this crystal form but not enough due the crystal decay under the radiations were collected from two crystals. These data were processed at 2.8 Å resolution and merged using MOSFLM and SCALA from CCP4. The other crystal forms have not been yet tested. The crystal characteristics are summarized hereafter:

Cell parameters: a=88.8 Å b=95.6 Å c=102.8 Å; $\alpha=101.2^\circ$ $\beta=107.1^\circ$ $\gamma=116.6^\circ$

Space group P1

Solvent content 71.8 % to 43.5 %

Molecule per ua 2 to 4

Wavelength 1.00 Å

Resolution 2.8 Å

Completeness 33 %

Multiplicity 1.3

Rsym 13.1 %

First protein structures from Protein Structure Factory

Babu A Manjasetty^{1,2,§}, Uwe Müller^{1,3}, Andrew Turnbull^{1,2}, Martin Fieber-Erdman^{1,3}, Ronald Förster^{1,3}, Ralf Splettstößer^{1,3}, Martin Ehlers^{1,3} and Udo Heinemann^{2,3,#}

¹Protein Structure Factory, c/o BESSY GmbH, Albert-Einstein-Str. 15, 12489 Berlin, Germany.

²Forschungsgruppe Kristallographie, Max-Delbrück-Centrum für Molekulare Medizin, Robert-Rössle-Str. 10, 13092 Berlin, Germany.

³Institut für Chemie/Kristallographie, Freie Universität, Takustr. 6, 14195 Berlin, Germany.

[§]On leave from: Government Science College, Bangalore 560002, India.

[#]To whom correspondence should be addressed

Abstract. *Three Protein Structure Factory beamlines dedicated to macromolecular crystallography were implemented at the BESSY light source which are ideally suited for MAD/SAD measurements. The PSF beamlines have a one-year track record as a powerful facility for macromolecular structure solution and provided more than 30 novel protein structures. During the year, beam time used by the Protein Structure Factory project yielded five new protein structures.*

1. Introduction. The Protein Structure Factory, a collaborative research project devoted to the high-throughput structure analysis of human proteins(1), has been implemented and started its production phase during the year 2003. The name, Protein Structure Factory, is now used as the synonym for structural genomics efforts worldwide. Within the Berlin-based Protein Structure Factory, the X-ray diffraction data collection facility and the subsequent structure determination unit are located at BESSY, a third generation synchrotron source. Within the reporting period, the Protein Structure Factory has carried out X-ray diffraction experiments on 10 different human proteins and solved five protein structures. In addition, the group has provided scientific support for external industrial and academic users. In total, about 30 independent protein structures were solved during the year 2003.

2. Results. X-ray diffraction experimental details are summarized in table 1. Three structures were solved by single-wavelength anomalous diffraction (SAD) and two structures were solved by molecular replacement methods. The biological insight gained from the protein structures is briefly described below.

2.1. Gankyrin, the product of a gene linked to hepatocellular carcinoma (2)

Gankyrin, a newly described oncoprotein, is identical to the p28 subunit of the 26S proteasome. The protein is derived from the first oncogene linked to hepatocellular carcinoma (HCC) and thus represents a potential target for drug therapy against liver cancer. As the name indicates, gankyrin contains an ankyrin repeat stack (6 repeats) with a 38-amino-acid N-terminal domain. The first letter 'g' stands for 'gann' which means cancer in Japanese. Similar to other ankyrin-repeat proteins, gankyrin mediates protein-protein interactions with diverse regulatory proteins, including the retinoblastoma tumor suppressor (Rb), the cyclin-dependent protein kinase 4 (CDK4), melanoma antigen (MAGE-A4), and the S6 ATPase of the 26S proteasome. The structure of gankyrin (Figure 1) consists of five complete ankyrin repeats, one incomplete ankyrin repeat at the C-terminus and the N-terminal domain. The fifth ankyrin repeat of gankyrin contains a previously defined retinoblastoma-binding motif, LXCXE which is in helical conformation, whereas two different Rb-bound LXCXE peptides adopt an extended, β -strand-like conformation (3, 4). Structural comparison between gankyrin and the CDK4 inhibitor p16^{INK4A} shows major structural differences at the second ankyrin

repeat, a site which might be important for CDK4 binding (5). On this basis, the binding sites on the gankyrin surface for Rb and CDK4/6 are proposed.

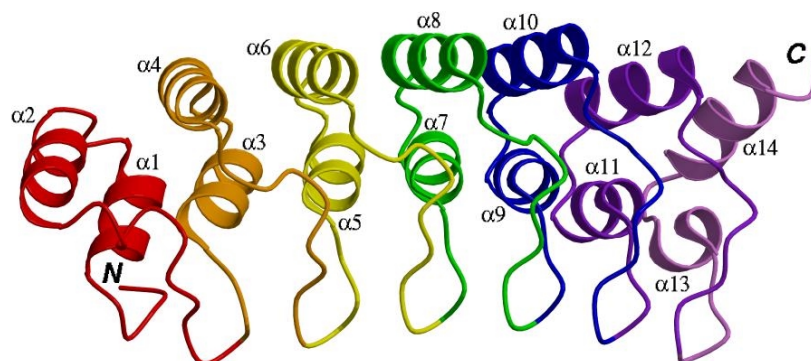


Figure 1. Secondary structure representation of gankyrin,

Table 1 : The first crystals from the Protein Structure Factory and their status

No.	Protein	Variant	Data Limit	Experimets	Status/PDB ID
1	Gankyrin	Native	2.8	1	Solved/1QYM
2a	hp14.5	Native	1.9	12	Solved/1ONI
2b	hp14.5	Hg	2.5	-	Solved
3a	BET3	Native	1.55	14	Solved
3b	BET3	SeMet	2.5	-	Solved
4a	Peptidase D	Native	1.9	18	Solved
4b	Peptidase D	SeMet	2.5	-	Solved
5	FLJ36880	Native	2.2	1	Solved
6	GADD45 γ	Native	2.65	30	Variant Search
7	CGI32	Native	1.8	24	Variant Search
8	Alacadin	Native	3.5	5	Variant Search
9	Translin	Native	5.0	5	Tested/Ended
10	Cys-Dioxygenase	Native	2.9	1	Tested

2.2 Translational inhibitor protein, hp14.5 (6)

Human trichloroacetic acid-soluble protein (hp14.5) is a member of the large YjgF/YER057c/UK114 protein family which to date comprises approximately 200 members, most with unclear biological function. The hp14.5 homologs belonging to the high-identity (>38%) groups (approximately 80 proteins) share nine completely invariant residues which are spread throughout the sequence. Proteins from this family are involved in various cellular functions reported in the literature, i.e. translation inhibition, ribonuclease activity, and involvement in the regulation of purine and isoleucine biosynthetic pathways (7-10). Like several homologous YjgF/YER057c/UK114 protein family members, the human translational inhibitor protein hp14.5 adopts a chorismate mutase-like subunit fold (Figure 2) and associates into a trimer. The deep clefts at the inter-subunit interfaces in the trimer are lined by the invariant residues that characterize the YjgF/YER057c/UK114 family. The protein has been crystallized in the presence of benzoate. In each cleft, a benzoate molecule is bound through bidentate salt bridges between the carboxylate group and the invariant arginine-107. A second

benzoate is located in alternating orientations in some, but not all of the clefts. It is likely that the benzoate ligands bound in the prominent cleft near invariant residues mark a site important for the function of hp14.5.

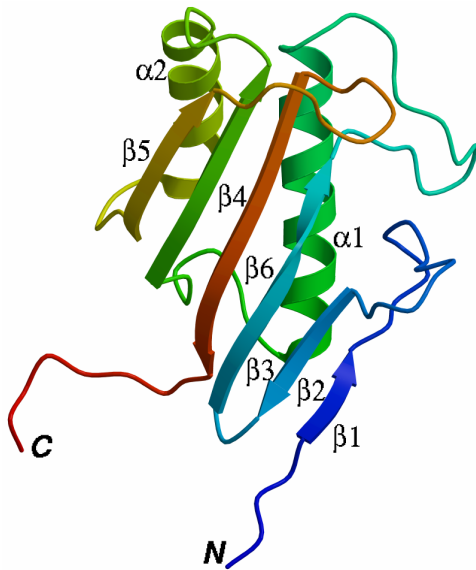


Figure 2. Secondary structure representation of hp14.5

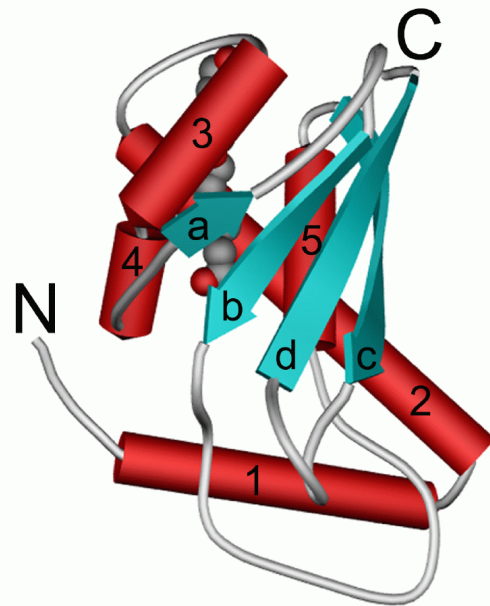


Figure 3. Secondary structure representation of Bet3p

2.3. Bet3p, a subunit of the TRAPP complex

The TRAPP (Transport Protein Particle) complex is involved in the targeting and/or fusion of endoplasmic reticulum to Golgi transport vesicles with their acceptor compartment (11, 12) and comprises at least 10 highly conserved proteins (Bet3p, Bet5p, Trs20p, Trs23p, Trs31p, Trs33p, Trs65p, Trs85p, Trs120p and Trs130p; yeast gene nomenclature) present in approximately equimolar amounts in the fully assembled complex (12, 13). The tertiary structure of Bet3p has a previously unknown α/β -plait fold (Figure 3) featuring an extensive tunnel lined predominantly by highly conserved hydrophobic residues. The presence of a hydrophobic ligand bound within this tunnel suggests that it may represent a putative binding site for a lipid anchor either from another constituent of the TRAPP complex or the Golgi or vesicle membrane, highlighting the importance of Bet3p in either TRAPP complex assembly or in its localization to the *cis*-Golgi membrane.

2.4 Peptidase D

Peptidase D (PEPD) is a ubiquitous metallo-aminopeptidase enzyme, which cleaves dipeptides with a C-terminal *trans*-Pro residue, with narrow substrate specificity. The biological function can be described as processing specific substrates including bioactive peptides involved in cardiovascular and pulmonary systems and degradation products of collagen. Several mutations in the PEPD encoding gene lead to PEPD deficiency, which has been described as a deadly autosomal recessive disorder for man (14). In order to analyze the three-dimensional structure of this 54 kDa protein, which is active as a homodimer, we have carried out X-ray diffraction experiments at BESSY, PSF-BL1+2. The three-dimensional structure model could be refined to a final R/R_{free} of 16.3/19.1 % up to 1.82 Å resolution. The structure solution was possible by applying the SAS method, using a Se-Met derivative of the PEPD polypeptide. Further analysis of the structure (Figure 4) is in progress.

2.5 Hypothetical protein FLJ36880

Hypothetical protein FLJ36880, an unnamed protein product of gene DKFZP566J2046 from *Homo sapiens*, belongs to the fumarylacetoacetate hydrolase (FAH) family. This family includes fumaryl acetoacetate hydrolase (FAH) which is the last enzyme in the tyrosine and phenylalanine catabolic pathway. FAH hydrolyses fumaryl acetoacetate into fumarate and acetoacetate which then enter the citric acid cycle (15). Mutations in FAH cause the metabolic disease hereditary tyrosinemia type I (HTI). In humans this is an inherited disorder mainly affecting the liver leading to liver cirrhosis, hepatocellular carcinoma, renal tubular damages and neurologic crisis. A second FAH family member is the bifunctional enzyme OPET decarboxylase / HHDD isomerase (HpcE in *E. coli*) which carries out the fourth and fifth steps of the homoprotocatechuate (3,4-dihydroxy phenylacetate, HPC) catabolism pathway (16). HPC is a product of tyrosine and phenylalanine metabolism which is also released by lignin catabolism. A third family member, ureidoglycolate lyase, catalyzes the breakdown of ureidoglycolate to glyoxylate and urea, which is the final step in the catabolic pathway leading from purines to urea (17). The structure of the hypothetical protein FLJ36880 adopts a mixed β -sandwich roll fold which forms a homodimer related by a pseudo 2-fold symmetry (Figure 5). Initial comparative studies suggest structural homology to isomerases, decarboxylases and hydrolases which in turn suggests that FLJ36880 may function as a multifunctional enzyme.

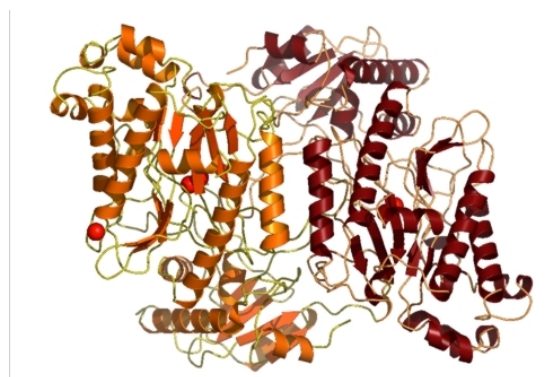


Figure 4. Secondary structure representation of Peptidase D

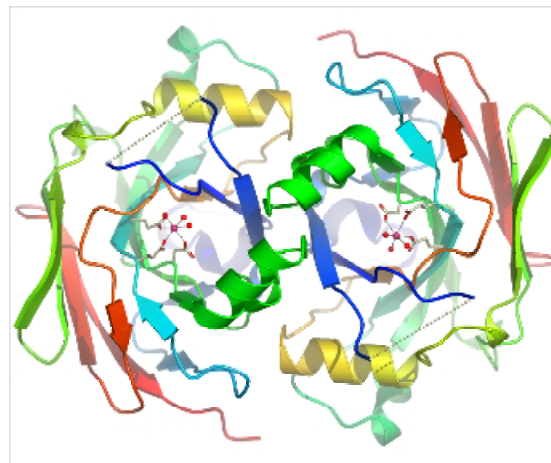


Figure 5. Secondary structure representation of FLJ36880

3. Conclusion

Our efforts have yielded several protein structures for the year 2003, some of them outlined here. All have interesting biological functions, some are clearly related to human diseases, and some provide the basis for further work aimed at structurally elucidating functional protein networks in which these proteins are active. Of course, current methodologies have to be further improved to increase the rate of protein structure determination. At present around the globe, attempts to streamline protocols, methods and implement new technologies to provide efficient rate of protein structures are in progress.

Acknowledgements

Funded by the German Federal Ministry for Education and Research (BMBF) through the "Leitprojektverbund Proteinstrukturfabrik" and with support by the Fonds der Chemischen Industrie to U.H. We wish to thank all Protein Structure Factory members.

References

1. Heinemann, U., Bussow, K., Mueller, U., and Umbach, P. (2003) *Acc Chem Res* **36**, 157-63.
2. Manjasetty, B. A., Quedenau, C., Seivert, V., Büssow, K., Niesen, F. H., Delbrück, H., and Heinemann, U. (2003) *Proteins-Structure Function and Genetics*, in press.
3. Kim, H. Y., Ahn, B. Y., and Cho, Y. (2001) *Embo J* **20**, 295-304.
4. Lee, J. O., Russo, A. A., and Pavletich, N. P. (1998) *Nature* **391**, 859-65.
5. Russo, A. A., Tong, L., Lee, J. O., Jeffrey, P. D., and Pavletich, N. P. (1998) *Nature* **395**, 237-43.
6. Manjasetty, B. A., Delbrueck, H., Pham, D.-T., Mueller, U., Fieber-Erdmann, M., Scheich, C., Sievert, V., Buessow, K., Niesen, F., Weihhofen, W., Loll, B., Saenger, W., and Heinemann, U. (2003) *Proteins-Structure Function and Genetics*, in press.
7. Oka, T., Tsuji, H., Noda, C., Sakai, K., Hong, Y. M., Suzuki, I., Munoz, S., and Natori, Y. (1995) *J Biol Chem* **270**, 30060-7.
8. Schmiedeknecht, G., Kerkhoff, C., Orso, E., Stohr, J., Aslanidis, C., Nagy, G. M., Knuechel, R., and Schmitz, G. (1996) *Eur J Biochem* **242**, 339-51.
9. Rappu, P., Shin, B. S., Zalkin, H., and Mantsala, P. (1999) *J Bacteriol* **181**, 3810-5.
10. Morishita, R., Kawagoshi, A., Sawasaki, T., Madin, K., Ogasawara, T., Oka, T., and Endo, Y. (1999) *J Biol Chem* **274**, 20688-92.
11. Sacher, M., Jiang, Y., Barrowman, J., Scarpa, A., Burston, J., Zhang, L., Schieltz, D., Yates, J. R., 3rd, Abeliovich, H., and Ferro-Novick, S. (1998) *Embo J* **17**, 2494-503.
12. Sacher, M., Barrowman, J., Schieltz, D., Yates, J. R., 3rd, and Ferro-Novick, S. (2000) *Eur J Cell Biol* **79**, 71-80.
13. Sacher, M., Barrowman, J., Wang, W., Horecka, J., Zhang, Y., Pypaert, M., and Ferro-Novick, S. (2001) *Mol Cell* **7**, 433-42.
14. Kikuchi, S., Tanoue, A., Endo, F., Wakasugi, S., Matsuo, N., and Tsujimoto, G. (2000) *J Hum Genet* **45**, 102-4.
15. Timm, D. E., Mueller, H. A., Bhanumoorthy, P., Harp, J. M., and Bunick, G. J. (1999) *Structure Fold Des* **7**, 1023-33.
16. Tame, J. R., Namba, K., Dodson, E. J., and Roper, D. I. (2002) *Biochemistry* **41**, 2982-9.
17. McNinch, J. K., McNinch, J. D., and May, S. W. (2003) *J Biol Chem* **278**, 50091-100.

Contact :

Udo Heinemann
Max Delbrück Center for Molecular Medicine
Robert-Rössle-Str. 10
D-13092, Berlin, Germany
Phone: +49 (30) 9406 3420
Fax: +49 (30) 9406 2548
E-mail: heinemann@mdc-berlin.de

Crystallographic Studies of the Carbonyl Reductase Sniffer, a β -alanine-CoA Ammonia Lyase and a Complex of Carbonic Anhydrase II

T. Sgraja, A. Heine, A. Weber, K. Reuter, G. Klebe
Institute of Pharmaceutical Chemistry
Philipps University Marburg, Marbacher Weg 6, 35032 Marburg

Abstract

In order to collect either MAD data to enable structure determination of novel proteins or to collect very high resolution data, X-ray diffraction experiments were carried out at the protein structure factory beamline II located at the Bessy synchrotron. All data sets were collected on a MAR345 imaging plate detector with exposure times ranging from 1 to 10 seconds and 45 seconds for the ultra-high resolution data, respectively. The structure of a carbonyl reductase was determined at 1.7Å resolution, a β -alanine-CoA ammonia lyase (ACL) at 0.97Å and a carbonic anhydrase II –inhibitor complex at 1.25Å resolution.

Introduction

A growing body of evidence suggests that oxidative stress is a common underlying mechanism in the pathogenesis of neurodegenerative disorders such as Alzheimer, Huntington, Creutzfeldt-Jakob and Parkinson diseases. The *Drosophila melanogaster* gene “sniffer” exerts an important function to assure neuronal cell survival. Sniffer, a carbonyl reductase, might be mainly involved in the detoxication or inactivation of chemical active compounds and is required to protect neurons from oxidative stress-induced neurodegeneration in *Drosophila* flies. The protein belongs to the superfamily of the short-chain dehydrogenases/reductases (SDR) and accepts a variety of substrates previously reported for carbonyl reductases, especially for phenanthrene-9,10-quinone which is processed with the highest catalytic turn over rate.

The enzyme ACL catalyzes the amination of acrylyl-CoA to form β -alanyl-CoA. This reaction has been shown to be fully reversible and is of interest for the biosynthesis of β -alanine and represents the first example of the formation of an acyl-CoA derivative of an amino acid [1]. In order to gain an insight into the mechanism of the reaction catalyzed by the enzyme structural studies were instigated.

Carbonic anhydrases (CA, EC 4.2.1.1) are zinc containing enzymes present in bacteria, plants and animals as efficient catalysts for the reversible hydration of carbon dioxide and a water molecule to bicarbonate and a proton. CAs occur in three distinct gene families (α , β , γ), which are variously expressed in all living organisms. In higher vertebrates, including humans, 14 different α -CA isozymes have been described so far. Since the conversion of CO_2 to HCO_3^- is a fundamental step in living organisms, the CA isozymes participate in numerous physiological processes. They are involved in respiration and transport of $\text{CO}_2/\text{HCO}_3^-$, pH and CO_2 homeostasis, electrolyte secretion and biosynthetic reactions. The human CA II belongs to the α -class and is the most studied CA isozyme. It is involved in the production of aqueous humor in the eye. The activity of this isozyme is linked to increased intraocular pressure, a major symptom of glaucoma. Sulfonamide CA II inhibitors are effective in lowering the intraocular pressure and therefore applied in the treatment of glaucoma.

Results

The crystal structure of the Sniffer protein in complex with NADP⁺ could be determined by multiple-wavelength anomalous dispersion at a resolution of 1.7Å using selenomethionine derivative protein crystals. The crystal structure of the binary complex with NADP⁺ was refined to an R_{cryst} of 21.5 % and an R_{free} of 27.8 %. The Sniffer protein consists of a seven parallel β-sheet in the center sandwiched between two arrays of three helices each. Crystal packing reveals that the protein is a dimer. The NADP⁺ molecule is well defined in the electron density. The structure contains a catalytic triad consisting of Tyr, Lys and Ser, a well conserved motif observed in enzymes of the SDR family.

β-alanine-CoA ammonia lyase
4-hydroxybenzoyl CoA thioesterase

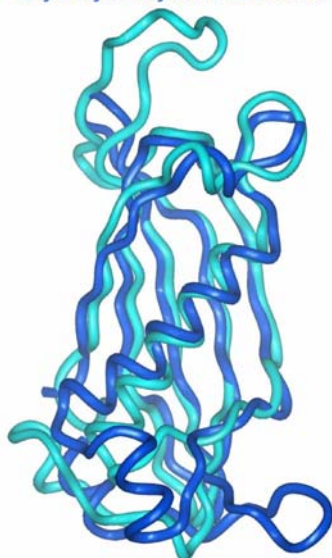


Figure 1

The crystal structure of the ACL protein was determined by multiple-wavelength anomalous dispersion collecting three data sets close to the zinc edge. The protein consists of 144 residues and contains one zinc atom per molecule, which was introduced during protein crystallization. Fortunately, crystals diffracted to ultra-high resolution and a high, medium and low resolution data set was recorded resulting in a very complete data set at 0.97Å resolution. The position of the zinc atom was unambiguously determined and used for initial phasing with SHELXE [2]. Automated model building was performed with ARP/wARP [3] and resulted in 139 out of 144 residues. The structure was refined with SHELXL [4] to R=15.8% and R_{free}=17.5%. The protein consists of a five-stranded anti-parallel β-sheet with a long α-helix lying across and resembles a high structural similarity to 4-hydroxybenzoyl CoA thioesterase (PDB code 1bvq) [5] (Figure 1).

The carbonic anhydrase structure was determined by molecular replacement at a resolution of 1.25Å resolution. The structure was refined to R=14.0% and R_{free}=19.2%. The electron density clearly revealed a bound inhibitor deeply buried in the active site. As previously shown by other groups [6] the sulphonamide group of the inhibitor coordinates the zinc ion by replacing the catalytically active water molecule.

References

- [1] P.R. Vagelos, J.M. Earl, E.R. Stadtman; *Biol. Chem.* 234, 1959, 490-497.
- [2] G.M. Sheldrick; *Z. Kristallogr.* 217, 2002, 1-7.
- [3] V.S. Lamzin, K.S. Wilson; *Acta Crystallogr. D*52, 1993, 129-149.
- [4] G.M. Sheldrick, T.R. Schneider; *Methods Enzymol.* 277B, 1997, 319-343.
- [5] M.M. Benning, G. Wesenberg, R. Liu, K.L. Taylor, D. Dunaway-Mariano, H.M. Holden; *Biol. Chem.* 273, 1998, 33572-33579.
- [6] S. Lindskog; *Pharmacol. Ther.* 74, 1997, 1-20.

The Schiff Base of Gossypol with 3,6,9-trioxa-decylamine forms Complexes with Monovalent Cations

Franz Bartl¹, Bogumil Brzezinski², Klaus Peter Hofmann¹, Ulrich Schade³, Piotr Przybylski²

¹*Institute of Medical Physics and Biophysics, Universitätsklinikum Charité,
Humboldt University, Ziegelstr. 5-9, D-10098 Berlin, Germany*

²*Faculty of Chemistry, A. Mickiewicz University, Grunwaldzka 6, 60-780 Poznan, Poland*

³*BESSY GmbH, Albert-Einsteinstr. 15, 12489 Berlin, Germany*

Introduction

Gossypol 2,2'-bis(8-formyl-1,6,7-trihydroxy-5-isopropyl-3-methylnaphthalene) is a yellow compound extracted from cottonseeds (1). To its broad spectrum of medical and biological applications belong also an antiviral (2) and antibacterial activity (3). The toxicity of gossypol, caused by aldehyd groups, is the main obstacle in using this compound in medical therapy (4). Hence we synthesized a new Schiff bases of gossypol, which show similar biological activity and lower toxicity in comparison to gossypol itself. This opens a wider use of this class of compounds in medical therapy.

The antibacterial effect of many antibiotics is based on the ability to form complexes with monovalent cations. Cell death is caused by an exchange of metal ions against H⁺. This leads to a pH shift and increased osmotic pressure inside, which destroys the cell.

Interestingly gossypol is not able to form complexes with monovalent cations, which limits its antibacterial activity. In order to generate the ability of complex formation and to enhance the antibacterial effect we introduced a new Schiff base with a polyoxaalkyl chain (3,6,9-trioxa-decylamine) to the gossypol molecule (5). This side chain was shown to form strong complexes with Li⁺, Na⁺ and K⁺ (6). The structure of the complexes between the Schiff bases of gossypol with 3,6,9-trioxa-decylamine (GSTB) and its complexes with cations and the mechanism of complex formation was investigated by conventional and synchrotron infrared spectroscopy.

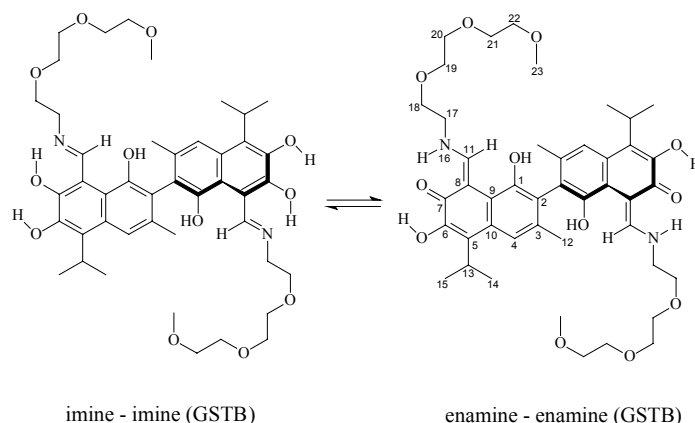


Fig. 1: Tautomeric forms of gossypol Schiff base.

Infrared spectroscopy of the complexes in the mid and in the far infrared regions

The Schiff bases of gossypol with 3,6,9-trioxa-decylamine (GSTB) and its complexes with cations can occur in imine-imine and enamine-enamine tautomeric forms (Fig.1). Fig. 2 shows the infrared spectra of GSTB (black line) and its complexes with 2 H⁺ (red line) and Li⁺ (blue

line). In the spectrum of the complex of GSTB with 2 H⁺ two bands at 1648 cm⁻¹ and at 1548 cm⁻¹ appear. The band at 1648 cm⁻¹ indicates the protonation of the N₁₆ and N_{16'} atom of the Schiff base and can be assigned to the N-H stretching vibration of the C=N⁺-H group. The band at 1548 cm⁻¹ is assigned to the C=C stretching vibrations of the naphthalene ring. The appearance of these two bands after protonation of the GSTB molecule indicate the formation of the imine-imine tautomeric form. A comparison of this spectra with the spectra of GSTB and its complex with Li⁺ reveal that in the latter no band of the naphthalene ring is found. Instead in both cases a strong band centered at 1625 cm⁻¹ of the C=O stretching vibration of the keto group is observed. This demonstrates that the GSTB molecule and its complex with Li⁺ exists in the enamine-enamine tautomeric form. The same is found for all other complexes of GSTB with cations (data not shown).

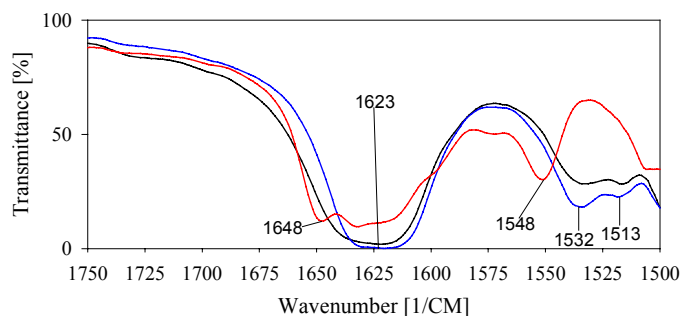


Fig. 2: FT-IR spectra with the extended scale 1750-1500 cm⁻¹ of GSTB (black) and its complexes with 2H⁺ (red) and 2Li⁺ (blue).

The far FTIR spectra of the GSTB-M (M = Li⁺, Na⁺) complexes are shown in Fig 3 a and b. In Fig 3 a the far FT-IR spectrum of the GSTB-2-Li⁺ complex is shown. This spectrum does not show the so called Li⁺-motion band usually observed at about 400 cm⁻¹ indicating vibrations of non-bonded Li⁺ cations. Instead of this band a broad band in the region 385- 258 cm⁻¹ with a maximum at 302 cm⁻¹ is observed. The shift of this band, compared to the Li⁺ motion band demonstrates, that the Li⁺ ions are strongly complexed by the GSTB molecule. The broadness of this band indicates, that the Li⁺ ions is not located at a certain oxygen atom, but shows a fluctuation between the oxygen atoms of the polyoxaalkyl chain.

The ion motion band of Na⁺ cation is observed at 195 cm⁻¹. In the spectrum of the GSTB-2-Na⁺ complex (Fig. 3b), this band is shifted to 182 cm⁻¹ indicating complex formation. The bandwidth of this band is however much smaller compared to the respective band in the Li⁺ complex. This shows that the mobility of the Na⁺ ion in the complex is lower than it is for the Li⁺ ions.

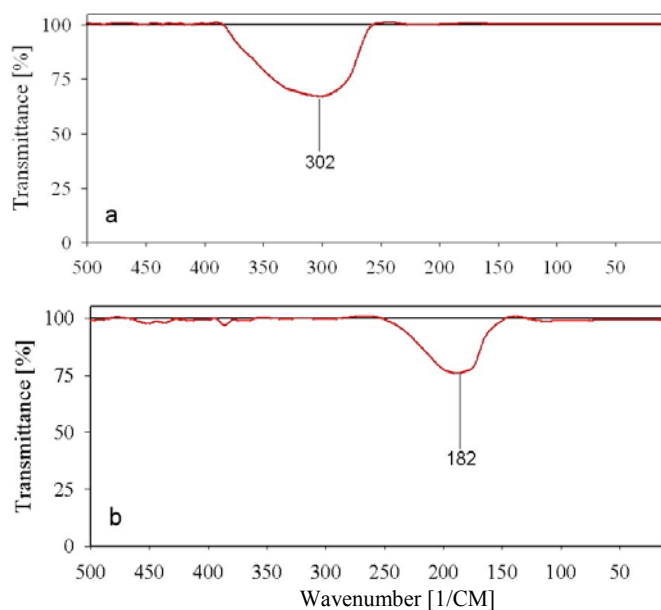


Fig. 3: Far FT-IR spectra of the complexes of GSTB with Li⁺ (a) and Na⁺ (b).

Conclusions

It was shown by FT-IR spectroscopy in the far IR region (Fig 3 a and b), that a new Schiff base of Gossypol with 3,6,9-trioxa-decylamine (GSTB) is able to form complexes with several cations such as H^+ , Li^+ and Na^+ . The spectra in the mid IR region (Fig. 2) show, that the complexes with metal cations are present in the enamine-enamine form, whereas the complex with protons exists in the imine-imine form. The proton is localized at the N_{16} and $N_{16'}$ atom of the Schiff base. The stoichiometry of the complexes was determined by electrospray mass spectrometry. The GSTB molecules form stable 1:1 and 1:2 complexes with Li^+ and Na^+ and exclusively 1:2 complexes with protons. The structures of the $GSTB:2H^+$; $GSTB:Li^+$ and of the $GSTB:2Na^+$ were calculated by the PM 5 semiempirical method (Fig. 4a bis 4c).

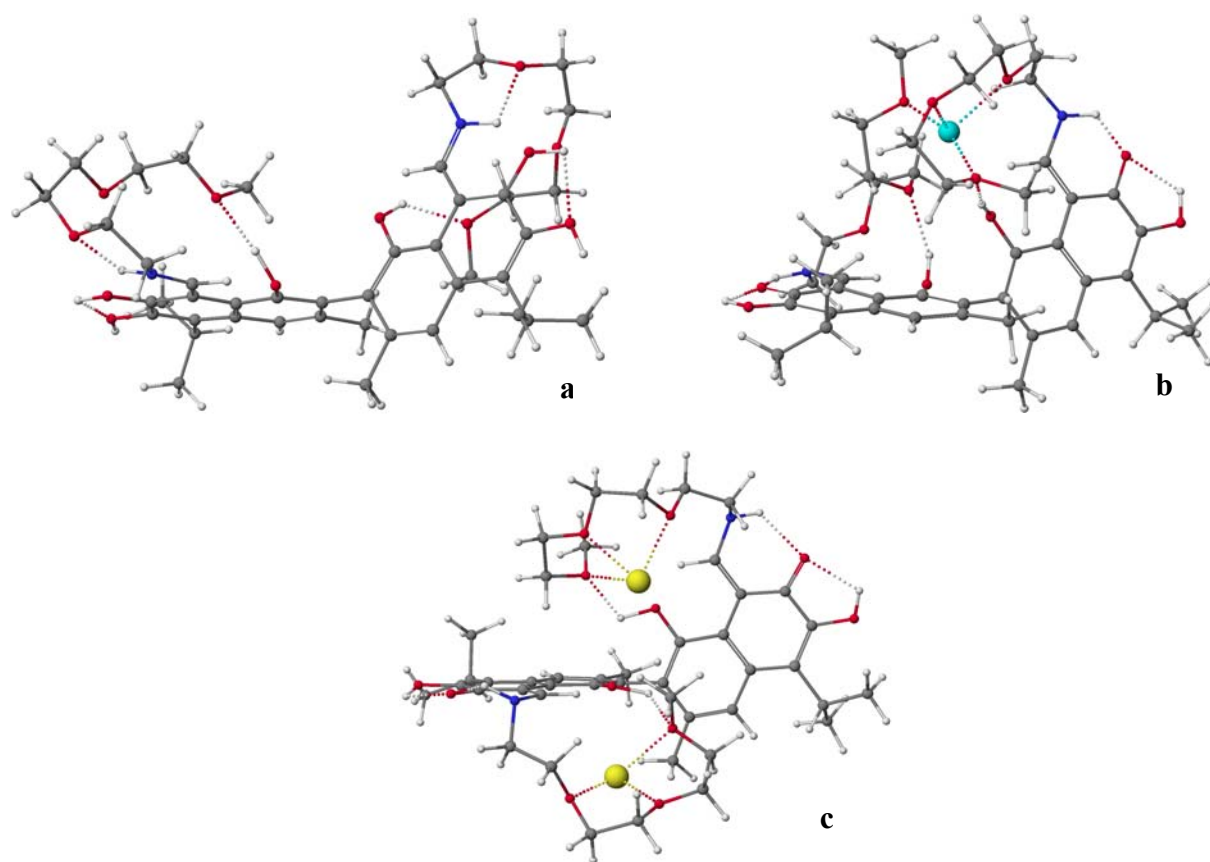


Fig. 4: Structure of the complex between the Schiffbase of gossypol with 3,6,9-trioxa-decylamine and H^+ (a), Li^+ (b) and with 3,6,9-trioxa-decylamine and Na^+ (c).

Literature:

- 1) Kulkarni, V.N.; Khadi, B.M.; Sangam V.S.; *Current Science*, **82**, 434. (2002).
- 2) L.M. Deck, D. L. Van der Jagt and R. E. Royer, *J. Med. Chem.*, **34**, 3001, (1991).
- 3) G. Tegos, F. Stermitz, O. Lomovskaya, K. Lewis, *Antimicrob. Agents Chemother.*, **46**, 3133, (2002).
- 4) Shelley, M.D., Hartley, L.; Groundwater, P.W.; Fish, R.G.; *Anti-Cancer Drugs*, **11**, 209, (2000).
- 5) Przybylski, P., Bartl, F., Brzezinski, B, *Biopolymers (Biospectroscopy)* **65**, 111, (2002).
- 6) G. Schroeder, B. Gierczyk, B. Leska, G. Wojciechowski, R. Pankiewicz, B. Brezinski. F. Bartl *J. Mol. Struct.* 607, 9-17, (2002).

Investigation of protein dynamics in crystals using fluorescence spectroscopy

Björn Klink & Axel J. Scheidig

*Max-Planck-Institut of Molecular Physiology, Otto-Hahn-Strasse 11,
D - 44202 Dortmund, Germany
Saarland University, Dept. Structural Biology, Saarland University Hospital, Bldg. 60,
D-66421 Homburg, Germany*

Background

Time-resolved and kinetic crystallography is an important technique for the investigation of protein dynamics. In solution protein dynamics are frequently characterized using fluorescence spectroscopy. The emphasis of our project is the combination of these two techniques in one single setup. For the initiation of protein reactions in crystals we make use of photolytic cleavage of photolabile protected molecules (caged molecules). For the detection of changes in fluorescence we either use intrinsic fluorophores or introduce artificial fluorophores into the protein using protein chemistry. For this project on the one hand we have to develop new techniques for the modification of proteins and, on the other hand have to develop new setups (laser for excitation of photolysis and fluorescence, and detectors for the fluorescence signal) which can be added to any synchrotron beam line. We propose to establish this technique using the model system Ras p21 and to apply this experimental setup to new proteins.

Results

The small (21 kDa) GTPase Ras p21 was chosen as a model system since its kinetic behavior in solution and in crystals is very well characterized. The different aspects of time-resolved and kinetic crystallography for this system (e.g. reaction initiation and freeze-trapping) are well understood. The in-cooperation of different fluorescence probes could be established using site directed mutagenesis and chemical modification of cysteine side-chains. Using different nucleotides and fluorophores different crystallization conditions had to be established in order to obtain well diffracting crystals. The structures of the individual constructs between protein, nucleotide and fluorophore, respectively were determined. The data collection for one of the complexes was performed at the BESSY II beamline BL1. For detailed statistics see Table 1. The new structures will serve as a starting point for new experiments for the combination of kinetic crystallography and fluorescence spectroscopy on protein crystals.

Table 1. Data statistics for Ras p21(C32-fluorophore)-R caged-GTP

detector	MAR CCD
temperature (K)	100
wavelength (Å)	1,0721
max. resolution (Å)	1.45
spacegroup	P4(1)
cell dimensions	a = b = 68,9; c = 35.1
multiplicity	4.5
R _{sym} (%)	6.3
completeness (%)	91.7
R _{cryst} (%) / R _{free} (%)	20.1 / 22.3

Acknowledgements

This work was funded by the BMBF (05 KS1EDA / 3).

Crystal structure determination of Rab4

Silke Huber & Axel J. Scheidig

*Max-Planck-Institut of molecular Physiology, Otto-Hahn-Strasse 11,
D - 44202 Dortmund, Germany
Saarland University, Dept. Structural Biology, Saarland University Hospital, Bldg. 60,
D-66421 Homburg, Germany*

Background

The Ras-related Ypt/Rab GTPases are central regulators of vesicular transport. The common key feature of this group appears to be the activation of specific effector molecules that bind exclusively to their GTP-bound form. The mammalian GTPase Rab4a is involved in the regulation of the recycling from the early endosome to the recycling compartment and to the plasma membrane, respectively. In its GTP-form, Rab4a interacts with the effector protein Rabaptin-5, a tethering protein interacting with Rab5 as well.

Results

We have determined the crystal structures of the GDP- and GppNHp-bound conformation of Rab4a solved at 1.8 Å and 1.6 Å resolution, respectively. Data collection for the GDP-form was performed at BESSY II beamline BL1. For detailed statistics see Table 1.

Despite the similarity of the overall structure to other Ypt/Rab proteins, Rab4a displays some significant differences in regions highlighted as Rab family (RabF) and Rab subfamily (RabSF) determinants. These differences are an example for the structural plasticity and variations at distinct surface epitopes characteristic for this protein family.

Conclusions

The results derived from the comparison of these two structures with the structures of other Ypt/Rab proteins will provide further insight into the determinants responsible for the specificity of the individual Ypt/Rab proteins for their respective effector proteins.

Figure 1:

Superposition of the structure from Rab4a•GDP (in light blue) and Rab4a•GppNHp (in light green). The switch regions are highlighted in blue (GDP-form) and green (GppNHp-Form).

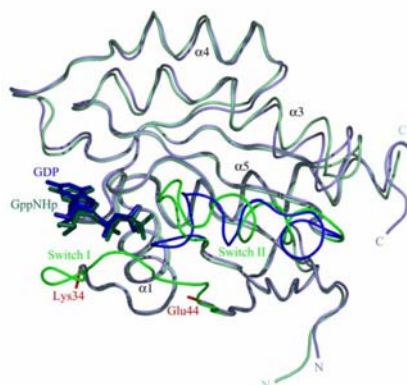


Table 1. Data statistics for Rab4-GDP

detector	MAR CCD
temperature (K)	100
wavelength (Å)	1,0721
max. resolution (Å)	1,8
spacegroup	C2
cell dimensions	a = 71,1; b = 63,7; c = 38,3; β = 100
multiplicity	4,3
R _{sym} (%)	7,1
completeness (%)	99,4
R _{crvst} (%) / R _{free} (%)	15,8 / 20,9

Acknowledgements

This work was funded by the Deutschen Forschungsgemeinschaft (DFG grant SCHE 545/4-1).

Structure determination of the L-amino acid oxidase from *Rhodococcus opacus*

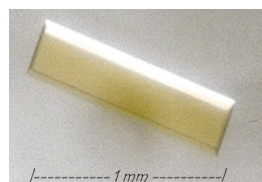
A. Faust, D. Schomburg, K. Niefind

Institute of Biochemistry, University of Cologne, Zuelpicher Strasse 47, 50674 Cologne,
Germany

L-amino acid oxidases catalyze the stereospecific oxidative deamination of an L-amino acid substrate to an α -keto acid along with the production of ammonia and hydrogen peroxide [1]. The enzymes are often found in snake and insect venom but also in fungi, algae and some cyano- and soil bacteria. The role of L-amino acid oxidase in bacterial metabolism is completely unknown until now.

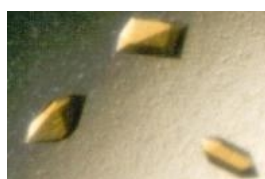
The L-amino acid oxidase from *Rhodococcus opacus* (LAO, EC: 1.4.3.2) is a dimeric flavoprotein which contains one non-covalently bound FAD per subunit as a cofactor. Each subunit consists of 489 amino acids corresponding to a molecular weight of 54.2KDa.

The LAO is overexpressed in *Rh. opacus* and *Streptomyces*, purified to homogeneity and crystallized. Two different crystal forms are obtained with very good diffraction properties:



(a) The crystals belong to the orthorhombic spacegroup $P2_12_12_1$ with lattice parameters of $a = 65.9 \text{ \AA}$, $b = 109.9 \text{ \AA}$, $c = 134.6 \text{ \AA}$. The most probable V_M -value is $2.24 \text{ \AA}^3/\text{Da}$ corresponding to a dimer in the asymmetric unit and a solvent content of 45 %.

Fig. 1: $P2_12_12_1$ crystals of LAO



(b) The crystals belong to the orthorhombic spacegroup $C222_1$ with lattice parameters of $a = 68.3 \text{ \AA}$, $b = 88.4 \text{ \AA}$, $c = 186.6 \text{ \AA}$. The asymmetric unit contains a monomer with a solvent content of 52 %.

Fig. 2: $C222_1$ crystals of LAO

The LAO from *Rhodococcus opacus* could not be heterologously expressed in *E. coli* in the active form. For *Streptomyces* which is used as an alternative heterologous expression system there are no methionine auxotrophic strains available to obtain seleno-methionine derivatives of the protein. Therefore it is necessary to do heavy atom derivative soaking of the native crystals to obtain the phase information.

A couple of derivatization reagents were tested with different concentrations and soak times. The derivatization of crystals in the crystallization buffer containing 10mM HgCl_2 for 24 hours leads to a

reproducible set of four Hg- sites in the dimer identified by a different Patterson function of derivative and native data.

Therefore a MAD experiment was done at the BL-2 beamline at the Protein Structure Factory (PSF). The peak, inflection and remote wavelengths as well as the concerning scattering factors were determined from a fluorescence scan of one P2₁2₁2₁ crystal.

So far the LAO structure could not be solved with these data, possibly because of the weak occupancy of the mercury-sites (5-12%). We are now forging the optimization of this derivatization condition to find crystals suitable for another MAD or SAD experiment.

The data statistics of the three data sets taken at the BL2 at the PSF are shown in the table below:

	peak	inflection	remote	peak	inflection
Wavelength	1.0086	1.00952	0.9311	1.0086	1.00952
Energy (eV)	12291.89	12281.64	13315.79	12291.89	12281.64
resolution range	100-2.25	100-2.25	100-2.25	100-2.25	100-2.0
Rsym	7.7 (10.4)	7.7 (10.4)	8.4 (12.2)	6.9 (9.5)	6.9 (14.4)
Multiplicity	14.3 (9.5)	7.9 (7.1)	8.2 (8.1)	6.8 (6.1)	8.4 (2.9)
Completeness	98.9 (89.2)	98.4 (97.3)	100 (100)	96.6 (94.6)	100 (25)

Table1: data statistics of the MAD data set of the Hg-derivative of LAO

References:

[1] Geueke, B.; Hummel, W.; 'Heterologous expression of *Rhodococcus opacus* L-Amino acid oxidase in *Streptomyces lividans*'; Protein Expr. Purif.; 2003 Apr.; 28 (2): 303-9.

On the evolutionary origin of the manganese complex of oxygenic photosynthesis: possible formation of a bicarbonate precursor complex

Peter Liebisch¹, Marcos Barra¹, Markus Grabolle¹, Claudia Müller¹
Alexej Erko², Holger Dau¹

¹*Institut für Experimentalphysik, Freie Universität Berlin, Arnimallee 14, 14195 Berlin*
²*BESSY GmbH, Albert-Einstein-Strasse 15, 12489 Berlin*

Oxygenic photosynthesis is well known to produce the atmospheric oxygen and to be the major primary energy source for life on Earth. The oxygen-evolving complex (OEC) of photosystem II, which is the protein complex responsible for conversion of light energy into reducing equivalents, consists of a four-manganese cluster that functions as the catalyst for water splitting and formation of molecular oxygen. Structure and function of the OEC are subject of intense research; BioXAS has played a particularly prominent role in the worldwide efforts to understand photosynthetic water oxidation at atomic level.¹⁻³ Recently hypotheses on the evolutionary origin of the OEC have been published.^{4,5} The first of these hypothesis involves that during early evolution of oxygenic photosynthesis, 2.5 billion years ago, the level of atmospheric CO₂ was considerably higher than it is now and that the bicarbonate dissolved in the ancient ocean formed complexes with free Mn²⁺ to become an OEC-precursor.

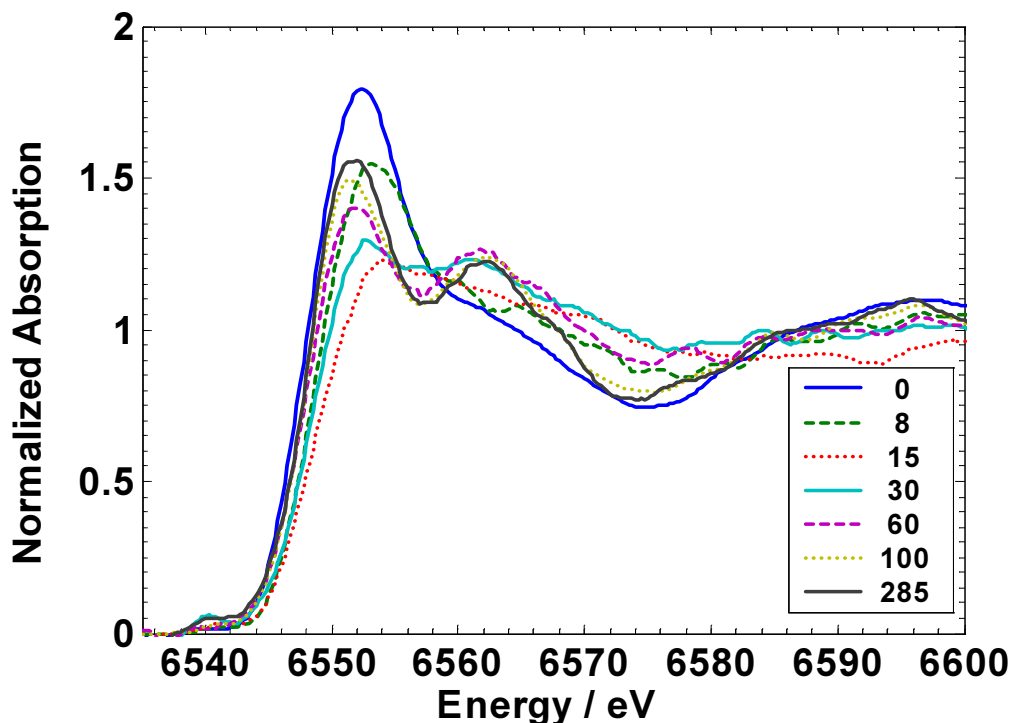


Figure 1. XANES spectra of a 250 μM Mn^{2+} -solution titrated with different NaCO_3 concentrations. The values given in the legend indicate bicarbonate concentrations in mM.

While the bicarbonate concentration-dependent two-step reduction of a Mn^{2+} -solution has been characterized electrochemically and by EPR⁴, we made an attempt to gain structural information using XAS.

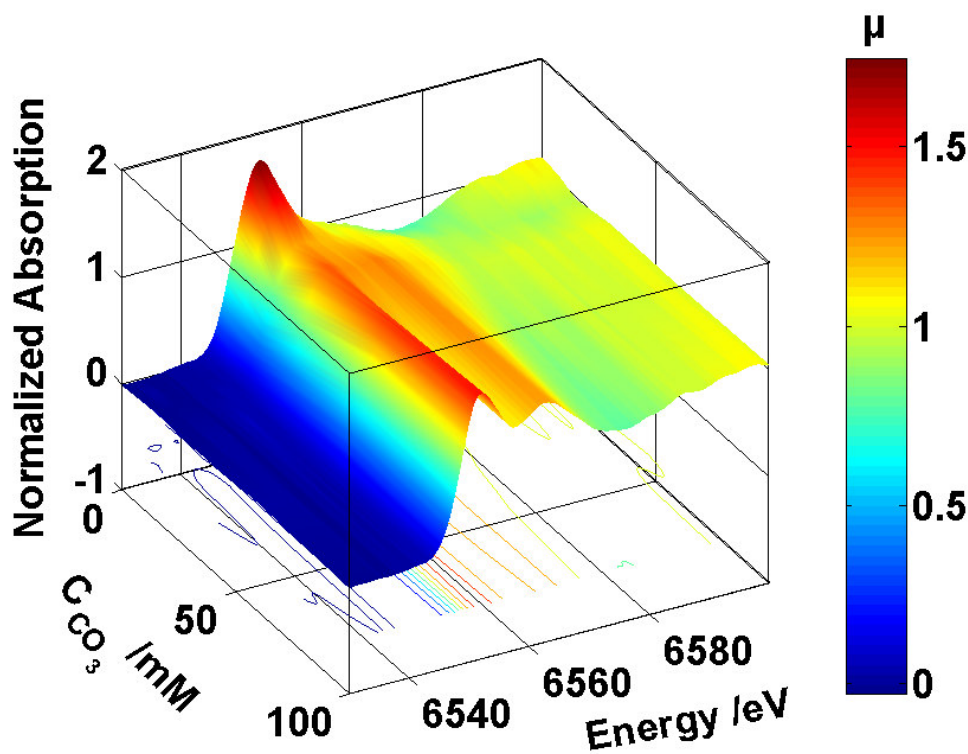


Figure 2. 3D-representation of the XANES spectra shown in Figure 1.

A glycerol-water solution containing 250 μM MnSO_4 was titrated with NaHCO_3 up to a maximum concentration of 300 mM and the EPR results of Dismukes et al.⁴ were reproduced. For seven selected concentrations, XAS spectra were collected at the bending-magnet beamline KMC-2 at room temperature at the Mn K-edge. Although the experiment was performed in fluorescence detection mode with an energy-resolving detector (RÖNTEC GmbH, Berlin), the low Mn concentration renders the experiment challenging. Figure 1 shows the XANES spectra for six different bicarbonate concentrations and a pure Mn^{2+} solution.

Starting with the Mn-hexaaquo spectrum with a pronounced edge peak at 6552 eV, the edge peak reduces in intensity up to a bicarbonate concentration of about 15 mM and then again rises. At the same time a second pronounced peak develops at around 6562 eV, as clearly visible in Figure 2.

Due to the low manganese concentration the quality of the EXAFS data is still insufficient so that a detailed structural analysis requires further measurements. However significant information can be derived from the XANES as well:

1. The bicarbonate titration causes significant structural changes.
2. The decrease of the edge peak at about 15 mM bicarbonate indicates loss of the symmetrical octahedral coordination of the hexaaquo complex.
3. The rise of a second peak indicates formation of a structure with higher long-range order than in the free ion with its disordered hydration shell.
4. The oxidation state of Mn(II) does not change during the titration.
5. The spectra represent a superposition of (at least) three different species of spectra, a finding which is inline with the interpretation of electrochemical data⁴.

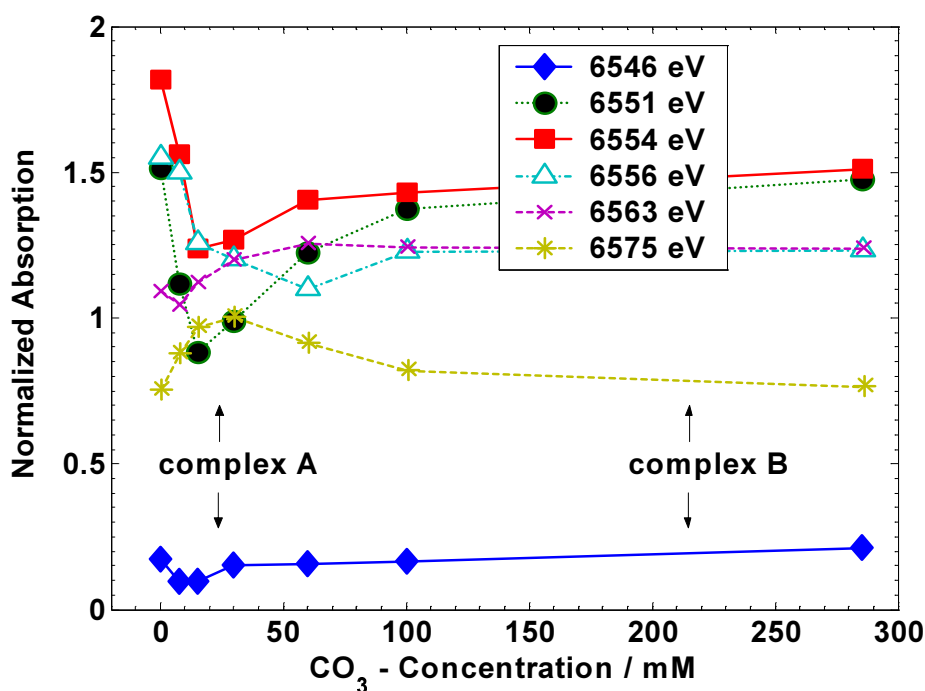


Figure 3. Normalized x-ray absorption at selected excitation energies as a function of bicarbonate concentration. At least three different chemical species are necessary to produce such a dependence.

To illustrate point 5., Figure 3 shows a plot of the X-ray absorption at selected energies as a function of the bicarbonate concentration. Each line represents the concentration dependence of a distinct spectral feature. The bicarbonate-concentration dependence is clearly biphasic indicating that two different manganese complexes (complex A and complex B) are formed in the course of the titration. Continuation of these promising experiments will involve structural characterization of complex A and complex B by EXAFS spectroscopy.

Acknowledgements

This work was supported by the DFG within the SFB 498 (project C6) and by the BMBF (grant 05/KS1KEA-6). We thank Drs. P. Tian and J. Pushkar of the Group of Prof. Stehlik at the FU Berlin for their help with the EPR measurements.

References

1. Dau, H.; Iuzzolino, L.; Dittmer, J., *Biochim. Biophys. Acta* **2001**, 1503, 24-39.
2. Dau, H.; Haumann, M., *J. Sync. Rad.* **2003**, 10, 76-85.
3. Dau, H.; Liebisch, P.; Haumann, M., *Anal. Bioanal. Chem.* **2003**, 376, (5), 562-583.
4. Dismukes, G. C.; Klimov, V. V.; Baranov, S. V.; Kozlov, Y. N.; DasGupta, J.; Tyryshkin, A., *Proc. Natl. Acad. Sci. USA* **2001**, 98, (5), 2170-2175.
5. Sauer, K.; Yachandra, V. K., *Proc. Natl. Acad. Sci. USA* **2002**, 99, 8631-8636.

Microfocus XAS measurements on volcano-shaped manganese deposits at the cell-wall of the green alga *Chara corallina*

Peter Liebisch¹, Claudia Müller¹, Christoph Plieth², Alexej Erko³, Holger Dau¹

¹*Institut für Experimentalphysik, Freie Universität Berlin, Arnimallee 14, 14195 Berlin*

²*Christian-Albrechts-Universität Am Botanischen Garten 5-9, 24118 Kiel*

³*BESSY GmbH, Albert-Einstein-Strasse 15, 12489 Berlin*

While it is well known that manganese is an essential trace element in plants and crucial for photosynthetic oxygen evolution¹ as well as for other enzymatic reactions, manganese toxicity has long been recognized as a factor limiting growth when organisms are exposed to high concentrations of Mn. Presumably related to a detoxification mechanism cells of the green alga *Chara corallina* develop brown deposits on the outer cell wall when cultured in alkaline water with a Mn-containing sediment.

To address the questions of spatial distribution and chemical speciation of relevant elements we performed microfocus XAS experiments. Elemental 2D-mapping by means of characteristic X-ray fluorescence as well as X-ray absorption measurements on selected spots on the cell wall were carried out successfully.

The measurements were carried out at the bending-magnet beamline KMC-2 using a single

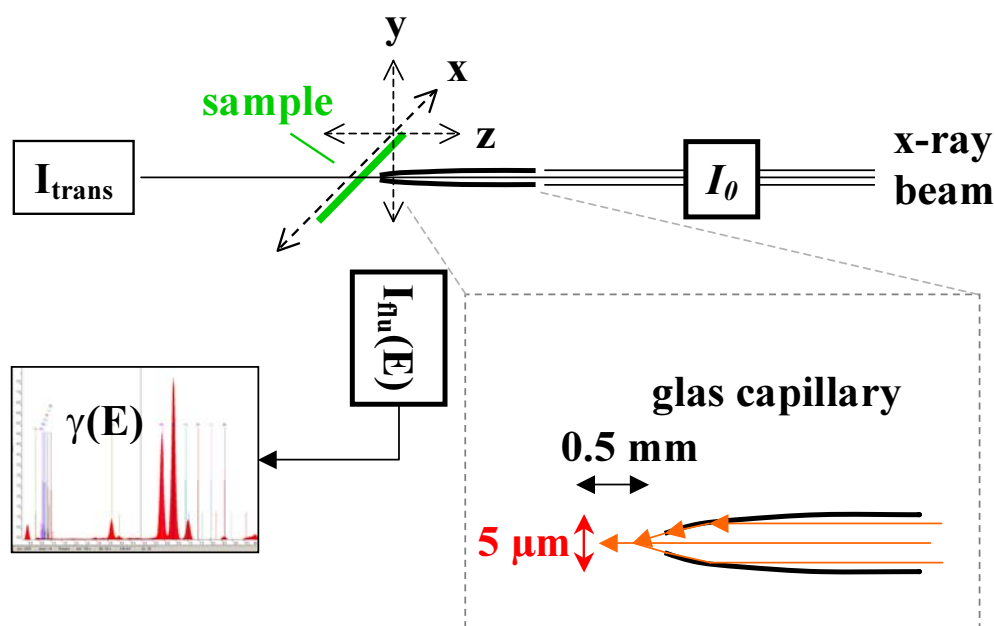


Figure 1. Experimental setup for micro-focus XAS experiment on KMC-2 at BESSY. For details see text.

crystal monochromator and an energy-resolving solid state detector (RÖNTEC GmbH, Berlin). The incident x-ray beam (preshaped by slits) was focused on the sample using either a focussing (a) monocapillary or (b) polycapillary. While (a) allowed a maximum spatial resolution of below 5 μm , (b) was the device of choice for local XAS measurements where a compromise between high flux and acceptable spatial resolution had to be found.

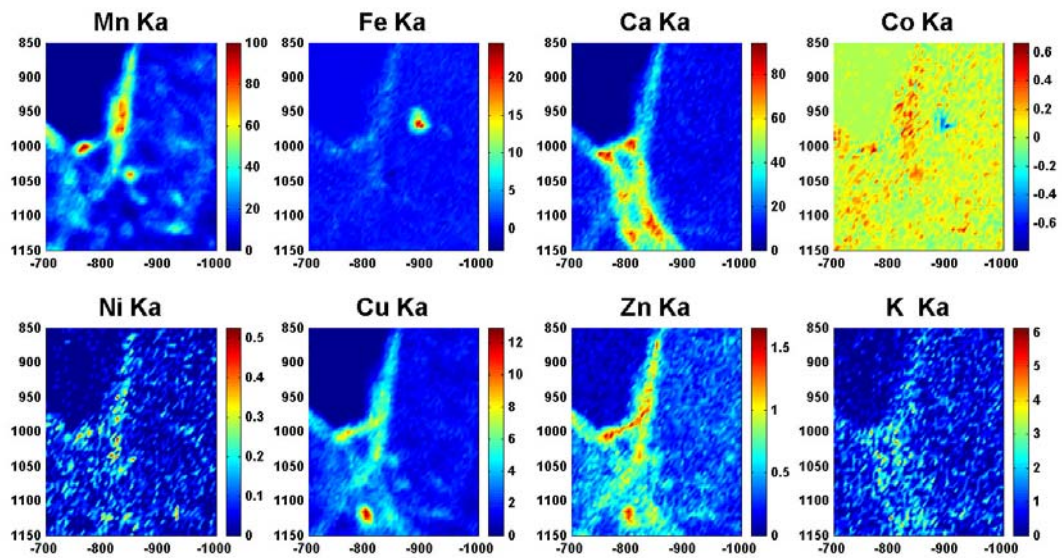


Figure 2. 2D-map of alga cell wall for different elements. The x- and y-dimensions are given in μm and the intensity represents the number of counts for each characteristic fluorescence line normalized to the maximum of Mn- $\text{K}\alpha$ counts and weighted by a calibration factor obtained for a stoichiometric standard.

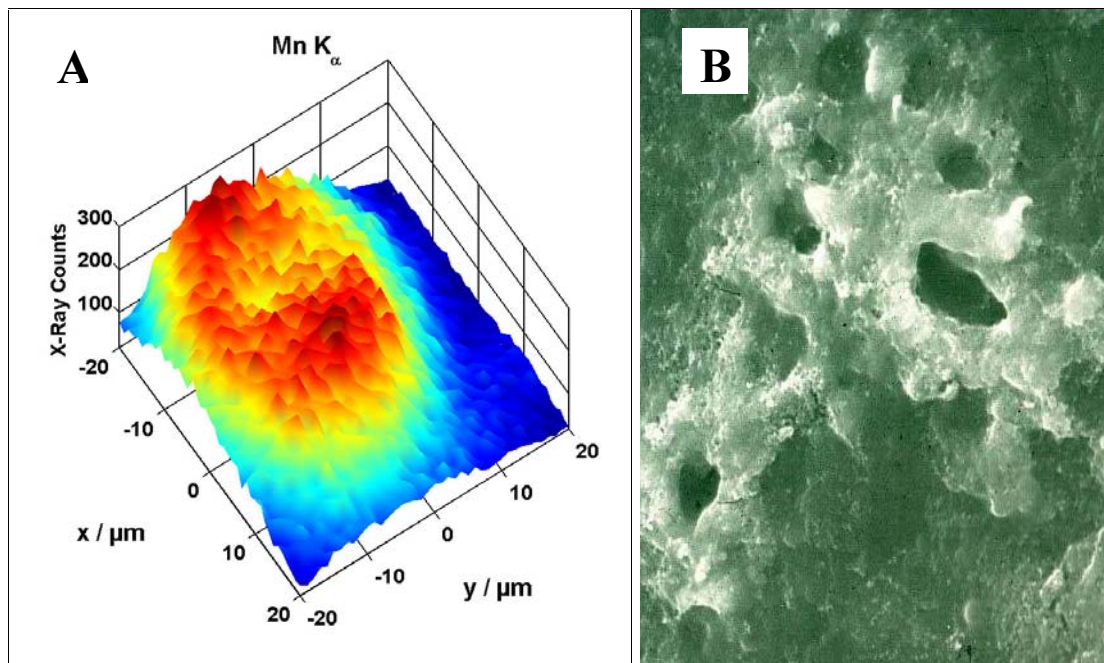


Figure 3. Crater structure on alga cell surface. (A) 2D-map of Mn $\text{K}\alpha$ fluorescence (B) electron microscopy (EM) image. Mn is predominantly found in such crater or volcano-like structures. While their existence and shape was known from EM images their element content can be mapped by microfocus XAS mapping. The resolution is high enough to resolve the crater structure, i.e. as good as $5\ \mu\text{m}$.

For data collection two types of samples were used: (1) Cell walls of unicellular alga placed between $25\ \mu\text{m}$ layers of cellophane and dried. Those samples were particularly flat and easy

to handle. (2) Fresh alga cells were cut and placed between two stretched 12.5 μm layers of Kapton foil immediately before the measurements. In contrast to (1), those samples remained wet and thus “chemically intact” for about 8 hours.

For selected elements (Mn, Fe, Ca, Co, Ni, Cu, Zn, K) the intensity of their characteristic x-ray fluorescence lines was measured across a 2D-mesh. The data was normalized and weighted according to factors gained from standard measurements with a sample of known element stoichiometry. For Fe and Co the K_{α} intensity was further corrected for contributions of Mn- K_{β} and Fe- K_{β} respectively. While Figure 2 shows a representative map for all measured elements, Figure 3 shows a Mn- K_{α} map of a crater structure on the cell surface. Those structures are of special interest in the light of Mn-sedimentation and detoxification strategies of cells. Detailed analysis of the element composition of the deposits is in progress. For selected spots on typical Mn-containing deposits, XAS measurements were performed with the polycapillary. Figure 4 shows XANES spectra of the Mn K-edge for a dried and a

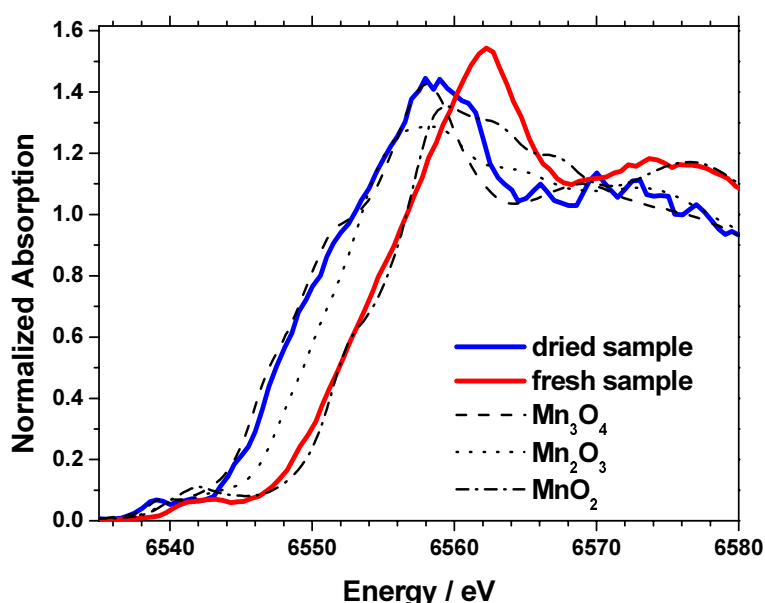


Figure 4 XAS measurement on Mn-containing spot. By comparison with reference substances, determination of the Mn oxidation state and eventually detailed chemical speciation can be achieved.

freshly prepared sample. As a first step of the chemical speciation, alga data is compared with reference spectra measured for known Mn oxides. Clearly one can assign the intact bio-sediment to a form of MnO_2 with an oxidation state of IV. The preliminary analysis of the elemental mapping suggests a Mn:Ca stoichiometry of 5:1. The analysis of microfocus EXAFS measurements (not shown) may lead to a structural model of these biogenic manganese deposits at the atomic level.

References

1. Dau, H.; Liebisch, P.; Haumann, M., *Anal. Bioanal. Chem.* **2003**, 376, (5), 562-583.
2. Hem, J. D.; Lind, C. J., *Geochimica et Cosmochimica Acta* **1994**, 58, (6), 1601-1613.
3. Morel, F. M. M.; Price, N. M., *Science* **2003**, 300, 944-947.

Characterisation of the UVIS Experimental Station for Circular Dichroism Spectroscopy and First Spectra of Standard Proteins

Peter Baumgärtel¹, Gerd Reichardt², Markus Sauerborn², Benjamin Schuler¹,

Monika Walter¹, Jan Lengefeld¹, Antje Emmerich¹, Robert Seckler¹

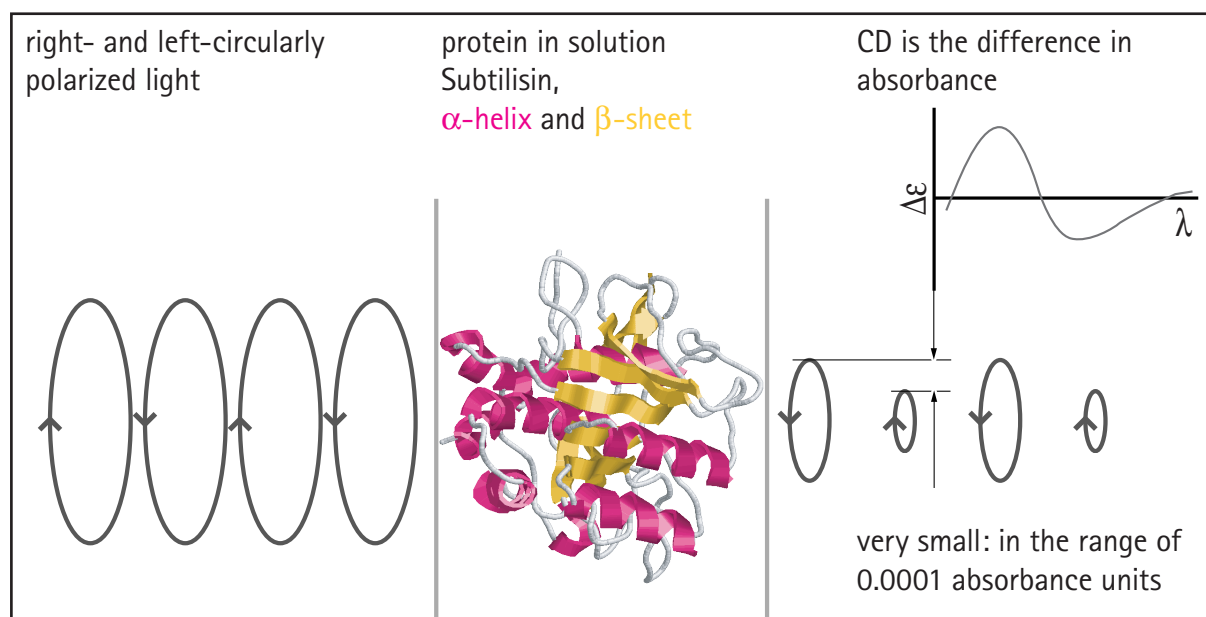
¹ Universität Potsdam, Physikalische Biochemie; ² BESSY GmbH

Circular dichroism spectroscopy on proteins

Circular dichroism spectroscopy (CD) is a form of light absorption spectroscopy that measures the difference in absorbance of right- and left-circularly polarized light by a substance. It has been shown that CD spectra can be analyzed for the different secondary structural types of proteins: alpha helix, parallel and antiparallel beta sheet, turn, and other (see box below). CD spectra of proteins arise from electronic transitions between ground and excited states of molecular orbitals. The most significant chromophore is the amide group of the polypeptide backbone. Secondary structures impose positional and intensity constraints on these transitions, and give rise to characteristic far-UV spectra (Wallace 2001). A very important requirement for successful secondary structure analysis is that the CD spectra need to be recorded from about 260 nm to at least 178 nm and preferable below (Johnson, 1990). Synchrotron light is the ideal light source for increasing this range. (Sutherland 1996). In addition, synchrotron light has an excellent beam characteristic regarding the polarisation and the spot size, which is essential for time resolved CD experiments.

Method of CD

A photoelastic modulator (PEM) generates left and right circular polarized light from the linear polarized synchrotron light at a fixed frequency. The principle of operation of the PEM is based on the photoelastic effect, in which a mechanically stressed sample exhibits birefringence proportional to the resulting strain. We use a PEM from Hinds Instruments with a CaF_2 optical element, which is stressed in a frequency of 50 kHz and the peak retardation from the birefringence corresponds to a quarter of the wavelength. The oscillating left and right circular polarized light shows after passing a protein solution slight differences in its amplitude depending on the protein secondary structure and wavelength. Only a lock-in system coupled to the frequency of the PEM and combined with a photomultiplier as detector can amplify this small dichroism.



Experimental station and characterisation

The experimental station was set up at the 3m-NIM Monochromator at beamline 12.1B (Reichardt 2001). The design of our set up basically follows that of Sutherland (Sutherland 1996). In addition, we use a polarizer in front of the photoelastic modulator for increasing and stabilizing the linear polarization. The absolute photon flux was measured and compared with simulations as it is highly connected to the performance of the experiment (see Fig. 1). The successful measurement of a CD-spectrum of (1S)- β -Camphor-10-sulfonic acid (CSA) (see Fig. 2) with its well defined peaks ratio validates the correct working of the experiment (Johnson 1996).

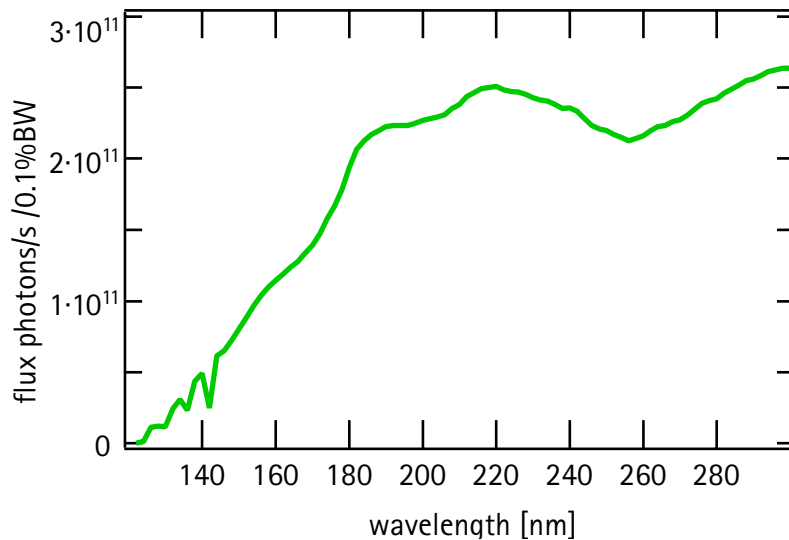


Fig. 1: Photonflux at the sample, measured with a GaAsP photodiode

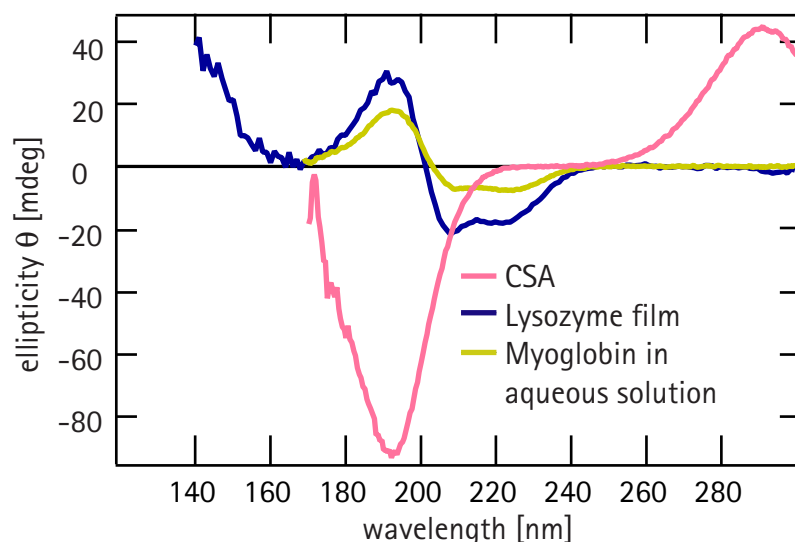
The intensity distribution mainly reflects the spectral properties of the optical components of the beamline (mirrors and grating). At lower wavelength optical instruments of the experimental setup and the purging gas nitrogen additionally diminish the photonflux. At 125 nm the CaF_2 window of the photoelastic modulator cuts off the flux. Up to 145 nm nitrogen absorption peaks are visible.

First studies on proteins in aqueous solution and protein films

One of our aims is to generate a database of CD-spectra of proteins. For this we are investigating standard proteins with known secondary structure and characterised by a well defined preparation. Using standard proteins we plan to establish a method to study proteins in aqueous solution

Fig. 2: CD spectra of CSA, Myoglobin solved in water and "dried" Lysozyme film

The ratio of the two peaks at 192.5 and 290.5 nm in the CD-spectrum of CSA should be about -2.0. In our measurements we found a ratio of $\theta_{192.5}/\theta_{290.5} = -2.06 \pm 0.09$. The depletion of water in the "dried" Lysozyme film allows for measurements down to shorter wavelength.



and additionally in „dried“ films (McPhie 2001). The latter method has the advantage not to be limited by the strong absorbance of H₂O at wavelength lower than 170 nm, but the integrity of the structure in the water depleted environment has to be investigated. (see Fig. 2. and Fig. 3). In combination both spectra of one protein will give us over the whole available wavelength range a reliable molar CD-signal (e. g. molar ellipticity). Further developments aim for time resolved CD-studies with a stopped-flow and continuous-flow cell and to start a regular user operation.

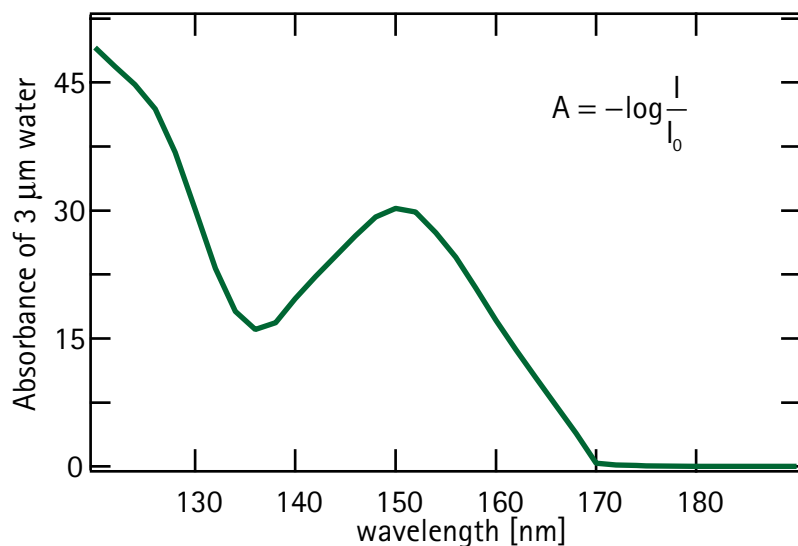


Fig. 3: Absorbance of water in the case of a aqueous solution in a "squish" cell

The shortest path length of 4 μm is achieved by pressing a high concentrated protein solution between two slips (Sutherland 1996). From the used concentration of the aqueous solution in such a "squish" cell we estimated the pathlength of H₂O to 3 μm the other part is filled out by the proteins. The absorbance of H₂O with this pathlength is shown in the diagram (Segelstein 1981). The strong absorbance of H₂O starting below 170 nm limits our spectra of proteins in aqueous solution. Even dramatically increased intensity will not help to overcome this limit.

References

Johnson WC jr., Proteins 7, 205 (1990); **Johnson** WC jr., in Circular Dichroism and the Conformational Analysis of Biomolecules, edited by Fasman GD, Plenum Press, 648 (1996); **McPhie** P, Analytical Biochemistry 293, 109 (2001); **Segelstein** <http://omlc.ogi.edu/spectra/water/data/segelstein81.dat> (1981); **Sutherland** JC, in Circular Dichroism and the Conformational Analysis of Biomolecules, edited by Fasman GD, Plenum Press, 599 (1996); **Reichardt** G et al., NIM A 467-468, 458 (2001); **Wallace** BA, Janes RW, Current Opinion in Chemical Biology 5, 567 (2001);

The project was initiated by the „UV/Vis Initiative Synchrotronstrahlung“ (UVIS).

The authors are pleased to acknowledge the financial support of the project by the German Federal Ministry of Education and Research (BMBF) under Contract 05 KS1IP1/1.

Crystal structure of amphomycin antibiotics

G. Bunkóczy¹, L. Vértesy² and G. M. Sheldrick¹

¹Lehrstuhl für Strukturchemie, Georg-August Universität, Tammannstr 4, 37077 Göttingen

²Aventis Pharma Deutschland GmbH, 65926 Frankfurt am Main

As a result of the spread of antibiotic resistance in antibacterial chemotherapy, novel agents are now urgently needed¹. Infections caused by multiresistant pathogens that cannot be adequately treated with existing drugs constitute a particularly acute problem. Antibiotics are thus required that develop their antibacterial action by a novel mechanism and are well tolerated by the human body.

An appropriate point of attack for therapeutically useful antibiotics is the synthesis of the bacterial cell wall. The acidic lipopeptide amphomycin² is a specific inhibitor of peptidoglycan synthesis³ and inhibits phospho-MurNAc-pentapeptide transferase, which catalyses the first step of the lipid cycle during murein biosynthesis. As none of the antibiotics in current medical use have this step as their site of action, amphomycin represents a highly promising starting point for the discovery of new treatment principles. Interestingly, these acidic lipopeptides are only inadequately described in the literature. Though several antibiotics belonging to the same group were isolated in addition to amphomycin, the mostly complex mixtures of antibiotics have not been separated into individual compounds, nor their chemical structures have been unambiguously clarified. It is therefore no surprise that the usefulness of acidic lipopeptide antibiotics in the treatment of bacterial infections has not yet been conclusively assessed.

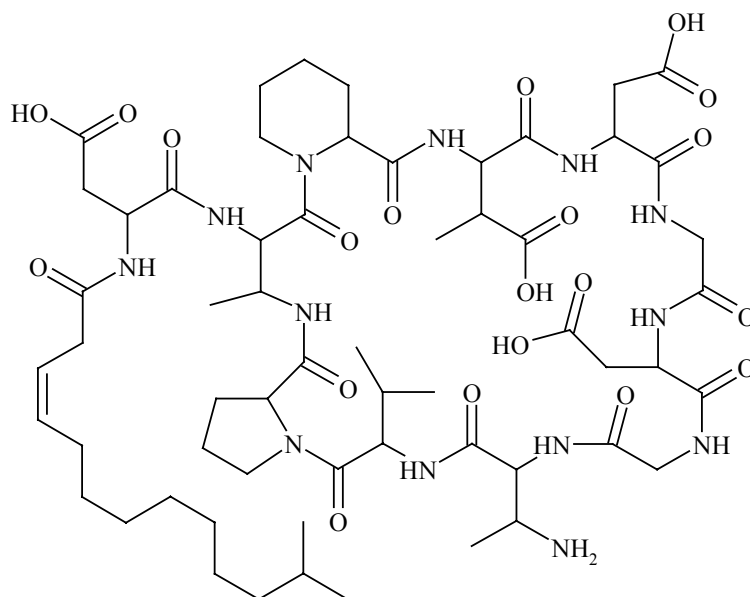


Figure 1. Chemical structure of the amphomycin antibiotic A 1437 B.

The amphomycin-related antibiotic A 1437 B has been crystallised using the hanging drop technique and thin plate crystals were obtained within a month. The crystals were mounted with a loop and shock-frozen in a cold nitrogen stream. Data were collected on the BL1 beamline at BESSY to 1 Å resolution. The data collection was complicated by the low crystal symmetry (P1,

$a=33.49 \text{ \AA}$, $b=36.38 \text{ \AA}$, $c=37.52 \text{ \AA}$, $\alpha=65.6^\circ$, $\beta=68.3^\circ$, $\gamma=69.9^\circ$) and the significant radiation damage that occurred to the crystal. To overcome these problems, the crystal was mounted on a goniometer head that allowed an angular offset to 15° in two directions. Data sets with an angular range of 90° were collected consecutively and were occasionally re-centred to irradiate new volumes in the crystal that had not decomposed yet. The resulting frames were processed using XDS to give 96.2% completeness (mean redundancy 4.50, $R_{\text{int}}=10.39\%$, $\langle I/\sigma \rangle=9.49$).

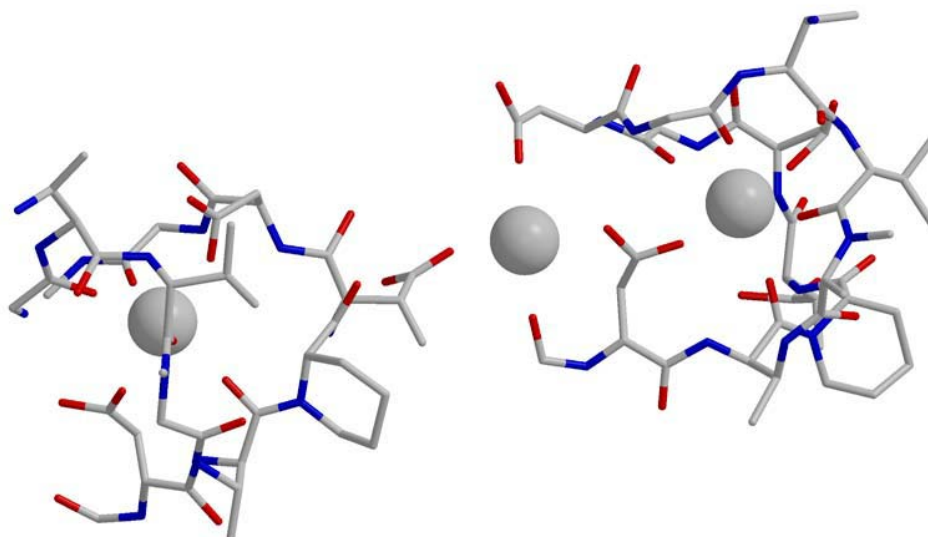


Figure 2. Calcium binding by A 1437 B.

The structure was solved surprisingly easily with *ab initio* direct methods using SHELXD. Although the asymmetric unit is larger than that of lysozyme and the number of atoms is well over a thousand, probably the relatively high calcium-content (2 per 10 amino acid residues) helped SHELXD to achieve a high success rate and to give a virtually complete structure. The structure is, however, not sufficiently refined, but current results seem to confirm the chemical structure assignment by Vértesy *et al.*⁴ (Figure 1).

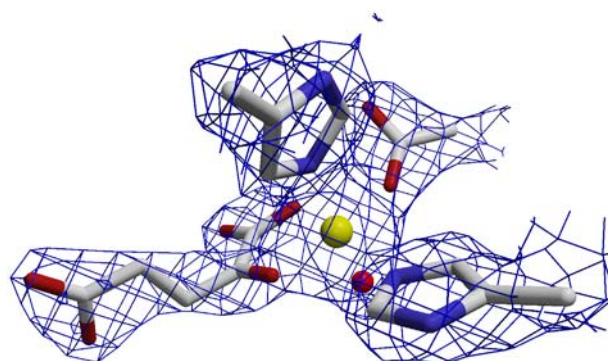
1. Neu, H. C. (1992). The crisis in antibiotic resistance. *Science* **257**, 1064-1073.
2. Heinemann, B., Kaplan, M. A., Muir, R. D. & Hooper, I. R. (1953). Amphomycin, a new antibiotic. *Antibiot. Chemother.* **3**, 1239-1242.
3. Tanaka H., Iwai Y., Oiwa R., Shinohara, S., Shimizu, S., Oka, T. & Omura, S. (1977). Studies on bacterial cell wall inhibitors. II. Inhibition of peptidoglycan synthesis in vivo and in vitro by amphomycin. *Biochim. Biophys. Acta* **497**, 633-640.
4. Vértesy, L., Ehlers, E., Kogler, H., Kurz, M., Meiwes, J., Seibert, G., Vogel, M. & Hammann P. (2000). Friulimycins: novel lipopeptide antibiotics with peptidoglycan synthesis inhibiting activity from *Actinoplanes friuliensis* sp. nov. *J. Antibiot.* **53**, 816-827.

Ligand Complexes of the Alkylsulfatase AtsK

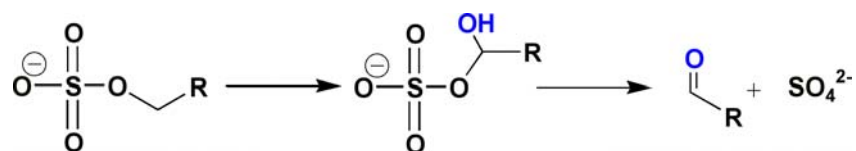
I. Müller and I. Usón

Lehrstuhl für Strukturchemie, University Göttingen, Tammannstr. 4, 37077 Göttingen, Germany

The alkylsulfatase AtsK from *Pseudomonas putida* S-313 catalyzes the oxygenolytic release of inorganic sulfate from a range of different aliphatic sulfate esters, in order to provide the strain with the sulfur it requires for growth in sulfate-limited conditions (1). The enzyme decarboxylates one molecule of α -ketoglutarate (α KG) into succinate per molecule of sulfate ester that is cleaved, and is hence a member of the family of non-heme iron(II) α KG dependent dioxygenases. Members of this remarkable enzyme family bind iron using a 2-His-1-carboxylate facial triad, a feature that is one of nature's recurring multifunctional bioinorganic motifs (like the heme group or iron sulfur clusters) (3).



AtsK is a very flexible enzyme, as it will desulfate a broad spectrum of linear and branched chain sulfate esters. AtsK cleaves alkylsulfate esters to yield the corresponding aldehyde and sulfate, and the initial hydroxylation in the cleavage reaction occurs at the non-activated carbon atom adjacent to the sulfate ester group.



The aim of the project is to compare the crystal structures of the enzyme bound to substrate iron, α KG or succinate to propose a general catalytic mechanism of this enzyme class which is still subject to considerable controversy.

The crystals of the ligand complexes were either obtained by co-crystallization or by soaking. We collected five datasets on different complexes of AtsK at BL2 at the Protein Structure Factory c/o BESSY. Crystallographic data is given in Table I. The structures were solved by molecular replacement with the structure of the *apo*-enzyme as a search model (2).

Table I Summary of crystallographic data.

	Na- α KG-AtsK-Complex	Na-Succinat-AtsK-Complex	Na- α KG-hexylsulfat-AtsK-Complex	Na-Succinat-AtsK-Complex	Fe-Succinat-AtsK-Complex
Cell [Å]	a=72.45	a=72.51	a=72.27	a=71.05	a=71.84
$\alpha = \beta = \gamma = 90^\circ$	b=145.68	b=145.82	b=143.27	b=142.83	b=140.97
	c=159.34	c=158.788	c=160.73	c=157.87	c=160.34
Beamline	BL2	BL2	BL2	BL2	BL2
Space group	$P2_12_12_1$	$P2_12_12_1$	$I2_12_12_1$	$P2_12_12_1$	$I2_12_12_1$
Resolution [Å]	29-1.8	25-2.0	25-2.7	20-2.1	20-2.0
No. observed Reflections	387421	628292	111490	434735	277978
No. independent Reflections	146181	92306	23225	89022	55198
Completeness %					
overall:	93.2	100	100	91.8	99.3
outer shell:	87.6 (1.8-1.9)	100 (2.0-2.1)	99.8 (2.8-2.7)	90.6 (2.1-2.2)	95.1 (2.1-2.0)
R_{merge}					
overall:	0.071	0.066	0.055	0.068	0.11
outer shell:	0.33	0.27	0.45	0.37	0.45
mean $I/\sigma(I)$					
overall:	12.4	10.7	12.4	18.0	16.4
outer shell:	3.4	3.6	2.5	3.1	2.7

¹ Kahnert, A. and Kertesz, M. A., (2000), Characterization of a sulfur-regulated oxygenative alkylsulfatase from *Pseudomonas putida* S-313. *J. Biol. Chem.* 275, 31661–31667.

² Schofield, C.J., Zhang, Z. (1999) Structural and mechanistic studies on 2-oxoglutarate-dependent oxygenases and related enzymes. *Current opinion in Structural Biology* 9, 772-731.

³ Müller, I., Kahnert, A., Pape, T., Sheldrick, G.M., Meyer-Klauke, W., Dierks, T., Kertesz, M. and Usón, I. Crystal structure of the alkylsulfatase AtsK: Insights into the catalytic mechanism of the Fe(II) α -ketoglutarate dependent dioxygenase superfamily, submitted.

Structure of complexes between Echinomycin and DNAs

Jose Antonio Cuesta-Seijo and George M. Sheldrick.

Institut fuer Anorganische Chemie, Tammannstrasse 4, Georg August Universitaet, Goettingen.

High and low resolution datasets were collected between 11-12-2003 and 12-12-2003 at the PSF (MARCCD detector) for the complexes between 3 different short duplex DNAs and echinomycin, one of them in two different crystal forms. The datasets are still being processed.

This work is funded by the SFB 416 project.

Structure of polyalanyl PNAs and chemical derivatives

Jose Antonio Cuesta-Seijo and George M. Sheldrick.

Institut fuer Anorganische Chemie, Tammannstrasse 4, Georg August Universitaet, Goettingen.

High and low resolution datasets were collected between 11-12-2003 and 12-12-2003 at the PSF (MARCCD detector) for 3 different crystal forms of a synthetic alanyl-homoalanyl nucleic acid. A fourth dataset from a Sodium Iodide derivative of one of them was also collected. The datasets are still being processed.

within the research project “**Structural characterisation of the enzymatic machinery for the desulfonation of arylsulfonates in *Pseudomonas putida* S-313**”

Crystal structure of SsuF

Ana Mirela Neculai, Dante Neculai, Isabel Usón Finkenzeller and George M. Sheldrick

Lehrstuhl für Stukturchemie, Institut für Anorganische Chemie, Universität Goettingen, Tammannstrasse 4, D-37077, Göttingen, Germany.

Arylsulfonates in aquifers are of particular environmental concern as they are used (e.g. detergents, dyestuffs) and released in significant quantities. Their microbiological degradation is best characterised in *Pseudomonas putida* S-313.

Central to the desulfonating reactions is the monooxygenase SsuD which needs at least four additional proteins - AsfAB (reductase and 2[4Fe-4S]-ferredoxin), SsuE (NADH:FMN oxidoreductase) and SsuF (function unknown).

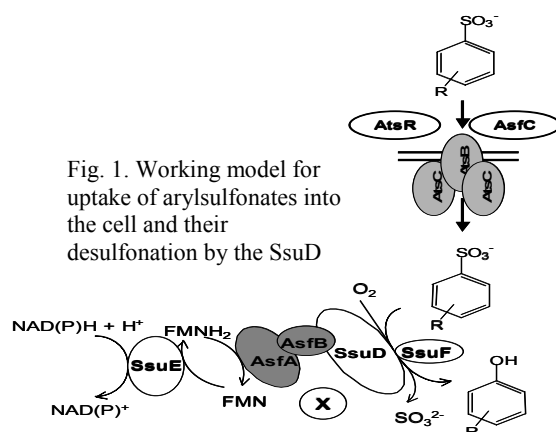


Fig. 1. Working model for uptake of arylsulfonates into the cell and their desulfonation by the SsuD

Figure 1 shows the postulated working model for arylsulfonate desulfonation in *P. putida* S-313, which remains to be substantiated (or refuted) by the structural and biochemical studies underway. NADPH serves as an electron source for the reduction of FMN by SsuE, and these reducing equivalents are passed via AsfAB to the oxygenase SsuD. SsuF may play a role in stabilising sulfur equivalents for transfer to the cysteine biosynthetic pathway. SsuF is a small protein (71 amino acids, 7.6 kDa) strongly upregulated during growth in the absence of sulfate, essential for growth with sulfate esters and sulfonates. Its function remains unknown. Sequence alignment (Figure 2) suggests it is related to a molybdopterin-binding protein, yet molybdenum starvation has no effect on growth.

Figure 2: The sequence of SsuF

MTIKAINVRNQFKGTVKEILEGPVLSEIDVQTASGIVTSVITTRS VKE LELQVGSEVIAF
VKSTEVSI AKLMSISARNQLKKGKVVGLKKGVVTA EVVLEIAGGNKITSIISLDSVEELG
VKEGAELTAVVKSTDVMILA

Needle-like crystals of SsuF were grown by the hanging drop method from H₂O/PEG/(NH₄)₂SO₄ mixtures at pH 4.6 (acetate buffer) (Figure 3).

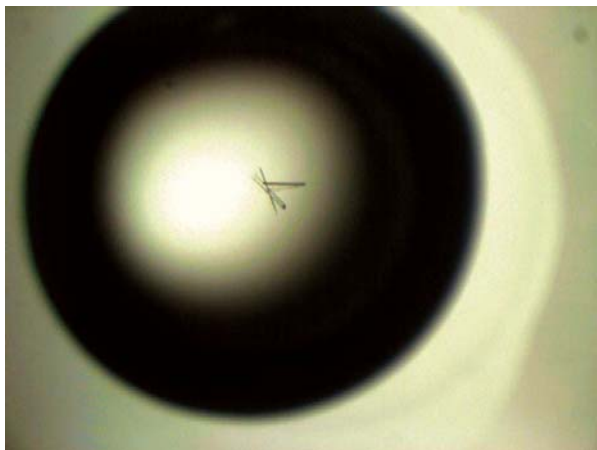


Fig. 3. SsuF crystals.

Data were collected between 11-12-2003 and 12-12-2003 at the PSF, at the BL2 fitted with a MAR 345 Image Plate detector at 100K using 15% glycerol as cryoprotectant using a wavelength of 0.8976 Å. Data from a single detector distance of 200 mm were processed with HKL2000 (completeness 99.4%, mean redundancy 4.7, $\langle I/\sigma \rangle$ 7.4) to a resolution of 2.55 Å. The structure was solved by molecular replacement (using the program EPMR) with the structure of MopII molybdenum from *Clostridium pasteurianum* (PDB ID 1GUN)^[1] as search model. The crystals were monoclinic, space group *C*2, $a = 141.540$, $b = 70.580$, $c = 87.390$, $\beta = 116.61$. One asymmetric unit contains 9 monomers, 1 hexamer and 1 trimer which is related to another trimer from the neighbour asymmetric unit through a crystallographic 2-fold axis. The solvent content is 51%. The refinement of the structure is still in progress using CNS, REFMAC and SHELXE for density modifications.

^[1] Schuttelkopf, AW; Harrison, JA; Boxer, DH; Hunter, WN "Passive acquisition of ligand by the MopII molybdenum from *Clostridium pasteurianum*: structures of apo and oxyanion-bound forms", *J. Biol. Chem.* 2002,277,15013-20.

The BESSY CD-Spectroscopy Beamline to Study the Domain Movement of 5'-Nucleotidase

Robert Schultz-Heienbrok, Timm Maier, Norbert Sträter

Introduction. 5'-nucleotidase (5'-NT) is a bacterial enzyme that hydrolyses a variety of nucleotides in the bacterial periplasm (Neu, 1967). Structural analysis revealed that the monomeric protein consists of a larger N-terminal domain and a smaller C-terminal domain that can rotate relative to each other with a maximum rotation of 96° around an axis that passes from the domain-connecting α -helix to the mass centre of the C-terminal domain (Knofel und Sträter, 1999; Knofel und Sträter, 2001). The domain motion is rather unusual in that the residues at the domain interface slide along the interface.

In order to analyse the motion, the enzyme has been trapped in two distinct conformations by engineered disulfide bridges (Schultz-Heienbrok et al. Protein Science, submitted). The different conformations are shown in figure 1. All structures have been experimentally determined by x-ray crystallography. In structure A the enzyme is trapped in an open conformation and in structure B the enzyme is trapped in an intermediate conformation. Structure C is the native structure in the most closed conformation found so far.

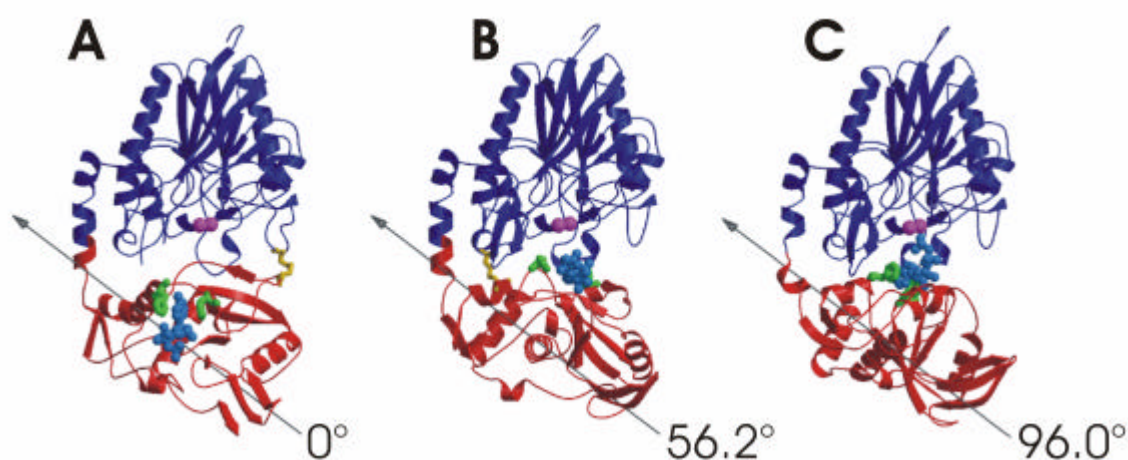


Figure 1. Comparison of different conformational states of 5'-nucleotidase. The axis of rotation between the most open (A) and most closed form (C) is drawn in grey. To follow the rotation a substrate (ATP) and two binding phenyl residues are shown in blue and green respectively in the C-terminal domain. The metal ions of the active site are depicted as CPK models in violet. The engineered disulfide bonds are drawn in yellow. **A.** 5'-nucleotidase trapped in an open form. **B.** 5'-nucleotidase trapped in an intermediate conformation. **C.** Wildtype structure of the most closed conformation found so far.

A major goal of the project was to establish the conformation of the enzyme in solution. It was hypothesised that the differences between the open and the closed states might be detectable by CD-spectroscopy.

Results. The newly established CD-spectroscopy beamline (3m-NIM-1c) at BESSY in Berlin has been used to test this hypothesis. Our preliminary results show that there is no detectable difference in the far UV-range (figure 2) between the wildtype protein and the trapped mutants. However, the results allow to accurately determine the secondary structure content of the enzymes (table 1). These agree well with the predicted content from the crystal structures. This result demonstrates that the domain rotation can be viewed as a rigid body movement of the two domains with no changes in the secondary structure involved.

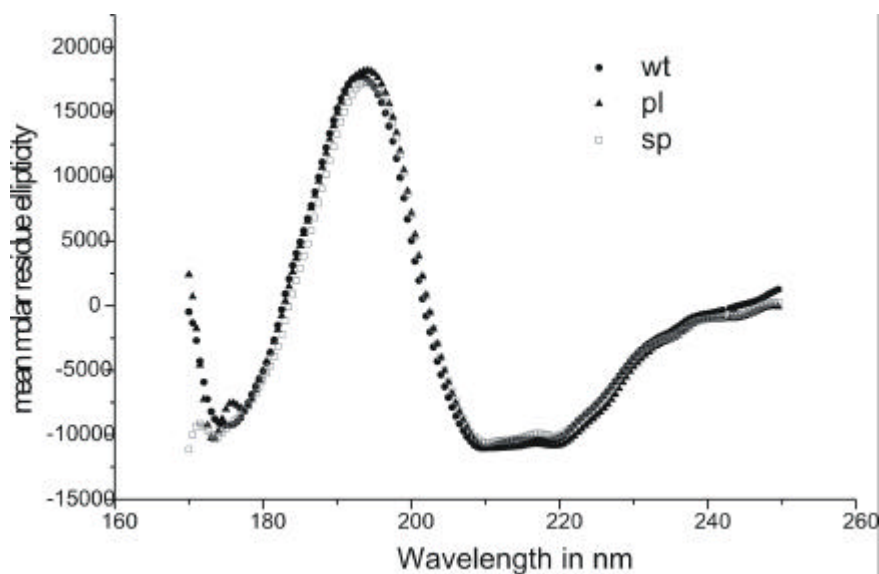


Figure2. CD-Spectra of the wildtype protein (wt), the cysteine double mutant (P90C, L424C) that locks the enzyme in an intermediate conformation (pl), and the cysteine double mutant (S228C, P513C) that locks the enzyme in an open conformation (sp).

Table 1. Comparison of secondary structure contents. WT is the wildtype protein, SP is the mutant trapped in the open conformation, PL the mutant trapped in the closed conformation. The inhibitor used here was α,β -methylene ADP.

structural element	CD-data (%)				crystallographic data	
	WT	WT + inhibitor	SP	PL	WT (1ho5)	WT (1ush)
α -helix	28,8	28,1	27,7	29,0	29,5	29,0
β -sheet	21,3	21,2	21,5	21,7	23,5	20,0
coil	22,6	23,4	23,1	22,6	22,2	22,3

Future Research. In future, experiments will focus on the detectable differences in the near UV spectra which have been measured with Jasco-600 CD spectrometer. These experiments have unambiguously demonstrated that the wild-type enzyme in solution resembles the trapped mutant in the open conformation. The CD-spectroscopy, therefore, has proven to be a diagnostic tool for different conformational states. Later the

BESSY beamline can be used to follow this conformational switch in real time by time resolved CD-measurements.

Experimental Details. The far UV spectra were obtained at the synchrotron beamline 3m-NIM-1c at BESSY in Berlin. The data were taken at 20° in 0.001 cm cuvettes with a protein concentration of 115 µM in 5 mM cacodylate buffer pH 7.4. Each protein sample was measured twice in independent runs. For each run a spectrum was acquired between 170 and 250 nm in steps of 0.5 nm with a 5 sec scan for each step. For calculation of secondary structure data between 185 and 245 nm were used and analysed with the SELCON 3 program for secondary structure calculation (Sreerama et al., 1999) using the DichroWeb-Server from the Birkbeck University, London (Lobley et al., 2002). The calculations of the secondary structure contents of the crystallographic structures was done with the program DSSP (Kabsch und Sander, 1983) using PDB ID 2ush as the input structure

Acknowledgements. We thank Dr. Peter Baumgärtel and Jan Lengefeld for their patient and extremely kind assistance during the measurements. This work was supported by the Deutsche Forschungsgemeinschaft.

References

- Kabsch, W. und Sander, C.** (1983) *Dictionary of protein secondary structure: pattern recognition of hydrogen-bonded and geometrical features.* Biopolymers, 22, 2577-2637.
- Knofel, T. und Strater, N.** (1999) *X-ray structure of the Escherichia coli periplasmic 5'-nucleotidase containing a dimetal catalytic site.* Nat. Struct. Biol., 6, 448-453.
- Knofel, T. und Strater, N.** (2001) *E. coli 5'-nucleotidase undergoes a hinge-bending domain rotation resembling a ball-and-socket motion.* J. Mol. Biol., 309, 255-266.
- Lobley, A., Whitmore, L. und Wallace, B.A.** (2002) *DICHROWEB: an interactive website for the analysis of protein secondary structure from circular dichroism spectra.* Bioinformatics, 18, 211-212.
- Neu, H.C.** (1967) *The 5'-nucleotidase of Escherichia coli. I. Purification and properties.* J. Biol. Chem., 242, 3896-3904.
- Sreerama, N., Venyaminov, S.Y. und Woody, R.W.** (1999) *Estimation of the number of alpha-helical and beta-strand segments in proteins using circular dichroism spectroscopy.* Protein Sci., 8, 370-380.

Measurements of multilayer optics : mirrors and gratings

J.-M. André*, Ph. Jonnard*

Laboratoire de Chimie Physique-Matière et Rayonnement, Université Pierre et Marie Curie, CNRS UMR 7614, 11 rue Pierre et Marie Curie, 75231 Paris CEDEX 05, France ;

andrejm@ccr.jussieu.fr

E. Filatova

Institute of Physics, St Petersburg University, Ulianovskaya 1, 198904 Russia

*Supported by E.U. program n° HPRI-CT-1999-00028 and A.C.O./CNRS 1999-2002

Periodic multilayer structures consisting of alternated layers of transparent and absorbing materials are of widespread use as Bragg reflectors for x-ray spectrometry. Wavelength Dispersive X-Ray Fluorescence or Electron Probe MicroAnalysis especially implements them for the detection of light chemical elements. Among these elements, boron is of particular interest in semiconductor and glass industries and also for geological investigations. We have developed new multilayer optical devices for this application. The first ones consist of small period La/B₄C multilayer mirrors developed in collaboration with Incoatec, and the second ones of Mo/B₄C multilayer gratings prepared in the Laboratory. La/B₄C multilayer mirrors are expected to increase the detection limit, while Mo/B₄C multilayer gratings are designed to improve the spectral resolution following an idea reported in different papers [1].

These optics were characterized by means of the diffractometer-polarimeter set-up at the UE56/1-PGM beamline.

La/B₄C multilayers were fabricated by Incoatec [2]. They were deposited onto Si wafers, one inch in diameter, by conventional diode magnetron sputtering. Figure 1 presents the experimental reflectivity versus glancing angle at 183 eV, corresponding to the energy of the B K α characteristic line, obtained with the circularly polarised radiation. In inset we have noted the values of the thicknesses retained for the fit and the value of the roughness r.m.s. height needed to take into account the interfacial roughness effect in the Debye-Waller model. Figure 2 shows the experimental reflectivity versus photon energy measured with the TE (s) polarised radiation respectively at a 45° glancing angle, together with the reflectivity calculated with the fitting parameters given in Figure 1. In this case, the TM (p) reflection is practically cancelled because the glancing angle is very closed to the Brewster angle. If Mo is used as absorbing material instead of La, the peak reflectivity for TE polarization which amounts to 42.8% with La falls to 21.2% with Mo, and the peak reflectivity for circular polarization which is equal to 21.4% with La becomes 10.6% with Mo. No significant change of the spectral bandwidth was noted by substituting La for Mo. These results show that the La/B₄C structure is more efficient in terms of peak reflectivity than the Mo/B₄C structure, at 183 eV.

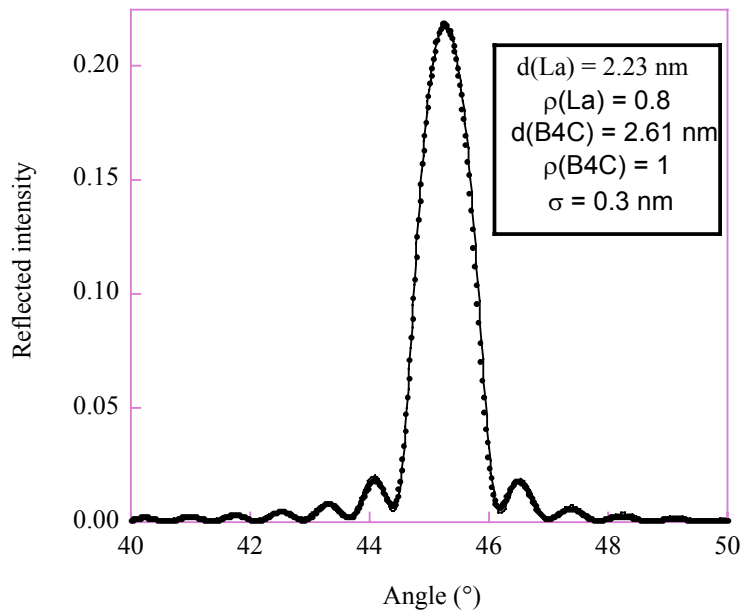


Figure 1 : Experimental (dots) and fitted (line) reflectivity versus glancing angle at 183 eV for circular polarization of the radiation. In inset, $d(\text{La})$ and $d(\text{B}_4\text{C})$ are the thicknesses of the La and B_4C layers, respectively, $\rho(\text{La})$ and $\rho(\text{B}_4\text{C})$ are the densities relative to those of the bulk materials, respectively, and σ is the Debye-Waller roughness factor.

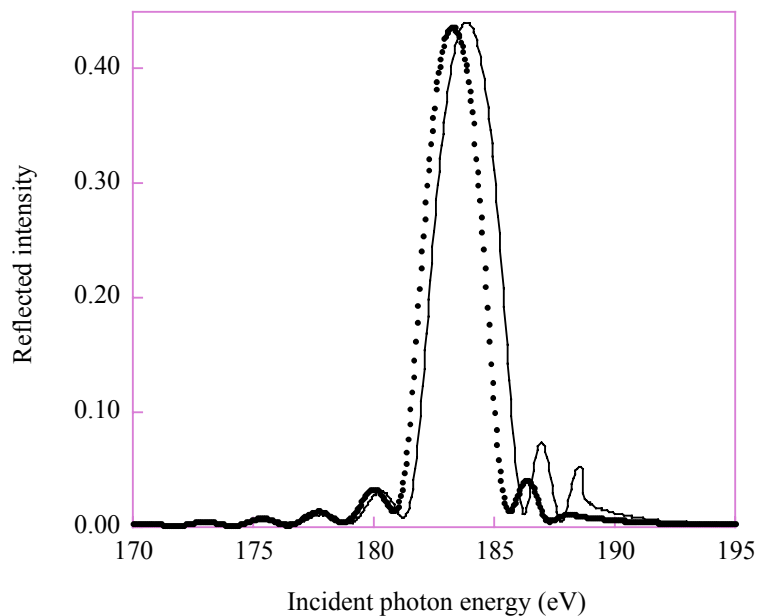


Figure 2 : Experimental reflectivity (dotted line) versus energy at 45° glancing angle for circular polarization of the radiation, and reflectivity calculated (solid line) with the fitting parameters given in Figure 1.

$\text{Mo}/\text{B}_4\text{C}$ multilayer gratings were fabricated by electron lithography and reactive ion etching, in the framework of the program A.C.O./CNRS [3]. These devices are designed to reduce the spectral bandwidth with respect to the mere multilayer mirrors. They have been tested at different energies and glancing angles. Figure 3 shows the normalized reflected intensity

versus the glancing angle of a Mo/B₄C grating in comparison with the corresponding Mo/B₄C mirror at 930 eV. The characteristics of the structure are : multilayer period = 6 nm, gamma ratio = 0.34, grating period = 1 μm. Four diffraction orders are observed with the grating which demonstrates the good quality of the grating. The Bragg angle of the zeroth diffraction order of the grating (6.48°) is shifted with respect to the Bragg angle of the mere mirror (6.7°) because of a refraction effect [3]. As expected by calculation, the bandwidth of the zeroth grating order is reduced by a factor of 4 with respect to the bandwidth of the mere mirror. Moreover, a reduction of bandwidth by a factor of 2, in agreement with the theory, was measured at 183 eV.

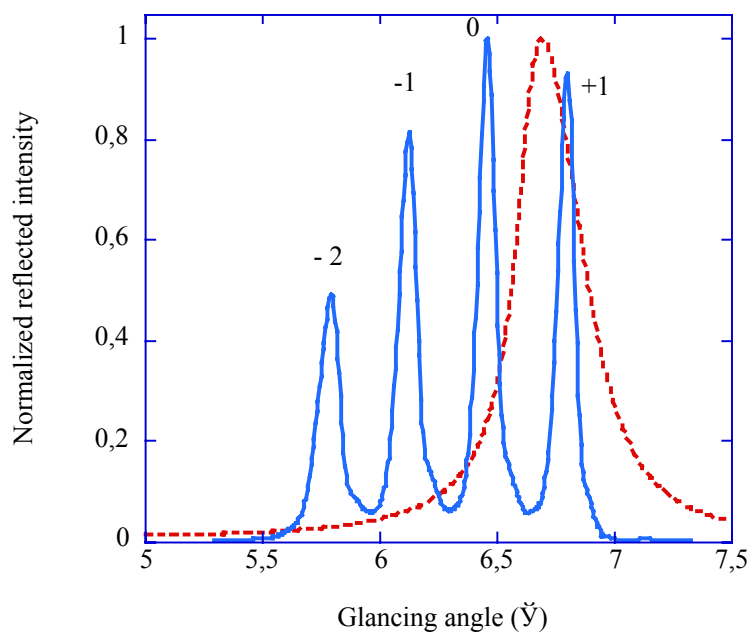


Figure 3: Reflected intensity versus the glancing angle at 930 eV of a Mo/B₄C multilayer mirror (dotted line) and a grating etched in this mirror (solid line). The numbers correspond to the diffraction order of the grating.

It appears that these gratings used at the zeroth order (i.e. in the specular condition) can be used as improved multilayer Bragg reflectors for soft-x-ray spectrometry.

Acknowledgments: We thank Dr Mertins, D. Abramsohn and the staff of BESSY for their help.

References:

[1] Benbalagh R., André J.-M., R. Barchewitz R. et al. *Applied Optics* 2002 ; 41: 239-244.
 [2] Michaelsen C., Ricardo P., Anders D., Schuster M., Schilling J. and Göbel H. *Adv. X-ray Anal* 2000; **42**: 308-320.
 [3] Benbalagh R., Thèse de l'Université Pierre et Marie Curie, Paris, June 2003.

Pinhole Interferometry with Hard X-rays

W. Leitenberger¹, H. Wendrock², L. Bischoff³, U. Pietsch¹, T. Panzner¹, J. Grenzer¹, A. Pucher¹

¹ *Universität Potsdam, Institut für Physik, Am Neuen Palais 10, D-14469 Potsdam, Germany*

² *Institut für Festkörper- und Werkstofforschung, P.O.B 270016, D-01171 Dresden, Germany*

³ *Forschungszentrum Rossendorf e.V., P.O.B. 510119, D-01314 Dresden, Germany*

Two types of pinhole interferometers for hard X-rays were experimentally realized in the same experimental set-up. The experiments were intended to demonstrate the possibility of measuring, in an energy-dispersive setup, the degree of coherence as a function of photon energy of a white hard X-ray spectrum from a bending magnet using a Young double slit setup^{1, 2}. The diffraction properties of white synchrotron radiation on small circular apertures in a thin metal foil were studied simultaneously in an energy range of $5 \text{ keV} < E < 20 \text{ keV}$ using an energy dispersive detector ($\Delta E/E \sim 200\text{eV}$) scanning a pinhole (diam. $5 \mu\text{m}$) in front for good lateral resolution. The experiments were done at the EDR-beamline at BESSY (energy-dispersive reflectometry). The pinholes in a $30\mu\text{m}$ thick tantalum foil (Fig. 1a) with different separations were fabricated with a focused ion beam (FIB). The principles of both types of interferometers are shown in Fig. 1 b,c. The X-ray absorption in the tantalum foil strongly depends on the energy of the incident radiation.

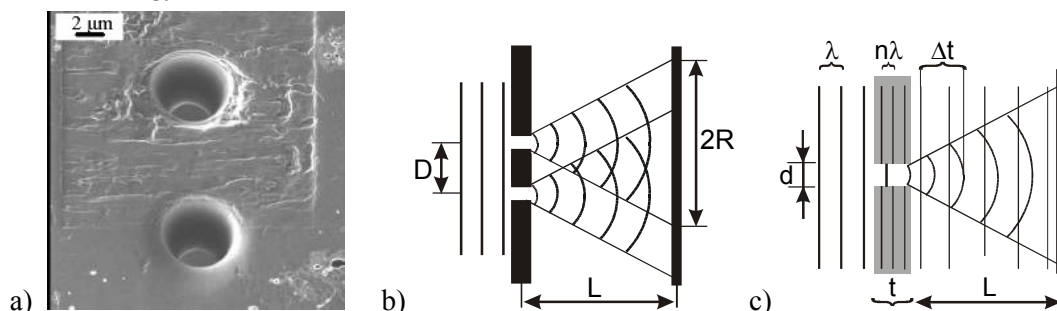


Fig 1 **a)** Electron micrograph of a double pinhole in a $30 \mu\text{m}$ thick tantalum foil; **b)** Propagation of waves in a double pinhole interferometer (DPI) and **c)** point diffraction interferometer (PDI).

For low energies the foil is opaque but it becomes more transparent as the energy increases (Fig. 2a). For opaque foil we have double pinhole interferometer while for a transparent foil the additional transmitted plane wave leads to the realization of a point diffraction interferometer. In a DPI two coherently illuminated tiny pinholes generate two spherical wavefronts that will interfere. The evaluation of the interference pattern is used for characterization of the coherence properties of the incident radiation. In Fig. 2a are shown two energy spectra, one of which was recorded on the optical axis of the system (center between both pinholes), while the other spectrum was recorded $200 \mu\text{m}$ below this axis. The off-axis spectrum coincides qualitatively with the absorption curve of a tantalum with its absorption edges at 9.9 and 11 keV. In the on-axis spectrum much higher intensity is observed due to radiation passing the pinhole directly. The maximum distance between the double pinhole and the detector was $L_{\text{exp}} = 1.4 \text{ m}$ which is a relatively small distance at this short wavelength - so we are mostly limited to the observation of quasi near-field diffraction.

Fig 2b shows, in a greyscale map, the raw data of the 151 energy spectra recorded at a region of $\pm 75 \mu\text{m}$ off the optical axis. In this image we see immediately the main properties of the pinhole interferometer over the accessible energy range. (i) Young's interference fringes appear as nearly horizontal dark bands whose distance decreases with increasing energy. (ii) "half circles" on the left side of Fig.2b are caused by interference of pinhole waves with the transmitted plane wave. Only if both amplitudes are of comparable strength do their interference fringes remain visible even for high orders. (iii) The absorption

edges of the tantalum foil are visible as vertical dark bands at 9.9 keV and 11.1 keV. Young's fringes are not visible above 13 keV due to the insufficient overlap of both pinhole waves. At these higher energies both "pinhole waves" do not interfere with each other and we only observe only their interference with the transmitted plane wave. From the visibility of Young's fringes (Fig 2c) which were observed we determined the spectral degree of coherence of X-rays (Fig 3a).

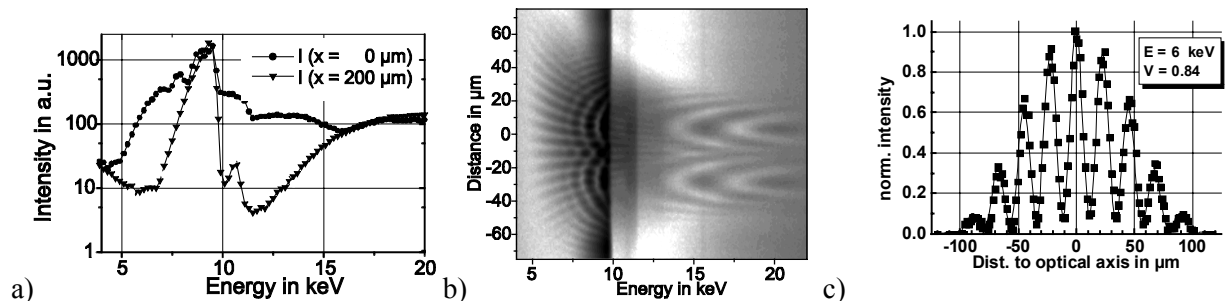


Fig. 2 a) Energy spectra of the transmitted intensity measured with an energy dispersive detector with $5 \mu\text{m}$ pinhole in front recorded on the optical axis and $200 \mu\text{m}$ off-axis. b) Grey scale map 151 energy spectra recorded 1.4m behind a double pinhole with $37\mu\text{m}$ separation. c) Young's fringes at 6 keV with $11\mu\text{m}$ pinhole separation.

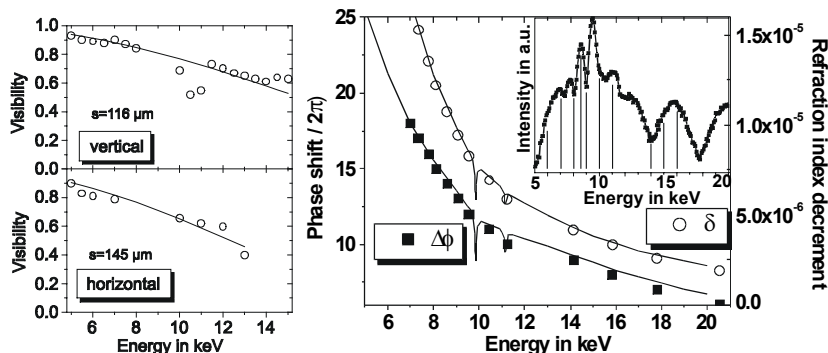


Fig.3 a) Visibility of Young's fringes as a function measured with $11\mu\text{m}$ pinhole separation, b) spectral phase shift between diffracted and transmitted wave for a PDI ($30 \mu\text{m}$ tantalum foil)

Fig 3a shows the experimental visibility for horizontal and vertical orientation as a function of energy measured with $11\mu\text{m}$ pinhole separation. From this data the effective, or virtual, size s of the X-ray source was calculated from the best fit of the experimental visibilities to theory. The effective source size of $116 \times 145 \mu\text{m}$ (v. \times h.) is large compared to the vertical source size of about $50 \mu\text{m}$ at the BESSY II³. One reason might be the loss of coherence due to nonperfect vacuum windows⁴.

An energy spectrum measured at the optical axis of an individual pinhole (at $-30\mu\text{m}$ in Fig 2b) directly gives the spectral intensity of the central Fresnel zone of the PDI (see inset of Fig 3b). The intensity oscillations are partially caused by the variable optical path difference of both interfering spherical and plane waves (introduced by the metal foil) and at lower energies by double pinhole interference. The maxima and minima coincides with phase shift of an integer multiple of π . The refraction index decrement of tantalum was determined at this positions over the whole energy range available and compared with tabulated data⁵.

The MPI for Colloids and Interfaces (Potsdam - Golm), the BESSY GmbH (Berlin) and the Hahn-Meitner-Institute (Berlin) are kindly acknowledged for financial support of beamline instrumentation.

¹ W. Leitenberger, H. Wendrock, L. Bischoff et al.; Physica B, Condensed Matter **336**, 63 (2003).

² W. Leitenberger, H. Wendrock, L. Bischoff et al.; J. Synchrotron Rad., in press (2004).

³ K. Holldack, J. Feikes and W. B. Peatman; Nucl. Instr. Meth. A **467-468**, 235 (2001).

⁴ I. K. Robinson, C. A. Kenney-Benson and I. A. Vartanyants; Physica B **336**, 56 (2003).

⁵ B. L. Henke, E. M. Gullikson and J. C. Davis; Atomic Data and Nuclear Data Tables **54**, 181 (1993).

3D micro X-ray fluorescence spectroscopy- Combining elemental analysis with chemical speciation

B. Kanngießer¹, W. Malzer¹, A. Fuentes Rodriguez¹, I. Reiche², F. Voigt³, M. Radtke⁴

¹ Technische Universität Berlin, ² Centre de Recherche et de Restauration de Musees de France, ³ Humboldt Universität Berlin, ⁴ Bundesanstalt für Materialforschung und -prüfung

The capabilities of micro X-ray fluorescence spectroscopy were expanded into a depth-resolved arrangement by realizing a confocal set-up consisting of X-ray optics in the excitation as well as in the detection channel. A micro-volume is defined by the overlap of the foci of both X-ray optics. If the sample is moved through this micro-volume, its chemical composition can be non-destructively investigated not only laterally along the surface but also within the sample at the depth of interest. Furthermore, the tuning of the excitation energy facilitates micro XAFS investigation for chemical speciation at the same spot in the sample. Thus, not only depth information concerning the elemental distribution but also chemical speciation and phase information are obtainable at the same point of interest in the sample.

The 3D micro-XRF set-up was realised at the BAMline located at a 7T wavelength shifter at BESSY [1,2]. The micro-volume formed was characterised by scanning the volume with a 2 µm thick Cu foil. The Cu foil was moved through the beam in 5 µm wide steps in the horizontal plane with respect to the storage ring and in the vertical direction. For an excitation energy of 17 keV a FWHM of about 20 µm was achieved, which can be regarded as the spatial resolution of the set-up. The 20 µm FWHM presents the lower limit of resolution achievable with this set-up.

The first application of the new 3D micro-XRF method was the investigation of ancient Indian Mughal miniatures from the Museum of Indian Art in Berlin [1,2]. Further investigations on the Mughal miniatures showed that it is also possible to distinguish the same element in different layers which can not be achieved by conventional XRF.

We could also show that 3D micro-XANES investigation is feasible at the same location where elemental depth profiles are obtained. The sample investigated was a Persian ceramic tile of the 19th c. presenting an underglaze painting from the Ethnological Museum of Berlin, see figure 1. For the art historians the question was the exact fabrication technique of the tilemakers. With the combination of 3D micro-XRF and micro-XANES a more clear characterisation of the colouring glass pigments was carried out. 3D micro-XANES spectroscopy was used to gain information on the specific chemical binding of Cu for the interfacial region between the pigment and the glaze layer.

For these investigations we used the double multilayer monochromator (DMM) and the double crystal monochromator (DCM) of the BAMline in series. Thus, the strong higher harmonics of the Si(111) DCM at the used excitation energy around 9 keV are reduced by five orders of magnitude. In this case the energy resolution of the series of monochromators is about 1 eV.



Figure 1: Persian Tile "Flying merchant of pomegranats", 19th c. Ethnological Museum Berlin (IB 9389)

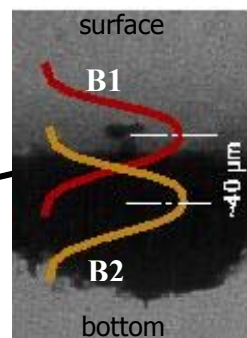


Figure 2: Sketch of the cross section of the tile.

Micro-XANES spectra were taken in two series of measurements in various depths in the pigment layer. Figure 3 shows the XANES spectra obtained in these two series.

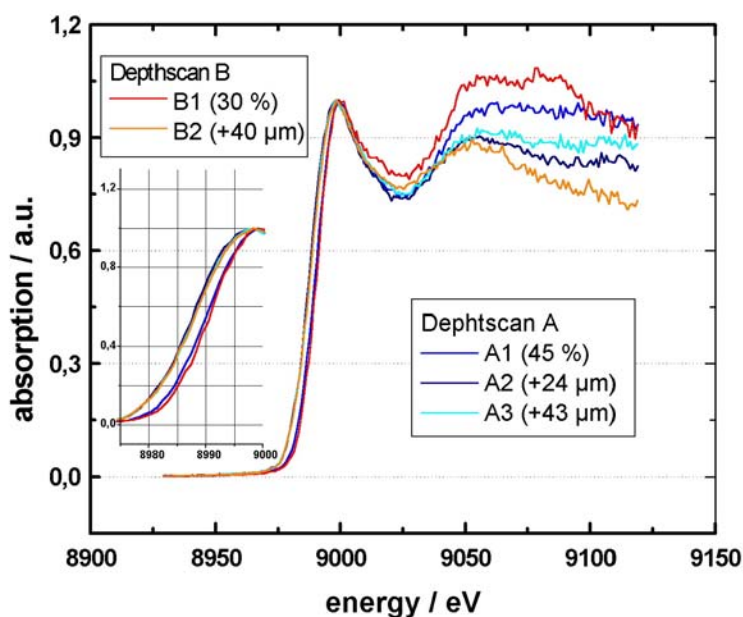


Figure 3: 3D micro-XANES spectra at two different sites of the tile.

Series A was started with a XANES measurement at 45% of the maximum Cu count rate of the Cu depth profile. The following spectra were taken at 24 μm and 43 μm , respectively, into the depth of the tile. Series B was started at 30% of the maximum Cu count rate at another location nearby the first one. The next spectrum was taken at 40 μm into the depth of the tile. Figure 2 shows a sketch of the cross section of the tile with the pigment layer in the centre. The position of the sensitivity profile depicted in red exemplifies where only one wing of the profile covers the pigment layer. Sketched in green is the position where spectra from the deeper regions of the colour layer were taken. The two series of spectra show a shift of about 2.5 eV of the absorption edge as well as of the region above for the spectra gained in deeper

lying locations. These results confirm the reproducibility of the depth resolved micro-XANES scans and clearly show the occurrence of two different chemical environments of the Cu containing layers.

Figure 4 shows the comparison of the XANES spectra of the B series with two different reference samples.

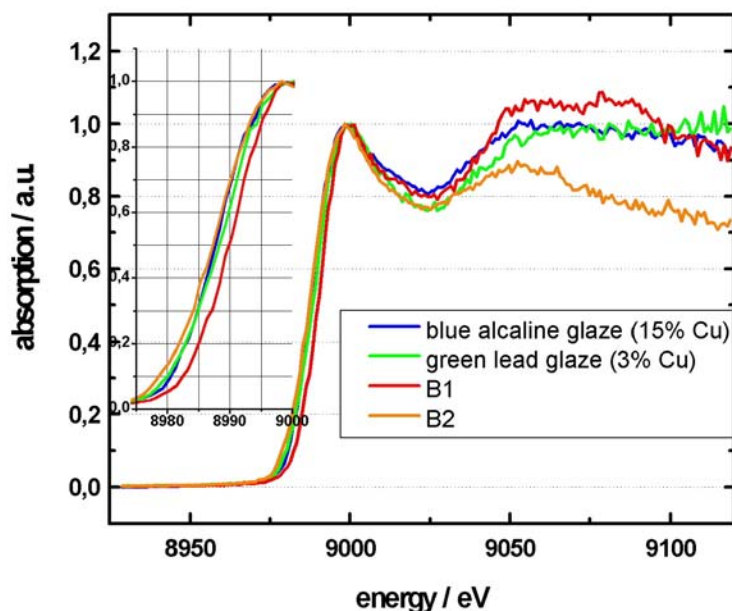


Figure 4: Comparison of the 3D micro-XANES spectra with XANES reference spectra.

Both reference samples are Cu containing glazes: the blue alkaline glaze has a 15% Cu content, the green lead glaze has a 3% Cu content. The Cu occurs in both samples in the Cu(II) oxidation state. The region after the edge of the B1 XANES spectrum is quite similar to this of the reference spectra, but the absorption edge position is shifted by 2.5 eV. The B2 XANES spectrum has the same edge position as the reference spectra, but shows a different region after the edge. Hence, the shape of the spectra corresponds to Cu²⁺ ions in a more or less distorted O_h environment in an amorphous silica-rich matrix. The difference in the two measured spectra of the B series lies basically in the site symmetry.

Acknowledgements

We gratefully thank A. Bjaoumikhov and N. Langhoff (IfG) for placing the half lens at our disposal and I. Schindlbeck (Ethnological Museum of Berlin) for placing the Persian tile at our disposal.

References

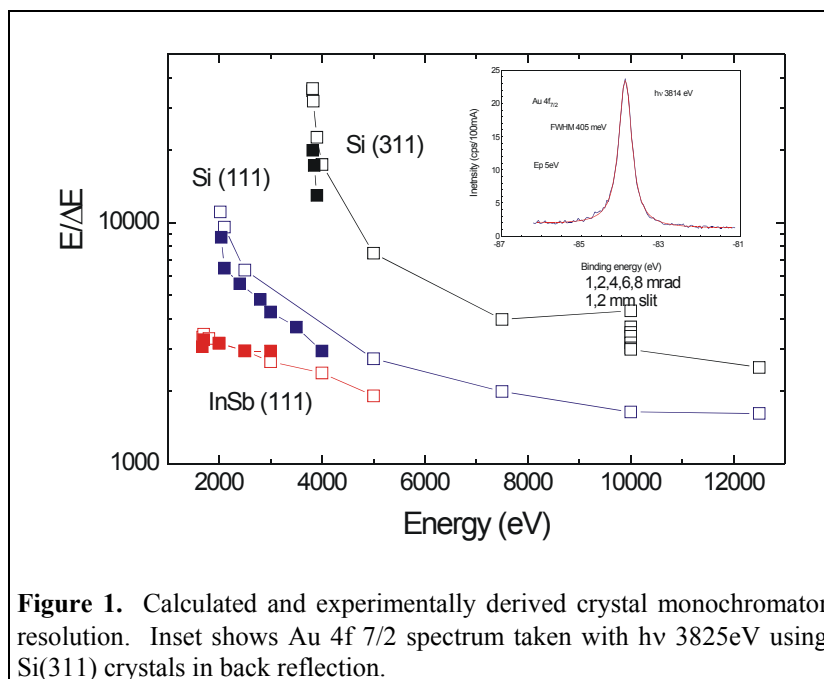
- [1] B. Kanngießer, W. Malzer, I. Reiche, Nucl. Instr. Meth. B 211/2, 259-264 (2003).
- [2] B. Kanngießer, W. Malzer, I. Reiche, BESSY-Highlights 2002 – Scientific Highlights (2003).

High resolution PES at high kinetic energies

D.R. Batchelor, P. Bressler, M. Mertin and F. Schäfers

BESSY, Albert Einstein Str. 15, 12489 Berlin

Photoelectron spectroscopy (PES) from solids finds a wide range of applications from conventional laboratory ESCA to PES studies at Synchrotrons. The former detects photoelectrons typically of ≈ 100 - 1000 eV and as a consequence of the size of the electron escape depth gives mixed information from both Surface and Bulk. It also suffers from poor energy resolution, ≈ 1 eV using conventional sources. Synchrotrons provide much better resolution, resolving powers of $\approx 10,000$, and the energy can be tuned so that one is surface sensitive by using kinetic energies of 50-100 eV. To obtain the complementary bulk information the escape depth needs to be in the range of a few to tens of nanometres which requires kinetic energies of a few thousand to tens of keV. It is only recently with parallel development of third generation Synchrotron sources and electron kinetic energy analysers that it has been possible to achieve a flux and resolution



needed for routine applications [1]. The use of a tuneable polarised X-ray source opens up other measurement possibilities to the relatively simple photoemission measurements of core levels and valence bands. The techniques of CFS and CIS measurements can be used to do resonance studies and photoelectron diffraction [2,3]. In addition the high photon energies open up the use of diffraction techniques such as X-ray standing waves enabling atom specific valence electronic structure to be obtained [4].

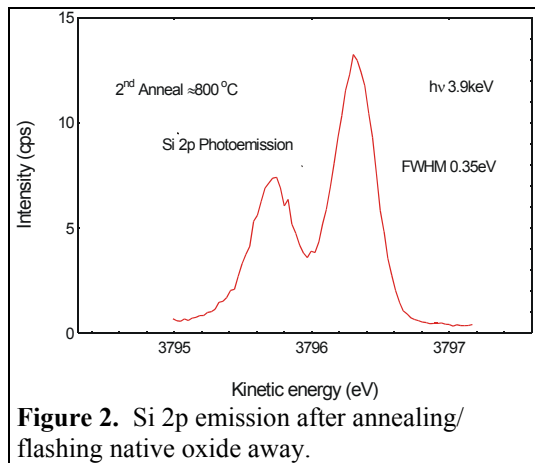


Figure 2. Si 2p emission after annealing/ flashing native oxide away.

At BESSY we have recently taken data from Gold and Silicon samples using an Oxford Instruments DCM monochromator equipped with Si(311), Si(111) and InSb(111) crystals and a SPECS Phoibos MCD-9 150 detector on a multi-purpose multi-sample chamber, the PHOENEX chamber, equipped with standard surface science instrumentation and a helium cooled manipulator.

Figure 1 shows the theoretical expected resolution calculated using ray tracing (RAY BESSY Technical report 202-96) as a function of energy and aperture for the three crystals and experimental results.

The experimental results are derived by measuring the Au 4f spectrum and curve fitting Gaussian convoluted Lorentz peaks with a Shirley type inelastic electron background. The pass energy of the analyser was sufficiently small such that no additional broadening in the spectrum was observed. The same Lorentz width was used to fit all of the spectra and the remaining Gaussian contribution taken to be the resolution due to the monochromator. The inset shows the fitted spectrum measured with the Si(311) crystals in back reflection, the highest possible monochromator energy resolution. The Lorentzian lineshape is clearly visible. The obtained Lorentzian width is in agreement with other measurements obtained on KMC-2 at BESSY [5] and also in good agreement with the original high energy measurements of Lindau et. al. [6].

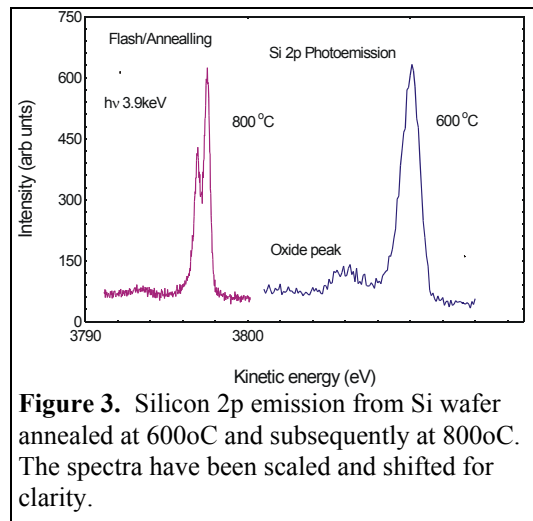


Figure 3. Silicon 2p emission from Si wafer annealed at 600oC and subsequently at 800oC. The spectra have been scaled and shifted for clarity.

As an additional check Si 2p emission from an annealed/flashed Silicon wafer is shown in Figure 2. The 2p spin orbit splitting is well resolved and curve fitting results indicate that the monochromator resolving power is of the order of $\approx 20,000$. An additional point is worth mentioning here in both spectra the inelastic background at these high energies underneath the peaks is small. As a consequence although the count rate is low the statistical noise is due to the signal and not the inelastically scattered electron background.

The Silicon wafer was prepared by stepwise annealing. Silicon 2p spectra are shown in Figure 3 for temperatures of 600 and 800°C (The spectra have been shifted and scaled for clarity). The oxide peak is clearly visible at $\approx 4\text{eV}$ lower kinetic energy for both spectra. The calculated inelastic mean free path (IMFP) for Silicon at these energies is $\approx 7\text{nm}$. Interestingly the oxide signal, which is a few percent of the total signal, is still clearly visible for the 800°C spectrum. This indicates that the IMFP is probably larger than the calculated value. In addition the 2p spin component shows a correlation of width with oxide amount. Assuming that this width is a function of the mixed oxide it is difficult to model the interface region as well defined layer and implies that interface region is much more diffuse, or another mechanism is responsible for the peak broadening.

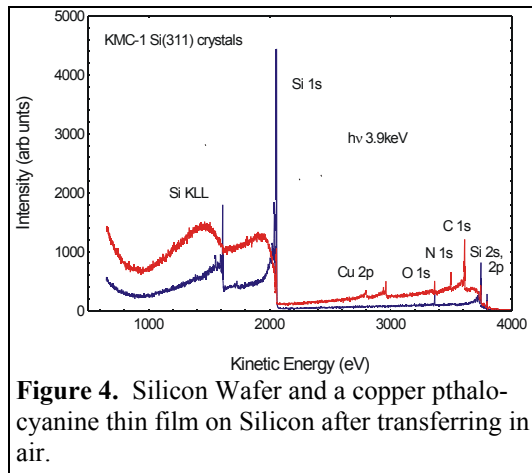


Figure 4. Silicon Wafer and a copper phthalocyanine thin film on Silicon after transferring in air.

Figure 4 shows an example of Copper Pthalocyanine evaporated on a Silicon substrate here the characteristic inelastic loss spectrum, rising to lower kinetic energy, of a buried substrate is seen for the Silicon peaks and peaks with a simple Shirley like background for the layer. The detailed analysis of the background using the procedures developed by Tougaard [7] is being pursued.

Acknowledgments

P. Hoffmann and D. Schmeißer (BTUC) for helpful discussions concerning the oxidation of Silicon. S. Mähl and O. Schaff from SPECS for advice concerning the analyser.

References

- [1] W. Drube Proceedings of SRI 2003, San Francisco
- [2] W. Drube et. al. Phys. Rev. Lett. **74** (1995) 42
- [3] K.A. Thompson and C.S. Fadley, J. Electron Spectroscopy, **33** (1989) 29, D.P. Woodruff and A.M. Bradshaw, Rep.Prog.Phys. 57 (1994) 1029
- [4] J.C. Woicik et. al. Phys Rev. B **64** (2001) 1926, D.P. Woodruff et. al. Surface Sci. **195** (1988) 237
- [5] D.R. Batchelor et. al. BESSY Annual Report 2003 pg 397
- [6] I. Lindau et. al. Nature **29** (1974) 215
- [7] S. Tougaard, Surface and Interface Analysis 25 (1997) 137

THz Near-Field Microscopy at BESSY

U. Schade, K. Holldack, P. Kuske and G. Wüstefeld
*Berliner Elektronenspeicherring-Gesellschaft für Synchrotronstrahlung mbH (BESSY),
Albert-Einstein-Straße 15, 12489 Berlin, Germany*

H.-W. Hübers
Deutsches Zentrum für Luft- und Raumfahrt (DLR), Rutherfordstraße 2, 12489 Berlin, Germany

A THz near-field imaging technique has been developed at BESSY which benefits from the broadband and highly brilliant coherent synchrotron radiation (CSR) from an electron storage ring^{1,2} together with a detection method based on locking on to the intrinsic time structure of the synchrotron radiation. The technique of THz scanning near-field infrared microscopy (SNIM) presented enables spectroscopic mapping of strongly absorbing, e.g., water containing, samples at a spatial resolution well below the diffraction limit. THz SNIM has been established at the infrared beamline IRIS^{3,4} at BESSY. The far-infrared port of the beamline provides a collimated CSR THz beam which is about 98% linearly polarized. The beam then passes through a Martin-Puplett spectrometer before being transferred to the SNIM where it is focussed into a conical waveguide with a circular cross-section and an exit aperture of a diameter smaller than the wavelength. The sample is placed in front of the exit aperture by a spring. Similar near-field probes have been proposed by Keilman⁵. Conical aperture probes with a cone angle of 50° with two different aperture diameters of 100 and 200 μm have been employed for the our experiments. Imaging is performed by moving the sample in front of the exit aperture by means of a computer controlled x-y stage. The evanescent field at the exit aperture penetrates the sample and the scattered radiation containing the spectral information is collected by an ellipsoidal mirror and is then focused onto a LHe-cooled InSb detector. The image is generated by interpretation of the 1.25 MHz modulated THz signal as provided by the source versus sample position relative to the cone axis.

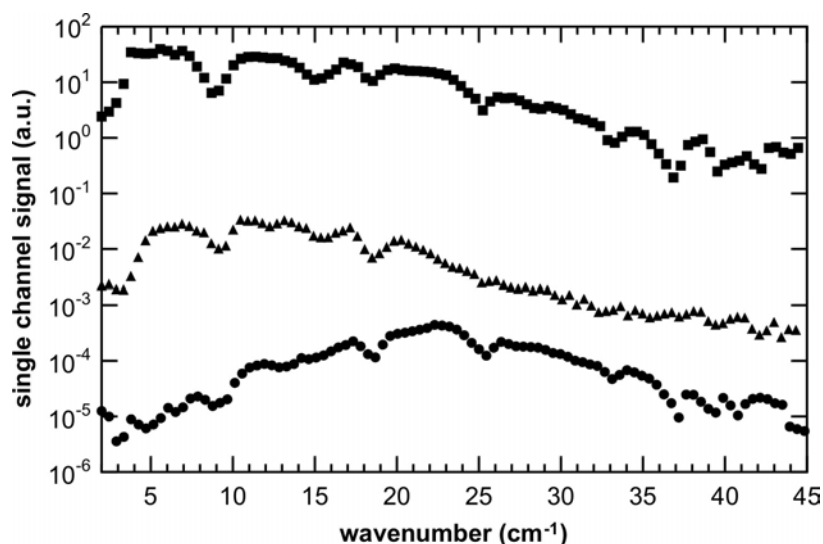


Fig. 1: Normalized empty channel spectra of the incoming beam (squares) from the coherent THz source and of the beam transmitted through the 200 μm aperture cone (triangles) in comparison to the spectra of the incoherent source (circles). All spectra are normalized to 1 mA bunch current. The two upper spectra were acquired in single bunch mode with a bunch length of about 30 ps at a ring current of 15 mA where the lower spectrum was taken in the normal mode of BESSY for 400 stored bunches at a ring current of 200 mA.

The conical aperture probe attenuates the free-space THz radiation for wavelengths longer than the cut-off wavelength, $\lambda_c = 1.71 d_c$, where d_c is the relevant cross-section diameter of the cone⁶. The power output of the near-field probe for a specific wavelength then depends on the cone angle and the diameter of the exit aperture⁷. The spectral transmittance of the cone was measured by means of the Martin-Puplett spectrometer. Fig. 1 shows the single channel spectra of the incident THz beam and the THz beam transmitted through a cone

with an exit aperture diameter of 200 μm . As expected from the geometry of the cone the transmitted power is reduced by about 4 orders of magnitude. This drastic decrease in transmittance is also in agreement with the findings of Keilmann for waveguides below the cut-off frequency⁶. However, since the transmitted intensity still lies 4 to 5 orders of magnitude above the detection limit of our system, even samples with a transmittance as low as of 0.01% can be mapped in transmission mode. The sensitivity of the detection schema applied is demonstrated by the weak incoherent synchrotron radiation spectrum shown in Fig. 1. Since the measurements are performed at ambient atmosphere all single channel spectra presented show distinct water absorption bands which do not interfere with our discussion.

The spatial resolution of the THz SNIM was investigated by scanning the edge of an aluminium film on a Si wafer along the near-field probe. The edge of the sample provides a strong contrast against the dielectric substrate. We obtained a spatial resolution which is on the order of the diameter of the aperture. From the 2σ -value of the Gaussian fit of the first derivative of the experimental data, the spatial resolution is estimated to be about 130 μm for the 200 μm aperture probe. At a cost of a further 2 orders of magnitude in intensity the resolution can be improved to 70 μm using the 100 μm aperture probe shown in Fig. 2. Together with the single channel spectra in Fig. 1 showing significant intensity from the source at 2 cm^{-1} for the 200 μm aperture probe a spatial resolution of about $\lambda/40$ wavenumber can be estimated for this wavenumber. Taking broad band near-field images the spectral center of gravity at around 12 cm^{-1} is transmitted yielding an average spatial resolution of $\lambda/6$ for the 200 μm aperture and $\lambda/12$ for the 100 μm aperture, respectively. Further attempts at higher resolution using a 50 μm aperture failed due to background effects caused by stray light. After a better screening of the setup and at higher ring current, this approach has the potential to work down to 10 μm resolution or better. To increase the transmitted power we also performed initial tests on coaxial wire cones as described by Keilmann⁶, but no significant progress could be achieved so far due to an insufficient coupling of the THz beam from the coherent synchrotron source into the coaxial waveguide.

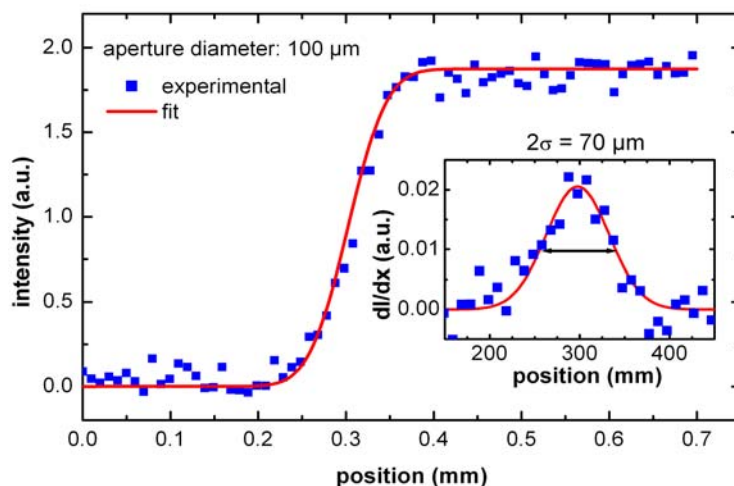


Fig. 2: Measured and fitted spatial resolution curves for an exit aperture of 100 μm diameter. The inset shows a Gaussian fit of the first derivative of the measured curve used to determine the spatial resolution.

The strength of the THz SNIM concept for applications on biological samples has been tested on strongly absorbing living leaves, where the contrast is mostly formed by the amount of liquid water present. Recently, images of living leaves have also been obtained by other authors^{8,9} from a confocal setup applying THz TDS to investigate the rehydration process of plants after watering. However, the spatial resolution of these investigations is restricted to the order of the wavelength applied. Using the THz SNIM technique presented much more detailed images is obtained. Fig. 3 shows a part of a freshly cut *parthenocissus* leaf imaged in transmission. In its THz

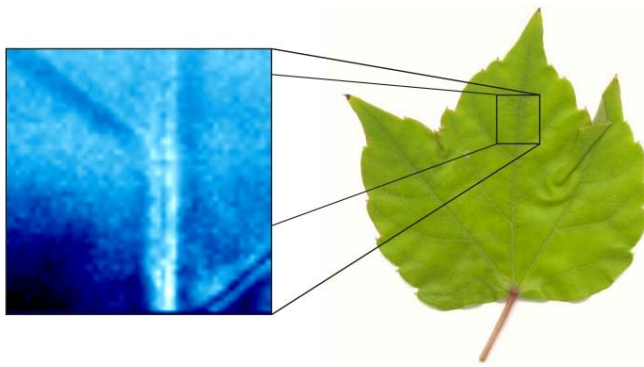


Fig. 3: Near-field THz image from a section of a *parthenocissus* leaf. Note, that less absorption is indicated by a darker blue in the THz image.

images shown in Fig. 3 and 4 clearly resolve the different leaf structures of the mesophytic *parthenocissus* and the xerophytic *laurus nobilis*. Both the THz and the visible light image reveal similar object features but the THz SNIM enables studies of hydration dynamics with a high spatial resolution as it is sensitive to the water concentration in the sample.

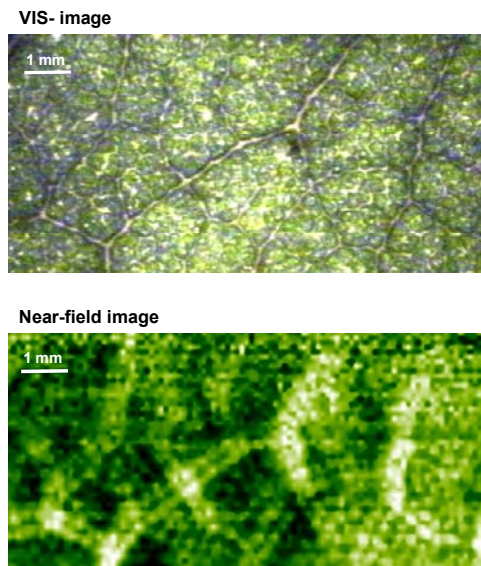


Fig. 4: Visible and near-field THz image from a section of a *laurus nobilis* leaf. Note, that less absorption is indicated by a darker green in the THz image.

near-field image an inner structure of the veins is apparent which is formed by a spectrally broad liquid water absorption and possible scattering at the structural boundaries. Topological effects may also contribute to the contrast. The image was taken using a 200 μm cone. In another example as depicted in Fig. 4 larger cellular structures of a freshly cut *laurus nobilis* leaf are imaged and compared to its bright field image in the visible. Our THz near-field

The high brilliance of an accelerator-based coherent source is employed for near-field microscopy in the THz and sub-THz range. The analysis of strongly absorbing specimen like living leaves or other biological tissue can be performed with sub-wavelength resolution due to the high power of the source together with a technique which exploits the time structure of the THz beam. Combined with a step scan spectrometer, spectral mapping based on the contrasts of different spectral features such as collective modes of biological relevant molecules in organic tissue is possible.

We acknowledge the support of D. Ponwitz, F. Höft (BESSY), K. Hinrichs, G. Hinte and R. Herzlieb (ISAS).

References:

- ¹ M. Abo-Bakr, J. Feikes, K. Holldack, G. Wüstefeld, and H.-W. Hübers, Phys. Rev. Lett. **88**, 254801 (2002).
- ² M. Abo-Bakr, J. Feikes, K. Holldack, P. Kuske, W. B. Peatman, U. Schade, G. Wüstefeld, and H.-W. Hübers, Phys. Rev. Lett. **90**, 094801 (2002).
- ³ W.B. Peatman and U. Schade, Rev. Sci. Instrum. **72**, 1620 (2001).
- ⁴ U. Schade, A. Röseler, E.H. Korte, F. Bartl, K.P. Hofmann, T. Noll, and W.B. Peatman, Rev. Sci. Instrum. **73**, 1568 (2002).
- ⁵ F. Keilmann, U.S. Patent No. 4,994,818 (1991, filed 1989).
- ⁶ F. Keilmann, Infrared Phys. Technol. **36**, 217 (1995).
- ⁷ B. Knoll and F. Keilmann, Opt. Commun. **162**, 177 (1999).
- ⁸ D. Mittelman, in *Sensing with Terahertz Radiation*, edited by D. Mittelman (Springer, Berlin, 2003), p. 137.
- ⁹ M. Koch, in *Sensing with Terahertz Radiation*, edited by D. Mittelman (Springer, Berlin, 2003), p. 303.

Comparison of Focus-PEEM and Elmitec-PEEM

Y.Burkov, P.Hoffmann, D.Schmeißer: BTU Cottbus, Universitätsplatz 3-4, 03046 Cottbus

Introduction:

The method of photo-emission-electron microscopy (PEEM) has been known for several years [1]. Microscopes, based on this principle, are used for the visualisation of magnetic domains [2], the characterisation of adsorbates [3], the mapping of doping inhomogeneities [4], of surface morphology or elemental distributions [5]. The use of Synchrotron radiation as a light source in a PEEM experiment is advantageous, not only for its tunability, but also for the high brilliance making small area detection of photoelectrons with reasonable counts rates possible. The comparison of results from different PEEM instruments for known system, for example CuInS₂ surfaces, is very interesting. Therefore two PEEM were used, the BTU (Firma Focus) and the HMI PEEM (Firma Elmitec). Focus-PEEM has electrostatic lenses whereas Elmitec-PEEM is build by electro-magnetic lenses and an addition analyser gives the opportunity to energy-filter the image so that the image consists of photo electrons with a certain kinetic energy.

Experimental :

For our measurement, we studied CuInS₂ films, deposited on a Mo film on a soda-lime-glass substrate by sputter deposition of Cu and In. The precursor layers are sulphurised in S₂- vapour at 500°C, according to [6], resulting in a thickness of the CuInS₂-layer of about 3µm. The films were prepared under excess of Cu to promote the grain growth [7]. An etching procedure in KCN solution, described by Weber et al. [8], was performed to remove phases like CuS on top of the absorber layer (3min, 5% KCN). Typically, the composition of such KCN-etched surfaces is In-rich. The bulk composition, as revealed by EDX, is stoichiometric (CuInS₂) and the distribution of Cu, In and S, detected by SEM, was homogenous [9]. To improve the stoichiometry of CuInS₂ surface it was annealed up to 400 °C.

In order to minimise the problem of interpretation, excitation at different photon energies is useful: By taking two images with energies around the absorption edges of the elements searched for and by subtracting the intensities at the related pixels, contrast of this so called difference-image should be a contrast of elemental distribution.

Results:

The images of the two PEEM are shown in Fig.1 for comparison. Like to be seen the images of the Elmitec-PEEM show stronger contrast and sharper projections. This is due to higher extractor voltage that is used by the Elmitec-PEEM. This also leads to the stronger contrast. But this strong contrast complicates the calculation of difference images. These difference images are shown also in Fig.1. Pictures C and D show the Cu distribution, Pictures E and F show the In distribution and Pictures G and H show the S distribution. In case of BTU-PEEM for Cu, bright and relatively homogeneous areas with dark spots are recorded. For In and S the situation is reverse, here exactly this spots (in the Cu-image) are the brighter ones. This leads to the following conclusions: Contrast is caused by differences of elemental content, topology would cause bright areas in every case, the bright areas must be congruent for Cu, In or S for this type of contrast.

Literature:

- [1] F. Eichhorn and K. Theis: BEDO 7, 363 (1974).
- [2] R. Fromter, Ch. Ziethen, G. Schönheise, and J.Kirschner et al.: BESSY Jahresbericht 1996, 482-484 .
- [3] H. Rotermund, W. Engel, S. Jakubith, A. von Oertzen, and G. ertl, Ultramicroscopy **36** (1991) 164.
- [4] R. Mikalo, P. Hoffmann, T. Heller, and D. Schmeißer, Solid State Phenomena **63 to 64** (1998), 317.
- [5] P. Hoffmann, R. Mikalo, D. Schmeißer, and M. Kittler: Phys. Stat. Sol. (b) **215** (1999) 743.
- [6] J. Klaer, J. Bruns et al., Proc. 2nd World Conf. Photovolt. Sol. Energy Conversion **1** (1998) 537.
- [7] R. Klenk, T. Walter, H.W. Shock and D. Cahen: Adv. Mat. **5** (1993) 114.
- [8] M.Weber, R.Scheer, H.J.Lewerenz, H.Jungblut, and U.Störkel: J.Electrochem.Soc. **149** (2002) G77-G84.
- [9] K. Müller, R. Scheer, Y. Burkov, D. Schmeißer, Thin Solid Films **413-432** (2003) 312-316

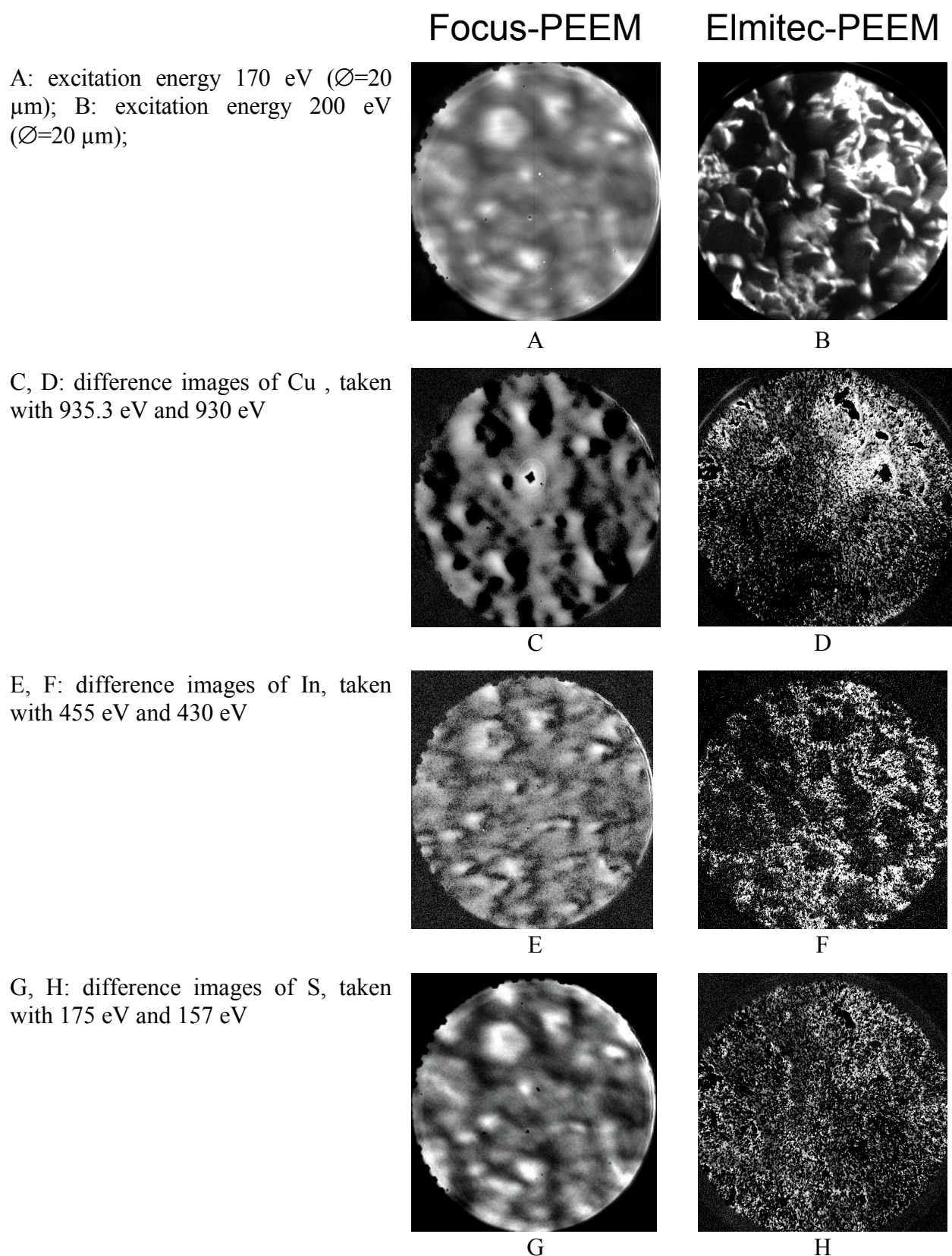


Fig.1: Comparison of the Focus- (left hand side) and the Elmitec-PEEM (right hand side)

Acknowledgements:

We would like to thank the workgroup of Prof. Dr Lewerenz (HMI) for the preparation of the used Cu-In-S-substrates and Prof. Dr Pettenkofer (HMI) for accordance of PEEM. Furthermore, we like to acknowledge the experimental assistance of W. Bremsteller as well as the help of the BESSY-staff.

Transmission Photoelectron Microscopy of dry and wet biomaterials at the Multilayer Monochromator Beamline U125-1/ML at BESSY II

M. Pohl, U. Kleineberg, U. Heinzmann

*University of Bielefeld, Faculty of Physics
Universitaetsstr. 25, D-33615 Bielefeld, Germany
kleineberg@physik.uni-bielefeld.de*

INTRODUCTION

Photoelectron Microscopy utilizing photoemission by energy-tunable soft x-ray radiation (X-PEEM) has been proven to be a valuable tool for spectromicroscopic imaging of surface structures (chemical, topographic or magnetic contrast) on a mesoscopic size scale (spatial resolution < 100 nm, energy resolution < 1 eV). While almost all experiments performed so far have been carried out by *directly illuminating the sample surface* under oblique angles of incidence (typ. 20 deg to the surface) only very few experiments have been reported about photoelectron microscopy *in transmission geometry* [1-3]. The transmission setup requires the use of thin samples attached to ultrathin silicon membranes (thickness 100-200 nm), both being (semi-) transparent for the incident soft x-ray radiation. Although Transmission Photoelectron Microscopy (T-PEEM) is similar in construction to the X-PEEM technique (using the same electron emission microscope) it is functionally different in that it images the secondary electrons produced by the *x-ray shadowgraph* of the sample on the backside of the transparent photocathode and not the photoelectron yield of the sample surface itself. Transmission spectromicroscopy has considerable applications beyond material sciences e.g. in life sciences where a major advantage is the compatibility to sealed environmental sample cells where the sample can be held under controlled (e.g. hydrated) conditions. Furthermore electrical charging effects which may cause image distortions in photoemission microscopy of non-conducting samples do not play any role in T-PEEM if the photocathode is sufficiently conducting. Transmission Photoelectron Microscopy is related to Transmission X-ray Microscopy (TXM) or Scanning Transmission X-ray Microscopy (STXM) the latter methods using the soft x-radiation transmitted through the sample for imaging by means of high resolution soft x-ray imaging or focusing optics.

Experimental Setup

The T-PEEM has been setup at the BESSY undulator beamline U125-1/ML as well as UE56 is displayed in Fig. 1. Undulator radiation emitted from the U125 is deflected by a plane Ni-coated Si-premirror at a deflection angle of 6 deg (resulting in a high energy cutoff photon energy at about 500 eV) and monochromized by a multilayer monochromator. The multilayer monochromator is equipped with a concave spherical multilayer mirror ($r = 2$ m) and a plane 3600 L/mm multilayer grating both operating at non-grazing incidence angles. Wavelength tuning is achieved by simultaneously varying the angle of incidence on both elements in a 15-65 deg angular range. Three sets of multilayer optics are available and can be exchanged in vacuo. A set of Mo/Si multilayer mirror [4] and grating is used for the 95-100 eV photon energy range while a second set of C/Ti multilayer optics is used in the 410-456 eV range.

A conventional electrostatic photoelectron microscope with a piezo-driven integrated sample stage (Focus IS-PEEM) has been used for T-PEEM imaging. The electron images are recorded by means of a twodimensional wire detector (delayline detector) operated in an electron detection mode.

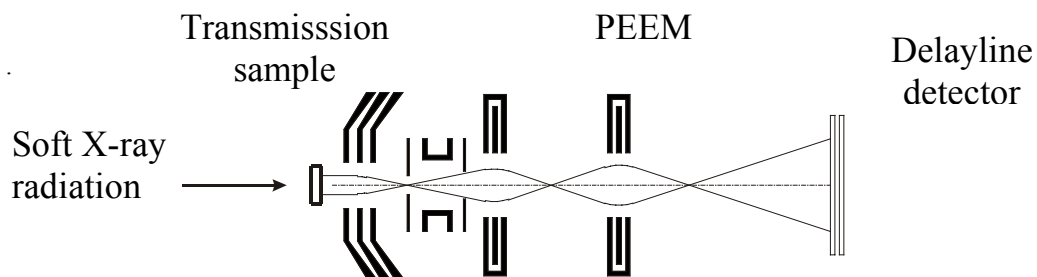


FIGURE 1. Scheme of the experimental setup of the T-PEEM

T-PEEM imaging experiments and resolution test on dry Diatom Algae

Transmission spectromicroscopy imaging experiments have been performed on silicate algae (Diatoms) using the Transmission Photoelectron Microscope setup. The dried algae have been dissolved and diluted in ultrapure water and spread onto the frontside of a silicon membrane (membrane thickness about 150 nm). The samples are loaded into a preparation chamber via a loadlock system where the flat backside of the membrane samples can be coated *in situ* with a CsI photocathode film to enhance the secondary electron yield from the membrane. Finally the samples are transferred *in vacuo* from the preparation chamber into the PEEM instrument.

Figure 2 shows a T-PEEM image recorded with an image field size of approx 13 μm at 95 eV photon energy. A finestructure consisting of a number of filaments is clearly visible within the diatoms (marked by white arrows). The lateral resolution of the recorded image has been determined from slope of the intensity linescans across the marked areas to be better than 60 nm.

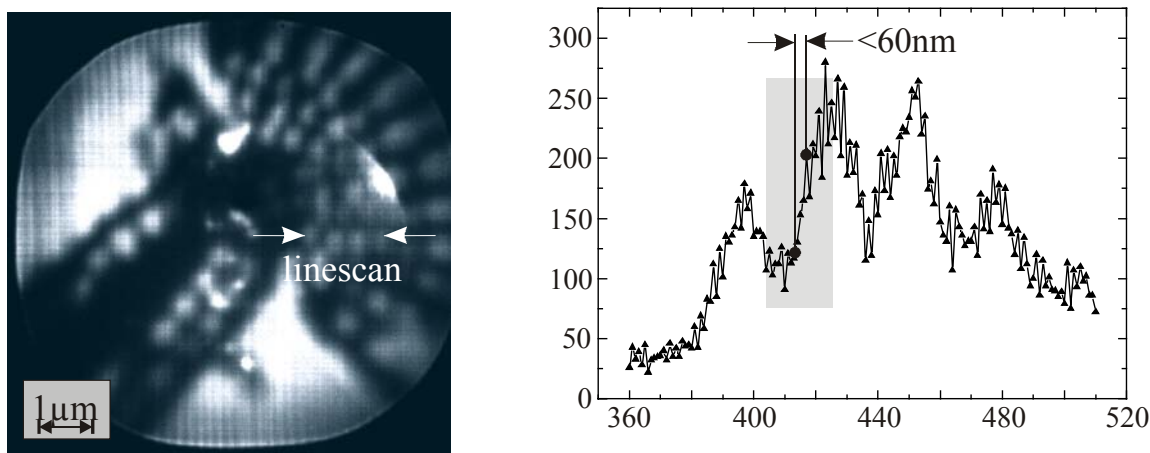


FIGURE 2. T-PEEM image of diatom at a photon energy of 95 eV and intensity line scan through marked image feature

The theoretical proximity resolution of the shadowgraph limited by diffraction is determined by the illuminating wavelength (13 nm) and the proximity distance of the object and the photocathode (approx. thickness of the membrane 150 nm) and can be estimated to be about 45 nm. Our experimentally achieved resolution has thus been found to be close to the theoretical limit and a further improvement may be achieved by reducing the membrane thickness (50-100 nm possible) and by imaging at higher photon energies. The aberration-limited resolution of the microscope sets a theoretical limit at about 20 nm.

T-PEEM spectromicroscopy of the Cu and O distribution of hemocyanine in a wet cell

First T-PEEM images of objects enclosed in a wet cell have been performed on the respiratory protein hemocyanine (Hc) which is a copper-containing protein responsible for oxygen transport in the blood of molluscs and

anthropodes. The T-PEEM image displayed in Fig. 3 (right) has been recorded at 530 eV photon energy with a field of view of approx. 150 μm and an acquisition time of 5 minutes. At this photon energy water and oxidized materials are highly transparent. The image displays absorbing materials (dark) agglomerated along the border lines of irregular shapes and a number of bright spots located within the objects. The image appears to be unchanged even after multiple exposures pointing to stable sample conditions due to the environmental sealing and immobilization of the Hc droplet in the wet cell. The complex nature of the sample (Hc protein in Tris buffer) does not allow to unambiguously distinguish the hemocyanine from salt complexes (dissolved in the buffer) in a single photon energy T-PEEM image.

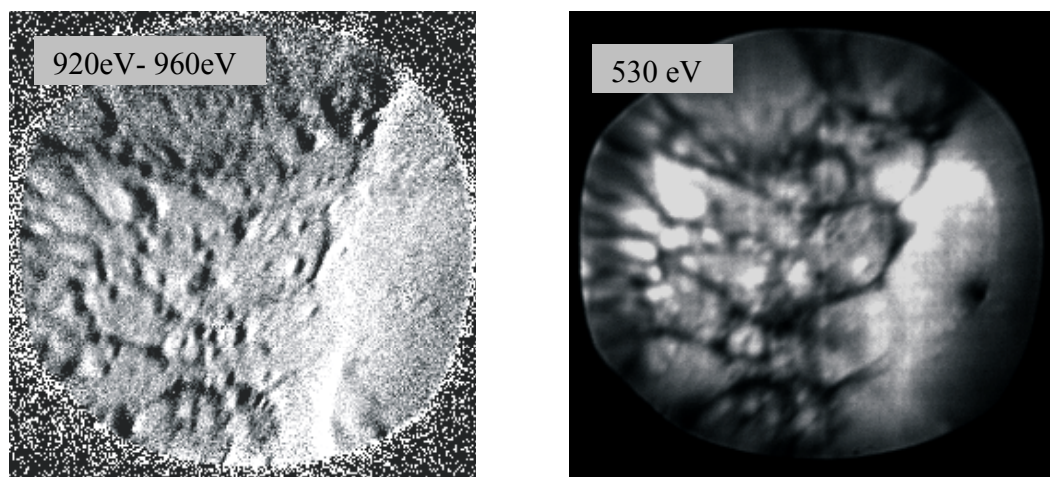


FIGURE 3. T-PEEM image of a hemocyanine film inclosed in a wet cell at the Cu-L edge (left) and O-K edge (right)

In order to identify hemocyanine-rich areas within the image two identical images have been recorded just below (920 eV) and above (960 eV) the Cu-L absorption edge. By calculating the normalized difference image the copper distribution is marked as bright image features. The difference image shows the distribution of Cu (bright) over the sample surface and therefore the distribution of hemocyanine. Note, that there are significant differences between the copper-distribution, as evaluated from the difference image, and the image recorded at the O-K edge pointing to differences with respect to the copper and oxygen distribution in hemocyanine.

Further experiments regarding the co-localization of oxygen and copper in hemocyanine require high resolution spectromicroscopic imaging of small regions of interests. Furthermore, chemical binding specificity may be achieved by XANES microspectroscopy evaluated from T-PEEM images at the Cu-L₂/L₃ edge.

ACKNOWLEDGMENTS

The authors like to thank Th. Woermann (group of Prof. T. Salditt, University of Goettingen, Germany) for providing the technology of ultrathin custom-made Si membranes and the excellent technical support by the BESSY staff. BMBF project funding under grant number 05KS1PBA-8 is acknowledged.

References

1. G. De Stasio et. al., Rev. Sci. Instrum 71 (1), 11-14 (2000)
2. G. De Stasio et. al., Rev. Sci. Instrum. 69 (9), 3106-3108 (1998)
3. R.N. Watts et.al., Rev. Sci. Instrum. 68 (9), 3464-3476 (1997)
4. U. Kleineberg et. al., Thin Solid Films 433, 230-236 (2003)

White beam x-ray waveguide experiments

A. Jarre, C. Fuhse, T.Salditt

Institut für Röntgenphysik, Universität Göttingen, Geiststr. 11, 37073 Göttingen, Germany

T.Panzner, U. Pietsch

Institut für Physik, Universität Potsdam, PO Box 601553, 14415 Potsdam, Germany

The use of x-ray waveguides for one dimensional beam compression and as coherence filter is a field of increasing interest. So far, x-ray waveguides were only used with monochromatic x-rays. In this report we want to point on the advantages of the use of x-ray waveguides in white synchrotron radiation beams as provided at the energy dispersive reflectometer (EDR) at BESSY II.

For hard x-rays very small beam sizes down to 10nm can be realized by making use of x-ray waveguides. Based on the principle of resonant beam coupling (RBC) well defined beam properties concerning coherence and the shape of the exiting beam are obtained. Anyway, aside from its optical properties related to (one-dimensional) beam compressing and coherence filtering, the coupling efficiency still is quite low and the flux of the waveguided beam too poor for many applications. The use of waveguides in a white synchrotron radiation beam increases the flux through the device, since the spectral acceptance of the waveguide is larger than the energetic width of beams typically provided on monochromatic beamlines. Depending on the waveguide material and geometry, the device either acts as broad bandpass monochromator in the case of single mode waveguides, or as multi-bandpass monochromator in the case of multimode waveguides.

While in monochromatic beams the waveguide has to be carefully aligned to the 'correct' incidence angle α_i in order to fulfill mode excitation condition in RBC scheme, in white synchrotron radiation the illuminated waveguide automatically 'finds' all energies which correspond to resonant mode excitation. The excited modes can be evidenced either as cusps in the plateau of total reflection (at fixed $\alpha_i = \alpha_f$), or directly in the energetic distribution of the farfield ($\alpha_f = 0$) of the waveguided beam as shown in Fig.1 for $\alpha_i = 0.194^\circ$. The WGs examined in the present experiment were prepared by magnetron sputtering, using Ni as a cladding and C as guiding layers on Si-wafers. Ni/C/Ni RBC waveguides with different layer thicknesses were prepared. Several of these structures were measured. The data shown in the illustrations correspond to a waveguide consisting of 5/32/20nm Ni/C/Ni on Si. Decreasing (increasing) α_i shifts the resonant mode energies to higher (lower) values, while the total number N of modes is set only by the waveguide geometry and index of refraction (s. Fig. 2). For the simulations shown, we have used the IMD software [1]. The internal intensity distribution for the waveguide parameters given above and the corresponding measured farfield is shown in Fig. 3.

The experiment was carried out at the EDR (energy dispersive reflectivity) dipole magnet beamline at BESSY II

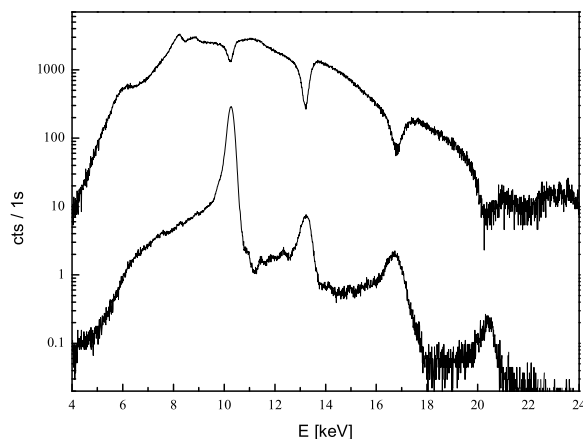


FIG. 1: The specular reflectivity (upper curve) shows characteristic cusps at energies E which satisfy the mode excitation condition. At $\alpha_f = 0$, the guided modes can be detected as a function of E (lower curve).

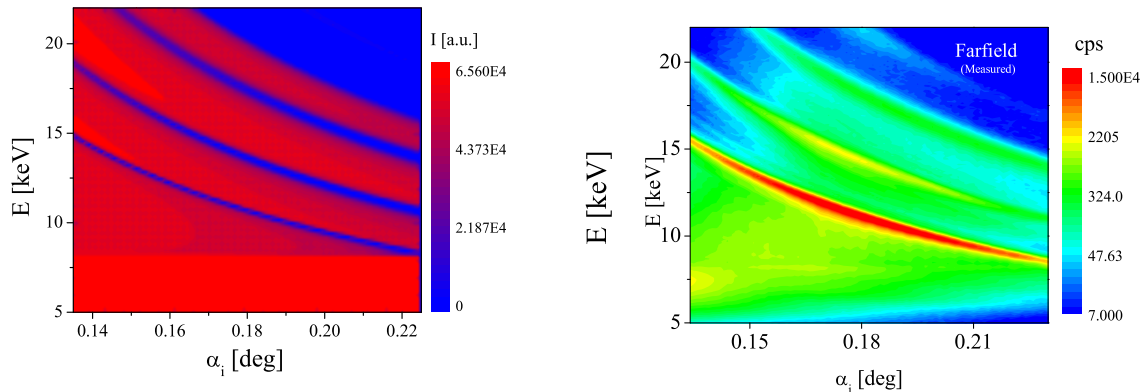


FIG. 2: left: The simulated reflectivity of the waveguide as a function of grazing incidence angle α_i and of energy E and right: the corresponding measured farfield.

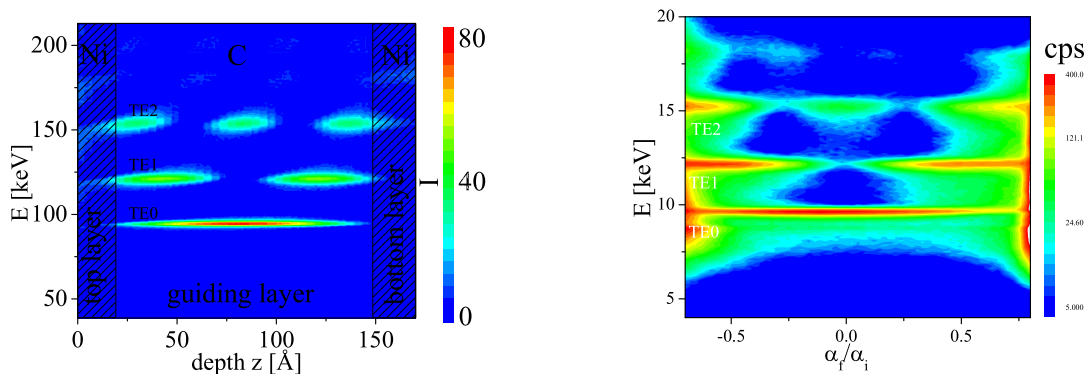


FIG. 3: left: The intensity distribution ($|\psi(E, z)|^2$) inside the waveguide structure calculated for $\alpha_i = 0.2^\circ$, as a function of E and z position in the guide and right: the corresponding measured farfield pattern of the waveguided beam exhibiting the expected angular distribution.

[2, 3]. We used the white beam with no optical components other than the $10 \mu\text{m}$ Pt-pinhole 350 mm in front of the waveguide, which was mounted on a HUBER goniometer [4]. The energy dispersive detector (Roentec Xflash 1000) was used to measure the reflected and the guided beam in the far-field at a distance of 1150 mm behind the sample.

Besides coupling the x-rays into the waveguide using the RBC method, we also performed experiments where the white beam was coupled directly into the front side of the waveguide ("front coupling"). Using this method, the flux at the exit of the waveguide is much lower than with the RBC method, but on the other hand this method has the advantage that for sufficiently long waveguides the contributions of the primary and specular reflected beam to the farfield are negligible. Depending on the x-ray energy and the angle of incidence, different combinations of modes are excited and are propagating through the waveguide with energy dependent propagation constants. Thus, a change of either energy or incidence angle changes the farfield pattern. In Fig. 4, three measured farfield patterns are shown as a function of energy for incidence angles ranging from -0.06° to 0.06° . The front coupling waveguide consists of 200 nm Ni/95 nm polyimide/20 nm Ni deposited on a Si substrate. It has a length of 4.2 mm and is supposed to have 8 modes. dzt denotes the position of the detector again placed 1150 mm behind the waveguide. The high intensities measured at dzt=0 result from the white beam transmitted through the Si substrate. Waveguide farfield patterns are seen for energies between approximately 7 keV and 20 keV. The center of the farfield pattern moves with the angle of incidence corresponding to a fixed exit angle. It is clearly seen that the shape of the farfield pattern varies strongly with energy. Due to the stronger absorption, no waveguide farfield can be detected for lower energies while for higher

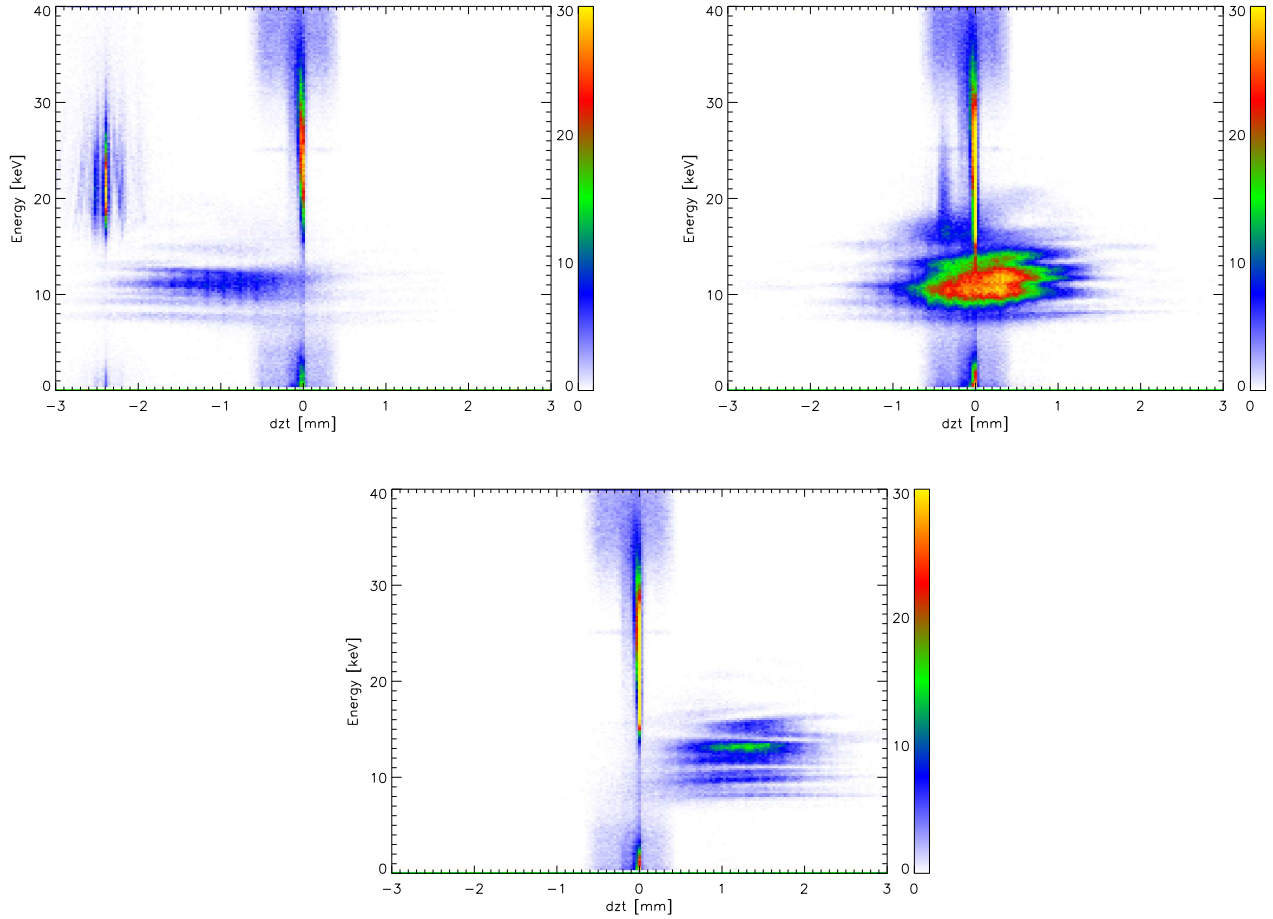


FIG. 4: The measured farfields of a front coupling waveguide as a function of energy E for different incidence angles $\alpha_i = -0.06^\circ, 0^\circ$ and 0.06° (from left to right).

energies the flux in the incident white beam is too low, which is due to the primary beam profile.

-
- [1] D. Windt, imd 4.1.1, 2000, <http://cletus.phys.columbia.edu/windt/idl>.
 - [2] T. Panzner, W. Leitenberger, J. Grenzer, Y. Bodenthin, T. Geue, U. Pietsch, and H. Möhwald, *J. Phys. D* **36**, A93 (2003).
 - [3] U. Pietsch, J. Grenzer, T. Geue, F. Neissendorfer, G. Brezesinski, C. Symietz, H. Möhwald, and W. Gudat, *Nucl. Instrum. Methods A* **47**, 777 (2001).
 - [4] A. Jarre, T. Salditt, T. Panzner, U. Pietsch, and F. Pfeiffer, submitted to APL.

FT-IR synchrotron ellipsometry for thin film analysis

M. Gensch¹, K. Hinrichs¹, R. Passmann^{1,2}, U. Schade³, N. Esser¹, E.H. Korte¹ and A. Röseler¹

¹Institut für Spektrochemie und Angewandte Spektroskopie, Institutsteil Berlin, Albert-Einstein-Straße 9, 12489 Berlin

²Institut für Festkörperphysik, Technische Universität Berlin, Hardenbergstraße 36, 10623 Berlin

³Berliner Elektronenspeicherring Gesellschaft für Synchrotronstrahlung mbH, Albert-Einstein-Straße 15, 12489 Berlin

email (local contact): hinrichs@isas-berlin.de

Ellipsometry in the infrared spectral range combines the advantages of ellipsometry with the merits of vibrational spectroscopy which gives access to the molecular fingerprint of the sample. Therefore by evaluating the ellipsometric parameters not only the thickness of the films but also the preferred orientations of dipole moments of molecular vibrations can be revealed.

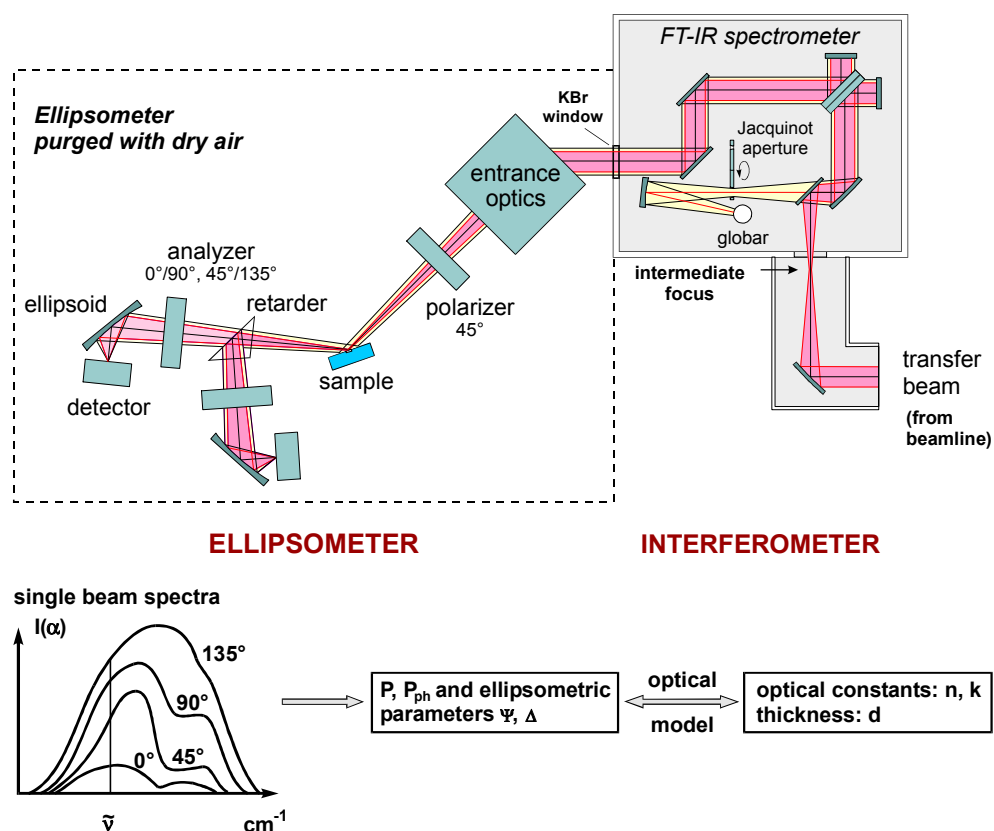


Fig.1: Schematic of set-up at the IRIS Beamline [1] and principle of the measurement [2]:

The ellipsometric parameters ψ and Δ as well as the degree of polarization P and of the phase polarization P_{ph} are measured. In the case of anisotropic samples the optical constants n , k and the thickness of a film are derived via best-fit calculations based on optical models[3,4].

The FT-IR ellipsometer at the IRIS beamline utilizes the brilliance of the synchrotron source for the investigation of small samples or sample areas [1]. The gain in intensity can in general be used either for investigation of samples that had previously been too small, or for studying samples that were too heterogeneous (due to laterally varying thickness or roughness) for conventional IR ellipsometry. The principle of the measurement and of the elucidation of the optical constants is shown in figure 1 together with a schematic of the set-up at the IRIS beamline. During the commissioning of the IRIS Beamline the set-up was tested by

investigating a $1 \times 1 \text{ mm}^2$ piece of a thin polyimide (PI2611, Du Pont) film on a silicon substrate [5] (see figure 2). Earlier studies of thicker films of this polyimide [6] indicated a predominately uniaxial anisotropy with the optical axis parallel to the substrate normal. A number of specific vibrational modes of organic groups like C-N-C, C=C and C=O are present in the spectra, therefore these films were considered as appropriate test samples.

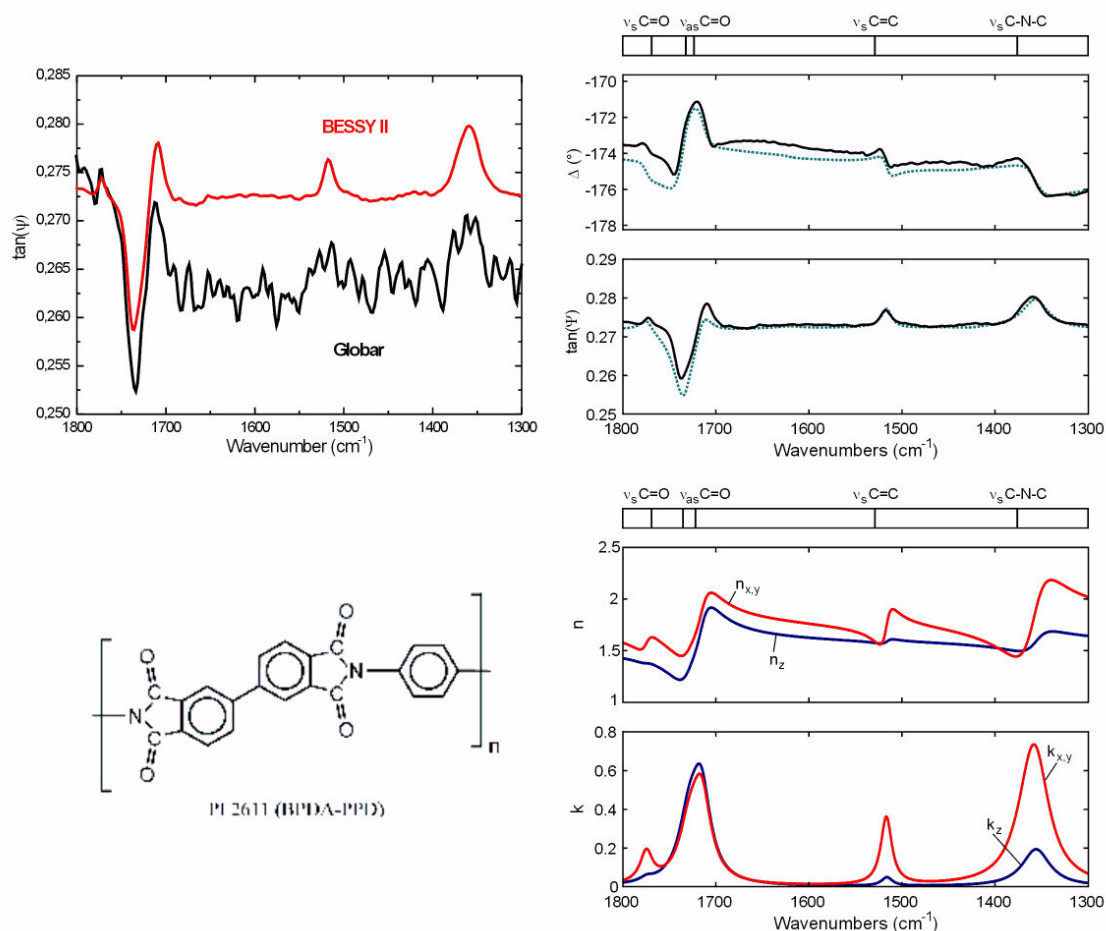


Fig. 2: Anisotropy in a $1 \times 1 \text{ mm}^2$ polyimide film on silicon sample

$\tan \psi$ spectra of the 1 mm^2 sample taken with the synchrotron source and the globar for comparison (**top left**) and structural formula of the investigated polyimide (**bottom left**) measurement (solid line) and calculation of the $\tan \psi$ and Δ spectrum of the polyimide film as well as the related anisotropic optical constants n_{xy} , n_z , k_{xy} , k_z (**right panels**). For an ideal uniaxial polyimide film with the optical axis along the substrate normal (along z) one expects only components within the plane of the substrate (xy) for the particular molecular vibrations present in the spectra. In contrast we find a rather isotropic distribution of transition dipole moments for the asymmetric C=O bands which can be interpreted as resulting from a perturbed Imide ring structure. The film thickness is determined to be 34 nm.

The optical models to describe the ellipsometric measurements of the sample generally also assume a sufficient homogeneity of the probed area. A variation of properties like thickness, roughness or molecular orientation over the investigated sample area make the elucidation of the optical constants difficult if not impossible [4]. The problem of heterogeneous samples can be tackled making use of the small focus of the FT-IR synchrotron ellipsometer as can be seen on the following example of a film of bacteriorhodopsin membrane fragments. The films were prepared by drying bacteriorhodopsin from *Halobacterium salinarium* onto a gold substrate. Bacteriorhodopsin is known to form a uniaxial 2D crystal-like structure known as purple membrane (see figure 3, bottom left). The function of this system in the bacterium is a light driven proton pump. The films are very stable, remain biologically active and therefore represent an important model system for biological energy transduction. There has been an ongoing interest in the anisotropic optical properties of these films for many years. However

the question for absolute values of the infrared optical constants remains essentially unresolved to this date. Exemplarily ellipsometric measurements on different spots of a purple membrane film are shown in figure 3. The finding of this mapping is that in the case of our sample the roughness of the film varies laterally while the molecular structure and the thickness of the film are rather preserved. The effect of a deviation from the ideal optical model due to the roughness is most obviously manifested in the damped amplitude of the interference fringes between 1900 cm^{-1} and 2800 cm^{-1} as well as in the decay of the degree of polarization P .

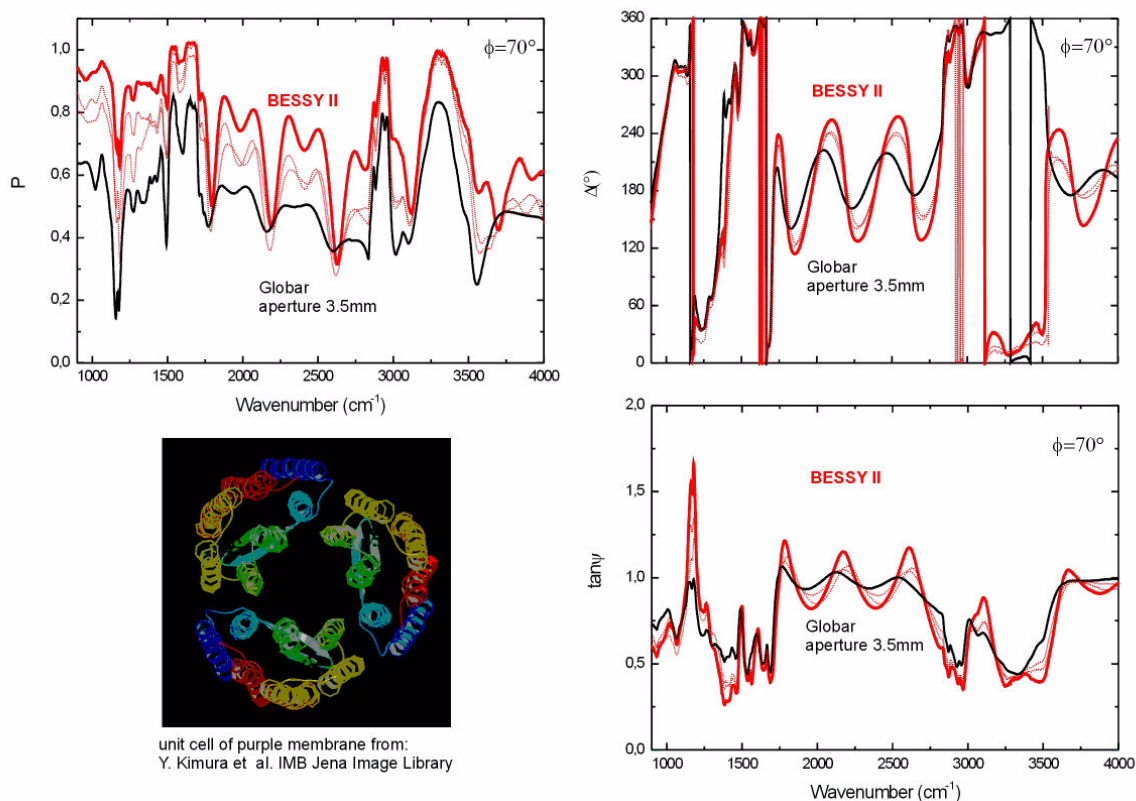


Fig.3: “mapping” of a purple membrane film

The degree of polarization P , the $\tan \psi$ and Δ spectra of purple membrane measured at different positions on the sample using the synchrotron source (red) are shown together with a lab experiment (black). P is a measure for the “optical” quality of the investigated spot and is poor (<0.6) in the lab experiment. By mapping the sample with the FT-IR synchrotron ellipsometer a spot on the sample exhibiting an optimum P value was identified (solid red). Ellipsometric parameters from this spot are currently evaluated for the determination of the optical constants. The angle of incidence ϕ was in all measurements 70° .

Acknowledgement: Support of this work through the BMBF grant 05 SR8kk19 is gratefully acknowledged.

- [1] M. Gensch, K. Hinrichs, A. Röseler, E.H. Korte and U. Schade, *Anal. Bioanal. Chem.*, 376 (2003) 626
- [2] A. Röseler, *Infrared Spectroscopic Ellipsometry*, (Akademie Verlag Berlin 1990)
- [3] R.M.A. Azzam and N.M. Bashara, *Ellipsometry and polarized light*, (North Holland Publishing Company, Amsterdam-New York-Oxford 1977)
- [4] M. Schubert, *Phys. Rev. B* 53 (1996) 4265
- [5] K. Hinrichs, M. Gensch, A. Röseler, E.H. Korte, K. Sahre, K.-J. Eichhorn, N. Esser and U. Schade, *Applied Spectroscopy*, 57 (2003) 1250
- [6] K. Hinrichs, D. Tsankov, E.H. Korte, A. Röseler, K. Sahre and K.-J. Eichhorn, *Applied Spectroscopy*, 56 (2002) 737

High Resolution Angle Resolving Toroidal Electron Spectrometer

A Tadich^a, L Broekman^a, E Huwald^a, R Leckey^a, J Riley^a, T Seyller^b and L Ley^b

^a *Department of Physics, La Trobe University, Victoria 3086, Australia.*

^b *Institut für Technische Physik, Universität Erlangen/Nürnberg, Erlangen, Germany.*

Introduction

Display electron analysers which detect electrons with a range of energies and range of emission angles, are now becoming the experimental norm. Spherical analysers can detect electrons with energy ranges of approximately 10% of the pass energy and with emission angles of up to $\pm 10^\circ$. An electron analyser with toroidal geometry operated at BESSY I for many years. This analyser had a single energy detection but with a range of emission angles of $\pm 90^\circ$.

The construction of a 2nd generation analyser with this geometry was completed in Australia in February, flown to Berlin and has been operated on TGM7 and TGM4 during 2003. This analyser has a significantly increased design resolution both in energy and angle and has the ability to detect electron energies for a range of 8% of the pass energy while retaining $\pm 90^\circ$ angular detection capability.

Analyser Design

The geometry of this analyser is shown in Figure 1.

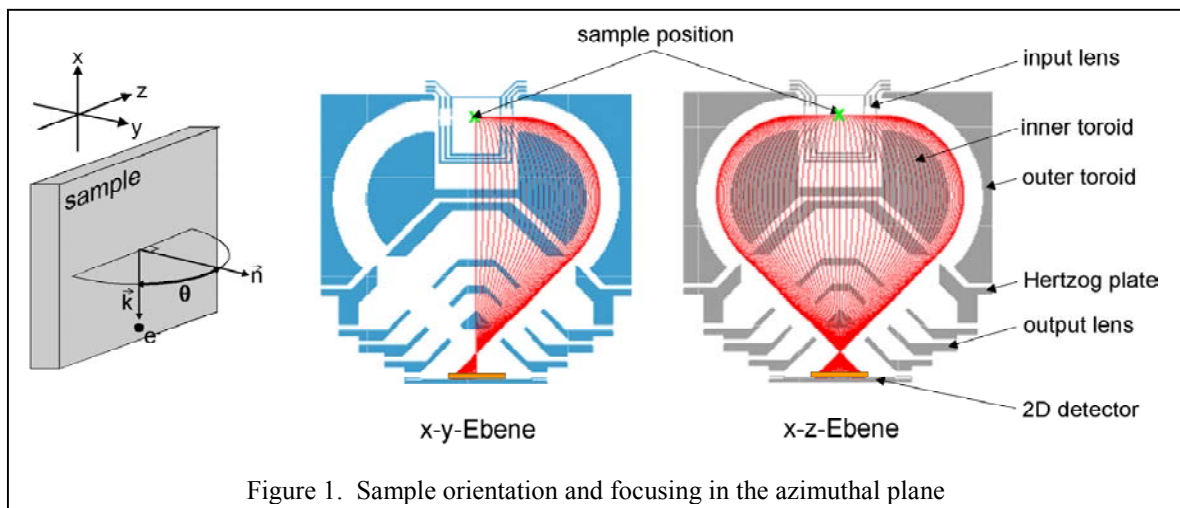


Figure 1. Sample orientation and focusing in the azimuthal plane

The sample surface is placed such that the cylindrical axis of the analyser lies in the surface and is perpendicular to the surface normal. Trajectories are shown for electrons with the same energy but with different emission angles forming a circular image on the detector. The position of the electron on the circle has a direct correlation with the angle of emission. Electrons emitted from a region around the centre of illumination are all focused at the same point with insignificant aberrations giving a high angle resolution. The position of this focus is determined by the input lens and by the geometry of the toroids and output lens. The output lens has only a small effect on this focus position.

Electron trajectories for electrons emitted at a range of angles of $\pm 0.5^\circ$ for different energies are shown in Figure 2.

The radial position on the detector increases with increasing energy permitting parallel detection. The focus in this plane is determined by the three elements, the input lens, the toroidal sectors and the output lens. Thus by suitable choice of voltages, the foci in the azimuthal plane and the “energy” plane can be brought into coincidence.

The design resolution is 1 part in 5000 of the kinetic energy. The resolution is limited by aberrations inherent in the toroidal sectors so does not remain a fixed fraction of the pass energy.

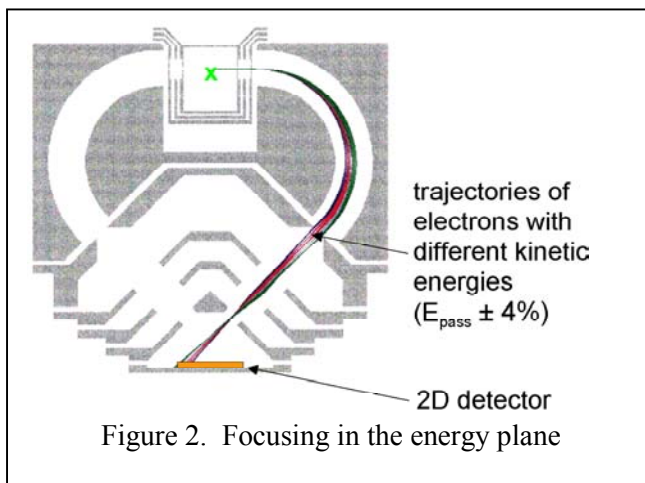


Figure 2. Focusing in the energy plane

The detector in this analyser consists of a 70 mm diameter channel plate stack with a phosphor screen. An external low noise cooled CCD camera acquires the image into an array 1200 X 1000. The pixel array currently limits the resolution in angle but this can be improved with an increase in the pixel density on the CCD.

Results.

The analyser has been operated on TGM4 and TGM7 which has not permitted the ultimate energy resolution to be determined. The angle resolution has been estimated from the surface states on Cu.

Cu (111) surface.

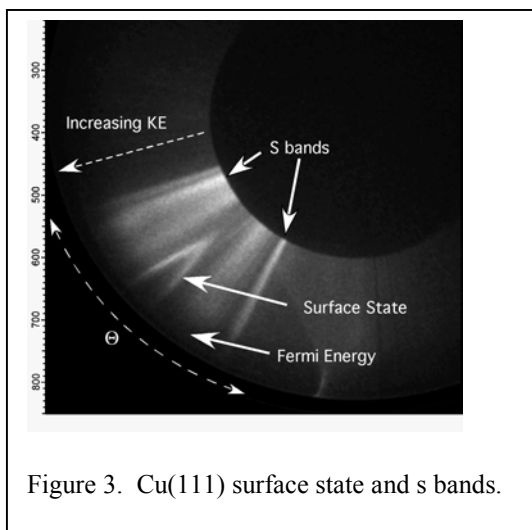


Figure 3. Cu(111) surface state and s bands.

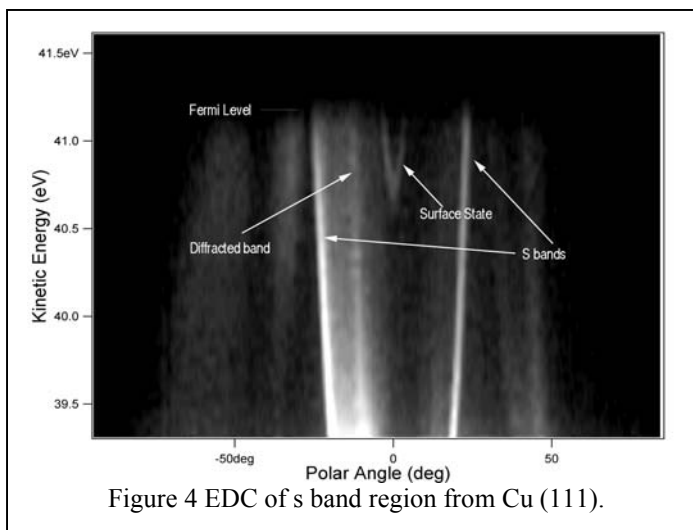


Figure 4 EDC of s band region from Cu (111).

The surface state on Cu (111) is shown in Figure 3 as seen by the detector illustrating the parallel detection capability in energy and angle. The surface state and the s-p bands dispersing to the Fermi level are clearly visible. An energy distribution is shown for the corresponding band region of Cu as observed from the Cu(111) surface. Data has also been obtained from SiC surfaces and from the alloy Cu₃Au, reports of which are contained elsewhere in this BESSY Year Book.

First Commissioning Results of the U125/2-10m-NIM

A. Balzer¹, R. Follath¹, G. Reichardt¹, A. Ehresmann², S. Klumpp², H. Molter², H. Schmoranzer²

¹ BESSY, Albert-Einstein-Strasse 15, 12489 Berlin

² TU Kaiserslautern, FB Physik, Erwin-Schrödinger-Straße, 67663 Kaiserslautern

The quasi-periodic undulator U125/2 is an ideal source for a normal incidence monochromator. Usually in this energy range spectral purity due to higher diffraction orders is a challenging problem. Especially in the range between the LiF-cut off and the transmission onset of thin metal filters only expensive and clumsy gas filters offer some possibilities to eliminate higher order light. With the quasi-periodic design of the undulator the problem is shifted into the source to a great extent. Higher undulator harmonics are shifted to lower energies compared to the integer multiples of the first harmonic, hence higher harmonics and higher diffraction orders no longer coincide. This feature gives the flexibility to optimize the other major monochromator characteristics like resolving power and transmission [1].

In the monochromator design new mechanical concepts have been incorporated. Stepping-motor driven sine drives have been completely replaced by in-vacuum piezo-motors (Nanomotion) which are capable to rotate the grating cradle with high speed and to reach nm resolution. Because the driving concept is based on friction a high precision angular encoder (Heidenhain UHV-RON 905) is indispensable. In order to obtain the utmost resolving power from this system a new control hard- and software was installed. The piezo-motor for the grating rotation is operated in closed loop with the angular encoder. For large driving ranges this concept is similar to a servo-motor. In the fine-tuning range a so-called DC-mode is activated, allowing the piezo-motor to be operated like a conventional piezo-translator over a range of ± 400 nm with nm resolution. Fig. 1 shows the mechanical setup of the grating chamber. The complete vacuum vessel is mounted on an air-side translational stage.

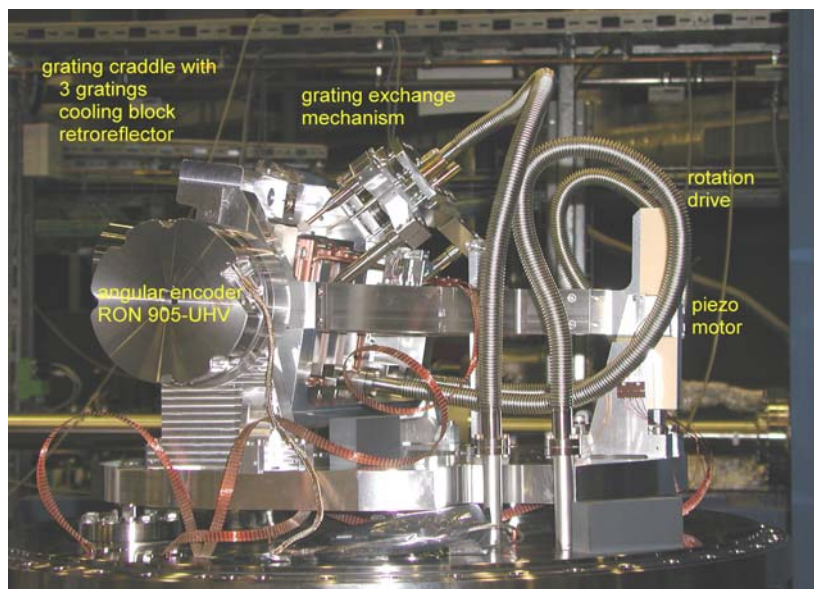


Fig. 1:
10m-NIM Grating Unit.

The matchbox-sized piezo motor is situated at the end of a 500 mm long lever arm. The angular encoder is mounted directly on the rotation axis. This design enables positioning increments as small as 0.0005 arcseconds.

Environmental noise, either from ground vibrations or from acoustic impact is a severe limiting factor for high resolution monochromators. Setting the drive unit to a fixed angle and sampling the angular encoder signal demonstrates this influence (Fig. 2). Oscillations with amplitudes of up to 0.1 arcsec and a distinct frequency pattern are detectable. The new piezo-drive allows for an efficient and fast active damping of these oscillations. Fig. 2 additionally

shows forced periodic oscillations up to 50 Hz, demonstrating the capability of the system to react on and hence damp frequencies to at least this limit.

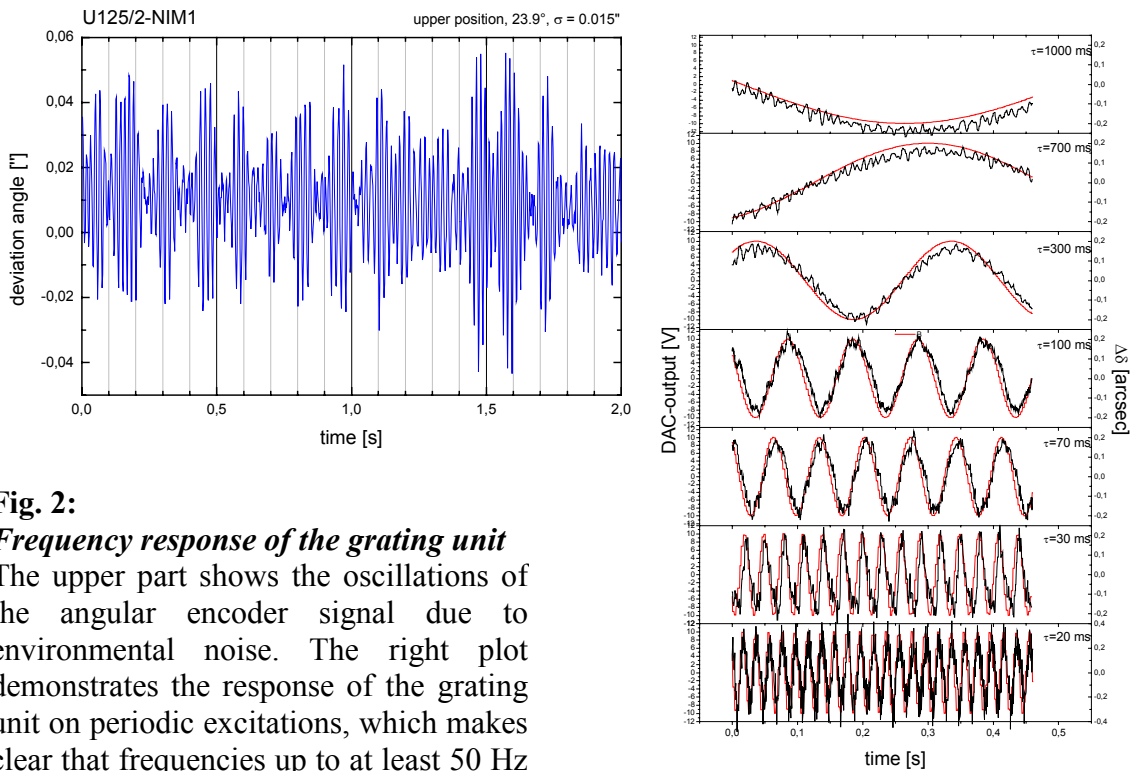


Fig. 2:
Frequency response of the grating unit
 The upper part shows the oscillations of the angular encoder signal due to environmental noise. The right plot demonstrates the response of the grating unit on periodic excitations, which makes clear that frequencies up to at least 50 Hz can be actively damped.

Of course resolving power is a major issue for a high dispersion instrument like the 10m-NIM. Therefore this was one of the first tests performed with the device after installation and optimisation of the control software. The Rydberg series of the noble gases like Neon, Argon or Xenon are ideal test cases for this energy range [2].

A differentially pumped ionisation chamber with a 10 mm long 1 mm diameter entrance aperture was used to record total ion yield (TIY) spectra. The gas pressure was as low as 10^{-5} to 10^{-4} mbar in order to minimize preabsorption and collisional broadening effects. The collection voltage was set to 5V. The ionisation current was measured with an electrometer (Keithley, model 6517) in high accuracy mode. By means of a photo diode at the end of the ionisation chamber absorption spectra can be recorded.

Fig. 3 shows a TIY-spectrum of Neon between the $I_{3/2}$ - and $I_{1/2}$ -thresholds recorded with the 1200 l/mm grating in second order and 10 μm entrance and exit slit size. The ionisation threshold $I_{3/2}$ between the $13s'$ and $12d'$ resonance is indicated by an arrow. The resonances below this threshold are only visible due to collisional ionisation. Due to the autoionisation character the ns^2 -($n-1$) d' -doublets show Fano-Beutler profiles with positive and negative form factor q , hence between these lines the intensity never goes back to the baseline. The doublets could be resolved up to $n=34$. A fit to the well resolved lines yields a raw linewidth of 195 μeV in average, consisting of the natural linewidth, Doppler-broadening and monochromator bandpass. This means that the instrumental resolving power is at least 110000. This excellent value can be easily obtained with still good intensities and remarkable long-term stability.

The absolute wavelength scale almost perfectly coincides with spectrographically recorded absorption data [1a]. Their value for the $12d'$ -resonance of 57.48912 nm only deviates 5 pm from ours yielding an absolute accuracy of $8 \cdot 10^{-5}$. Hence, only by carefully calibrating the

zero order the absolute angle measurement with the RON905 gives an almost perfect wavelength scale.

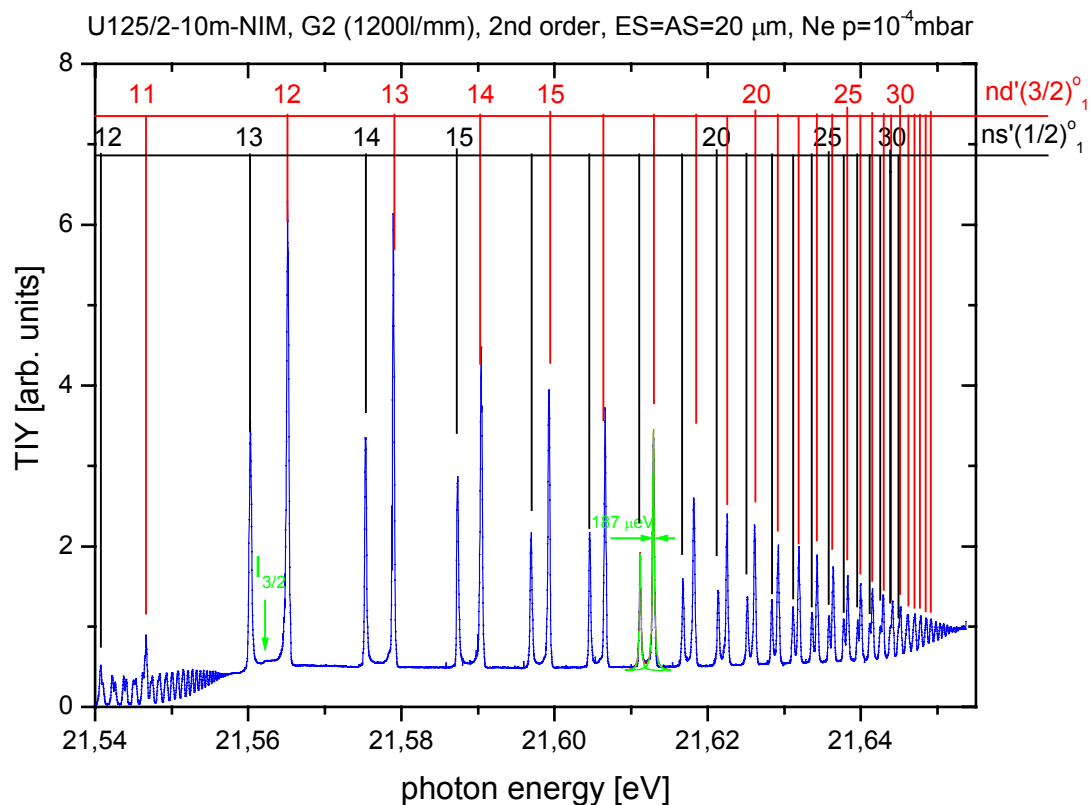


Fig 3: Neon autoionisation spectrum between the two $2p^{-1}$ thresholds recorded with $10 \mu\text{m}$ slits in second order of the 1200 l/mm grating. A fit of Lorentzian profiles to the well resolved lines yields a linewidth of $195 \mu\text{eV}$ in average.

Unfortunately the grating planned for highest resolving power (2400 l/mm) shows severe “ghosts”. Experiments with only partial illumination demonstrated that on one half of the grating the grating period deviates from the 2400 l/mm and changes continuously. This grating will be replaced in the next shut down.

Although the transmission of the beamline even with a very small entrance slit ($10 \mu\text{m}$) is already very good, the plane elliptical focusing mirror M2 will be replaced by a better one. The calculated focus of $<10 \mu\text{m}$ will then make the entrance slit practically dispensable. A further upgrade concerns the monochromator mechanics. An in-situ adjustment for the dispersion plane will be retrofitted to the grating goniometer. In addition a position detector will be mounted in front of the exit slit slightly above the optical axis. By means of the M1 rotational adjustment the position measured with this detector will be held constant on the μm -scale and so cancels out any misadjustment or instability.

- [1] Reichardt et al, NIM A **467-468**, 462 (2001)
- [2] (a) Ito et al, J.Opt.Soc.Am. B **5**, 2006 (1988),
- (b) Yoshino et al, J. Opt. Soc. Am. B **2**, 1268 (1985),
- (c) Yoshino et al, J. Opt. Soc. Am. **60**, 1220 (1970)

Compressed Electron Bunches for THz-Generation: Operating BESSY II in a Dedicated Low Alpha Mode

J. Feikes, K. Holldack, P. Kuske, G. Wüstefeld
BESSY mbH, Albert-Einstein-Str. 15, D-12489 Berlin

For the first time an electron storage ring has been operated during regular user shifts in a dedicated 'low alpha' (short electron bunch) mode, where electron bunches are shortened by a factor of 5 for THz-radiation and short X-ray pulses experiments. Operation experiences as compared to the regular user mode are presented.

BESSY II is presently the only electron storage ring worldwide which can generate stable, broadband coherent THz radiation (CSR) [1]. This radiation is up to 10^7 more powerful than the incoherent radiation, Fig. 1. There are two machine modi where enhanced THz radiation is produced. One mode is the regular user optics, where no changes of the optics are required only the beam current has to be at least 4 mA per bunch. In the multi bunch shift at 250mA the single bunch current is less than 0.7 mA, but in the regular single bunch user shifts bunch currents up to 20 mA are realized. Above the 4 mA threshold the bunch becomes unstable and powerful bursts of CSR are emitted [2] in a more or less irregular temporal manner.

The second mode is a dedicated 'low alpha' machine optics. In this case the bunches are longitudinally compressed and, depending on the beam current, stable CSR below and bursting CSR above an α dependent threshold current is emitted. The 'low alpha' bursting mode is, in comparison to the bursting mode of the user optics, much more stable and well suited for experimental applications [3],[4], [5]. In the 'low alpha' mode the 'momentum compaction factor', α , of the machine is reduced. The term α describes the relative increase of the electron orbit, dL/L_0 , with deviating momenta, dp/p_0 :

$$dL/L_0 = \alpha dp/p_0.$$

Table 1: Parameters of the Low Alpha Optics

optics parameter	normal optics	low alpha optics
nat. emittance	6 nmrad	30 nmrad
beta hor./vert. at D-ID	18.0 m/ 3.5 m	16.0 m / 2.5 m
beta hor./vert. at T-ID	1.3 m/ 1.3 m	16.0 m / 2.5 m
dispersion at ID	0.0 m	-0.35 m
bunch fill pattern	buckets filled	buckets empty
multi bunch (MB)	200	200
single bunch (SB)	1	399
SB and MB current	<i>rms</i> bunch length	life time
0.25 mA 50 mA	7.5 ps	8 h
0.10 mA 20 mA	5.5 ps	20 h
0.025 mA 5 mA	3.5 ps	40 h

By an appropriate detuning of the quadrupoles α can be varied, starting with $7.3 \cdot 10^{-4}$ of the regular user optics down to $7.3 \cdot 10^{-6}$ and less. Parallel with the reduction of α , the bunch length is lowered, following a $\sqrt{\alpha}$ dependency at lower bunch currents. A special optics, the so called 'low alpha' optics is set up for the purpose of bunch shortening. This optics requires carefully tuned sextupole corrections and has a 16-fold symmetry, different from the 8-fold symmetry of the standard user optics. In the low alpha optics the electron bunch length becomes comparable to the wavelength of the emitted THz radiation, which is then able to superimpose coherently in phase and become extremely powerful. These short bunches also emit short X-ray pulses of 3 ps *rms*-length which are of interest for time resolved X-ray experiments. In this case, even a low current, single bunch filling was offered.

For the BESSY 'low alpha' user shift a value of $\alpha = 3.5 \cdot 10^{-5}$ was chosen, where the zero current bunch *rms*-length is about 1 mm, five times shorter than the bunchlength in the regular user optics. This value of α is balanced between less stable operation with a further reduced bunch length and a reliable operation of the machine. With this α value it is possible to inject at a good rate into the machine - no detuning of the optics just for the injection process is necessary. A smaller α value leads to less stable beam orbits, for example to thermally dependent orbit shifts.

A specially adapted, automatic orbit correction procedure was developed (R. Müller, BESSY). For this correction scheme the rf-correction was excluded. The present rf bit-resolution of 1 Hz at 500 MHz rf-frequency is not sufficiently fine in case of the small α orbit corrections and lead to steplike orbit changes of up to 40 micrometers. With the smoothly running orbit correction it is possible to operate insertion devices. Hence, other users, who are not interested in this special mode are not excluded. The THz experiments are not sensitive to small orbit changes. Strong insertions like the superconducting wave length shifters and wigglers with small gaps were not operated since the distortion of the beam optics would be too large.

The helical insertion devices affected significantly the far infrared intensity if the polarization was changed. This is normally performed by a longitudinal shift of the magnetic rows and leads to a change of the horizontal focussing, which in turn affects the low alpha setting (α -change up to 20%). The power of the emitted THz radiation is dependent on α and sensitively reacts to the horizontal tune change. However, a reset of the horizontal tune shift by the global quadrupoles does reset the α value, as long as the tune shift is not too large. A tune feed forward will be developed to control this [6]. It is very likely, but not yet proven, that the THz-intensity will recover with this correction.

The THz radiation was analyzed by means of a Martin-Puplett far infrared spectrometer, detecting the intensity modulation by a liquid helium cooled InSb detector. The time constant of the detector is faster than the revolution time of the electrons in the storage ring of 800 ns. A beam filling of 200 bunches out of 400 possible buckets was chosen to have an optimum signal modulation.

The initial beam filling was 40 mA providing a sufficiently strong THz-signal in combination with a good lifetime of more than 10 h. From earlier measurements it was shown, that the corresponding single bunch current of 0.25 mA is far above the bursting threshold, which is α -dependent and now at about 0.08mA. It was also shown that the bursting in the low alpha multibunch mode does not deteriorate the quality of the spectra.

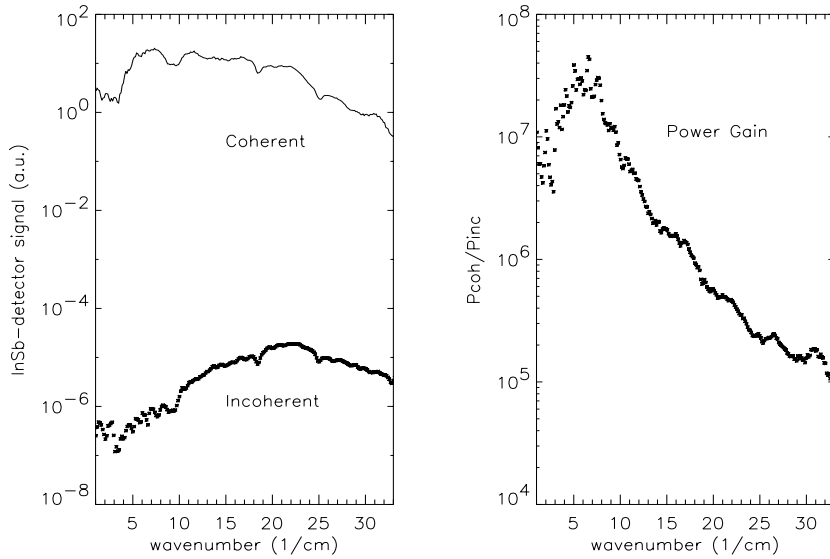


Figure 1: Emitted THz-Power at 20 mA in the low alpha optics. The left figure shows raw data of the coherent and incoherent THz power measurements with an InSb-detector. The right figure shows the ratio of these two intensities, yielding a power gain of more than 10^7 achieved by the coherent emission process.

The low alpha week for user operation proved that this optics mode is running very reliably with good beam stability and lifetime. It is not limited to special machine shifts of experts only. It can be offered as a regular, dedicated user shift and is well handled by the machine operators.

1 REFERENCES

- [1] M. Abo-Bakr et al., Phys. Rev. Lett. 88, 254801 (2002).
M. Abo-Bakr et al., Phys. Rev. Lett. 90, 094801 (2003).
G. Wüstefeld, BESSY Highlights2002, p. 49.
- [2] J. M. Byrd et al., Phys. Rev. Lett. 89, 224801 (2002).
- [3] E.J. Singley, M. Abo-Bakr, D.N. Basov, J. Feikes, et al. "New scientific opportunities with intense coherent THz synchrotron radiation: Measuring the Josephson plasma resonance in $\text{Bi}_2\text{Sr}_2\text{CaCu}_2\text{O}_8$ ", to appear in Phys. Rev. B., 2004.
- [4] U. Schade, K. Holldack, H.-W. Hübers (DLR), P. Kuske, G. Wüstefeld, "THz Near-Field Microscopy at BESSY", this annual report, and Applied Physics Letter, Februar, 2004.
- [5] H.-W. Hübers (DLR) and S. G. Pavlov (DLR), K. Holldack, P. Kuske, U. Schade, and G. Wüstefeld, "THz Spectroscopy of excited acceptor states in p-type Germanium", this annual report, to be published.
- [6] J. Bahrtdt, A. Gaupp, J. Feikes, W. Frentrup, M. Scheer, "Insertion Devices", this annual report.

The Crystal-based Bragg-Fresnel lenses.

A.Firsov

BESSY, Berliner Elektronenspeicherring-Gesellschaft für Synchrotronstrahlung mbH, Albert-Einstein-Str. 15, D-12489, Berlin, Germany.

Recently we have reported about design and test of a crystal-based Bragg-Fresnel lenses [1]. This type of focusing elements can be effectively used in the energy range from 4 keV to 200 keV and has an energy resolution of a crystal ($E/\Delta E > 5000$). We have combined in focal plane the first and second order of diffraction to increase the lens aperture. The lens structure has been made by e-beam lithography and chemical etching with the depth of profile corresponding to an optimal value. Later experiments with synthetic x-ray holograms on crystal (Si) substrates have shown that very high efficiency and spatial resolution can be obtained using the structure which consists of a phase-shift layer on a top of the crystal instead of profile inside the crystal. It was achieved 2.5 μm resolution at the energy of 8 keV in a ‘white’ X-ray beam [2].

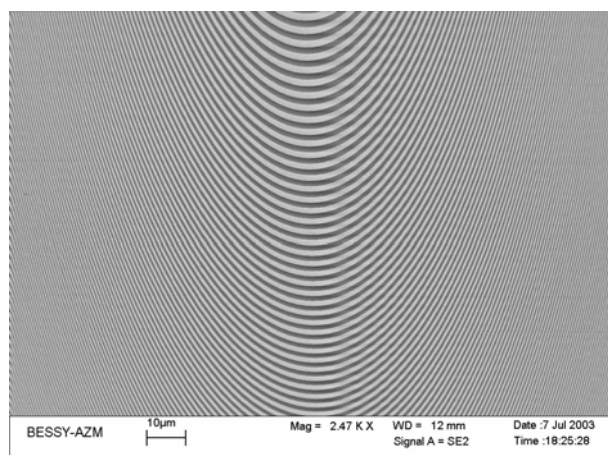


Figure 1. Part of an elliptical lens based on Si crystal.

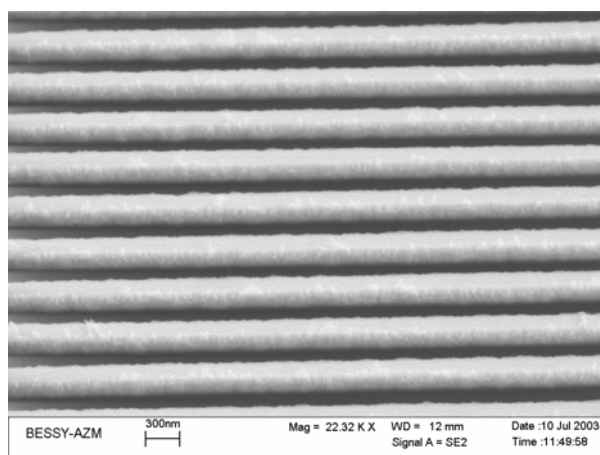


Figure 2. View of the smallest zones. Thickness of a gold phase-shift layer is equal to 200 nm.

The goal of present experiment is to test experimentally different Bragg-Fresnel lens structures made on the surface of Si and Ge crystals by e-bam lithography and “lift-off” technology. These tests will lead to the development of the technology of BFL with high-efficiency.

Figures 1 and 2 show the quality of the diffraction focusing elements fabrication. The photos were made with scanning electron microscope LEO1560. On one Si crystal substrate were fabricated three different types of focusing elements – elliptical, linear, and meridional. All three lenses have the same focus distance of 40 centimeters and minimum diffraction feature size of 200 nanometers.

The experiments were performed at BESSY beam line 13.2 (EDR). Preliminary alignment of the lens system was performed with the help of a CCD X-ray camera (Figure 3). Final alignment of the lens system position was reached in a process of scanning with a 5 microns pinhole of a lens focal plane and analysis of an intensity distribution. Linear scans (horizontal and vertical) via pick of intensity are of the main interest. We need to compare width of a picks at a half-height with supposed geometrical size of a source image. A rate of a maximum intensity to a noise (signal from substrate out of diffraction structure) is of the interest as well.

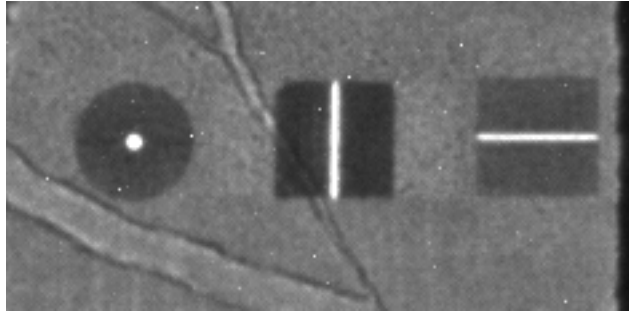


Figure 3. Image from X-ray CCD camera of three different type lenses.

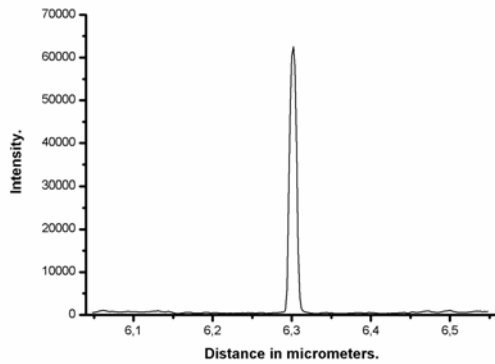


Figure 4. Horizontal scan with 5 micrometers pinhole via maximum intensity.

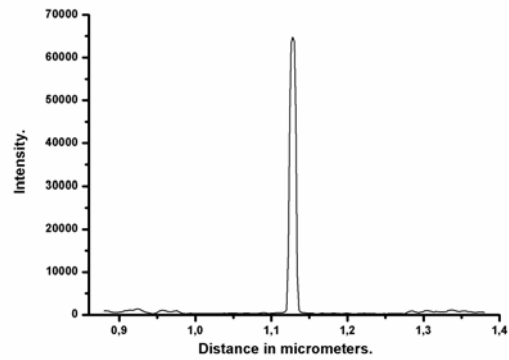


Figure 5. Vertical scan with 5 micrometers pinhole via maximum intensity.

1. Firsov, V. Aristov, A. Asryan, A. Erko, M. Ferstl, W. Gudat, S. Shapoval, A. Svintsov "Crystal-based diffraction focusing elements for third-generation synchrotron radiation sources", Nuclear Instruments and Methods in Physics Research A 467-468 (2001) 366-369.
2. A. Firsov, A. Svintsov, S.I. Zaitsev, A. Erko, V. Aristov "The first synthetic X-ray hologram: results", Optics Communications, 202 (2002) 55–59.

Insertion Devices

J. Bahrtdt, J. Feikes, W. Frentrup, A. Gaupp, M. Scheer

The Femto-Second-Slicing Project

Using the bunch slicing technique femto second pulses can be produced at storage rings [1], [2]. BESSY will implement such a bunch slicing facility at the straight section H11. The upstream module of the UE56/1 double undulator has been removed in summer 2003 to provide space for the modulator module. The downstream module will be used as the radiator. Thus, XUV-femto second pulses with variable polarization will be available.

The energy modulation of the electron bunch due to the laser field scales with the square root of the number of modulator periods. The period length has to be chosen such that the number of periods is maximized under the constraint that the first harmonic can be tuned up to 800 nm, the wavelength of the Ti:Sapphire laser. The period length for a conventional Halbach type hybrid design is 139 mm. Side magnets at the poles permit a slightly shorter period of 127 mm. Nevertheless, the Halbach design has been chosen because one sacrifices only ten percent of the periods with the much simpler mechanical design.

The device has ten periods which is the maximum number within the available space. The maximum and effective fields at a magnetic gap of 16 mm are 1.53 Tesla and 1.38 Tesla, respectively, which tunes to the laser wavelength at an electron energy of 1.9 GeV. The endpoles have been optimized for small kicks and displacements. Simulations give values below 14 μ rad and 15 μ m at an electron energy of 1.7 GeV.

The device has been assembled and will be installed in March 2004.

The UE49 Undulator

The device is of the APPLE II type and will provide light with variable polarization in the photon energy regimes listed in table 1 assuming an electron energy of 1.7 GeV. The K-values are derived from measured magnetic fields at a gap of 16 mm. The low energy limit for the elliptical mode (3rd and 5th harmonic) corresponds to the case where the product of the intensity and the degree of polarization squared is maximum.

Table 1: Tuning ranges of the UE49 undulator

polarization	K_{max}	1 st harmonic	3 rd harmonic	5 th harmonic
horizontal linear	3.221	91-498	272-1120	453-1518
vertical linear	2.117	173-498	518-1120	864-1518
circular / elliptical	2.499	136-498	300-1120	520-1518

The UE49 undulator comprises several new developments which originate from the experiences with the existing BESSY APPLE II devices:

- 1: Four magnet rows instead of two can be moved. This provides the flexibility to rotate the linear polarization vector by 180° compared to 90° for two movable rows.
- 2: All brakes (longitudinal and vertical) are now pneumatically powered. This eliminates any interaction of the brakes with the electron beam. Electromagnetic brakes produce beam displacements of the order of 5 μ m even at a distance of 1 m to the electron beam.
- 3: A new system for the gap measurement is located at either end of the magnet girder (figure 1 left). The linear encoder is mounted right above the electron beam which eliminates the Abbe comparator error. The gap repeatability is now below 1.5 μ m independent from the speed and direction of gap movement (figure 1 right).

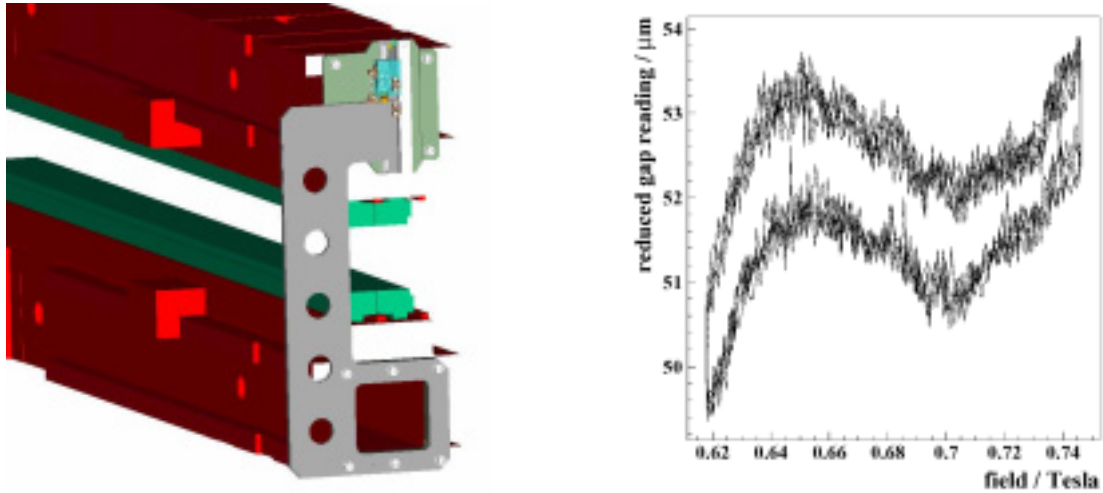


Figure 1: Left: The gap measurement system of the UE49. Right: Reduced gap reading (a third order polynomial has been subtracted from the measured gap) versus magnetic field for several gap movements from 15 to 18 mm and back.

Sorting and Shimming of the UE49 APPLE II Undulator

The sorting and shimming procedures of APPLE II undulators have been described in detail in [3]. These procedures have been applied successfully to the UE49 and some of the results will be presented in the following. The 1060 magnets of the UE49 have been characterized individually with an automated Helmholtz coil as well as with a stretched wire system. The data are used in a simulated annealing code which determines a magnet configuration with low integrated field errors. Two magnets are glued into one keeper. The keepers were measured again with the stretched wire system and sorted accordingly. No further measurements or optimizations have been done during assembly. Figure 2 demonstrates an excellent agreement between the predicted and the measured field integrals on axis for the complete structure at the smallest gap of 15 mm.

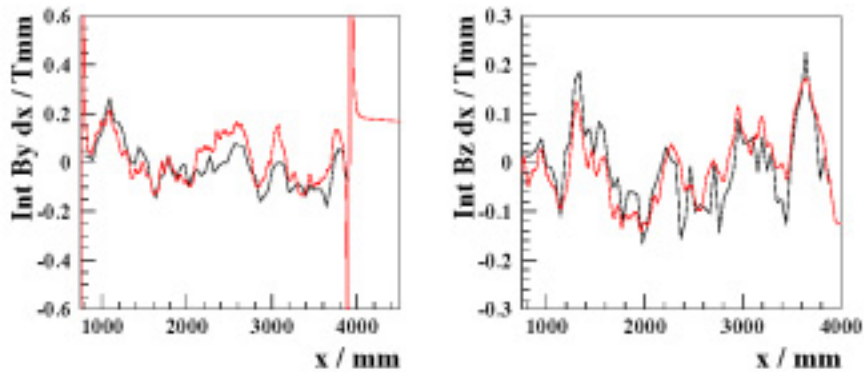


Figure 2: Predicted (black) and measured (red) field integrals at smallest gap of 15 mm. The periodic part has been filtered out.

Based on the stretched wire data of the keepers the completed structure has been further optimized by a rearrangement of about 20 keeper (in situ sorting). Then, the horizontal and vertical on axis trajectories have been flattened by horizontal and vertical block movement (virtual shimming). After this step the phase errors in the horizontal and vertical linear polarization mode are 3.6, 3.0, 2.0, 0.7 degree and 3.3, 2.7, 1.4, 0.3 degree for gaps of 15, 20, 30, 50 mm, respectively.

APPLE II structures show a variation of the field integral distribution with row shift. The variations can be reduced with appropriate iron shims which have a row shift dependent signature. Figure 3 shows the shift dependent terms without and with Fe-shims. Finally, the shift independent field integrals have been minimized with permanent magnet arrays at both ends of the device similar to the ones used for the UE52 APPLE II undulator.

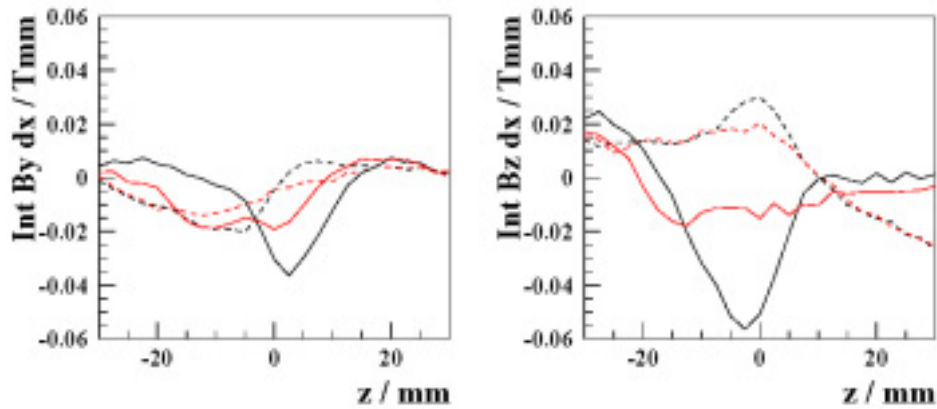


Figure 3: Shift dependent field integrals at row shifts of $\pi/2$ (dashed) and π (solid) with (red) and without (black) Fe-shims.

The undulator will be installed in the straight section L8 in March 2004.

Undulator Operation

Beam lifetime, source size and other important operation parameters depend among other parameters on the horizontal (f_x), vertical (f_z) and longitudinal (f_s) tune. Changing an ID gap causes a change of these tunes. Closing all ID gaps simultaneously, their natural focussing induces a vertical tune-shift of $\Delta f_z \approx +100\text{kHz}$. This can result in a reduction of the beam lifetime of up to 40% which is not tolerable for user operation. The tune shift can be compensated by correcting the settings of quadrupole magnets of the storage ring. At BESSY a Tune Feed Forward System was established to change the quadrupole settings as a function of the ID gaps. As a result, the vertical tune-shift for all IDs is reduced to 5kHz, sufficiently small to avoid any resonance (see for example U125-2 in figure 4) [5,6].

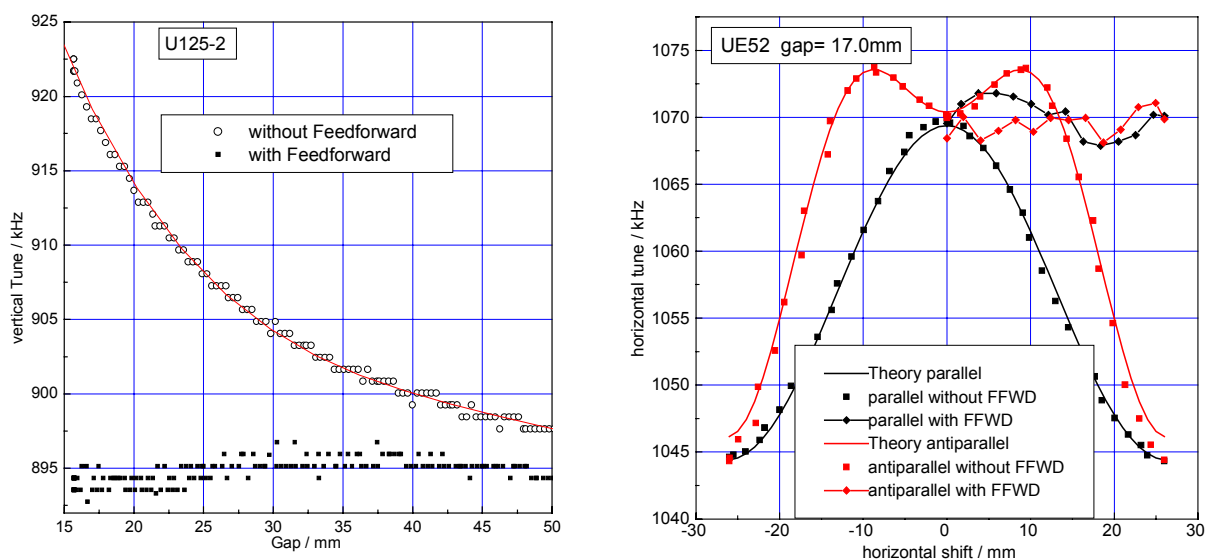


Figure 4: U125 gap-dependence of vertical tune and its compensation with feed forward correction (left). UE52 shift-dependence of horizontal tune and its compensation with feed forward correction (right).

Besides the influence of the gap-changes on the vertical tune, the elliptical insertion devices (UE46, UE52, UE56-1, UE56-2, UE49) also modify the horizontal tune up to $\Delta f_x = 30\text{kHz}$ per undulator when shifting the magnetic rows at constant gap. The measured tune shifts agree well with calculations for an ideal device as demonstrated for the UE52 (see figure 4). With tune feed forward the horizontal tune is held fixed within $\pm 2\text{ kHz}$ (figure 2). In 2004 the Tune Feed Forward System will be improved to a two-dimensional (gap, shift) scheme.

In 2003 at BESSY a new optic has been introduced for user applications, the so called "Low Alpha-Mode" where Alpha is the Momentum-Compaction-Factor. The aim is to reduce the length of the electron bunches down to 3.5ps in order to generate powerful THz radiation. The short bunch length is also used for time resolved measurements. A simple measure for the value of Alpha is the longitudinal tune ($\text{Alpha} \sim f_s^2$). The Low Alpha-Mode has a different working point as the common user optics. The symmetry is changed from an 8-fold (low beta, high beta) to a 16-fold (high beta, high beta) one [7]. Besides the described influence of the ID movements on f_x and f_z , the longitudinal tune shift Δf_s during ID-shifts becomes very important because it changes the intensity of the THz radiation. The effect of tune shift will have to be compensated again with new feed forward tables for all IDs to guarantee a stable working point and stable user conditions. The continuous work over the last years on the compensation of the ID influence in the standard user optic has now to be done again for the Low Alpha-Mode which is inherently less stable than the standard user mode.

During an energy scan of a monochromator the undulator's gap (and shift) is changed stepwise with a resolution of $0.1\ \mu\text{m}$. Every step of a mechanical component needs a dead time in the order of 1...2 seconds (communication, brakes, movement, position control, ...). But in many cases fine steps are not necessary due to the width of the harmonic of the

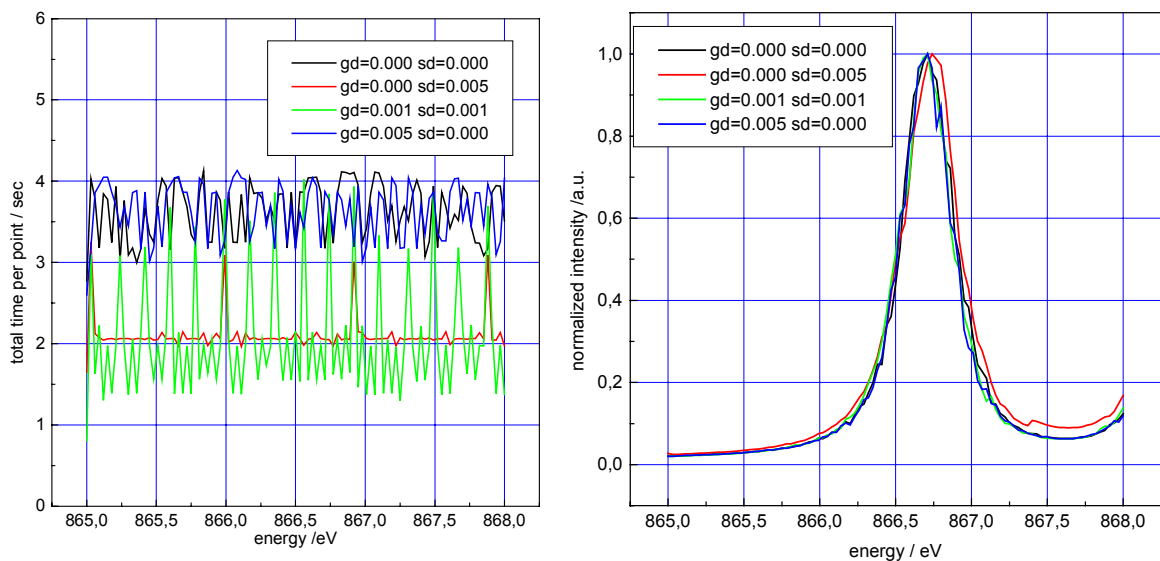


Figure 5: Influence of the gap-filter (=gd /mm) and the shift-filter (=gs /mm) on time per point and intensity for the UE52 operating at the 3rd harm., elliptical polarization mode ($P_3=0.9$).

undulator of a few eV. The following numbers are related to the UE52. At 100eV an energy step of 0.1eV is achieved by a gap step of $10\ \mu\text{m}$ (1st harm.) and at 500eV (5th harm.) $2\ \mu\text{m}$ results in the same energy shift of the harmonic. Without moving the undulator, the intensity will only be changed by about 2%. This is in the order of the accuracy of the drive tables. Especially for finest energy steps it is useful to limit the minimum step width of the undulator movement. Now an external tunable variable defines a filter for the minimum gap (and shift) movement.

As an example we measured the Ne 1s Rydberg line near 867eV at the UE52 with a monochromator step width of 0.03eV and a measuring time per point of 1 sec (see figure 5).

The average dead time was reduced with the special filter conditions by up to 60% without changing the resolution of the spectrum.

References

- [1] A. A. Zolenths, M. S. Zoloterev, Phys. Rev. Lett. 76 (1996) 912.
- [2] R. W. Schoenlein et al, Science, 287 (2000) 2237.
- [3] H.-J. Bäcker et al, Proceedings of the 2003 Particle Accelerator Conference, 836-838.
- [4] J. Bahrdt et al., Nucl. Instr. and Meth., 516 (2004) 575-585.
- [5] J. Feikes, G. Wüstefeld, "Lifetime Reduction due to Insertion Devices at BESSY II", PAC'2003, California, USA, May 2003
- [6] T. Birke, J. Feikes, B. Franksen, R. Lange, I. Müller, G. Pfeiffer, J. Rahn (BESSY), "A Tune Feed Forward System for the BESSY II Storage Ring", ICALEPCS, October 2003, Gyeongju, Korea
- [7] M. Abo-Bakr, J. Feikes, K. Holldack, G. Wüstefeld, H.-W- Hübers, "Steady-State Far Infrared Coherent Synchrotron Radiation detected at BESSY II" Phys.Rev.Lett. 88, 254801(2002)

Breakthrough in the Metrology and Manufacture of Optical Components for Synchrotron Radiation

Heiner Lammert, Tino Noll, Thomas Schlegel, Fred Senf, Frank Siewert, Thomas Zeschke
BESSY GmbH, Albert Einstein Strasse 15, D 12489 Berlin. <http://www.bessy.de/>

E-mail: Lammert@Bessy.de

BESSY Annual Report 2003, (30.1.2004)

Introduction

The technological limit for producing mirrors and gratings is determined by the metrology available to measure the figure quality. Until recently, the lowest attainable slope errors for spherical and plane surfaces was 0.1 arcsec rms and for aspherical surfaces about 0.5 arcsec rms. With the advent of synchrotron radiation (SR) sources of the third generation with a source emittance on the order of a few nm-rad, these limits had to be overcome.

With the cooperative research project "Nanometer-Optikkomponenten" NOK, ten partners from German industries and scientific institutes under the coordination of BESSY have accepted the challenge to improve the figure quality of optical elements [1]. The success of this endeavor was dependent upon major improvements both in the metrology and in the final finishing processes.

The metrology team, under the leadership of BESSY, was responsible for the development of a new profiler with two main characteristics [2]:

1. Line scan accuracy below 0.03 arc sec over a length of a 1000 mm or more
2. Area measurements of similar accuracy over a surface of ca. 1200 mm x 300 mm.

The second stage, the improvement of the final finishing process, was the responsibility of the second team in the project. In a three step process, (1) manufacture of a "good" mirror, (2) mapping its surface and then (3) correction of the surface, the goal was to make mirrors and gratings of hitherto unreachable figure accuracy.

Improvement of the Metrology

Up to now the best figure accuracy for commercially available optical components is 0.1 arcsec rms for the slope error or, accordingly, for the shape error 10 nm rms for plane or spherical surfaces. For aspherical surfaces it is five times worse. The accuracy of the measuring techniques, interferometers or profilers, is not better than this 0.1 arcsec rms limit. If the optical surfaces are to be improved, the measuring uncertainty must be 3-5 times superior to this. The present state of the art and the goals of the NOK project [1] are summarized in table 1.

Table 1: Slope errors for various geometries

Geometry	Present state of the art: slope error (arc sec)	Goal of this NOK-project slope error (arc sec)	
		Tolerances for manufacturing	Measuring accuracy
plane	0.1	0.02	< 0.01
sphere	0.1	0.03	0.01
Asphere (cylinder, torus, ellipse)	0.5	0.05	0.01

At BESSY the Nanometer Optical Component Measuring Machine, NOM, employing the non-contact principle of optical deflectometry, was developed [2]. For reasons explained below, it utilizes two different measurement sensors, an LTP-head [3] and an autocollimator head [4]. The construction of a high precision stone carriage and table system enables measurements over an area of 1200mm x 300 mm to be made. The following main results have been achieved:

1. The measurement accuracy has been improved from 0.1 arcsec rms to less than 0.01 arc sec rms with a reproducibility in the range of 0.002 arcsec rms.
2. Three dimensional mapping over up to a 1200mm x 300 mm surface. The reproducibility of a map over a test surface of 500mm x 110 mm was determined to be < 0.3 nm rms.
3. Automatic measurement of complete surfaces and data workup.

Measurement Accuracy

The absolute accuracy of measurements is a function of the systematic errors in the concept and of the equipment while the reproducibility mainly results from random noise. One direct method to counter systematic errors is to employ two different methods for the measurement. This approach has been employed in two ways in the NOK project: (1) A test surface was measured with the NOM and by the PTB with a different method and the results compared. (2) Two different measuring heads, employing different measurement principles, are an intrinsic feature of the NOM itself.

The influence of random errors such as mechanical vibrations, thermal effects, and electronic noise was determined by comparing measurement data taken under otherwise identical conditions. The reproducibility achieved is better than 0.002 arcsec rms or 0.5 nm rms over 480 mm (Fig. 1).

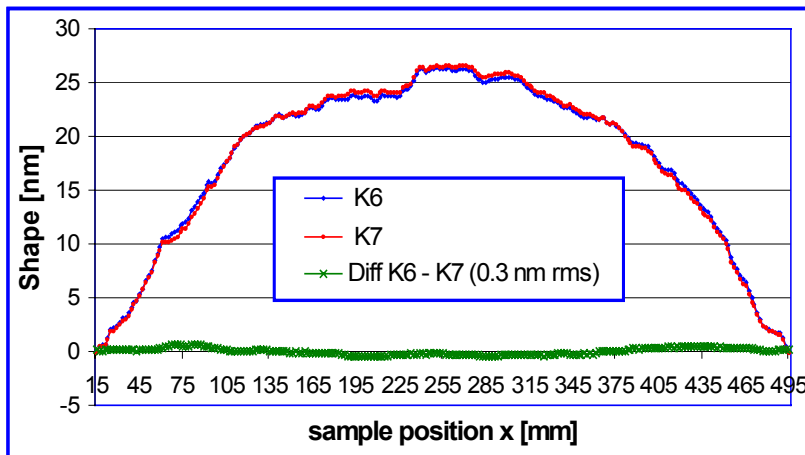


Fig.1: Comparison of measurements of a 480 mm long trace. The 510 mm long plane surface on Zerodur is curved with a maximal height of 26.5 nm p-v and a radius of curvature of 1083 km. The difference over the 480 mm is < 0.5 nm rms or 0.002 arc sec rms and demonstrates the reproducibility of the NOM.

The elimination of all sources of systematic error is difficult and may even not be possible. However, comparison of two fundamentally different methods is a very reliable test. A special measuring principle for making line scans of plane surfaces and surfaces with a large radius of curvature was developed at the Physikalisch Technische Bundesanstalt Braunschweig (PTB): the Extended Shear Angle Difference (ESAD) method [5]. In cooperation with the NOK project several different plane substrates of different lengths were measured at the PTB by the ESAD method and again at BESSY using the NOM. In figure 2 the ESAD and NOM results for a plane surface are presented. The conformity of both measurements in a central section of 130 mm of a 510 mm x 118 mm Zerodur mirror lies within 0.3 nm rms or 0.02 arcsec rms slope deviations.

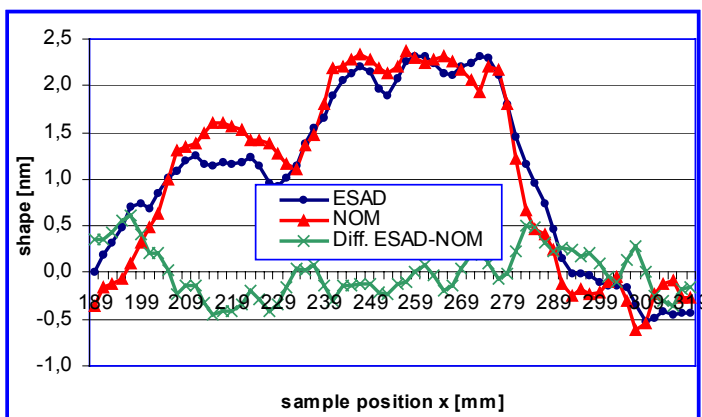


Fig. 2: Comparison of measurement results: ESAD (PTB) and NOM (BESSY): Conformity of the results < 0.3 nm rms

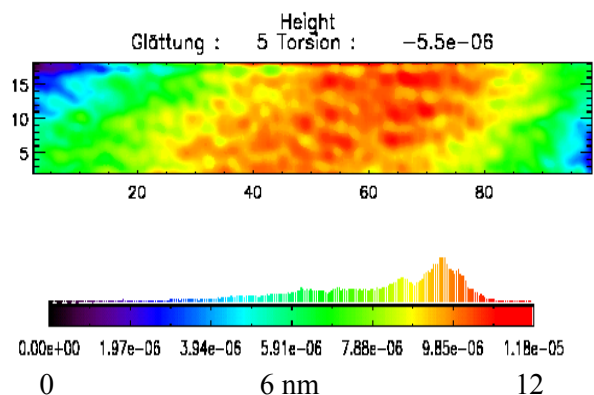


Fig. 3: 3D-mapping of a plane surface of 100 mm x 20 mm with a reproducibility < 0.3 nm rms

For surfaces with a short radius of curvature, e.g. 10 - 500 meters, the comparisons are made using two different measuring heads installed in the NOM: an LTP-head [3c] and an autocollimator head [4]. In this way, systematic errors in the measuring principle have been avoided.

Three Dimensional Mapping

Highly accurate area measurements of an optical surface are necessary if good optical elements are to be reworked to make them more perfect. With the NOM it is possible to make 3D maps in different ways, depending upon the accuracy required. For the highest accuracy, the map is generated in three steps: (1) equidistant line scans in the meridional direction of the sample with a spacing of 2 mm (footprint of the measuring beam) or less; (2) equidistant line scans orthogonal to those of 1 above also with a spacing of 2 mm or less; (3) line scans across the two diagonals. After taking the above data, the root mean squares of the height measurements of steps 1 and 2 are minimized and the points of the surface that lie on one of the measured diagonals selected. Using the directly measured diagonal as a reference, the rms values of the differences between these two diagonals is obtained. In this way, any twisting of the surface, which is recognized and measured in the direct measurement, is superimposed onto the generated diagonal and correspondingly onto the entire array of x,y data, yielding the genuine shape of the surface. These results are then compared with those of the second diagonal. In the test case presented here, the final difference in the two diagonal line scans was less than 0.3 nm rms [6]. Such 3D maps provide the basis for a sequential shape optimization by ion beam figuring, the production part of the NOK project [7].

Automation of the Measurements

Because of the extensive and time consuming nature of the measurements, it was advisable to automate them: (1) hardware drivers with readout of the two heads; (2) selection of the measurement strategy and (3) the workup and presentation of the data. In addition to reducing the work load for the operator the automation makes it possible to choose the optimal time windows for the measurements: nights and weekends. The time required for the complete measurement of, for example, a 100 mm x 20 mm plane surface (eg. fig. 3) is 90 minutes for an uncertainty of 0.5 nm rms.

Results Achieved

In the course of this project several substrates were measured and the results compared with those obtained by other methods. It has been shown that the desired measurement accuracy of 0.02 arc sec rms or lower has indeed been achieved. In addition, the mapping of optical surfaces again to the necessary accuracy has been accomplished (e.g. figure 3). The final test of all of the aspects of this project, the mapping and the correction of an optical surface to a new degree of perfection, has also been performed.

A plane elliptical mirror, the most desirable geometric form for focusing a quasi-point object with a large demagnification factor in one plane [8], was mapped and reworked by ion beam milling. The result is a mirror of nearly perfect geometry: the final slope error was of 0.14 arc sec rms. This mirror was designed for use as the sole horizontally focusing mirror in a monochromator on an undulator at BESSY and has a very large theoretical demagnification factor of 47, the ratio of the entrance and exit arm lengths. The extreme effect of slope errors in the demagnification had in the past precluded achieving such a factor with a single optical element. A horizontal focus width of 8 μm rms was measured verifying that the desired demagnification had been reached. This achievement was only possible through the successful, cooperative efforts of the partners in the NOK project. For more details regarding this mirror, see the paper immediately following in this annual report [9].

Conclusion and Perspectives

The fivefold improvement of the technological limit to 0.01 arcsec rms for the metrology of plane, spherical and aspherical optical surfaces together with improvements in the methods used to correct these surfaces represent an essential breakthrough for synchrotron radiation facilities of the third generation and for the needs of VUV and soft x-ray free electron lasers of the future. In addition, the new standards of accuracy will be used for hitherto unattainable goals, for instance: mirror and grating substrates of 0.02 arcsec rms; bending mirrors < 0.1 arcsec rms; mechanical influence of the mounting

system below 0.1 arcsec rms; determination of thickness constancy of coatings to less than 1 nm; radius determination of test glasses to < 0.01 % ; reference normal specimen for interferometry with subnanometer accuracy ($\lambda/1000$) ; plane surface measurements with radii > 1000 km; determination of long term shape stability of optical materials in the nm range; determination of inhomogenities in optical glasses in the range of $\Delta n < 10^{-6}$. With the development of the Nanometer-Optikkomponenten-Messmaschine -NOM- an essential step has been made towards making the “Measuring technique an outrider of the optics technology development”. Despite these very significant successes, there is still much work to be done.

Acknowledgements

This work has been supported by the Bundesministerium für Bildung und Forschung and the Verein Deutscher Ingenieure VDI under Contract No.: 13 N 7929. We thank the partners of the cooperative research project Nanometer-Optikkomponenten -NOK-: Leibnizinstitut für Oberflächenmodifizierung IOM Leipzig; Möller Wedel Optical GmbH Wedel; Schnabel Elektrische Messtechnik Wedel; Physikalisch Technische Bundesanstalt Braunschweig; Berliner Glas KG Berlin; Jenoptik Laser Optik Systeme GmbH Jena; Carl Zeiss Oberkochen; Optikkomponenten und Kristalle GmbH Berlin; Optik Elektronik & Gerätetechnik GmbH Frankfurt (Oder); Friedrich Schiller Universität Jena.

References

- [1] Heiner Lammert “Nanometer Optical Components for Synchrotron Radiation Beamlines”, BESSY annual report , Berlin 2001, p. 301-304
304. www.bessy.de
- [2] Heiner Lammert, Tino Noll, Thomas Schlegel, Fred Senf, Frank Siewert, Thomas Zeschke, “The Nanometer Optical Component Measuring Machine – NOM – at BESSY”, BESSY annual report , Berlin 2002, p. 399-404. www.bessy.de
- [3] (a) Takacs, P.Z., K. Furenlid; Measurement of Surface Finish and Figure Accuracy; Proc. of the Int. Workshop High Performance Monochromators and Optics for Synchrotron Radiation in the Soft X-Ray Region, held at BESSY GmbH, Berlin, 1991;
(b) Takacs, P.Z., Qian, S.-N.; Pat. 4,884,697; Intern’l Class: G01B 009/02, filed: June 21, 1988;
(c) Takacs, Peter Z., and Qian, Shinan, Profilometry of X-ray Optics: Current Progress”, www.inst.bnl.gov/seminars/pdf/04102002.pdf BNL, Brookhaven, April 10, 2002, 21-25
- [4] Möller-Wedel Optical GmbH, Wedel; www.moeller-wedel-optical.com/ .
- [5] Ralf Geckeler, Ingolf Weingärtner, “Sub-nm Topography Measurement by deflectometry - flatness standard and wafer nanotopography, Proc. 3rdInternational Conference, euspen 1 (2002) 497 – 500.
- [6] Frank Siewert, Tino Noll, Thomas Schlegel, Thomas Zeschke and Heiner Lammert; “The Nanometer Optical Component Measuring Machine: a new Sub-nm Topography Measuring device for X-ray Optics at BESSY”, SRI 2003 Conference, San Francisco, 2003
- [7] Axel Schindler, Thomas Haensel, Andreas Nickel, Hans-Jürgen Thomas, Heiner Lammert, Frank Siewert, “Finishing procedure for high performance synchrotron optics”, SPIE’s 48th annual meeting, San Diego 2003
- [8] William B. Peatman; Gratings, Mirrors and Slits, Taylor & Francis books, inc., New York, 1997, 133-138
- [9] Frank Siewert, Kai Godehusen, Heiner Lammert, Thomas Schlegel, Fred Senf, Thomas Zeschke, Thomas Hänsel, Andreas Nickel, Axel Schindler, “NOM measurement supported ion beam finishing of a plan-elliptical refocusing mirror for the UE52-SGM1 beamline at BESSY”, BESSY annual report , Berlin 2003, next page of this issue. www.bessy.de



NOM measurement supported ion beam finishing of a plane-elliptical refocusing mirror for the UE52-SGM1 beamline at BESSY

Frank Siewert, Kai Godehusen, Heiner Lammert, Thomas Schlegel, Fred Senf, Thomas Zeschke
Thomas Hänsel*, Andreas Nickel*, Axel Schindler*

BESSY GmbH, Albert-Einstein-Str. 15, D-12489 Berlin, Germany

** Leibnitz Institut für Oberflächenmodifizierung IOM, Permoserstr. 15, 04303 Leipzig, Germany*

Abstract

Advanced surface measuring techniques of sub-nm accuracy enables the surface finishing of a new generation of X-ray optics by Ion Beam Finishing (IBF) technology. An ion beam finished plane-elliptical refocussing mirror characterized by a slope error of about 0.1 arcsec rms is in use now at the UE52-SGM1 beamline at BESSY. The coaction of measurements at the Nanometer Optical component measuring Machine (NOM) and ion beam milling will be discussed. The improved performance of the beamline is demonstrated by measurements of the spot size.

Introduction

The performance of x-ray beamlines at 3rd generation synchrotron radiation sources like BESSY II is limited by the quality of the optical components used. To enable a surface figuring of optical elements with an exactness that exceeds the limit of 0.5 arcsec rms for aspheres with the goal of obtaining slope deviations in the range of 0.1 arcsec rms or better (for aspherical surfaces up to 200 mm in length) by ion beam finishing (IBF) technology, it is essential that these components are characterized using metrology tools of at least five to ten times superior accuracy. To address this problem the Nanometer Optical component measuring Machine (NOM) has been developed at BESSY [1][2][3]. The development of the NOM is a partial result of the BESSY coordinated cooperative research project “Nanometer Optikkomponenten” (NOK) a cooperation of 11 partners from German industries and science to provide a new generation of optical components for Synchrotron Radiation beamlines [4]. In the discussed example a plane-elliptical mirror has been finished by ion beam technology supported by 3D-NOM measurements.

Surface Measurement and Surface finishing

In the shown case a plane-elliptical (elliptical cylinder) mirror (substrate material: ZerodurTM) characterized by a slope error of 1.21 arcsec rms (best fit) was the initial substrate to be finished by 3 iterations of ion beam milling. The dimensions of this demonstration model are 190 mm in length, 37 mm in width and 40 mm in height. The topography data matrix used for the three surface correcting trails was gained by 3D-measurements at the BESSY NOM [1, 2]. To generate a 3D-data matrix two surface scans each consisting of a multitude of parallel sampled line-scans were traced in meridional and in saggital direction successively. Each single surface linescan was taken on the fly and contains of 915 measurement points (for IBF step one and two). The lateral step size was 0.2 mm. At least a 3D-datamatrix of $dx = 0.2$ mm, $dy = 0.2$ mm measuring point spacing was achieved. The 3D-datamatrix used for the final 3rd IBF step contained a measuring point spacing of $dx = 0.5$ mm x $dy = 0.5$ mm. Related to the used aperture of the NOM-autocollimator the spatial resolution was 3 mm. Based on the gained topography data matrix it was possible to calculate the simulation of the surface removal rate required for the dwell time controlled ion beam treatment.

The figuring process was realized by a computer controlled scanning of a small sized ion beam with a near Gaussian distributed beam profile across the surface line by linewidth and dwell time distributed proportional to the desired material removal [5]. In our case the substrate was moved to the fixed ion beam. The simulation of the figuring is based on a modification of van Citter deconvolution in the local coordinate space using the Fourier transformation and contains an optimal turn and smoothing of the output topology, a graphic output of the topologies and profiles as well as the generation of the dwell times. A 40 mm Kaufmann-type ion source developed by the IOM with a focussing grid system was used [6]. The ion source parameters for the figuring were: ion beam voltage: 800 eV, ion beam current: 20 mA using Ar⁺ as the etch gas. The positive charged ion beam was neutralized by a hot filament neutralizer. Due to the high requirements for X-ray optics these elements have to be finished by tools working at different optical relevant spatial frequency ranges. The size of the rotational symmetric Gaussian beam with different parameters has been adjusted with the help of circular

diaphragms of different hole diameters. The beam profiles and the etch rates have been determined by etching a “footprint” for a certain time into a test blank. The “footprint” has been measured by interferometry. The mirror substrate was figured in three IBF Steps with the following ion current density profiles:

- For IBF step 1 and 2 a beam size of 6 mm FWHM (diaphragm hole diameter: 4mm) came into operation and
- for the final IBF step a beam size of 2.1 mm (diaphragm hole diameter: 2mm) was used.

Figure 1 and Table 1 shows the progress of shape optimization as result of the IBF procedure. The achieved result of an slope deviation of 0.138 arcsec rms \pm 0.02 arcsec at the center line and a saggita of 8.8 nm pv \pm 0.5 nm (fitted curve) represents a ten fold improvement compared to the refocussing optics in use before at UE52-SGM1. It is also to notice that related to the initial state before the ion beam etching no change of the microroughness (0.5 - 0.8 nm rms) has been observed finally. At least the mirror was coated by a PVD Platinum coating (thickness 40 nm) and installed at the beamline for use.

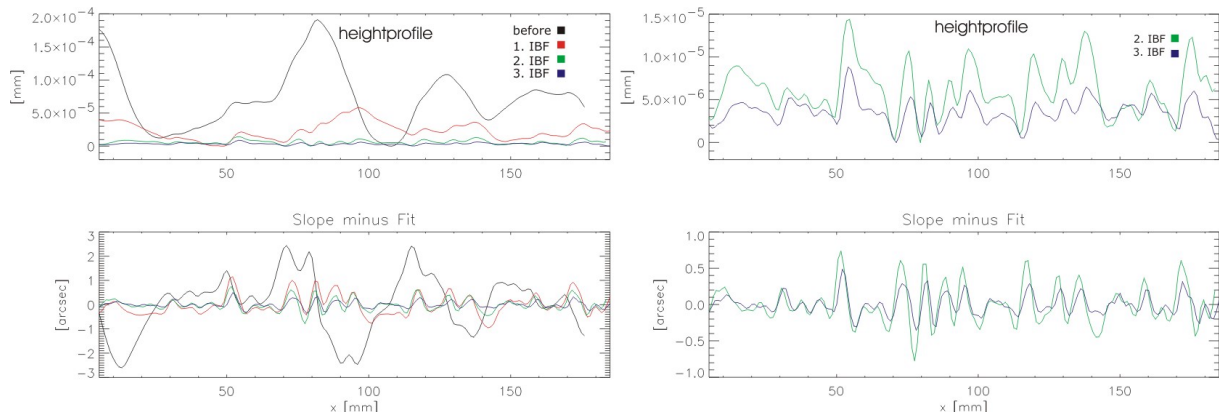


Figure 1. Left: best fit Height and slope profile at center line of the mirror before and after each iteration of ion beam milling, right: best fit height and slope profile at the same line of the mirror after 2nd and 3rd Iteration of ion beam milling. After 3 iterations of ion beam milling a slope error of 0.138 arcsec rms \pm 0.02 arcsec rms is achieved.

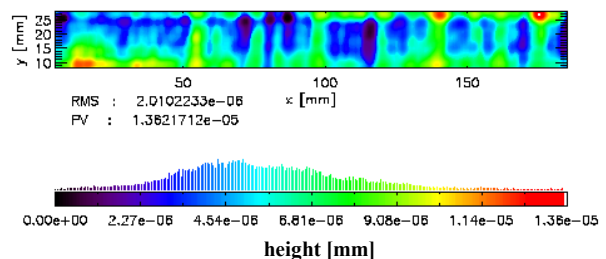
finishing step	slope [arcsec rms]	slope [arcsec pv]	height [nm rms]	height [nm pv]	beam width [mm FWHM]
initial state	1.21	5.02	47.3	191.1	
1 st run	0.44	2.43	13.3	58.1	4
2 nd run	0.26	1.51	2.9	14.3	4
3 rd run (final state)	0.138	0.85	1.4	8.8	2

Table 1. slope and height data measured at the center line of the refocussing mirror, the estimated measuring accuracy is in the range of 0.02 arcsec rms respectively 0.5 nm pv

parameter	specification	measurement results (best fit)
entrance arm length: r_a	34150.0 mm \pm 200.0 mm	34273.6 mm
exit arm length r_b	750.0 \pm mm 3.0 mm	748.4 mm
angle of incidence: ϕ	2° \pm 0.04°	1.971°
long half axis: a	17450.0 mm \pm 300 mm	17511.0 mm
short half axis: b	176.6 mm \pm 1 mm	174.2 mm

Table 2 parameter of the plane-elliptical refocussing mirror: specified and measured

Figure 2. 3-dimensional surface scan of the plane-elliptical mirror after the final ion beam treatment – ellipse fit corrected topography of the optical active surface area (180 x 20 mm², measuring point spacing: dx = 0.5 mm, dy = 0.5 mm) Height: 14 nm pv, (8.8 nm pv \pm 0.7 nm at the center line).



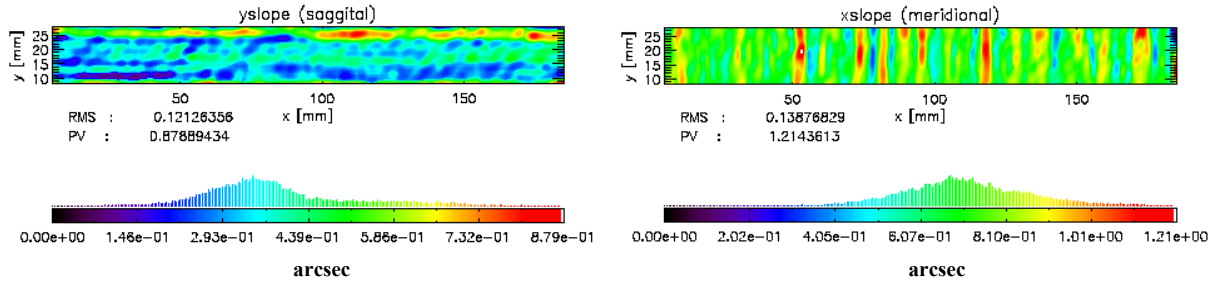


Figure 3. left: map of slope deviation in meridional direction (slope optimized ellipse fit), the average of the slope deviation is 0.139 arcsec rms - and right: in saggital direction (best fit). The saggital slope map shows a substructure presumably caused by the finishing of the initial blank using a polishing robot, average of slope deviation: 0.121 arcsec rms. The estimated measuring uncertainty is in the range of 0.02 arcsec rms.

Focus size / Commissioning of the UE52-SGM1 beamline

The UE52-SGM1 is a undulator based beamline covering the energy range from 90 to 1500 eV. The optimization of the beamline focus was made in the energy range between 350 - 1100 eV. The focus size was optimized and determined with the BESSY microfocus imaging system utilizing a layer of P43 ($\text{Gd}_2\text{O}_2\text{S:Tb}$) with a spatial resolution of $3\mu\text{m}$ and a CCD-camera [7]. Figure 4 shows the optimized foci of three different horizontal refocusing mirrors before and currently in use at the beamline.: The focus size by use of the new refocussing mirror (green color) is less than $20 \times 20 \mu\text{m}^2$ for the inspected range of energy (350 – 1100 eV) at an exit slit width of 3 - 4 μm . For horizontal intensity distribution a value of $17.4 \mu\text{m}$ ($\pm 10\%$) FWHM has been obtained. This represents a two fold improvement compared to the previous state of the beamline. Due to the characteristics of the undulator source UE52 the minimum limit of focus size is achieved. A further improvement of the mirror shape beyond a slope deviation of 0.1 arcsec rms would not provide a smaller focus size for this beamline. Nevertheless the implementation of plane-elliptical mirrors beyond the limit of 0.1 arcsec rms at low β -sections would lead to a significant improvement of beamline performance.

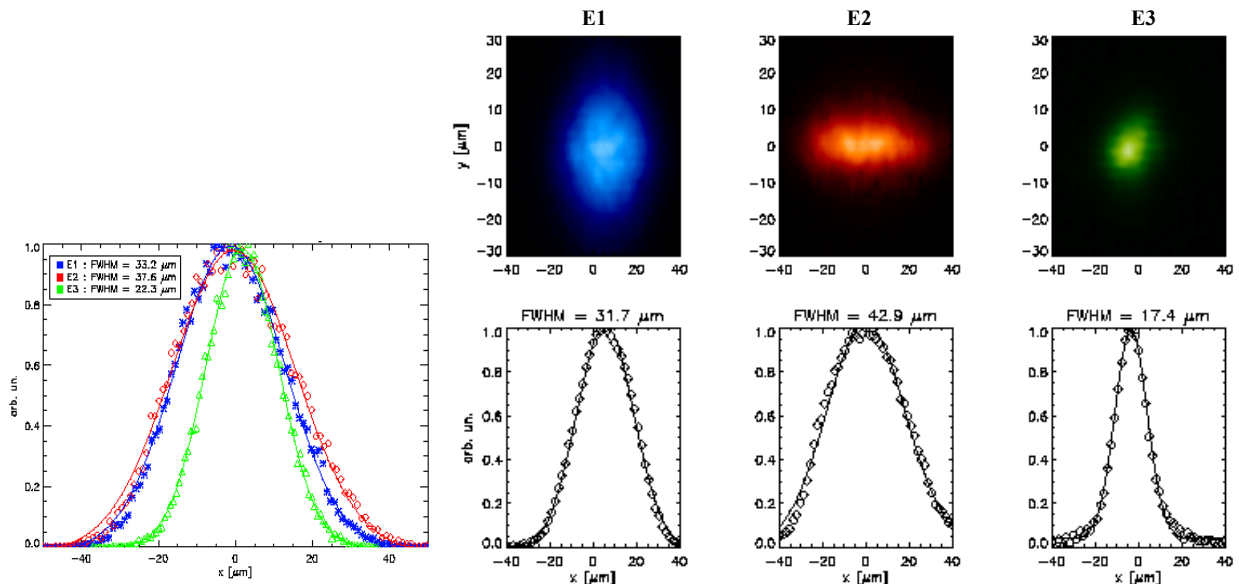


Figure 4. Foci and horizontal intensity distribution of three different refocussing mirrors at beamline UE52-SGM1, left: ray simulation and right: microfocus measurements at the beamline. The green color marks the results of the simulation and the focus measurements during the beamline commissioning at an exit slit with of 3-4 μm for the new demonstration-mirror E3 (slope error: 0.138 arcsec rms.). Blue and red color indicates the results achieved for refocussing mirrors characterized by slope deviations of 1.08 arcsec rms E1(blue, exit slit width: 10 μm) and 1.49 arcsec rms E2 (red, exit slit width: 3-4 μm).

Conclusions

The coaction of advanced metrology devices like the BESSY-NOM and Ion Beam Finishing technology enables the manufacturing of a new generation of aspherical X-ray optics. The shown plan-elliptical refocussing mirror represents a five fold improvement to the present state of the art of commercial available optical components. A further progress in the manufacturing of aspherical optics beyond the limit of 0.1 arcsec rms can be expected for instance by use of a new type of "1-mm ion source". Microfocus measurements at beamline UE52-SGM1 demonstrated that a substantial increase of beamline performance is obtained by use of high performance optical elements.

Acknowledgements

This work has been supported by the Bundesministerium für Bildung und Forschung and the Verein Deutscher Ingenieure VDI under Contract No.: 13 N 7929.

References:

- [1] F. Siewert, T. Noll, T. Schlegel, T. Zeschke and H. Lammert; "The Nanometer Optical Component Measuring Machine: a new Sub-nm Topography Measuring device for X-ray Optics at BESSY", SRI2003 Conference, San Francisco, 2003
- [2] H. Lammert, T. Noll, T. Schlegel, F. Siewert, T. Zeschke, The Nanometer Optical Component Measuring Machine - NOM - at BESSY", BESSY annual report , Berlin 2002, p 399 – 403
- [3] H. Lammert, T. Noll, T. Schlegel, F. Senf, F. Siewert, T. Zeschke, „Breakthrough in the Metrology and Manufacture of Optical Components for Synchrotron Radiation", BESSY annual report, Berlin 2004 (this issue), www.bessy.deb-exp
- [4] H. Lammert "Nanometer Optical Components for Synchrotron Radiation Beamlines", BESSY annual report , Berlin 2001, p. 301-304. www.bessy.de
- [5] A. Schindler, T. Haensel, A. Nickel, H.-J. Thomas, H. Lammert, F. Siewert, "Finishing procedure for high performance synchrotron optics", SPIE's 48th annual meeting, San Diego 2003
- [6] T. Haensel, A. Schindler, B. Dissing, "Multiple high period accuracy gratings fabricated by holographic exposure and ion beam etching with nanometer depth accuracy in silicon" , SPIE's 48th annual meeting, San Diego 2003
- [7] K. Holldack, T. Zeschke, F. Senf, C. Jung, R. Follath, D. Ponwitz, "A Microfocus Imaging System", BESSY annual report, Berlin 2000, p. 336 - 338,

Fe in silicate melt at high temperature

M. Wilke, G.M. Partzsch*, F. Farges**

Institut für Geowissenschaften, Universität Potsdam, Postfach 601553, 14415 Potsdam, Germany

**Mineralogisches Institut, Universität Heidelberg, INF 236, 69120 Heidelberg, Germany*

***Laboratoire des Geomateriaux, Université Marne-la-Vallée, 77454 Marne la Vallée Cedex 2, France*

In geological magmatic systems, Fe is the most abundant transition element. Due to the heterovalent nature and the different crystal-chemical behaviour of the two species, Fe affects a wide number of physical and chemical properties of melts, such as viscosity, stability of phases and nucleation during crystallization. This study explores the structural environment of Fe in silicate glass and melt by using XANES (pre-edge) and EXAFS. The structure found in the glass represents the structure of the melt as it is frozen in at the glass transformation temperature (T_g). Usually it is assumed that the melt structure at T_g to be similar to the one at higher temperature. Previous studies, however, have found evidence that this assumption may be not be true indicating that relaxation kinetics around T_g may be sufficient to re-organize the melt structure even at high quench rates ([1], [2], [3]).

We investigated synthetic $\text{Na}_2\text{Si}_3\text{O}_7$, $\text{K}_2\text{Si}_3\text{O}_7$, $\text{Rb}_2\text{Si}_3\text{O}_7$ and haplogranitic glass and melt, doped with ca. 5 wt% Fe_2O_3 using Fe K-edge XAS spectroscopy to compare the local environment of Fe in melt and glasses. The spectra of were collected at BESSY, beamline KMC-2 using the Si-Ge gradient (111) 2-crystal monochromator. Spectra were collected in fluorescence mode using a Stern-Heald type detector (Lytle detector) filled with Krypton. Samples were heated on a $\text{Pt}_{70}\text{Rh}_{30}$ -loop using a S-type thermocouple for temperature control. The furnace was filled with air for oxidizing conditions and with N_2 containing 5% H_2 for reducing conditions.

Pre-edges of the XANES of reduced and oxidized glass show strong changes in position, shape and intensity with Fe-oxidation state (see [4] and Fig. 1). The pre-edge positions indicate ca. 90 % of Fe in either ferric or ferrous state, respectively. The pre-edge intensities of the glasses indicate mixtures of 4-fold and 6-fold or even presence of 5-fold co-ordinated Fe in reduced and oxidised cases (intensity of 5-fold geometry inbetween 4 and 6, see [5]). The pre-edges of reduced melts and glasses are pretty similar, which indicates only small differences between glass and melt. In contrast, at oxidising conditions the pre-edge intensity e.g. of the $\text{Na}_2\text{Si}_3\text{O}_7$ melt is considerably higher than the one of the corresponding glass. In case of the more polymerised haplogranitic composition differences are much smaller and moreover, the pre-edge intensity of the melt decreases compared to the one of the glass. The differences at oxidising conditions may be assigned to a difference in the amount of low co-ordinated (i.e. tetrahedral) Fe between melt and glass, especially in the case of depolymerised compositions like $\text{Na}_2\text{Si}_3\text{O}_7$. The smaller differences observed on the haplogranitic composition may indicate only small changes in the average co-ordination geometry (e.g. distortion).

The observations made in the pre-edge region are consistent with changes that may be observed at the maximum of the first EXAFS oscillation. The position of the first maximum varies as a function of the Fe-O interatomic distance: longer distances will shift the maximum to lower energy (if the oxidation state remains constant). The interatomic Fe-O distance can be taken as a sensitive proxy for the Fe-coordination [6]. In case of the oxidised $\text{Na}_2\text{Si}_3\text{O}_7$ glass, the maximum shifts to higher energy for the molten state, thus indicating a decrease in the interatomic Fe-O distance or decrease of the average Fe co-ordination (towards tetrahedral). The oxidised haplogranitic glass shows a slight shift to lower energy for the molten state indicating the opposite behavior. Only small shifts towards higher energy are observed at reducing conditions for both compositions, which indicates slight decrease of the Fe co-ordination. Preliminary fit results of the EXAFS indicate a clear decrease of the Fe-O distance for oxidised $\text{Na}_2\text{Si}_3\text{O}_7$ (1.96 Å glass, 1.92 Å melt) indicating an average co-ordination around 5, which is consistent with the observations in the pre-edge region. Reduced samples indicate a much smaller decrease (around 0.02 Å) but the absolute value (ca. 2 Å) is too short to be consistent with the average co-ordination expected from the pre-edge (around 5). Expected Fe-O distances should be around 2.05 Å. The spectra of the reduced samples are probably significantly affected by

anharmonicity due to high static and thermal disorder, which has not been fully accounted for in the fit model, so far.

The results shown here indicate that the structural environment of Fe in silicate glass may considerably differ from the one found in the molten state at temperatures above T_g .

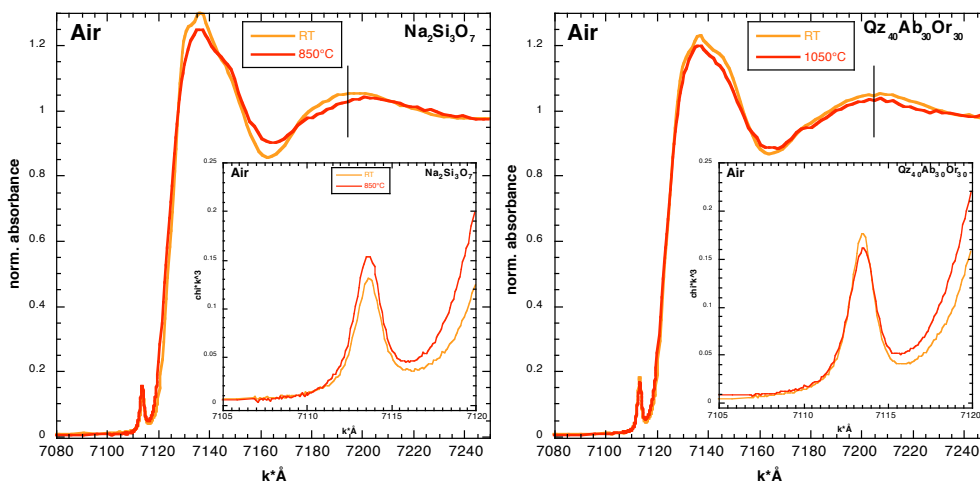


Figure 1: Normalised XANES of oxidised Fe in $\text{Na}_2\text{Si}_3\text{O}_7$ (left) and haplogranitic (right) glass and melt. Qz: SiO_2 ; Ab: $\text{NaAlSi}_3\text{O}_8$; Or: KAlSi_3O_8 . Data taken from [4].

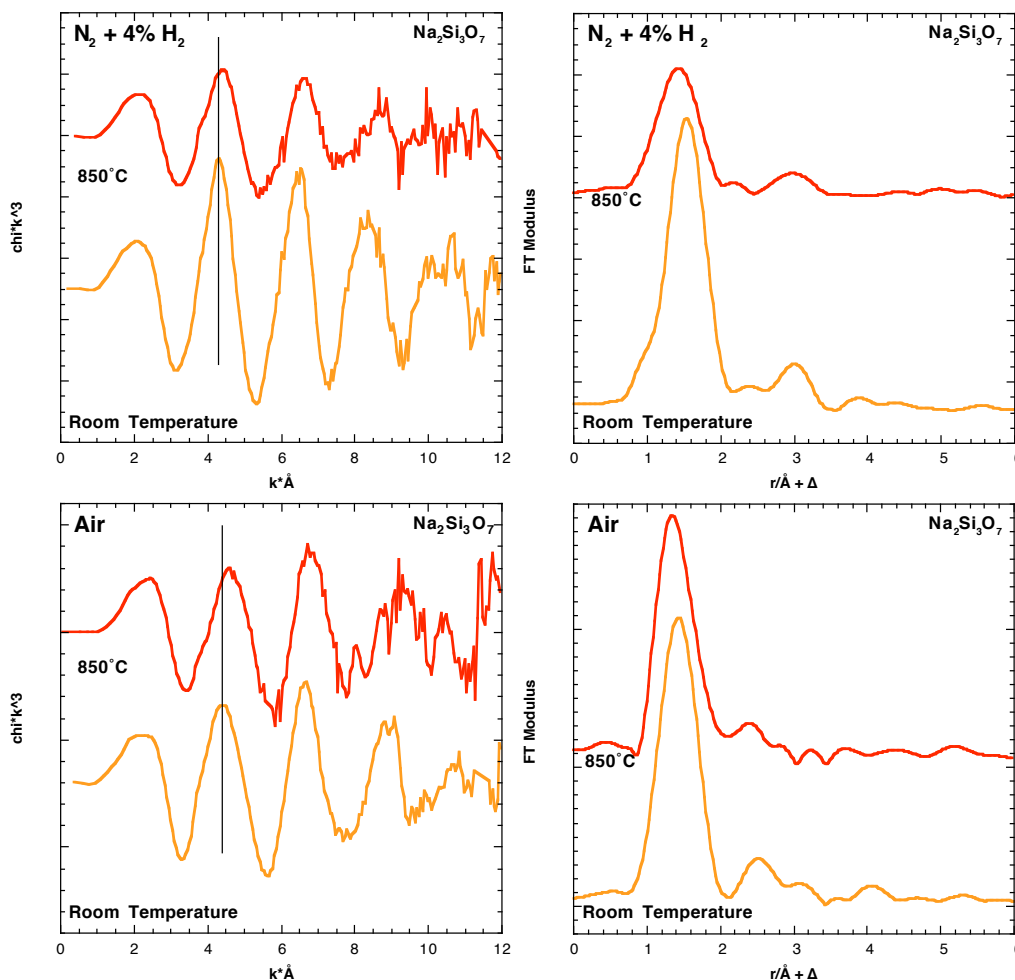


Figure 2: Normalised and k^3 -weighted EXAFS and fourier transform of Fe in $\text{Na}_2\text{Si}_3\text{O}_7$ at reducing (top) and oxidising (bottom) conditions. Note the significant shift in the first EXAFS oscillation at oxidising conditions

Acknowledgements: We thank A. Erko (BESSY), M. Borchert and I. Sommerweiß for support during beamtime.

References

- [1] Farges, F., Hao Gan, Rehr J.R., Brown G.E. Jr, Navrotsky A. *Geochim. Cosmochim Acta* 60, 3055-3065 (1996).
- [2] Farges, F., Waychunas, G.A., Brown Jr G.E., Calas G., Galois L. *Geophys. Res. Letters* 21, 1931-1934 (1994).
- [3] Jackson, W.E., Mustrede, Leon M., Brown, G.E. Jr., Waychunas, G.A., Conradsen, S.D., Combes, J.M. *Science* 262, 229-233 (1993).
- [4] Wilke, M., Partzsch G.M., Farges, F., Welter E. *HASYLAB Annual Report* (2003)
- [5] Wilke, M., Farges, F., Petit, P.E., Brown, Jr., G.E., Martin, F. *Am. Mineral.*, 86, 714-730 (2001).
- [6] Brown, G.E. Jr., Farges F., Calas G. *Rev. Mineralogy*, 32, 317-410 (1995).

Organic molecular beam epitaxy of perylene on Cu(110) investigated by NEXAFS spectroscopy

K. Hänel, T. Strunskus, G. Witte, and Ch. Wöll

Physikalische Chemie I, Ruhr-Universität Bochum,

Universitätstraße 150, 44801 Bochum

The electron and hole mobilities of small aromatic hydrocarbons, like pentacene or perylene are limited by the presence of defects like domain boundaries. For applications it will be necessary to build devices with less domain boundaries, ultimately transistors consisting of single domain organic semiconductors would be desirable. A true epitaxial growth of molecular compounds on solid substrates will be required for fabricating these devices. The growth of soft materials, like perylene, on hard substrates is therefore a new interesting field of research¹⁻⁷.

In this work we present the results of near-edge x-ray fine-structure (NEXAFS) measurements of perylene films on Cu(110) starting with low coverages in the monolayer regime up to coverages of several nanometers.

The copper surface was prepared in UHV by Ar⁺ ion sputtering (1000 eV) and annealing to 900 K. Perylene (Fluka, ≥ 99%) was degassed in vacuum for four hours at 350 K and for two hours at 400 K before it was deposited on the Cu(110) single crystal by organic molecular beam deposition (OMBD). The flux of the perylene molecules was monitored using a quartz crystal microbalance (Leybold Inficon). The NEXAFS spectra were measured in the partial electron yield (PEY) mode using a home made electron detector based on double channel plates (Galileo). Simultaneously with each spectrum a spectrum of a carbon contaminated gold grid was recorded for the energy calibration of the NEXAFS spectra. This grid was also used as a radiation flux monitor. The C1s NEXAFS raw data were normalized by a procedure consisting of several steps, see⁸. Rotation around two axes allowed to conduct measurements at different polar and azimuthal angles. The average tilt angle of the perylene ring-plane relative to the surface plane was determined quantitatively by utilizing that this intensity variation is given by $I_{\pi^*} \sim |\vec{E} \cdot \vec{T}|^2$, where \vec{T} denotes the transition dipole moment which is oriented normal to the perylene plane⁹.

The monolayer, also called interface layer, is the starting point of the growth of perylene films on Cu(110). In Fig. 1 we present NEXAFS spectra of different perylene coverages on

Cu(110) ranging from a monolayer to a thickness of nominal 170 nm (according to the reading on the quartz crystal microbalance). The monolayer perylene film was prepared by saturating the Cu(110) substrate with perylene at a surface temperature of 450 K. The overall shape of the spectra is dominated by the π^* -resonance at 285 eV. The width of the NEXAFS-resonances, however, is clearly broader than in the case of the multilayer data (shown in Fig. 1b) and the splitting of the π^* -resonance into three components (see below) is not resolved. The near edge X-ray absorption fine-structure spectra exhibit a dichroism. For the grazing incidence of 30° a very intense π^* -resonance is observed. In fact, the π^* -resonance at 285 eV is hardly visible at normal incidence (grey curve). A quantitative analysis of the NEXAFS data yields an average tilt-angle of $10^\circ \pm 5^\circ$ between the molecular plane and the surface plane. This could indicate that the molecules are slightly tilted with respect to the Cu(110) surface. But other work on aromatic compounds interacting with metal surfaces suggest a different interpretation. It has been observed that adsorption-induced intramolecular distortions, involving a bent of C-H bonds out of the aromatic ring plane lead to an average tilt-angle different from zero, although the plane of the aromatic ring system is oriented parallel to the surface. As a matter of fact NEXAFS is the method of choice to detect such distortions¹⁰⁻¹². The Fig. 1b shows NEXAFS spectra of a thick perylene film on Cu(110). The π^* -resonance is split into closely spaced components located at 283.8 eV, 284.3 eV and 285.2 eV. In contrast to the perylene monolayer the dichroism is found to be reversed, now the π^* -resonances are most intense for normal x-ray photon incidence. A quantitative analysis of the angular variation of the NEXAFS resonance intensities with angle of incidence yields an average tilt angle of $70^\circ \pm 5^\circ$ between the molecular plane and the surface plane. The NEXAFS spectra exhibit no azimuthal dependence for thick perylene films, i. e., the symmetry information of the substrate is lost.

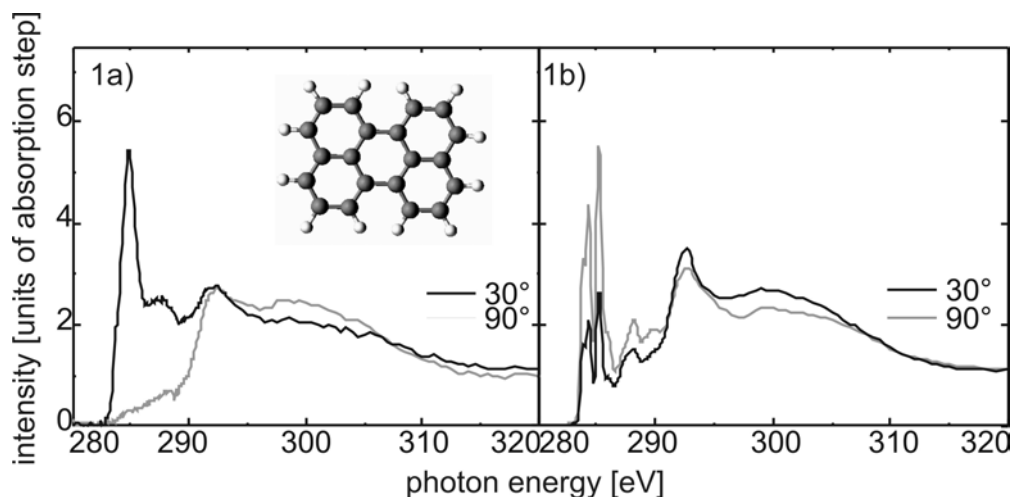


Fig. 1: NEXAFS spectra of perylene on Cu(110) for different angles of incidence of the x-ray beam relative to the sample and along [1-10] azimuth direction of the substrate. (a) saturated perylene layer at 450 K the inset shows a structural model of perylene (b) 170 nm thick perylene film at 300 K

Acknowledgements

This work has been funded by the german research council (DFG focus program OFET, WO 464/17-2).

- 1 Q. Chen, T. Rada, A. Mc Dowall, et al., Chem. Mater. **14**, 743 (2002).
- 2 Q. Chen, A. Mc Dowall, and N. V. Richardson, Chemistry of Materials **15**, 4113 (2003).
- 3 L. Gross, C. Seidel, and H. Fuchs, Organic Electronics **3**, 1 (2002).
- 4 C. Seidel, R. Ellerbrake, L. Gross, et al., Phys. Rev. B **64**, 195418 (2001).
- 5 D. Wang, L.-J. Wan, Q.-M. Xu, et al., Surf. Sci. Lett. **478**, L320 (2001).
- 6 P. Yannoulis, R. Dudde, K. H. Frank, et al., Surf. Sci. **189/190**, 519 (1987).
- 7 U. Zimmermann, G. Schnitzler, V. Wüstenhagen, et al., Sec. A Mol. Cryst. Liq. Cryst. **339**, 231 (2000).
- 8 S. Reiß, H. Krumm, A. Niklewski, et al., Journal of Chemical Physics **116**, 7704 (2002).
- 9 J. Stöhr, *NEXAFS spectroscopy* (Springer Verlag, Berlin, Heidelberg, 1992).
- 10 S. Lukas, S. Söhnchen, G. Witte, et al., ChemPhysChem (in print).
- 11 C. Mainka, P. S. Bagus, A. Schertel, et al., Surf. Sci. **341**, L1055 (1995).
- 12 K. Weiss, S. Gebert, M. Wühn, et al., Journ. Vac. Sci. Technol. **A 16**, 1017 (1998).

Study of Ag and Au based historical and archaeological objects by high energy Sy-XRF

A. Berger¹, T. Calligaro², A. Duval², W. Görner¹, M.-F. Guerra², S. Merchel¹,
M. Radtke¹, I. Reiche², H. Riesemeier¹, M. Roth³

¹Bundesanstalt für Materialforschung und –prüfung (BAM), 12200 Berlin, Germany

²Laboratoire du C2RMF – UMR 171 CNRS, 75001 Paris, France

³Kupferstichkabinett (KK), Staatliche Museen zu Berlin, 10785 Berlin, Germany

Introduction

After two years of intensive and successful studies of silverpoint drawings of the Netherlands sketch book (1520-21) by Albrecht Dürer and of one famous Flemish drawing by Jan van Eyck [1, 2], we now enlarge the research to other archaeometric problems.

Further drawings of Albrecht Dürer realized with different materials as well as drawings of Dürer's contemporaries, of Hans Holbein the Ancient and his workshop, were investigated by Sy-XRF to broaden the expertise on ancient drawing materials. In contrast to pure metal point drawings of Albrecht Dürer already analysed by us, the works by Hans Holbein and his workshop present the particularity to be made with a more complex drawing technique including namely metal point, gouache, white and red pigments. It is arguable if the latter materials were added by the artist himself, his sons, or a later collector. The aim of our investigations is to clarify the genesis of the drawings and to determine the origin and authenticity of the other drawing materials applied. Additionally, we addressed the issue of the particular alteration phenomenon of ancient silverpoint drawings, the enrichment in Hg, by studying more recent silverpoint drawings in order to detect the presence of Hg.

A new methodological project on the provenance and manufacturing technology of ancient gold objects was also considered [3]. The study of the origin of Au used to fabricate ancient objects is generally restricted to non-destructive measurements of characteristic trace and ultra trace elements present in the final alloy. Among those, Pb, Pt, and Sn are very representative of the exploitation of major ancient Au deposits, those of secondary type (such as alluvial deposits) [4]. However, only very few analytical techniques fulfil the requirements. The most common techniques for the determination of trace element concentrations are proton activation analysis, ion beam analysis, and mass-spectrometry analysis or atomic emission spectroscopy in combination with ICP. 3 MeV PIXE with selective filters, in the case of Au alloys a Cu foil [5], is a good compromise for totally non-destructive analysis. Unfortunately, Pb and Pt are the most important elements that cannot be easily measured by PIXE in Au alloys (the limits of detection which can be attained are 300 ppm and 2000 ppm, respectively). To solve the problem of Pt, a PIXE-XRF set-up was developed based on an As primary target. However, the Raman and the Raleigh effects observed for Au give an upper limit of detection of about 80 ppm [5]. In order to find out how far the detection limits for Pt and Pb in Au alloys can be improved for a totally non-destructive technique, first measurements were performed at the BAMline using beam energies close to the Au K and the Au L absorption edges.

Investigated objects

Drawings by Albrecht Dürer: “Agnes Dürer in niederländischer Tracht”, 1521, indicated as metal point, brown on deep-violet paper, 407 x 271 mm, from the Kupferstichkabinett (KK) Berlin (KdZ 36); “Beweinung Christi”, 1522, indicated as metal point or chalk on prepared paper, from the Kunsthalle Bremen. Furthermore, complex drawings attributed to Hans Holbein the Ancient of the KK Berlin were investigated: “Sigmund, der Bruder des Künstlers“, unknown date (KdZ 2508); “Leonhard Wagner, Profil nach rechts“, before 1512 (KdZ 2525); “Konrad Merlin, Abt von St. Ulrich“, unknown date (KdZ 2526); “Schneider Grün Profil links“, unknown date (KdZ 2545); “Schneider Grün, halb links“, unknown date

(KdZ 2546); “Gumprecht Rauner”, unknown date (KdZ 2549); “Laienbruder Hans, halb rechts”, unknown date, (KdZ 2550); and two recent silverpoint drawings: “Joseph Senn”, 1934, by Otto Dix conserved in the KK Berlin; “Die Kirche St. Maria im Speicherring“, 1997, modified in 2003, by Heinrich Wunderlich, private collection.

Gold objects: Only few certified standards are available for quantitative trace element analysis in Au. For this first experiment, we used a Canadian Mint reference standard NIST 8056 with (40.8 ± 1.0) ppm Pt (also named “FAU8”), a pure Au standard from Lyon Allemand, and a pure Pt standard from NIST. Three ancient samples, which were previously analysed by PIXE, PIGE, and PIXE-XRF as well as by ICP-MS were also analysed. Finally four archaeological samples, for which the concentration of Pt in the alloy was fundamental to understand the provenance of the Au, were investigated.

Experimental set-up at BAMline

Drawings: We used the Sy-XRF set-up at the wavelength shifter beamline, BAMline [6], to determine major and minor element contents in the lines of the drawings. A W/Si Double-Multilayer-Monochromator (DMM) was used to produce an X-ray beam of 32 keV with a beam diameter of $100 \times 100 \mu\text{m}^2$. The drawings were fixed in air on a sample frame on a motorized xyz-stage at an angle of 45° to the X-ray beam. Fluorescence signals were collected during 300 s by a Si(Li)-detector, covered with an Al or a polyethylene filter, at 90° with respect to the incident beam. Data processing was performed by means of AXIL. Relative concentrations of the silverpoints were determined by a procedure based on different silver standards after background subtraction using a thin layer approximation.

Gold objects: The same Sy-XRF set-up was used for the analysis of trace concentrations of Pt in Au. Measurements were performed at different excitation energies above and below the Pt L_3 edge, as well as at the K absorption edge. The X-ray fluorescence signals were detected for about 1500 s with a Si(Li) detector, shielded by a $200 \mu\text{m}$ Cu filter for excitation with 78.5 keV. Beam diameter varied for the standard and archaeological samples between $250 \mu\text{m}$ and 2 mm as a function of their size and Pt content.

Results and discussion

Drawings: About 20 points per drawing were analysed. All drawings of Hans Holbein the Ancient and his workshop were revealed to be realised with silverpoints. The detailed quantitative analysis of the silverpoint and the exact identification of the other drawing materials used by the artists are still in progress. Contrarily to what was formerly described, both drawings, “Beweinung Christi” and “Agnes Dürer in niederländischer Tracht”, have not been performed with a silverpoint but with black chalk on a Pb-white containing preparation. This illustrates that much confusion still exists on drawing materials. The more recent drawing by Otto Dix (1934) was realised by one silverpoint on a zinc white preparation (Fig. 1a). The contemporary drawing by Wunderlich was made with three silverpoints varying in minor elements. No Hg ($< 2\%$) was detected in the metal strokes of neither of the recent drawings. This confirms that the presence of Hg in ancient drawings might be due to an alteration phenomenon.

Gold objects: Several measurements of the Pt concentration were carried out on the “FAU8” as well as on pure Au and Pt standards using a beam energy below and above the Pt L absorption edges. The Pt signal was calculated in a way, that the spectrum above the Pt edge was approximated by the sum of the shifted spectrum below the edge and the spectrum of the pure Pt foil. The chosen energy range was 9.255 to 9.576 keV (Fig. 1b). In this range, the Pt signal is bigger than one third of the maximal Pt signal. Quantification was done by Monte Carlo simulation of the Pt intensity at the FAU 8 sample in comparison to the pure Pt. By this method we calculated a concentration of 58.1 ppm for Pt in the “FAU8” standard using a beam energy of 11.554 and 11.574 keV. With an excitation energy of 78.5 keV and by

comparing the spectrum obtained from the FAU8 standard with those from pure Au and Pt standards a concentration of 46 ppm for Pt was determined. Thus, the latter measurements showed the best performance for determination of low Pt contents. At this beam energy, we could largely improve the detection limit for Pt. Using the same experimental conditions, we could find a good agreement between the expected and the calculated Pt concentrations for ancient Au samples.

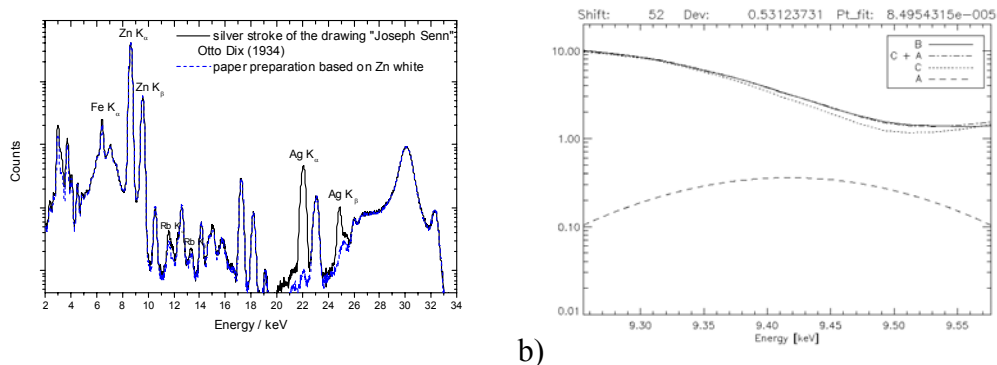


Fig. 1a) XRF spectra of the drawing "Joseph Senn" by Otto Dix (1934). **b)** Superposition of the spectra A=pure Pt sample at 11.574 keV (above Pt L_3 edge) and C="FAU8" at 11.547 keV (below Pt L_3 edge) to approximate spectra B="FAU8" at 11.574 keV (above Pt L_3 edge).

Conclusion and perspectives

The spatially resolved XRF investigations were revealed to be a powerful tool for the non-destructive study of different drawing materials and of trace elements such as Pt in Au. New results on a recent silverpoint drawing by Otto Dix, on chalk drawings by Albrecht Dürer as well as on complex drawings by Hans Holbein the Ancient were obtained. The results showed the potential of physico-chemical analyses for the unambiguous identification of the artists' materials and the definition of new criteria for the attribution to a particular artist or workshop. Moreover, first measurements of Pt at trace concentrations in Au alloys illustrate the possibility for achieving a very low limit of detection and, therefore, for improving the determination of new provenance criteria for archaeological Au objects. We hope to continue the projects on the analysis of drawing materials and of trace elements in archaeological gold objects, namely on Pt and Pb traces in Au. Further measurements using an X-ray detector with an appropriate efficiency for the considered high-energy region will certainly improve the detection limits for Pt and Pb.

References

- [1] I. Reiche, A. Berger, W. Görner, S. Merchel, M. Radtke, J. Riederer, H. Riesemeier, M. Roth, Following the traces of Albrecht Dürer: Analysis of silverpoint drawings by spatially resolved synchrotron-induced X-ray fluorescence analysis, submitted to *Nucl. Instr. and Meth. B*.
- [2] I. Reiche, M. Radtke, A. Berger, W. Görner, T. Ketelsen, S. Merchel, J. Riederer, H. Riesemeier, M. Roth, Spatially resolved Synchrotron-induced X-ray fluorescence analyses of metal point drawings and their mysterious inscriptions, submitted to *Spectrochimica Acta B*.
- [3] M.F. Guerra, Th. Calligaro, The analysis of gold: manufacture technologies and provenance of the metal, *Measur. Scien. Techn.* **14** (2003) 1527-1537.
- [4] A. Gondonneau, M.F. Guerra, The circulation of precious metals in the Arabic Empire: the case of the Near and the Middle East, *Archaeometry*, **44:4** (2002) 573-599.
- [5] M.F. Guerra, Th. Calligaro, Gold traces to trace gold, *J. Archaeol. Scien.*, in press.
- [6] W. Görner, M.P. Hentschel, B.R. Müller, H. Riesemeier, M. Krumrey, G. Ulm, W. Diete, U. Klein, R. Frahm, BAMline: The first hard X-ray beamline at BESSY II, *Nucl. Instr. and Meth. A* **467-468** (2001) 703-706.

Acknowledgements

We gratefully acknowledge the support during beam time of E. Alex, C. Severit, R. Fricke, R. Wittich (KK Berlin) and A. Röver-Kann (Kunsthalle Bremen). This work was supported by the DAAD and the French Ministry of Research and Education (contract n° D/0122896). We thank BESSY for allowing beam time.

SEARCHING FOR WATER IN THE EARTH'S UPPER MANTLE

Koch-Müller, M.(1), Matsyuk S.(2) and Wirth R.(1)

(1) GeoForschungsZentrum Potsdam, Telegrafenberg, 14473 Potsdam, Germany
(mkoch@gfz-potsdam.de),

(2) Institute of Geochemistry, Mineralogy and Ore Formation,
Ukrainian Academy of Science, Pr. Palladina 34, Kiev-252 142, Ukraine

Water plays an important role in geodynamic processes in the Earth's upper mantle. Beside in nominally hydrous minerals such as amphibole, serpentine, mica and talc hydrogen may be stored in nominally anhydrous minerals (NAMs) such as pyroxene, garnet and olivine. NAMs can dissolve traces of OH as point defects. Although the amount of water in these minerals is generally very low (up to 0.1 wt % H₂O), the water content that can be dissolved in NAMs in the upper mantle is large and may exceed the amount of water in the hydrosphere. The presence of water in the earth's crust and mantle has enormous effects on the dynamic of processes of the earth, because the incorporated hydrogen changes the physical properties of the minerals such as the melting point, rheological behavior (hydrolytical weakening) and the transformation kinetics.

An appropriate method for detecting traces of hydrogen in minerals is IR spectroscopy. IR spectroscopy using a conventional laboratory source needs a comparatively large beam size to get an acceptable signal to noise ratio (about 60 µm). But for small synthetic crystals and to check the homogeneity of natural samples it would be desirable to have a smaller lateral resolution. Therefore, we used the facilities of the infrared synchrotron beamline at Bessy II. An infrared microscope and interferometer is coupled to the synchrotron beam and allowed us to collect IR spectra with a spatial resolution of 5 x 5 µm. We adjusted an IR-polarizer (KRS5) to the microscope and we were able to take polarized measurements with the same aperture size of 5 x 5 µm as the unpolarized measurements. As far as we know are these the first polarized measurements obtained on small oriented crystals with such a small aperture size.

The quantitative importance of hydrogen in mantle processes depend on how much water or hydrogen can be stored in nominally anhydrous minerals and on where hydrogen resides in the crystal lattice. We report here the results of our studies on the location and quantification of OH in two geologically very important nominally anhydrous minerals:

- a) clinopyroxene, (Na, Ca)(Fe, Mg, Al) (Si, Al)₃O₆
- b) coesite, SiO₂, the high-pressure polymorph of quartz

a) Clinopyroxene

Clinopyroxene (cpx) is a major constituent of the Earth's crust and mantle. From experimental studies as well as from studies of natural systems it is well known that cpx can store hydrogen in its structure. Hydrogen concentration varies widely from 0.01 to 0.13 wt % H₂O as a function of geological setting with the greatest amount occurring in mantle-derived samples of omphacitic cpx. In a recent study an omphacitic cpx from a diamond-grade eclogite from the Kokchetav massif, Kazakstan, with a water content as high as 0.30 wt % H₂O has been reported (Katayama and Nakashima 2003).

We investigated a series of omphacitic clinopyroxenes from lower crust to upper mantle origin beneath the Siberian platform by FTIR spectroscopy and transmission electron microscopy. The IR spectra of all our samples exhibit three groups: group (a) 3445-3465 cm⁻¹, group (b) 3500 – 3540 cm⁻¹ and group (c) 3600 – 3624 cm⁻¹. When applying synchrotron IR

radiation, which allows a spot size of only $5 \times 5 \mu\text{m}$, we realized that the intensities mostly of the absorption bands of group (c) vary extremely within one crystal. By the combination of transmission electron microscopy (TEM) and synchrotron IR spectroscopy we showed convincingly that the OH is partly incorporated by micro- and nano-inclusions of sheet silicates (Fig. 1). The inclusions are of secondary origin (alteration during up-lift) (Koch-Müller et al. 2004).

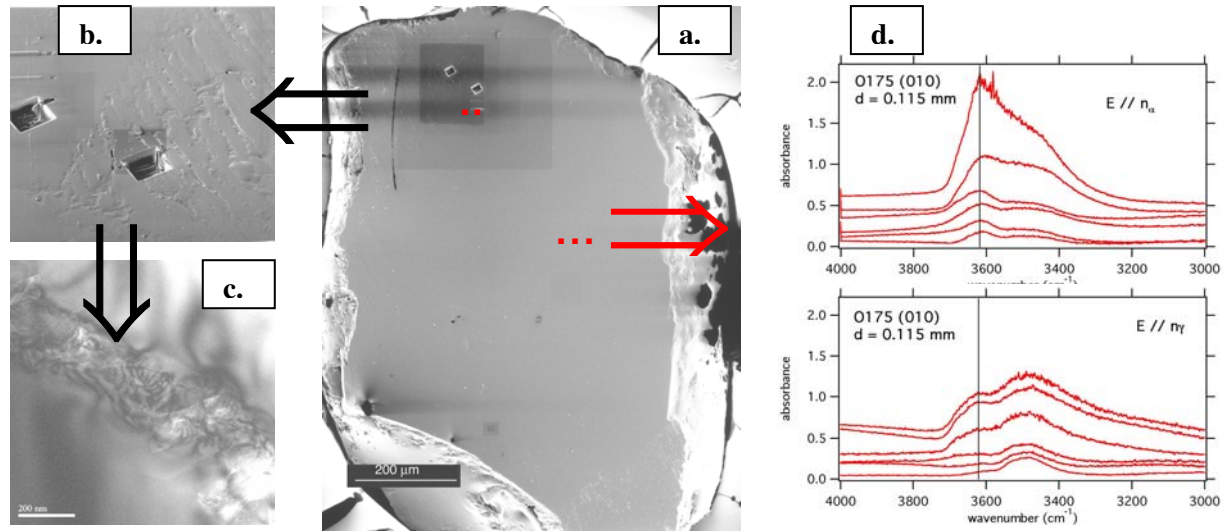


Figure 1: (a) SE image of an cpx grain showing the position and spot size of the polarized synchrotron IR measurements (red squares) and the location of the TEM foils (black squares). (b) SE image of a part of the grain in Fig.1a at higher magnification. The grooves where the TEM foils have been cut by Focused Ion Beam (FIB)-technique are visible. The TEM foils are removed. c) TEM bright field image of a part of the FIB-foil showing a narrow vein of sheet silicates in cpx. (d) Polarized infrared spectra with (a) $E // Z$ (n_{γ}) and (b) $E // X$ (n_{α}) taken on different parts on the (010) wafer of cpx (red squares) with an aperture of 5 by 5 μm showing the variation in band intensity.

To quantify the water content we excluded absorption peaks of group (c) from the calculation. The structural bonded water content of the omphacitic cpx range from 0.003 to 0.051 wt % H_2O . Surprisingly, the lowest contents were found for cpx of the highest pressure region, i.e. for the diamond bearing eclogite xenoliths of the Mir kimberlite pipe; the highest values were obtained for omphacitic cpx of the low pressure grospydites and granulites of the Zagadotschnaya and Udatschnaya kimberlite pipe, respectively. The low water concentrations of the cpx from the high-pressure region seems to be controlled by low water activity during crystallization. But hydrogen loss during the uplift cannot be ruled out.

b) Coesite

Recent experimental studies showed that the SiO_2 polymorph coesite belongs to the group of nominally anhydrous minerals which incorporates hydrogen in the form of hydroxyl groups (e.g. Koch-Müller et al. 2001). FTIR spectra from OH-bearing coesite samples published so far show at least six bands: four intense bands at 3575, 3528, 3508, and 3459 cm^{-1} , and two weak bands at 3296 and 3210 cm^{-1} . All six bands are due to OH-stretching vibrations (Koch-Müller et al. 2001). Using ion probe analysis along with polarized and in-situ high-pressure FTIR spectroscopy, Koch-Müller et al. (2001) concluded that hydrogen incorporation into coesite was consistent with the hydrogarnet substitution mechanism, $\text{Si}^{4+(\text{Si}2)}$

+ $4\text{O}^{2-} = {}^{[4]}\text{va}^{(\text{Si}2)} + 4\text{OH}$. The vibrations of the low symmetry $(\text{OH})_4$ group in coesite (point symmetry 1) must give rise to four bands as observed. To investigate the hydrogen solubility of coesite as a function of pressure synthesis runs were performed at 8.5 and 9.0 GPa and 1200 °C. Infrared spectra taken on these HP-coesite show four sharp new IR bands in the energy range of 3380 – 3460 cm^{-1} (ν_7 - ν_{10}) together with weak ν_1 - ν_3 bands. To insure that the new bands were intrinsic the crystals were investigated by single crystal X-ray diffraction, Raman spectroscopy, polarized single crystal and in-situ high pressure FTIR spectroscopy. Fig. 2 shows the synchrotron IR-spectra of four different crystals taken with an aperture size of 5 x 5 μm on different parts of the 100 μm -sized crystals. Considering the small aperture size, the spectra are of high quality. Our investigation confirmed that the new bands are due to OH in coesite. The polarisation and high-pressure behaviour of the ν_7 - ν_{10} OH bands is quite different from that of the ν_1 - ν_3 bands indicating that the H incorporation in coesite changes dramatically at these P and T conditions. At these high pressures the OH defects are introduced into the structure by another type of hydrogarnet substitution with much shorter O-H...O distances as those previously described for coesite (Koch-Müller et al. 2001 and 2003).

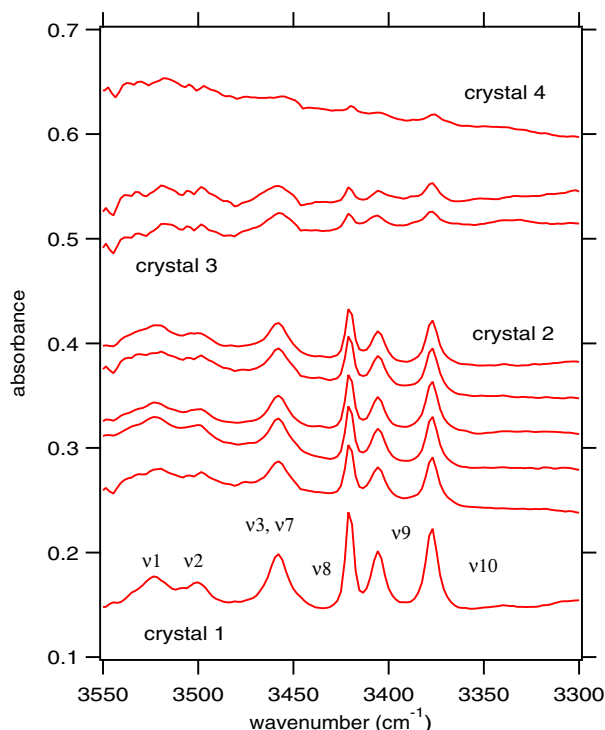


Figure 2: Infrared spectra of synthetic coesite crystals, taken with synchrotron IR with an aperture of 5 x 5 μm . The crystal 1 to 4 are of different thickness.

References

- Katayama I., and Nakashima S. (2002) *American Mineralogist*, 88, 229 –234.
 Koch-Müller M., Fei Y., Hauri E. and Liu Z. (2001) *Physics and Chemistry of Minerals*, 28, 693-705.
 Koch-Müller M., Dera P., Fei Y., Reno B., Sobolev N., Hauri E., and Wysoczanski R. (2003) *American Mineralogist*, 88, 1436 – 1445.
 Koch-Müller M., Matsyuk S.S. and Wirth R. (2004) *American Mineralogist* (in press).

Kostenträger (BMBF 05KS1KK1/4)

Projects in Basic Research 2003

Project leader	Affiliation	Project title	Funding	Contract number
Ageev	Ioffe Physical-Technical Institute RAS, St.Petersburg	Mechanism for great alkali metal ions enhancements in electron stimulated desorption		
Akerboom	Wageningen University, Laboratory of Microbiology	Surface Layer Protein from <i>Pyrococcus furiosus</i>	EU	
Akerboom / Brouns	Wageningen University, Laboratory of Microbiology	Bleomycin binding Protein (Sshble)	EU	
Andersen	Aarhus University, Dep. Molecular Biology	Structures of yeast translation factors	EU	
Andersen / Nissen	Aarhus University, Dep. Molecular Biology	Structures of the Ca ²⁺ ATPase in various functional states	EU	
Andersen / Thirup	Aarhus University, Dep. Molecular Biology	Structure of bovine mitochondrial EFTu-EFTs complex	EU	
Andersen / Thirup	Aarhus University, Dep. Molecular Biology	Elongation factor T (EF-Tu:EF-Ts) in complex with pulvomycin	EU	
Andersen/ Thirup	Aarhus University, Dep. Molecular Biology	Mitochondrial seryl-tRNA synthetase	EU	
Andre	Université Pierre et Marie Curie Laboratoire de Chimie Physique	Measurement of multilayer optics mirrors and gratings	EU	HPP33/150902
Arvanitis	Uppsala University Department of Physics	Novel interlayer exchange in epitaxial 3d bi and tri-layers by means of XMCD and XRMS	EU	
Arvanitis	Uppsala University Department of Physics	X-ray magnetic circular dichroism on large-scale magnetic nanostructures	EU	
Assmann	Universität München Sektion Physik	Texture modification in polycrystalline Ti layers on Si by irradiation with swift heavy ions		
Babanov / Baberschke	Institute of Metal Physics RAS Yekaterinburg / FU Berlin	EXAFS study of L-edges for FeCr systems		
Baczewski	Polish Academy of Sciences Institute of Physics	Magnetic structure in Re/Tm thin films studied by MXCD	EU	
Bansmann	Universität Rostock Fachbereich Physik	Magnetische Cluster auf Oberflächen: Korrelation von geometrischen, elektronischen und magnetischen Eigenschaften	DFG	BA 1612/3-1
Bansmann	Universität Rostock Fachbereich Physik	Magnetismus von Inselfschichten und Clustern auf Oberflächen	DFG	835/H-3

Barth	Institut de Physique des Nanostructures (IPN) Faculté des Sciences de Base	Bonding of a trimesic acid on a Cu(100) surface		
Barth	MPI-FKF	Engineering low-dimensional metal-organic coordination systems at metal surfaces	DFG	
Bartl	Institute of Medical Physics and Biophysics, Universitätsklinik Charite	Complexes of Gossypol Schiff bases with cations. Structure and Mechanism of complex formation		
Batchelor	BESSY	Switching of annealation in metal-TAPs		
Baumgärtl	FU Berlin FB Chemie			
Becker / Viefhaus	Fritz-Haber-Institut der Max-Planck-Gesellschaft	Coherence properties in atomic and molecular photoionization	BMBF DFG	05 KS1EB12 BE 860/18-2
Becker/Prümper	Fritz-Haber-Institut der Max-Planck-Gesellschaft	Vollständige Experimente zur Photoionisation mittels Koinzidenzspektroskopie oder Targetpräparation	DFG	
Behne	Hahn-Meitner-Institut SF6	Identifizierung und Analyse von metallhaltigen Proteinen aus dem Zentralnervensystem und der männlichen Reproduktionsorgane mit Hilfe der Röntgenfluoreszenzanalyse		
Behne	Hahn-Meitner-Institut SF6	Lokalisation von Proteinablagerungen bei Morbus Alzheimer mit Hilfe der Synchrotron-FTIR-Mikroskopie		
Behne	HMI	Lokalisation von Proteeablagerungen bei Scrapie mit Hilfe der Synchrotron-FTIR Mikroskopie		
Beigang	Universität Kaiserslautern FB Physik	Untersuchung der Plasmonen-unterstützten Transmission elektromagnetischer Wellen durch Öffnungen im sub-Wellenlängen-Bereich		
Birch	Linköping University IFM	Characterization of reflectivity and interfaces of Scandium-based soft X-ray multilayer mirrors grown by ion-assisted magnetron sputter deposition	EU	
Bolse	Universität Stuttgart Institut für Strahlenphysik	Surface modification by irradiation with swift heavy ions	DFG	BO 1130/1
Borisenko	IFW Dresden	Momentum and temperature dependence of the pseudogap phenomenon in the high-Tc cuprates		
Boronin	Inst. of Catalysis RAS, Novosibirsk	Photoemission study of Ag and Au oxide films formed by microwave-excited oxygen		

Boyen	Universität Ulm Abt. Festkörperphysik	Magnetization studies on ordered arrays of size-selected pure Co and exchange-biased Co/CoO nanoparticles	BMBF	
Boyen	Universität Ulm Abt. Festkörperphysik	Electronic properties of size-selected supported nanoparticles	BMBF	05 KS1VUA/8
Braun (PDI)	Paul-Drude-Institut für Festkörperelektronik	Surface interface and layer structure of MnAs on GaAs during heteroepitaxy	BMBF	
Braun (PDI)	Paul-Drude-Institut für Festkörperelektronik	Structural studies of ferromagnet-semiconductor structures during growth using in situ X-ray diffraction	BMBF	DI BM159
Bressler	BESSY	High kinetic energy Photoelectron Spectroscopy		
Brückel	IFF, FZ Jülich	Magnetization profile in epitaxial Fe/Cr/Fe trilayers exhibiting the giant magnetoresistance effect		
Brückel/Kenzinger	IFF, FZ Jülich	The magnetic structure of $\text{Fe}_{(1-x)}\text{Co}_x/\text{Mn}/\text{Fe}_{(1-x)}\text{Co}_x$ epitaxial trilayers probed by resonant soft x-ray magnetic scattering		
Bürgler	IFF, FZ Jülich	Electronic structure of Ge in epitaxial Fe/Ge/Fe trilayers and its correlation to magnetic and magnetotransport properties		
Calvet	Hahn-Meitner-Institut Berlin SE 6	Electronic bandstructure of epitaxial $\text{CuIn}_x\text{Ga}_{(1-x)}\text{S}_2$ films ($x=0\dots 1$)		
Cobessi	ESBS	Structural studies of the pyoverdine receptor FpvA from <i>Pseudomonas aeruginosa</i>	EU	
Cobessi	ESBS	Structural studies of the pyochelin receptor FptA from <i>Pseudomonas aeruginosa</i>	EU	
Dähne	Technische Universität Berlin Institut für Festkörperphysik	Photoemission at MIS structures with external gate bias	BMBF	
Dähne	Technische Universität Berlin Institut für Festkörperphysik	Electronic structure of self-organized lanthanide silicide nanowires on Si(001)	BMBF	05 KSIKTA/4
de Groot	Utrecht University	In situ soft X-ray absorption at low-loaded framework Fe-ZSM5	Eu	
Deb	Bhabha Atomic Research Centre Synchrotron Radiation Section	Investigation of high pressure phase transition in organic compounds using IR spectroscopy		
Dodelet	INRS-Energie et Matériaux	Non-noble metal catalysts for oxygen reduction in PEM fuel cells		

Dürr	BESSY	Magnetic spectromicroscopy of magnetoresistive $\text{Co}_2\text{Cr}_{0.6}\text{Fe}_{0.4}$ AL Heusler alloys		
Dürr	BESSY	Time-resolved magnetic polaron dynamics in (GaMn)As magnetic semiconductors		
Dürr	BESSY	Valence electronic and magnetic structure of magnetorestrictive $\text{Co}_2\text{Cr}_{1-x}\text{Fe}_x\text{Al}$ Heusler alloys probed by circular dichroism in 2p resonant photoemission		
Ehresmann	Universität Kaiserlautern FB Physik	Nachweis von Dissoziationsprozessen molekularer N_2 -Rydbergzustände in atomare Rydbergzustände unter Erhaltung der Hauptquantenzahl des Rydbergelektrons	DFG	
Ehresmann	Universität Kaiserlautern FB Physik	Autoionisation der N_2 ($1s\text{-}\pi^*$)-Resonanz in die Zustände N_2^+ B und C	DFG	
Ehresmann	Universität Kaiserlautern FB Physik	Rotationsaufgelöste Photodissoziation in neutrale Fragmente u. Ionenausbeuten aufgrund der Prädissoziation u. Autoionisation molekularer Rydbergzustände in NO und O_2	DFG	Eh187/4
Ehresmann	Universität Kaiserlautern FB Physik	Resonante magnetische Reflexion an $\text{NiO}(50\text{nm})\text{Ni}(5\text{nm})/\text{Ta}(2\text{nm})$ Zweilagigen-Schicht-Systemen und FeMn Spinvalves nach deren Modifikation durch He-Ionenbeschuss	DFG	Eh187/2
Ehresmann	Universität Kaiserlautern FB Physik	Anregungsenergieabhängigkeit des Alignments angeregter Xe II-Zustände bevölkert durch resonanten (Raman-) Augerprozess innerhalb der natürlichen Linienbreite der Xe I $4d^9 np$ Autoionisationsresonanzen	DFG	Schm 379/12
Einsle	Universität Göttingen, Institut für Mikrobiologie und Genetik	Cytochrome c Nitrite Reductase Complex NrfHA		
Einsle	Universität Göttingen, Institut für Mikrobiologie und Genetik	Nitrous oxide reductase		
Eisebitt	BESSY	Coherent resonant X-ray scattering from magnetic domain patterns		

Eisebitt	BESSY	Soft X-ray spectroscopy in liquid environments		
Erdmann / Klusmann (Noxxon Pharma AG)	Freie Universität Berlin, Institut für Biologie, Chemie, Pharmazie	Crystallization and structure analysis of Spiegelmers		
Erko	BESSY	Investigations of Ge concentration micro-variations in a $\text{Si}_{(1-x)}\text{Ge}_{(x)}$ crystal		
Erko	BESSY	Confocal capillary X-ray microscope		
Esser	TU Berlin	IR-Ellipsometrie: Elektronische und vibronische Anregungen nanoskopischer Strukturen auf Halbleiteroberflächen	DFG BMBF	
Esser	TU Berlin Institut für Festkörperphysik	Optical anisotropy in the VUV-spectral region: surface core level excitations	BMBF	
Esser	TU Berlin Institut für Festkörperphysik	Aufbau und Betrieb eines VUV-XUV-Ellipsometers mit Synchrotronstrahlung	BMBF	055E8KTA3
Esser/Richter/Braun	TU Berlin Institut für Festkörperphysik BESSY	Identifizierung ferromagnetischer Komponenten bei der Reaktion von Kobalt mit GaAs(001) und $\text{In}_{0.52}\text{Ga}_{0.48}\text{P}(001)$ Oberflächen	DFG	
Fabian	Robert-Koch-Institut, P12	Infrared microspectroscopy of breast tumor tissue sections	Deutsche Krebshilfe	70-2420
Fauth	Universität Würzburg Physikalisches Institut Exp.-Physik IV	XMCD und XAS-Untersuchungen von Übergangsmetallclustern auf nichtmagnetischen Metallsubstraten		
Fauth	Universität Würzburg Physikalisches Institut Exp.-Physik IV	Charakterisierung deponierter Übergangsmetallcluster mittels (resonanter) Photoemission		
Fauth	Universität Würzburg Physikalisches Institut Exp.-Physik IV	XMCD und XAS-Untersuchungen des Magnetismus von Übergangsmetallclustern sowie ihrer Wechselwirkung mit nichtmagnetischen Substraten		
Feigl	Fraunhofer IOF	Sc-based multilayer optics for the EUV/Soft X-ray range		SFB 602, TPA 1
Felsch	Universität Göttingen Physikalisches Institut	Electronic structure and magnetism of GdN thin layers: X-ray absorption and XMCD at the N-K and Gd- $M_{2,3}$ edges	DFG	
Ficner / Dickmanns	Universität Göttingen, Molekulare Strukturbiologie	Nuclear transport factor snurportin 1		

Fiechter	Hahn-Meitner-Institut Berlin GmbH SE 5	Investigations of catalytic centers in noble metal free catalysts for direct methanol PEM fuel cell. EXAFS measurements		
Filatova	St. Petersburg University Institute of Physics	Anisotropy of X-ray reflection from one axis crystals		
Fink J. / Borisenko	IFW Dresden	Anisotropy of the coupling strength in Bi-based cuprates	DFG	Fi-439/10-1
Fink R.	Universität Erlangen Physikalisches Institut Lehrstuhl f. Exp. Physik II	Elektronische und vibronische Feinstruktur in quinon- basierenden Ladungstransfersalzen	BMBF	
Fink R.	Universität Erlangen Institut für Physikal. U. Theoret. Chemie	NEXAFS Feinstruktur in quinon- basierenden Ladungstransfersalzen und aromatischen Molekülen	BMBF	05 KSIWWA/2
Firsov	BESSY	The Crystal-Based Bragg-Fresnel- Lens		
Freiwald	BESSY	Soft X-ray spectroscopy in liquid environment: Towards an understanding of the electronic structure in active centers of biomolecules		
Freund	Fritz-Haber-Institut der Max-Planck-Gesellschaft Abt. Chemische Physik	Elektronische Struktur molekularer Schichten auf reinen und modifizierten Oxid-, Karbid- und Nitridsubstraten	MPG	
Fried	UoC, San Francisco	THz Near-field Imaging of Caries Lesions		
Galakhov	Institute of Metal Physics, Russian Academy of Sciences - Ural Division	Nature of electronic holes in doped oxides		
Gambardella	Ecole Polytechnique Federale de Lausanne Institut de Physique des Nanostructures, EPFL	XPS investigation of localized 3d impurity states on free-electron hosts	EU	
Gießel / Widdra	Max-Born-Institut, Universität Halle	Bestimmung der lokalen Adsorptionsgeometrie von Stufenkantenadsorbaten auf vizinalen Halbleiteroberflächen		
Gisler	Uni Konstanz	Untersuchung von Konformationsunordnungen in Protein-Einkristallen mittels THz Strahlung		
Godehusen	BESSY	Bestimmung des β -Parameters an freien 3d-Übergangsmetall- Atomen		

Goering/Schütz	MPI für Metallforschung	Untersuchung der magnetokristallinen Anisotropie ferromagnetischer Übergangsmetalloxide mittels XMCD		
Goering/Schütz	MPI für Metallforschung	Untersuchungen zur induzierten Kupfermagnetisierung von "Spin-Valve-Systemen" mit resonanter magnetischer Röntgenreflektometrie		
Golden	Universiteit van Amsterdam Van der Waals-Zeeman Institut	k-space microscopy of the high temperature superconductors	EU	
Goldhahn	Technische Universität Ilmenau	Bestimmung der dielektrischen Funktion von InN im VUV	BMBF	055SE8KTA3
Goldmann/Tepper	Universität Kassel	Commissioning "multi-user-multi-purpose" station at BESSY		
Gomoyunova	A.F.Ioffe Physico-Technical Institute	Initial stages of oxygen mediated growth of CoSi ₂ at the Si(100)-2x1 surface		
Gordeev	Ioffe Physical-Technical Institute, Russian Academy of Sciences	Fullerite C ₆₀ Modification by Monochromatic Synchrotron Radiation		
Gordeev	Ioffe Physical-Technical Institute, Russian Academy of Sciences	Study of Element Composition, Electron Structure, and Shape of InAs Quantum Dots in the GaAs matrix		
Grenzer	University of Potsdam, Institute for Physics	X-ray investigations of a heat sink mounted disk laser device		
Grunze / Zarnikov	Universität Heidelberg Angewandte Physikalische Chemie	Neutronenstreu- und Synchrotronstrahlungsexperimente an biologisch relevanten organischen Monoschichten. Teilprojekt: Homogene und heterogene organische Schichten als Substrate für Anwendungen in der Biosensorik	BMBF	03 GRE1HD
Grunze / Zarnikov	Universität Heidelberg Angewandte Physikalische Chemie	Röntgenspektroskopie an organischen Grenzflächen und Biomaterialien in Kontakt mit Lösungen	BMBF	
Gudat/Mertins	Universität Potsdam/BESSY	Magneto-optische Polarisationspektroskopie mit Synchrotronstrahlung an magnetischen Schichtsystemen	BMBF	
Güntherodt	RWTH Aachen II. Physikalisches Institut	High -resolved spin-polarized photoemission of ferromagnetic oxide interfaces and oxide half-metallic ferromagnets	BMBF	05KS1PAA/7

Hague	Universität Pierre et Marie Curie Laboratoire de Chimie Physique	Low energy electron excitations in complex oxides studied by X-ray Raman spectroscopy	EU	HPR1-1999-CT-00028
Haibel	HMI	Investigation of pore formation in metallic foams by synchrotron computed tomography	DFG	Ba 1170/4-2
Haumann / Dau	FU Berlin Physik	X-ray absorption spectroscopy on biological samples (BioXAS): The manganese complex of photosystem II in functionally relevant substates.	BMBF DFG	
Haumann / Dau	FU Berlin Physik	Setup and test of a helium cryostat at beamline KMC-2 for XAS on metalloenzymes	DFG	SFB496/C6,C8
Heberle	Forschungszentrum Jülich	Functional mid- and far-infrared spectroscopy on monolayers of biological membranes		
Heinemann / Felber	Max-Delbrück-Centrum für Molekulare Medizin, FG Kristallographie	IF2 in complex with initiator tRNA	MDC	
Heinemann / Halavaty	Max-Delbrück-Centrum für Molekulare Medizin, FG Kristallographie	Studies of the electron transfer between components of the vertebrate mitochondrial hydroxylase system	MDC	
Heinemann / Khare	Max-Delbrück-Centrum für Molekulare Medizin, FG Kristallographie	Crystal structure analysis of a transcriptional repressor, KorB, in complex with operator DNA and with its interacting partner IncC	MDC	
Heinemann / Kolbe	Max-Delbrück-Centrum für Molekulare Medizin, FG Kristallographie	Structural studies on tight junction proteins	MDC	
Heinemann / Kolbe	Max-Delbrück-Centrum für Molekulare Medizin, FG Kristallographie	Structural studies of the TTSS	MDC	
Heinemann / Kolbe, Kumar	Max-Delbrück-Centrum für Molekulare Medizin, FG Kristallographie	Structure determination of SycD and SycD/YopB complex from <i>Yersinia enterocolitica</i>	MDC	
Heinemann / Kolbe, Max, Klaas	Max-Delbrück-Centrum für Molekulare Medizin, FG Kristallographie	Structure determination of full-length Coenzyme A Synthase	MDC	
Heinemann / Max, Klaas, Wanker	Max-Delbrück-Centrum für Molekulare Medizin, FG Kristallographie	Structure determination of full-length human p97	MDC	
Heinemann / Müller	Max-Delbrück-Centrum für Molekulare Medizin, FG Kristallographie	Tail Spike protein HK620 from Bacteriophage E. Coli	MDC	
Heinemann / Roske	Max-Delbrück-Centrum für Molekulare Medizin, FG Kristallographie	The second carbohydrate binding module of family 27 of Caldicellulosiruptor strain Rt8B.4	MDC	

Heinzmann	Universität Bielefeld Fakultät für Physik	Spinpolarisationstransfer an Photo- und Auger-Elektronen aus freien Atomen	DFG	He 1049/7-2
Heister	MBI	Electron dynamics studies of PTCDA layers on Si(001)		
Held	University of Cambridge Dept. Of Chemistry	Probing chiral surfaces using circularly polarised light - the adsorption of chiral organic molecules	EU	HPR-1999-0028
Herein	Institut für Angeandte Chemie	XAS investigations on vanadium based catalysts	BMBF	
Hergenhahn	MPI für Plasmaphysik, München	Photoionization of a free cluster beam		
Heske	Universität Würzburg Physikalisches Institut Lehrstuhl f. Exp. Physik II	NEXAFS investigations of organic materials for field effect transistors	BMBF DFG	05KS1WW1/5 Um6/8-1
Heske / Umbach	Universität Würzburg Physikalisches Institut Lehrstuhl f. Exp. Physik II	Charakterisierung der elektronischen Struktur von II-VI und organischen Halbleitern mit resonanter inelastischer Röntgenstreuung	BMBF DFG	
Heske / Umbach	Universität Würzburg Physikalisches Institut Lehrstuhl f. Exp. Physik II	Elektronische und chemische Eigenschaften von Halbleiter- Nanopartikeln	DFG	
Hess	RWTH Aachen II. Physikalisches Institut	Temperature dependence of the hole distribution in $Sr_{14}Cu_{24}O_{41}$		
Hingerl	Universität Linz Institut für Halbleiterphysik	Spannungsinduzierte optische Anisotropien von Gruppe-III- Nitriden im VUV Ellipsometer		
Hinrichs	ISAS	IR-Ellipsometrie für die Untersuchung der Struktur und der optischen Eigenschaften anisotropischer Proben und Schichten	BMBF	05 SR8KK19
Hirschmugl	University of Wi Milwaukee Dept. Of Physics	Infrared imaging of microalgae		
Hirschmugl	University of Wi Milwaukee Dept. Of Physics	Infrared ellipsometric measurements of V_2O_3 /water interface		
Hofmann	Institut f. Med. Physik und Biophysik	Infrarotspektroskopische Untersuchungen am Rhodopsin Mechanismus des Zonentransportes in Ionophorantibiotika	DFG	
Horn, K.	Fritz-Haber-Institut der Max-Planck-Gesellschaft	Low-dimentional metal structures: magnetism and quantum size effects		

Horn, S.	Universität Augsburg	Kooperative Phänomene im Festkörper: Metall-Isolator-Übergänge und Ordnung mikroskopischer Freiheitsgrade	DFG	SFB 484
Hübers	DLR	Characterization of superconducting photon counters		
Hübers	DLR	THz spectroscopy of impurity centers in semiconductors		
Hunger	TU Darmstadt Surface Science Division	Band mapping of CuInSe ₂ and CuGaSe ₂		
Ionov	Inst. of Solid State Physics RAS Chernogolovka	Investigation of electronic structure of 2D ordered array of epitaxial nanodots and metalattice conductors		
Jaegermann	Technische Universität Darmstadt FB Materialwissenschaften Fachgebiet Oberflächenforschung	Electronic structure of ion conducting materials	DFG	SFB595
Jaegermann	Technische Universität Darmstadt FB Materialwissenschaften Fachgebiet Oberflächenforschung	Potential inhomogenities at semiconductor and - interfaces	BMBF	0329857
Jaegermann	Technische Universität Darmstadt FB Materialwissenschaften Fachgebiet Oberflächenforschung	Characterisation of solid/electrolyte interfaces: Modification of CuInSe ₂ surfaces and interfaces by chemical-bath deposited II-VI compounds		
Jaegermann	Technische Universität Darmstadt FB Materialwissenschaften Fachgebiet Oberflächenforschung	Characterisation of solid/electrolyte interfaces: elementary processes in contact formation and interface engineering	BMBF	
Jaskolski / Bujacz (Lodz Univ. of Technology)	Inst. Bioorg. Chem., Pol. Acad. Sci.	Plant hormone binding proteins	EU	
Jaskolski / Kochman (Wroclaw Univ. Techn.)	Inst. Bioorg. Chem., Pol. Acad. Sci.	Insect hormone binding proteins	EU	
Jenichen	Paul-Drude-Institut	Phase transitions in epitaxial MnAs layers on GaAs		
Kanngießer	Technische Universität Berlin	Depth sensitive micro-X-ray fluorescence analysis	DFG	

Kanngießer / Hahn	Technische Universität Berlin Institut für Atomare und Analytische Physik, BAM	Untersuchung von Migrations- und Oxidationsprozessen anorganischer Verbindungen in Tintenfraß-geschädigten Manuskripten		
Kanunnikova	Phys-Technical Institute, Ural Branch RAS, Izhevsk	Composition and structure of spin-on-glass thin silica films		
Kern	Max-Planck-Institut für Festkörperforschung	Magnetism of novel two-dimensional molecule-based magnetic systems		
Kisker	Heinrich-Heine-Universität Düsseldorf Institut für Angewandte Physik	Interface reactions in FM-AF-layered materials studied by micro-spectroscopy using magnetic dichroism	BMBF	05 KS1PFA/3
Kisker	Heinrich-Heine-Universität Düsseldorf Institut für Angewandte Physik	Magnetic domain structure and interface coupling in ferromagnetic and antiferromagnetic metal/oxide heterostructures	BMBF	05 KSPFB/1
Klein	TU Darmstadt FB 11	Defektbildung an Cu, (In,Ga) Se ₂ surfaces and interfaces	BMBF	01SF0114
Klein	TU Darmstadt FB 11	Interfaces of polycrystalline conducting oxides	BMBF	SFB 595-D3
Klein/Jaegermann	TU Darmstadt	Elektronische Eigenschaften von quasi-van der Waals-Epitaxie Grenzflächen	BMBF	
Kleineberg	Uni Bielefeld Bereich Physik	In-vitro Transmissions-Photoemission-Elektronenemissionsmikroskopie im Wasserfenster am U125/1-ML bei BESSY II	BMBF	05 KS1PBA-8
Knop-Gericke / Häveker / Schlögl	Fritz-Haber-Institut der Max-Planck-Gesellschaft	Investigation of the catalytic oxidation of n-butane over vanadium-phosphorous-oxide using in situ X-ray photoelectron spectroscopy		
Knop-Gericke / Schlögl	Fritz-Haber-Institut der Max-Planck-Gesellschaft	X-ray photoelectron spectroscopy of catalytic relevant systems under reaction conditions		
Knop-Gericke / Schlögl	Fritz-Haber-Institut der Max-Planck-Gesellschaft	In Situ high pressure NEXAFS study of ammonia oxidation on Pt(533)		
Knop-Gericke / Schlögl	Fritz-Haber-Institut der Max-Planck-Gesellschaft	Combined application of in situ X-ray absorption near edge structure (XANES) spectroscopy and mass-spectrometry to study ethylene epoxidation over silver		
Knop-Gericke / Teschner / Schlögl	Fritz-Haber-Institut der Max-Planck-Gesellschaft	Vom Einkristallsystem zu realen Katalysatoren am Beispiel der Hydrierung an Silberkatalysatoren	DFG	SP 1091

Koch-Müller	Geoforschung (Zentrum Potsdam) Projektbereich 4.1	Location and quantification of OH in nominally anhydrous minerals	BMBF	05KS1KK1/4
Kuch	Max-Planck-Institut für Mikrostrukturphysik	Elementspezifische Abbildung magnetischer Domänen in gekoppelten magnetischen Dünnschichtsystemen	BMBF	05 KSIEFA6
Kuch	Max-Planck-Institut für Mikrostrukturphysik	Depth-resolved study of magnetic properties of fcc-Fe layers	MPG	
Kuch	Max-Planck-Institut für Mikrostrukturphysik	Time and layer resolved magnetic imaging of spin-valve structures using PEEM	EU	HPRI-1999-0028
Lamont	University of Huddersfield Department of Chemical and Biological Sciences Centre for Applied Catalysis	Application of photoelectron diffraction and circular dichroism photoelectron spectroscopy to the study of enantioselective heterogeneous catalysis	EU	
Lasch	Robert-Koch-Institut Berlin Biophysical structure analysis	Infrared microspectroscopy of tissue sections		
Laubschat	Technische Universität Dresden Inst. f. Oberflächen- und Mikrostrukturphysik	High-resolution angle-resolved resonant photoemission study of CePd ₃ and CeSi ₂	BMBF/ DFG	05 KS10DA/2 SFB 463 TPA1 u. B4
Leach	Observatoire de Paris-Meudon Laboratoire d'Etude du rayonnement et de la matière en astrophysique	Photophysics of exobiological molecules		
Lendl	TU Wien	Time-resolved FTIR Spectroscopy of Biochemical Reactions in Solutions		
Lewerenz	HMI	Anodic oxidation of silicon: a photoelectron spectroscopy investigation		
Lewerenz	HMI	Initial phases of alkaline etching of silicon		
Ley / Seyller	Uni Erlangen	Photoelektronenspektroskopie an SiC		
Ley / Seyller	Uni Erlangen	Determination of the Fermi surface of Cu ₃ Au and the surface bands of ZnO		
Ley / Seyller	Uni Erlangen	Elektronische und strukturelle Eigenschaften der Grenzflächen zwischen SiC und ALD-Dielektrika		
Ley / Seyller	Uni Erlangen	Interactions of Mn overlayers with GaAs surfaces		

Locht	Université de Liège Dtp. de Chimie	High Resolution Photoabsorption spectroscopy and photoionization of CH ₃ X and C ₂ H ₃ X (X=F, Cl, Br, and I)	EU/HPP	HPP21/221001
Locht	Université de Liège Dtp. de Chimie	High resolution photoabsorption spectroscopy and photoionization of C ₂ H ₂ X (X=F, and/or Cl) and isomers)	EU	
Luecke	University of California, Depts of Biochemistry, Biophysics and Computer Science	Crystal structure determination of various eubacterial proteorhodopsins		
Luecke / Spudich (Univ. Texas, Med. School)	University of California, Depts of Biochemistry, Biophysics and Computer Science	Crystal structure determination of Anabaena sp. sensory rhodopsin (ASR)		
Luecke / Spudich (Univ. Texas, Med. School)	University of California, Depts of Biochemistry, Biophysics and Computer Science	Crystal structure determination of Anabaena sp. sensory rhodopsin associated transducer (ASRT)		
Luecke / Spudich (Univ. Texas, Med. School)	University of California, Depts of Biochemistry, Biophysics and Computer Science	Crystal structure improvement of Sensory Rhodopsin II of Natronobacterium pharaonis (NpSRII)		
Lux-Steiner	Hahn-Meitner-Institut Berlin GmbH	Röntgenemissions- und Photoelektronen-Spektroskopie an Dünnschichtsolarzellen auf Basis von Cu(in,Ga)(S,Se) ₂	BMBF BMWf	01 SF0007 03 N8605/8
Makhov / Kirm	Lebedev Physical Institute RAS, Moscow / University of Hamburg	High-resolution, low-temperature photoelectron spectroscopy of insulating crystals		
Maletta	Hahn-Meitner-Institut Berlin GmbH	Spin structure at exchange-coupled CoO/ferromagnet interfaces		
Maletta	Hahn-Meitner-Institut Berlin GmbH	Magnetism of nanoparticles synthesized by colloidal chemistry methods		
Maletta	Hahn-Meitner-Institut Berlin GmbH	Exploration of the (M)EXAFS method at the UE46-PGM		
Maletta	Hahn-Meitner-Institut Berlin GmbH	Installation and test of the high-field reflectometer		
Maletta	Hahn-Meitner-Institut Berlin GmbH	Element-specific, in-situ investigation of the magnetization at the interface of Fe on V(110)		
Maletta	Hahn-Meitner-Institut Berlin GmbH	Magnetism of nanoparticles prepared by magnetophoretic deposition		
Manzke	Humboldt Universität zu Berlin Institut für Physik / EES	Photoelektronenspektroskopie höchster Auflösung an kondensierter Materie mit Synchrotronstrahlung	BMBF	05 K51KH1/1

Martin	ALS, Berkeley	THz-Pump FIR-Probe Experiments on the superconductor MgB2		
Martins	Universität Hamburg II. Institut für Experimentalphysik	Correlations in free atoms and molecules		
Menzel	TU München	Photon induced dynamics by inner shell excitations	MP	
Mertins	Potsdam/BESSY	Magneto-optische Polarisationspektroskopie mit Synchrotronstrahlung an magnetischen Schichtsystemen	BMBF	05 KS1IPB/8
Meyer	Laboratoire Louis Neel - CNRS BP 165	Magnetic scattering on Tb nanoparticles	EU	HPRI-1999-0028+E191
Mikhlin / Szargan	Institute of Chemistry and Chemical Technology SB RAS, Wilhelm-Ostwald-Institut für Physikalische und Theoretische Chemie, Universität Leipzig	SR-XPS and X-ray absorption studies of chemically modified surface and subsurface layers of metal sulphides		
Mittsev	Ioffe Institute, Russian Academy of Sciences	Growth mechanism and electronic/geometric structure of Eu-Si(100) interface at various stages of its formation		
Molodtsov	TU Dresden Inst. f. Oberflächen- und Mikrostrukturphysik	Magnetic oscillations in photoemission spectroscopy of Cr/Fe(100) and Cr/W(100)	DFG	SFB 463TPB16
Molodtsov	TU Dresden Inst. f. Oberflächen- und Mikrostrukturphysik	Electron correlation effects in Yb and Eu compounds	DFG	463 TPB14 und B16
Müller	FU Berlin Proteinstrukturfabrik c/o BESSY	3D-structure determination of proteins from KeV, German structural genomics initiative - Protein Structure Factory		
Murin	Department of Chemistry, St. Petersburg State University	X-ray absorption and photoemission study of electronic structure for magnetic oxide nanostructures of a given topology		RFBR N 02-03-32748
Naumann	Robert-Koch-Institut Berlin Projekt 13	Infrared microspectroscopy of CNS tissue from scrapie-infected Syrian hamsters		
Nazin	Kurchatov Institute, Moscow	UPS study of partly oxidated zirconium surface		
Netzer	Universität Graz Experimentalphysik IV	Wechselwirkung von Aminosäuren und Wasser auf Oxidoberflächen: hochaufgelöste NEXAFS und XPS Spektroskopie	EU/HPP	

Neumann	Universität Osnabrück Fachbereich Physik	Study of A-side doped Lanthanum manganites by resonant inelastic X-ray scattering techniques	BMBF	05 SR8 OL1-2
Nordlund	Stockholm University, Department of Biochemistry and Biophysics	Structural studies of the human mitochondrial deoxyribonucleotidase dNT-2	EU	
Nordlund	Stockholm University, Department of Biochemistry and Biophysics	Allosteric regulation and reaction mechanism in class II ribonucleotide reductase	EU	
Nordlund	Stockholm University, Department of Biochemistry and Biophysics	Structural studies of the human cytosolic deoxyribonucleotidase dNT-1	EU	
Nordlund / Hallberg	Stockholm University, Department of Biochemistry and Biophysics	Structural basis for eukaryotic and prokaryotic RNA-modification: pseudouridine synthases	EU	
Norlund / Divne	Stockholm University, Department of Biochemistry and Biophysics	Studies of the flavoprotein domain of cellbiose dehydrogenase from <i>Sclerotium rolfsii</i>	EU	
Norlund / Divne	Stockholm University, Department of Biochemistry and Biophysics	Studies of the cytochrome domain of cellbiose dehydrogenase from <i>Sclerotium rolfsii</i>	EU	
Norlund / Divne	Stockholm University, Department of Biochemistry and Biophysics	Studies of the flavoprotein domain of cellbiose dehydrogenase from <i>Corynascus</i>	EU	
Norlund / Divne	Stockholm University, Department of Biochemistry and Biophysics	Studies of the cytochrome domain of cellbiose dehydrogenase from <i>Corynascus</i>	EU	
Norlund / Divne	Stockholm University, Department of Biochemistry and Biophysics	Studies on fungal pyranose-oxidizing enzymes	EU	
Norlund / Divne	Stockholm University, Department of Biochemistry and Biophysics	Mechanistic studies on lipase B from <i>Candida antarctica</i>	EU	
Norlund / Hallberg	Stockholm University, Department of Biochemistry and Biophysics	Structural studies on a novel m5c rRNA methylase	EU	
Novikova	Institute of Crystallography, RAS	X-ray standing wave studies of CdS nanoparticle location in Langmuir-Blodgett films		
Okotrub	NIIC RAS, Novosibirsk, Russia	Electronic state of carbons occurred in the carbonaceous chondrite meteorites		

Olsbye	University of Oslo Institute of Chemistry	XPS study of a working Pt, Sn/Mg(Al)O catalyst	Eu	
Oswald	IFW Dresden	Zerstörungsfreie Tiefenprofilanalyse ultradünner Oberflächenschichten	DFG	
Oubrie	University of East Anglia, School of Biological Sciences	Structure determination of ResA, a cytochrome c maturation factor of Bacillus subtilis	EU	
Oubrie	University of East Anglia, School of Biological Sciences	Structural basis of substrate oxidation and specificity in a soluble glucose dehydrogenase	EU	
Ovchinnikov / Starke	Inst. of Physics RAS Krasnoyarsk / FU Berlin	The magnetic structure and magnetic properties of rare-earth ferroborates $Gd_{1-x}Nd_xFe_3(BO_3)_4$, $GdFe_{3-x}Ga_x(BO_3)_4$ and ludwigites $Cu_{2-x}Co_xGaBO_5$, $Cu_{2-x}Fe_{1-y}V_yGa_xBO_5$ single crystals by magnetic X-ray scattering, XMLD and MEXAFS		
Paloura	Aristotle University of Thessaloniki Dept of Physics	X-ray absorption studies on glasses containing industrial wastes	EU	HPP08/301000
Peisert	IFW Dresden	Einfluß von Grenzflächenphänomenen auf die Funktion organischer Feldeffekt- Transistoren	BMBF	01 BI163
Pesin	Pedagogical University Chelyabinsk	A comprehensive study of electron structure of carbynoids using synchrotron radiation		
Pettenkofer	Hahn-Meitner-Institut Berlin GmbH SE 6	Untersuchung der elektronischen Struktur der initiellen Wachstumsphase von hetero- epitaktischen $CuInS_2$ Filmen		
Pettenkofer	Hahn-Meitner-Institut Berlin GmbH SE 6	Laterale Inhomogenitäten in den Grenzflächenpotentialen und elektronische Struktur von epitaktisch gewachsenen $Ag(111)$ Filmen		
Pettenkofer	Hahn-Meitner-Institut Berlin GmbH SE 6	Untersuchung der Struktur der Si- GaSe Grenzfläche als Modellsystem für neuartige Pufferschichten in der Photovoltaik		
Pettenkofer	Hahn-Meitner-Institut Berlin GmbH SE 6	On the nature of hydroxide in polycrystalline ZnO		
Piancastelli	University "Tor Vergata" Dept of Chem. Sciences and Technology	Surface-induced circular dichroism in adsorbates	EU	

Pietsch	Universität Potsdam Institut für Physik	Temperatue and time dependent X-ray scattering on thin organic films	DAAD mit Indien	
Pietsch	Universität Potsdam Institut für Physik	Molecular magnetism in thin metallo-supramolecular films	DFG	Pie217/21-1
Pietsch/Brezesinski	Universität Potsdam Institut für Physik	Structure investigation of organic monolayers on solid support		
Pietsch/Grenzer	Universität Potsdam Institut für Physik	Investigation of lateral modulated InP templates defined by ion implantation		
Pietsch/Grenzer	Universität Potsdam Institut für Physik	Application of coherent X-ray scattering in structural research		
Pietsch/Henneberg	Universität Potsdam Institut für Physik	Energy dispersive reflectometry at polymer surface gratings		
Pietsch/Reiche	Universität Potsdam Institut für Physik	Investigations of phase transitions at memory polymers		
Polcik	Fritz-Haber-Institut der Max-Planck-Gesellschaft	Photoelectron diffraction of adsorbed atoms, molecules and thin films		
Powis	University of Nottingham School of Chemistry	Circular dichroism in the photoionization of free chiral molecules	DFG EU	
Püttner	Freie Universität Berlin Fachbereich Physik	Kanal- und winkelaufgelöste Messungen an den Doppelanregungszuständen in Helium	DFG	Pu 180/2-1
Rader	BESSY	Which Mn is ferromagnetic in $Ga_{1-x}Mn_xAs$?	BMBF	05 KS1IPA/0
Rader	BESSY	Magnetic coupling and RKKY interaction of rare earths on flat Fe(110) and on Fe stripes		
Rader	BESSY	Quantum confinement versus supercell effects		
Rader / Gudat	BESSY	Elektronische Struktur von Spin- Gap-Materialien	BMBF	05 KS1-IPB/8
Rader / Shikin	BESSY	Antiferromagnetic band structure		
Rader / Shikin	BESSY	Nanowires on stepped graphite	DFG	Ra 1041/1-1
Ramsey	Karl-Franzens Universität Graz	Monolayers and thin films of sexiphenyl on clean and oxygen modified A(111) and Cu(110)	EU	HPRI-1999-0028
Reiche	Centre de Recherche et de Restauration des Musées de France, Rathgen- Forschungslabor, SMPK	Spatial resolved ultra trace analysis of medieval silver point drawings by means of XRF	DAAD	
Reinert	Universität des Saarlandes FR 7.2 Experimentalphysik	Spektroskopie und Mikroskopie mit dem NanoESCA	BMBF	13N7847

Rettig	Humboldt-University Berlin	Time-resolved Fluorescence		
Reuter	Philipps-University Marburg	Crystallographic Studies of the Carbonyl Reductase Sniffer, a β - alanine-CoA Ammonia Lyase and a Complex of Carbonic Anhydrase II		
Rieseemeier	Bundesanstalt für Materialforschung und - prüfung (BAM)	Charakterisierung keramischer Grünkörper mit SR-CT; Synchrotron-Refraktions- Topografie; X-ray fluorescence experiments; μ -XRF		DAAD D/0122896
Riley	La Trobe University	Mn overlayers on GaAs		
Roßbach	DESY	Bunch length diagnostics on TTF- 2		
Rotenberg	Lawrence Berkeley Nat. Lab. ALS	Photoemission dichroism of valence bands as a probe of surface-adsorbate interactions		
Rühl	Universität Osnabrück Fachbereich Physik	Projektverbund zum Aufbau und Test eines Messstandes zur Untersuchung gespeicherter Nanopartikel mit Synchrotronstrahlung	BMBF	05 KSIMPA/8, 05 KSIOCI/2, 05 KSIBMA/0
Rühl	Universität Osnabrück Fachbereich Physik	Experimentelle und theoretische Untersuchungen zur hochaufgelösten Anregung der Rumpfniveaus von Molekülen, Clustern und Adsorbaten	DFG	RU 420/5-1
Rühl	Universität Osnabrück Fachbereich Physik	Innerschalenanregung von S ₂ O	DFG	
Saenger	Frei Universität Berlin, Institut für Kristallographie	MTH177		
Saenger / Alonso (CNB, Madrid)	Frei Universität Berlin, Institut für Kristallographie	Omega-DNA-complex		
Saenger / Athina (Max- Vollmer-Inst.)	Frei Universität Berlin, Institut für Kristallographie	Crystallographic studies of Photosystem II and single subunits		
Saenger / Chames (Collectis, Paris)	Frei Universität Berlin, Institut für Kristallographie	HLA-A1:MAGE:Fab complex		
Saenger / Lanka (MPI für Mol. Gen.)	Frei Universität Berlin, Institut für Kristallographie	Structure studies on the inhibition of the hexameric DNA helicase RepA		
Saenger / Sandhoff	Frei Universität Berlin, Institut für Kristallographie	Structure and Mechanism of human beta-Hexosaminidase B		
Saenger / Sandhoff (Kekulé-Inst. für Org. Ch.)	Frei Universität Berlin, Institut für Kristallographie	Human SA-proteins and their role in membrane lipid metabolism		

Saenger / Uchanska-Ziegler (Charité)	Frei Universität Berlin, Institut für Kristallographie	Peptide Presentation by Differentially Disease-Associated HLA-B27 Subtypes		
Salditt	Universität Göttingen Institut für Röntgenphysik	Energy dispersive waveguide experiments and waveguide monochromators	BMBF	05 KS1TSA/7
Schade	BESSY	IR-Ellipsometrie an planetaren Analogmaterialien	BMBF	
Schäfers	BESSY	Development of multilayer optical elements		
Schartner	Justus-Liebig-Universität I. Physikalisches Institut	Radiative Zerfälle doppelt angeregter Zustände der He- und Ne-Valenzschalen	DFG	Scha 235/17-1
Schartner / Schmoranzer	Justus-Liebig-Universität I. Physikalisches Institut	Orientierung O ₁₀ und Alignment A ₂₀ von Kr+ 4p ⁴ 5p-Zustände bei Interferenz resonanter Raman-Auger-3d ⁹ 5p-Prozesse nach Anregung mit zirkular polarisierter Synchrotronstrahlung	DFG	
Schartner / Schmoranzer	Justus-Liebig-Universität I. Physikalisches Institut	Messung von Verzweigungsverhältnissen beim radiativen Zerfall doppelt angeregter He-Atome	DFG	
Schedel-Niedrig	Hahn-Meitner Institut	In situ monitoring of the interfacial Gas/Solid-reaction of H ₂ O and CuGaSe ₂ -thin film solar cell absorber by means of X-ray absorption spectroscopy		
Scheidig	Saarland University	Investigation of protein dynamics in crystals using fluorescence spectroscopy	BMBF	05 KS1EDA / 3
Schilling	Uni Kaiserslautern	Hilbert transform spectroscopy using THz CSR		
Schmahl / Guttman	Georg-August-Universität Göttingen Institut für Röntgenphysik	Weiterentwicklung des röntgenmikroskopischen Messplatzes am Undulator U41 am BESSY II und röntgenmikroskopische Experimente	BMBF	05 KS1MG1/9
Schmeißer	Brandenburgische Technische Universität Cottbus Angewandte Physik - Sensorik	Photoelektronen-spektroskopische Untersuchungen an oxidischen Praseodym/Silizium Verbindungen	DFG	Schm 745/9-1
Schmeißer	Brandenburgische Technische Universität Cottbus Angewandte Physik - Sensorik	Photoelektronen-spektroskopische Untersuchungen an verborgenen SiC-Grenzflächen		
Schmeißer	Brandenburgische Technische Universität Cottbus Angewandte Physik - Sensorik	ZnS-CuInS ₂ Legierungen	DFG	Gep-Schm 745/3

Schmidt-Böcking	Universität Frankfurt/M Institut für Kernphysik	Elektronenkorrelation in doppelt hoch angeregten Heliumszuständen nahe der Kontinuumsgrenze untersucht mit Elektron-Ion-Photon-Koinzidenz		
Schneider	FZ Jülich	Soft X-ray magnetooptics with full polarization analysis	BMBF	05 KS1BD1/0
Schneider	FZ Jülich	Magnetic domain structures and interdot coupling in submicron dot arrays	BMBF	05 KS1BDA/9
Schneider	FZ Jülich	Magneto-optical anisotropy at the 3d transition metal M edges	BMBF	05 KS1BD1/0
Schneider	FZ Jülich	Spin-resolved band mapping of ultrathin magnetic films along low symmetry directions	BMBF	05 KS1BD1/0
Schneider	FZ Jülich	Element-selective magnetization reversal in GMR Systems	BMBF	
Schneider	FZ Jülich	Spin-resolved electronic study of the full-Heussler alloy Co ₂ CrAl	BMBF	
Schneider	FZ Jülich	XMOKE microscopy in reflection	BMBF	
Schneider	FZ Jülich	Domain formation in coupled magnetic micro- and nanostructures	BMBF	
Schoenes	TU Braunschweig Institut für Halbleiterphysik und Optik	VUV-Ellipsometrie an - YH _x (2.3<x<3)		
Schoenes	TU Braunschweig Institut für Halbleiterphysik und Optik	VUV-Ellipsometrie an Seltenen-Erd-Hydriden		
Schoenes	TU Braunschweig Institut für Halbleiterphysik und Optik	Spin- und winkelaufgelöste Photoemissions-spektroskopie an epitaktischen T/Pt Schichtsystemen (T=Cr, Mn)		
Schomburg	Universität Köln, Institut für Biochemie	LAO MAD		
Schomburg	Universität Köln, Institut für Biochemie	HNE		
Schomburg	Universität Köln, Institut für Biochemie	Crystal Structure of Human Protein Kinase CK2 Catalytic Subunit		
Schönhense	Johannes-Gutenberg-Universität Mainz Institut für Physik	Picosekunden PEEM. Photoemissionsmikroskop für die zeitaufgelöste Beobachtung dynamischer Prozesse	BMBF	
Schönhense	Johannes-Gutenberg-Universität Mainz Institut für Physik	Magnetic circular dichroism of Heusler alloys	BMBF	05 KS1UM1/5

Schönhense	Johannes-Gutenberg-Universität Mainz Institut für Physik	Mikroskop mit Flugzeitspektrometer und Bunch Selektor (Picosekunden PEEM)	BMBF	05 KS1UM1/5
Schroeder	Molecular Materials Centre, UMIST	Closing the pressure and material gap between model and practical catalysis: High-pressure XPS and XAS of Au/TiO _x catalysts		
Schumacher	Hahn-Meitner Institut	Lattice misfit in single crystal nickel base superalloy SC16 of the early stages of rafting	DFG	Ne 645/5-4, Schu 1253/3-4
Schüßler-Langeheine	Universität Köln II. Physikalisches Institut	Resonant soft X-ray scattering from transition-metal compounds	DFG	SFB 608TPC4
Schüßler-Langeheine	Universität Köln II. Physikalisches Institut	Energy analysis for resonant soft X-ray scattering	BMBF DFG	
Schwarz	Biozentrum der TU Berlin, Institut für Pflanzenbiologie	Structural Analysis of Cnx1 G Domain in Complex with Molybdopterin		
Schwarz	Biozentrum der TU Berlin, Institut für Pflanzenbiologie	Crystal Structure of the Molybdenum Cofactor Carrier Rotein from Chlamydomonas Reinhardtii		
Schwarz / Fischer	Biozentrum der TU Berlin, Institut für Pflanzenbiologie	Structural Analysis of Arabidopsis Molybdopterin Synthase (Cnx6/7)		
Schwarz / Schrader	Biozentrum der TU Berlin, Institut für Pflanzenbiologie	Structural Analysis of human Gephyrin E Domain		
Schwarz / Schrader	Biozentrum der TU Berlin, Institut für Pflanzenbiologie	Structural Analysis of Holo-Gephyrin		
Schwentner	Freie Universität Berlin Institut für Experimentalphysik	Lichtinduziertes Trockenätzen		
Seckler	Universität Potsdam Physikalische Biochemie	Untersuchungen von Proteinen mittels Synchrotron Circular Dichroismus Spektroskopie (SRCD)	BMBF	05 KS1IP1/1
Sepiol	Universität Wien Institut für Materialphysik	Near surface clusters of gold in ultrathin iron films on Au(001)		
Sepiol	Universität Wien Institut für Materialphysik	Interface motion on nanoscale		
Shabanova	Physical-Technical Institute, Ural Branch of RAS	The study of the electronic structure and magnetic properties of Invar alloys based on transition metals	BMBF	
Shabanova	Institute of Surface Physics RAS, Izhevsk	The study of the electronic structure of compound copper oxides		

Sheldrick	Universität Göttingen, Lehrstuhl für Strukturchemie	Sulfatases and Sulfonatases		
Sheldrick	Universität Göttingen, Lehrstuhl für Strukturchemie	Proteins in sulfur metabolism		
Sheldrick	Universität Göttingen, Lehrstuhl für Strukturchemie	Crystal structure of Wind - a PDI related protein		
Sheldrick	Universität Göttingen, Lehrstuhl für Strukturchemie	Structure of complexes between Echinomycin and DNAs.		
Sheldrick	Universität Göttingen, Lehrstuhl für Strukturchemie	Structure of polyalanyl PNAs and chemical derivates.		
Sheldrick	Universität Göttingen, Lehrstuhl für Strukturchemie	Structures of d,l-alternating peptides		
Soriano	Universidad Autónoma de Madrid	Study of the electronic structure of small particles and ultra-thin-films of metal oxides, nitrides and carbides: The NiO/HOPG system	EU	
Spiegel	MPI für Eisenforschung	In situ measurement on ultrathin oxide scales		
Stamm	Institut für Polymerforschung	Fabrication of polymeric nanotemplates	BMBF	05 RS1BPA/4
Starke	Freie Universität Berlin Institut für Exp.-Physik	Looking quantitatively at magnetization reversal	BMBF	
Starke	Freie Universität Berlin Institut für Exp.-Physik	Spin structure of Gd- and Eu- oxide/metal interfaces	BMBF	05 KS1 KEC/2
Starke	Freie Universität Berlin Institut für Exp.-Physik	Ferrimagnetic spin order in O/Gd surface monoxide	BMBF	
Steinrück	Universität Erlangen- Nürnberg Institut für Physikal. und Theoret. Chemie Physikalische Chemie II	Höchstaufgelöste Photoelektronenspektroskopie mit Synchrotronstrahlung zur in-situ Untersuchung von Oberflächenreaktionen	DFG	STE 620/4-2
Stöhr	SSRL, Stanford USA	Critical fluctuations in thin magnetic films and polymers observed by resonant soft X-ray scattering		
Stubbs	Martin-Luther-Universität, Institut für Biotechnologie	Tungsten binding protein TupA		
Stubbs	Martin-Luther-Universität, Institut für Biotechnologie	D-Ala adenylation domain DltA		
Svensson	Uppsala University Dept. Of Physics	Investigation of Fano type interference pattern in resonant Raman Auger spectra of the HI/DI molecule in the gasphase	EU	

Szargan	Universität Leipzig Wilhelm-Oswald-Institut f. Physik. U. Theor. Chemie	Valenzbanddiskontinuität und Grenzflächenreaktionen an Heteroübergängen von Dünnschichtmaterial auf CIS- Basis	BMBF DFG	
Szargan	Universität Leipzig Wilhelm-Oswald-Institut f. Physik. U. Theor. Chemie	Reduced dimensionality in transition metal monoxide interfaces studied by resonant photoemission and X-ray fluorescence	BMBF DFG	05 KS10L1/3
Temst	K.U. Leuven Lab. V. Vaste-Stoffysica	The exchange Bias effect in nanostructured films	EU	
Titov	Institute of Metal Physics RAS	X-ray resonance emission spectra of titanium dichalcogenides intercalated by transition metals near the semimetallic state		
Troyanov / Sidorov (Moscow State Univ.)	Humboldt Universität Berlin, Institut für Chemie	Structural Chemistry of Fullerenes and their Derivatives		
Umbach	Universität Würzburg Physikalisches Institut Lehrstuhl f. Exp. Physik II	Höchstauflösende elektronen- Spektro-Mikroskopie mit dem fehler-korrigierten SMART- Spektromikroskop	BMBF	
Umbach	Universität Würzburg Physikalisches Institut Lehrstuhl f. Exp. Physik II	Röntgenabsorptionsspektroskopie an organischen und biologischen Dünnschichten und Grenzflächen	BMBF DFG	
Unger	Bundesanstalt für Materialforschung und - prüfung (BAM)	Untersuchung dünner, im Pulsplasma hergestellter Polymer- und Blockcopolymerfilme mit der Röntgenabsorptionsspektroskopie (NEXAFS)		
Unger	Bundesanstalt für Materialforschung und - prüfung (BAM)	Charakterisierung neuartiger Kohlenstoffsichten mit der Röntgenabsorptionsspektroskopie (NEXAFS) unter Berücksichtigung der Anforderungen industrieller QM Systeme	DFG	M1QN03114600
Vincze	University of Antwerp Department of Chemistry	Measurement of X-ray resonant Raman scattering cross sections for selected materials		
Vincze	University of Antwerp Department of Chemistry	Study of X-ray resonant Raman scattering in the atomic number range of 24-82		
Vinogradov	St. Petersburg State University Institute of Physics	Resonant soft X-ray emission spectroscopy of FeF_2 , $\text{KFe}(\text{CN})_6$, FeF_3 and $\text{K}_3\text{Fe}(\text{CN})_6$		RFBR N01-03- 32285

Wende	Freie Universität Berlin Fachbereich Physik	Electron core-hole interaction in X-ray magnetic circular dichroism for early 3d elements: Ti L _{3,2} -edge XMCD of Fe/Ti/Fe(110) trilayers as a model system	BMBF	
Wende	Freie Universität Berlin Fachbereich Physik	Spin-fluctuations in 2D ultrathin ferromagnets	BMBF	05 KS1 KEB4
Wernet	BESSY	Röntgenabsorptions- und Röntgenemissionsspektroskopie an flüssigem Wasser - der Einfluss räumlicher Einschränkung		
Weschke	Freie Universität Berlin Institut für Experimentalphysik	Magnetic scattering from thin antiferromagnetic and ferromagnetic films	BMBF	05 KS1 KEE/8
Weschke	Freie Universität Berlin Institut für Experimentalphysik	Finite-size cross over in thin epitaxial lanthanide metal films	BMBF	
Weschke	Freie Universität Berlin Institut für Experimentalphysik	Finite size effect in antiferromagnets with long period spin structures	BMBF	
Widdra	Max-Born-Institut für Nichtlineare Optik und Kurzzeitspektroskopie	Pump-Probe Untersuchungen zur Dynamik von Halbleiteradsorbat- und Oberflächenzuständen		
Widdra/Johannson	Max-Born-Institut für Nichtlineare Optik und Kurzzeitspektroskopie	Electron dynamics studies of PTCDA layers on Si(001)		
Wieder	TU Darmstadt Institut für Materialwissenschaft	Resonante inelastische Streuung an amorphem Siliziummonoxid		
Wilke	Universität Potsdam Inst. f. Geowissenschaften	XAFS of Fe in silicate glasses and melts	DFG	Wi 2000/1-2
Winkler	MPI für Mikrostrukturphysik	Two electron photoemission from surfaces		
Winter	Max-Born-Institut für Nichtlineare Optik und Kurzzeitspektroskopie im Forschungsverbund Berlin e.V.	Electronic Structure of Liquid Water and Aqueous Solutions		
Winter	Max-Born-Institut für Nichtlineare Optik und Kurzzeitspektroskopie im Forschungsverbund Berlin e.V.	Electronic structure of organic thin films		
Wittmann	Universität Göttingen, Dep. Of Molecular Structural Biology	Structure of GTPase Rab9, involved in endosomal protein trafficking, complexed with GDP		
Wöll	Ruhr-Universität Bochum, NL 5 Lehrstuhl für Phys. Chemie I	Tiefendifferenzierende Photoelektronenspektroskopie	DFG	Wo 464/17-3

Wöll	Ruhr-Universität Bochum, NL 5 Lehrstuhl für Phys. Chemie I	Mikroskopische Mechanismen der Abscheidung von Palladiumschichten mittels CVD-Verfahren	DFG	Wo464/19-2
Woodruff	University of Warwick Physics Department Surface Science Group	Scanned-energy mode photoelectron diffraction at BESSY II	EU	
Wurth	Universität Hamburg 2. Institut für Experimentalphysik	Magnetic properties of small, size-selected, deposited transition metal clusters	BMBF	KS1-GUB/5
Wurth	Universität Hamburg 2. Institut für Experimentalphysik	Molecular precursors in the initial stages of Si oxidation: Resonant inelastic X-ray scattering and NEXAFS	DFG	
Wurth	Universität Hamburg 2. Institut für Experimentalphysik	Spin polarized charge transfer processes and core-hole clock spectroscopy	DFG	SPP 1093, Wu 207/1-1
Wurth	Universität Hamburg 2. Institut für Experimentalphysik	Resonante Rumpfelektronenspektroskopie als Sonde für ultraschnelle Elektronendynamik an Oberflächen	DFG	
Yashina	Moscow State university	Impurity charge state, surface core level shifts and surface oxidation of (100) PbTe(X) surface (X=Ge,Ga,In)		
Zabel	Ruhr Universität Bochum Inst. für Experimentalphysik	Study of Heusler-based superlattices by soft X-ray resonant magnetic scattering	BMBF	03ZAE7BO
Zabel	Ruhr Universität Bochum Inst. für Experimentalphysik	Investigation of the magnetic properties of the antiferromagnet/ferromagnet exchange interface in CoO/ferromagnet exchange biased bilayers	DFG	SFB491
Zabel	Ruhr Universität Bochum Inst. für Experimentalphysik	Study of FeCr/C ₂ superlattices by soft X-ray resonant magnetic scattering	BMBF	
Zahn	Technische Universität Chemnitz Institut für Physik	Vacuum ultraviolet spectroscopic ellipsometry investigations of DNA bases layers on semiconductor surfaces	BMBF	05 622 ESA 2
Zahn / Braun	Technische Universität Chemnitz Institut für Physik, BESSY	Organisch modifizierte Metall/Halbleiterkontakte	BMBF	05 KS1 OCA/1
Zimina	BESSY	Orientation and electronic structure in polymers for integrated plastic circuits		
Zimina	BESSY	Electronic structure of Si nanocrystals in SiO ₂ matrices		

Zimmermann	Technische Universität Berlin Institut für Atomare und Analytische Physik	Hochauflösende Elektronenspektroskopie an freien Atomen der 3d- Übergangselemente	DFG	Zi 183/16-3
Zimmermann	Technische Universität Berlin Institut für Atomare und Analytische Physik	Dichroismusexperimente mit laserpolarisierten freien Atomen der 3d-Übergangsmetalle	DFG	

LIST OF PUBLICATIONS 2003

L. Aballe, C. Rogero, K. Horn

Quantum-size effects in ultrathin Mg films: electronic structure and collective excitations
Surface Science, **518**, 141, (2002)

M. Abo-Bakr, J. Feikes, K. Holldack, H.-W. Hübers, P. Kuske, W.B. Peatman, U. Schade, G. Wüstefeld

Brilliant, Coherent Far Infrared (THz) Synchrotron Radiation
Phys. Rev. Lett., **90**, 94801, (2003)

K. Adlkofer, A. Shaporenko, M. Zharnikov, M. Grunze, A. Ulman, M. Tanaka

Chemical engineering of gallium arsenide surfaces with 4'-methyl-4-mercaptobiphenyl and 4'-hydroxy-4-mercaptobiphenyl monolayers
J. Phys. Chem. B, **107**, 11737-11741, (2003)

Ch. Ammon, A. Bayer, H.-P. Steinrück, G. Held

Low-temperature partial dissociation of water on Cu(110)
Chemical Physics Letters, **377**, 163-169, (2003)

S. Andreev, A.D. Akhsakhalyan, M.A. Bibishkin, N.I. Chkhalo, S.V. Gaponov, S.A. Gusev, E.B. Klunokov,

K.A. Prokhorov, N.N. Salashchenko, F. Schäfers, S.Yu. Zev

Multilayer optics for XUV spectral region: technology fabrication and applications
Central European Journal of Physics: CEJP, **1**, 191-209, (2003)

D. Attwood, E. Anderson, G. Denbeaux, K. Goldberg, P. Naulleau, and G. Schneider

Soft X-ray microscopy and EUV Lithography: An update on Imaging at 20 - 40 nm Spatial Resolution
8th International Conference on X-Ray Lasers, 461 - 468, (2003)

K. Baberschke

Ferromagnetic Monolayers: A Fresh Look at Fundamentals
Physica Status Solidi (b), **236**, 233, (2003)

B. Beckhoff, R. Fliegau, G. Ulm, J. Weser, G. Pepponi, C. Strel, P. Wobrauschek, T. Ehmman, L. Fabry, C. Mantler, S. Pahlke, B. Kanngießer, W. Malzer

Ultra-trace analysis of light elements and speciation of minute organic contaminants on silicon wafer surfaces by means of TXRF in combination with NEXAFS
Electrochem. So. Proc., **2003-03**, 120-128, (2003)

B. Beckhoff, R. Fliegau, G. Ulm, J. Weser, G. Pepponi, C. Strel, P. Wobrauschek, T. Ehmman, L. Fabry, S. Pahlke, B. Kanngießer, W. Malzer

TXRF Analysis of Low Z Elements and TXRF-NEXAFS Speciation of Organic Contaminants on Silicon Wafer Surfaces Excited by Monochromatized Undulator Radiation
Solid State Phenomena, **92**, 165-170, (2003)

B. Beckhoff, R. Fliegau, J. Weser and G. Ulm

A Novel Instrumentation for Contamination and Deposition Control on 300 mm Silicon Wafers Employing Synchrotron Radiation Based TXRF and EDXRF Analysis
Solid State Phenomena, **92**, 89-92, (2003)

B. Beckhoff, R. Fliegau, G. Ulm

Investigation of high-resolution superconducting tunnel junction detectors for low-energy X-ray fluorescence analysis
Spectrochimica Acta B, **58**, 615-626, (2003)

S. Bengió, H. Ascolani, N. Franco, J. Avila, M.C. Asensio, E. Dudzik, I.T. McGovern, T. Gießel, R. Lindsay, A.M. Bradshaw and D.P. Woodruff

Quantitative determination of the adsorption site of the OH radicals in the H₂O/Si(100) system
Phys. Rev. B, **66**, 195322-1-8, (2002)

- M. Bhattacharya, M. Mukherjee, M.K. Sanyal, T. Geue, J. Grenzer, and U. Pietsch
Energy dispersive x-ray reflectivity technique to study thermal properties of polymer films
 J. App. Phys., **94**, 2882-2887, (2003)
- R.I.R. Blyth, J. Thomson, Y. Zou, R. Fink, E. Umbach, G. Gigli and R. Cingolani
Characterization of Thin Films of the Organic Infra-red Emitters Yb- and Er-tris(8-hydroxyquinoline) by X-ray Photoemission Spectroscopy
 Synth. Metals, **139**, 209, (2003)
- C. Bolm, M. Martin, G. Gescheidt, C. Palivan, D. Neshchadin, H. Bertagnolli, M. Feth, A. Schweiger, G. Mitrikas, J. Harmer
Spectroscopic Investigations of Bis(sulfoximine) Copper (II) Complexes and their Relevance in Asymmetric Catalysis
 J. Am. Chem. Soc., **125**, 6222, (2003)
- S. V. Borisenko, A. A. Kordyuk, T. K. Kim, A. Koitzsch, M. Knupfer, J. Fink, M. S. Golden, M. Eschrig, H. Berger, R. Follath
Anomalous enhancement of the coupling to the magnetic resonance mode in underdoped Pb-Bi2212
 Physical Review Letters, **90**, 207001, (2003)
- W. Braun, B. Jenichen, V. M. Kaganer, A. S. Shtukenberg, L. Däweritz, K. H. Ploog
Island and pit kinetics on the growing GaAs (001) surface studied by synchrotron X-ray diffraction
 Journal of Crystal Growth, **251**, 56-61, (2003)
- W. Braun, B. Jenichen, V. M. Kaganer, A. G. Shtukenberg, L. Däweritz, K. H. Ploog
Layer-by-layer growth of GaAs(001) studied by in situ synchrotron X-ray diffraction
 Surf. Sci., **525**, 126-136, (2003)
- A. Brechling, M. Sundermann, U. Kleineberg and U. Heinzmann
Characterization of DMPC bilayers and multilamellar islands on hydrophobic Self-Assembled Monolayers of ODS/Si (100) and mixed ODS-DDS/Si (100) by nc-AFM and X-ray reflectometry
 Thin Solid Films, **433**, 281, (2003)
- M. Broschwitz
Optische und magnetooptische Eigenschaften von UxLa1-xS Einkristallen und epitaktischen MnPt3 und CrPt3-Filmen ,
 Dissertation
 TU Braunschweig, (2003)
- M. Brunnbauer
Röntgenstabilität und Struktur von Monolagen aliphatischer und araliphatischer Aliphatische Thiole auf Münzmetallen - Eine Synchrotronstudie , Dissertation
 Universität Hamburg, (2003)
- V. I. Bukhtiyarov, M. Hävecker, V. V. Kaichev, A. Knop-Gericke, R. W. Mayer, R. Schlögl
Atomic oxygen species on silver: Photoelectron spectroscopy and X-ray absorption studies
 Phys. Rev. B, **67**, 235422, (2003)
- Y. Burkov
Untersuchungen von Oberflächenprozessen des Mischkristalls CuInS2/ZnS , Diploma
 BTU Cottbus, (2003)
- D. Bürgler, M. Buchmeier, S. Cramm, S. Eisebitt, R. R. Gareev, P. Grünberg, C. Jia, L. Pohlmann, R. Schreiber, M. Siegel, Y. Quin, K. Urban, A. Zimina
Exchange coupling of ferromagnetic films across metallic and semi conducting interlayers
 Journal of Physics - Condensed Matter, **15**, 443, (2003)
- L. I. Chelaru
Microscopic studies of interlayer magnetic coupling across nonmagnetic and antiferromagnetic spacer layers ,
 Dissertation
 Martin-Luther-Universität Halle-Wittenberg, (2003)

- N. A. Cherepkov, S.K. Semenov, M. Drescher, U. Heinzmann
Resonance enhancement of non-dipole effects in spin polarization of atomic photoelectrons
 J. Phys. B: At. Mol. Opt. Phys., **36**, 3063-3078, (2003)
- N. Darowski, I. Zizak, G. Schumacher, S. Klaumünzer, E. Wendler
Surface Crystallinity and Radiation-Amorphization of InP - an X-ray Grazing Incidence Study
 Nucl. Instr. and Meth. B, **209**, 131-135, (2003)
- R. Denecke, B. Tränkenschuh, M. P. Engelhardt and H.-P. Steinrück
Adsorption kinetics of CO on Cr/Ru surfaces
 Surface Science, **532-535**, 173-178, (2003)
- A. Denker, O. Hahn, B. Kanngießer, W. Malzer, S. Merchel, M. Radtke, S. Röhrs, I. Reiche, H. Stege
Chemie der Kunst - Zerstörungsfreie Analyse von Kunst- und Kulturgütern
 MP Materialprüfung / Carl Hanser Verlag München, **45 (11-12)**, 485-503, (2003)
- Y.M. Desta, Y. Jin, J. Goettert, Louisiana State Univ., L. Jian, M. Bednarzik, B. Löchel, H. Scheunemann
Borosilicate Glass Based X-ray Masks for LIGA Microfabrication
 SPIE (2003) Int. Symposium on Micromachining and Microfabrication, 514-522, (2003)
- S.S. Dhesi, H.A. Dürr, M. Münzenberg, W. Felsch
Isolating the interface magneto crystalline anisotropy contributions in magnetic multilayer
 Phys. Rev. Lett., **90**, 117204, (2003)
- V. Dietz, and N. Schwentner
Online measurement of photochemical reaction rates in the VUV with a quartz microbalance: Cl₂ and Cu
 Surf. Sci., **528**, 215-218, (2003)
- E.P. Domashevskaya, V.A. Terekhov, V.M. Kashkarov, S.Yu. Turishchev, S.L. Molodtsov, D.V. Vyalykh,
 D.A. Vinokurov, V.P. Ulin, M.V. Shishkov, I.N. Arsentev, I.S. Tarasov, and Zh.I. Alferov
Synchrotron investigations of electron-energy spectra in A3B5 nanostructures
 Semiconductors, **37**, 992, (2003)
- S.-L. Drechsler, Z. Hu, J. Malek, H. Rosner, R. Neudert, M. Knupfer, M. S. Golden, J. Fink
X-ray absorption spectroscopy of CuO₂ chains
 J. Low Temp. Phys., **131**, 369-373, (2003)
- S. Dreiner, C. Westphal, M. Schürmann, and H. Zacharias
Angle-Scanned X-ray Photoelectron Diffraction of Clean and Hydrogen Terminated 2x1-reconstructed Si(100) Surfaces
 Thin Sol. Films, **428**, 123, (2003)
- M. Drescher, T. Khalil, N. Müller, S. Fritzsche, N.M. Kabachnik, U. Heinzmann
Spin polarization transfer in the resonant Auger decay following Kr 3dⁿ⁻¹ 5p photoexcitation
 J. Phys. B: At. Mol. Opt. Phys., **36**, 3337-3347, (2003)
- A.-C. Dupuis, M. Abu Haija, B. Richter, H. Kühlenbeck, H.-J. Freund
V₂O₃(0001) on Au(111) and W(110): growth, termination and electronic structure
 Surf. Sci., **539**, 99, (2002)
- A. Ehresmann, H. Liebel, M. von Kröger, H. Schmoranzer
Vibrationally resolved band profiles for autoionisation of NO $\left(c^3\Pi\right)n\ell\lambda(\nu_R=0)$ Rydberg states into NO⁺ A¹ $\Pi(\nu_i = 0, 1, 2)$ vibronic levels
 J. El. Spectrosc. Rel. Phen., **130**, 49-56, (2003)
- A. Ehresmann, H. Liebel, H. Schmoranzer, B. Zimmermann, S. Kammer, K.-H. Schartner, Ph.V. Demekhin,
 V.L. Sukhorukov
Double photoionization of N₂ into the N₂²⁺ D¹ Σ_u^+ -state
 J. Phys. B: At. Mol. Opt. Phys., **36**, 3669-3681, (2003)

- A. Ehrmann, J. Rau, A. Wolter, F.M. Kamm, J. Mathuni, F. Scholze, J. Tümmeler, G. Ulm
Mask CD characterization with EUV reflectometry at the electron storage ring BESSY II
 GMM-Fachbericht, **39**, 59-64, (2003)
- A. Eichler
Flugzeitmassenspektroskopie zur Untersuchung von Photoionisation und Photodissoziation ionischer Bindungen, Diploma
 TU Berlin, (2003)
- T. Eimüller, B. Niemann, P. Guttman, G. Schmahl, P. Fischer, G. Schütz
The magnetic transmission X-ray microscopy project at BESSY II
 J. Phys. IV, **104**, 91-94, (2003)
- T. Eimüller, P. Fischer, P. Guttman, G. Denbeaux, M. Scholz, M. Köhler, G. Schmahl, G. Bayreuther, G. Schütz
Multilayered magnetic nanostrips studied by transmission X-ray microscopy
 J. Phys. IV, **104**, 483-486, (2003)
- S. Eisebitt, M. Lörger, W. Eberhardt, J. Lüning, J. Stöhr, C. T. Rettner, O. Hellwig, E. E. Fullerton, G. Denbeaux
Polarization effects in coherent scattering from magnetic specimen: implications for x-ray holography, lensless imaging and correlation spectroscopy
 Phys. Rev. B, **68**, 104419, (2003)
- H. J. Elmers, G. H. Fecher, D. Valdaitsev, S. A. Nepijko, A. Gloskovskii, G. Jakob, G. Schönhense, S. Wurmehl,
 T. Block, C. Felser, P.-C. Hsu and W.-L. Tsai
Element specific magnetic moments from core-absorption magnetic circular dichroism of the doped Heusler alloy
 $Co_{2-x}Cr_xFe_{0.4}Al$
 Phys. Rev. B, **67**, 104412, (2003)
- D. Enslin, R. Hunger, D. Kraft, T. Mayer, W. Jaegermann, M. Rodriguez-Girones, V. Ichizli, H. L. Hartnagel
Pulse plating of Pt on n-GaAs (100) wafer surfaces: Synchrotron induced photoelectron spectroscopy and XPS of wet fabrication processes
 Nuclear Instruments & Methods in Physics Research Section B- Beam Interactions with Materials and Atoms, **200**, 432-438, (2003)
- M. Farle, H. Wende, D. Arvanitis (editors)
Spin-Orbit Interaction and Local Structure in Magnetic Systems with Reduced Dimensions (Proceedings of the 281. Wilhelm and Else Heraeus Seminar)
 J. Phys.: Condens. Matter, **15**, No. 5, (2003)
- K. Fauth, M. Heßler, D. Batchelor and G. Schütz
Strong influence of defects on the electronic structure of Pt adatoms and clusters on graphite
 Surf. Sci, **529**, 397, (2003)
- S.I. Fedoseenko, D. V. Vyalikh, I. E. Iossifov, R. Follath, S. A. Gorovikov, R. Püttner, J.-S. Schmidt, S. L. Molodtsov,
 V. K. Adamchuk, W. Gudat, and G. Kaindl
Commissioning results and performance of the high-resolution Russian-German beamline at BESSY II
 Nucl. Instr. Meth. A, **718**, 505, (2003)
- C. Felser, B. Heitkamp, F. Kronast, D. Schmitz, S. Cramm, H. A. Dürr, H.-J. Elmers, G. H. Fecher, S. Wurmehl,
 T. Block, D Valdaitsev, SA Nepijko, A Gloskovskii, GJakob, G Schönhense, W. Eberhardt
Investigation of a novel material for magnetoelectronics: $Co_2Cr_{0.6}Fe_{0.4}Al$
 J. of Phys.: Condens. Matter, **15**, 7019, (2003)
- M.P. Feth, A. Klein, H. Bertagnolli
Investigation of the ligand exchange behavior of square planar nickel(II) complexes by X-ray absorption spectroscopy and X-ray diffraction
 Eur. J. Inorg. Chem, 839-852, (2003)
- J.-H. Fillion, Dulieu F., Baouche S., Lemaire J.-L., Jochims H.-W., and Leach S.
Ionisation yield and absorption spectra reveal superexcited Rydberg state relaxation processes in H₂O and D₂O
 J. Phys. B.: At.Mol.Opt.Phys, **36**, 2767 - 2776, (2003)

- M. Fonin, Yu. Dedkov, Ch. Kunig, G. Güntherodt, U. Rüdiger, J. Mayer, D. Vyalikh and S.L. Molodtsov
Room Temperature Spin Polarization of Epitaxial Half-Metallic Fe₃O₄(111) and CrO₂(100)
Adv. Solid State Phys, **43**, 487, (2003)
- S. Frey, A. Shaporenko, M. Zharnikov, P. Harder, D. L. Allara
Self-assembled monolayers of nitrile-functionalized alkanethiols on gold and silver substrates
J. Phys. Chem. B, **107**, 7716-7725, (2003)
- J. Fritsche
Grenzflächen und Inhomogenitäten polykristalliner CdTe-Dünnschichtsolarzellen: Charakterisierung und zielgerichtete Modifizierung, Dissertation
Technische Universität Darmstadt, (2003)
- K.Y. Gao, Th. Seyller, L. Ley, F. Ciobanu, G. Pensl, A. Tadich, J.D. Riley, R.G.C. Leckey
Al₂O₃ prepared by atomic layer deposition as gate dielectric on 6H-SiC(0001)
Appl. Phys. Lett., **83**, 1830, (2003)
- F. Gard, Riley J D, Leckey R, Usher BF
A RHEED Study of MBE Growth of ZnSe on GaAs (111) A-(2 x 2)
Surface Review and Letters, **10 (4)**, 669, (2003)
- M. Gensch, K. Hinrichs, A. Röseler, E.H. Korte, and U. Schade
Instrumentation for FT-IR reflection spectroscopy with synchrotron radiation
Anal. Bioanal. Chem., **376**, 626-630, (2003)
- T. Gießel, D. Bröcker, P. Schmidt, W. Widdra
Time-Resolving and Energy-Dispersive Photoelectron Detector for combined Laser and Synchrotron Radiation Experiments
Review of Scientific Instruments, **74**, 11, (2003)
- L. Glaser
Präparation von ultradinnen Metallschichten und Analyse mit Thermodesorptionsspektroskopie, Diploma
Universität Hamburg, (2003)
- S. Gleber, C. Knöchel, J. Thieme, D. Rudolph, G. Schmahl
3-D computer reconstruction of X-ray microscopy objects from stereo images
J. Phys. IV, **104**, 639-642, (2003)
- Th. Gleim, L. Weinhardt, Th. Schmidt, R. Fink, C. Heske, E. Umbach, L. Hansen, G. Landwehr, A. Waag, A. Fleszar, B. Richter, Ch. Ammon, M. Probst, H.-P. Steinrück
Influence of As passivation on the electronic level alignment at BeTe/Si(111) interfaces
Physical Review B, **67**, 205315, (2003)
- Th. Gleim, C. Heske, E. Umbach, C. Schumacher, S. Gundel, W. Faschinger, A. Fleszar, Ch. Ammon, M. Probst, H.-P. Steinrück
Formation of the ZnSe/(Te)GaAs(100) heterojunction
Surface Science, **531**, 77-85, (2003)
- K. Godehusen, T. Richter, P. Zimmermann, M. Martins
Ion charge resolved 3p photoabsorption measurements of atomic Cr
J. Phys. B, **36**, L387, (2003)
- K. Godehusen, H.-C. Mertins, T. Richter, P. Zimmermann, M. Martins
Electron-correlation effects in the angular distribution of photoelectrons from Kr investigated by rotating the polarization axis of undulator radiation
Phys. Rev. A, **68**, 12711, (2003)
- K. Godehusen, Ph. Wernet, T. Richter, P. Zimmermann, M. Martins
Determination of the beta parameter for atomic Mn and Cr 2p photoemission: A benchmark test for core-electron photoionization theories
Phys. Rev. A, **68**, 52707, (2003)

- M. S. Golden, T. Pichler, P. Rudolf
Charge transfer and bonding in endohedral fullerenes from high energy spectroscopy
Springer Series Structure and Bonding (Ed. K. Prassides), in print, (2003)
- M.V. Gomoyunova, I.I. Pronin, N.R. Gall, S.L. Molodsov, and D.V. Vyalikh
*Si 2p photoemission spectra of thin films of CoSi₂ formed on Si(100)2*1*
J. Solid State Physics (Russian), **45**, 180, (2003)
- M.V. Gomoyunova, I.I. Pronin, N.R. Gall, S.L. Molodsov, and D.V. Vyalikh
Disappearance of surface reconstruction of Si after adsorption of Co
J. Technical Physics Letters (Russian), **29**, 115, (2003)
- M.J. Gottfried, K.J. Schmidt, S.L.M. Schroeder & K. Christmann
Oxygen Chemisorption on Au(110)-(1x2). II. Spectroscopic and Reactive Thermal Desorption Measurements
Surf. Sci., **525**, 197-206, (2003)
- J. Grabis, A. Nefedov, H. Zabel
A diffractometer for soft x-ray resonant magnetic scattering
Rev. Sci. Instr., **74(9)**, 4048-4051, (2003)
- P. Guttman, B. Niemann, S. Rehbein, C. Knöchel, D. Rudolph, G. Schmahl
The transmission X-ray microscope at BESSY II
J. Phys. IV, **104**, 85-90, (2003)
- M. Hecker, H.-Ch. Mertins, D. Abramsohn, C.M. Schneider
Soft X-Ray L-MOKE measured from Co/Cu Multilayers at the Co L_{2,3}Edges
J. Appl. Phys., **93**, 6516 - 6518, (2003)
- W.M. Heijboer, A.A. Battiston, A. Knop-Gericke, M. Hävecker, H. Bluhm, B.M. Weckhuysen, D. C. Koningsberger, F. M. F. De Groot
Redox behavior of over-exchanged Fe/ZSM5 zeolites studied with in-situ soft X-ray absorption spectroscopy
Phys. Chem. Chem. Phys., **5**, 4484-4491, (2003)
- S. Heim, S. Rudolph, D. Rudolph, G. Schmahl
Hard real time control software for use in electron beam lithography with an emphasis on patterns with radial symmetry
J. Phys. IV, **104**, 197-201, (2003)
- B. Heitkamp
Charakterisierung magnetischer Materialien mit X-PEEM
Berichte des Forschungszentrums Jülich, **4068**, (2003)
- G. Held, H.-P. Steinrück
Cyclic hydrocarbons
Landolt-Börnstein "Physics of Covered Solid Surfaces - I. Adsorbed Layers on Surfaces", H. P. Bonzel (ed.), **in print**, (2003)
- U. Hergenhahn, A. Rüdell, K. Maier, A.M. Bradshaw, R.F. Fink, A.T. Wen
The Resonant Auger Spectra of Formic Acid, Acetaldehyde, Acetic Acid and Methyl Formate
Chemical Physics, **289**, 57-67, (2003)
- C. Heske, U. Groh, O. Fuchs, E. Umbach, Th. Schedel-Niedrig, Ch.-H. Fischer, M.Ch. Lux-Steiner, S. Zweigart, F. Karg, J.D. Denlinger, B. Rude, C. Andrus, and F. Powell
Monitoring chemical reactions on surfaces in liquids: water on CuIn(S,Se)₂ thin film solar cell absorbers
J. Chem. Phys. (Comm.), **119**, 10467, (2003)
- C. Heske
Studying buried interfaces with soft x-ray spectroscopy
Synchrotron Radiation in Natural Sciences, **2**, 35, (2003)

C. Heske

Untersuchungen zur elektronischen Struktur verborgener Grenzflächen und Schichten in Halbleitern, Habilitation
Universität Würzburg, (2003)

J.T. Hoeft, M.Polcik, D.Sayago, M. Kittel, R. Terborg, R.L. Toomes, J. Robinson, D.P.Woodruff, M.Pascal,
G. Nisbet, C.L.A.Lamont

Local adsorption sites and bondlength changes in Ni(100)/H/CO and Ni(100)/CO
Surface Science, **540**, 441-456, (2003)

P. Hoffmann, D. Schmeißer, G. Roters, Z. Nenyei

Non-Destructive Probing of Interfacial Oxidation and Nitridation Stages at RTP Si-Oxides
Thin Solid Films, **428**, 216-222, (2003)

P. Hoffmann

Untersuchungen zu Inhomogenitäten an der Halbleitergrenzfläche Silizium-Siliziumoxynitrid, Dissertation
TU Cottbus, (2003)

K. Horn, M. Moreno, M. Alonso, M. Hörnicke, R. Hey, J.L. Sacedon, K.H. Ploog

Photoemission from Heterojunctions with intralayers: band offset changes vs. Band bending effects
Vacuum, **67**, 115, (2002)

G. J. Hutchings, J. A. Lopez-Sanchez, J. K. Bartley, J. M. Webster, A. Burrows, C. J. Kiely, A. F. Carley, C. Rhodes,
M. Hävecker, A. Knop-Gericke, R. W. Mayer, R. Schlögl, J. C. Volta, M. Poliakoff

Amorphous Vanadium Phosphate Catalysts Prepared using Precipitation with Supercritical CO₂ as an Antisolvent
J. Catal., **208**, 197-210, (2002)

F. Hübinger, A. S. Shulakov, K. Starke, A. Y. Grigoriev, and G. Kaindl

Surface X-ray Emission from Lanthanide Metals
Surf. Sci. Lett., **526**, L137, (2003)

M. Hävecker, A. Knop-Gericke, R. W. Mayer, M. Fait, H. Bluhm, R. Schlögl

Influence of the geometric structure on the VL3 near edge X-ray absorption fine structure of vanadium phosphorous oxide catalysts

J. Elec. Relat. Phen., **125**, 79-87, (2002)

M. Hävecker, R. W. Mayer, A. Knop-Gericke, H. Bluhm, E. Kleimenov, A. Liskowski, D. Su, R. Follath,

F. G. Requejo, D. F. Olgetree, M. Salmeron, J. A. Lopez-Sanchez, J. K. Bartley, G. J. Hutchings, R. Schlögl

In situ investigations of the nature of the active surface of a vanadyl pyrophosphate catalyst during n-butane oxidation to maleic anhydride

J. Phys. Chem., **107**, 4587-4596, (2003)

B. Illerhaus, N. Hort, C. Potzies, H. Frank, J. Goebbels

Non-destructive Testing of Cast Magnesium Alloys by Computerized Tomography

Proc. of the 6th Int. Conf. Magnesium Alloys and their Applications, Ed. **K.U. Kainer, Wiley-VCH**, 746-751, (2003)

W. Jaegermann, T. Mayer, eds

Adsorption of H₂O on Semiconductors in: Physics of Covered Surfaces

LANDOLT-BÖRNSTEIN, ed. H.P. Bonzel, in print, (2003)

J. Jakubowicz, H. Jungblut and H. J. Lewerenz

Initial Surface Topography Changes During Divalent Dissolution of Silicon Electrodes

Electrochim. Acta, **49**, 137, (2003)

C. Janowitz, R. Müller, L. Dudy, R.-St. Unger, A. Krapf, R. Manzke, C. Ast, H. Höchst

Progress in the understanding of the normal state of the cuprates

Applied Phys. A, **76**, 673, (2003)

Ch. Janowitz

Photoemission an 3-, 2- und 2-delta dimensionalen Festkörpern, Habilitation

HU Berlin, (2003)

- B. Jenichen, V. M. Kaganer, M. Kästner, C. Herrmann, L. Däweritz, K. H. Ploog, N. Darowski, and I. Zizak
Constrained phase coexistence near the Curie Temperature in MnAs(0001)/GaAs(111) epitaxial films
Phys. Rev. B., **68**, 132301, (2003)
- B. Jenichen, V.M. Kaganer, M. Kästner, C. Herrmann, L. Däweritz, K.H. Ploog, N. Darowski, I. Zizak
Structural and magnetic phase transition in MnAs(0001)/GaAs(111) epitaxial films
Physical Review B, **68**, 132301, (2003)
- B. Jenichen, W. Braun, V. M. Kaganer, A. G. Shtukenberg, L. Däweritz, C. Schulz, and K. H. Ploog
Combined molecular beam epitaxy and diffractometer system for in situ x-ray studies of crystal growth
Rev. Sci. Instrum, **74**, 1267-1273, (2003)
- V.M. Kaganer, W. Braun, B. Jenichen, L. Däweritz, and K. H. Ploog
Two-Dimensional Coarsening Kinetics of Reconstruction Domains: GaAs(001)-beta(2x4),
Phys. Rev. Lett., **90**, 16101, (2003)
- T.U. Kampen, D.R.T. Zahn, W. Braun, C. Gonzáles, I. Benito, J. Ortega, L. Jurczyszyn, J.M. Blanco, R. Pérez, F. Flores
Surface Properties of Chalcogen Passivated GaAs(100)
Appl. Surf. Sci., **212-213**, 850, (2003)
- T.U. Kampen, G. Gavrila, H. Méndez, D.R.T. Zahn, A.R. Vearey-Roberts, D.A. Evans, J. Wells, I. McGovern, W. Braun
Electronic Properties of Interfaces between Perylene Derivatives and GaAs(001) Surfaces
J. Phys.: Condens. Matter, Special issue: „Organic-Inorganic Semiconductor Interfaces“, **15**, 2679, (2003)
- T.U. Kampen, S. Park, D.R.T. Zahn
Organic modified Schottky contacts: Barrier height engineering and chemical stability
J. Vac. Sci. Technol. B, **21**, 879, (2003)
- T.U. Kampen
Organic-Inorganic Semiconductor Interfaces: Physical Properties and Application in Schottky Contacts, Habilitation
TU Chemnitz, (2003)
- J-H. Kang, R. L. Toomes, M. Polcik, M. Kittel, J. T. Hoelt, V. Efstathiou, D. P. Woodruff and A. M. Bradshaw
Structural investigation of glycine on Cu(100) and comparison to glycine on Cu(110)
J. Chem. Phys., **118**, 6059-6071, (2003)
- B. Kanngiesser, W. Malzer, M. Müller, N. Schmidt, P. Zimmermann, A.G. Kochur, V.L. Sukhorukov
Cascade decay of atomic magnesium after photoionization with a photoelectron-photoion coincidence method
Phys. Rev. A, **68**, 22704, (2003)
- M. Katsikini, F. Pinakidou, E. C. Paloura, W. Wesch
Identification of implantation - induced defects in GaN: A near edge x-ray absorption fine structure study
Applied Physics Letters, **82**, 1556, (2003)
- M. Katsikini, F. Pinakidou, N. Vouroutzis, R. Mitdank, A. Markwitz, E. C. Paloura
NEXAFS and AFM characterization of Si implanted GaN
Nuclear Instruments and Methods B, **200**, 120, (2003)
- Tarek Khalil
New resonant behavior in the spin resolved photoionization of the rare gas atoms Kr 3d and Xe 4p, Dissertation
Universität Bielefeld, (2003)
- T. K. Kim, A. A. Kordyuk, S. V. Borisenko, A. Koitzsch, M. Knupfer, H. Berger, J. Finkl
Doping Dependence of the Mass Enhancement in (Pb,Bi)₂Sr₂CaCu₂O₈ at the Antinodal Point in the Superconducting and Normal States
Physical Review Letters, **91**, 167002, (2003)
- A. Klein
Electronic Properties of Thin Film Semiconductors, Habilitation
Technische Universität Darmstadt, (2003)

- U. Kleineberg, Th. Westerwalbesloh, W. Hachmann, U. Heinzmann, J. Tümmeler, F. Scholze, G. Ulm, S. Müllender
Effect of substrate roughness on Mo/Si multilayer optics for EUVL produced by UHV-e-beam evaporation and ion polishing
 Thin Solid Films, **433**, 230-236, (2003)
- S. Klumpp
Spektroskopie von Rydbergserien zweifach angeregter Zustände in der Nähe der Kr-4s Ionisationsschwelle, Diploma
 Universität Kaiserslautern, (2003)
- J. Knobloch
The 'Q disease' in superconducting niobium rf cavities
 AIP Conf. Proc., **671**, 133, (2003)
- M. Koch-Müller, P. Dera, Y. Fei, B. Reno, N. Sobolev, E. Hauri, R. Wysoczanski
OH in synthetic and natural coesite
 American Mineralogist, **88**, 1436-1445, (2003)
- A.G. Kochur, V.L. Sukhorukov, V.F. Demekhin, C. Gerth, B. Kanngießler, P. Zimmermann
Cascading Decays of Innershell Vacancies
 AIP Conf. Proc., **652**, 256, (2003)
- A. Koebbel, M. Polcik, D.R. Lloyd, I.T. McGovern, O. Schaff, R. Lindsay, A.J. Patchett, A.M. Bradshaw, D.P. Woodruff
*Local structure of OH adsorbed on the Ge(001)(2*1) surface using scanned-energy mode photoelectron diffraction*
 Surface Science, **540**, 246-254, (2003)
- G. Koller, R.I.R. Blyth, S.A. Sardar, S. Eck, F.P. Netzer, M.G. Ramsey
Growth of ordered bithiophene layers on the p(2x1)O reconstructed Cu(110)
 Surf. Sci., **536**, 155-165, (2003)
- M. Kotsugi, W. Kuch, F. Offi, L. I. Chelaru, J. Kirschner
Microspectroscopic Fermi surface mapping using a photoemission electron microscope
 Rev. Sci. Instrum., **74**, 2754-2758, (2003)
- O. Krupin, J. E. Prieto, S. Gorovikov, K. Starke and G. Kaindl
Ferrimagnetic spin order in O/Gd surface monoxide
 Thin Solid Films, **428**, 98, (2003)
- W. Kuch
Layer-resolved microscopy of magnetic domains in multi-layered systems
 Appl. Phys. A, **76**, 665-671, (2003)
- W. Kuch, L. I. Chelaru, K. Fukumoto, F. Porrati, F. Offi, M. Kotsugi, J. Kirschner
Layer-resolved imaging of magnetic interlayer coupling by domain wall stray fields
 Phys. Rev. B, **67**, 214403, (2003)
- O. Kugeler, S. Marburger and U. Hergenhan
Calculation and Experimental Verification of the Time-of-Flight Spread in a Hemispherical Electron Energy Analyser
 Review of Scientific Instruments, **74**, 3955-3961, (2003)
- O. Kugeler
Aufbau einer Elektronen-Koinzidenz Apparatur für Experimente mit Synchrotronstrahlung, Dissertation
 Technische Universität Berlin, (2003)
- B.M. Lagutin, Ph. V. Demekhin, V.L. Sukhorukov, A. Ehresmann, H. Schmoranzler
Interference Effects in Auger spectra at the 3dⁿnp resonances in Kr
 J. Phys. B: At. Mol. Opt. Phys., **36**, L163-68, (2003)
- B.M. Lagutin, I.D. Petrov, V.L. Sukhorukov, Ph.V. Demekhin, B. Zimmermann, S. Mickat, S. Kammer, K.-H. Schartner,
 A. Ehresmann, Yu.A. Shutov and H. Schmoranzler
The interference effects in the alignment and orientation of KrII 4p45p states following KrI 3d95p resonance excitation
 J. Phys. B: At.Mol.Opt.Phys., **36**, 3252-3268, (2003)

- B.M. Lagutin, I.D. Petrov, V.L. Sukhorukov, A. Ehresmann, Yu.A. Schutov, H. Schmoranzler, B. Zimmermann, S. Mickat, S. Kammer, K.-H. Schartner
Raman regime energy dependence of alignment and orientation of KrII states populated by the resonant Auger effect
Phys. Rev. Lett., **90**, 73001, (2003)
- J.T. Lau, Ehrke, H.-U., Achleitner A., and Wurth, W.
Soft-landing of Size Selected Clusters in Rare Gas Matrices
Low Temp. Phys., **29**, 223, (2003)
- C. Laubschat, S.L. Molodtsov, Yu. Kucherenko, M. Finken, M. Heber, and G. Behr
Configuration Mixing in Pr and Nd Transition-Metal Compounds
J. Electron. Spectrosc. Relat. Phenom, **128**, 45-50, (2003)
- I. Lauer mann, M. Bär, A. Ennaoui, U. Fiedeler, C.-H. Fischer, A. Grimm, I. M. Kötschau, M. C. Lux-Steiner, J. Reichardt, B. R. Sankapal, S. Siebentritt, S. Sokoll, L. Weinhardt, O. Fuchs, C. Heske, C. Jung, W. Gudat, F. Karg, and T. P. Niesen
Analysis of zinc compound buffer layers in Cu(In,Ga)(S,Se)₂ thin film solar cells by synchrotron-based soft X-ray spectroscopy
Mat. Res. Soc. Symp. Proc., **B4.5.1**, 763, (2003)
- S. Leach, Schwell, M., Talbi D., Berthier G., Hottmann K., Jochims H.-W., Baumgärtel H.
He I Photoelectron Spectroscopy of Four Isotopologues of Formic Acid : HCOOH, HCOOD,
Chem.Phys, **286**, 15 - 43, (2003)
- M. V. Lebedev, Th. Mayer, W. Jaegermann
Sulfur adsorption at GaAs(100) from solution: role of the solvent in surface chemistry
Surface Science, **547**, 171–183, (2003)
- R. Leckey
Ultraviolet Photoelectron Spectroscopy of Solids
Surface Analysis Methods in Materials Science, Eds. O'Connor, Sexton, Smart. 2nd Edition, 37-345, (2003)
- W. Leitenberger, Wendrock, H., Bischoff, L., Panzner, T., Pietsch, U., Grenzer, J., Pucher, A.
Double Pinhole Diffraction of White Synchrotron Radiation
Physica B, Condensed Matter, **336**, 63-67, (2003)
- M. Letz, L. Parthier, A. Gottwald, M. Richter
Spatial anisotropy of the exciton level in CaF₂ at 11.1 eV and its relation to the weak optical anisotropy at 157 nm
Phys. Rev. B, **67**, 233101-1, (2003)
- M. Letz, A. Gottwald, M. Richter, M. Brinkmann, G. Wehrhan, L. Parthier
On the optical anisotropy in the cubic crystal of CaF₂: Scaling arguments and their relation to dispersing absorption
Proc. SPIE, **5040**, 662-666, (2003)
- H.J. Lewerenz, M. Aggour, C. Murrell, J. Jakubowicz, M. Kanis, S. A. Campbell, P. A. Cox, P. Hoffmann, H. Jungblut and D. Schmeißer
High Resolution Surface Analysis of Si Roughening in Dilute Ammonium Fluoride Solution
J. Electroanal. Chem., **540**, 3, (2003)
- H.J. Lewerenz, M. Aggour, C. Murrell, M. Kanis, H. Jungblut, J. Jakubowicz, P. A. Cox, S. A. Campbell, P. Hoffmann and D. Schmeißer
Initial Stages of Structure Formation on Silicon Electrodes Investigated by Photoelectron Spectroscopy Using Synchrotron Radiation and in-situ Atomic Force Microscopy
J. Electrochem. Soc., **150**, E185-E189, (2003)
- M.F. López, A. Gutiérrez, F. J. Pérez, M. P. Hierro y F. Pedraza
Soft X-ray absorption spectroscopy study of the effects of Si, Ce and Mo ion implantation on the passive layer of AISI 304 stainless steel
Corrosion Science, **45**, 2043-2053, (2003)

- K. Lüdge, P. Vogt, W. Braun, W. Richter, N. Esser
Cobalt growth on InGaP (001) (2x4): Interface formation
J Vac. Sci. Technol. B, **21**(4), 1749, (2003)
- S. Marburger, O. Kugeler, U. Hergenhan, T. Möller
Experimental Evidence for Interatomic Coulombic Decay in Ne Clusters
Physical Review Letters, **90**, 203401, (2003)
- M. Martins, K. Godehusen, T. Richter, P. Zimmermann
2p photoionization of atomic cobalt and nickel
AIP Conf. Proc., **652**, 153, (2003)
- N. Matsuie, Y. Ouchi, H. Oji, E. Ito, H. Ishii, K. Seki, M. Hasegawa, M. Zharnikov
UV-photoinduced surface anisotropy of polyimide studied by near-edge x-ray absorption fine structure spectroscopy
Jpn. J. Appl. Phys., **42**, L67-L69, (2003)
- R.W. Mayer, M. Melzer, M. Hävecker, A. Knop-Gericke, K. Weiss, J. Urban, H.J. Freund, R. Schlögl
Comparison of polycrystalline copper foil with small deposited copper cluster on their behaviour in the ammonia oxidation: An investigation by means of in situ NEXAFS spectroscopy in the soft X-ray range
Catal. Lett., **86**, 245-250, (2003)
- J.-S. McEwen, S.H. Payne, H.J. Kreuzer, M. Kinne, R. Denecke, H.-P. Steinrück
Adsorption and desorption of CO on Pt(111): a comprehensive analysis
Surface Science, **545**, 47, (2003)
- I. Melnikov, I. Radu, U. Bovensiepen, O. Krupin, K. Starke, E. Matthias and M. Wolf
Coherent Optical Phonons and Parametrically Coupled Magnons Induced by Femtosecond Laser Excitation of the Gd(0001) Surface
Phys. Rev. Lett., **91**, 227403, (2003)
- B. Mertens, B. Wolschrijn, R. Jansen, N. Koster, M. Weiss, M. Wedowski, R. Klein, T. Bock, R. Thornagel
EUV time resolved studies on carbon growth and cleaning
Proc. SPIE, **5037**, 95-102, (2003)
- R. Mikalo
Elektronische Eigenschaften von leitfähigen konjugierten Polymeren und deren Grenzflächenreaktionen im elektronischen Kontakt mit Metallen, Dissertation
TU Cottbus, (2003)
- S.L. Molodtsov, F. Schiller, S. Danzenbäcker, Manuel Richter, J. Avila, C. Laubschat, and M.C. Asensio
Folded Bands in Photoemission Spectra of La-Graphite Intercalation Compounds
Phys. Rev. B, **67**, 115105, (2003)
- S.L. Molodtsov, Yu. Kucherenko, D.V. Vyalikh, G. Behr, A. Starodubov and C. Laubschat
Strong Hybridization of 4f States of Heavy Rare-Earth's in Intermetallic Compounds
Phys. Rev. B, **68**, 193101, (2003)
- M. Moreno, B. Jenichen, V. Kaganer, W. Braun, A. Trampert, L. Däweritz and K. H. Ploog
MnAs nanoclusters embedded in GaAs studied by x-ray diffuse and coherent scattering
Phys. Rev. B., **67**, 235206, (2003)
- B.R. Müller, A. Lange, M. Harwardt, M.P. Hentschel, B. Illerhaus, J. Goebbels, J. Bamberg, F. Heutling
Refraction Computed Tomography Applied to Metal Matrix Composites
35th Int. SAMPE Technical Conference, **CD-ROM ISBN 0-93994-95-6**, (2003)
- R. Müller
Die Physik der CuO₂ Ebene am Beispiel des Modell-Hochtemperatur Supraleiters Bi₂Sr_{2-x}La_xCuO_{6+delta}, Dissertation
HU Berlin, (2003)

B.R. Müller, A. Lange, M. Harwardt, M.P. Hentschel, B. Illerhaus, J. Goebbels
First Refraction Enhanced 3D Computed Tomography - Application to Metal Matrix Composites
Int. Symp. on Computed Tomography and Image Processing for Industrial Radiology, **CD-ROM ISBN 3-931381-48-X**, (2003)

B.R. Müller, A. Lange, M.P. Hentschel
Non-Destructive Characterization of High Performance Composites by use of X-Ray Refraction Topography
SAMPE 2003 ISBN 0-938994-94-8, **CD-ROM**, 1203 - 1211, (2003)

K. Müller, P. Hoffmann, S. Milko, Y. Burkov, D. Schmeißer
Preparation of stoichiometric CuInS₂-surfaces – an XPS, UPS-study
Thin Solid Films, **312**, 431, (2003)

A. Navratil
Kerreffekt von Seltenen Erden, Diploma
TU Braunschweig, (2003)

U. Neuhäusler, G. Schneider, W. Ludwig, M.A. Meyer, E. Zschech, D. Hambach
X-ray microscopy in Zernike phase contrast at 4 keV photon energy with 60 nm resolution
J. Phys. D: Appl. Phys., **36**, A79-A82, (2003)

B. Niemann, P. Guttmann, S. Rehbein
Concept and realization of the novel rotating condenser-monochromator at the Göttingen TXM at BESSY II
J. Phys. IV, **104**, 273-276, (2003)

R. Nünthel, T. Gleitsmann, P. Pouloupoulos, A. Scherz, J. Lindner, E. Kosubek, Ch. Litwinski, Z. Li, H. Wende, K. Baberschke, S. Stolbov and T.S. Rahman
Epitaxial growth of Ni on Cu(001) with the assistance of O-surfactant and its magnetism compared to Ni/Cu(001)
Surf. Sci., **531**, 53, (2003)

F. Offi, W. Kuch, L. I. Chelaru, M. Kotsugi, J. Kirschner
Local exchange bias observed by photoemission microscopy
J. Magn. Mater., **261**, L1-L6, (2003)

F. Offi, W. Kuch, L. I. Chelaru, K. Fukumoto, M. Kotsugi, J. Kirschner
Induced Fe and Mn magnetic moments in Co-FeMn bilayers on Cu(001)
Phys. Rev. B, **67**, 094419, (2003)

P.M. Oppeneer, H.-Ch. Mertins, O. Zaharko
Alternative Geometries for the Determination of X-Ray Magneto-Optical Coefficients
J. Phys. Cond. Matter, **15**, 7803, (2003)

P.M. Oppeneer, H.-Ch. Mertins, D. Abramsohn, A. Gaupp, W. Gudat, J. Kunes, C.M. Schneider
Buried Antiferromagnetic Films Investigated by X-Ray Magneto-Optical Reflection Spectroscopy
Phys. Rev. B, **67**, 52401, (2003)

A.A. Owens, M. Bavdaz, G. Brammertz, V. Gostilo, H. Graafsma, A. Kozerezov, M. Krumrey, I. Lisjutin, A. Peacock, A. Puig, H. Sipila, S. Zatoloka
The X-ray response on TIBr
Nucl. Instr. and Meth. A, **497**, 370-380, (2003)

T. Panzner, Leitenberger, W., Grenzer, J. and Pietsch, U.
Coherence experiments at the energy-dispersive reflectometry beamline at BESSY II
J. Phys. D Appl. Phys., **36**, A93 - A97, (2003)

A. Parge
Magnetische Eigenschaften von GdN-Einfach- und GdN/Fe-Vielfachschichten, Diploma
Universität Göttingen, (2003)

G. Pepponi, B. Beckhoff, T. Ehmann, G. Ulm, C. Strelt, L. Fabry, S. Pahlke and P. Wobrauschek
Analysis of organic contaminants on Si wafers with TXRF-NEXAFS
Spectrochimica Acta Part B: Atomic Spectroscopy, **58**, 2245-2253, (2003)

A. Pietzsch
Electronic Structure and Dynamics: Core Hole Spectroscopy on semiconductor Surfaces, Diploma
Universität Hamburg, (2003)

F. Pinakidou, M. Katsikini, E. C. Paloura
XAFS characterization of buried SixNyOz samples
Nuclear Instruments and methods B, **200**, 66, (2003)

N. Pontius, M. Neeb, W. Eberhardt, G. Lüttgens and P.S. Bechthold
Ultrafast relaxation dynamics of optically excited electrons in Ni3
Phys. Rev. B, **67**, 35425, (2003)

D. Pop
Photoelectron Spectroscopy on Thin Films on Cu-, Zn-, and Metal-Free Extended Porphyrazines, Dissertation
FU Berlin, (2003)

D. Pop, B. Winter, W. Freyer, I. V. Hertel and W. Widdra
Electronic structure of metal-free porphyrazines in thin films
J. Phys. Chem, **107**, 11643, (2003)

I. Powis, E.E. Rennie, U. Hergenbahn, O. Kugeler, R. Bussy-Socrate
Investigation of the Gas-Phase Amino Acid Alanine by Synchrotron Radiation Photoelectron Spectroscopy
Journal of Physical Chemistry A, **107**, 25-34, (2003)

P. K. Pranzas, R. Willumeit, R. Gehrke, J. Thieme, A. Knöchel
Characterization of structure and aggregation processes of aquatic humic substances using small-angle scattering and X-ray microscopy
Anal. Bioanal. Chem., **376**, 618-625, (2003)

J.E. Prieto, F. Heigl, O. Krupin, G. Kaindl, K. Starke
Magneto-optics of Gd and Tb in the soft x-ray resonance regions
Physical Review B, **68**, 134453, (2003)

M. Probst
Photoelektronenspektroskopische Untersuchungen zu reaktiven Übergangsmetalloberflächen auf MoO3- und Si-Substraten, Dissertation
Universität Erlangen-Nürnberg, (2003)

G. Prümper, S. Kröger, R. Müller, M. Martins, J. Viefhaus, P. Zimmermann and U. Becker
Magnetic circular dichroism in the ion yield of polarized chromium atoms at the 2p edge
Phys. Rev. A, **68**, 32710, (2003)

T. Rabe, R. Rudert, J. Goebbels, K-W. Harbich
Nondestructive Evaluation of Green Components
American Ceramic Society Bulletin, **82**, **3**, 28-32, (2003)

K. Rahne
Surface modification and Interface characterisation of chalcopyrite solar cells with a ZnSe buffer layer using X-ray emission and photoelectron spectroscopies, Diploma
Freie Universität Berlin, (2003)

A. Montaigne Ramil
In-situ monitoring and growth of III-nitrides
Universität Linz, (2003)

- S. Rehbein
Nanofabrication of diffractive optics for soft X-ray and atom beam focusing
J. Phys. IV, **104**, 207-210, (2003)
- J. Reichardt
X-Ray emission and photoelectron spectroscopy of chalcopyrite thin film solar cells Humboldt-Universität Berlin,
Diploma
Humboldt-Universität Berlin, (2003)
- I. Reiche, M. Radtke, C. Brouder
Röntgenanalyse in der Kunst Antike Gläser und versteinertes Elfenbein
Physik in unserer Zeit, **34(2)**, 80-86, (2003)
- H.-S. Rhie, H. A. Dürr and W. Eberhardt
Femtosecond Electron and Spin Dynamics in Ni/W(110) Films
Phys. Rev. Lett., **90**, 247201, (2003)
- M. Richter, G. Ulm, C. Gerth, K. Tiedtke, J. Feldhaus, A.A. Sorokin, L.A. Shgmaenok, S.V. Bobashev
Photoionization cross sections of Kr and Xe from threshold up to 1000 eV
AIP Conf. Proc., **652**, 165-171, (2003)
- M. Richter, A. Gottwald, U. Kroth, A.A. Sorokin, s.V. Bobashev, I.A. Shmaenok, J. Feldhaus, Ch. Gerth, B. Steeg,
K. Tiedtke, R. Treusch
Measurement of gigawatt radiation pulses from a vacuum and extreme ultraviolet free-electron laser
Appl. Phys. Lett., **83**, 2970-2972, (2003)
- T. Richter, B. Obst, M. Martins, P. Zimmermann
The decay of the 2p resonances of atomic Scandium studied by photoelectron spectroscopy
J. Phys. B, **36**, 155, (2003)
- M. Richter, J. Hollandt, U. Kroth, W. Paustian, H. Rabus, R. Thornagel and G. Ulm
Source and detector calibration in the UV and VUV at BESSY II
Metrologia, **40**, 107-110, (2003)
- R. Romberg, B. Kassühlke, P. Wiethoff, D. Menzel, P. Feulner
Condensation effects in K-shell excitation and de-excitation of solid neon
Chemical Physics, **289**, 69-79, (2003)
- K. Rotkiewicz, W. Rettig, N. Detzer, A. Rothe
Substituent-Induced Coupling of the Two Lowest Excited Singlet States of 2-Methoxy- Derivatives
Phys. Chem. Chem. Phys., **5**, 998-1002, (2003)
- S. Rudolph, S. Heim, D. Rudolph, G. Schmahl
Fast control unit for electron beam lithography systems especially for X-ray and EUV optics
J. Phys. IV, **104**, 203-205, (2003)
- E. Rühl
Core Level Excitation of Clusters
in: "Progress in Experimental and Theoretical Studies of Clusters", Eds.: T. Kondow, F. Mafune, World Scientific,
Singapore, **Advanced Series in Physical Chemistry, Vol. 13**, 189-237, (2003)
- E. Rühl
Core level excitation, ionization, relaxation, and fragmentation of free clusters
Int. J. Mass Spec., **229**, 117, (2003)
- D. I. Sayago, J. T. Hoefl, M. Polcik, M. Kittel, R. L. Toomes, J. Robinson, D. P. Woodruff, M. Pascal,
C. L. A. Lamont and G. Nisbet
Bond Lengths and Bond Strengths in Weak and Strong Chemisorption: N₂, CO, and CO/H on Nickel Surfaces
Phys. Rev. Lett., **90**, 116104, (2003)

- D.I. Sayago, M.Kittel, J.T.Hoeft, M.Polcik, M.Pascal, C.L.A.Lamont, R.L.Toomes, J.Robinson and D.P.Woodruff
The structure of the Ni(100)c(2x2)-N2 surface: a chemical-state-specific scanned-energy mode photoelectron diffraction determination
Surface Science, **538**, 59-75, (2003)
- J. Schaefer, S.C. Erwin, M. Hansmann, Z. Song, E. Rotenberg, S.D. Kevan, C.S. Hellberg, und K. Horn
Random Registry shifts in Quasi-one-dimensional Adsorbate Systems
Phys. Rev. B, **67**, 85411, (2003)
- A. Scherz, P. Pouloupoulos, R. Nünthel, J. Lindner, H. Wende, F. Wilhelm, and K. Baberschke
Direct probe of interdiffusion effects on the induced V spin-polarization at Fe/V interfaces
Phys. Rev. B, **68**, 140401(R), (2003)
- H.-U. Scheunemann, B. Löchel, L. K. Jian, D. Schondelmaier
Cost Effective Masks for Deep X-ray Lithography
SPIE Microtechnologies for the New Millennium, **5116**, 775-781, (2003)
- R.H. Schill, D. Hasselkamp, S. Kammer, S. Mickat, B. Zimmermann, K.-H. Schartner, A. Ehresmann, H. Schmoranzer, B. M. Lagutin, V. L. Sukhorukov
Partial wave analysis of the photon induced Kr 3d95/2 -> Kr+ 4p4(1D)5p2F7/2 decay by orientation and alignment transfer
J. Phys. B: At.Mol.Opt.Phys., **36**, L57-61, (2003)
- G. Schmahl, D. Rudolph, B. Niemann, P. Guttman, J. Thieme, U. Wiesemann, G. Schneider, T. Eimüller, P. Fischer, G. Schütz
X-ray microscopy at BESSY
Synchrotron Radiation News, **16/3**, 3-10, (2003)
- D. Schmeißer, K. Pressel, Y. Yamamoto, B. Tillack, D. Krüger
Ge instabilities near interfaces in Si-SiGe-Si heterostructures
Materials Science & Engineering B, **B101**, 208, (2003)
- D. Schmeißer, H.-J. Müssig
The Pr2O3 / Si(001) interface studied by synchrotron radiation photo-electron spectroscopy
Solid State Electronics, **47**, 1607, (2003)
- E. Schmid, M. Krumrey, G. Ulm, H. Roos, D. Regulla
The maximum low-dose RBE of 17.4 and 40 keV monochromatic x rays for the induction of dicentric chromosomes in human peripheral lymphocytes
Radiat. Res., **160**, 499-504, (2003)
- D. Schmitz, J. Hauschild, P. Imperia, Y.T. Liu, H. Maletta
Element-specific investigation of the magnetization of ultrathin Fe on a V(110) single crystal
Journal of Magnetism and Magnetic Materials, **269/1**, 89-94, (2003)
- G. Schneider, M.-A. Meyer, E. Zschech, G. Denbeaux, U. Neuhäusler, P. Guttman
In situ X-ray microscopy studies of electromigration in copper interconnects
D.G. Seiler et al. (Eds.): Characterization and Metrology for ULSI Technology: 2003 International Conference, **CP683**, 480-484, (2003)
- G. Schneider, E. Anderson, B. Bates, F. Salmassi, P. Nachimuthu, A. Pearson, D. Hambach, N. Hoffmann, W. Hasse, K. Hoffmann
Electromigration in Integrated Circuit Interconnects studied by X-ray Microscopy
Nucl. Instr. Meth. B, **199**, 469 - 474, (2003)
- G. Schneider
X-ray microscopy: methods and perspectives
Anal. Bioanal. Chem., **376**, 558 - 561, (2003)

- F. Scholze, R. Klein, and T. Bock
Irradiation stability of silicon photodiodes for extreme-ultraviolet radiation
Appl. Opt., **42**, 5621-5626, (2003)
- F. Scholze, J. Tümmeler, E. Gullikson, A. Aquila
Comparison of extreme ultraviolet reflectance measurements
J. Microlith., Microfab., Microsyst., **2**, 233-235, (2003)
- F. Scholze, J. Tümmeler and G. Ulm
High-accuracy radiometry in the EUV range at the PTB soft x-ray beamline
Metrologia, **40**, 224-228, (2003)
- F. Scholze, F. Scholz, J. Tümmeler, G. Ulm, H. Legall, P.V. Nickles, W. Sandner, H. Stiel, L. van Loyen
Characterization of a laser produced plasma source for a laboratory EUV reflectometer
Proc. SPIE, **5037**, 670-681, (2003)
- S. Schrader
Elektronische Struktur und Anregungsprozesse organischer Halbleiter, Habilitation
Uni Potsdam, (2003)
- B. Schreder, C. Dem, M. Schmitt, A. Materny, W. Kiefer, U. Winkler, and E. Umbach
Raman Spectroscopy of II-VI Semiconductor Nanostructures: CdS Quantum Dots
J. Raman Spectrosc, **34**, 100-103, (2003)
- H. Schröter
Optische Eigenschaften von YHx zwischen 1 eV und 10 eV, Diploma
TU Braunschweig, (2003)
- J. Schulz, Ph. Wernet, M. Martins, B. Sonntag, R. Müller, K. Godehusen, P. Zimmermann
Linear dichroism of the 4f photoemission in the giant resonance of atomic Europium
Phys. Rev. A, **67**, 12502, (2003)
- M. Schürmann, S. Dreiner, U. Berges and C. Westphal
Sb/Si(110)-2x3 - A photoelectron diffraction study
Appl. Surf. Sci., **212**, 131, (2003)
- M.C. Schürmann, T. Missalla, K.R. Mann, S. Kranzusch, R.M. Klein, F. Scholze, G. Ulm, R. Lebert, L. Juschkina
Metrology tools for EUVL-source characterization and optimization
Proc. SPIE, **5037**, 378-388, (2003)
- F. Schäfers, S. Yulin, T. Feigl, N. Kaiser
At-wavelength Metrology on Sc-based Multilayers for the VUV and Water Window
Advanced Metrology: Advanced Characterization, Techniques for Optics, Semiconductors, and Nanotechnologies, SPIE-Proc., **5188**, 17, (2003)
- A. Schöll, Y. Zou, T. Schmidt, R. Fink, and E. Umbach
Energy Calibration and Intensity Normalization in High-Resolution NEXAFS Spectroscopy
J. Electron Spectrosc, **129**, 1, (2003)
- A. Schöll
High-resolution investigation of the electronic structure of organic thin films, Dissertation
Universität Würzburg, (2003)
- H. Schöppe
Untersuchung der Temperaturabhängigkeit optischer Eigenschaften von CaF₂ im Spektralbereich von Vakuum-UV-Strahlung, Diploma
TFH Wildau, (2003)

- M. Sczegan, W. Rettig and A.I. Tolmachev
Spectral and Photophysical Characteristics of Unsymmetric Polymethine Dyes as Model Compounds for the Colour Shift of Visual Pigments
 Photochem. Photobiol Sciences, **2**, 1264-1271, (2003)
- S. Shaikhutdinov, M. Heemeier, J. Hoffmann, I. Meusel, B. Richter, M. Bäumer, H. Kuhlenbeck, J. Libuda, H.-J. Freund, R. Oldman, S. D. Jackson, C. Konvicka, M. Schmid, P. Varga
Interaction of oxygen with Pd deposited on a thin alumina film
 Surf. Sci., **501**, 270, (2002)
- A. Shaporenko, K. Adlkofer, L. S. O. Johansson, M. Tanaka, M. Zharnikov
Functionalization of GaAs surfaces with aromatic self-assembled monolayers: a synchrotron-based spectroscopic study
 Langmuir, **19**, 4992-4998, (2003)
- A. M. Shikin, S. A. Gorovikov, V. K. Adamchuk, W. Gudat, O. Rader
Electronic structure of carbon nanostripes
 Phys. Rev. Lett., **90**, 256803, (2003)
- N. Sieber, Th. Seyller, L. Ley, D. James, J.D. Riley, et al.
Synchrotron x-ray photoelectron spectroscopy study of hydrogen-terminated 6H-SiC{0001} surfaces
 Phys Rev B, **67**, 205304, (2003)
- R. Stoian
The Thermal Stability of WO₃ Thin Films, Diploma
 BTU Cottbus, (2003)
- C. Strelt, G. Pepponi, P. Wobrauschek, B. Beckhoff, G. Ulm, S. Pahlke, L. Fabry, Th. Ehmann, B. Kanngießer, W. Malzer and W. Jark
Analysis of low Z elements on Si wafer surfaces with undulator radiation induced total reflection X-ray fluorescence at the PTB beamline at BESSY II
 Spectrochimica Acta Part B: Atomic Spectroscopy, **58**, 2113-2121, (2003)
- D.S. Su, H.W. Zandbergen, P.C. Tiemeijer, G. Kothleithner, M. Hävecker, C. Hebert, A. Knop-Gericke, B. H. Freitag, F. Hofer, R. Schlögl
High Resolution EELS Using Monochromator and High Performance Spectrometer: Comparison of V₂O₅ ELNES with NEXAFS and Band Structure Calculations
 Micron, **34**, 235-238, (2003)
- B. Tepper, B. Richter, A.-C. Dupuis, H. Kuhlenbeck, C. Hucho, P. Schilbe, M. A. bin Yarmo, H.-J. Freund
Adsorption of molecular and atomic hydrogen on vacuum cleaved V₂O₅(001)
 Surf. Sci., **496**, 64, (2002)
- W. Theis, E. Rotenberg, K. Franke, K. Horn
Electronic structure in quasicrystals and approximants
 "Quasicrystals, Structure and Physical Properties", ed. H.-R. Trebin, Wiley-VCH, 615, (2003)
- J. Thieme, G. Schneider, C. Knöchel
X-ray tomography of a microhabitat of bacteria and other soil colloids with sub-100 nm resolution
 Micron, **34**, 339 - 344, (2003)
- J. Thompson, R.I.R. Blyth, V. Arima, Y. Zou, R. Fink, E. Umbach, G. Gigli, and R. Cingolani
4f Energies in an Organic-Rare Earth Guest-Host System: The Rare Earth Tris-8-hydroxyquinolines
 Mat. Sci. Eng. B, **40**, 105, (2003)
- R. L. Toomes, J. -H. Kang, D. P. Woodruff, M. Polcik, M. Kittel and J. T. Hoefl,
Can glycine form homochiral structural domains on low-index copper surfaces?
 Surface Science, **522**, L9-L14, (2003)
- J. Tümmler, H. Blume, G. Brandt, J. Eden, B. Meyer, H. Scherr, F. Scholz, F. Scholze, G. Ulm
Characterization of the PTB EUV reflectometry facility for large EUVL optical components
 Proc. SPIE, **5037**, 265-273, (2003)

- G. Tzvetkov, Y. Zubavichus, G. Koller, Th. Schmidt, C. Heske, E., Umbach, M.Grunze, M. G. Ramsey and F. P. Netzer
Growth of H₂O Layers on an Ultra-Thin Al₂O₃ Film: from Monomeric Species to Ice
 Surf. Sci., **543**, 131-140, (2003)
- G. Ulm
Radiometry with synchrotron radiation
 Metrologia, **40**, 101-106, (2003)
- L. van Loyen, T. Böttger, S. Braun, H. Mai, A. Leson, F. Scholze, J. Tümmeler, G. Ulm, H. Legall, P.V. Nickles, W. Sandner, H. Stiel, C. Rempel, M. Schulze, J. Brutscher, F. Macco, S. Müllender
A new laboratory EUV reflectometer for large optics using a laser plasma source
 Proc. SPIE, **5038**, 12, (2003)
- J. Vogel, W. Kuch, M. Bonfim, J. Camarero, Y. Pennec, F. Offi, K. Fukumoto, J. Kirschner, A. Fontaine, S. Pizzini
Time-resolved magnetic domain imaging by x-ray photoemission electron microscopy
 Appl. Phys. Lett., **82**, 2299-2301, (2003)
- O. Vormoor
Techniques for characterization of fractal clusters using X-ray microscopy
 J. Phys. IV, **104**, 513-516, (2003)
- R.L. Weber
Photoelectron Spectroscopy of Liquid Water and Aqueous Solutions in Free Microjets Using Synchrotron Radiation,
 Dissertation
 FU Berlin, (2003)
- L. Weinhardt, Th. Gleim, O. Fuchs, C. Heske, E. Umbach, M. Bär, H.-J. Muffler, Ch.-H. Fischer, M.C. Lux-Steiner, Y. Zubavichus, T.P. Niesen, and F. Karg
CdS- and Cd(OH)₂-formation during Cd-treatments of Cu(In,Ga)(S,Se)₂ thin film solar cell absorbers
 Appl. Phys. Lett., **82**, 571, (2003)
- H. Wende, A. Scherz, F. Wilhelm and K. Baberschke
Induced magnetism at thin-film interfaces probed by x-ray magnetic circular dichroism
 J. Phys.: Condens. Matter, **15**, 547, (2003)
- H. Wende, Ch. Litwinski, A. Scherz, T. Gleitsmann, Z. Li, C. Sorg, K. Baberschke, A. Ankudinov, J.J. Rehr and Ch. Jung
A systematic study of embedded atom EXAFS: The (2x1)O/Cu(110) reconstruction as an ideal prototype system
 J. Phys.: Condens. Matter, **15**, 5197, (2003)
- L. Werner
Untersuchungen der Autoionisation und Dissoziation der O₂(c⁴||Sigma_u⁻) ns/nd ||sigma_g(||nu = 0,1)-Rydbergzustände nach Anregung mit monochromatisierter Synchrotronstrahlung, Diploma
 Universität Kaiserslautern, (2003)
- C. Westphal
Buried Interfaces Studied by photoelectron diffraction
 Appl. Phys. A, **76**, 721, (2003)
- C. Westphal
The Study of the Local Atomic Structure at and below Surfaces by Means of X-ray Photoelectron Diffraction
 Surf. Sci. Rep., **50**, 1, (2003)
- W. Widdra, D. Bröcker, T. Gießel, I.V. Hertel, W. Krüger, A. Liero, F. Noack, V. Petrov, D. Pop, P.M. Schmidt, R. Weber, I. Will, B. Winter
Time-resolved core level photoemission:surface photovoltage dynamics of the SiO₂/Si(100)interface
 Surface Science, **548**, 87-94, (2003)
- U. Wiesemann, J. Thieme, P. Guttmann, R. Früke, S. Rehbein, B. Niemann, D. Rudolph, G. Schmahl
First results of the new scanning transmission X-ray microscope at BESSY II
 J. Phys. IV, **104**, 95-98, (2003)

- U. Wiesemann
The scanning transmission X-ray microscope at BESSY II, Dissertation
 Universität Göttingen, (2003)
- P. Wiethoff, B. Kassühlke, D. Menzel, P. Feulner
Biexcitons in solid neon
 Fizika Nizkikh Temperatur, **29**, 351-355, (2003)
- T. Wolff
Untersuchungen von Photoionisationsprozessen an atomarem Eisen und molekularem Eisenchlorid im Bereich der 2p-Anregung mittels Synchrotronstrahlung, Diploma
 TU Berlin, (2003)
- Q. Wu
Interkalationsreaktionen von Oxiden, Dissertation
 Technische Universität Darmstadt, (2003)
- S. Yulin, F. Schäfers, T. Feigl, N. Kaiser
Enhanced reflectivity and stability of Sc/Si multilayers
 Advances in Mirror Technology for X-Ray, EUVL, Laser and Other Applications, SPIE-Proc., **5193**, 20, (2003)
- S. Yulin, F. Schäfers, T. Feigl, N. Kaiser
High performance Cr/Sc multilayers for the soft X-ray range
 Advances in Mirror Technology for X-Ray, EUVL, Laser and Other Applications, SPIE-Proc., **5193**, 23, (2003)
- D.R.T Zahn, T.U. Kampen, H. Mendez
Transport Gap of Organic Semiconductor in Organic Modified Schottky Contacts
 Appl. Surf. Sci., **212-213**, 423, (2003)
- M. Zharnikov, A. Küller, A. Shaporenko, E. Schmidt, and W. Eck
Aromatic self-assembled monolayers on hydrogenated silicon
 Langmuir, **19**, 4682-4687, (2003)
- J.F. Zhu, M. Kinne, T. Fuhrmann, B. Tränkenschuh, R. Denecke, H.-P. Steinrück
The adsorption of NO on an oxygen pre-covered Pt(111) surface: in-situ high-resolution XPS combined with molecular beam studies
 Surface Science, **547**, 410-420, (2003)
- J.F. Zhu, M. Kinne, T. Fuhrmann, R. Denecke, H.-P. Steinrück
In-situ high resolution XPS studies on adsorption of NO on Pt(111) surfaces
 Surface Science, **529**, 384, (2003)
- B. Zimmermann
Dynamische Prozesse bei der Photoneninduzierten Ne⁺-Satellitenproduktion: Direkte Besetzung und Autoionisation doppelt angeregter Zustände, Dissertation
 Uni Giessen, (2003)
- Y. Zou
Electronic properties of organic molecular thin films in condensed and interfacial states with metal substrates,
 Dissertation
 Universität Würzburg, (2003)
- Y. Zubavichus, M. Zharnikov, A. Shaporenko, M. Grunze
NEXAFS study of glycine and glycine-based oligopeptides
 J. Electron Spectrosc. Relat. Phenom., **134**, 25-33, (2003)

Keyword Index

(click on page number to open selected page)

(2x1)O/Cu(110) reconstruction	180	binary alloy	397
(GaMn)As	417	block copolymer	85
10m-NIM	517	blowing agent	443
2PPE	228	branching ratio	148, 188
3,6,9-trioxa-decylamine	463	bulk properties	498
3D micro XANES	495	C60	59, 91
3D micro XRF	495	calibration	21
3d-metal-atoms	52	carbon nanotubes	238
3p edges	163	carbonaceous chondritic meteorites	300
6T	145	catalysis	249, 254, 277
A 3B5 semiconductors	94	catalyst	403
absorption	190, 240, 316, 338	cathode	196
acrolein	257	CD3Br	48
adsorption	265, 267, 269, 290	Cd3I	48
Al	428	CdTe	369
amino acids	288	CH2DI	48
ammonia oxidation	274	CH3Br	48, 50
analysis of the phase compositions	283	CH3I	48, 50
angle-resolved	445	charge transfer	226
angle-resolved fragmentation	78	charge transfer fluorescence	44
angle-resolved photoelectron spectroscopy	57	chemical etching	369
angular distribution	52	chemisorption	111, 252
anisotropy	153, 188, 377, 512	chiral surfaces	280
anisotropy of embedded atom potential	180	chirality	67
antiferromagnetic	386	chlorine	286
archaeometry	371, 544	chromium dioxide	139
ARUPS	145	circular dichroism	476, 67
atomic EXAFS	180	circular polarization	231
atoms	64, 78	CIS	413, 504
auger decay	231	clusters	73, 76, 78, 88
autoionization	231, 64	CO	269
AZM	35, 38, 41	cobalt	186, 286
B acteriorhodopsin	512	cobaltites	105
band gap	97	coherence	440, 493, 509, 57
battery	196	coherent X-ray	319
Bayes-Turchin approach	335	colossal magneto resistance	161
beam collimation	5	complexes with cations	463
beta-parameter	52	computed tomography	403
		confinement	240
		cooper minimum	224
		core level	434
		core level excitation	76

core-hole-clock	226	excited-state nonradiative decays	46
correlated electrons	214		
covalent bonding	158	F ar FTIR spectroscopy	463
creep-deformation	294	far-infrared	374
crystal growth	312	Fe on V(110)	150
crystals	466, 523	Fe/NiO	386
Cu ₃ Au	425	femtosecond	226
CuInS ₂	413, 504	fermi level	178
cuprates	134	ferromagnetic	386
CVD	394	ferromagnetic semiconductors	417
D efects	105	films	124, 312
delocalization	57	fine structure	316
depth profiling	356, 445	finite-size effect	392
depth resolved analysis	495	fluorescence	240, 64
detectors	21, 28, 374	fluorescence spectroscopy	466
dichalcogenides of transition metal	338	focus	534
dielectric function	377	FptA membrane protein crystal	455
different atmospheres	283	fragmentation	59
diffractometry	383	fresnel lens	523
diffusion	397	FTIR spectroscopy	463
diffusion barrier	445	fullerene	59, 91
dissociation	267	G aAs	312
DNA bases	209	galvanik	38
donor	374	GaN	349
doping	238, 349, 431	Gd	231, 88
drawings	544	germanium	374
dry etching	286	GISAXS	380
E lectronic configurations	105	glasses	347
electronic structure	105, 116, 118, 142, 158, 161, 190, 204, 218, 300, 498	glycine	288
electrophilic oxygen	262	gold	544
elemental mapping	473	gossypol	463
ellipsometry	209, 377, 512	gossypol schiffbases	463
energie-dispersive	319	grain boundaries	399
energy resolution	5	graphene	118
epitaxial growth	383	graphite	118
epitaxial layer	292	green alga	473
epitaxy	312	growth kinetics	410
ethylene epoxidation on silver	262	H ard X-Rays	498
EUV	11, 14, 17, 25, 28, 8	Heusler alloys	124, 360
EXAFS	349, 538	high kinetic energies	498
exchange bias	364, 367	high Resolution	48
exchange coupling	386	high resolving power	517
		HMF	130, 136, 139
		hole-distribution	134

holography	440	localization	57
hydrogen	236	low-alpha	329, 520
hydrogenation	257	luminescence	240
I ce	288	MAD	468
image reconstruction	440	magnesium alloy	403
imaging	501	magnetic domain imaging	307
imaging ESCA	399, 401	magnetic domains	307, 401
imaging spectroscopy	399, 401	magnetic interlayer coupling	307
impurity	374	magnetic materials	292
in situ diffraction	443	magnetic multilayers	307, 314
in situ spectroscopy	254	magnetic scattering	360, 367
in situ TEY cell	283	magnetisation	150
in situ XAS	257	magnetism	163, 171, 175, 73, 80, 88
in situ XPS	257, 262, 271	magnetite	130, 136, 188
In ₂ O ₃	178	magnetization dynamics	329
InAs/GaAs	94	magneto-optical Kerr-effect	163
infrared	501	magneto-optics	221
infrared spectroscopy	512	maleic anhydride	271
InN	377	manganese complex	470
inner-shell excitation	78	manganese deposits	473
insertion devices	525	materials characterisation	403
interface properties	211	metal coated	326
interface sharpening	397	metallic foams	324, 326, 443
interfaces	178, 236, 364	methane	267
interlayer exchange coupling	175	methanol steam reforming	254
invar alloys	434	Mg	211
ion bombardment	364	Micro-CT	321
ion sputtering	94	micro-focus	473
ion tracks	380	micro-magnetic structure	329
iron gall ink corrosion	371	micro-XANES	371
isotope	57	micro-XRF	371, 448
K err spectra	221	microscopy	440
Kr	52, 64	Mn	52
L -edges EXAFS	335	MnAs	312
LAO	468	Moessbauer spectra	183
laser	228	molecular magnets	204
lateral quantization	142	molecular orientation	436
lattice distortion	294	molecules	78
layer thickness	23	moment analysis	188
lensless imaging	440	morphology	190
LiCoO ₂	196	MOSFET	236
light elements	148	multilayer	490, 506
lithography	305, 41	multiplet splitting	434
		MXCD	124

N -butane	271	phase retrieval	440
N ₂	54	phase transitions	292, 389
NaCl	214	photoabsorption	48
nanocrystal	240	photodiodes	21
nanoESCA	399, 401	photodissociation	54
nanoparticles	80, 83, 97, 240	photoelectron emission microscopy	307
nanostripes	118	photoelectron spectroscopy	94, 247, 434
nanostructures	85, 88, 142, 351	photoelectrons	52
nanostructures of magnetic oxide	183	photoemission	97, 116, 118, 142, 145, 238, 358, 498
nanowires	452	photoionization	57, 59, 67, 83
NDE	403	photoionization cross section	224
near-edge spectra	83	photosynthesis	470
near-field	501	photovoltage	358
neon-autoionisation	517	piezo-motor	517
NEXAFS	91, 97, 206, 211, 277, 288, 297, 303, 347, 394, 428	PIX	224
nickel compounds	158	plasma polymers	297
nitric oxide	265	platinum	280
NOK	530	polarimeter	221
NOM	530, 534	polarised radiation	316
		polarization	78
O FET	436	polyimide	512
one axis crystals	316	pore formation	324
optical components	530	Pr	408
optical conductivity	155	propane	206
optical pumped laser	310	protein	476
optoelectronic	240	protein crystallography	456
orbital moments	148, 188	protein dynamics	466
organic electronics	428	PrOx	415
organic materials	436	PSD	419
organic thin films	145	Pt(533)	274
orientation	190	PTCDA	211
oxidation	236	pump-probe	228
oxide	445	pump-probe experiments	166
oxygen	186, 265, 280	PVBDOs	196
oxynitride	356	PVD evaporated iron	410
		Q uantum	240
P -wave	153	quantum dots	94
palladium	394	quantum stripes	116
partial wave analysis	64	quantum well states	116
particle traps	83	quantum wells	247
PEEM	329, 369, 413, 504	quasi-periodic undulator	517
pentacene	190		
PES	186, 356	R ab protein	467
PGM	254	radiation damage	419

radiation induced modification	91	spectral shifts	76
radiometry	8, 11, 14, 17, 21, 25, 28	spectroscopy	240, 476
rare earth	80, 171	spin moments	148
rare-earth pnictides	129	spin polarization	231
reaction	290	spin-ladders	134
reduction of CuO	283	spin-polarized states	338
reflection	316	stepped surface	116
reflectometry	8, 11, 14, 19, 23, 25	steps	269
refraction index	493	STM	142
resonance photoemission	91	stress	349
resonances	64	strongly correlated systems	99, 102
resonant inelastic x-ray scattering	161	structural biology	456
resonant magnetic scattering	314	structural forces	303
resonant photoemission	196	structural genomics	456
resonant soft X-ray emission spectra	218	suboxide	236
resonant X-ray raman spectroscopy	389	sum rules	148, 188
RIXS	193, 438	superalloys	294
Rydberg states	54	superconducting tunnel junction (STJ)	5
Röntgenmasken	35	superconductivity	99, 102, 153
SAMs	419	surface	73, 186, 214, 380, 431
SCLS	431	surface magnetism	153
segregation	445	surface photovoltage	166
selective bond breaking	419	surface science	252
self-assembled monolayers	303, 305	surface structure	111, 252
semiconductor	290, 431	symmetries	145
sexiphenyl	428	synchrotron	228
sexithiophene	145	synchrotron radiation	448
SHIM	380, 383	T-PEEM	506
Si	166, 186, 240, 351	temperature effects	419
SiC	236, 408	temperature-dependent interlayer exchange coupling	171
SiGe crystals	448	temperature-programmed XPS	267
silicate	408	terahertz	374
silicate formation	415	texture	383
silicide formation	415	thermal oxidation	410
silicon dioxide	236	thin film solar cells	369
silicon monoxide	438	thin films	186
silver	257	thin magnetic films	364
small angle scattering	440	thin metal films	247
soft X-ray scattering	392	thin-film magnetism	392
soft X-rays	171, 440	THz	501, 520
solar cells	358	TiO ₂	428
speckle	319	TMO	136
		tomography	324, 326

toroidal electron analyzer	425, 515	XMCD	88, 124, 148, 150, 153, 175, 188, 401, 417
transition metal oxides	161	XMLD	364, 401
transmission photoelectron microscopy	506	XMLDAD	401
		XPEEM	85
UE52	534	XPS	206, 211, 254, 274, 277, 399, 401, 419, 445
ultrathin films	175		
ultrathin oxide scales	410	XRF analysis	544
umklapp	118	XRF mapping	347
UN	155	XRMS	80
UPtGe	155		
		ZnO	193, 277
V2O3	206	ZnPc	178
V2O5	206		
valence band	434		
vanadium oxides	389		
vicinal surface	116		
VPO	271		
VUV	19, 48		
VUV-ellipsometry	155		
Waste management	347		
water	206, 288		
wet chemical synthesis	97		
white beam	310, 493		
X-ray absorption	129, 193, 249		
X-ray absorption spectra	158, 183		
X-ray diffraction	310		
X-ray emission	193		
X-ray fluorescence (XRF) analysis	5		
X-ray interferometer	493		
X-ray magnetic circular dichroism	129		
X-ray magneto-optical Kerr effect	171		
X-ray optics	490		
X-ray photoelectron spectroscopy	265, 267, 269		
X-ray scattering	345		
X-ray spectra	105		
X-ray waveguide	509		
X-rays	316		
XANES	193, 470, 538		
XAS	190, 419		

Authors Index

(click on page number to open selected page)

A braham, J.	238	Bodenthin, Y.	354, 362
Abramsohn, D.	221, 316, 364	Bolse, W.	380
Abrosimov, N.V.	448	Bontempi, E.	80
Adamchuk, V.K.	118	Borisenko, S.V.	99, 102
Aggour, M.	351	Bradeanu, I.L.	76, 78
Albrecht, D.	274	Brandt, G.	25
Aliev, I.	118	Braun, W.	211, 312, 452
Ambacher, O.	377	Braune, M.	57
Ando, Y.	102	Bressler, P.	244, 498
André, J.-M.	316, 490	Broekman, L.	425, 515
Andrews, S.	440	Bron, M.	257
Ankudinov, A.	180	Brunnbauer, M.	303
Assmann, W.	383	Brunner, K.	417
		Bryzgalov, V.V.	91, 94
B aberschke, K.	175, 180	Brzezinski, B.	463
Bahrdt, J.	525	Bröcker, D.	166
Balzer, A.	517	Buchholz, C.	8, 11
Banhart, J.	324, 326, 443	Bukhtiyarov, V.I.	262
Bansmann, J.	73, 163	Bulusheva, L.G.	300
Barkow, U.	155	Bulut, F.	73
Barra, M.	470	Bunkóczy, G.	479
Barth, A.	41	Burkov, Y.	85, 413, 504
Barth, J.V.	342	Buturovich, D.V.	121
Bartl, F.	463	Büchner, B.	134
Bartley, J.K.	271	Bütow, A.	326
Batchelor, D.R.	498	Bär, M.	405
Bauchspieß, K.R.	288, 436		
Baumgärtel, H.	48, 50	C alligaro, T.	544
Baumgärtel, P.	476	Carbone, M.	290
Bavdaz, M.	31	Carsteanu, A.-M.	155
Bechstein, S.	5	Casaletto, M.P.	290
Becker, U.	57, 59, 70, 83	Casper, F.	124
Beckhoff, B.	5, 31	Casu, M.B.	288, 436
Bednarzik, M.	35, 38	Cava, R.J.	153
Beke, D.L.	397	Célia, H.	455
Berger, A.	544	Chassé, T.	198, 201
Berger, H.	99, 102, 244	Chelaru, L.I.	307
Bergmann, A.	314, 360	Cimalla, V.	377
Berkebile, S.	428	Claus, P.	257
Bernien, M.	175	Cobessi, D.	455
Bischoff, L.	493	Cobet, C.	155, 377, 422
Biswas, I.	201	Cox, P.	351
Bluhm, H.	249, 254, 257, 262, 271, 274	Crainic, T.	204

Cuesta-Seijo, J.A.	483	Fedoseenko, S.I.	183
Cvejanovic, S.	57	Feikes, J.	520, 525
D anel, A.	46	Felsch, W.	129
Danzenbächer, S.	91, 233	Felser, C.	124
Darowski, N.	292, 294, 345, 380, 383, 443	Fernandez-Madrigal, F.J.	196
Dau, H.	470, 473	Feulner, P.	419
Dedkov, Yu.S.	130, 136, 139, 218, 233	Fieber-Erdman, M.	456
Deisenhofer, J.	153	Filatova, E.O.	316, 490
Delaunay, R.	389	Fink, J.	99, 102
Denecke, R.	265, 267, 269	Fink, R.	97
Dikov, Yu.P.	300	Finkenzeller, I.U.	485
Dil, J.H.	247, 290	Firsov, A.	35, 38, 523
Dini, D.	201	Fischer, A.	11, 25
Dmitriev, A.	342	Fischer, Ch.-H.	405
Drago, M.	422	Flammini, R.	290
Duval, A.	544	Flesch, R.	76, 78
Dwelk, H.	168, 173	Fliegauf, R.	5
Dürr, H.A.	417	Foerster, R.	456
Däweritz, L.	292, 312	Follath, R.	102, 244, 517
Döbrich, K.	171	Fonin, M.	130, 136, 139, 218
E bbinghaus, S.G.	153	Forster, F.	399, 401
Eberhardt, W.	240, 338, 417, 440	Fraser, G.	31
Eberle, K.	419	Frentrup, W.	525
Ehlers, A.	364	Freund, H.-J	206
Ehresmann, A.	54, 64, 364, 517	Frey, S.	305
Ehters, M.	456	Friedrich, M.	209
Eisebitt, S.	240, 338, 389, 438, 440	Fuchs, O.	405
El-Gezawy, H.	46	Fuess, H.	438
Elmers, H.J.	124	Fuhrmann, T.	265, 267, 269
Emmerich, A.	476	Fuhse, C.	509
Emtsev, K.V.	236, 425	Fukumoto, K.	307
Engel, D.	364	Funnemann, D.	399, 401
Ensling, D.	196	Föhlisch, A.	226, 228
Erdelyi, Z.	397	G alakhov, V.R.	105, 161
Erko, A.I.	332, 347, 371, 448, 470, 473	Gall, N.R.	186
Escher, M.	399, 401	Galyametdinov, Yu.G.	332
Esser, N.	377, 422, 452, 512	Gassenbauer, Y.	178
Evtikhiev, V.P.	94	Gaupp, A.	221, 525
F arges, F.	538	Gavrishkov, V.A.	168
Faubel, M.	126	Gavrila, G.	211
Faust, A.	468	Gebhardt, R.K.	73
Fauth, K.	129	Gensch, M.	512
Fecher, G.H.	124	Gerlach, J.	383
		Gerlich, D.	83
		Getzlaff, M.	73

Geue, Th.	354, 362	Harwardt, M.	321
Gießel, T.	166	Hasselkamp, D.	64
Girol, S. Gil	277	Heigl, F.	231
Glaser, L.	88	Heine, A.	461
Glatzel, P.	249	Heinemann, U.	456
Gleitsmann, T.	175, 180	Heiner, C.	145
Gloskovskii, A.	124	Heinzmann, U.	231, 506
Godehusen, K.	52, 59, 62, 534	Heister, K.	305
Goebbels, J.	324, 326, 403	Heitmann, J.	240
Goering, E.	148, 153, 188	Held, G.	280
Gokhale, S.	247	Helwig, H.-M.	326
Gold, S.	153, 188	Hennies, F.	226, 228
Golden, M.S.	102, 244	Hentges, R.	57, 70
Goldhahn, R.	377	Hentschel, M.P.	321
Gomoyunova, M.V.	186	Herein, D.	283
Goncalves, E.	351	Hergenhahn, U.	67
Gordan, O. D.	209	Herrmann, C.	292
Gordeev, Yu.S.	91, 94	Hertel, I.V.	126, 145, 166
Gorgoi, M.	211	Heske, C.	97, 288, 405, 436
Gottwald, A.	17, 19	Hess, C.	134
Grabis, J.	314, 360, 367	Heßler, M.	129
Grabolle, M.	470	Himcinschi, C.	209
Graf, C.	83	Hinrichs, K.	512
Graupner, R.	236, 238	Hirsch, A.	238
Grenzer, J.	310, 319, 345, 354, 362, 493	Hoeft, J.T.	111, 252, 260
Grimm, A.	405	Hoffmann, M.	21, 23
Grimm, M.	83	Hoffmann, P.	356, 369, 504
Groot, F. de	249	Hofmann, K.P.	463
Großhans, I.	383	Hohl, A.	438
Grunze, M.	303, 305	Holldack, K.	374, 501, 520
Gudat, W.	116, 118, 142, 221, 364, 405	Holub-Krappe, E.	73
Guentherodt, G.	218	Horn, K.	247, 290
Guerra, M.-F.	544	Huang, Y.	244
Guimond, S.	206	Huber, S.	467
Gusel'nikov, A.V.	300	Hunger, R.	196, 358
Günther, S.	274	Hutchings, G.J.	271
Güntherodt, G.	130, 136, 139	Huwald, E.	515
Görner, W.	544	Hübers, H.-W.	374, 501
		Hänel, K.	541
Haase, W.	332	Hänsel, Th.	534
Hague, C.F.	389	Hävecker, M.	249, 254, 257, 262, 271, 274
Hahn, O.	371		
Haibel, A.	324, 326	Illerhaus, B.	403
Haija, M. Abu	206	Imbühl, R.	274
Hanack, M.	201	Imperia, P.	150, 417
Harding, C. J.	67		

J aeckel, B.	369	Kleimenov, E.Yu.	139, 249
Jaegermann, W.	196, 369	Klein, A.	178, 358
Jakob, G.	124	Klein, R.	28
Jakubowicz, J.	351	Kleineberg, U.	506
James, D.	236	Klink, B.	466
Janowitz, C.	168, 173	Klumpp, S.	54, 64, 517
Jarre, A.	509	Kniep, B.L.	254
Jenichen, B.	292, 312	Knop-Gericke, A.	249, 254, 257, 262, 271, 274
Jian, L.	35, 38	Knupfer, M.	99, 102, 134, 190, 201
Jiang, Y.H.	70	Knyazev, A.A.	332
Jochims, H.W.	48, 50	Koch-Müller, M.	547
Jones, L.B.	280	Koitzsch, A.	99, 102
Jonnard, Ph.	490	Kolbe, M.	31
Joshi, S.	97	Koller, G.	288, 428
Journel, L.	389	Komninou, Ph.	347
Jung, C.	405	Koops, W.	102
Jung, Ch.	180	Kordyuk, A.A.	99, 102
Jungblut, H.	351	Korica, S.	57, 59
		Korte, E.H.	512
K abachnik, N.	231	Korte, L.	178
Kaganer, V.M.	292, 312	Kotsugi, M.	307
Kaindl, G.	70, 171, 392	Kraft, D.	369
Kammer, S.	54, 64	Krapf, A.	168, 173
Kampen, T.U.	209, 211	Krasnikov, S.A.	139, 158, 218
Kanis, M.	351	Krasyuk, A.	329
Kanngießler, B.	371, 495	Krenek, R.	85
Karakostas, Th.	347	Kronast, F.	417
Karg, F.	405	Kropf, H.	326
Katsikini, M.	347, 349	Kroth, U.	19
Kavouras, P.	347	Krumrey, M.	21, 23, 31
Keimer, B.	102	Krupin, O.	171
Kellerman, D.G.	105	Krömker, B.	399, 401
Kerherve, G.	214	Kuch, W.	307
Kern, K.	342	Kuepper, K.	105, 161, 204
Khalil, T.	231	Kuhlenbeck, H.	206
Kim, J.W.	247, 290	Kuksov, A.	329
Kim, T.K.	99, 102, 134	Kulkarni, S.K.	97
Kinne, M.	265, 267	Kumpf, C.	97
Kirchner, A.	233	Kurth, D. G.	354, 362
Kirschner, J.	214, 307	Kuske, P.	374, 501, 520
Kis-Varga, M.	397	Kuzmin, M.V.	121
Kisker, E.	386	Köhlich, H.	35, 38, 41
Kittel, M.	111, 252, 260	König, C.	139
Klaumünzer, S.	345, 380, 383	Kötschau, I.	405
Klebe, G.	461		
Kleibert, A.	73, 163		
Kleimenov, E.	254, 257, 271, 274		

L agutin, B.M.	64	M aier, T.	487
Lammert, H.	530, 534	Maletta, H.	73, 150, 335
Lamont, C.L.A.	111, 252	Malzer, W.	371, 495
Lange, A.	321	Manjasetty, B.A.	456
Langer, B.	83	Mans, A.	244
Langer, G.A.	397	Mantler, M.	31
Lapouyade, R.	44	Manzke, R.	168, 173
Laubis, C.	25	Marburger, S.	67
Laubschat, C.	218	Mariot, J.M.	389
Lauermann, I.	405	Martins, M.	52, 62, 88
Leckey, R.	236, 425, 515	Marutzy, M.	155
Lehner, A.	419	Mast, M.	59
Leitenberger, W.	319, 410, 493	Matijasevic, B.	443
Lengefeld, J.	476	Matsyuk, S.	547
Letz, M.	19	Matthes, F.	108, 130
Leuenberger, F.	129	Meiwes-Broer, K.H.	73
Lewerenz, H.J.	351	Menzel, D.	155, 419
Ley, L.	236, 238, 515	Merchel, S.	544
Leyh, B.	48, 50	Merkel, M.	399, 401
Li, Z.	175, 180	Mertig, M.	233
Lider, V.V.	332	Mertin, M.	498
Liebisch, P.	470, 473	Mertins, H.-Ch.	163, 221, 316, 364
Lin, C.T.	102	Methling, R.P.	73
Lin, N.	342	Meyer, C.	80
Lingenfelder, M.	342	Mick, U.	386
Lippitz, A.	297	Mickat, S.	54, 64
Lischke, T.	83	Mikhlin, Yu.	113
Litwinski, Ch.	175, 180	Mikoushkin, V.M.	91, 94
Liu, X.	190	Mitdank, R.	173
Locht, R.	48, 50	Mittsev, M.A.	121
Loidl, A.	153	Molenkamp, L.	417
Lomova, N.V.	434	Molodtsov, S.L.	91, 94, 105, 136, 139, 158, 183, 186, 218, 233, 300, 431, 434
Lopez-Sanchez, J.A.	271	Molter, H.	517
Lorenz, M.	193	Morales, F.	249
Lu, H.	377	Morawetz, K.	319
Lucht, S.	54	Mueller, U.	456
Lupina, G.	408, 415	Muessig, H.J.	408
Lux-Steiner, M.C.	405	Mukowskii, Ya.M.	161
Lußky, T.	178	Murali, S.	44
Lüdge, K.	452	Murin, I.V.	183
Lüning, J.	440	Murrell, C.	351
Löchel, B.	35, 38, 41	Müller, B.R.	321
Lörger, M.	440	Müller, C.	470, 473
		Müller, I.	481
		Müller, K.	413

Müller, N.	231	Ovchinnikov, S.G.	168
Müller, P.	21, 23	Ovechkina, N.A.	105
Müller, R.	17, 28	Owens, A.	31
Müssig, H.-J.	415		
Möhwald, H.	319, 354, 362	P aloura, E.C.	347, 349
		Panchuk, V.V.	183
N agasono, M.	226	Panzner, T.	319, 493, 509
Nagel, M.	198	Papp, C.	267, 269
Nagel, P.	134	Parge, A.	129
Navratil, A.	155	Park, W.G.	386
Naymushina, E.A.	434	Partzsch, G.M.	538
Neculai, A.M.	485	Pascal, M.	111, 252
Neculai, D.	485	Passmann, R.	512
Nefedov, A.	314, 360, 367	Pattus, F.	455
Nekat, B.	371	Paulus, H.	380
Nepijko, S.A.	124, 329	Pavlov, S.G.	374
Nesterov, M.A.	139	Pavlychev, A.A.	76, 78
Netzer, F.P.	288	Peacock, A.	31
Neudachina, V.S.	431	Peisert, H.	198, 201
Neumann, M.	105, 161, 204	Pestryakov, A.	254, 257, 271
Ney, V.	286	Petrov, I.D.	64
Nickel, A.	534	Pettenkofer, C.	196
Niedermayer, T.	419	Piancastelli, M.N.	290
Niefind, K.	468	Pietsch, U.	310, 319, 345, 354, 362, 493, 509
Niesen, T.P.	405		
Niklewski, A.	394	Pietzsch, A.	226, 228
Nikolaeva, E.V.	158	Pinakidou, F.	347, 349
Nisbet, G.	252	Plieth, Ch.	473
Nizovskii, A.I.	262	Ploog, K.H.	292, 312
Njeh, A.	438	Plöger, S.	11, 25, 28
Noll, T.	530	Pohl, M.	231, 506
Novikova, N.N.	332	Poiguine, M.V.	70, 434
Nowak, G.	367	Pokrant, S.	80
Nücker, N.	134	Polcik, M.	111, 231, 236, 252, 260
		Pompe, W.	233
O elsner, A.	329	Popov, D.	118
Offi, F.	307	Postnikov, A.V.	338
Okotrub, A.V.	300	Powis, I.	67
Olligs, D.	190	Poygin, M.	300
Ono, S.	102	Pratt, S.J.	280
Oppeneer, P.M.	221	Preobrajenski, A.B.	139, 158, 218
Oran, U.	297	Prieto, J.E.	171
Ortega, L.	80	Procop, M.	14
Oswald, S.	445	Pronin, I.I.	186
Osyannikov, R.	417	Pruemper, G.	57, 59
Ott, H.	392	Przybylski, P.	463

Pucher, A.	493	Saalfrank, R.W.	204
Pucher, K.	153	Sacchi, M.	389
Pullan, D.	31	Salditt, T.	509
Püttner, R.	70	Salvan, G.	209
		Santoso, I.	244
R ack, A.	324, 326	Satapathy, D.K.	312
Rader, O.	116, 118, 142, 231	Sauerborn, M.	476
Radnik, J.	283	Sawicki, M.	417
Radtke, M.	283, 495, 544	Sayago, D.I.	111, 252, 260
Radu, F.	314, 367	Schade, U.	374, 463, 501, 512
Rahne, K.	405	Schaff, W.J.	377
Rakel, M.	422	Schartner, K.-H.	54, 64
Ramirez, E.G.	193	Schattat, B.	380
Ramsey, M.G.	288, 428	Scheer, M.	525
Rehr, J.J.	180	Scheibe, A.	274
Reichardt, G.	54, 476, 517	Scheidig, A.J.	466, 467
Reichardt, J.	405	Scherz, A.	175, 180
Reiche, I.	495, 544	Scheunemann, H.-U.	35, 38, 41
Reiche, R.	445	Scheurer, A.	204
Reif, M.	88	Schierle, E.	80, 392
Reinert, F.	399, 401	Schill, R.	54
Reinkoester, A.	57, 59	Schill, R.H.	64
Ressler, T.	254	Schindler, A.	534
Rettig, W.	44, 46	Schlegel, Th.	530, 534
Reuter, K.	461	Schlemmer, S.	83
Richter, M.	17, 19	Schlögl, R.	254, 257, 262, 271
Richter, T.	52, 62	Schmeißer, D.	85, 224, 356, 369, 408, 413, 415, 504
Richter, W.	377, 422, 452	Schmich, E.	419
Riesemeier, H.	283, 324, 326, 403, 544	Schmidt, H.	193
Riley, J.	236, 425, 515	Schmidt, M.	178
Robinson, J.	111, 252	Schmidt, P.M.	126
Rodriguez, A. Fuentes	495	Schmidt, S.	399, 401
Rolles, D.	57	Schmidt, T.	97
Rossner, H.	335	Schmidt, Th.	190, 436
Rost, J.M.	70	Schmidting, T.	422
Roth, M.	544	Schmitz, D.	73, 150, 335, 417
Rudolph, I.	38	Schmoranzner, H.	54, 64, 364, 517
Rueff, J.P.	389	Schneider, C.M.	108, 130, 329
Rüdiger, U.	130, 136, 139	Schneider, M.	168, 173, 283
Rügamer, S.	97	Schneider, R.	419
Rühl, E.	76, 78, 83	Schoenes, J.	155
Rüthers, E.	351	Schoeppe, H.	19
Rüttinger, S.	175	Scholz, F.	11, 25
Röseler, A.	512	Scholze, F.	8, 11, 14, 25, 28, 31
		Schomburg, D.	468
		Schondelmaier, D.	35, 38

Schott, G.	417	Stamm, M.	85
Schröter, H.	155	Starke, K.	171, 434
Schuler, B.	476	Steinhauer, B.	257
Schulmeyer, T.	358	Steinrück, H.-P.	265, 267, 269
Schultz-Heienbrok, R.	487	Stepanow, S.	342
Schulze, D.	193, 198	Stepina, N.D.	332
Schulze, R.-D.	297	Storch, G.	405
Schumacher, G.	294, 383, 443	Strunskus, Th.	277, 342, 394, 541
Schuppler, S.	134	Sträter, N.	487
Schwarz, U.	28	Stöhr, J.	440
Schwarzkopf, O.	59	Sukhorukov, V.L.	64
Schwentner, N.	286	Suzuki, Yu J.	209
Schwieger, T.	190, 201	Swaraj, S.	297
Schütz, G.	129, 153, 188	Szargan, R.	158, 193, 198, 204, 218
Schäfers, F.	498		
Schöll, A.	436	T adich, A.	236, 425, 515
Schönhense, G.	124, 329	Taeger, S.	369
Schöpke, A.	178	Tai, Y.	419
Seckler, R.	476	Takács, A.	161, 204
Seidel, U.	168	Tallarida, M.	247, 290
Semenov, V.G.	183	Taracheva, E.Yu.	316
Senf, F.	530, 534	Tavaddod, S.	244
Sepiol, B.	397	Tepper, B.	211
Seyller, Th.	236, 238, 425, 515	Terborg, R.	252, 260
Sgraja, T.	461	Terfort, A.	303
Shabanova, I.N.	434	Teschner, D.	254, 257, 271
Shamin, S.N.	105	Thißen, A.	196, 369
Shaporenko, A.	303	Tikhonov, E.V.	431
Shcolnic, A.S.	94	Timergaleev, N.Z.	173
Sheldrick, G.M.	479, 483, 485	Titov, A.N.	338
Shikin, A.M.	116, 118	Tokarev, I.	85
Shnitov, V.V.	91, 94	Tomashevich, Ye.	113
Shtanov, V.I.	431	Tong, L.N.	108, 130
Sidorenko, A.	85	Tonnerre, J.M.	80
Sieber, N.	236	Toomes, R.L.	111, 252, 260
Siewert, F.	530, 534	Trampert, A.	312
Silaghi, S.D.	209	Troc, R.	155
Sladeczek, M.	397	Tränkenschuh, B.	265, 267, 269
Smirnov, V.M.	183	Turnbull, A.	456
Sokoll, S.	405	Tzvetkov, G.	288, 428
Sorg, C.	175, 180		
Sorokin, A.A.	17	U lm, G.	5, 21, 23, 25, 28, 31
Sperlich, M.	130, 139	Ulman, A.	305
Spiegel, M.	410	Umbach, E.	97, 288, 436
Splettstosser, R.	456	Unger, R.-St.	168, 173
Stadler, L.-M.	397	Unger, W.	297

Uphues, T.	231	Wolk, Th.	403
Usón, I.	481	Woodruff, D.P.	111, 252, 260
Ustinov, V.M.	94	Wurmehl, S.	124
V alencia, S.	163, 221	Wurth, W.	88, 226, 228
Varykhalov, A.	116, 121, 142	Wüstefeld, G.	374, 501, 520
Venceleova, A.	238	Wöll, Ch.	277, 342, 394, 541
Vértesy, L.	479	Y armoshenko, Yu. M.	338
Viefhaus, J.	57, 59, 70	Yashina, L.V.	431
Vijayalakshmi, S.	226, 228	Z abel, H.	314, 360, 367
Vinogradov, A.S.	139, 158, 183, 218	Zacharias, M.	240
Visbeck, S.	405	Zahn, D.R.T.	209, 211
Vogel, D.	410	Zeimer, U.	310
Vogt, P.	452	Zemtsova, E.G.	183
Voigt, F.	495	Zeschke, Th.	530, 534
Vollenhoven, J. van	244	Zhang, F.	67
Vollmer, A.	417	Zhang, L.	113, 198, 201
Vyalikh, D.V.	91, 94, 105, 113, 136, 139, 158, 183, 186, 218, 233	Zharnikov, M.	303, 305, 419
W agner, H.	11, 25	Zheludeva, S.I.	332
Walter, M.	476	Zhu, J.F.	265, 267, 269
Wanderka, N.	294	Zhukov, A.E.	94
Weber, A.	461	Zier, M.	445
Weber, N.	399, 401	Zimina, A.	240, 338, 438
Weber, R.	126	Zimmermann, B.	64
Weber, S.	155	Zimmermann, P.	52, 62
Weckhuysen, B.	249	Zizak, I.	292, 294, 380, 383, 397, 443
Weidemann, G.	324, 326, 403		
Weinhardt, L.	405		
Wende, H.	175, 180		
Wendrock, H.	493		
Werner, L.	54, 64		
Wernet, Ph.	52		
Weschke, E.	80, 392		
Weser, J.	5		
Westerholt, K.	360		
Wett, D.	193, 204		
Wichert, I.	35, 38		
Widdra, W.	83, 126, 145, 166		
Wieder, T.	438		
Wilde, L.	283		
Wilke, M.	371, 538		
Winkler, C.	214		
Winter, B.	126, 145		
Wirth, R.	547		
Witte, G.	394, 541		